AD-A273 665

12th International Corrosion Congress

PROCEEDINGS

September 19-24, 1993

VOLUME 4

Houston, Texas USA

OIL/GAS/PIPELINE

NACE
International

CORROSION CONTROL FOR LOW-COST RELIABILITY

12th International Corrosion Congress

PRECEEDINGS

VOLUME 4

OIL/GAS/PIPELINE

Accesion For

NTIS CRA&I		☑
DTIC TAB		
U..a ..o.....		
Ju.til c...un		

By Vol. 4 - 85. ⁰⁰

D. ... Set ³400

Dist Special

A-1 | 2-)

NACE
International

DTIC QUALITY INSPECTED 3

PREECEEDINGS CONTENTS

NON-METALLIC COATINGS ON STEEL SUBSTRATES

VOLUME 2

ATMOSPHERIC CORROSION

VOLUME 3A

CORROSION: MATERIALS PERFORMANCE

CORROSION: MODES AND BEHAVIOR

PASSIVITY AND BREAKDOWN

VOLUME 4

CATHODIC PROTECTION

HYDROGEN EFFECTS

OIL AND GAS PRODUCTION AND REFINING WORKSHOP

VOLUME 5A

AIRCRAFT

SURFACE ANALYSIS TECHNIQUES

NUCLEAR ENERGY AND WASTE STORAGE

WATER

VOLUME 6

ELECTRIC POWER INDUSTRY WORKSHOP

STRAY CURRENT INTERACTION IN THE SYSTEM OF TWO EXTENSIVE UNDERGROUND CONDUCTORS

Wojciech Machczyński
Technical University of Poznań
ul. Piotrowo 3 a
60 - 965 Poznań, Poland

Abstract

The important problem, technically, is to evaluate the harmful effects that an electrified railway has on nearby earth-return circuits (cables, pipelines).
This paper considers the effects of a DC - electrified railway system on two extensive metal conductors buried in parallel in the vicinity of the tracks. The interaction between currents flowing in both underground conductors is taken into account, whereas the reaction of the conductors' currents on the track current is disregarded. The analysis given is applicable to any DC railway system in which tracks may be represented by a single earth return circuit with current energisation. It is assumed in the paper that the system considered is linear and that the earth is homogeneous. The technical application of the method is illustrated by an example of computer simulation.

Key terms : interference, stray currents, earth return circuit, electric traction, computer simulation.

Introduction

There are many practical cases where one is interested in the stray current influence on underground metal structures. The important problem, technically, is to evaluate harmful effects (corrosion) that electric traction may have on nearby installations and to design a protection system. This is a complex task involving many technical and economic aspects for consideration. The computer simulation of stray currents effects can be useful tool in this case.

The calculations given in the paper are based on the general solution, which has been obtained in [1] for currents in two earth return-circuits exposed to alternating current electric railways. By specialising the driving electric field, calculation are made and formulas obtained, applicable to the analysis of currents and potentials along two underground leaky conductors laid in a stray current area.

The electric flow field caused in the earth by stray currents is determined under the assumption that the system of rails of a DC electrified railway system is modelled by sections of equivalent earth return circuits lying on the surface of the homogeneous soil. It is also assumed in the paper that the system considered is linear and that the effects of currents in the underground installations on the track current can be disregarded.

The knowledge of the potential of the underground metallic conductors caused by stray currents may be used as one of the criterions participating in the decisions of planning of routes of underground structures in the stray current

areas.

The literature on the problem of calculating potentials of metal underground structures located in an electric flow field does not deal with the polarisation, treating that phenomenon as insignificant when compared with the ohm drop of potential [4]. Because of the above and also because of the lack of analytic methods of calculating the polarisation potential of underground metal structures being affected by external currents the considerations presented in the following sections of the paper deal mainly with the ohm drop of potential.

Scalar potential in the earth due to current in conductor with earth return

The basic circuit for the calculation of the earth potential is shown in Fig.1.

The potential due to the segment $d\tau$ with the current $I(\tau)$ takes the form

$$dV^{o}(P) = \frac{- \dfrac{dI(\tau)}{d\tau}}{4\pi\kappa \sqrt{(x-\tau)^{2}+y^{2}}} \, d\tau \quad . \tag{1}$$

The distribution of the longitudinal current depends on the mode of the current excitation in the conductor. In the stray current theory the current (shunt) energisation [2] of the conductor with earth return lying on the surface of the earth, Fig.2, is of great importance.

If the conductor with the shunt energisation at point $x = x_{s}$ is finite in the length, the current along the conductor is given by

$$I(x) = \text{sign} \, (x - x_{s}) \, \frac{I_{s}}{2} \, e^{-\alpha_{0}|x-x_{s}|} + A \, e^{-\alpha_{0}x} + B \, e^{\alpha_{0}x} \tag{2}$$

where α_{o} is the propagation coefficient of the conductor, A and B are constants, which are to determined from the boundary conditions.

The insertion of eqn.(2) into eqn.(1) and integrating gives the relation of the potential in the earth owing to the current flowing in the conductor with the current energisation. This relationship is numerically solved only. Efficient techniques of calculation have been applied in the computation algorithm developed.

Model of an electrified railway system

The system shown in Fig.2 may be used to the modelling of the DC electric railway system for the case of concentrated load, as in Fig.3.
In this system tracks are represented by a single conductor – equivalent to a

rail continuously in contact with the earth through the track ballast. The conductor is energised with the currents I_s and $-I_s$ by a feeder station and a load at points $x = 0$ and $x = a$, respectively.

It should be noted that the basic model may be applied directly by superposition if there are a number of loads to be considered. The computation of the earth potential near an electrified railway system of a complicated configuration is also possible by the use of the elementary model.

Currents in the system of two underground conductors

The elimination of the potentials in equations for potentials and currents along two underground conductors gives a non-homogeneous 2-nd order system of differential equations

$$\frac{1}{G_1} \frac{d^2 I_1(x)}{dx^2} - R_1 I_1(x) + \frac{1}{G_{12}} \frac{d^2 I_2(x)}{dx^2} = - E_1^0(x) \quad ,$$

$$\frac{1}{G_{12}} \frac{d^2 I_1(x)}{dx^2} + \frac{1}{G_2} \frac{d^2 I_2(x)}{dx^2} - R_2 I_2(x) = - E_2^0(x) \quad ,$$

(3)

where $E_n^0(x)$ is the intensity of a primary, driving electric field, R_n – series resistance, G_n – shunt conductance of the conductor n ($n = 1$, 2) and G_{12} – mutual conductance between conductors [5].

It is easy to solve this system of equations using the Fourier integral if the conductors are assumed to be infinitely long. It is shown in [1] that if the electric field within the underground conductor n results in a scalar potential V_n^0, the currents along both conductors become

$$I_1^\infty(x) = \frac{\alpha_{02}^2 \, G_1}{2(1-\lambda)(\alpha_1^2-\alpha_2^2)} \left\{ (1- \frac{\alpha_2^2}{\alpha_{02}^2}) \int_{-\infty}^\infty \text{sign}(x-v) \, V_1^0(v) \, e^{-\alpha_2|x-v|} \, dv + \right.$$

$$-(1- \frac{\alpha_1^2}{\alpha_0^2}) \int_{-\infty}^\infty \text{sign}(x-v) \, V_1^0(v) \, e^{-\alpha_1|x-v|} \, dv + \frac{G_2 \, \alpha_2^2}{G_{12}\alpha_{02}^2} \int_{-\infty}^\infty \text{sign}(x-v) \, V_2^0(v) \, e^{-\alpha_2|x-v|} \, dv$$

$$\left. - \frac{G_2 \, \alpha_1^2}{G_{12}\alpha_{02}^2} \int_{-\infty}^\infty \text{sign}(x-v) \, V_2^0(v) \, e^{-\alpha_1|x-v|} \, dv \right\} \quad , \tag{4}$$

$$I_2^\infty(x) = \frac{\alpha_{01}^2 \, G_2}{2(1-\lambda)(\alpha_1^2-\alpha_2^2)}\left\{(1-\frac{\alpha_2^2}{\alpha_{01}^2}) \int_{-\infty}^{\infty} \text{sign}(x-v) \, V_2^O(v) \, e^{-\alpha_2|x-v|} \, dv + \right.$$

$$- (1-\frac{\alpha_1^2}{\alpha_0^2})\int_{-\infty}^{\infty} \text{sign}(x-v) \, V_2^O(v) \, e^{-\alpha_1|x-v|} \, dv + \frac{G_1 \, \alpha_2^2}{G_{12}\alpha_{01}^2} \int_{-\infty}^{\infty}\text{sign}(x-v) \, V_1^O(v) \, e^{-\alpha_2|x-v|} \, dv$$

$$\left. - \frac{G_1 \, \alpha_1^2}{G_{12}\alpha_{01}^2} \int_{-\infty}^{\infty}\text{sign}(x-v) \, V_2^O(v) \, e^{-\alpha_1|x-v|} \, dv \right\}$$

where :

$$\left.\begin{matrix}\alpha_1^2\\[10pt]\alpha_2^2\end{matrix}\right\} = \frac{\alpha_{01}^2+\alpha_{02}^2 \pm \sqrt{(\alpha_{01}^2+\alpha_{02}^2)^2-4(1-\lambda)\alpha_{01}^2\alpha_{02}^2}}{2(1-\lambda)} \quad , \tag{5}$$

where α_{on} is the propagation coefficient of the conductor n. The conductive coupling coefficient λ, appearing in the equations, which is the measure of the interaction between the conductors is defined as

$$\lambda = \frac{G_1 G_2}{G_{12}^2} \quad . \tag{6}$$

The integrating of eqn.(4) yields

$$I_n^\infty(x) = \frac{I_s \alpha_o^2 G_n}{2\pi\kappa(1-\lambda)(\alpha_1^2-\alpha_2^2)}\left[A_{n1}\Psi(\alpha_o x,\alpha_o s_1) + A_{n2}\Psi(\alpha_o x,\alpha_o s_2) + A_{n3}\Psi(\alpha_1 x,\alpha_1 s_1) + \right.$$

$$\left. + A_{n4}\Psi(\alpha_1 x,\alpha_1 s_2) + A_{n5}\Psi(\alpha_2 x,\alpha_2 s_1) + A_{n6}\Psi(\alpha_2 x,\alpha_2 s_2)\right], \quad n = 1,2 \tag{7}$$

where

$$A_{11}= \frac{(\alpha_1^2-\alpha_2^2)(\alpha_{02}^2-\alpha_0^2)}{(\alpha_1^2-\alpha_0^2)(\alpha_2^2-\alpha_0^2)} \; ; \quad A_{12}= \frac{G_2(\alpha_1^2-\alpha_2^2)\alpha_0^2}{G_{12}(\alpha_1^2-\alpha_0^2)(\alpha_2^2-\alpha_0^2)} \; ; \quad A_{13}= \frac{(\alpha_{02}^2-\alpha_1^2)}{(\alpha_1^2-\alpha_0^2)} \; ;$$

$$A_{14}= \frac{G_2\alpha_1^2}{G_{12}(\alpha_1^2-\alpha_0^2)} \; ; \quad A_{15}= \frac{(\alpha_2^2-\alpha_{02}^2)}{(\alpha_2^2-\alpha_0^2)} \; ; \quad A_{16}= -\frac{G_2\,\alpha_2^2}{G_{12}(\alpha_2^2-\alpha_0^2)} \; ; \tag{8}$$

$$A_{21} = A_{12}\frac{G_1}{G_2} \;;\quad A_{22} = A_{11}\frac{(\alpha_{o1}^2 - \alpha_o^2)}{(\alpha_{o2}^2 - \alpha_o^2)} \;;\quad A_{23} = A_{14}\frac{G_1}{G_2} \;;\quad A_{24} = A_{13}\frac{(\alpha_{o1}^2 - \alpha_1^2)}{(\alpha_{o2}^2 - \alpha_1^2)} \;;$$

$$A_{25} = A_{16}\frac{G_1}{G_2} \;;\quad A_{26} = A_{15}\frac{(\alpha_2^2 - \alpha_{o1}^2)}{(\alpha_2^2 - \alpha_{o2}^2)} \;;$$

whereas

$$s_n = \sqrt{d_n^2 + a_n^2} \;;\quad n = 1, 2 \tag{9}$$

where :

d_n – burial depth of the conductor n , a_n – horizontal distance between the equivalent rail and the underground conductor n.

The voltage to the adjacent earth of the underground conductor n may be obtained from the relation [1]

$$U_n^\infty (x) = -\frac{1}{G_{in}}\frac{dI_n^\infty(x)}{dx} \;, \tag{10}$$

where G_{in} is the conductance of insulation of the conductor n.

Hence, the voltages to the adjacent earth of conductors 1 and 2, caused by the effects of the stray current flowing out of the equivalent rail shown in Fig.2, take the form

$$U_n^\infty(x) = \frac{I_s\alpha_o^2 G_n}{2\pi\kappa(1-\lambda)(\alpha_1^2 - \alpha_2^2)G_{in}}\Bigg[A_{n1}\alpha_o\Omega(\alpha_o x,\alpha_o s_1) + A_{n2}\alpha_o\Omega(\alpha_o x,\alpha_o s_2) +$$

$$+ A_{n3}\alpha_1\Omega(\alpha_1 x,\alpha_1 s_1) + A_{n4}\alpha_1\Omega(\alpha_1 x,\alpha_1 s_2) + A_{n5}\alpha_2\Omega(\alpha_2 x,\alpha_2 s_1) +$$

$$+ A_{n6}\alpha_2\Omega(\alpha_2 x,\alpha_2 s_2) - (A_{n1} + A_{n3} + A_{n5})\frac{1}{\sqrt{x^2 + s_1^2}} + \tag{11}$$

$$- (A_{n2} + A_{n4} + A_{n6})\frac{1}{\sqrt{x^2 + s_2^2}}\Bigg] \;,\quad n = 1, 2 \quad .$$

The functions Ω and Ψ appearing in the equations (7) and (11) are defined as follows [2,3] :

$$\left.\begin{array}{c}\Omega\,(u,v)\\[6pt]\Psi\,(u,v)\end{array}\right\} = \frac{1}{2}\left[e^{-u}\,\Phi(u,v) \pm e^{u}\,\Phi(-u,v)\right] \tag{12}$$

where

$$\Phi(u,v) = \int_{-u}^{\infty} \frac{e^{-\tau}}{\sqrt{\tau^2 + v^2}} \, d\tau \quad . \tag{13}$$

Voltages to the remote earth (potentials) along the conductors under considerations, may be obtained from the relations [1]

$$V_1(x) = V_1^0(x) + U_1(x) \frac{G_{11}}{G_1} + U_2(x) \frac{G_{12}}{G_{12}} \quad , \tag{14}$$

$$V_2(x) = V_2^0(x) + U_1(x) \frac{G_{11}}{G_{12}} + U_2(x) \frac{G_{12}}{G_2} \quad .$$

Conductors finite in the length

To solve the problem of the conductors finite in the length and terminated through the earthing electrodes at their end points, consider the homogeneous system of differential equations, which is obtained from the system (3) with $E_n^0 = 0$. The elimination of the current I_2 from these equations gives as the result the biquadratic equation (15) for the current I_1

$$\frac{1-\lambda}{G_1 \alpha_{02}^2} \frac{d^4 I_1(x)}{dx^4} - \frac{\alpha_{02}^2 + \alpha_{01}^2}{G_1 \alpha_{02}^2} \frac{d^2 I(x)}{dx^2} + \frac{G_2 R_1 R_2}{\alpha_{02}^2} I_1(x) = 0 \quad . \tag{15}$$

Thus the solution for the current I_1 has the form

$$I_1(x) = A_1 e^{r_1 x} + A_2 e^{r_2 x} + A_3 e^{r_3 x} + A_4 e^{r_4 x} \tag{16}$$

where $r_1 - r_4$ are the roots of the characteristic equation of the eqn.(15) and $A_1 - A_4$ are arbitrary constants. It is easy to show, that

$$r_1 = \alpha_1, \ r_2 = -\alpha_1 \ , \ r_3 = \alpha_2 \ , \ r_4 = -\alpha_2 \ . \tag{17}$$

The current $I_2(x)$ can be next obtained from the equation (18)

$$I_2(x) = (A_1 e^{\alpha_1 x} + A_2 e^{-\alpha_1 x})(C_1 \alpha_1^2 + C_2) + (A_3 e^{\alpha_2 x} + A_4 e^{-\alpha_2 x})(C_1 \alpha_2^2 + C_2) \tag{18}$$

and

$$C_1 = - \frac{G_{12}(1-\lambda)}{G_1 \alpha_{02}^2} \quad , \quad C_2 = \frac{R_1 G_{12}}{\alpha_{02}^2} \quad . \tag{19}$$

The complete solution of the non-homogeneous system of differential equations

(4), for the case of the conductors finite in the length, is assumed to have the following form

$$I_n^f(x) = I_n^\infty(x) + I_n(x) \qquad n = 1,2 \quad .\tag{20}$$

From the mathematical point of view I_n^∞ is the particular solution of the system (3) and I_n is the general solution of the homogeneous system of differential equations.

The potentials along the conductors are

$$V_1'^f(x) = -\frac{1}{G_1}\frac{dI_1^f(x)}{dx} - \frac{1}{G_{12}}\frac{dI_2^f(x)}{dx} \quad ,$$

$$\tag{21}$$

$$V_2'^f(x) = -\frac{1}{G_{12}}\frac{dI_1^f(x)}{dx} - \frac{1}{G_2}\frac{dI_2^f(x)}{dx} \quad .$$

The constants which appear in the solution can be obtained from the boundary conditions

$$Z_A = -\frac{V_1'^f(x_1)}{I_1^f(x_1)} \ , \quad Z_B = \frac{V_1'^f(x_2)}{I_1^f(x_2)} \ , \quad Z_C = -\frac{V_2'^f(x_3)}{I_2^f(x_3)} \ , \quad Z_D = \frac{V_2'^f(x_4)}{I_2^f(x_4)} \ . \tag{22}$$

The potentials to the adjacent earth (ohm drop of potential) can be next derived from the realtion

$$V_n^f(x) = -\frac{1}{G_{ln}}\frac{dI_n^f(x)}{dx} \ , \quad n = 1,2 \quad . \tag{23}$$

Computer results – example

The usefulness of the computation algorithm developed shall be demonstrated by the example of conductors buried in a stray current area, Fig.4.

The following conductors buried in the soil with the conductivity κ = 0.01 S/m have been considered :

(i)   conductor 1 – pipeline with parameters r_1= 0.3 m, d_1 = 1.4 m, R_1 =0.013 Ω/km, G_{11} = 1 S/km,

(ii)   conductor 2 – cable with parameters r_2 = 0.03 m, d_2 = 0.8 m, R_2= 0.737 Ω/km, G_{12} = 0.1 S/km.

The lengths of the pipeline and the cable are 5 km . The distance between the conductors is 5 m. The pipeline is terminated through the earth electrodes : $Z_A = Z_B$ = 1 Ω ($x_1 = x_3$ = – 2.5 km ; $x_2 = x_4$ = 2.5 km). The cable is earthed through the resistances Z_C = 1 Ω, Z_D = 4 Ω. The tracks of the DC electrified railway system have been approximated by an equivalent earth return circuit

with α_0 = 0.123 1/km. The current of the feeder station is I_s = 500 A.

The calculated maximum voltages between the conductors and the adjacent earth are shown in Fig.5. The voltages are ploted as functions of the horizontal distance between the conductors and the equivalent rail. The primary earth potential of the electric flow field is also shown in this Figure. The calculations have been carried out for the worst case, i.e. when the loads are far away from the feeder station.

Fig.5 shows that the voltages U between the conductors and the sorrounding soil exceed, even for the remote localisation of the conductors, the tolerable corrosion limit i.e. + 100 mV according to the German standard [4]. The protective measures should be undertaken to avoid the stray current corrosion of the conductors.

Final remarks

A computer program has been developed for the calculation of the potential distribution in a system of underground metal installations buried in a stray current area.

The computer simulation of the harmful effects that the DC electric traction may have on nearby underground structures may be useful in planning of localisation of the installations affected by stray currents and in designing the protective measures against the stray current corrosion as well.

The extensive parametric analysis to examine the roles of various factors which affect the interference levels caused in extensive metal underground conductors by stray currents may be performed using the method described.

References

[1]. W. Machczyński : Currents and potentials in earth-return circuits exposed to alternating current electric railways.IEE PROC., Vol. 129, Pt.B, No.5, September 1982, pp. 279-288

[2]. E.D. Sunde : Earth conduction effects in transmission systems. Dover Publications, Inc., New York, 1968

[3]. M. Krakowski : Earth return circuits (in polish). WNT, Warszawa, 1979

[4]. W. v. Baeckmann , W. Schwenk : Handbuch des kathodischen Korrosions-schutzes. Verlag Chemie, Weinheim, Deerfield Beach, Florida – Basel, 1980

[5]. W. Machczyński : Contribution to studies on problems resulting from the close proximity of cathodically protected structures to the unprotected ones. 9th International Congress on Metallic Corrosion, Toronto, June 3-7 1984, Vol.1, pp.274 -279
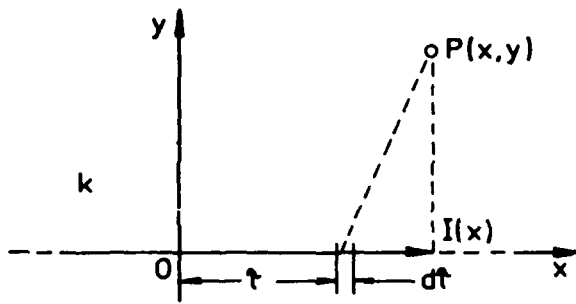
Fig.1. Conductor with longitudinal current flow in the infinite space with conductivity κ
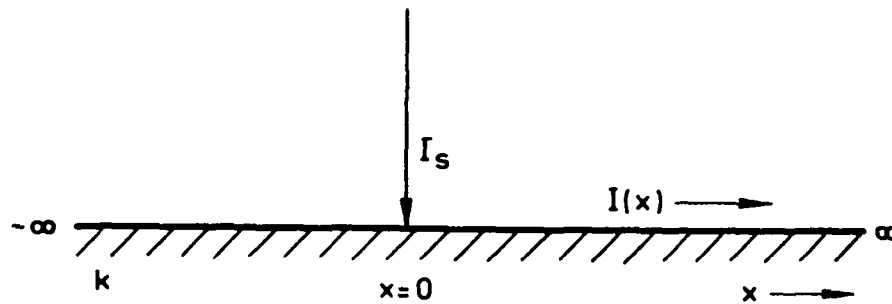
Fig.2. Current energisation of the conductor with earth return
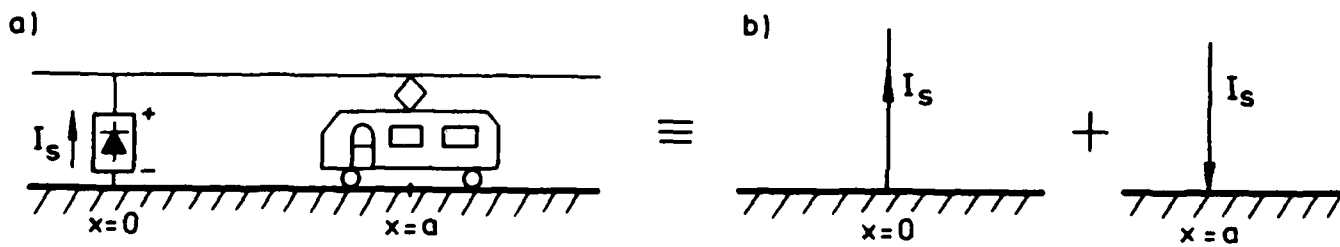
Fig.3. DC railway system and its equivalents
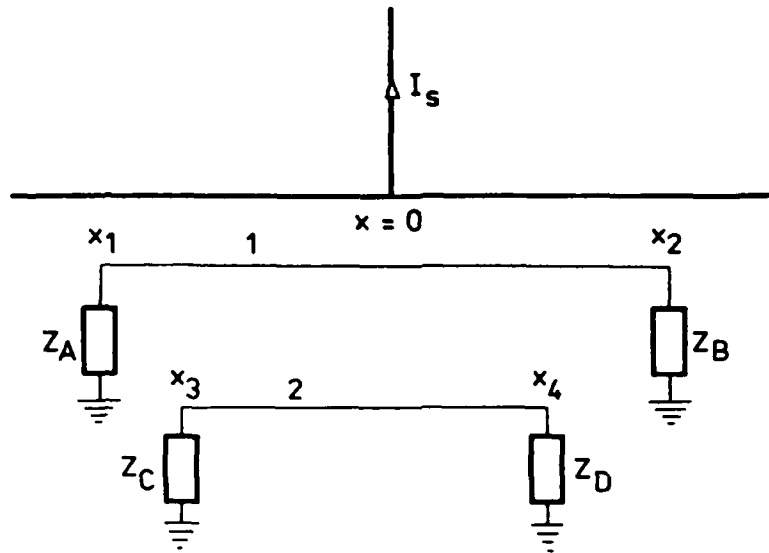
Fig.4. Two underground conductors in the vicinity of the DC railway system
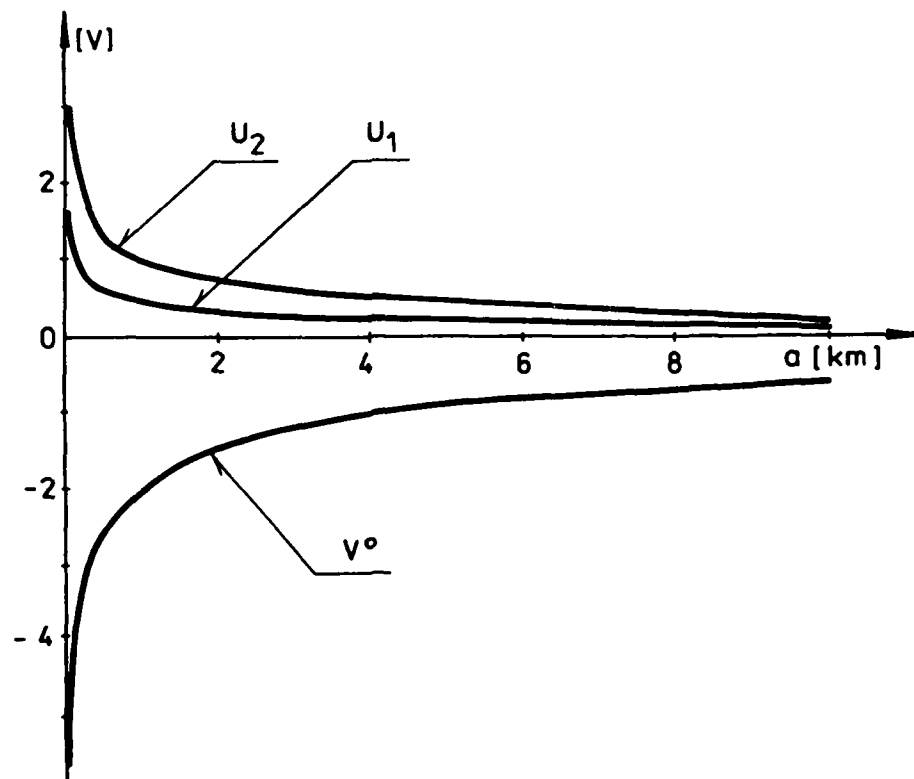
Fig.5. Maximal conductors' voltages U to the local earth vs distance a between the equivalent rail and the conductors

An Initial Investigation of Calcareous Deposits Upon Cathodically Polarized Steel in Brazilian Deep Water

Ruth de Oliveira Vianna
COMCORR - Consultoria em Materiais e Corrosão Ltda.
Rua Evaristo da Veiga, 55 - grupo 1409
20031-040 - Rio de Janeiro - RJ - Brazil

Gutemberg de Souza Pimenta
PETROBRÁS Research and Development Center
Cidade Universitária - Quadra 7
21949-900 - Rio de Janeiro - RJ - Brazil

Abstract

Field testing has been carried out on the Brazilian continental shelf at depths down to approximately 800 m, using mooring systems to evaluate corrosion and corrosion protection. Zinc anode/cathode assembles with different cathodic current densities were exposed for 14 months at depths of 300, 400, 500 and 770 m to establish preliminary design data for cathodic protection in deep waters. The paper presents measurements of the effects of depth, current density, and the physical and chemical parameters of seawater on the formation of calcareous deposits. This preliminary investigation was limited to quantitative results.

Key terms: calcareous deposits, polarized steel, deep water.

Introduction

Each year Brazilian offshore oil production moves into deeper and deeper waters. In the near future, discoveries of oil fields in very deep water will require the location of facilities at water depths of over 1,000 m. Consequently, the nature and characteristics of calcareous deposits formed under high hydrostatic pressure are of prime interest to the corrosion engineers responsible for protecting equipment.

Studies of the calcareous deposits formed during the cathodic protection of steel in seawater have focused on the effects of applied potential[1], current density[2,3,4], and water flow[1,5] on the properties of the deposits, but little information is available on the effects of depth. This parameter influences the formation of the calcareous deposit since it affects pH, dissolved oxygen, and temperature and, consequently, the solubility of the $CaCO_3$ and $Mg(OH)_2$ on the steel/seawater interface.

At present, the correct design of cathodic protection procedures based on the use of galvanic anodes is achieved by applying an initial high-density current to promote rapid cathodic polarization and the formation of calcareous deposits. Well-formed deposits reduce the velocity with which the oxygen dissolved in the seawater diffuses to the steel surface, thereby sharply reducing the current density needed to maintain polarization. A thorough understanding of the physical and chemical characteristics of seawater as a function of depth and

of the water's long-term effects on cathodic polarization is necessary to optimize design parameters in deep water cathodic protection. Since the values of these parameters vary not only with depth but also with geographic location and exposure time, long-term in-situ testing is necessary to establish the proper design criteria for deep water cathodic protection.

This paper examines the effects of depth, current density, and the physical and chemical parameters of seawater on the formation of calcareous deposits in Brazilian deep waters.

Experimental

A mooring system was installed in the Albacora Field of the Campos Basin (Rio de Janeiro) to carry out in-situ testing. Equipment design and operational details are presented in earlier papers[6,7].

Test specimens were placed at water depths of 300, 400, 500, and 770 m and were left exposed for about 14 months. Twelve anode/cathode assemblies were placed at each depth to evaluate cathodic protection. Two of every twelve assemblies were left unconnected and were assessed for corrosion at the end of the test period. Five initial current densities were specified for the other ten assemblies placed at each depth: 50, 100, 200, 300, and 400 mA/m^2. The cathodic protection system is presented and assessed in another paper[8].

Environmental Conditions

Although the vertical structure of the sea currents in the Campos Basin is quite complex, it is possible to identify some characteristics that appear to represent stationary or dynamic equilibrium conditions. The strongest currents are observed in the surface layer (0 to 100 m) and usually run toward the southern quadrant; their average flow varies from 0.15 to 0.70 m/s. The Brazilian current is located at a depth of around 100 to 300 m but may run the entire length of the water column (down to 700 to 800 m); it is usually observed flowing toward the southern quadrant as well, at an average rate varying from 0.05 to 0.32 m/s. The Brazilian countercurrent is generally observed below a depth of 300 m but at times may reach the surface. It flows toward the northern quadrant, varying from WNW to ENE, at average rates of 0.07 to 0.26 m/s (Fig. 1).

Environmental parameters pertinent to this study are shown in Figures 2 through 5.

Results

Following the exposure period, test specimens with an initial current density of 200, 300, or 400 mA/m^2 displayed protection[8]. Deposits removed from the samples were chemically analyzed. The atomic absorption spectrometry technique was used to measure Ca and Mg contents at the various current densities.

Figure 6 shows percentages of calcium as a function of the applied current density and of depth, while Figure 7 shows magnesium contents as a function of these same two parameters.

Figure 8 shows concentrations of Ca + Mg as a function of the current density initially applied, at different depths.

Discussion

The environmental parameters that affect the deposition and quantity of calcareous deposits and whose values vary with depth include sea currents, dissolved oxygen, temperature, salinity, and pH. It is of course very difficult to identify the effect of a single parameter since they are all interdependent.

In relation to the environmental conditions at the test location, the variations in oxygen content, salinity, and pH detected at these four depths were not significant enough to permit correlations with the quantify of calcareous deposits obtained. The parameters displaying greatest variations were temperature and sea currents.

As can be seen in Figure 6, Ca content generally increased with depth and more intensely so at greater initial current densities (i.e., 300 and 400 mA/m^2). At all depths, the concentration of Ca grew with current density. At all specified current densities, the highest Ca values were observed at 700 m. With a current density of 300 mA/m^2, a sharp elevation in Ca occurred at a depth of 770 m; with 400 mA/m^2, a sharp elevation was observed at all depths.

Variations in Mg content were not uniform as a function of either depth or current density (Fig. 7). The highest values were obtained with a current density of 200 mA/m2, at all depths. Of the current densities that resulted in protection, the lowest Mg contents were observed with 400 mA/m^2, again at all depths.

As to Ca + Mg content – a parameter used by Finnegan and Fisher[9], the effects were practically identical at depths of 300, 400, and 500 m with current densities of 200 and 300 mA/m^2. At 770 m there was a pronounced increase in the concentration of Ca + Mg, especially with current densities of 300 and 400 mA/m^2.

Figure 8 shows a significant increase in the Ca + Mg deposit at 400 mA/m^2, at all depths. This result confirms tests conducted by other researchers, who concluded that an initial current of over 350 mA/m^2 is needed to form a good calcareous layer and, further, that the quantity of calcareous deposits formed increases with increases in current density[2].

It has been found that the solubility of calcium carbonate increases as temperature drops, and the solubilities of calcite and aragonite increase with increases in water depth. In this study, however, calcium content generally increased with depth, thereby reinforcing Hartt's recommendation[10] that the role of the calcareous deposit in polarizing structures be assessed at each location.

The formation and growth of calcareous deposits depends heavily on the flow of sea currents[1]. While calcareous deposits may develop very slowly at locations where currents are strong, relatively thick deposits will form in calm waters[3]. The

present experiment observed the effect of water flow, associated with high current densities, on the formation of deposits. Indeed, the greatest concentrations of Ca + Mg were obtained at 700 m, where lowest flowrates are observed; even at lower current densities (i.e., 200 and 300 mA/m^2), Ca + Mg contents were also higher at 700 m than at other depths.

Temperature can have different effects on calcareous deposition and can influence diffusion, solubility, adsorption, or other parameters[11]. In the present study, however, water flow appeared to have the greatest effect.

Conclusions

Quantitative data on calcareous deposits were obtained at four depths and five initial current densities, following 14 months of field testing on the Brazilian continental shelf. Results indicate that:

1. Water flow had the greatest effect on the formation of calcareous deposits.

2. A high initial current density clearly favored the formation of a denser calcareous layer.

3. Concentrations of Ca generally increased with depth, which means that in-situ tests should be conducted to clarify questions concerning the formation of calcareous deposits in very deep waters.

4. The slower rate of flow observed at 770 m must have contributed to the formation of a denser layer of Ca + Mg, even at lower current densities (i.e., 200 and 300 mA/m^2).

References

1. WOLFSON, S. L. and HARTT, W. H. "An initial investigation of calcareous deposits upon cathodic steel surfaces in sea water". Corrosion, vol. 37 (2), pp. 70-76 (February 1981).

2. FISCHER, K. P. and FINNEGAN, J. E. "Cathodic polarization behaviour of steel in seawater and the protective properties of the calcareous deposits". Corrosion/89, Paper No. 582, NACE, Houston (1989).

3. FISCHER, K. P., SYDBERGER, T. and LYE, R. "Field testing of deep water cathodic protection on the Norwegian Continental Shelf". Materials Performance, vol. 27 (1), pp. 49-56 (1988).

4. EVANS, S. "Use of initial current density in cathodic protection design". Materials Performance, vol. 27 (2), pp. 9-11 (1988).

5. FISCHER, K. P. and SYDBERGER, T. "In-situ testing of cathodic protection on the northern Norwegian Continental Shelf". Corrosion/84, Paper No. 344, NACE, Houston (1984).

6. VIANNA, R. O. et al. "Mooring system for corrosion evaluation in deep water". 9th Symposium of Materials, Inspection and Corrosion Control (Proceedings). Rio de Janeiro (1987). In portuguese.

7. VIANNA, R. O. "Evaluation of cathodic protection in deep water". 1st Argentine-Brazilian Meeting of Corrosion and Corrosion Protection (Proceedings). Foz do Iguaçu (1989). In portuguese.

8. VIANNA, R. O. "In-situ testing of deep water cathodic protection on the Brazilian continental shelf". To be published.

9. FINNEGAN, J. E. and FISCHER, K. P. "Calcareous deposits: calcium and magnesium ion concentrations". Corrosion/89, Paper No. 581, NACE, Houston (1989).

10. HARTT, W. H., WANG, W. and CHEN, T. Y. "Critical questions pertaining to deep water cathodic protection". Corrosion/89, Paper No. 576, NACE, Houston (1989).

11. HARTT, W. H., CULBERSON, C. H. and SMITH, S. W. "Calcareous deposits on metal surfaces in sea water - a critical review". Corrosion/83, No. 59, NACE, Houston (1983).
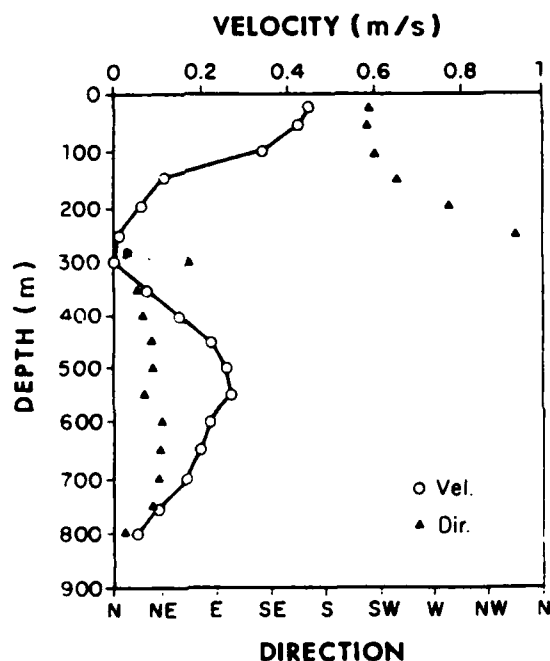
Fig. 1 - Seawater current profile in Campos Basin.
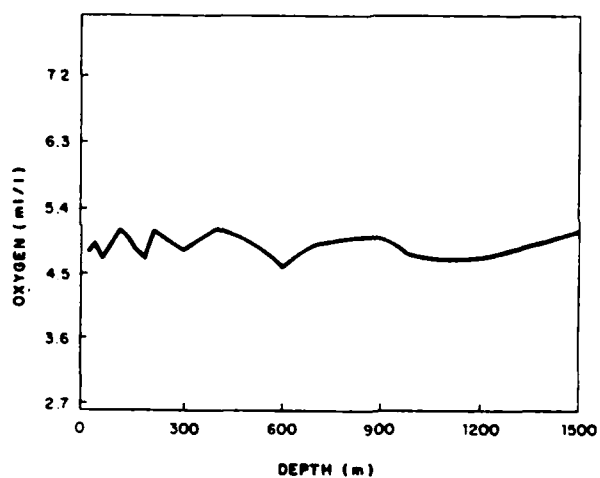
Fig. 2 - Oxigen concentration versus depth.
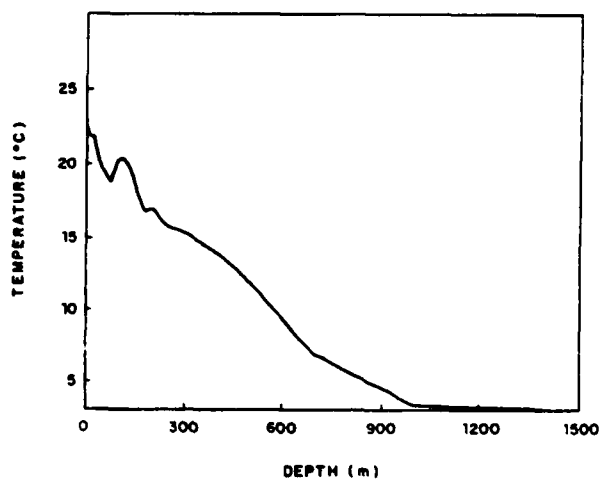
Fig. 3 – Variation of seawater temperature with depth.
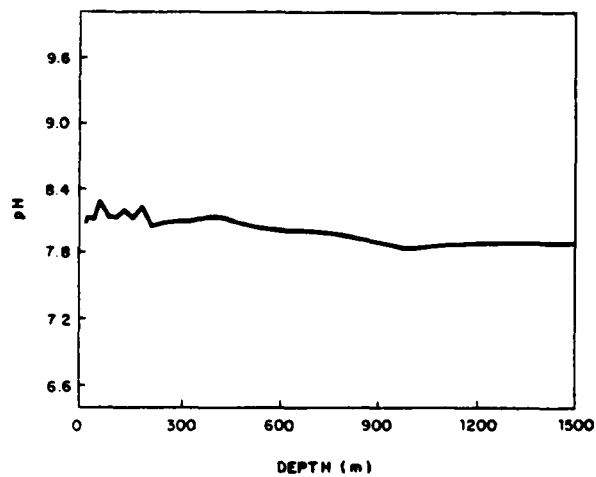
Fig. 4 – Variation of seawater pH with depth.
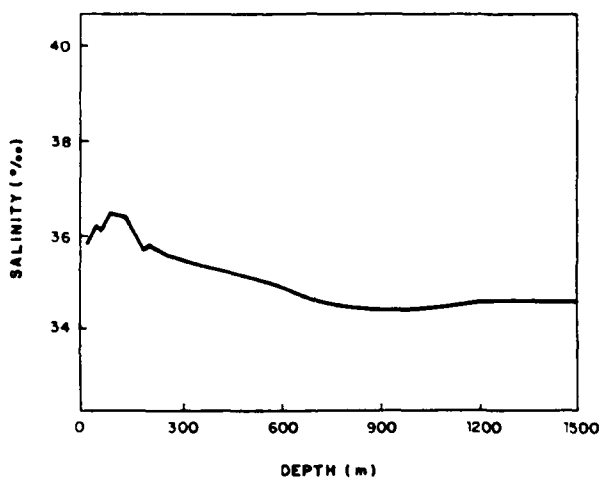
Fig. 5 – Seawater salinity versus depth.
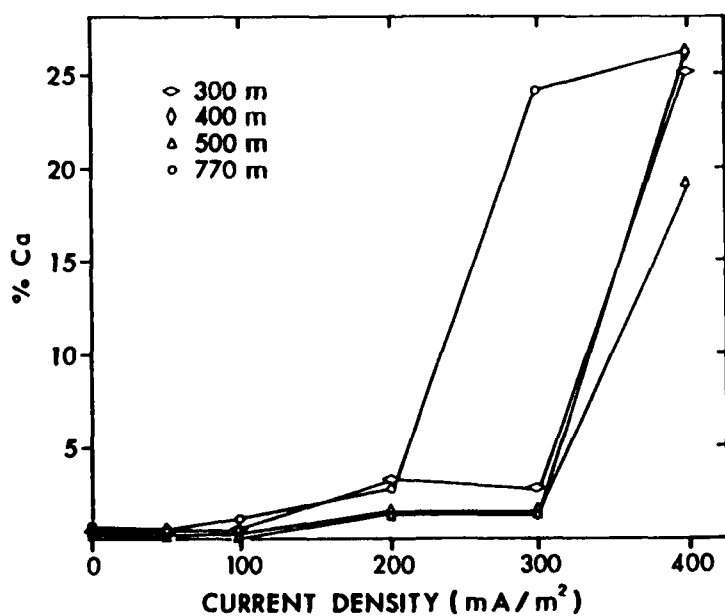
Fig. 6 – Variation in calcium concentration as a function of design current density and of depth.
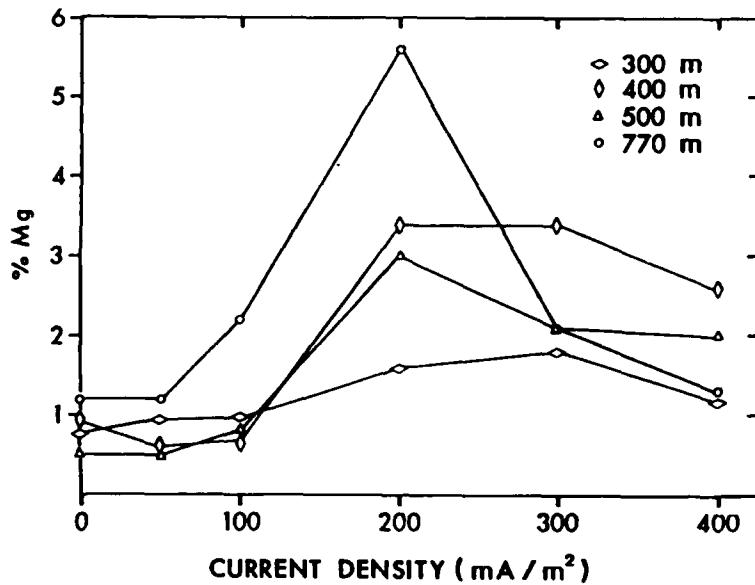
Fig. 7 – Variation in magnesium concentration as a
function of design current density and of
depth.
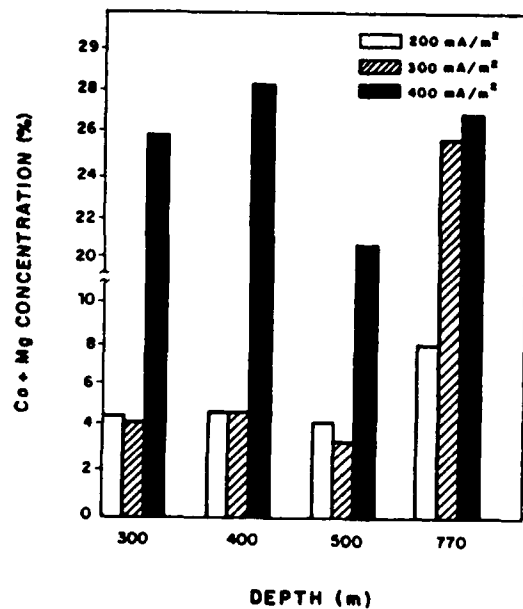
Fig. 8 – Concentrations of Ca + Mg as a
function of initial current density
and of depth.

The Isolator/Surge Protector: A Superior Alternative to Polarization Cells

Tom Scharf
Dairyland Electrical Industries, Inc.
P.O. Box 30
Oregon, WI 53575

Abstract

Cathodically protected systems utilizing impressed DC current have for years used polarization cells to simultaneously isolate and ground structures being protected. The old polarization cell technology is in conflict with current concerns for worker safety and the environment. Dairyland Electrical Industries has developed a solid-state product which can be used to replace (or in place of) polarization cells. This paper will describe the device and its application.

Introduction

The Isolator/Surge Protector (ISP) is a solid-state device with logic-controlled circuitry which simultaneously provides DC isolation and AC continuity; common requirements for protective devices used with cathodically protected systems. Its use is intended for safe electrical isolation of:

° Systems subject to 60 Hz power system faults. The ISP diverts these faults to ground, preventing unsafe AC voltage on the cathodically protected structure.

° Systems which are coupled to an AC source. The ISP provides a low impedance path to ground for AC current, preventing potentially hazardous AC voltage from being developed on the structure.

° Systems subject to lightning and/or switching transients.

It is important to recognize that cathodically protected systems which are not part of a power system may still be subject to the voltages and fault currents associated with power systems. For example, pipelines which are adjacent to power lines are subject to fault currents and induced voltage due to inductive and/or capacitive coupling.

Typical applications include cathodically protected:[1]

° Pipelines (Including insulated flanges)

---

[1]Reference Appendix A for application examples.

°High-Voltage pipe-type or lead-covered cable
°Power Plants
°Fueling Facilities

How the ISP Functions

The Isolator/Surge Protector achieves both isolation and protection by presenting a significantly different impedance to DC versus AC. Under steady-state ("normal") conditions, the ISP has extremely high impedance to DC and low impedance to AC. This mode is always in effect unless the voltage across the terminals of the ISP exceeds a predetermined level. This level is selected at 10.0 volts peak for most applications.

When the voltage across the terminals of the ISP attempts to exceed 10.0 volts peak, the DC and AC impedance both drop to extremely low values and the ISP effectively becomes a short circuit. This prevents high voltage--potentially dangerous to personnel or equipment--from occurring between the two points to which the ISP is connected. The peak voltage across the ISP just prior to transition to its "shorted" mode is 12.5 volts. Typical situations which would cause the voltage to exceed this transition level include 60 Hz fault currents or lightning/switching transients. When the absolute value of voltage drops below the 10.0 volt level, the device automatically reverts to its normal operating mode (blocking DC, conducting AC).

An ISP model should be selected so that under steady-state conditions the voltage across the ISP terminals is never more than 10 volts peak[2]. The peak voltage is the sum of DC voltage and the peak value of the AC voltage as measured between the ISP terminals. The peak value of the AC voltage is the AC-RMS value (as measured with a typical voltmeter) times the $\sqrt{2}$ (Note: $V_{AC\ peak} = V_{AC-RMS} \sqrt{2}$).

Why Isolation is Desirable

Isolation is desirable because it prevents the flow of DC current from the structure being protected, thus minimizing the DC current required for corrosion protection, and thereby reducing cathodic protection costs. Isolation also minimizes the effects of stray currents which may cause a structure to corrode at a faster rate.

---

[2]This 10 volt maximum does not limit the ISP from handling voltages significantly higher than 10 volts, because even voltages exceeding 100 volts will be reduced to only a few volts across the terminals of the ISP when it is properly selected and installed. Refer to Appendix A for details.

Product Features and Characteristics

Solid-State Design: Eliminates the use of potentially hazardous electrolytes and eliminates routine maintenance requirements.

Over-Voltage Protection: Significantly limits voltage that personnel and equipment may be exposed to.

Fail-Safe: If subject to currents in excess of rating which would cause failure, failure will occur in the shorted mode (AC and DC impedance low).

Number of Operations: Virtually unlimited under maximum 60 Hz and I^2t ratings, provided the operations are not repetitive.

Field Testing: May be partially field tested with a standard AC/DC multimeter and clamp-on AC ammeter to verify operability. Comprehensive testing in-situ is possible when the "Test Point" option is specified, and a custom designed field tester is purchased or rented from Dairyland Electrical Industries.

Enclosure: Enclosures are offered in 14 gauge #304 stainless steel and are suitable for submersible and non-submersible applications. A valve fitting is provided on all enclosures for factory leak testing purposes. All enclosures are 100% leak tested when a submersible application is specified. Enclosures are powder paint coated light gray.

Mounting: The unit is made to mount to a flat surface with two 1/2" diameter bolts furnished by user. Auxiliary add-on brackets are available to improve rigidity when mounting to a round pole. An outline drawing to aid in installation is provided with each unit.

Size:

60 Hz Rating Code	Dimensions		
	Length	Width	Height
3	23 9/16"	10 5/8"	8 7/16"
	59.8 cm	27.0 cm	21.4 cm
24,35,60	32 7/16"	10 5/8"	8 7/16"
	82.4 cm	27.0 cm	21.4 cm
68	36 1/2"	10 5/8"	8 7/16"
	92.7 cm	27.0 cm	21.4 cm

Weight: 50 to 115 pounds (23 to 52 kg) depending on model selected.

Energy Requirements: None. The device is totally autonomous.

Ambient Operating Temperature: -40°C to +60°C (-40°F to +140F).

Polarity/Electrical Connection: Polarity marks (- and +) are embossed on the enclosure above the NEMA[3] two-hole terminal pads to aid in proper connection. Stainless steel bolts, nuts, and washers are provided.

Product Ratings

60 Hertz Current (Steady-State)

The maximum 60 Hz steady-state current through the ISP that is allowable while the unit is still blocking DC is determined from the equation $I_{AC-RMS} \leq (10.0 - |V_{DC}|) + \sqrt{2} \times X_C$, where X_C = 0.088 ohms, 0.133 ohms, or 0.265 ohms, depending on model selected.

As the impressed DC voltage increases, the maximum allowable steady-state AC current must decrease. This is necessary to keep the peak (i.e., absolute) voltage below 10 volts; the level above which the ISP ceases to block DC and transitions from its steady-state impedance (X_C) to a virtual short circuit. The relationship between the allowable steady-state current and DC voltage is graphically illustrated in Figure 1:
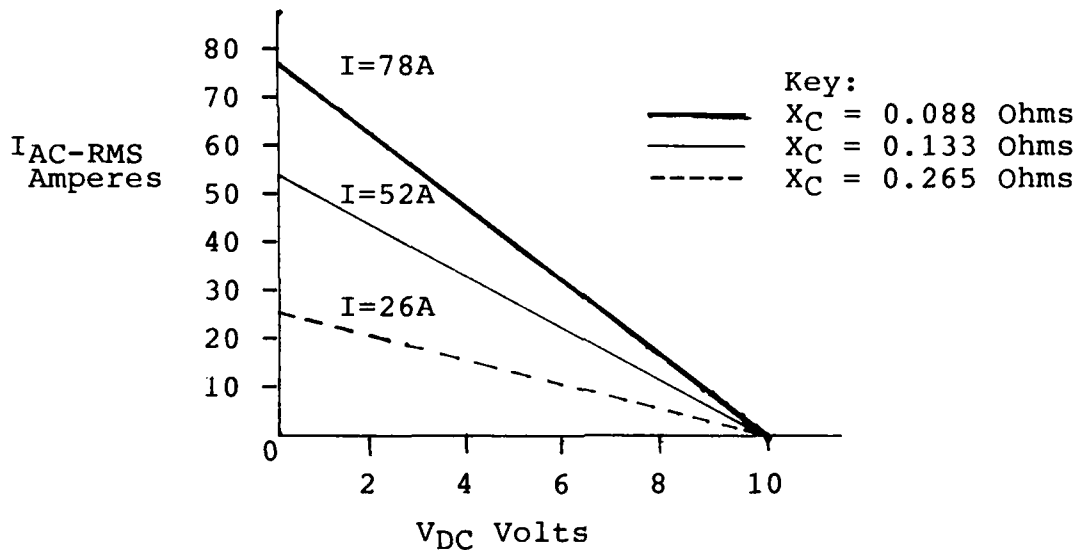
Figure 1: Maximum Steady-State 60 Hz AC Current versus DC Voltage

The allowable value of AC-RMS current at V_{DC} = 0 has been incorporated into a rating code as a means of selecting the appropriate steady-state current rating. The right column of the following rating code table ($V_{DC} \neq 0$) provides the same information as Figure 1 above.

---

[3]National Electrical Manufacturers Association.

"D" Code   Max. 60 Hz Steady-State Current (Amperes AC-RMS)

	@ $V_{DC} = 0$	@ $V_{DC} \neq 0$
26	26	$26 - (2.6 \times V_{DC})$
52	52	$52 - (5.2 \times V_{DC})$
78	78	$78 - (7.8 \times V_{DC})$

For example, under rating code 52, if 1.2 volts DC were present, the maximum continuous 60 Hz current allowable would be:

$52 - (5.2 \times 1.2 \ V_{DC}) \approx 46$ amperes.

60 Hertz Current (Short Duration)

The five 60 Hz short duration (fault current) ratings are summarized as follows:

"C" Code   Max. 60 Hz AC-RMS Amperes, Symmetrical[4]

3	3,000A @ 1$\sim$	2,700A @ 3$\sim$	2,400A @ 10$\sim$	2,100A @ 30$\sim$
24	24,000A @ "	18,000A @ "	14,000A @ "	11,000A @ "
35	35,000A @ "	28,000A @ "	21,000A @ "	14,000A @ "
68	68,000A @ "	55,000A @ "	40,000A @ "	30,000A @ "

Lightning Surge Current

Two lightning surge current ratings are available, with values of 50,000A or 75,000A crest. These ratings should not be confused with 60 Hz fault current ratings as the waveforms associated with each are distinctly different and have different effects. In an area with moderate to high incidence of lightning, the higher rating is suggested.

"A" Code   Surge Current Rating

50	50,000 A crest
75	75,000 A crest

These lightning surge current ratings are based on an 8 x 20 microsecond waveform considered representative of lightning. (The crest value of current is reached in 8 microseconds after which the current decays exponentially, reaching one-half of its crest value in 20 microseconds.)

For Additional Information

Model Number Structure of the ISP: A guide to selecting appropriate ratings for any application.

Installation and Operating Instructions of the ISP: Provided

---

[4] "$\sim$" is the symbol for cycles.

with each unit. Lists the ratings of the unit, with instructions on mounting the ISP and conducting simple field tests if desired.

Summary

The ISP is the only product which provides isolation and grounding with solid-state components and logic-controlled circuitry. All parameters are precisely defined and readily tailored to specific applications.

Appendix A

Isolator/Surge Protector Application Examples

The following examples are intended to aid in understanding how the ISP is applied in representative situations.

A. Cathodically protected systems subject to 60 Hz power system faults.

A pipeline located in the corridor of an electric utility power line may be subject to the power system voltage and the available fault current during fault conditions, because the pipeline may be the lowest impedance path back to the current source. Therefore, even if the pipeline does not physically come in contact with the power line, it may still be subject to system voltage and current. An ISP connected to the pipeline would then be subject to the system voltage and current.

The power utility can provide information on the available fault current and the time duration that this current can flow. This information is necessary to select an ISP with the proper short duration current (i.e. fault current) rating. For example, if the available fault current were 10,000 amperes AC-RMS symmetrical for 10 cycles, an ISP with a 60 Hz rating code 24 would be selected because this is the lowest rating that meets or exceeds this requirement. (Refer to the "60 Hz Short Duration" rating information table.) The voltage of the power utility system is not relevant to the select;on of an ISP rating because an ISP immediately becomes a "short circuit" to any voltage that attempts to exceed a peak value of 10 volts. The available current is the factor that determines the rating.

B. Cathodically protected systems subject to induced 60 Hz voltage.

It is not uncommon for a cathodically protected pipeline located in an electric utility powerline corridor to have a steady-state (continuous) voltage induced. Again, even if there is no physical contact between the power line and the pipeline, the elec-

tromagnetic field of the powerline can create voltage on the pipeline. Induced voltages of 100 volts are not uncommon and represent a potential shock hazard upon contact. Proper application of an ISP can reduce this voltage to non-hazardous levels.

One frequently asked question is "How can an ISP with a peak voltage blocking level of 10 volts be used in a system which may have 100 volts available? Doesn't this exceed the capabilities of the ISP?" The answer lies in the fact that the available current from a system with induced AC voltage is usually very limited. This limited current flowing through an ISP of relatively low steady-state impedance (i.e. X_C = 0.088, 0.133, or 0.265 ohms, depending on model selected) reduces the voltage to a value determined by "$I \cdot X_C$," where I is the available induced current and X_C is the steady-state impedance of the ISP. (X_L values are not to be confused with the ISP's impedance during 60 Hz fault/lightning conditions, since the ISP momentarily becomes a short circuit to provide safe, immediate grounding in such conditions.)

For example, assume that the voltage on a cathodically protected pipeline is 100 volts AC-RMS and that the maximum available current is 15 amperes AC-RMS when the pipeline is shorted to the same ground connection to which the ISP would be connected. This means that the equivalent internal resistance of this voltage source is 6.67 ohms (because 100V $\div$ 15A = 6.67 ohms). Since the impedance of the ISP is negligible compared to the voltage source resistance, it will not affect the available current; therefore the available current can be assumed to remain at 15 amperes. The voltage across the ISP terminals becomes $I \cdot X_C$.

Steady-State Voltage Across ISP Terminals For I = 15 A AC-RMS

For X_C =	0.265 Ohms	0.133 Ohms	0.088 Ohms
$I \cdot X_C$ =	3.98 Volts-RMS	2.0 Volts-RMS	1.32 Volts-RMS
$I \cdot X_C \sqrt{2}$ =	5.63 Volts peak	2.83 Volts peak	1.87 Volts peak

Note that the voltage across the ISP has been reduced to a small fraction of the original 100 volt value, thereby illustrating how a protective device with a 10 volt blocking level can be used on a system with significant levels of open-circuit voltage. For this example, the maximum DC voltage that could also be impressed across the ISP, due to impressed cathodic protection voltage and stray DC, would be 4.37 volts, 7.17 volts, and 8.13 volts respectively; this is determined by subtracting the peak AC voltage across the ISP from its 10 Volt blocking rating. Note that all references to the 10 volts blocking level always pertain to "peak" or "absolute" voltage; not RMS values as measured with a typical voltmeter.

Another key factor to consider is that the voltage developed across the ISP is not necessarily the voltage that a person would experience by making contact with this pipeline. The reason is that a person contacting the pipeline has internal resistance as well as resistance to the ground connection point for the ISP. Further, these parameters can vary with distance from the point at which the ISP is installed. In addition, there is resistance from the ISP ground connection point to true earth ground and from the pipeline to true earth ground. Many different factors affect these various resistance values and therefore affect the actual voltage that a person may experience. As a general rule, the lower the voltage across the ISP, the lower the voltage available to a person making contact. For this reason, when these additional factors are not completely known, it is preferable to select an ISP with a higher steady-state AC current rating than may otherwise be considered necessary because this will result in an ISP with the lowest steady state voltage across it for a given value of current. Due to the complex nature of grounding and voltage mitigation, a thorough presentation of this aspect is beyond the scope of this application example. Due to the several factors mentioned above, it is not possible to casually give a recommended interval at which ISPs should be installed. Consulting engineering firms that specialize in this type of analysis are available to assure that proper voltage mitigation is achieved when all relevant factors are considered.

Laboratory Evaluation of the Effectiveness of Cathodic Protection in the Presence of Iron Bacteria

Kiyoshi Okamura
Yukio Koyama
Fumio Kajiyama
Komei Kasahara
Fundamental Technology Research Laboratory
Tokyo Gas Co., Ltd.
1-16-25 Shibaura, Tokyo 105, Japan

Abstract

Laboratory cathodic protection test was carried out to investigate off-potential requirements to achieve complete cathodic protection on the steel pipes buried in the microbiologically active soils containing iron bacteria (IB) with other species of bacteria. Off-potentials were changed over a range from -0.65 V to -1.1 V (Cu/CuSO$_4$).

Practical sufficient protection in active IB sand was shown to be obtainable at the off-potentials more negative than -0.8 V.

General mechanisms whereby protection was achieved included the reduced proliferation of bacteria due to environmental changes caused by the enhanced cathodic reactions, that is, a pH shift toward alkaline and an aeration change into anaerobic.

1. Introduction

Cathodic protection has received a worldwide recognition as the most effective and economical method to protect buried coated steel pipes against corrosion[1,2]. This technique first became practical in 1933 when Kuhn proposed a -0.85 V (Cu/CuSO$_4$) potential criterion, that is, potentials more negative than -0.85 V were required to attain complete protection.

Possible microbiologically influenced corrosion (MIC) of steel pipes buried in anaerobic clayey soils containing sulfate-reducing bacteria (SRB), which was first reported in 1934 by Kühr and van der Vlugt[3], raised a need for an alternative potential criterion, and on the basis of thermodynamic considerations, a -0.95 V criterion was proposed by Hovarth and Novak[4] in 1964 for the cathodic protection in the presence of SRB; which was afterwards experimentally verified by Fischer[5].

Although SRB have thus been the focus of many investigations involving MIC, the roles in MIC of other species of bacteria, such as acid producing bacteria and metal depositing bacteria, have increasingly been emphasized. The authors carried out a number of site-surveys on buried pipes to clarify the causes of a wide variety of corrosion failures caused by local action cells or localized cells, and demonstrated[6,7,8] that iron-oxidizing bacteria (IOB), sulfur-oxidizing bacteria (SOB) and iron bacteria

(IB) could have played a major role in the significant corrosion of the buried pipes. The contribution of SRB was found to be small.

As such, the need has naturally been increased for the revised cathodic protection criteria. Therefore, in the present study, the effectiveness of cathodic protection was reinvestigated in the laboratory to protect steel pipes against corrosion in the soils with high activity of bacteria as IB. Potentiostatic test was conducted with an emphasis on examining the action and behavior of IB under conditions applied with cathodic currents.

2. Experimental Procedures

In the present laboratory study, a simulated cathodic protection cell as shown in Figure 1 was used; wherein three electrodes, a working, counter and reference electrodes, respectively, were buried in a PVC soil box of 110 mm wide × 150 mm long × 110 mm deep. The working electrode of carbon steel plate to simulate a coated steel pipe having a 7.1 cm^2 of coating holiday was obtained by covering the steel plate surface with a PVC cap of 5 mm in thickness. The surface of the working electrode was slightly abraded with 2/0 Emery paper, followed by degreasing with acetone. A carbon plate of 100 mm wide × 100 mm long × 10 mm thick was used to simulate a counter electrode in an impressed current type of cathodic protection system. This counter electrode was placed at a distance of 120 mm from the working electrode. A commercial double-junction type of saturated Ag/AgCl electrode as a reference electrode was placed in between the working and the counter electrodes at the distance of 20 mm from the working electrode. These three electrodes were then buried in the soil held in a PVC box in order to create a simulated cathodic protection test cell, and wired to a potentiostat as indicated in the figure. These test cells were set in an incubator at 298 K for 90 days. The soil used in the test was a sandy soil which was sampled on-site where the presence and high activity of IB had been recognized.

Cathodic protection was applied potentiostatically by applying cathodic currents via the counter electrode to the working electrode so that off-potentials of the electrode should drop in the range from -0.533 to -0.983 V vs. Ag/AgCl. Potential values, however, are given below with reference to Cu/CuSO$_4$ at 298K. During the testing period, currents flowing between working and counter electrodes were monitored continuously by means of a potentiostat.

Spontaneous burial corrosion testing was also carried out in the same manner so as to highlight the effectiveness of cathodic protection.

Potentiostatic polarization measurements were taken before and after the testing. Measurements were undertaken in a range ±500 mV around the corrosion potential (Ecorr) by alternating polarity in a discrete manner at steps of 2 mV, and maintaining each level for a sufficient time period of 5 to 10 min to attain the steady state measurements. Solution resistance calibration, that is, IR-drop compensation, was made.

Soils used in the tests were investigated with respect to pH, Eh, and bacteria counts

(IOB, SOB, IB,SRB and methane–producing bacteria: MPB) before and after the exposure. Samples were collected from the immediate vicinity of each working electrode surface (< 1 mm). Bacterial counts (IOB, SOB, SRB and MPB) were made in accordance with the most probable number method. Postgate's medium B[9] was used for SRB enumeration. IOB, SOB, IB and MPB enumerations were made according to the recommendation appearing in Reference[10]. The rest of environmental factors was determined in accordance with the Japanese Standardized Manual for Soil Analysis.

Upon conclusion of the test, every working electrode was removed from each cell, followed by cleaning and weight loss determination. The weight loss measurements were then converted into uniform corrosion rate (mm y^{-1}). Maximum corrosion rate (mm y^{-1}) was obtained by means of an optical microscope equipped with a depth gauge.

3. Results and Discussion

3.1 Cathodic Protection Tests in the Presence of IB

Figures 2 and 3 show the effect of applied potential on the uniform and the maximum corrosion rates, respectively, in active IB sand. The potentials grouped in the category of "free corrosion" stand for those of the working electrodes without cathodic protection, that is, those subjected to free corrosion. Measurements were taken at 90 days of the termination of exposure testing.

From comparison of these two figures, it is evident that the maximum corrosion rates were more than one order of magnitude higher than those of the uniform corrosion; indicating that the type of corrosion was localized corrosion. Rates of uniform corrosion at free corrosion potentials fell well within the range of average uniform corrosion rates experienced in the Kanto area (in and around Tokyo metropolitan area)[8]. On the other hand, the rates of localized corrosion were around 0.7 mm y^{-1}. These rates can be classified in the top range for the natural soil corrosion of steels in Kanto–area[8]. A characteristic feature of the corrosion attack included an extensive tubercle formation; which was similar to that observed in the site–surveys on the pipes buried in sands with active IB[8].

It can be seen in the figure that in such cases as off–potentials were controlled to fall within the range from Ecorr to –0.75V, maximum corrosion rates still remained at rather higher levels, sometimes exceeding those of free corrosion; which would have been due to the limited cathodic current distribution that stifled the vast majority of anodic sites leaving only small anodic sites to continue to proceed anodic reaction.

On the other hand, in the potential range more negative than –0.8 V, localized corrosion was depressed significantly at slower rates; leading to a temporary conclusion that complete, or practical sufficient, cathodic protection in a sand with active IB may be achieved at the off– potentials more negative than –0.8 V.

Figure 4 shows semi–log plots of the cathodic current density versus time relationship monitored during the cathodic protection tests. A slight decrease in cathodic current

density from the beginning of the test till the day 10 was replaced by the gradual increase, eventually attaining a steady level depending on the each respective applied potential. Such was a feature common to every testing cell. As apparent in the figure, the order of magnitude of applied potential corresponded simply to that of resulting cathodic current density; indicating a simple mechanism wherein the protection against corrosion could be achieved by the enhanced cathodic reaction.

Figure 5 shows the relationship between the maximum localized corrosion rate and the cathodic current density averaged over the testing periods. It can be drawn from this result that the minimum required cathodic current density to achieve complete cathodic protection would be 0.25 A m^{-2}. It may be worth noting that this current density is about three times greater than the level critical for the common soils in Kanto area[2].

3.2 Cathodic Protection and Microbial Action

The contribution of bacteria species to corrosion have not yet been fully clarified; the present understanding is summarized in Table 1. From analogy with such an understanding, environmental changes accompanied by the progress of cathodic protection could bring about not insignificant amount of influence on the proliferation and activities of bacteria species involved in the soil corrosion process. Therefore, studies were undertaken with an emphasis on examining the action of bacteria.

Figure 6 shows the effect of applied potential on the pH and Eh in the soil close to the working electrode surface (< 1 mm). Readings for free corrosion are also plotted in the figure. It can be seen in the figure that the change of pH with applied potential was such that it increased rapidly, starting at around 7 of free corrosion, with increasing cathodic polarization, hence with enhancing cathodic protection, rising up to around 10 at -0.8 V and thereafter increasing gradually and that almost in linear with potential, reaching a steady state level of 12 in the range in between -0.95 and -1.1 V. It may be worth noting that the inflection point occurred at around -0.8 V exactly corresponded the potential where a practical sufficient protection against corrosion could be attained.

On the other hand, the change of Eh with applied potential was in somewhat different; it started at around 0.45 V (NHE) of free corrosion and decreased (hence, shifted toward anaerobic site) linearly with increasing cathodic polarization within the potential range tested.

Such pH and Eh changes observed in the study seem to be rationally explained by a cathodic reaction of Equation (1) because this should bring about the build up of alkalinity in the soil close to the working electrode surface, together with the consumption of dissolved oxygen leading to an anaerobic environment. Alternative cathodic reaction as represented by Equation (2) could not be involved in the present cathodic protection mechanism because potentials applied were not sufficient enough to activate the reaction, and hence no hydrogen production was noticed.

$$1/2O_2 + 2H_2O + 2e^- \rightarrow 2OH^- \tag{1}$$
$$2H_2O + 2e^- \rightarrow H_2 + 2OH^- \tag{2}$$

Table 2 compares bacteria counts in the soil close to the working electrode surface (< 1 mm) before and after 90-day laboratory burial tests. As one-by-one counting of IB is not easy because these bacteria usually form agglomerated strings, a 3-level semi-quantitative indicator system, +, ++, and +++, is employed here to classify the IB population.

At free corrosion and -0.65 V, counts of both IB and SOB increased appreciably during the test run, whereas counts of SRB and MPB decreased. This is thought to exactly correspond to the above-mentioned observation that severe localized attack, accompanied tuberculation, was noticed at both free corrosion and -0.65 V.

On the other hand, at -0.95 V, activity of every bacteria species reduced without exception; wherein both IB and SRB counts could still be detected, though at significantly lower levels, whereas both SOB and MPB became entirely extinct.

From analogy with the present understanding shown in Table 1, in combination with the pH and Eh observation, both the buildup of alkalinity and the consumption of dissolved oxygen was thought to be responsible for the decreased activities of bacteria. It has been well established that both IB and SRB can survive the unfavorable conditions of environments by confining themselves to sheaths of their own making.

Figure 7 shows the polarization curves obtained before and after the testing. At the off-potential of -0.8 V, significant amount of anodic polarization was noticed accompanied by the Ecorr shift toward nobler potential direction, presumably as a result of formation of stable and high resistivity of oxide layers. The buildup of alkalinity in the immediate vicinity of the working electrode surface was thought to be mostly responsible for the formation of such stable oxide layers.

On the other hand, at the off-potentials of free corrosion and -0.7 V, the extent of anodic and cathodic polarizations was not changed in consistent with the site-surveys as well as the present laboratory corrosion tests resulting in severe localized attack accompanied tuberculation.

4. Conclusions

Laboratory evaluation of the effectiveness of cathodic protection in the presence of iron bacteria was conducted. The conclusions based on the test are as follows:

(1) Complete cathodic protection in a sand with active IB could be achieved at the off-potentials more negative than -0.8 V (Cu/CuSO$_4$).

(2) Cathodic protection in a sand with active IB was mainly brought about by the decrease in IB activity due to the environmental changes as pH shift into alkaline and aerobic shift into anaerobic.

References

1. NACE Recommended Practice RP-01-69.

2. K. Kasahara and H. Adachi, "A Proposal for Cathodic Protection Criterion for Buried Steel Pipelines", 8th International Corrosion Congress on Metallic Corrosion, paper no.49 (Mainz, Germany: International Corrosion Council, 1981).

3. C. A. H. von Wolzogen Kühr and L.S. van der Vlugt, Water, 186 (1934):p.147-165.

4. J. Hovarth and M. Novak, Corrosion Science, 4 (1964): p.159.

5. K. P. Fischer, Material Performance, 20 10 (1981): p.41.

6. K. Kasahara and K. Kajiyama, "Electrochemical Aspects of Microbiologically Influenced Corrosion on Buried Pipes", International Congress on Microbiologically Influenced Corrosion and Biodeterioration (Knoxville, TN: National Association of Corrosion and Engineers,1990): p.2-33.

7. F. Kajiyama, K. Okamura, Y. Koyama and K. Kasahara, "Microbiologically Influenced Corrosion on Ductile Iron Pipes in Soils", International Symposium on Microbiologically Influenced Corrosion (MIC) Testing (Miami, FL: American Society for Testing and Materials, 1992).

8. K.Kasahara, F.Kajiyama and K.Okamura, Zairyo-to-Kankyo, 40 12 (1991): p.806 (in Japanese).

9. J.R.Postgate, The Sulphate-reducing Bacteria, (Cambridge University Press, 1979): p.26.

10. Handbook of Classification of Microorganisms, R and D Planning, Japan (1986).

Table 1 Action of bacteria implicated in the soil corrosion[a].

Species	Oxygenr equirement	pH range	Temperature range (°C)	Action
IB Gallionella	Aerobic	7.5~9.5	20~30	Oxidize Fe^{2+} to Fe^{3+} Promote tuberculation
IOB Thiobacillus ferrooxidans	Aerobic	0.5~6.0	10~40	Oxidize Fe^{2+} to Fe^{3+} in H_2SO_4 and HCl environments
SOB Thiobacillus thiooxidans	Aerobic	0.5~7.5	10~40	Oxidize S and sulfides to form H_2SO_4
SRB Desulfovibrio	Anaerobic	5.5~7.5	25~45	Reduce SO_4^{2-} to S^{2-}
MPB	Anaerobic	4~8	25~45	Consume acetic acid to form methane

Table 2 Change in bacteria counts observed in the laboratory cathodic protection testing.

Time/Days	Location	Applied potential/V vs. Cu/CuSO$_4$	Number of bacteria / Cell g^{-1}				
			IB	IOB	SOB	SRB	MPB
Before test	Bulk	——	++	0	4×10^2	2×10^2	1×10^2
90	Interface	Free corrosion	+++	0	5×10^3	7×10	2×10
90	Interface	− 0.65	+++	0	1×10^2	3×10	1×10
90	Interface	− 0.95	+	0	0	3×10	0

Interface : Electrode/soil interface
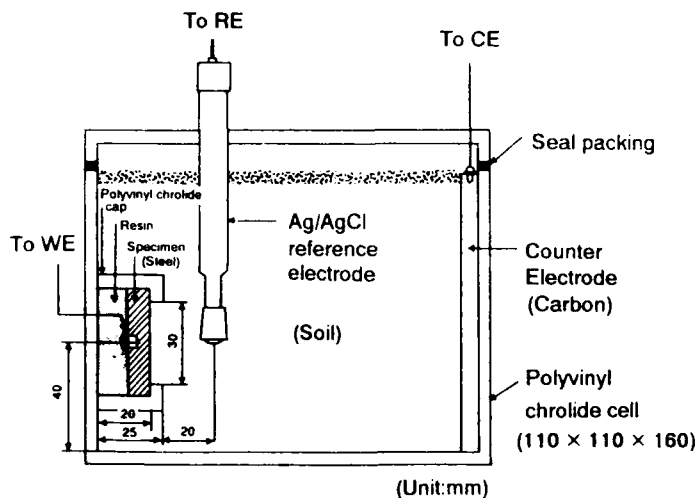
Figure 1 Shematic diagram of the testing cell.
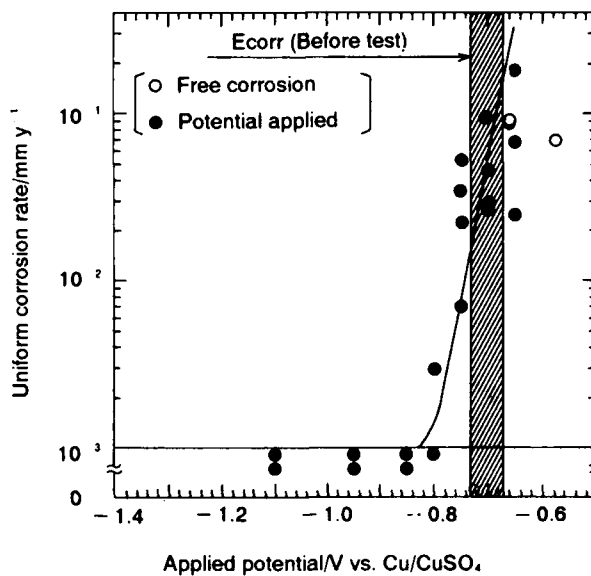
Figure 2 Effect of applied potential on uniform corrosion rate in sand.
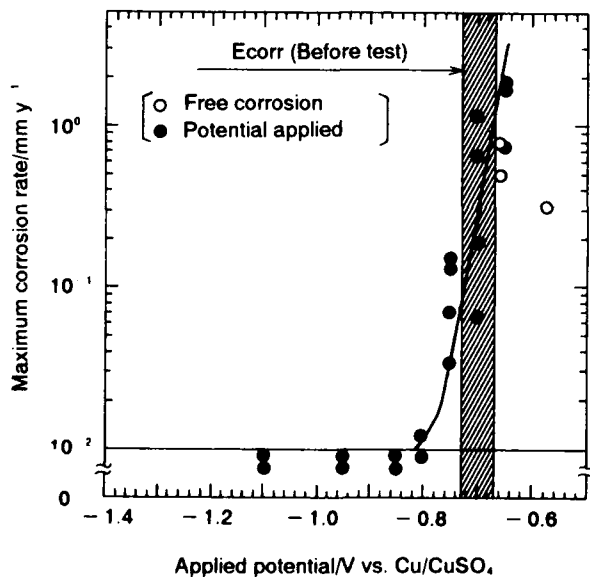
Figure 3 Effect of applied potential on maximum corrosion rate in sand.
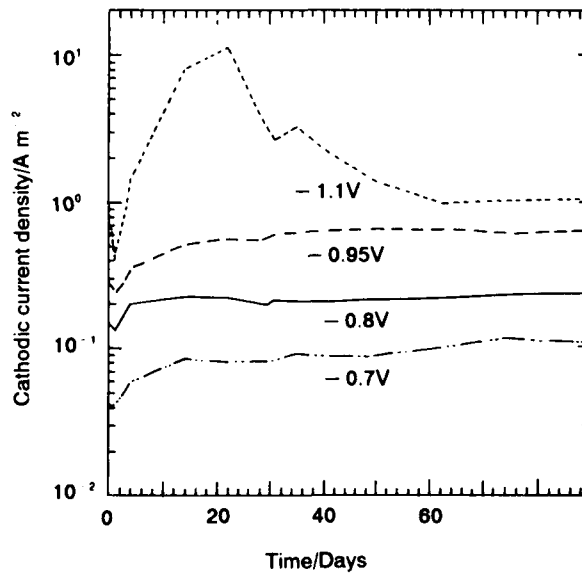
Figure 4 Cathodic current density/time variations for various applied potentials in sand. Potentials on the diagram are presented with respect to $Cu/CuSO_4$.
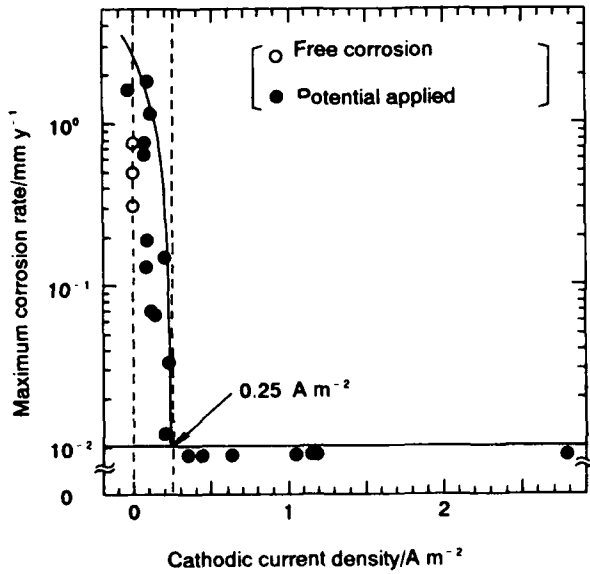
Figure 5 Relation ship between maximum corrosion rate and cathodic current density averaged over extented period in sand.
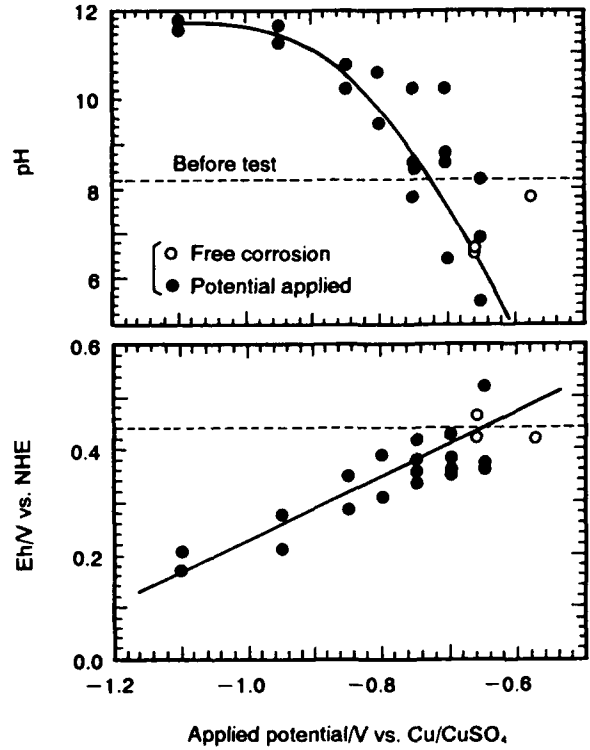
Figure 6 Polarization curves before and after the testing in sand.
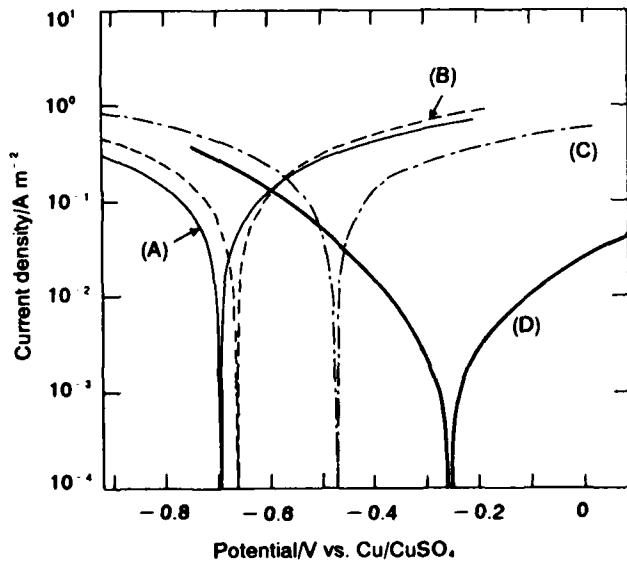
Figure 7 Values of pH and Eh at the electrode/soil interface in sand after the testing as a function applied potential.

Before test	————	(A)
	free corrosion	(B)
After test	~ 0.7V applied	(C)
	~ 0.8V applied	(D)

Modification of the Corrosion Environment Beneath Disbonded Coatings by Cathodic Protection

Klaus Fink
The Case School of Engineering
Department of Materials Science and Engineering
Case Western Reserve University
10900 Euclid Ave.
Cleveland OH 44106

Joe H. Payer
The Case School of Engineering
Department of Materials Science and Engineering
Case Western Reserve University
10900 Euclid Ave.
Cleveland OH 44106

Abstract

Disbonded coatings on steel can interfere with the current distribution from cathodic protection. Shielding the current under disbonded coatings can affect the level of protection for steel. Steel can be protected by modifying the corrosion environment via a cathodic protection system. Recent work completed in low conductivity electrolytes as well as strategies for continued investigation of hydroxide generation and distribution beneath disbonded coatings will be discussed. The experimental results will be related to the corrosion behavior of steel as well as to possible defects in pipeline coatings. Further work will focus on the mechanistic processes and guiding issues within the disbonded region which determine the level of protection to the steel.

Key Words: cathodic protection, disbonded coatings, hydroxide, passivation

Introduction

Corrosion beneath damaged and disbonded coating systems on pipelines is a concern. In high conductivity soils and waters, the ability of cathodic protection systems to distribute current and protect the steel in crevices beneath a disbonded coating system has been examined. The effectiveness of cathodic protection for steel beneath damaged coatings has not been clearly demonstrated under conditions of low solution conductivity. The premise of this work is that the corrosion rate of the steel will be negligible if an alkaline, deaerated environment can be generated and maintained beneath the damaged coating system by using cathodic protection techniques.

The goal of this program is to determine if the chemical changes which occur during cathodic protection can protect crevices created by damaged coating systems. In low conductivity solutions, penetration of cathodic current into crevices is reduced. The concept of mitigating corrosion of steel by altering the corrosion environment is illustrated in Figure 1. By increasing the local pH and reducing the level of dissolved oxygen within the crevice, the corrosion rates can be significantly reduced and the steel can be protected without penetration of cathodic currents under the coating system.

The goal of this work is to develop a total picture of the local chemistry and electrochemistry of cathodically protected steel beneath disbonded coatings.

Background

It is well documented that where access to the inside of a crevice is restricted, a significantly different chemistry may be present than found in the bulk electrolyte.

These altered chemistries have been observed in crevice studies for cathodic protection technology in laboratory experiments and in the field. An increase in local pH has been noted and results from the consumption of hydrogen ions and generation of hydroxyl ions during cathodic protection. Most of the available literature documents work using high conductivity solutions. Parkin's (et al) work showed that cathodic protection currents were able to penetrate deeply into disbonded tape crevices when conductive solutions were filled beneath the tape[1].

Several groups working on pipeline protection issues in Saudi Arabia have attempted to make measurements on segments of pipe buried beneath the soil in Saudi Arabia[2-4]. These groups identified the electrolyte present as very conductive (20 ohm-cm). Toncre and Ahmad[2] conducted testing in brackish, high conductivity waters and showed that a degree of cathodic protection can be obtained within a crevice. Clean crevices with large openings were easier to polarize than those containing mill scale or corrosion products. These results were measured on test cells submerged in electrolyte. The cell's plastic top contained reference electrodes for measurements. The crevice opening was 0.40 mm wide. The pH was also measured during the tests by removing solution from the crevice and using pH paper. The results showed alkaline pH's inside the crevice of 8-12 while the bulk solution just outside the crevice remained neutral.

Additional work on pipe sections in the field in Saudi Arabia has been reported by Orton[3]. Instrumented pipe sections were buried in the Saudi Arabian soil, and the pipe potential was measured via internal reference electrodes. Results indicated that cathodic protection can be achieved for crevice ratios of 1:6000 in highly conductive soils. Attempts were made to measure the pH within the crevices, and values of pH 8-12 were measured in the crevice while the bulk remained constant at pH 6-7. These measurements were made with pH paper.

Toncre[4] discusses the cases for and against effective cathodic protection of pipelines. In the case for, Toncre presents the theoretical arguments and laboratory studies which indicate that cathodic protection should provide effective protection of steel. The case against consists of a series of field studies which show either good CP survey data and corroded pipe or poor survey data and good condition pipe. Areas where the cathodic protection data indicated good protection, corroded steel was found beneath disbonded tape during excavation. In other regions, the cathodic protection data indicated an inadequate protection level and steel with insignificant corrosion was found. In this case, an alkaline environment was present beneath the disbonded tape. The paper concluded that standard pipeline surveys are not solely adequate for determining the level of protection of the pipeline.

Cherry and Gould[5] indicated that maintaining a high pH environment will help to protect the steel beneath a disbonded coating by passivation of the steel. Interruption or removal of the cathodic protection system may cause a decrease in the alkaline environment and cause the crevice potentials to shift to more positive rest potentials. At the more positive potentials, pitting corrosion may result in carbonate environments.

The test cells used for the Cherry and Gould project were based on a cell design published by Fessler et al.[6,7]. Fessler tracked potential shifts inside a crevice due to applied potentials at a

holiday in tape. Their cells were constructed of Lucite and were 20cm in length. The group used a 2N sodium carbonate/bicarbonate solution. They found that 20cm crevices (0.13mm thick) were polarized to -0.780V-SCE after 1000 hours even if the holiday potential was set at -0.850V-SCE. Bubble formation was also studied using the same cells. The applied potential had an effect on the formation of hydrogen bubbles. At potentials above -1.2V-SCE, hydrogen bubbles caused blockage of the crevice. The potential distribution was monitored during the test and the bubble formation within the crevice was photographed through the acrylic crevice cell cover. As the crevice potential equilibrated, bubble formation became uniform throughout the crevice. Reproducibility was a problem with small crevice thicknesses.

Thompson and Barlo[8] studied changes in solution chemistry within crevices due to cathodic protection, with particular emphasis on pH changes. They found a significant increase in pH due to the applied potential by reduction of oxygen or water depending on the state of aeration. The initial pH and the pH of the bulk solution had little effect on the final pH attained, while the polarized potential only indirectly influenced the final pH. Their work showed a rapid increase in pH after the applied potential was activated. The chloride and sodium ion concentration of the solution were also monitored; however they showed no significant change during the tests.

Work done at The Case School of Engineering[9] has shown that alkalinity can be generated at a crevice using a cathodic protection system and that this alkalinity will proceed down the length of a narrow crevice to protect the steel beneath disbonded tape. The work showed rapid pH increases during the first several days of testing, tapering to a more gradual increase to a steady state after 15-20 days. Movement of the alkalinity was also studied and showed a rapid spread of the hydroxyl ions beneath the crevice.

In summary, the literature shows that there are chemical changes within crevices. The pH can shift to more alkaline values and it is anticipated that the oxygen concentration will decrease within a crevice, both in the lab and in the field. The conductivity of the solution has a major effect on current penetrating the crevice. Also, the geometry of the crevice may have a major effect. The objective of this work is to continue to explain these changes in low conductivity solutions.

Experimental Procedures

Several different cell variations were developed for the experiments. The material chosen for the electrochemical cells was clear polyvinyl chloride (PVC) covering a 1/4" steel plate.[9]

A general schematic of the test cell is shown in Figure 2 and is discussed in detail in a previous publication[9]. The crevice was formed with an FEP spacer shim. Other variations to this cell will continue to be developed.

For tests with applied potentials, an anode chamber was bolted to the holiday end of the test cells as shown in Figure 2. Two long screws were used to secure the anode chamber to the cell. A 1.1cm hole was drilled into both the cell and the anode chamber to connect the two sections. An ion permeable membrane was inserted between the chambers to prevent solution transfer.

An ASTM 516 steel plate was used for all tests. Cutting of the plates was done by band saw to minimize metal distortion along the edges. The plates were grit blasted with a fine glass bead blaster to remove all mill scale, and the grit blastd plates were stored in a dessicator. Before testing, the plates were cleaned with methanol and abraded with a wire brush. The plates were rinsed again with methanol and force air dried before assembly into test cells.

Three different solutions were used for testing in the disbonded tape simulation cells as well as for the corrosion coupons and polarization tests: 0.01M Na_2SO_4, 0.1M Na_2SO_4 and 1.0M NaOH All solutions were prepared with distilled water and reagent grade chemicals. The conductivity of the 0.01M Na_2SO_4 solution was 1900 $\mu S/cm$, while the 0.1M solution had a conductivity of 15,000 $\mu S/cm$.

In order to monitor the pH beneath the crevice, metal/metal oxide pH electrodes were prepared and inserted into the cells. The pH electrodes were calibrated before each test. Potentials of the steel and the pH electrodes were measured against external Ag/AgCl reference electrodes.

Two additional cells have been designed to complement the cell described above in further work. The microcell shown in Figure 3 will be used to study the spatial distribution of chemical species during testing. This will be done with pH electrodes for both the vertical direction into the environment as well as for the horizontal plane along the steel plate. Oxygen probes will be distributed as needed around the 3 mm holiday in the coating system. A flow through cell design is shown in Figure 4. This cell will be used in conjunction with two electrode linear polarization resistance specimens to determine the effects of solution changes on the instantaneous corrosion rate of the steel sample. The crevice width will be varied over a range from greater than several millimeters to a very snug, tight crevice.

Results

I. Generation of Alkalinity.

A potential was applied to the steel at a holiday using the cell shown in Figure 2 and changes in local pH and potential were monitored within the crevice. Measurement sites were located at the holiday and continued every 5 cm to the rear of the crevice. The data from these tests are presented as two graphs, one for changes in pH and the other for changes in steel potential. Each line on the graph represents the data set collected at the stated distance from the holiday.

The applied potential at the opening for this test was -1.0 V-SCE, and the crevice was filled with 0.01M Na_2SO_4 solution. The applied potential was controlled at the holiday opening with a standard laboratory saturated calomel electrode and a potentiostat. A micro reference electrode and pH electrode were also present in the holiday next to the crevice opening for pH measurements. All data are presented standardized to the Ag/AgCl electrodes. The equivalent value for -1.000 V-SCE is -0.932 V-Ag/AgCl.

The data for a 0.8 mm thick crevice are shown in Figures 5 and 6. The pH data in Figure 5 shows a rapid increase in pH within the crevice with values greater than pH 11 recorded within the first day. After the initial increase, the pH remained essentially constant throughout the remainder of the 15 day test. Figure 6 shows the steel potential data for the 0.8 mm crevice test. The potentials within the crevice dropped 75-80 mV within the first day, followed by a positive shift from -0.700 V-Ag/AgCl to -0.500 V-Ag/AgCl at all locations in the crevice after 9 days, after which a steady state condition was reached.

II. Transport of Alkalinity.

In order to measure the transport of alkaline solution within a crevice, a series of tests were run with cells similar to those described above, however, no potential was applied at the holiday nor was there an anode chamber. The crevice was filled with a solution of predetermined pH and a second solution with different pH was filled into the holiday chamber to start the test. Two series of experiments were run: (a) to measure the transport of alkalinity into a neutral crevice

and (b) to measure the transport rate out of the crevice by an alkaline solution when neutral water is added at the holiday. The pH and the potential were monitored in the crevice as described above. Tests for type (a) began with neutral 0.01M Na$_2$SO$_4$ solution in the crevice and 1M NaOH solution added to the holiday to start the test, and type (b) experiments began with 1M NaOH solution in the crevice and 0.01M Na$_2$SO$_4$ solution was added and dripped into the holiday. Data from electrochemical polarization tests were used to aid in interpreting the potential data generated from the transport experiments.

The pH changes in a test of type (a) where alkaline solution was added to a neutral crevice are shown in Figure 7 for a test with disbonded tape. The disbonded tape test cell had electrodes mounted at the 2.5 cm, 12.5 cm and 20 cm locations. Immediately after filling the alkaline solution into the crevice at 1 hour, the pH began to increase in the holiday as well as in the crevice. The initial pH rise to pH 10 when the alkaline solution was added is due to mixing of neutral solution in the holiday with the more alkaline fill solution. The pH leveled off at greater than pH 9 within the crevice after the 18 hour test. The potential data for this test are shown in Figure 8. The data indicated a shift in potential within the crevice which corresponds to the increased pH measured.

In order to investigate the retention of alkalinity within the crevice with fresh neutral solution in the holiday, a dripping reservoir was added above the holiday. The drip rate for the experiments was fixed at 5 cc/min throughout the 34 hour test. The crevice was filled with 1M NaOH. Figure 9 shows the pH data over time with solution dripping into the holiday chamber and a test crevice opening of 0.8mm. The alkaline condition established before the test began was reduced within hours of startup, even deep in the crevice. The pH equilibrated at pH 9.5 in this test, which was terminated after 80 hours. Data are shown for the first 20 hours. The potential data for the test is shown in Figure 10. The shift of pH and potential corresponded within the crevice. The shift to more negative values occurred in the same time frame as the pH decrease. The potential data indicated that the pH shift at the rear of the crevice was from pH 13 to pH 11 and at the holiday the pH shifted from pH 13 to pH 7-8.

Discussion

Cathodic protection systems can modify the electrolyte chemistry to protect the steel surface from corrosion in addition to polarizing the steel into a protective potential regime. Two benefits were observed: (a) an increase in alkalinity at the holiday, followed by transport of hydroxyl ions beneath the disbonded coatings and (b) the deaeration and reduction of dissolved oxygen in the solution within the crevice. Under these conditions, a low corrosion rate will be maintained.

The increase in hydroxyl concentration is due to the electrochemical reduction of oxygen in solution, followed by the reduction of water and is governed by the general reaction:

$$O_2 + 2H_2O + 4e^- \rightarrow 4OH^- \qquad (1)$$

Polarization tests showed that the free corrosion potential of the steel shifts to significantly more positive values as the pH was increased above pH 9. Also, corrosion coupon tests showed a decreased corrosion rate above pH 9.

All experiments performed in the generation of alkalinity experiments showed an increase in alkalinity to pH 10 or greater during the test period. The results also showed that the applied potential did not penetrate deeply into the crevice. The crevice was not polarized to the potential at the holiday. Since no difficulty was encountered in polarizing the holiday, modification of the environment did not require polarization current down the crevice.

If the rear of the crevice is to be protected, the alkalinity generated at the holiday must be transported into the crevice and/or local processes within the crevice must alter the environment. The alkalinity from the holiday was transported down the various crevice geometries to protect the steel beneath the tape and the local reduction of dissolved oxygen also increased the pH. Protective pH values of greater than '2 were measured in many tests with the insitu pH electrodes and verified manually by pH paper measurements after testing. Visual observation of the steel plates after test completion showed samples free of significant corrosion, even at the rear of the 25-30 cm long crevices.

It is possible to generate increased alkaline conditions at a holiday in a coating, and this alkalinity will move beneath the disbonded regions of the coating. The hydroxyl ions cause the local pH within the crevice to shift significantly, and the testing has shown protective conditions can be established beneath the disbonded coating.

Several issues remain to be investigated with respect to the changes in local conditions beneath disbonded coatings. Further testing will examine several other important variables such as temperature, effects of prior corrosion products and crevice geometry. Tests will be run at 50 and 60°C to determine if significant differences exist under these conditions.

Wet/dry cycles beneath disbonded tape are an important issue. With an increase of oxygen during air exposure. It is anticipated that any magnetite corrosion products on the steel surface will oxidize to hematite. After rewetting, the corrosion reaction will cause the solution to deaerate and the hematite to transform back to magnetite. In order to investigate the changes in corrosion products and their effects on the generation and movement of alkalinity, two approaches will be used. First, the crevices in the test cells will be filled with predetermined corrosion products. The effects on generation and movement of alkalinity will be measured under these conditions. To quantify the changes in the corrosion products themselves, samples of the post test corrosion products will be analyzed using X-ray Photoelectron Spectroscopy (XPS) and Fourier Transform Infrared Spectroscopy (FTIR).

Further work willl investigate the processes which control the solution chemistry beneath a disbonded coating section. The work will examine the relationship and effects of chemical and electrochemical reactions and transport, hydrolysis, generation of corrosion products on the steel surface, consumption of oxygen, precipitation of calcareous deposits as well as the effects of soluble gases. Coating interactions such as permeability by gases and water as well as organic and inorganic species will be considered.

Summary

The corrosion of steel and the effectiveness of a cathodic protection system is determined by the chemistry and electrochemistry near the steel surface. Much of the prior work has emphasized the determination of potential by measurements and predictive modeling. In addition to the work described above in which the solution pH was monitored under CP conditions, further work will continue to examine the changes in solution chemistry simultaneously with potential measurements beneath crevices. The results of these tests will provide useful information for development of improved coatings, surface treatments, and CP technology. As models for the cathodic protection of pipelines become more sophisticated, a knowledge of the local chemical and electrochemical conditions at holidays and disbonded areas becomes essential. Similarly, knowledge of these conditions is essential to the rational estimation of the conditions present and the expected life of pipelines.

The results of this research project demonstrated the feasibility of protecting a steel substrate beneath unbonded and disbonded coating. The theoretical concept for corrosion transport beneath disbonded coatings is to apply sufficient current to the pipeline to modify the corrosive

environment at the holiday and to reduce the corrosion rate of steel to acceptable levels. Two beneficial modifications were (a) to increase the alkalinity of the environment and (b) to decrease the concentration of oxygen in the environment.

The results demonstrate that beneficial changes occur to decrease the corrosion of steel by the local generation of alkalinity and the transport of alkalinity with and without external polarization of the steel. Where the solution is trapped and there is little or no exchange with fresh solution, the corrosion rate of steel can decrease rapidly and remain at low values. Where exchange of solution (flow of water beneath the coating) can occur, a frequent or continual generation of alkalinity by external polarization may be required.

Planned work will identify other critical areas of research. Also, the work will increase the electrochemical database for steel under cathodic protection, This will aid efforts to create more sophisticated models of the system. Also, the knowledge base used to make decisions regarding monitoring of CP systems and useful life assesments of the pipelines will be enhanced.

Acknowledgements

References

1. R.N. Parkins, A.J. Markworth,, J.H. Holbrook, and R.R. Fessler, , Corrosion Vol 41, No.7, (1985) p389-397
2. A.C. Toncre, and N. Ahmad,.., Materials Performance, p. 39-43 June (1980).
3. M.D. Orton, Materials Performance, p. 17-20 June (1985).
4. A.C. Toncre, Materials Performance, p. 22-27, August (1984).
5. B.W. Cherry, and A.N. Gould, Materials Performance, p. 22-26, August (1990).
6. R.R. Fessler, A.J. Markworth, and R.N. Parkins, Corrosion Vol 39, No.1, p. 20-25, (1983).
7. R.N. Parkins, A.J. Markworth, J.H. Holbrook, and R.R. Fessler, Corrosion Vol 41, No.7, p389-397, , (1985).
8. N.G. Thompson, and T.J. Barlo, 1983 International Gas Research Conference Proceedings, p274-283, 1983.
9. K. Fink and J.H. Payer, Corrosion'93, Paper #93578 (Houston, TX NACE, 1993).
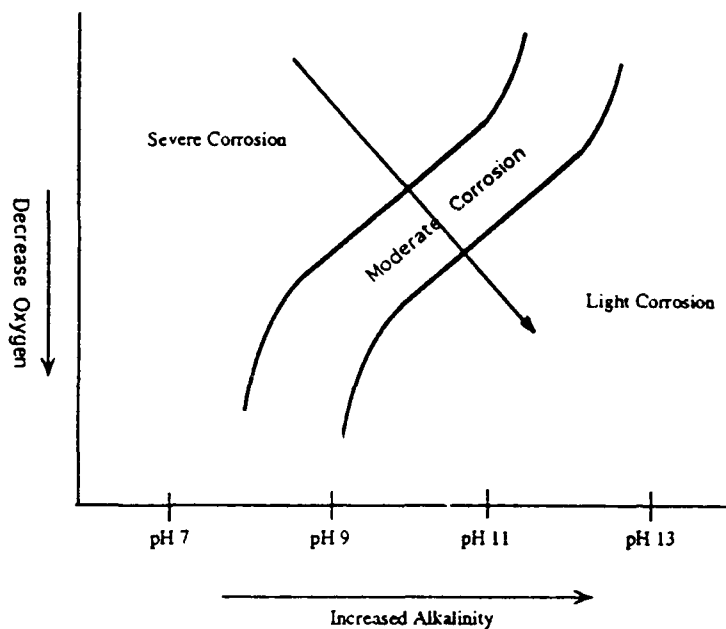
Figure 1 - Modify the Corrosion Environment
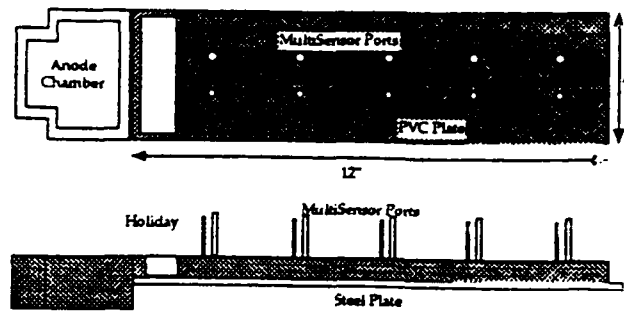
Figure 2 - MacroCell for Study of Chemical and Electrochemical Changes beneath Disbonded Tape Section
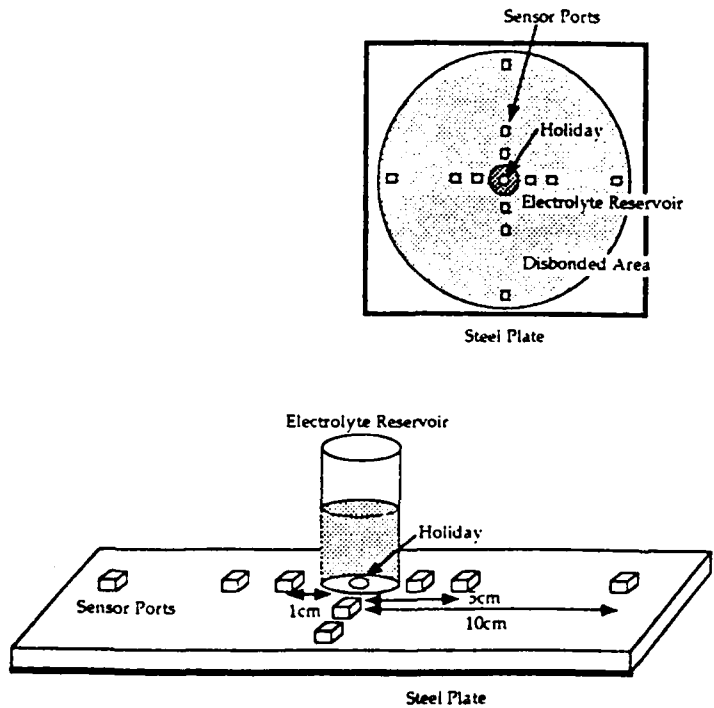
Figure 3 - MicroCell for Studying Chemical and Electrochemical Changes Beneath Disbonded Tape
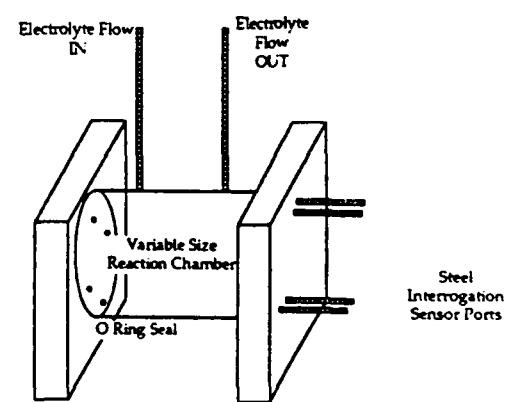
Figure 4 - Flow Through Cell for InSitu Steel Polarization and Monitoring Chemical Changes.
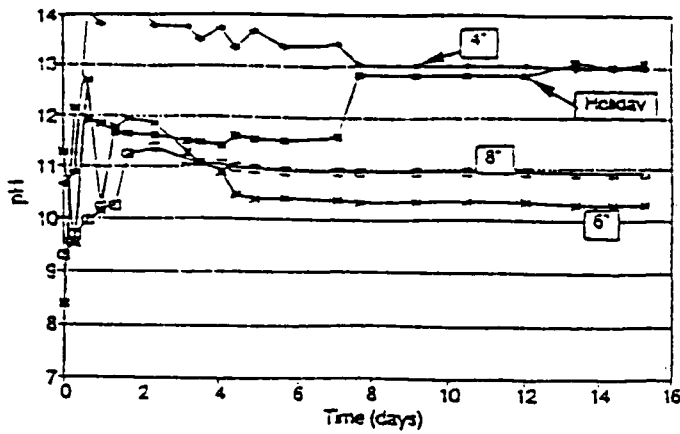
Figure 5 - Generation and Migration of Alkalinity; 30cm x10cm x 0.8mm; -1.000 V-SCE applied; pH plot;.
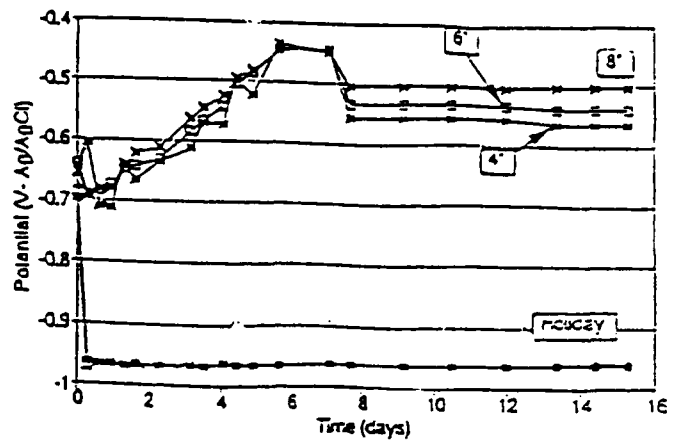
Figure 6 - Generation and Migration of Alkalinity; 30cm x10cm x 0.8mm; -1.000 V-SCE applied; potential plot.
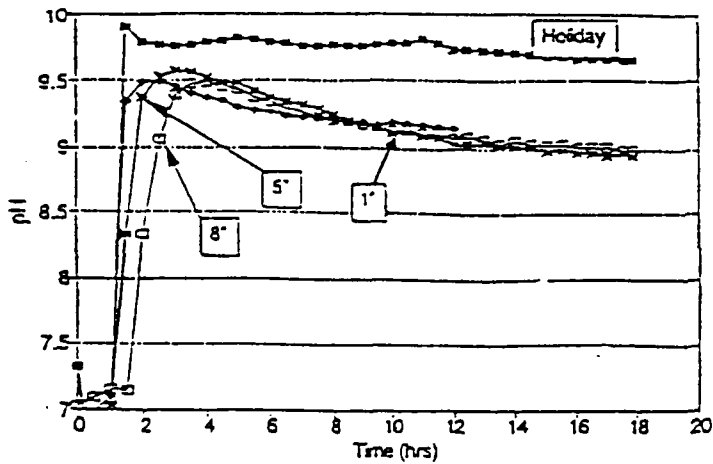
FIGURE 7 - Migration of alkaline solution into neutral crevice; 30cm x 10cm disbonded tape; pH plot.
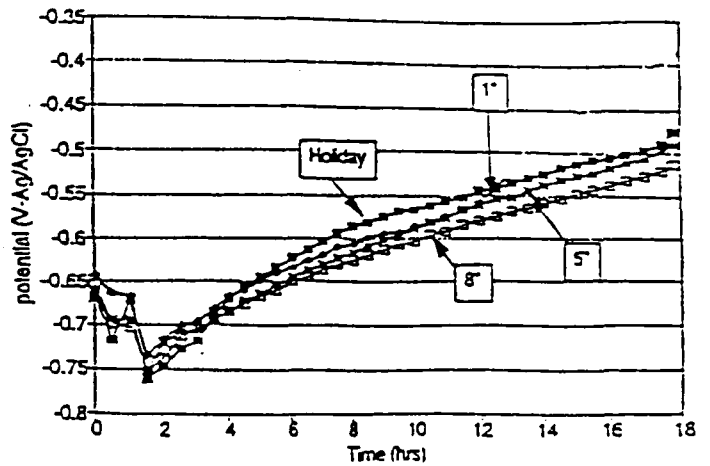
FIGURE 8 - Migration of alkaline solution into neutral crevice; 30cm x 10cm disbonded tape; potential plot.
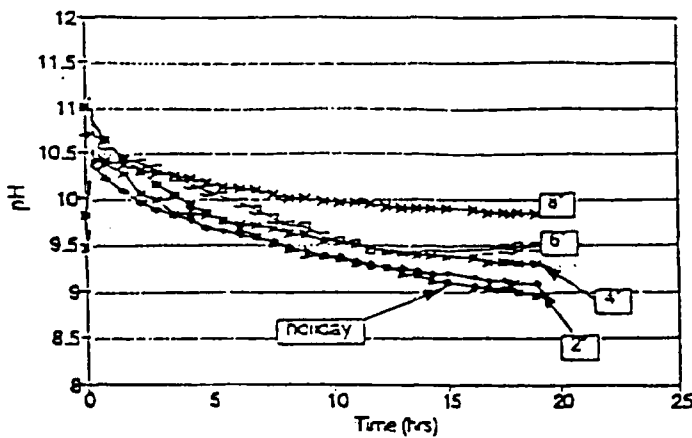
FIGURE 9 - Migration of dripping neutral solution into alkaline crevice; 30cm x 10cm x 0.8mm; pH plot.
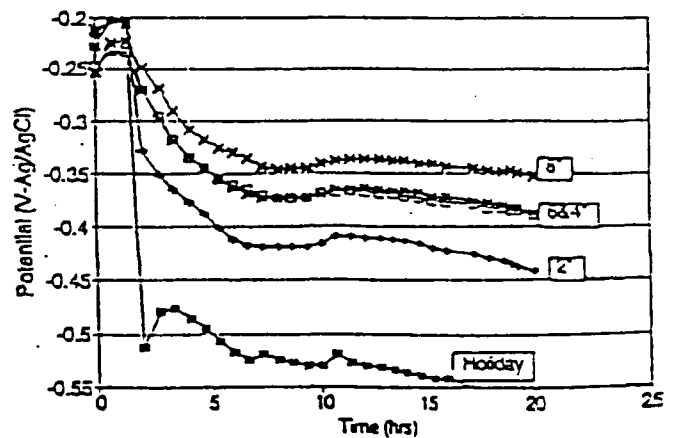
FIGURE 10 - Migration of dripping neutral solution into alkaline crevice; 30cm x 10cm x 0.8mm; potential plot.

PIPELINE INSPECTION AND REHABILITATION
An Overview

Garry Matocha
Corrpro Companies, Inc.
P. O. Box 100
Spring, Texas 77383

Abstract

A pipeline system is capable of operating for an indefinite period of time provided it is properly maintained. In most instances, government regulations dictate specific maintenance standards but do not detail how they should be met. This paper describes several inspection techniques developed by industry to determine the condition of the pipeline, as well as methods that have been developed to resolve any problems found. These inspections techniques include close interval pipe-to-soil surveys, bell hole inspections, hydrotesting and the running of smart pigs. The results of one or more of these inspection techniques dictate whether remedial actions such as additional cathodic protection or recoating is necessary.

Introduction

The leading oil and gas pipeline companies in the United States operate over 630,000 miles (1,013,670 km) of pipeline consisting of natural gas transmission (361,000 miles or 580,850 km), liquids pipelines (179,000 miles or 288,011 km)), and gathering pipelines (90,000 miles or 144,810 km). These pipelines represent an investment of over $52.5 billion and generated operating revenues in excess of $46.6 billion in 1991.[1] Therefore, there is a large incentive for the pipeline industry to properly operate and maintain their systems. In addition to the obvious economic factors, regulatory and environmental concerns throughout the world have also become major factors when decisions are made concerning the pipeline systems.

Due to the economic, regulatory and environmental factors involved in operating a pipeline system, it is necessary and often required by government regulations that the pipeline systems be inspected to determine their integrity. It is estimated that over 50% of the above mentioned pipelines are over 40 years old, therefore, there is no inspection technique which will be suitable for all circumstances.[2] However, a combination of techniques can provide the pipeline operator with information to make an intelligent decision regarding the appropriate actions to take to correct any deficiencies found.

Based on the results of the inspection, follow-up action may often need to be taken to correct any deficiencies found. These actions could involve additional cathodic protection or recoating. In 1993, it has been estimated that such remedial action will result in over 2,600 miles (4,183 km) of pipeline (United States only) being either repaired, replaced, or rehabilitated at a projected cost of $342 M.[3]

Justifications for Inspection and Rehabilitation

Pipelines are primarily protected from external corrosion by first coating the pipeline and then using cathodic protection to protect any bare areas or holidays on the pipeline. However, over a period of time the coating may lose its integrity and fail to provide the protection for which it was intended. As this happens, the amount of cathodic protection current needed for adequate protection increases. In some instances the coating will disbond from the pipe and shield the cathodic protection from the pipe surface. Because of the economic, environmental and safety consequences of a failure a prudent operator should have an inspection program in place to determine the pipeline's condition and its suitability for service.

Economically a dependable delivery system is essential. It has been estimated that in 1991 the top pipeline companies in the US moved over 43.081 Tcf (1.22 Tcm) of natural gas and 12.5 billion barrels of liquid product. This translated into an operating income of over $5.3 billion.[4] Therefore, with this tremendous amount of money involved, it is easy to see why prudent operators should be concerned about the condition of their pipeline system.

In addition to economic concerns, safety, regulatory and environmental issues have become very important in determining how companies operate. In many areas, the pipeline right-of ways were in rural areas 30 years ago but are now part of the yards of many suburban homeowners The results of a pipeline failure could now be catastrophic.

Regulations within the United States and Canada are pushing the pipeline companies toward even greater use of internal inspection tools. In October, 1988 the US Congress passed the Pipelines Safety Reauthorization Act law requiring the Department of Transportation's Research and Special Programs Administration (RSPA) to establish minimum federal safety standards so that all new and replacement pipelines would be able to accommodate smart pigs. In 1992, the new reauthorization of the pipelines safety law allowed the Office of Pipeline Safety to require transmission pipelines be modified to accommodate smart pigs. A recent General Accounting Office report stated that "Due to the effects of corrosion over time, pipelines tend to have more ruptures and leakage as they age. These incidents can result in fatalities, injuries and property damage. Considering smart pig's potential to improve pipeline safety, RSPA needs to complete the mandated feasibility study and regulations."[5]

In Canada the Canadian Standards Association has established standards for smart pigging of hazardous liquids pipelines and natural gas transmission pipelines. The Canadian National Energy Board intends to adopt these standards this year to make them enforceable as regulations on smart pig inspections.

Worldwide, countries are becoming more environmentally aware and are requiring pipeline operators to take on additional responsibilities to insure the integrity of their systems. Even in remote areas, the consequences of a hazardous liquid spill can be very great due to the environmental havoc it can create. The effects of such a spill can be even further magnified if the spill should get into a body of water. A river or stream can expand the area effected and bring the consequences into the public eye even further.

Inspection Techniques

Determining the suitability of a pipeline for continued operation and/or rehabilitation may require a variety of inspection techniques. They consists of:

* Close Interval Surveys (CIS)

* Bell Hole Inspections

* Hydrotesting

* Smart Pigging

These techniques complement each other and do not preclude the use of the others. Each technique can provide a piece of information on the condition of the pipeline which an operator can use to prioritize line segments for rehabilitation. Pipeline operators are then able to direct their resources to those critical areas where the probability of failure is the greatest.

Close Interval Surveys.

Close interval pipe-to-soil surveys involve taking a reading at 2.5 foot (0.76 meter) increments with the data and distance being recorded on a field computer. These surveys allow the pipeline operator to evaluate the level of cathodic protection and to locate anomalies in the potential profile that can be caused by:

* Coating Defects

* Localized Soil Conditions

* Foreign Contacts

* AC/DC Interference

* Current Shielding

When evaluating the level of cathodic protection it is necessary to consider all voltage (IR) drops in the circuit including those caused by current flow through the soil and along the structure. These IR drops should be compensated for when determining the polarized potential of the structure and evaluating the level of corrosion protection. This is particularly true in the case of buried pipelines when the reference electrode is placed at a distance from the point of electrical connection to the pipeline during the close interval survey.

The most common method involved in eliminating the IR drop in the readings involves installing electronically synchronized current interrupters in all the cathodic protection rectifiers affecting the area under test. The Instant Off potential is recorded, which, when all current sources are off, is equivalent to the polarized potential of the pipeline. The interrupters continuously switch the rectifiers on and off during the survey at cycles determined by the operator. The on/off cycle frequently used is a 3:1 ratio. This results in a saw tooth type graph showing both the on and off potentials on the same graph (Figure 1). The appropriate on/off ratio must be used so that an instant off potential can be determined but also a short enough interval so that the pipeline is not allowed to depolarize.

A variation of the standard CIS survey involves taking remote (side drain) potential readings at the same time the over the line potentials are being obtained. The remote readings are taken ten to twelve feet (three to four meters) perpendicular to the over the line readings. The difference between the two potential readings is automatically recorded in the field computer. The resultant graph has two separate lines. The first set of data shown is the on/off potential readings taken during a conventional survey. The second set of data shown is the difference between the over the line and the side drain readings. The differential data will remain fairly constant for a well coated pipeline. If there is a holiday in the coating, there will be a peak in the line showing the difference between the two potentials (Figure 2). This is a result of the increased current flow to the location from the cathodic protection system. Both the on/off and the side drain readings are used in order to differentiate between holidays and metal objects which may be in the immediate vicinity of the pipeline. This type of survey has proven to be very successful in locating holidays not only on older lines but in locating holidays during the commissioning of new pipelines.

Bellhole Inspections.

A limitation of the CIS survey is that it can only determine the condition of the pipeline coating and measure the level of cathodic protection on the line. It cannot determine the integrity of the pipe. Bellhole inspection is the only method available for the operator to visually confirm the condition of the coating and the condition of the pipe surface. Locations which are likely candidates for bellhole inspections include:

* Areas with low pipe-to-soil potentials

* Areas with possible coating damage.

* Areas of low soil resistivity

* Areas of possible corrosion determined by smart pigging.

* Areas with interference problems.

Although bellhole inspections are the best method of determining the condition of the pipeline, only a small percentage of the pipeline is inspected at any one time because of the costs involved. It is also very difficult or impossible to perform bellhole inspections through wetlands, swamps or other continuously wet area. In addition, pipelines running through cities and other urban areas are becoming increasingly difficult to inspect because of the right-of-way limitations.

Hydrotesting.

Hydrostatic testing is used and often required on pipelines to substantiate the maximum operating pressure, to locate any potentially hazardous leaks or to uprate the operating pressure on a pipeline. More companies are now hydrotesting their older pipelines to simply verify the integrity of the line by detecting and destructively removing all defects on the pipeline. The hydrotest pressure is determined by the operator and is often related to the maximum operating pressure and to the specified minimum yield strength of the pipe. The US Department of Transportation requires that new pipelines be hydrotested from 1.1 to 1.5 times its maximum operating pressure depending upon the population density along the pipeline.

Hydrostatic testing of pipelines has been used for many years to test pipelines. Companies have become very proficient with the testing and are able to monitor the test pressures and the factors affecting the test through the use of computers. It is a good method of certifying to the operator the immediate pressure-carrying capacity of the pipeline. It is also the only means capable of assuring the integrity of the pipeline against cracking such as fatigue-crack growth or stress-related cracking. However, it does not locate any anomalies which do not fail. It is possible for very deep pitting to survive the test and then to develop into a leak shortly after a test.

Smart Pigging.

Smart pigging of a pipeline is used to detect anomalies such as corrosion, dents or gouges in the pipe wall. There are various types of pigs used for in-line inspection. The three types of pigs used for determining the wall thickness of pipelines include the low resolution magnetic-flux pig, the high resolution magnetic-flux pig, and the ultrasonic pig. These pigs are the most accurate and economical tools available to determine the metal loss along a pipeline segment. A recent GAO report has concluded that the widespread use of smart pigs could save lives and protect property by improving the safety and reliability of pipelines.

The magnetic leakage technique is able to survey pipelines in either gas or liquid service. This is done by inducing a magnetic flux into the pipe wall between two magnets. Any metal loss which occurs in the wall results in the flux lines being distorted; this distortion is sensed by a detector, which then generates an electrical signal, indicating metal loss. These signals are passed through microprocessors and the resulting data is stored for detailed analysis upon completion of the run.

The low resolution tools are able to provide an accurate count of the number of corrosion damage sites, their location, and an approximate indication of the length and depth of damage. They do this by grouping sensors to form inspection bands. The sensor data is stored in analog form and a graphical report is generated upon completion of the survey. It is then necessary to interpret the data so as to determine the location and size of the defects found. Because the data obtained from the smart pig is relative and not absolute, the defects are graded by categories such as light, moderate or severe.

The high resolution tool is similar to the low resolution tool but improvements were made in the resolution as a result of microelectronics advances made in the 1980's. One of the results of these developments was the reduction in the size of the sensors while their number increased. This was necessary because the smaller the sampling area of the sensor the greater the resolution of the data. The large amount of data gathered from the increased number of data channels also required significant advances in data storage and processing. This is typically done by digitizing the data and storing it on a data tape prior to it being processed. The additional data available makes it possible for the pigging companies to provide the pipeline companies with a comprehensive report on the status of the pipeline. It is now possible through the use of a personal computer to scan the length of the pipeline and zoom in on suspect areas or individual defects of particular interest. It is also possible to accurately size the defects and make a determination to allow the operator to calculate the failure pressure for each corrosion damage feature. This has given the high resolution tool the following advantages over the low resolution tool:

* It can give the operator an accurate baseline condition of his pipeline.

* The data gathered is sufficient to develop long term maintenance plans.

* Corrosion growth rates can be determined from subsequent inspections.

* The number of correlation digs and subsequent repairs can be minimized.

* Environmentally sensitive areas or those with limited access can be inspected with minimal damage.

The disadvantage to the high resolution tool is that the cost is 2 to 4 times greater than the low resolution tool. Also, because the data must be processed, immediate data analysis is also not always available. These factors must be factored in when deciding which type of tool is appropriate for an operator's pipeline inspection program.

The most accurate of the inspection tools is the ultrasonic pig. It has a greater number of sensors than even the high resolution tool and each sensor measures the wall thickness and continuously records the sensor stand-off. This allows the tool to easily distinguish between internal and external corrosion, since the stand-off function will not respond to external defect but will fully display internal defects. The measurements are acquired at sufficiently small intervals, so that the pipe wall is mapped like a contour map. Also because the pipe wall thickness is being measured directly, corrosion in and around the girth welds can be more effectively picked up than with the magnetic flux tools.

The data from the numerous sensor channels are assessed and condensed by a multi-microprocessor system and then stored on digital tape. The ultrasonic pig, like the magnetic flux pigs, carries several odometer wheels to measure distance, a marker system to provide additional zero points for distance measurement, a method for determining circumferential orientation, and a master system to pre-program and monitor the survey run. This entire system is typically powered by a lithium battery system.

The data from the ultrasonic pig is interpreted with a personal computer. Defects can be displayed on the screen in graphical format to aid in interpretation. Three dimensional representations of the defects are often available.

The quality of ultrasonic data is superior to the high resolution tools but the inspection costs are also higher than the cost of a high resolution tool run. Also, the tool can only be run in a liquid line or within a liquid slug because a couplant is needed for this technique. Therefore, the pipeline operator must make a cost-benefit analysis as to whether the quality of data is worth the additional costs.

It has to be recognized that the smart pigs are only looking for changes in the pipe wall thickness, are not able to directly determine the condition of the coating or the level of cathodic protection along the pipeline. Also, no inspection tool is 100% accurate and it is always possible that an unidentified defect may remain on the line.

Rehabilitation Techniques

Using the results of the various inspection techniques, the pipeline operator should be able to determine next course of action. The most drastic action an operator can take is to replace the portion of pipe which no longer meets the required safety criteria. However, in the majority of the cases, rehabilitation of the pipeline can often be done economically to extend the operating life of the pipeline system. The appropriate method of rehabilitation is often dictated by the condition of pipeline coating and the amount of corrosion present in the bare areas. The two methods primarily used for rehabilitation are additional cathodic protection and/or recoating.

Cathodic Protection

Additional cathodic protection is needed if the pipeline coating has deteriorated to the point where the cathodic protection levels as defined in NACE Standard RPO-169-92 are no longer adequate to protect the pipeline. On those areas with low pipe-to-soil potentials and no extensive corrosion, additional cathodic protection is often the answer. This additional protection can be achieved through the use of sacrificial anode systems, impressed current systems, or conductive polymer anode systems.

Sacrificial Anodes Systems. These systems are most often used where the cathodic protection current demands are small. This is often the case for well coated lines, small diameter lines, or for localized hot spots. The anodes are typically made of either a magnesium alloy or zinc. These anodes are often used because of their relatively low cost, low maintenance and because they do not need a source of electrical power. However, they are limited in their current output and their service life is dependent upon the quantity of anode material.

Impressed Current System. These systems are used where the cathodic protection current demands are very large or a single point source is desired for long lengths of pipeline. The current output can be controlled and is limited only to the capacity of the source of power. Many different types of anode materials can be used as anode material such as graphite, silicon iron and mixed metal oxide.

One of the main drawbacks of impressed current systems is the fact that access to electrical power is often limited. In such cases solar powered units are used. The amount of current available from these units is limited by the amount of solar panels that can be erected on the site. At night or during cloudy periods batteries which are charged during the daylight hours are used as the power source. A system has even been developed whereby magnesium anodes are used in the system to provide the necessary cathodic protection current during the night, thus, not allowing the line to depolarize.

Conductive Polymer Anode Systems. In areas where it is hard to get good current distribution or where there are concerns with hydrogen overvoltage, a conductive polymer anode system can be used. The polymeric cable is simply plowed in over or next to a pipeline with a coke breeze backfill. To further assist in current distribution, the positive lead from the rectifier can be laid in the ditch above the coke backfill and tied into the anode cable at various locations. The costs for this system are normally greater than a typical impressed current system but less than those for recoating the pipeline.

Recoating

Pipeline recoating becomes an alternative to cathodic protection where additional cathodic protection is no longer economical or where shielding is a problem. Shielding results when the coating disbonds from the pipe but "shields" the cathodic protection current from reaching the pipe.. This can lead to severe corrosion or even stress corrosion cracking.

The pipeline recoating process can be broken into five parts:

* Coating Selection

* Cleaning

- Blasting

- Application

- Inspection

Coating Selection. Selecting a suitable coating to recoat a pipeline in the field is often a series of compromises. Preferred coating systems for new pipelines such as fusion bond epoxies and extruded polyethylenes do not lend themselves to field application. Some of the factors which affect the coating selection are:

Weather
- Rain
- Wind
- Temperature
- Humidity

Logistics
- What is the length of pipe to be recoated?
- Is the pipe to be recoated in the ditch or cut and taken out of the ditch?
- Is the pipe to be recoated while it is in service?

Coating Quality
- Cathodic Disbondment Characteristics
- Resistance to Soil Stress
- Moisture Permeability
- Resistnace to Handling Damage
- Adhension

Because of the varying factors on each operator's pipeline numerous coatings have been used for recoating. A few will be discussed briefly.

Coal tar enamel has been successfully used for many years in the pipeline industry. It is a four component system consisting of a primer, the coal tar enamel, an inner reinforcing material consisting of a glass fiber mat and an outer wrap consisting of a coal tar saturated mineral felt or a coal tar impregnated fiber glass mat. This coating has been applied in the field for many years but the lack of adequate surface preparation has led to failures of the system. It has also been found to be susceptible to soil stress.

Tape systems are probably the most common systems used for recoating. They are relatively easy to apply, typically use a primer and due not require surface preparation beyond a commercial blast. Some of the tape systems used are:

Polyethylene Tapes

Hot Applied Tapes

Shrink Sleeves

Fabric Strengthened Tapes

Although the surface preparation requirements are not as stringent for tapes as for other types of coatings, it is still a very critical factor. Inadequate surface preparation can often lead to premature failure. The failure of a polyethylene tape system can lead to shielding problems which could result in problems greater than if the pipeline was bare.

Coal tar epoxy is also a good coating which has been used for recoating purposes. It is relatively hard and has a high resistance to soil stress. However, as with most spray applied coatings, there are several areas which can hamper its use in the field.

Surface Preparation - Most of the existing coal tar epoxies require a white metal blast which can be difficult to attain and maintain in the field.

Mixing - A proper mixture of epoxy and the curing agent must be maintained.

Cure Time - Many coal tar epoxies require from 8-24 hours of cure time before they can be handled and backfilled. This often requires the company to set the pipe on skids and then to come back and coat the skid marks.

Spray applied coal tar polyurethanes have been developed and used to alleviate some of the problems associated with the cure time of coal tar epoxies. However, adequate surface preparation and mixing are still crucial.

Cleaning. Rehabilitating the pipe involves the removal of the old coating prior to recoating. The cleaning of the old pipe can be critical since the old coating may or may not be compatible with the new coating system. Several cleaning methods used are:

Manual cleaning with hammers and scrapers.

Mechanical cleaning with machines that use knives and brushes.

Water blasting with pressures from 12,000 to 30,000 psi.

Mechanical cleaning with machinery that utilizes a serieds of rotating chains.

Only the water blasting method can remove all of the old primer and surface contaminants. The amount of pressure required varies with the type and condition of the old coating.

Blasting. The preparation of the pipe surface by blasting is critical no matter what type of coating system is used. It is possible with the water blasting technique to get a near white metal surface provided the pressure is adequate (This pressure varies according to the type of coating previously on the pipe). Manual air blast systems have been used for surface preparation for many years but this method has proven to be too slow for long sections of pipe. The use of mechanical processes to provide the necessary surface preparation is a much more attractive alternative. The wheel blast system utilizes either a metal shot or grit for cleaning the pipe surface. The air blast system has also been automated for line travel purposes and uses grit or sand as a blast medium. Both systems recycle the shot or grit to reduce the amount of material consumed.

The choice of what type of machinery to use for surface preparation is partially dependent upon whether the pipeline can be taken out of service and cut into long sections. Some of the machinery must be slipped onto the end of a pipeline while others can "clam shell" onto a pipeline that is still in service or one that cannot be cut.

Application. Although it is preferable to choose the type of coating and then to determine how the coating will be applied, this may not always be possible. If a pipeline cannot be cut and taken out of the ditch, machinery must be chosen that will "clam shell" onto the pipeline. For those pipelines that can be cut and taken out of the ditch, there is a greater flexibility on the types of coating that can be applied.

Tape systems can be applied on a pipeline that is either in service or out of the ditch. For long sections of line, hand wrapping is not economical. Motor driven line travel machinery is available that can be clam shelled onto the pipeline It is possible to achieve coating rates of up to 1 mile (1.6 km) a day depending upon the type of machine used and the diameter of the pipeline

If a pipeline must be recoated in the ditch, spray applied coating are normally applied by coating applicators with spray equipment specified by the coating manufacturer. There is machinery available for spray applied coatings but the pipeline must normally be taken out of service, cut and taken out of the ditch. Machine application rates can reach 1 mile (1.6 km) a day with the limiting factors being material cure time and the machine reliability.

Unless adequate padding is provided under the skids, the pipe should be lowered into the ditch and buried as soon as possible. This is because air temperature changes will cause the pipe to move and could possibly cause holidays at the skid locations.

Inspection. An operator must have the proper procedures in place throughout the process to insure an adequate recoating job. These procedures should include having an inspector (in-house or third party) on the job to insure that the specifications were followed. A failure in any part of the process could result in holidays in the new coating and eventually to corrosion problems. A set of specifications must be agreed upon by all parties involved in the rehabilitation process and provisions must be made to insure that they are followed. Provisions should be made on how to repair holidays as they will happen no matter the amount of care taken. The inspector is needed to not only provide expertise in areas that the contractor is not comfortable or unfamiliar with but also to provide a different perspective on the project.

Summary

As a pipeline system ages, decisions must be made on how best to preserve this valuable asset. Proper inspection of the pipeline will often dictate the appropriate measures to be taken. The type of inspection techniques available include close interval pipe-to-soil surveys, bell hole inspections, hydrotesting and intelligent pigging of the pipeline. Just as critical to the maintenance of the pipeline are the decisions on how to handle problems found on the line. Each particular situation will dictate whether cathodic protection, recoating or even replacement is appropriate. Ultimately the pipeline operator must make a decision as to what course of action is feasible based on safety, environmental and economic considerations.

References

1 & 4. Jim Watts, "The 12th P&GJ 500 Report, Pipe Line & Gas Journal, September, 1992, p. 12.

2. J. D. Lormand, "Pipeline Rehabilitation - A Contractor's Perspective", Proceedings of the Pipeline Rehabilitation Seminar, Houston, Texas, January, 1992, p 206.

3. Jim Watts, "US/Canada Pipeline Work Remains At High Level", Pipe Line & Gas Journal, January, 1993, p. 23

5. <u>Greater Use of Instrumented Inspection Technology Can Improve Safety</u>, General Accounting Office, GAO/RCED 92-237, September, 1992, p. 3.

Bibliography

1. General Accounting Office, <u>Greater Use of Instrumented Inspection Technology Can Improve Safety</u>, GAO/RECED 92-237, September, 1992

2. D. H. Kroon, "Electrical Surveys in Pipeline Rehabilitation", Proceedings of the Pipeline Rehabilitation Seminar, Houston, Texas, September, 1990.

3. J. D. Lormand, "Pipeline Rehabilitation - A Contractor's Perspective", Proceedings of the Pipeline Rehabilitation Seminar, Houston, Texas, January, 1992.

4. Daniel P. Werner, " State-of-the-Art in Anti-Corrosion Coatings", Proceedings of the Pipeline Rehabilitation Seminar, Houston, Texas, January, 1992.

5. Jim Watts, "The 12th P&GJ 500 Report", Pipe Line & Gas Journal, September, 1992.

6 Jim Watts, "US/Canada Pipeline Work Remains At High Level", Pipe Line & Gas Journal, January, 1993.

Pipe/Soil Potential (mv)

FIGURE 1

36+00 CROP EDGE
36+53 MARKER
36+63 CL GRAVEL RD.
36+70 MARKER
37+06 CROP EDGE

Distance (feet)
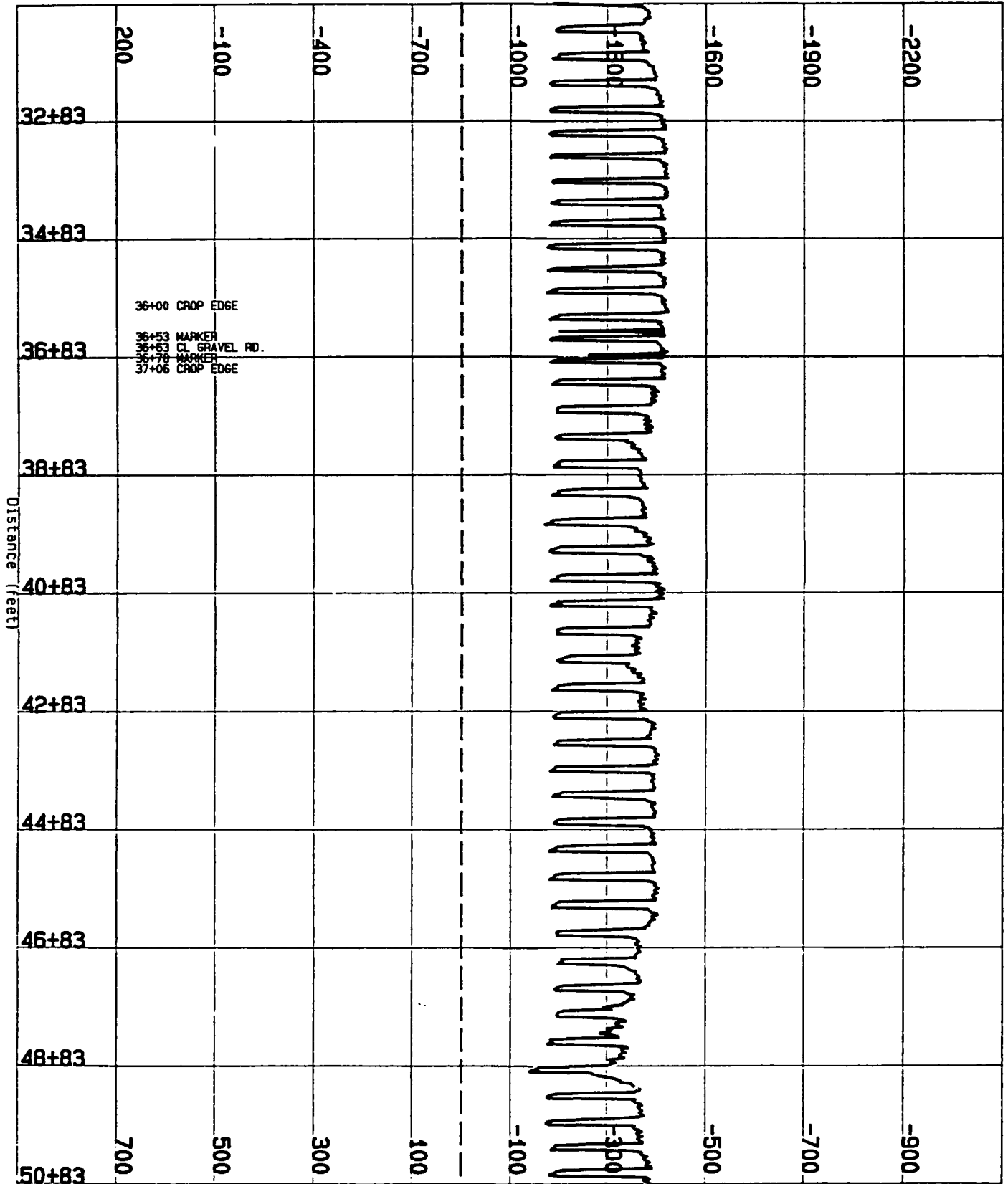
Pipe/Soil Potential (mv)
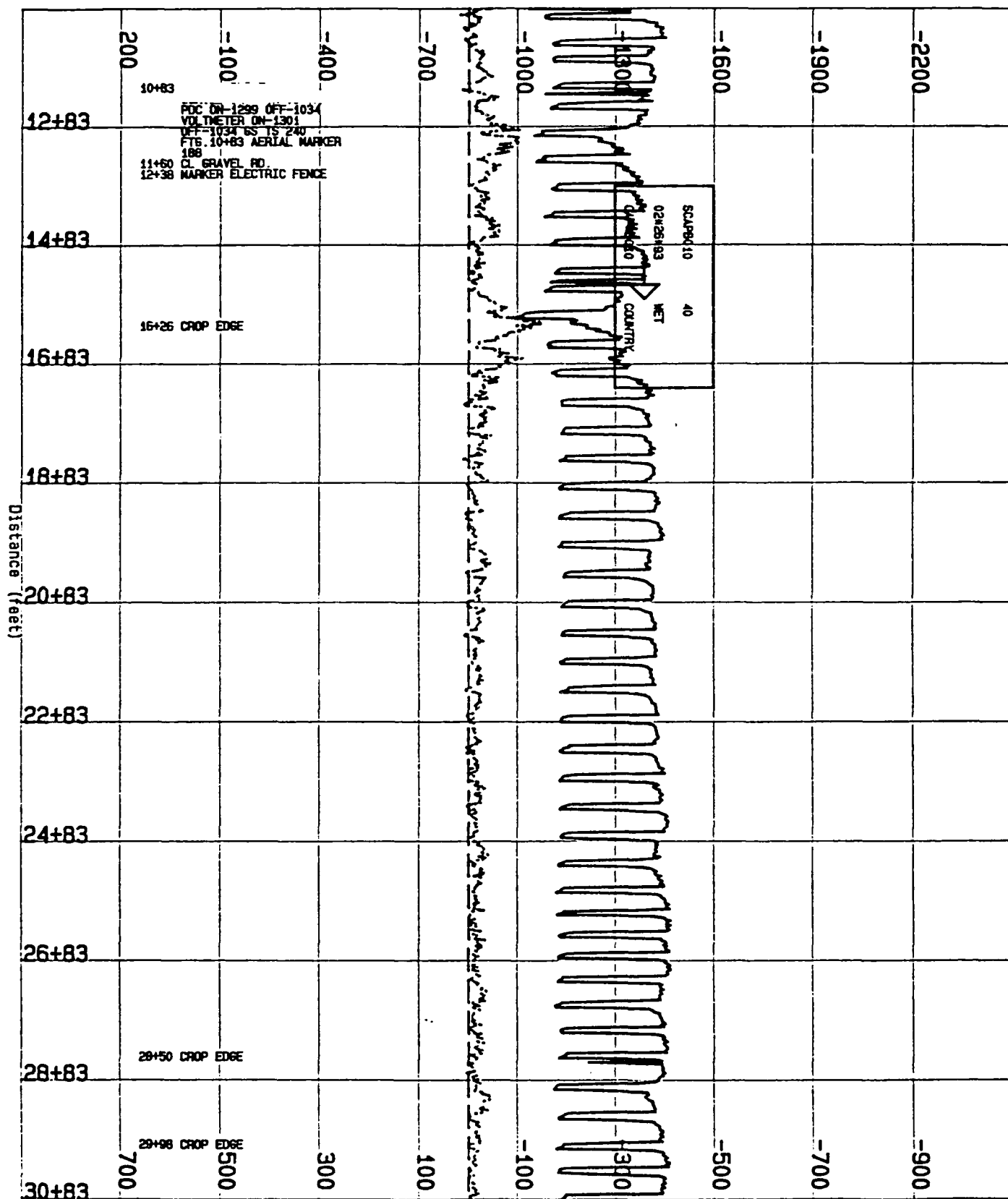
FIGURE 2

PREDICTION OF DYNAMIC CURRENT DENSITY ON CATHODICALLY PROTECTED STEEL IN SEAWATER AT DIFFERENT DEPTHS

R. B. Griffin

Department of Mechanical Engineering

Texas A&M University

College Station, Texas 77843

J.-F. Yan

Department of Chemical Engineering

North Carolina State University

Raleigh, NC 27695–7905

R. E. White

Department of Chemical Engineering

University of North Carolina

Columbia, SC 29208

ABSTRACT

A first principle mathematical model was developed to predict the dynamic current density developed on cathodically protected steel in seawater at different depths. The results show that the decrease in the current density is associated with the formation of the calcareous deposits on the steel surface. The formation rate of calcareous deposits is governed by the pH at the metal surface, which is controlled by electrochemical reactions, especially oxygen reduction. The predictions from the model showed that the formation rate of calcareous deposits is much slower in deeper water than in the water near the surface. Consequently, it would take more time to reach a steady-state residual current density in deeper waters.

INTRODUCTION

Cathodic protection has been recognized as an effective method for preventing immersed offshore structures from corroding. Under cathodic protection, the oxidation of iron can be prohibited by supplying electrons to the metal structure to be protected by means of sacrificial anodes or impressed current (1). One feature associated with the marine cathodic protection is the formation of calcareous deposits at the metal surfaces (2-4).

Calcareous deposits are the minerals precipitated on the structure's surface due to the increased alkalinity resulting from the cathodic polarization process. It is believed that these porous films act as resistant layers and reduce the transport rate of oxygen to the metal surface, where the electrochemical reactions occur. Consequently, the current density required to protect the structure is reduced.

In the first part of this research, a first principles mathematical model was presented for the formation of calcareous deposits on cathodically protected steel in seawater (5). The results from the model are helpful in understanding the mechanism of the formation of calcareous deposits on cathodically protected steel in seawater and their effects on cathodic protection systems. The model is also capable of predicting the changes in current density and composition of the deposits with time. The model has been used to examine how the physical and chemical properties of seawater and cathodic protection parameters influence the formation of calcareous deposits and their ability to lower the cathodic current density (6).

The development of offshore energy resources is rapidly moving into water depths greater than 300 meters (3). Results from Ref. (6) show that the formation of calcareous deposits is sensitive to the chemical and physical properties of seawater, which vary at depth. Whether the calcareous deposits can form in deep cold water and whether these deposits will adhere to the steel surface under high hydrostatic pressure are still unclear. Therefore, the main objective of this research is to predict the dynamic current density on cathodically protected steel at depth due to the formation of calcareous deposits.

SUMMARY OF THE MODEL

Observations from SEM pictures (5) showed the main change on the electrode surface was the increasing surface area covered by the calcareous deposits not the increasing thickness. Therefore, the model that is derived in detail in Ref. (5) is based on the fact that calcareous deposits block the active surface area available for the electrochemical reactions and consequently the current density is reduced.

The main electrochemical reactions occurring during the corrosion of steel structures in seawater are the oxidation reaction of iron:

$$Fe \rightarrow Fe^{2+} + 2e^-$$ [1]

the oxygen reduction:

$$O_2 + 2H_2O + 4e^- \rightarrow 4OH^-$$ [2]
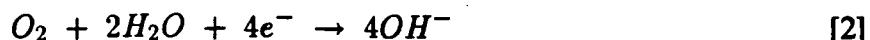
and the hydrogen evolution:

$$2H_2O + 2e^- \rightarrow H_2 + 2OH^-$$ [3]

The proposed mechanism for the formation of calcareous deposits on cathodically protected steel in seawater is presented below. The higher concentration of OH⁻ ions generated by the reduction reactions at the metal surface causes the precipitation of $Mg(OH)_2$ to occur:

$$Mg^{2+} + 2OH^- \rightarrow Mg(OH)_2 \downarrow$$ [4]
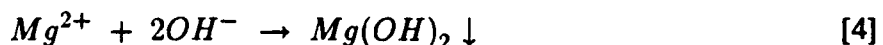
Meanwhile, the production of OH⁻ ions changes the inorganic carbon equilibria in seawater and facilitates the following buffering reaction (7):

$$OH^- + HCO_3^- \rightleftharpoons H_2O + CO_3^{2-}$$ [5]

As a result, $CaCO_3$ also precipitates:

$$Ca^{2+} + CO_3^{2-} \rightarrow CaCO_3 \downarrow$$ [6]

Diffusion, migration, and convection have been taken into consideration for the mass transfer of the components in seawater inside the diffusion layer.

The model equations will be cast in the finite difference form and solved using Newman's BAND(J) subroutine (8) with an implicit time-stepping technique to obtain the surface coverage of the calcareous deposits, the concentrations, and potential distributions throughout the diffusion layer. Once these values are known, the current density due to the individual electrochemical reaction can be determined using the Butler–Volmer equation (9–11). The details of the model were reported in Ref. (5).

RESULTS AND DISCUSSION

Before presenting the results in deep waters, a case study based on the parameters at sea level is used to explain quantitatively the mechanism of the formation of calcareous deposits. The primary driving force for the formation of calcareous deposits is the electrochemical reactions, particularly the oxygen reduction. This causes the pH in seawater to increase from 8.2 in bulk solution to 9.9 at the metal surface as shown in Fig. 1. Meanwhile, the high pH facilitates the buffering reaction and produces CO_3^{2-} ions on the electrode surface. As a result, the concentration of CO_3^{2-} ions increases about eight times higher than that in the bulk solution as shown in Fig. 2, and the precipitation rate of $CaCO_3$ is increased.

The surface area occupied by the calcareous deposits (surface coverage) was found to increase with time as shown in Fig. 3. This leads to a decreasing cathodic current density. Figure 3 also indicates that the decrease in the current density on marine structures under cathodic protection is associated with the formation of the calcareous deposits at the metal surface. After the metal surface was almost covered, the current density became nearly constant. However, the residual current density was never equal to zero due to the porous nature of the calcareous deposits.

Instead of doing experiments of growing the calcareous deposits under different environmental conditions, the model has been used to predict the dynamic current density on cathodically protected steel in seawater at different depths. The temperature, salinity, oxygen concentration, and pH at different depths in the northern half of the Gulf of Mexico were obtained from Ref. (12). The vertical changes of oxygen concentration and temperature are plotted in Fig. 4. The detailed methods of predicting depth-dependent parameters used in the modeling were reported in Ref. (6).

Figure 5 shows the computed surface coverage on cathodically protected steel in seawater at different depths. The surface coverage of calcareous deposits decreases with depth; however, below 500 m, the change of surface coverage increases with depth. As shown in the above mechanism, the formation rate of calcareous deposits is related to the pH at the metal surface, which is controlled by electrochemical reactions, especially by oxygen reduction. Since oxygen reduction is mass-transfer controlled, a higher oxygen concentration in the bulk solution leads to a faster oxygen reduction rate, which causes a higher pH at the metal surface. In the Gulf of Mexico, a minimum value of oxygen content occurs about at 400–500 m. Therefore, the predictions in Fig. 5 can be explained from the vertical change of oxygen concentration as shown in Fig. 4.

Another reason for smaller formation rate of calcareous deposits at depths is contributed to the lower temperature of the seawater, which results in an increase in the solubility constant

(K_{sp}) and a decrease in reaction constant (k) of $CaCO_3$, as shows in Fig. 6. The solubility constant of $CaCO_3$ is also influenced by the higher hydrostatic pressure.

The formation of calcareous deposits results in the decrease of the cathodic current density as shown in Fig. 7. Therefore, it would take longer time to reach a residual current density in deeper waters.

CONCLUSION

From the results and discussion, the following conclusions are presented:

1. The decrease in the current density on marine structures under cathodic protection is associated with the formation of the calcareous deposits at the metal surface.
2. The seawater pH increases from 8.2 in bulk solution to 9.9 on the cathodically protected steel surface. The higher pH causes the precipitation of $Mg(OH)_2$ to occur and also accelerates the precipitation rate of $CaCO_3$.
3. The formation rate of calcareous deposits would be expected to be smaller in deep water.

ACKNOWLEDGMENT

REFERENCES

1. M. G. Fontana, "Corrosion Engineering," 3nd. *ed.*, McGraw-Hill, NY (1986).
2. W. H. Hartt, W. Wang and T. Y. Chen, Paper No. 576, CORROSION/89, National Association of Corrosion Engineers, Houston, TX (1989).
3. K. P. Fischer and W. H. Thomason, Paper No. 577, CORROSION/89, National Association of Corrosion Engineers, Houston, TX (1989).
4. W. H. Hartt, C. H. Culberson and S. W. Smith, *Corrosion*, 40, 11, 609 (1984).
5. J.-F. Yan, T. V. Nguyen, R. E. White, and R. B. Griffin,, *J. Electrochem. Soc.*, 140, 733 (1993).
6. J.-F. Yan, R. E. White, and R. B. Griffin, "Parametric Studies of the Formation of Calcareous Deposits on Cathodically Protected Steel in Seawater," *J. Electrochem. Soc.*, will be published in May (1993).
7. A. Turnbull and D. H. Ferriss, *Corrosion Science*, 26, 601 (1986).
8. J. S. Newman, *Ind. Eng. Chem. Fundam.*, 7, 514 (1968).

9. Ken-Ming Yin and R. E. White, *AIChE J.*, **36**, 187 (1990).

10. H. Gu, T. V. Nguyen, and R. E. White, *J. Electrochem. Soc.*, **134**, 2953 (1987).

11. T. Yeu, T. V. Nguyen, and R. E. White, *J. Electrochem. Soc.*, **135**, 1971 (1988).

12. A. D. Goolsby and B. M. Ruggles, *Corrosion*, **47**, 5, 387 (1991).
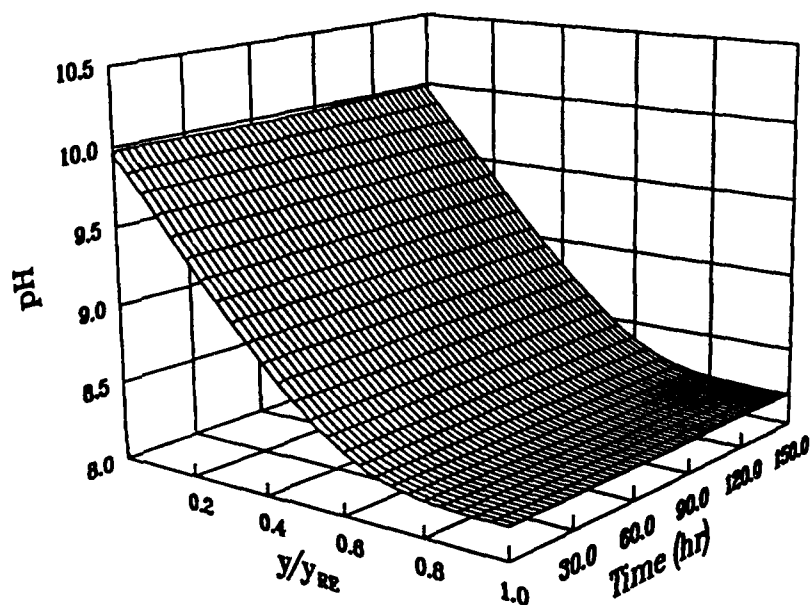
Fig. 1. Variation of pH inside the diffusion layer (y_{RE}=1.5×10^{-2} cm).
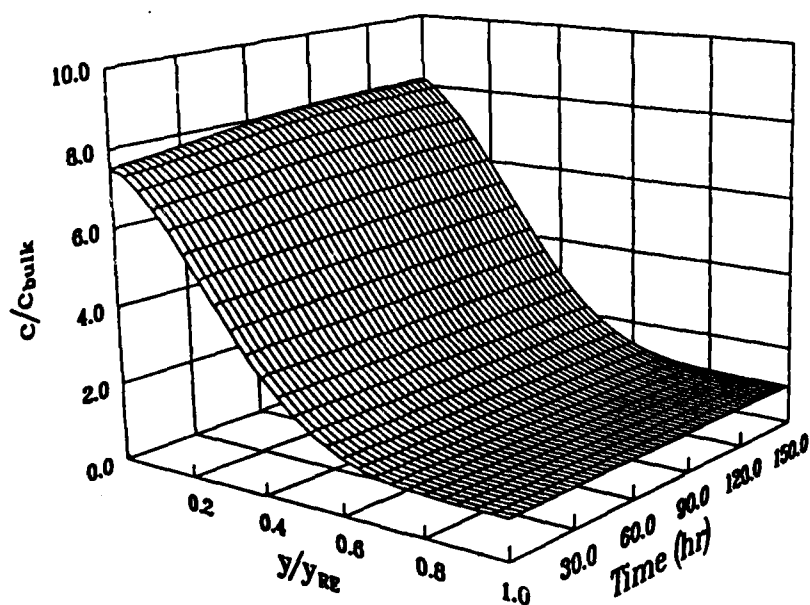
Fig. 2. Concentration profile of CO_3^{2-} ions inside the
diffusion layer (y_{RE}=1.5×10^{-2} cm, c_{bulk}=1.8×10^{-7} mol/cm^3).
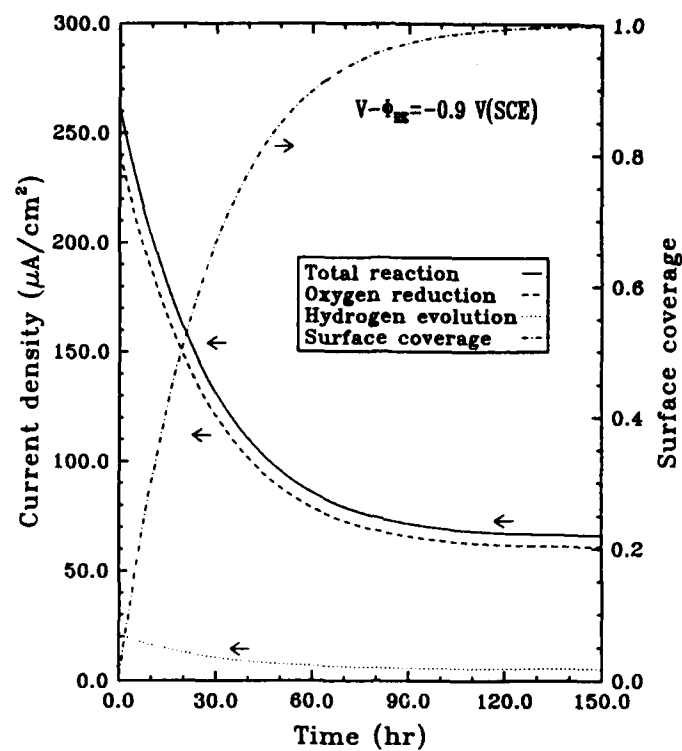
Fig. 3. Changes of current density and surface coverage
on cathodically protected steel in seawater with time.
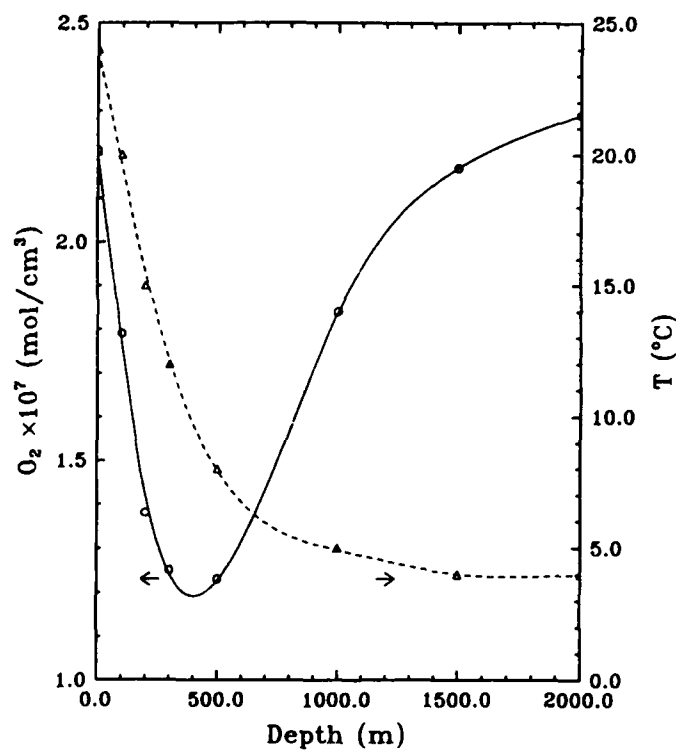
Fig. 4. The vertical changes of oxygen concentration and temperature in seawater.
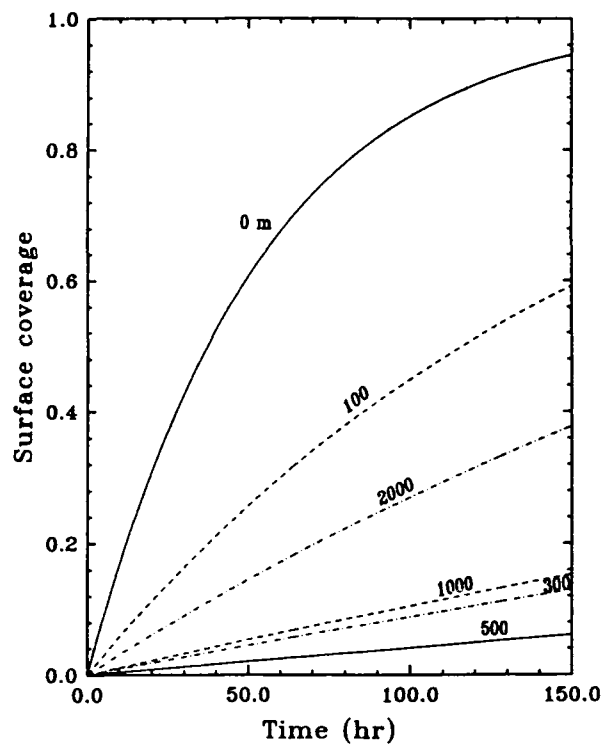
Fig. 5. Effect of depth on the change of surface coverage
on cathodically protected steel in seawater with time.
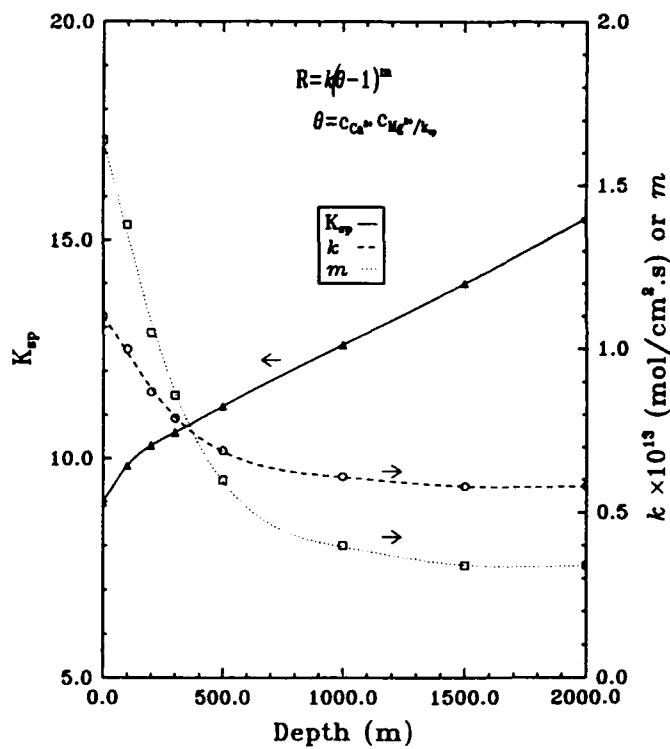
Fig. 6. Effect of depth on the change of solubility
constant, reaction constant, and reaction order of $CaCO_3$.
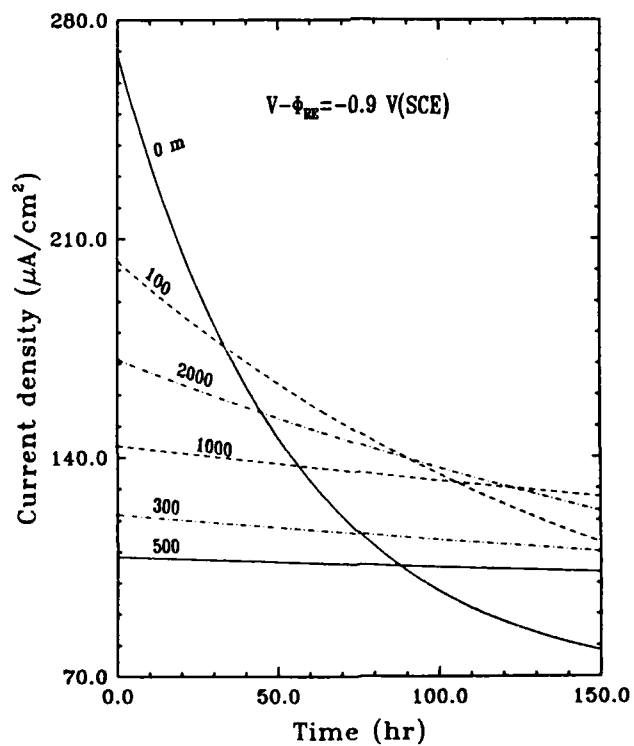
Fig. 7. Effect of depth on the change of current density
on cathodically protected steel in seawater with time.

Hydrogen Embrittlement in Steels:
Mechanical Aspects

Ruth Magdowski
Institute of Metallurgy
Swiss Federal Institute of Technology, ETH
CH-8092 Zurich, Switzerland

Abstract

Hydrogen embrittlement is the mechanism responsible for environment-assisted crackii.g of various materials such as medium and high strength steels under static or cyclic loads. The present paper illustrates some mechanical aspects of environment-assisted cracking with emphasis on stress corrosion cracking. Various testing methods are presented and the conditions for crack branching and leak before break under stress corrosion are shown.

Key terms: hydrogen embrittlement, stress corrosion cracking, crack branching

Hydrogen Embrittlement versus Stress Corrosion Cracking

Environmental degradation can be defined as the initiation and the subsequent growth of cracks under the simultaneous action of stresses and an aggressive environment. Hydrogen has been found to be the predominant embrittling and thus degrading species for various materials. The severity of environmental degradation of a material depends on the supply of atomic hydrogen generated by its interaction with a wide range of environmental conditions. Indeed, for a number of materials, e.g. medium and high strength steels, hydrogen embrittlement has been accepted to be the mechanism for stress corrosion cracking. Therefore, both concepts, hydrogen embrittlement and stress corrosion cracking, can be interpreted and treated as the same process which is affected by at least three different groups of parameters: metallurgical, environmental and mechanical. Out of these groups, this paper concentrates on the effect of various mechanical aspects that influence hydrogen embrittlement and/or stress corrosion cracking.

Loading Modes and Environmental Cracking

There are two extremes of a continuum considering the applied loading mode which may cause environmental cracking in an aggressive environment: the sustained load yielding pure stress corrosion cracking and cyclic load yielding pure corrosion fatigue. It is impossible to draw a strict boundary between these two extremes, as indicated in Figure 1. The transitions between load wave shapes underlying stress corrosion cracking and corrosion fatigue are illustrated. It is obvious that there exist load wave shapes which clearly would cause stress corrosion cracking and there are load wave shapes which clearly would cause corrosion fatigue. However, in addition, there are loading modes which could cause either stress corrosion cracking

or corrosion fatigue, such as, for example, ripple effects and large start-stop cycles which are common and known to adversely affect the growth of environment-induced cracks. Some elements of the latter loading modes are frequently encountered on various components in service. Often, however, the stresses responsible for stress corrosion cracking are not service stresses but residual stresses originating from various sources, for example the production or manufacturing process.

Figure 1 also shows possible ways of testing and quantifying the susceptibility of a material to environmental cracking. Starting with sustained loads, one can distinguish between the testing of smooth and precracked specimens exposed to the environment. For smooth specimens, time-to-failure curves are measured in a given environment. As a matter of fact, by using this testing method, often the crack incubation time is consuming the major part of the specimen life time. Therefore, a more conservative way of testing is to measure the stress corrosion crack growth rate of a precracked specimen as a function of the applied stress intensity. The result of such tests are stress corrosion crack growth curves ($\Delta a/\Delta t$ versus K curves) which are characterized by a threshold value K_{ISCC} below which no crack growth is observed and a characteristic shape of the curve, often revealing a plateau-region where the crack growth rate is independent of the applied stress intensity. More details will be discussed later in this paper.

Another way to investigate and to present the stress corrosion properties of a material is to perform slow strain rate tests or constant extension rate tests. Here, smooth or notched tensile specimens are pulled apart slowly in an aggressive environment. Two different effects of the applied strain rate on stress corrosion resistance are observed, as indicated by the two curves in the respective diagram of Figure 1. Depending on the material/environment combination, extremely low strain rates may cause high susceptibility to stress corrosion cracking, e.g. there is time enough for the environment to degrade the material by forming cracks. At the same low strain rates, however, a different material/environment combination may show very good stress corrosion resistance because the material passivates continuously at locations where bare metal is produced by straining. At higher strain rates, however, passivation cannot be completed rapidly enough, therefore the susceptibility to stress corrosion cracking increases. At even higher strain rates, there is not enough time for the environment to affect the material, thus no environmental degradation is observed. Slow strain rate testing is a typical situation between true stress corrosion cracking and true corrosion fatigue: the load is slowly increased. This can also be interpreted as one half of a fatigue cycle at extremely low frequency.

True corrosion fatigue is measured by applying cyclic load on either smooth or precracked specimens. In the former case, the number of cycles to failure under a given stress range is measured. This number is usually considerably smaller when - at a given stress level - an aggressive environment is present. Fatigue and corrosion fatigue crack growth is illustrated in Figure 1. Here the fatigue crack growth rates are plotted as a function of the applied cyclic stress intensity range. The environment typically increases the propagation rates in the linear range of the log $\Delta a/\Delta N$ versus log ΔK plot compared to inert environment. This effect is frequency dependent, due to similar reasons as for slow strain rate loading. In summary, Figure 1 gives a systematic overview of the various aspects of loading and environmental cracking, the two extremes being stress corrosion cracking and corrosion fatigue, respectively.

The Effect of Stress Intensity

Stress intensity may have a major effect on the growth of stress corrosion cracks. Only a complete crack growth curve of a particular material/environment combination gives sufficient information on this influence. It is an important advantage of fracture mechanics that the stress intensity at the tip of cracks can be calculated for different geometries, as indicated in Figure 2, provided the geometry correction factor is known as well as the crack depth and the nominal tensile stress. In principle, stress corrosion crack growth curves can be experimentally determined by following the steps that are illustrated in Figure 3. A notched and fatigue-precracked specimen is stressed to a well-defined stress intensity by either inserting a wedge or by mounting the specimen into a loading frame. Then the specimen is exposed to the environment for a certain period of time. By dividing the crack elongation due to stress corrosion by the testing time, the stress corrosion crack growth rate is calculated and plotted as a function of the stress intensity. The results of such tests are stress corrosion crack growth curves which are characterized by a threshold value K_{ISCC} below which no crack growth is observed, and, eventually, by a so-called plateau crack growth rate where the crack velocity is independent of the applied stress intensity. Whether such a plateau occurs usually depends on the material/environment combination.

As an example, Figure 4 shows a number of stress corrosion crack growth curves of a quench and temper steel used for springs. This steel has been heat treated to different strength levels, as indicated in the figure. The crack growth curves measured in room temperature water differ from each other in various ways: most important, the shapes of the curves are not identical. For example, with the lower strength steels, there is a distinct plateau region, where an increase of the stress intensity does not result in higher crack velocities. The crack growth rates are independent of the applied stress intensity. The actual velocities, however, differ from each other: higher strength steels suffer faster crack growth rates. With even higher yield strength levels, the crack growth curves do not exhibit distinct plateaus anymore, but the crack growth rates increase with increasing stress intensities. As to the threshold stress intensities K_{ISCC}, these values are lowest for high strength steels, as obvious from Figure 4.

There is a general relationship between K_{ISCC} and the yield strength of a steel: threshold stress intensities are usually low in high strength steels and higher when the yield strength is lowered. This is shown in Figure 5. For a number of steels the threshold stress intensities observed in pure water and in H_2S-solution are plotted as a function of the yield strength. In both environments, there is the same trend obvious: the higher the yield strength, the lower is K_{ISCC}. In absolute values, K_{ISCC} not only depends on the yield strength but also on the environment. Therefore, at a given yield strength, K_{ISCC} has been measured to be considerably lower in the aggressive environment H_2S-solution than in pure water.

Branching of Stress Corrosion Cracks

Stress corrosion cracks can - and often do - develop branch cracks. Two types of branching can be distinguished: microbranching, in which the crack front splits into several local cracks with separation distances of the order of a grain diameter, and

macrobranching, in which the crack separates into two or more macroscopic components that tend to diverge or continue to grow in parallel. Three conditions are necessary, but not always sufficient for macrobranching to occur with stress corrosion cracks, as indicated in Figure 6 [1]. First, the crack growth rate must be (almost) independent of the crack tip stress intensity, i.e. the crack velocity versus stress intensity curve must exhibit a plateau. Second, the crack tip stress intensity K_B, above which macrobranching may occur, must be equal to or larger than 1.4 times the stress intensity K_P (where the plateau region starts), as illustrated in Figure 6. This precondition is necessary for each branch crack to respond to a high enough stress intensity to be driven further, even though the stress intensity at each crack tip is reduced by $1/\sqrt{n}$ with n being the number of branch cracks, as illustrated in Figure 7. Third, the fracture path must be relatively isotropic [1].

Microbranching can occur under less restrictive conditions. The crack velocity does not have to be stress independent, but the stress intensity limit for microbranching is a certain multiple of K_{ISCC}. At extremely low stress intensities, no microbranching is observed.

Leak Before Break

This section gives an example for how important it is to know the influence of mechanical parameters on environmental cracking in practical life. For pressure boundary components which contain liquids or humidity, the question arises, which path eventual stress corrosion cracks would take, e.g. would there be a leak before break or a break without leakage, as illustrated in Figure 8. In other words, are there conditions that can guarantee leak before break? In order to answer this question, it is again a precondition to know the exact stress corrosion crack growth curve of the material in the given environment.

Break before leak in cylindrical pressure boundary components can be excluded only if at least one of the following preconditions is fulfilled: First, if there is no possibility for stress corrosion to occur. Second, if stress intensities at the inner side of the component are smaller than K_{ISCC} or even negative. Third, if unsymmetric crack initiation can be guaranteed. Fourth, if the stresses at the inner side differ highly from each other and, in addition, the stress corrosion crack growth rate is strongly stress-dependent, e.g. there exists no plateau region in the crack growth curve. Fifth, if stresses along a sufficient part of the inner circumference are compressive rather than tensile, such as may be the case in pipe bending. If none of these preconditions is met with, a leak before break due to stress corrosion cracking cannot be guaranteed.

References

1) Ruth Magdowski, Peter J. Uggowitzer and Markus O. Speidel: "The Effect of Crack Branching on the Residual Lifetime of Machine Components Containing Stress Corrosion Cracks", Corrosion Science, vol. 25, No. 8/9, 1985, pp. 745-756
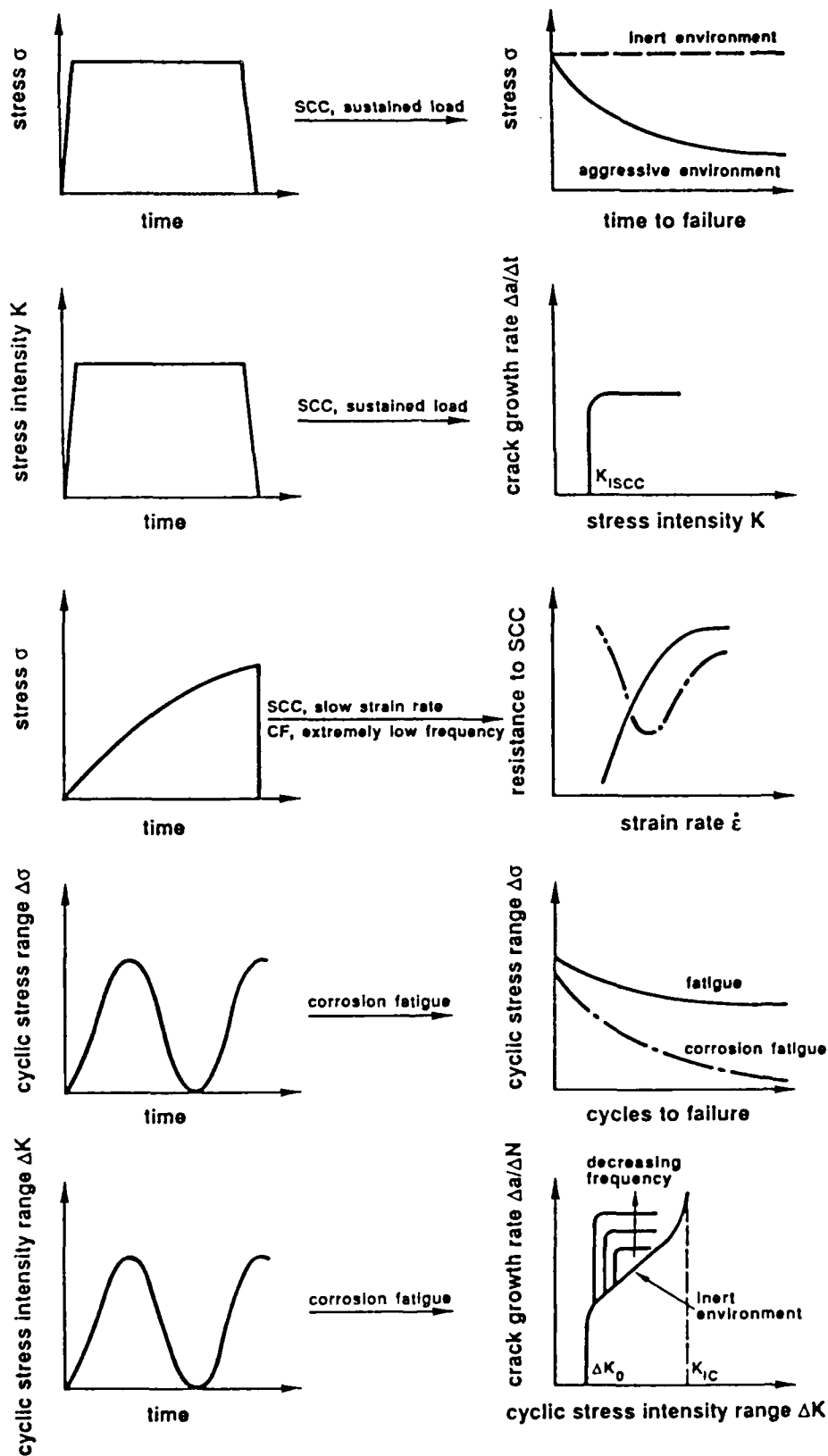
Figure 1: Load wave shapes and resulting testing methods. Stress corrosion cracking and corrosion fatigue as the two extreme aspects of a continuum.
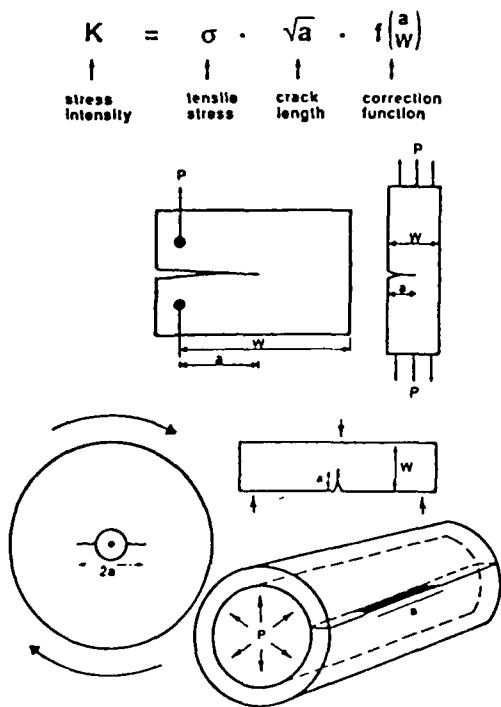
Figure 2: The stress intensity parameter K.
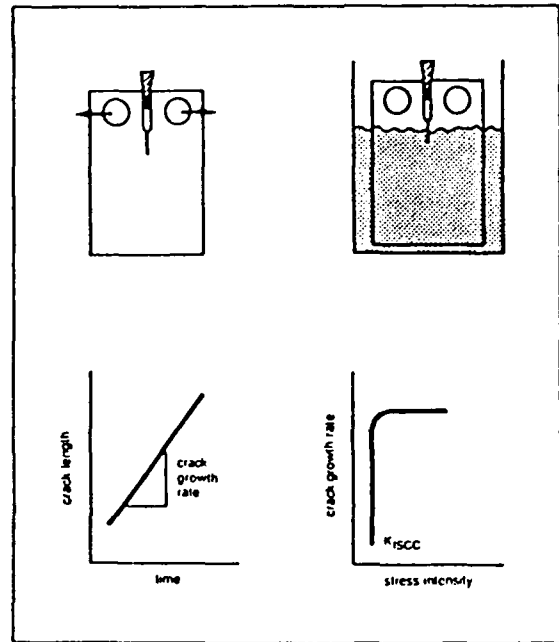
Figure 3: Fracture mechanics stress corrosion testing procedure.
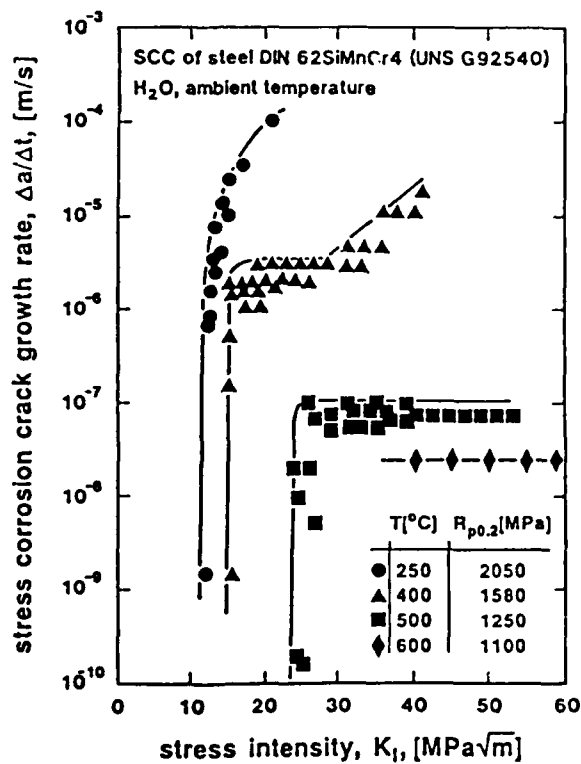
Figure 4: Various shapes of stress corrosion crack growth curves, depending on material and environment.
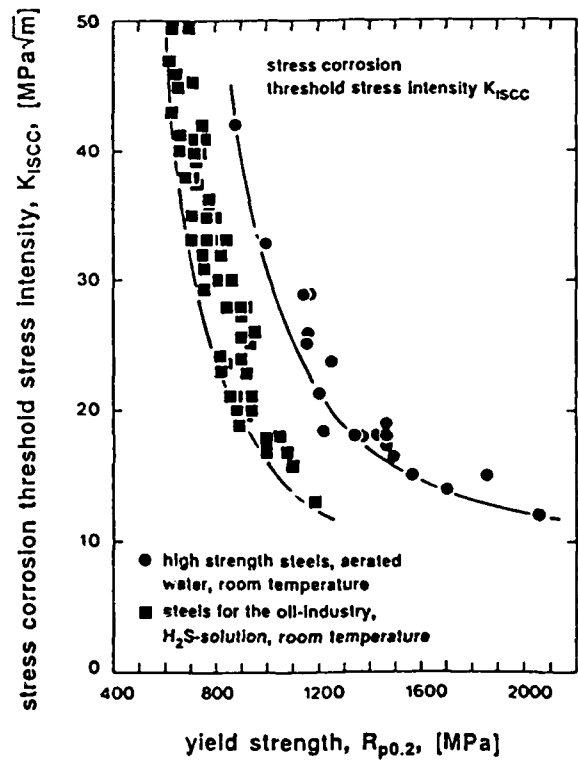
Figure 5: The threshold stress intensity K_{ISCC} depends on the yield strength and the aggressivity of the environment.

2337
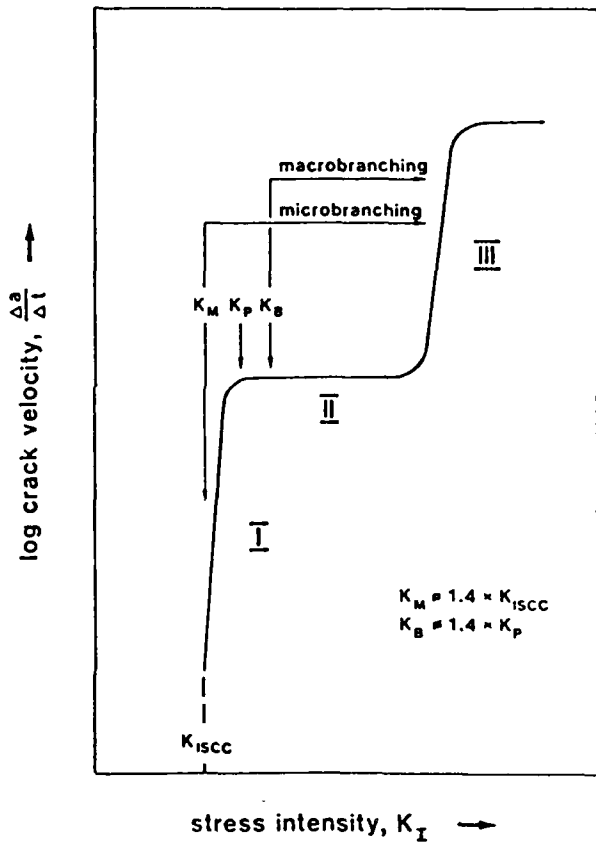
Figure 6: Macrobranching and microbranching of a stress corrosion crack.
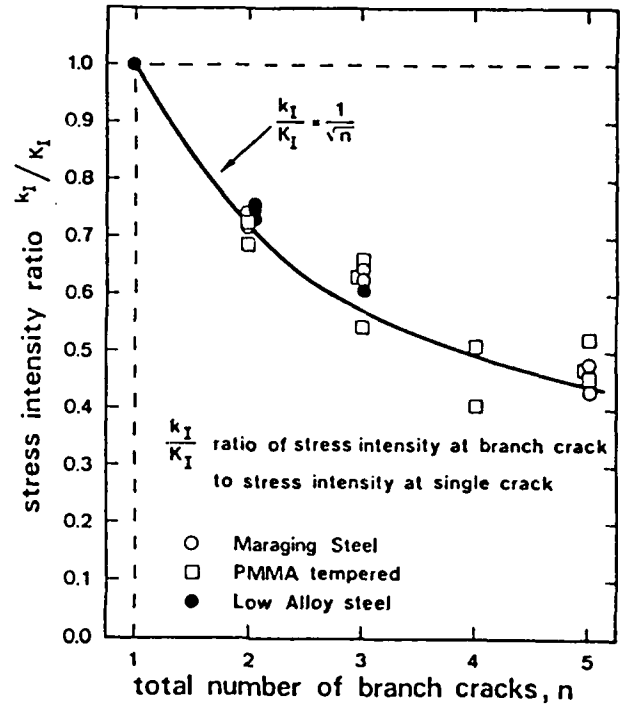
Figure 7: Reduction of the stress intensity on the crack tips due to the presence of branch cracks.
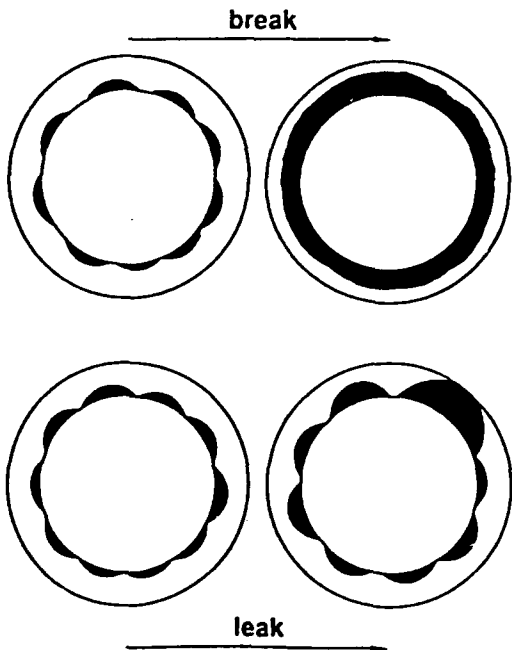
Figure 8: Schematic illustration of the leak before break or break before leak situation.

Hydrogen Embrittlement in Steels:
Metallurgical Aspects

Markus O. Speidel
Institute of Metallurgy
Swiss Federal Institute of Technology, ETH
CH-8092 Zurich, Switzerland

Abstract

Hydrogen embrittlement, that is hydrogen-related, slow, subcritical crack growth, occurs with high-strength steels in at least three different forms: cracking due to the presence of hydrogen-containing gases such as H_2 or H_2S, cracking due to the presence of hydrogen in the steel, and cracking due to the presence of hydrogen-containing liquids such as water or hydrocarbons. This paper illustrates some of the major metallurgical influences on hydrogen embrittlement of steels in water, a phenomenon which is also known as stress corrosion cracking. The major metallurgical influences are exerted by the strength of the steel, the strengthening mechanism, the concentration of major alloying elements, the carbon and the sulfur content of the steels. These influential parameters, however, cannot be measured in a meaningful way or be modeled by theory unless the effect of stress intensity and temperature is systematically taken into account.

Key terms: hydrogen embrittlement, stress corrosion cracking, steels.

Hydrogen Embrittlement versus Stress Corrosion Cracking

Environmental degradation can be defined as the initiation and the subsequent growth of cracks under the simultaneous action of stresses and an aggressive environment. Hydrogen has been found to be the predominant embrittling and thus degrading species for various materials. The severity of environmental degradation of a material depends on the supply of atomic hydrogen generated by its interaction with a wide range of environmental conditions. Indeed, for a number of materials, e.g. medium and high strength steels, hydrogen embrittlement has been accepted to be the mechanism for stress corrosion cracking. The similarity between gaseous hydrogen embrittlement, internal hydrogen embrittlement (after electrolytic charging) and stress corrosion cracking in water is obvious in Figure 1. Therefore, both concepts, hydrogen embrittlement and stress corrosion cracking, can be interpreted and treated as the same process which is affected by at least three different groups of parameters: metallurgical, environmental and mechanical. Out of these groups, this paper concentrates on the effect of various metallurgical aspects that influence hydrogen embrittlement and/or stress corrosion cracking.

Yield Strength and Threshold Stress Intensity

The yield strength of a quenched and tempered steel depends, of course, strongly on the tempering temperature. This is illustrated in Figure 2. It is evident from the same figure that either tempering temperature or yield strength have a strong influence on the threshold stress intensity, K_{ISCC}, below which environment-assisted cracking is not observed. In contrast, it can be seen from Figure 3 that different high strength steels may have quite different plateau crack growth rates, yet their threshold stress intensities are all between 10 and 20 MPa $\sqrt{m}$. These observations are reconciled in Figure 4 which illustrates the fact that at ambient temperature the threshold stress intensity K_{ISCC} depends markedly on the yield strength only when the strength is below about 1200 to 1300 MPa. A further surprising observation revealed in Figure 4 is that K_{ISCC} does not depend on the yield strength in the high temperature regime above about 100°C. This high temperature regime is to the left of the maxima in Figures 1 and 5. Obviously, theories modeling the effect of strength on K_{ISCC}[3] must take into account two different temperature regimes.

Crystal Structure: Ferritic versus Austenitic

Direct comparisons of austenitic versus ferritic steels are presented in Figures 3 and 5. Quite generally, austenitic steels exhibit lower crack growth rates than ferritic steels in water, but care must be taken not to draw too far-reaching conclusions from such a general statement. For example, steel X5MnCrN1818K may have similar yield strength as the steel D6AC it is compared to in Figure 3 but it contains 18 weight percent chromium and has therefore much higher corrosion resistance than all the other steels mentioned in Figure 3. On the other hand, in Figure 5, two steels with vastly different yield strengths are compared. The austenitic steel 304 which exhibits two orders of magnitude slower crack growth rates has a yield strength of 240 MPa while steel D6AC has a yield strength of 1425 MPa. It would be extremely difficult to find two steels, one austenitic, the other ferritic with otherwise identical compositions and yield strengths. Thus, an ideal comparison of ferritic versus austenitic is impossible. Nevertheless, the analogy shown in Figure 5 permits the notion that similar temperature dependencies and maybe similar mechanisms are responsible for subcritical crack growth rates of austenitic and ferritic steels in water. Figure 1 permits the thought that there is a parallel to gaseous hydrogen embrittlement, internal hydrogen embrittlement and stress corrosion cracking of high strength ferritic steels. A very similar argument can also be made for austenitic stainless steels, when one considers not only the stress corrosion data of Figure 5 but also the fact that internal hydrogen embrittlement (after electrolytic charging) and crack growth in hydrogen gas have been observed [4, 5].

Yield Strength and Crack Growth Rates

The strong effect of the yield strength on the crack growth rates of various ferritic steels exposed to water is illustrated in Figures 6 and 7. Obviously, meaningful comparisons of crack growth rates at a given temperature are possible only in the temperature ranges where all steels are below or above the drop-off in crack growth rates which occurs at intermediate temperatures, Figure 6. Naturally, a meaningful comparison also presupposes that all crack growth rates to be compared are measured in the plateau range where, according to Figures 2 and 3, the effect of

stress intensity is negligible. Such a comparison is illustrated in Figure 7 primarily for low alloy steels. Yet, a great difference in crack growth rates is observed at any given yield strength. This indicates that either the microstructure or the minor alloying elements or both are of prime importance. In fact, both are, as will be seen from Figures 8, 9 and 11.

Carbon and Sulfur Content in Steels

The widely scattering observations of crack growth rates at any given yield strength in Figure 7 cluster together along specific trendlines if one separates them into groups of similar carbon and sulfur content. The effect of carbon and sulfur is illustrated in Figures 8 and 9 for specific strength levels. It is now clear that meaningful experimental comparisons and theoretical predictions of crack growth rates - for example to elucidate the effect of yield strength - can be made only for fixed carbon contents and sulfur contents since these can affect the crack growth rates by three to four orders of magnitude. Moreover, the effect of sulfur and carbon in the steels needs to be addressed specifically in models and theories of stress corrosion cracking or hydrogen embrittlement of steels. Figure 9 gives a clear danger signal concerning the enhanced susceptibility of resulfurized steels to environmental cracking. Naturally, the strong effect of sulfur content of the steel will in some way be related to the strong effect of H_2S in the environment which is well known from oilfield tubular goods and which is also observed in laboratory tests of K_{ISCC} [6] and which is also addressed theoretically [7].

High Temperature Water

It is often believed that hydrogen embrittlement disappears at elevated temperatures, and such belief is supported by observations such as those shown in Figure 1. However, it is quite clear from Figures 5 and 6 that there are also extensive high temperature regimes where water as an environment can result in environment-assisted subcritical cracking and the question may then be asked whether this is also a form of hydrogen embrittlement. In Figure 10 we have illustrated the combined effect of material yield strength and temperature on the K-plateau crack growth rates of steels in high temperature water. It is well known that the mere existence of such cracking in low alloy steels has caused huge service failure problems, for example in the power generating industry.

Maraging Steels

The salient point of Figure 11 is that the growth rates of the subcritical cracks in water environment do not parallel the yield strength as a function of the annealing temperature. This means that the yield strength is not the decisive factor controlling the stress corrosion (hydrogen embrittlement) crack growth rate. This is evident from the fact that the crack growth rates peak below 400°C annealing temperature while the yield strength peaks near 500°C. Consider in Figure 11 a yield strength of 1300 MPa. In the underaged condition this entails a crack growth rate of 5×10^{-6} m/s while in the overaged condition this entails a crack growth rate of 5×10^{-11} m/s, a difference by a factor of 100'000 at identical yield strengths ! Clearly, it is not only the strength level but also the microstructure responsible for the strength which controls the crack growth rate.

Discussion and Conclusions

The metallurgical parameters which influence hydrogen embrittlement (and therefore stress corrosion cracking) of steels are many and effective. Yield strength, crystal structure, carbon content, sulfur content, and strengthening mechanism, all can influence the crack growth rate by several orders of magnitude. These influential parameters in turn can only be properly assessed if they are determined systematically as functions of temperature and stress intensity. At present we do not have a reasonably complete quantitative knowledge of all the major influences on crack growth rates. It is thus impossible to compare theoretical predictions to the experimental results. A continuing major research effort is therefore necessary in order to obtain both the quantitative experimental basis and the quantitative modeling or theory which can explain such observations and thus help with steel development and with failure prevention in actual service. The results of such efforts will be valuable to all concerned.

References

1)   R.P. Wei, K. Klier, G.W. Simmons, and Y.T. Chou in "Hydrogen Embrittlement and Stress Corrosion Cracking, A. Troiano Festschrift", ASM, 1984, pp. 103

2)   W.W. Gerberich, "Fracture Mechanics: Microstructure and Micromechanisms", 1987 ASM Materials Science Seminar, Cincinnati, Ohio, pp. 201

3)   W. W. Gerberich, P.G. Marsh and H. Huang in Fundamental Aspects of Stress Corrosion Cracking, Parkins Symposium, TMS, Warrendale, Pennsylvania, 1992, pp. 191-204

4)   Hsun-Kai Juang and Carl Altstetter, Ref. 3, pp. 205-213

5)   J.H. Huang and C.J. Altstetter, Metall. Trans., Vol. 22A, 1991, pp. 2605-2618

6)   R. Magdowski, this volume

7)   H. Pickering, this volume
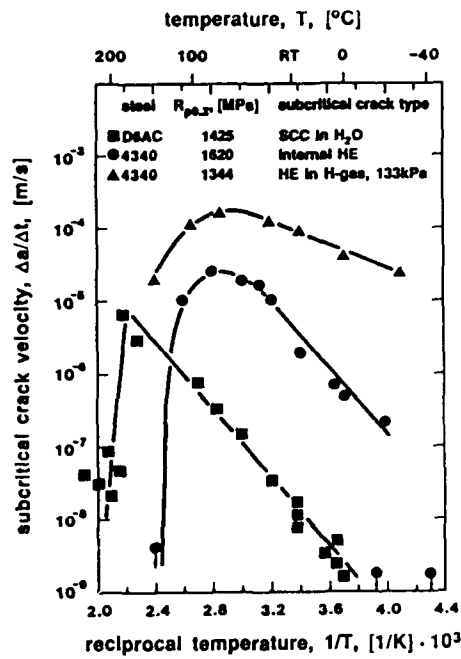
Figure 1: Hydrogen embrittlement is slow subcritical crack growth due to the presence of hydrogen. Hydrogen may be either already in the steel (internal HE) or in a gas or a liquid which may react with the steel at the crack lip. Crack growth rates due to H_2-gas and to internal HE are based on data in references 1) and 2).
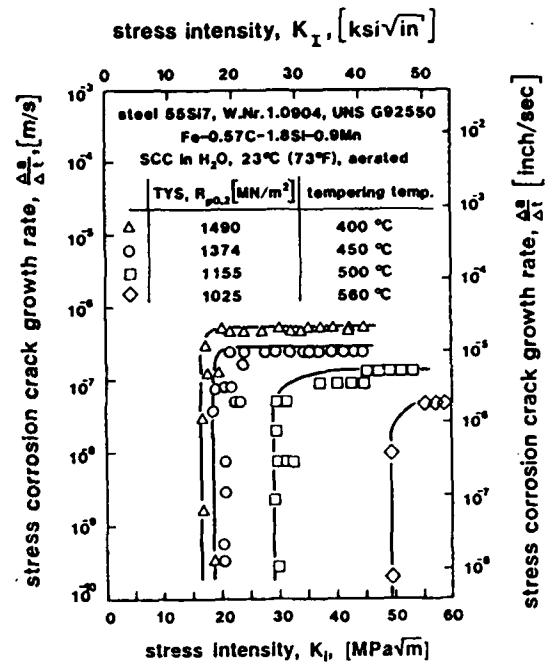
Figure 2: Hydrogen embrittlement (stress corrosion) crack growth curves of a low alloy quenched and tempered steel exposed to water at ambient temperature. Lower yield strengths result in lower crack growth rates and higher threshold stress intensities.
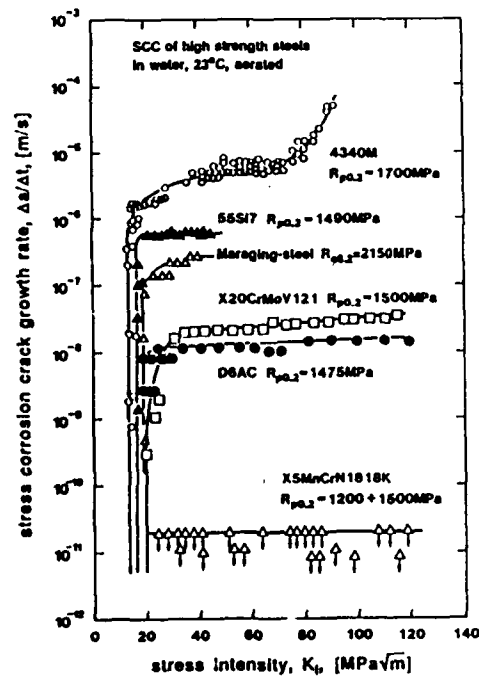
Figure 3: Hydrogen embrittlement (stress corrosion) crack growth rate curves of different high strength steels in water at ambient temperature. Threshold stress intensities are all beetwen 10 and 20 MPa√m although the plateau crack growth rates differ strongly.
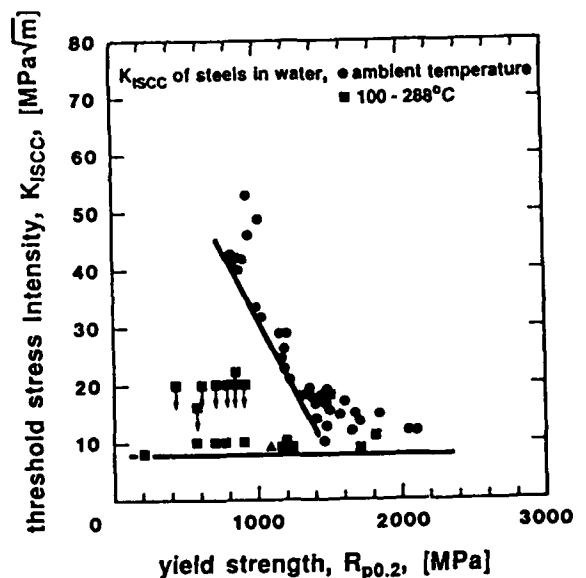
Figure 4: Threshold stress intensities depend on yield strength - but only at temperatures below about 100°C.

2343
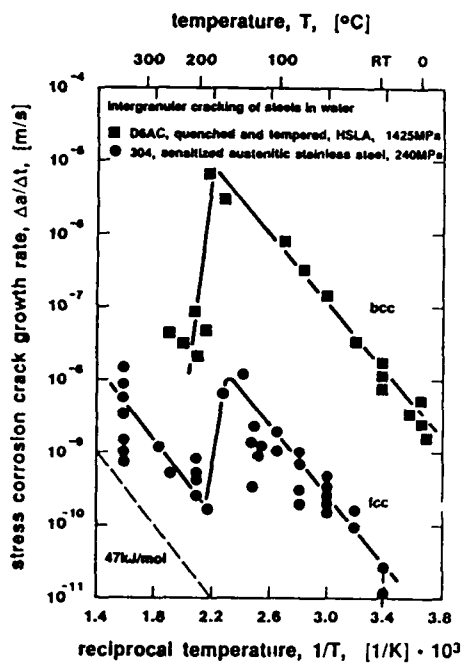
Figure 5: Effect of temperature on the crack growth rates of a ferritic and an austenitic steel, exposed to water. Note also the difference in yield strength of the two steels.
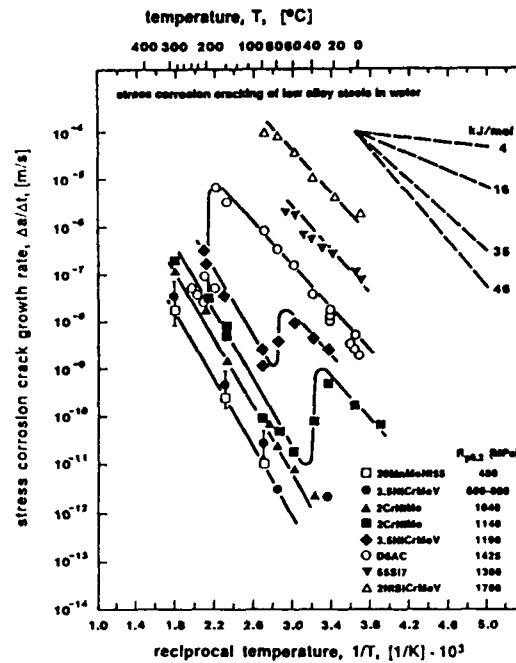
Figure 6: Effect of yield strength and temperature on the crack growth rates of ferritic steels exposed to water. Note that at a given temperature crack growth rates of steels in water may differ by a factor of ten million.
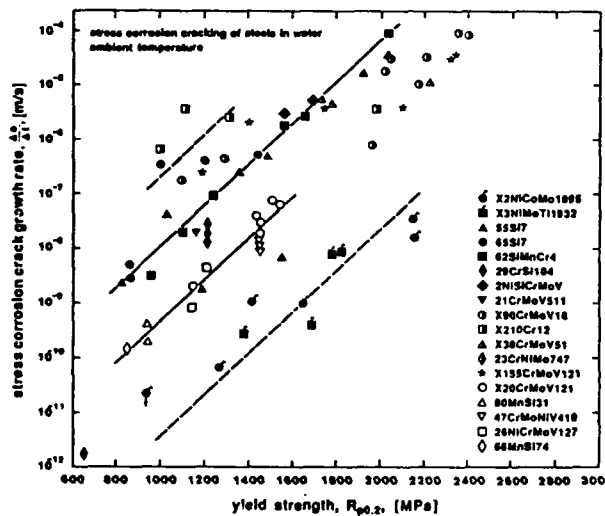
Figure 7: Effect of yield strength on stress corrosion crack growth rates of a large number of various steels.
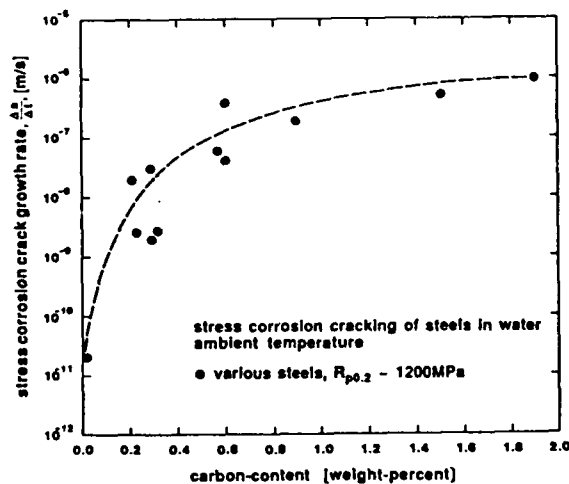
Figure 8: Effect of carbon on the crack growth rates of steels in water.
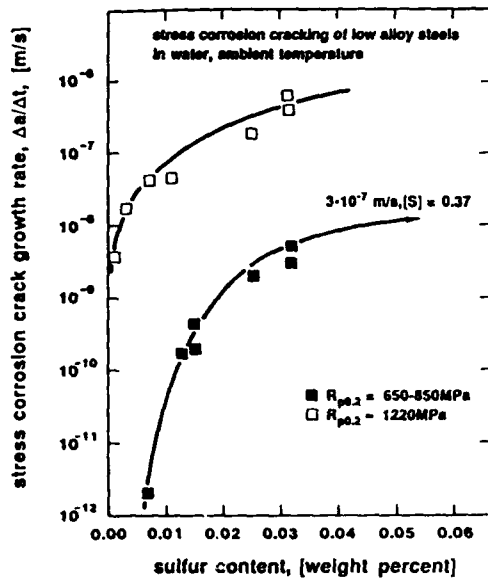
Figure 9: Effect of sulfur on the crack growth rates of steels in water.
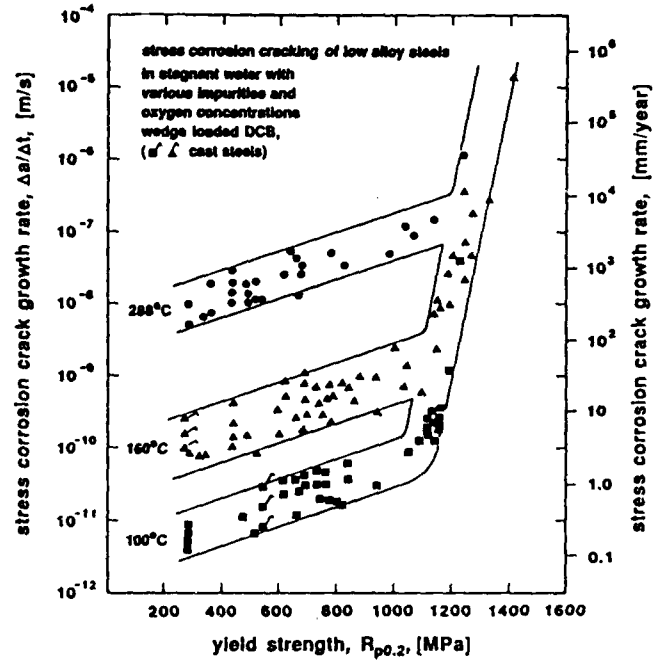
Figure 10: Effect of temperature and yield strength on the growth rates of low alloy steels in high temperature water.
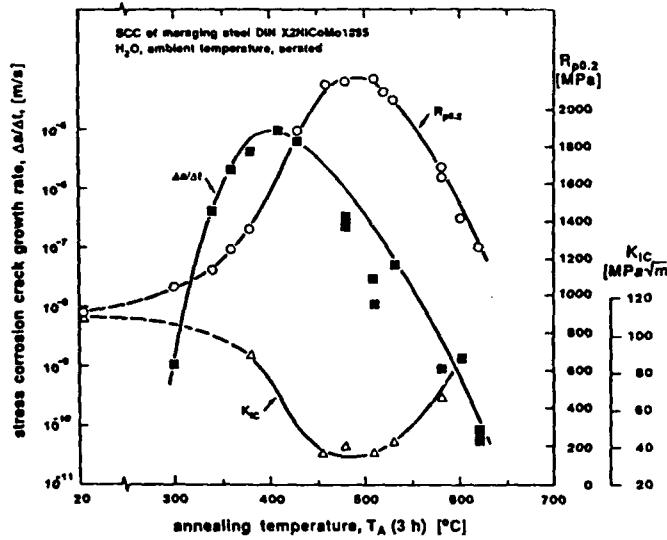
Figure 11: Fracture toughness K_{IC}, yield strength $R_{p0.2}$ and crack growth rate $\Delta a/\Delta t$ in water of a maraging steel as a function of ageing temperature.

Electrochemical Aspects of Hydrogen Embrittlement in Steels: (i) IPZ Model of Hydrogen Permeation (ii) IR Voltage-Induced Hydrogen Charging

Howard W. Pickering
Department of Materials Science and Engineering
The Pennsylvania State University
University Park, PA

Abstract

This paper reviews results of the past decade in the author's laboratory on (i) the Iyer, et. al. (IPZ) model of hydrogen absorption and permeation into metals from aqueous solution for studying the hydrogen absorption mechanism and factors such as H_2S that modify the absorption rate, and (ii) the IR (ohmic) voltage within recesses and holidays, and its impact on the tendency for hydrogen evolution and hydrogen charging inside the cavity for both open circuit corrosion and the protected (anodic protection or cathodic protection) surface.

Key terms: environmentally assisted cracking, hydrogen absorption, hydrogen permeation, H_2S poison mechanism, hydrogen evolution reaction, h.e.r./entry rate constants, IR-induced cracking, hydrogen charging within cracks and holidays, cathodic protection, anodic protection.

Introduction

The problems of environmentally assisted cracking (hydrogen embrittlement, stress corrosion, corrosion fatigue) are interdisciplinary and varied, and the resulting economic loss and safety aspects are a major concern in, for example, the power generation and petrochemical industries.[1] All these forms of environmentally assisted cracking start with the entry of hydrogen into the metal. This paper focuses on (i) the study of mechanistic aspects of hydrogen entry from aqueous solution using the Iyer, et. al. (IPZ) model[2,3], and (ii) the role of IR voltage in modifying the tendency for hydrogen charging and evolution from within cavities (cracks, crevices, holidays).

Electrochemical Aspects of Hydrogen Entry

Experiments in the Penn State Corrosion Laboratory are providing information as to why certain solution species (the so-called poisons) promote hydrogen entry into steels, e.g., H_2S. The key to this improved understanding is the recent development by Iyer, et. al.[2] of a rigorous, quantitative steady-state model of the hydrogen evolution/hydrogen permeation process. This section of the paper briefly describes this model and then illustrates an impressive application of the model for analyzing one of the most encountered deleterious poisons (H_2S)[4].

For aqueous hydrogen charging, the charging conditions can be precisely varied and very high fugacities on the order of 10^6 atm. (corresponding to pressures of 10^4 atm.), can be achieved[5,6]. The first step of H_3O^+ reduction is now fairly well understood to take place by a single electron transfer

$$H_3O^+ + e^- = H_x + H_2O \qquad (1)$$

where x refers to the state of the reduced hydrogen atom on the metallic phase. The electron transfer reaction is followed by two parallel processes which are the evolution of gaseous

hydrogen that forms from the adsorbed hydrogen atoms on the surface and the entry of other adsorbed hydrogen atoms into the metallic phase itself.[7-10] These are:

$$H_{ads} + H_{ads} = H_2 \tag{2a}$$
or
$$H_{ads} + H_3O^+ + e^- = H_2 + H_2O \tag{2b}$$
and
$$H_{ads} = H_{abs} \tag{3}$$

Although widely debated a few decades ago, it is now accepted that hydrogen attains an adsorbed state on the metallic surface, immediately following the discharge step (Reaction 1)[11,12]. But controversy exists as to whether hydrogen atoms are on, or interstitially in, the surface[11,13-15] and whether hydrogen adsorption can cause rearrangement of surface metal atoms, such as occurs in vacuum as shown for a nickel surface by low energy electron diffraction (LEED)[16]. Much of the work in this area strongly suggests an intermediate step in which the discharged hydrogen dissolves just under the metallic surface and equilibrates with hydrogen covering the surface itself[12,16,17]. This is termed the absorption-adsorption reaction, which if in equilibrium means, the permeation process itself is the slow step in the overall permeation process. But for very thin membranes or for high values of hydrogen diffusivity, this equilibrium is not achieved and the overall permeation process becomes interface controlled[3,18]. Both the h.e.r. and the hydrogen permeation characteristics of a metal cathode are easily measured by using an electrochemical hydrogen permeation procedure, in which protons are reduced at one surface of a foil specimen, and the fraction of the discharged hydrogen entering the metallic material and permeating through the foil is oxidized back to the proton at the exit surface, with the oxidation current being a measure of the hydrogen flux. Details of the set-up and circuitry for this procedure are widely available in the literature[19-21]. Models[8,9,22] developed to understand the relationship between the h.e.r. flux and hydrogen permeation flux that predate the Iyer, et. al. model, are not sufficiently detailed to evaluate the various rate constants, surface coverages, and other kinetic parameters relating to hydrogen discharge, evolution, and permeation. These earlier models have even less value in those cases of significant absorption of hydrogen into metallic materials, such as in poisoned electrolytes[9] since the assumption in these models that hydrogen permeation is negligible is invalidated. It is in this background that the more rigorous model (referred to as the IPZ model) by Iyer, Pickering and Zamanzadeh[2] was developed.

In a hydrogen permeation cell the hydrogen discharge reaction rate is given by the cathodic current density, i_c. The relationship between i_c and the cathodic overvoltage, η, is given by the Butler-Volmer equation for a well polarized electrode: $i_c = i_o{'} (1-\theta_H) e^{-a\alpha\eta}$. Here, $i_o{'} = i_o/(1-\theta_e)$, i_o = the exchange current density; θ_H = the surface (hydrogen) coverage, which depends on η; θ_e = the equilibrium surface (hydrogen) coverage (at $\eta = 0$); $a = F/RT = 19.4$ V^{-1} at 25 °C; α = the hydrogen discharge transfer coefficient; $\eta = E_c - E_{eq}$; E_c = the electrode potential during hydrogen discharge; and E_{eq} = the equilibrium electrode potential. The hydrogen recombination reaction rate is given by $i_r = F k_r (\theta_H)^2$, where, k_r is the chemical recombination reaction rate constant. The hydrogen permeation rate (at steady state) is given by $i_\infty = F (D_l/L) c_s$. Here, L = the membrane thickness, c_s = the charging (sub)surface hydrogen concentration and D_l = the hydrogen diffusivity in the metal. If the hydrogen absorption-adsorption reaction is assumed to be in local equilibrium, $c_s = k'' \theta_H$, where k'' = the absorption-adsorption constant that is thickness-dependent.

The IPZ Model

Assumptions in the IPZ model[2,3] that combines hydrogen evolution and hydrogen permeation are the following: (a) The reactions are at steady state and the only reactions occurring on the cathode surface are hydrogen discharge (Reaction 1), chemical recombination(Reaction 2a), and hydrogen absorption (Reaction 3). (b) The cathode surface is sufficiently polarized so that no oxidation of hydrogen or any other oxidation reaction can occur at this surface. (c) The absorption-adsorption reaction is in local equilibrium. (d) The hydrogen permeation process involves simple diffusion of hydrogen atoms through the bulk metal. (e) The surface coverage by hydrogen is low enough to follow Langmuir conditions, i.e., the free energy of hydrogen adsorption is coverage independent. This is generally true for $\theta_H \lesssim 0.2$ and $\theta_H \gtrsim 0.8$.

One of the major relationships of the IPZ model[2,3] is between the steady state permeation flux, i_∞, and the hydrogen recombination flux, i_r. Another is the relation between the charging flux, i_c, overvoltage, η, and permeation flux, i_∞. These two equations are[2,3]

$$i_\infty = \frac{k''}{b}(F\,k_r)^{-0.5}\,\sqrt{i_r} \tag{8}$$

and

$$i_c\,e^{a\alpha\eta} = -(b\,i_0'/k'')\,i_\infty + i_0' \tag{9}$$

Equation 8 states that i_∞ is proportional to $\sqrt{i_r}$ (rather than $\sqrt{i_c}$ as in less rigorous models[8,22]) for a coupled discharge-recombination process; i_r is obtained by subtracting the value of i_∞ from i_c (using Assumption a). Equation 8 is an important relationship enabling one to determine the fraction of the discharged hydrogen that goes off as hydrogen gas and the fraction that actually enters the metal. The constants in Equation 8 consist of the rate constant for the hydrogen recombination reaction, k_r, the rate constant for the hydrogen absorption-adsorption reaction, k'', the Faraday constant, $F=96485$ C/equiv. and $b = L/(FD_l)$.

Equation 9 is derived by considering some electrochemical details of the polarization of the cathode[2] and is needed because $\theta_H = \dfrac{b i_\infty}{k''}$ cannot be determined by a direct experimental method. The IPZ model is the first of its kind to include such a useful relationship. For derivation of Equation 9, the transfer coefficient, α, has to be determined by a procedure described elsewhere[2]. Accurate determination of α is very important since it is in the exponential term. Construction of the true α plots at constant θ_H is discussed in detail elsewhere[23]. The various kinetic parameters such as k_r, k'' and i_0' can be evaluated by plotting i_∞ versus $\sqrt{i_r}$ (Equation 8) and $i_c\,e^{a\alpha\eta}$ versus i_∞ (Equation 9) and performing regression analyses of these equations (if these plots are linear). Subsequently, θ_H ($=bi_\infty/k''$) can be plotted as a function of η and by extrapolating this plot to $\eta = 0$, θ_e can be obtained and, thus, $i_0[= i_0' (1-\theta_e)]$ evaluated. The i_0 values for various metal electrodes are generally available in the literature for comparison with the i_0 values determined using the IPZ model.

Determination of i_o, α, and the various rate constants is important for understanding the electrolytic hydrogen discharge and permeation process and for determining the parameters that control the process. For example, the discharge reaction rate constant, k_1^o $(= i'_o/(a_{H^+}\, e^{-a\alpha E^{eq}}))$, gives the rate of proton reduction (a_{H^+} = the hydrogen ion activity and E_{eq} = the equilibrium potential for the h.e.r.). k_1^o is directly proportional to the proton jump frequency and exponentially related to the activation energy for proton discharge, while α is related to the symmetry factor describing the ease with which a proton can get to the top of the activation energy barrier[24]. The chemical recombination kinetics are characterized by k_r which describes the surface diffusion of hydrogen, mean displacement for hydrogen recombination and site specificity, if any.

In order to understand the h.e.r. mechanism and rate controlling step, the intrinsic (coverage-independent) rates (i.e., the rate constants) of the discharge ($v_d = k_1^o$ $(a_{H^+})\, e^{-a\alpha E^{eq}}$) and of the recombination ($v_r = k_r$) reactions have to be compared. If v_d and v_r are within one order of magnitude of each other, then the discharge and recombination reactions are considered to be coupled[2,24]. If the reactions are coupled, any factor that changes the rate of one reaction will affect the rate of the other reaction as well as the rate of the overall reaction. For example, if the pH of the electrolyte or the cathodic potential is changed it will directly affect v_d and in a coupled discharge-recombination process, it will also affect v_r.

The hydrogen absorption-adsorption rate constant, k'', (obtained from Equations 8 and 9) is a very important parameter characterizing hydrogen absorption and adsorption. It contains quantitative terms describing surface and subsurface kinetic properties of the metal-hydrogen interaction. If k'' is increased, hydrogen absorption is enhanced and if k'' is decreased, hydrogen evolution is enhanced. The k'' values can be altered by the presence of films or adsorbed species on the surface, or impurities in the metal.

If the absorption-adsorption reaction is in local equilibrium, a complete steady state flux balance at the subsurface will yield[17,18]: $i_\infty = F\, k_{abs}\, \theta_H - F\, k_{ads}\, c_s$, where k_{abs} is the hydrogen absorption rate constant and k_{ads} is the hydrogen adsorption rate constant, and $(i_\infty)^{-1} =$ $[k_{ads}/(FD_l k_{abs}\theta_H)]\, L + (Fk_{abs}\theta_H)^{-1}$. Under diffusion controlled permeation conditions, i.e., i_∞ is inversely proportional to L, the latter relation becomes[2,18]: $i_\infty \cong F(D_l/L)k'\theta_H$, where $k' = k_{abs}/k_{ads}$. This steady state criterion will thus serve as an additional check for the diffusion controlled condition, apart from the transient stage condition of the square-root of time lag being proportional to L. Furthermore, to overcome grain boundary effects L has to be much larger than the average grain diameter for a polycrystalline membrane.

The IPZ model provides an analytical means of evaluating both k_{abs} and k_{ads} using a range of membrane thicknesses that avoid the above-mentioned problems. The relationship is given by[2,3]:

$$(k'')^{-1} = (k_{ads}/k_{abs}) + (D_l/k_{abs})\, (L)^{-1} \tag{10}$$

Thus, by determining k'' as a function of L, k_{abs} and k_{ads} are easily found [if the $(k'')^{-1}$ versus $(L)^{-1}$ plot is linear]. The L values have to be chosen within a small dimensional window, typically ten to a few tens of the grain diameter since, in addition to avoiding the above mentioned grain boundary effects, if the membrane is too thick, $(k'')^{-1} \cong (k')^{-1} = (k_{ads}/k_{abs})$, and so k'' becomes thickness independent. If the permeation experiments are also carried out as a function of temperature, T, k_{abs} and k_{ads}, which are respectively proportional to $e^{-(\Delta G_{abs}/RT)}$, and $e^{-(\Delta G_{ads}/RT)}$ where ΔG_{abs} and ΔG_{ads} are the activation energies of hydrogen absorption and adsorption, then ΔG_{abs} and ΔG_{ads} can be determine if the plots of log (k_{abs}) versus $(T)^{-1}$ and log (k_{ads}) versus $(T)^{-1}$ are linear. At present, there are no alternative ways of determining k_{abs} and k_{ads}. However, the activation energies can be determined from pseudocapacitance[12] and B.E.T.[15,25] measurements. Such determinations can also be compared with those obtained in gas phase hydrogen charging, correcting for the fugacities involved. These approaches may offer unique means of not only correlating aqueous charging data with gas phase charging data but also provide a broad unification of the entry and embrittlement by hydrogen originating from two independent hydrogen sources.

Modified IPZ Model for Poisoned Electrolytes

When metallic materials encounter poisoned environments, the hydrogen permeation is significantly enhanced indicating significant coverages of the surface by hydrogen in which case the Langmuir condition ($\theta_H \lesssim 0.2$) may no longer hold. For higher coverages ($0.2 \lesssim \theta_H \lesssim 0.8$) Equations 8 and 9 were modified to include the Frumkin-Temkin correction[12] for the discharge and chemical recombination rate equations to give[3,4]

$$\log_e (\sqrt{i_r}/i_\infty) = (\alpha f b/k'') i_\infty + \log_e[b(Fk_r)^{0.5}/k''] \qquad (11)$$

$$\log_e (f_{i_c, i_\infty}) = -\alpha a \eta + \log_e(i_o{'}) \qquad (12)$$

where

$$f_{i_c, i_\infty} = i_c\, e^{(\alpha f b i_\infty/k'')}/(1-bi_\infty/k'') \qquad (12a)$$

Here $f = \gamma/RT$, where γ is the gradient of the apparent free energy of adsorption with coverage and the value of $f = 4.5$ has been assumed. However, an accurate value of f has to be obtained for each specific metal-solution system for a more rigorous analysis; techniques such as the adsorption pseudocapacitance measurements[12] can be utilized for evaluating f. Once f is known, Equations 11 and 12 will unambiguously yield the values of α, k'', k_r and $i_o{'}$. A detailed evaluation procedure is described elsewhere[4]. Essentially, log $(\sqrt{i_r}/i_\infty)$ versus i_∞ is plotted, and if this plot is linear, the slope and intercept will contain the values of α, k'' and k_r. Then, in Equation 12, k'' can be expressed in terms of α and iteratively solved for α. If α values converge to a fixed value, it will indicate that $\log(f_{i_c, i_\infty})$ is linear with η. But if α does not converge, it will indicate that the system is not following these relationships and that one or more of the assumptions may not be valid. Such cases can arise if the recombination reaction becomes rate limiting or if it involves electrochemical desorption (Reaction 2b). If α does converge, then k'', k_r and $i_o{'}$ are easily evaluated by regression analyses of Equations 11 and 12. These quantities provide very

useful information about the way in which poisons promote hydrogen entry. For example, it is well established that a large hydrogen entry into the metal occurs when H_2S is present in highly acidic solutions, but the hydrogen overvoltage is reduced. Analysis with the modified IPZ model showed that the increased hydrogen entry is largely due to the recombination step being slowed considerably, probably in conjunction with the reaction:

$$H_2S + e^-_{cathode} \longrightarrow H_2S^-_{cathode} \qquad (13)$$

This side reaction can occur quite fast at the cathodic metal surface and affect the discharge and recombination steps in various ways[4]:

1. H_2S can work as a bridge for hydrogen discharge through H_2S^-, as originally proposed by Kawashima, et .al .[26]:

$$H_2S^-_{cathode} + H_3O^+ + M \longrightarrow M\text{-}H + H_2S + H_2O \qquad (14)$$
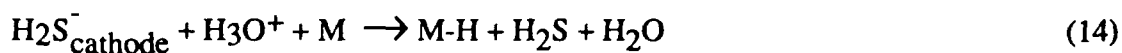
Reaction 14 leads to a decrease in the overvoltage for the discharge reaction.

2. The recombination reaction can be poisoned by the $(H...H_2S)$ intermediate forming on the cathode and slowing the diffusion of H adatoms and/or blocking the recombination sites (if the recombination reaction is heterogeneous) on the metallic surface.

The value of α obtained using the IPZ model, slightly increased with small additions of H_2S, consistent with the Kawashima, et .al .bridge mechanism. Thus, the primary function of H_2S^- acting as a bridge is to facilitate transfer of protons across the double layer and, thus, decrease the overvoltage necessary for hydrogen discharge. But the intermediate product $(H...H_2S)$ poisons the recombination reaction and this has been quantitatively illustrated by the precipitous decrease in k_r with small additions of H_2S. This is further quantified by the increase in θ_H with increasing $[H_2S]$ at a particular η showing the build up of H adatoms due to slowing down of the recombination reaction. The model evaluations also showed that k'' increased with increasing $[H_2S]$, although not significantly. In order to attain yet a clearer picture of the role of H_2S in enhancing hydrogen entry into metallic materials, the absorbates have to be experimentally analyzed.

Hydrogen Entry from Within Cavities

For a decade in the Penn State Corrosion Laboratory, the IR (ohmic) voltage within cavities (crevices and artificial pits) has been systematically investigated. In principle, the explanation of stable localized corrosion as a shift of the cavity electrode potential out of the potential region of stable passivity, is well founded on potential theory, and a computational model with the ability to quantitatively predict geometrical features has already been derived.[27] Nevertheless, the importance of the IR voltage in stabilizing localized corrosion has not been considered by the corrosion science community and so this study was designed to see how important the IR voltage is in practice. One result (large ohmic voltages) stands out by its reproducibility and novelty. Reproducibility refers to the every-time observation (out of many tens of experiments) that crevice corrosion in iron, nickel and stainless steel only occurs when the voltage difference between the anodic site inside the crevice and the cathodic site on the outer surface (where the oxidant is

plentiful) is so large that the electrode potential at the corroding anodic site is below (less noble than) the potential region of stable passivity.[28-32] This same result has been obtained also for pit growth in nickel.[33] In brief, these experimental results, which are documented by simultaneous in-situ measurement of several parameters using a powerful, new crevice design,[28-31] show that the IR voltage in cavities is an essential ingredient in at least some forms of localized corrosion. The results go further in that they show how the IR mechanism can explain the roles of acidification and chloride ion buildup in promoting localized corrosion and the role of some inhibitors in decreasing its occurrence. Readers can learn more about the IR voltage as it pertains to localized corrosion in this writer's other paper in this volume.[34] In what follows in this paper, the role of the IR voltage in promoting the hydrogen evolution reaction (h.e.r.) and hydrogen absorption into the metal is evaluated.

Whenever the anodic and cathodic sites are separated, the IR voltage accompanying current flow between these sites can be an appreciable fraction of the cell voltage, in which case the IR voltage must be taken into account in a mechanistic analysis of the cell process. This situation is typically encountered in localized corrosion and in anodic and cathodic protection of surfaces that contain recesses (crevices, cracks, holidays, etc.). The resulting electrode potential distribution and its relation to the IR voltage is given by

$$E_x = E_{surf} + IR \tag{15}$$

and depends on the direction of current flow within the cavity as follows: If the current flow direction is from the cavity electrolyte to the bulk electrolyte, as in the case of localized corrosion or anodic protection, the electrode potential in the cavity, E_x where x increases with distance into the cavity, is less noble than the surface potential, E_{surf}, since the current, I, flows in the negative x direction; thus I is negative in Equation 15 for anodic protection or open circuit corrosion.[†] During anodic protection with E_{surf} in the passive region, the measured current can be cathodic as a result of reduction of dissolved oxygen. Since the dissolved oxygen is not readily replenished inside the cavity, the cavity surface, beyond the deepest point of oxygen transport into the cavity, can support only the anodic reaction. Consequently, regardless of whether or not an oxidant is present in the bulk electrolyte, current flows in the negative x direction through the cavity electrolyte, i.e., from the anodic sites on the cavity wall to the cathodic sites on the outer surface (oxidant present) or to the counter electrode in the absence of an oxidant during anodic protection.

On the other hand, if the current flow is in the opposite direction (positive x direction) within the cavity electrolyte, as in the case of cathodic protection, the electrode potential in the cavity, E_x, is more noble than the set potential at the outer surface, E_{surf}, where now I is positive in Equation 15 since I flows in the positive x direction. For more description of these factors in establishing the potential distribution within cavities for cathodic and anodic polarization, the reader is referred to References 28-31, 35-41.

We are now ready for an evaluation of the tendency for hydrogen evolution and absorption into the metal from within the cavity, relative to the same tendency at the outer surface for both a protected and unprotected surface. In the case of open circuit corrosion or an anodically protected surface, the tendency for the h.e.r. and hydrogen absorption increases with increasing distance x into the cavity. Very often, this means the situation changes from a condition at the outer surface where no

---

[†] In previous papers[28-31,35-41], Equation 15 was sometimes given as $E_x = E_{surf} - |IR|$ for open circuit corrosion or anodic protection, and as $E_x = E_{surf} + |IR|$ for cathodic polarization except that the absolute magnitude of IR was only implied. Equation 15 as presented above in the text is equivalent but can be used for all three situations since it considers that the current I is negative when it flows out of the cavity (negative x direction) as in the case of anodic protection and open circuit corrosion, and is positive when it flows into the cavity as in the case of cathodic protection.

hydrogen absorption occurs because E_{corr} or E_{surf} is more noble than the h.e.r. equilibrium potential, E_h^{eq}, to a condition beyond some distance into the cavity where E_x is less noble than E_h^{eq}, i.e., $E_x < E_h^{eq}$, and the h.e.r. occurs and hydrogen is charged into the metal from within the cavity. Thus, the larger the IR in Equation 15, the greater is the tendency for hydrogen charging into the metal from within the cavity during open circuit corrosion or anodic protection. On the other hand, in the case of cathodic protection, the opposite tendency is encountered, i.e., with increasing distance, x, into the cavity, the tendency for the h.e.r. and hydrogen charging into the metal decreases compared to the tendency at the outer surface (whereas the tendency for oxidation reactions, including metal dissolution, increases). This follows again from the basic criterion expressed in Equation 15 which shows that $E_x > E_{surf}$, i.e., E_x is more noble than E_{surf}, for cathodic protection. It follows (for cathodic protection) that the driving force, η for the h.e.r. for constant E_h^{eq} is less (a less negative value of η) at E_x than at E_{surf}, where η is defined as the departure of the electrode potential from E_h^{eq}, and the converse is true for anodic protection or open circuit localized corrosion.

Conclusions

Theoretical and experimental results of the past decade in the authors laboratory have provided new insight into two aspects of the hydrogen embrittlement issue, as follows:

(i) The Iyer, et. al., (IPZ) computational model has put the hydrogen permeation experimental technique on a more rigorous basis than was previously available. As a result information about the details of the hydrogen evolution and hydrogen permeation process can now be obtained from the application of the model to the measured steady-state permeation rate as a function of charging current density and membrane thickness. Thus, new understanding should be forthcoming on how different variables affect the hydrogen charging process, such as the so-called poisons, compressive stress in the surface, segregates in the surface layer, temperature, etc.. The first application of the model for understanding how H_2S promotes hydrogen entry nicely supports this prognosis.

(ii) Applying the IR voltage concept of localized corrosion to the hydrogen entry question shows that the tendency for hydrogen evolution and entry into the metal is affected by IR voltages in cavities: For open circuit corrosion and anodic protection, the hydrogen charging tendency is greater inside cavities and holidays than on the outer surface. The converse holds during cathodic protection.

Acknowledgment

References

1. C. M. Hudgins, Materials Protections, 8 (1969): p. 41.

2. R. N. Iyer, H. W. Pickering and M. Zamanzadeh, J. Electrochem. Soc., 136 (1989): p. 2436.

3. R. N. Iyer and H. W. Pickering, Annu. Rev. Mater. Sci., 20 (1990): p. 299; ibid, Hydrogen Effects on Material Behavior, N. R. Moody, A. W. Thompson, ed., (Warrendale, PA, The Minerals, Metals and Materials Soc., 1990), pp. 195-206.

4. R. N. Iyer, I. Takeuchi, M. Zamanzadeh and H. W. Pickering, Corrosion, 46 (1990): p. 460.

5. I. M. Bernstein, Metall. Trans, (1970): p. 3143.

6. R. A. Oriani, Annu. Rev. Mater. Sci., 8 (1978): p. 327.

7. K. J. Vetter, Electrochemical Kinetics, (London, Academic Press, 1967), pp. 516-40.

8. J. O'M. Bockris, J. McBreen, L. Nanis, J. Electrochem. Soc., 112 (1965): p. 1025.

9. E. G. Dafft, K. Bohnenkamp, H. J. Engell, Corros. Sci., 19 (1979): p. 591.

10. M. Enyo, Comprehensive Treatise of Electrochemistry, (New York, NY, Plenum, 1983), pp. 241-300.

11. B. E. Conway, Electrode Processes, (New York, NY, Ronald Press, 1965), pp. 136-69.

12. E. Gileadi, B. E. Conway, Modern Aspects of Electrochemistry, J. O'M. Bockris, B. E. Conway, ed., (Washington, DC, Butterworth, 1964), pp. 347-442.

13. B. E. Conway, J. O'M. Bockris, Can. J. Chem., 35 (1957): p. 1124.

14. B. E. Conway, M. Salomon, Ber. Bunsenges. Phys. Chem., 68 (1964): p. 331.

15. O. Beeck, Adv. Catal., 2 (1950): p. 151.

16. L. H. Germer, A. U. MacRae, J. Chem. Phys., 37 (1962): p. 1382.

17. C. D. Kim, B. E. Wilde, J. Electrochem. Soc., 118 (1971): p. 202.

18. B. G. Ateya, H. E. Abd Elal, Proc. Conf. Corrosion - Industrial Problems, Treatment and Control Techniques, V. Ashworth, ed., (Kuwait, Kuwait Found Adv. Sci., Vol. 2, 1984), pp. 201-222.

19. M. A. V. Devanathan, Z. Stachurski, J. Electrochem. Soc., 111 (1964): p. 619.

20. S. S. Chatterjee, B. G. Ateya, H. W. Pickering, Metall. Trans., A9 (1978): p. 389.

21. M. A. V. Devanathan, Z. Stachurski, J. Electrochem. Soc., 110 (1963): p. 886.

22. J. McBreen, M. A. Genshaw, Proc. Conf. Fundamental Aspects of Stress Corrosion Cracking, R. W. Staehle, A. J. Forty, D. van-Rooyen, ed., (Houston, TX, Nat. Assoc. Corrosion Engineers, 1969), pp. 159-177.

23. R. N. Iyer, H. W. Pickering, J. Electrochem. Soc., 137 (1990): p. 3512.

24. J. O'M. Bockris, A. K. N. Reddy, Modern Electrochemistry (New York, NY, Plenum, 1970), pp. 1231-38, 1261, 1262.

25. S. Brunauer, P. H. Emmett, E. Teller, J. Am. Chem. Soc., 60 (1938): p. 309.

26. A. Kawashime, K. Hashimoto, S. Shimodaira, Corrosion, 32 (1976): p. 321.

27. Y. Xu, H. W. Pickering, J. Electrochem. Soc., 140 (1993): p. 658; ibid, Critical Factors in Localized Corrosion, G. Frankel and R. Newman, ed., Vol. 92-9, (Pennington, NJ, The Electrochemical Society Softbound Proceedings Series, 1992), p. 389.

28. A. Valdes, H. W. Pickering, Adv. Localized Corrosion, ed. H. Isaacs, U. Bertocci, J. Kruger and S. Smialowska, (Houston, TX, National Association of Corrosion Engineers, 1990), p. 393; ibid, H. W. Pickering, p. 77.

29. H. W. Pickering, Corros. Sci., 29 (1989): p. 325.

30. K. Cho, H. W. Pickering, J. Electrochem. Soc., 137 (1990): p. 3313; ibid, 138 (1991), p. L56; ibid, Critical Factors in Localized Corrosion, G. Frankel and R. Newman, ed., Vol. 92-9, (Pennington, NJ, The Electrochemical Society Softbound Series, 1992), p. 407.

31. H. W. Pickering, K. Cho, E. A. Nystrom, Corrosion Sci., in press.

32. E. A. Nystrom, J. B. Lee, A. A. Sagüés, H. W. Pickering, Electrochem. Soc., in press.

33. M. Wang, Y. Xu, H. W. Pickering, in preparation.

34. H. W. Pickering, This Proceedings.

35. H. W. Pickering, Corrosion, 42 (1986): p. 125.

36. B. G. Ateya, H. W. Pickering, J. Electrochem. Soc., 122 (1975), p. 1018; ibid, J. Appl. Electrochem., 11 (1981); p. 453.

37. B. G. Ateya, H. W. Pickering, Hydrogen in Metals, I. M. Bernstein, A. W. Thompson, ed., (Metals Park, OH, Am. Soc. Metals, 1974), pp. 207-222.

38. B. G. Ateya, H. W. Pickering, Stress Corrosion Cracking and Embrittlement of Iron Base Alloys, R. W. Staehle, J. Hockmann, R. D. McCright, J. E. Slater, ed. (Houston, TX, National Association of Corrosion Engineers, 1977), pp. 1183-88.

39. B. G. Ateya, H. W. Pickering, Passivity of Metals, R. P. Frankenthal, J. Kruger, ed., (Pennington, NJ, The Electrochemical Society, 1978), pp. 350-367.

40. H. W. Pickering, R. P. Frankenthal, J. Electrochem. Soc., 119, (1972): p. 1297.

41. H. W. Pickering, P. J. Byrne, J. Electrochem. Soc., 120 (1973): p. 607.

Predicting the Susceptibility to Hydrogen Embrittlement

B. G. Pound

Materials Research Center
SRI International
333 Ravenswood Ave
Menlo Park, CA 94025
U.S.A.

Abstract

The susceptibility of an alloy to hydrogen embrittlement (HE) is critically affected by the trapping of hydrogen at microstructural defects, so a knowledge of the trapping characteristics is crucial in predicting the susceptibility to HE. Hydrogen trapping in various high-strength steels, precipitation-hardened and work-hardened nickel-base alloys, and titanium has been investigated using a technique referred to as hydrogen ingress analysis by potentiostatic pulsing (HIAPP). HIAPP was found to be effective in evaluating the irreversible trapping characteristics of alloys containing both single and multiple principal traps. The results showed that a range of microstructural features can be identified as the principal irreversible traps and so demonstrated the ability of HIAPP to provide a basis for explaining differences in the resistance of alloys to HE. Furthermore, it was established that the irreversible trapping capability of the alloys can be correlated with the susceptibility to embrittlement. Hence, HIAPP appears to provide a convenient means of quantitatively characterizing the propensity of an alloy to undergo HE.

Key terms: hydrogen embrittlement, hydrogen trapping, potentiostatic pulse, high-strength alloys.

Introduction

The susceptibility of an alloy to hydrogen embrittlement (HE) is highly dependent on the interaction of hydrogen with microstructural defects such as precipitates, grain boundaries, and dislocations. These defects provide potential trapping sites for hydrogen and so critically influence the series of events leading to failure. The accumulation of hydrogen at second-phase particles and precipitates, for example, is generally considered to promote microvoid initiation via the fracture of particles or the weakening of particle-matrix interfaces. Traps with a large saturability and a high binding energy for hydrogen are highly conducive to HE,[1,2] whereas metals containing a high density of well-distributed strong traps (high binding energy) that have a low specific saturability should be more resistant. Accordingly, a knowledge of the trapping characteristics is crucial in predicting the susceptibility to embrittlement.

The approach currently used to assess HE susceptibility is based on time-to-failure results from mechanical cracking tests. The disadvantage of these tests is that they require exposure times typically of days or longer and are often laborious. Furthermore, the results are at best only semi-quantitative, and it is frequently difficult, if not impossible, to discriminate between more resistant alloys that do not fail within the given test period.

Over the last few years, hydrogen trapping in various high-strength alloys has been investigated in our laboratory by using an electrochemical technique referred to as hydrogen ingress analysis by potentiostatic pulsing (HIAPP).[3-6] As the name indicates, the alloy of interest is subjected to a potentiostatic pulse and the resulting current transients are analyzed by using a model for hydrogen diffusion and trapping.[7,8] Test data can be acquired rapidly (typically within a few hours) for a range of charging potentials using only small bulk samples of an alloy. In addition, the data yield both the hydrogen trapping constants and the rates of hydrogen entry into

the alloy. A crucial finding was that the hydrogen trapping constants represent an index of HE susceptibility, and so it was shown that HIAPP can provide two key parameters required to characterize the performance of an alloy in an environment conducive to HE.

HIAPP has been applied to high-strength steels,[3,4] precipitation-hardened and work-hardened nickel-base alloys,[4,5] and titanium,[6] and was found to be effective in evaluating the trapping characteristics of alloys containing both single and multiple principal traps. In this paper, we review the use of HIAPP as a technique for examining hydrogen ingress, particularly in terms of irreversible trapping. The research was aimed at not only characterizing the susceptibility to HE but also, wherever possible, identifying the dominant type of irreversible trap in different alloys. In essence, the goal was to use the data provided by HIAPP as a basis for explaining differences in the resistance of these alloys to HE.

Role of HIAPP

Techniques

Membrane permeation methods have been used extensively to determine diffusion and trapping characteristics but they suffer from several disadvantages, as discussed elsewhere.[9] Long charging times (of the order of days) may be required for hydrogen to diffuse through many metals, especially those with a fcc lattice, thereby increasing the likelihood of changes in the surface condition. If a surface film is present, progressive thinning of the film may result from reduction, and the bare metal may eventually be exposed. Prolonged charging times may also result in deposition of significant amounts of impurities on the cathode surface.

A further disadvantage is that most, if not all, diffusion/trapping models for permeation techniques are based on an input boundary condition of constant concentration, which implies that they are strictly applicable only for charging conditions without any entry limitation. Hence, existing permeation models may well yield incorrect values of diffusivity and trapping parameters, if the prevailing boundary condition involves a constant or time-dependent flux. Unfortunately, the limitations of the constant concentration condition are not always recognized, even though it underlies virtually all permeation analyses involving trapping.

In the potentiostatic pulse technique, the metal is cathodically charged with hydrogen for a certain time, and the potential is then stepped to a more positive value, resulting in an anodic current transient associated with the reoxidation of H atoms as they diffuse back to the same surface. Pulse methods are suitable for bulk specimens, since only a single surface need be exposed to the electrolyte. Hence, they offer practical advantages over permeation methods in terms of specimen shape and charging times. Also, diffusion in bulk specimens can be treated in terms of a semi-infinite boundary condition, which is mathematically appealing.

Diffusion/Trapping Model For Pulse Technique

A model has been developed to allow for the effect of trapping on diffusion without *or* with surface constraints; that is, for cases involving either constant concentration or constant flux at the input surface. These two cases are characterized by the kinetics of hydrogen entry into the metal: (1) pure diffusion control, in which hydrogen entry is assumed to be fast enough that equilibrium is rapidly achieved between adsorbed and subsurface hydrogen; and (2) interface-limited diffusion control (referred to simply as interface control), in which the rate of hydrogen ingress is controlled by diffusion but the entry flux of hydrogen across the interface is restricted.

The interface control model is found to be applicable for all alloys studied to date. According to this model, the total charge passed out is given in nondimensional form by[7]

$$Q'(\infty) = \sqrt{R}\{1 - e^{-R}/\sqrt{(\pi R)} - [1 - 1/(2R)]erf\sqrt{R}\}$$ (1)

The nondimensional terms are defined by $Q = q/[FJ\sqrt{(t_c/k_a)}]$ and $R = k_a t_c$ where q is the dimensionalized charge in C cm^{-2}, F is the Faraday constant, and J is the ingress flux in mol cm^{-2} s^{-1}. The charge $q'(\infty)$ corresponding to $Q'(\infty)$ is equated to the charge (q_a) associated with the experimental anodic transients; the adsorbed charge is almost invariably found to be negligible, so q_a can be associated entirely with absorbed hydrogen. k_a is an apparent trapping constant measured for irreversible traps in the presence of reversible traps and can be expressed by $k(D_a/D_L)$ where k is the irreversible trapping constant, D_a is the apparent diffusivity, and D_L is the lattice diffusivity of hydrogen in the metal.

Eq. (1) was fitted to data for q_a as a function of t_c to obtain values of k_a and J such that J was constant over the range of charging times and k_a was independent of charging potential, as is required for the diffusion/trapping model to be valid, since the traps are assumed to be unperturbed by electrochemical variables and remain unsaturated. The values of k_a and J can be used to calculate the irreversibly trapped charge (q_T) given nondimensionally by

$$Q_T = [R^{1/2} - 1/(2R^{1/2})]\,\mathrm{erf}(R^{1/2}) + e^{-R}/\pi^{1/2} \qquad (2)$$

The charge associated with the entry of hydrogen into the metal (q_{in}) can be determined from its nondimensional form of $Q_{in} = \sqrt{R}$ by using the value of k_a. The data for q_{in}, q_T, and the cathodic charge (q_c) can then be used to obtain two ratios: (1) The trapping efficiency (q_T/q_{in}), corresponding to the fraction of hydrogen trapped in the metal; and (2) the entry efficiency (q_{in}/q_c), representing the fraction of hydrogen entering the metal during charging.

Trap Density

The density of particles or defects (N_i) providing irreversible traps can be obtained from the apparent trapping constant by using a model based on spherical traps:[4,8]

$$N_i = k_a a/(4\pi d^2 D_a) \qquad (3)$$

where a is the diameter of the metal atom and d is the trap radius, which is estimated from the dimensions of heterogeneities that are potential irreversible traps. The value of a for an alloy is taken as the mean of the atomic diameters weighted in accordance with the atomic fraction of each element. The predominant irreversible trap can be identified by comparing the calculated trap density with the actual concentration of a particular heterogeneity in the alloy.

The assumption of spherical traps is an approximation in most cases. However, for various alloys studied to date, the calculated trap densities have shown close agreement with the concentrations of potential trap particles that are clearly not spherical, suggesting that use of a more applicable trap geometry would make little difference in identifying the principal traps.

Experimental

The composition and yield strength of each alloy are given in Tables 1 and 2, respectively. Also shown in Table 2 is the thermo-mechanical treatment used for each alloy. A number of the alloys contained micrometer-size particles such as carbides or, in the case of 4340 steel, sulfide inclusions. The characteristic dimension of these particles was determined as the mean of the linear dimensions in the exposed plane.

The test electrodes of each alloy consisted of a length (1.3-3.8 cm) of rod press-fitted into a Teflon sheath so that only the planar end surface was exposed to the electrolyte. The surface was

polished before each experiment with SiC paper followed by 0.05-μm alumina powder. The electrolyte was an acetate buffer (1 mol L^{-1} acetic acid/1 mol L^{-1} sodium acetate) containing 15 ppm As$_2$O$_3$ as a hydrogen entry promoter. The electrolyte was deaerated with argon for 1 hr before measurements began and throughout data acquisition. The potentials were measured with respect to a saturated calomel electrode (SCE). All tests were performed at 22 $\pm$ 2°C. Details of the electrochemical cell and instrumentation have been given elsewhere.[3]

The test electrode was charged with hydrogen at a constant potential E$_c$ for a time t$_c$, after which the potential was stepped in the positive direction to a value 10 mV negative of the open-circuit potential E$_{oc}$.[3,7,8] Anodic current transients with a charge q_a were obtained over a range of charging times (0.5-60 s) at different overpotentials (η = E$_c$ - E$_{oc}$). The open-circuit potential of the test electrode was sampled immediately before each charging time and was also used to monitor the stability of the surface oxide; reduction of the film was evident from a progressive shift of E$_{oc}$ to more negative values with each t$_c$ at a sufficiently high charging potential. A typical transient is shown in Figure 1. Experimental and fitted values of q_a for various charging times are compared in Figure 2, which illustrates the level of agreement obtained for the alloys in this work.

Initial Application of HIAPP

The application of HIAPP to alloys was explored initially with a high-strength steel — AISI 4340 (UNS G43400), and two nickel-containing alloys — Monel K-500 (UNS N05500) and MP35N (UNS R30035).[3] The aim was to determine their hydrogen ingress characteristics and compare them in relation to differences in their HE susceptibility.

Hydrogen Ingress Characteristics

The values of k_a and k are shown in Table 3. k_a was found to be independent of heat treatment in the case of 4340 steel. Initial results[3] for alloy K-500 indicated that there was no apparent difference in trapping behavior between the unaged and aged alloy, but improvements in data aquisition have since revealed that the trapping constant of the aged alloy is a little higher than that of the unaged alloy.[10]

The values of both k and J are higher for 4340 steel than those for alloys K-500 and 35N. Hence, both of these parameters are consistent with the steel being more susceptible to HE than the two nickel-containing alloys. The reduction of H$^+$ and subsequent entry of H atoms into alloys K-500 and 35N occurred on an oxide-covered surface, which undoubtedly explains the lower hydrogen flux for these alloys. Perhaps of more significance in terms of susceptibility is the nature of the irreversible traps reflected by the values of k. This issue was explored further by calculating the density of irreversible trap defects (commonly second-phase particles and precipitates) from k_a [Eq. (3)] and comparing it with the actual defect concentration in the alloy.

Identification of Traps

4340 Steel. The trap density was calculated in terms of MnS inclusions and was found to be in reasonable agreement with the actual concentration of inclusions, indicating that they did indeed provide the primary irreversible traps in this alloy. The lack of change in k_a and therefore N$_i$ with heat treatment was further evidence that the irreversible traps were associated with some stable species such as MnS inclusions.

Alloys K-500 and 35N. HE in Ni-Cu base alloys and alloy 35N is known to be assisted by sulfur and phosphorus segregated at grain boundaries.[11,12] Since hydrogen also probably segregates to the grain boundaries as in Ni,[13] grain boundary S and P were assumed to provide the irreversible traps predominantly encountered by hydrogen in alloys K-500 and 35N. However, a lack of data for S and P segregation in these alloys makes it difficult to verify the nature of the traps by the approach used here.

The density of irreversible traps provided by atomic S and P is three orders of magnitude less than the overall S and P content determined from the alloy composition (Table 1). Hence, it is clear that, providing that S and P are the principal irreversible traps, any useful comparison of N_i must be made with respect to grain boundary concentrations. Subsequent work[5] on Hastelloy C-276 (UNS N10276) has shown that it is possible for the trap density to agree closely with the amount of grain boundary P distributed per unit volume of the alloy. Hence, it does seem reasonable in the case of alloys K-500 and 35N to consider S and P at grain boundaries, rather than in the bulk alloy, to be the primary irreversible traps.

Rationale for HE Susceptibility

Two significant findings emerged from this work in terms of rationalizing differences in the HE susceptibility of the three alloys. First, values of k and J for 4340 steel were higher than those for alloys K-500 and 35N. Second, the irreversible traps in the steel appeared to be associated with inclusions, whereas those in alloys K-500 and 35N were considered to be elements segregated at grain boundaries. The difference in both the nature of the irreversible traps and the interfacial flux must play a major role in the different susceptibilities of the steel and the two Ni-containing alloys. The sulfide inclusions, in particular, can be linked to the susceptibility of 4340 steel, since they are strong traps with a large hydrogen capacity; in other words, these inclusions possess the two characteristics that are most detrimental.

Further Application of HIAPP

The application of HIAPP was extended to alloys of various groups: Precipitation-hardened alloys — Inconel 718 (UNS N07718), Incoloy 925 (UNS N09925), and 18Ni maraging steel;[4] work-hardened alloys — Inconel 625 (UNS N06625) and Hastelloy C-276;[5] and pure (99.99%) and grade 2 (UNS R50400) titanium.[6] In the case of pure Ti, the anodic charge was invariant with t_c, indicating that negligible hydrogen enters the metal. The resistance of pure Ti to hydrogen entry was attributed to the surface film, which is known to be a highly effective barrier.

Hydrogen Ingress Characteristics

The mean values of k_a and k are summarized in Table 3. The maraging steel has the highest value of k, followed by alloys 718, C-276, 925, Ti grade 2, and alloy 625. Stress-rupture tests during electrolytic charging have shown that 18Ni (1723 MPa) maraging steel undergoes severe embrittlement, whereas alloy 718 exhibits negligible susceptibility.[14] In addition, test results suggest that Incoloy 903 (UNS N09903)[15] and, by implication, alloy 925 are less sensitive than alloy 718[14] to HE. Hence, the irreversible trapping constants for the precipitation-hardened alloys are consistent with their relative susceptibilities to HE.

A similar comparison of the susceptibilities of alloys C-276 and 625 is complicated by their sensitivity to the amount of cold work performed in each case. However, the ranking of these alloys can be assessed indirectly from previous studies of alloys C-276 and G (UNS N06007).[16] The composition of alloy G is comparable to that of alloy 625, and it can be reasoned[5] that, for the degree of cold work involved, alloy C-276 should be more susceptible to embrittlement, as indeed indicated by the trapping constants. The susceptibility of alloy C-276 relative to the other alloys, as reflected by its trapping constant, is subject to some question because of the uncertainty in k.

Titanium grade 2 exhibited two values of k, depending on the level of hydrogen present in the metal. The similarity in trapping constants for Ti grade 2 and alloy 925 fits their relative resistance to HE in that long exposure times are required for the concentration of hydrogen to exceed the level necessary to result in a loss of mechanical properties.[15,17] Furthermore, the higher trapping constant coincides with the increasing susceptibility to embrittlement with hydrogen concentration due to hydride precipitation.

Identification of Traps

Alloy 718. The irreversible traps were assumed to be niobium carbide particles, and the density of trap particles was calculated to be 2.0×10^{13} m^{-3}, as compared with 2.2×10^{13} m^{-3} for the actual concentration of carbide particles. This close agreement was remarkable in view of the spherical shape assumed for the traps and carbides, but it indicates clearly that large traps with both a high surface area and a high trapping energy can overwhelmingly dominate the irreversible trapping behavior of an alloy.

Alloy 925. TiC particles were assumed to provide the irreversible traps in Incoloy 925, and the density of trap particles was calculated to be 4.1×10^{13} m^{-3}. The actual concentration of carbide particles (4.6×10^{13} m^{-3}) and the trap density were again found to be in close agreement, despite treating both the traps and carbides as spherical.

18Ni Maraging Steel. A combination of irreversible traps and quasi-irreversible traps appeared to be present in this alloy. The quasi-irreversible traps were difficult to identify, although autoradiography studies have shown that trapping occurs at grain boundaries and martensite boundaries in maraging steel.[18] Both sites appear to be moderately strong traps. However, grain boundaries are generally considered to be reversible traps in ferritic steels, and so the martensite boundaries may well be stronger traps. The martensite boundaries, like grain boundaries,[19] were assumed to have an influence diameter of 3 nm, which gave a trap density of 9×10^{17} m^{-3}.

The irreversible traps were able to be identified more closely with qualified support from the comparison of N_i with particle concentration. Trapping has been observed at carbo-nitride interfaces in maraging steels,[18] and so the density of irreversible traps was calculated on the basis of TiC/Ti(CN) particles. N_i was found to be 3.4×10^{11} m^{-3}, as compared with $(1.1 \pm 0.6) \times 10^{13}$ m^{-3} for the actual concentration of particles. The two values differ by a factor of ~30, which can largely be accounted for by uncertainties in both the concentration of particles and the value of D_a assumed for the maraging steel. In view of these uncertainties, the calculated trap density and carbide/nitride concentration were considered to correlate moderately well.

Alloy 625. NbTi carbide particles were assumed to act as the principal irreversible traps, and the density of trap particles was calculated to be 2.5×10^{13} m^{-3}. Since there was some uncertainty in D_a for this alloy, the trap density was regarded as being in good agreement with the actual concentration of particles (7.4×10^{13} m^{-3}).

Alloy C-276. The trapping behavior can be interpreted on a similar basis to that for 18Ni maraging steel, in which both irreversible and quasi-irreversible traps exist. The quasi-irreversible trapping was consistent with the formation of an unstable hydride during charging. In the irreversible case, the traps were clearly different from those in the other cold worked alloy (625), since carbide particles appeared to be absent in alloy C-276. The HE susceptibility of this alloy, like that of alloy 35N, has been correlated with the concentration of phosphorus segregated at grain boundaries.[20] Hydrogen probably segregates to the grain boundaries also in this case, so grain boundary P was again assumed to provide the irreversible traps. It should be noted that although P may play a role in alloy 625, the carbide particles appear to dominate the irreversible trapping.

The concentration of grain boundary P was estimated on the basis of a simple microstructural model involving cubic grains of length b (in m).[5] By using data for P enrichment at grain boundaries in alloy C-276,[20] it was shown that the amount of grain boundary P per unit volume (C_b) is given by $9 \times 10^{16}/b$ atoms m^{-3}. The value of b for the C-276 alloy was estimated to be 10 μm, and therefore, C_b was calculated to be ~9×10^{21} P atoms m^{-3}. In contrast, the total P content of the alloy corresponded to 8.6×10^{24} atoms m^{-3}, while the trap density calculated on the basis of atomic P was found to be 1.9×10^{22} m^{-3}. The close agreement between the values of C_b

and N_i was somewhat fortuitous but demonstrated that grain boundary P can in fact provide the primary irreversible traps.

Titanium Grade 2. The increase in trapping constant at a high enough overpotential can be ascribed to an additional type of irreversible trap participating concurrently with the irreversible traps detected at low overpotentials. The trap density at low hydrogen levels was calculated in terms of the minor elements (C, N, O, and Fe), and it was found that all of them except nitrogen could be discounted as the principal irreversible trap. Interestingly, among the interstitials, nitrogen is particularly effective in reducing the ductility of titanium,[21] which coincides with its apparent role as the principal trap. Hence, nitrogen may strongly affect the susceptibility of Ti grade 2 to HE through its combined influence on brittleness and hydrogen trapping.

The additional trapping constant obtained at high hydrogen levels [E_c <-0.93 V(SCE)] is probably associated with the accelerated formation of hydrides reported[22] to occur at potentials more negative than -1.0 V (SCE). A decrease observed in the entry efficiency (Figure 3) in this potential region is consistent with the presence of a partial barrier to hydrogen entry and so provides support for the formation of a thick hydride layer.

Rationale for HE Susceptibility

Two key features marked the work extending the use of HIAPP. First, the trapping capability of the individual alloys was shown to be consistent with their relative susceptibilities to HE. Second, a range of microstructural features were identified as the predominant irreversible traps, present as either a single type or multiple types.

Alloys 625, 718, and 925 were each characterized by a single type of irreversible trap — (NbTi)C, NbTi(CN), and TiC particles, respectively — whereas alloy C-276 and 18Ni maraging steel were characterized by both an unidentified quasi-irreversible trap and an irreversible trap thought to be grain boundary phosphorus in the case of alloy C-276 and TiC/Ti(CN) particles in the case of the steel. Ti grade 2 exhibits two types of irreversible trap — probably involving interstitial nitrogen and hydride formation — depending on the concentration of hydrogen in the metal. The type of trap defect tends to be reflected by its size, so the type, together with the defect concentration (N_i) and the hydrogen diffusivity, determines the magnitude of k.[4] Thus, in view of the diversity of microstructural features that act as the predominant traps, it is not surprising that the HE susceptibility varies considerably between alloys.

Ranking Susceptibility to Hydrogen Embrittlement

The irreversible trapping constants for all the alloys tested in this work are listed in Table 4 in descending order. Clearly, there is a strong correlation between the HE susceptibility and the trapping capability of the alloy as represented by k. The trapping constants, as might be expected, indicate that the 4340 steel is the most susceptible, followed by the maraging steel, which is predicted to be somewhat less so on the basis of its k. The sequence of k values for the two steels is in agreement with experimental results, which showed that 4340 steel was more susceptible to hydrogen-induced cracking than 18 Ni(250) maraging steel.[23] At the other extreme, the low trapping constant for alloy 35N is consistent with the high resistance to HE found in practice for this alloy.[24]

It is difficult to determine whether the two cold-worked alloys follow the observed pattern for the trapping constants because of a lack of relevant results for HE. Moreover, some uncertainty in the values of k for alloys C-276 and 625 compounds the difficulty in evaluating the position of these alloys in Table 3, other than noting that, as discussed above, the C-276 alloy in this study is somewhat more susceptible to embrittlement than alloy 625. The position of alloy 625 is comparable to that of alloy 35N within the uncertainty of k. Failure tests[24] indicate that alloy 625 with 17% cold work should be at least as resistant to HE as alloy 35N in the condition (40%

cold reduced and aged) of interest in our work. In fact, the Inconel may be more resistant than the alloy 35N specimen, as implied by their different values of k. Hence, the trapping constants of alloys 625 and 35N appear to be consistent with the relative HE susceptibilities.

Summary

A correlation was shown to exist between trapping capability and HE susceptibility for a wide range of alloys. In the case of 4340 steel and 18Ni maraging steel, the trapping constants reflect their relatively high susceptibility, whereas the nickel-base alloys display less trapping capability than the two steels and, as expected, are found to be more resistant to HE. Differences in the resistance of the nickel-base alloys are smaller than those for the steels, but they can still be resolved from the trapping constants. In particular, the trapping constants for alloys within groups defined by thermo-mechanical treatment (precipitation- and work-hardening) are consistent with their relative susceptibilities to embrittlement. Thus, HIAPP appears to provide a convenient means of quantitatively characterizing the susceptibility of an alloy to HE. In addition, a range of microstructural features can be identified as the predominant irreversible traps, either singly or in the presence of multiple principal traps.

Acknowledgment

References

1. G. M. Pressouyre and I. M. Bernstein, Metall. Trans., **9A** (1978): p. 1571.
2. G. M. Pressouyre and I. M. Bernstein, Acta Metall., **27** (1979): p. 89.
3 B. G. Pound, Corrosion, **45** (1989): p. 18.
4. B. G. Pound, Acta Metall., **38** (1990): p. 2373.
5. B. G. Pound, Acta Metall., **39** (1991): p. 2099.
6. B. G. Pound, Corrosion, **47** (1991): p. 99.
7. R. McKibbin, D. A. Harrington, B. G. Pound, R. M. Sharp, G. A. Wright, Acta Metall., **35** (1987): p. 253.
8. B. G. Pound, R. M. Sharp, and G. A. Wright, Acta Metall., **35** (1987): p. 263.
9. B. G. Pound, in Modern Aspects of Electrochemistry, J. O'M. Bockris, B. E. Conway, and R. E. White, eds., No. 25, in press.
10. B. G. Pound, Corrosion, submitted for publication.
11. J. D. Fransen and H. L. Marcus, Effect of Hydrogen on the Behavior of Materials, I. M. Bernstein and A. W. Thompson, eds. (Warrendale, PA: The Metallurgical Society of AIME, 1976), p. 233.
12. R. D. Kane and B. J. Berkowitz, Corrosion, **36** (1980): p. 29.
13. D. H. Lassila and H. K. Birnbaum, Acta Metall., **35** (1987): p. 1815.
14. R. J. Walter, R. P. Jewett, and W. T. Chandler, Mater. Sci. Eng., **5** (1969/70): p. 98.
15. C. G. Rhodes and A. W. Thompson, Metall. Trans., **8A** (1977): p. 949.
16. D. A. Mezzanotte, J. A. Kargol, and N. F. Fiore, Metall. Trans., **13A** (1982): p. 1181.
17. R. W. Schutz and D. E. Thomas, in Metals Handbook, 9th ed., Vol. 13 (Metals Park, OH: American Society for Metals, 1987), p. 669.
18. M. Aucouturier, G. Lapasset, and T. Asaoka, Metallography, **11** (1978): p. 5.
19. M. Pressouyre, Metall. Trans., **10A** (1979): p. 1571.
20. B. J. Berkowitz and R. D. Kane, Corrosion, **36** (1980): p. 24.
21. A. E. Jenkins and H. W. Worner, J. Inst. Metal., **80** (1951/52): p. 157.
22. H. Sato, T. Fukuzuka, K. Shimogori, and H. Tanabe, 2nd Int. Cong. Hydrogen in Metals, **3** (Paris, 1977).
23. T. P. Groeneveld, E. E. Fletcher, and A. R. Elsea, "A Study of Hydrogen Embrittlement of Various Alloys," Tech. Support Package to Tech. Brief No. 67-10141, (Washington D.C.: NASA, 1967), p. 135.
24. R. D. Kane, M. Watkins, D. F. Jacobs, and G. L. Hancock, Corrosion, **33** (1977): p. 309.

Table 1
ALLOY COMPOSITION (wt %)

Alloy	Al	C	Co	Cr	Cu	Fe	Mn	Mo	Ni	P	S	Si	Ti	Other
4340 Steel	0.031	0.42		0.89	0.19	bal	0.46	0.21	1.74	0.009	0.001	0.28		0.005 N, 0.001 O, 0.05 Ca
18Ni Steel	0.13	0.009	9.15	0.06	0.11	bal	0.01	4.82	18.42	0.004	0.001	0.04	0.65	0.003 B, 0.01 W, 0.02 Zr
K-500	2.92	0.16			29.99	0.64	0.72		64.96		0.001	0.15	0.46	
35N		0.003	bal	20.19		0.34	<0.01	9.55	35.88	0.003	0.002	0.02	0.85	
718	0.60	0.03	0.16	18.97	0.04	16.25	0.10	3.04	54.41	0.009	0.002	0.11	0.98	0.003 B, 5.30 Nb+Ta
925	0.30	0.02		22.20	1.93	28.96	0.62	2.74	40.95		0.001	0.17	2.11	
C-276		0.002	0.83	15.27		5 84	0.48	16.04	57.5	<0.005	<0.002	<0.02		3.90 W
625	0.18	0.03		22.06		4.37	0.17	8.70	60.33	0.012	0.001	0.38	0.27	0.12 V, 3.50 Nb+Ta
Ti grade 2		0.021				0.17							bal	0.007 N, 0.16 O, <0.005 H

Table 2
Thermo-Mechanical Treatment of Alloys

Alloy	Heat Treatment[a]	Test Condition	Yield Strength (MPa)
4340 Steel	Annealed	Austenized/Tempered to HRC 41 and 53	1206 &1792
18Ni Steel	Aged (482°C, 4 hr)	As received	1954
K-500	Cold drawn, unaged	As received Aged (600°C, 8 hr)	758 1096
35N	Cold drawn and aged	As received	1854
718	Hot finish, solution treated	As received	1238
925	Hot finish, annealed, aged	As received	758
625	Hot finish, annealed	17% cold work	1195
C-276	Hot rolled	27% cold work	1237
Ti Grade 2	Annealed (620°C, 1 hr)	As received	380

[a] Provided by producer.

Table 3
Trapping Parameters

Alloy	k_a (s^{-1})	D_L/D_a	k (s^{-1})
4340 Steel	0.008 ± 0.001	500	4.0 ± 0.5
K-500 Unaged	0.017 ± 0.003	2.0	0.034 ± 0.006
Aged	0.021 ± 0.003	2.0	0.042 ± 0.006
35N	0.026 ± 0.002	1	0.026 ± 0.002
718	0.031 ± 0.002	4.0 ± 0.5	0.124 ± 0.024
925	0.006 ± 0.003	4.6 ± 0.6	0.034 ± 0.004
18Ni Steel	0.005 ± 0.002	300 ± 90	1.50 ± 1.05
	0.010 ± 0.005[a]	300 ± 90	3.00 ± 2.40
625	0.004 ± 0.002	2.6 ± 0.8	0.014 ± 0.010
C-276	0.025 ± 0.003	2.6 ± 0.8	0.090 ± 0.030
	0.019 ± 0.010[a]	2.6 ± 0.8	0.068 ± 0.051
Ti pure	na[b]	1	na
Ti grade 2	0.028 ± 0.002	1	0.028 ± 0.002
	0.012 ± 0.006[c]	1	0.012 ± 0.006

[a] Quasi-irreversible trapping; [b] na = not available; [c] Hydride formation.

Table 4
Irreversible Trapping Constants

Alloy	k (s^{-1})
4340 steel	4.0 ± 0.5
18Ni (300) steel	1.50 ± 1.05
718	0.128 ± 0.024
C-276 (27% cw[a])	0.090 ± 0.030
K-500	0.040 ± 0.010
Ti grade 2 (high H)	0.040 ± 0.008
925	0.034 ± 0.004
Ti grade 2 (low H)	0.028 ± 0.002
35N	0.026 ± 0.002
625 (17% cw)	0.014 ± 0.010

[a] cw = cold work
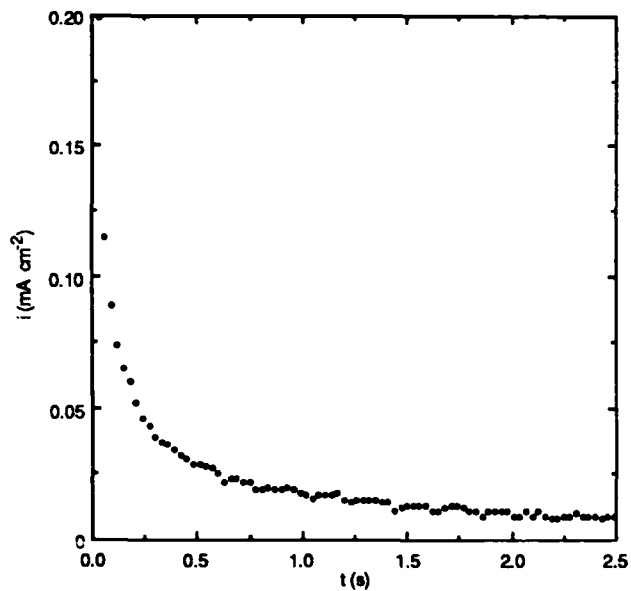
Figure 1. Anodic transient for titanium grade 2 in acetate buffer.
$t_c = 15$ s; $E_c = -0.742$ V (SCE).

The full transient is not shown.
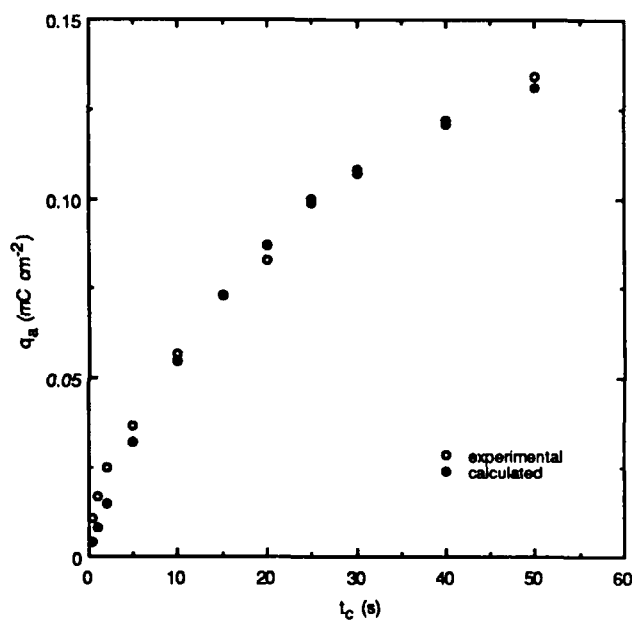
Figure 2. Comparison of experimental and calculated anodic charge data for titanium grade 2 in acetate buffer.

$E_c = -0.741$ V (SCE).
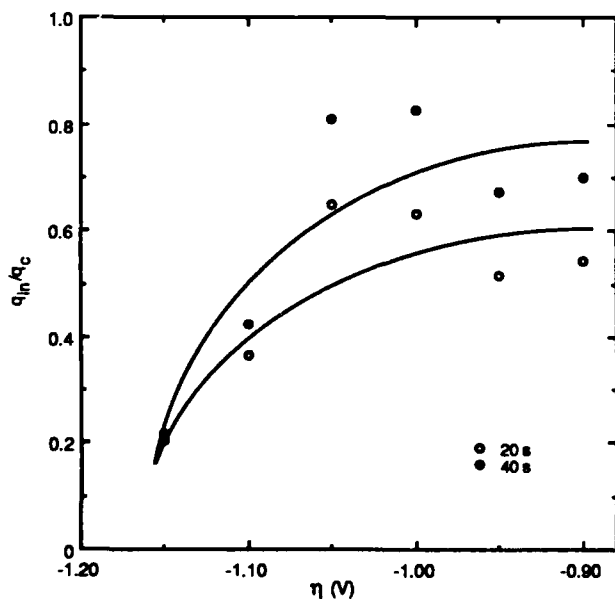
Figure 3. Dependence of q_{in}/q_c on overpotential for titanium grade 2 at high overpotentials and charging times of 20 s and 40 s.

Evaluation of Three Different Surface Modification Techniques for Resisting Hydrogen Embrittlement in Steel

C.L. Ho
Chinese Petroleum Corp.
Refining & Manufacturing Research Center
239, Min Sheng S.Road, Chia-Yi, Taiwan, 60036, R.O.C.

S.L.I. Chan
Institute of Materials Science and Engineering
National Taiwan University
Taipei, Taiwan, 10764, R.O.C.

J.Y. Lin
Chinese Petroleum Corp.
Refining & Manufacturing Research Center
239, Min Sheng S. Road, Chia-Yi, Taiwan, 60036, R.O.C.

Abstract

The purpose of this investigation was to evaluate the effects of three different types of surface modifications on the hydrogen embrittlement (H.E.) of 4130 steel. The surface modification processes employed here were laser surface hardening, cold rolling and shot peening . The specimens were fully annealed before the test, and then subjected to the surface modifications listed above. To assess the degree of H.E., slow strain rate tensile test (C.E.R.T.) and constant load rupture test (C.L.R.T.) were carried out in NACE H_2S-saturated solutions. Under external stress application, cracks were found near the interface of the hardened zone and the base metal. Consequently, the ductility of the specimens was severely degraded. In the case of cold rolling, the results in this work suggest that cold rolling increased the resistance to H.E. under all types of loadings. It was mainly because of the compressive stresses on the surface and the amount of uniform trapping sites produced by cold rolling. The critical amount of rolling under which no cracking was found, however, depended on the steel composition, heat treatment as well as the service conditions. Shot peening resulted in a residual compressive stress on the surface, thus retarding the formation of crack induced by hydrogen. The amount of loading was found to have a significant effect on the H.E. susceptibility of steel after shot peening. For instance, it was sensitive to H.E. when the external stress applied was higher than the yield strength of material. However, when the applied stress was lower than the yield strength, the compressive stress resulted from shot peening can resist H.E..

Keyterms: AISI 4130 Steel, hydrogen embrittlement, laser surface hardening, cold rolling, shot peening

Introduction

There are many failure modes in petroleum refining processes. Figure 1 illustrates examples of failure for furnace tubes : oxidation, external crack, degradation, creep, corrosion, hydrogen attack and carburization[1]. Thus ways to prevent premature failure of steel induced by hydrogen are always emphasized in the petrochemical industry. The purpose of this investigation was to study the effects of surface modification on the hydrogen embrittlement (H.E.) of AISI 4130 steel. A high power CO_2 laser provided a controllable, precise energy source for phase transformation of steels to produce a martensitic layer on the steel surface. The existence of this martensitic layer delays the hydrogen diffusion into the steel. Many reports [2,3] state that shot peening and cold rolling also increase the resistance of a steel to hydrogen embrittlement. This is because these types of cold deformation increase the dislocation density, produce a compressive stress on the steel surface, and change the hydrogen diffusion path. However, adverse effects of cold working have also been reported on spheroidized 1045 [4,5] and 1095 [5,6] steels. It is possible that the cold working can enhance hydrogen-induced failures by facilitating the particle-matrix separation, void initiation and growth, local stress concentration caused by plastic incompatibility and particle cracking. These contrasting results illustrate the complexity of the effect of cold working, and that different types of steel, because of their chemical compositions and microstructures, might behave differently after surface treatment. This paper focuses on the evaluation of the above different surface modification techniques for resisting hydrogen embrittlement in the 4130 steel.

Experimental Procedure

The chemical composition of AISI 4130 steel used in this work was determined by XRF analysis (Table 1). Before surface modification, specimens were austenised at 870°C for 1 hour, then furnace-cooled to room temperature. The resulting microstructure was a ferrite/pearlite banded structure(figure 2), with a hardness around Hv 200. The specimens were then subjected to different kinds of surface modifications. In order to increase the absorptivity of specimen during the laser surface hardening, black paint was coated on the surface before the laser surface treatment. The laser power, traveling speed and defocused distance were 1200 watts, 2500 mm/min and 15 mm respectively. Careful controlling of the laser treating process was followed in order that the surface layer of the material exceeded the austenising temperature. Overheating the specimen which might give rise to melting was avoided. In the cold rolling process, the specimens were subjected to different degree of rolling reductions (10%, 20% and 30%). To avoid specimen distortion, each pass of the cold rolling was less than 2% reduction. Shot peening conditions used in this work are shown in Table 2. Shot peening for 10 minutes was found to be the best condition after preliminary testing on H.E., it was then chosen to evaluate the effects of shot peening treatment. Hydrogen charging following the specifications of NACE TM-01-77 (5% NaCl +0.5% acetic acid) was used to evaluate the degree of H.E.. During tensile testing, H_2S was charged continuously into the solution to ensure that the solution was saturated with the gas. Both constant extension rate tensile testing (CERT) and constant load rupture testing (CLRT) were employed. In CERT, three different extension rates ($5*10^{-6}$, $10*10^{-6}$ and $20*10^{-6}$ sec^{-1}) have been used. Figure 3 shows the dimensions of the tensile specimens . The loss in elongation of specimens with hydrogen charging, as compared to that of the hydrogen-free specimens, was chosen as the index on H.E. susceptibility. For CLRT, a load corresponding to 70%, 80% and 90% of the tensile yield stress of materials was applied to the specimen while being hydrogen charged. The time to failure (TTF) was recorded as an indication of the H.E. susceptibility.

Results and Discussion

Laser Surface Modification

Martensitic layers were produced by the laser treatment. The interaction time between laser beam and specimens was so short that banding was retained after the hardening. Figure 4 shows the cross-sectional hardness of a specimen after laser treatment. An average hardened layer of about 0.5 mm was

formed. Figure 5 shows the load-elongation curves of specimens. When the specimens were charged with H_2S, the U.T.S. and elongation decreased significantly. On application of an external load, microcracks were formed in the martensitic layer. When the stress level increased, the cracks propagated through the specimen. At the same time, hydrogen was transported to the cracks. So U.T.S. and elongation were decreased by the action of hydrogen in the crack tip. The same phenomenon was also observed under constant load rupture testing. Figure 6 shows the micrographs of failure specimens. There were several cracks on CERT and CLRT specimens if H_2S-charged. Figure 7 shows the elongation loss under different strain rate tensile testing. Figure 8 shows the time to failure under different applied stress. When an external stress was applied, cracks were produced quickly in the martensitic layers. These cracks propagated through the specimens and failure occurred shortly. Thus under external stress condition, laser hardening was found to be detrimental to the H.E. resistance of 4130 steel.

Cold Rolling Treatment

Figure 9 shows that without hydrogen charging, the U.T.S. of cold-rolled specimens increased with increasing amount of cold deformation, and that it also decreased slightly with increasing strain rate. It is very obvious from the CERT and CLRT studies that the susceptibility of steel to hydrogen embrittlement was significantly reduced by cold working. In Figure 10, where the results of elongation losses of the hydrogen-charged specimens is plotted against the degree of cold rolling, it is evident that under constant extension rate, the specimens suffered more elongation loss when a slower extension rate was used. This was as expected since with a slower extension rate, more hydrogen was allowed to diffuse to the stress concentration sites, hence allowing hydrogen embrittlement to take place. Figure 10 also shows that the elongation losses decreased with increasing degrees of cold rolling, a result that was different from that obtained in CLRT (Figure 11). Thus in CERT, a specimen with 30% rolling reduction was more resistant to H.E. than that with 20% or 10% reduction, while the opposite result was observed in CLRT. An explanation for this apparent discrepancy is given as follows. Cold rolling increased the dislocation density, created heterogeneity, and depending on the degree of deformation, some voids or small cracks were formed in the steel. For CERT, the testing duration was less than 6 hours. Taking into account the relatively short charging periods, only a limited amount of hydrogen can diffuse into the specimens. With increasing degree of cold deformation, hydrogen diffusion was slow, and the hydrogen was evenly distributed in traps such as deformed grain boundaries, microvoids or microcracks, dislocations etc. Thus a critical hydrogen concentration, C, which gave rise to hydrogen embrittlement, could not be achieved easily. Consequently the degree of H.E. for 30% reduction specimens was reduced. On the other hand, for un-deformed or lightly deformed specimens (e.g.. 10% reduction), hydrogen diffusion in these specimens was high, and there were relatively less number of defects available for innocuous hydrogen trapping. In this case hydrogen diffused to the cracking zone easily and induced failure. However, for CLRT the situation was different. The hydrogen charging period was ten times or more than that in the CERT. Diffusion of hydrogen was no longer a problem and all the traps were filled with hydrogen. Thus the specimens with 30% reduction, which have more defects and microvoids with a large amount of hydrogen within these traps, were more prone to hydrogen embrittlement than those lightly deformed specimens. In a study on the stepwise cracking (SWC) of cold-rolled steel, where the stress-free specimens were immersed in NACE H_2S solution for 96 hours, it was found that the cold rolling increased the SWC resistance of the specimens, but the resistance diminished as the degree of cold rolling exceed 15%[7]. In summary, the above results of CERT and CLRT can be explained by the trapping theory, and the effect of cold rolling varied with the form of stress application and the hydrogen charging period.

Shot Peening Treatment

Figure 12 shows the results of CERT of specimens after shot-peening. Elongation loss of these specimens was higher than that of the as-received specimens. Figure 13 shows the results of CLRT of shot peened specimens. The result obtained was different from that obtained in CERT. In CLRT, a specimen after shot peening treatment was more resistant to H.E. than the as-received one. Shot peening treatment created localized deformation and increased heterogeneity in the steel. It also induced a compressive stress on the surface. In CERT, the treatment could change the surface stress

distribution, destroy the compressive stresses on the surface, and allow hydrogen to reach stress concentration areas easily . The higher stress level in CERT, as compared with that in CLRT, may also reduce the critical hydrogen concentration levels required for hydrogen embrittlement. In any case both factors increased the H.E. susceptibility of the specimens. For the CLRT results, hydrogen transport by dislocation was not so obvious when applied stress was lower than yield stress of material. The movement of dislocations at these stress levels was very much restricted, and diffusion was the main mechanism for hydrogen transport. This is the reason why the shot peening specimen could help in resisting hydrogen embrittlement . Figure 14 shows the fracture mode of charging-free and charged, shot peened specimens. Under a charging-free condition, the specimens shows ductile failure with a dimple pattern that can be seen clearly. After H_2S charging, metals were embrittled severely by hydrogen, the fracture mode of the base metal changing from ductile to quasi-cleavage failure.

Conclusions

For the safe and economical operations, it is necessary to investigate the effect of different types of surface treatment on the hydrogen embrittlement of the AISI 4130 steels. Three major conclusions were obtained which provide some information on the prevention of material failure in hydrogen charging environment:

1. For the laser-hardened specimens, cracks were found near the interface of the hardened zone and the base metal under tensile stress in hydrogen charging environment. The mechanical properties were severely degraded. Thus suggests that laser surface hardening is not a suitable way for improving the hydrogen embrittlement resistance of steels under external stress.

2. Cold rolling can reduce the sensitivity of AISI 4130 steel to hydrogen embrittlement. This is due to the increase in dislocation density and defects which delays the hydrogen diffusion in the steel. The defects may act as innocuous trapping sites for hydrogen. The optimum degree of cold rolling may depend on the service conditions such as the stress state, hydrogen contents etc.

3. Shot peening made the steel more resistant to hydrogen embrittlement than the as-received condition if the applied stress was lower than yield strength of material.

References

1. Material Research Laboratory,"Research of Furnace Tube for Chinese Petroleum Corp." MRL-TAT 8101, (1992), P.1
2. G.M. Pressouyre, J. Dollet and B.Vieillard-Baron, Met. Sci. Rev., 79 (1982): p.161
3. K.N. Akhurst and P.H. Pumphrey, 2nd. International Congress on Hydrogen in Metals, 3B1, Paris-France, 1977
4. H. Cialone and R.J. Asaro, Met. Trans., 10A (1979): p.367
5. R.A. Oriani and P.H. Josephic, Met. Trans., 11A (1980): p.1809
6. M.W. Joosten,T.D. Lee,T. Goldenberg and J.P. Hirth in "Hydrogen effects in metals", Eds. I.M. Bernstein and A.W. Thompson, Met. Soc. of AIME (1981), p..839
7. J.S. Wu, Master's Thesis, National Taiwan University, 1988

Table 1. Chemical composition of AISI 4130 steel by XRF analysis

Material	Fe	C	Si	Mn	P	S	Ni	Cr	Mo
4130	-Bal-	.315	0.26	0.49	.004	.003	0.27	0.99	0.16

Table 2. Conditions of shot Peening used in this experiment

ball hardness	HRc 55 ~ 60
ball diameter	0.4 ~ 0.7 mm
motor power	5 hp
motor speed	1720 rpm
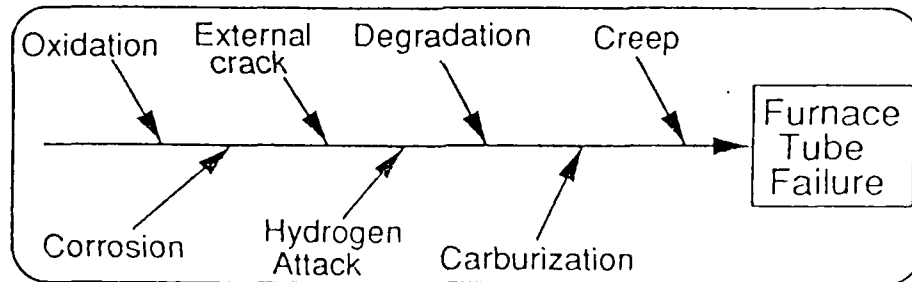
Figure 1. Typical failure modes of furnace tubes in refining processes
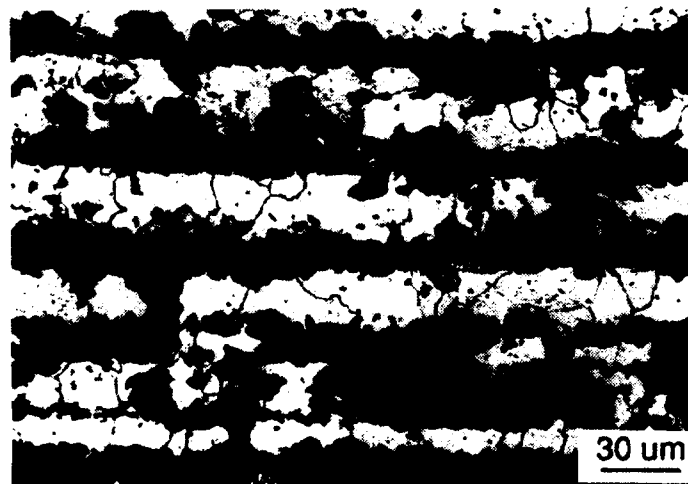
Figure 2. Microstructure of steel before surface nodification
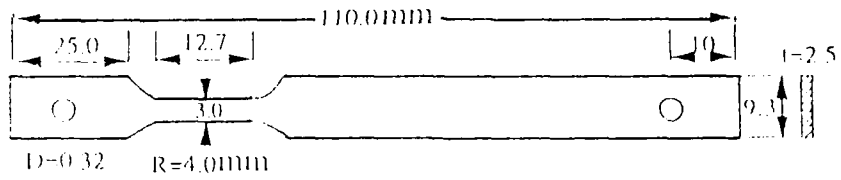
Figure 3. Dimensions of the tensile specimen
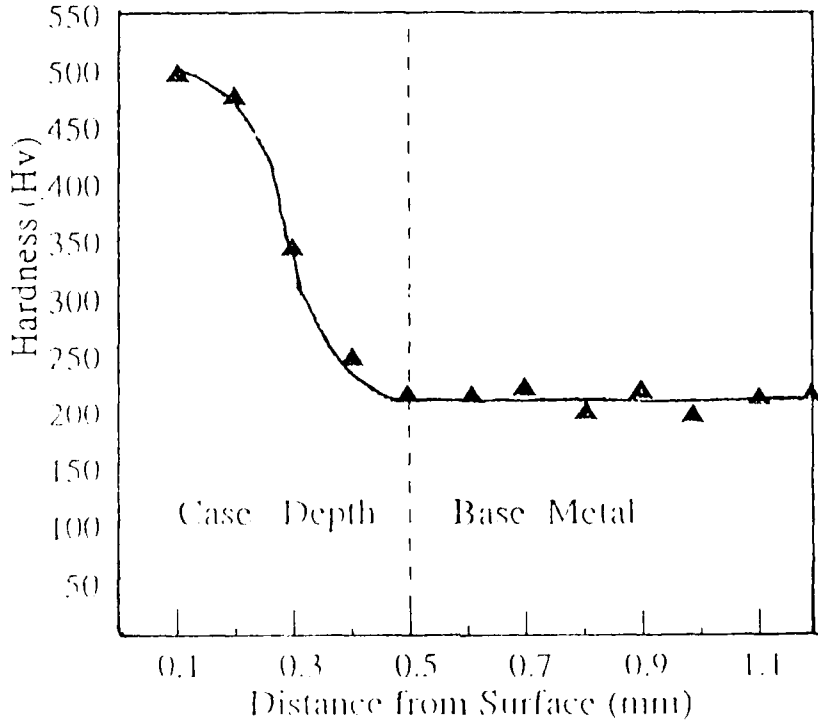
Figure 4. Cross-sectional hardness of specimen after laser treatment
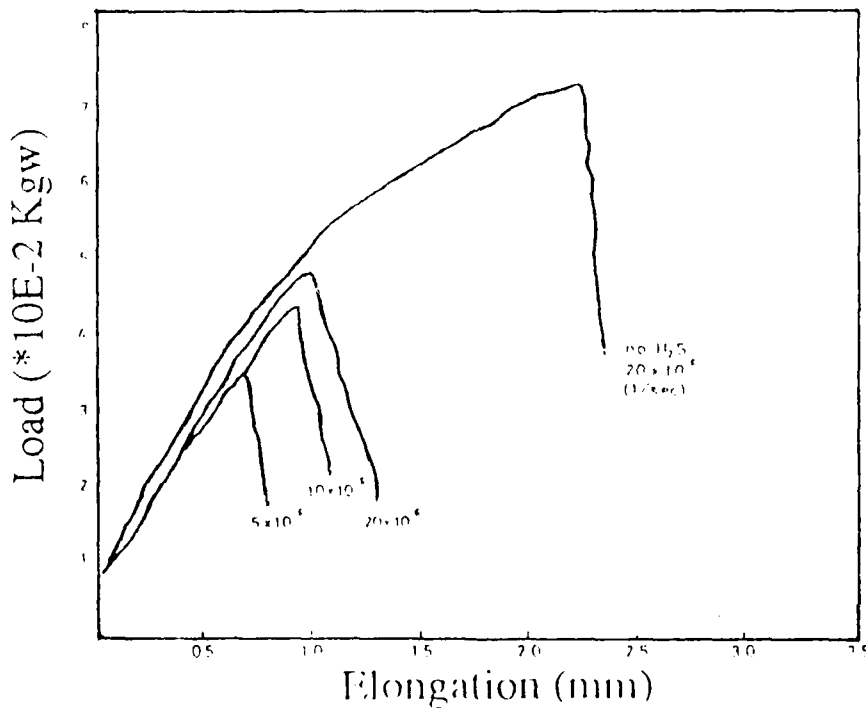
Figure 5. Load-elongation curves of laser-treated specimens

Figure 6. Micrograph of failed specimens under CERT and CLRT
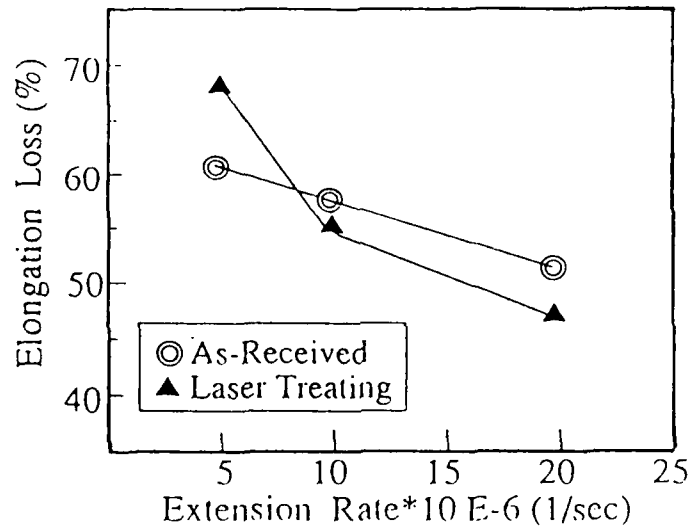
Figure 7. Elongation loss of laser-treated specimens
under different strain rate tensile testing
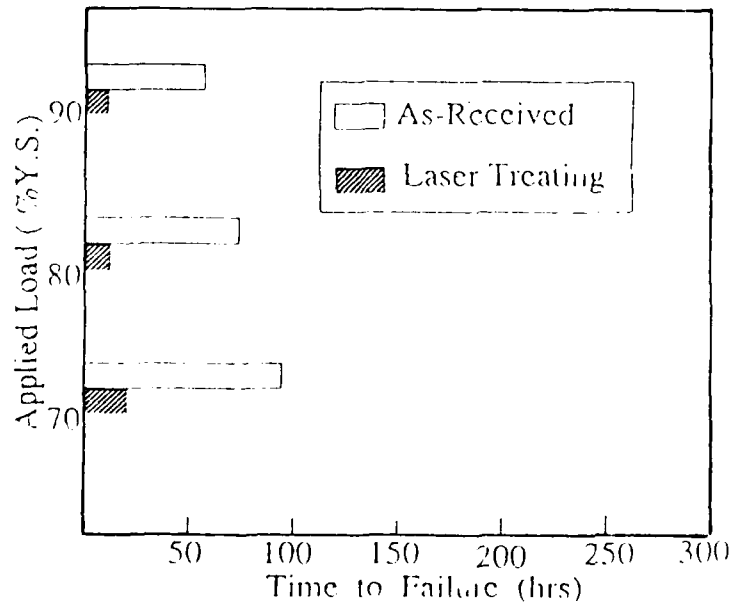
Figure 8. Time to failure of laser treating specimens under different applied load
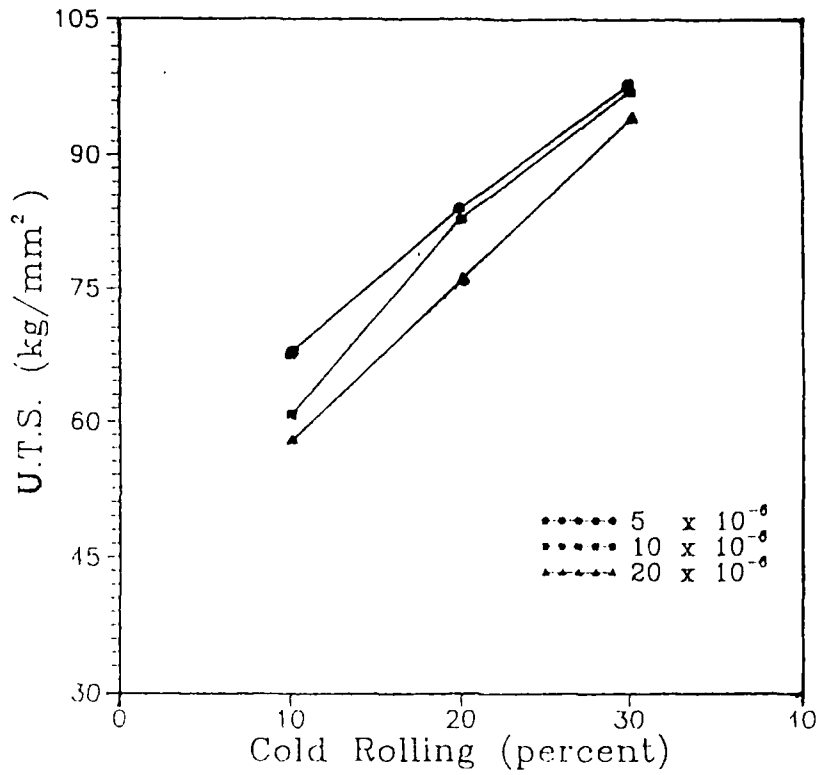
Figure 9. Results of U.T.S. of the tensile specimens against the degree
of cold rolling treatment under different strain rate
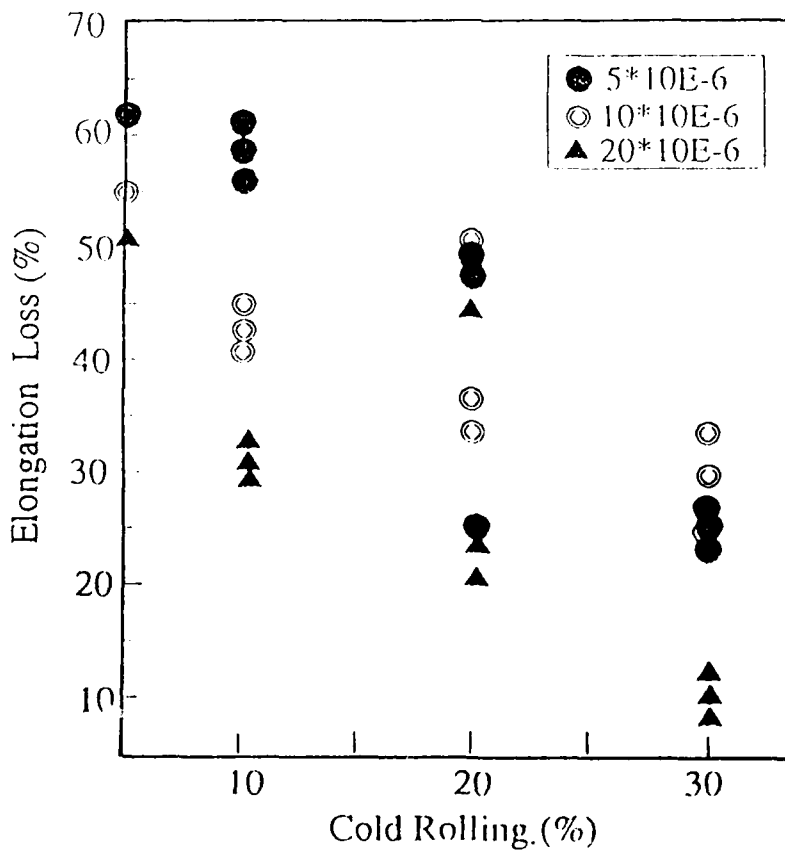
Figure 10. Elongation loss of cold-rolled specimens under different strain rate
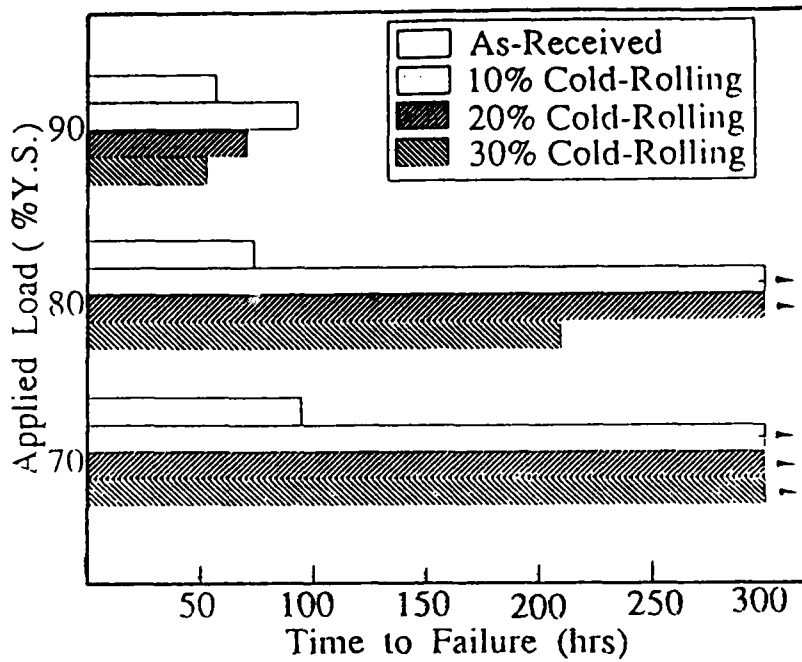
Figure 11. Time to faiure of cold-rolled specimens
under different amount of applied stress
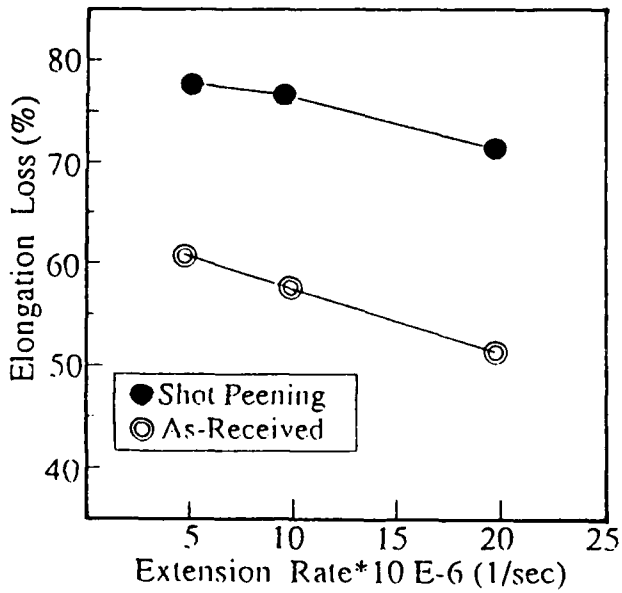
Figure 12. Elongation loss of shot-peened
specimens under different strain rate
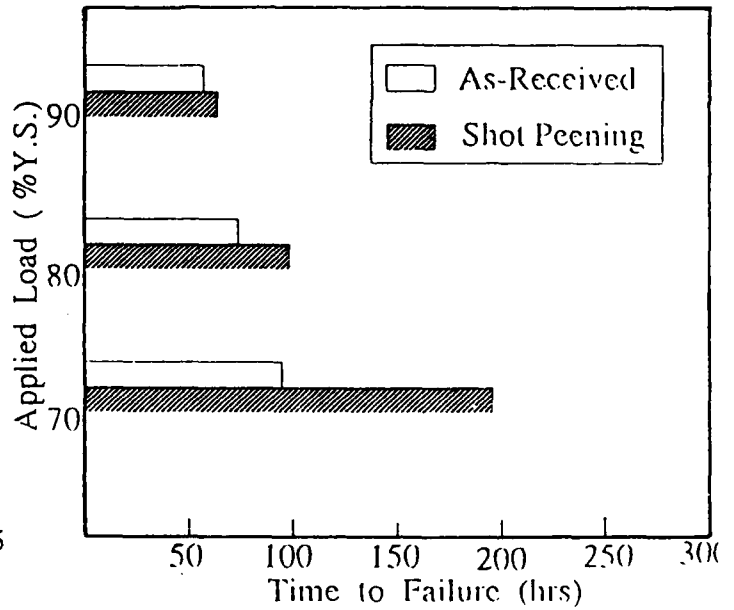
Figure 13. Time to failure of shot-peened
specimens under different amount
of applied stress
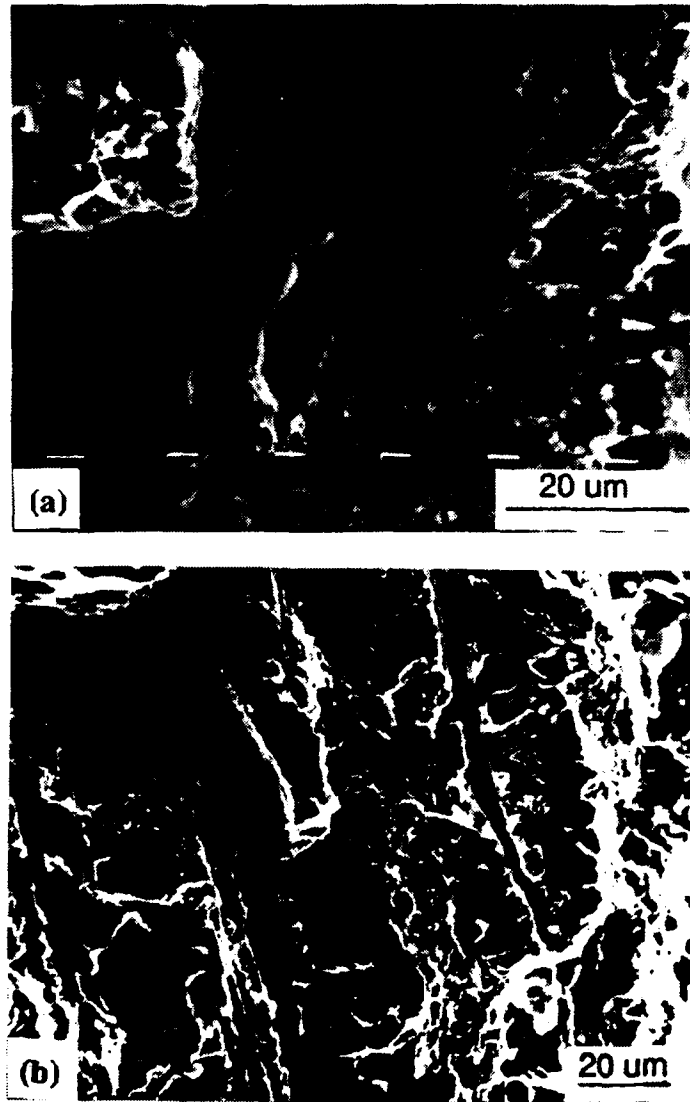
Figure 14. Fracture modes of shot-peened specimens
(a)under charging-free (b)under charging conditions

Modeling of Nonsteady State Hydrogen Permeation

P. Janavicius
Case Western Reserve University
The Case School of Engineering
Dept. of Materials Science and Engineering
Cleveland, OH 44106-7204

S.L. Amey
Master Builders, Inc.
23700 Chargin Blvd.
Cleveland, OH 44122-5554

J.H. Payer
Case Western Reserve University
The Case School of Engineering
Dept. of Materials Science and Engineering
Cleveland, OH 44106-7204

G.M. Michal
Case Western Reserve University
The Case School of Engineering
Dept. of Materials Science and Engineering
Cleveland, OH 44106-7204

Abstract

The transport of hydrogen through low carbon sheet steels has been studied using the electrochemical permeation test. When high current densities (> 50 mA/cm^2) are used, the anodic current maximum is followed by a decrease in current to a plateau level. This nonsteady state behavior has been attributed to the formation of hydrogen damage and trapping in the material. An empirical model has been developed which considers the hydrogen entry and exit reactions and surface effects. The nonsteady state conditions have been evaluated in model simulations.

Key terms: hydrogen, steel, modeling

Introduction

There has been recent interest[1,2] in hydrogen absorption by low carbon sheet steels (< 0.04 % C) during the industrial process of electrogalvanization. During this process the steels are subject to high current density (100-500 mA/cm^2) alkaline

electrocleaning, acid electropickling, and electroplating. The hydrogen absorption behavior during these conditions is of interest.

The interaction between hydrogen and steels has been well documented in several reviews[3,4,5]. Specific studies have emphasized the effects of pH[6,7], cathodic current[8,9,10,11], electrolyte agitation[12], surface finish[13] or hydrogen diffusion[14,15]. However, most of these studies have been conducted under benign conditions (i.e., low current densities and minimal agitation). Commercial electroprocesses associated with electrogalvanizing (the electrocleaning, electropickling and electroplating steps) operate under severe conditions of electrolyte pH, high current densities (100 to 500 mA/cm^2), vigorous agitation (line speeds of 90 to 150 m/min) and moderate temperatures (55 - 71°C). Under these extreme conditions the hydrogen that enters the steel sheet can cause damage, and the damage may affect subsequent hydrogen absorption behavior.

The phenomenon of nonsteady state hydrogen permeation has been previously reported by Beck and Bockris[16]. Figure 1 illustrates two permeation curves that were obtained under different charging conditions (100 and 0.5 mA/cm^2 respectively). In both cases ultra low carbon steel was tested. The high cathodic charging (100 mA/cm^2) resulted in a maximum in the anodic current versus time curve, followed by a decrease to a plateau. This "hump" is the nonsteady state behavior attributed to hydrogen damage and trapping. The permeation curve obtained at the low charging current conditions resulted in no such "hump." For studies on iron it has been recommended that cathodic currents < 1 mA/cm^2 be used in permeation testing to prevent the occurrence of damage in the material.[17] These low current densities are far below those used commercially.

It has been hypothesized[16] that the decrease in permeation current is due to subsurface damage. Such damage is thought to result from a high and non uniform distribution of dissolved hydrogen in the metal lattice. The non uniform expansion of the lattice could lead to the formation of a significant dislocation density. The high degree of hydrogen in solution could also lead to void formation. From a phenomenological point of view during charging under high current density conditions the surface of the metal is undergoing changes as a function of time. These changes limit hydrogen transport across a generalized electrolyte/metal interface. This paper will explore the effect of changing the resistance to hydrogen transport across the cathodic electrolyte/metal interface on the permeation current measured during a permeation test. A model will be used to examine this effect that represents the interfacial resistance by a single parameter called the mass transfer coefficient (κ).

Modeling Overview

An analytical model was developed which describes the hydrogen entry and transport during the extreme conditions of the industrial processes used during electrogalvanizing. The details of the development of the model are described elsewhere[18], but a summary of the model will be given. Figure 2 illustrates several parameters utilized in the model. The model is applied to the geometry of a permeation

experiment. The parameters c_1 and c_2 are the hydrogen concentrations predicted by the Nernst equation and Hirth's[19] equation for the absorption of hydrogen in iron. The actual concentrations of hydrogen beneath the metal surfaces at x=0 and x=L are c(0,t) and c(L,t) respectively. J is the hydrogen flux through the sheet. The motion of the hydrogen through the sheet is controlled by Fick's second law with D as an effective diffusivity as described by McNabb[20]. The parameters κ_1 and κ_2 are constants termed mass transfer coefficients. These terms define the deviation from Sievert/Nernstian behavior.

The deviation from Sievert/Nernstian behavior is described in the following manner. When κ is large (e.g., approaching ∞) the deviation from Sievert/Nernstian behavior is small. Conversely, when κ is small (e.g., approaching 0) deviations from Sievert/Nernstian behavior are significant. The steady state permeation current is given by the following expression:

$$J^{\infty} = \frac{c_1 - c_2}{\left(\dfrac{L}{D} + \dfrac{1}{\kappa_1} + \dfrac{1}{\kappa_2}\right)} \tag{1}$$

where J^{∞} is the steady state permeation current and the other parameters are as previously defined. The effect of varying the diffusivity and the two κ values was demonstrated under constant charging conditions on low carbon steel used for electrogalvanizing (L = 1 mm, D ~ 10^{-5}-10^{-6} cm^2/s)[18]. It was shown that κ_1 had the greatest impact on hydrogen permeation as is shown in Figure 3. As such, the decrease in permeation current seen in nonsteady state behavior can be described by a situation in which κ_1 decreases as a function of time.

Experimental

Using the model, several simulations of permeation experiments were performed. The diffusivity was kept constant at 6×10^{-6} cm^2/s. The value for κ_2 was held constant at 10^3 cm/s. The value of κ_1 was set at 5×10^{-7} cm/s initially and decreased at a rate of 10^{-8} (cm/s)/s to values of 3.5×10^{-7}, 2.5×10^{-7}, and 1×10^{-7} cm/s.

The effect of the rate of variation of κ_1 was also investigated. For the simulation D and κ_2 were held constant as before. The value of κ_1 was changed from 5×10^{-7} cm/s to 1×10^{-7} cm/s. The rates of change were: A, 1×10^{-8} (cm/s)/s; B, 5×10^{-9} (cm)/s.

Results and Discussion

The results of the first set of simulations is shown in Figure 4. Each value of κ_1 represents a different surface state. The most notable feature of the simulations in Figure 4 is the "hump" in the curve. This "hump" is the anomalous behavior which resulted for all of the curves which had changing κ_1. Clearly, if there is minimal overall change in κ_1, as seen in the curve A (5×10^{-7} to 3.5×10^{-7} cm/s), there is negligible "anomalous"

behavior (i.e., only a slight hump in the curve). However, for curves B and C, a significant hump exists which is typical of the anomalous, non-steady state permeation noted by Beck and Bockris[16].

The results of the simulations with κ_1 changing at different rates are shown in Figure 5. The rate of change of κ_1 had a significant effect on the size of hump. Decreasing the rate of change led to a higher maximum current and a wider hump in the curve.

These results suggest two ramifications relevant to permeation testing under such conditions. First, changes in the surface or subsurface can significantly affect the permeation current. These changes could give rise to a "hump" in the permeation curve. The size of the hump is dependent upon the initial and final κ_1 values and the rate with which the surface changes from one value to the next. Secondly, κ_1 values are estimated from experimental permeation curves. Two values are one for the permeation maximum and one for the steady-state behavior. The κ_1 value taken from the current maximum will under estimate its initial value since κ_1 is decreasing as a function of time during such permeation tests.

Conclusions

A phenomenological model was applied to permeation curves that exhibit nonsteady state hydrogen permeation behavior. The nonsteady state behavior was studied via changes in the mass transfer coefficient, κ_1, associated with the metal sheets entrance surface. Decreasing κ_1 produced the anomalous "hump" which is characteristic of non steady state behavior. In addition, the rate of change of κ_1 controls the shape of the "hump."

Acknowledgements

References

1. J.H. Payer and G.M. Michal, *Proc. of 5th Auto.Prev.of Corr.*, **P-250**, Dearborn, MI, (1991), 53-63.

2. J.H. Payer, G.M. Michal and C. Rogers: *Corrosion/91*, (1991): paper no. 405.

3. M. Smialowski, <u>Hydrogen in Steel</u>, Pergamon Press, Oxford and Addison-Wesley Publishing, Reading MA, (1962) 88-90.

4. J.P. Hirth, *Met. Trans.*, **11A**, (1980): pp. 861-890.

5. E.E. Fletcher and A.R. Elsea, "Hydrogen Movement in Steel--Entry, Diffusion and Elimination," *DMIC Report*, **219** Battelle Memorial Institute, (1965).

6. R.M. Hudson, *Corrosion*, **20**, (1969): p. 24t.

7. J.O'M. Bockris, *Chem. Rev.*, **43** (1948): pp. 525-577.

8. H. Zeilmaker, *Electrodepos. & Surf. Treat.*, **1**, (1972/73): p. 109.

9. J.O'M.Bockris, Proceedings of Stress Corrosion Cracking and Hydrogen Embrittlement of Iron Base Alloys, NACE, 1973: p. 286.

10. J.O.'M. Bockris, J. McBreen and L. Nanis, *J. Electrochem. Soc.*, **112**, [10](1965): p. 1028.

11. K. Bolton and L.L. Shreir, *Corrosion Sci.*, **3** (1963): pp. 17-33.

12. M. Shirkhanzadeh, *Corrosion Sci.*, **28** (1988): pp. 201-206.

13. M. M. Makhlouf and R.D. Sisson, Jr., *Met. Trans. A*, **22A** (1991): pp. 1001-1006.

14. W. Beck, J.O'M. Bockris, M.S. Genshaw and P.K. Subramanyan, *Met. Trans.*, **2A**, (1971): p. 883.

15. A.S. Nowick and J.J. Burton, Diffusion in Solids, Academic Press, New York, (1975) pp. 281-284.

16. W.Beck, J.O'M. Bockris, J. McBreen, and L. Nanis, *Proceedings of the Royal Society of London*, Series A, Vol. 290, (1965): pp. 191-206.

17. L. Coudreuse and J. Charles, *Corrosion Science*, **27**, No. 10/11, (1987): pp. 1169-1181.

18. S.L. Amey, G.M. Michal, and J.H. Payer, Submitted to *Met. Trans. A*, spring 1992.

19. J.P. Hirth, *Met. Trans.*, **11A**, (1980): pp. 1001-1006.

20. A. McNabb and P. Foster, *Trans. TMS-AIME*, **227**, (1963): PP. 618-627.
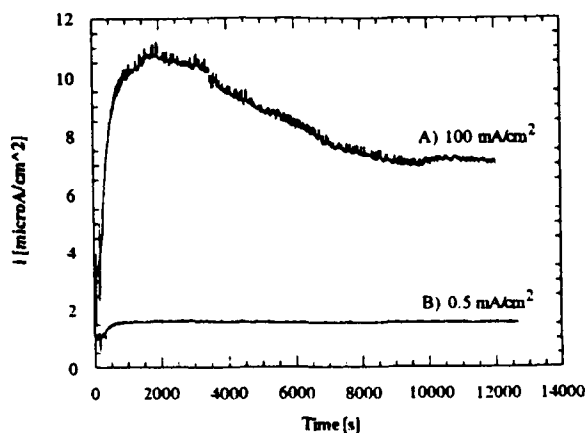
Figure 1. Permeation curves for 0.005 wt%C steel at current densities of 100 mA/cm^2 and 0.5 mA/cm^2 in 0.1N H$_2$SO$_4$.
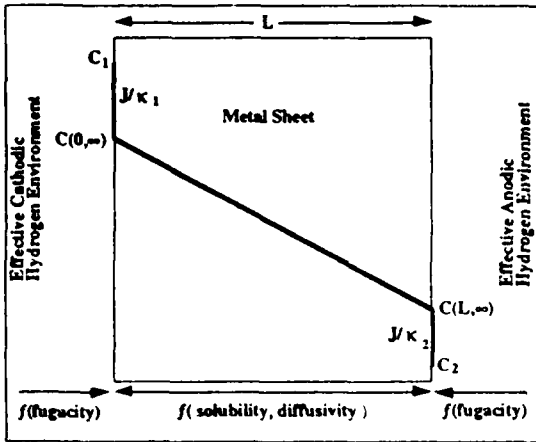
Figure 2. The effective geometry of a permeation test as viewed by our model.
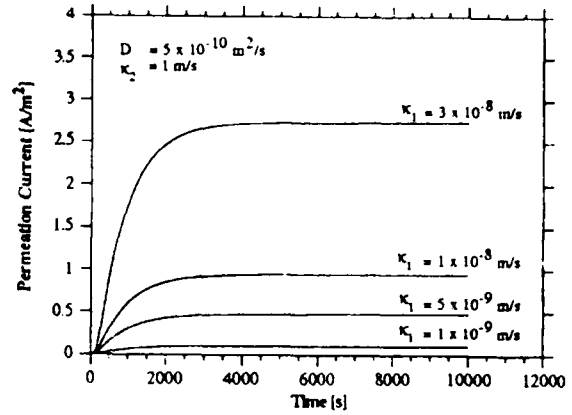
Figure 3. The effect of κ_1 on the hydrogen permeation current. D and κ_2 are held constant and L = 10^{-3} m.
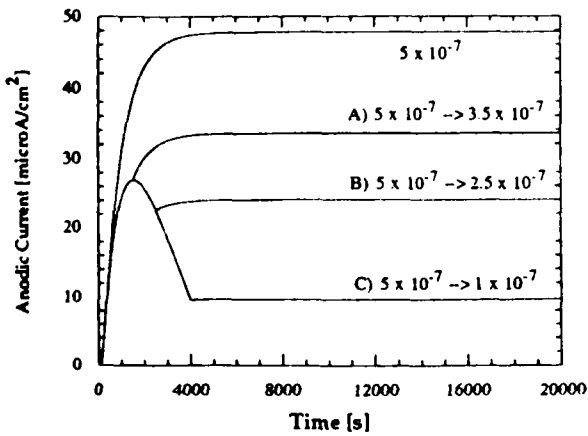
Figure 4. The effect of changing κ_1 over time at a constant rate upon permeation behavior.
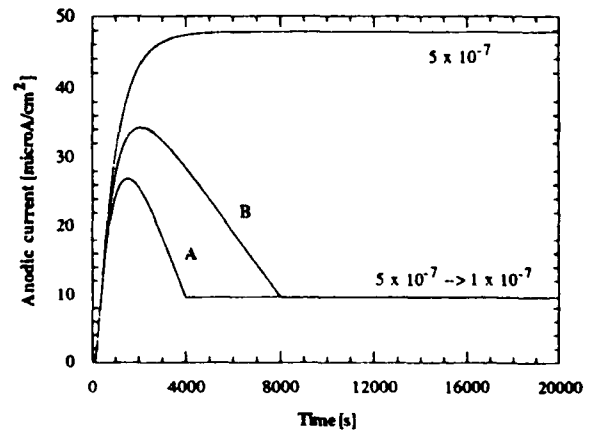
Figure 5. The effect of changing κ_1 over time at different rates upon permeation behavior. (A, 1 x 10^{-8} ((cm/s)/s); B, 5 x 10^{-9} ((cm/s)/s))

2382

A Sensor for Measuring the Permeation Rate of Atomic Hydrogen and its Applications in HIC Inspection*

Yuan-long Du
Corrosion Science Laboratory
Institute of Corrosion and Protection of Metals
Chinese Academy of Sciences
62 Wencui Road
110015 Shenyang, China

Abstract

Hydrogen induced cracking (HIC) of steel is widely present in various industrial processes with reduction of hydrogen ion as the cathodic reaction. For measuring and evaluating the HIC susceptibility of steel better than some commercially available hydrogen probe, a fuel cell type sensor in the shape of a hermetically sealed button was developed and studied. It is a modified Devanathan-Stachurski(D-S) cell with a fast response (few minutes to tens of minutes) controlled by a simple measuring system. In this paper, the structural design and the properties of the sensor are presented. After caliberating/correlating the levels of the signal output of the sensor with the strength/embrittlement of the steel in the same media, the HIC/sulfide stress corrosion cracking(SSCC) susceptibility of the steel can be evaluated comprehensively. The sensor has been successfully used in the following computerized probe techniques for assessing and judging the HIC/SSCC susceptibilities of the steels: offshore platform joints, pipeline/vessel for sour oil/gas, boiler/pipe in pickling etc. Some of these techniques are presented and discussed in detail.

Key terms: sensor, permeation rate, hydrogen atom, hydrogen induced cracking, HIC, HE susceptibility and in-situ inspection.

Introduction

In the most commercially available hydrogen probe techniques, e.g., the hydrogen patch probe or hydrogen probe with a barnacle electrode[1,2] the levels of the signal output of the sensors are rather low and there is a fairly long time lag of the permeation of hydrogen atoms (in the order of tens of hours) from the internal surface directly in contact with the corrosive media to the external surface of the wall of pipe/vessel where the sensor is mounted. Therefore, if the steel is sensitive to hydrogen damage, by the time a significant current response is measured by the above-mentioned probes, irreversible hydrogen damage might be possibly produced. Arup's probe cannot be used in a pressurized system[3].

According to the demands of safety inspection from the various industrial or engineering structures, a fuel cell type sensor in the shape of a hermetically sealed button was developed and studied for pressurized and corrosive systems by the author and coworkers. In this paper, the design of the sensor structure and its properties are presented. Some probe techniques were then developed to evaluate the HIC/SSCC susceptibility of the steels

for diverse uses in offshore platform joint, pipeline/vessel for sour oil/gas, for boiler/pipe in pickling, etc. Some of these techniques are also presented and discussed

Design and Structure

In the D-S cell[4], the permeation of hydrogen atoms takes place from the hydrogen charging side to the other side. The anodic oxidation of hydrogen atoms is proportional to the concentration of hydrogen atoms on the charging side and inversely proportional to the specimen thickness. Therefore, in any design of this kind of hydrogen probe, the thinner the foil and the higher concentration of hydrogen atoms on the charging surface, the higher will be the output current response and the shorter the time lag of the permeation of hydrogen atoms across the specimen. Moreover, in the general D-S cell two sets of potentiostats, a recorder, power supply, reference electrode and counter electrode are needed. For engineering purposes, the controlling/measuring systems of the hydrogen probe need to be as simple as possible. Following modifications to the D-S cell make a simpler probe:

  --use a simple galvanostatic power supply to replace one of the potentiostats for cathodic charging of hydrogen atoms;

  --use a stable, non-polarized powder oxide cathode with large specific surface to replace the reference electrode and the counter electrode on the anodic oxidation side of the cell;

  --use the short-circuited discharge current of the following cell as a measure of the permeation rate of hydrogen atoms and to remove the other potentiostat:

Anode	Electrolyte	Cathode
steel foil with catalyst coating	alkaline electrolyte in separating membrane	powder metallic oxide electrode

As the two potentiostats and reference electrodes are no longer required, the power supply and the measuring/recording systems can be simplified. For engineering purposes, the above-mentioned conversions are more reasonable than the original setup.

Based on the above-mentioned conversions, a fuel cell type sensor in the shape of hermetically sealed button was designed and constructed for measuring the permeation rate of hydrogen atoms in steel (Fig. 1)[5].

In the sensor (Fig. 2), the steel electrode is made of 08F high quality carbon steel (Table 1), cold- rolled and bright annealed in an argon atmosphere. Its thickness is 0.3 mm. Powder metallic oxide electrode is used as cathode, in which other metallic oxides are doped for optimization of its electrochemical properties. Separating membrane of kraft paper is thoroughly wetted with saturated potassium hydroxide solution to provide a good contact with the powder oxide cathode and the internal side of the steel foil plated with catalyst. The geometric area of the dual-electrode in the probe (1 on Fig.1), both the cathodic charging and anodic oxidation surfaces of hydrogen atoms, is 1.15 square centimeters. Thermoplastic polyvinyl gasket is used for sealing and electrical insulation. Two kinds of catalyst coatings and three cathodes were studied. Therefore, there were six kinds of sensors to be tested and optimized. They are labelled as PH, PHA, PHM, NH, NHA and NHM, respectively.

Experimental

The measuring system is shown schematically in Fig. 2.

Test solutions used were 5% sodium chloride, artificial seawater (ASTM-D1141-52), hydrochloric or sulfuric acids with or without hydrogen sulfide or corrosion inhibitor. In preparing and transferring the test solutions, high grade nitrogen atmosphere (99.999% and further de-oxygenated with active copper column) was used. In order to avoid serious corrosion of the surface for hydrogen charging of the sensor was directly contacted with the corrosive media, and to increase the amplitude of the signal output, cathodic polarization with a constant current of 1 mA was given. During the experiment, the change of the anodic oxidation current of the hydrogen atoms within the sensor with time was measured up till steady output was reached. All tests were carried out in a 25°C thermostatic chamber.

Pressure-resistant testing of the sensor was carried out as follows: the test sensor was degreased in organic solvents, washed with distilled water; put into a beaker with distilled water and then into an autoclave. It was then pressurized with pure nitrogen for two hours. The pH change of water was measured before and after the test to record any changes.

Service life of the sensor was studied by the following cyclic tests: the NHA sensor was charged with hydrogen atoms on various levels by dipping the sensor into 0.001, 0.01, 0.05 and 0.1 M sulfuric acid. The anodic oxidation current was measured up till its steady (maximum) value was reached. The sensor was then taken out of the acid, and rinsed with water. After drying, the sensor was short-circuited for 30 minutes. The test was then repeated to observe the cyclic times (service life), over which the original discharge current could not be sustained. The testing was carried out at temperatures of 10, 20, 30 and 40°C.

Applications of the Sensor

To inspect and evaluate the HIC/SSCC susceptibility of the steel in the corresponding corrosive media, the levels of the signal output of the sensor were caliberated/correlated with the strength and the embrittlement of the steel (including its matrix, HAZ and welded seam) in the same media by slow strain rate tensile technique (SSRT) and SEM analysis of the corresponding fractograph. Then the HIC or SSCC susceptibilities for various systems were correlated and defined with the Index of Hydrogen Embrittlement (F%) of the steels in media. It is commomly known that, when the stress of the steel exceeds its critical value and the F% value is larger than 35%, the steel is considered as sensitive to HIC or SSCC. But for F% values lower than 25%, or for some systems even 20%, it will be safe from HIC or SSCC. If F% lies between them, there is a latent danger of HIC or SSCC[6-8]. According to the relationship and the above-mentioned criteria, the probe, the computer on slice with the specially designed software and the peripheral attachment can be designed and constructed to fit the various engineering purposes. The schematic is shown in Fig. 3. By dipping the working surface of the sensor mounted on the front of the appropriate probe, the relative permeation rate of the hydrogen atoms in the steel in corresponding media and the HIC or SSCC susceptibility of the steel structure can be measured, judged and tabulated out on an ultramicroprinter on a peripheral attachment.

So far, following computerized probe techniques for in-situ inspection of the steel structure have been developed by the author and coworkers:
　　1. Probe for inspection of the HIC susceptibility for offshore platform joint[9] (Fig.4).
　　2. Probe for inspection of the SSCC susceptibility of the pipeline for sour oil/gas[10] (Fig.5).
　　3. Probe for inspection of the HIC susceptibility of the boiler/pipe in pickling[11].

Research/development of other probe techniques for in-situ inspection of the HIC/SSCC susceptibility of the steel concerned are also under the way respectively for following

systems, acidification of oil/gas wells, acidic cleaning of the water injection well of oil field and the drilling rod operated in mud with hydrogen sulfide, etc.

Results and Discussion

Optimization of the Catalyst Coating and the Oxide Cathode

For selecting/optimizing the structure of the sensor, the change of the anodic oxidation current of the permeated hydrogen atoms were measured and compared in sodium chloride solution with hydrogen sulfide for the sensors (as shown in Fig.1) with different catalyst coatings and metallic oxide cathodes. The results are shown on Fig. 6.

It can be seen that, only after 4 minutes, the maximum current response (140 and 120 microampere) was reached for PHA and NHA type sensors. They are much higher than the other four sensors.

In comparing the various sensors, the NHA sensor is more attractive than the others for practical applications, as it can give almost the same current output as PHA and uses a cheaper catalyst coating to decrease the oxidation overpotential of the hydrogen atoms into water in alkaline solutions.

It is obvious that the structural design of the sensor is acceptable for engineering purposes. Some peripheral instruments, such as the potentiostats and reference electrodes in the original D-S cell, can be removed or simplified for practical purposes.

Influence of Cathodic Charging on the Current Response

The current response (with time) of the anodic oxidation of permeating hydrogen atoms, from cathodic charging and corrosion charging, is shown in Fig. 7 (in seawater polluted by hydrogen sulfide) and in Fig. 8 (in 0.2N sulfuric acid). It can be seen that the amplitude of the current output from the sensor will be increased appreciably by cathodic charging of hydrogen atoms. Not only can the sensitivity of the signal output be increased, but the sensor is well protected by cathodic protection and serious corrosion of the sensor used in strongly corrosive media could be greatly diminished so as to avoid its failure in a short time and prolong its service life. Obviously, this is very important for sensors used in corrosion monitoring.

In comparison with the hydrogen patch probe and hydrogen probe with barnacle electrode[1,2] the current output of NHA sensor was fairly higher than obtained with the former probes. In a hydrochloric acid solution, a signal output less than 6 and 2 $\mu A/cm^2$ could be measured respectively for the former two probes[1,2]. But for the NHA sensor in sulfuric acid, 300 $\mu A/cm^2$ for cathodic charging and 40 $\mu A/cm^2$ for corrosion charging was found (Fig. 8). Additionally, for the former two probes, the time lag of permeation of hydrogen atoms from the hydrogen charging side to the oxidation side of the wall of pressurized pipe/vessel, will be in the order of tens of hours. If the structure is sensitive to HIC and the wrong corrosion inhibitor is selected or is not operated in its optimum concentration, irreversible hydrogen damage might possibly result.

As far as an ideal sensor for corrosion inspection/monitoring is concerned, the following characteristics are desirable: fast response, significant signal output, long service life (without appreciable corrosion), peripheral instruments as simple as possible, and low

cost. In these aspects, the NHA sensor can satisfy all of these demands for practical purposes.

Influence of Environment on the Signal Output of the Sensor

In figures 9 and 10, the influence of environment on the levels of the signal output of the NHA sensor are shown for well-fluid with different hydrogen sulfide contents and in hydrochloric acid for pickling with different corrosion inhibitors, respectively.

It is obvious that the levels of the signal output of the NHA sensor will be appreciably influenced by the concentration of hydrogen sulfide in saline water and by the concentration of corrosion inhibitor. If a wrong inhibitor is selected for pickling, e.g., thiourea in hydrochloric acid, the permeation of hydrogen atoms and then the signal output of the sensor will be greatly promoted/increased.

Pressure-Resistance of the Sensor

The results in Fig. 11 show that although the sealed sensors were mounted in atmospheric pressure, any concentrated alkaline solution was not squeezed out from the sensor under pressure, at least, up to 3 MPa. This might satisfy the demands in the region of offshore exploitation in the near future, or of general transportation pipeline for sour oil/gas etc. without any design as a supplement to balance the working pressure of the system inspected.

The results of the service life tests show that, even after 20 cycles of high discharge current in 0.1 M and 40 cycles in 0.001 M sulfuric acid, there is not any discernable decrease on current output level on the NHA sensor. Obviously, the service life of the sensor is long enough and acceptable for use of HIC/SSCC inspection.

The Relationship between I (μA) and F% of Various Systems

As an example of the application of the sensor, the relationship between the signal output of the sensor (I) and F% of the boiler steels is tabulated in Table 2. SEM analysis of the corresponding fractograph of the steels is reported elsewhere[11].

Based on the results for the above-mentioned sour oil/gas system and similar systems, the microcomputer on slice with the software specially designed for the corresponding system and the probe techniques could be developed for data sampling, logging, storing, processing and evaluation/judgement of the inspection result, so as to fulfill the engineering demands concerned with safety inspection.

So far, the probe for inspection of the HIC susceptibility for offshore platform joint has been used on the annual and special underwater inspections of five offshore platforms, located on Bohai Sea and Nanhai Sea, China. SSCC susceptibility of pipeline for sour oil/gas was measured by in-situ inspections in the sour gas field southwest of Sichuan Province, China. Nine sour gases with different contents of hydrogen sulfide were tested from desulfurized gas to that containing hydrogen sulfide contents higher than 1000 mg/L under ambient pressure in brine.

As revealed by the results taken from practical inspections in-situ by the above-mentioned probes,[12-14] these hydrogen probes could be successfully used for assessing the HIC or SSCC susceptibility of steel structures with a fast response (few minutes to tens of minutes), good working stability, data reproducibility and high resolution to different

environmental conditions. Based on the inspections, latent hazard of environmental sensitive cracking could be found and the proper repair/maintenance could be taken.

In recognition of the creativity and utility of these patents, Gold Medals were presented by the International Invention/New Produc; Exposition (INPEX), Pittsburgh, Pennsylvania (May, 1992) and by the China Patent Products and Technology Fair (CPPTF), Yantai, China (Sept, 1992), respectively.

Conclusions

1. Among the six types of the sensors tested for measuring the permeation rate of hydrogen atoms, the NHA type has the best technical-economic characteristics.
2. Based on the NHA type sensor, computerized hydrogen probe techniques developed by author and coworkers can be successfully used for in-situ inspection and evaluation of the susceptibility of HIC/SSCC of steel structure with stable/large signal output, fast response, pressure resistant, low cost and long service life in corrosive media.

References

1. E.C. French and L.D. Hurst, Corrosion, 47 2 (1980): p.1.

2. J.J. Delvccia and D.A. Berman, Electrochemical Corrosion Testing, ASTM STP 727, F. Mansfeld, U. Bertocci Eds., ASTM (1981): p.256.

3. H. Arup, Proceeding of the 9th Scandinavian Corrosion Congress, Vol. 2, Copenhagen (1983): p.825.

4. M.A.V. Devanathan and Z. Stachurski, Proceedings of the Royal Society, 270A (1962): p.90.

5. Chin. Pat: 90106448.3; Int.Cl.G01N 27/407; CN 1061849A.

6. P. Bastien, H. Vernon and C. Roques, Revue de Metallurgie, 55, Paris, France (1958): p.310; Hydrogen Sulfide Corrosion in Oil Gas Production--A Compilation of Classic Papers, R.N. Tuttle, R.D. Kane, Eds.(Houston, TX: National Association of Corrosion Engineers, 1981): p.61.

7. Yuan-long Du, Corrosion and Protection (Chinese), 1 (1975): p.13.

8. Yuan-long Du, Chao Fu, Zheng Lu and Wei Wei, European Federation of Corrosion Series No.10, paper no.16 (1991): p.104; Proceedings of the International Symposium on Marine and Microbial Corrosion, Stockholm, Sweden (Sept. 1991).

9. Chin. Pat: 89105157.0; Int.Cl.G01N 27/00; CN 1050090A.

10. Chin. Pat: 90106449.1; Int.Cl.G01N 27/406; CN 106184ბA.

11. Yu-feng Cheng and Yuan-long Du, Corrosion Science and Protection Technique (In Chinese with English abstract), 5, 2 (1993):In press.

12. Yuan-long Du, Shun-ji Shi, Peng Du, Er-ru Zhang and Wei Wei., A Study on the Hydrogen Probe Technique for Assessing the SSCC Susceptibility of Pipeline Steels in Sour Gas, Technical paper of the Institute of Corrosion & Protection of Metals, Chinese Academy of Sciences (Jun, 1990): p.19.

13. Wei Wei, Peng Du, Chao Fu, Zheng Lu and Yuan-long Du, European Federation of Corrosion Series No.10, paper no.11 (1991): p.69; Proceedings of the International Symposium on Marine and Microbial Corrosion, Stockholm, Sweden (Sept,1991).

14. Yuan-long Du, Peng Du, Wei Wei and Chao Fu, Proceeding of the 6th Asian-Pacific Corrosion Control Conference, Singapore, (Sept. 1989).

Table 1. Chemical composition (%, w / w) of 08F high quality carbon steel

C	Si	Mn	Ni	Cr	S	P
0.08	0.03	0.32	0.25	0.10	0.04	0.04

Table 2. The relationship between the signal output of the sensor (I) and status and F% of the boiler steels

I (μA) Status Steel	Sensitive (F>35%)	Dangerous (34% > F>21%)	Safe (F < 20%)
Carbon Steel Matrix	>27	22–26	<22
Carbon Steel Welded	>17	13–16	<13
16Mn Steel Matrix	>14	11–13	<11
16Mn Steel Welded	>12	7–11	<7
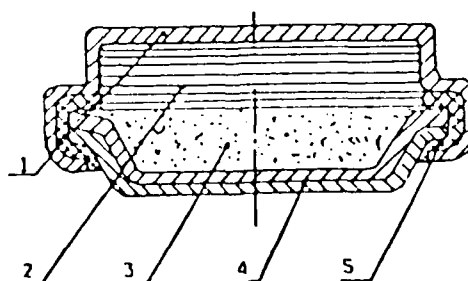
1 — dual–electrode with internal catalyst coating;

2 — separating membrane wetted with alkaline solution;

3 — non–polarizing cathode with metallic oxide powder;

4 — metal back cover;   5 — hermetical gasket.

Fig.1. Schematic diagram of the sensor
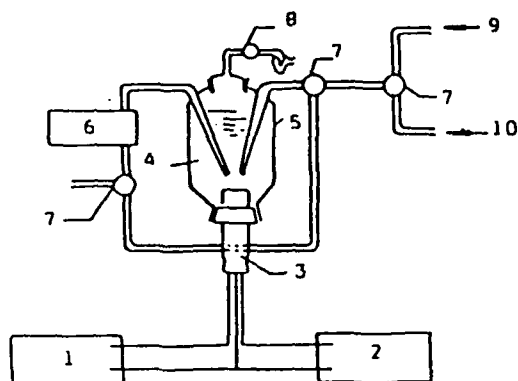
1 — zero resistance ammeter;   2 — galvanostatic power supply;
3 — hydrogen probe;   4 — test solution;
5 — electrolytic cell;   6 — lift pump;
7 — rectangular two-way stopcock;   8 — stopcock;
9 — N₂ inlet;   10 — solution inlet.

Fig.2. Schematic diagram of experimental device for measuring
the hydrogen permeation rate
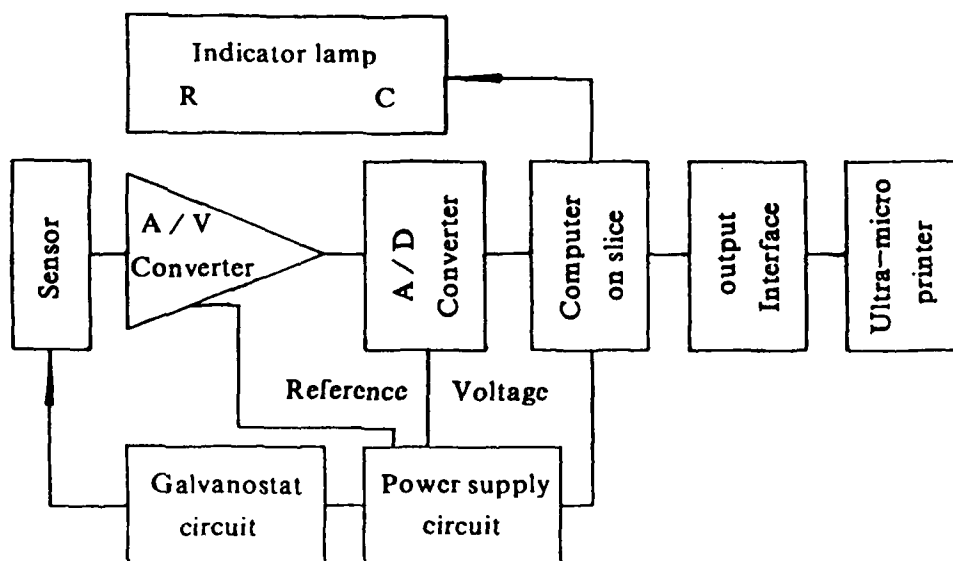
Fig.3. Schematic diagram of hydrogen probe
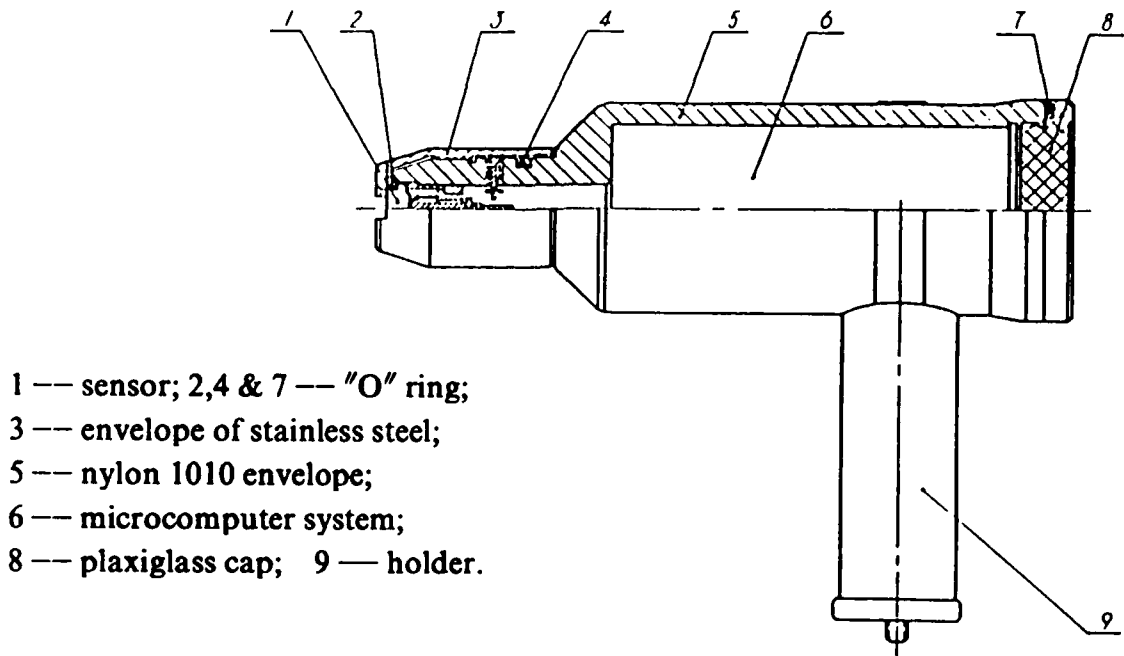
1 — sensor; 2,4 & 7 — "O" ring;
3 — envelope of stainless steel;
5 — nylon 1010 envelope;
6 — microcomputer system;
8 — plaxiglass cap;   9 — holder.

Fig.4. Probe for inspection of the HIC susceptibility
for offshore platform joint

To microcomputer system
&
periphery attachment box

1 — pressure gauge;   2 — flow meter;   3— outlet of sour gas;
4 — sampling outlet for analysis;   5— inlet of sour gas;
6 — autoclave;   7 — probe;   8— brine;
9 — microcomputer system & periphery attachment box.

(a). by-path connected type   (b). directly inserted type
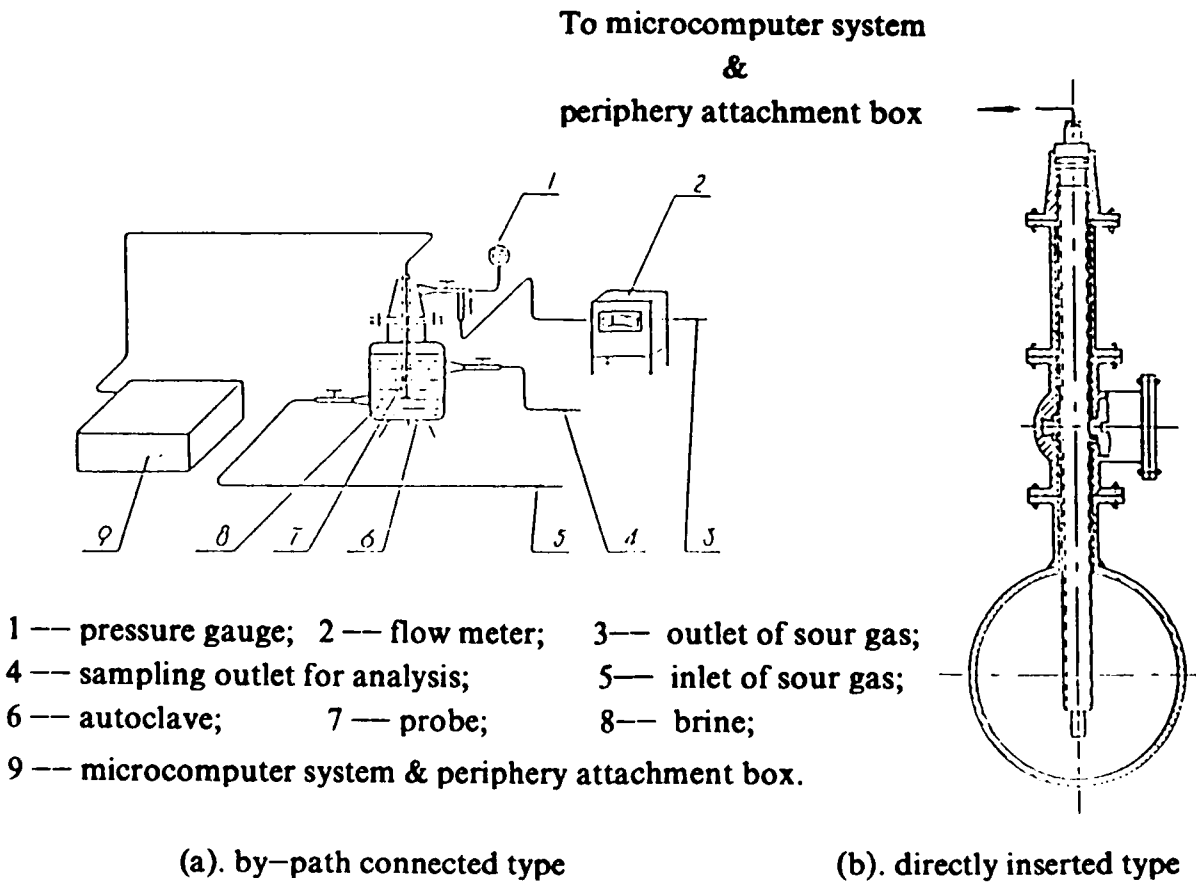
Fig.5. Probe for inspection of the SSCC susceptibility
of pipeline for sour oil / gas
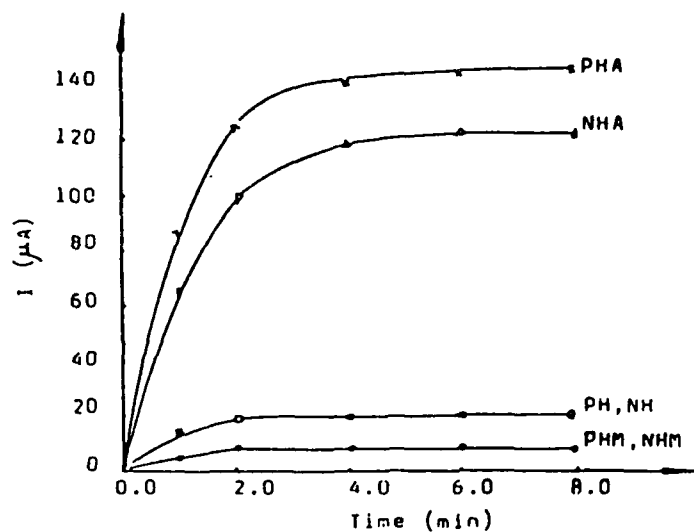
Fig.6. Change of anodic oxidation current of permeating
hydrogen atoms with time in a 5% NaCl
+ 0.0476N H₂S solution
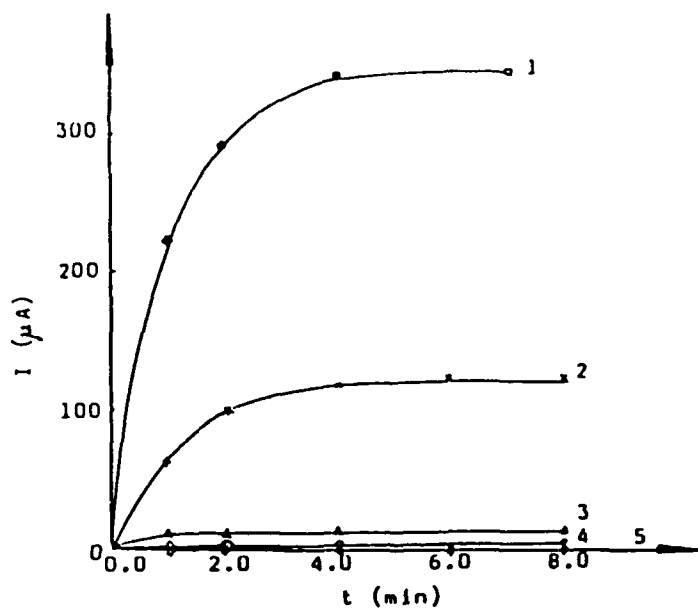
1 — H₂S 800ppm, cathodic charging
2 — H₂S   8ppm, cathodic charging
3 — H₂S 800ppm, corrosion charging
4 — H₂S   8ppm, corrosion charging
5 — H₂S   0ppm, cathodic charging

Fig.7. Influence of cathodic polarization on the current
response of NHA type sensor in seawater
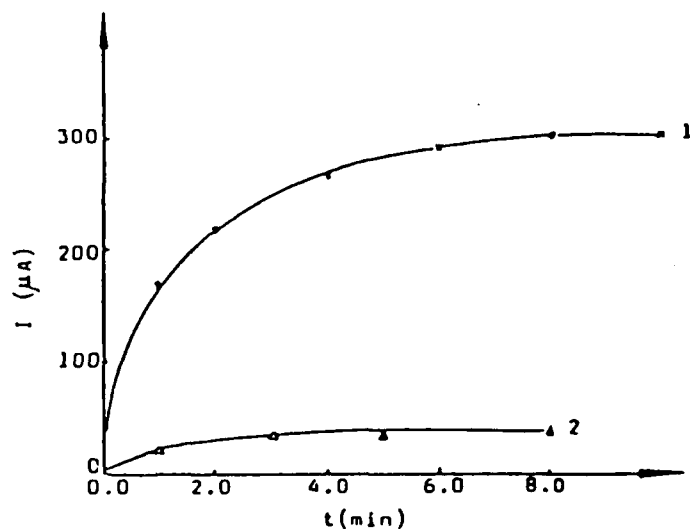
1 — cathodic charging;   2 — corrosion charging

Fig.8. Current output of NHA type probe in
0.2N H_2SO_4, 25℃
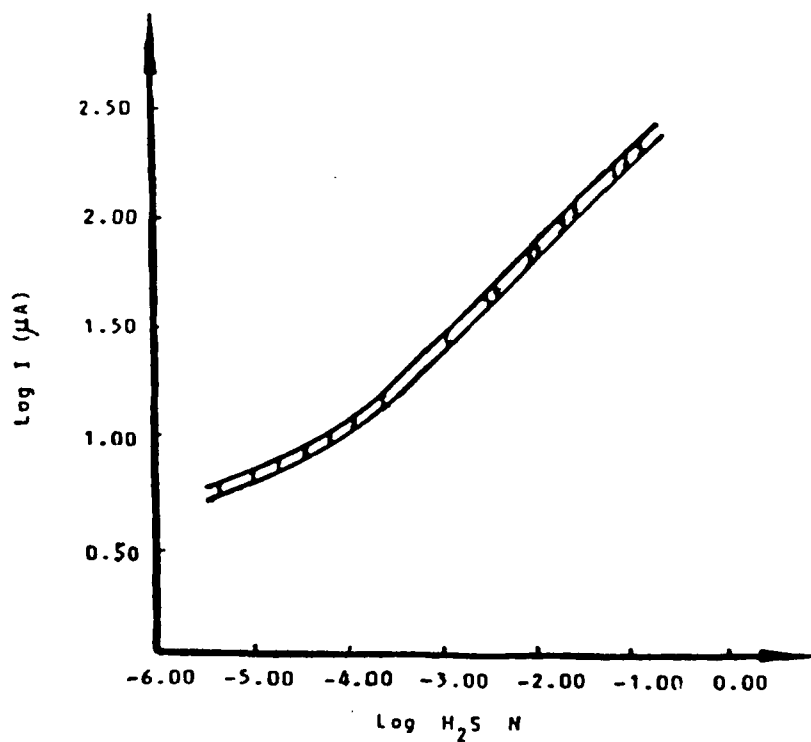
Fig.9. Influence of H_2S concentration on the anodic
oxidation current of hydrogen atoms for the
NHA type sensor in well–fluid

● — thiourea (TU)

◆ — dodecyldimethylbenzylamine bromide (DDB)
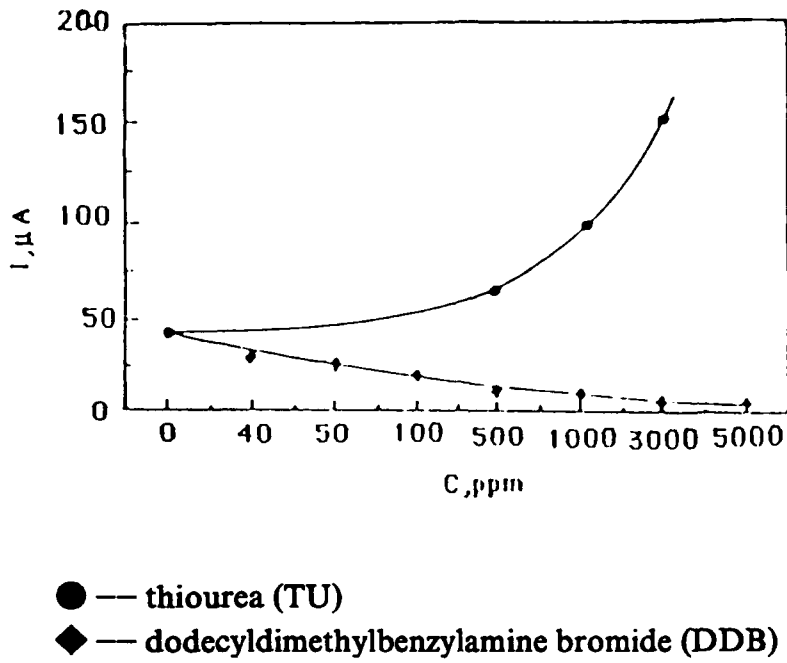
Fig.10. Influence of DDB and TU concentration on the
permeating hydrogen current in the sensor
in HCl solution
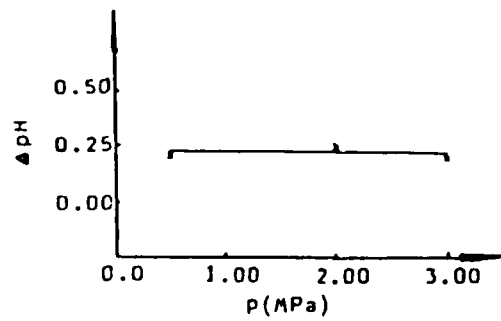
Fig.11. Change of pH of pressurized water
(with submerged sensor) with time

The Effect of Oxygen-Containing Oxidants on the Rates of Hydrogen Permeation into Iron and Hydrogen Cathodic Evolution on Various Metals.

Ludmila Maksaeva
The Institute of Physical Chemistry
Russian Academy of Sciences
31 Leninsky pr., Moscow
117915 Russia

Andrey Marshakov
The Institute of Physical Chemistry
Russian Academy of Sciences
31 Leninsky pr., Moscow
117915 Russia

Yuriy Mikhailovsky
The Institute of Physical Chemistry
Russian Academy of Sciences
31 Leninsky pr., Moscow
117915 Russia

Valentina Popova
The Institute of Physical Chemistry
Russian Academy of Sciences
31 Leninsky pr., Moscow
117915 Russia

Abstract

The effect of inorganic oxygen – containing oxidants (Ox) on the rate of hydrogen cathodic evolution (i_H) on Fe, as well as on the rate of hydrogen permeation (i_p) through a Fe membrane in acidic sulphate solutions (pH 0.3 – 3) have been investigated. Depending upon the form of existence in the solution the oxidant can be both an inhibitor and accelerator of hydrogen generation. It was shown that at a pH value $>$ pK_a an increase in the concentration of the oxyanions monotonically decreases the rate of hydrogen permeation into the metal. At pH values $<$ pK_a the reduction of the adsorbed molecules of the oxyacid increases hydrogen absorption into the metal. The critical concentration of oxidants ($C_{Ox,o}$) at which the permeation rate was minimum was determined both theoretically and experimentally. The degree of the accelerating effect was determined as a difference between the maximum hydrogen permeation rate (or gas evolution rate) in the presence of the oxidant and the rate in the oxidant free solution. The accelerating effect of oxidants on the discharge rate of hydrogen ions was found to depend on the following factors: the electrode potential, the pH of the solution and the nature of the metal.

Key terms: hydrogen permeation, iron, oxidant.

Introduction

The cathodic electrode reactions occurring under the corrosion of iron in acid oxidizing media, namely the hydrogen evolution reaction and the electroreduction of an oxidant, are usually considered to be independent processes[1,2]. However, the reduction of oxygen-containing oxidants (Ox) and cathodic evolution of hydrogen may be interactive processes since the donor protons in both reactions are hydroxonium ions[3]. One would expect that a alteration in the rate of h.e.r. (hydrogen evolution reaction) during Ox reduction will lead to a change in the amount of hydrogen absorbed into the metal. Then, by measuring the hydrogen permeation rate into metal, one can obtain information on the change in H_3O^+ ions concentration on the metal surface.

The aim of this study was to examine the effects of oxygen-containing oxidants on the rates of hydrogen cathodic evolution and hydrogen permeation into metal and to elucidate the mechanism of this phenomenon.

Experimental

The experiments were carried out in a two-section cell (Devanathan's technique)[4] using an iron membrane (an area of 4.23 cm^2 and a thickness of 0.1 mm). A horizontally flat membrane configuration allowed the hydrogen permeation and evolution rates to be determined simultaneously. The latter rate was determined using the volume metric technique[5]. One side of the membrane was covered with a layer of Pd, following the procedure described[6]. The diffusion part of the cell was filled with the 0.1 M NaOH solution and the membrane was polarized at a potential of 0.45 V (potentials are given relative to the normal hydrogen electrode). The deaerated (0.5-x) M Na_2SO_4 + xM H_2SO_4 solution (pH 0.3 - 2.0) was the background electrolyte. After keeping the membrane in the background solution at a constant potential, oxidant was added to the cell, and the steady state current due to hydrogen permeation through the membrane (i_p) was recorded.

Results and Discussion

During corrosion of metal in acid oxidizing media two cathodic reactions occur: reduction of the oxidant and cathodic evolution of hydrogen:

$$Ox + pH_3O^+ + me \longrightarrow Red + nH_2O \qquad (1)$$
$$2H_3O^+ + 2e \longrightarrow H_2 + 2H_2O \qquad (2)$$
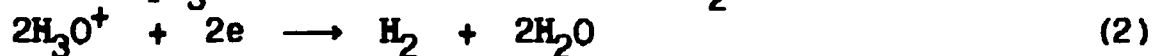
where p, m, n are stoichiometric coefficients. If the total rate of consumption of hydrogen ions is essentially lower than its transport rate to the electrode surface, reactions (1) and (2) may be considered independent. But an increase in the oxidant concentration must lead to the appearance of diffusion limitations on hydrogen ions and to the decrease in their surface concentration. As a result, the rate of hydrogen ions discharge will decrease at a constant electrode potential. When some critical oxidant concentration is achieved, the hydrogen evolution rate must be come zero (Fig. 1)[3,7].

Assuming that the reduction of the oxidant occurs under the condition of diffusion limiting current, the rate of hydrogen evolution (i_H) and the value of critical oxidant concentration are described by the simple expressions:

$$i_H = i_H^O - F\ p\ D_{Ox}\ C_{Ox}\ /\ \delta \qquad (3)$$

$$C_{Ox,c} = D_H\ C_H\ /\ D_{Ox}\ p \qquad (4)$$

where i_H^O - rate of h.e.r. in the background electrolyte, D_H and D_{Ox} - diffusion coefficients of H_3O^+ ions and oxidant, respectively, C_H , C_{Ox} - concentrations of H_3O^+ ions and oxidant, respectively, δ - thickness of the diffusion layer. In concentrated sulphate solution the diffusion flow of buffer substance (HSO_4^- ions) must be taken into account and the value of critical Ox concentration will be determined by the expression:

$$C_{Ox,c} = (D_H\ C_H + D_{HSO_4^-}\ C_{HSO_4^-}\ )\ /\ D_{Ox}\ p \qquad (5)$$

where D_{HSO_4} and C_{HSO_4} are the diffusion coefficient and concentration of HSO_4^- ions, respectively. It is known that part of hydrogen atoms formed during the cathodic evolution are absorbed by the metal. One can expect that the rate of hydrogen permeation into the metal will be determined by the oxidant concentration.

Fig. 2 represents the curves of the changes in the hydrogen permeation rate depending on the concentration of the following oxidants: Fe^{3+}, BrO_3^-, $Cr_2O_7^{2-}$, MnO_4^- ions. As can be seen, the increase in the concentration of oxyanions monotonically decreases the hydrogen permeation rate, while the cation-type oxidant (ferric ions) does not affect the permeation rate. The

oxidant concentrations at which i_p becomes equal to zero or attains a minimum value is in good agreement with calculated values of a critical concentration of the respective oxidants (Table 1). Thus, the reduction of oxyanions was expected to lead to an increase in the electrode pH and to a decrease in the hydrogen permeation rate.

One can assume that a layer of the reaction products which occur after reduction of MnO_4^- and $Cr_2O_7^{2-}$ ions forms on the membrane surface and as a result, the value of pH_s stabilizes at a level corresponding to the pH of hydroxide formation of the respective compounds involved. If the hydroxide formation pH of a reduction product such as $Cr(OH)_3$, for example, is rather low, then the permeation rate does not come zero even at $C_{Ox} > C_{Ox,c}$.

However, the introduction into solution of such oxidants, as H_2O_2, $NaNO_3$, Na_2MoO_4 and Na_2WO_4 increased the permeation rate (Fig. 3). It should be noted, that in the pH 2 solution the given oxidants exist partially as undissociated molecules of oxyacids as can be seen from their respective dissociation constants:

HOx:	H_2O_2	HNO_3	H_2MoO_4	H_2WO_4	$HBrO_3$
pK_a:	11.6	3.4	3.7	3.7	0.7

As can be seen in Fig.3, small additions of oxyacid ($C_{Ox} < C_{Ox,c}$) lead to a significant increase in the value of i_p. Upon further increase in the concentration of oxyacid the permeation rate begins to decrease. The concentration of the oxidant at which i_p becomes equal to zero (in the case of H_2O_2 and $NaNO_2$) or constant (in the case of Na_2MoO_4 and Na_2WO_4) is in good agreement with the values of the critical concentrations (Table 1).

One can assume that an electroneutral molecule of oxyacid is able to penetrate through the energy barrier, caused by the potential drop across the double electric layer, and approach the metal surface as closely as possible. Supposing oxyacids dissociate on the iron surface:

$$HOx_{ads} + H_2O_{ads} \longrightarrow H_3O^+_{ads} + Ox^- \qquad (6)$$

where HOx is the oxyacid and Ox^- is the oxyanion.

As it follows from the elementary act theory[8], only hydrogen ions which have penetrated into the first layer of water molecules, are discharged. The major part of cations including

hydrogen ions are located in the second water mono layer. If the oxyanion reduction occurs with the participation of hydrogen ions adsorbed on the outer Helmholtz plane, the concentration of hydrogen ions on the inner Helmholtz plane of the double layer should increase as a result of reaction (6). Hence, the oxyacids reduction occurs with the evolution of more reactive hydrogen ions and consumption of less reactive ones. This leads to the acceleration of cathodic hydrogen evolution and consequently to the increase in the rate of hydrogen permeation into the metal.

Thus, the oxidant effect depends on the pH of the medium and on the ionization constant of the respective oxyacids. For example, the addition of bromate to the pH 2 solution decreases the permeation rate, because in this medium the bromate exists in the form of ions. However, in the pH 0 solution bromate exists in the form of molecules, resulting in an increase in the permeation rate. Hence, depending on the form of existence in the solution one and the same oxidant can be both an inhibitor and accelerator of the hydrogen generation.

The accelerating effect of oxyacids on the discharge rate of hydrogen ions also depends on the following factors: the electrode potential value, the pH of the solution and the nature of the metal[9]. The degree of the accelerating effect was determined as a difference between the maximum hydrogen permeation rate i_p^{max} (or gas evolution rate- i_H^{max}) in the presence of the oxidizer and the related rate in the background solution (i_p^0, i_H^0):

$$\Delta i_p = i_p^{max} - i_p^0 \tag{7}$$

$$\Delta i_H = i_H^{max} - i_H^0 \tag{8}$$

It was found that oxyacid equally increased both the hydrogen evolution rate and the hydrogen permeation rate into the iron:

$$\Delta i_H / I_H^0 = \Delta i_p / I_p^0 \tag{9}$$

Let us consider the influence of the potential and pH of the solution for the case of change in the hydrogen permeation rate into iron in the presence of H_2O_2. i_p increases appreciably on the introduction of small quantities of H_2O_2 in the solution. A further increase in H_2O_2 concentration results in a decrease of i_p and at a certain critical oxidant concentration the hydrogen permeation rate becomes equal to zero (Fig.3). Fig. 4 shows the change in the permeation rate at different pH of the solution.

The maximum accelerating effect of H_2O_2 is observed in pH 2 solution. In electrolytes with pH > 3 and with pH < 0.4 the accelerating effect is absent. We believe that this is related to the prevention of the oxyacid dissociation on the metal surface. In more acidic solutions dissociation of the H_2O_2 is suppressed because of the higher coverage of the metal surface by hydrogen ions. In more alkaline solutions a oxide layer with good electron conductivity is formed on iron, and the H_2O_2 molecules reduce on its surface[9].

Fig. 5 shows the accelerating effect of hydrogen peroxide at different potentials. As shown, the greatest increase in the hydrogen permeation rate into iron is observed at the potentials corresponding to the Tafel part of the polarization curve of cathodic hydrogen evolution (E = -0.4 - -0.6 V). At more negative potentials the discharge of hydrogen ions occurs under the conditions of the diffusion limiting current which increases the pH of the solution electrode layer and consequently decreases the accelerating effect of H_2O_2. At sufficiently positive potentials corresponding to intensive metal dissolution, i_p again tends to zero. If oxidation of the Fe takes place via formation of hydroxide complexes then the surface of the anodically dissolving metal may be enriched in hydroxonium ions formed during dissociation of adsorbed water molecules:

$$\text{Fe} + 2H_2O_{ads} \longrightarrow \text{Fe(OH)}^-_{ads} + H_3O^+_{ads} \qquad (10)$$

If dissociation of the iron hydroxo complex takes place on the outer surface of the electrical double layer, then the reactions of surface dissociation of water with formation of $H_3O^+_{ads}$ and breakdown of the hydroxo complex involving H_3O^+ are spatially separate. This is probably a prerequisite for hydrogen discharge, gas evolution and permeation into the metal during anodic dissolution of Fe. The higher the dissolution rate of Fe, the higher should be the surface concentration of hydroxonium ions. This is consistent with the fact that i_p values in the potential region for anodic dissolution of Fe increase with a positive shift in potential (Fig.6).

The accelerating effect of oxyacids also increases with increasing hydrophilicity of the metal surface. Metal hydrophilicity is known to increase in the series[10,11]:

Ga > Zn > Cu > Ag > In > Cd > Sn > Ni > Pb > Hg

As can be seen from the Table 2, the increase in the evolution rate is higher on hydrophilic metals (Cu, Zn, Ga) and is absent on hydrophobic metals (Hg, Pb, Sn). These data confirm the

assumptions about dissociative adsorption of the oxyacid molecules[11].

The effect of oxygen on hydrogen permeation into iron have been investigated. The reduction of oxygen is known to proceed in two ways: directly to water (equation 11) or with formation of hydrogen peroxide as an intermediate compound (equation 12):

$$O_2 + 4H^+ + 4e \longrightarrow 2H_2O \tag{11}$$

$$O_2 + 2H^+ + 2e \longrightarrow H_2O_2 + 2H^+ + 2e \longrightarrow 2H_2O \tag{12}$$

Iron belongs to the group of metals on which oxygen may be reduced to water directly[12]. If H_2O_2 is not formed, the reduction of oxygen will be inhibit the hydrogen permeation into Fe by reason of the alkalification of the solution electrode layer. Usually a constant oxygen concentration is maintained under the conditions of natural aeration. Then, at a definite pH of the solution the given oxygen concentration will be critical, and the electrode concentration of hydrogen ions will decrease abruptly. Let us call the pH value at which hydrogen permeation rate is expected to decrease ten-fold as the critical pH (pH_c). The value of pH_c will depend on the anionic composition of the solution because not only hydroxonium ions but also acid molecules and partially dissociated anions will act as carriers of protons to the electrode surface. The critical pH values may be calculated according to the equation that includes the oxygen concentration in the solution, diffusion coefficients of the respective particles and dissociation constants of the buffer compounds. The calculated and experimental pH_c values show good agreement as can be seen in Table 3. In a carbonate solution oxygen reduction cannot increase the pH of the solution electrode layer and does not effect on hydrogen permeation rate into iron. Thus, knowing the oxygen concentration, the anionic composition and pH of the medium, one can classify the corrosion media according to the danger of hydrogen embrittlement of steel.

References.

1. A.N. Frumkin, V.S. Bagotsky, Z.A. Iofa, B.N. Kabanov, Kinetics of electrode processes, (Moscow, Russia: Moscow University Publishers, 1952), p.278.

2. H. Kaesche, Die Korrosion der Metalle, (Berlin -Heidelberg, Germany: Springer-Verlag, 1979), p.97.

3. A.I. Marshakov, Yu.N. Mikhailovsky, V.M. Popova, Zaschita metallov, 22 6 (1986): p.629.

4. M.A. Devanathan, Z. Stachurski, Proceeding of the Royal Society, Ser. A, Mathematical and Physical Science, A270 (1962): p.91.

5. I.L. Rozenfeld, K.L. Zhigalova, Uskorennye metody korrosionnykh ispytanii metallov, (Moscow, Russia: "Metallyrgiya", 1966), p.347.

6. B.S. Choudhari, T.P.Radhakrishnan, Corrosion Science, 25 11 (1985): p.1077.

7. A.I. Marshakov, O.V. Batisheva, Yu.N. Mikhailovsky, Zaschita metallov, 25 6 (1989): p.888.

8. L.I. Krishtalik, Electrode reactions. The mechanism of the elementary act, (Moscow, Russia: "Nauka", 1979), p.224.

9. A.I. Marshakov, O.V. Batisheva, L.B. Maksaeva, Yu.N. Mikhailovsky, Zaschita metallov, 27 5 (1991): p.713.

10. A.N. Frumkin, Potentials of zero charge, (Moscow, Russia: "Nauka", 1979), p.157.

11. A.I. Marshakov, L.B. Maksaeva, V.M. Popova, Yu.N. Mikhailovsky, Zaschita metallov, 29 1 (1993): p.130.

12. M.P. Tarasevich, E.I. Khruscheva, Itogi nauki i techniki, (Moscow, Russia: VINITI, 1981), p.42.

Table 1. Critical concentration of oxidants calculated according to equation (5) and those experimentally determined.

Oxidant	$C_{Ox,c} \cdot 10^{-2}$, M	
	calculated	experiment
H_2O_2	4.4	4.4
$NaBrO_3$	1.8	2.1
$Na_2Cr_2O_7$	1.0	0.9
$NaMnO_4$	2.4	2.4
Na_2MoO_4	4.1	4.5
Na_2WO_4	4.3	4.0
$NaNO_2$	1.2	1.2

Table 2. Increase in permeation rate on addition of H_2O_2
on various metals.

Me	Zn	Cu	Ag	Ga	In	Cd	Fe	Sn	Pb	Ni	Hg
Δi_H	8.9	3.9	3.8	1.7	1.4	1.6	0.65	0	0	0	0

Table 3. Experimental and calculated values of pH_c in aerated
solutions with different anionic composition.

Solution	HAn	pH_c(calcul.)	pH_c(experim.)
0.1-x)M NaCl + + xM HCl	—	3.1	2.8
0.1-x)M Na_2SO_4 + xM H_2SO_4	HSO_4^-	3.7	3.5
0.07-x)M CH_3COON xM CH_3COOH	CH_3COOH	5.9	5.4
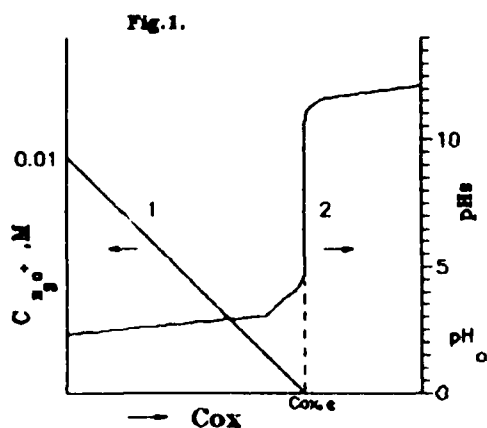
Fig.1. Scheme of the change in h.e.r. rate (1) and in the electrode pH (2) depending on oxidant concentration.
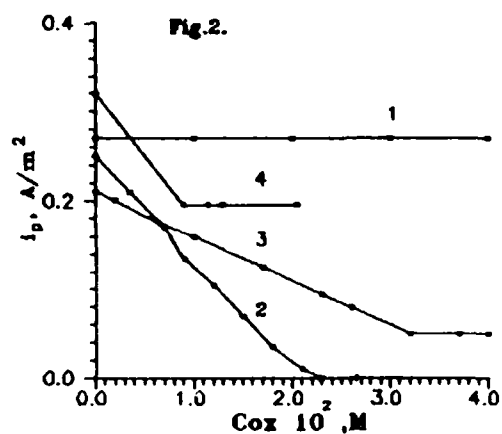
Fig.2. Dependence of permeation rate on oxidant concentration in 0.5M SO_4^{2-}, pH 2.0 at $E = -0.47$ V: Fe^{3+} (1), BrO_3^- (2), MnO_4^- (3), $Cr_2O_7^{2-}$ (4).
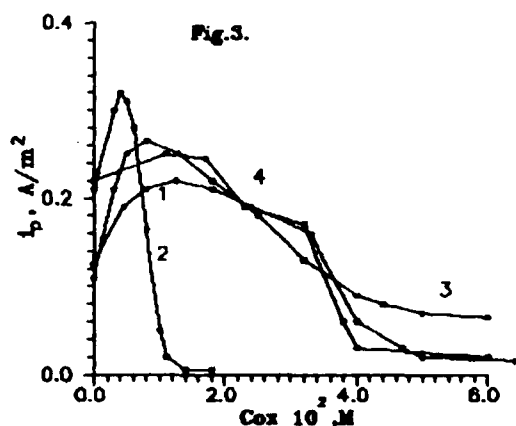
Fig.3. Permeation rate vs. oxidant concentration. pH 2.0, E = -0.47 V: H_2O_2 (1), $NaNO_2$ (2), Na_2MoO_4 (3), Na_2WO_4 (4).
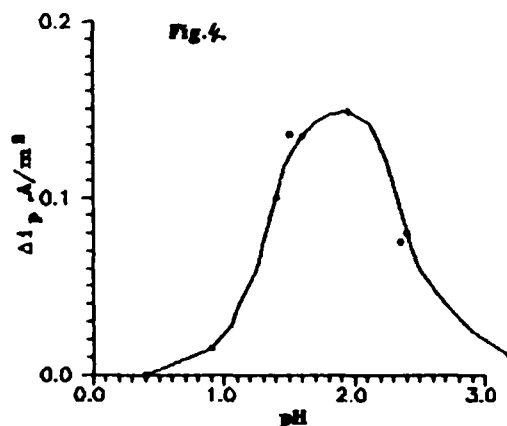
Fig.4. Increase in permeation rate on addition of H_2O_2 as a function of pH of the solution.
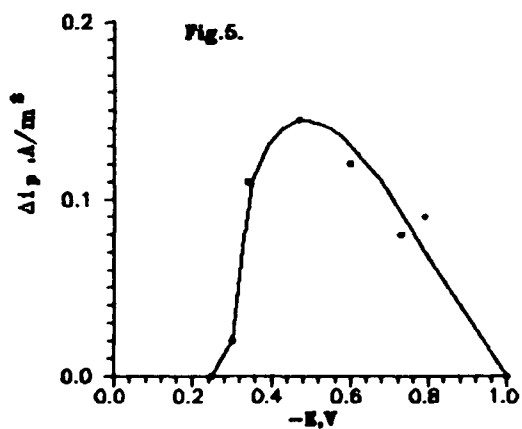
Fig.5. Increase in permeation rate on addition of H_2O_2 as a function of potential.
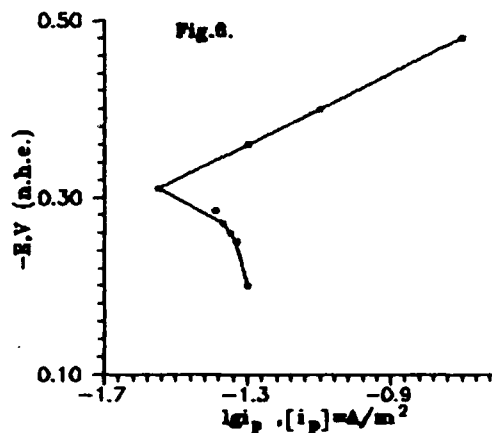
Fig.6. Dependence of hydrogen permeation rate on electrode potential in 0.5M SO_4^{2-}, pH 1.3.

ON HYDROGEN EMBRITTLEMENT OF METALS AND ALLOYS

Yu.I.Archakov

All-Union Scientific-Research Institute for Petrochemical Processes, Zheleznodorozhny Pr. 40, 193148 St.Petersburg, Russia

A great number of works on this problem has been published in literature. Up to now, however, there is no a common point of view explaining the mechanism of metal hydrogen embrittlement. To our mind, it is connected with the influence of many factors, complexity and insufficient exploreness of individual elementary physico-chemical processes.

In our opinion, it is expedient to subdivide the influence of hydrogen on metal mechanical properties into two main aspects: (a) purely physical hydrogen influence connected with absorption of gas by metals which is not accompanied by formation of new phases and by alteration of microstructure and (b) physico-chemical influence of hydrogen accompanied by chemical interaction of gas with individual phases and components (reduction of carbide and other phases by hydrogen, formation of hydrides) which provokes alteration of metal microstructure. The hydrogen embrittlement of the 1st kind is frequently reversible: absorbed hydrogen is released when heating metal and its mechanical properties are restored to initial values. The hydrogen embrittlement of the 2nd kind is irreversible and no thermal treatment can restore initial propeties of metal.

Low hydrogen concentrations (5-8 ppm) at comparatively low temperatures have practically no influence on the resistance to plastic deformation of carbon, low-alloyed and medium-alloyed steels, but sharply decrease plastic limit and resistance to failure.

Comparative mild conditions of high-temperature hydrogen occlusion do not provoke irreversible changes of mechanical propeties and, when subsequent tempering, properties are completely restored.

In the case of hydrogen chemical influence on steel, complete disappearance of physical yield point takes plase (Fig. 1). In this case, even small concentration of hydrogen in steel (Fig. 2) results in sharp decrease in ductility and

impact strength of steel. It is confirmed by microscopic investigations of specimen breakage zones. For the breakage of specimens having no visible signs of decarburization, the presence of grain deformation is typical, but the absence of grain deformation and noticable "crowling" of microcracks along grain boundaries are typical for specimens which underwent decarburization.

Low- and medium-alloyed steels as well as high-alloyed ones carbide phases of which are more thermodynamically stable as compared with cementite have higher corrosion resistance in hydrogen. However, the character of hydrogen content influence on mechanical properties of steel is analogous to that on carbon steels and technical iron. In the case when there is no noticable decarburization of steel, the hydrogen influence on mechanical properties is practically reversible. It is confirmed by the results of steel testing at pressure of 70 MPa and temperature of $600^{\circ}C$ at different exposition times (Fig. 3). Austenitic steels were tested under the analogous conditions. In this case, the analogous picture is observed. In the case, when the steel with 18%Cr, 10%Ni, 0.5%Ti is hydrogen resistant, the following thermal treatment restores initial mechanical properties. Austenitic steels with 0.45%C, 18%Mn and 3%Al undergoes strong decarburization under these conditions and no thermal treatment can restore its properties.

The results obtained shows that to impart hydrogen resistance to steel the total number of alloying elements and a type of lattice are not of considerable importance, but the presence of strong carbide-forming elements, and if their amount is insufficient to bind all carbon it results in sharp and irreversible decrease in all mechanical properties.

It has been determined by means of microscopic study of the character of failure of the investigated steels that the intracrystalline failure of metal took place in initial condition and after thermal treatment. As a rule, failure of austenitic steels took place on grain boundaries immediately after hydrogen influence. Hydrogen-resistant austenitic steels again displayed intracrystalline character of failure after saturation with hydrogen followed by high-temperature tempering, and aus-

tenitic steels which underwent decarburization had distinctly pronouced intercrystallite character of failure in this state.

The microscopic analysis shows that accumulation of absorbed hydrogen occurs in general on grain boundaries and it results in formation of incipient cracks in these volumes and in premature failure of metal structure. In the case of steel decarburization,this effect is increased by accumulation of methane under high pressure on grain boundaries.

The results obtained when investigating long-term strength under hydrogen pressure are given in Fig. 4. An interesting behaviour is also observed here. In the case when steel undergoes hydrogen influence (curves 1,2), the long-term strength in hydrogen sharply decreases as compared to tests in argon and the more the longer the test time is. In the case of hydrogen resistance of steel under given test conditions, the long-term strength in hydrogen does not practically differ from values obtained in inert medium (Figs. 4,5). The analogous dependences are also observed when investigating long-term strength of steel containing 18%Cr, 10%Ni, 0.5%Ti in hydrogen and argon at pressures 20-40 MPa and temperatures 600-800°C. All the values of long-term strength limits are practically identical. However, the character of specimen failure is changed when testing this steel in hydrogen. The plastic limit of this steel in hydrogen is significantly lower than that in argon and it decreases with the increase in hydrogen pressure. When carrying out microscopic investigation of metal structure, the origin and development of cracks are observed on inner surfaces of tubular specimens while the origin and development of cracks in specimens failured by argon pressure take place on their outer surfaces.

Therefore, not lowering long-term strength limit of hydrogen-resistant steel, hydrogen gives rise to appreciable decrease in ultimate strain of specimens. To all appearance, it is provoked by an increase in hydrogen concentration in metal which prevents proceeding relaxation processes under conditions of hampered strain, i.e. by an increase in the resistance to plastic flow of metal.

Thus, sufficiently definite regularities for alteration of

mechanical properties and long-term strength after hydrogen influence at high temperatures and pressures have been obtained for all the individual steels. Steels which possess sufficient hydrogen resistance and do not undergo hydrogen corrosion display slight decrease in ductility and impact strength. In the case of decarburization, the irreversible decrease in steel properties takes place. The following tempering does not result in restoring structure and mechanical properties.
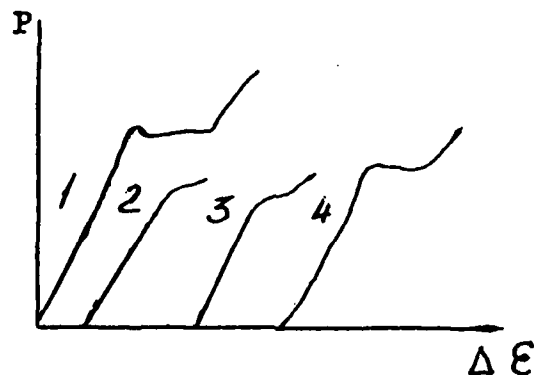
Fig. 1. Tension diagram of steel with 0.2% C.
1 - Initial state; 2 - After high-temperature hydrogen occlusion (P_{H_2} = 20 MPa, t = 450°C); 3 - After tempering at 550°C in vacuo; 4 - After normalizing in vacuo.
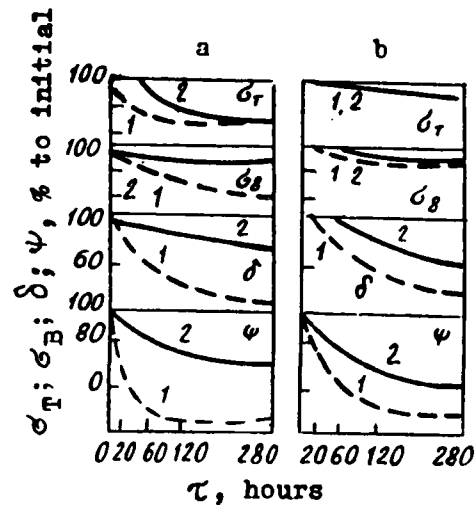
Fig. 2. Alteration of mechanical properties of technical iron
(a) and of steel with 0.2% C (b) depending on duration
(τ, hrs.) of hydrogen influence (P_{H_2} = 20 MPa, t =
400°C).

1 - After hydrogen occlusion; 2 - After hydrogen oc-
clusion and tempering.
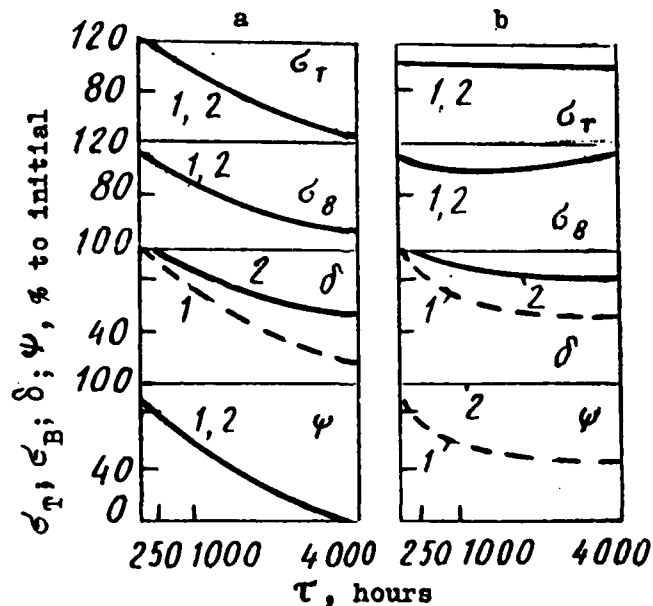
Fig. 3. Alteration of mechanical properties of steels contai-
ning 0.2% C, 3% Cr, up to 1% of W, Mo, V (a) and 0.15%
C, 12% Cr, up to 1% of W, Mo, V (b) depending on ex-
position time (P_{H_2} = 70 MPa, t = 600°C).

1 - Immediately after hydrogen occlusion; 2 - After
hydrogen occlusion and tempering.
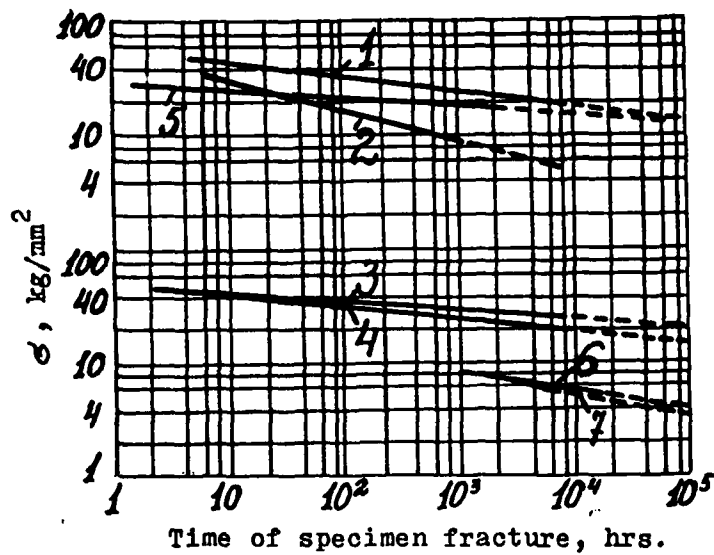
Fig. 4. Long-term strength of steels containing 0.2% C, 3% Cr,
up to 1% of W, Mo, V (1,2), 0.2% C, 3% Cr, up to 1% of
Mo, V, Nb (3,4), 0.15% C, 12% Cr, up to 1% of W, Mo, V
(5) at 600°C and P_{H_2} = 60 MPa, and of steel containing
0.15% C, 5% Cr, 0.5% Mo (6,7) at t = 600°C and P_{H_2} =
15 MPa.

1,3 - In argon; 2,4,7 - In hydrogen; 5 - In argon and
hydrogen; 6 - In air.

Time of the specimen fracture, hrs.
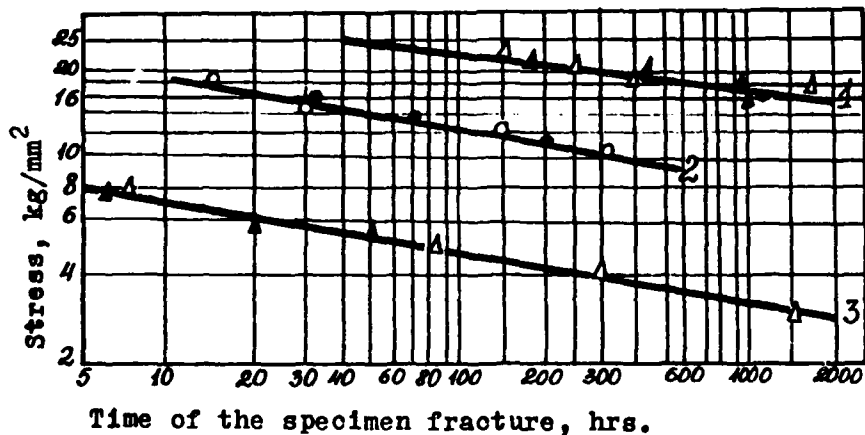
Fig. 5. Long-term strength of Cr-Ni steels in air (light cir-
cles and triangles) and hydrogen medium at 300 MPa
(black circles and triangles).

1 and 3 - Steel containing 0.08% C, 15% Cr, 26% Ni,
2% W, 4% Mo, 0.5% Nb; 2 - Steel containing 18% Cr,
10% Ni, 0.9% Ti.

2410

EFFECT OF COMPOSITION ON HYDROGEN INDUCED DUCTILITY LOSS AND K_{IH} IN Ni-Fe FCC ALLOYS

Wei Hu
Yan-Bin Wang
Wu-Yang Chu
Chi-Mei Hsiao
Dept. of Materials Physics
Univ. of Science and Technology, Beijing
Beijing 100083, P.R.China

Abstract

The ductility loss and threshold stress intensity K_{IH} during dynamic charging were measured for pure Ni and four Ni-Fe fcc alloys. The results showed that ductility loss in 60Ni40Fe alloy and K_{IH} in 50Ni50Fe alloy had a minimum value. The variations of the amounts of hydride phase and hydrogen evolution and dislocation structure with composition have been investigated. The difference between the variation of hydrogen embrittlement susceptibility measured by ductility loss with composition and that by K_{IH} or K_{IH}/K_C could be explained by the use of synthetical effects of amount of hydride and solutionizing hydrogen and the extent of dislocation planarity on hydrogen embrittlement susceptibility.

Introduction

Several investigations [1-4] have been concerned with the embrittlement of Ni-Fe austenitic alloys by hydrogen. The early results obtained for this alloy system indicated that the hydrogen embrittlement susceptibility decreased as the iron content of the alloy increased [1,2]. The recent investigations [3,4], however, showed that the hydrogen embrittlement susceptibility increased again with increasing iron content after Fe > 50-60%, as shown in Figure 1. Figure 1 shows that the hydrogen embrittlement suscep-tibility for Ni-Fe alloys has a minimum at about 50-60%Fe. While there is no known basis for this phenomenon, it is of significance, as the Ni-Fe system is the basis of many commercially important alloy systems. The early explanation considered that the hydrogen embrittlement of Ni and Ni-Fe alloys was associated with the grain boundary precipitation of unstable hydride,and the tendency for hydride formation and then the hydrogen embrittlement decreased with increasing iron content [2,3]. Supposing this is true, it still can not explain the further increase of hydrogen embrittle-ment susceptibility when Fe > 50-60%.

Up to now, all data of hydrogen embrittlement susceptibility for Ni-Fe alloys were hydrogen induced ductility loss measured by using smooth tensile specimens. There was not any delayed fracture test. Maybe the variation of the ductility loss for Ni-Fe alloys with the iron content is different from that of threshold stress intensity of hydrogen induced cracking, K_{IH}. Therefore, the present work will study the hydrogen induced delayed fracture for Ni-Fe alloys and the effect of alloy composition on K_{IH}.

Besides the tendency for hydride formation and hydride content, the atomic hydrogen concentration in the Ni-Fe alloys, which maybe depends upon the iron content, will strongly influence the hydrogen embrittlement susceptibility. For austenitic stainless steels and alloys, the

dislocation planarity and then stacking fault energy plays a dominant or important role for hydrogen embrittlement susceptibility [5,6]. The stacking fault energy for Ni-Fe alloys is dependent upon the iron content [7,8] and has a minimum for 35Ni65Fe alloy [8]. Therefore, the other purpose for this work is to investigate the variations of hydride content, atomic hydrogen concentration and dislocation planarity with iron content in Ni-Fe alloys and explain the effect of alloy composition on both ductility loss and K_{IH}.

Experimental Procedures

The alloys used in the present study were prepared by vacuum melting, casting into ingots, and hot rolling to plates of 6.4mm in thick. They were then cold rolled into strips of 0.25mm or 0.1mm in thick. The compositions of the alloys used in this study were determined by analysis, with the C, S, N and O contents being measured by vacuum extraction, and are given in Table 1.

Table 1. Alloy Composition (in wppm)

Alloy	C	S	O	N
Ni	28	16	281	16
60Ni40Fe	110	12	14	5
50Ni50Fe	110	10	18	5
40Ni60Fe	120	12	18	5
30Ni70Fe	64	3	119	3

The specimens included flat tensile ones with a gage section of 4mmX0.1mm for Ni or 4mmX0.25mm for the others, and single-edge notched tensile ones with a notch of 1mm in depth and root radius of 0.1mm. All specimens were oriented such that the tensile axis paralleled to the rolling direction. All samples were sealed in evacuated quartz tunes and heat treated at 950°C for 2 hours, followed by oil quenching without removing the samples from the quartz tubes. X-ray diffraction analysis of the samples revealed that all specimens including the 30Ni70Fe were single-phase fcc gamma in structure. No martensite was found to form on quenching.

Hydrogen was introduced by cathodic charging at current density of 100A/m² in 1N H_2SO_4 with 250mg/l $NaAsO_2$.

After precharging for 24 hours, the specimens were tensile tested at room temperature at a strain rate of $10^{-5}s^{-1}$, while the same hydrogen-charging condition as used in the precharging was maintained. Two or three specimens were tested under identical condition, and the results reported are averages of the individual behavior.

Delayed fracture test of hydrogen induced cracking (HIC) under constant load [9] was performed using single-edge notched specimens with thickness of 0.1mm for Ni and 0,25mm for the others. To obtain the normalized threshold stress intensity ,K_{IH}/K_c, the time to- failure under different K_I/K_c was measured during dynamic charging after precharging for 24 hours.

To examine the fracture surfaces on scanning electronic microscope, the failure specimens were ultrasonically cleaned in 15pct HCl + 1pct $(CH_2)_6N_4$ solution and then in acetone.

Thin foils for TEM were prepared from tensile specimens deformed 10pct by first electrolytic thinning in 1N H_2SO_4 methanol solution and then ionic thinning.

Waiting for 20min after precharging for 24 hours, X-ray diffraction were performed within 4min to determine hydride content. Supposing that the intensity of the diffraction peaks depends only on hydride content and the diffraction angle, the difference between the absorption coefficient of Ni and Fe is ignored, the volume fraction of hydride should be:

$$C = [\ 1 + \frac{I}{I_H} \frac{(1-\cos^2 2\theta_H)/\sin^2\theta_H \cos\theta_H}{(1+\cos^2 2\theta)/\sin^2\theta\cos\theta}]^{-1}$$

where I, I_H and i, i_H are intensities and angles of diffraction peaks for matrix and hydride, respectively.

The amount of hydrogen evolution at room temperature for the specimens precharged for 24 hours was collected using a glass tube filled with liquid paraffin [10].

Experimental Results

1. Ductility loss for Ni-Fe alloys

Table 2. Relative change of ductility, strengths and intergranular fracture induced by H (%)

Alloy	ductility loss	increase in YS	decrease in UTS	IG
Ni	54	2	0	34
60Ni40Fe	55	18	27	55
50Ni50Fe	40	16	18	14
40Ni60Fe	22	4	8	24
30Ni70Fe	72	0	28	49

The relative changes of uniform elongation, yield strength and ultimate tensile strength induced by hydrogen for pure Ni and Ni-Fe alloys are listed in Table 2. The intergranular fracture percent in the charged specimens for Ni-Fe alloys is also listed in Table 2. There was no intergranular fracture for Ni and Ni-Fe alloys in the absence of hydrogen.

Table 2 shows that a small increase in yield strength is caused by hydrogen and embrittlement takes place as evidenced by the reduction in uniform elongation and ultimate tensile strength.

The variations of hydrogen induced ductility loss and inter- granular fracture fraction with alloy composition, i.e., iron content, are shown in Figure 1. Comparing the curve of present work with that of previous work in Figure 1, it is evident that the variation in ductility loss with iron content obtained in the present work has the same tendency as that in the references. i.e., the hydrogen embrittlement susceptibility decreases with increasing iron content when Fe<60%,

and then increases again when Fe > 60%. There is a minimum hydrogen embrittle-ment susceptibility for the 40Ni60Fe alloy. The variation of inter-granular fracture, however, with iron content is not consistent with that of ductility loss.

2. Threshold values of hydrogen induced cracking

An average fracture load in air for the single-edge notched specimen was used to calculate the critical stress intensity in plane stress condition, K_C, as shown in Table 3. The failure times for notched specimens precharged for 24 hours under different but constant loads during dynamic charging were recorded. The curves of K_I vs time-to-failure for Ni and the Ni-Fe alloys were obtained. The threshold stress intensity of HIC can be calculated as follows [11].

$$K_{IH} = (K_{Ii} + K_{Ig})/2$$

where K_{Ii} stands for the minimum K_I at which delayed failure occurs and K_{Ig} for the maximum value at which delayed failure will not occur within the fixed time, e.g., 100 hours. To ensure that the error measuring of K_{IH} will be not more than 10pct, (K_{Ii} - K_{Ig}) must be less than $0.2K_{IH}$. The K_{IH}, K_{IH}/K_C and the intergranular fracture percent on the delayed failure surfaces for the five materials are listed in Table 3.

Table 3. K_{IH}, K_{IH}/K_C and intergranular fracture

Alloy	Ni	60Ni40Fe	50Ni50Fe	40Ni60Fe	30Ni70Fe
K_C (MPam$^{1/2}$)	18.4	21.6	21.7	19.6	15.9
K_{IH}, (MPam$^{1/2}$)	16.2	14.3	12.0	15.7	14.3
K_{IH}/K_C	0.88	0.66	0.56	0.79	0.90
I.G.,%	26	23	30	32	48

The variation in K_{IH} and K_{IH}/K_C with iron content is shown in Figure 2. Figure 2 indicates that the hydrogen embrittlement susceptibility measured by K_{IH} or K_{IH}/K_C increases with increasing iron content within Fe < 50%, and then decreases again with increasing iron content when Fe > 50%. To one's great surprise, the variation of hydrogen embrittlement susceptibility measured by K_{IH}/K_C with iron content, as shown in Figure 2, has just contrary tendency to that measured by ductility loss, as shown in Figure 1. Again, the variation in intergranular fracture fraction with iron content is not consistent with that in K_{IH}/K_C, as shown in Table 3.

3. Hydride and amount of hydrogen evolution

X-ray diffraction revealed that hydride phase could form after cathodic charging for 24 hours in the five fcc materials. The diffraction peaks of hydride phase for pure and Ni-Fe alloys would disappear if laying aside for 24 hours at room temperature after precharging. This means that the hydride formed during charging is unstable. The volume percent of hydride phase estimated based on the X-ray diffraction data are shown in Figure 3. The total amounts of hydrogen evolution at room temperature for pure Ni and Ni-Fe alloys precharged for 24 hours are also shown in Figure 3.

4. Dislocation structure

The dislocation structures for the Ni-Fe alloys deformed 10pct. are shown in Figure 4. For

50Ni50Fe alloy, there was a planar dislocation arrangement without dislocation tangle and a lowest dislocation density, as shown in Figure 4(a). For 30Ni70Fe, 60Ni40Fe and Ni, there were lots of dislocation tangles, corresponding cross-slip dislocation arrangement, as shown in Figure 4(b) and 4(c). For 40Ni60Fe there were a few dislocation tangles, as shown in Figure 4(d). Figure 4 shows that the extent of dislocation planarity is the maximum for 50Ni50Fe alloy, the minimum for 30Ni70Fe, 60Ni40Fe and pure Ni and the middle for 40Ni60Fe alloy.

Discussion

The main factors influencing the hydrogen embrittlement susceptibility for the Ni-Fe alloys are as follows.

1. Yield strength
For high strength steels, hydrogen embrittlement susceptibility measured by either ductility loss or K_{IH} increased with increasing yield strength [12,13]. For the five fcc materials used in the present work, the yield strength are very low, i.e., 130MPa to 180MPa, and the effect of composition on yield strength is very small. Therefore, the variation of ductility loss and K_{IH} with composition is not due to the small difference of yield strength for the Ni-Fe alloys.

2. Volume fraction of hydride
Hydride is one kind of brittle phase, the elongation and K_{IH} would decrease with increasing volume fraction of hydride phase. Unfortunately, it is not possible to investigate the effect of hydride on elongation and K_{IH} in pure Ni and the Ni-Fe alloys independently, since the hydride phase formed during charging is unstable and will begin to decompose immediately at room temperature after stopping charging. For titanium aluminide, in which hydride is a stable phase, strain-to failure and K_{IH} decreased exponentially with increasing hydride [14].

For the Ni-Fe alloys, hydride could reduce elongation and K_{IH} during dynamic charging because of no decomposition of hydride in this case. The volume fraction of hydride phase in the Ni-Fe alloys was dependent on the iron content (Figure 3), thus the hydrogen embrittlement susceptibility induced by hydride alone should depend upon the composition, similar to Figure 3. A schematic effect of hydride on hydrogen embrittlement susceptibility is indicated using curve (b) in Figure 5.

3. Solutionizing hydrogen concentration
Hydrogen embrittlement susceptibility should increase with increasing atomic hydrogen concentration entering into the sample during charging. The solubility of hydrogen in the Ni-Fe fcc alloys should depend on composition, although there is no data available. Figure 3 shows that the total amount of hydrogen evolution, which is the sum of hydrogen solutionizing in lattice and that resulting from decomposition of hydride, has a maximum value for pure Ni and a minimum value for 60Ni40Fe, 50Ni50Fe and 40Ni60Fe alloys. However, the amount of hydride in 50Ni50Fe alloy had a maximum value, as shown in Figure 3. Therefore, the atomic hydrogen solutionizing in lattice had a minimum value for 50Ni50Fe alloy. The variation of hydrogen embrittlement susceptibility induced by solutionizing hydrogen alone with composition is schematically shown by curve (c) in Figure 5.

4. Dislocation or slip planarity
The role of slip character in HIC process is that planar slip enhances dislocation transport

[15], and prevent dislocations from cross-slipping around small particles and escaping. Thus the larger the extent of slip planarity is, which is mainly controlled by stacking fault energy, the larger the hydrogen embrittlement susceptibility will be. Figure 4 shows that the extent of dislocation planarity in 50Ni50Fe alloy has the maximum value and that in pure Ni, 30Ni70Fe and 60Ni40Fe the minimum value. Therefore, the variation of the hydrogen embrittlement susceptibility with composition resulted from dislocation planarity is schematically plotted by curve (a) in Figure 5.

Investigating synthetically the effect of hydride, solutionizing hydrogen and dislocation planarity on the hydrogen embrittlement susceptibility is maybe able to explain the different variations of ductility loss and K_{IH} with composition because the weights of the effect of the three above-mentioned factors on ductility loss and K_{IH} are different. Supposing that the ductility loss are controlled by hydride and the amount solutionizing hydrogen, the combination of curve (b) and (c) in Figure 5 can result in a minimum ductility loss for 60Ni40Fe or/and 50Ni50Fe alloy. Supposing that the K_{IH} for HIC is controlled by hydride and dislocation planarity, the combination of curve (a) and (b) in Figure 5 can result in a minimum K_{IH} value in 50Ni50Fe alloy.

Conclusions

1. The hydrogen induced ductility loss for pure Ni and 60Ni40Fe, 50Ni50Fe, 40Ni60Fe and 30Ni70Fe fcc alloys were 54%, 55%, 40%, 22% and 72%, respectively, i.e., there was a minimum ductility loss for the 60Ni40Fe alloy.

2. The normalized threshold value of HIC, K_{IH}/K_C, for Ni, 60Ni40Fe, 50Ni50Fe, 40Ni60Fe and 30Ni70Fe alloys were 0.88, 0.66, 0.56, 0.79, and 0.90, respectively, i.e., there was a minimum K_{IH} or K_{IH}/K_C for 50Ni50Fe alloy.

3. A unstable hydride phase could form during charging for the five fcc materials and the volume fraction of hydride depend on composition.

4. The amount of hydrogen evolution and then the solutionizing hydrogen had a minimum value for the 50Ni50Fe alloy.

5. The extent of dislocation planarity was the maximum for the 50Ni50Fe alloy and the minimum for pure Ni, 60Ni40Fe and 30Ni70Fe alloys.

Acknowledgement

References

1. P.Blanchard and A.R.Troiano, Mem.Sci.Rev.Met., 57(1960), 409.

2. M.L.Wayman and G.C.Smith, Acta Metall., 19(1971), 227.

3. G.C.Smith, Hydrogen in Metals, eds. I.M. Bernstein and A.W.Thompson, ASTM 1974,

p485.

4. W.Y.Chu and H.K.Birnbaum, Metall. Trans.A, 20A(1989), 1475.

5. B.C.Odegard, J.A.Brooks and A.J.West, Effect of Hydrogen on Behavior of Materials, eds. A.W.Thompson and I.M.Berstein, AIME, 1976, p116.

6. A.W.Thompson and I.M.Bernstein, Advance in Corrosion Sci. and Tech., eds. M.G.Fontana and R.W.Stachle, vol.7, 1980, 53.

7. B.E.P.Beeston and L.K.France, J. Institute of Metals, 96(1968), 105.

8. W.Charnock and J.Natting, Met. Sci. J., 1(1967), 78.

9. W.Y.Chu, J.Yao and C.M.Hsiao, Metall. Trans.A, 15A(1984), 749.

10. W.Y.Chu, Y.B.Wang and C.M.Hsiao, Corrosion, 38(1982), 561.

11. W.Y.Chu, C.M.Hsiao and J.W.Wang, Metall. Trans.A, 16A(1985), 1663.

12. W.Y.Chu, T.H.Liu, C.M.Hsiao and S.Q.Li, Corrosion, 37(1981), 320.

13. M.Smialawski, Hydrogen in Steel, Pergamon press, 1962, p207.

14. W.Y.Chu and A.W.Thompson, Metall. Trans.A, 22A(1991), in press.

15. J.K.Tien, A.W.Thompson, I.M.Bernstein and J.R.Richards, Metall. Trans.A, 7A(1976), 821.
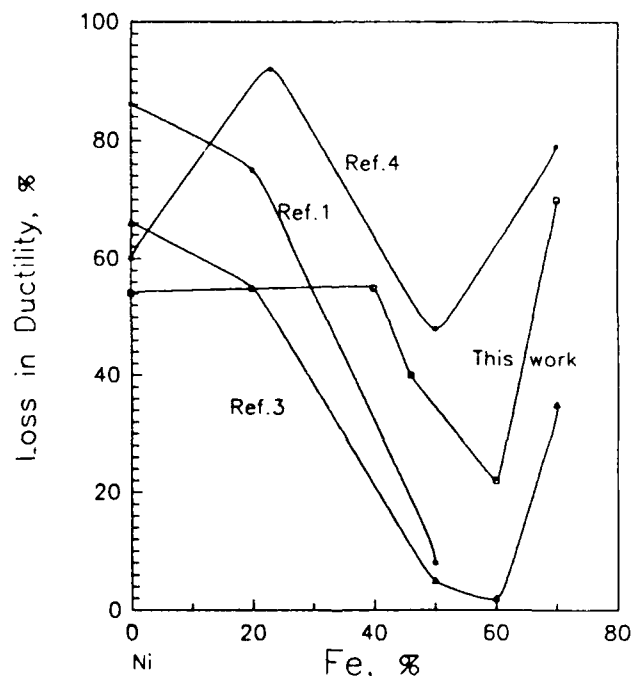
Fig. 1   Hydrogen induced ductility loss VS composition (Fe %) present work
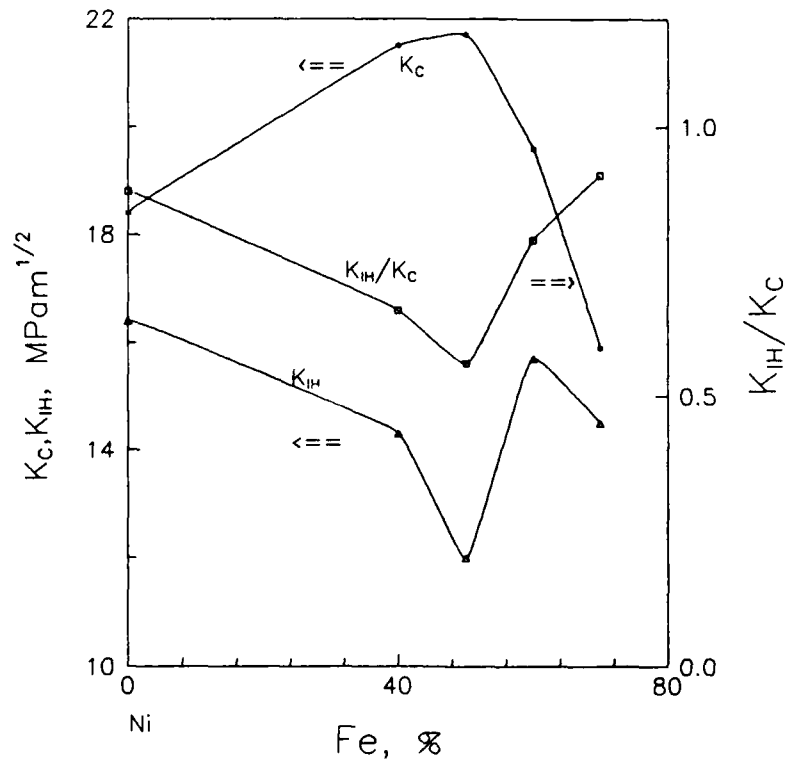
Fig.2 K_C, K_{IH} and K_{IH}/K_C as a function of
amount of iron in Ni—Fe alloy
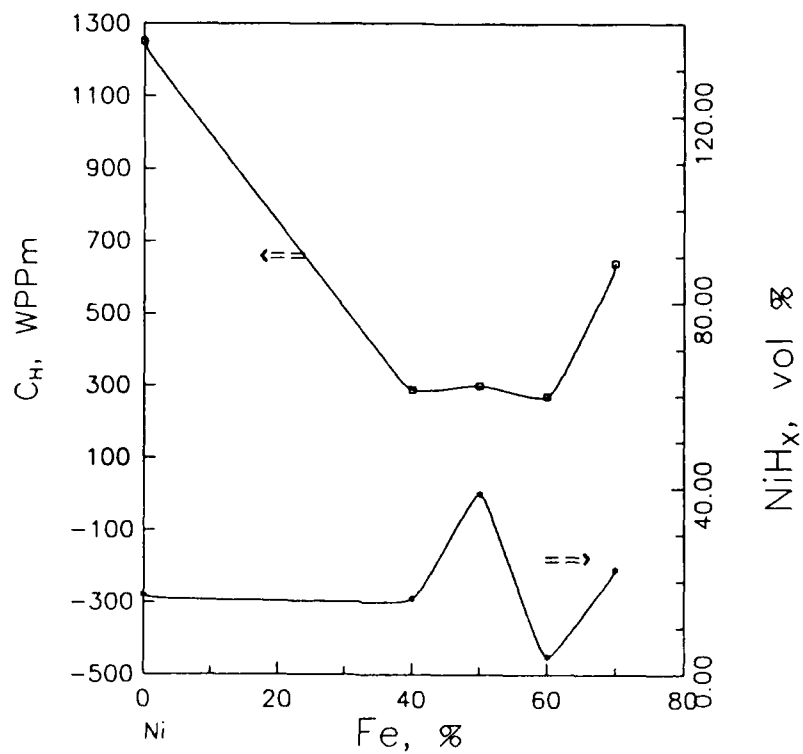
Fig.3 The variation of the volume percent of the hydride and
total hydrogen evolution with composition (Fe%)

(a)

(b)

(c)

(d)
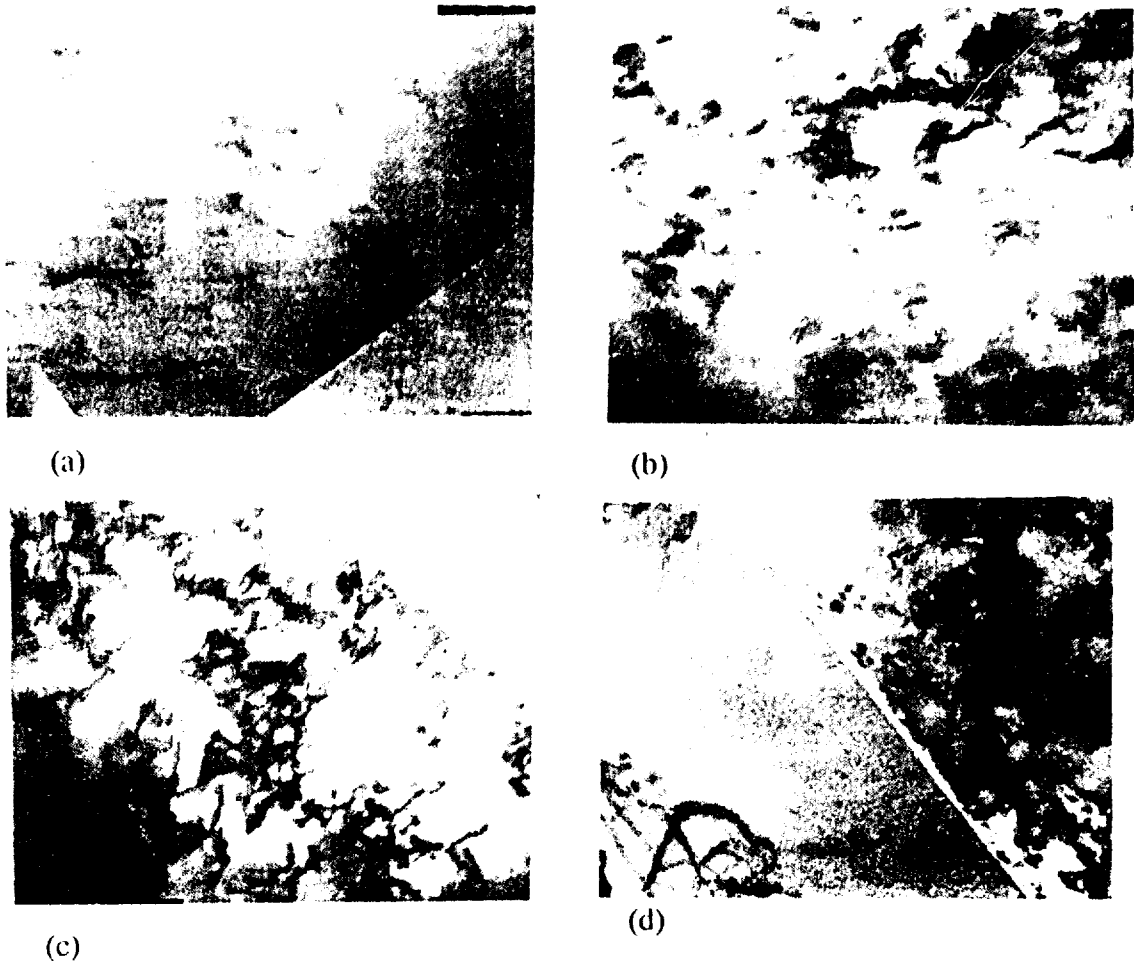
Fig. 4 Dislocation structure for Ni-Fe alloys

(a) 50Ni50Fe   (b) 30Ni70Fe

(c) 60Ni40Fe   (c) 40Ni60Fe
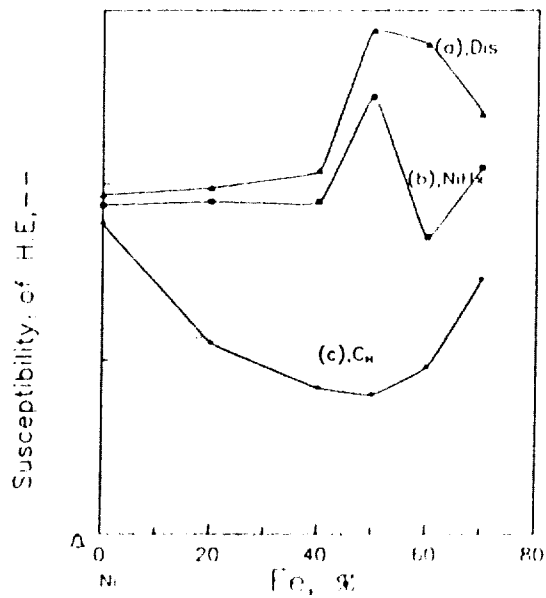
Fig.5 The schematic effect of dislocation structure (a),

hydride (b) and soluble hydrogen (c) on

the susceptibility of hydrogen embrittlement

2419

Corrosion Management

Derek Milliams,
Shell Internationale Petroleum Maatschappij B.V.,
PO Box 162,
2501 AN The Hague, The Netherlands

Abstract

Corrosion in installations, if not managed adequately, can increase the risks to personnel, to the environment and to the value of an asset.

The corrosion and materials engineer has an important role to play in a multi-disciplined team, with operations, maintenance and inspection engineers to ensure that a broad awareness of corrosion is translated into day to day actions to reduce these risks.

It is important that the constraints applied by the corrosion and materials engineer at the design stage are fully appreciated by staff involved in operating an installation. Equally the maximum use should be made of corrosion monitoring and inspection data in the day to day operation of equipment and in indicating where future designs could be improved.

When systematically registered and analysed, inspection and corrosion findings will highlight recurring problems allowing the use of either existing technology or that developed by carefully focussed research to provide optimised solutions. This can lead to substantial financial savings.

A model is provided describing the information flows in Corrosion Management. It has the aim of ensuring optimum use is made of the skills of the corrosion and materials engineer.

Key terms: technical integrity, corrosion management, deviation control, audit, cost saving

Introduction

Society and company interests both demand that the achievement and maintenance of the technical integrity of installations for oil and gas production and refining is given high priority. This reflects the need to ensure the safety of the public and company personnel, the avoidance of unacceptable environmental impact and the preservation of asset value. The demonstration of such integrity to regulatory authorities is increasingly required.

Minimising life cycle costs whilst achieving technical integrity is often dependent on the use of materials which can be expected to corrode during normal service. As a consequence, to ensure continued integrity at minimum cost, corrosion has to be actively managed throughout an installation's life from the early stages of design until it is taken out of service.

Corrosion and materials engineers, however detailed their knowledge of the corrosion processes occurring in a plant or piece of equipment, cannot, alone, ensure that the necessary measures to contain corrosion threats are being applied on a day to day basis. It follows that they have the responsibility to see that all involved in the design, construction, commissioning, operation, inspection and maintenance of an installation are alert to the need to manage corrosion and to the potential consequences, in terms of safety, environmental effects and cost, of a failure to do this adequately.

To achieve the maximum impact of the corrosion and materials engineers' skills, it is important that the flows of related information are clearly defined and recognised by all who should be involved with their use.

A Model for Corrosion Management

A model for Corrosion Management, which illustrates the information flows required and emphasises the multi-disciplined nature of the process, is shown in Figure 1. The information cycle which results from this model can provide a basis to ensure that optimum use is made of corrosion and materials engineering knowledge.

All stages of this cycle require excellent two way communication between corrosion and materials engineers, as advisers, and their clients throughout an organisation.

The Tools to Achieve the Management of Corrosion

Standards

Standards represent a wealth of knowledge often based upon experience built up over many years.

Clearly it is important that National and Industry Standards, for example, for the fabrication and construction of an installation, are accurately followed if the full benefit of existing knowledge is to be gained.

Equally, internal company Standards and reference documents related to corrosion and materials should also be established and applied. These documents will go further than published information and will contain the product of, sometimes costly, prior operating experience. Amongst many possibilities, such a document might offer guidance on the corrosion rates to be expected in a particular process stream or piece of equipment, it might reflect

company preferences for structural painting systems and their application or it might provide details of company policy on cathodic protection design for pipelines.

In all cases standards organisations, both external and internal, should be open to Feed-Back from standards users which, with appropriate authorization, can be used to update their documents. An obligation on users is that they should provide technically sound and well reasoned documentation to justify any proposed change.

Corrosion Management Manuals

Corrosion Management Manuals prepared, possibly by the project team during the design phase of an installation, provide a formal method of ensuring "Feed-Forward" of essential corrosion design, control and measurement information. To be effective such documents should make the reasoning for the materials' choices transparent in terms of the corrosion processes expected to occur, the anticipated rates of attack and the corrosion mitigation methods chosen.

In addition, they should contain information on the operating and maintenance practices and inspection planning requirements to achieve the defined installation life.

For the operator this might involve the definition of his responsibilities with respect to ensuring the continuous injection of corrosion inhibitors downhole. For the maintenance engineer information might be provided on the expected life of an internal vessel coating under the expected process conditions so that likely necessary repairs can be planned. For the inspector this might involve the initial definition of the frequency of intelligent pig inspections of a pipeline based upon the rates of corrosion expected, the planned design life and the corrosion allowance provided.

Inspection / Corrosion Data Bases and Data Analysis

Measurements made during inspections and corrosion monitoring of installations are a major asset, this applies whether they show deviations from the design assumptions or confirm the design approach chosen. Such data, in many cases accumulated at considerable cost, are often under-utilised.

Data collected may identify possible threats to an installation's integrity which require immediate and urgent action. However, a key factor in the use of inspection / corrosion data for the longer term planning of operations, maintenance and inspection requirements is the availability of a data base system to facilitate the collation and analysis of information over longer periods. The ready availability of design data and operating information to the corrosion and materials engineer for the data analysis step will also enhance the efficient and effective use of the available inspection / corrosion data.

The coupling of inspection findings to process condition data is a valuable source of field experience in optimising the operation of an installation from a corrosion and materials viewpoint and in providing a basis for the confirmation or modification of Standards for future designs. In view of the potential influence of this "Feed-Back", the data analysis step is of major importance in the corrosion management cycle.

Status Reports

The analysis of inspection and monitoring results should lead to condition status reports, which may contain proposals to revise operating and maintenance practices and inspection plans, for individual pieces of equipment, based on the observed operational experience.

It is of particular importance that summary status reports, for installations as a whole, be provided for management on a regular basis. These reports should highlight the areas of concern, review the progress made towards their resolution and define clearly the actions and responsibilities within a multi-disciplined team for the period ahead.

Status reports raise the general awareness of corrosion and materials engineering concerns and provide for technical continuity in the event of staff transfers. They are an essential contribution to establishing management confidence in the achievement of technical integrity.

Potential Benefits of a Transparent Corrosion Management Approach

Deviation Control

Corrosion Management Manuals provide a basis for deviation control through the establishment of base line operating conditions and practices and maintenance and inspection plans. Changes in these practices for an installation, possibly prompted by operating experience or operational needs, can be evaluated against this base line, agreed by all relevant disciplines and fully documented in a revised manual before their introduction. This sequence of documentation will provide an audit trail through an installation's operational history.

Audit

The Corrosion Management model suggested provides a basis for audit at two levels. It defines a possible set of corrosion management tools which should be in place if effective Corrosion Management is to be achieved and at a more detailed level, information concerning an individual piece of equipment can be examined to ensure that its integrity with respect to corrosion has been established and is being adequately safeguarded.

Enhanced application of technology

The systematic analysis of corrosion failures, promoted by this approach to Corrosion Management, will help with the identification of recurring problems allowing the optimised use of existing technology or the focussing of research effort on areas where no economic solution exists. In the latter case, well defined experience data collected for and generated during the analysis step will be available as a foundation for the research work.

Financial benefits

The development of this approach to Corrosion Management has been stimulated by indications that the more efficient use of corrosion and materials technology and inspection and monitoring data would result in a reduction of avoidable corrosion costs by at least twenty five percent.

Concluding remarks

The management of corrosion is a concern which extends beyond the responsibilities of corrosion and materials engineers. Whilst they should provide advice during both the design and operational phases, they are dependent upon the co-operation of other disciplines if an installation's projected design life is to be achieved. The model proposed provides a framework for that co-operation and for optimising the contribution the corrosion and materials engineers make to an organisation.
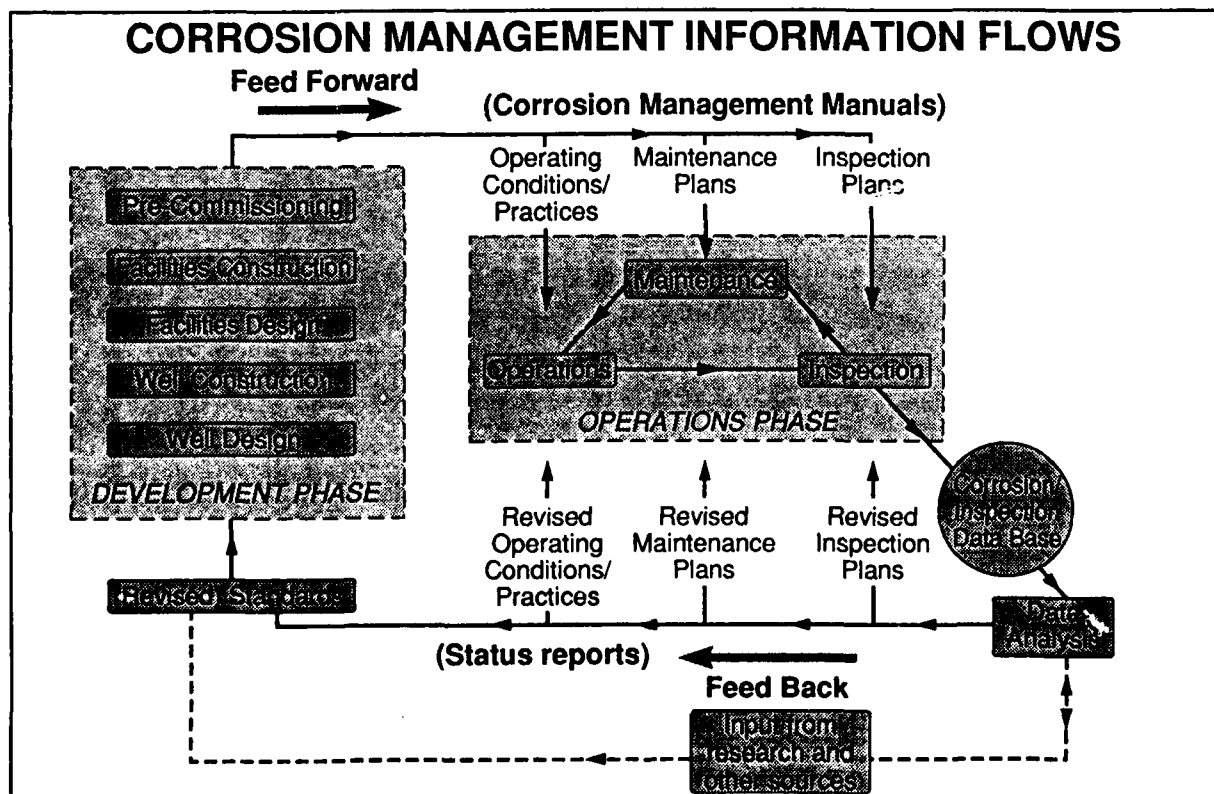
Figure 1

Development of Super 13Cr Stainless Steel
for CO_2 Environments Containing a Small Amount of H_2S

Tohru Okazawa, Tsuneaki Kobayashi
Sumitomo Metal Industries Ltd.
Wakayama Steel Works
1850 Minato
Wakayama, Japan 640

Masakatsu Ueda, Takahiro Kushida
Sumitomo Metal Industries Ltd.
Iron & Steel Reseach Laboratories
1-8 Fuso-cho
Amagasaki, Japan 660

Abstract

Recently, a super 13Cr martensitic stainless steel (LowC-13Cr-5Ni-2Mc) has been developed at SMI. Its chemical composition was determined from the view-point of both SSC at ambient temperatures and the general/localized corrosion at elevated temperatures in CO_2 environments with a small amount of H_2S. Carbon content was controlled to a low value of less than 0.05mass% in order to increase the effective Cr for corrosion resistance. 2mass% Mo was necessary for improving the SSC resistance at up to 0.003MPa of H_2S partial pressure. Ni of 5mass% was added in order to obtain a martensitic, single-phase structure.

The super 13Cr stainless steel seamless tubulars of 95ksi grade were manufactured by the mannesmann-mandrel mill process. The tubulars were quenched and tempered into 95ksi grade having a hardness of lower than 28HRC. These tubulars showed a higher SSC resistance at ambient temperatures than the conventional 13Cr steel, and the H_2S threshold pressure was 0.003MPa in 5% NaCl solution with 30MPa CO_2.

In the field application of 95ksi(665MPa) grade tubulars made from the super 13Cr stainless steel, these tubulars showed good corrosion resistance in simulated environments of North Sea fields, whose conditions were composed of high CO_2 partial pressure, low H_2S partial pressure and high chloride concentration. No SSC occurred in the specimens at ambient temperatures. Corrosion rate of C-ring specimens was less than 0.01mm/y and no localized corrosion occurred at elevated temperatures.

In addition, the super 13Cr stainless steel has good fracture toughness and weldability. So, the corrosion tests on welded portions were investigated to clarify the applicability of the super 13Cr stainless steel to line pipe.

Key terms: oil country tubuler goods, super 13Cr stainless steel, martensitic stainless steel, sulfide stress cracking, SSC, corrosion resistance, CO_2

Introduction

The field application of 13Cr martensitic stainless steel(AISI 420) has been increasing due to its good corrosion resistance in CO_2 environments and lower cost than 22Cr duplex stainless steel[1][2]. However, it is well known that 13Cr steel is susceptible to SSC in CO_2 environments with H_2S partial pressure more than 0.0003MPa(0.003atm or 0.045psi), and it is less resistant to general and localized corrosions at elevated temperatures above 150°C[3]. In particuler, the existence of H_2S extremely deteriorates the corrosion resistance of 13Cr steel in laboratory tests. On the other hand, the exploration of deep and hot oil and gas wells has expanded, and the CO_2 environments have begun to contain a small amount of H_2S.

Recently, several super 13Cr stainless steels with improved corrosion resistance have been proposed by some researchers[4][5][6][7]. In this paper, newly developed super 13Cr martensitic stainless steel is introduced. It has an intermediate corrosion resistance between conventional 13Cr martensitic stainless steel and 22Cr duplex stainless steel.

In the first section of this paper, the alloying design of the super 13Cr stainless steel is introduced. This design enhances the SSC resistance at ambient temperatures and the localized corrosion resistance at elevated temperatures. In the section II, the corrosion resistance of the super 13Cr stainless steel is presented. An application limit and effect of environmental factors such as H_2S partial pressure, Cl^- ion concentration and temperature are also discussed in consideration of the environmental variables. In addition, concerning the field application of tubulars made from super 13Cr stainless steel, the results of long term corrosion testing in simulated environments are introduced. Finally, the results on fracture toughness and weldability are introduced in section III.

Experimental Procedure

I. Tested Materials

Materials with the chemical composition given in **Table 1** were used for the investigation. The mechanical properties of these materials are shown in **Table 2**. The super 13Cr stainless steel seamless tubulars were manufactured by the mannesmman-mandrel mill process. These tubulars were quenched and tempered into 80ksi, 95ksi and 110ksi grades.

The effects of environmental factors on corrosion were studied using the super 13Cr stainless steel with 95ksi grade. The conventional 13Cr steel and 22Cr duplex stainless steel were used as comparative materials.

II. Corrosion Test

SSC resistance was evaluated by constant-strain test methods. The four-point bent beam specimen of 2mm by 10mm by 75mm with notch (stress concentration factor of notched-bottom portion = 2.1) and C-ring specimens were used for the constant-strain test. The specimens were stressed to 100% of the yield strength. The 4-point bent beam and tensile specimens were stressed longitudinally to the rolling direction.

In crevice-corrosion tests at elevated temperatures, metal-to-metal crevice specimens were used[4].

III. Test Method

The specimens were polished with silicon carbide No.600 paper. The C-ring specimen was pickled in HNO_3 + HF solution. Then these specimens were rinsed with distilled water and degreased in ethanol and aceton. Deaeration was carried out by a repetition of vacuum and bubbling of N_2 gas. H_2S gas and CO_2 gas were charged to the experimental pressure at room temperature. After the corrosion test, a visual observation was done and then weight loss was measured after descaling. The specimens were mounted in epoxy resin and further examined at high magnification to detect cracking.

Result and Discussion

I. Alloying Design of Super 13Cr Stainless Steel

The SCC at ambient temperatures and the general and localized corrosion at elevated temperatures are the most important corrosion problems for the martensitic 13Cr stainless steel in CO_2 environments with a small amount of H_2S. So, the chemical composition of super 13Cr stainless steel was determined in consideration of both corrosion resistances.

Carbon content was controlled to a low value of less than 0.05mass% in this study in order to suppress the reduction of the Cr concentration in the matrix as Cr carbide precipitation($Cr_{23}C_6$). The martensitic single-phase region, when austenized at 1050° C, is shown in **Figure 1**. The region was reduced with the increase of Mo content in the steels.

The SCC resistance of these steels was investigated in 5% NaCl solution with 3.0MPa(450psi) CO_2 and 0.001MPa(0.15psi) H_2S at 25° and 60° C. The test results on the corrosion rate and SCC susceptibility are given in **Figure 2**. The corrosion rate was remarkably decreased with Mo content. The steels with 2mass% Mo or higher had a corrosion rate of less than 0.01mm/y and did not suffer SSC. Therefore, the addition of 2mass% Mo to LowC-13Cr- Ni martensitic stainless steel is very effective for the improvement of SCC resistance.

The corrosion test at elevated temperature was carried out in the concentrated 25% NaCl solution with 3.0MPa(450psi) CO_2 at 150° C. The corrosion rate decreased enormously as shown in **Figure 3** when the Cr content was higher than 11mass%. Accordingly, it is thought that the decrease in carbon content to 13Cr martensitic stainless steel improves the general corrosion resistance in CO_2 environments at elevated temperatures.

Based on the test results mentioned above, the chemical composition region of super 13Cr stainless steel is given in **Figure 4**. The Ni content was fixed at 5mass% for economic reasons. LowC-13Cr-5Ni-2Mo is a suitable chemical composition for the super 13Cr stainless steel.

II. Corrosion Resistance of Super 13Cr Stainless Steel

First, the effects of environmental factors such as H_2S partial pressure and Cl^- ion concentration on SSC resistance of the steel which was melted in the laboratory and manufactured in the mill was studied. Next, the localized corrosion and SSC resistances of these steels were investigated at elevated temperatures.

II.1 SSC Resistance

The effect of H_2S partial pressure and Cl^- ion concentration on SSC susceptibility is given in **Figure 5**. The susceptibilities of the laboratory-melted steel and mill-melted steel were evaluated using a 4-point bent beam and C-ring method, respectively. The conventional 0.2C-13Cr steel suffered SSC in 5% NaCl solution with 0.001MPa(0.15psi) H_2S, while the super 13Cr stainless steel melted in the laboratory and mill did not. When the H_2S was increased to 0.003MPa(0.45psi), only the laboratory-melted super 13Cr stainless steel suffered cracking in the notched 4-point bent beam specimen, under the condition of high Cl^- ion concentration. This fact indicates that SSC susceptibility was increased by the introduction of plastic deformation at the notched-bottom portion. The SCC susceptibility of mill-produced steel with a yield strengthof 95ksi was the same as that of the 80ksi grade. Therefore, the threshold value of H_2S partial pressure for SSC occurrence would be 0.001 to 0.003MPa(0.15 to 0.45psi) for the super 13Cr stainless steels. On the other hand, SSC did not occur even at 0.01MPa(1.5psi) H_2S when the Cl^- ion concentration was 100ppm or below. Namely, if Cl^- ion concentration is low, the H_2S threshold pressure for SSC occurrence is increased.

II.2 Corrosion Resistance at Elevated Temperatures

Effects of temperature on the resistance to general and localized corrosions and also cracking were investigated in 25% NaCl solution with 3.0MPa(450psi) CO_2. The super 13Cr stainless steel had high corrosion resistance at 150° C or belowand suffered pitting corrosion only at 200° C, as shown in **Figure 6**. On the other hand, the conventional 13Cr steel suffered pitting corrosion at 100° C, and general corrosion with corrosion rates above 1mm/y at temperatures of more than 150° C.

Next, a corrosion test was carried out in 5% NaCl solution with 3.0MPa(450psi) CO_2 containing 0.001MPa(0.15psi) H_2S. The results are given in **Figure 7**. The conventional 13Cr steel suffered cracking at 25° and 60° C, pitting corrosion at 120° C and general corrosion at 150° C or above. The corrosion rate in the CO_2 environment without H_2S was slightly higher than that with H_2S. This fact suggests that Cl^- ion accelerated corrosion, but on the contrary, H_2S depressed the corrosion. The super 13Cr stainless steel showed good corrosion resistance to localized corrosion and SSC up to 150° C, but it suffered pitting corrosion with corrosion rate of 0.3mm/y at 200° C in a similar manner as in the CO_2 environment. The super 13Cr stainless steel manufactured by the mill was tested using C-ring specimens in a similar environment. The steels with yield strength of 80, 95 and 110ksi grades showed the same resistance as that of the steel melted in the laboratory, except at 200° C. Namely, the mill-manufactured super 13Cr stainless steel which was pickled in HNO_3 + HF solution did not suffer pitting corrosion.

The results of the crevice corrosion test are shown in **Figure 8**. The crevice corrosion occurred at 100° C or above on the conventional 13Cr steel, and at 200° C on the super 13Cr stainless steel.

It is thought from these results that the addition of Mo element improves not only SSC resistance at ambient temperatures, but also localized corrosion and SSC resistance at elevated temperatures. Further, the temperature limitation of super 13Cr stainless steel would be 150° C in CO_2 environments both with and without 0.001MPa(0.15psi) H_2S considering corrosion rate and occurrence of localized corrosion.

Ⅱ.3   Long Term Corrosion Test in Simulated Environments
In order to apply the tubulars made from the super 13Cr stainless steel to the North Sea fields, long term corrosion tests were carried out in simulated environments, whose conditions were composed of high CO_2 partial pressure, low H_2S partial pressure and high Cl^- ion concentration. Tested tubulars are shown as follows. The conventional 13Cr steel and 22Cr duplex stainless steel were used as comparative materials.
    A.   Super 13Cr(95ksi), 2-7/8"(73.0mm)O.D. x 0.217"(5.51mm)W.T.
    B.   0.2C-13Cr(80ksi),   3-1/2"(88.9mm)O.D. x 0.254"(6.45mm)W.T.
    C.   22Cr(110ksi),   2-7/8"(73.0mm)O.D. x 0.276"(7.01mm)W.T.

The SSC test results are summarized in **Table 3**. In the case of the super 13Cr stainless steel, no SSC occurred on the specimens at ambient temperatures. On the other hand, the conventional 13Cr steel suffered SSC in environmental No.A-2, whose temperature was 25° C with 0.02atm(0.002MPa or 0.3psi) H_2S.

The corrosion rates of tested materials are shown in **Figure 9**. Regarding the super 13Cr stainless steel, the corrosion rate was less than 0.01mm/y and no localized corrosion occurred at elevated temperatures. The super 13Cr stainless steel has an intermediate corrosion resistance between conventional 13Cr steel and 22Cr duplex stainless steel. In this manner, the application

of the super 13Cr stainless steel tubuler of 95ksi grade for a certain field
in the North Sea was determined.

III. Fracture Toughness and Weldability of Super 13Cr Stainless Steel

As a further application of the super 13Cr stainless steel to line pipe, the
fracture toughness, weldability and the corrosion resistance of welded
portions were investigated.

III.1 Fracture Toughness

Charpy impact tests were carried out, and the results are shown in **Figure 10**.
The tubulars made from the super 13Cr stainless steel of 73mmO.D. x 14mmW.T.
with the yield strength of 95 and 110ksi grade were tested. The test specimens
were sampled longitudinally in the rolling direction. As shown in Figure 10.
The tubulars had a much better fracture toughness than conventional 13Cr
steel. The transition temperature of 95ksi grade tubular was approximately
-100° C(-150° F).

III.2 Weldability and Corrosion Resistance of Welded Portion

The weldability of the super 13Cr stainless steel and the corrosion resistance
of the welded portion in a CO_2 environment were investigated to clarify the
applicability of the steel to line pipe.

The tubulars of 2-7/8"(73.0mm)O.D. x 0.217"(5.51mm)W.T. were girth welded, and
the welding conditions are summarized in **Table 4**. The GTAW(gas tungsten arc
welding) process was applied in non-preheating conditions. The super 13Cr
stainless steel had enough toughness, although PWHT(post weld heat treatment
for a stress relief) was not applied.

The corrosion test results on the welded portion are shown in **Table 5**. By
using a welding material similar to super 13Cr stainless steel, the corrosion
rate was suppressed to a low level even under as-welded conditions.

Conclusions

The alloying design of the super 13Cr stainless steel was carried out for the
improvements of both the SSC resistance at ambient temperatures and localized
corrosion and SSC resistance at elevated temperatures in a CO_2 environment
containing a small amount of H_2S. Further, effects of environmental factors
on corrosion resistance of the super 13Cr stainless steel were investigated
compared with the conventional 13Cr steel. The results obtained are summarized
as follows:

1. A super 13Cr stainless steel(LowC-13Cr-5Ni-2Mo) has been developed at
SMI. It is a more corrosion resistant material than conventional 13Cr steel.

2. The super 13Cr stainless steel showed a higher SSC resistance at ambient temperatures than the conventional 13Cr steel, and the H_2S threshold pressure was 0.001 to 0.003MPa(0.15 to 0.45psi) in 5% NaCl solution with 3.0MPa(450psi) CO_2.

3. The H_2S threshold pressure changed depending on Cl^- ion concentration. For example, the super 13Cr stainless steel did not suffer SSC even at 0.01MPa (1.5psi) H_2S when Cl^- ion concentration was 100ppm or below.

4. The super 13Cr stainless steel had a higher resistance to general corrosion and localized corrosion at elevated temperatures compared to the conventional 13Cr steel, and the limitation of temperature was 150° C in CO_2 environments both with and without a small amount of H_2S.

5. The super 13Cr stainless steel showed a good fracture toughness and weldability, so it is considered that the steel could be applied to line pipe.

Acknowledgements

References

1. J. D. Combes, J. G. Kerr and L. J. Klein, "13Cr Tubulers Solve Corrosion Problems in The Tuscaloosa Trend," Petroleum Engineer International, March, 1983.

2. L. J. Klein, "H_2S Cracking Resistance of 420 Stainless Tubulers," Material Performance, October, p29, 1984.

3. A. Ikeda, M. Ueda and S. Mukai, "CO_2 Corrosion Behavior and Mechanism of Carbn Steel and Alloy Steel," CORROSION/83, Paper no.45 (Houston, TX: National Association of Corrosion Engineers,1983).

4. M. Ueda, T. Kushida, K. Kondo and T. Kudo, "Corrosion Resistance of 13Cr-5Ni-2Mo Martensitic Stainless Steel in CO_2 Environment Containing a Small Amount of H_2S," CORROSION/92, Paper no.55 (Houston, TX: National Association of Corrosion Engineers, 1992).

5. A. Tamaki, "A New 13Cr OCTG for High Temperature and High Chloride CO_2 Environment," CORROSION/89, Paper no.469 (Houston,TX: National Association of Corrosion Engineers, 1989).

6. S. Hashizume, T. Takaoka, Y. Minami, Y. Ishizawa and T. Yamada, "A New 15 Percent Cr Steel Developed for OCTG,"CORROSION/91, Paper no.28(Houston, TX: National Association of Corrosion Engineers, 1991).

7. A. Miyasaka and H. Ogawa, "Influence of Metallurgical Factors on Corrosion Behaviors of Modified 13Cr Martensitic Stainless Steels,"CORROSION /90, Paper no.67 (Houston, TX: National Association of Corrosion Engineers, 1990).

Table 1. Chemical composition of steels used for the investigation.

Material		Chemical composition (mass%)							
		C	Si	Mn	P	S	Ni	Cr	Mo
Super 13Cr	Lab. melted	0.02	0.13	0.44	0.016	0.001	4.96	12.89	2.0
	Mill melted	0.02	0.19	0.44	0.014	0.001	5.60	12.00	2.0
0.2C-13Cr(AISI420)		0.21	0.35	0.67	0.017	0.001	0.10	12.43	—
22Cr		0.02	0.49	1.61	0.022	0.001	5.20	22.25	2.8

Table 2. Mechanical properties of steels used for the investigation.

Material	Y.S.		T.S.		El	Hardness
	(MPa)	(ksi)	(MPa)	(ksi)	(%)	(HRC)
Super 13Cr (80ksi)	585	85	846	123	37	24.9
Super 13Cr (95ksi)	712* 702	103* 102	867* 861	126* 125	— 36	— 25.7
Super 13Cr (110ksi)	827	120	889	129	22	26.5
0.2C-13Cr (80ksi)	632* 620	92* 90	785* 799	114* 116	— 22	— 22.5
22Cr (110ksi)	792	115	868	126	19	29.0

* ; Lab. melted material

Table 3. Long term SSC test results in simulated enviroments

E-No.	Test Condition					SSC test results***		
	H₂S (atm)	CO₂ (atm)	Salt (%)	Temp. (°C)	Time (h)	Super13Cr (95ksi)	0.2C-13Cr (80ksi)	22Cr (110ksi)
A-1	0.02*	40*	10% NaCl	135	1440	No SSC	No SSC	No SSC
A-2	0.02*	40*	10% NaCl	25	1440	No SSC	SSC	No SSC
B-1	0.005*	62*	9% NaCl	125	1440	No SSC	No SSC	No SSC
B-2	0.005*	62*	9% NaCl	25	720	No SSC	No SSC	No SSC
C-1	—	30**	25% NaCl	150	1440	No SSC	No SSC	No SSC

* ; at test temperature
** ; at ambient temperature
*** ; 4-point bent beam method according to ASTM G3979

Table 4. Welding test condition
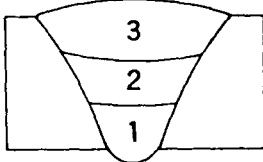
Chemical composition of welding materials (%)											
Welding material	C	Si	Mn	P	S	Ni	Cr	Mo	Ti	N	—
W1	0.02	0.19	0.44	0.019	0.001	5.46	11.91	2.05	0.29	0.0043	Ms
W2	0.03	0.61	0.57	0.021	0.005	1.00	11.90	—	—	—	Ms
W3	0.01	0.37	1.60	0.009	0.001	8.82	22.16	3.37	—	0.08	Duplex

Welding condition: GTAW process, Non-preheating

Pass No.	Welding current (A)	Welding voltage (V)	Welding speed (cm/min)	Welding sequence
1	110	13	10	
2	130	16	10	
3	130	16	10	

PWHT condition

PWHT \ Welding material	W1	W2	W3
As weld	○ : tested	○	○
640℃×30min, AC	○	—	—
720℃×20min, AC	—	○	—

Table 5. Corrosion test results on the welded portion

Welding condition			Corrosion rate (mm/y)		
Mother metal	Welding material	PWHT	4 point bent beam	Coupon-1	Coupon-2
Super 13Cr 73mmO.D. × 5.51mmW.T.	W1	Yes	0.041	0.067	—
	〃	No	0.030	0.050	—
	W2	Yes	0.046	0.137	—
	〃	No	0.030	0.073	—
	W3	Yes	0.028	0.040	—
	〃	No	0.029	0.077	0.029

Corrosion test condition ; 3.0MPa(450psi)CO_2, 5%NaCl, 150°C, 240h
Coupon-1 shows as welded specimen
Coupon-2 shows machined specimen
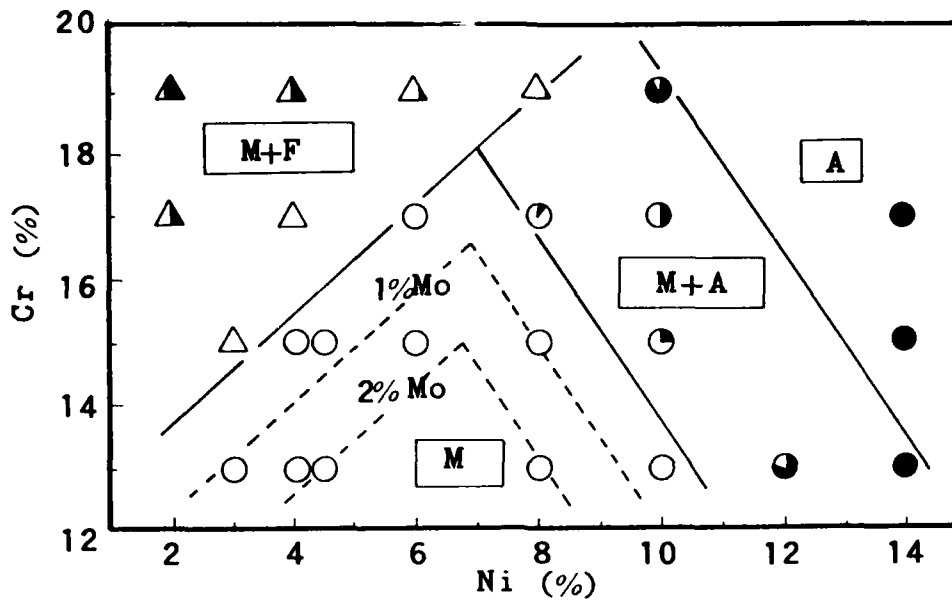
Figure 1. Effect of Mo content on martensitic, single-phase range.

(0%(△): Ferrite content in martensitic phase : 100%(▲))
(0%(◯): Austenite content in martensitic phase: 100%(●))
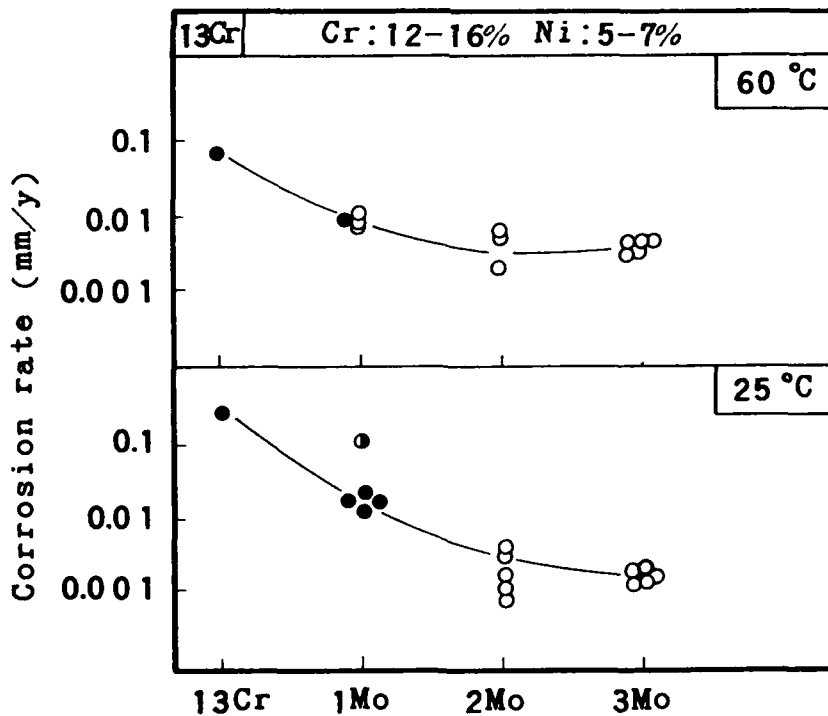
Figure 2. Effect of Mo content on corrosion rate and craking susceptibility.

(5%NaCl+3.0MPa (450psi) CO2+0.001MPa (0.15psi)H2S, 336h, 4-point)
(bent beam with notch, 1σy, 336h, ●:cracked , ◯:no cracked,)
(◐:pitting)
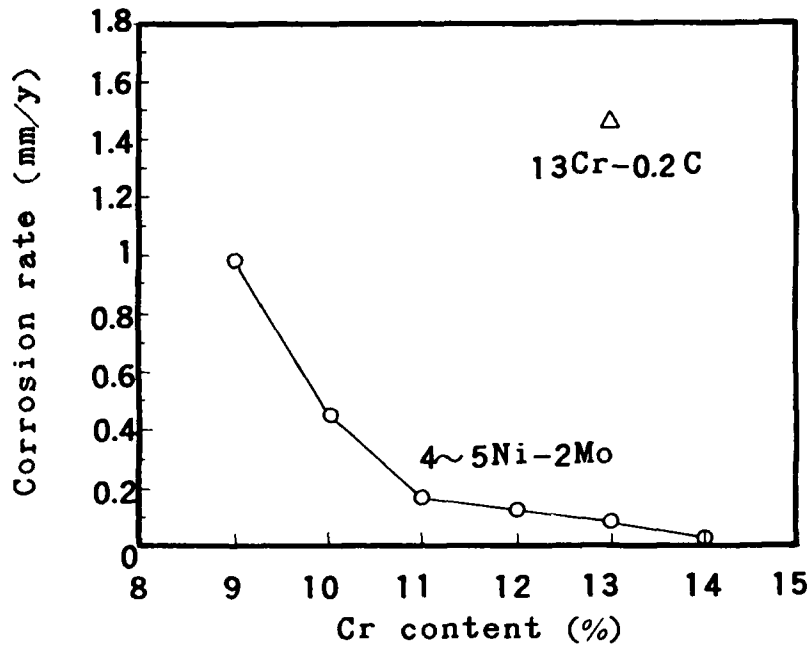
Figure 3. Effect of Cr content of materials with 4 to 5% Ni and 2%Mo on corrosion rate.

(3.0MPa(450psi) CO_2, 25%NaCl,150℃, 336h)
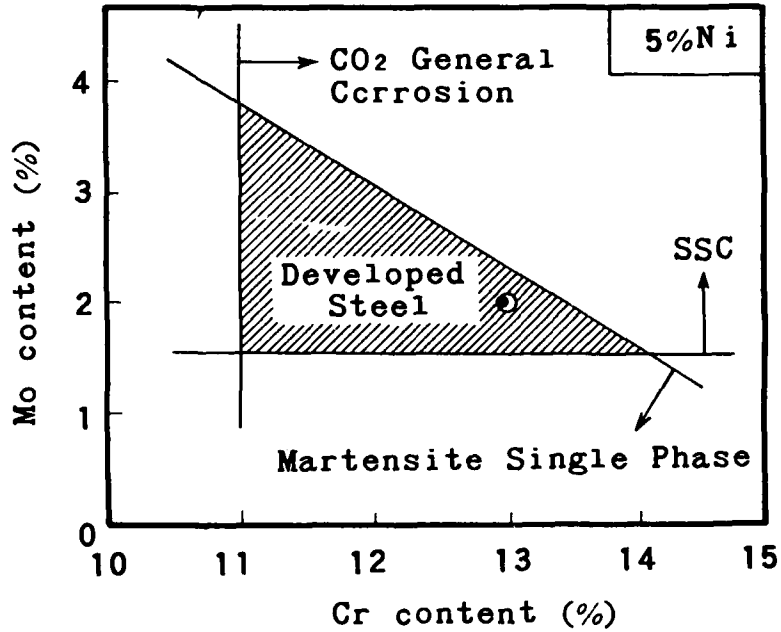
Figure 4. Recommendable Cr and Mo contents of the super 13Cr martensitic stainless steel for CO_2 environment containing a small amount of H_2S.
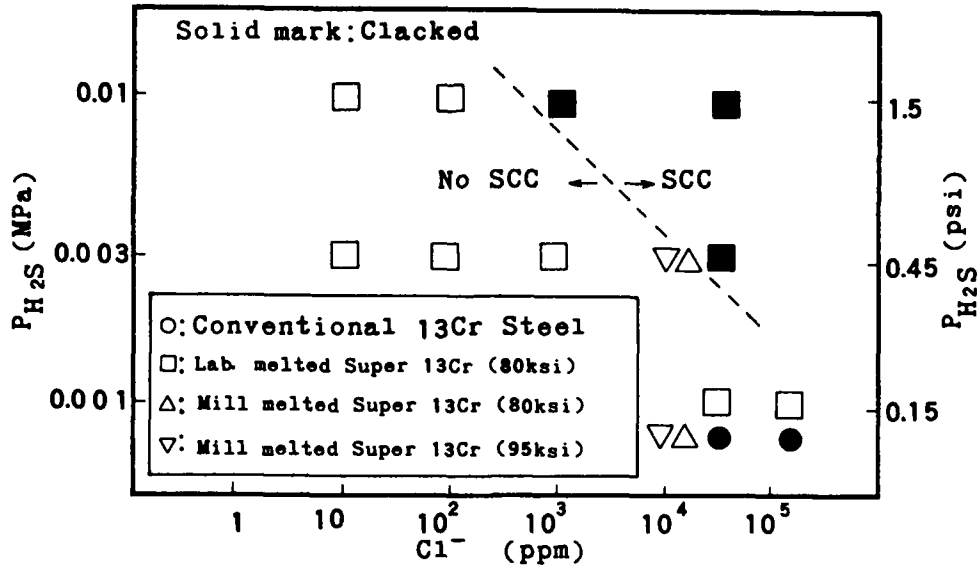
Figure 5. Effect of H₂S partial pressure and Cl⁻ ion
concentration on SSC susceptibility super
13Cr martensitic stainless steel

$$\left(\begin{array}{l} \text{3.0 MPa (450psi) CO}_2, \text{ 25}℃, \text{ 1}σ\text{y, 336h} \\ \text{Lab. melted material} \quad\quad ; \text{ 4-point bent beam with notch} \\ \text{Mill melted material (80, 95ksi); C-ring} \end{array}\right)$$
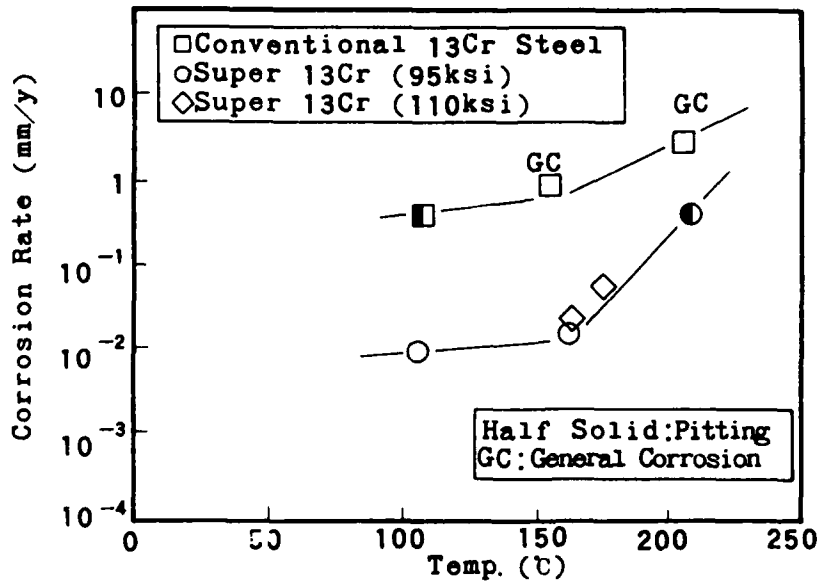
Figure 6. Effect of temperature on corrosion rate, localized
corrosion and SCC susceptibility of conventional 13Cr
and super 13Cr steels in CO2 environment.
(3.0MPa (450psi) CO2, 25%NaCl, 1σy, 336h, 4-point bent beam
with notch)
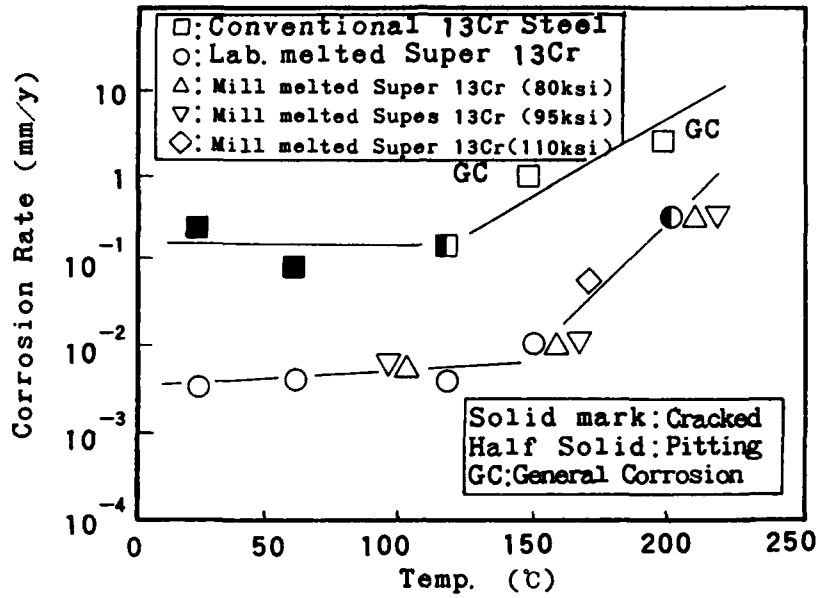
Figure 7. Effect of temperature on corrosion rate, localized
corrosion and SCC susceptibility of conventional 13Cr
and super 13Cr steels in CO2 environment with 0.001MPa
(0.15psi)H2S.

$\left(\begin{array}{l}\text{3.0MPa (450psi) CO2 + 0.001MPa(0.15psi) H2S, 5\%NaCl, } 1\sigma y, \text{ 336h}\\ \text{Lab. melted material} \qquad \text{; 4-point bent beam with notch}\\ \text{Mill melted material (80, 95ksi); C-ring}\end{array}\right)$
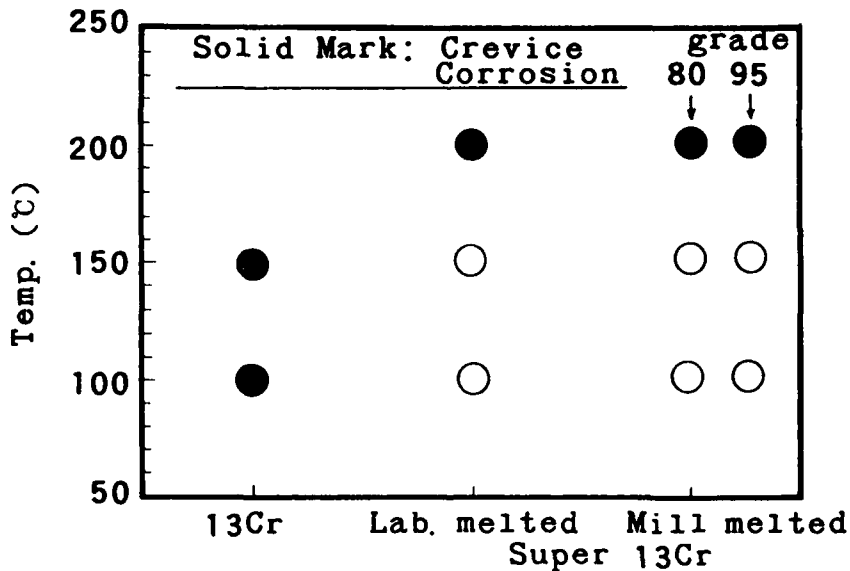
Figure 8. Comparison of crevice corrosion resistance among conventional
13Cr, lab. melted and mill-melted super 13Cr steels in CO2
environment with 0.001MPa (0.15psi) H2S.
(3.0MPa (450psi) CO2 + 0.001MPa (0.15psi) H2S, 5%NaCl, 336h)
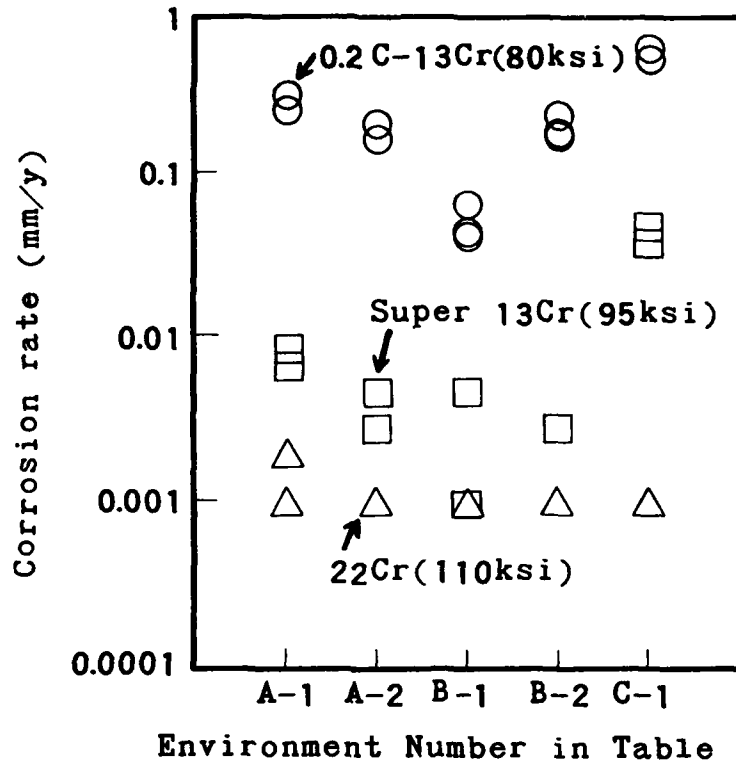
Figure 9. Long term corrosion test results in
simulated environments (Test conditions
are listed in Table 3).
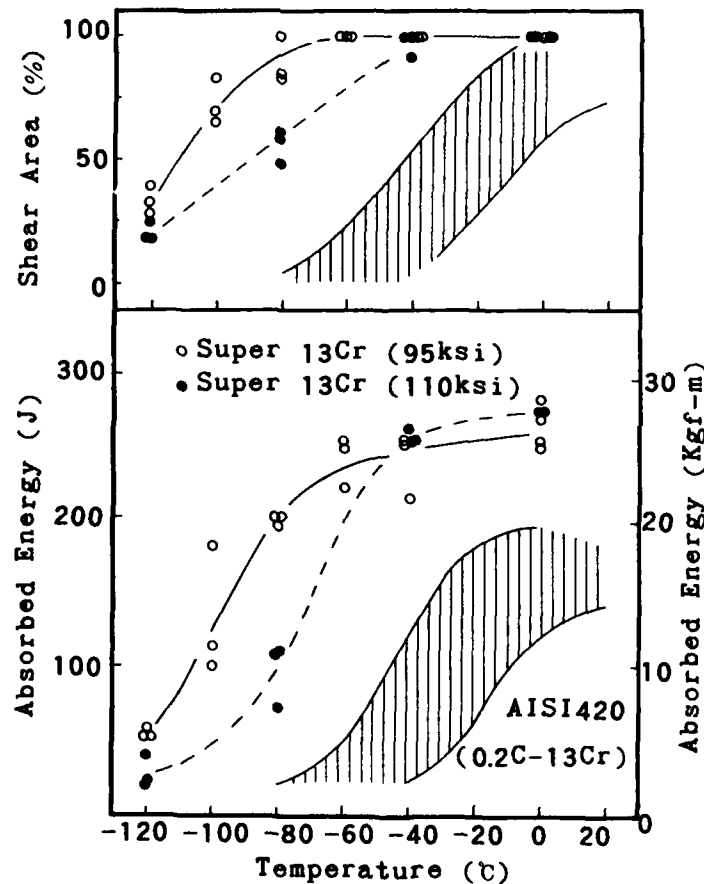
Figure 10. Charpy impact test results of
super 13Cr stainless steel.

Corrosion Resistance of 13 and 15% Cr Martensitic Stainless Steels in Oil and Gas Wells

SHUJI HASHIZUME
NKK CORPORATION
MATERIALS and PROCESSING RESEARCH CENTER
1-1, MINAMIWATARIDA, KAWASAKI-KU, KAWASAKI, 210, JAPAN

YUSUKE MINAMI
NKK CORPORATION
MATERIALS and PROCESSING RESEARCH CENTER
1-1, MINAMIWATARIDA, KAWASAKI-KU, KAWASAKI, 210, JAPAN

YOSHIICHI ISHIZAWA
NKK CORPORATION
MATERIALS and PROCESSING RESEARCH CENTER
1-1, MINAMIWATARIDA, KAWASAKI-KU, KAWASAKI, 210, JAPAN

ABSTRACT

From the view points of CO_2 corrosion resistance, phase stability and cost performance, 15% Cr martensitic stainless steel (15%Cr-0.5%Mo-1.5%Ni-0.12%C-0.07%N, UNS No. is S42500) has been developed as a partial substitute for duplex stainless steels. Eighty ksi grade 15% Cr stainless steel manufactured shows excellent corrosion resistance in conditions of several percent NaCl solution at temperatures below 200°C. This steel shows higher CO_2 corrosion resistance, a little higher pitting corrosion resistance compared to Type 420 (13%Cr-0.2%C, UNS No. is S42000). From the Auger analysis of 15% Cr stainless steel immersed in conditions simulating CO_2 gas well environments, Cr-oxide or -hydroxide was assumed to be formed near the surface even if at 180°C. Increasing Cr content from 13 to 15% leads to producing the stable Cr-oxide or -hydroxide in such a severe condition. Improving CO_2 corrosion resistance of 15% Cr stainless steel results from the existence of the stable Cr-oxide or -hydroxide.

Key terms: 15% Cr stainless steel, Type 420, Oil country tubular goods, Toughness, CO_2 corrosion resistance, Pitting corrosion resistance, 80 ksi grade, Auger analysis

INTRODUCTION

Corrosion Resistant Alloys have been widely used in oil and gas wells recently. In a lot of cases, martensitic stainless steels have been selected for CO_2 gas wells from the economical view point. Typical martensitic stainless steel, Type 420 shows good resistance to CO_2 corrosion at elevated temperatures up to 150°C, to pitting corrosion in several percent NaCl solution and to sulfide stress corrosion cracking when partial pressure of H_2S is lower than 0.1 atm.. In the conditions in which Type 420 does not show good resistance to corrosion, austenitic/ferritic duplex stainless steel has been recommended. However, duplex stainless steel is twice or three times expensive compared to Type 420. For solving the upper problem, much attention has been paid to modified martensitic stainless steels[1-6]. Modified martensitic stainless steels show better resistance to corrosion than Type 420 and are cheaper than duplex stainless steel.

From the view points of CO_2 corrosion resistance, phase stability and cost performance, 15% Cr martensitic stainless steel has been developed as a partial substitute for duplex stainless steels[6]. In this study, 13 and 15% Cr martensitic stainless steels in oil and gas wells are discussed from the view points of mechanical properties and resistance to CO_2 corrosion, pitting corrosion. The mechanism of preventing CO_2 corrosion by using high Cr stainless steel is also discussed.

EXPERIMENTAL PROCEDURE

Materials

Mill product seamless tubing of Type 420 and 15% Cr stainless steel were used. Both steels were quenched and tempered to the strength level of 80 ksi grade. Chemical compositions of Type 420 and 15% Cr stainless steel tested are listed in Table 1.

For clarifying the mechanism of preventing CO_2 corrosion by using high Cr stainless steel, laboratory melt steels were used. The range of chemical compositions of materials used were listed in Table 2. These steels were quenched and tempered.

Experimental methods

The following mechanical properties were measured:
1. Longitudinally-oriented tensile strength at R.T.
2. Rockwell hardness C scale
3. Longitudinally-oriented, half size Charpy impact energy and shear area from -120°C to 20°C

The following corrosion tests were conducted:
1. Immersion tests in autoclaves were carried out in 3 - 20% NaCl solutions with P_{H2S} = 0 - 0.05 atm. and P_{CO2} = 30 atm. at 60 - 200°C for 336 - 2160 hours.
2. Measurements of pitting potential in autoclaves were conducted in 5% NaCl solution with P_{H2S} = 0.025 atm. and P_{CO2} = 10 atm. at 130°C. Ag/AgCl inner reference electrode was used. Polarization started at corrosion potential and potential was swept with 20 mV/min. to the noble direction.

The following measurements were conducted for clarifying the mechanism of preventing CO_2 corrosion by using high Cr stainless steel:
1. Polarization behavior for laboratory melt steels were measured in 3.5% NaCl solution with 1 atm. CO_2 at 60°C. Polarization started at -1000 mV vs. S.C.E. and potential was swept with 20 mV/min. to the noble direction. Peak current density of active state and cathodic current density at -800 mV vs. S.C.E. were measured.
2. Auger electron spectroscopy technique was applied to surface analysis of immersed test specimens. Test specimens of 15% Cr steel were immersed in 3% NaCl solution with P_{CO2} = 25 atm. at 180 and 150 °C for 100 hours.

TEST RESULTS AND DISCUSSION

Mechanical properties

Mechanical properties of Type 420 and 15% Cr stainless steel manufactured are listed in Table 3. The results of Charpy impact tests of Type 420 and 15% Cr stainless steel with half size specimens are shown in Figure 1. The energy transition temperature (vTre) of Type 420 and 15% Cr stainless steel are -25 and -80°C, respectively. Fifteen percent Cr stainless steel shows better toughness than Type 420. Reducing C is effective for improving toughness.

Corrosion resistance

Immersion test. Immersion test results of Type 420 and 15% Cr stainless steel in 3% NaCl solutions at 100 - 200°C are shown in Figure 2. The corrosion rate of 15% Cr stainless steel and Type 420 increases with increasing temperature. The corrosion rate of 15% Cr stainless steel is less than Type 420.

The effect of test duration on corrosion rate of Type 420 and 15% Cr stainless steel is shown in Figure 3. After 3 months immersion, corrosion depth of 15% Cr stainless steel is around 0.0035 mm, while that of Type 420 is over 0.06 mm. No pitting corrosion of 15% Cr stainless steel was observed after 3 months immersion in 10% NaCl solution with P_{CO2} = 30 atm. at 100°C.

Immersion test results of 15% Cr stainless steel in 3 - 20% NaCl solutions with $P_{H2S} \leq 0.05$atm. and P_{CO2} = 30atm. at 60 - 200°C for 336 hours are summarized in Figure 4. Severe general corrosion of which the corrosion rate was more than 0.3g/m²/hr (0.33 mm/year) was observed in 10 and 20% NaCl solutions at 200°C. Pitting corrosion was observed in 20% NaCl solutions at 80 - 120°C. In these conditions, the corrosion rate was very low and a little corrosion product was observed on the surface of the specimens after test. In 20% NaCl solutions at 150 - 180°C, the corrosion rate was greater than that at 80-120°C, and black- colored corrosion product covered all of the surface. However, pitting corrosion was not observed under the corrosion product after removing it. The corrosion resistance of 15% Cr stainless steel seems to depend on whether the corrosion product behaves as protective or not. At 60°C, 15% Cr stainless steel shows excellent passivation remaining its shiny, original surface. From these observations, 15% Cr stainless steel may show less localized corrosion resistance in the active-passive transitional region when Cl⁻ concentration is high. No severe general corrosion and no pitting corrosion was observed in 10% NaCl solutions at less than 180°C and in 3% NaCl solutions at less than 200°C.

Material selection chart based on the immersion test results of Type 420 and 15% Cr stainless steel in 3 - 20% NaCl solutions with $P_{H2S} \leq 0.05$atm. and P_{CO2} = 30atm. at 60 -200°C for 336 hours is shown in Figure 5. Conditions where 15% Cr stainless steel shows no pitting corrosion and no severe general corrosion (less than 0.3 g/m²/hr) are shown as a upper hatched region in Figure 5. The use of 15% Cr stainless steel is permissible in several percent NaCl solutions up to

200°C. The limit of use for Type 420 is also shown in Figure 5 as a lower hatched region. Fifteen percent Cr stainless steel is useable in solutions with higher concentrations of NaCl at higher temperatures than Type 420.

Measurement of pitting potential. Polarization curves of Type 420 and 15% Cr stainless steel in 5% NaCl solution with P_{H2S} = 0.025 atm. and P_{CO2} = 10 atm. at 130°C are shown in Figure 6. The pitting potentials at which material indicates 100 micro A/cm^2 caused by pitting corrosion of Type 420 and 15% Cr stainless steel are -420 and - 280 mV vs. Ag/AgCl, respectively. The pitting potential of 15% Cr stainless steel is 140 mV nobler than that of Type 420. Passive region is clearly observed in curve of 15% Cr stainless steel and peak current density at active region of 15% Cr stainless steel is smaller than that of Type 420. These results suggest that 15% Cr stainless steel shows better resistance to CO_2 general corrosion and pitting corrosion than Type 420.

Mechanism of preventing CO_2 corrosion by using high Cr stainless steel. Corrosion rate of martensitic stainless steel in CO_2 environments depends on the following equation[6]:

GCI = Cr-12C+0.75Ni+10N (%, GCI, General Corrosion Index)   (1)

Corrosion rate decreases with increasing GCI value. Increasing Cr, Ni and N is effective to decreasing corrosion rate. Decreasing C is also effective to decreasing corrosion rate. When martensitic stainless steel is tempered to obtain the strength level of 80 to 110 ksi, $M_{23}C_6$ precipitates. Cr content in $M_{23}C_6$ is large. When $M_{23}C_6$ precipitates, Cr content in matrix reduces. Therefore, Increasing Cr content is equal to reducing C content.

To clarify the effect of GCI value on anodic and cathodic reaction of corrosion process, polarization behavior of laboratory melt steels of which GCI value varies from 13 to 17% was measured in CO_2 environment. Effect of GCI value on peak current density of active state ($i_{cri.}$) and cathodic current density at -800 mV vs. S.C.E. (i_{-800}) measured are shown in Figure 7. Peak current density of active state decreases with increasing GCI value. Cathodic current density at -800 mV vs. S.C.E. is independent on GCI value. These results suggest that increasing GCI value is effective to restricting anodic reaction of

corrosion process.

Surface analysis of immersed 15% Cr stainless steel by using Auger electron spectroscopy technique was conducted to examine the corrosion film formed in CO_2 environment at high temperature. The concentration profiles of some elements from the surface to matrix are shown in Figure 8. Cr enrichment is observed at the outer surface of corrosion film formed at temperatures both 150 and 180°C. Cr-oxide or -hydroxide (Fe free) is considered to be formed at the outer corrosion film. At the inner corrosion film, Fe and Cr are observed. Cr and Fe-oxide or -hydroxide is considered to be formed. Cr content in corrosion film is larger than that in matrix. Corrosion film formed at 180°C is thicker than that formed at 150°C. This corrosion film is different from air formed Cr-oxide. Therefore, this corrosion film does not behave as a perfect passive film just like air formed Cr-oxide. However, judging from the fact that corrosion rate decreases with increasing Cr content, Cr enrichment at the outer corrosion film will work effectively to reduce corrosion rate in CO_2 environment. High Cr content in matrix leads to formation of stable Cr-oxide or -hydroxide.

Mo enrichment is observed at the most outer surface. It is considered that MoO_4^{2-} is formed at the interface of solution and Cr-oxide or -hydroxide. Mo is considered to be effective to preventing localized corrosion[6]. Ni is not observed at anywhere. Ni content is too small to detect by using Auger electron spectroscopy technique.

The followings regarding to 15% Cr stainless steel immersed in CO_2 environment are expected by immersion test results and surface analysis by Auger electron spectroscopy technique:
1. When temperature is less than 60°C, air formed Cr-oxide film at surface behaves as a perfect passive film. No general corrosion and no pitting corrosion is observed.
2. When temperature is 80 to 120°C, Cr-oxide or -hydroxide film will be formed at the outer surface. Under it, thin Cr and Fe-oxide or - hydroxide will be formed. Corrosion film does not show passivity perfectly. Therefore, 15% Cr stainless steel shows less localized corrosion resistance in the active-passive transition region when Cl- concentration is high. No general corrosion is observed.
3. When temperature is 150 to 200°C, Cr-oxide or -hydroxide film is formed at outer surface. Under it, thick Cr and Fe-oxide or -hydroxide is formed. Fifteen percent Cr stainless steel shows active state. However, corrosion rate is kept low by the formation of Cr-oxide or - hydroxide. No severe general corrosion and no pitting corrosion is

observed.

CONCLUSIONS

Thirteen and 15% Cr martensitic stainless steels in oil and gas wells are discussed from the view points of mechanical properties and resistance to CO_2 corrosion, pitting corrosion. The mechanism of preventing CO_2 corrosion by using high Cr stainless steel is also discussed. The following conclusions are drawn:

1. Fifteen percent Cr stainless steel has better toughness than Type 420.

2. Fifteen percent Cr stainless steel shows higher CO_2 corrosion resistance, a little higher pitting corrosion resistance compared to Type 420.

3. Fifteen percent Cr steel shows superior resistance to CO_2 general corrosion up to 200°C in several percent NaCl solutions.

4. From the Auger analysis of 15% Cr stainless steel immersed in conditions simulating CO_2 gas well environments, Cr-oxide or -hydroxide was assumed to be formed near the surface even if at 180°C. Increasing Cr content leads to forming the stable Cr-oxide or -hydroxide in such a severe condition. Improving CO_2 corrosion resistance results from the existence of the stable Cr-oxide or -hydroxide.

ACKNOWLEDGMENTS

REFERENCES

1. K. Tamaki, CORROSION/89, Paper No.469 (1989) New Orleans, LA.
2. L. J. Klein, R. M. Thompson and D. E. Moore, CORROSION/90, Paper No.52 (1990) Las Vegas, Nevada
3. W. C. Chen, CORROSION/90, Paper No.61 (1990) Las Vegas, Nevada

4. A. Miyasaka and H. Ogawa, CORROSION/90, Paper No.67 (1990) Las Vegas, Nevada

5. W. J. Sisak and R. D. Cadwell, CORROSION/91, Paper No.12 (1991) Cincinnati, Ohio

6. S. Hashizume, T. Takaoka, Y. Minami, Y. Ishizawa and T. Yamada, CORROSION/91, Paper No.28 (1991) Cincinnati, Ohio

Table 1 Chemical compositions of Type 420 and 15% Cr stainless steel used (%)

Steel	UNS No.	C	Si	Mn	Cr	Mo	Ni	N
Type420	S42000	0.20	0.28	0.49	13.1	tr.	0.12	0.009
15% Cr stainless steel	S42500	0.12	0.26	0.70	14.7	0.5	1.5	0.08

Table 2 Range of chemical compositions of laboratory melt steels used (%)

C	Si	Mn	Cr	Mo	Ni	N
0.05 - 0.22	0.22	0.79	14.0 - 15.1	0.52	1.0 - 2.0	0.08 - 0.09

Table 3 Mechanical properties of Type 420 and 15% Cr stainless steel used

Steel	Yield strength,ksi	Tensile strength, ksi	Hardness, HRC	vE-40C, J (Half size)	vTre, degree C
Type420	88	110	20	24	-25
15% Cr stainless steel	85	114	20	75	-80
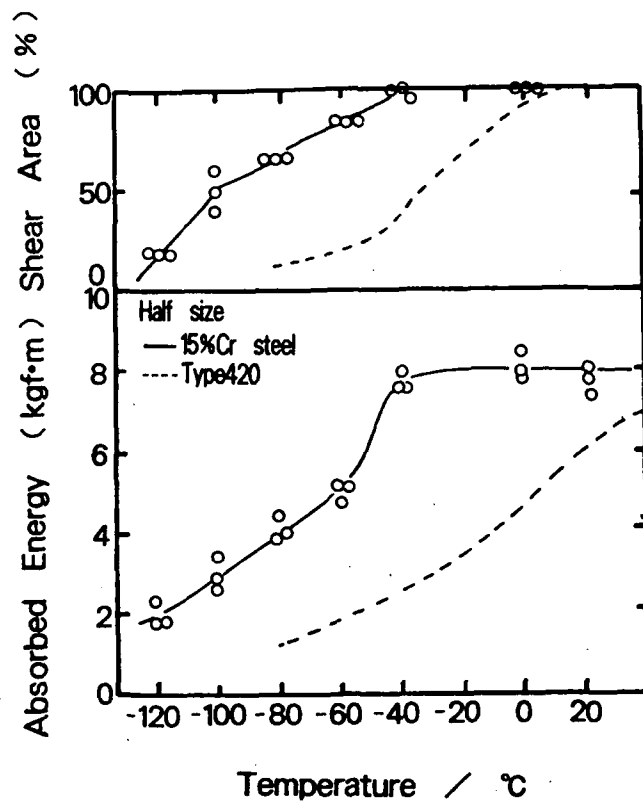
Figure 1   The results of Charpy impact tests of Type 420 and 15% Cr
stainless steel with half size specimens

△ Type420
O 15%Cr steel

3% $NaCl, P_{H_2}S = 0.05atm, P_{CO_2} = 29.95atm, 336hrs$
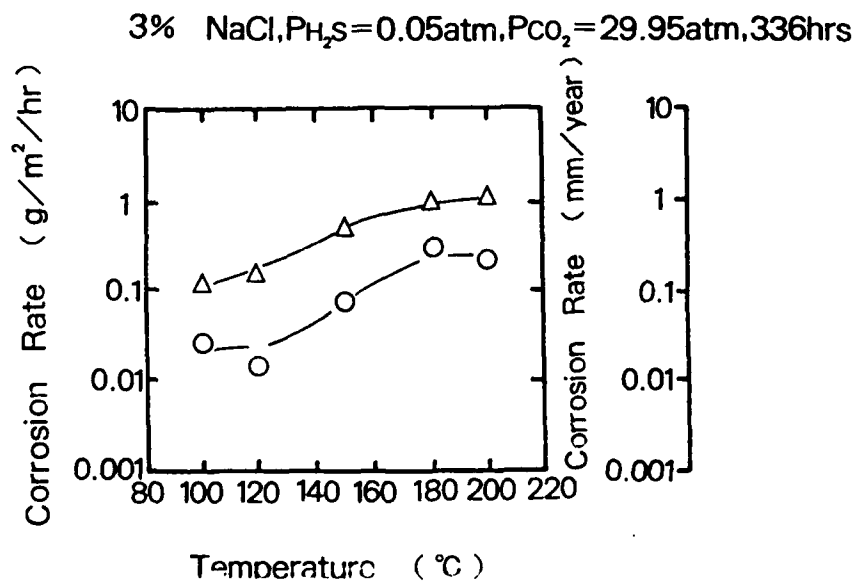
Figure 2   Effect of temperature on corrosion rate of Type 420 and 15%
Cr stainless steel

100°C, 10%NaCl, Pco₂=30atm.
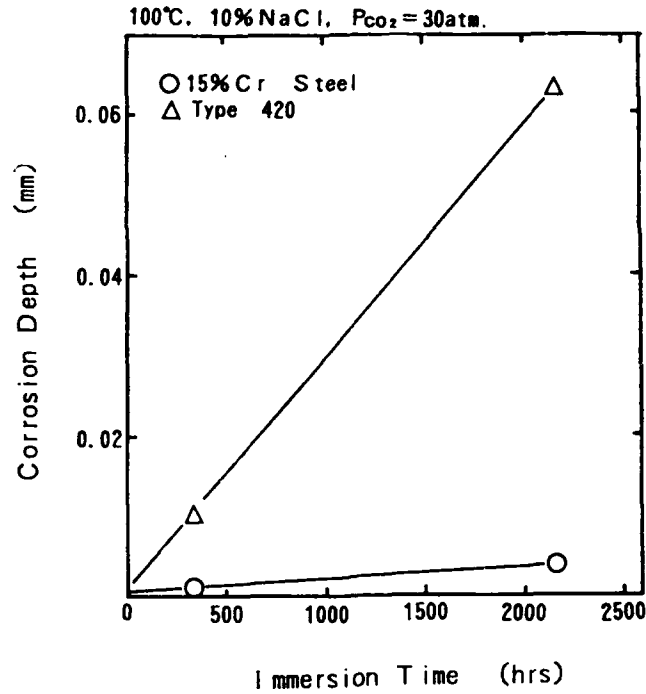
Figure 3 Effect of test duration on corrosion rate of Type 420 and 15% Cr stainless steel

Pco₂≒30atm, Pₕ₂ₛ≦0.05atm, 336hrs

Solid : Severe general corrosion
Half solid : Pitting corrosion
Open : No severe general corrosion and no pitting corrosion
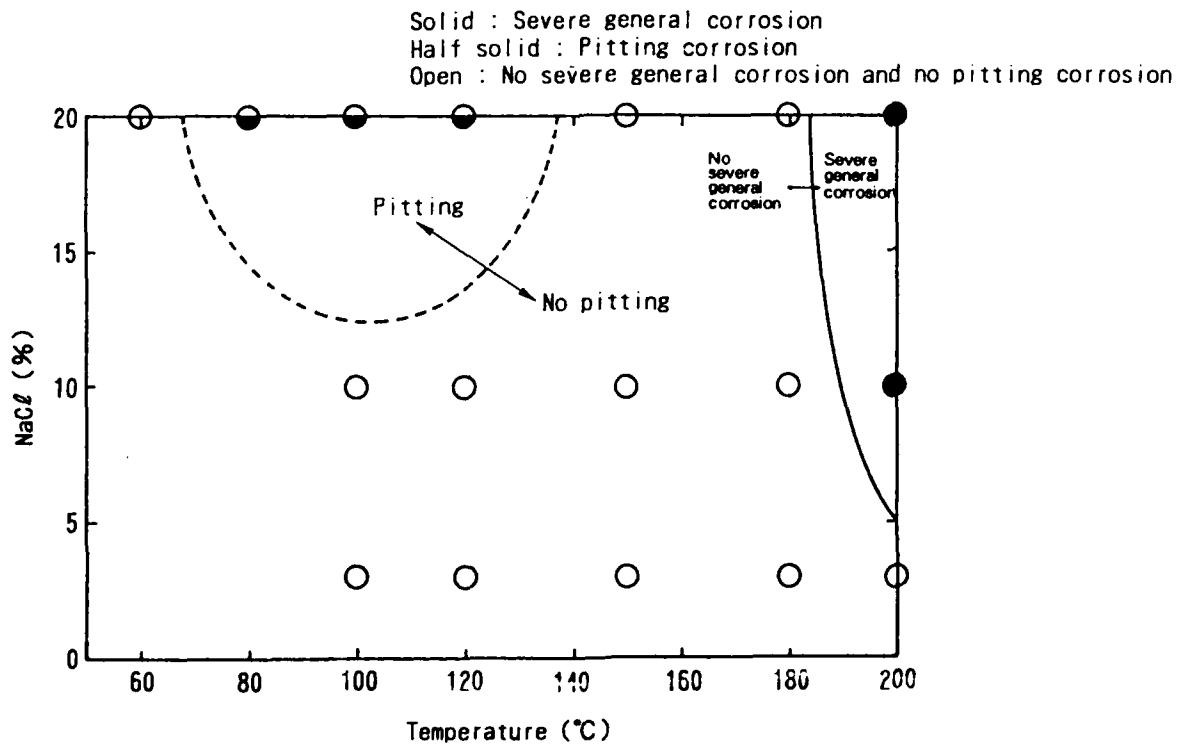
Figure 4 Immersion test results of 15% Cr stainless steel

2448
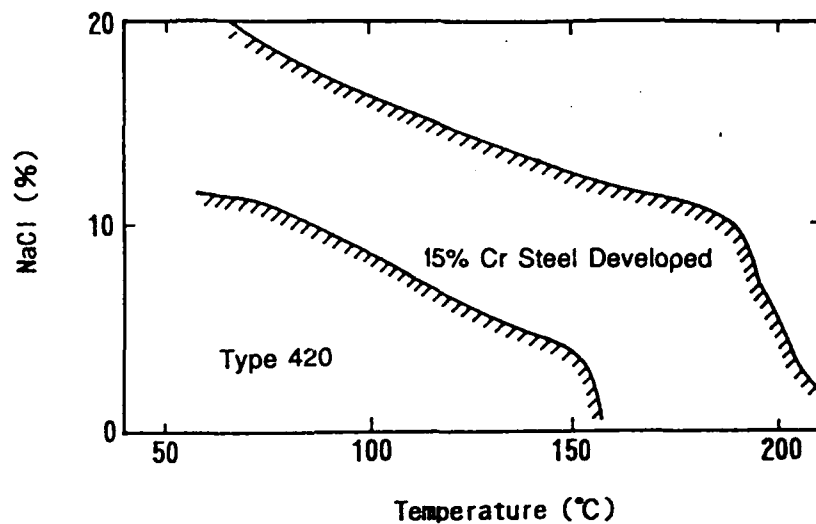
Figure 5   Material selection chart based on the immersion test results
of Type 420 and 15% Cr stainless steel
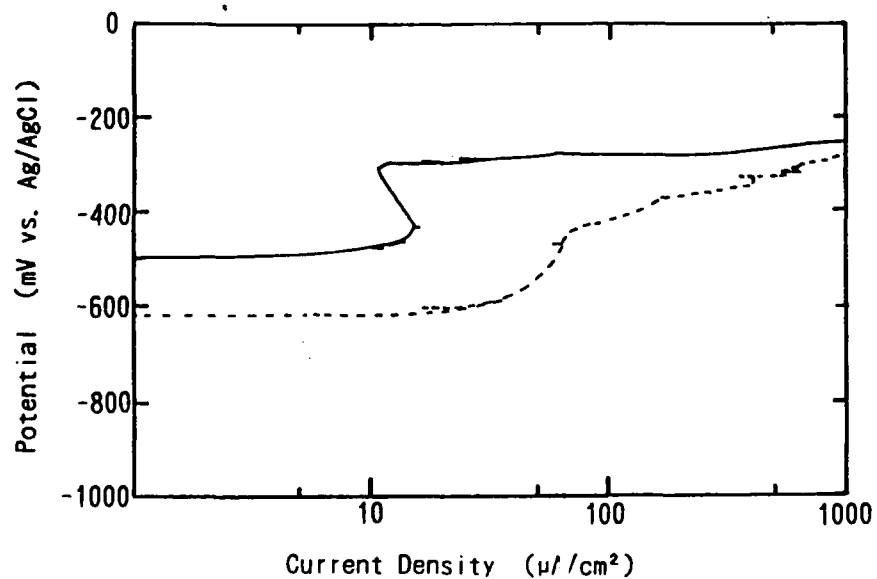
Figure 6   Polarization curves of Type 420 (Dotted line) and 15% Cr
stainless steel (Solid line) measured in 5% NaCl solution with P_{H2S} =
0.025 atm. and P_{CO2} = 10 atm. at 130°C
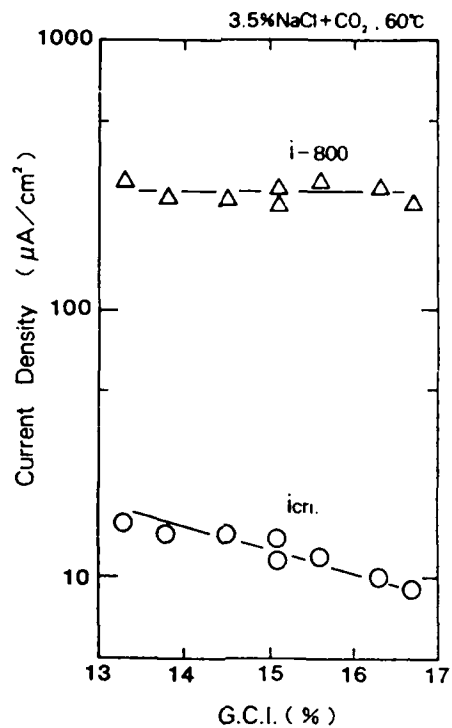
Figure 7　Effect of GCl value on peak current density of active state ($i_{cri.}$) and cathodic current density at -800 mV vs. S.C.E. (i_{-800}) measured
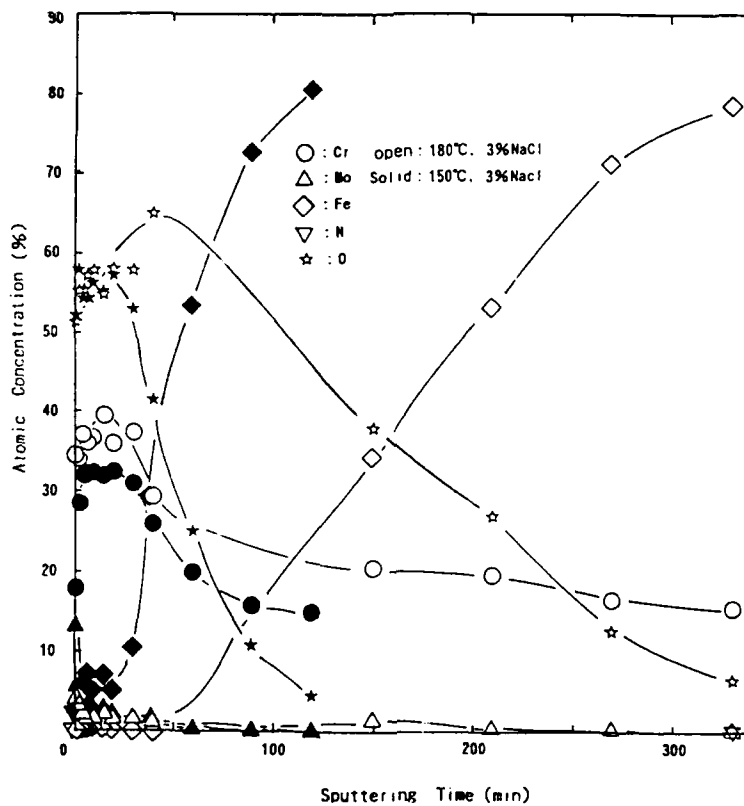
Figure 8　Surface analysis of immersed 15% Cr stainless steel by using Auger electron spectroscopy technique

Development of Safe Use Limits for Martensitic and Duplex Stainless Steels

Dr. Russell D. Kane
Cortest Laboratories, Inc.
P.O. Box 691505
Houston, Texas 77269

Sridhar Srinivasan
Cortest Laboratories, Inc.
P.O. Box 691505
Houston, Texas 77269

Abstract

Selection of martensitic stainless steels (9Cr-1Mo, 13Cr) and duplex stainless steels (22Cr, 25Cr) for sour production service requires an understanding of the effects of different environmental components on these alloys. The individual as well as synergistic effects of pH, H_2S and chlorides in the selection of martensitic and duplex stainless steels have been examined to identify safe use limits for these materials from a stand point of general corrosion and SSC/SCC. A method to assess resistance to pitting has been developed using an environmental severity index and maximum operating temperature.

Keywords: selection, Duplex, Martensitic, stainless steels, expert systems, stress corrosion cracking, pitting indices

Introduction

In recent years, the use of Corrosion Resistant Alloys (CRA) for mitigation of corrosion in oil and gas production systems has increased dramatically. However, appropriate selection of these alloys for oil and gas field service has remained a difficult task which needs significant knowledge of materials behavior and experience[1]. This is particularly true for martensitic and duplex stainless steels which exhibit complex corrosion and stress corrosion cracking behavior in systems containing H_2S and chlorides.

In order to select martensitic and duplex stainless materials for a given oilfield application involving exposure to H_2S, CO_2, water and chlorides, it is necessary to understand the role of various factors that affect the corrosion performance of these materials. These factors include environmental, chemical, mechanical and metallurgical attributes. In characterizing the role of these attributes on material selection, it is required to evaluate the effect of the individual parameters on material choices as well as the effect of the attribute interactions.

General corrosion, pitting, sulfide stress cracking and anodic stress corrosion cracking are of particular concern when selecting CRA materials[2]. Further, for many CRAs, there is relatively limited documented field experience to define their limits of use. Selection of CRAs often

involves decision-making based on seemingly contradictory laboratory data. Also, selection involves understanding and characterizing the effects of the following variables in terms of mechanical, corrosion and cracking considerations, such as[3]:

- Mechanical requirements such as strength, heat treatment and hardness criteria
- Environmental parameters such as
    H_2S partial pressure
    CO_2 partial pressure
    Minimum and maximum operating temperatures
    Bicarbonates
    Hydrogen ion concentration (pH)
    Sulfur
    Gas to Oil ratio
    Water to Gas ratio
- Metallurgical composition

The purpose of this paper is to discuss the development of guidelines for selection of martensitic and duplex stainless steels based on safe use limit concepts. These guidelines have been implemented along with other important factors as an expert system to assist the materials/corrosion engineer in the complex process of selection of CRA materials for oil and gas service. Specifically, an expert system entitled "Selection of CRAs Through Environment Specifications" (SOCRATES™)* is described, along with a discussion of the technical approach, methodologies and data incorporated into the software[4]. Particular focus is directed towards rules developed for the use of martensitic 13 Cr and duplex 22 Cr and 25Cr stainless steels in relation to sulfide stress cracking, stress corrosion cracking and localized corrosion.

Expert Systems, Rules and Knowledge Representation

Expert systems are defined as intelligent computer programs using expert knowledge to attain high levels of performance in narrow problem domains[5]. The term *expert* in the expert system implies the narrow specialization and competence of a human expert which has been embodied into the system. Expert systems have a specific structure that distinguishes them from conventional computer programs. Structural components in an expert system are shown in Figure 1. The knowledge base and the inference engine form the heart of the expert system. The knowledge base houses the expertise that is embodied in an expert system. The inference engine controls the manner or the logical path used by the expert system to utilize the information (facts and rules) in the knowledge base to make decisions.

Knowledge or expertise in a particular area (termed as domain-expertise) is stored in the knowledge base in terms of facts and rules. *Knowledge representation* in the expert system refers to the scheme used to represent a given piece of information in an expert system. Decision making in an expert system can be represented through interconnected rules. The rules are used

in a specific sequence in order to reach decisions. The structure of the SOCRATES system and the role of rules is briefly described in the Sections 3 and 4.

Domain Knowledge: Corrosion and Cracking in CRAs

The organization of different frames in the SOCRATES system is shown in Figure 2. The system performs material selection by applying constraints at different hierarchical levels. The constraints are organized such that a comprehensive initial solution set of applicable materials is refined and reduced in size as the system proceeds through the different levels.

At level 1, the initial set of applicable materials is obtained by determining the application for which the CRA is to be selected. If the application is not known, all classes of materials known to the system become part of the solution set. These include the following classes of materials:

- Stainless Steels: Conventional austenitic, high alloy austenitic, martensitic, precipitation hardened, duplex and ferritic.
- Precipitation hardened and solid solution nickel base alloys, nickel copper alloys.
- Cobalt-base, titanium and zirconium alloys.

The constraints at this level include yield strength, material condition (heat treatment/cold work) and hardness limitations. At this level, the constraints operate independently and hence are applied sequentially. For example, a material in a required yield strength (SMYS) range (say, 110-130 ksi; 760-900 MPa) can also be cold worked. Here, materials available in the required yield strength range are selected prior to applying the material condition (cold worked) requirement.

At level 2, the environment is characterized in terms of severity for general corrosion using the following environmental parameters:

- H_2S and CO_2 partial pressure
- Bicarbonates
- pH
- Minimum operating temperature
- Chlorides and Sulfur
- Water to gas ratio and gas to oil ratio

The parameters used in the material evaluation here operate concurrently. When materials are evaluated at this level, the system considers both the effect of the individual parameter as well as the effect of the cumulative interactions. An environmental severity index, based on the environmental parameters, is computed to represent the synergistic effect of the different parameters operating in cor ~rrence. This environmental severity index is in turn used to select the set of applicable materials.

At level 3, materials are evaluated for their susceptibility to stress corrosion cracking. Factors in evaluation here include,

- H_2S partial pressure
- pH
- Chlorides
- Maximum operating temperature
- Material composition in terms of nickel, chromium, molybdenum, tungsten and columbium

At level 4, the materials are evaluated for their susceptibility to pitting corrosion. A Required Minimum Pitting Index (RMPI) is computed based on maximum temperature, and environmental severity determined at level 2. Further, a pitting index is computed for each of the materials in the solution set using the relation[6],

$$Pitting\ Index = Cr + 3.3Mo + 11N + 1.5(W + Cb)$$

Where Cr, Mo, N, W and Cb represent Chromiu n, Molybdenum, Nitrogen, Tungsten and Columbium content of the alloy. All alloys that have a pitting index greater than or equal to the RMPI are selected for further evaluation.

At level 5, all applicable materials from level 4 are evaluated for qualification based on sulfide stress cracking requirements as well as certain rules of thumb based on application requirements.

Selection of martensitic and Duplex Stainless Steels

As shown in Figure 3, as the acid gas partial pressure in the production environment increases, the pH generally decreases[7]. Typically, stainless alloys are expected to have reduced corrosion performance with lower pH. The "lean" alloys such as martensitic 13Cr and 22-25Cr duplex stainless steels generally degrade more severely at pH values less than 4.0. However, it has also been observed that there are absolute effects of H_2S partial pressure and chloride concentration. Therefore, the system corrosivity can be estimated based on,

- parameters which control pH in the aqueous phase (H_2S and CO_2 partial pressure, bicarbonate concentration and temperature)
- H_2S partial pressure
- chloride concentration (See Table 1).

In the expert system for selection of CRAs, the empirical relationships shown in Figure 3 and Table 1 are utilized to develop a "window" of conditions where martensitic and duplex stainless steels can be used based initially only on their corrosion resistance (*and not their cracking behavior*). The sulfide stress cracking, stress corrosion cracking and localized corrosion behaviors of these materials are dealt with separately in subsequent modules in the system. This "window" of conditions is based on available weight loss corrosion data and applying limitations on acceptable values (typically 2 mpy maximum) [8,9].

SSC and SCC Considerations for 13Cr

13Cr is typical of martensitic stainless steels in it being susceptible to sulfide stress cracking (SSC). In some cases, nickel containing and high strength materials may also exhibit stress corrosion cracking (SCC). For typical oilfield applications limited to restricted yield grades of tubulars yield strengths ranging from 75 - 90 to 85 - 100 ksi, (520-620 to 585-690 MPa) maximum susceptibility to SSC occurs near room temperature (23 C). This susceptibility decreases with increasing temperature with essentially no SSC observed above 80 C [10].

As shown in Figure 4, one commonly used guideline for the SSC resistance of 13Cr is to limit its service to conditions which have a partial pressure of H_2S less than or equal to 1.5 psia (0.01MPa). Additionally, 13 Cr materials with a yield strength greater than 110 ksi and/or those with a nickel content greater than one percent, can exhibit SCC particularly at temperatures greater than 60 C.

SOCRATES utilizes such guidelines for environmentally induced cracking in the form of IF/THEN rules to define limits for service conditions where 13Cr is recommended. A typical rule for martensitic stainless steels is given below:

IF

  Yield strength $\geq$ 110 ksi (760 MPa) and
  {Chlorides > 10000 ppm   or
  H_2S > 0.05 psia or }   and
  Max. temperature $\geq$ 60 C

THEN

  Martensitic stainless steels are susceptible to stress corrosion cracking.

Cracking Considerations for Duplex Stainless Steels

Characterization of environmentally induced cracking of duplex stainless steels and determining safe use limits are complex issues. As identified in a previous study, these materials can exhibit more than one mechanism of cracking depending on the nature of the exposure conditions and test method utilized[11]. At low temperatures (<100 C), a hydrogen embrittlement mechanism tends to predominate where as at high temperatures (>150 C) anodic SCC is the most active cracking mode. Therefore, maximum susceptibility to environmentally induced cracking is often observed to occur at temperatures around (100 C) .

However, to establish basic guidelines for coldworked 22 and 25 Cr duplex stainless steels for use in the expert system, the data from several studies were evaluated and common trends identified[12,13]. Figures 5 and 6 show cracking data for these materials under conditions of low pH (approx. 3) at low and high temperatures, respectively. This data indicates that, for general considerations,

- the differences between 22 and 25 Cr stainless steels are usually minor but may be significant particularly at borderline conditions,
- the low temperature cracking behavior is effectively controlled by the chloride concentration in the range of H_2S partial pressures up to 100 psi (0.69 MPa), and

- at high temperatures, the more effective parameter for assessing cracking behavior is H_2S partial pressure.

Further, cracking behavior for 22 Cr duplex can be summarized as follows:

- Typically, SSC occurs at less than 65 C. When temperature is greater than 65 C, SCC occurs. Maximum cracking susceptibility to SCC is observed near 90 to 120 C.
- Chloride concentration predominates SCC behavior at low temperatures.
- H_2S and chloride concentrations both contribute to SCC behavior at high temperatures.

A typical rule for determining occurrence of stress corrosion cracking in 22-Cr duplex stainless steels is given below:

IF   [Temp $\geq$ 60 C < 80 C   and
                     {(Chlorides 100000 $\geq$ ppm and H_2S $\geq$ 0.01 MPa)   or
                     (Chlorides 10000 ^{3} ppm and H_2S ^{3} 15 psia)}   ]
      or
      [Temp $\geq$ 80 C < 120 C   and
                     {(Chlorides 10000 $\geq$ ppm and H_2S $\geq$ 0.01 MPa)   or
                     (Chlorides 1000 $\geq$ ppm and H_2S $\geq$ 0.1 MPa)}   ]
      or
      [Temp $\geq$ 120 C   and
                     {(Chlorides 10000 $\geq$ ppm and H_2S $\geq$ 0.01 MPa)   or
                     (Chlorides 1000 $\geq$ ppm and H_2S $\geq$ 0.1 MPa)}   ]
THEN
      Duplex stainless steels are susceptible to stress corrosion cracking.

Evaluation of Pitting Resistance of Stainless Steels

As indicated in Section 3, published literature on localized corrosion of stainless and nickel based alloys was reviewed to develop a pitting relationship for these materials in sulfide/chloride environments[14]. The relationship (Cr + 3.3Mo + 11N + 1.5[W+Cb]) was used in determining a pitting index for a wide variety of materials in the expert system. This relationship for pitting index was considered to be conservative relative to other pitting index equations available in literature. Pitting resistance of different materials was evaluated on the basis of a Required Minimum Pitting Index (RMPI). The RMPI was calculated as a function of the environmental severity index determined in Table 1 and the maximum operating temperature for a range of applicable service conditions.

The methodology of empirically achieving this relationship applied in SOCRATES is presented in Table 2. This table combines the environmental severity, maximum temperature and an RMPI value. As the environmental severity and temperature increase, so does the RMPI value required. Typical values of pitting index for 13Cr, 22Cr and 25Cr materials was determined to be 13, 32.0 and 35.6 respectively.

Application of the SOCRATES System

One of the most important aspects of expert systems formulated on empirical data and state-of-the-art knowledge is that they must be flexible and be able to accommodate changes in our fundamental knowledge and available data used in the materials selection process. The methodologies utilized in SOCRATES can be easily modified through changes to the associated rules and databases. The importance of the ability of an adaptive system for selection of stainless alloys has been highlighted by the rapid growth of databases and operating experience with these materials.

In two recent studies performed by Cortest Laboratories[15], SOCRATES accurately predicted problems associated with SCC of duplex stainless steels and localized corrosion problems in martensitic stainless steels based on the definition of the service environment. This aspect of the expert system, to assist in accurate selection of stainless alloys and reproducibly monitor the effects of up to seven environmental variables critical to alloy corrosion performance, we believe, underscores the relevance of such systems. Furthermore, these studies has also shown that such expert systems can significantly reduce the time required to conduct a proper selection of stainless alloys and have shown a cost benefit of at least 5 to 1 based on the engineering time saved.

Other environmental factors have also been incorporated into the SOCRATES system to better characterize real field production environments. These factors include consideration of gas-to-oil ratio (GOR). GOR basically is a measure of the relative amounts of gas and oil phase in the production environment. In cases of low GOR (i.e. oil wells) it has been found that corrosion and corrosion related cracking phenomena are of less concern. SOCRATES handles this by derating the environmental severity index.

Other factors also incorporated into SOCRATES include water-to-gas ratio (WGR) for gas wells and percent water cut in oil wells. Gas wells (i.e. high GOR) which produce high amount of water (i.e. high WGR) typically s how maximum corrosive severity and tendencies for SSC and SCC. However, in oil wells (i.e. low GOR) with low water cut, corrosivity can be very low. This can allow for the safe use of martensitic and duplex stainless steels at substantially higher levels of H_2S than predicted based on laboratory tests conducted in aqueous environments. The results of these laboratory tests typically predict behavior more typical of that experienced in wet gas well environments.

Conclusions

Martensitic and duplex stainless steels are intended for use in "mildly" corrosive environments. Martensitic stainless steels (13 Cr) are particularly susceptible to SSC and pitting. The higher alloy content in duplex stainless steels makes them more corrosion resistant than martensitic alloys. Also, duplex materials are susceptible to stress corrosion cracking and pitting in severe environments.

Selection evaluation methods for martensitic and duplex stainless steels have been formalized to facilitate implementation in the SOCRATES system. Environmental severity from a stand point of general corrosion has been represented as a function of H_2S partial pressure, chlorides and pH.

It has been shown that the minimum pitting index required to assess resistance to pitting can be represented in terms of environmental severity and maximum temperature. Practical applications have shown the effectiveness of the expert system in evaluating and selecting martensitic and duplex stainless steels.

Acknowledgments

References

1. M. C. Place, "The development and Application of Corrosion Resistant Alloys in Natural Gas Production", Paper No. 282, Corrosion/87, NACE, San Francisco, CA, 1987.

2. Crolet J., and Bonis M. R. "Evaluation of the resistance of some highly alloyed stainless steels to stress corrosion cracking in high chloride solutions under high pressures of CO_2 and H_2S" Corrosion/85, Paper No. 232, Boston, MA, 1985.

3. A. Ikeda, T. Kudo, Y. Okada, S. Mukai, F. Terasaki, "Corrosion behavior of high alloy oil country tubular goods for deep sour gas wells" Paper No. 206, Corrosion/84, New Orleans, LA, 1984.

4. S. Srinivasan and S. Cook, SOCRATES: Selection of Corrosion Resistant Alloys Through Environment Specifications: A User's Manual, Cortest Internal Publication No. L83203KS, August 1991.

5. Hayes-Roth F., Et al., Building Expert Systems, Addison Wesley Publishing Co., MA, 1983, pp 1-37.

6. H. Miyuki, et al, Localized corrosion of duplex stainless steels in CO_2-H_2S-Cl environments at elevated temperatures, Corrosion/84, Paper No. 293, New Orleans, LA, 1984.

7. Bonis M., and Crolet J. L. Practical aspects of the influence of in-situ pH on H_2S induced cracking, Corrosion Science, Vol. 27, No. 10/11, pp 1059-1070, 1987.

8. Aspahani A. I., Highly alloyed stainless steels for CO_2/H_2S environments, Corrosion/80, Paper No. 12.

9. H. Ogawa et al., "An estimating method for the critical limit of corrosion resistance of high alloy OCTG and line pipe in sour environments", Corrosion/87, No. 294, San Francisco, CA, 1987.

10. L. Kline et al., "9 Cr - 1 Mo and 13 Cr tubulars for sour service", Corrosion/90, No. 52, Las Vegas, NV, 1990.

11. R. Ottra et al., "The stress corrosion cracking of duplex stainless steels in environments containing chlorides and H2S", Proceeding of the conference on "H2S induced environment sensitive fracture of steels", Amsterdam, Sep. 10-12, 1986.

12. M. Barteri et al., "Microstructural study and corrosion performance of duplex and super austenitic steels in sour well environment", Corrosion/86, Paper No. 157, Houston, TX., 1986.

13. Bernhardsson S. O., "Properties of a duplex stainless steel in corrosive oil and gas wells", Corrosion/80, Paper No. 85.

14. R. D. Kane, S. M. Wilhelm and D. R. McIntyre, Application of Critical Pitting Temperature Test to the Evaluation of Duplex Stainless Steel, Corrosion Testing and Evaluation: Silver Anniversary Volume, ASTM STP 1000, Philadelphia, 1990, pp 289-302.

15. R. D. Kane, Cortest Laboratories' internal report on applications of SOCRATES, September 1991.

	Low (pH ≤ 4)	Moderate (4 < pH ≤ 5.5)	High (pH > 5.5)	
H,S pp ≤ 1 psi	20 (R037)	15 (R036)	10 (R035)	Low (Cl⁻ ≤ 10,000 ppm)
	25 (R038)	20 (R037)	15 (R036)	Moderate (10,000 < Cl⁻ ≤ 100,000ppm)
	30 (R039)	25 (R038)	20 (R037)	High (Cl⁻ > 100,000 ppm)
1 psi < H,S pp ≤ 10 psi	30 (R039)	15 (R036)	10 (R035)	Low
	50 (R041)	40 (R040)	20 (R037)	Moderate
	60 (R042)	50 (R041)	30 (R039)	High
10 psi< H,S pp ≤ 100 psi	60 (R042)	30 (R039)	20 (R037)	Low
	85 (R044)	50 (R041)	40 (R040)	Moderate
	100 (R045)	85 (R044)	60 (R042)	High
H,S pp > 100 psi	100 (R045)	50 (R041)	50 (R041)	Low
	110 (R046)	70 (R043)	70 (R043)	Moderate
	120 (R060)	100 (R045)	100 (R045)	High
H,S > 100 psi + Sulfur	120 (R060)	100 (R045)	100 (R045)	Low
	140 (R061)	120 (R060)	120 (R060)	Moderate
	150 (R047)	150 (R047)	150 (R047)	High

The associated rule for each environmental rating is shown in parentheses.

Table 1 -- Environmental severity rankings for different combinations of pH, H_2S and chlorides

Environmental Severity	T≤150F	150< T≤ 350F	350<T≤450F	450<T≤500F
10	12	12	12	30
15	12	12	13	30
20	12	13	25	30
25	16.5	25	35	37
30	16.5	25	35	37
40	25	30	35	37
50	25	30	35	38
60	25	31	35	40
70	25	31	35	40
85	25	31	35	40
100	30	31	40	45
120	30	40	43	50
150	40	43	50	60

Table 2 -- Required Minimum Pitting Index (RMPI) Values for Different Environments
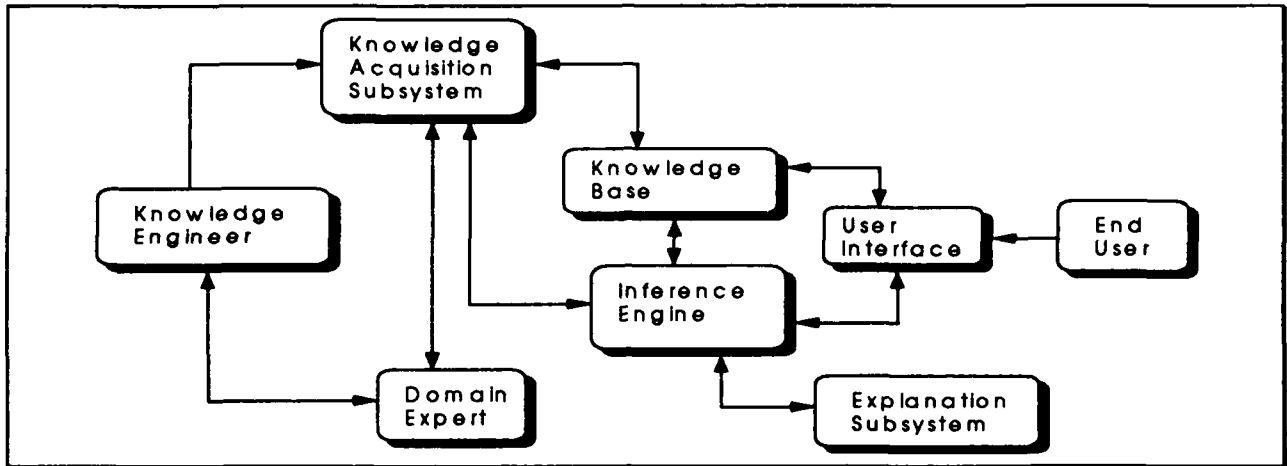
Figure 1 - Structural Components in Expert System Development
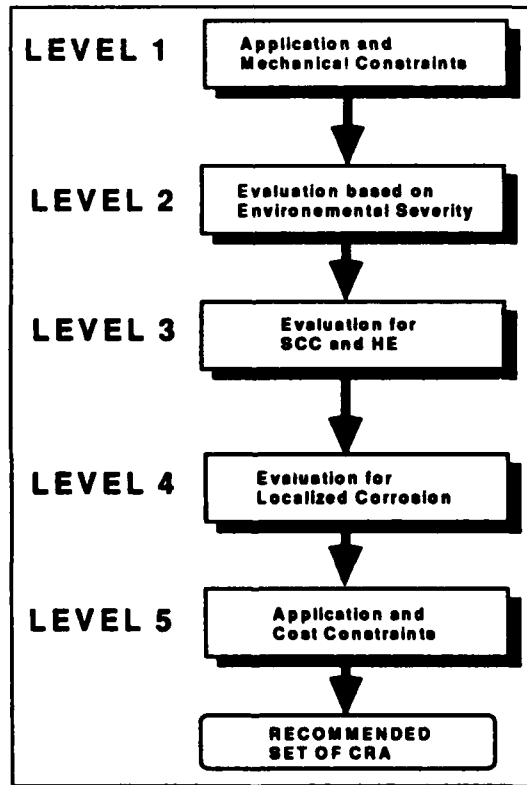
Figure 2 - Structure of the SOCRATES expert System
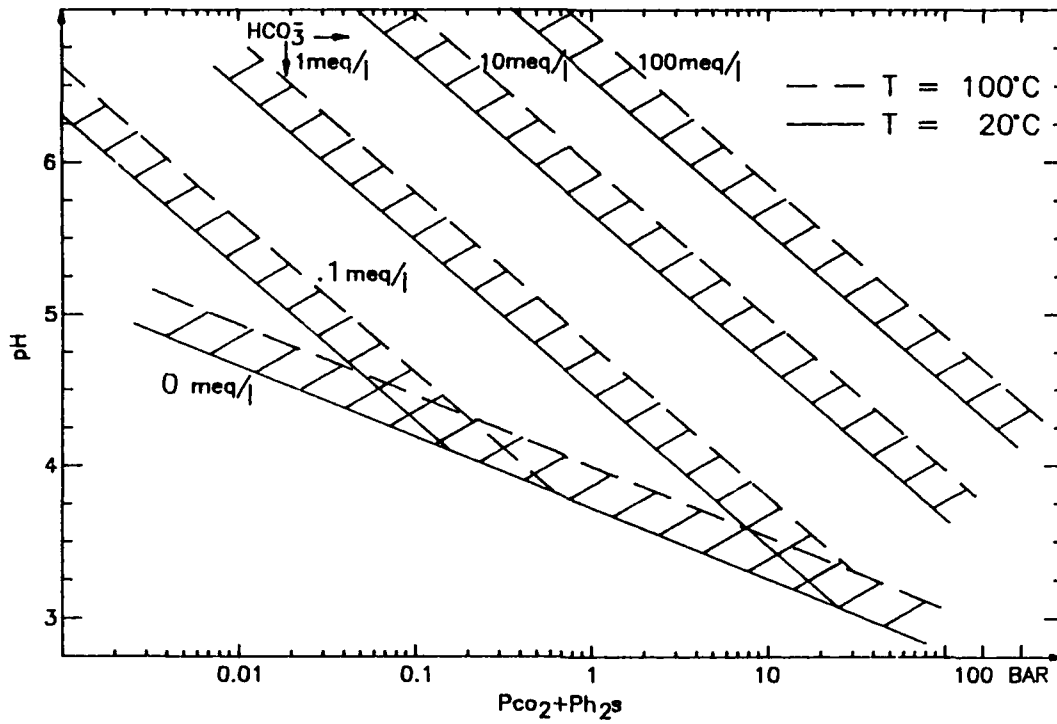
Figure 3 - The pH of Limestone - unsaturated formation
waters under CO_2 and H_2S pressure.
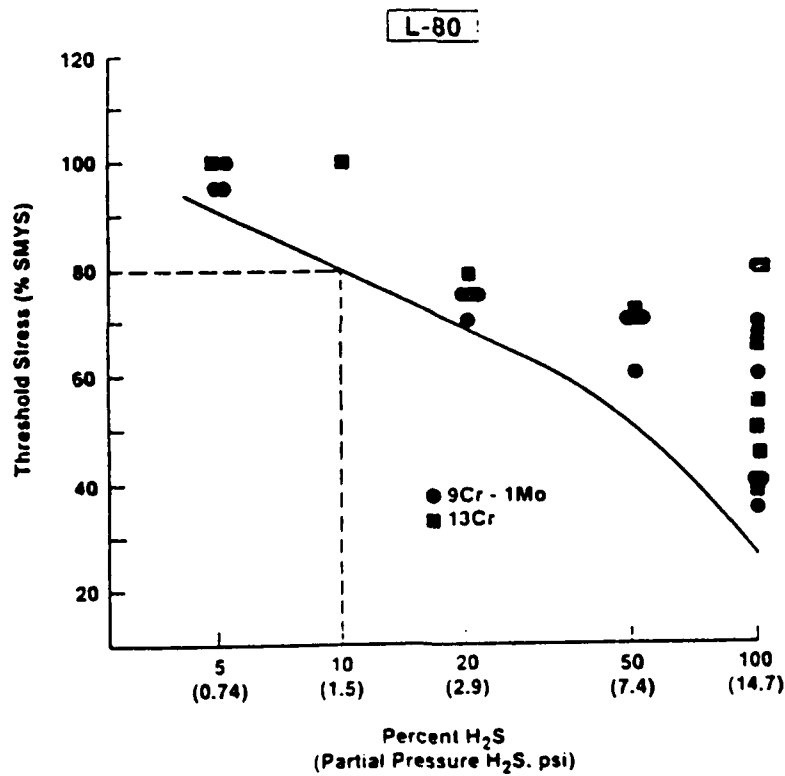
Figure 4 - Threshold stress as a function of
H_2S partial pressure for L-80 steel.
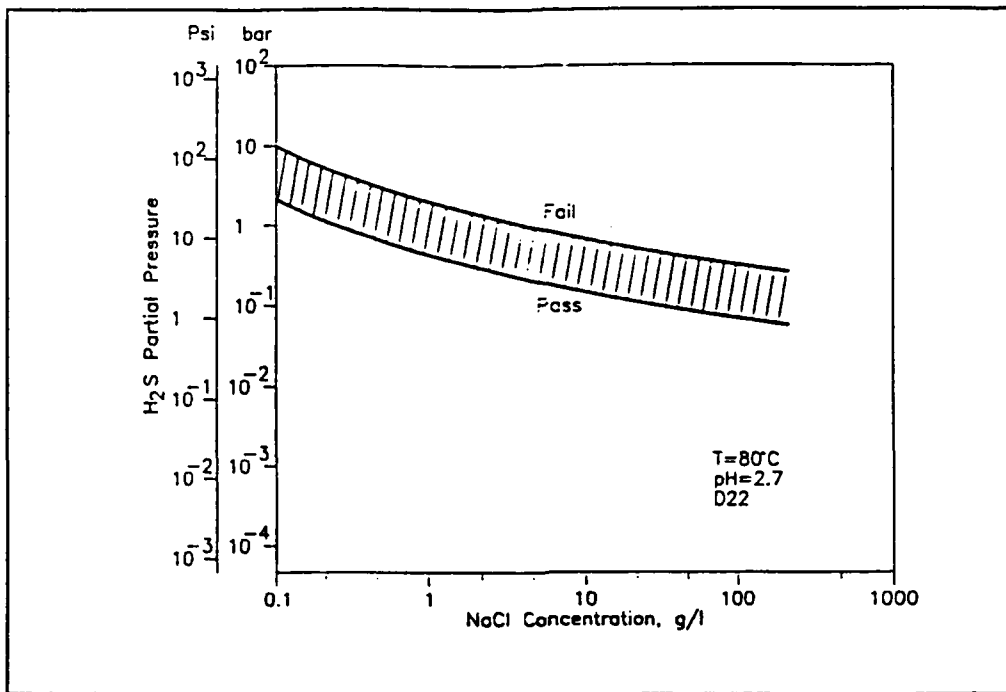
Figure 5 - Range of corrosion stability as a function of
NaCl concentration, partial pressure of H_2S
and cold worked state.
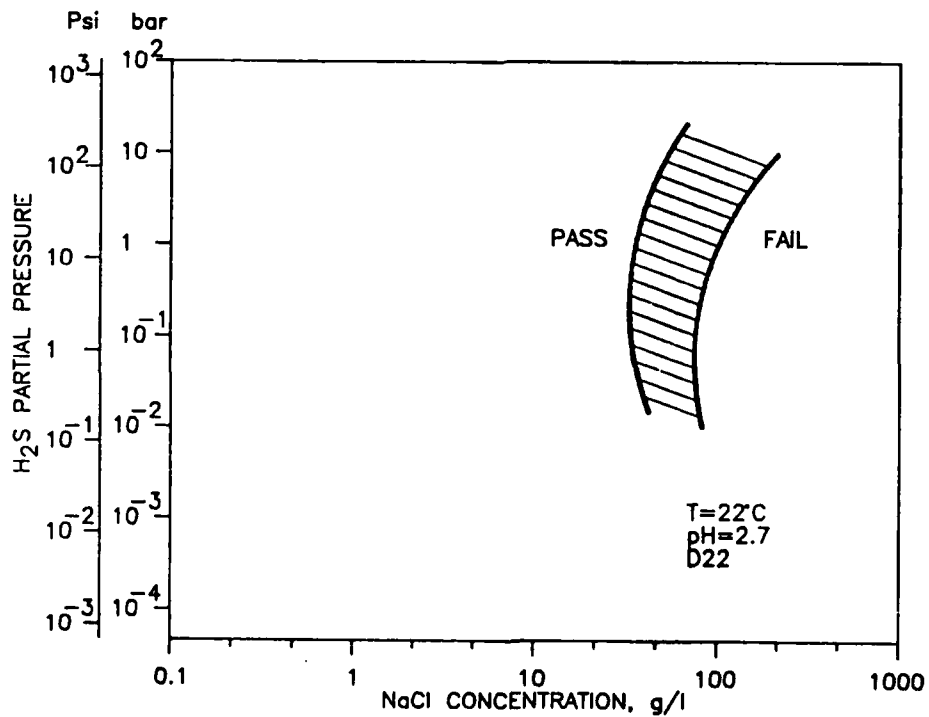
Figure 6 - Range of corrosion stability as a function
of NaCl concentration, partial pressure of
H_2S and cold worked state.

Effect of Flow Velocity on CO_2 Corrosion Performance of 13Cr, Super 13Cr and α-γ Duplex Phase Stainless Steels

Akio Ikeda and Masakatu Ueda
Osaka Head Office, Sumitomo Metal Industries Ltd.
5-33, Kitahama 4-chome, Chuo-ku , Osaka, Japan

Jose Vera, Alfred Viloria and Jose L. Moralez
INTEVEP S.A. P.O. Box 76343, Caracas, Venezuela

Abstract

A newly developed dynamic field tester(DFT) was installed at the gas well containing 6 vol.% CO_2 in the vicinity of Anaco, Venezuela. Cylindrical specimens of various kinds of corrosion resistant alloys with different internal diameter were mounted vertically in the DFT. Particularly, in the present paper, corrosion behavior of four stainless steels, i.e. 420 type (0.2C-13Cr) martensitic stainless steel(ss), low carbon martensitic super 13Cr martensitic stainless steel (0.01C-12Cr-5Ni-2Mo) and 18Cr and 22Cr α-γ duplex phase stainless steels is analyzed and discussed. The production fluid is mainly composed from methane and light hydrocarbon. The average gas oil ratio(GOR) is 400,000 to 600,000 SCFPD/BBPD and water cut is about 50%. Test temperatures at the outlet of test section are 360K(190F) in the first test and 350K(170F) in the second test. Any material discussed in this paper is practically categorized to corrosion resistant alloy in this corrosion media. Although corrosion rate is small, the difference in weight loss among different alloys can be assessed in the long time test.

As the result , an effect of flow rate and alloy composition on weight loss corrosion is clarified. The film of corrosion product is analyzed by the electron probe microanalyzer and ion mass microanalyzer. It is presumed from the results of surface appearance and depth analysis of composition of surface film that erosional flow effect on CO_2 corrosion rate of corrosion resistant alloys does not occur in the flow rate below 78.2m/s, but above 131.4 m/s. It is also clarified that passive films formed in the open air are restructured to the ones with different compositions and thickness in the corrosive environment.

Key terms: CO_2 corrosion , corrosion resistant alloy, CRA, 13Cr steel, Duplex stainless steel, flow effect, passive film, Cr-Ni-Mo alloy, annular mist , erosion

Introduction

Since late 1970's, CO_2 corrosion behaviors of corrosion resistant alloys(CRAs) tubing and casing have been systematically studied in laboratories. [1]-[5]The usage of those alloys in the field has been also expanded. [6]-[10] Although those laboratory data are effective to understand CO_2 corrosion phenomena, they have various short points to clarify the effect of various factors on CO_2 corrosion ;i.e. flow , fluids, oxygen contamination, interference of dissolved metallic ion due to corrosion, test duration etc. On the other hand, it is difficult to obtain some systematical information from the field experience. In order to accumulate the systematical field data on CO_2 corrosion and use them effectively for the engineering purpose, a dynamic field tester(DFT) was designed and fabricated. The details of the facilities and preliminary test data have been published elsewhere.[10] A flow effect on CO_2 corrosion of carbon steel and Cr contained low alloys in the DFT experiment has been also discussed elsewhere.[11]

In this paper, a flow effect on CO_2 corrosion behaviors of corrosion resistant alloys is studied. Particularly, corrosion behavior of four stainless steels(ss), i.e. 420 type (0.2C-13Cr) martensitic-ss, low carbon super 13Cr martensitic - ss (0.01C-12Cr-5Ni-2Mo) and 18Cr and 22Cr $\alpha-\gamma$ duplex phase stainless steels(dss), is analyzed and discussed on the basis of corrosion rate data and information of corrosion product film.

Experimental

1. Test Facility
A design of a dynamic field tester (DFT) is shown in Figure 1. The essential design condition is as follows:
    (1) max. temperature : 472K(392F),
    (2) max. pressure : 20MPa(2800psi),
    (3) material for flow section contacting with produced fluids:
        SM2535 alloy, which chemical composition is the same as shown in Table 1

        and which is corrosion resistant to H_2S-CO_2-Cl^-·

The detailed description of DFT and installation in the well head flow section has been described elsewhere.[10]

2. Materials tested
A long-run DFT experiments for flow effect on CO_2 corrosion behavior of alloys were carried out twice at JM101well in Anaco, Venezuela. They are called the DFT experiments 1 and 2. Materials tested are shown in Tables 1 and 2. A large part of materials with internal diameter(I.D.) of 52mm$^\phi$ was sampled from tubular products except of S13Cr and DP1. All of materials with smaller diameters were sampled from forged bar. A configuration of specimen is cylindrical, and the specimen dimensions were shown in the previous paper.[10] An electrical insulation between materials mounting in the specimen holder was carried out by a poly- ether ether ketone(PEEK) spacer or SM2535 spacer with plasma CVD Al2O3 ceramic coating . A materials arrangement at the vertical specimen holder in the DFT experiment 2 is shown in Fig.3. That in the DFT experiment 1 was described in the previous paper. [10] Materials S13Cr and DP1 were tested only in the DFT experiment 2. In order to obtain a stabilized flow at the test section, preparatory flow sections with the same I.D., which lengths are more than 50 times of I.D. are allocated at the upper flow site of specimen holders shown in Fig.3. A dummy material used for preparatory flow section is the same 22Cr-dss as shown in Tables 1 and 2.

3. Test conditions in the DFT experiment
The experimental condition in the DFT experiment has been described precisely in the previous paper. [10] The chemical composition of production fluids is shown in Table 3.
It is a typical gas well, i.e. average gas oil ratio(GOR) : 400,000 to 600,000 (SCFPD/BBPD). A total liquid flow rate is 50 to 130 BBPD and water cut is about 50%. The partial pressure of CO_2 is about 1MPa. Severe corrosion has occurred in production tubing and line pipe during the operation of this well without inhibitor injection. The down hole production tubing has been made of 420 type13Cr-ss. The well head piping system for installation of the DFT was mainly constructed with 22Cr-dss. During the DFT experiments, this section including the DFT has been operated in the ordinary production condition without inhibitor injection in order to represent the severest corrosion condition. In order to maintain corrosion performance of down stream facilities, corrosion inhibitor has been injected at the section right after the second choke shown in Fig. 1.

The testing time is 3672h in the experiment 1 except shut down time of 720h and 4493h in the

experiment 2 except shut down time of 816h. During the shut down time, the DFT was sustained in the high pressure condition by the production fluid. A typical vertical flow regime map indicating the conditions in the DFT experiments 1 and 2 is shown in Fig. 3.

4. Measurement

Three specimens of each material were mounted in each sections of I.D. 52, 27 and 20 mm$^\phi$, respectively. In the section of I.D. 15 mm$^\phi$, two specimens of 22Cr-dss was mounted in the DFT experiment 1, and each two specimens of 13Cr-ss and S13Cr -ss were tested in the DFT experiment 2. In the case installing three specimens, two specimens were used for measuring weight loss and one was used for analyzing surface film or corrosion products. In the case mounting two specimens, one for corrosion loss and one for analysis of corrosion products. In measuring weight loss after test, specimens were descaled in 10 wt. % ammonium citrate aqueous solution. The weight loss was measured by the difference of weight before and after the corrosion test. A corrosion rate was calculated by means of dividing the weight loss with testing time. Each precision of measurement for corrosion rate is 0.0002 mm/y in the DFT experiment 1 and 0.00005 mm/y in the DFT experiment 2.

In order to study the corrosion products and surface films, the specimens were cut along the longitudinal axis, observed visually and microscopically, and analyzed by the electron probe microanalyzer[EPMA] and ion microprobe mass analyzer[IMMA].

Result and discussion

Corrosion test results of 13Cr-ss and 22Cr-dss in the DFT experiment 1 are shown in Table 5. Although other high alloys, i.e. 25Cr, SM2535, SM2242 and SM2550, were also tested at the flow rate up to 131.4 m/s, all of corrosion rate were less than 0.0002 mm/y. Corrosion test results in the DFT experiment 2 are shown in Table 6. Even if a flow effect on corrosion rate of alloys with more excellent corrosion resistance than DP1- dss exists, it is negligibly small at the flow rate less than 78.2 m/s. I t is, particularly, assessed that SM2550 alloy above all is immune to corrosion in all of these test conditions. An effect of flow rate on corrosion rate of lower grade corrosion resistant alloys is shown in Fig. 4. Corrosion behavior of DP1-dss is mostly resemble to that of 22Cr- dss. Therefore, each flow effect on corrosion behaviors of 13Cr- ss, S13Cr- ss and 22Cr- dss is discussed precisely at the following sections, respectively.

1. Martensitic 13Cr ss

This material is categorized to UNSS42000, AISI 420 and API specification 5CT - group 2 of casing and tubing.[12] Generally speaking from engineering view points, this material is resistant to CO_2 corrosion at the temperature less than 423 k(300F).[1]-[4] Sondtvedt described that 13Cr-ss for choke in production equipment for unprocessed hydrocarbon had an allowable flow rate of 300 m/s, while that of carbon steel was 260 m/s in the same condition, which was classified to non corrosive environment.[13] It is noted that the allowable flow rate is an engineering criterion. It is reviewed in Table 7 how CO_2 corrosion behaviors of 13Cr-ss depend upon the flow rate in the experiment in the vicinity of 373K(212F). [1][3][14]-[18] It is shown in Table 7 that CO_2 corrosion rates of AISI 420 type martensitic 13Cr- ss are less than 0.1mm/y in the laboratory short time tests at the temperature below 373K(212F), and do not depend upon the flow rate in the range less than 26m/s. As corrosion rate and film thickness of corrosion product increases with increasing temperature, different flow effects could occur in the temperatures higher than 373K(212F). Denpo et al showed in the short periods loop test of 96h that corrosion rate at 393K(248F) increased with the flow rate up to 3 m/s and was sustained to a plateau level of about 0.46mm/y in the range of flow rate between 3 and 17 m/s.[18] On the other hands, Ciaraldi reported that a pitting corrosion at the pin end of metal-to-metal connection occurred in the 13Cr-ss tubing string used for one or two years in the gas-condensate well containing 1.0 to 1.4MPa CO_2 and organic acid of 800ppm, and its penetration

rate through wall was maximum 1.7 mm/y in the fluctuated flow rate in the range of 10.7 to 21.3 m/s, while it was more moderate value in the constant flow rate of 12 m/s, which corresponded to an allowable limiting flow velocity recommended with API RP14E.[17] In the field test in the same flow line at the flowing temperature of 383 K(270F), it was also reported that AISI 410- ss specimen did not suffer any pitting corrosion in 8.5 m/s, but in 14 m/s, and F6NM(13Cr-4Ni-0.5Mo) was immune to corrosion in the flow rate less than 17.9m/s.[17] It suggests that a long run of operation or test could result in a flow effect on CO_2 corrosion different from a short periods test such as the conventional laboratory tests shown in Table 7, because an accumulation of corrosion product occur, even if corrosion rate be small.

The corrosion rate of 420-ss in the flow rate less than 78.2 m/s in the DFT experiment is below 0.03 mm/y as shown in Fig. 4, and 420-ss is corrosion resistant at the temperature below 373K(212F) in consistency with the published data as shown in Table 7. In addition to this information, it is noted in Fig. 4 that the corrosion rate of 420-ss decreases as the flow rate increases in the range of 10.6 to 78.2 m/s, even if the difference of corrosion rate due to flow effect is not so much. Another fact is that its corrosion rate in the DFT experiment 2 increases significantly at the high flow rate, i.e. 157.1m/s. It suggests that a critical flow rate for 420-ss to erosion-corrosion could exist in the range of 78.2 m/s to 157.1 m/s. In order to discuss precisely these phenomena, corrosion product deposited on the specimen was studied. Surface appearance of specimen after tested, cross sectional view of corrosion products and EPMA analysis of corrosion product are shown in Figs. 5 to 7. On the basis of observation of cross sectional view of corrosion products, an effect of flow rate on the variation of film thickness of corrosion product is shown in Fig. 8. It is recognized that the specimens after tested are covered with the chromium and oxygen enriched corrosion product as shown in Fig. 6 and 7. This result of EPMA for 13Cr- ss is different from that for 3%Cr steel, where enriched Cr, O, and C, and Fe exist in the film of corrosion product.[1] It is presumed that a tight and adhesive hydrated chromium oxide film is formed for corrosion products of 420-ss as described by Fierro et al.[19] Existence of many cracks in film is shown in Fig.5. It is notable that existence of cracks is significantly less in the specimen tested at the flow rate of 157.1 m/s than in the others tested at the low flow rates. A cause of cracks is not clarified. The variance of film thickness is the largest at the flow rate of 157.1 m/s as shown in Fig.8. In this highest flow rate, maximum film thickness is closely related to the pit-wise sites of matrix, and minimum film thickness is located on the flat heights of matrix. This suggests the following corrosion process; At first, ferrous iron dissolves preferentially and enrichment of chromium and oxygen occurs, and the protective film of corrosion product is nucleated and grown, and it is locally peeled off by the mechanism of erosion corrosion after the film thickness attained to some level, and cured by localized corrosion of matrix at that site. Adherence of film at the cured site is stronger than at the other site, because of anchor effects. It results in the dispersion of corrosion site, and the surface morphology of corroded matrix becomes a general corrosion rather than a localized corrosion. It is also noted that a minimum corrosion rate at the flow rate of 78.2 m/s is related with a formation of adherent and tight protective film, which result in the minimal variance of film of corrosion product as shown in Fig. 8.

2. Low carbon martensitic S13Cr stainless steel
This material is a newly developed engineering material to improve CO_2 corrosion resistance of 420-ss both in high temperature and in H_2S contamination.[20] In Fig. 4, corrosion rate of S13Cr-ss is 1/40 to 1/15 of that of 420-ss in the flow rate below 78.2 m/s. In the high flow rate 157.1 m/s, the corrosion rate of S13Cr- ss, i.e. 0.0012mm/y, is about 1/120 of that of 420-ss and nearly equal to that of 22Cr- dss. A film of corrosion product is too thin to observe a cross sectional structure by either optical microscope or SEM. Results of surface appearance by SEM and depth analysis by IMMA are shown in Figs. 9 and 10. The surface appearance in the flow rate below 78.2 m/s is completely different from that in 157.1 m/s. In the latter, a fine structure of machining trail is almost disappear and erosional pits along the flow direction are appeared, while the surface as machined is observed in the former. The results of IMMA clarify for the surface passive film to restructure from a Fe -rich thin film formed in the open air to a new thicker film enriched with Cr -(Si) in the corrosion environment without the erosional

damage in low flow rate. The film formed in the high flow rate 157.1 m/s have a film composition similar to one in the open air, although the zone with chromium depletion is thicker in the former than in the latter. This difference might be resulted from the fact that the corrosion specimen was exposed to the static humid environment and a passive film in the stagnant corrosion environment was restructured, even after the corrosion test in the high flow rate was finished. It is concluded that the increased weight loss in the high flow rate 157.1 m/s is due to the erosional effect rather than the contribution of corrosion and the repassivation reaction of S13Cr-ss is rapid enough to maintain the low corrosion rate such as 0.0012 mm/y.

3. 22Cr α-γ duplex phase stainless steel
22Cr-dss is immune to corrosion at the flow rate below 66.6 m/s. A slightly effective weight loss is measured at the flow rate of 78.2 m/s. The surface appearance by SEM shown in Fig. 11 indicates some evidence of flow effect at 78.2 m/s, although it is very local. However, results of depth analysis shown in Fig. 12 does not indicate any evidence of erosional flow effect, but an existence of restructured passivation film in the corrosion environment different from that in the open air. A characteristic feature of the restructured passivation film of 22Cr-dss is an enrichment of Cr and Si and depletion of Fe in the film.This is also supported by the fact that both 420-ss and S13Cr-ss less resistance than 22Cr-dss does not show any evidence of erosional flow effect in the flow rate 78.2 m/s as mentioned above. In the flow rate more than 131.4 m/s, the weight loss increases as the flow rate increases. An erosional flow effect would result in the weight loss as discussed for S13Cr-ss. It is noted that the corrosion rate of 22Cr-dss is 0.0034mm/y even in the high flow rate 250.5 m/s, and this material is still immune to corrosion in this environment from the engineering view point. This corrosion rate corresponds to about 3 times of the corrosion rate in the flow rate 131.4 m/s. As it is not an abnormal increase, it is presumed that an increase of frequency damaging film by the erosional effect results in the increased corrosion rate, but a self-curing capability of passive film due to the repassivation reaction is sufficient to prevent corrosion.

Conclusion

1. Corrosion resistant alloys more than martensitic 13Cr- ss(420-ss) are resistant to CO_2 corrosion at the temperature of about 360k in the flow rate up to 78. 2 m/s. At this temperature, 420-ss shows a moderate corrosion rate of about 0.14 mm/y in the flow rate 157.1m/s. From engineering view point, other materials tested, i.e. S13Cr-ss (0.01C-5Ni-2Mo12Cr), α-γ duplex phase stainless steels and high nickel austenitic CRAs are resistant to CO_2 corrosion in the flow rate below the maximum flow rate tested; 157.1m/s for S13Cr- ss , 250.5 m/s for 22Cr- dss,78.2 m/s for DP1-dss and 131.4 m/s for high Ni-CRAs.

2. Corrosion rate of 420-ss decreases as the flow rate increases up to 78.2 m/s. It is presumed that a hydrated chromium oxide film with thickness of 1.5 to 6 mm is formed on the surface. In the film, many cracks exist. In the high flow rate 157.1 m/s, the film thickness is 1 to 11 mm, and the film is crackless.

3. S13Cr- ss and 22Cr- dss have not an evidence of erosional damage due to in the flow rate below 78.2 m/s, but in the flow rate 157.1 and 131.4 m/s, respectively. The weight loss due to the erosional damage is minor, and a self-curing capability of passive film due to the repassivation reaction is sufficient to prevent corrosion at the sites suffering erosional damage. As for 22Cr- dss, the same mechanism of flow effect is sustained up to 250.5 m/s.

4. In exposed to the corrosion environment, a passive film enriched with Cr and depleted with Fe different from one formed in the open air is restructured. In suffering erosional flow effect, the passive film with compositions similar to ones in the open air is represented, but the film thickness in the corrosion environment is thicker than in the open air.

References

(1) A.Ikeda, M.Ueda,S.Mukai, Corrosion'83 Paper No.43, Advances in CO_2 corrosion vol.1, (Houston TX, NACE,1984), pp 39-51

(2)   A.Ikeda, M.Ueda,S.Mukai, Advances in CO_2 corrosion vol.2, (Houston TX, NACE,1985), pp 1-22

(3)   A.Ikeda,S.Mukai, M.Ueda, Corrosion, 41(1985);p185 , Advances in CO_2 corrosion vol.2, (Houston TX, NACE ,1985), pp 47-54,

(4) S.Mukai, M. Ueda, T. Tsumura, A. Ikeda, Proc. 4th Asian Pacific Corrosion Conf. in Tokyo(May, 1985) p664

(5) S.Mukai, H. Okamoto, T. Kudo, A. Ikeda, J. materials Energy System 5,(1983);p59

(6) L.J. Klein, Materials Performance 23, 10(1984);p29

(7) G.A. Welch, R.B. Stanbery, L.M. Fergason, D. W. Jenkins, G.A. Myers, C.M. Maryan, Corrosion' 86(Houston, NACE,1986) paper No. 337.

(8) L. Abrego, Corrosion' 86(Houston, NACE,1986) paper No. 335.

(9) H. Erikson, S. Bernhardson, Corrosion' 90 (Houston, NACE,1990) paper No. 64

(10) A. Ikeda, M. Ueda, J. Vera, M. Castillo, A. Viloria, Corrosion' 90 (Houston, NACE, 1992) paper No. 48

(11) J. Vera, M. Castillo, A. Viloria,A. Ikeda, M. Ueda, " Flow Velocity Effect on Carbon Steel CO_2 Corrosion Using a Dynamic Field Tester" 1st Pan -American Congresson Corrosion and Protection (October ,1992)

(12) API Specification 5CT, 3rd edition(Dallas, TX, American Petroleum Institute,1990)

(13) T. Sontvedt, "Production Rate Limits Due to Internal Erosion and Corrosion in Offshore Production-Pipes and chokes" Two phase flow lecture series No.8   (Tronthiem, Norway,1985)

(14) B.Lefevre, G. Guntz, J.C. Prouheze, J.J. Renault, P. Bounie, Advances in CO_2 corrosion vol.2, (Houston TX, NACE ,1985), pp 55-71

(15) K. Satoh, K. Yamamoto, N. Kagawa, Advances in CO_2 corrosion vol.1, (Houston TX, NACE,1984), pp 151-156

(16) K. Masamura, S. Hashizume, K. Nunomura, J. Sakai,   Advances in CO_2 corrosion vol.1, (Houston TX, NACE,1984), pp 143-150

(17) S.W. Ciaraldi, Corrosion '90, Paper No.71(Houston TX, NACE,1990)

(18) K. Denpo, H. Ogawa, Corrosion '90, Paper No.28(Houston TX, NACE,1990)

(19) G. Fierro, G.M. Ingo, F. Mancia, L. Scoppio, N. Zacchetti , J. Materials Science 25 (1991) pp1407-1415

(20) M. Ueda, T. Kushida, K. Kondo, T. Kudo, Corrosion '92, Paper No. 55(Houston TX, NACE,1992)

Table 1   Chemical composition and mechanical properties materials used in the DFT experiments 1 and 2 [test specimens with I.D. 52 mm]

Material	Chemical composition (wt%)										Tensile properties			
	C	Si	Mn	P	S	Cu	Cr	Ni	Mo	Others	Y.S. (MPa)	T.S. (MPa)	El (%)	R.A. (%)
13Cr*	0.20	0.42	0.66	0.023	0.001	0.02	13.1	0.1	<0.1		601	784	25.2	66.9
S13Cr**	0.01	0.18	0.44	0.016	0.002	0.09	13.0	5.2	2.1		624	853	24.4	76.6
DP1**	0.02	1.58	1.68	0.019	0.001	0.08	18.4	5.0	2.8		596	801	47.0	72.4
22Cr*	0.02	0.51	1.52	0.021	<0.001	0.07	22.1	5.3	2.8	N	811	878	25.8	78.2
25Cr*	0.02	0.43	0.84	0.021	0.001	0.49	25.1	7.2	3.2	W:0.42,N	605	802	29.6	71.6
SM2535*	0.02	0.22	0.59	0.016	0.001	0.80	24.8	30.9	3.1		908	956	18.0	79.0
SM2242*	0.02	0.31	0.79	0.016	0.001	1.84	21.1	43.1	3.2	Ti:0.75	879	920	16.0	64.0
SM2550*	0.01	0.41	9.61	0.012	0.001	0.96	24.8	49.8	5.7	Ti:0.89	866	929	19.0	72.0

* Commercial tubular materials
** Forged bar materials

Table 2   Chemical composition and mechanical properties of materials used in the DFT experiments 1 and 2 [test specimens with I.D. 15, 20 and 27 mm]*

Material	Chemical composition (wt%)										Tensile properties			
	C	Si	Mn	P	S	Cu	Cr	Ni	Mo	Others	Y.S. (MPa)	T.S. (MPa)	El (%)	R.A. (%)
13Cr	0.19	0.37	0.58	0.021	<0.001	0.02	13.3	<0.1	<0.1		589	756	26.8	68.8
13Cr	0.01	0.18	0.44	0.016	0.002	0.09	13.0	5.2	2.1		624	853	24.4	56.6
DP1	0.02	1.58	1.68	0.019	0.001	0.08	18.4	5.0	2.8		596	801	47.0	72.4
22Cr	0.02	0.51	1.50	0.015	<0.001	0.08	22.0	4.9	2.8	N	491	713	43.0	79.0
25Cr	0.02	0.35	0.82	0.017	0.001	0.47	24.7	6.8	3.2	W:0.28,N	548	753	39.8	82.4
SM2535	0.02	0.32	0.63	0.011	0.001	0.78	24.5	30.5	3.3		853	902	21.6	81.9
SM2242	0.02	0.34	0.82	0.013	0.001	1.79	21.3	43.5	3.4	Ti:0.93	769	829	22.2	76.6
SM2550	0.02	0.37	0.57	0.012	0.001	0.91	23.3	49.9	6.8	Ti:0.46	890	949	22.4	68.8

* Forged bar materials

Table 3 Chemical analysis of production fluids at JM-101 well (Dec.1989)

Gas composition (mol%)	C_1	90.35
	C_2	1.49
	C_3	0.56
	C_4^+	0.95
	CO_2	6.65
	H_2S	$\leq$ 5 ppm
Chemical analysis of condensed water (ppm)	Fe	0.57
	Cr	< 0.5
	Ni	< 0.5
	Cl^-	23

Table 4 Average test conditions in the DFT experiments 1 and 2

Experiment	Internal diameter (mm)	Gas flow rate (Nm^3/min)	Pressure (psi)	Pressure (MPa)	Temperature (°F)	Temperature (K)	Gas velocity Vsg (m/s)	N_{gv}*	N_{LV}*	Flow pattern*
1	52	9000	1960	13.8	190	361	17.6	145.5	0.60	Transition Annular mist
	27	9000	1917	13.5	190	361	66.6	560.0	2.27	Annular mist
	20	9000	1775	12.5	188	360	131.4	1155.1	4.33	Annular mist
	15	9000	1661	11.7	188	360	250.5	2257.7	7.89	Annular mist
2	52	7860	1755	12.1	181	355	10.6	87.96	0.36	Transition
	27	7860	1726	11.9	175	352	39.7	334.0	1.35	Annular mist
	20	7860	1598	11.1	175	352	78.2	687.8	2.66	Annular mist
	15	7860	1406	9.9	171	350	157.1	1380.8	5.18	Annular mist

* According to Taitel and Dukler and calculated using correlation based on Duns & Ros dimensionless parameter[8][9]

$N_{LV} = 1.938 \, V_{sl}(\rho_{liq} \gamma)^{-1/4}$

$N_{gv} = 1.938 \, V_{sv}(\rho_{liq} \gamma)^{-1/4}$

ρ_{liq} = Liquid(water+condensate) density (lb/ft^3)

γ = Surface tension (dyne/cm)

Table 5 Corrosion test result in the DFT experiment 1

Specimen[1] I.D. (mm)		15	15	20	20	27	27	52	52
Vsg (m/s)[2]		250.5	250.5	131.4	131.4	66.6	66.6	17.6	17.6
Materials	S.G. (g/cm^3)[4] C.R.[3]	g/m^2/h	mm/y	g/m^2/h	mm/y	g/m^2/h	mm/y	g/m^2/h	mm/y
13Cr	7.68	-	-	0.0079	0.009	0.0028	0.0032	0.0035	0.004
22Cr	7.85	0.0027	0.0034	0.0009	0.0011	<0.0001	<0.0001	<0.0001	<0.0001

Note
(1) I.D. : Internal diameter
(2) Vsg : Gas velocity
(3) C.R.: Corrosion rate
(4) S.G.: Specific gravity

Table 6   Corrosion test result in the DFT experiment 2

Specimen[1] I.D. (mm)		15			20			39.7			52		
V_{SG} (m/s)[2]		157			78.2			39.7			10.6		
C.R.[3]		g/m²/h		mm/y	g/m²/h		mm/y	g/m²/h		mm/y	g/m²/h		mm/y
Materials / S.G. (g/cm³)[4]		each	av.		each	av.		each	av.		each	av.	
13Cr	7.68	0.1261	(0.1103) 0.1261	(0.125) 0.143	0.00612 0.00677	(0.0056) 0.0064	(0.0064) 0.0074	0.01038 0.01078	(0.0093) 0.0106	(0.0105) 0.0120	0.01698 0.01767	(0.0151) 0.0173	(0.0173) 0.0198
S13Cr	7.79	0.0010	0.0010	0.0012	0.00066 0.00035	0.0005	0.0006	0.00045 0.00040	0.00043	0.0005	0.00038 0.00044	0.0004	0.0005
DP1	7.85	-	-	-	0.00022 0.00012	0.00017	0.0002	0.00010 0.00003	0.00006	0.0001	-0.00005 0.00002	-0.00001	<0.0001
22Cr	7.85	-	-	-	0.00015 0.00018	0.00016	0.0002	0.00008 0.00010	0.00009	0.0001	0.00015 0.00010	0.00007	0.0001
25Cr	7.85	-	-	-	0.00015 0.00031	0.00023	0.0002	0.00010 0.00013	0.00011	0.0001	-0.00003 0.00006	0.00001	<0.0001
SM2535	8.13	-	-	-	0.00017 0.00018	0.00019	0.0002	0.00017 0.00017	0.00017	0.0002	-0.00013 -0.00013	-0.00013	<0.0001
SM2242	8.14	-	-	-	0.00018 0.00020	0.00019	0.0002	0.00013 0.00015	0.00014	0.0002	-0.00001 -0.00008	-0.00005	<0.0001
SM2550	8.29	-	-	-	-0.00055 0.00032	-0.00023	<0.0001	-0.00058 0.00017	-0.00020	<0.0001	-0.00119 0.00009	-0.00055	<0.0001

Note   (1) I.D. : Internal diameter   * ( ) : Corrosion rate calculated with the testing time including shut-down time.
(2) Vsg : Gas velocity
(3) C.R. : Corrosion rate
(4) S.G. : Specific gravity

Table 7   Review of flow effect on CO_2 corrosion rate of 13Cr steels
in the vicinity of 373K (212F)

No.	Materials	Cl⁻	P_{CO_2}	Temperature	Testing duration	Flow rate	Remarks	Corrosion rate	References
		ppm	MPa	K (F)	h	m/s		mm/y	
1	0.005C-13Cr	10	3.0	423(300)	96	2.5	Autoclave	0.015	
2	(Ferritic)	500	3.0	423(300)	96	2.5		0.3	Ikeda et al.
3		30,000	3.0	373(212)	96	2.5		0.25	(3)
4		30,000	0.1	373(212)	96	2.5		<0.1	
5	AISI 420	30,000	3.0	373(212)	200	7.0	Solution loop	<0.1	Ikeda et al.
6	Martensitic	30,000	3.0	373(212)	200	15.0		<0.1	(1)
7	AISI 420	30,000	0.15	373(212)	200	26.0	Gas loop	<0.1	Ikeda et al.
8		30,000	0.15	423(300)	200	26.0		0.15-0.3	(3)
9	AISI 420 (Ni-added)	500	1.5	353(176)	168	0.5	Autoclave	0.2-0.3	Lofebvre et al. (14)
10	AISI 410 CA15	18,000	0.3	413(284)	96	1.5	Solution loop	<0.1	Satoh et al. (15)
11	AISI 420	18,000	5.5	423(300)	96	Static	Circulation	0.1	Masamura
12			5.5		500	Static	autoclave	0.4	et al. (16)
13	AISI 420	800	1.0/1.4			10.2/21.3	Field	1.7	Ciaraldi
14	420			383/400	8760	12.0	Organic acid	moderate	(17)
15	410				~17520	<8.5	: 230ppm	<0.025*	
16	410			(270/261)		14	pH 4.6	Pitting	
17	F6NM					17.9		<0.025	
18	AISI 420	18,000	4	353(176)	96	0	Solution loop	0.05	Denpo et
19						3		0.07	al. (18)
20						17		0.07	
21		18,000	4	393(248)	96	0	Solution loop	0.05	
22						3		0.46	
23						17		0.46	
24		18,000	4	393(248)		100	Gas loop	0.05	

* below measurable limit

Fig. 1 Schematic illustration of the dynamic field tester[DFT]
T : Temperature,   CM : Corrosion monitor(coupon)
P : Pressure,   EM : Electrochemical corrosion monitor
F : Flow rate

Note

* 22Cr was used for dummy tube
* (2), (3) ; Specimen numbers
* Each different material is mounted with the electrical insulation

Fig. 2　Materials arrangement at the vertical specimen holder in the DFT experiment 2

2474
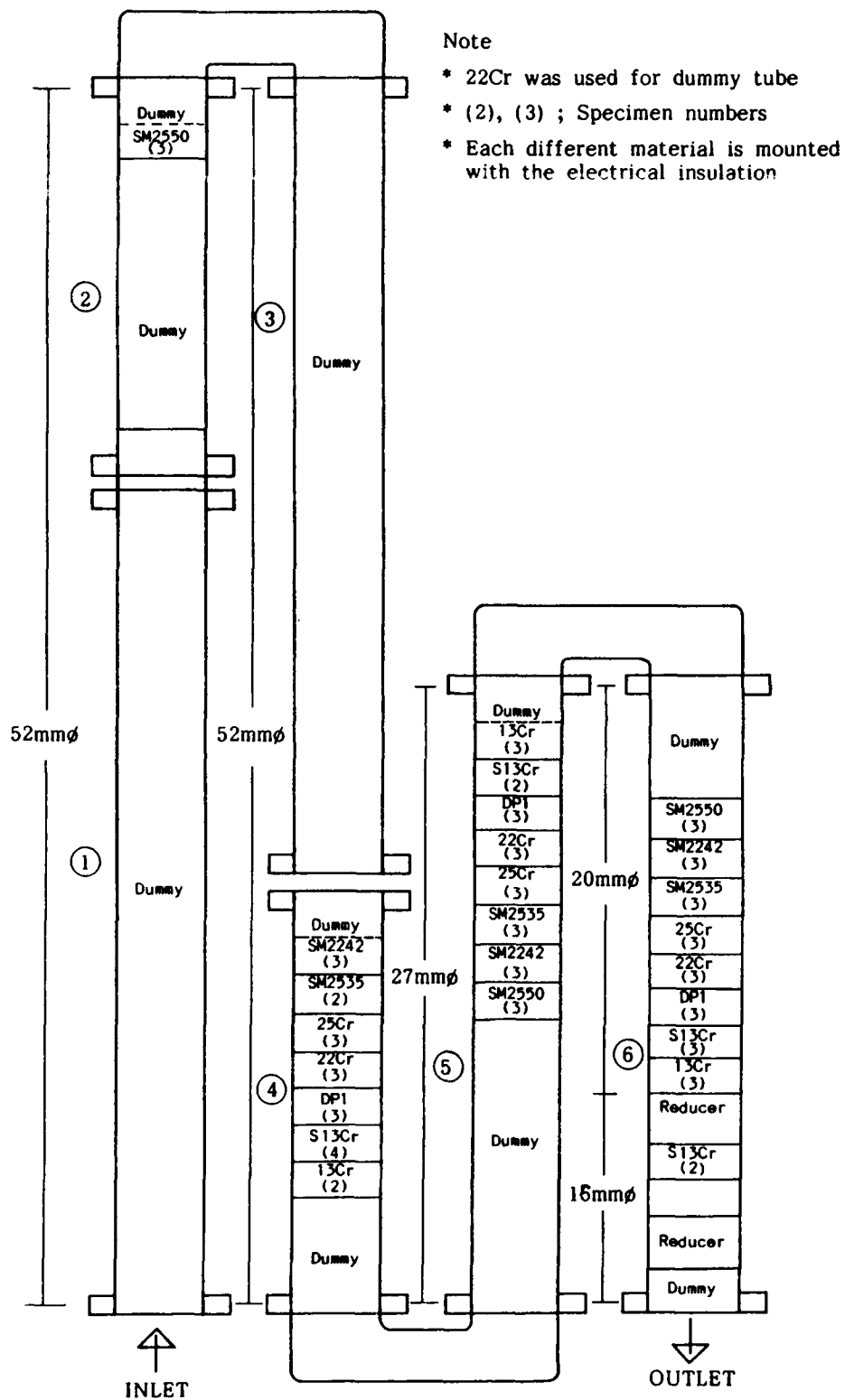
I.D. (mm)	52	27	20	15
Experiment 1	■	◪	□	▣
Experiment 2	▲	◮	△	◬
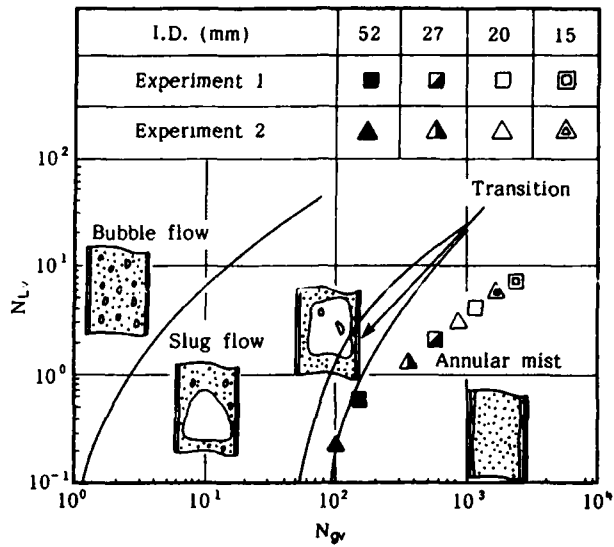
Fig. 3 Typical vertical flow regime map and conditions in the DFT experiments 1 and 2
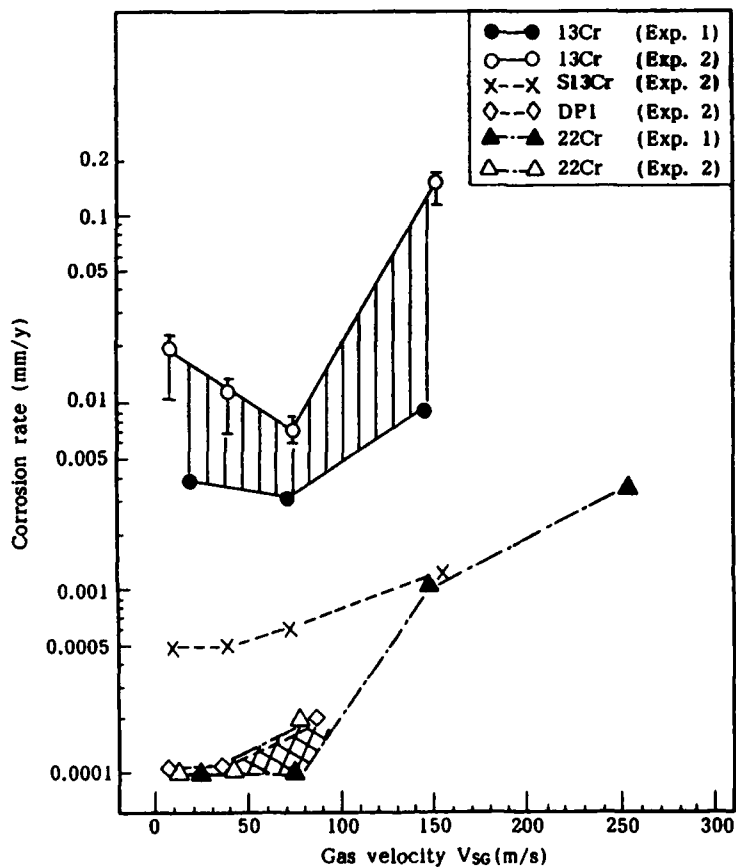
Fig. 4 Effect of flow velocity on corrosion rate of 13Cr, S13Cr, DP1 and 22Cr steels in the DFT experiments 1 and 2

Flow direction

Gas velocity(Vsg)=10.6 m/s   Vsg=157.1 m/s

40µm

Vsg=78.2 m/s   Vsg=157.1 m/s

40µm   40µm

40µm   10µm
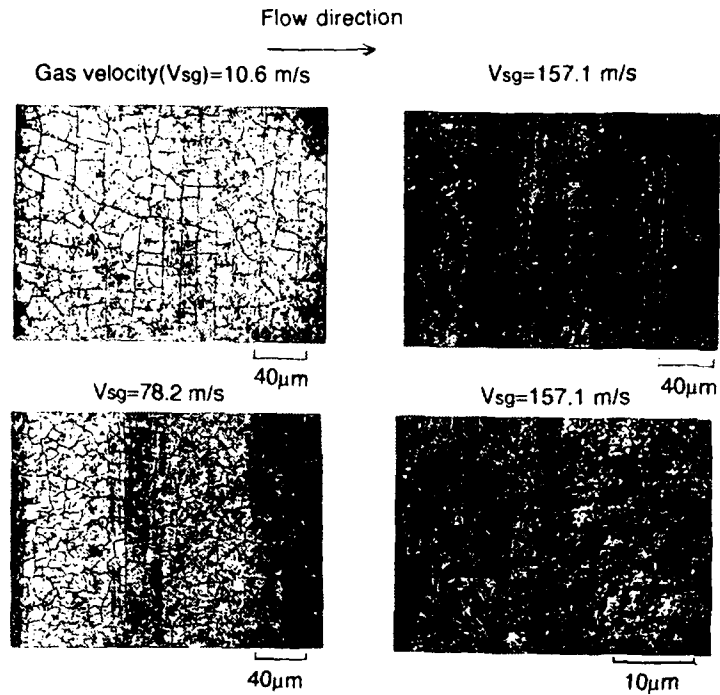
Fig. 5 Surface appearance by SEM of 13Cr steel in the DFT experiment 2

OM   SEM   Corrosion product

Gas velocity(Vsg)
=10.6 m/s

Vsg=39.8 m/s

Vsg=78.2 m/s

Vsg=157.1 m/s

20µm   2 µm
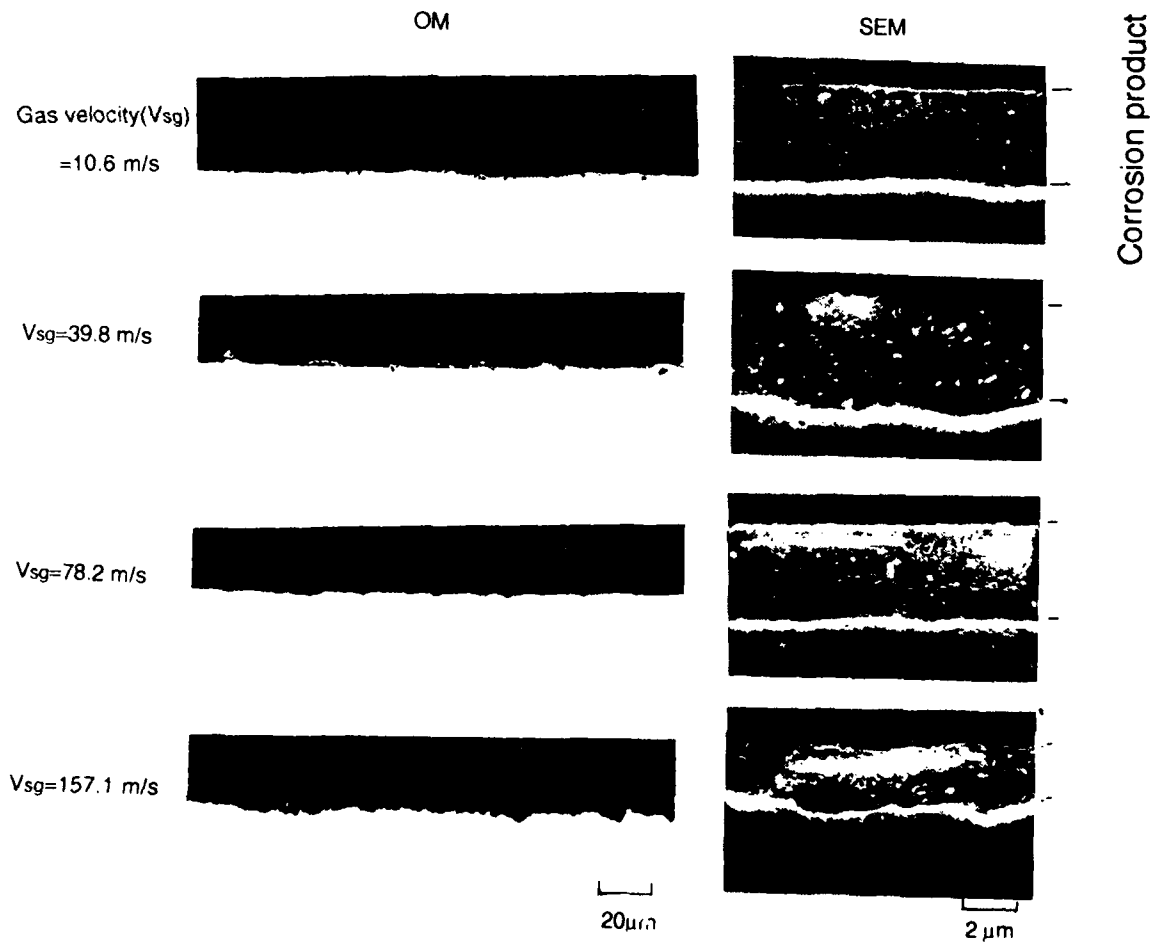
Fig. 6 Cross-sectional view of corrosion products of 13Cr steel in the DFT
experiment 2   [OM : optical microscopy,   SEM : scanning electron
microscopy]
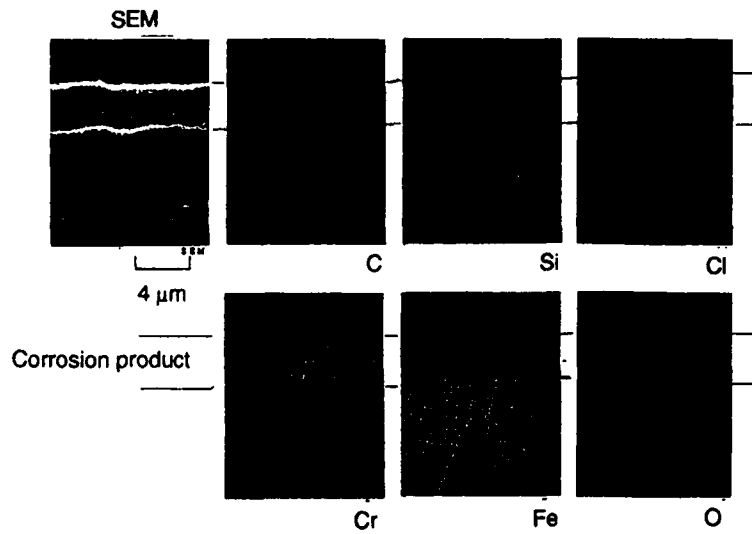
Fig. 7　EPMA analysis of corrosion product of 13Cr steel in the
DFT experiment 2　[Gas velocity $V_{sg} = 157.1$ m/s]
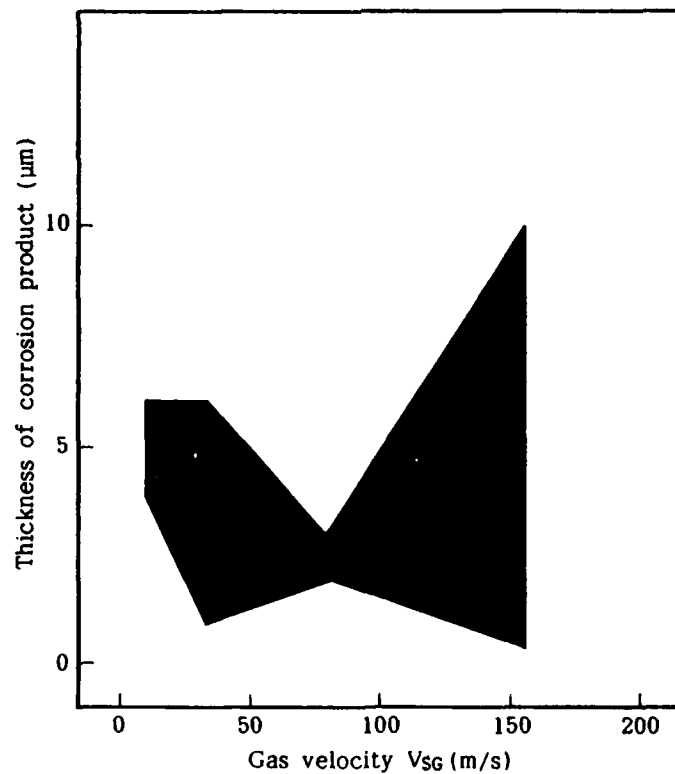
Fig. 8　Effect of gas velocity on thickness of corrosion product
of 13Cr steel in the DFT experiment 2
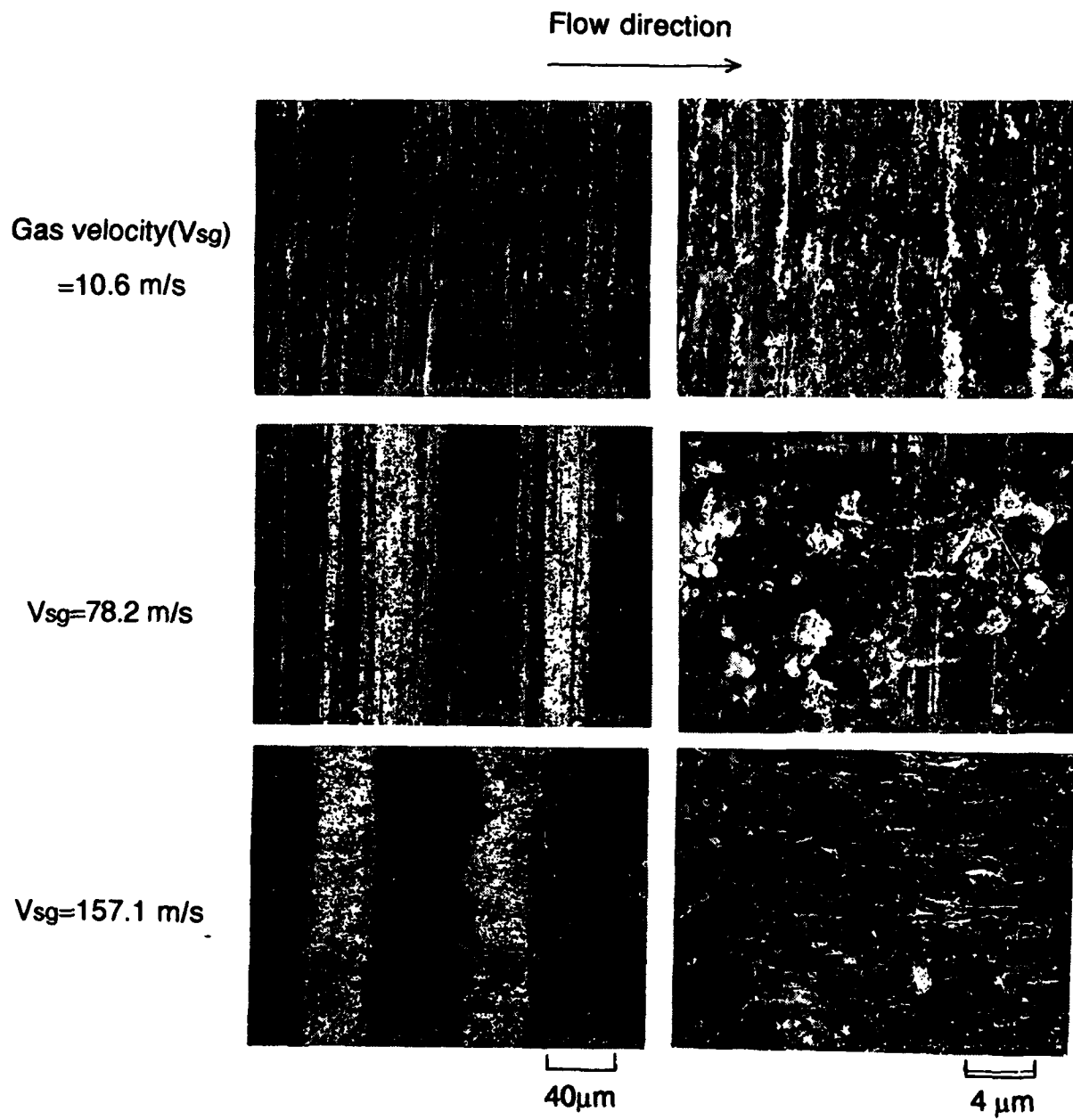
Fig. 9 Surface appearance by SEM of S13Cr steel after tested in the DFT experiment 2
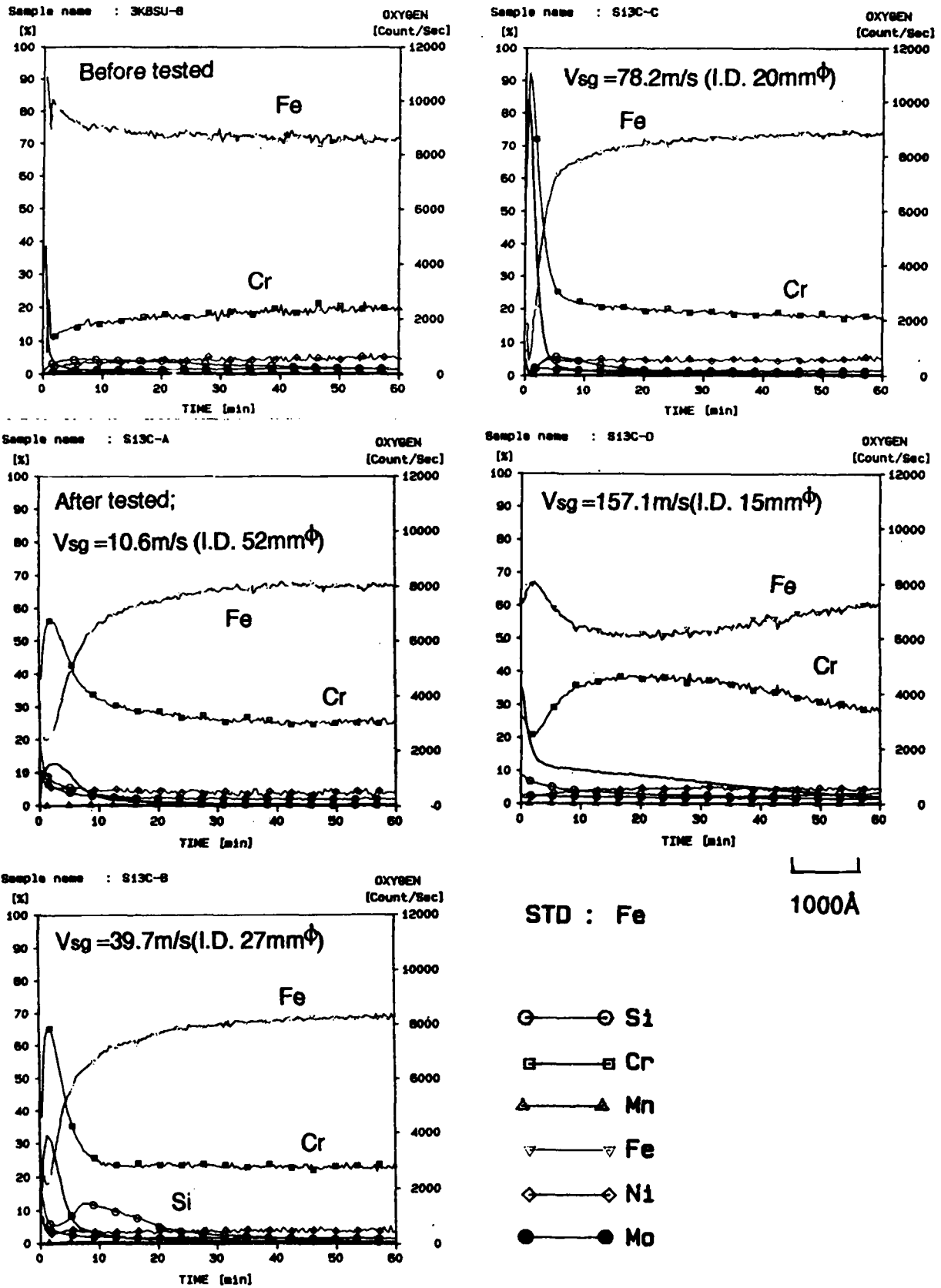
Fig. 10 Depth analysis by IMMA of surface film of S13Cr steel before and after tested in the DFT experiment 2

Flow direction →

Gas velocity(Vsg) =10.6 m/s

Vsg=78.2 m/s

40µm
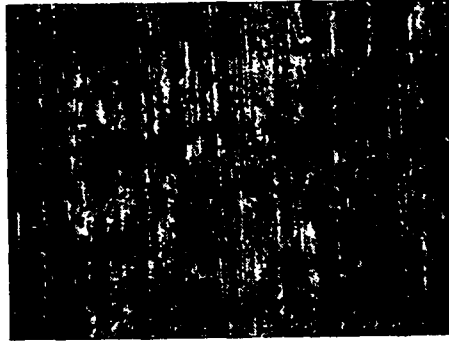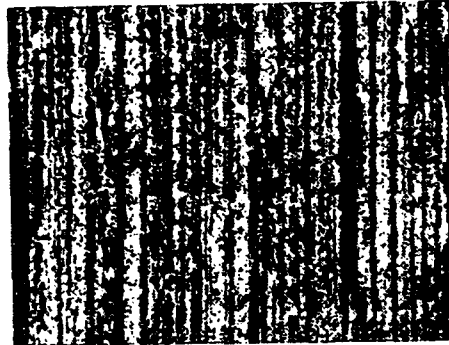
4 µm

Fig. 11 Surface appearance by SEM of 22Cr steel after tested in the DFT experiment 2

2480
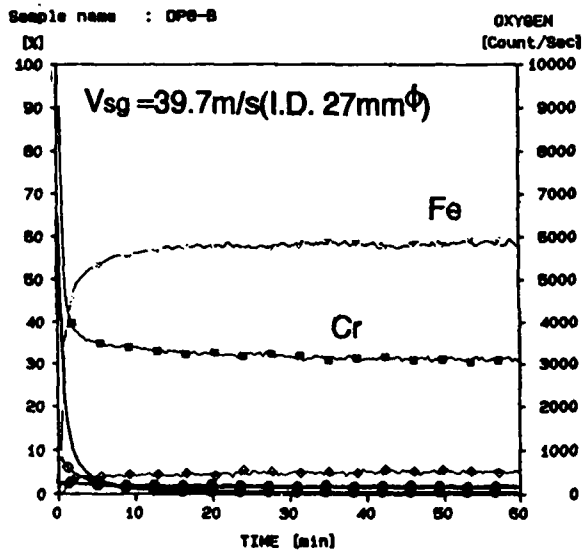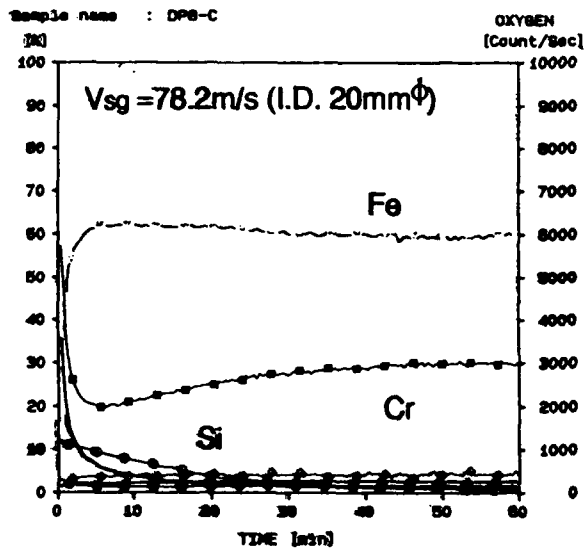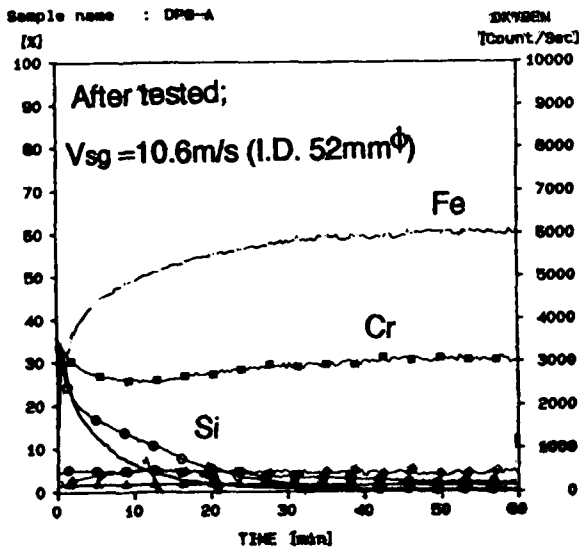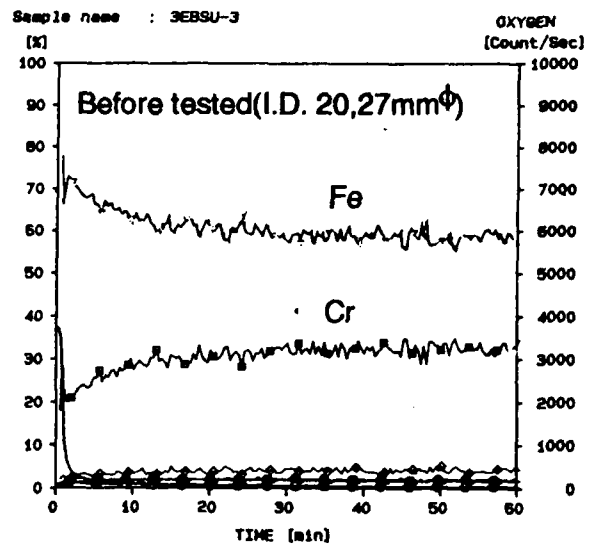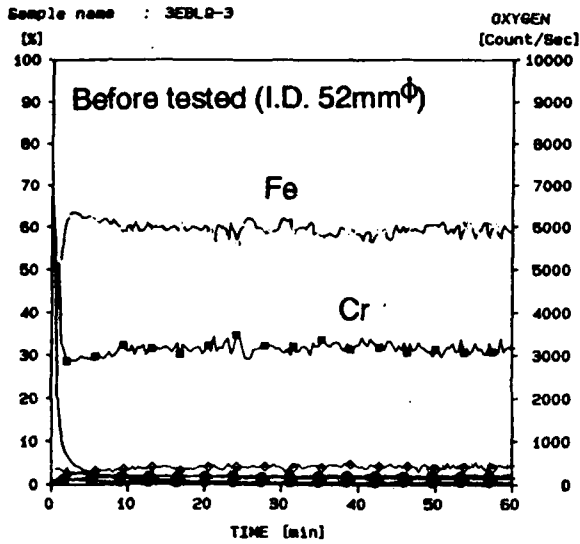
Fig. 12 Depth analysis by IMMA of surface film of 22Cr steel before and after tested in the Di-T experiment 2

The Effect of Temperature on Sulphide Stress Corrosion Cracking Resistance of Martensitic Stainless Steels used in Oil and Gas Industry

T. Cheldi, A. Kopliku
Agip S.p.A., 20097 San Donato Milanese, Milano, Italy

A.Cigada, M.Cabrini
Dipartimento di Chimica Fisica Applicata, Politecnico di Milano, Piazza L. da Vinci, 32, 20133, Milano, Italy

G. Rondelli, B.Vicentini
CNR - Istituto Tecnologia Materiali - Via Bassini, 15, 20133, Milano, Italy

Abstract

Environmental cracking of two martensitic stainless steels types AISI 410 and F6NM in 20g/L NaCl, pH_2S 0.016 - 0.3 bar and pCO_2 3 bar was evaluated by Constant Deformation (CD) tests and Slow Strain Rate (SSR) test ($\dot{\epsilon} = 2.17 \times 10^{-6}$) at room temperature, 60°C and 125°C. Tests conducted on CD specimens showed better cracking behaviour of F6NM, and a decrease of cracking severity from room temperature to 125°C. SSR tests showed that the steels studied are highly susceptible to environmental cracking also at pH_2S 0.016 bar. An inverse trend of cracking severity vs temperature compared with CD tests was detected by SSR technique. Finally SSR tests carried out in absence of H_2S evidenced no cracking susceptibility.

Key Words: 13%Cr Martensitic Stainless Steels, F6NM, Sulphide Stress Corrosion Cracking, Hydrogen Embritlement, Weel Head.

Introduction

The oil and gas industry interest as regards martensitic stainless steels is greatly increasing in the last years thanks to their good resistance to uniform corrosion at high CO_2 partial pressure. Many authors[1-5] have studied the corrosion behaviour of those steels, in particular for a possible use in low pH environments due to CO_2 presence and in absence or at low H_2S partial pressure limited to traces (a few mbar). If H_2S is present, even at limited levels, the main problem to consider is the Sulphide Stress Corrosion Cracking (SSCC): the high susceptibility of this class of materials to SSCC limit its use for high applied stress values, limiting the field applicability to less stressed components as valves or well head. In fact several failure analysis of martensitic stainless steel components are reported in literature[6-7].

In order to characterize the behaviour of steels for well heads it is not easy to fix the exact environmental parameters: in particular the system temperature is not constant, contrarily to the bottom hole system, but depends on operating conditions. For example during shut down the temperature changes from flowing production fluid to ambient temperature, crossing a large spectrum of intermediate values. For these reasons it is very important to study the SSCC of martensitic stainless steels in presence of H_2S, CO_2 and Cl⁻ and, in particular, its dependence on temperature.

The aim of this work has been the determination of the dependence of temperature as regards the SSCC resistance of martensitic stainless steels type AISI 410 and F6NM in simulating oil field environments.

Experimental

Materials

The specimens were obtained from two billets (300mm×300mm×300mm) of AISI 410 Vacuum Melted and F6NM steels. The billets were processed by hot forging, quenching and double tempering. Table 1 reports the chemical composition of the examined materials, the performed heat treatment are reported in Table 2. The microstructure of the steels consists primarily of quenched and tempered martensite; grain size was 5.5 for AISI 410 and 5 for F6NM steel. The mechanical properties are given in Table 3.

Test Environments

Constant Deformation (CD) and Slow Strain Rate (SSR) tests were performed in the following environment simulating the aggressive conditions of an oil field:

A)   20 g/L NaCl, pH_2S 0.3 bar, pCO_2 3 bar

SSR tests were also performed in the following environments:

B)   20 g/L NaCl, pH_2S 0 bar, pCO_2 3 bar
C)   20 g/L NaCl, pH_2S 0.016 bar, pCO_2 3 bar

The tests were carried out at Room Temperature (RT), 60 and 125°C.

Stress Corrosion Tests

The stress corrosion behaviour of the steels was detected by CD tests and constant SSR tests. CD and SSR specimens were obtained from the billets by machining and final grinding; surface finishing with No 1200 emery paper and ultrasonically degreasing in acetone were carried out. CD tests were performed in 1.5 L autoclaves made of alloy C-276; 63.3±1.3mm long, 4.57± 0.13mm large, 1.52±0.03mm thick specimens were utilised. Galvanic coupling between the specimens and the specimens holders was avoided by insertion of glass insulators. The specimens were loaded at stress levels ranging from 40 to 100% of the yield strength according to ASTM G39-90 Standard Practice. The exposure time was 720 hours. At the end of the tests the specimens were observed at 50x magnification under a stereo microscope to detect cracks presence.

For the SSR tests a 0.45 L autoclave, made of alloy C-276 was utilised. Care was taken to avoid galvanic contact among the specimens and between each specimen and the autoclave; for SSR tests the specimens were electrically insulated from the autoclave using suitable gaskets made of hot-oxided Zircaloy-2. SSR tests were performed on subside cylindrical tensile specimens according to NACE TM0177-90. The SSR tests were conducted on a four position slow strain rate testing machine, having a maximum load of 30 kN and 2.18·10⁻⁵

mm/N compliance. Tests were carried out at a clevis displacement rate of $5.62 \cdot 10^{-5}$ mm/s corresponding to a strain rate of $2.17 \cdot 10^{-6}$ s^{-1}. At the end of the tests the specimens were observed at 50x magnification under stereo microscope and the reduction of area was determined.

The values of the parameters: elongation to fracture (El_{tot}), maximum stress (σ_{max}), reduction of area (RA) obtained in aggressive medium were compared with those obtained in glycerine.

After arranging the specimens in the autoclaves, a 24 hours deaeration step by means of a constant flow of high purity nitrogen, was performed, for both the solution and the autoclave. The autoclaves were then filled with the aggressive solution and the deaeration process was carried out for further 24 hours. Hence a 6 hours saturation step of the solution using the selected gaseous mixture CO_2/H_2S at room temperature and atmospheric pressure was conducted. The autoclaves were pressurized with CO_2 at RT and, finally, heated up to the selected temperature.

Results and Discussion

The understanding of environmental cracking behaviour of 13%Cr type martensitic stainless steels in $H_2S/Cl^-/CO_2$ media is complex since the parameters that play a role in cracking phenomena can be differently influenced by changes in the experimental test conditions. The main features of the sulphide stress corrosion cracking can be summarised as follows:

- the incidence of pitting is increased by dissolved H_2S[8-9] and there is a synergic action between H_2S and chloride ions in promoting pits[10].

- often cracking is associated with pits[5.10.11];

- in sour environments the complementary counter reaction to pits onset is the hydrogen evolution, whose recombination to hydrogen molecular is inhibited by H_2S; hydrogen absorption or adsorption at the bottom of pits gives rise to cracking by Hydrogen Embritlement (HE) mechanism[12.13.14].

In the literature there is not complete agreement on the above scheme of cracking mechanism; in particular some authors[9.10] suggest an involvement, in the overall fracture mechanism, of anodic dissolution of the crack tip. Other factors, such as the formation at high temperatures, in presence of CO_2, of covering films which act as barrier against corrosion and hydrogen uptake should also be considered[15].

SSR tests in absence of H_2S, whose results are reported on tables 4 and 5, were carried out to verify if, in the experimental conditions adopted, the steels studied are susceptible to stress corrosion by active dissolution at the crack tip. In some cases, in particular on AISI 410 steel, RA ratios sensibly lower than 1 were detected and at the end of tests many pits were observed on the specimen gage length. However fractographic examination clearly pointed out the absence of stress corrosion since no secondary cracks outside the necked region and no brittle areas on the fractur surface were found. The low RA ratios observed also in absence of stress corrosion are ascribable to the coalescence of several pits that give rise to the final fracture (Figure 1).

The results of tests conducted in H_2S bearing media on CD specimens are reported in figure 2 and can be condensed as follows:

- the F6NM steel shows better cracking resistance than AISI 410;

- the cracking severity decreases from RT to 125°C.

The first result can be explained taking into account the role played by pitting on cracking process; the better pitting corrosion resistance of F6NM, found also in previous experiments[16] and related to the beneficial effect of Mo, Ni and to the reduced carbon content[17], can account for its better cracking behaviour. Figure 3 shows an example of the microscopic nature of cracking observed on AISI 410 CD specimens.

The second outcome fits the generally accepted picture of cracking behaviour for martensitic stainless steels in sour media[2] and can be explained considering the key role played by HE, whose severity is highest at room temperature.

The results of SSR tests in H_2S bearing media, reported in tables 4-5 and figure 4, can be summarised as follows:

- both materials are highly susceptible to cracking in all experimental conditions adopted;

- the severity of test increases by increasing the temperature.

Regarding the first point it has been reported[18] that SSR technique is more severe than other tests like CD; it is conceivable that, since this test gives rise in the present experimental conditions to severe cracking, no differentiation between the two steels considered can be made. An example of the fracture surface aspect observed in SSR tests is reported in figure 5. Regarding the second aspect it should be outlined that the trend detected does not fit the generally accepted cracking behaviour picture, revealed also in our CD tests; however our data are in accordance with SSR test results of other authors[13].

Even though a reasonable explanation has not been found it can be thought that the temperature effect is mainly related to the presence of a slow and continuous straining that, on one hand emphasises the destabilization of passive film[19] and increases pitting corrosion tendency (Figure 6), and on the other hand substantially modify the transport mechanism of hydrogen inside the material, that is not any more determined by diffusion processes.

Conclusions

On the basis of our data the following conclusions can be drawn:

- Constant Deformation tests indicated that F6NM steel has better cracking resistance than AISI 410 steel; this is related to the better pitting resistance of F6NM steel;

- Constant Deformation tests pointed out that the severity of cracking decreases from Room Temperature to 125°C, while SSR tests pointed out an inverse trend;

- Slow Strain Rate tests showed cracking on both steels and in all experimental conditions also at pH_2S 0.016 bar;

- Slow Strain Rate tests conducted in absence of H_2S evidenced no cracking susceptibility.

References

(1) A.Ikeda, M.Ueda e S.Mukai, "CO_2 Corrosion Behaviour and Mechanism of Carbon Steel and Alloy Steel", CORROSION/83, paper no. 45, (Houston, TX: National Association of Corrosion Engineers, 1983).

(2) M.F.Galis e J.J.Damman, "13 Percent Chromium Steels for Slightly Sour Service", CORROSION/91, paper 20, (Houston, TX: National Association of Corrosion Engineers, 1991).

(3) U.Lotz e T.Sydberger, Corrosion, 44 11 (1988): p. 800.

(4) M.F.Galis e J.P.Peter, "Corrosion Behaviour of martensitic and Duplex Stainless Steels tubes for Oil and Gas Wells", 11th ICC, Florence, Italy, 2-6 April 1990, Vol.4, p.483.

(5) A.K.Agrawal, W.N.Stiegelmeyer e J.H.Payer, Materials Performance, 26 3(1987): p. 24.

(6) J.D.Alkire, S.W.Ciaraldi, "Failures of Martensitic Stainless Steels in sweet and sour Gas Service", CORROSION/88, paper 210, (Houston, TX: National Association of Corrosion Engineers, 1988).

(7) R.M.Thompson G.B.Kohut, D.R.Canfield e W.R.Bass, "Sulphide Stress Cracking Failures of 12Cr and 17-4 PH Stainless Steels weel Head Equipment", CORROSION/90, paper 53, (Houston, TX: National Association of Corrosion Engineers, 1990).

(8) Y.Yoshino and A.Ikegaya, Corrosion, 41 2 (1985): p. 105.

(9) F.Mancia, Corrosion Science, 27 10/11 (1987): p.1225.

(10) J.E.Truman, International Metals Review, 26 6 (1981): p. 301.

(11) M.Pressouyre, L.Bretin, and C.Zmudzinski, "New Steels for Use in H_2S Environment", CORROSION/81, paper 181, (Houston, TX: National Association of Corrosion Engineers, 1981).

(12) B.E.Wilde, Corrosion, 27 8 (1971): p. 326.

(13) W.J.Sisak, R.D.Cadwell, "Stress Corrosion Cracking of F6NM Stainless Steel in $H_2S/CO_2/S$ Environments", CORROSION/91, paper 12, (Houston, TX: National Association of Corrosion Engineers, 1991).

(14) M.Ueda, T.Kushida, K.Kondo and T.Kudo, "Corrosion Resistance of 13Cr-5Ni-2Mo Martensitic Stainless Steel in CO_2 environment containing a small amount of H_2S", CORROSION/92, paper 55, (Houston, TX: National Association of Corrosion Engineers, 1992).

(15) A.Ikeda, S.Mukai, M.Ueda, "Prevention of CO_2 Corrosion of Line Pipe and Oil Country Tubulars Goods" CORROSION/84, paper 289, (Houston, TX: National Association of Corrosion Engineers, 1984).

(16) A.Cigada, M.Cabrini, G.Rondelli, B.Vicentini, T.Cheldi, A.Kopliku, G.Fontana, "Corrosion Behavior in Sour Gas of Hot Forged Stainless Steels", 10th European Corrosion Congress, in press.

(17) M.O.Speidel, R.M.Pedrazzoli, "High Nitrogen Stainless Steels in Chloride Solutions", CORROSION/92, paper 398 (Houston, TX: National Association of Corrosion Engineers, 1992).

(18) H.Eriksson, S.Berhardsson, "The Applicability of Duplex Steels in Sour Environments", CORROSION/90, paper 64, (Houston, TX: National Association of Corrosion Engineers, 1990).

(19) M.Saenz de Santa Maria and A.Turnbull, Corrosion Science, 29 1 (1989): p. 69.

Table 1: Chemical composition of the tested steels (%)

Materials	C	Si	Mn	S	P	Cr	Ni	Mo
AISI 410	0.14	0.16	0.64	0.011	0.021	11.79	0.54	-
F6NM	0.03	0.3	0.51	0.008	0.025	12.4	3.5	0.37

Table 2: Heat Treatments of the tested steels

Heat Treatments / Materials	Austenitizing	Quenching	1st Tempering	Cooling medium	2nd Tempering	Cooling medium
AISI 410	940°C for 3.5 hours	Water	660°C for 5 hours	Water	620°C for 5 hours	Water
F6NM	1020°C for 4 hours	Oil	670°C for 6 hours	Air	630°C for 6 hours	Air

Table 3: Mechanical properties of the tested steels

Materials	YS (0.2%) (MPa)	UTS (MPa)	E (25mm) (%)	RA (%)	HRB	Transition Temperature (°C)	Impact Energy at 0°C (J)
AISI 410	600	760	20	54	-	45	26
F6NM	585	784	22	60	243	-95	168

Table 4: Results of SSR tests on AISI 410 steel

Environment	Temperature	σ_{max} (MPa)	σ_{max} ratio	El_{tot} (mm)	El_{tot} ratio	RA (%)	RA ratio
inert	60°C	693	-	3.4	-	65.4	-
A 20g/L NaCl, pH$_2$S 0.3bar, pCO$_2$ 3 bar	RT	667	0.96	1.7	0.50	11.3	0.17
	60°C	597	0.86	1.0	0.29	12.9	0.20
	125°C	592	0.85	0.7	0.21	8.6	0.13
B 20g/L NaCl, pH$_2$S 0 bar, pCO$_2$ 3 bar	RT	710	1	3.3	0.97	38.6	0.59
	60°C	670	0.97	3.6	1	37.7	0.58
	125°C	656	0.95	3.6	1	56.3	0.86
C 20g/L NaCl, pH$_2$S 0.016 bar, pCO$_2$ 3bar	RT	731	1	1.3	0.38	6.9	0.11
	60°C	669	0.97	1.1	0.32	1.2	0.02
	125°C	674	0.97	1.5	0.44	8.1	0.12

Table 5: Results of SSR tests on F6NM steel

Environment	Temperature	σ_{max} (MPa)	σ_{max} ratio	El_{tot} (mm)	El_{tot} ratio	RA (%)	RA ratio
inert	60°C	736	-	4.3	-	72.2	-
A 20g/L NaCl, pH$_2$S 0.3bar, pCO$_2$ 3 bar	RT	721	0.98	1.8	0.42	10.4	0.14
	60°C	648	0.88	1.5	0.35	6.1	0.08
	125°C	634	0.86	1.4	0.33	2.4	0.03
B 20g/L NaCl, pH$_2$S 0 bar, pCO$_2$ 3 bar	RT	781	1	5.0	1.16	64.2	0.89
	60°C	744	1	4.6	1	68.9	0.95
	125°C	714	0.97	4.2	0.98	62.2	0.86
C 20g/L NaCl, pH$_2$S 0.016 bar, pCO$_2$ 3bar	RT	779	1	2.7	0.63	10.8	0.15
	60°C	656	0.89	1.9	0.44	4.6	0.06
	125°C	652	0.89	1.9	0.44	16.3	0.23
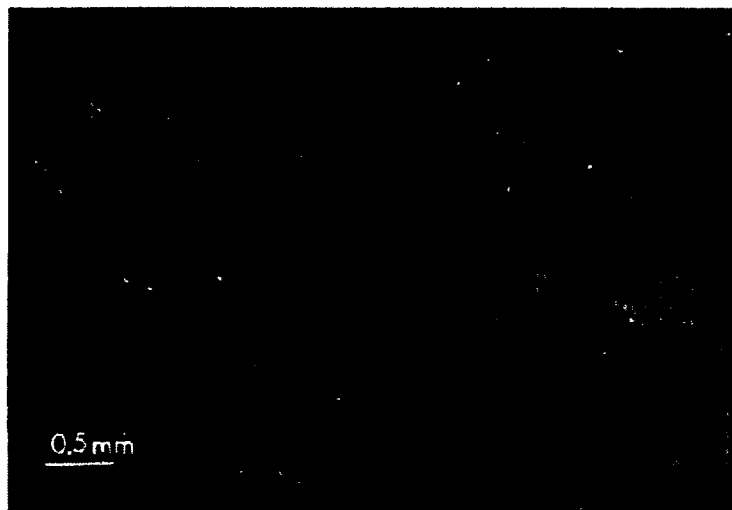
Figure 1: Microscopic nature of fracture of AISI 410 steel after SSR test in 20 g/L NaCl at 60°C in absence of H_2S

NO SCC ■ SCC
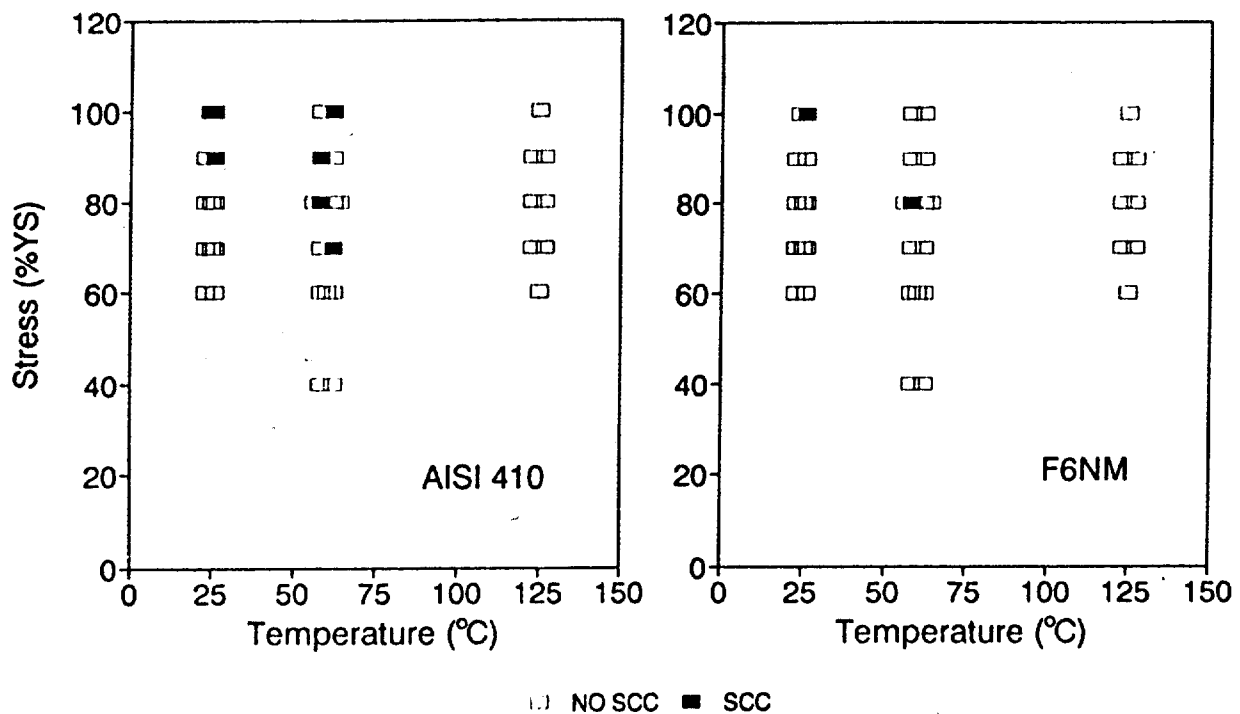
Figure 2: Results of Three Point-Bent-Beam tests conducted in 20 g/L NaCl, pH_2S 0.3 bar, pCO_2 3 bar
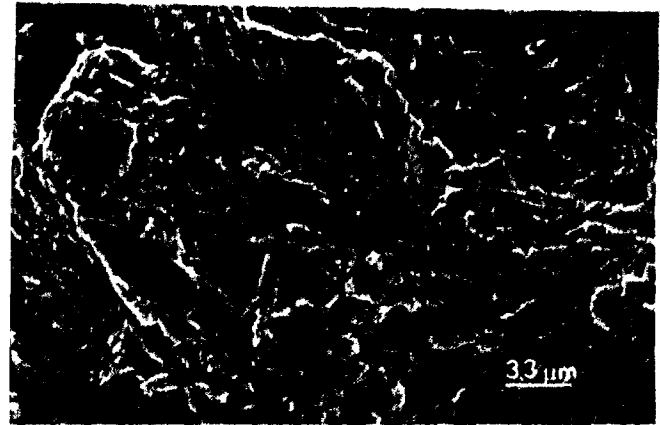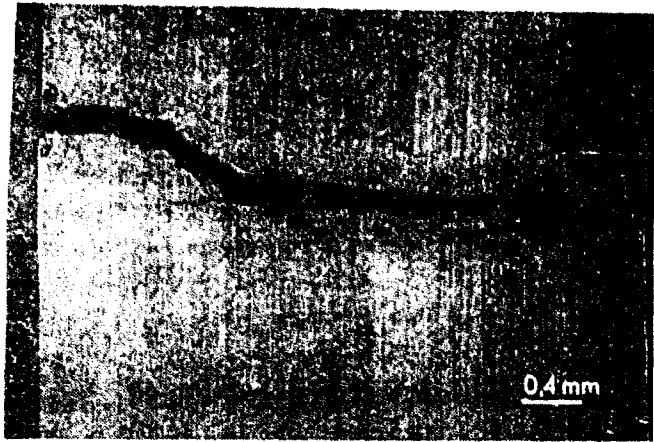
A

B

Figure 3   Microscopic nature of cracking of AISI 410 steel Three Point-Bent-Beam specimen (90% YS) tested in 20 g/L NaCl pH₂S 0.3 bar, pCO₂ 3 bar at RT, a) pit-initiated crack, b) fracture surface aspect
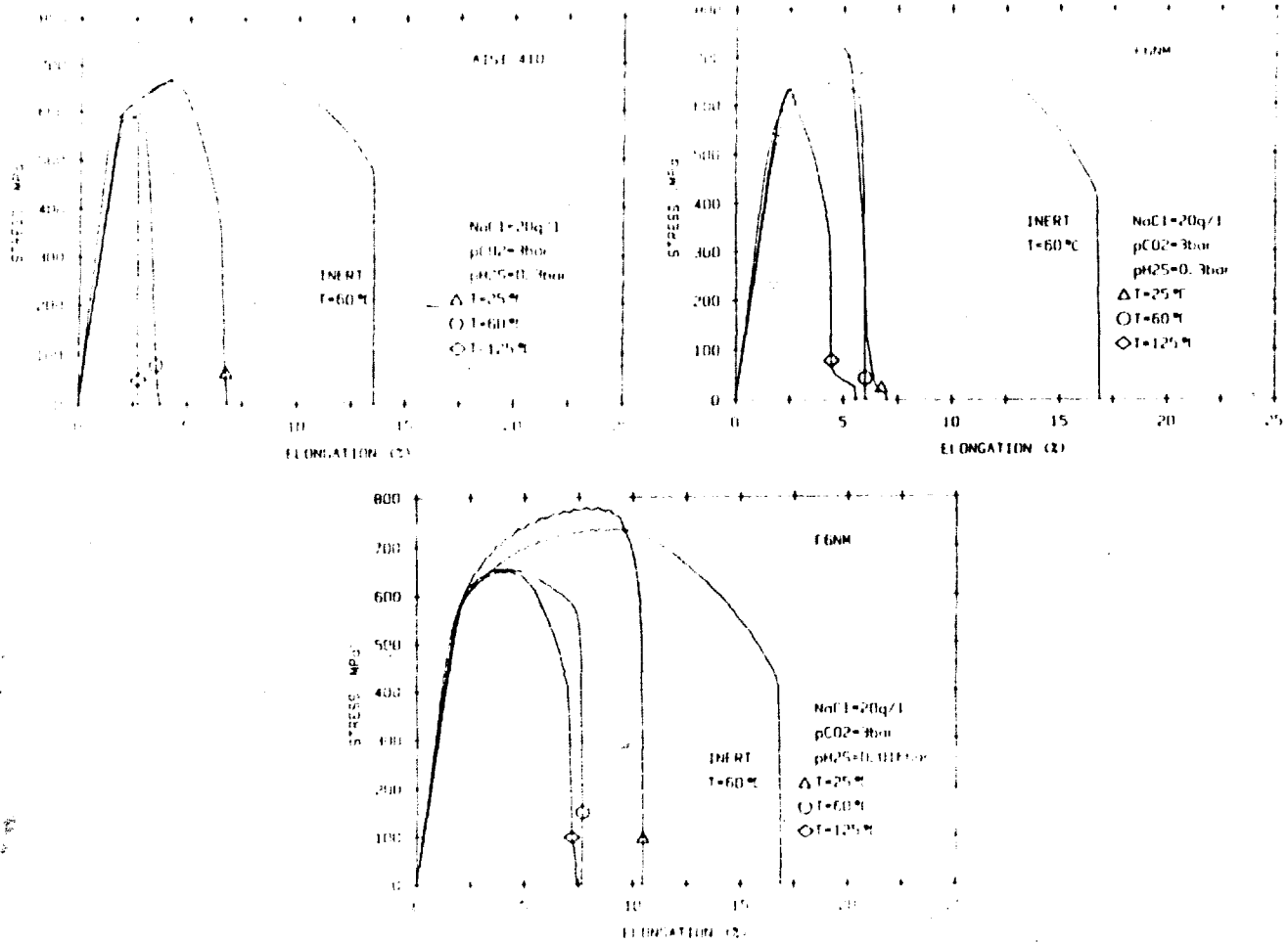
Figure 4   Results of SSR tests

A   B
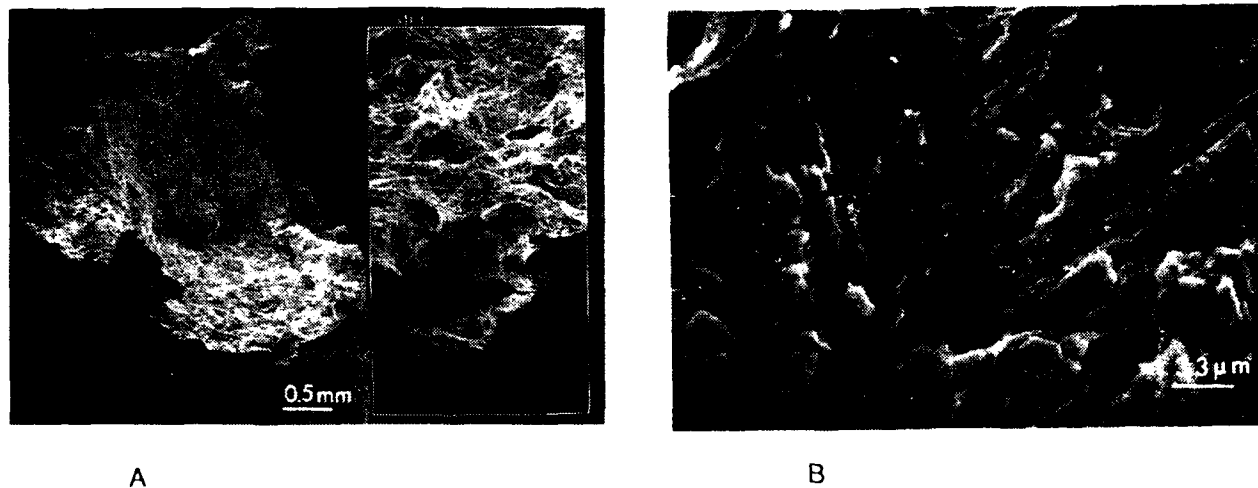
Figure 5 Microscopic nature of cracking of F6NM steel tested in 20 g/L NaCl, pH$_2$S 0.3 bar, pCO$_2$ 3 bar at RT by SSR technique. a) pit-initiated crack, b) fracture surface aspect
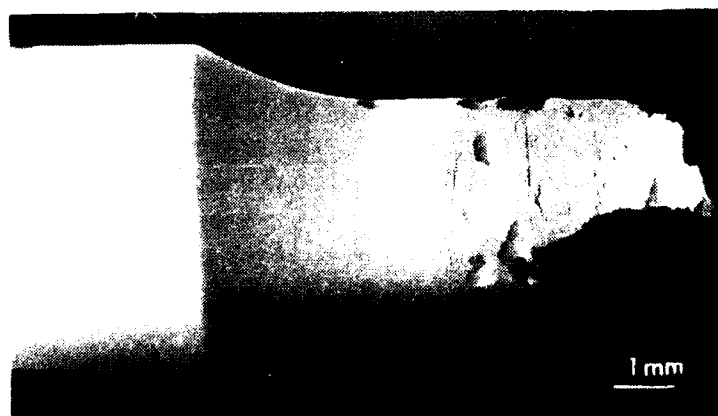
Figure 6 Microscopic nature of pitting attack observed on AISI 410 steel tested in 20 g/L NaCl, pH$_2$S 0.3 bar, pCO$_2$ 3 bar at 60°C by SSR technique, many pits can be observed on the specimen's gage length

Environment Sensitive Cracking of Titanium Alloys in Offshore Equipment

Iñaki Azkarate
INASMET
Camino Portuetxe, 12
20009 San Sebastián Spain

Harvey M. Flower
Imperial College
Prince Consort. South Kensington
SW7 2BP London United Kingdom

Irina Aho-Mantila
VTT. Metals Laboratory
Kemistintie, 3
02150 Espoo Finland

Liv Lunde
Institute for Energy Technology
PO Box 40
2007 Kjeller Norway

Abstract

The behaviour of severall Titanium alloys under different hydrogen uptake conditions has been studied in this work. Hydrogen absorption, hydrogen assisted stress cracking and fatigue crack growth and optical, scanning electron and transmission electron microscopy studies have been performed. It was concluded that the beta phase content is of major importance in the hydrogen absorption and hydriding phenomena. Titanium Grade 12 and 5 have experienced important losses of ductility. Titanium Grade 2 has shown only superficial hydriding but Grade 12 has suffered extensive and deep hydride precipitation.

Key terms: titanium alloys, hydrogen, hydrides, embrittlement.

Introduction

Titanium and its alloys are attractive materials for seawater applications because of their excellent corrosion resistance and "mechanical properties/density" ratio. However, hydriding and hydrogen assisted cracking can be a problem mainly in cases where hydrogen uptake occurs. It is then of paramount importance to study the conditions where hydriding takes place, and the effect of hydrogen and hydrides in the mechanical properties and the cracking mechanism.

The overall objectives of this work have been to study the extent and nature of the hydrogen embrittlement process in comercially pure Titanium and various Titanium alloys, and to assess their suitability to applications, particularly in the offshore oil industry.

Experimental

This work has concentrated mainly on Titanium Grades 2, 5 and 12 alloys, although Titanium Grade 9, Beta-C, Beta 21S and Ti 0,05% Pd, 0,3% Co alloys have been also considered in some parts. Chemical composition and mechanical properties of these materials are given in Tables I and II.
Experimental studies carried out in this work have been concentrated on:

I. Hydrogen absorption.
The influence of various paremeters in the hydriding of Titanium alloys in seawater with relevance to offshore oil applications has been studied. Cathodic charging of Grade 2, 5,

9, 12 and Beta-C Titanium alloys has been carried out in artificial seawater, with CO_2 and H_2S in some tests -700 and -1050 mV (Ag/AgCl) were the potentials used. The effect of some superficial treatments as pickling, anodizing, air oxidizing and sand abrasion on hydrogen absorption has also been studied. The experiments list is given in Table III.

Before inmersion into the cell, specimens (with surface area/volume ratio 10 cm^{-1}) were ground, etched in a HNO_3-HF-H_2O mixture, rinsed in distilled water and dryed in 96 % ethanol. Then the specimens were exposed to air at room temperature for 1 day before inmersion in the cell solution. Abraded and oxidized specimens have also been tested.

The experiments were performed inside a glass jar with no metal parts, except the specimens and the counter electrode (ruthenium oxide coated titanium), within the bath. The counter electrode was placed in its own compartment separated from the cell solution by a glass filter. The cell solution was renewed every two month. The specimens were kept at constant potential by means of a potentiostat.

In the experiments at -1050 mV, automatic pH adjustment were used to mantain the pH constant. In the other experiments it was necessary to add HCl occasionally (only 1-5 times per week). The pH electrode was checked against standard buffer solutions at the same temperature as the test solution at least once a week.

The results obtained show that the following parameters influence the hydrogen absorption in titanium: alloying elements, pH, potential, temperature, hydrogen sulphide and surface treatment. Amount of hydrogen penetrating the surface has been the way selected for reporting data in this section.

I.A. Carbondioxide saturated solutions. The absorption rate of hydrogen in all specimens decreased with time. All specimens, with the exception of grade 12, have a low hydrogen absorption -less than 5µg/cm^{-2}- after one year exposure at a maximum temperature of 95°C and minimun pH of 4. The hydrogen absorption rate in grade 12 is about one decade higher than for the other alpha alloys. Continuous hydride layers are observed even after 10 days at -1050 mV (Ag/AgCl) at pH 4. Hydrogen absorption was also significant at -700 mV (Ag/AgCl) pH 4.0 and 80°C. No effect of the temperature was observed on the absorption of hydrogen for grade 12 whwn tested at pH 4.

The cathodic current densities of all specimens were measured during the experiments. No correlation between the total charge density and the amount of absorbed hydrogen has been found. This result shows that the specimen surface's nature is of major importance for hydrogen absorption.

Hydrogen absorption increased strongly when specimens were tested in the presence of eroding sand. case. The explanation of this finding is that the eroding sand particles destroy the oxide film - which acts as a barrier against hydrogen absorption.

No significant effect of temperature was observed on the rate of hydrogen absorption for grade 12 when tested at pH 4.

Addition of 50 ppm H_2S did not influence the hydrogen absorption rate of any of the specimens when tested at -700 mV (Ag/AgCl) and pH 6.5.

I.B. Nitrogen - saturated solution. Hydrogen absorption rate in nitrogen-saturated solutions was found to be higher than in solutions with carbondioxide; it is suggested that some protective carbonate films are formed, such films being unstable at pH 4. The results of the amount of absorbed hydrogen in the specimens tested at room temperature and 40°C (at -1050 mV Ag/AgCl) are given in Table IV.

At room temperature (with N_2-atmosfhere) precipitated hydrides were found in Titanium grade 2 and grade 9 alloys after 40 days at -1050 mV (Ag/AgCl) and 40°C. Grade 12 had massive hydride layers (Figure 1).

Abraded specimens often had more absorbed hydrogen compared to pickled specimens. Hydrogen content could not in any case be related to the measured cathodic current density. The protective quality of the surface film seemed to be more important than the cathodic charge through the surface.

II. Hydrogen Assisted Stress Cracking (HASC)

The behaviour of titanium alloys in HASC conditions has been studied on two different ways: the first one consisted in testing previously hydrided materials and the second with uncharged materials and "in situ" generation of hydrogen on the specimen surface during the test.

II.A. <u>HASC of previously hydrided Titanium alloys</u>. TiGr-2 and TiGr-12 alloys were cathodically hydrogen charged and heat treated for hydrogen contents of 100, 200, 500 and 700 ppm. Slow strain rate tests were carried out in air with flat tensile specimens. The strain rate used was $3,75.10^{-7}s^{-1}$ although in some cases $2,5.10^{-4}$ and $1,1.10^{-8}s^{-1}$ were also employed.

The results of the slow strain rate tests carried out at room temperature in air with a strain rate of $3,75.10^{-7}s^{-1}$ for grade 2 and 12 specimens did not show any evidence of marked changes in such mechanical properties as yield and tensile strength or elongation as a function of bulk hydrogen content (up to 700 ppm). After the slow strain rate tests, there were several cracks on the side surfaces of the specimens. A narrow brittle zone was to be seen on the fracture surfaces near the side surfaces. The cracks and corresponding narrow brittle zone on the edges of the fracture surfaces may partly be caused by the specimen preparation, e.g., initial cathodic hydrogen charging which has caused high surface hydrogen contents. According to the tests with different strain rates the brittle zone on the fracture surface widened with the lower strain rate.

According to the mechanical tests performed in this study for notched specimens, Titanium Grades 2 and 12 are not affected by bulk hydrogen contents of up to 700 pm. Locally higher hydrogen contents in the surface layer caused the brittle surface cracks noticed in flat tensile test specimens. High surface hydrogen contents con lead to surface nuclei which may grow under stress but according to this study, local hydrogen contents should then be higher than 700 ppm.

II.B. <u>HASC of Titanium alloys with "in situ" hydriding condidions</u>. In this case 3 mm diameter round TiGr-2, TiGr-5 and TiGr-12 alloys specimens were tensile tested at slow strain rate in air and in 3.5% NaCl aqueous solution at room temperature. Hydrogen was cathodically produced on the specimen surface during the test by means of a potentiostat. Three different potentials were used: free potential, -1000 mV and -1500 mV (SEC). Strain rates used were $1,5x10^{-6}$, $3x10^{-7}$ and $2x10^{-7}s^{-1}$. In order to quantify the hydriding of the alloys under different test conditions, samples from the specimens' gauge length were analyzed using an automatic hydrogen analyzer.

Results obtained in tests performed at the strain rate of $2x10^{-7}s^{-1}$ are summarized in figure 2 where maximum load, elongation, true stress at fracture and reduction of area are plotted versus applied polarization potential for each material . Hydrogen analysis results are given in Table V.

TiGr-2 has shown no loss of ductility as a function of the cathodic potential for any of the strain rate used. Hydrogen analysis show that appreciable hydriding does not occur until the -1500 mV cathodic potential is applied to the specimen. This is in agreement with what is observed in the metallographic studies where no hydrides are detected until the highest cathodic polarization is applied; in this case superficial hydriding and some lateral

secondary cracks near the surface were present for all the strain rates used. Secondary cracking was more severe in the specimen tested at the lower strain rate (Figure 3). Specimens' fracture surfaces were studied by means of the scanning electron microscope (SEM). The fracture mode was ductile for all test conditions, even when the highest cathodic potential was applied to the specimen the fracture surface was mainly ductile and only some short brittle areas have been observed in the crak initiation.

Sensitivity to the hydrogen assisted stress cracking has been more evident for TiGr-12 since it has suffered some loss of ductility mainly manifested in the reduction of area and consequently in the true stress at fracture. As in the case of TiGr-2, metallographic studies and hydrogen analysis showed no important hydriding until the highest cathodic potential was applied to the specimen. Figure 4 shows an optical micrograph of a specimen tested at $2.10^{-7}s^{-1}$ strain rate; considerable hydriding with important diffusion of hydrogen towards the bulk material and extensive secondary cracking along the gauge length of the specimens is seen. The fracture mode observed in scanning electron microscope studies is ductile for all testing conditions except when -1500 mV (SCE) polarization is used, case in which a more brittle like manner in the begining of main crack is detected.

Finally, TiGr-5 has been the alloy that has sustained the bigest loss in ductility clearly manifested in the values of elongation, reduction of area and stress at fracture for specimens tested with the highest cathodic polarization. Unlike TiGr-2 and TiGr-12 alloys, no hydride formation nor secondary cracking has been observed in the metallographic study but chcmical analysis show that TiGr-5 specimens tested in the -1500 mV polarization condition have also suffered an important hydrogen uptake. The fracture surface mode observed in SEM studies was ductile for all test conditions except for the specimen polarized at -1500 mV, which has shown a large area with brittle fracture mode.

III. Hydrogen assisted fatigue crack growth (HAFCG).

Corrosion fatigue studies have been carried out with TiGr-2 (base and TIG welded), TiGr-5 and TiGr-12 alloys. Three and six mm thick CT specimens according to ASTM E 647-88a have been tested at room temperature in air and in 3,5 % NaCl aqueous solution using a servohydraulic closed loop universal testing machine equiped with a plastic cell. In order to study the effect of hydrogen on the fatigue crack growth rate the specimens were electrochemically polarized during the test to several cathodic potentials up to -1500 mV (SCE).

Fatigue tests were performed under load control with sinusoidal load wave form, 2 and 0,2 Hz frecuencies and 0,5 and 0,7 load ratios. Crack length was measured by using a travelling microscope and a clip gauge. A special arrangement which transfered the crack opening motion above the water level, where the opening was measured by the clip gauge, was used. Crack length was defined using the compliance method and recorded in a computer as a fuction of cycles. The crack growth rate analysis was carried out according to the polynomial fit method of the ASTM E 647-88a standard.

The results obtained in these tests showed no important effect of the enviroment on the fatigue crack growth rate (da/dN) versus increment of the stress intensity factor (ΔK) for Ti Gr-2, in both base and welded materials, and Ti Gr-12 alloys (Figures 5 and 6). The effect of the testing enviroment and the hydrogen produced on the specimen surface during the test has been more evident for the Ti Gr-5 alloy (Figure 6); in this case the crack growth rate was clearly higher for the specimen tested in seawater than for the specimen tested in air, and even higher when the -1000 mV cathodic polarization was applied to the specimen; but when the specimen was polarized to -1500 mV the crack growth rate

decreased to values similar to those obtained in air.

IV. Microstructural characterisation and mechanism of embrittlement.

Optical, transmission electron and scanning electron microscopy methods were used to study the microstructural characterisation of the materials before and after the exposure to a hydriding environment.

All samples were initially electropolished using standard procedures for Titanium, in order to obtain a standard surface for hydrogen-charging. The hydrogen-charging was electrochemical, the samples being immersed in 0.1M sulphuric acid and made negative with respect to the stainless steel container, various potential differences being used, in all cases a current density on the exposed sample surface of 10mA/cm^2 being maintained. The experiments were conducted at room temperature, and the charging times were from 1 to 20 days. The solution was renewed every 5 days for the longer charging periods, and the current was maintained by having a load resistance at least 10 times the resistance of the charging cell in series with it, thus preventing a current variation of more than 10 %.

IV.A. <u>Study of Titanium Grade 2</u>. Tensile specimens of 5 x 15 mm gauge were stamped and drilled from a 0,5 mm thick Ti Gr-2 sheet. The presence of substantial quantities of an iron-rich grain boundary phase were revealed by transmission electron microscopy (TEM) in combination with energy-dispersive X-ray (EDX) analysis. Some of the specimens were annealed at 800°C and others were annealed at 950°C, both for half an hour under argon, followed by air cooling. The lower annealing temperature, below the alpha-beta transus, produced an equiaxed alpha structure, grain size 50 microns; the higher temperature produced the transformed beta structure of lamellar alpha grains within the prior beta grain structure, the alpha grains being 20 x 200 microns.

The samples were hydrogen-charged for periods up to 14 days and examined using the optical microscope. The transformed beta structure showed no effects but the equiaxed structure showed needle-shaped intragranular precipitates after short hydrogen-charging periods, which were replaced by larger transgranular whiskers after longer periods. These precipitates were confirmed as titanium hydride, TiH$_2$, by means of electron diffraction in the TEM. The hydrides were seen in both types of samples in the TEM, but only in thin foils made from near-surface regions of these. A diffraction study of hydrides and matrix gave an orientation relationship.

$$\{111\}_H//\{1\bar{1}01\}_{Ti}$$
$$<011>_H//<2\bar{1}\bar{1}3>_{Ti}$$

The samples were tested in tension to faliure at strain rate of 2.5 x 10^{-4} s^{-1}. A trend of a slight increase in ductility for increasing hydriding times was noticed for both microstructures, the opposite of what had been expected. Fractography in the scanning electron microscope (SEM) revealed, however, a layer of intergranular fracture at he surfaces of the hydrided samples, not present in the unhydrided samples, which showed entirely ductile fracture characteristics. The surface layer was observed after 3 days charging in the trasformed beta samples, but only after 14 days charging in the equiaxed samples. This, it was surmised, was due to the higher grain boundary density in the former. Hydrogen is thus believed to partition to the grain boundaries in this material.

IV.B. <u>Study of Titanium Grade 12</u>

The alpha-beta transition in grade 12 was determined to be between 800 and 850°C, and annealing above this temperature for 1 hour produced a basketweave-type structure, annealing just below for 24 hours produced an equiaxed structure with some residual deformation due to rolling. Tensile specimens were made similar to those described for

grade 2. Hydriding for 20 days at -2.3 v, 10 mA/cm^2 and tensile testing at a strain rate of 2 x 10^{-4}s^{-1} showed that major differences in the hydriding behavior between these microstructures were reflected in major differences in the mechanical behaviour. The unhydrided ductility of the basketweave was about half that of the equiaxed, but after hydriding, basketweave ductility was reduced by 80 % , equiaxed ductility by 60 %. The ductility of the basketweave after hydriding was only 2.5 %, representing very severe embrittlement. The peak stress and yield point were about the same for the unhydrided materials, but hydriding caused them to diverge, the basketweave again being more affected.

The fracture surfaces of these materials, viewed in the SEM, showed distinctive changes, in the equiaxed materials from a typical ductile fracture appearance to a type of ridged fracture surface, and in the basketweave material from a ductile to a flat cleavage fracture appearence.

Polished sections of the specimens were made, as before, perpendicular to the gauge length. These showed, under backscattered imaging, that the grain pattern in the basketweave material had allowed the hydride to completely penetrate the thickness of the sample along beta paths, thus accounting for the severe embrittlement observed. The hydride in the equiaxed material, in contrast, was concentrated in an almost homogeneous layer stopping 100 microns in from the surface. Thus embrittlement of grade 12 is seen to be highly dependent on the distribution of the beta phase, since the actual quantity of hydride in the two materials was about the same.

The thickness of the surface hydride layer in equiaxed grade 12 samples was also measured for various charging times and voltages, keeping the current density constant by employing charging cells of different resistances. For periods of up to 20 days and in the voltage range -2.3 to -0.8v, it was found that the thickness of the layer is directly proportional to charging time and independent of voltage. Thus the total quantity of charge passed should be known in order to assess whether equiaxed grade 12 will become embrittled.

IV.C. In-Situ Straining experiment on Hydrided Titanium Grade 2. The object of this work was to strain, into the plastic region, a pre-hydrided specimen while it was under observation in a high-voltage transmission microscope. This was done in order to study the interaction between growing cracks and hydrides. It was hoped to be able to observe the nucleation of new hydrides from hydrogen in solid solution in the metal in response to the applied stress at a crack tip. This was not observed, possibly because of the duration of the experiments, limited to about 3 hours.

The samples were 1x3 mm, 0.025 mm thick. They were produced by mechanical polishing and finally jet electropolishing to produce the electron-transparent area. The samples were observed at accelerating voltages between 500 and 1000 KeV, and the straining was achieved by means of a stage in which varying the current to a heater wire varied the tension in a spring holding the specimen.

The growth of cracks in the metal was followed, and some cracks were observed to grow along large, pre-existing hydrides. These cracks differed from those in the matrix in their episodic growth, with voids forming ahead of the crack tip and subsequent failure of the connecting hydrides regions. Hence the experiment showed that hydride-assisted cracking seems to occur by a partly ductile failure of the hydrides themselves.

IV.D. Characterisation of Titanium Grade 2, 5 and 12 Hydrogen-Assisted Stress Cracking Specimens. Specimens strained at very slow rates in a hydrogen-charging seawater solution, for various periods up to 300 days, as described in section II.B, were necked but not broken. The cylindrical specimens were sectioned across the hydrided part

of the gauge and metallographically mounted, polished and etched. The specimens were examined optically and by means of secondary and backscattered electrons in the SEM. Hydriding in needles was observed in all types of image, extending 50 microns in from the surface in Titanium grade 2. Hydriding was mainly transgranular. In grade 12 hydriding was observed optically along the grain boundaries. This alloy had an alpha-beta microstructure with elongated grains left over the processing of the material. The identity of the alpha and beta phases was confirmed by electron diffraction in the TEM and partitioning of nickel to the beta phase of the order of 2 % was observed using thin foil EDX analysis. Optically, the hydriding was observed to extend further into the material where the elongated grains intersected the surface at right angles, suggesting hydrogen conduction either down grain boundaries or beta grains. Grade 5 Titanium also had an alpha-beta microstructure with partitioning observed of aluminium to the beta grains and vanadium to the alpha grains as expected. A finer-grained microstructure than in the other materials with some banding was observed, but without the long contiuous paths present in the grade 12. No hydrides were observed in grade 5 using any type of image.

Lateral sections of the cylindrical samples were also made and examined as before in order to study the cracks. In grade 2 these were frequent and blunt, only extending through the hydride layer but not into the metal. In grade 12 the cracks were less frequent, but sharper and typically extending into the material 2-3 times the depth of the hydride layer. This was despite the fact that grade 2 had undergone much greater extension than grade 12, 236 hours as opposed to 165 hours, both at a strain rate of $3 \times 10^{-7} s^{-1}$. In grade 2 the situation appears to reflect the breaking up of a brittle surface film as the metal beneath it extends plastically, while in grade 12 there seems to be genuine internal embrittlement. The cracks in grade 12 did not always have hydrides at their tips, suggesting the possibility of a component of the embrittlement due to interstitial hydrogen.

Titanium grade 12 was studied in the SEM using highly polished, unetched surfaces in the backcattered imaging mode. This showed the morphology clearly owing to the low atomic number hydride appearing darker than the alpha Titanium and the higher mean atomic number, nickel-stabilised beta phase appearing brighter than the alpha Titanium. Electropolishing was avoided where possible in order to preserve the crack shapes, though it was found necessary in grade 5 in order to obtain adequate alpha-beta contrast.

Grade 12 had a typical morphology consisting of polygons of beta surrounding alpha grains and lined with intergranular hydride. Hydride also extended into the alpha grains in transgranular needles in places. Hydrides could be seen following paths of beta phase deep into the sample. This shows a preferential diffusion of hydrogen through the beta phase, but with actual precipitation in the alpha (Figure 7). This conforms with the known facts that hydrogen diffusion is about 100 times faster in beta than in alpha titanium, and that hydrogen solubility is much lower in the alpha than it is in the beta. The hydride layer in grade 12 was typically twice the depth of that in grade 2 specimens, but it was not continuous as it was in grade 2, being related to the microstructure of the beta phase. In these samples the rate of hydride growth in terms of depth was 4 times greater in grade 12 than in grade 2. Grade 5, hydrided for 40 days, exhibited no cracking.

Conclusions

The main conclusions that can be drawn from the results obtained in this work are:
- In Hydrogen absorption studies performed on unloaded specimens:
    * Ti Gr-12 is the alloy that has experienced the highest hydrogen absorption rate and hydride precipitation.
    * Hydrogen absorption rate in nitrogen saturated solutions is considerably higher than in solutions with carbondioxide.
    * Hydrogen absorption rate is higher in abraded than in pickled specimens.
    * The higher the temperature, acidity, cathodic potential and stress level the higher the hydrogen absorption.
- In slow strain rate tests performed in air, bulk hydrogen contents of up to 700 ppm have no effect in the mechanical properties of Ti Gr-2 and Ti Gr-12.
- In slow strain rate test performed in air and seawater with cathodic polarization:
    * No effect of seawater, nor of -1000 mV (SCE) cathodic potential on ductility of Ti Gr-2, Ti Gr-5 and Ti Gr-12 alloys has been observed. No hydriding, nor secondary cracks are noticed.
    * Cathodic potencial of -1500 mV (SCE) produces losses in ductility of Ti Gr-5 and Ti Gr-12 alloys. Superficial hydriding with small secondary cracks are observed for Ti Gr-2, Ti Gr-12 shows more in deep hydriding and larger secondary cracks. No hydriding nor secondary cracks are noticed for Ti Gr-5.
- In hydrogen assisted fatigue crack growth studies.
    * No important effect of seawater nor of cathodic potentiols up to -1500 mV (SCE) on the fatigue crack growth rate is noticed for Ti Gr-2 (base and welded) and Ti Gr-12 alloys.
    * The fatigue crack growth rate of Ti Gr-5 has experimented a clear aceleration when the testing media changes from air to seawater and seawater with -1000 mV (SCE) cathodic polarization, but when the -1500 mV (SCE) potential is aplied, the crack growth rate diminishes.
- Beta phase content and distribution strongly affects Titanium alloys' embritllement.
- The mechanism of embritllement of Ti Gr-12 has been found to be hydrogen conduction down beta paths and hydride precipitation in the alpha. Embrittlement depends of the depth of hydride formation which is dependent on the total quantity of charge passed, for a particular microstructure and temperature.
The hydrogen absorbtion in grade 12 can be minimised by ensuring recovery to an equiaxed structure. This can be done by annealing at 850°C for at least 24 hours (under argon), but care must be taken not to exceed this temperature in order to avoid the undesirable basketweave microstructure.
- Another mechanism seems to be responsible for Ti Gr-5 loss of ductility in slow strain rate tests. Its higher beta phase content admits more hydrogen entering the material by interstitial solid solution without forming hydrides. When the hydrogen content reaches a certain level, lattice decohesion occurs with a brittle rupture.

Acknowledgement

TABLE I. Chemical composition (Weight %).

Alloy	Element														
	N	C	H	Fe	O	Al	V	Mo	Ni	Cr	Zr	Nb	Si	Pd	Co
Ti Gr-2	0,03	0,10	0,015	0,30	0,25	--	--	--	--	--	--	--	--	--	--
Ti Gr-5	0,05	0,10	0,015	0,50	0,40	6,4	3,8	--	--	--	--	--	--	--	--
Ti Gr-12	0,03	0,08	0,015	0,30	0,25	--	--	0,26	0,66	--	--	--	--	--	--
Ti Gr-9	0,02	0,05	0,015	0,30	0,12	3	2.5	--	--	--	--	--	--	--	--
Ti Beta-C	0,03	0,05	0,015	0,03	0,14	3,5	8	4	--	6	4	--	--	--	--
Ti Beta-21S	0,03	0,05	0,015	0,03	0,14	3	--	15	--	--	--	2,6	0,2	--	--
Ti0.05 Pd-0.3Co	0,07	0,10	0,013	0,07	0,30	--	--	--	--	--	--	--	--	0,05	0,3

TABLE II. Mechanical properties.

Alloy	Y.S. 0,2% (PMa)	U.T.S. (MPa)	E (%)
Ti Gr-2 annealed	430	499	31
Ti Gr-5 annealed	988	1030	13
Ti Gr-12 annealed	484	587	20

TABLE III. Hydrogen absorption experiments list.

Exp.	pH	Potential mV(Ag/AgCl)	T(°C)	Gas	Alloys	Duration (days)
1	4.0	-700	80	CO_2	2,5,9,12 beta-C	360
2	4.0	-1050	80	CO_2	2,5,9,12 beta-C	700
3	6.2	-1050	80	N_2	12	12
4	13	-1050	80	CO_2	2,12	41
5	6.5	-700	80	CO_2 + 50 ppm H_2S	2,5,9,12 and beta-C	340
6	4.0	-1050	60	CO_2	12	40
7	4.0	-1050	40	CO_2	12	40
8	4.0	-1050	20	CO_2	12	40
9*	4.0	-1050	80	CO_2	2. (Eroding sand particles)	7
10*	4.0	-700	80	CO_2	2. (Eroding sand particles)	7
11	4.0	-1050	95	CO_2	2,5,9,12, beta-C	440
12	4.0	-1050	80	CC	2. (Co cathodically deposited)	20
13	4.0	-1050	20	N_2	2,5,9,12 beta-C Ti0.05Pd0.3Co	120
14	4.0	-1050	40	N_2	2,5,9,12 beta-C Ti0.05Pd0.3Co	40
15	4.0	-1050	80	N_2	2,5,9,12 beta-C Ti0.05Pd0.3Co	40

TABLE IV. Absorbed hydrogen in $\mu g/mm^{-2}$ after 40 days exposure time. (* Abraded specimens).

Titanium grade	CO_2 -1050mV 80°C	N_2 -1050mV 40°C	N_2 -1050mV RT	
2	0,02-0,09	0,13	0,08	0,21*
5	0,03-0,05	0,16	0,15	0,45*
9	0,12-0,16	0,43	0,02	1,66*
12	0,2-0,7	2,5	0,57	0,34*
β-C	0,02	1,0	0,36	0,50*
β-21S	0,6	1,0	0,07	0,98*

TABLE V. Total hydrogen content (ppm) of tested specimens.

Alloy	Test Conditions		
	Air	-1000 mV	-1500 mV
Ti Gr-2	20	39	232
Ti Gr-12	23	60	320
Ti Gr-5	69	104	253
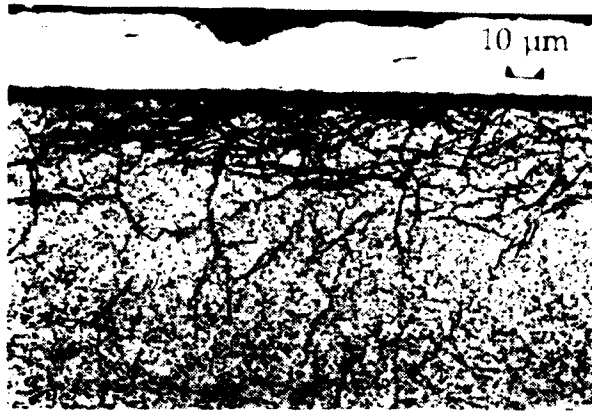
Figure 1. Hydride layer on specimens 12-6 and 12-11 after 40 days at
-1050 mV, pH=4, CO_2 and 80°C. (x400).

ELONGATION (%)

★ Ti Gr-2 ◆ Ti Gr-5 ✦ Ti Gr-12

REDUCTION OF AREA (%)

★ Ti Gr-2 ◆ Ti Gr-5 ✦ Ti Gr-12

MAXIMUM LOAD (MPa)

★ Ti Gr-2 ◆ Ti Gr-5 ✦ Ti Gr-12

TRUE STRESS AT FRACTURE (MPa)

★ Ti Gr-2 ◆ Ti Gr-5 ✦ Ti Gr-12
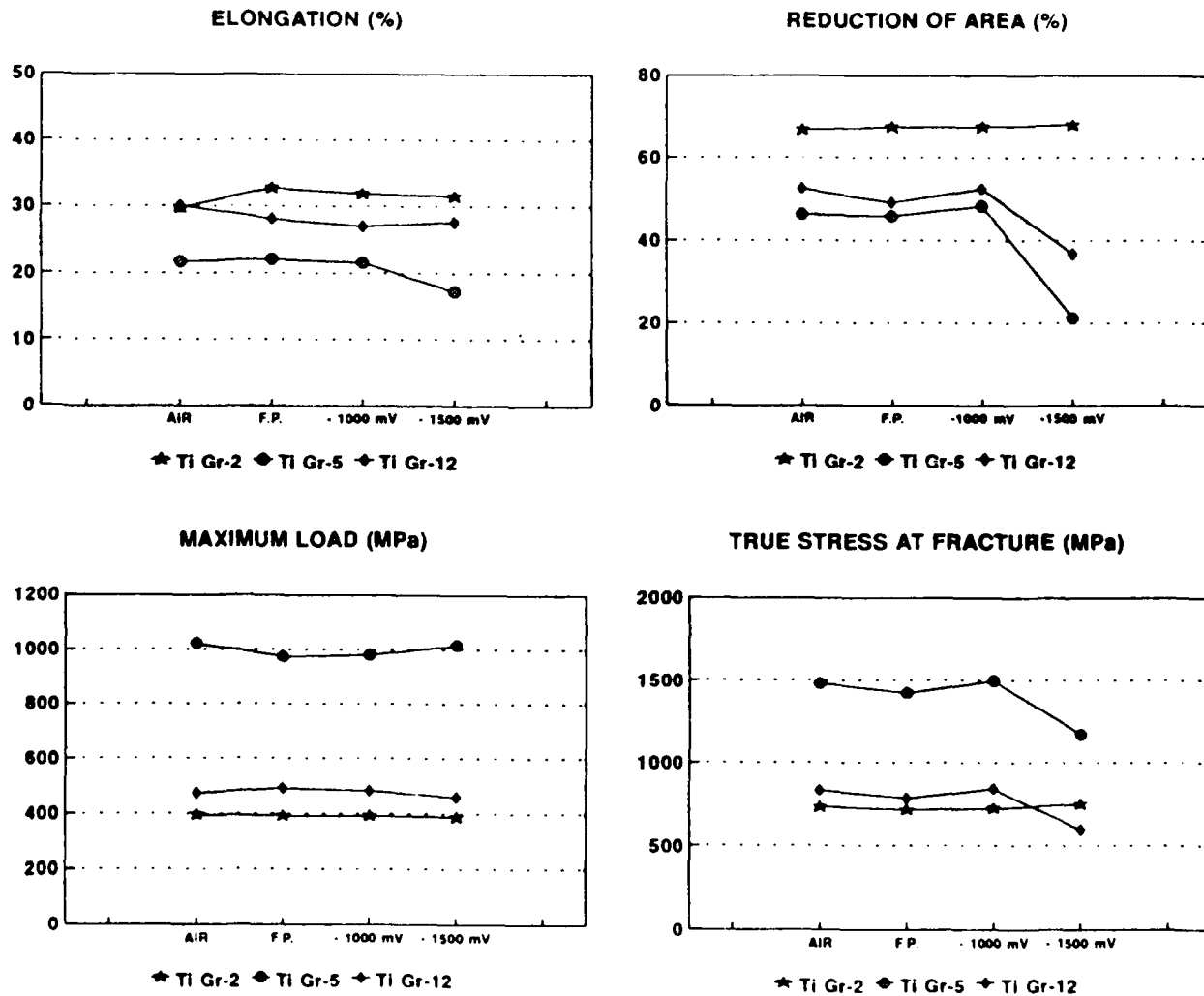
Figure 2. Results of SSRT tests
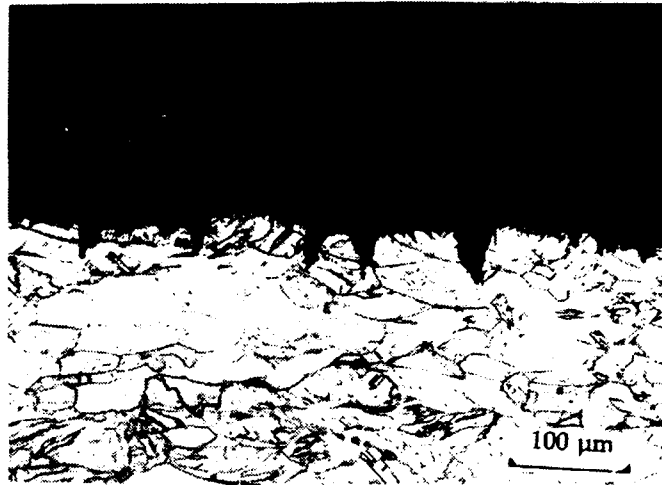
Figure 3. Optical micrograph of TiGr-2 tested at 2 x $10^{-7}s^{-1}$ strain rate with -1500 mV (SCE) cathodic polarization.
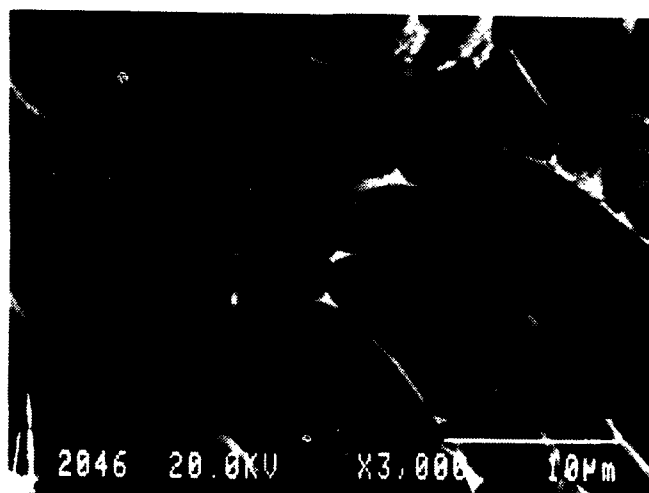
Figure 4. Optical micrograph of TiGr-12 tested at 2 x $10^{-7}s^{-1}$ strain rate with -1500 mV (SCE) cathodic polarization.
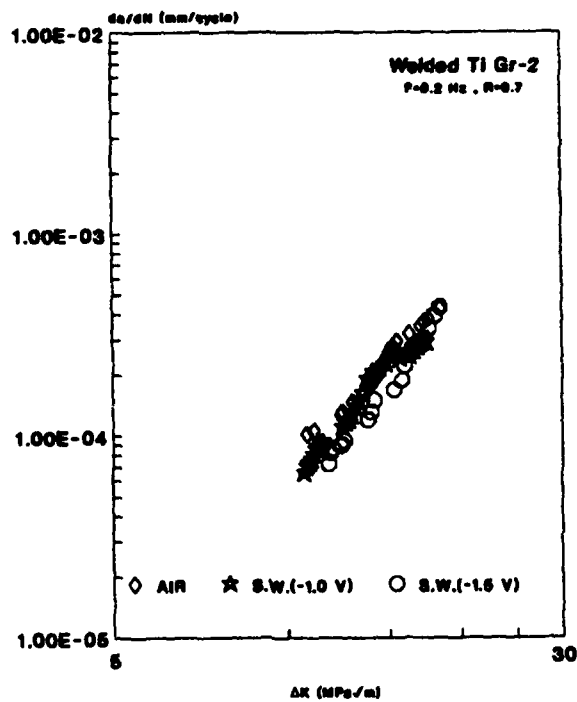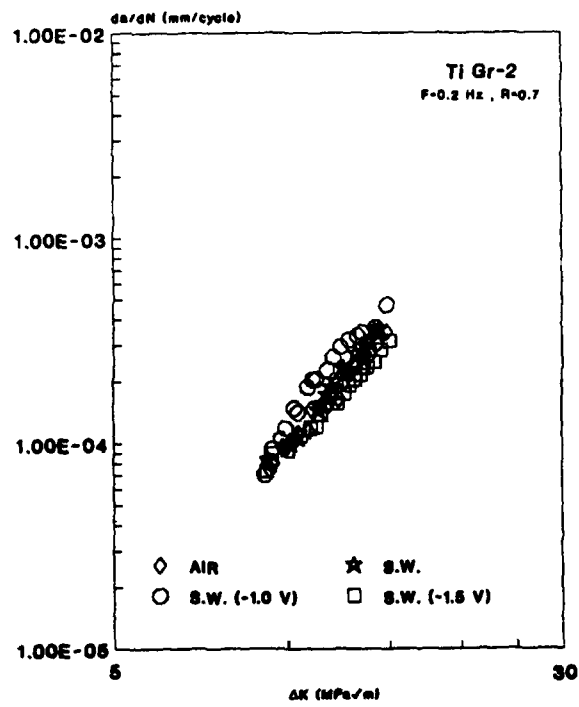
Figure 5. da/dN versus ΔK for TiGr-2 base and TiG welded materials tested in air and seawater with different cathodic polarization.
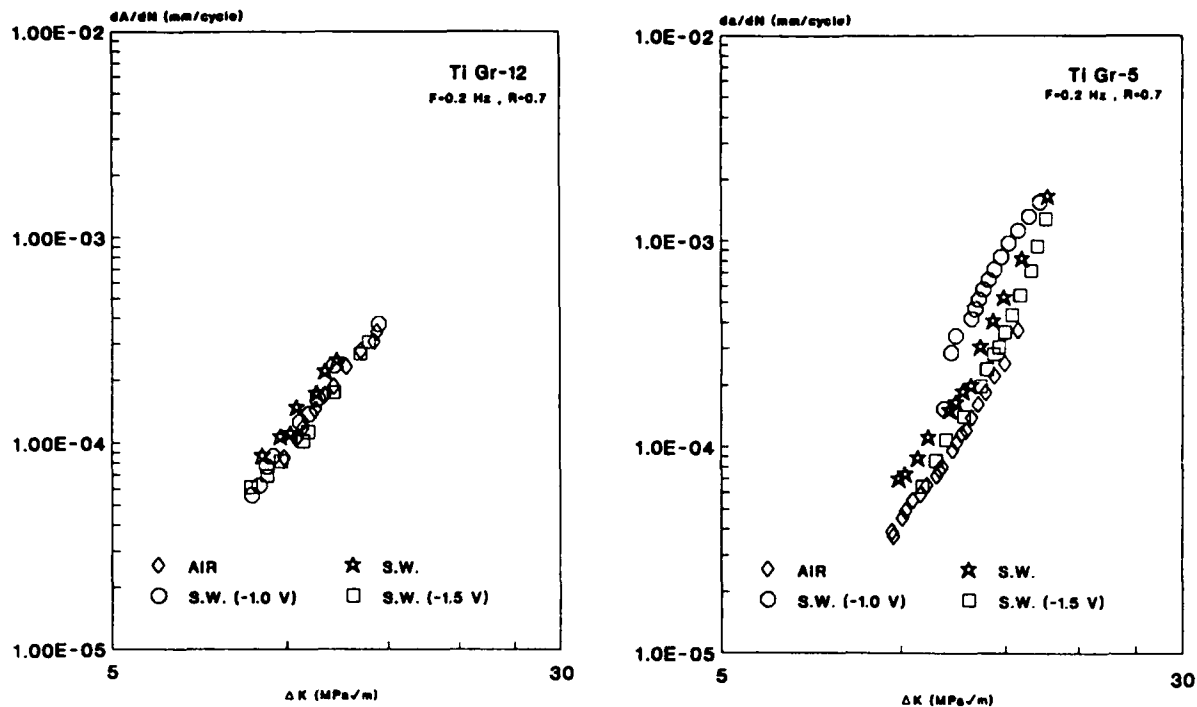
Figure 6. da/dN versus ΔK for Ti Gr-12 and TiGr-5 alloys tested in air and seawater with different cathodic polarization.

Figure 7. Backscattered electron image of TiGr-12 showing hydride
precipitates (black) occurring in the alpha phase (grey) near the
intergranular beta paths (white).

Stress Cracking and Crevice Corrosion Resistance of Pd-enhanced Ti-38644 Titanium Alloy Products In Deep Sour Gas Well Environments

R. W. Schutz and M. Xiao
RMI Titanium Company
1000 Warren Avenue
Niles, OH 44446

J. W. Skogsberg
Chevron Services Company
Drilling Technology Center
2202 Oil Center Court
Houston, TX 77073

Abstract

A substantial, rigorous stress corrosion and crevice corrosion database for Pd-enhanced Ti-38644 alloy pipe and billet mill products has been generated in a worst-case deep sour gas well brine fluid up to 260°C. Long term C-ring, discriminating SSR, and Teflon®-metal crevice test results indicate useful alloy resistance to at least 246°C and 204°C for pipe and billet products, respectively, which are significantly higher than those for the standard Ti-38644 alloy.

Introduction

The quest for vast gas reserves has led to drilling depths of 7,600 - 10,600 meters, where higher downhole temperatures and more aggressive sour brine conditions often prevail. Gas fields currently under development, such as the Mobile Bay (Gulf of Mexico), Madden (W. Wyoming), and Arun (Indonesia) fields, for example, typically produce near-saturated brines at downhole temperatures of 190 - 230°C with H_2S and CO_2 partial pressures exceeding 0.7 MPa, often with elemental sulfur. Only the most resistant CRA's are candidates for these severe sour brine environments, which become limited by chloride crevice corrosion and/or stress corrosion cracking as temperatures increase.

The Ti-38644 beta titanium alloy (Ti-3Al-8V-6Cr-4Zr-4Mo/UNS #R58640) has become an attractive CRA for deep sour gas well applications based on its successful service in hypersaline geothermal brine wells up to 270°C (1), and its known resistance to hot sour brine environments (2-4). Along with superior corrosion resistance, this NACE MR-01-75-approved alloy offers potential design and cost advantages for production tubulars (3), safety valves and other critical deep gas well components based on its elevated strength to density ratio, low modulus, and low thermal expansivity. The standard Ti-38644 alloy, however, has demonstrated finite susceptibility to both chloride crevice and stress corrosion (3,4) in severe laboratory sour brine tests when temperatures exceed approximately 190°C. These corrosion limitations are effectively addressed by enhancing the alloy with 0.04 - 0.1 wt.% Pd, as discussed in prior publications (3,4), thereby expanding the safe, useful temperature limits for this alloy in sour brine media.

This paper is intended to offer a substantial data base for both the stress corrosion cracking (SCC) and crevice corrosion resistance of Pd-enhanced Ti-38644 alloy mill products typically utilized in oilfield applications in a worst-case deep sour gas well brine fluid environment. Conservative laboratory SCC data for mill-produced pipe and billet products are derived from long term (2 - 6 month) C-ring and slow strain rate (SSR) tests. Based on the stress and crevice corrosion temperature thresholds identified from these tests, conservative operating windows for these Pd-enhanced Ti-38644 alloy products are identified, and compared tothose of the standard Ti-38644 alloy.

Experimental

Stress Corrosion Testing

The general test matrix for SCC evaluation of Pd-enhanced Ti-38644 products is outlined in Table 1. Long term (2-6 month) C-ring and slow strain rate (SSR) tests were performed on the cold-pilgered/PASTA pipe and forged/STA billet products described in Table 2. These RMI Titanium Company mill products are representative of alloy stock utilized for deep sour gas well production tubulars, subsurface safety valves, oil tools, and other critical well components. The "PASTA" treatment for Ti-38644 pipe refers to a proprietary final heat treatment process (5) for uniformly aging cold-worked beta titanium alloy products, while providing high ductility and thermal stability. "STA" refers to the solution treat and age treatment traditionally used to strengthen beta titanium alloys.

Test Environment. The C-ring and SSR tests were all conducted in laboratory autoclaves containing a simulated worst-case sour gas well production fluid consisting of:

- fully deaerated 20 wt.% NaCl
- 6.9 MPa (1000 psi) H_2S
- 3.4 MPa (500 psi) CO_2
- 1 or 10 gpl elemental sulfur
- with or without 0.5 wt.% acetic acid

The partial pressures of H_2S and CO_2 indicated are those at test temperature. The addition of either 0.5% acetic acid or 10 gpl sulfur was made in a few tests to create ultra-aggressive test conditions.

Successful simulation of downhole production fluids in laboratory tests requires total deoxygenation within the autoclave. This includes de-adsorption of oxygen from autoclave internals and specimen surfaces and crevices, in conjunction with thorough brine and gas phase deaeration. To achieve this test condition, an autoclave loading procedure was qualified that reproducibly precluded significant oxygen/air contamination. This procedure incorporates multiple autoclave evacuation and argon backfilling cycles at ~150°C once samples are loaded, prior to brine filling. Once filled with argon-spared deaerated brine, the autoclave is sequentially "cold-charged" with liquid H_2S and liquid CO_2 at room temperature. These weighed liquid additions are based on trial gas pressure calibration curves empirically established in prior autoclave heat-up trials. Final autoclave heat-up to test temperature raises the partial pressures to desired values. This technique eliminates the alternative high pressure "hot charge" procedure for H_2S and CO_2 gases, which may increase the risk of leakage and air intrusion into the autoclave.

C-Ring Testing.   C-ring test samples from both Ti-38644/Pd pipe and billet products (Table 2) represented the circumferential orientation of each product. In the case of the billet, the stressed test portion of the C-ring was derived from the billet outer radius. The billet stock for C-ring testing possessed yield strength and hardness values of 1117 MPa and 36.5 HRC, respectively. Billet C-ring samples were 146 mm x 26 mm width x 6.4 mm thick, whereas pipe samples were 73 mm OD x 26 mm width x 7 mm thick in dimension. C-rings were prepared and loaded by deflection measurement in accordance with ASTM G-38 specifications. Specimen surfaces were either as-machined to a 25 RMS finish or, as for a few pipe C-ring samples, in a sandblasted and heavily pickled condition. C-rings were stressed using Ti-38644/Pd alloy bolts, washers, and nuts to avoid galvanic interferences. These samples were loaded to either 80, 90, 95, or 100% of product L-direction yield strength at test temperature. C-ring stressing calculations were based on product yield strength and elastic modulus values measured at test temperature.

Testing was conducted in nonstirred Ti-38644 (non-stirred) titanium autoclaves of 6 - 15 liters in volume, which permitted exposure of 9 - 10 C-rings per autoclave test. C-ring samples were mounted to a central titanium sheet fixture attached to the autoclave lid, as pictured in Figure 1a for pipe samples and in Figure 1b for the billet samples. Most C-ring samples were galvanically-isolated via ceramic washers. The balance of Ti-38644/Pd C-ring samples were galvanically coupled with Ni-Cr-Mo alloys in a 1:1 surface area ratio. Two pipe C-ring samples per autoclave test were coupled to alloy C-276 sheet (see Fig. 1a), whereas duplicate billet C-rings were independently coupled to C-276 and 625 plus®/725 alloy sheets (see Fig. 1b). The number of C-ring samples exposed per product form, test time, temperature and stress level was typically two to three. Post-exposure C-ring evaluation consisted of visual examination for cracking at 1-40X, and if cracking occurred, high magnification SEM examination of sample fracture surfaces.

Slow Strain Rate Testing (SSRT). SSR testing was performed on L-direction samples of 7 mm and 11 mm wall x 73 mm OD Ti-38644/Pd pipe, and on L-direction mid-radius and outer radius samples of the Ti-38644/Pd billet in two conditions.   These billet (STA) conditions represented yield strengths of 1013 MPa (147 ksi) and 1110 MPa (161 ksi).

SSR testing was performed in Ti-38644 titanium autoclaves at a strain rate of $4 \times 10^{-6} \sec^{-1}$ utilizing a 4.8 mm diameter x 25.4 mm length gage (smooth) SSRT sample. Ceramic washers assured electrical isolation of the sample from the load train and autoclave. This strain rate was chosen based on its discriminating traits established in prior Ti-38644 alloy SSR studies in hot sour brines (4). Sample % RA (Reduction of Area) and TTF (Time to Failure) values derived from the test environment were compared (by ratio) to those measured in an inert helium gas atmosphere at each test temperature. Post exposure evaluation of SSRT samples included visual examination of fracture surfaces at 1-40X for secondary cracking, and SEM examination at 50-2000X for fracture mode determination.

Crevice Corrosion Testing

The test matrix for crevice corrosion evaluation of Ti-38644 alloy products in high temperature sour and sweet brines is presented in Table 3. These test brine variations permitted identification of which species (i.e. H_2S and S°) promoted crevice attack in these deaerated NaCl brine exposures. Ti-38644 alloy sheet stock was chosen for alloy crevice corrosion evaluation since the geometries

of billet and pipe products did not readily lend themselves to this mode of testing. Testing was performed on both Pd-enhanced and standard versions of the Ti-38644 alloy to develop a comparative data base in sweet and sour brines. The strength and metallurgical conditions of these sheet test materials (described in Table 2) mimicked those of production tubular products.

The test media, detailed in Table 3, consisted of an argon-spared, deaerated 20% NaCl brine which was loaded into evacuated autoclaves using the same meticulous deaeration procedures described for the SCC tests. However, considering all of the tight Teflon-metal sample crevices involved, it is possible that a limited but finite amount of adsorbed air/oxygen remained within sample crevices. If oxygen was indeed retained within sample test crevices, more aggressive (and conservative) test results would be expected. This is based on the oxidation of sulfur species (H_2S and S°) to highly acidic sulfite/sulfate species within the crevice. The H_2S gas partial pressure in these tests was achieved by direct pressurization from an H_2S gas cylinder. In brine tests where H_2S gas was not injected, brine pH was adjusted to a value of 3.5 at room temperature (using dilute HCl additions) to maintain a consistent brine pH in all tests. Carbon dioxide gas was intentionally omitted from these tests since it tends to buffer brine pH upward and could act to reduce susceptibility of titanium alloys to crevice attack in sour brines.

Each autoclave test included two crevice test assemblies per alloy tested. Each crevice assembly consisted of five 38 x 38 mm alloy sheet coupons interspersed with 25 x 25 x 0.8 mm sheets of virgin PTFE (Teflon)®. These sandwich assemblies, described elsewhere (6), were tighted together via centerline Ti-38644 bolts and nuts to a torque of 40 in·lbs, producing very discriminating, severe gasket-to-metal crevices. Sheet coupons were exposed in the wet-ground (200 grit) and lightly pickled surface condition. Test exposure period was 30 days in all cases.

Results

C-Ring Test Data

The C-ring SCC test data for Pd-enhanced Ti-38644 pipe and billet products are presented in Table 4. No evidence of SCC was revealed by any of the three and six month pipe C-rings at the 232° and 260°C test temperatures, regardless of stress level (90 - 100% YS), surface condition (pickled or machined), or galvanic coupling to Alloy C-276. The more aggressive brine additions of 0.5 wt.% acetic acid at 260°C (3 months) and/or the relatively high elemental sulfur level (10 gpl) also failed to induce cracking in pipe samples. The several C-ring samples exposed to vapor phase only also proved to be resistant. Similarly, billet C-ring samples exhibited SCC resistance in the 2 and 6 month sour brine exposures, regardless of stress level (80 and 100% YS) and whether they were galvanically coupled to Alloys C-276 or 625 plus® or not.

Weight loss determinations of all cleaned C-ring samples revealed slight weight gains, with no measurable dimensional changes or localized surface attack. Hydrogen analyses of numerous coupled and uncoupled Ti-38644/Pd C-ring samples indicated no significant increase (<15 ppm) in sample hydrogen level.

C-ring SCC test results for Ti-38644/Pd pipe and billet are plotted as a function of temperature in Figure 2, and are compared to those for standard Ti-38644 tubulars derived from prior work (4).

SSR Test Data

SSR test results for Pd-enhanced Ti-38644 pipe and billet products are outlined in Table 5 and plotted in Figure 3. Pipe samples resisted SCC to at least 246°C, even with an 0.5 wt.% acetic acid brine addition, exhibiting high % RA and TTF ratios ($\geq$0.90) and a fully ductile fracture mode. At 260°C and above, pipe samples displayed susceptibility to SCC, which was confirmed by transgranular quasi-cleavage initiation sites identified during SEM fracture examination.

Billet SSRT samples exhibited SCC resistance to at least 204°C in this worst-case sour brine fluid. SCC temperature thresholds, however, were more variable, and dependent on billet sample location and strength level. Greater scatter in %RA and TTF ratio values was noted, along with a weak correlation of ratio values with SCC occurrence as assessed by fractographic examination. For example, samples with ratio values in the 0.95 - 1.00 range still exhibited fracture initiation via (minor) transgranular cleavage. The SSRT data, plotted in Figure 3, suggest that finite improvements in SCC resistance appear to be associated with the higher strength level tested (1110 MPa YS) and the mid-radius location of the billet.

Crevice Corrosion Test Results

The comparative crevice corrosion resistance of the Pd-enhanced and standard Ti-38644 alloys as a function of temperature in sweet and sour deaerated NaCl brines is depicted in Figure 4. The Pd-enhanced alloy coupons exhibited full resistance to localized crevice attack to temperatures as high as 246°C in all sweet and sour brines tested. Some minor discoloration of Teflon sheet-creviced coupon surfaces was observed (see Figure 5a), and is typical of protective oxide film growth within passive titanium alloy crevices in hot brine exposures.

The standard Ti-38644 alloy, in contrast, experienced severe localized crevice attack in all sour and sulfur-containing brines at 232°C. After removing heavy black crevice corrosion deposits on attacked sites, pits as deep as 20 mils were measured after 30 days exposure as shown in Figure 5b. Results from the worst-case brine (containing H_2S and $S°$) tested indicate that crevice attack of the standard alloy is possible at 150°C or above. On the other hand, crevice attack was not observed in the nonsulfur-containing (sweet) deaerated brine to temperatures as high as 232°C.

Discussion

SCC Database for Ti-38644/Pd

The long term C-ring tests and SSR tests conducted in this worst-case sour brine fluid generate an exceptionally conservative SCC database for Ti-38644/Pd pipe and billet products. These were rather rigorous, discriminating tests due to the high stress levels imposed (80 - 100% YS), long test duration (2 - 6 months), the highly aggressive brine chemistry, and the elevated test temperatures imposed. Aggressive aspects of this test environment relative to those associated with deep sour gas wells include the rather high (20%) NaCl concentration, elevated H_2S and CO_2 partial pressures, the abundance of elemental sulfur, and the 0.5 wt.% acetic acid addition made in a few tests. The SSR tests are also known to be an especially rigorous and conservative SCC test method for passive metals such as titanium alloys, since continued depassivation and damage to the passive oxide surface film is incurred during slow plastic straining.

Influence of Product Metallurgy - A comparison of SSRT data between the pipe and billet products (Fig. 3) clearly suggests that SCC behavior is a function of product metallurgical condition. The pipe product was produced by cold pilgering (cold working) down to final size, followed by preaging, recrystallization annealing and a final aging (PASTA treatment). This produces a highly refined, equiaxed beta microstructure with a highly uniform age, exhibiting a high degree of ductility at a medium strength level (~965 MPa). The hot GFM forged billet product, on the other hand, is solution treated and aged to a higher yield strength of 1103 MPa, and exhibits very coarse, partially recrystallized grain structure (ASTM grain size below 0).

The greater variability and somewhat reduced SCC temperature thresholds for the billet product may be explained by the billet's higher strength level and/or increased grain size. Higher strength means a higher volume fraction of alpha phase precipitates in the beta matrix and, possibly, increased grain boundary alpha precipitation. The alpha phase is the molybdenum- and palladium-lean phase compared to the beta phase, which could make it the more anodic (susceptible) phase. If a less likely cathodic SCC mechanism is considered, greater amounts of the less hydrogen-tolerant alpha phase might also rationalize the increased billet susceptibility. Alloy SCC susceptibility also increases with increasing mean-free path length (grain size) of the beta phase, as shown for other beta titanium alloys in aqueous media (7). Reduced ductility and larger grain size favor achievement of a critical stress crack size.

Pd-enhancement Mechanism - Although the SCC mechanism in Ti-38644 titanium in high temperature sour brine is not fully understood, SCC is either a cathodic (hydrogen embrittlement) or an anodic (chloride-assisted) controlled phenomenon. In the author's opinion, a cathodic mechanism is considered unlikely due to the very high solubility and diffusivity of hydrogen in alpha and beta phase at these high test temperatures. Little or no generation of atomic hydrogen at metal surfaces resulting from the near-nil corrosion rates observed in these brines also implies that a significant source for hydrogen was absent. An anodic explanation appears more plausible, and has been diagnosed in a Mo-rich alpha-beta titanium alloy in a similar environment (8). The case for anodic control is further supported by the lack of influence of sulfur and sulfide species on Ti-38644 alloy SCC thresholds revealed in prior hot brine studies (4,9).

The significant elevation of SCC temperature thresholds noted in both C-ring (Fig. 2 and SSR testing of the Ti-38644 alloy by Pd-enhancement (alloy addition of 0.04 - 0.1 wt.% Pd) has been expressed in prior work (3,4). As an alloy addition, palladium's well known ennobling effect can be expected to enhance SCC resistance. By reducing hydrogen overvoltage and depolarizing the cathodic process, palladium serves to shift alloy corrosion potential in the positive direction where formation of stable, protective titanium oxide surface films is favored. Thus, Ti-38644 alloy passivity is extended into hotter, more reducing acid conditions, manifesting itself as enhanced resistance to hot HCl solutions and chloride crevice corrosion. This positive effect on SCC resistance can be rationalized whether the cracking mechanism is cathodically or anodically controlled. Rate of oxide film repassivation is enhanced, thereby limiting hydrogen absorption or anodic attack when localized oxide film breakdown occurs, such as during slow straining. Resistance to crack initiation on stressed metal surfaces is also realized where local sites of reducing acid chlorides may develop (i.e., within flaws, crevices, under deposits).

Crevice Corrosion Database

Based on the same ennobling/passivation mechanism discussed for alloy SCC behavior, the predicted improvement in Ti-38644 alloy crevice corrosion resistance with Pd enhancement was noted in the crevice tests. The data presented in Figure 4 reveals that the Pd-enhanced alloy fully resisted crevice attack in all sweet and sour brines up to at least 246°C, whether or not elemental sulfur was present. Unlike the standard alloy, this Pd-enhanced alloy also did not experience incipient crevice attack under heavy elemental sulfur deposits adhering to specimen surfaces.

On the other hand, the standard Ti-38644 alloy did exhibit crevice attack in sulfide-and/or sulfur-containing brines at temperatures above 150°C. Since no attack occurred in deaerated sweet brines up to at least 232°C, the results imply that either sulfide or sulfur (or both) is responsible for aggravating the crevice attack observed. Since pH was normalized in the sweet and sour test brines, variation in brine pH was not a factor. A more plausible explanation stems from the minute amounts of adsorbed air/oxygen gas retained within the tight Teflon sheet-metal crevices. The oxygen gas is known to react with either sulfide or sulfur species to form acidic sulfites or sulfates (i.e., sulfuric acid) (10), producing high local acidification within the crevice. If one could practically remove all traces of adsorbed oxygen from specimen crevices/surfaces, then the crevice resistance of the standard alloy would probably approach that observed in sweet brine.

It should be noted that these crevice tests are considered to be severe and highly conservative since they incorporate very tight, large Teflon sheet-to-metal crevices. Secondly, the adsorbed oxygen retained within these test crevices enhance local crevice acidity in sulfide-and/or sulfur-containing brines (as discussed above), providing worst-case crevice test conditions.

<h3 style="text-align:center">Conclusions</h3>

1. A substantial, rigorous stress-corrosion and crevice corrosion database for Pd-enhanced Ti-38644 alloy pipe and billet mill products has been generated in a worst-case deep sour gas well brine fluid up to 260°C.

2. Long term (3-6 month) C-ring tests indicate SCC resistance to at least 260°C for Ti-38644/Pd pipe, and to at least 204°C for billet. No detrimental influence of galvanic coupling to Ni-Cr-Mo alloys on alloy SCC behavior is indicated.

3. Highly discriminating SSR tests revealed SCC resistance up to 246°C for Ti-38644/Pd pipe, which is ~70°C higher than that for standard Ti-38644 in similar product form.

4. SSR testing of billet revealed variable susceptibility to (transgranular) SCC above 204°C, which appeared to be dependent on billet location and strength level.

5. The Pd-enhanced alloy fully resists crevice corrosion in sweet and sour brines to temperatures as high as 260°C. The standard alloy, in comparison, may experience attack above 150°C in sour brines, while remaining resistant in deaerated sweet brines.

6. Based on this conservative SCC and crevice corrosion database, upper service limits of 246°C and 204°C in sour gas well brine fluids are considered to be reasonable for Ti-38644/Pd pipe and billet products, respectively.

References

1. W. W. Love, et. al., "The Use of Ti-38644 Titanium for Downhole Production Casing in Geothermal Wells," Sixth World Conference on Titanium Proceedings, Cannes, June 6-9, 1988, Société Française de Métallurgie, Les Ulix Cedex, France, pp. 443-448.

2. D. E. Thomas and S. R. Seagle, "Stress Corrosion Cracking Behavior of Ti-38-6-44 in Sour Gas Environments," Titanium Science and Technology, Proceedings of the 5th International Conference on Titanium, Munich, Germany, Sept. 10-14, 1984, Deutsche Gesellschaft für Metallkunde E.V., pp. 2533-2540.

3. D. R. Klink and R. W. Schutz, "Engineering Incentives for Utilizing Ti-3Al-8V-6Cr-4Zr-4Mo Titanium Tubulars in Highly Aggressive Deep Sour Gas Wells," Paper No. 63, presented at NACE Corrosion '92, Nashville, TN, April 27-May 1, 1992.

4. R. W. Schutz, M. Xiao and T. A. Bednarowicz, "Stress Corrosion Behavior of the Ti-3Al-8V-6Cr-4Zr-4Mo Titanium Under Deep Sour Gas Well Conditions," Paper No. 51, presented at NACE Corrosion '92, Nashville, TN, April 27-May 1, 1992.

5. R. W. Schutz and S. R. Seagle, "Method for Improving Aging Response and Uniformity in Beta Titanium Alloys," U.S. Patent Application #991,989, Dec. 17, 1992, RMI Titanium Company, Niles, OH.

6. R. W. Schutz and L. C. Covington, "Guidlines for Corrosion Testing Titanium," ASTM STP 728, ASTM, Philadelphia, PA, 1981, pp. 59-70.

7. Stress-Cracking Cracking - Materials Performance and Evaluation, Edited by R. H. Jones, ASM International, Materials Park, OH, 1992, pp. 272-273.

8. M. Ueda, et. al., "Corrosion Behavior of Titanium Alloys in a Sulfur-Containing H_2S-CO_2-Cl⁻ Environment," Paper No. 271, NACE Corrosion '90, April 23-27, 1990, Las Vegas, NV.

9. W. J. Sisak and D. E. Knox, "Stress Corrosion Cracking of Ti-3Al-8V-6Cr-4Zr-4Mo in a Sour Brine," presentation made at an AIME-TMS Annual Meeting Symposium, New Orleans, LA, Feb. 17-18, 1991.

10. G. Schmitt, "Effect of Elemental Sulfur on Corrosion in Sour Gas Systems," Corrosion, Vol. 47, No. 4, April 1991, pp. 285.

Table 1.   Test Matrix for Stress Corrosion Evaluation of Pd-enhanced Ti-38644 Products

Product	SCC Test Method	Test Temp °C (°F)	Test Environment*	Test Duration (mo.)
Pd-enhanced Ti-38644 pipe	C-ring	232 (450)	Brine with 6.9 MPa H_2S, 3.4 MPa CO_2 and 10 gpl S	6
		260 (500)		3
		260 (500)	Brine with 6.9 MPa H_2S, 3.4 MPa CO_2, 10 gpl H_2S, and 0.5% acetic acid	3
	SSRT	204 - 274 (400 - 525)	Brine with 6.9 MPa H_2S, 3.4 MPa CO_2, 1 gpl S (with and w/o 0.5 wt.% acetic acid)	--
Pd-enhanced Ti-38644 billet	C-ring	204 (400)	Brine with 6.9 MPa H_2S, 3.4 MPa CO_2 and 1 gpl S	2
		204 (400)		6
	SSRT	204 - 246 (400 - 475)	Brine with 1000 psi H_2S, 500 psi CO_2 and 1 gpl S	--

* Brine is deaerated 20% NaCl

Table 2.   Description and Composition of Ti-38644 Alloy Product Forms Tested

Product	Cold-Pilgered/ PASTA Pd-enhanced Ti-38644 Pipe	Forged/STA Pd-enhanced Ti-38644 Billet	Cold-Worked/PASTA Pd-enhanced Ti-38644 Sheet	Hot-Rolled/STA Standard Ti-38644 Sheet
Size(s)	- 73 mm OD x 7 mm AW - 73 mm OD x 11 mm AW	152 mm dia.	1.8 mm thick	1.0 mm thick
RMI Heat No.:	882836	863084	X-20040	860390
Composition (wt.%):				
% Al	3.1	3.3	2.7	3.5
% V	7.9	8.0	7.8	8.1
% Cr	6.0	5.8	6.0	5.8
% Zr	4.0	4.3	4.0	3.9
% Mo	4.2	4.5	4.1	3.9
% Pd	0.06	0.06	0.05	--
% O	0.08	0.08	0.08	0.09
Tensile Properties:				
YS (MPa)	945	1117	965	965
UTS (MPa)	993	1207	--	--
% El	21	8	--	--
% RA	47	12	--	--

Table 3. Test Matrix for Crevice Corrosion Evaluation of Ti-38644 Products

Product	Test Environment*	Test Temp. °C (°F)
Pd-enhanced Ti-38644 sheet	Brine with 1.38 MPa H₂S and 1 gpl S	232 - 260 (450 - 500)
	Brine with 1.38 MPa H₂S	246 (475)
	Brine with 1 gpl S	246 (475)
	Brine	246 (475)
Standard Ti-38644 sheet	Brine with 1.38 MPa H₂S and 1 gpl S	121 - 232 (250 - 450)
	Brine with 1.38 MPa H₂S	232 (450)
	Brine with 1 gpl S	232 (450)
	Brine	232 (450)

* Brine is deaerated 20% NaCl

Table 4. C-ring Test Results for Pd-enhanced Ti-38644 Products Exposed to the Worst-case Sour Gas Well Brine Fluid

Product	Test Temp. °C (°F)	Exposure Period (Mo.)	Replicate Samples (per stress level)	Stress Level (% YS)	Surface condition	Alloy Coupled to	SCC ?
Pipe	232 (450)	6	2	90	Pickled	None	No
			3**	95	Machined	None	No
			2	95	Machined	C-276	No
			2	100	Machined	None	No
	260 (500)	3 + 3*	2	90	Pickled	None	No
			3**	95	Machined	None	No
			2	95	Machined	C-276	No
			2	100	Machined	None	No
Billet	204 (400)	2	1	80, 100	Machined	None	No
			2	80, 100	Machined	C-276	No
			2	80, 100	Machined	625 plus	No
	204 (400)	6	1	80, 100	Machined	None	No
			2	80, 100	Machined	C-276	No
			2	80, 100	Machined	625 plus	No

* 0.5 wt.% acetic acid was added to brine in the second 3 month exposure.
** One C-ring sample was exposed to vapor phase during test.

Table 5. SSRT Results for Pd-Enhanced Ti-38644 Products Tested in a Worst-case Sour Gas Well Environment

Product Form/Size	Sample Location/ Orientation	RT YS MPa (ksi)	Test Temp. (°C)	Envi- ronmental % RA	RA Ratio	TTF Ratio	SCC ?
152 mm dia. billet	mid-radius (L)	1013 (147)	218	24.7	0.95	0.99	No
			232	20.5	0.79	0.91	Yes
			246	26.1	1.00	0.97	Yes
	outer-radius (L)		204	--	1.00	0.77	No
			218	18.3	0.81	0.63	Yes
			232	19.4	0.86	0.66	Yes
	mid-radius (L)	1110 (161)	204	19.8	1.00	1.00	No
			218	14.3	0.93	0.85	No
			232	15.4	1.00	0.75	No
			246	19.1	1.00	1.00	No
	outer-radius (L)		204	16.2	1.00	1.00	No
			218	17.3	1.00	1.00	Yes
			218	10.5	0.71	0.71	Yes
73 mm OD x 7 mm wall pipe	thru-section (L)	945 (137)	232	36.5	0.94	0.94	No
			246	40.6	1.00	1.00	No
			246	42.4*	1.00*	1.00*	No
			260	43.9	1.00	1.00	No
			274	18.6	0.48	0.72	Yes
73 mm OD x 11 mm wall pipe	thru-section (L)	945 (137)	246	39.4	0.99	0.97	No
			246	35.0*	0.90*	1.00*	No
			260	39.8	1.00	1.00	No
			260	30.4	0.83	0.91	Yes

* 0.5 wt.% acetic acid added
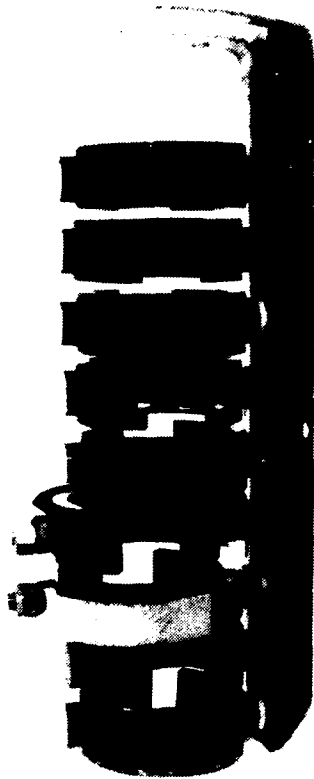
1a.   Fixtured arrangement of pipe C-ring samples.
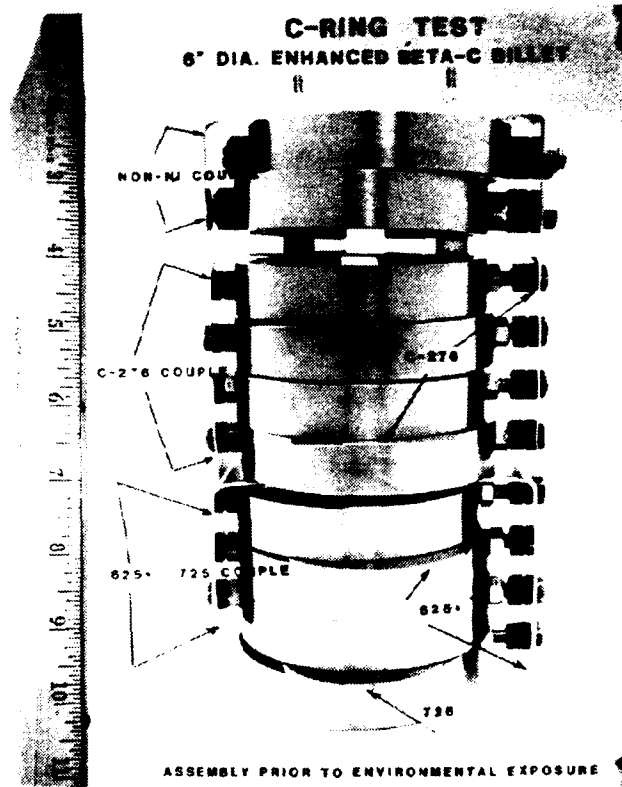
1b.   Fixtured arrangement of billet C-ring samples.

Figure 1a, b. View of pipe and billet C-rings positioned on internal fixtures for autoclave exposures.
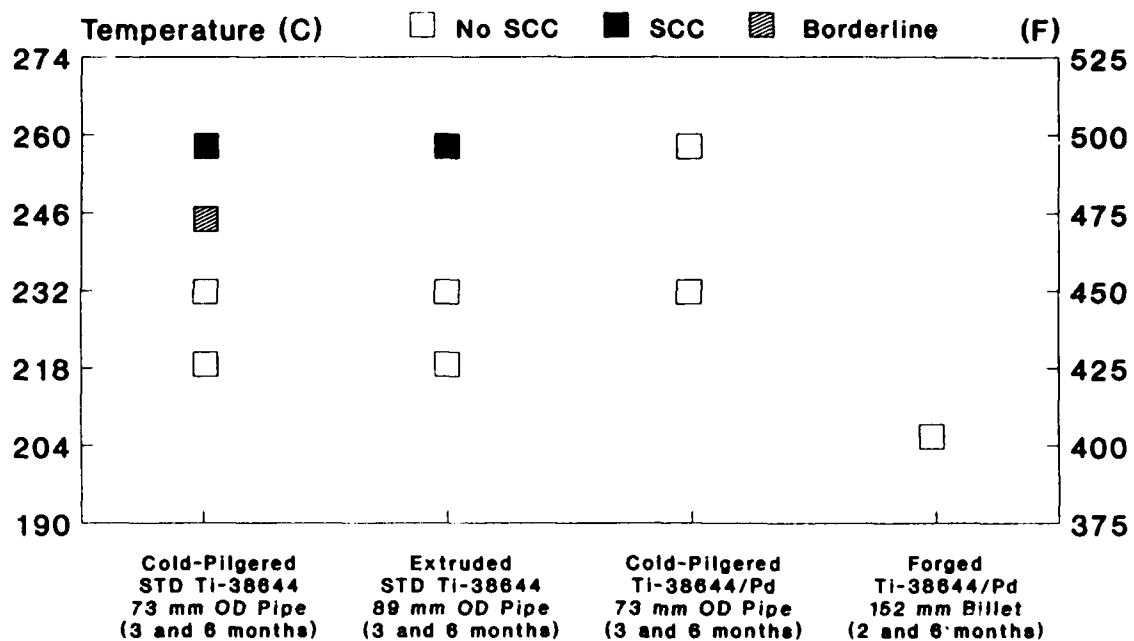
Figure 2. C-ring test results for standard and Pd-enhanced Ti-38644 products in a worst-case sour gas well brine fluid.
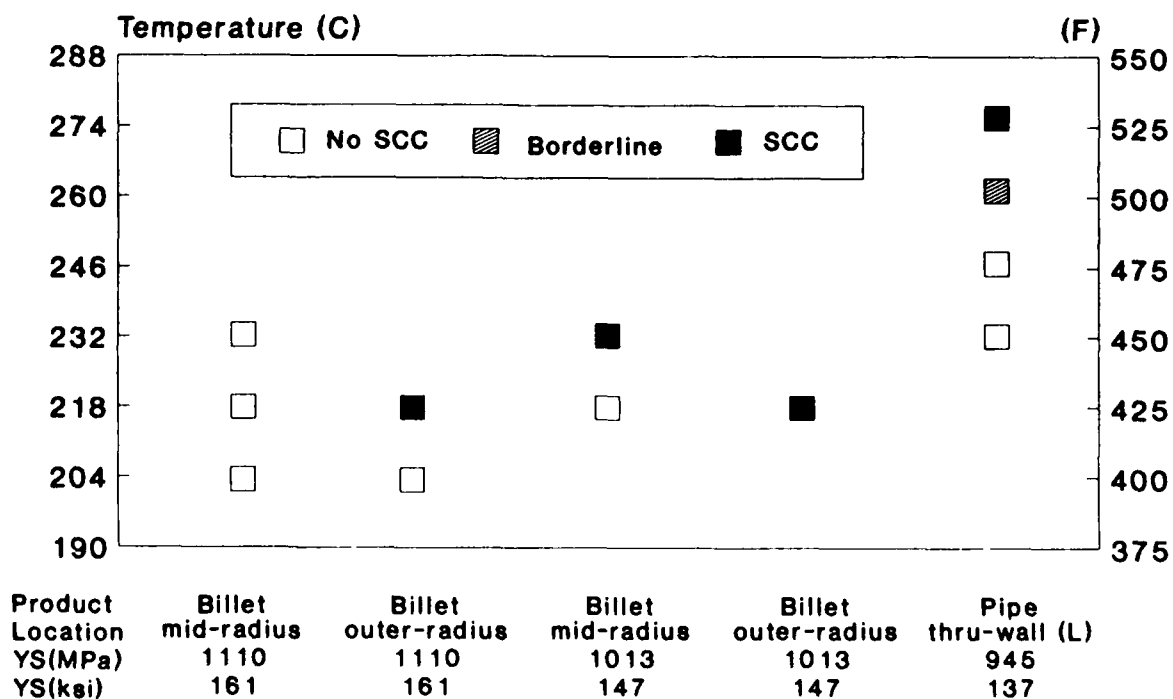
Figure 3. SSRT results for Pd-enhanced Ti-38644 products in a worst-case sour gas well brine fluid.
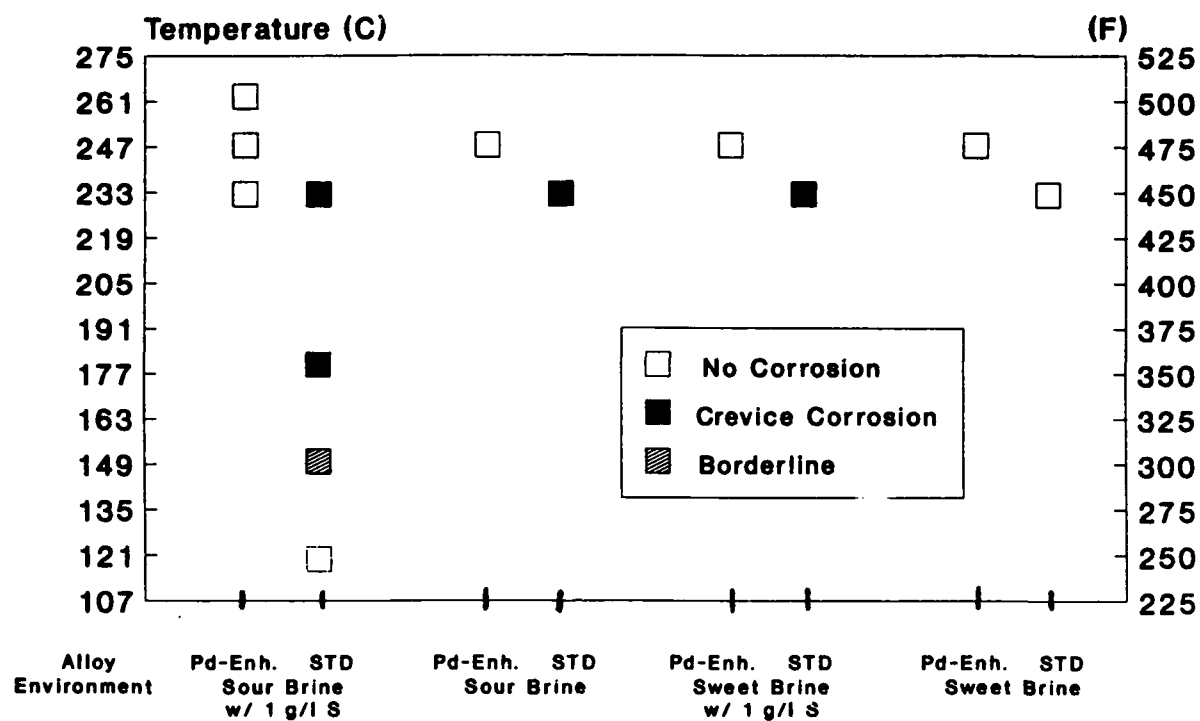
Figure 4.   Crevice corrosion test results for standard and Pd-enhanced Ti-38644 in hot brines.
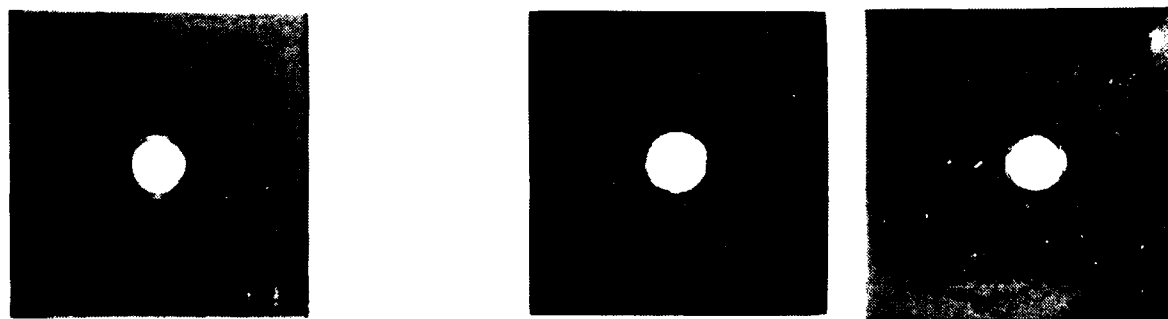
5a. Unattacked Pd-enhanced Ti-38644 coupon.   5b. Severe crevice attack on standard Ti-38644 coupons.

Figure 5a, b.   Susceptibility of Ti-38644 sheet coupons to crevice corrosion in (>150°C) sour brines.

Study of Oil Aluminium Alloy Pipes
with Improved Corrosion Resistance

V.S. Sinyavsky
All-Russia Institute of Light Alloys
121596, Moscow, Gorbunova st. 2, Russia

V.D. Kalinin
All-Russia Institute of Light Alloys
121596, Moscow, Gorbunova st. 2, Russia

L.S. Kagan
All-Russia Institute of Oil Pipelines
443069 Samara, Avrora 110

V.E. Dorokhina
All-Russia Institute of Light Alloys
121596, Moscow, Gorbunova st. 2, Russia

V.A. Kuznetsova
All-Russia Institute of Light Alloys
121596, Moscow, Gorbunova st. 2, Russia

Abstract

The objective of this work was to study the potentiostatic and corrosion resistance of various alloys used for pipes and protective layers depending on the chemical composition, structure of alloys and operating conditions of oil fields. The protection system developed on the basis of these experiments for protecting pipes with metal layers coated on their surface during their production provide an effective electrochemical inhibition of the corrosion process. Based on the prediction, the service life of pipes in terms of corrosion will amount at least to 15 years.

Key words: corrosion potential, pitting initiation potential, protecting current, tests in autoclave, tests in oil fields, pitting corrosion , exfoliation corrosion

Introduction

Steel pipes used in oil production and transportation show rapid signs of failure due to the action of mineralized water contained in oil and soil corrosion. The situation is significantly aggravated when oil is extracted with a high content of sulfurous compounds. In this case the service life of steel pipes usually equals 0.5 – 2 years. Preliminary investigations showed that the use of pipes based on aluminium alloys offers substantial advantages. However, without additional protection they can fail due to corrosion within a relatively short period (2-3 years) in particularly aggressive media.

The developed protection system owing to metal protecting layers applied to pipes during their production provides an effective inhibition of the corrosion process. The corrosion rate in the plating layer in this case drops 2-3-fold due to anodic protection effects.

The subject of the present work is to select the most corrosion resistant cladded aluminium alloys designed for the production of pipes for oil production systems.

Materials and Methods
Materials.

Materials for studies were experimental series of plated and uncladded pipes of AlMg3 108 x 4 mm in dia and AlCuMg alloys (D16T2 according to Russian standards or 2024 T72 according to US standards) 74 x 7 mm in dia.

For plating material use was made of AlZn1, AlZn2 and AlMgSi alloys with different Zn content from 0 to 1.4% with limiting content of other components.

Methods

Tests for pitting corrosion were carried out in tap water with addition of 0.1 g/l NaCl, 0.0005 g/l $CuCl_2$ at pH 5.5-7.2 for up to 6 months according to a cycle of 16 h at 60-70oC, 8 h at room temperature.

Tests for exfoliation corrosion (EXCO) were carried out in two solutions (Table 1) [1,2]. Bench tests for total corrosion with assessment for the depth of damage were run in a 700 l autoclave in a solution 30 g/l NaCl + 6 at H_2S = 6 at CO_2.

Pipes 1800 mm long were placed into the autoclave. The pipes was filled with one of the liquid media containing 0.1, 30, 150 g/l NaCl; 0; 20% of oil, the remaining part was water, then carbon dioxide was fed into some of them at a pressure of 10 at and/or hydrogen sulfide at 15 at and the pressure was raised up to 40 at. by means of nitrogen. During the tests the pressure was maintained constant. The oil was taken from one of the wells in the Volga region. The hermetically sealed pipes were arranged vertically in the autoclave. One charge into the

autoclave consisted of 5 pipes. The tests were carried out for 1000 h.

Tests for stress corrosion cracking (SCC) were carried out by a bending method at preset strain using C-shaped specimens at a stress of 0.9 of YS [1] in accordance with ISO 95-91.

Potentiokinetic polarization curves were taken with the rate of potential change 2 mV/s at room temperature without stirring the electrolyte. A chlorine silver electrode was used as a reference electrode. Platinum wire served as an auxiliary electrode. Prior to polarization the specimens were left in the solution for 30 min. The surface of the specimens before measuring was scoured with emery cloth, cleaned with alcohol and stored in an exsiccator for one hour.

Operation tests were carried out in the line of one of the wells in Yakushisky oil field of the Volga region. Pipes dia. 110 x 4 mm of AlMg3 cladded from either side were assembled in the experimental section 1141 m long of the pipeline. The pipeline ran in the open air. The pipeline was used to pumping over oil products of the following composition (g/l): Cl^- – 139.18; SO_4 – 2.66; HCO_3 – 0.35; Ca^{2+} – 4.0; Mg^{2+} – 1.58; K^+ + Na^+ – 2256.

Total mineralization – 230.19 g/l; density – 1.149 g/l; pH – 5, temperature 19-24°C, pressure – 6 at. The water content of the pumped over medium was 82%. The throughput of the line was 6 m^3/d. The oil contained (mol%): H_2SO_4 – 0.14; CO_2 – 0.42, N_2 –3.68.

Results and Discussion

Electrochemical Characteristics

Fig. 1 presents a combined diagram of anodic (cladding material) and cathodic (base material) curves, and Table 2 summarizes the electrochemical characteristics: corrosion potential – Ec, corrosion potential in active state – Ec*, pitting initiation potential Epi, repassivation potential – Erp, current density in passive region – ipr, density of diffusion current – id, density of protecting current ip. Coincidence of anodic and cathodic curves obtained in the investigations by the potentiokinetic method shows the possibility of cathodic protection of metal-base by using all the indicated alloys for cladding [3]. Protecting current in all the cases is greater than diffusion current. The value of protecting current for AlZn2 and AlMgSiZn2 alloys is about the same. This points to their equal possibilities from the point of view of electrochemical protection level. In cladding material of AlMgSi of a standard composition (without zinc) this value is 1.5 times lower. Comparison of the electrochemical characteristics with the data of corrosion tests shows that the value of protecting current correlated with the distance action of the protector ("distance protection"). Alloying with zinc at a concentration of 0.3% a alone provides a certain degreee of distance protection.

Tests for Pitting Corrosion in Model Solutions

The results obtained from tests of uncladded and cladded pipes of AlMg3 are illustrated in Fig. 2. Similar results were obtained for pipes of AlCuMg T72 alloy. Studies showed that the maximum depth of pitting corrosion of uncladded pipes at the initial period only 1.5-2 times higher than that of cladded pipes. However after 6 months of tests, for uncladded pipes this drastically rises, reaching 1.2 mm. The maximum depth of corrosion damage of pipes cladded with AlZn1, AlZn2 and AlMgSiZn2 alloys does not exceed beyond the thickness of cladding and after 6 months of tests 0.2 mm when the cladding alloy composition is optimal. An increase in the concentration of chlorides from 0.1 g/l NaCl to 150 g/l NaCl, leaving the depth of pitting corrosion invariable, slightly deteriorates the protecting properties of cladding, expanding the area of corrosion damage. In acid medium (pH = 5.5) it is possible to observed a noticeable decline in the protecting properties, the surface of specimens shows larger spots corrosion with partial or complete removal of cladding. However, the impaired continuity of the cladding layer does not lead to an increase in corrosion depth in the alloy-base. Here the effect of distance protection is manifested.

Optimization of the composition of protective layers and technology of their application with obligatory introduction of zinc makes it possible to limit the progress of pitting corrosion within the cladding thickness. As in the case of distance protection, this occurs when the selection of a basic alloy – cladding alloy pair with regard to the influence of the adhesive transitional layer provides an excess of the protective layer over the diffusion layer at least by 4 times. Fig. 4 displays that the value of protective current is determined not only by corrosion potential and pitting initiation potential, but also by the current in passive region. The literature data [4] shows that pitting corrosion in aqueous media spreads according to parabolic dependence in conformity with the equation:

$$h = K \cdot \tau^n,$$

where h = pitting depth;
K = coefficient depending on the structure and;
   composition of alloy;
τ = time of medium influence;
n = coefficient depending on the composition and parameters of medium.

For aqueous medium coefficient "n" approaches three. Then, by rectifying the dependence of change in corrosion depth on time, it is possible to predict metal behavior in long operation (Fig. 3). In the case of protecting the pipes of AlMgSi alloys with AlZn1 and AlZn2 alloys as well as the pipes of AlCuMg T72 alloy with AlMgSiZn1 and AlMgSiZn2 in hard tap water with chloride content up to 150 g/l and copper chloride 0.0005 g/l at pH = 3.5 at elevated temperature the corrosion should not exceed the thickness of the cladding layer for at least 5 years of operation. Cladding of AlMgSi (without zinc) alloy on AlCuMg alloy also markedly inhibits corrosion.

However, it persists within the cladding layer for a relatively short period. By the 5-th year, according to forecasting, the depth of corrosion may reach a rather considerable value – about 1 mm. On uncladded pipes both of AlCuMg and Al-Mg3 alloys perforations may occur in about 1.5 –2 years.

Bench Tests in Autoclave

The tests carried out with pipes of AlMg3 alloy cladded with AlZn1 alloy (Table 3) demonstrated that carbon dioxide up to 15 at. had no influence on corrosion resistance. Hydrogen sulfide up to 10 at and more considerably inhibits corrosion of oil. In terms of mass loss hydrogen sulfide reduces corrosion by about 15% and oil by 1.5-2 times. Prediction of the corrosion resistance of pipes in terms of their inner surface (Fig. 4) shows that by the 5-th year in oil-containing medium the depth of damage does not go beyond half of cladding layer thickness (0.1 mm). For medium containing no oil, corrosion by this time is not to exceed cladding layer thickness)0.16 mm).

Determination of Distance Protective Action.

In order to determine electrochemical protection kinetics, pipe specimens 150 mm long were cut longitudinally. The cladding was partly left (ÿ20%) on the inner surface, the remaining inner surface of the specimen was milled to the depth exceeding cladding thickness by 3 times. Specimens with complete removal of the cladding layer were tested in parallel. The tests were carried out by the method of complete and alternate immersion into solution: tap water + 0.1 g/l NaCl + 0.0005 g/l $CuCl_2$.

The cladding of AlMgSi alloy with a high content of Zn(1.4%) displayed a full protective effect, the entire specimen surface 120 mm long was protected. The milled surface showed slight corrosion damage 0.03 mm deep, at the ends there was no corrosion . However it was observed that high zinc content in the cladding reduced the resistance to exfoliation corrosion of the cladding layer itself. A decrease in zinc content in the cladding down to 0.7 and even to 0.3% also provides complete electrochemical protection of A16 T2 alloy with simultaneous increase in EXCO resistance of a cladding layer. The cladding of AlMgSi alloy without zinc displays the effect of partial electrochemical protection. The range of its action is limited to 6 mm. Cladded specimens showed numerous corrosion damages up to 1.2 mm deep. Considerable corrosion was also observed at the ends.

Under natural conditions in sea water pipes 4 m long with protectors at one of the ends were tested. The protector was 50 mm long. AlZn2 and AlZn5 alloys were chosen for protectors. After a year of testing the corrosion depth on the pipes was not in excess of 0.1 mm. The protector of AlZn5 alloy was destroyed by 80% and that of AlZn2 alloy by 45%.

Additional experiments showed that the protector of AlMgSiZn in this respect may proved to be even more effective.

The pipes without protectors were damaged by pitting to a depth approaching perforations. No exfoliation corrosion was observed on unprotected pipes, which can be explained by the conditions

of their heat treatment (T72).

Tests of Pipes for Exfoliation Corrosion Resistance

Uncladded and cladded pipes of AlMg3 alloy are insensitive to EXCO. Pipes of D16 T2 alloy protected with cladding of the AlMgSi alloy type with Zn content up to 0.85% are unsusceptible to EXCO. Further increase of Zn in the cladding up to 1.4% considerably reduces resistance to EXCO down to point 7. Uncladded pipes of AlCuMg T72 alloys have low resistance to EXCO, corresponding to point 8 in 4 S solution and quite satisfactory resistance (points 4-5) in 2 S solution. As seen from paper (4), this is related to the nature of exfoliation corrosion development during heat treatment of the T72 type.

It progresses in a transcrystalline way. However, in 4 S solution with such development of EXCO a considerable exfoliation occurs. As shown by natural trials, tests in 2 S solution match the actual operating conditions of oil fields in a larger measure. Thus, under these conditions pipes of AlCuMg T72 alloy display no considerable sensitivity to EXCO, which is an important factor in their long service of life.

Tests for Stress Corrosion Cracking

All the investigated version had high resistance to SCC. None of the specimens was damages under a stress up to 0.9 of YS and a test period of 90 days. This was determined a correct choice of the chemical composition (magnesium content is below 3.5%) in AlMg3 alloy and by the condition of artificial ageing of AlCuMg alloy. The protective layers in this case prevent additional adverse effects, which are possible in stress corrosion .

Service Tests

The outer surface of pipes of AlMg3 alloy cladded with AlZn1 after 9 months of use showed sporadic pittings 0.02 mm deep and the inner surface had pittings 0.06 mm deep. Thus, in media similar in composition in terms of aggressivity to components in laboratory and service tests the pipes under actual conditions are noted for higher corrosion resistance. This offers the grounds to consider their service life of at least 15 years to be justified.

Conclusions

1. Unlike steel pipes, sulfur-containing media for pipes of aluminium alloys not only accelerate corrosion processes, but even inhibit them. Therefore, the pipes of aluminium alloys can be successfully used in oil production and transportation irrespective of sulfur contained in it.

2. Pipes of AlMg3 and AlCuMg alloys protected with cladding layers of AlZn1 and AlMgSiZn1 alloys are noted for high corrosion resistance in the operation in oil fields. Their service life according to the foresting compiled will amount to

at least 15 years.

References

1. Sinyavsky V.S. Methods of Control and Research of Light Alloys (Moscow, Metallurgiya, 1985), p.359-430 (in Russian).

2. Sinyavsky V.S., Kalinin V.D., Dorokhina V.E. Aluminium Alloys 90 (Proceedings of the Second International Conference on Aluminium Alloys, International Academic Publisher, Beijing. China 1990), p. 692-697.

3. Tomashov V.D. The Theory of Corrosion and Protection Metals (Moscow, AN SSR, 1960) 480 p (in Russian).

4. Sinyavsky V.S., Valkov V.D., Kalinin V.D. Corrosion and Protection of Aluminium Alloys (Moscow "Metallurgiya", 1986) 368 p (in Russian).

Table 1

Chemical composition of solutions used for exfoliation corrosion tests

Solution No.*	Content of components, g/dm³					Test duration days
	$K_2Cr_2O_7$	HCL	NaCL	KNO_3	HNO_3	
2S	10	–	225	50	5.5	2
4S	20	13.5	–	–	–	7

*Designations are given in accordance with the draft of International Standard ISO/CD 1181

Table 2

Electrochemical characteristics of investigated alloys

No	Alloy	-Ec mV 24 h	-Ec	-Ep	-Erp	ipp	ipr (id) A/cm2	
							AlCuMg	AlMg3
1	AlCuMg T72	480	870	440	600	60	(10)	
2	AlMg3	680	1070	480	650	55		(4)
3	AlZn2	750	1100	690	770	75	75	
4	AlMgSiZn2	660	1050	580	650	55	60	
5	AlMgSiZn1	630	1030	510	630	45	49	
6	AlMgSiZn0.5	616	1030	600	620	40	46	
7	AlMgSi	550	1000	460	670	35	38	
8	AlMgSiZn0.05	550	1050	450	700	31	37.5	
9	AlZn1	690	990	625	680	14	–	18

Table 3

Results of Tests in Autoclave

No	Medium	Corrosion depth, mm			
		500 h		1000 h	
		Outer surface	Inner surface	Outer surface	Inner surface
1	NaCl-150 g/l CO_2 -0 at H_2S - 15 at Oil - 0	0.08	0.1	0.13	0.1
2	NaCl-150 g/l CO_2 -0 at H_2S - 15 at Oil - 20%	0.07	0.08	-	-
3	NaCl-150 g/l CO_2 -10at H_2S - 15 at Oil - 20%	0.03	0.06	0.12	0.06
4	NaCl-0.1 g/l CO_2 -10at H_2S - 0 at Oil - 20%	0.02	0.06	-	-
5	NaCl-150 g/l CO_2 -0 at H_2S - 15 at Oil - 0	0.02	0.09	-	-
6	NaCl-0.1 g/l CO_2 -10at H_2S - 15 at Oil - 0	0.13	0.1	-	-
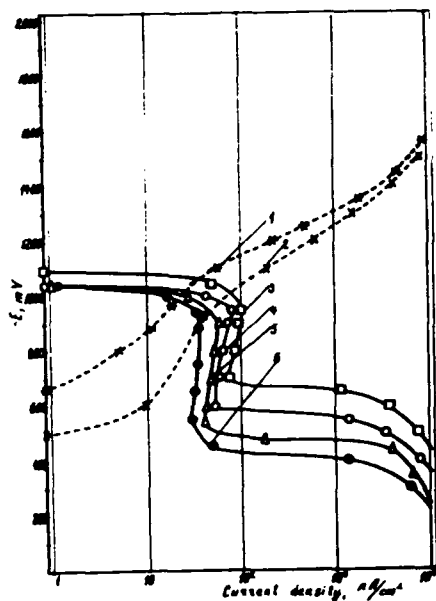
Fig. 1. Combined cathodic
(1-AlMg3, 2-AlCuMg T72) and
anodic (3-AlZn2, 4-AlMgSiZn2,
5-AlMgSiZn1, 6-AlMgSi)
polarization diagrams
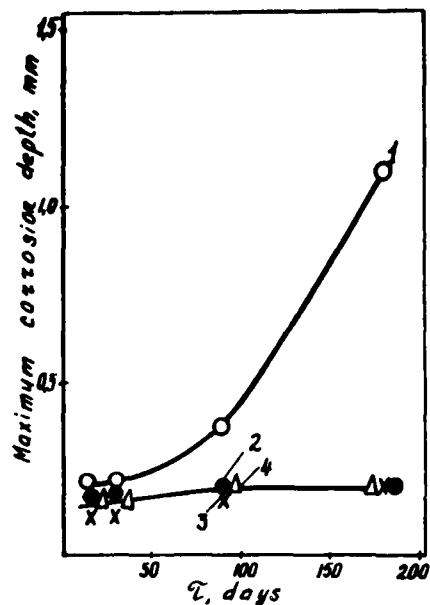
Fig. 2. Pitting
corrosion
of uncladded (1) and
cladded (2-4) pipes of
AlMg3 alloy:1.2 — H_2O +
0.1 g/l NaCl +
0.0005 g/l $CuCl_2$;
3 — same 150 g/l NaCl;
4 — same as 3, pH 5.5
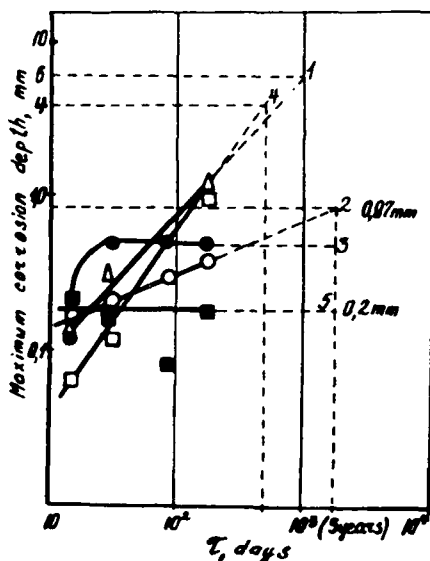
Fig. 3. Development of local corro-
sion in medium H_2O+150 g/l NaCl+
+0.0005 g/l $CuCl_2$, pH 5.5: 1 —
— AlCuMg alloy without cladding;
2,3 — with cladding of AlMgSi and
AlMgSiZn1 alloys; 4 — AlMg3 alloy
without cladding; 5 — with cladding
of AlZn1 alloy
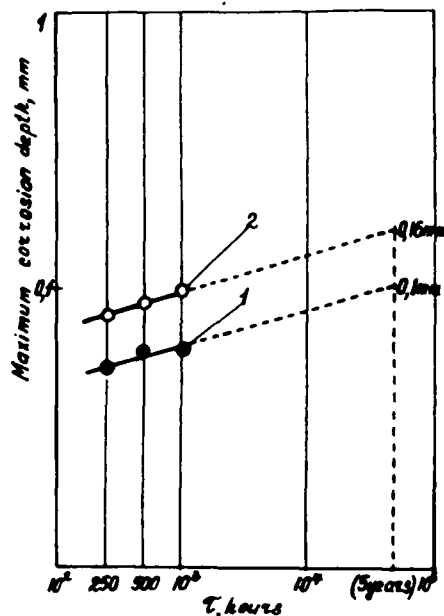
Fig. 4. Development of
local corrosion of
cladded pipes AlMg3
in autoclave: 150 g/l
NaCl, CO_2 — 10 at.,
H_2S — 15 at.,
oil 20 % — H_2O

USE OF COMPOSITE MATERIALS ON OFFSHORE PLATFORMS

Oddvar Sætre
AMAT a/s
P.O box 243
N-3201 Sandefjord
Norway

ABSTRACT

The petroleum industry is moving into deeper waters and colder climates. The demand for safer platforms with low operating and maintenance costs and long design lives is increasing. Life cycle costs is receiving increased attention. All of this puts new demands on the materials.

This paper gives a general overview on the present use of glassfibre reinforced polymer (GRP) materials on offshore platforms, mainly in the Norwegian sector of the North Sea. Ongoing development work in Norway is referred to, and promising fields for future use of GRP are highlighted. Some limitations associated with the materials and some fields where more research and developments are required are pointed out.

INTRODUCTION

A general trend in offshore engineering is to reduce weight, installation costs, and need for maintenance on the installations, in order to minimize the required manning, which reduces the operating costs. Another trend is: longer design life. The first installations in the North Sea were designed for 20 years service, the Statfjord platforms were designed for 30 years, while Troll and the Europipe installations have 50 years as design life.

To meet the above mentioned demands, composite materials, which in this paper means glassfibre reinforced polymers (GRP), are used more and more on offshore installations as alternatives to steel in a number of applications, in particular in seawater carrying piping systems. GRP materials possess four assets which make them attractive for the offshore oil industry: corrosion resistance, light weight, fatigue resistance and ability to tailor make components to the exact need in each case.

Although GRP materials have been commonly used for more than 30 years, e.g.. in leisure boats, skis, and fishing rods, the general knowledge about such materials is low. Hence, in some cases, psychological barriers may be more difficult to overcome than solving the technical problems.

EXISTING INSTALLATIONS

Drain pipes.

GRP materials are well suited for drain pipes. In the North Sea, 5 different systems, originally designed in carbon steel, have been replaced by GRP piping. (Ref. /4/).

On offshore platforms, GRP piping is easier to install than steel piping because:

1   Hot work (welding) is greatly reduced. GRP pipes and fittings are adhesively bonded together. Heat blankets may be required, but not open flames.
2   The lightweight GRP pipes and fittings can easily be carried by the fitters, so the need for cranes and trucks is reduced.

As a result, modifications and repairs are easier to carry out on a platform while in production.

Shaft drain.

Statfjord C is a concrete platform, with subsea storage cells and 4 concrete shafts extending up above the sea level. 3 of the shafts are water filled. A shaft drain system was installed to skim off and pump away any oil spills collecting on the water surface inside the shafts.

The vertical parts of the piping system was installed and cast into the concrete walls while the slipform was moving upwards. Thus, both curing of the adhesive in every joint and pressure testing of it had to be performed and accepted before the joint was submerged in concrete. Once the slipform was started, stopping it had to be avoided at almost any cost.

A special adhesive was developed which could be applied in the humid conditions likely to be experienced on the moving slipform in the middle of the winter in Norway.

Before the job commenced, the following experiment was carried out: Two pipes to be joined were submerged in water along with the adhesive. The application of the adhesive was performed with a brush, submerged, and the two pipe ends were joined. After 24 hours submerged curing, the pipe joint was pressure tested to 10 times it's pressure rating.

The Gullfaks C platform was built in 1988, and the shaft skimmer system is still operative.

Ballast water and crude oil pipes.

According to reference /4/, 7 GRP ballast water systems (2"-12") are installed on platforms in the North sea. One particular installation requires special attention:

On the Draugen platform, which is another of the Norwegian giant concrete structures, the lower part of the ballast water system was made from GRP (Vinylester) and cast into concrete. Besides, the concrete covered Crude Oil to Storage-piping system was designed in glassfibre reinforced vinylester. This system comprised 7 vertical pipes, 240 m long, 16" diameter, cast into the concrete as the slipform moved upwards. The total height of the concrete shaft is 276 m !

Process piping

An emerging design philosophy is to use non-corrosive composites in the process equipment to permit elimination of chemicals such as corrosion inhibitors which otherwise would have been required to protect steel pipes.

According to reference /4/, the following systems are installed on different platforms in the North Sea:

- Sea water pump, 3" - 8", 4 systems.
- Sea water cooling, 1" - 24", 15 systems.
- Produced water, 2" - 30", 9 systems.
- Potable water, 2" - 4", 3 systems.
- Sea water injection, 3" - 24", 3 systems.

Phillips Petroleum Company Norway has installed the following systems:

- Produced water, 680 m, 6" - 14".
- Cooling water, 730 m, 10" - 30".
- Vacuum service, 55 m, 6".
- Seawater supply pipes, 2 installations, 130 m, 6" and 8".
- Seawater lift pipes, 2 installations, 60 m, 6" and 8".

The latter installations are of particular interest. The weight of the pumps supported by the lift pipes is 900 kg each, and the lift pipes are tested to have 7 and 10, respectively, as safety factors against break.

In order to reduce weight and space requirements of process equipment, pipe diameters are minimized, resulting in increased water velocities. Some uncertainty existed regarding the maximum water velocity that could be tolerated in composite pipes. The pipe manufacturers seemed to state low limits, to be on the safe side. Reference /7/ reports a test loop for GRP pipes installed in Norway. A test program was carried out to document the behaviour of composite pipes exposed to large velocities, i.e up to 10 m/s, of clean, natural sea water without particles or chemical additives. The idea was to simulate the conditions in the low pressure part of a sea water injection system.

The conclusion from the tests state that velocities in the order of 10 m/s do not seem to have harmful effects on the pipes, provided the combination of geometrical design, local pressure and large velocity does not produce cavitation.

Figure 1 shows another test loop erected in Norway, designed to evaluate the behaviour of GRP pipes in a flow of sea water containing particles. This loop simulates or accelerates the conditions in a produced water system.

Fire water pipes.

Dry deluge firewater systems are found throughout nearly all platform areas, with many kilometers of piping used for typical offshore platforms. Internal corrosion problems are reported in offshore firewater systems with carbon steel piping, resulting in blocking of the deluge nozzles by rust scales. (Reference /1/). Costly maintenance is required to keep the systems operative. GRP pipes with 8 mm fire insulation have been tested in hydrocarbon

fires, and are now accepted by the Norwegian Petroleum Directorate for use in firewater systems. (ref. /2/).

In reference /1/, Amoco Norway Oil Company reports a "pilot" system of fire insulated dry deluge pipes in glassfibre reinforced epoxy installed at the Valhall field in the Norwegian sector of the North Sea in 1991. The experience with the system is good, both technically and economically, so Amoco is working further to install GRP firewater systems on one platform offshore Netherlands, two offshore Trinidad and is considering a system for a platform in the South China Sea.

Conoco have 3 platforms in the Gulf of Mexico (Marquette, Ewing Bank 305, Green Canyon Central Production Platform), and one in Dubai (Southwest Fateh Complex) equipped with GRP firewater piping. (Ref. /3/).

Phillips Petroleum Company Norway installed a 24" firewater header in glassfibre reinforced epoxy between the platforms on the Ekofisk field, in the Norwegian sector of the North Sea in 1992. The header pipe is not in an area with a high risk of fire.

Antennas

On all ships and offshore structures, there is a large number of rod shaped antennas. GRP is well suited for this service, because as a non-metallic material it does not influence the radio signals, it is light, strong, flexible, fatigue resistant, and requires no maintenance. The technology for production of antennas originates from design of fishing rods, but is further developed.

Structural elements

As offshore petroleum activities are performed in deeper and deeper waters, sea bottom based structures become more slender, and topside weight becomes increasingly important. Tension leg platforms (TLP) (i.e. Hutton and Snorre) are attractive alternatives to gravity based structures. A TLP is a floating structure tethered to the bottom, a cost effective platform concept where weight is even more crucial to the economical performance.

So far, the primary material used by the offshore industry is steel. However, the density of steel is 3.9 times higher than glassfiber reinforced epoxy, 5.1 times higher than graphite fibre reinforced epoxy, and 5.8 times higher than Kevlar fibre reinforced epoxy.(Ref. /5/). The low density of GRP, combined with an attractive strength-to-weight ratio provide a potential for substantial weight reduction with resulting cost savings on offshore installations.

One ton saved on the topside weight of a TLP saves 1.3 tons of steel weight on the hull and 0.65 tons of pretension requirement for the tethers. Thus one ton of component weight saved will permit two additional tons of weight savings in the rest of the structure. (Ref. /5/).

Because of the improved strength-to-weight ratio, equipment such as walkways, gratings and handrails in GRP will be lighter than equivalent equipment made from steel. If a cost of NOK 20,000 per ton of steel, (2,850 USD/ton) installed, is used as an estimate, each ton of reduced weight on the topside equipment saves NOK 40,000 (5,700 USD) in steel on

the support structure of a TLP, in addition to the money saved by making the topside equipment itself more cost effective.

Structural elements in GRP materials are available "off the shelf" in the form of I-beams, U-beams, angle bars, hollow rectangular bars and hollow cylindrical bars. A wide variety of sizes are offered. Gratings (for walkways), (Weight: 11 kg/m²), ladders and complete handrail systems (weight: 15 kg pr linear metre) are also available.

A frequently used method of designing in GRP is by using "sandwich" elements, consisting of two laminates with an expanded foam between them, Such elements exhibit exceptional performance related to strength vs. weight. The protection structure around the Draugen subsea units are made from Sandwich elements.

Sandwich elements are available in many forms and sizes. One supplier offers a panel with thickness 66 mm, weight 52 kg pr m². This panel has fire rating H 120 J, which means that it is jet fire-tested and blast resistant, and after 120 minutes exposed to a hydrocarbon fire from one side, the integrity of the plate is still intact, and the temperature on the "cool side" of the panel is lower than 139 °C.

ONGOING DEVELOPMENTS

Spoolable pipes

The growing emphasis on sub-sea equipment in offshore oil production, including satellite production systems, has resulted in an increased need for high performance pipes designed for injection of chemicals and water, or as hydraulic control lines between satellite wells and a main platform. Present piping used for this purpose is mainly constructed of either steel or thermoplastic piping with an external braided fiber structural body.

The main limitations involved with these are corrosion of the steel pipes, and flexibility of the thermoplastic piping resulting in a long response time to operate hydraulic valves.

A new class of continuous pipe is being developed in Norway for this purpose. (ref /6/). The pipe consists of a thermoplastic inner liner and a load carrying GRP (epoxy) laminate. A prototype pipe with inner diameter 35 mm has been short term burst tested to 900 bars pressure, uniaxial loading. The pipe can be spooled to a diameter of 7.2 m. Another prototype was bent 50,000 times at a frequency of 24 cycles per minute to simulate spooling onto a 6.1 m minimum diameter spool, and then pressure tested until rupture, which occurred at 507 bars.

Spoolable pipes can be supplied in long lengths, which simplifies the installation, lowers the offshore installation cost, and eliminates a majority of the connections presently used, which are common sources for leaks.

Three sections of the pipe has been field tested onshore by Conoco on a South Texan oil field, in a water injection line at 85 bar (1200 psi). The pipes have operated successfully without problems since installation in June 1991.

Reach rod for downhole service

One of the latest developments where composite materials are utilized, is a spoolable, solid rod for TFL service (Through Flowline Logging of oil reservoirs). At present, the most common method for logging a satellite well, is to position a vessel above the well and lower down a chain of 3 m long sucker rods, linked together, through the access valves into the well.

The new system under development consists of a solid rod, 20 mm in diameter, with couplings in both ends. The yield strength of the system is more than 9 tons. The rod can be spooled on a reel with only 3 m in diameter.

The rod with driving units is pumped through the flowline from the main platform to the satellite well, and driven downwards to the "no-go nozzle" far down in the well. Further down from there, only the rod with the required instruments is able to penetrate. The length of the rod is designed to reach to the required depth of the well below the nozzle, which may be 300 m, where the readings are taken. Subsequently, the rod and the driver units are driven back through the flowline to the main platform by means of the well pressure. Finally, the rod is retrieved and stored on the reel on board the platform.

Pressure vessels

The Norwegian government and oil industry are cooperating in a program called "KAPOF" (Capitalisation of Offshore research). One of the tasks in that program is to qualify (i.e. document the performance of) process vessels in GRP materials for use offshore:

Phase 1: Investigating the range 0-10 bar operating pressures, containing water with traces of hydrocarbons. Installation of the first "pilot" unit is expected in 1995.

Phase 2: If GRP materials show acceptable performance in water containing process systems (phase 1), other areas with higher hydrocarbon content will be addressed. Other process units, such as pumps, and valves could also be included.

Items for low temperature service

Material properties at low temperatures (-75°C or lower) is important for the oil companies as their activities are moving into arctic regions. According to reference /8/, among others, fibre reinforced polymer materials are considered to be promising candidates for use in arctic and other cold regions. These materials at least retain their physical and mechanical properties at low and cryogenic temperatures, have high specific strength, are corrosion resistant and require less maintenance than steel materials.

No dramatic degradation in physical or mechanical properties for GRP composites were reported. Properties like tensile strength and stiffness, compressive strength and stiffness, and flexural strength and stiffness at low or cryogenic temperature are retained or even improved.

Composite modules and containers both for transportation and for living quarters are considered to be feasible due to the low weight, the insulation properties and the low maintenance requirements.

The use of fibre reinforced polymers in tanks and vessels for storage and transportation of liquefied gas is considered challenging, and should be considered further.

DISADVANTAGES / SUBJECTS FOR IMPROVEMENTS

Some features related to GRP materials need urgent improvements, because they limit the use of GRP:

Lack of standardization. This problem is associated with pipes and fittings. The different suppliers have their own non-compatible standards. As a consequence of this, piping designers are not able to work out detailed drawings until the supplier of the materials is nominated. This is unlike most other engineering, and is considered to be a disadvantage connected to GRP piping installations. Besides, it complicates storage of spare parts.

Techniques and acceptance criteria for NDT examination, as well as methods for stress / strain analysis of GRP structures are presently not reliable enough to be trusted for design and control of GRP components to be used in applications where failures would result in a high risk of pollution or damage to human lives, (e.g. high pressure hydrocarbons).

GRP materials have low impact strength. Metal objects may only be bent or dented, while GRP laminates may develop smaller or larger cracks when exposed to impacts. Special precautions should be taken during the design (positioning / shielding) to prevent GRP from being mechanically damaged.

Ultraviolet radiation (sunshine), may alter the surface finish of GRP laminates. This is more of a cosmetic than a technical problem. Shielding from direct sunshine or coating with UV resistant top coat will prevent the degradation.

The temperature and humidity must be controlled when performing lamination and adhesively bonding of GRP materials. In the North Sea this may be a problem during the winter season.

CONCLUSIONS

The petroleum industry is moving into deeper waters and colder climates. At the same time, more and more emphasis is put on cost reductions, for new as well as for existing installations. GRP materials can contribute to this development.

GRP materials offer attractive properties, such as low cost, light weight, corrosion resistance, fatigue resistance and flexibility to be tailor made. They are well suited for low-temperature service, e.g. in arctic regions.

A substantial potential exists for cost reductions by increased use of GRP materials in structures, accommodation modules and process equipment on new as well as on existing offshore petroleum installations.

ACKNOWLEDGEMENTS

REFERENCES.

/1/   Stephen W. Ciaraldi, J.D. Alkire and G.G Huntoon: Fiberglass Firewater
        Systems for Offshore Platforms. Paper no. OTC 6926 from the 24. annual
        Offshore Technology Conference in Houston, Texas, May 1992.

/2/   The Norwegian Petroleum Directorate: "Regulations concerning explosion and
        fire protection of installations in the petroleum activities", with guidelines (1992)
        1SBN 82-7257-356-3.

/3/   Oddvar Sætre and John L. Sundt: "Composite Pipes in Firewater Systems" Paper
        presented at the NACE conference "Engineering Solutions to Industrial Corrosion
        Problems", 7-9 June 1993, Sandefjord, Norway.

/4/   Reidar Matre: "Erfaringer ved bruk av Glassfiber Armerte Plastrør på Ekofisk
        Feltet". (Experience from use of GRP pipes at the Ekofisk field). Paper presented
        at the conference "Offshore Drift og Vedlikehold '91", Bergen, Norway 16-17
        October1991.

/5/   Jerry G. Williams: "Development in Composite Structures for the Offshore Oil
        Industry". (OTC 6579). Paper presented at the 23rd Annual OTC in Houston,
        Texas, May 69, 1991.

/6/   Tore W. Moe and Jerry G. Williams: "Spoolable Composite Pipes". Paper
        presented at the NACE conference "Engineering Solutions to Industrial Corrosion
        Problems", 7-9 June 1993, Sandefjord, Norway.

/7/   OJdvar Sætre: "Testing of Composite Pipes in High Velocity Sea Water". Paper
        presented at the Offshore Mechanics and Arctic Engineering (OMAE) conference
        in Stavanger, Norway, June 1991.

/8/   Kasen, M.B.: "Cryogenic Properties of Filamentary-Reinforced Compoaites: an
        Update". Cryogenics, June 1982, Page 323-340.

FIGURE
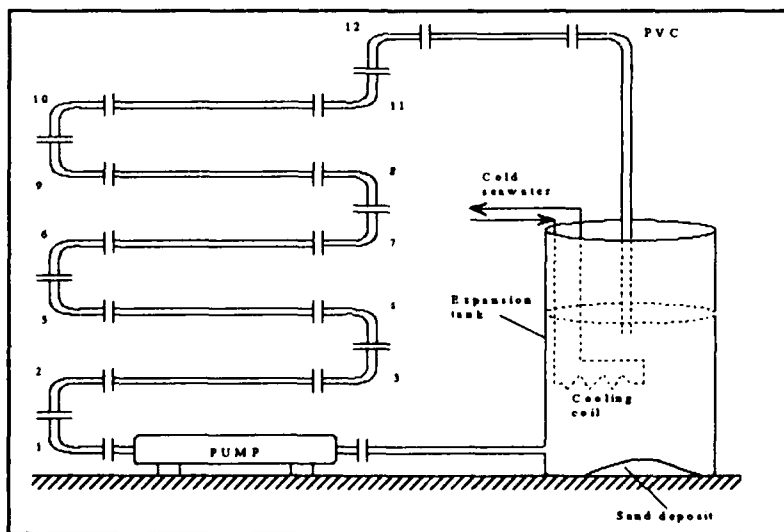
Figure 1.Sand erosion test loop.

Corrosion Performance and Application Limits of Materials in Oil Fields

Akihiro Miyasaka
NIPPON STEEL CORPORATION, Nagoya R&D Laboratories
5-3 Tokai-machi, Tokai, Aichi, Japan

Hiroyuki Ogawa
NIPPON STEEL CORPORATION, Steel Research Laboratories

Abstract

The corrosion behavior of corrosion resistant alloys (CRAs) in sour environments was investigated intensively by using a duplex stainless steel as a representative CRA. The changes in corrosion morphologies due to changes in environmental aggressiveness were elucidated. It was found that the application limits of CRAs were determined by whether pitting corrosion occurs or not. A new theory was proposed for predicting the corrosion morphologies and thus determining the application limits of CRAs. The validity of prediction by the new theory was confirmed by good agreement with the long-term immersion test results and the field test for the actual size test pipes. Since this theory is based on the corrosion mechanism, it has many advantages; the prediction is accurate; the results for one environments can be extended to other environments; the prediction is conducted very quickly.

Key terms: sour gas, corrosion resistant alloys, stress corrosion cracking, pH,
localized corrosion

Introduction

Oil and natural gas that are produced recently sometimes contain a large amount of hydrogen sulfide (H_2S) and carbon dioxide (CO_2). For the exploitation of such corrosive and hostile reservoirs, low-alloy steel tubulars have been traditionally used with the application of corrosion inhibitors for corrosion prevention. Chemical inhibitors, however, is low in effect for very deep wells and is expensive for offshore wells. Thus, the demand for corrosion resistant alloy (CRA) O.C.T.G. (oil country tubular goods) has been increasing, because their use can abolish chemical inhibition.

A great variety of CRAs, from 13%Cr martensitic stainless steel up to Cr-Ni-Mo superalloys, have been proposed for sour service. Each CRA has its own application limit not to corrode or crack, depending principally on its alloy chemistry. The selection of CRAs with necessary and sufficient corrosion resistance to a given environment is indispensable to assure the structural integrity of production wells at the least possible expenditure. This necessitates precise information on the critical environments for each CRA.

Conventionally, such application limits have been determined experimentally[1] by "go/no go" type test methods. The test results by these techniques, however, are significantly dependent on the test conditions. For example, the test results of constant-load type and constant-strain type stress corrosion cracking (SCC) tests are affected by the applied stress and test duration. It is now well known that strain rate has remarkable influence on the results of slow strain rate technique (SSRT) tests. For this reason, the application of conventional SCC test results

has been confined primarily to the relative comparison of corrosion resistance between CRAs.

In this study, the corrosion and cracking mechanism of CRAs in sour gas environments is extensively investigated. On the basis of the results, the new criteria for rational determination of the application limits of CRAs, not affected by test conditions, are proposed. Its versatility will also be discussed briefly.

Characterization of environmental aggressiveness

The aggressiveness of environments can be characterized by the following two factors: pH and the redox potential of the environments.

pH estimation of oil field environments

In considering the following conditions, Eq.[1] was obtained for calculating the pH of sour and sweet environments[2]. The deduction of Eq.[1] was introduced in detail in the previous paper[2]. The m_{H^+} is obtained as a positive solution of Eq.[1], and by substituting m_{H^+} into the definition of pH in Eq.[8], the pH value can be calculated.

1. Dissociation equilibria of H_2S, CO_2, H_2O and HSO_4^-.
2. Electric neutrality condition for aqueous solutions.
3. Mass balance of bicarbonate- and sulfate-related substances.

$$m_{H^+}{}^4 + (X + C_2 + Z + C_4)m_{H^+}{}^3 - (C_1 m_{H_2S} + C_3 - ZC_2 - XC_4 - C_2C_4)m_{H^+}{}^2$$
$$- (C_2 - C_4)(C_1 m_{H_2S} + C_3)m_{H^+} - C_2C_4(C_1 m_{H_2S} + C_3) = 0 \qquad [1]$$

$$\text{where,} \quad C_1 = K_{1,H}\, \gamma_{H_2S} / \gamma^2_{\pm H_2S} \qquad [2]$$
$$C_2 = K_{1,C}\, \gamma_{CO_2} / \gamma^2_{\pm CO_2} \qquad [3]$$
$$C_3 = K_w / \gamma^2_{\pm H_2O} \qquad [4]$$
$$C_4 = K_{1,S}\, \gamma_{HSO_4^-} / \gamma^2_{\pm HSO_4^-} \qquad [5]$$
$$X = m_{CO_2} + m_{HCO_3^-} \qquad [6]$$
$$Z = m_{SO_4^{2-}} + m_{HSO_4^-} \qquad [7]$$

$$\text{pH} = - \log a_{H^+}$$
$$= - \log \gamma_{H^+} m_{H^+} \qquad [8]$$

The physico-chemical parameters that are required to account the effect of concentrated ions on ionic activity coefficients, and mean activity coefficients are estimated or extrapolated from the data for those in NaCl aqueous solutions[2]. The dissociation constants and solubility coefficients of H_2S and CO_2 were thermodynamically estimated[2,3]. The estimation for physico-chemical parameters were also introduced in detail in the previous paper[2,4]. The validity of the above approximation and estimation has already been confirmed for concentrated NaCl aqueous solutions by direct measurements of the pH by using an n-type TiO_2 semi-conductor electrode up to elevated temperatures[4]. Figure 1 gives a typical example for the change of pH with an increasing content of bicarbonate.

Redox potential of the environments

In every service environment, the most noble immersion potential (E_{ip}) that an alloy can take is the redox potential (E_1) of the cathodic reaction that controls the corrosion of the alloy in the environment. Strictly speaking, the immersion potential of the alloy never agree with the

redox potential of the cathodic reaction, because the immersion potential is controlled by the balance of anodic and cathodic reactions. However, the approximation of $E_1 = E_{ip}$ enables a simple and prompt prediction with a slightly conservative estimation.

The cathodic reaction that controls corrosion and SCC of CRAs in sour environments is the reduction of elemental sulfur[5] in Eq.[9]. Then the redox potential E_1, and approximately the immersion potential E_{ip}, can be calculated by using Eq.[10][6]. In Eq.[10], the pH value can be obtained by the procedure introduced in the previous section and H_2S activity can be thermodynamically calculated[3].

$$S + 2H^+ + 2e^- = H_2S \qquad [9]$$

$$E_1 = E_T^0 - (2.303RT/F)\, pH - (2.303RT/2F)\, \log a_{H_2S} \qquad [10]$$

Figure 2 shows a typical example for the influence of bicarbonate concentration on the redox potential of reaction [9] at various temperatures.

Experimental Procedure and conditions

Test Materials

A 20 mm thick plate, in accordance with DIN standard 1.4462 (UNS S31803), was used as a representative CRA for oil and gas production. It was solution heat treated at 1323 K for 300 s followed by water quenching. The steel was used both in as-solution treated and in cold rolled conditions. The total reduction in thickness in the latter was 20%. The major chemical composition was 0.019%C-0.43%Si-1.78%Mn-21.4%Cr-5.3%Ni-2.78%Mo-0.146%N-Fe bal.

Test Procedure

Electrochemical Measurements. Critical pitting potential (V_c') and depassivation pH (pH_d) were measured. Test coupons of 3 mm thick, 15 mm wide and 20 mm long were machined from the middle of the wall. They were degreased in acetone, polished with #320 grit paper and coated with silicon resin leaving 1 cm x 1 cm area for measurements. Just before being immersed in test solutions, the specimens were pickled in 50% sulfuric acid at 333 K to remove the air-formed film.

Potentio-dynamic experiments were conducted at a scan rate of 10 mV/min. The potential scan was made from the spontaneous potential in the positive direction. The potential corresponding to the current density of 100 microamperes/cm^2 was adopted as V_c'.

For measuring pH_d, specimens were immersed in test solutions with various pH values adjusted before immersion and potential changes were continuously monitored for 8.64×10^4 s. The pH_d values was the pH at which the potential shifted in the noble direction on the potential-pH diagram.

Immersion Tests. The relationship between environmental conditions and corrosion morphologies was examined by immersion tests. The dimensions of the test coupons were 2 mm thick, 15 mm wide and 20 mm long. They were degreased in acetone and polished with #320 grit paper just before the tests. Atmospheric pressure tests were performed in glass vessels, whereas high pressure tests and high temperature tests above 373 K were conducted in high pressure autoclaves. Test duration was principally 1.21×10^6 s. Tests for 1.56×10^7 s

were also carried out where the corrosion morphologies had been marginal. After immersion, corrosion morphologies were determined by visual and opto-microscopic observations. They were classified into the following three types: no attack (N), pitting (L), and general corrosion (G).

SCC Tests. Four point bent beam tests and SSRT tests were performed. The former was made for cold-rolled materials, as per ASTM standard G39-79. Specimens of 2 mm thick, 10 mm wide and 65 mm long were sampled lengthwise from the middle of the wall. Stress equal to 0.2% offset proof stress was applied in the rolling direction. Test duration was 1.21×10^6 s. SSRT specimens with gage sections 4 mm in diameter and 20 mm long were sampled in the rolling direction from the as-solution treated material. The SSRT tests were conducted at a nominal strain rate of 2.0×10^{-6} s^{-1} until failure. The reduction-in-area ratio (RAR= RA_{env}/RA_{inert}) was used to express the SSRT test results, where $RA_{env.}$ and RA_{inert} are the reduction in area in the test environments and in an inert environment. 5 MPa dry nitrogen gas was used as an inert environment to obtain the baseline data for SSRT tests. Without aqueous solutions, corrosion did not take place. The scanning electron microscopy for fracture surface and cross sectional observation were conducted for both types of SCC tests when necessary.

Test Environments

Deaerated aqueous solutions that contained 20 mass% (4.28 mol/kg-H$_2$O) NaCl and were in equilibrium with H$_2$S at the scheduled pressure were selected as the test solutions. For examining the influence of anions, sodium bicarbonate or sodium sulfate, ranging from 10^{-4} to 0.1 mol/kg, was added in the solutions. Ion-exchanged and distilled pure water and analytical grade chemicals were used for preparing the test solutions. All the tests were performed at temperatures ranging from 298 to 523 K. H$_2$S partial pressure was varied between 0.001 to 4 MPa.

Test Results

Electrochemical Measurements

Figure 3 shows the influence of temperature and H$_2$S partial pressure on V_c'. V_c' shifted in the less noble direction with temperature rise from 298 to 353 K. The further temperature rise resulted in a slight decrease of V_c'. V_c' took a less noble value with increasing H$_2$S partial pressure. The effects of temperature and H$_2$S partial pressure on depassivation pH (pH$_d$) are given in Fig. 4. The pH$_d$ value increased with a temperature rise and an increase in H$_2$S partial pressure. These results indicate that the passivation capability of the CRAs decreases, i.e., the passive film becomes unstable, at high temperature and under high H$_2$S partial pressure.

The influence of sulfate and bicarbonate ion concentrations on V_c' is shown in Fig. 5. It is obvious from the figure that sulfate raised the V_c', when the molar ratio of sulfate ion to chloride ion was approximately greater than 0.5. Bicarbonate ion did not affect V_c' up to $m_{HCO_3}/m_{Cl} = 1$. A similar tendency for the effect of anions was also observed for 5%NaCl (0.90 mol/kg) aqueous solutions.

Immersion Tests

The relationship between the corrosion morphologies and the environmental conditions

obtained as a result of the immersion tests is illustrated in Fig. 6. At low temperature and low H_2S partial pressure, the alloy underwent no attack (N). The corrosion morphology changed to localized corrosion (L) with a temperature rise and an increase in H_2S partial pressure and finally exhibited general corrosion (G). Among test results in Fig. 6, those for H_2S partial pressure of 0.05 and 0.5 MPa and temperature of 333 and 423 K are the test results after 1.56 x 10^7 s immersion. At H_2S partial pressure of 0.05 MPa and at 423 K (point A in Fig. 6), the corrosion morphology was initially determined as L after a 1.21 x 10^6 s immersion, where on the other hand that after 1.56 x 10^7 s was general corrosion. The quasi-pitting after 1.21 x 10^6 s was attributed to the incomplete dissolution of the air-formed film within a limited time of 1.21 x 10^6 s. At point B in Fig. 6, the corrosion morphology was marginal between N and L after 1.21 x 10^6 s, but it changed to complete L (pitting) after 1.56 x 10^7 s. It is obvious from these results that the results of conventional immersion-type tests are significantly affected by test duration. No changes in corrosion morphology due to prolongation of test duration were observed at points C and D.

SCC Tests

Figures 7 and 8 give the SCC test results for four point bent beam tests and SSRT tests, respectively. In four point bent beam test, the SCC/no SCC boundary was found between H_2S partial pressure of 0.01 and 0.03 MPa. The influence of temperature as well as that of H_2S partial pressure is considerable for SSRT tests. Also in this case, the transition from no SCC to SCC was observed at an H_2S partial pressure of approximately 0.03 MPa. These critical H_2S partial pressure are slightly greater than those previously reported by other researchers[7,8]. Visual and opto-microscopic examination for cracking morphology revealed that cracks initiated at pits and propagated by connecting pits when H_2S partial pressure was small. At higher H_2S partial pressure, SCC cracks initiated directly at the metal surface without pitting.

Figure 9 shows the influence of bicarbonate ion concentration on the reduction in area ratio (RAR). The RAR remained unchanged up to bicarbonate concentration of 10^{-2} mol/kg. At $m_{HCO_3^-}$ of 0.1 mol/kg, the RAR reached approximately unity and no SCC was observed on the fracture surface. The failure was caused by completely ductile fracture. This mitigation of SCC susceptibility by presence of bicarbonate was attributed to the raise of the pH and the resultant shift of the redox potential E_1 in the less noble direction, as can be expected by Figs. 1 and 2, because bicarbonate buffers and raises the pH . Such SCC mitigation effect could not be observed in the case of sulfate ion up to its concentration of 10^{-1} mol/kg. This was because the pH buffering el.ect of sulfate was much smaller than that of bicarbonate.

Criteria for Determining the Application Limits on the Basis of Corrosion Mechanism

Prediction of "No attack/Pitting" Transition

It has been well understood that V_c corresponds to the critical potential above which macroscopic pitting takes place[9,10]. The pit embryo continues to grow at the potential more noble than V_c, whereas it stops propagation when the potential is less noble than V_c. Therefore, if the potential of a given alloy (E_{ip}) in a given environment is known, the occurrence of pitting can be predicted by comparing V_c with E_{ip}. Then, the following criterion predicts the critical environments for the occurrence of pitting.

$V_c < E_1$ Macroscopic pits propagate.

$V_c > E_1$ Macroscopic pitting does not occur.

V_c can be obtained electrochemical measurements. E_1 can be thermodynamically calculated by using Eq.[7] as is already stated in the previous section. The predicted boundary for No attack to pitting transition is given in Fig. 8.

Prediction of "Pitting/General corrosion" Transition

The pH_d is defined as a critical pH value for an alloy to exhibit passive to active and active to passive transition. Therefore, if the pH value of a given environment is known, it is possible to determine whether or not the alloy can be passivated in the environment. If the alloy cannot be passive, the passive film does not form on the alloy surface so that the corrosion morphology must be general corrosion (active dissolution). The corrosion morphology in a situation where the alloy is passive should be no attack or pitting. Since the passive film is quite unstable in the vicinity of passive to active transition, the critical environments for the transition should coincide with the boundary between pitting and general corrosion. Therefore, the critical environments for general corrosion of an alloy can be predicted by comparing the pH of environments with the pH_d of the alloy as follows:

$pH < pH_d$ The alloy undergoes general corrosion

$pH > pH_d$ The alloy exhibits pitting or no attack

The pH_d can be obtained by electrochemical measurements. The predicted boundary for pitting to general corrosion transition is also given in Fig. 8, in which the critical environment is a locus of the node of the equi-pH lines and the equi-pH_d lines.

Comparison of electrochemical prediction with experimental results

Figure 8 compares the electrochemically predicted transitions of corrosion morphologies with long-term immersion test results. Here, the boundary A is the electrochemical prediction for no attack/pitting transition, and the boundary B for pitting/general corrosion transition. The letters in circles indicate the corrosion morphologies determined in the immersion tests. It is obvious from the figure that the electrochemically predicted transitions of corrosion morphologies are in good agreement with experimental results. This strongly validates the proposed criteria.

Prediction of "No SCC/SCC" Transition

In Fig. 8, the no SCC/SCC boundary C mentioned in the previous section is also shown. The boundary C is fairly close to the critical environments for pitting. Considering that SCC in sour environments initiates at pits, the two boundaries may well be expected to coincide with each other after a sufficiently long time. By substituting the transition B (no attack/pitting) for the transition C (no SCC/SCC), the transition C may also be predicted by electrochemical techniques.

Application of the Proposed Technique

The electrochemical prediction of corrosion morphology proposed in this paper has the

following advantages:

    (1) The predicted results are not dependent on test duration.

    (2) The corrosion morphology can be theoretically predicted on the basis of the corrosion mechanism.

    (3) It may be possible to guarantee the performance of alloys for the lifetime of oil and gas wells.

    (4) Each measurement takes a very short time.

In addition to the above advantages, the proposed technique has another unique character. The corrosion morphology with the co-existence of H_2S and CO_2 can be predicted by using the results obtained in CO_2-free conditions. Or, the influence of anions such as bicarbonate and sulfate can also be taken into account without repeating the corrosion and SCC tests. This is because the technique is based on the corrosion mechanism. The conventional techniques require that tests be repeated when the environmental constituents are changed. On the contrary, the present technique easily predicts the corrosion morphology even with the existence of CO_2 and/or bicarbonate ion, since CO_2 or bicarbonate does not affect the V_c' and pH_d of CRAs in sour environments. Some examples are given below.

The effect of CO_2 is only to lower the pH of the environment. The pH of sour environment shifts to a smaller value with increasing CO_2 pressure. This slightly raises E_1 as is obvious from Eq.[7]. As V_c' is independent of pH in acidic environments[10], V_c' values obtained in CO_2-free conditions stand also for CO_2-containing environments. Figure 9 shows the calculated results for the change in the no attack/pitting transition as a function of CO_2 partial pressure. The no attack region shrank with an increase in CO_2 partial pressure.

Similarly, the influence of CO_2 partial pressure on the pitting/general corrosion boundary was calculated. The pH_d values obtained in CO_2-free conditions are also applicable to CO_2-containing environments, because CO_2 does not affect the pH_d of CRAs. An increase in CO_2 partial pressure enlarges the general corrosion area towards the lower temperature and lower H_2S partial pressure region.

Verification by the field tests

To confirm the accuracy of the newly proposed prediction technique for the application limits of CRAs, the two field tests were performed in C.I.S. (formerly U.S.S.R.). One was for CII pipes (Nippon Steel's double wall pipe, licensed by Kawasaki Heavy Industries) with the liner material of AISI 316L and UNS N06625[12]. The pipes were exposed to the actual produced fluid from the natural sour gas reservoir having total pressure of 100 bar. It was expected, before the test, that alloy 316L would exhibit pitting in presence of produced water and the high pressure natural gas containing 7.20 vol.% CO_2, 4.98 vol.% H_2S and 0.28 vol.% N_2, whereas alloy 625 would not. After the test for 6 months, the detailed examination for the liner material revealed that the laboratory prediction was completely in good agreement with the field test results[12].

The other test[13] was conducted, in Astrakhan gas field in C.I.S., for solid (mono-wall) and double wall pipe consisting of NT-2225 alloy (22%Cr-25%Mo-4%Mo) in 5%NaCl+ 0.5%CH3COOH aqueous solution in equilibrium with 15 bar H_2S plus 9 bar CO_2. It was considered, before the test, that the alloy would not undergo any pitting or cracking in the test environment. This was certified by the detailed observation for the materials tested after the

end of the field test.

Conclusions

The corrosion behavior of CRAs in sour environments was extensively investigated by using a duplex stainless steel as a representative CRA. On the basis of the examination, electrochemical techniques to predict the corrosion morphology of CRAs were proposed. Since the proposed technique is based on the corrosion mechanism, they produce accurate predictions which are unaffected by the test conditions. Thus they enable the rational determination of application limits of CRAs. It should be noted that the validity of the prediction was confirmed by good agreements with both the long-term laboratory tests and the field tests using the full scale section of the CRA pipes.

Acknowledgments

Nomenclature

a_i : activity of i chemical $\quad\quad\quad\quad$ E_T^0 : equilibrium potential at temperature T

F : Faraday constant $\quad\quad\quad\quad\quad$ $K_{H,i}$: solubility constant of i chemical (mol/l/atm)

$K_{1,i}$: first dissociation constant of i chemical (C:CO_2, H:H_2S, S:SO_4^{2-}, w:H_2O)

m_i : molar concentration of i chemical P_G : partial pressure of G gas

R : gas constant (8.314 J/K/mol) $\quad\quad$ T : Temperature (K)

γ_i : activity coefficient of i chemical $\quad$ $\gamma_{\pm i}$: mean activity coefficient of i chemical

References

1. For example, A. Ikeda et al.: Corrosion/84, paper No.206, (Houston, TX: National Association of Corrosion Engineers, 1984).
2. A. Miyasaka : Corrosion/92, paper No.5, (Houston, TX: National Association of Corrosion Engineers, 1992).
3. J.W. Sweeton et al. : EPRI NP-2400 Project, Report No.1167-1, (1982).
4. A. Miyasaka et al. : ISIJ International, 29(1989): p.85.
5. A. Miyasaka et al. : Corrosion, 45(1989): p.771.
6. R.J. Biernat and R.G. Robins : Electrochim. Acta, 14(1969): p.809.
7. J. Sakai et al.: 1982 ASM Metals Congress, No.8201-012, (1982).
8. A. Ikeda et al.: Corrosion/84, paper No.289, (Houston, TX: National Association of Corrosion Engineers, 1984).
9. Y. Hisamatsu : Boshoku-Gijutsu, 21(1972):p.504.
10. Z. Szklarska-Smialowska : Pitting corrosion of metals, (Houston, TX: National Association of Corrosion Engineers, 1986).
11. H.P. Leckie and H.H. Uhlig : J. Electrochem. Soc., 121(1974): p.1137.
12. H. Ogawa et al. : Proceedings of 11th International Corrosion Congress, (1990): p.4.466.
13. A. Miyasaka et al. : Corrosion/92, paper No.38, (Houston, TX: National Association of Corrosion Engineers, 1992).
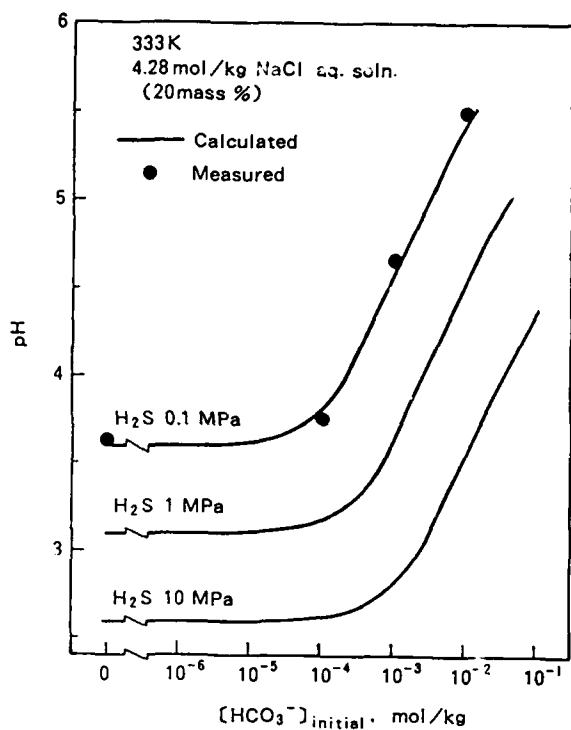
Fig.1 Influence of HCO₃⁻ content on pH of 20%NaCl aqueous solution saturated with H₂S at 333K.
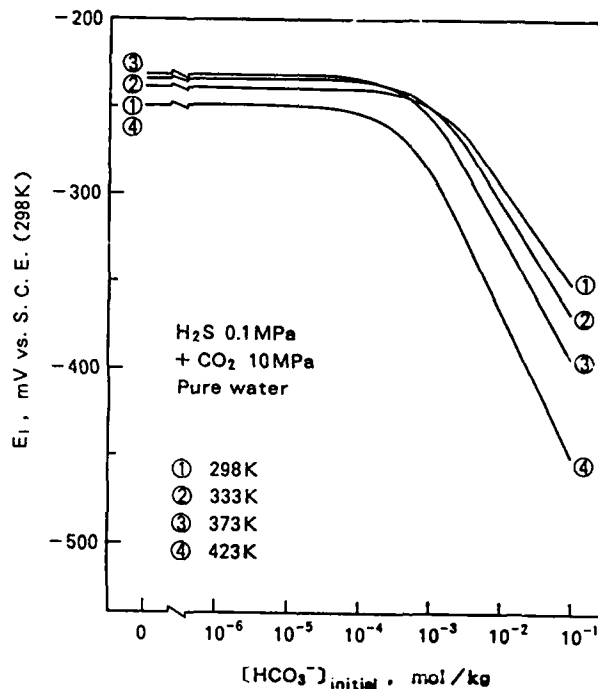
Fig. 2 Changes of S/H₂S redox potential as a function of bicarbonate addition.
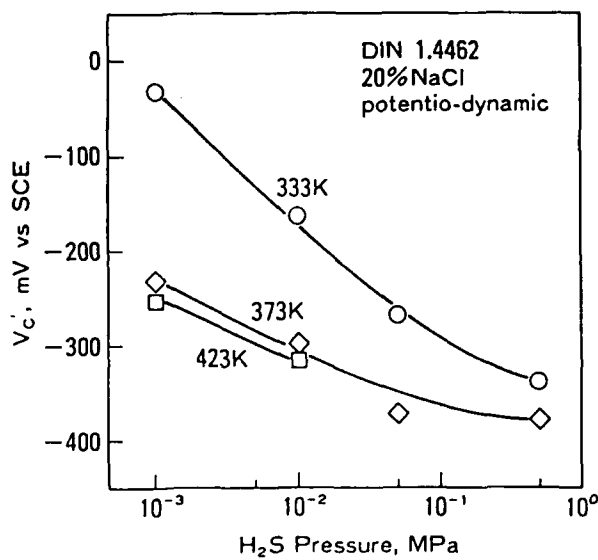
Fig. 3 Influence of temperature and H₂S pressure on V_c'.
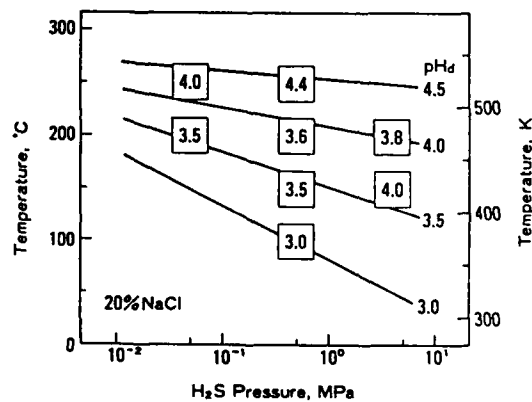
Fig. 4 Influence of temperature and H₂S on pH_d.
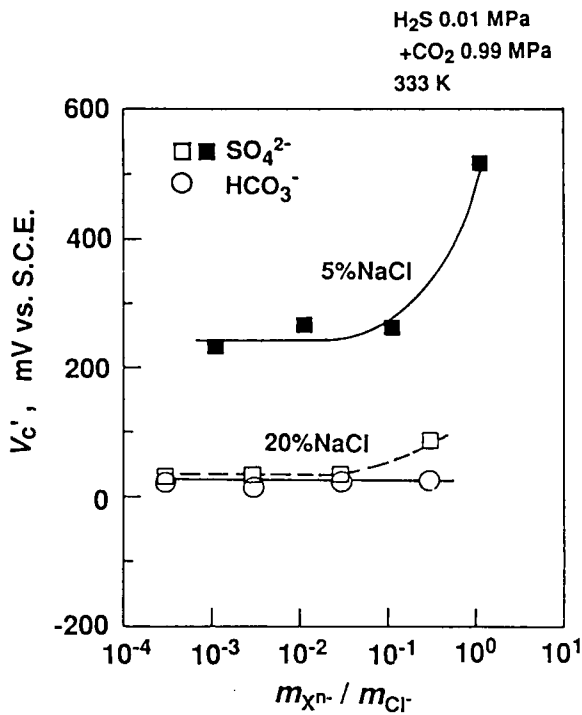
Fig. 5 Effect of sulfate and bicarbonate ion concentration on V_c'.
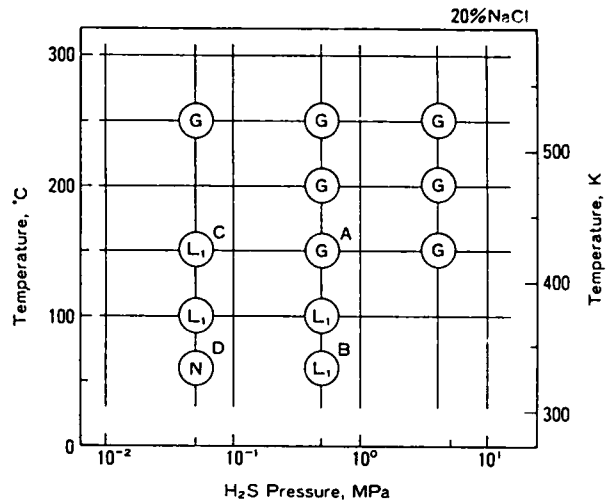
Fig. 6 Relationship between corrosion morphologies and environmental conditions.
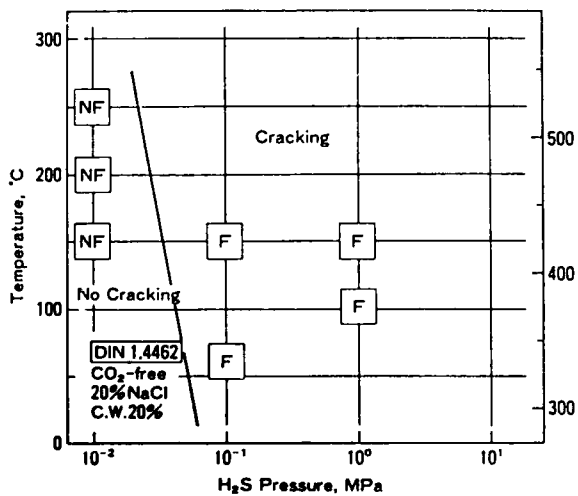
Fig. 7 Four-point bent beam test results. (F: failed, NF: not failed)
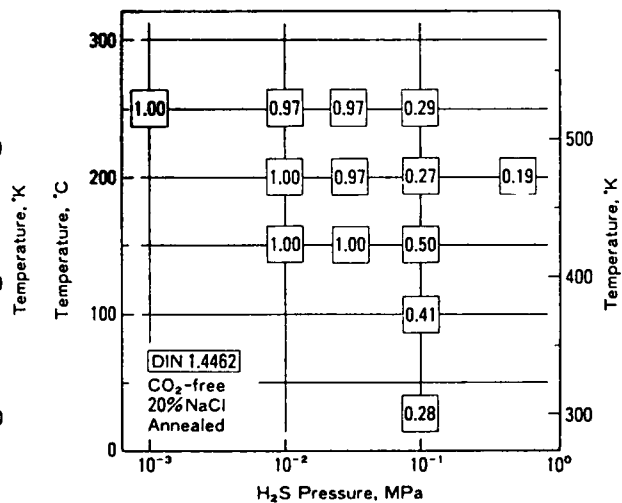
Fig. 8 Elongation ratio obtained by SSRT tests.
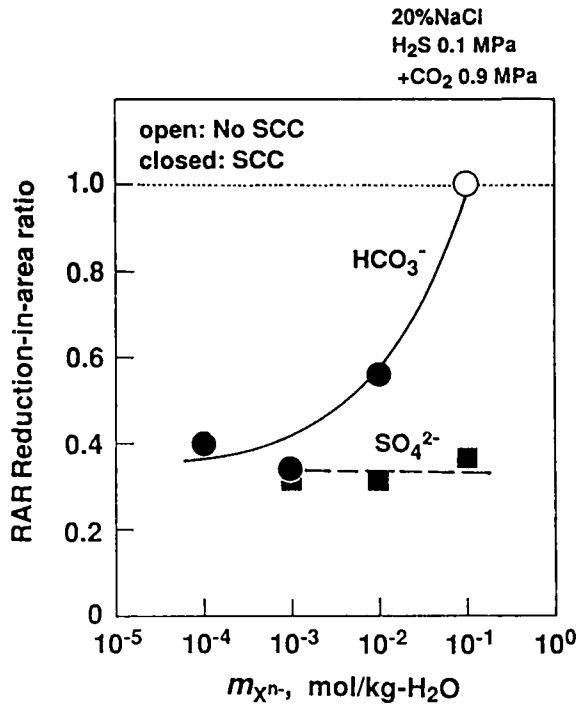
Fig. 9 Influence of co-existing anion contents on RAR obtained by SSRT tests.
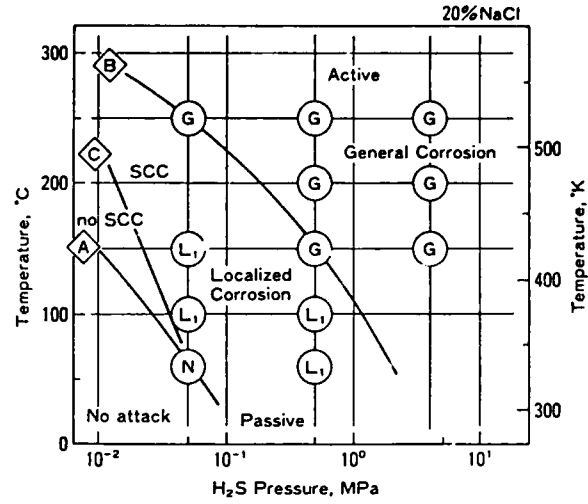
Fig. 10 Comparison of predictions for "no attack/pitting" and "pitting/general corrosion" transitions with the experimental results.
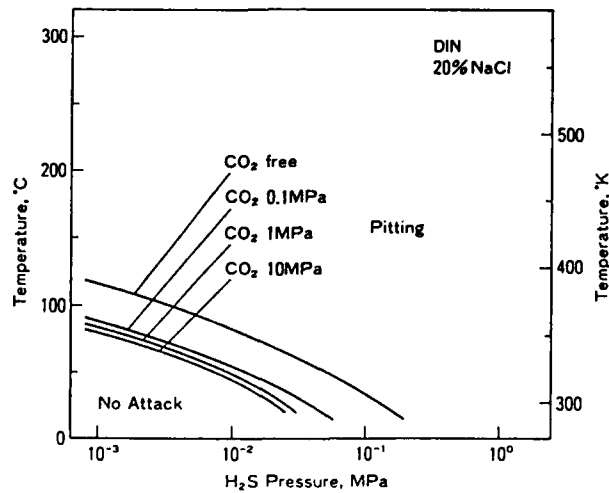
Fig. 11 Change in "no attack/pitting" boundary as a function of CO_2 pressure.

Corrosion Resistant Alloys UNS N09925 and N07725 for Oil Field and Other Applications

Edward L. Hibner and Ralph H. Moeller
Inco Alloys International, Inc.
Huntington, WV 25720

Abstract

Alloy 925 (UNS N09925) and alloy 725 (UNS N07725) are highly corrosion resistant alloys capable of being age hardened to minimum 0.2% yield strengths of 105 ksi (724 MPa) and 120 ksi (827 MPa), respectively. Alloy 925 and alloy 725 are austenitic nickel base alloys strengthened by precipitation of gamma prime (γ') and gamma double-prime (γ''), respectively. Large section sizes can achieve uniform hardening throughout the cross section. Both alloys are resistant to pitting and Stress Corrosion Cracking (SCC) in Deep Sour Gas Well (DSGW) environments containing NaCl, H_2S, and S, and are resistant to Sulfide Stress Cracking (SSC) as illustrated by laboratory and field test data. The alloys also exhibit excellent resistance to other environments such as seawater and mineral acids. This paper is an in-depth summary of the mechanical properties and corrosion resistance of age-hardenable corrosion resistant alloys 925 and 725.

Introduction

The trend in oil and gas production has been toward deeper wells, enhanced recovery methods, and offshore field exploration. Deeper wells and enhanced recovery methods, such as steam injection, in combination with CO_2 result in hostile environments due to increased temperatures, pressures and presence of H_2S, CO_2 and chlorides. For several decades, much research has centered around the need for Corrosion Resistant Alloys (CRA's) that can withstand the high temperature, high pressure and corrosive oil field production environments.[1] Alloy 625 (UNS N06625) and alloy C-276 (UNS N10276) have the necessary corrosion resistance, but can only be strengthened through cold work, therefore, some large sizes cannot be produced with the exception of alloy C-276.[2] Age-hardenable alloy X-750 (UNS N07750) and alloy 718 (UNS N07718) have been used in these applications but have insufficient corrosion resistance in many severe environments.[3,4] INCOLOY® alloy 925 (UNS N09925), strengthened by precipitation of gamma prime [$Ni_3(Ti,Al)$], and INCONEL® alloy 725 (UNS N07725), strengthened by precipitation of gamma double-prime [$Ni_3(Nb,Ti,Al)$] are capable of being age hardened to minimum 0.2% yield strengths of 105 ksi (724 MPa) and 120 ksi (827 MPa), respectively. Aging treatments given each alloy result in the optimum combination of strength, toughness, and corrosion resistance. Alloy 925 was developed for use in oil production tubular products, tool joints, and equipment for surface and down hole hardware for intermediate sour gas wells. Alloy 725 was developed for tubing hangers, SubSurface Safety Valves (SSSV's), wellheads, Christmas trees, valve trim, packers, Polished Bore Receptacles (PBR's), and other down hole equipment for severe sour service. Alloy 725 has been used as pressure-containing, flow-wetted components in subsurface safety valves and as valve components and other down hole components in sour service[5] at temperatures exceeding 175°C (350°F). Alloy 925 is resistant to pitting and Stress Corrosion Cracking (SCC) in Deep Sour Gas Well (DSGW) environments containing NaCl, H_2S and S at temperatures up to about 149 to163°C(300 to 325°F). Alloy 725 is resistant to pitting and Stress Corrosion Cracking (SCC) in Deep Sour Gas Well (DSGW) environments containing NaCl, H_2S and S at temperatures up to about 232 to 260°C (450 to 500°F). Sulfide stress cracking is extremely detrimental to down hole equipment and should be taken into account when designing metal components.[6] Both alloys are resistant to sulfide stress cracking (SSC) in the NACE TM-0177 environment.[7] Alloy 725 also has excellent capabilities in other environ-

---

INCOLOY and INCONEL are registered trademarks of the Inco family of companies.

Key Terms: alloy UNS N09925, alloy UNS N07725, oil field, corrosion prevention, stress corrosion cracking, hydrogen embrittlement, salt solution, inorganic acid, organic acid.

ments such as seawater, where it exhibits excellent corrosion fatigue, pitting, crevice corrosion resistance, and mineral acids, where it exhibits corrosion resistance equivalent to alloys 625 and C-276. Welding of alloy 725 is required for some applications. Welding with alloy 725 serves as a high strength alternative to alloy 625 welding products which have found extensive use in oil patch applications. Data generated on commercially produced alloy 725 weldments, show excellent weldability, mechanical properties and corrosion resistance.[8]

Discussion

Composition and Heat Treating

The nominal chemical composition ranges of alloys 925 and 725 are displayed in Table 1.

Since alloy 925 is strengthened by precipitation of gamma prime $[Ni_3(Ti,Al)]$, a solution anneal of 1850°F (1010°C) air cooling or faster, is required to put the material into the proper condition before aging. A dual aging treatment of 1365°F (740.5°C)/8h, furnace cool (FC) at 50°F (28°C)/h to 1150°F (620°C)/8h/air cool (AC) was found to provide the best combination of strength and toughness.

Alloy 725 is strengthened by precipitation of gamma double-prime $[Ni_3(Nb,Ti,Al)]$ during aging. A solution anneal of 1900°F (1038°C) air cooling or faster, is required to put the material into the proper condition before aging. A dual aging treatment of 1350°F (732°C)/8h, furnace cool (FC) at 100°F (56°C)/h to 1150°F (620°C)/8h/air cool (AC) was found to provide the best combination of strength and toughness.

Mechanical Properties

Table 2 displays representative mechanical properties for various mill forms of nickel alloys for Oil Country Applications. As can be seen, alloys 925 and 725 provide excellent high strength alternatives to cold worked products. In addition, large section sizes can achieve uniform hardening throughout the cross section.[9] The properties for alloys 925 and 725 displayed in Table 2 represent material in the optimum solution annealed plus dual aged conditions.

Alloys 925 and 725 can be provided in the solution treated plus single aged, solution treated plus dual aged, direct aged, and cold worked plus aged conditions to obtain a variety of strength levels.[9-14]

Table 3 displays average Room Temperature Tensile (RTT) and Charpy-V- Notch (CVN) impact properties for both alloys, 0.625 to 7.5 in. (1.6 to 19.0cm) diameter hot finished rod and bar in the optimum solution annealed plus dual aged conditions. Excellent strength, ductility, and toughness were observed. These are average properties and do not represent specification minimums which are a function of hot finish technique and rod diameter.

Table 4 shows average RTT and CVN impact properties for alloy 725 0.5 in. (1.27cm) plate, solution annealed at 1900°F (1038°C), then given a variety of single and double aging treatments. The RTT results obtained from the various aging treatments on alloy 725 were similar to those exhibited by hot finished rod and bar products in Table 3. Longitudinal and transverse orientations exhibited similar properties, i.e., 122 to 128 ksi (841 to 883 MPa) 0.2% yield strength, 173 to 182 ksi (1193 to 1255 MPa) tensile strength, 31 to 36% elongation (%El), and 44 to 54% reduction of area (%RA). Transverse CVN impact energies of $\cap$ to 112 ft-lb (84 to 152 J) were obtained.

Table 5 displays RTT properties for alloy 725 0.217 in. (5.51 mm) wall x 2.375 in. (60.3 mm) O.D. tubing, cold drawn 17%, then evaluated in various annealed plus dual aged conditions. The annealed plus aged tubing also displayed RRT properties similar to the rod and bar mentioned in Table 3, i.e., approximately a 132 ksi (910 MPa) 0.2% yield strength, 184 ksi (1268 MPa) tensile strength, 28%El, and 39%RA.

Table 6 exhibits average High Temperature Tensile (HTT) properties for alloy 725, 0.625 to 7.5 in. (1.6 to 19.0cm) diameter hot finished rod and bar, in the optimum solution annealed plus aged condition. As expected, the drop in strength is low over the room temperature to 1000°F (538°C) temperature range, with alloy 725 exhibiting excellent ductility.

Corrosion Resistance to DSGW Environments

Table 7 contains room temperature sulfide stress cracking (hydrogen embrittlement) data for steel coupled nickel alloy C-rings evaluated in the cold worked, annealed and aged, and cold worked and aged conditions in the NACE TM-0177 environment. For alloy 725, aged material representing yield strengths up to 139 ksi (958 MPa) and hardnesses up to 41.5 HRc did not crack when coupled to carbon steel for 720 to 1000 hours. Aged alloy 718 , yield strength 130 ksi (896 MPa) and hardness HRc 34, did not crack in 720 hours of exposure. For alloy 925, aged material representing yield strengths up to 185.5 ksi (1279 MPa) and hardnesses up to 46 HRc did not crack. See Table 7 for details.

C-ring stress corrosion cracking data for nickel alloys evaluated in high temperature sour brine environments is shown in Table 8. These autoclave environments were designed to simulate conditions in severe deep sour gas wells. For alloy 925, material representing yield strength up to 185.5 ksi (1279 MPa) and hardnesses up to 42 Rc, evaluated in 15% NaCl saturated with H_2S plus 1000 psi (6.9 MPa) gas phase of 1% H_2S, 50% CO_2, 49% N_2 at 500°F (260°C), no cracking occurred. As expected in 15 to 25% NaCl sour environments containing 200 psi (1380 kPa) H_2S plus 100 psi (690 kPa) CO_2 plus 1 g/L elemental sulfur at 400 to 450°F (204 to 232°C), cracking occurred.

Stress corrosion cracking data for C-rings evaluated in a 25% NaCl + 0.5% acetic acid + 120 psi (827 kPa) H_2S + 1 g/L sulfur environment is displayed in Table 9. Alloy 725 was resistant to SCC up to 450 to 500°F (232 to 260°C). Alloy 718, age-hardened to 130 ksi (896 MPa) yield strength, cracked at 275°F (135°C) in this environment. Cold-drawn alloy 625, yield strength 144 to 160 ksi (993 to 1,103 MPa), cracked at 375°F (191°C). And, cold-drawn alloy C-276, yield strength 127 to 168 ksi (876 to 1,158 MPa), resisted SCC up to about 500°F (260°C).

Figure 1 displays the results of C-ring tests, in a severely aggressive 25% NaCl, 0.5% acetic acid, 1 g/L sulfur environment with 120 psi (825 kPa) H_2S, plotted as Test Temperature versus Test Stress. For the conditions tested the nickel alloys ranked as to decreasing resistance to SCC as follows: Alloy C-276 (N10276) > alloy 725 (N07725) > alloy G-3 (N09685) > alloy 925 (N09925) > alloy 825 (N08825) > alloy 718 (N07718).

Tables 10 and 11 display mass loss corrosion data for nickel alloy evaluated in sour brine environments with and without free-sulfur. Alloy 925 consistently exhibited very low corrosion rates comparable to alloys 718 (N07718), 825 (N08825), 625 (N06625) and C-276 (N10276). In contrast, alloys K-500 (N05500), 9Cr/1Mo Steel and type 316 SS (S31600) exhibited significantly higher corrosion rates.

Corrosion Resistance to Mineral and Organic Acids

Corrosion results for alloy 725 in mineral acids, compared to alloys 625 (N06625) and C-276 (N10276) are shown in Table 12. In all of the mineral acid environments of this study, both annealed and annealed plus aged alloy 725 exhibited corrosion resistance comparable to mill annealed alloys 625 and C-276.

Table 13 and 14 display corrosion rates for 0.125 in. (3.2 mm) sheet of alloy 925 and 725, respectively, evaluated in mineral acid environments for varied exposure times and temperatures as per Materials Technology Institute (MTI) of the Chemical Process Industries (CPI) Manual No.3 Procedures. A planned interval exposure test is used (0-96, 96-192, and 0-192 hours) to provide information on any initial corrosion effects which might influence interpretation of the data. Both alloys exhibited low corrosion rates in many environments.

Corrosion Resistance to Seawater

Table 15 is a summary of crevice corrosion test data for alloy 625 and alloy 725 sheet specimens, evaluated in nominally quiescent seawater at 30°C for 30 days using an acrylic crevice device with plastic tape insert torqued to 25 in.-lbs. (2.9 Nm). Alloy 625 suffered significant corrosion, with a large percentage of the crevices attacked up to a maximum depth of 0.66 mm. In the 1850°F (1010°C)/1h/WQ + 1375°F (746°C) dual aged condition, alloy 725 exhibited excellent crevice corrosion resistance, with no attack observed in the 30-day exposure.

A summary of crevice corrosion test results for alloy 625 and alloy 725 tube sections, evaluated with flowing seawater on the inside surface (I.D.) of tubes is shown in Table 16. Vinyl sleeves which connected the tube specimens provided crevice formers in the seawater environment. Tests were conducted in flowing seawater at a mean temperature of 24.5°C for 145.8 days.

As seen in Table 16, two of the three alloy 625 specimens initiated attack in 26 to 40 days of exposure, which penetrated to a maximum depth of 0.78 mm. There was no attack observed in the 145.8 days of exposure, for duplicate specimens of alloy 725 in the solution annealed condition. For alloy 725 in the 1375°F (746°C) dual aged condition, just two of the three specimens were attacked with a maximum penetration of only 0.4 mm.

Figure 2 is a plot of Mean Axial Stress vs. Cycles of Fatigue for alloy 725 in the 1350°F (732°C) dual aged condition, as determined by the axial tension-tension method. The general fatigue behavior in seawater and air was similar The seawater corrosion fatigue strength was determined to be 105.8 ksi (729 MPa) for 107 cycles life.

A similar plot of Mean Axial Stress vs. Cycles of Fatigue for alloy 925 in the 1365°F (740.5°C) dual aged condition is found in Figure 3. As with alloy 725, the general fatigue behavior in seawater and air was similar. The seawater corrosion fatigue strength is 72.5 ksi (500 MPa) for 107 cycles life for alloy 925. Table 17 shows a comparison of the seawater corrosion fatigue life of alloys 725 and 925 compared to other alloys evaluated by the same technique.

Figure 4 is a plot of anodic current (galvanic coupling) versus time for alloy K-500 (N05500) and for alloy 725 in both the annealed and the 1350°F (732°C) dual aged condition. Tests were performed in natural seawater, ambient temperature. The surface area ratio of alloy 625 to alloy 725 and to alloy K-500 was 10:1. Alloy K-500 displayed a significantly high anodic current (corrosion rate) in the 92 days of exposure. Whereas, alloy 725 in both annealed and aged conditions showed an extremely low anodic current with a negligible corrosion rate.

Welding

Applications may require welding of alloy 725. Commercially available alloy 725 welding products provide a high strength alternative to alloy 625 welding wire.[8] Gas Tungsten Arc Welding (GTAW) and Gas Metal Arc Welding (GMAW) are the preferred methods of weld fabrication. Submerged Arc Welding (SAW) and Shielded Metal Arc Welding (SMAW) are not applicable methods of welding alloy 725.

Typical welding parameters for alloy 725 filler metal are listed in Table 18. One-half inch (12.7mm) plate was Gas Metal Arc Welded with matching filler wire to produce all weld metal samples for mechanical properties. Tables 19 and 20, respectively, display RTT and CVN impact test results for all weld metal samples of alloy 725 in the as welded, direct aged and annealed plus aged conditions. The annealed plus aged material exhibited mechanical properties similar to wrought products. As-welded material exhibited excellent impact properties and somewhat lower yield strengths than the annealed plus aged material. As expected, the direct aged material exhibited low impact strength and failed 2T side bend tests. Direct aging of alloy 725 weldments is therefore not recommended. Optimum results for welding

age- hardenable alloys are typically obtained by annealing the material to be welded prior to welding, then solution annealing and aging after welding.

In the Oil Patch, welding has been used to overlay a corrosion resistant alloy on low alloy steel. One of the main concerns with the use of weld overlays has been the mechanical properties. Historically, alloy 625 has been used for such applications. Because of relatively low room temperature mechanical properties, alloy 625 weld overlays have been limited in areas where galling and high contact stress are of concern. Alloy 725 provides an excellent high strength alternative to alloy 625 weld overlays.[8] Weld overlays of alloy 725 deposited on 4130 and 4140 steel and aged in the 1175 to 1225°F (635-663°C) stress relieving range of the steels for 2 to 8 hours exhibited excellent SCC resistance to a sour oil field environment at 300°F (149°C). Slow Strain Rate (SSR) tests were conducted on all weld metal samples of alloys 625 and 725, deposited on alloy steel, in the 5% NaCl + 75 psig H_2S + 400 psig CO_2 environment at 300°F (149°C). The alloy 725 weld overlays, aged during the steel stress relieving process, exhibited excellent stress corrosion cracking resistance equivalent to or better than the alloy 625 weld overlay. i.e., the TTF, %RA and %El ratios were high (average > 1.00) and there was no secondary cracking as summarized below:

	Alloy 725 Overlays		Alloy 625 Overlay	
	Mean	Range	Mean	Range
Time to Failure Ratio	1.00	0.83 – 1.15	0.93	0.90 – 0.95
%RA Ratio	1.09	0.97 – 1.24	1.06	0.92 – 1.20
%El Ratio	1.01	0.82 – 1.17	0.93	0.90 – 0.95

In review, the most common pass/fail criteria for SSR testing is a ratio of Time to Failure (TTF), % Reduction of Area (%RA) and/or % Elongation (%El) measured in a simulated oil patch environment relative to the same parameter in an inert environment (air or nitrogen). TTF and %RA ratios of >0.80 typically represent passing behavior in SSR tests. If the ratios are below 0.80, the specimen is examined under the Scanning Electron Microscope (SEM) for evidence of ductile or brittle fracture of the primary fracture surface. Ductile behavior passes and brittle behavior fails. All specimens are examined for secondary cracking in the gage length, away from the primary fracture. The absence of secondary cracking is indicative of good Stress Corrosion Cracking resistance is considered passing.

The presence of secondary cracks fails. One to two inert SSR tests were conducted along with one to three environmental SSR tests for each test lot of weld overlay. Air test results were averaged for calculation of critical ratios.

Conclusions

1. Alloy 925 (UNS N09925) and alloy 725 (UNS N07725) are resistant to pitting and to stress corrosion cracking in Deep Sour Gas Well environments containing NaCl, H2S and S, and are resistant to sulfide stress cracking.

2. Alloys 925 and 725 also exhibit excellent resistance to other environments, such as seawater and mineral acids.

3. Alloy 725 welding products provide a high strength alternative to alloy 625 welding wire, for welding age-hardenable alloys or for weld overlay on low alloy steel.

References

1. Kane, R.D., International Metals Reviews, Vol. 30, No.6, p.291, 1985.

2. Moeller, R.H., et.al., "Large Diameter Cold Worked C-276 for Downhole Equipment," CORROSION/91, March 11-15, 1991, Paper No. 30.

3. Hibner, E.L., "A New Age-Hardenable Corrosion Resistant Alloy for Deep Sour Gas Well Service," CORROSION/91, March 11-15, 1991, Paper No. 18.

4. DeBold, T.A. and Frank, R., Materials Performance, Vol.27, No.9, p.59, September, 1988.

5. Publication 1F192, "Use of Corrosion Resistant Alloys for Resistance to Environmental Cracking in Oilfield Environments," National Association of Corrosion Engineers, Houston TX, 1992 revision.

6. Rice, P.W., "Selecting Metallic Materials for Down Hole Service," World Oil, Vol.209, No.5, p.70, November, 1989.

7. Standard TM-0177, "Testing of Metals for Resistance to Sulfide Stress Cracking at Ambient Temperatures," National Association of Corrosion Engineers, Houston TX, 1990 revision.

8. Hibner, E.L. and Maligas, M.N., "High Strength Weld Overlay for Oil Patch Applications," CORROSION/93, March 8-12, 1993, Paper No.144.

9. Hibner, E.L., "Corrosion Behavior of Age Hardenable alloy UNS N07725 for Oil Field and Other Applications," Proceedings of ADVMAT/91 p.14-1, June 19-21, 1991.

10. Harris, J.A., et.al., "The Development of a Corrosion Resistant Alloy for Sour Gas Service," CORROSION/84, April 2-6, 1984, Paper No. 216.

11. Harris, J.A. and Clatworthy, E.F., "Hydrogen Embrittlement of INCOLOY alloy 925, MONEL alloy K-500, and INCONEL alloy 625 by Slow Strain Method," CORROSION/86, March 17-21, 1986, Paper No. 150.

12. Ganesan, P.G., et.al., "Development of a Time-Temperature Transformation Diagram for Alloy 925," Corrosion, Vol.44, No.11, p. 827, November, 1988.

13. Hibner, E.L., "A New Age-Hardenable Corrosion Resistant Alloy for Deep Sour Gas Well Service," CORROSION/90, April 23-27, 1990, Paper No. 50.

14. Hibner, E.L., "Corrosion Behavior of Age- Hardenable Alloy UNS N07725 for Oil Field Applications," CORROSION/91, March 11-15, 1991, Paper No. 18.

Table 1. Chemical Composition of Evaluated Heats (wt. %)

	UNS N09925	UNS N07725
Ni	42 – 46	55 – 59
Cr	19.5 – 22.5	19 – 22.5
Mo	2.5 – 3.5	7 – 9.5
Fe	22 min.	7 – 11
Cu	1.5 – 3.0	–
Al	0.5 max.	0.35 max.
Ti	1.9 – 2.4	1.0 – 1.7
Nb	–	2.75 – 4.0

Table 2. Representative Mechanical Properties of Nickel Alloys for Oil-Country Applications*

Alloy	Material Condition	Y. S. (0.2% Offset)		Tensile Strength		El. (%)	Hard. R$_C$
		1000 psi	MPa	1000 psi	MPa		
400 (UNS N04400)	Annealed	31.3	216	78.6	542	52	60B
	Cold Worked	93.7	646	108.8	716	19	20C
K-500 (UNS N05500)	Aged	97.5	672	152.5	1051	25	28C
600 (UNS N06600)	Annealed	39.7	274	99.2	684	43	77B
	Cold Worked	118.5	817	123.5	852	16	28C
625 (UNS N06625)	Annealed	69.5	479	140.0	965	54	95B
	Cold Worked	125.7	867	150.4	1037	30	33C
718 (UNS N07718)	Aged	159.0	1096	191.5	1320	20	40C
725 (UNS7725)	Annealed & Aged	132.0	910	181.0	1248	30	37C
	Cold Worked & Aged	>160.0	>1103	>189.0	>1303	>15	≥38C
X-750 (UNS N07750)	Aged	132.8	916	188.0	1296	27	34C
800 (UNS N08800)	Annealed	43.0	296	87.0	600	44	80B
	Cold Worked	100.0	690	111.8	771	17	25C
825 (UNS N08825)	Annealed	47.0	324	100.0	690	45	85B
	Cold Worked	114.0	786	130.5	900	15	28C
925 (UNS N09925)	Annealed & Aged	112.0	772	168.0	1158	29	34C
	Cold Worked	129.0	889	140.0	965	17	32C
	Cold Worked & Aged	153.0	1055	176.0	1214	19	–
25-6MO (UNS N08926)	Annealed	48.0	331	100.0	690	42	88B
	Cold Worked	138.0	952	162.0	1117	12	32C
G-3 (UNS N06985)	Annealed	41.4	285	99.3	685	54	83B
	Cold Worked	119.7	825	141.1	973	18	28C
C-276 (UNS N10276)	Annealed	52.0	359	110.4	761	64	83B
	Cold Worked	156.9	1082	172.5	1189	17	35C

*Properties represent various product forms. Tubular goods are supplied to specified minimum yield strengths that may differ from values in this table.

Table 3. Average Room Temperature Tensile and Charpy V-Notch Impact Properties for Alloy 925 and Alloy 725, 0.625 to 7.5 in. (1.6 to 19.0 cm) Diameter Hot Finished, Solution Annealed Plus Aged* Rod and Bar

| Alloy | Room Temperature Tensile | | | | | | -75°F (-59°C) Charpy V-Impact | | | |
| | 0.2% Yield Strength | | Tensile Strength | | | | Energy | | Lateral Expansion | |
	ksi	MPa	ksi	MPa	% El	% RA	ft-lb	J	in.	mm
925* (UNS N09925)	112	772	168	1158	29	45	65	88		
725**(UNS N07725)	132	910	181	1248	30	44	65	88	0.032	0.81

* Solution Treated at 1850°F (1010°C) aged at 1365°F (740°C)/8h, at 100°F (56°C)/h to 1150°F (620°C)/8h/AC.
** Solution Treated at 1900°F (1038°C) aged at 1350°F (732°C)/8h, at 100°F (56°C)/h to 1150°F (620°C)/8h/AC.

Table 4. Average Room Temperature Tensile and Charpy V-Notch Impact Properties for Alloy 725, 0.5 (1.27 cm) Plate, Solution Annealed at 1900°F (1038°C), then Aged*

| Aged Condition | Test Orientation | Room Temperature Tensile | | | | | | -75°F (-59°C) Charpy V-Impact | | | |
| | | 0.2% Yield Strength | | Tensile Strength | | | | Energy | | Lateral Expansion | |
		ksi	MPa	ksi	MPa	% El	% RA	ft-lb	J	in.	mm
1	Long.	128	883	182	1255	33	46				
1	Trans.	128	883	181	1248	31	46	77	104	0.040	1.02
2	Long.	125	862	180	1241	35	51				
2	Trans.	125	862	178	1227	36	54	112	152	0.056	1.42
3	Long.	127	876	177	1220	33	44				
3	Trans.	124	855	174	1200	34	45	62	84	0.039	0.99
4	Long.	123	848	175	1207	35	51				
4	Trans.	122	841	173	1193	36	51	112	152	0.059	1.50

*Aged Condition:
1. 1350°F (732°C)/8h at 100°F (56°C)/h to 1150°F (620°C)/8h/AC
2. 1325°F (718.5°C)/8h at 100°F (56°C)/h to 1150°F (620°C)/8h/AC
3. 1400°F (760°C)/6h AC
4. 1350°F (732°C)/8h AC

Table 5. Room Temperature Tensile Properties for Alloy 725 (UNS N07725) Cold Drawn* 0.217 in. (5.51 mm) Wall x 2.375 in. (60.3 mm) O.D. Tubing

Anneal	Dual Age	Yield Strength (0.2% Offset)		Tensile Strength		Elong	Hardness
		ksi	MPa	ksi	MPa	(%)	Rc
1850°F (1010°C)	1375°F(746°C)	128	882	184	1268	28	40
1875°F (1024°C)	1375°F (746°C)	132	910	183	1262	28	39
1900°F (1038°C)	1375°F (746°C)	133	917	183	1262	27	39
1900°F (1038°C)	1350°F (7432°C)	133	917	185	1275	30	38

Cold Drawn 17%, Longitudinal Properties
Heat Treatment:
    Anneal = Temperature/1h/Water Quench
    Dual Age = Temperature/8h, Furnace Cool 100°F (56°C)/h to 1150°F (620°C)/8h/Air Cool

Table 6. Average High Temperature Tensile Properties for Alloy 725, 0.625 to 7.5 in. (1.6 to 19.0 cm) Diameter Hot Finished, Solution Annealed Plus Aged* Rod and Bar

Test Temperature		Yield Strength (0.2% Offset)		Tensile Strength		Elon-gation	Reduction of Area
°F	°C	ksi	MPa	ksi	MPa	(%)	(%)
75	23	132.3	912	181.9	1254	30.8	47.3
100	38	134.4	927	183.9	1268	30.8	47.8
200	93	129.9	896	180.2	1242	28.5	45.6
300	149	126.5	872	174.3	1202	29.3	48.8
400	204	125.6	866	170.8	1178	29.7	51.3
500	260	120.5	831	166.3	1147	30.7	53.1
600	315	118.2	815	161.4	1113	31.0	54.3
650	343	120.8	833	161.2	1111	30.5	53.7
700	371	117.6	811	160.0	1103	30.3	54.4
750	399	118.9	820	158.7	1094	30.3	53.6
800	426	117.5	810	160.2	1105	30.0	52.0
850	454	117.2	808	155.9	1075	31.3	50.9
900	482	118.9	820	157.9	1089	30.7	49.8
950	510	115.1	794	153.7	1060	30.7	49.5
1000	538	117.3	809	157.3	1085	29.7	44.5

*Solution Treated at 1900°F (1038°C)/h then Aged at 1350°F (732°C)/8h, at 100°F (56°C)/h to 1150°F (620°C)/8h/AC

Table 7. Sulfide Stress Cracking C-Ring Test Results for Nickel
Alloys Evaluated as Per NACE Standard Test Methods TM-0177[a]

| Alloy | Material Condition | Simulated Well Age | Yield Strength (0.2% Offset) | | Hard-ness Rc | Dura-tion Days | Sulfide Stress Cracking |
			1000 psi	MPa			
625 (UNS N06625)	Cold Worked	None	125.0	862	30.5	42	No
	Cold Worked	None	160.0	1103	37.5	10	Yes
	Cold Worked	None	176.0	1214	41	6	Yes
718 (UNS N07718)	Annealed & Aged	None	120.0	827	30	42	No
	Annealed & Aged	None	130.0	896	37	42	No
	Annealed & Aged	None	134.0	924	38.5	42	No
	Annealed & Aged	None	139.0	958	38	42	No
	Annealed & Aged	None	156.0	1076	41	60	No
	Cold Worked	None	197.0	1358	37.5	2	Yes
			197.0[b]	1358[b]	37.5	25	Yes
725 (UNS N07725)	Cold Worked	None	90.0	621	25	30	No
	Annealed & Aged	None	117.6	811	37	30	No
	Annealed & Aged	None	128.6	887	40	30	No
	Annealed & Aged	600°F(315°C)/1000h	130.8	902	41.5	30	No
	Annealed & Aged	None	132.9	916	36	42	No
	Annealed & Aged	None	133.0	917	39	30	No
	Cold Worked & Aged	None	137.8	950	39	42	No
825 (UNS N08825)	Cold Worked	None	138.0	952	30	42	No
	Cold Worked	None	147.0	1014	33	42	No
925 (UNS N09925)	Annealed & Aged	None	114.0	786	38	42	No
	Cold Worked	None	139.0	958	35.5	42	No
	Cold Worked & Aged	None	176.0	1214	43.5	42	No
	Cold Worked & Aged	None	186.0	1282	46	42	No
	Annealed & Aged	500°F(260°C)/1000h	113.5	783	38	42	No
	Cold Worked	500°F(260°C)/1000h	139.5	962	35.5	42	No
	Cold Worked & Aged	500°F(260°C)/1000h	176.0	1214	43.5	42	No
	Cold Worked & Aged	500°F(260°C)/1000h	180.0	1214	44	42	No
	Cold Worked & Aged	500°F(260°C)/1000h	185.5	1279	46	42	No
G-3 (UNS N09685)	Cold Worked	600°F(315°C)/1000h	119.4	823	26	43	No
	Cold Worked	600°F(315°C)/1000h	132.3	912	30	43	No
	Cold Worked	600°F(315°C)/1000h	135.3	933	31	43	No
	Cold Worked	600°F(315°C)/1000h	136.9	944	–	30	No,No[c]
	Cold Worked	600°F(315°C)/1000h	137.7	949	–	30	No,No[c]
	Cold Worked	600°F(315°C)/1000h	181.7	1253	–	30	No,No[c]
C-276 (UNS N10276)	Cold Worked	600°F(315°C)/1000h	126.6	873	32	43	No
	Cold Worked	600°F(315°C)/1000h	155.1	1069	38	43	No
	Cold Worked	600°F(315°C)/1000h	166.8	1150	35	43	No
	Cold Worked	600°F(315°C)/1000h	188.7	1301	43	43	No

[a]Room temperature tests at 100% of yield strength in 5% NaCl plus 0.5% acetic acid saturated with H2S. All specimens were coupled to carbon steel.
[b]Test stress was 85% of yield strength: 165,000 psi (1138 MPa).
[c]Duplicate test specimens.

Table 8. C-Ring Stress Corrosion Cracking Data* for Nickel Alloys Evaluated in High Temperature Sour Brine Environments

Alloy	Material Condition	Yield Strength (0.2% Offset) 1000 psi	MPa	Hard-ness R$_C$	Test Media**	Duration Days	Stress Corrosion Cracking
625 (UNS N06625)	Cold Worked	128.0	883	37	A	15	No
	Cold Worked	177.1	1221	41	A	15	No
	Cold Worked	128.0	883	37	B	15	No
	Cold Worked	177.1	1221	41	B	15	No
	Cold Worked	125.0	862	30.5	C	42	No
	Cold Worked	160.0	1103	37.5	C	42	No
	Cold Worked	176.0	1214	41	C	42	No
718 (UNS N07718)	Annealed & Aged	120.0	827	30	C	42	No
	Annealed & Aged	134.0	924	38.5	C	42	No
	Cold Worked	197.0	1358	37.5	C	20	Yes
825 (UNS N08825)	Cold Worked	131.0	903	30	A	15	Yes
	Cold Worked	138.0	952	30	C	42	No
	Cold Worked	147.0	1014	33	C	42	No
925 (UNS N09925)	Annealed & Aged	166.0	1145	40.5	A	15	Yes
	Annealed & Aged	133.5	783	38	B	15	Yes
	Annealed & Age	185.5	1279	46	B	15	Yes
	Cold Worked & Aged	114.0	786	38	C	42	No
	Cold Worked	139.0	958	35.5	C	42	No
	Cold Worked & Aged	176.0	1214	43.5	C	42	No
	Annealed & Aged	185.5	1279	46	C	42	No
G-3 (UNS N09685)	Cold Worked	133.5	920	33	D	60	No
	Cold Worked	133.5	920	33	D	120	No
	Cold Worked	137.5	948	30	D	90	Yes
	Cold Worked	137.5	948	30	D	120	No
	Cold Worked	183.3	1264	38	D	120	No
	Cold Worked	133.5	920	33	E	60	No
	Cold Worked	133.5	920	33	E	120	No
	Cold Worked	137.5	948	30	E	120	No
	Cold Worked	183.3	1264	38	E	120	No
C-276 (UNS N10276)	Cold Worked	194.7	1342	43.5	A	15	No
	Cold Worked	194.7	1342	43.5	B	15	No

*Autoclave tests on C-ring specimens stressed at 100% of yield strength.

**Test Media:

A = 15% NaCl plus 200 psi (1380 kPa) H$_2$S plus 100 psi (690 kPa) CO$_2$ plus 1g/L of sulfur at 450°F(232°C).

B = 25% NaCl plus 200 psi (1380 kPa) H$_2$S plus 100 psi (690 kPa) CO$_2$ plus 1g/L of sulfur at 400°F(204°C).

C = 15% NaCl saturated with H$_2$S plus 1000 psi (6.9 MPa) gas phase of 1% H$_2$S, 50% CO$_2$, 49% N$_2$ at 500°F(260°C).

D = 25% NaCl plus 100 psi (690 kPa) H$_2$S plus 200 psi (1380 kPa) CO$_2$ at 400°F(204°C).

E = Same as D but at 425°F (218°C).

Table 9. C-Ring Stress Corrosion Cracking Data Nickel Alloys
Evaluated in a Sour Brine Environment Containing Free-Sulfur

Alloy	Material Condition	Y.S. (0.2% Offset) 1000 psi	MPa	Stress Corrosion Cracking 350°F (177°C)	375°F (191°C)	400°F (204°C)	425°F (218°C)	450°F (232°C)	475°F (246°C)	500°F (260°C)
725 (UNS N07725)	Annealed & Aged	117.6	811	No	No	No	No	No	Yes[b]	No
	Annealed & Aged	128.6	887	No	No	No	No	Yes	–	–
	Annealed & Aged	132.9	916	No	No	No	No	No	No	No
	Annealed & Aged	133.0	917	No	No	No	No	No	Yes[b]	No
718 (UNS N07718)	Annealed & Aged	130.3	898	Yes[c]	–	–	–	–	–	–
625 (UNS N06625)	Cold Worked	144.0	993	No	Yes	–	–	–	–	–
	Cold Worked	160.0	1103	No	Yes	–	–	–	–	–
C-276 (UNS N10276)	Cold Worked	127.0	876	No	No	No	No	No	No	No
	Cold Worked	155.0	1069	No	No	No	No	No	No	Yes
	Cold Worked	167.0	1151	No	No	No	No	No	No	No
	Cold Worked	168.0	1158	No	No	No	No	No	No	Yes

a. C-ring autoclave tests of 14-day duration at 100% of yield strength in 25% NaCl plus 0.5% acetic acid plus 1 g/L sulfur plus 120 psi (827 kPa) H_2S.
b. One of two specimens cracked.
c. At 275°F (135°C).

Table 10. Mass Loss Corrosion Data[a] for Nickel Alloys Evaluated in a Sour Brine Environment

Alloy	H$_2$S Pressure		Corrosion Rate			
			300°F (149°C)		400°F (204°C)	
	psi	kPa	mpy	mm/y	mpy	mm/y
625 (UNS N06625)	10	69	0.0	0.000	0.1	0.003
	50	345	0.3	0.008	0.4	0.010
	100	690	0.1	0.003	0.2	0.005
825 (UNS N08825)	10	69	0.1	0.003	0.1	0.003
	50	345	0.4	0.010	0.5	0.013
	100	690	0.1	0.003	0.5	0.013
925 (UNS N09925)	0	69	0.1	0.003	0.1	0.003
	50	345	0.4	0.010	0.5	0.013
	100	690	0.1	0.003	0.4	0.010
718 (UNS N07718)	10	69	3.0	0.076	0.3	0.008
	50	345	0.7	0.018	2.3	0.058
	100	690	0.1	0.003	1.2	0.030
K-500 (UNS N05500)	10	69	27	0.69	11	0.28
	50	345	78	1.98	113	2.87
	100	690	221	5.61	169	4.29
9Cr/1Mo Steel	50	345	206	5.23	278	7.06
	100	690	299	7.59	172	4.37

[a] Autoclave tests of 14-day duration in 15% NaCl/distilled water with total gas pressure of 1000 psi (6.9 MPa) consisting of 500 psi (3.4 MPa) CO2 plus N$_2$ and H$_2$S.

Table 11. Mass Loss Corrosion Data[a] for Nickel Alloys
Evaluated in a Sour Brine Environment Containing Free-Sulfur

Alloy	Test Media[b]	Corrosion Rate	
		mpy	mm/y
C-276 (UNS N10276)	A	0.2	0.005
	B	0.1	0.003
625 (UNS N06625)	A	0.7	0.018
	B	0.2	0.005
925 (UNS N09925)	A	1.1	0.028
	B	1.2	0.030
825 (UNS N08825)	A	1.1	0.028
	B	1.6	0.041
Type 316SS (UNS S31600)	A	3.9	0.099
	B	4.5	0.114

[a] Autoclave tests of 15-day duration on unstressed coupons.
[b] Solution A: 15% NaCl plus 200 psi (1380 kPa) H$_2$S plus 100 psi (690 kPa) CO$_2$ plus 1 g/L of sulfur at 450°F (232°C).
Solution B: 25% NaCl plus 200 psi (1380 kPa) H$_2$S plus 100 psi (690 kPa) CO$_2$ plus 1 g/L of sulfur at 400°F (204°C).

Table 12. Average Corrosion Rates for Alloy 725 (N07725) in Mineral Acids*
Compared to Literature Data for Alloy 625 (N06625) and Alloy C-276 (N10276)

Alloy 725 Condition	3% HC1 150°F (66°C)		5% HC1 150°F (66°C)		10% HC1 150°F (66°C)		Boiling 10% H₂SO₄		Boiling 10% HNO₃		Boiling 30% H₃PO₄		Boiling 85% H₃PO₄	
	mpy	mm/y	mpy	mm/y	mpy	mm/y	mpy	mm/y	mpy	mm/y	mpy	mm/y	mpy	mm/y
1	<1	<0.03	<1	<0.03	105	2.67	25	0.64	<1	<0.03	3	0.08	73	1.85
2	<1	<0.03	<1	<0.03	268	6.81	25	0.64	<1	<0.03	5	0.13	62	1.57
3	<1	<0.03	<1	<0.03	250	6.35	25	0.64	<1	<0.03	3	0.08	45	1.14
4	<1	<0.03	<1	<0.03	218	5.54	28	0.71	<1	<0.03	2	0.05	35	0.89
Literature														
Alloy 625	<1	<0.03	69	1.75	93	2.36	18	0.45	<1	<0.03	<10	<0.25	25	0.63
Alloy C-276	<5	<0.03	5-20	0.13-0.51	20	0.51	20	0.51	16	0.41	<5	<0.13	5-25	0.13-0.64

Condition: *Two Week Duration
1. 1900°F(1038°C) anneal
2. 1900°F(1038°C) anneal + 1400°F(760°C)/6h/AC
3. 1900°F(1038°C) anneal + 1375°F(746°C)/8h, FC at 100°F(56°C)/h to 1150°F(620°C)/8h/AC
4. 1900°F(1038°C) anneal + 1350°F(732°C)/8h, FC at 100°F(56°C)/h to 1150°F(620°C)/8h/AC

Table 13. Corrosion Rates for Alloy 925 (UNS N09925), 0.125" Sheet, Evaluated in Acid
Environments for Varied Exposure Times and Temperatures as per MTI Manual No.3 Procedures

Environment	Temp (°C)	Corrosion Rate					
		0-96 Hours		96-192 Hours		0-192 Hours	
		mpy	mm/y	mpy	mm/y	mpy	mm/y
0.2% HCl	Boiling	<0.1	<0.01	<0.1	<0.1	<0.1	<0.01
1% HCl	70	1	0.03	<1	<0.03	11	0.28
10% H₂SO₄	70	3	0.08	<1	<0.03	2	0.05
85% H₂PO₄	Boiling 90	46 <1	1.17 <0.03	47 <1	1.19 <0.03	47 <1	1.19 <0.03
80% CH₃CO₂H	Boiling	<0.1	<0.01	<0.1	<0.01	<0.1	<0.01

Table 14 Corrosion Rates for Alloy 725 (UNS N07725), 0.125" Sheet, Evaluated in Acid Environments for Varied Exposure Times and Temperatures as per MTI Manual No.3 Procedures

Environment	Temp.(°C)	Corrosion Rate					
		0–96 Hours		96–192 Hours		0–192 Hours	
		mpy	mm/y	mpy	mm/y	mpy	mm/y
0.2% HCl	Boiling	<0.1	<0.01	<0.1	<0.01	<0.1	<0.01
1% HCl	Boiling	4.6	0.12	1.9	0.05	10.2	0.26
	90	25.0	0.64	2.0	0.05	2.0	0.05
5% HCl	70	193.8	4.92	203.3	5.16	169.7	4.31
	50	52.8	1.34	52.5	1.33	44.7	1.14
	30	9.4	0.24	6.6	0.17	7.8	0.18
10% H_2SO_4	Boiling	9.9	0.25	21.5	0.55	4.6	0.12
60% H_2SO_4	70	25.5	0.65	25.6	0.65	16.0	0.41
	50	23.1	0.59	0.71	0.02	29.0	0.74
	30	1.5	0.04	1.3	0.03	7.1	0.18
95% H_2SO_4	70	66.3	1.68	67.5	1.71	42.0	1.07
	50	72.6	1.84	50.1	1.27	23.0	0.58
	30	11.0	0.28	13.3	0.34	13.0	0.33
85% H_2PO_4	Boiling	30.7	0.78	31.2	0.79	58.0	1.47
	90	0.54	0.01	0.50	0.01	0.32	0.01
80% CH_3CO_2H	Boiling	<0.1	<0.01	<0.1	<0.01	<0.1	<0.01

Table 15. Summary of Crevice Corrosion Test Data for Sheet and Strip Specimens of Alloy 625 (N06625) and Alloy 725 (N07725), Evaluated in Quiescent Seawater at 30°C for 30 Days Using an Acrylic Plastic Crevice Torqued to 25 in.-lbs. (2.9 Nm)

Alloy	Observed Initiation (days)	Percent of Sites Attacked	Maximum Depth of Attack (mm)
625 (N06625)[a]	2 to 5	25 to 75	0.02 to 0.66 (Average 0.26)
725 (N07725)[b]	None at 30 days	0	0.00
[a] Data for 4 heats of mill annealed commercial sheet, duplicate specimens. [b] Data for 1 heat of hot rolled commercial strip in condition: 1850°F(1010°C)/1h/AC + 1375°F(746°C)/8h, FC at 100°F(56°C)/h to 1150°F(620°C)/8h/AC.			

Table 16. Summary of Crevice Corrosion Test Data for Tube Specimens of Alloy 625 (N06625) and Alloy 725 (N07725), Evaluated with Flowing Seawater on the ID Surface at a Mean Temperature of 24.5°C for 145.8 Days Using Vinyl Sleeves Secured with Clamps as a Crevice Former

Alloy	Observed Initiation (days)	Maximum Depth of Attack (mm)
625 (N06625)[a]	26 to 40 (no attack of 1 specimen)	<0.01 to 0.78
725 (N07725)[b]	0	0
725 (N07725)[c]	42 to 80 (no attack of 1 specimen	<0.01 to 0.04

[a] Data for 3 specimens of commercially produced welded tubing.
[b] Data for 2 machined tube specimens in the 1900°F(1038°C)/1h/WQ solution annealed condition.

[c] Data for 3 machined tube specimens in condition: 1900°F(1038°C)/1h/WQ + 1375°F(746°C)/8h, FC at
100°F(56°C)/h to 1150°F(620°C)/8h/AC.

Table 17. Seawater Corrosion Fatigue Strength for alloy 725 (N07725) in the Solution Annealed plus 1350°F (732°C)Dual Aged Condition, Compared to Other Commercially Significant Alloys

Alloy	Ultimate Tensile Strength ksi (MPa)	Corrosion Fatigue Strength* in Seawater at 107 Cycles ksi (MPa)
MP-35N	303 (2089)	124.1 (856)
718 (N07718)	238 (1641)	130.0 (896)
AISI 4140	236 (1627)	42.5 (293)
PH 13-8Mo	219 (1510)	67.5 (465)
925 (N09925)	170 (1172)	72.5 (500)
725 (N07725)	180 (1241)	105.8 (729)

*Axial tension-tension fatigue test.

Table 18. Typical Hobart Ultra-Arc 350 Programs for Alloy 725 Filler Metals

Wire Diameter (inches)	0.035	0.045
Peak Current (amp)	324	400
Time at Peak (mil sec)	3.0	3.4
Minimum Current (amp)	30	40
Delta Current (amp)	350	100
Wire Feed Speed/100 amp (ipm)	310	170
Starting Current (amp) Useful down to;	350 – 45 amp	350 – 60 amp
Shielding Gas:	100% Ar or 75% Ar, 25% He	100% Ar or 75% Ar, 25% He
Flow (cfh)	50-60	50-60

Table 19. Typical Alloy 725 Filler Metal All Weld
Metal GMAW Room Temperature Tensile Properties

Test Orienta-tion	Base Metal Pre-Weld Condition	Post Weld Treatment	Tensile Strength		Yield Strength		El	R.A.	Side Bend Indications
			ksi	MPa	ksi	MPa	%	%	
Transv.	Anneal	As Welded	124.9	861	73.6	507	39.0	34.4	P 2T
Long.	--	As Welded	119.8	826	76.0	524	33.0	30.6	P 2T
Long.	--	Age	172.1	1187	130.1	897	20.0	22.5	F 2T
Transv.	Anneal	Age	179.8	1240	141.0	972	13.0	19.5	P 4T
Long.	--	Ann,Age	173.9	1199	129.9	896	19.0	28.6	P 4T
Transv.	Ann,Age	Ann,Age	171.4	1181	131.8	909	25.0	29.8	P 4T
Long.	--	Ann2,Age	174.8	1205	126.5	872	21.0	28.4	P 4T
Transv.	Anneal	Ann2,Age	172.8	1191	126.6	873	28.0	42.7	P 4T

Ann = 1900°F (1038°C)/1h/AC   P = Pass
Ann2 = 1950°F (1066°C)/1h/AC   F = Fail
Age = 1350°F (732°C)/8h, FC 100°F (56°C)/h to 1150°F (620°C)/8h/AC

Table 20. Typical Alloy 725 Filler Metal All Weld Metal GMAW Impact Prope-ties

Post Weld Heat Treatment	75°F (23.9°C) CVN Impact		-75°F (-59.3°C) CVN Impact	
	ft – lb	J	ft – lb	J
1	66	89		
2	16	22	18	24
3	42	57	39	53
4	56	76	79	107

Condition: 1. As Welded
           2. 1350°F(732°C)/8h, FC at 100°F(56°C)/h to 1150°F(620°C)/8h/AC
           3. 1900°F(1038°C) anneal + 1350°F(732°C)/8h, FC at 100°F(56°C)/h to 1150°F
               (620°C)/8hAC
           4. 1950°F(1066°C) anneal + 1350°F(732°C)/8h, FC at 100°F(56°C)/h to
               1150°F(620°C)/8hAC
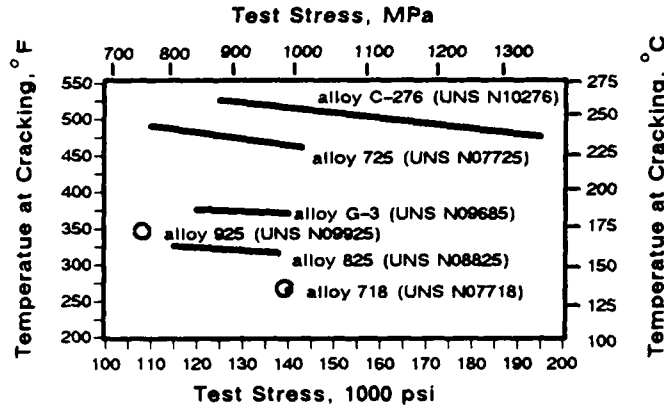
Figure 1. Results of autoclave C-ring tests in a solution of distilled water containing 25% sodium chloride, 0.5% acetic acid, and 1g/L sulfur with pressure of 120 psi (825 kPa) hydrogen sulfide. Test stresses were 100% of yield strength (0.2% offset).
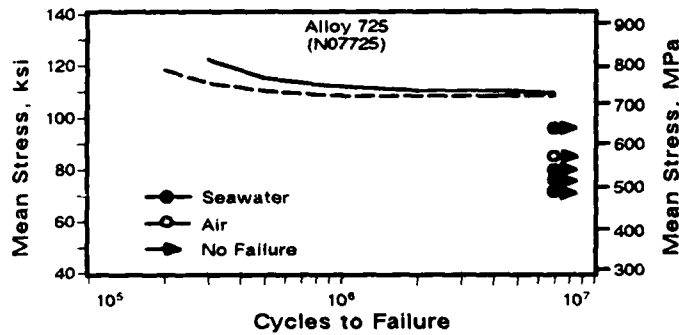
Figure 2. Mean Axial Stress Versus Cycles of Fatigue for Alloy 725 in the 1350°F Dual Aged Condition, Tension-Tension Test
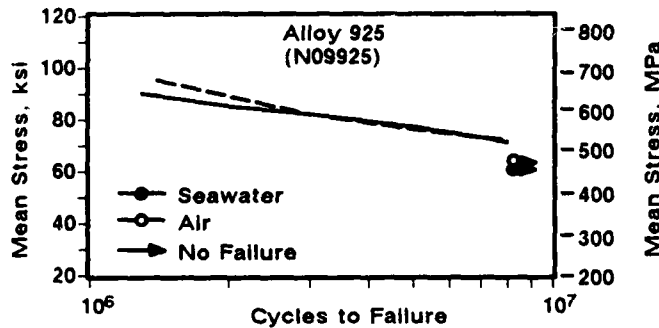
Figure 3. Mean Axial Stress Versus Cycles of Fatigue for Alloy 925 in the 1365°F (740.5°C) Dual Aged Condition, Tension-Tension Test.
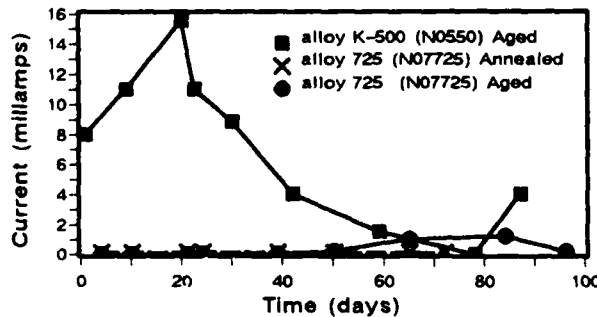
Figure 4. Anodic Current versus Time (Galvanic Coupling to alloy 625) for Aged Alloy K-500 and for Alloy 725 in Both the Annealed and Annealed + Aged Conditions.

Stress Corrosion Cracking Behavior of Austenitic and Duplex Stainless Steels in Simulated Sour Environments

Kari Saarinen
VTT, Technical Research Centre of Finland
P.O. Box 26 (Kemistintie 3)
SF-02151 Espoo, Finland

Abstract

The exploitation of the new oil fields or the chemical changes in the environment of the fields already in operation usually means that the production facility will be operated in more hostile environments than earlier. This is due to higher temperatures and pressures or increased contents of hydrogen sulphide, carbon dioxide or chlorides. To evaluate the effects of these more hostile environments on the reliability and durability of tǐ structural materials, stress corrosion cracking behavior of several austenitic and duplex stainless steels has been studied by using stressed specimens immersed into simulated sour environments.

The studies were carried out in a NACE solution (5% NaCl + 0.5% CH_3COOH, deaerated, pH = 3 and saturated with H_2S at room temperature) and in the modified NACE solution (20% NaCl + 0.5% CH_3COOH, deaerated, pH = 3 and saturated with H_2S at room temperature) by using four-point loaded as well as U-bend specimens. The testing temperature was 200 °C and the pressure 300 bar in the NACE solution test. In the modified NACE solution the testing temperature was 150 °C and the pressure was 150 bar. The materials studied were commercial stainless steels delivered by Outokumpu Polarit Oy and Materials Technology Oy (Subsidiary of Rauma Oy). For failure cases a fractographical inspection was performed.

In the NACE solution failures were observed in the austenitic alloys POLARIT 725, 757 and in the duplex alloys DUPLOK 22 and 25. In the austenitic alloys the fracture mode was mainly intergranular, whereas in the duplex alloys the fracture has occurred mainly transgranular. To compare the sulphide stress corrosion cracking susceptibility of the different alloys, a SCEN (stress corrosion equivalent number) that was gained by dividing the pitting resistance equivalent number (PREN) with the applied stress, was used. According to the results failures were observed in the duplex alloys as the SCEN number was less than about $80 \cdot 10^{-3}$, whereas for the austenitic alloys the critical SCEN number was about $90 \cdot 10^{-3}$. In the modified NACE solution failures were observed in the alloys POLARIT 725 and POLARIT 757. The failure mode was mainly intergranular as observed also in the studies conducted in the NACE solution. In the failure cases in these austenitic alloys the critical SCEN was observed to be the same about $90 \cdot 10^{-3}$ as was observed in the NACE solution.

Key terms: Stainless steels, stress corrosion cracking, oil production, sour environment, hydrogen sulphide, high temperature, high pressure

Introduction

The exploitation of the new oil fields or the chemical changes in the environment of the fields already at operation usually means that the production facility will be operated in more hostile environments than earlier. This is due to higher temperatures and pressures or increased contents of hydrogen sulphide, carbon dioxide or chlorides. The changed environments usually also mean that the maintenance costs and the corrosion requirements of the construction materials will increase. To meet the changed material requirements and to reduce the demand for maintenance, new materials are being introduced for the offshore industry and more corrosion resistant alloys are being used in the offshore constructions.

In sour wells the oil and natural gas are often contaminated by hydrogen sulphide, the content of which may vary from a few parts per million up to 30 %[1]. In the presence of hydrogen sulphide the atomic hydrogen that is produced on the surface of the steel by the corrosion reactions tends to enter the steel and cause embrittlement. This phenomenon is called sulphide stress corrosion cracking (SSC). The SSC susceptibility is enhanced by chlorides and the results obtained by Fliethmann et al. indicate that the cracking mechanism is a mixed mechanism of hydrogen- and chloride induced SSC[2]. Beside cracking, considerable general corrosion can be observed due to presence of carbon dioxide that acidifies the mixture of brine and oil[1]. In order to optimize the SSC behavior of the austenitic and duplex stainless steels, the chemical composition and the ferrite / austenite ratio have to be considered[3]. Also microstructure, heat treatment conditions, grain size and form of nonmetallic inclusions plays an important role in the SSC resistance of construction materials[4]. Thus, for reasonable assessment of the applicability of a duplex stainless steels in a certain sour environment, it is important to consider practical experience and to use suitable SSC test methods, both regarding the loading procedure and the environment[6].

The localized corrosion resistance is related to the chemical composition and thereby to the pitting resistance number (PREN) of an alloy. The initial process of SSC could be the breakdown of the passive film[3] and thereby the increase of the chromium and molybdenum content of the alloys increases the passivity of the surface layer. However, it has been pointed out that the ferritic phase of duplex stainless steels is richer in chromium and molybdenum than the austenitic phase and hence the PREN of the austenitic phase seems to play a more important role on the pitting resistance and hence on the SSC resistance of the duplex stainless steels than the PREN of the ferritic phase[3]. The SSC susceptibility of the duplex stainless steels is also greatly affected by the ferrite / austenite ratio, distribution and grain size. The threshold stress for SSC in simulated sour environments have been observed to be highest at the α-content of 40 to 45 %[5] and an alloy with a α-content exceeding 80 % is reported to have a high susceptibility to pitting and intergranular corrosion[5].

To evaluate the effects of hostile environments on the reliability and durability of the structural materials, stress corrosion cracking behavior of several austenitic and duplex stainless steels has been studied by using stressed specimens immersed into simulated sour environments.

Experimental

I.   Test Materials

The materials investigated in this study are commercial austenitic and duplex stainless steels delivered by Outokumpu Polarit Oy and Materials Technology Oy. For reference materials were selected SAF 2205 delivered and manufactured by SANDVIK Co. and Nicrofer 6020, Nicrofer 5716 and Nicrofer 5923 delivered by Cronimo Co. and manufactured by VDM Nickel-Technologie AG. The chemical compositions of the test materials, their pitting resistance equivalent numbers (PREN = Cr + 3,3 Mo + 32 N) and stress corrosion cracking equivalent numbers (SCEN = PREN / applied stress * 1000) are presented in Table 1.

II.   Test Equipment and Environments

The high temperature studies were carried out by using the unique Materials Research Shuttle Laboratory facility that can withstand hostile environments and pressures up to 1500 bar and temperatures up to 300 °C. The facility consists of a high temperature and high pressure autoclave with a room temperature storage tank and a recirculation loop "Figure 1". The facility is also equipped with an environment monitoring system to control the water chemistry of the autoclave. The facility is assembled into a freight container "Figure 2" that was transferred outside the laboratory facilities in order to avoid any indoor leakages of hydrogen sulphide.

The corrosion potential measurements were carried out by using $Ni/NiSO_4$ reference electrode and the results are presented in a scale of standard hydrogen electrode.

In the NACE solution (5% NaCl + 0.5% CH_3COOH, deaerated, pH = 3 and saturated with H_2S at room temperature) both four-point loaded specimens and U-bend specimens were used. The four-point loaded specimens were prepared from commercial austenitic stainless Polarit alloys grades 774 and 778 and duplex alloys DUPLOK 25, DUPLOK 27, DUPLOK 27 HS PM, CF8M and SAF 2205. The preparation and the stress calculations of the specimens followed the ASTM standard G 39-79. The stress applied on the four-point loaded specimens was 90 % of the yield strength of each material. The U-bend specimens were prepared from alloys POLARIT 725, 757, DUPLOK 22 and CF8M. The applied stress for U-bends was considered to be the yield strength. The testing temperature was 200 °C and the pressure was 300 bar. The exposing time for four-point loaded specimens was 250 hours and for U-bend specimens 100 hours.

In the modified NACE solution (20% NaCl + 0.5% CH_3COOH, pH = 3, deaerated, saturated with H_2S at room temperature) U-bend specimens were used. The specimens were prepared from all alloys mentioned in Table 1. The testing temperature was 150 °C and the pressure was 150 bar. The exposing time was 400 hours and the applied stress was considered to be the yield strength.

After testing the specimens were examined by using an optical microscope and the failures were reported. For failure cases a fractographical inspection was performed.

Results

In the NACE solution the failures were observed in the austenitic alloys POLARIT 725, 757 and in the duplex alloys DUPLOK 22 and 25. In the austenitic alloys the fracture mode was mainly intergranular "Figures 3a, 3b". In the duplex alloys the fracture partly follows grain boundaries between the ferrite and austenitic faces, but mainly the fracture is transgranular "Figure 3c". When the susceptibility of the alloys was compared by dividing the PREN with the applied stress related to the yield strength differences between austenitic and duplex alloys were observed. In the duplex alloys failures were observed as the SCEN was less than about $80 \cdot 10^{-3}$, whereas a failure was observed in the austenitic alloy having a SCEN of about $90 \cdot 10^{-3}$. The corrosion potential of all the alloys during the experiment was near -100 mV(SHE).

In the modified NACE solution the failures were observed in the alloys POLARIT 725 and POLARIT 757. The failure mode in these austenitic alloys was mainly intergranular as observed also in the NACE solution. The critical SCEN for cracking was also observed to be the same about $90 \cdot 10^{-3}$ as was observed in the NACE solution. The corrosion potential of all the alloys during experiment was near -100 mV(SHE). A small change to a positive direction in the corrosion potentials of the austenitic alloys could be observed.

Discussion

It is known that the corrosion cracking susceptibility of austenitic alloys increases as the temperature increases. The more alloying elements the material has the higher the critical cracking temperature is. In this study the temperature of 150 °C was high enough to cause intergranular corrosion cracking in the austenitic alloys having a PREN under about 30 and SCEN under about $90 \cdot 10^{-3}$. The cracking behavior of the austenitic alloys was the same in the NACE solution and in the modified NACE solution. According to the high temperature pH-potential diagrams for the $Fe-S-H_2O$, $Cr-S-H_2O$, $Ni-S-H_2O$ and $Mo-S-H_2O$ systems[7] at pH 3, only iron and nickel sulphides are stable in the environments studied. Therefore the failure cases of the austenitic alloys are apparently related to the various nickel contents of the different alloys, since the nickel contents of the unfailed specimens were clearly higher than the nickel contents of the failure cases.

It is also known that the cracking resistance of duplex alloys is enhanced compared to the austenitic alloys having the same level of alloying elements and mechanical properties. According to the SCEN examination the same effect was also observed in this study, since the SCEN boundary for no cracking was lower in the duplex alloys than in the austenitic alloys. This was observed inspite of the fact that the SCEN does not include the nickel content of the alloys and thereby the volume of the austenitic phase in the duplex micro-structure that effects on the stress corrosion cracking susceptibility of the duplex alloys[5]. Normally the initiation and the growth of the cracks in the duplex stainless steels takes place in the austenitic part of the material. In this case, however the cracking was observed to grow not only in the austenitic structure, but also in the ferrite phase. This was probably due to the high contents of hydrogen sulphide and thereby high contents of hydrogen in the environment.

Conclusion

In this work the evaluation of sulphide stress corrosion cracking behavior of several austenitic and duplex stainless steels in simulated sour environments has been made by using U-bend and four-point loaded specimens. According to the results

- in the high temperature and pressure NACE solution test failures were observed in the austenitic alloys POLARIT 725, 757 and in the duplex alloys DUPLOK 22 and 25,
- in the austenitic alloys the fracture mode was mainly intergranular,
- in the duplex alloys the fracture occurred partly on the grain boundaries of the ferrite and austenitic faces, but mainly the fracture was transgranular,
- in the duplex alloys failures were observed in the NACE solution as the SCEN number was less than about $80 \cdot 10^{-3}$,
- in the austenitic alloys failures were observed in the alloys having a SCEN number less than about $90 \cdot 10^{-3}$,
- the corrosion potential of all the alloys during the experiments was near -100 mV(SHE),
- in the modified NACE solution the failures were observed in the alloys POLARIT 725 and POLARIT 757,
- the failure mode in the austenitic alloys was mainly intergranular as observed also in the studies conducted in the NACE solution,
- in the austenitic alloys the critical SCEN for cracking was observed to be about $90 \cdot 10^{-3}$ in the modified NACE solution.

Acknowledgements

References

1. Garber, R. et al. Sulfide Stress Cracking Resistant Steels for Heavy Section Wellhead Components. J. of Materials for Energy Systems. 1985, pp. 91-103.

2. Fliethmann, J. et al. Autoklaven-Untersuchungen der Spannungsriβkorrosion von Fe-Cr-Ni-Legierungen in NaCl/CO₂/H₂S-Medien. Werkstoffe und Korrosion 43(1992), pp.467 - 474.

3. Brunella, M. F. et al. Stress Corrosion Cracking in Sour Environments of Martensitic and Duplex Stainless Steels. Proc. of Int. Conference on Stainless Steels. Chiba, 10-13 June 1991. Tokyo 1991, ISIJ. Vol 1. pp. 264 - 271.

4. Artamoshkin, S. V. Effect of the Microstructure and Nonmentallic Inclusions on the Susceptibility of Low-alloy Steels to Sulfide Stress Corrosion Cracking. Translated from Fiziko-Khimicheskaya Mekhanika Materilov. 27(1991)6, pp. 60 - 66.

5. Kudo, T. et al. Stress Corrosion Cracking Resistance of 22% Cr Duplex Stainless Steel in Simulated Sour Environments. Corrosion 45(1989)10, pp. 831 - 838.

6. Eriksson, H., Bernhardsson, S. The Applicability of Duplex Stainless Steels in Sour Environments. Corrosion 47(1991)8, pp. 719 -727.

7. Chen, C. M. et al. Computer-Calculated Potential pH Diagrams to 300 °C. Palo Alto 1983, Electric Power Research Institute, EPRI NP-3137, Vol. 1-2.

Table 1.   Nominal composition of the materials used in the study given by the manufactures.

Material	C	Si	Mn	S	P	Cr	Ni	Mo	Cu	Al	Co	Nb	Fe	N_2	PREN	SCEN U-bend	SCEN Four-point
POLARIT 725	0.027	0.41	1.45	0.001	0.034	18	8.6	0.019	0.18	0.001	0.17	0	bal	0.0565	20	74	-
POLARIT 757	0.049	0.49	1.51	0.007	0.029	17.1	10.6	2.51	0.16	0	0.21	0	bal	0.046	27	91	-
POLARIT 774	0.02	0.55	1.46	0.001	0.015	20	24.7	4.48	1.67	0.022	0.22	0	bal	0.0765	37	118	131
POLARIT 778	0.024	0.4	0.46	0.001	0.019	19.8	21.5	6.15	0.79	0.024	0.37	0	bal	0.21	47	123	137
LOK-Mo 5	0.024	0.35	0.49	0.005	0.032	20.7	24.0	5.2	0.57	0.01	0.05	0.02	bal	0.20	44	176	-
LOK-Mo 6	0.025	0.30	0.48	0.003	0.030	19.6	17.9	6.1	0.66	0.02	0.05	0.03	bal	0.20	46	184	204
DUPLOK 21	0.012	0.60	0.58	0.008	0.032	20.7	8.3	2.8	1.25	0.03	0.05	0.06	bal	< 0.06	32	86	-
DUPLOK 22	0.013	0.53	0.52	0.010	0.033	23.0	6.1	3.0	0.19	0.02	0.10	0.02	bal	0.15	38	77	-
DUPLOK 25	0.015	0.43	0.62	0.008	0.030	24.5	6.4	3.0	1.45	0.03	0.07	0.04	bal	0.14	39	71	79
DUPLOK 26	0.023	0.20	0.72	0.010	0.030	26.2	7.6	2.95	0.68	0.02	0.07	0.02	bal	0.22	43	84	-
DUPLOK 27	0.01	0.28	0.52	0.008	0.032	27.1	7.9	3.0	2.5	0.01	0.05	0.03	bal	0.24	45	83	93
DUPLOK 27 HS PM	0.01	0.50	0.55	0.005	0.030	27	8	4	2.5	0.010	0.05	-	bal	0.3	50	77	85
CF8M	0.005	0.68	0.87	0.007	0.030	18.7	9.6	2.1	0.26	0.03	0.15	0.02	bal	<0.06	28	122	135
CA6NM	0.01	0.55	1.02	0.005	0.020	12.5	3.8	0.40	0.16	0.01	0.10	0.02	bal	<0.02	14	25	-
SAF 2205	0.018	0.40	1.51	0.007	0.025	22.5	5.7	3.0	0.07	0.01	0.05	0.02	bal	0.14	37	72	80
Nicrofer 6020	0.01	0.13	0.17	-	0.005	21.8	bal	8.5	0.06	0.16	0.05	3.4	3	-	53	101	-
Nicrofer 5716*	0.01	0.05	0.37	-	0.005	19	bal	15	0.08	0.09	0.10	0.04	6.5	-	72	170	-
Nicrofer 5923	0.01	0.12	0.15	-	0.005	22.5	bal	14	0.01	0.2	0.00	0.03	0.5	-	72	-	-

* The tungsten (W) content of the alloy Nicrofer 5716 is 4 %.
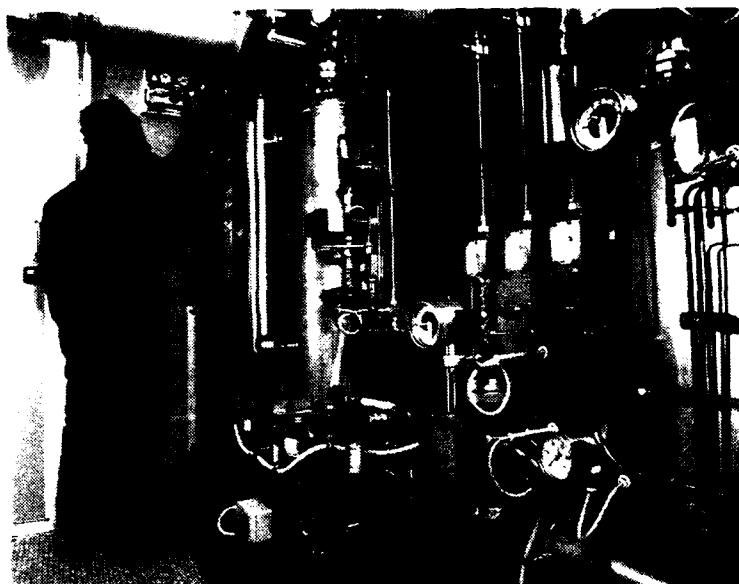
Figure 1.   The chemistry and flow of the test environment can be monitored and controlled with sophisticated instrumentation. In the figure the 120 liter storage tank, H_2S-cylinder, high pressure pumps and part of the recirculation loop can be seen.
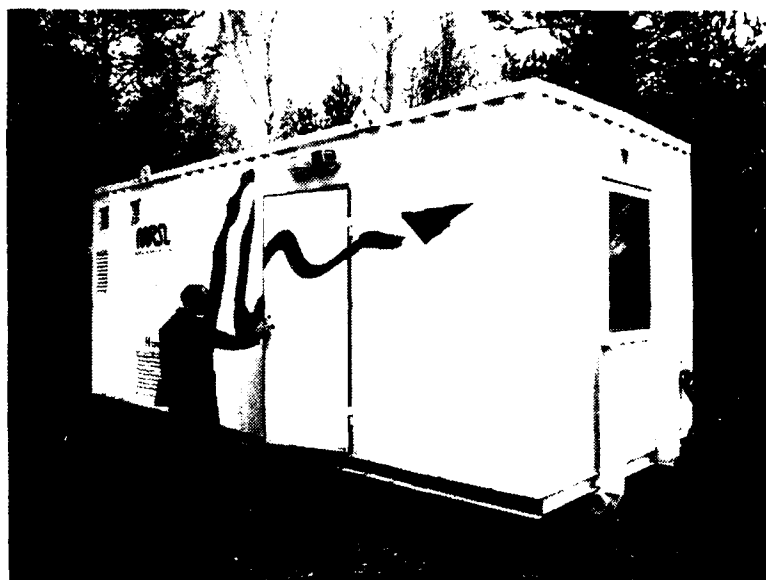
Figure 2.   The process autoclave facility is assembled into a freight container. For operators safety, the container is divided between autoclave area and protected compartment, which contains all control and measurement devices.
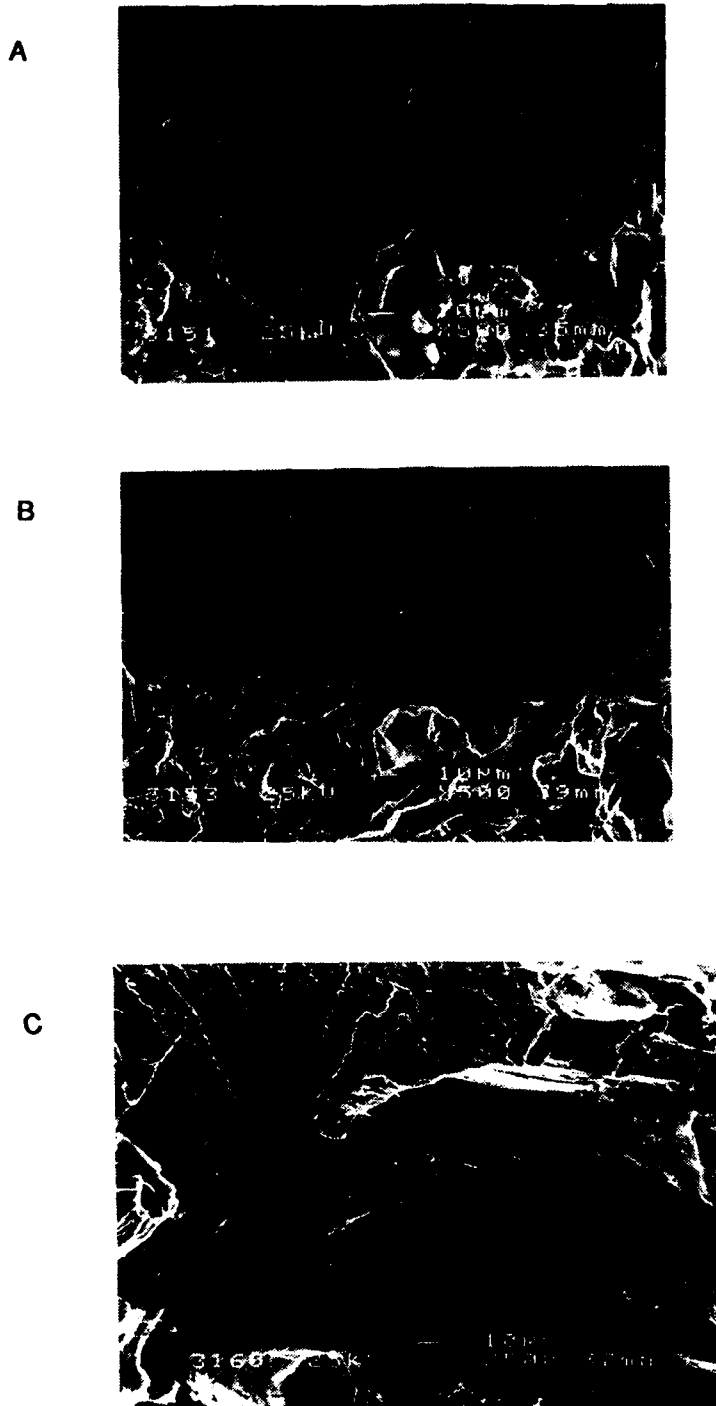
Figure 3.   The fracture surfaces of a) alloy POLARIT 725, x 500 and b) alloy POLARIT 757, x 500 are mainly intergranular. The fracture in the alloy DUPLOK 22 has partly occurred on the grain boundaries between the ferrite and austenitic faces, but the fracture is mainly transgranular c), x 500.

Role of Expert Systems in Technology Transfer of Materials for Petroleum Applications

Sridhar Srinivasan
Cortest Laboratories, Inc.
P. O. Box 691505
Houston, Texas 77269-1505

Abstract

Material evaluation for oil and gas applications requires an in-depth understanding of corrosion phenomena and materials behavior. Expert systems developed at Cortest Laboratories have been shown to be valuable tools in assimilating and disseminating hard to access expertise to end-users, so as to create consistent methods of material evaluation across the band-width of users. This paper describes a series of expert systems related to material selection in different areas that have played a catalytic role in bringing together pooled expertise from different sources: (i) Evaluation of metallic materials for resistance to SSC in sour environments (SUSCEPT) (ii) Selection of corrosion resistant alloys (CRAs) for oil and gas production (SOCRATES) (iii) Selection of corrosion resistant alloys (CRAs) in non-production environments (SOCRATES-B) (iv) Evaluation of steels for resistance to HIC and SSC in sour pipelines (STRATEGY-A) and (v) Evaluation of steels for resistance to HIC and SSC in wet H2S refineries (STRATEGY-B). Such programs have enabled *technology transfer* across different companies and countries in critical applications related to petroleum production and in doing so, have become vehicles for sharing corrosion and materials information and knowledge.

Keywords: Expert systems, sour service, corrosion, cracking, environmental severity, material selection

1. Introduction

Selection and evaluation of materials for different types of petroleum applications related to oil and gas production, transmission and refining requires extensive knowledge into behavior of materials in different types of environments and development of methods to utilize existing experience and data to create appropriate material and environment characterization techniques. Given the enormous amount of information that is involved in decision-making for material evaluation in petroleum applications, a natural need has arisen to encapsulate this body of knowledge in a medium that would facilitate access to appropriate information and promote consistency in material selection decision-making. Expert systems have been developed at Cortest Laboratories over the last five years to address different aspects of materials associated with several types of oil and gas production service[1,2]. These include expert systems for:

- Evaluation of metallic materials for resistance to SSC (Suscept)
- Selection of Corrosion Resistant Alloys Production Service (Socrates)
- Evaluation of steels and weldments in sour pipeline and refinery service (Strategy)
- Selection of CRAs in non-production environments (Socrates - B)

All these programs have been developed as multi-client sponsored programs that bring together a representative industry group together to create the specifications for development. The group of companies in these development programs typically span the gamut of materials scientists and engineers, from material manufacturers and equipment suppliers to end users such as oil companies. All the programs have been developed by creating a body of material selection and

environmental evaluation rules gleaned from available literature, laboratory test data and field experience. In developing these expert systems, there was a significant exchange of information between the different participant companies, an effort to create a consistent and accurate decision-making logic to be embodied in the computer. This exchange of information in developing these expert systems has several obvious benefits to the end-user community:

- Access to material selection and corrosion evaluation information representing the state-of-the-art expertise in these areas
- Creation of a consistent methodology for environment and material characterization, representing a consensus view of available technology
- Creation of a knowledge base of material evaluation information which can be easily distributed and augmented
- Access to a tool that can be used to disseminate domain expertise about materials for petroleum production service and relevant corrosion concerns to non-specialist end-users

Most of these expert systems provide a framework for further development and customization of both the knowledge bases and the databases. They can play a critical role in training personnel in technical areas and to impart a measure of consistency coupled with correctness in decision-making across a company and industry groups. The experience from the development of these systems has created a two way technology transfer and communication channel that allows all participants in the development benefit from shared experiences and expertise.

The rest of the paper is organized as follows: The organization of the different expert systems developed at Cortest Laboratories for sour service material selection is given in Section 2. Section 3 describes fundamentals of expert systems and knowledge base system development. The Socrates expert system is described in Section 4 and the Strategy system is described in Section 5. The role of expert systems in materials for petroleum applications are examined and conclusions are presented in Section 6.

2. Expert Systems for Selection of Sour Service Materials

The expert system development effort for selection of sour service materials has been broadly divided into three phases: Phase I (SUSCEPT) deals with evaluation and specification of metallic materials for resistance to sulfide stress cracking (SSC). This system embodies information about different types of oil and gas applications and metallurgical conditions for different materials for SSC resistance. This system is also coupled with a database containing information from literature and field experience. The Phase II system (SOCRATES)[3,4] provides access to the material selection decisions and the decision logic of a domain expert in the selection of Corrosion Resistant Alloys (CRAs). The SOCRATES system also embodies information from published literature and proprietary test data on evaluation CRAs. The SOCRATES system also allows the user to perform a cost analysis to compare costs of using CRAs and steels for a given application. The SOCRATES-b program evaluates CRAs based on considerations relevant to non-production environments such as those with injected water, acidizing and well completions[5].

General corrosion, pitting, sulfide stress cracking and anodic stress corrosion cracking are of particular concern when selecting CRA materials[6]. Further, for many CRAs, there is relatively limited documented field experience to define their limits of use. Selection of CRAs often involves decision-making based on seemingly contradictory laboratory data. Also, selection involves

understanding and characterizing the effects of the following variables in terms of mechanical, corrosion and cracking considerations, such as[7]:

- Mechanical requirements such as strength, heat treatment and hardness criteria
- H_2S partial pressure
- CO_2 partial pressure
- Minimum and maximum operating temperatures
- Bicarbonates and Hydrogen ion concentration (pH)
- Sulfur
- Gas to Oil ratio and Water to Gas ratio
- Metallurgical composition

Conventional steels, on the other hand, are quite susceptible to different types of hydrogen cracking (sulfide stress cracking, hydrogen blistering, hydrogen induced cracking, stress-oriented hydrogen induced cracking and sulfide stress cracking) which can occur in sour pipeline and wet H_2S refinery applications[8]. Environmental factors affecting performance of steels in these applications include:

- H_2S, CO_2 concentration
- Minimum and maximum operating temperatures
- Bicarbonates and pH
- Cyanides
- Ammonia
- Gas to Oil ratio and water cut

The Phase III program (STRATEGY)[9] evaluates refinery and sour pipeline environments and provides recommendations for HIC and SSC resistant steels. The overall structure and organization of the different expert systems in given in Figure 1. The different components of Figure 1 address different aspects critical to sour service material selection. Each of the different systems encapsulate significant domain expertise; however, together they provide a comprehensive reasoning and decision-making tool. The SOCRATES and the STRATEGY systems are discussed in the sections 4 and 5 from a stand point of providing an overview of the development methodology and the knowledge stored in these systems. Fundamentals of expert systems are discussed in the next section.

3. Expert Systems, Rules and Knowledge Representation

Expert systems are defined as intelligent computer programs using expert knowledge to attain high levels of performance in narrow problem domains[10]. The term *expert* in the expert system implies the narrow specialization and competence of a human expert which has been embodied into the system. Expert systems have a specific structure that distinguishes them from conventional computer programs. Structural components in an expert system are shown in Figure 2. The knowledge base and the inference engine form the heart of the expert system. The knowledge base houses the expertise that is embodied in an expert system. The inference engine controls the manner or the logical path used by the expert system to utilize the information (facts and rules) in the knowledge base to make decisions.

Knowledge or expertise in a particular area (termed as domain-expertise) is stored in the knowledge base in terms of facts and rules. *Knowledge representation* in the expert system refers to the scheme used to represent a given piece of information in an expert system. Decision

making in an expert system can be represented through interconnected rules. The rules are used in a specific sequence in order to reach decisions.

Each of the programs discussed in this paper have been developed through support from a multi-client industrial group to create knowledge bases that represent a consensus view point on many aspects of materials characterization for different environments and focusing on different aspects of corrosion and cracking, as well as capture expertise within each organization. The Socrates expert system is described in Section 4.

4. Socrates: Expert System for Selection of CRAs

The organization of different frames in the SOCRATES system is shown in Figure 3. The system performs material selection by applying constraints at different hierarchical levels. The constraints are organized such that a comprehensive initial solution set of applicable materials is refined and reduced in size as the system proceeds through the different levels.

At level 1, the initial set of applicable materials is obtained by determining the application for which the CRA is to be selected. If the application is not known, all classes of materials known to the system become part of the solution set. These include the following classes of materials:

- **Stainless Steels**: Conventional austenitic, high alloy austenitic, martensitic, precipitation hardened, duplex and ferritic.
- Precipitation hardened and solid solution nickel base alloys, nickel copper alloys.
- Cobalt-base, titanium and zirconium alloys.

The constraints at this level include yield strength, material condition (heat treatment/cold work) and hardness limitations. At this level, the constraints operate independently and hence are applied sequentially. For example, a material in a required yield strength (SMYS) range (say, 110-130) can also be cold worked. Here, materials available in the required yield strength range are selected prior to applying the material condition (cold worked) requirement.

At level 2, the environment is characterized in terms of severity for general corrosion using the following environmental parameters:

- H_2S and CO_2 partial pressure
- Bicarbonates
- pH
- Minimum operating temperature
- Chlorides and Sulfur
- Water to gas ratio and gas to oil ratio

The parameters used in the material evaluation based on the environment operate concurrently. When materials are evaluated at this level, the system considers both the effect of the individual parameter as well as the effect of the cumulative interactions. An environmental severity index, based on the environmental parameters, is computed to represent the synergistic effect of the different parameters operating in concurrence. The environmental severity index is determined based on the pH, chloride content and the H_2S partial pressure of the environment. The program determines the pH based on this environmental severity index which is used to select the set of

applicable materials. Typical environmental variables and corresponding severity indices are shown in Table 1.

At level 3, materials are evaluated for their susceptibility to stress corrosion cracking. Factors in evaluation here include,

- H_2S partial pressure
- pH
- Chlorides
- Maximum operating temperature
- Material composition in terms of nickel, chromium, molybdenum, tungsten and columbium

A typical rule for material evaluation for resistance to SCC is given in Table 2.

At level 4, the materials are evaluated for their susceptibility to pitting corrosion. A Required Minimum Pitting Index (RMPI) is computed based on maximum temperature, and environmental severity determined at level 2. Further, a pitting index is computed for each of the materials in the solution set using the relation[11],

$$\text{Pitting Index} = Cr + 3.3Mo + 11N + 1.5(W + Cb)$$

Where Cr, Mo, N, W and Cb represent Chromium, Molybdenum, Nitrogen, Tungsten and Columbium content of the alloy. All alloys that have a pitting index greater than or equal to the RMPI are selected for further evaluation. At level 5, all applicable materials from level 4 are evaluated for qualification based on sulfide stress cracking requirements as well as certain rules of thumb based on application requirements. The SOCRATES system contains 115 commonly used CRAs and their metallurgies which are used during the evaluation process. The architecture of the expert system facilitates easy modification of the database and its alloys without affecting the reasoning embodied in the system or the knowledge base. The knowledge base for the STRATEGY system is described in Section 5.

5. STRATEGY: Evaluation of Steels in Sour Pipelines and Wet H_2S Refineries

Serviceability of refinery process equipment exposed to wet H2S environments and pipelines exposed to sour (H_2S-containing constituents) have been issues of significant concern in recent years. Most of these concerns stem from premature failure of steel equipment in these applications related to absorbed hydrogen produced by the sulfide corrosion process. Cracking problems in these applications arise from one of the following four phenomena:

- **SSC** - formation of brittle cracks in high strength steels
- **Hydrogen blistering** - formation of internal blisters in low strength steels
- **Hydrogen Induced Cracking** (HIC) - the linking of small blister cracks that can traverse the cross-section in a step-wise manner
- **Stress-Oriented Hydrogen Induced Cracking** (SOHIC) - Similar to HIC, but the small blister cracks are aligned in the through-thickness direction by the action of tensile stress.

The STRATEGY system evaluates steels for specific types of service typically seen in wet H_2S refineries and sour pipelines. The structure of the Strategy system for refinery service is shown in Figure 4. The steel evaluation and selection process, as in the SOCRATES system, is accomplished through a four step process, specified below:

1. Ranking of the refinery/pipeline environment in terms of severity from a stand point of hydrogen cracking.
2. Ranking of steels based on metallurgical parameters affecting cracking resistance.
3. Normalization and synthesis of the environmental and material ranks to assess suitability of a given steel to a given environment.
4. Determination of a reliability factor as a function of the materials resistance factor and the environmental severity factor.

5.1 Determination of Environmental Severity

There are two types of wet H_2S environments found in refinery and pipeline service:
1. The mildly acidic sour pipeline environments, whose pH and severity vary in correspondence with acid gas content.
2. The typically alkaline refinery environments, which under some conditions may turn slightly acidic.

System pH and the H_2S contents are the two most significant components of the pipeline environment. Based on the pH and H_2S values, the pipeline environment can be categorized into different regimes of severity such as mild, intermediate, severe and very severe. Other parameters that have an effect on severity of hydrogen charging include effective dehydration, the presence of a persistent oil phase and chemical inhibition.

Refinery environments are generally more complex and unstable as opposed to pipeline environments. However, in the STRATEGY system, refinery environments are ranked on an interval scale of 1-10, based on the following parameters:
- pH
- Cyanide concentration
- Maximum temperature
- H_2S concentration
- Ammonia, Bicarbonates and Polysulfides

5.2 Methodology for Ranking Steels

Critical material parameters are combined in this step to determine a material rank on an interval scale that represents the cracking resistance of the material[12]. For example, for HIC resistance, the following parameters are important:
- Product form (hot-rolled plate or pipe, forging, casting etc.)
- Heat treatment (as-rolled, annealed, normalized or quenched & tempered)
- Micro structure (centerline segregation, ferrite/pearlite banding, minor banding, no banding)
- Presence of inclusions (elongated clusters/stringers, isolated globular etc.)
- De-oxidation practice (Si-Al killed, Si-killed, Ca-treated)

Each steel is ranked with respect to each of the above parameters on a scale, in the order of increasing HIC resistance. Also, the following alloying elements have been determined to be critical factors in determining HIC cracking behavior of steels:

- **Sulfur**   Very low   < 0.002%
            Low   0.002 - 0.01%
            Medium   0.011 - 0.02%
            High   > 0.02%
- **Phosphorus** Low   ≤ 0.01%
            High   >0.1%
- **Carbon**   Very Low   ≤ 0.1%
            Low   0.11 - 0.15%
            Medium   0.16 - 0.2%

High   > 0.2%

All these compositional elements affect HIC resistance such that increasing levels of these elements typically reduce HIC resistance of both pipeline and plate steels. Other parameters such as yield strength, tensile strength and hardness do not play a major role in determining HIC resistance of the steel whereas maximum susceptibility to hydrogen blistering is typically seen in lower strength steels. However, hardness is very critical to determining SSC resistance and strength ratio is critical to SOHIC resistance in steels.

In the STRATEGY system, the different parameters are combined in such a way as to produce a material rank that represents the overall HIC resistance of the material. The system compares the environmental ranking and the material rank to guide the user about the applicability of a given steel in a specific refinery or pipeline environment.

5.3 Applications of the SOCRATES and STRATEGY Systems

One of the most important aspects of expert systems formulated on empirical data and state-of-the-art knowledge is that they must be flexible and be able to accommodate changes in our fundamental knowledge and available data used in the materials selection process. The methodologies utilized in SOCRATES and STRATEGY systems can be easily modified through changes to the associated rules and databases. The importance of the ability of an adaptive system for selection of materials for sour service applications has been highlighted by the rapid growth of databases and operating experience with these materials.

In two recent studies performed by Cortest Laboratories[13], SOCRATES accurately predicted problems associated with SCC of duplex stainless steels and localized corrosion problems in martensitic stainless steels based on the definition of the service environment. This aspect of the expert system, to assist in accurate selection of stainless alloys and reproducibly monitor the effects of up to seven environmental variables critical to alloy corrosion performance, we believe, underscores the relevance of such systems. Furthermore, these studies has also shown that such expert systems can significantly reduce the time required to conduct a proper selection of sour service materials and have shown a cost benefit of at least 5 to 1 based on the engineering time saved.

6. Conclusions

Expert systems have been developed to provide material selection guidelines for different aspects of petroleum production and processing applications. The SOCRATES system performs comprehensive evaluation of CRAs from a stand point of general corrosion, stress corrosion cracking and localized corrosion where as the STRATEGY system evaluates different types of steels for wet H_2S refinery and sour pipeline service. Both systems have been developed using a group of experts who have come together to provide state-of-the-art information to the development of these systems. All the expert systems have been developed so as to facilitate customization of their knowledge bases as well as to allow for incorporation of updated information on material performance as technologies progress.

The knowledge bases for the different expert systems were developed using available expertise from industry and literature as well as field and lab data. The creation and review of the knowledge bases proved to be a convenient vehicle for exchanging information about material behavior between different companies and facilitated transfer of technology as a means to the

creation of consistent material selection and evaluation methodologies. The growth of the development program into other allied areas indicates the success of this type of development where expert systems bring together the expertise from different companies around the world in creating an effective approach to documenting and disseminating critical material evaluation and corrosion characterization technologies.

7. Acknowledgments

References

1. S. Srinivasan and R. D. Kane, "Expert systems for selection of materials in sour service", 72nd Annual GPA convention, San Antonio, Texas, March 1993

2. R. D. Kane and S. Srinivasan "Reliability assessment of Wet H_2S Refinery and pipeline equipments: A Knowledge-based systems approach", Serviceability of Petroleum, Process and Power Equipment, Eds. D. Bagnoli, M. Prager and D. M. Schlader, PVP Vol. 239, ASME, NY, 1992.

3. S. Srinivasan and R. D. Kane "Selection of Martensitic and Duplex stainless steels for oil and gas production service", Corrosion 92, Paper No.56, NACE, April 1992.

4. S. Srinivasan and R. D. Kane "Methods of data synthesis in a rule-based representation for characterization of corrosion and cracking in CRAs", Corrosion 92, Paper No. 267, NACE, April 1992.

5. S. Srinivasan and R. D. Kane, Socrates-b: Expert System for evaluation of CRAs in non-production environments, Cortest proposal no. P002135SK, November 1991.

6. Crolet J., and Bonis M. R. "Evaluation of the resistance of some highly alloyed stainless steels to stress corrosion cracking in high chloride solutions under high pressures of CO_2 and H_2S" Corrosion/85, Paper No. 232, Boston, MA, 1985.

7. A. Ikeda, T. Kudo, Y. Okada, S. Mukai, F. Terasaki, "Corrosion behavior of high alloy oil country tubular goods for deep sour gas wells" Paper No. 206, Corrosion/84, New Orleans, LA, 1984.

8. S. Srinivasan and R. D. Kane, Strategy - Expert system for Evaluation of steels in wet H_2S refinery environments, Cortest document No. L912022SK, March 1993.

9. S. Srinivasan and R. D. Kane, "An approach to the development of an expert system for reliability assessment of sour pipelines", Proceedings of the International Conference on Pipeline Reliability, Calgary, Alberta, June 1992.

10. Hayes-Roth F., Et al., Building Expert Systems, Addison Wesley Publishing Co., MA, 1983, pp 1-37.

11. H. Ogawa et al., "An estimating method for the critical limit of corrosion resistance of high alloy OCTG and line pipe in sour environments", Corrosion/87, No. 294, San Francisco, CA, 1987.

12. R. D. Kane, "Metallurgical considerations for wet H2S service", Cortest Laboratories' 2nd International H2S Materials Conference, Paper No. 2, Houston, TX, Jan. 1992.

13. R. D. Kane, Cortest Laboraotories' internal report on applications of SOCRATES, September 1991.

Table 1 -- Typical Environmental severity rankings for different combinations of pH, H2S and chlorides

	Low (pH ≤ 4)	Moderate (4 < pH ≤ 5.5)	High (pH > 5.5)	
	20	15	10	Low (Cl⁻ ≤ 10,000 ppm)
H₂S pp ≤ 1 psi	25	20	15	Moderate (10,000 < Cl⁻ ≤ 100,000ppm)
	30	25	20	High (Cl⁻ > 100,000 ppm)
	30	15	10	Low
1 psi < H₂S pp ≤ 10 psi	50	40	20	Moderate
	60	50	30	High
	60	30	20	Low
10 psi< H₂S pp ≤ 100 psi	85	50	40	Moderate
H₂S > 100 psi + Sulfur	140	120	120	Moderate
	150	150	150	High

Table 2 -- A Typical Rule in Socrates

```
IF
        [       Temp ≥ 60 C < 80 C                and
                {(Chlorides  100000 ≥ ppm and H₂S ≥ 1.5 psia)  or
                (Chlorides  10000 ≥ ppm and H₂S ≥ 15 psia)}              ]
        or
        [       Temp ≥  80 C   < 120 C and
                {(Chlorides  10000 ≥ ppm and H₂S ≥ 1.5 psia)  or
                (Chlorides  1000 ≥ ppm and H₂S ≥ 15 psia)}              ]
        or
        [       Temp ≥ 120 C   and
                {(Chlorides  10000 ≥ ppm and H₂S ≥ 0.15 psia)  or
                (Chlorides  1000 ≥ ppm and H₂S ≥ 15 psia)}              ]
THEN
        Duplex stainless steels are susceptible to stress corrosion cracking.
```
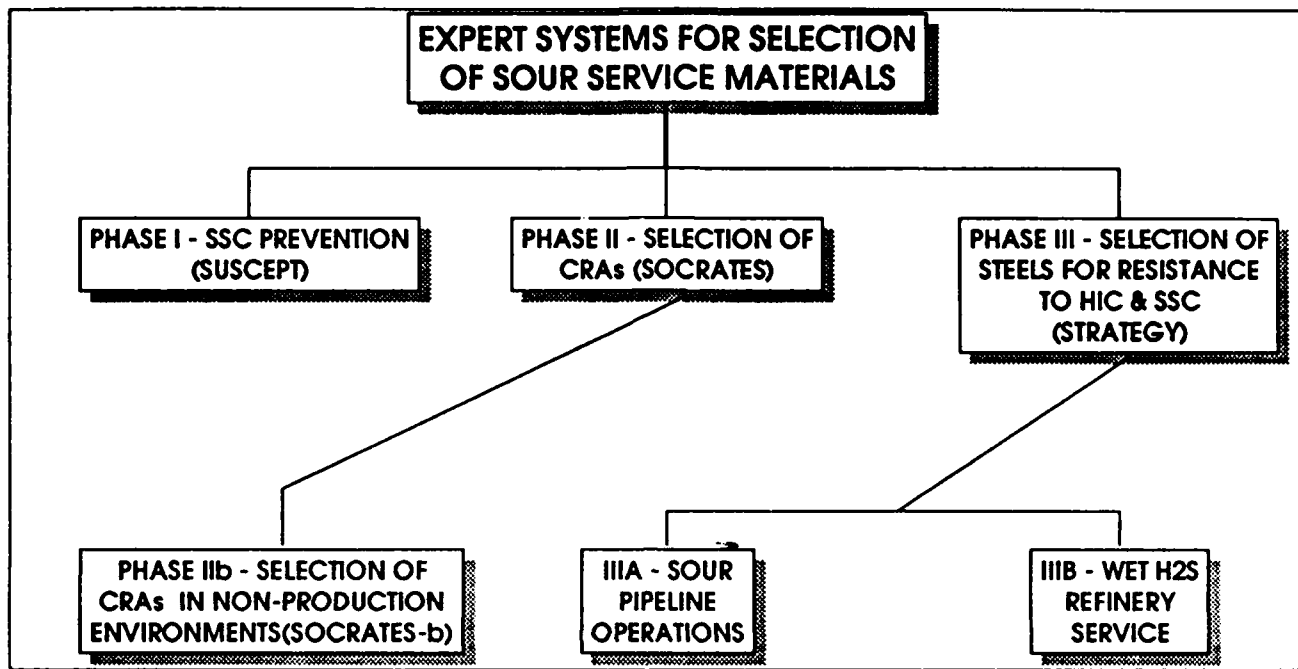
Figure 1 - Organization of different expert systems for selection of sour service materials
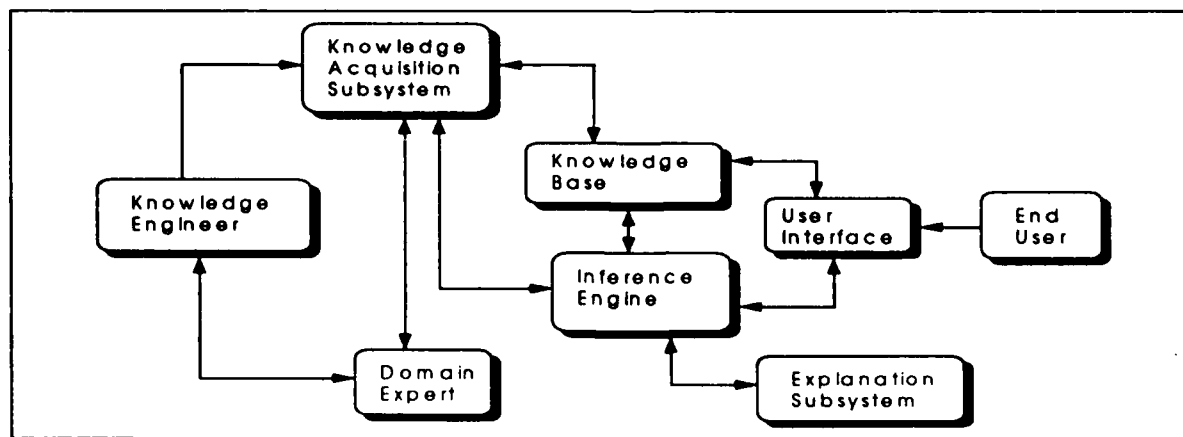
Figure 2 - Structural Components in Expert System Development
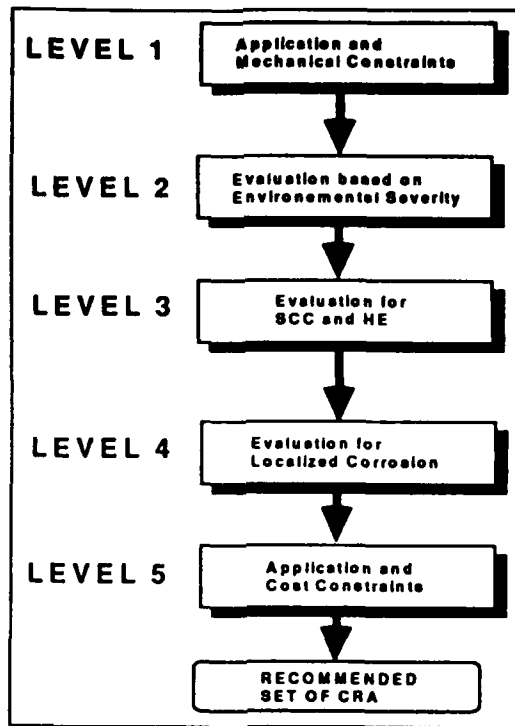
Figure 3 - Structure of the SOCRATES expert System
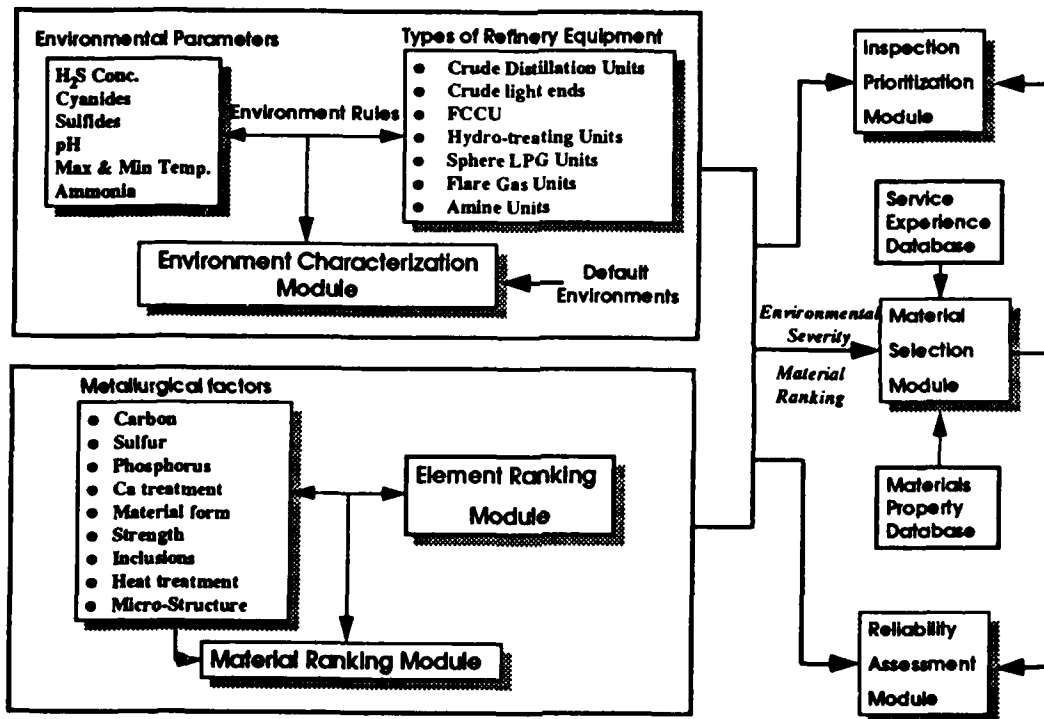
Figure 4 - Knowledge base structure for the STRATEGY system

The Effect of Certain Compositional Aspects on the Behavior of Tank and Pipe Linings under Laboratory and Field Conditions

Max A. Winkeler
Sigma Coatings USA
PO Box 816
Harvey, LA 70059

Abstract

In spite of all the progress made in analytical and testing techniques, certain aspects of the performance of chemical resistant linings are marginally understood. Although this paper will not give an answer to all of the causes and effects, it will address the theories behind the blistering of coatings under immersion conditions; the adhesive forces that have to counteract the separation of the film from the steel surface to prevent blistering; the influence of the transition temperature of the lining on the performance under high temperature immersion conditions and more specifically the effect of a temperature gradient over the coating film. As test methods the use of autoclave and atlas cell equipment will be discussed. Finally some results will be mentioned, obtained with coatings made according to new insights.

Introduction

In general, organic coatings used for the protection of metals are composed of resins or binders, pigments, solvents and almost always one or more additives to assist in obtaining the required properties of the liquid as well as the cured coating material.

After WW II complete new resin technologies announced the era of the thermoset materials. Unless triggered by high temperatures or moisture in which case the reaction partners are latent, most of these coatings consist of two separate components. Mixed together, these components will react and form a continuous, flexible or hard film after application. Two-component epoxy coatings and polyurethane coatings are not the only, but certainly the most prominent representatives of this class of materials, although unsaturated polyester and vinylester products are important as well. This paper will predominantly address the category of two-component epoxy resin based thermoset coatings.

All the coating ingredients: Resin(s) (including curing agents), pigments, solvents and additives play their own, specific role in the properties of the coating before, during and after application. The following presentation addresses some of the effects caused by the choice of ingredients on the behavior of linings for tanks and pipelines. In many instances such coatings are exposed to harsh environments such as high temperatures, pressures, aggressive chemicals and often steep temperature gradients over the film if no thermal insulation is used.

I. COATING COMPOSITION

For a coating applied in a liquid form , a resin or binder is indispensable. Pigments and solvents only, even with the help of additives will not adhere to any substrate. Clear, transparent coatings or varnishes, don't make use of color pigments but some fillers, extender pigments or flatting agents may still be incorporated. Most anticorrosive primers and coatings contain both color pigments and inert pigments. It is disappointing that still some end users of coatings believe that extender pigments are only used to make the product cheaper.   It should be recognized by now, that extender pigments play an extremely important reinforcing role in the protective and mechanical properties of coatings.

A. Resin (Binder)

The purpose of the resin is to attach the composition to the metal and in the case of a pigmented composition, to "glue" the solid pigment particles together.

The chemical structure of the resin has a great effect on the physical, chemical and mechanical properties of the resulting film. As far as epoxy resins are concerned, many different oxirane ring terminated resin species have been synthesized since their initial introduction in the early 50's.   The best known are the bisphenol A based resins with molecular weights ranging from 380 for the liquid type to 8000 for the extreme hard type. These resins are mainly bi-functional and although they are excellent for many applications, they lack high temperature and very high chemical resistance. As reaction partner(s), mainly amines, polyamines, polyamides or polyamidoamines are used in air drying compositions.   The chemical structure of these curing agents play of course also an important role in the overall properties of the cured material. No more will be said here than that in general amines, polyamines and their epoxy adducts are preferred when high chemical resistance is required.

To improve further on those resistance properties, multifunctional epoxy resins are used alone or in combination with phenolic resins, standard bisphenol A resins or the newer, lower viscosity bisphenol F based epoxy resins.   Representatives of these multifunctional resins are the novolac and cresol-novolac epoxy resins. Figure 1. illustrates one of the reasons of the enhanced properties. The diagram shows schematically the difference between 3 and 4 functional epoxy resins after reaction with a two functional amine compound. The higher crosslink density of the higher functional resins combined with the high concentration of the aromatic rings in the cured coating film leads to greater solvent and heat resistance. Still, the choice of curing agent will have a markedly effect on the end results.   Aliphatic amines in general are relatively good resistant against alkalies and reasonable against diluted mineral acids. The solvent resistance is in general not

very high. Aromatic amines have a much better acid resistance both mineral and organic, but their cure rate is much slower and often insufficient for curing at ambient temperatures. Heat curing is therefore often necessary although specific accelerators may overcome that problem. Due to recent regulations, the use of MDA containing aromatic amine curing agents will most likely be drastically curtailed. Cycloaliphatic amines, as more or less expected, seem to have properties in between.

Reaction mechanisms between epoxy resins and amine type curing agents are well described and analyzed in many books and papers of which the handbook of epoxy resins from Lee & Neville [1] is still a good example. It has to be mentioned however, that the specific reaction kinetics, when more than one resin, curing agent or catalyst is involved, are quite complicated. In the literature of most coating manufacturers a time of 7 days drying at room temperature is mentioned until "full" cure is reached. Although the coating may be hard by then and resistant against the service conditions, a 100% cure is seldom achieved for a long time. As a rule of thumb the degree of curing after 7 days will be at best in the neighborhood of 60 to 75 %. The coating film may even never reach the 100%, unless heat cured. Solvent retention in the film will slow down the curing and keep the T_g below that of the fully cured composition. Another important factor related to curing is the ratio between epoxy resin and amine hardener. Stoichiometric amounts don't always give the optimum results under specific exposure conditions. A slight excess of epoxy for instance will increase the water resistance, but decrease the solvent resistance, where on the other hand an excess of amine gives better solvent resistance but the water resistance decreases.

By increasing the functionality, the resin will in general be more reactive. Gelation of the mixture will take place faster and the growing molecules become immobilized before a high degree of crosslinking is reached. Further reaction will not take place unless higher curing temperatures are exercised. (Fig. 2)

The crosslink density of the reacted mixture is expressed as the distance between the crosslinks per unit of length. A short distance between the crosslinks adds to higher chemical resistance but also greater hardness or brittleness.
The following diagrams and table schematize the effects of functionality and molecular size of epoxy resin and curing agent on the properties of the cured network.

Functionality 4   Short Molecule

A

```
┌─────────────────────────────────────────────────────────────┐
│         Functionality 4      Long Molecule                   │
│                                                              │
│         ┌──────────────────────────┬─────────────────────┐   │
│         │                          │                     │   │
│   B                                                          │
└─────────────────────────────────────────────────────────────┘

┌─────────────────────────────────────────────────────────────┐
│         Functionality 2      Short Molecule                  │
│                                                              │
│                        ┌─────────────────┐                   │
│                        │                 │                   │
│   C                                                          │
└─────────────────────────────────────────────────────────────┘

┌─────────────────────────────────────────────────────────────┐
│         Functionality 2      Long Molecule                   │
│                                                              │
│         ┌──────────────────────────────────────────────┐     │
│         │                                              │     │
│   D                                                          │
└─────────────────────────────────────────────────────────────┘
```
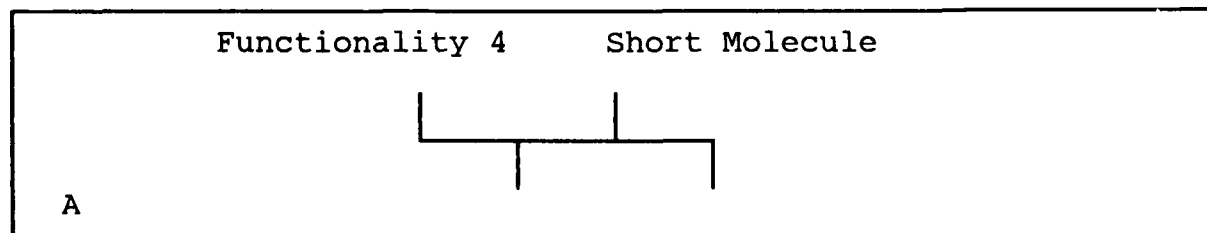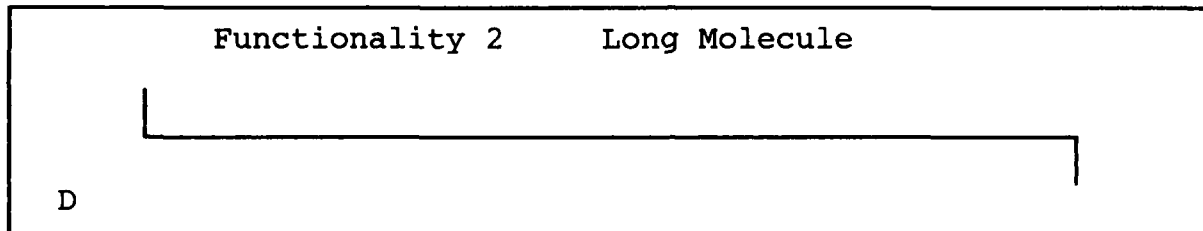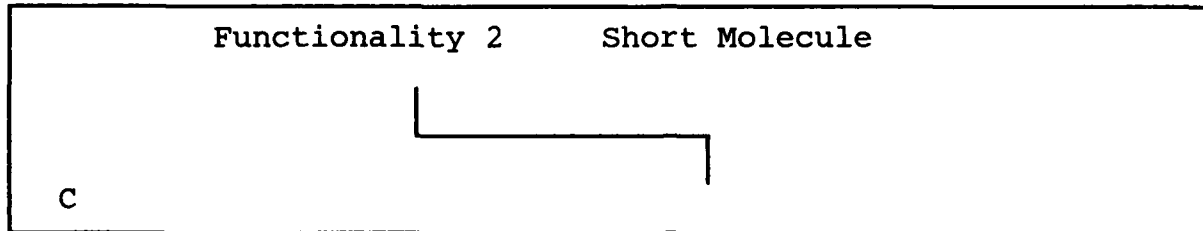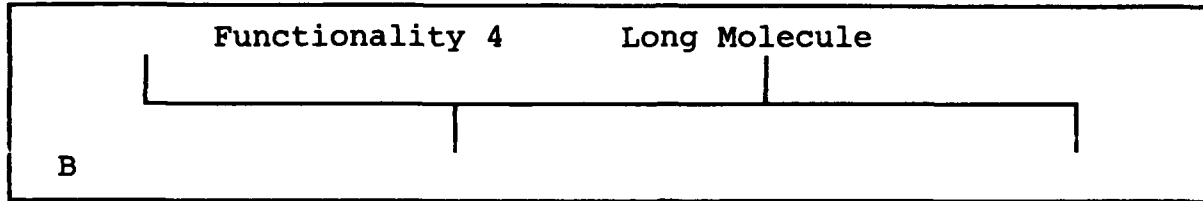
The next tables give a general idea about some important coating properties related to the difference in resin functionality and size of molecules. The effect of side chains, steric hindrance and the presence of other specific groups are neglected here for simplicity reasons.

Property	Order		
Hardness	1>2>3>4	Highest ——— Lowest
Flexibility	1>2>3>4	Highest ——— Lowest
Geltime	1<2<3<4	Shortest ——— Longest
Viscosity	1<2<3<4	Lowest ——— Highest
Crosslink Density	1>2>3>4	Highest ——— Lowest
T_g	1>2>3>4	Highest ——— Lowest
Chem. Resistance	1>2>3>4	Highest ——— Lowest

	A	B	C	D
Hardness	1	3	2	4
Flexibility	4	2	3	1
Gel Time	1	2	3	4
Viscosity	2	4	1	3
Crosslink Density	1	2	3	4
T_g	1	2	3	4
Chemical Resistance	1	2	4	3

Other characteristics than functionality and length of molecule play a role in the properties of the final composition. Although known already for some time, the use of Bisphenol F i.s.o. Bisphenol A in the reaction with epichlorohydrin gives epoxy resins of lower viscosity with the same or better chemical resistance of the cured film.

Epoxy phenol novolacs contain a higher concentration of phenol groups per molecule and have therefore a higher temperature resistance than bisphenol A or bisphenol F based epoxy resins. Together with the higher functionality, they can give very chemical and temperature resistant coatings, with a high crosslink density, higher HDT and higher T_g. It is however more difficult for such resin/curing agent system to come to adequate cure when simultaneously short molecular and high functionality amino type curing agents are used. The workable period after mixing of the components (potlife) is often short and further decreased by the exothermic reaction. Only by using the correct combinations of polyamines and catalysts, an acceptable level of degree of curing can be achieved at room temperature. Many of the combinations need forced curing at higher temperatures to achieve their full resistance capabilities. There are ways to adjust the overall functionality to the point, that more complete curing can be achieved, although this takes somewhat away from the crosslink density. (Fig.2)

Summarizing this resin section, we can say that for use as internal pipe and tank lining exposed to sever conditions of heat and aggressive liquids often accompanied by pressure, it is important to select resin systems, that result in a high T_g, because a more compact and complete cured network can control better the penetration of liquids and gases through the film.

B. Pigmentation

The role of pigments in the properties of coatings is in general reasonable well understood by coating developers, but less by end users. Many in the last mentioned category still believe, that good pigments are only used in the coating to obtain a certain color, or for anti-corrosive properties, other "pigments" are only used to make the coating cheaper (fillers!). Some specifiers go even so far to reject coatings with a PVC above a certain level because they insist on getting their money's worth of "resins" and not cheap fillers. Many extender pigments however have a reinforcing effect and contribute to better protective properties of the coating. Not only the chemical composition differs from pigment, but also the shape, size and the surface topography.

PVC stands for Pigment Volume Concentration and is expressed as the volume of pigment as a percentage of the total volume solids of the coating. This % can readily be calculated from the weight and the specific density of the components in the coating.

In 1956, M. van Loo, published a schematic to illustrate the relation between the Pigment Volume Concentration and several

coating film properties[2][4](see fig 3). The curves for gloss, blistering, rusting and permeability showed a more or less sharp break at approximately the same point where the lines intersect, which he called the Critical Pigment Volume Concentration (CPVC). For the products he examined, the CPVC was around 45%. Van Loo used the following definition for CPVC : "It represent the condition of tightest possible packing of the pigment particles, compatible with the presence of the minimum amount of binder needed to provide the adsorption layer on the pigment particles and to fill the interstices between the wetted particles."

Since then, the concepts of PVC and CPVC have been further developed, but in the middle 70's the shortcomings of these concepts in explaining many coating characteristics came to light. Compare two particles of the same pigment but one with a radius 2x (A) that of the other(B) (fig 4).
The volume of A is then 8x the volume of B, so that 8 particles of B take the same space as 1 particle of A. The surface area (assuming perfect smooth round surfaces) of A is however 4x that of the surface area of one particle B, so that 4 particles of B have the same surface area as 1 particle of B. In fact, we need almost twice as much resin to encapsulate the same volume of pigment.

Dittrich[3][4] in 1976 and 1977 describes the relation between packing density, critical wetting point and corrosion resistance. He introduced the pigment surface area concentration in stead of the pigment volume concentration as the determining parameter in many properties of coatings. In fact the absorption of oil used to characterize a pigment, is clearly related to the available surface area of the pigment and not its volume. Of one specific, well defined pigment (a micronised red iron oxide), he determined the specific surface area and through the resin adsorption values (rather than oil adsorption values!) calculated the relative active surface area of other pigments.

The reference pigment was almost ideal in the sense, that the particles were perfectly round and equal in size with an average particle radius of 0.15 micrometer. The specific Volume (V) of 100 grams of this pigment was 19.6 cm^3 (100 / 5.1, where 5.1 is the specific gravity of the pigment). The specific Surface Area (A) was therefore 3 x 19.6 / 0.15 x 10^{-4} = 392 m^2 for 100 grams pigment.

To determine the minimum amount of resin necessary to just wet the pigment, the coating industry is usually using the oil absorption number (ASTM ....). Dittrich used other model liquids, which better imitate the polarity range of the actual resin used in specific coatings. After determining the Resin Adsorption Value of the reference pigment as well as the pigment(s) he used for his experiments, he calculated the Relative Active Surface Area of those pigments with the relational equation:

$$A_1 / A_2 = RAV_1 / RAV_2$$

A_1 = relative active surface area of the new pigment $(m^2/100g)$
A_2 = active surface area of the reference pigment $(m^2/100g)$
RAV_1 = resin adsorption value of the new pigment $(cm^3/100g)$
RAV_2 = resin adsorption value of the reference pigment $(cm^3/100g)$

The Pigment Surface Area Concentration (PAC) is calculated from the Relative Active Pigment Surface Area (A) divided by the volume of resin in the coating or film and expressed in m^2/cm^3. (fig. 5)

The Critical Pigment Surface Area Concentration (CPAC) is then the Relative Active Pigment Surface Area (A) divided by the Resin Adsorption Value (RAV) and also expressed in m^2/cm^3.

There are obviously big differences between the PVC/CPVC and the PAC/CPAC approach (Fig. 7). The volume of pigment will not change with increased dispersion. Nevertheless, the resin demand increases with further de-agglomeration of the pigment and that can only be due to the increasing pigment surface area. A thin layer of resin is adsorbed on the surface of the pigment (Fig. 7). Coarser particles will need less resin before the flow point is reached in comparison to finer particles. The distance between the fine, dispersed particles is bigger than between coarse particles which is best understood after realizing, that there is more resin in a certain quantity of paint with fine particles than in the same volume of coarse particles. Why is this discussion about PVC and PSAC so important ? Some of the main mechanisms of water permeation through a coating film is the diffusion through the resin matrix and along the pigment surface where it can move from one pigment particle to another. By increasing the surface area of pigments through intense dispersion, not only more resin is adsorbed, but it will also be easier for water to travel alongside the pigment particles because of the greater surface area. "Finer" is therefore not always "better". [2][5][14]

By using the method of Dittrich, the optimum packings density can be obtained from the resin adsorption values and he could prove, that a primer with good protective properties, using active anticorrosive pigment (zinc chromate), could be equaled or even improved upon without zinc chromate as long as the same or a tighter packings density was achieved with inert pigments. The critical particle distance was calculated to be approximately $0.5\mu m$ [4].

The following table shows the differences between the Volume and the Surface Area approach.

Specific Volume (V) cm^3/100g	Specific Surface Area (A) m^2/100g
Pigment Volume Concentration (PVC) in % $$\frac{\text{Pigment Volume x 100}}{\text{Volume(Pigment+Resin)}}$$	Pigment Surface Area Concentration (PAC) in m^2/cm^3 $$\frac{\text{Active Pigment Surface Area}}{\text{Volume Resin}}$$
Critical Pigment Volume Conc. (CPVC) in % $$\frac{100}{1 + RAV_v}$$ RAV_v = Resin Adsorption Value in cm^3 per cm^3 of pigment	Critical Pigment Surface Area Conc. (CPAC) in m^2/cm^3 $$\frac{\text{Active Pigment Surface Area}}{\text{Resin Adsorption Value}}$$

Note: The CPVC is normally expressed in the same way as the PVC but using for the resin volume, the resin (oil) adsorption value expressed in cm^3 per 100 gram of pigment

The blistering of paint films under immersion conditions has been and still is the subject of quite a number of studies. W. Funke[10] and H. Leidheiser[12]. There is no doubt, that the pigmentation in quality and quantity plays an important role in the blistering phenomena.

Summarizing the pigment section we can state, that a high packing density, which not automatically implies a finer particle size, and a strong bond between resin and pigment, will contribute to better performance under severe immersion conditions. Moreover a high packing density results in less resin, which often is the weakest link in the resistance against blistering.

C. Additives

Most coatings contain one or more additives to add specific properties. They range from flow agents, wetting and dispersing aids to air release and thixotropic additives. All these additives have different effects in specific coating composition and a lot of trial and error is involved to find the correct compounds.

Wetting agents and dispersion aids help to remove air from the surface of the pigments and contribute to a better bond between pigment and resin. This is necessary to decrease or eliminate the possibility of water transport along the surface of the pigment particles inwards in the direction of the metal substrate.

Pigments are available in all shapes and sizes. The pigments in their dry form will reach the coating manufacturer in a more or less agglomerated form. Dispersion is necessary to break up those agglomerates and wet the particle surface with resin. This dispersion is accomplished by putting the mixture of resin and pigment under high shear. Sometimes the word "grinding" is used for this process, but it seldom happens, that the agglomerates are broken down further than the elementary particle size. Especially when high concentrations of pigments are used, such as in primers, a wetting or dispersion aid will assist in having most of the particles wetted out properly.

Still, the bond created between pigment and resin with the help of conventional wetting aids is open for improvement. In the early 60's , adhesion promoters and coupling agents were examined for their properties in reinforced plastics and composites. Around 1975 the use in coatings was studied (cleveland society for Paint Technology, J. Coatings Technology 1979, 51, 653)

In a series of 5 articles, P. Walker [16] discusses the mechanisms and the improvement of the adhesion of organic coatings in the "dry" stage and the "wet" adhesion after exposure in liquids. The silanes were all of the type $R-Si(OR^1)_3$, where R is group capable reacting with a polymer matrix and the (OR^1) is a hydrolisable ester group. This last group is responsible for the improved adhesion to the substrate not only in the dry state, but primarily during and after long term immersion in liquids. Since then a variety of other adhesion promoters have been studied such as titanates and zirconates. The effects of all these agents which are added in very small quantities are very specific and much work is involved not only in testing these adhesion effects under different conditions, but also in monitoring stability and studying the reproducibility of the results.

Although primarily intended to improve the adhesion to substrates, the adhesion promoters have also an effect on the wetting of the pigments and the resulting bond between pigment and resin. Because of the combination of a resin-reactive side and a hydrolizable side, these additives are able to decrease the adsorbed resin layer on the pigment, so that less resin is necessary to reach the "flow" point. The distance between the pigment particles can be decreased.

Other additives are used to improve specific properties such as deaeration aids, which help release the air during prcduction of the coating and during the application.

2. Testing

Apart from a long list of physical, mechanical and chemical tests which have to be performed on tank and pipelinings, there are two which are of specific interest. The Autoclave Test and the Atlas Cell Test.

    a. Autoclave Test
    NACE Standard TM-01-85 [16] describes this method for the

evaluation of internal plastic coatings of tubular goods, but the same method can very well be used for tanklinings. In general three phases are used: hydrocarbon (kerosine/toluene 1/1), water (brine or fresh) and gas. Depending on the expected composition, the gas phase can contain H_2S, CO_2, CH_4 as the main components. The other variables in the test are: temperature, pressure, length of pressure period, speed of depressurization and the number of cycles.

Temperatures as high as 500°F and pressures as high as 10,000 psi have been used. For air drying coatings, these temperatures are in first instance far above the T_g. The coating will therefore go through a transition phase and melt or rubberize before it hardens again due to a shift upwards of the T_g. Every coating material will have its specific maximum T_g. During the transition towards a higher T_g, the film is much more sensitive to attack by the environment than when in the glass phase. Liquids and gases molecules can enter the film more easily and deform the resin matrix. All vacuoles between the molecules are filled quickly and the rubber film will accommodate more foreign incoming molecules of liquid and gas than in the glass phase. Because inside the cylinder of the autoclave pressure and temperature will reach the same conditions.

The pressurization step by itself does not seem to be so destructive, it is the depressurization, that does the most harm, especially when this is done in a matter of minutes. The pressurized gas in the film has to expend and can only do that by rupturing the film. If the coating is very hard, the expansion (temperature under T_g) may take longer and it is not uncommon, that the coated panels immediately removed from the autoclave show no defects, but 5 or 10 minutes later the blisters become clearly visible.

Our experiments indicate that, apart from the necessary chemical resistance, better results are obtained at higher temperatures and pressures when the coated panels meet the following properties:

> High T_g (higher than testing temperature)
> Complete cure
> No air inclusion in the film
> High packing density of the pigments
> Maximum bond between pigment and resin
> Perfectly clean metal substrate
> Maximum bond strength between metal and coating

Because seldom all these criteria are met, the results are less than perfect. Because some of the factors are likely to differ from time to time, such as the metal substrate itself, application and curing conditions, results are not always consistent.

For airdrying coating systems our experiments indicate, that the maximum acceptable pressure followed by rapid depressurization is in the neighborhood of 3500 psi but in that case the

temperature has to stay under or close to the T_g. When on the other hand the temperature in the autoclave is around 225°F to 250°F, any more pressure than that due to the heating in the closed cylinder, will effect the coating. Although far from scientifically proven, the relation between temperature and pressure of some coatings is practically linear.

b. Atlas Cell Test

An atlas cell is an open, metal or glass cylinder, in which liquids are in contact with coated metal panels. The liquid in the cylinder can be heated and in the case of the metal cell, also pressure can be exerted, which opens the possibility for adding special gases. In our experiments a glass cylinder type was used. The uncoated backside of the panels are cooled with water to variable temperatures. Most Atlas cells have the uncoated backside of the panels in contact with room conditions.

The creation of a temperature difference between the coated frontside and the cooled backside, while at the same time the frontside is exposed to hot water with a hydrocarbon layer on top, has a strong effect on the coating film. Depending on the temperature difference inside and out, blistering may occur within one day or may take many weeks. Schenk [15] did some experiments with polyamide cured epoxy coatings in an atlas cell partly filled with water and "tube material". At 80°C and a temperature difference over the panel of 10°C he saw blistering after 14 hours, while the same system under isothermal heating at 80°C showed only blisters after 2300 hrs. He also found, that with the same temperature difference, but at a lower inside temperature (60°C), the blister free period increased from 14 hours to 68 hours. Polyamide cured epoxy coatings have in general lower heat distortion temperatures than amine cured epoxy coatings, moreover Schenk did not address other particulars such as pigmentation, surface preparation.

Our experiments show, that also in the case of the Atlas Cell test the same compositional aspects mentioned under the section "Autoclave Test" play a decisive role. Again, the packing density, the use of additives to improve the bond between pigment and resin as well as between resin and substrate, the T_g of the coating film, and also the surface preparation play a decisive role in the prevention of blistering.

Much work has to be done to increase the understanding of the blister phenomena due to hot/cold wall effect. Fig. 8 shows one of the effects of penetrating liquids in the film. It is expected, that the liquid molecules enter the film individually or at least in small clusters, but condense on their way to the cold wall. the growing clusters take more space and will after reaching the metal surface start lifting the film in discrete areas which may be related to the phase separation theory of Funke. It is interesting and intriguing to see that most times the blistering occurs right at the water/ hydrocarbon interface

and mainly on the waterside. It is sure, that distilled water (used for these experiments) has a tremendous penetrating power and the temperature difference over the film works as a pressure difference so that there is definitely a reason for the water to penetrate deep into the film. Most likely there are at the same time inside the film vertical movements of liquid molecules taking place. At high temperatures, the toluene could soften the coating inside the film and under the outside waterline, so that the water has an even stronger effect in that area. Fig. 9 gives a schematic picture of a typical Atlas cell panel after the test.

As mentioned earlier, by optimizing the composition in all aspects and removing all foreign materials from the metal surface before coating application, almost perfect results can be obtained in the presence of steep temperature gradients. In our work no pressure was used inside the cell and it is known, that this definitely has an effect on the performance of the coating. By itself, the temperature gradient is already a destructive factor and a coating that does not resist this test, will certainly not succeed when the extra pressure is used.

Fig. 10 gives the relation between the blister free time and the PVC for a certain product composition and a 70°C/10°C gradient. Other aspects of the coating were optimized previously and used in all the coatings tested. In fact, the Relative Active Pigment Surface Area approach was used in the optimization and afterwards recalculated as PVC.

3. Conclusion

It is possible to improve on the protective properties of tank and pipelinings by using modern techniques and understanding. Blistering of coatings is considered to be an important negative aspect often encountered and although blisters may not always
cause corrosion, it is highly likely, that eventually those blisters will open, after which corrosion will definitely take place. Unfortunately, coatings resistant against steep temperature gradients are very inflexible because of their high T_g and high packing density of the pigments. However because of their high bond strength to the metal substrate, they will survive the normal mechanical effects in tanks and pipes.

Bibliography

1. Handbook of Epoxy Resins
    H. Lee and K. Neville, Mc Graw-Hill Reissue 1982
2. M. van Loo
    Official Digest 28, (1956) 1141
3. Korrosionsschutz infolge neuer Erkentnisse bei der
    Formulierung pigmentierter Anstrichstoffe nach dem Prinzip
    relativ benetzbarer Oberflächen.
    H.K. Dittrich
    Farbe und Lack no. 5, 1977
4. Dr. J. Sickfeld
    Farbe und Lack no. 12, 1975
5. Neue Untersuchungen über die Zusammenhang von Korrosion und
    Wasser Diffusion durch Lackfilme.
    Dr. P. Kresse
    Deutsche Farben Zeitung no. 9, 1972
6. Modern Surface Coatings
    Nylen & Sunderland
    John Wiley & Sons Ltd, 1965
7. Helmut Haagen   (blistering)
    Journal of Coatings Technology, Vol. 56, 1984
8. W. Funke   (Blistering of paint films)
    Prog. Org. Coatings 9 (1981) 29
9 . Corrosion of Painted Metals - A Review   (Blistering)
    H. Leidheiser, Jr
    Corrosion Vol. 38, No.7, July, 1982
10. Zur direkten Ermittlung gunstiger Dispergieransatze
    H. Dittrich, K.M. Oesterle   (PVC/PSAC)
    Fatipec Congres 1974 ?
11. Influence of Pigments on the Effectiveness of Anticorrosive
    Primers.   (Packing density and particle distance)
    P. Kresse, V. Szadkowski, R.H. Odenthal
12. Neue Korrosionsschutzpigmente auf Phosphat-Basis
    G. Adrian, A. Bittner und M. Gawol (Particle Size)
    Farbe und Lack, 10/1981
13. Corrosions tests for organic coatings.
    W. Funke   (permeability gases/liquids,Tg)
    JOCCA, 1979, 62
14. Beurteilung des korrosionsschutzenden Verhaltens von
    Lackfilmen und Beschichtung.
    W. Funke, E. Machunsky, G. Handloser
    Farbe und Lack, 7, 1978   (permeability and pigmentation)
15. W. Schwenk, 1980   (Temp. Gradient blistering)
16. Organosilanes as adhesion promoters for organic coatings
    P. Walker
    JOCCA, 65, 1982 , 66, 1983, 67, 1984
17. NACE Standard TM-01-85
    Test Method for the Evaluation of Internal Plastic Coatings
    for Corrosion Control of Tubular Goods by Autoclave Testing.
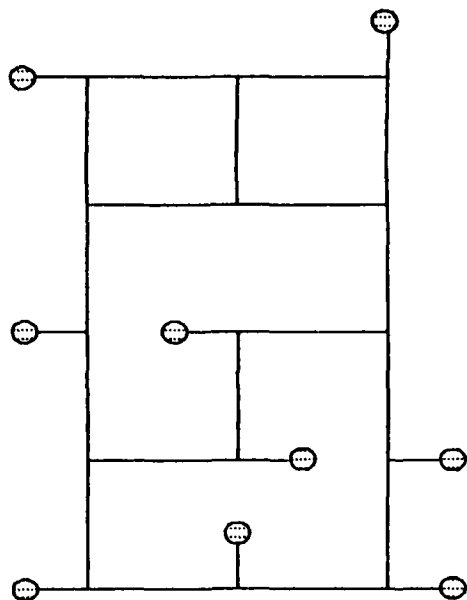
Epoxy functionality: 3
Amino-hydrogen functionality: 2
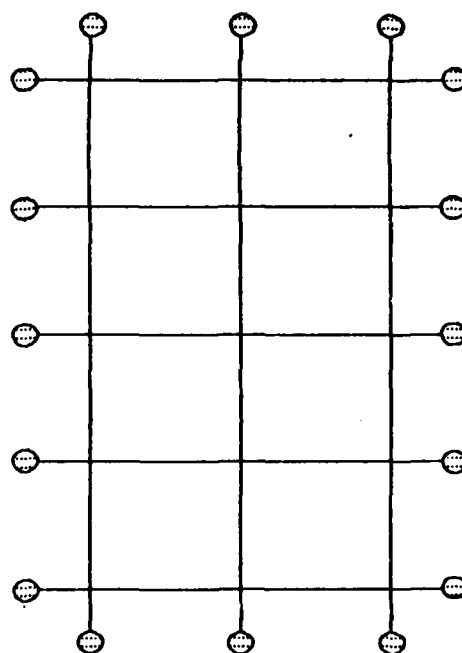
Epoxy Functionality: 4
Amino-hydrogen functionality: 2

Fig. 1
Crosslink Density relative
to Functionality

HIGH RESIN FUNCTIONALITY

ADJUSTED RESIN FUNCTIONALITY
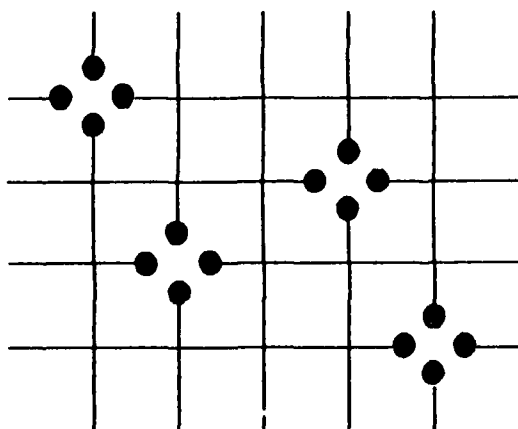
Incomplete cure. Low crosslink density
Residual chemical-sensitive sites
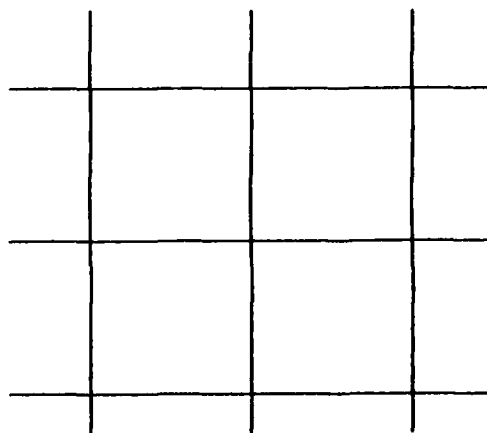
Complete cure. Higher crosslink density.
Higher chemical resistance

Fig. 2

Incomplete and Complete Cure

Fig. 3

SURFACE AREA VS VOLUME

$$R_1 = 2 R_2$$

$$V = 4/3 \, \Pi \, R^3 \qquad A = 4 \, \Pi \, R^2$$

$$V_1 = 8 \, V_2 \qquad A_1 = 4 \, A_2$$

Fig. 4

SURFACE AREA VS. VOLUME

Pigment Surface Area Concentration   vs   Pigment Volume Concentration

PAC   vs   PVC

$$\frac{\text{Pigment Surface Area} \ (m^2/100g)}{\text{Volume of Solid Resin} \ (cm^3/100g)} \qquad \frac{\text{Pigment Volume} \times 100}{\text{Volume of Pigment + Resin}}$$

$$m^2 / cm^3 \qquad\qquad \%$$

Fig. 5
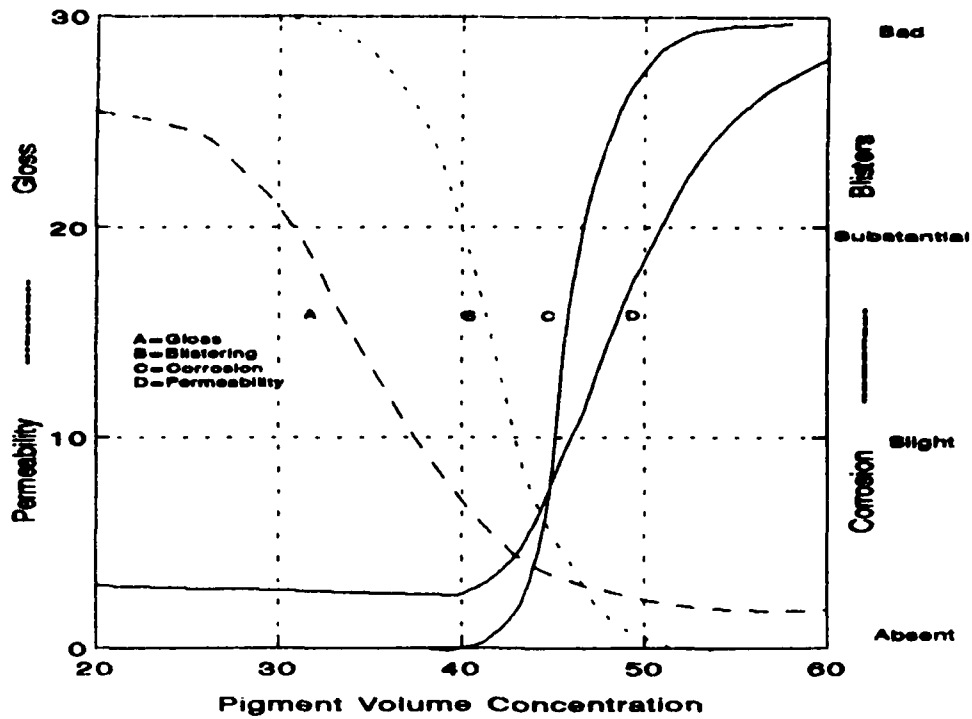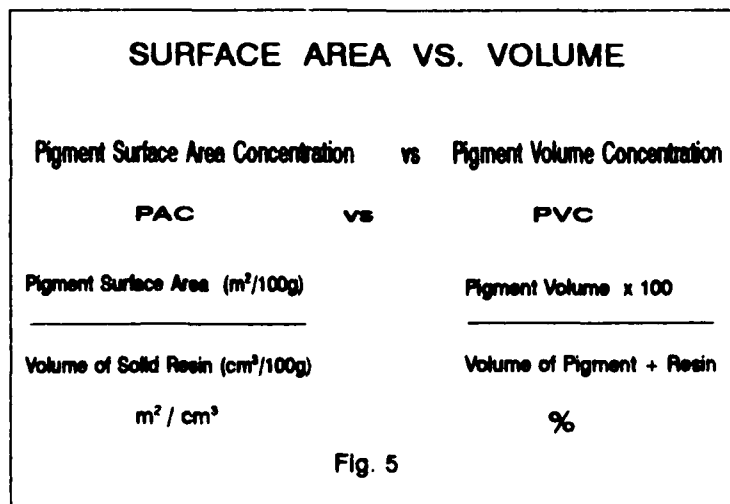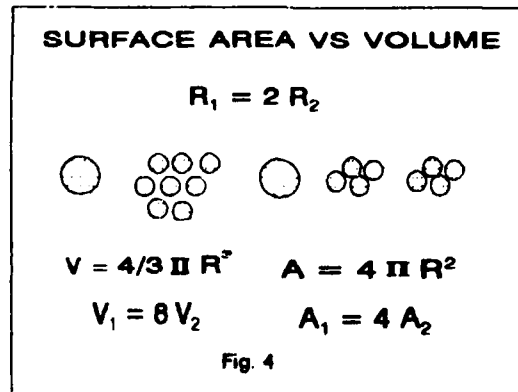
Pigment Surface Area Concentration

Dependent on Degree of Dispersion

Pigment Volume Concentration

Independent on Degree of Dispersion

Fig. 6

RESIN ADSORPTION

Fig. 7

free resin

adsorbed resin

hot

cold

Water condensation in film due
to temperature gradient

Fig. 8

Vapor

Kerosine/Toluene 1:1

Distilled Water
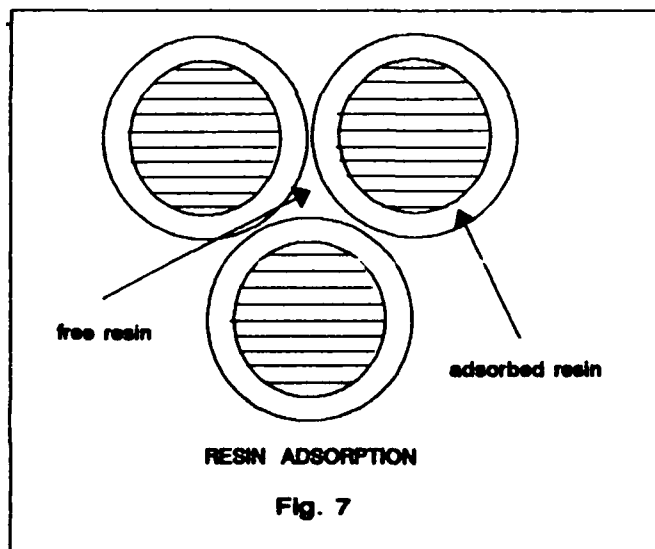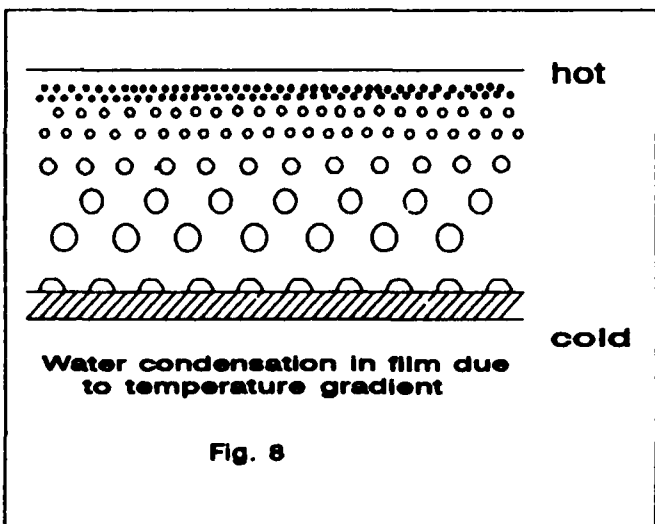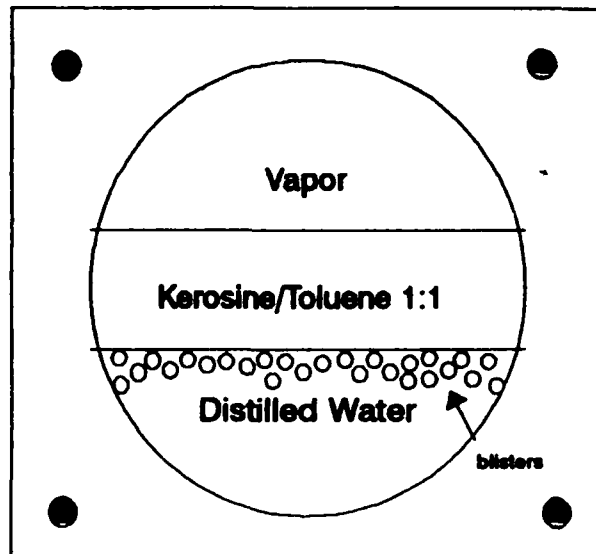
blisters

TYPICAL ATLAS CELL PANEL AFTER EXPOSURE

Fig. 9

BLISTERING VS PVC
Temperature Gradient 70°C / 10°C
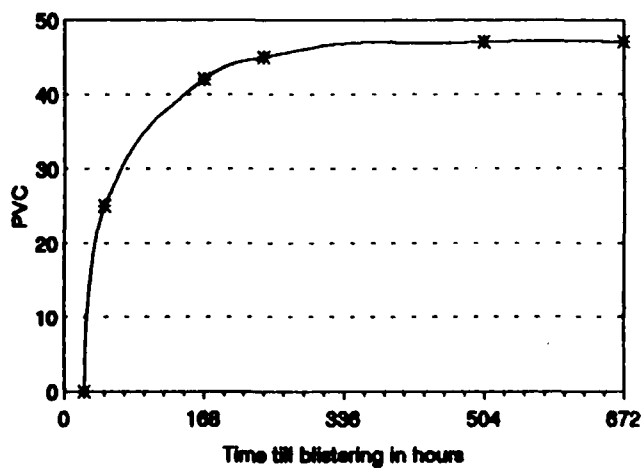
Fig. 10

Methods to Develop a Performance Envelope for Internal Linings in Oilfield Production Environments

Gregory Ruschau
ARCO Exploration and Production Technology
2300 W. Plano Pkwy
Plano, TX 75075

Lee Bone III
ARCO Exploration and Production Technology
2300 W. Plano Pkwy
Plano, TX 75075

Oliver Moghissi
ARCO Exploration and Production Technology
2300 W. Plano Pkwy
Plano, TX 75075

Abstract

Various laboratory testing methods for the performance of internal linings in oilfield production environments have been evaluated. In general, the testing methods involve two separate components; exposure to the production environment, and evaluation of properties after exposure.

The exposure methods include stationary autoclaves, circulating pressure vessels, atlas cells, pressured atlas cells, and rocker arm machines. The goal of an exposure test is to accelerate the aging process, but it is difficult to accomplish this without unfairly "punishing" the coating. The pressured atlas cell has been found to be the best method for simulating actual operating conditions inside production vessels, while the rocker arm tests better simulate stratified three-phase flow for internal pipe linings.

Evaluating the panels after exposure is often a mix of objective and subjective analysis. The most important coating property for corrosion mitigation is adhesion of the coating to the steel substrate, although interlayer disbonding may also lead to failure. Blistering is a dramatic indication of poor adhesion; the number, size, and depth of the blisters can be counted for an objective performance rating. Physical deformities such as cracks are often an indication of application problems, but nonetheless must count against coating performance.

Electrochemical impedance spectroscopy is a non-destructive method for evaluating the adhesion of a coating. It combines the exposure and evaluation steps, allowing the coating performance to be measured with time. Impedance data is difficult to interpret and is therefore most valuable when used together with traditional coating evaluation techniques.

Key terms: coating, lining, atlas cell, rocker arm, adhesion, impedance specroscopy

Introduction

A. Coatings in Oilfield Production

Protective coatings and linings are an integral part of all aspects of the oil industry. Corrosion mitigation is essential for avoiding costly production shutdowns and to prevent hazardous environmental leaks. Common areas of corrosion in oilfield production include downhole tubulars, three-phase flow lines, separator vessels, and above ground storage tanks.

Protective coatings and linings for the oil industry often must withstand the harshest of environments. The most common corrosives in production vessels are carbon dioxide, hydrogen sulfide, and condensed water, in addition to crude oil and natural gas. Along with the chemical environment, process vessels are often operated at high temperatures and pressures, increasing the severity of the corrosion problems.

The choice of protective coatings must be based on not only the expected performance in service, but also on the economics of coatings versus other corrosion mitigation methods, such as the use of corrosion resistant alloys, non-metallic alternatives such as fiberglass pipe and plastic sleeves, and chemical inhibition. Thus, oil companies must continuously search for coatings which will perform satisfactorily for many years to justify the selection of coating as corrosion mitigation.

B. Coatings as Materials

In order to consider a coating from a materials perspective, one must break down the behavior of a protective coating in terms of its component parts. The relative weighting factor for each component depends on factors such as the coating thickness, operating temperature, and overall chemistry of the system. These factors, for the purposes of this paper, do not consider the variation in surface preparation and cleanliness, but focus solely on the performance of the coating.

First of all, the coating itself is a composite material, and has its own unique set of stand-alone properties. A composite may be defined as a combination of dissimilar materials (in this case, organic resins combined with inorganic fillers) which maintain their individual characteristics after combination and which make a separate contribution to the overall properties. This definition distinguishes a composite from a compound, in which single phase materials are formed. The innerconnectivity of each phase determines the properties of the coating; coatings with a high PVC (pigment volume content) often have a more highly connected filler phase and tend to be more brittle. If the PVC is increased to near the critical PVC, at which the filler phase becomes continuous, porosity may appear in the coating film.

Second, the integrity of every coating is determined by maintaining of interfacial adhesion to the substrate. In the case of protective coatings for the oil industry, the substrate is usually carbon steel, although alloys are sometimes coated for acid protection. Optimal adhesion is obtained when the interfacial bond is as strong as the bonding within the coating. For the purposes of corrosion protection, the interfacial bond must be able to absorb as much energy as is imparted by the atmosphere. Cumulative damage to the interface lowers the amount of energy required to break this bond.

Exposure Tests

A. Methods of Exposure

Exposure tests are intended to provide an estimate of the long term performance of coatings in a short time period by pinpointing signs of material deterioration or adhesion failure. Exposure tests for internal linings differ greatly from atmospheric coatings[1,2] due to the nature of the corrosive agents.

Simple immersion testing is a quick, easy way of determining the chemical compatibility of a coating with the production environment. Chemically, immersion tests indicate (1) the solubility of the coating in the atmosphere, and (2) any chemical reaction (e.g. acid/base reactions, crosslinking, etc.) which takes place between the coating and the atmosphere at the test temperature. For a simple screening of materials, some "negative" answers can be obtained; in other words, gross incompatibility can be determined. Certainly, a coating which dissolves, blisters, or cracks in immersion testing can be immediately dismissed as a potential candidate. However, in typical oilfield production environments, immersion testing provides few answers.

The next step "up" in severity is to add gas pressure to the atmosphere, in order to "force" the chemical constituents into the coating film as well as to evaluate gaseous corrosives such as CO_2 and H_2S. Pressure vessels may be stationary or circulating, and the degree of circulation can vary. In a circulating autoclave, the entire pressure vessel is rotated so that all parts of the coated sample are exposed to all phases within the environment. In a stationary autoclave, the coated panel is exposed to the atmosphere in distinct zones, usually an oil phase, a water phase, and a gas phase. The effect of pressure on coatings is an increase in the solubility of the chemical atmosphere in the coating.

The conventional atlas cell, as diagrammed in Fig. 1, adds another variable into the exposure; the "cold wall" effect. By exposing the coated panel to the production fluids at temperature while the back side of the panel is exposed to ambient temperature, a continuous thermal gradient is maintained. ΔT's of up to $5^\circ F$ have been measured across the 3/16" panels. Unfortunately, the conventional atlas cell, made of glass, must be run at ambient pressure and nominal gas phase.

The pressured atlas cell, developed by ARCO in the early 1970's, combines the cold wall effect with the utilization of pressure and a concise gas phase. The pressured atlas cell (see Fig. 2) is made from stainless steel or hastelloy, depending on the amount of corrosion resistance desired within the cell. For sour oilfield testing, hastelloy cells are essential. Pressured atlas cells simulate oilfield separator vessels, into which three phase production lines empty and separate into three separate phases, with the gas phase vented off of the top into gas lines or to flare stacks, the oil phase drawn into production lines, and the heavier water phase falling to the bottom of the vessel.

The final exposure method, also developed at ARCO, is the rocker arm machine. In the rocker arm exposure, a section of pipe approximately 2' long and 2"-4" in diameter is internally coated and fitted with pressure-tight end plugs, as pictured

in Fig. 3. The production fluids are added through the fitted end plug and the pipe is pressured with the gas phases to the test pressure. This sample pipe is placed in the rocker machine which rocks the pipe at a predetermined rate, accurately simulating stratified flow through a pipeline.

B. Discussion of Exposure Methods

Autoclave testing is a standard method of materials evaluation, and has great flexibility along with a potentially large sample throughput and low operating cost. The stationary autoclave also permits separate evaluation of the coating in all three phases, while the circulating pressure vessel continuously "washes" the coating in the atmosphere. The circulating pressure vessel may be thought of as a pressured immersion test, since the coating sample is more or less immersed in a mix of all three phases. In the field, the three phases act separately on the coating; inspection of vessels during shutdowns reveals differing degrees of damage severity in the three phases. Thus, the stationary autoclave is preferred for oilfield environments. However, many coatings pass the autoclave test but fail in the field; it is not a severe enough test on which to base coating selection.

The atlas cell lends itself to visual observation of the coating during exposure, since the cell itself is transparent. The condition of the coated panel can be monitored daily, and the effects of varying temperature in-situ can be observed. The weakness of the conventional atlas cell is that a pressured gaseous atmosphere is not possible; the most common oilfield corrosives are CO_2 and H_2S, neither of which can be fairly evaluated in the glass atlas cell.

The pressured atlas cell test has been found to be the most severe of all of these exposure methods. The most severe damage, in all cases, is seen at the oil-water interface. When a coating fails badly in the atlas cell test, a common appearance is seen, as illustrated in Fig. 4. A complete row of blisters is seen at the oil water interface; these blisters continue down into the water phase, becoming smaller and more spread apart, until they disappear. The severity of the damage appears to be proportional to the distance from this interface.

The remarkable property of the pressured atlas cell is that it not only simulates the conditions in separator vessels, but the same type of failure is seen in the field when the separator vessels are inspected. Rows of blisters near the water/oil interface are common, as well as some blistering at the oil/gas interface. We have seen samples perform well in both stationary and circulating autoclaves while blistering in the atlas cell.

Both standard and pressured atlas cells illustrate the severity of the "cold wall" effect. This effect is present in all above ground production facilities in the oilfield. The thermal gradient and resulting heat flux results in a non-equilibrium situation inside of the atlas cell and through the coating. Thus, while a stationary autoclave may be considered a static test in which the conditions do not change with time, panels in an atlas cell test are subject to a constant thermal stress and resulting fluid movement, particularly at the oil/water interface where there is additional energy of the water going into and coming out of solution with the oil phase.

Rocker arm testing is the standard test procedure for downhole tubulars; again, the

results of the rocker arm test accurately reflect field performance. The value of the rocker arm test is that in addition to a cold wall effect, the internal stresses related to cylindrical coatings can be investigated, and "weak" areas of the coating such as near welds, mechanical joints, and irregularities can be examined after long periods of exposure to the corrosive atmosphere.

Evaluation Methods

A. Quantitative Ratings

After exposure, the relative amount of "damage" to a coating must be somehow quantified in order to compare the performance of different coating systems, to compare results of tests run by different people, and to compare new data to old data. Quite often, a coating which "looks bumpy" to one eye might later look "textured" to the same observer, even though those observations convey different meanings. Nevertheless, a highly detailed quantitative rating system also has inherent problems; such systems often make sense only to the person devising the test. In addition, the rating system must correlate with field data exactly or the test is of no use.

It is for these reasons that ARCO has developed a rating system for coatings based on a mix of subjective and objective analysis. Table I lists the quantitative "scoring" for the different evaluation components; the lower the score, the better the rating for a coating. The first quantitative ratings were developed by examining the atlas cell and rocker arm test performance of coatings which were proven performers in the field. Since their performance was a proven commodity, any shortcomings were necessarily downgraded in significance. Thus, the first quantitative ratings were "massaged" in order to provide us with the answers that we already knew, so to speak.

The primary consideration for internal linings is adhesion of the coating to the substrate; it is the loss of adhesion which results in corrosion of the steel. The numerical rating therefore concentrates on factors related to interfacial bonding.

Many coatings evaluators rely on pull tests for adhesion, in which a knob is cemented onto the coating and pulled off with a device that records the adhesive strength. Problems with pull tests are numerous: they yield inconsistent results, sometimes they do not work at all (if the coating adhesion is stronger than the pull knob cement), and the results are an average over a rather wide area on the coating.

A simple knife test can yield a wealth of information in a very short time. By shear scribing an "X" in the coating then popping off areas of the coating around the scribe, a subjective estimate of the adhesion is possible. The shear stress imparted by the scribe creates a natural tendency for the coating to "lift off" the substrate or to delaminate. Our rating system uses a standard A through F grading system with numerical values attached to each grade to assign this subjective measurement a quantitative value. An "A" adhesion means that when coating is popped off, none of the substrate is visible underneath. For "B" adhesion, less than 50% of the substrate is visible under the popped off coating. A "C" means that greater than 50% but less than 100% of the substrate is visible. "D" ratings are for cases in which no coating is left within the blast profile on the substrate, and "F" ratings are reserved for cases in which the coating completely pops off during scribing before we even try to evaluate it.

Numerical values are assigned to each grade, with a sharp difference between a "C" and a "D", while little differences exist between an "A", a "B", and a "C". This is necessary for two reasons. First, since the test is somewhat subjective, some coatings take a lot more to "pop off" than others, so they should not be penalized if after they pop off there is more substrate showing than for a soft coating which is easy to pop off. Second, a "D" or "F" rating means that there is no coating left on the substrate, the worst of all cases from a material protection standpoint. Penalizing a coating which leaves 55% substrate showing vs. 45% substrate showing for a rival coating is counterproductive; again, all of these decisions are based on comparison of test data with actual field life data.

Blistering is the most dramatic indication of poor adhesion. The most important aspect of a blister is what is underneath; is there bare metal underneath, or is it merely an interlayer blister? For maximum metal protection, we have found that primer coats are not only unnecessary but undesirable since high-performance materials tend to have both good adhesion and good cohesion. Topcoat materials which perform well generally don't need primer.

The causes of blistering are not well understood. A blister may be the result of local corrosion concentration cells, but on test panels blistering is usually uniform and repeatable, not what would be expected from random defects. Blistering could be the result of electrochemical responses to the thermal gradient across the panel, an effect which appears to be concentrated at the oil/water interface in the the atlas cell. Water molecules are in a constant state of flux at this interface, going into limited solution with the crude oil (particularly at high temperatures). For coatings which have a great deal of cohesive strength, the interfacial bond is weaker than the intrinsic coating bonding, so that blistering occurs rather than splitting or tearing. That helps to explain why we have seen, over the years, that "loose" coatings which do not show a great deal of cohesive strength perform better in atlas cell tests than "tight" coatings which have high cohesive strengths.

Blistering between coating layers is not as significant, due to the simple fact that corrosion will not occur between coating layers. Often interlayer adhesion problems are a result of contamination between coats rather than an inherent bonding problem. Nevertheless, interlayer blistering and disbonding results in an overall weakening of the coating system. The protective nature of coatings implies that the entire coating system must act in unison to protect the steel; thus, any damage to the outer layer of coatings affects the protective action of the coating system.

When a blister is noticed in service, the first question which comes to mind is, how significant is this with regards to the corrosion of the entire system? That is why our coatings evaluation rating system notes not only the presence of blisters but the size and number of blisters. Very large blisters convey that general disbonding has been seen. A large number of smaller blisters indicates that while general disbonding is not present, a large number of disbonding sites is present; thus, a poor rating is necessary. The rating system measures the size and number of blisters, with a certain maximum amount (by number and size) not differentiated; once a coating has blistered to a point, it may be assumed that the coating will not perform in service.

One problem with this type of rating system is that blisters are almost always accompanied by "D" or "F" adhesion. While it may be that such coatings are being

doubly penalized for blisters (by receiving correspondingly poor marks in adhesion), it is this property which is a precursor to field failure.

Cracks in a coating are almost always the result of solvent entrapment. Coatings with a high solvent content are most susceptible to cracking, and as such receive lower performance ratings. Cracking results when the evaporation rate of the solvent from the surface is greater than the diffusion rate of solvent to the surface. In addition, the cohesive energy of the coating must be lower than energy of vaporization of the solvent to avoid cracking. When several layers are applied, any one of these layers, if applied too quickly, may result in a layer which contains a high level of solvent. This will increase the level of energy of vaporization to a point beyond the cohesive energy, resulting in cracking. Thus, cracking may be avoided by (a) keeping the solids level high and (b) controlling the application so that the wet film thickness is not too great and that the necessary time for drying is allowed.

It is unclear whether slight mud cracking is detrimental to coating performance, since this cracking is often limited to the top layer of coating. In addition, since it has been seen that slightly porous coatings provide excellent corrosion protection, it can be argued that a small, discontinuous crack differs little from a pore. The true detriment to cracking may in fact be the reaction of field personnel to cracked coatings, since cracks convey poor properties and become accentuated when saturated with black crude oil.

B. Impedance Spectroscopy

While previous in-house testing methods have successfully provided information to guide coatings decisions, a need exists for improved evaluation methods and better understanding of the mechanism behind corrosion mitigation by coatings. Until the mechanisms of failure are understood, the development of products with improved performance will be a struggle.

The next generation of coatings evaluation techniques will monitor performance during exposure. One promising candidate is electrochemical impedance spectroscopy (EIS). By separating the electrical effects of the coating from the electrochemical corrosion reactions through the use of models, the performance of a coating can be evaluated long before any visual evidence of degradation is apparent. Analysis of EIS data also provides insight to the protection mechanism of each coating. This information can be used to correlate physical coating properties with performance in a particular environment.

A rapid test for coating degradation is to examine the change in polarization resistance with time. The measured polarization resistance will be small for a damaged coating relative to a fully protective layer. This change in corrosion resistance can usually be identified well before any change in the coating characteristics can be visually identified. Collecting impedance data from coated steel can be difficult because of the high electrical resistance of organic coatings. The current resulting from a potential perturbation is small and therefore difficult to measure. However, as the coating degrades, the current associated with a defect or blister can be easily measured.

The analysis of impedance data collected from coated steel has been performed with the aid of equivalent circuits. The goal of a circuit design is to model the response of each important physical process by an element. The most commonly used circuit[3] is shown in Figure 5. A perfect barrier coating will act as a capacitor whose impedance, Z, can be

represented by

$$Z = R_s - \frac{j}{\omega C_c}.$$

(1)

where R_s is the resistance of the coating material and C_c is the coating capacitance at frequency ω. With time, the dielectric film will be short circuited by electrolytic paths created by microscopic defects. This phenomenon can be represented by a pore resistance R_{po} in parallel with C_c. This resistance depends on defect area[4]:

$$R_{po} = \frac{\rho d}{A_d}$$

(2)

where ρ is the intrinsic coating resistivity, d is the coating thickness, and A_d is the defect or delaminated area. The charge transfer resistance R_{ct} and double layer capacitance associated with a reaction at the base of the pore are in series with R_{po} and in parallel with C_c. Both of these parameters depend on defect area by:

$$R_{ct} = \frac{R_{ct,bare}}{A_d} \text{ and } C_{dl} = \frac{C_{dl,bare}}{A_d}.$$

(3)

By regressing the equivalent circuit to experimental data, the defect area of a coated metal can be determined. However, the technique is limited to coatings which can be represented as dielectrics whose properties are constant with time and simple charge transfer reactions unaffected by mass transfer. The breakpoint frequency method is a method for determining $R_{po}C_c$ without regressing a circuit[4].

The success of EIS methods for quantitative determination of defect area will be limited by the ability to correctly simulate the behavior of coating systems. More complete models must be developed that include the properties of specific coatings, the reactions occuring underneath them, and the transport of chemical species involved in the reactions.

References

. L.Bone III, "A Unique Method for Accelerated Testing of Atmospheric Coatings for Offshore Structures," CORROSION/89, paper no. 217 (Houston TX:National Association of Corrosion Engineers, 1989).

2. J.F.Montle, Y.Korobov, "Coatings Manufacturer's Use of Accelerated and Field Tests to Evaluate Coatings," CORROSION/92, paper no. 327 (Houston TX:National Association of Corrosion Engineers, 1992).

3. F.Mansfeld, C.H.Tsai, and H.Shih, Proceedings of the Symposium on Advances in Corrosion Protection by Organic Coatings, (Cambridge UK·Electrochemical Society, 1989), p.228-240.

4. H.P.Hack, J.R.Scully, Journal of the Electrochemical Society, 138 1 (1991): p. 33.

TABLE I: Scoring system for the performance of internal linings

Adhesion	Rating	Points		
	A	0		
	B	2		
	C	4		
	D	12		
	F	40		

Blisters	Number	Diameter	Points (if not to metal)	Points (if to metal)
	0	0	0	0
	1-2	<=.0625	4	12
	1	.125	4	12
	2	.125	6	16
	1	.25	8	18
	2	.25	10	30
	>=3	any	20	40

Delamination	?	Points		
	No	0		
	Yes	20		

Cracks	?	Points		
	No	0		
	Yes	20		

Application	?	Points		
	Not Difficult	0		
	Difficult	20		
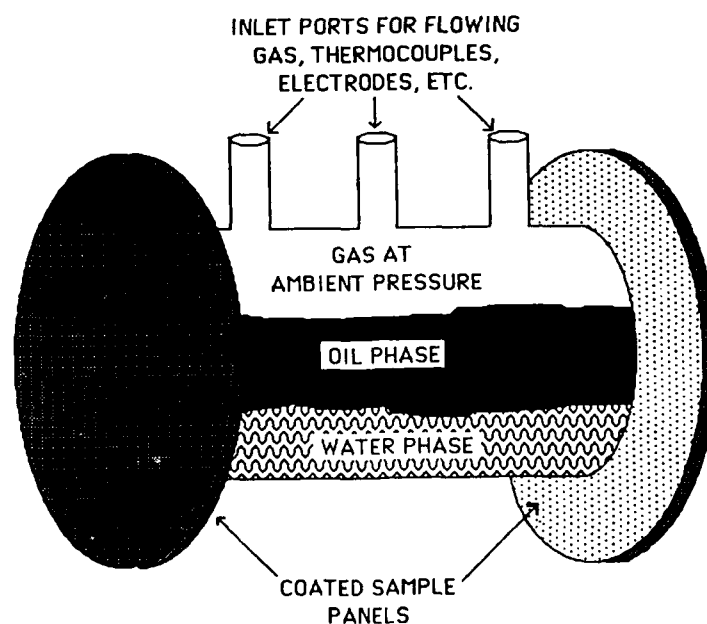
Figure 1: The conventional glass atlas cell.
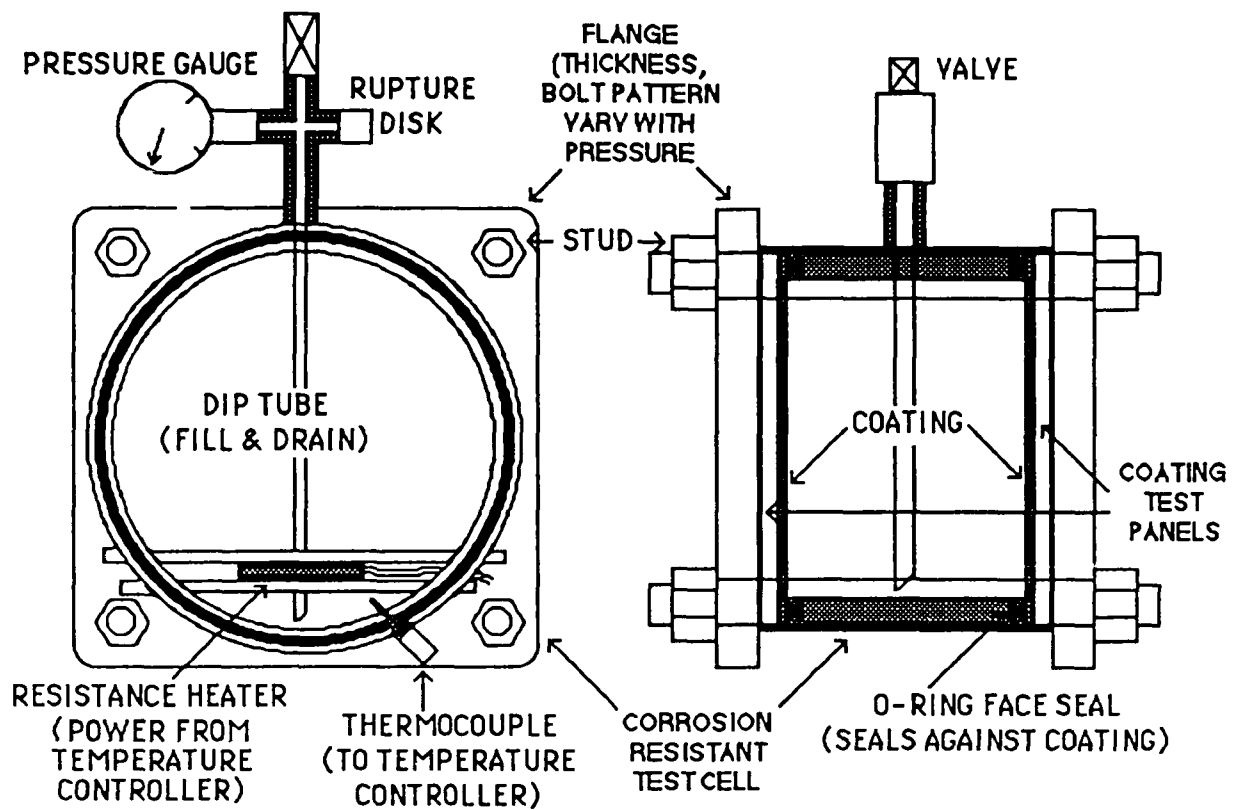
Figure 2: Schematic of the pressured atlas cell (not drawn to scale).
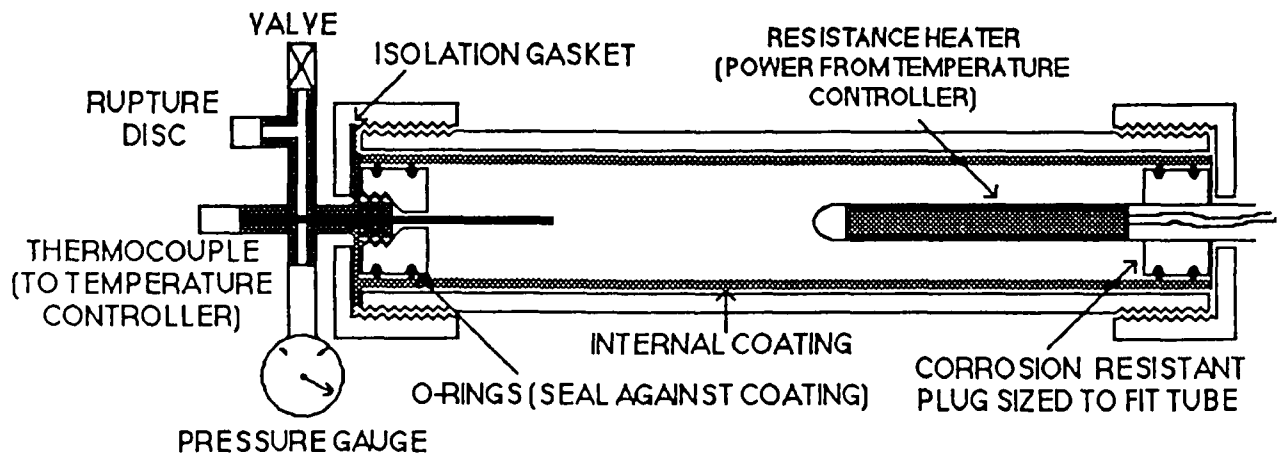
Figure 3: Schematic of the rocker arm test sample with plugs and control attachments (not drawn to scale).
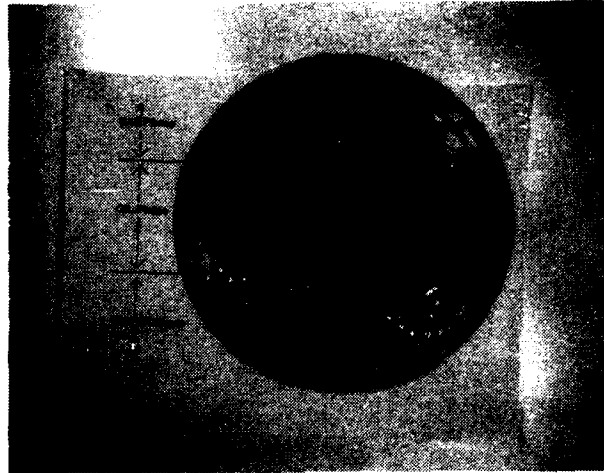
Figure 4: Failed coating panel, illustrating the row of blisters at the oil/water interface. The scratch marks in the oil and gas phases are knife scribes from the evaluation process.
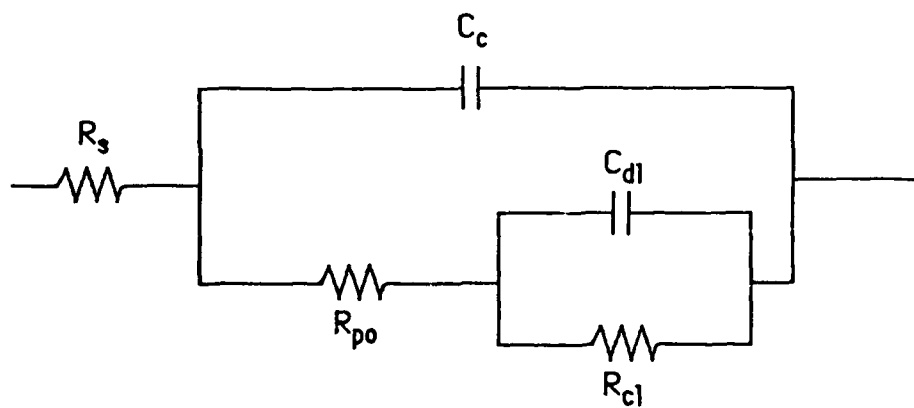
Figure 5: Equivalent circuit model for impedance spectroscopy

Polymer Coatings Degradation Mechanisms Related to Hot Production

Richard D. Granata
Lehigh University
Zettlemoyer Center for Surface Studies
7 Asa Drive, Sinclair Lab
Bethlehem, PA 18015

Richard C. MacQueen and
Kevin J. Kovaleski
Lehigh University
Department of Chemistry
6 E. Packer Avenue
Bethlehem, PA 18015

Abstract

Polymer coatings degradation mechanisms are described for hot production service performance on internal metal surfaces of vessels and pipes. The degradation mechanisms are described: blistering, wet adhesion, cathodic delamination, and anodic undermining. Other coatings barrier properties provide corrosion protection by limiting transport of corrosive- or polymer-degradation agents. Thermal behavior and stability affect the performance characteristics by altering the polymer chemistry and diffusion properties. Hydrothermal properties of coatings are the combined action of water and temperature and can have strong influence on the degradation processes. Electrochemical impedance and positron annihilation data for protective polymer coatings materials are presented with emphasis on processes affecting their degradation while under hot production service.

Key terms: polymer coating, degradation, steel, corrosion, cathode, delamination, hydrothermal, blistering, adhesion, deadhesion, disbondment, electrochemical impedance, free volume, positron annihilation lifetime.

Introduction

Internal polymer coatings have been described in detail for use in hot petroleum production[1-3] Coatings degradation and failure occur by diverse mechanisms. Pressure, heat and aggressive agents have strong influences[3] on protective coatings degradation mechanisms particularly for hot petroleum production systems. Failure mechanisms include blistering, wet adhesion loss, cathodic delamination and anodic undermining. Barrier properties of polymer coatings systems are important for corrosion protection and are related to failure mechanisms. The barrier properties can be strongly influenced by pressure, heat and the type and concentration of materials in production vessels or pipes. A better understanding of the degradation processes or mechanisms provides for more successful use of internal protective coatings. The focus of this paper is to describe the general degradation mechanisms and some of our current work related to the mechanisms.

Background

Polymer coatings degradation mechanisms associated with corrosion processes have been studied extensively in our laboratory[4-11]. Particular emphasis has been placed upon innovative methods for investigating the coating/metal interface. Detailed discussions of specific processes are beyond the scope of this paper.

Coatings Degradation Mechanisms

General descriptions of blistering, wet adhesion, cathodic delamination and anodic undermining are described in the subsequent sections.

Cathodic blistering. The formation of blisters associated with the electrochemical reduction of oxygen or hydrogen ion forming alkali beneath a coating having no physical damage (defect) is termed cathodic blistering. Oxygen, water and cations diffuse through the paint film as cathodic reactants (see following Cathodic Delamination) and the center of the blister is considered the anode. The blister is usually liquid-filled due to alkali formation or may contain some gas in the cases of very low pH.

Gas blistering. This blistering is due to hydrogen ion reduction to form hydrogen gas, H_2. It is associated with acidic environments where hydrogen ion reduction is more likely than oxygen reduction, for example in the absence of oxygen. Thus the process is unusual in environments containing oxygen but is more likely in petroleum production environments.

Osmotic blistering. A process by which blistering occurs due to high liquid phase pressure induced by soluble materials beneath polymer films is termed osmotic blistering. For production environments in which soluble salt concentrations change, blisters may occur upon exposure to low salt or potable water.

Polymer swelling. Swelling of the polymer in some coatings is due to uptake of water or other liquid phase and induces stress on the coating leading to possible disbondment in systems with poor adhesion. Blisters may form as a result of the stresses, particularly when wet adhesion is poor.

Wet adhesion. The loss of adhesion upon permeation of water or a liquid phase to the polymer/metal interface is wet adhesion. The adhesion loss may be regained after drying. Physical damage to the coating is more likely while the coating system possesses decreased adhesive strength.

Cathodic Delamination. This mechanism is caused by cathodic processes leading to disbondment and separation of a coating from a metallic substrate[12-17]. The main feature of the mechanism is reduction of oxygen or hydrogen ion at the coating/substrate interface, seen as

$$O_2 + 2H_2O + 4e^- = 4OH^- \; , \tag{1}$$

or

$$2H^+ + 2e^- = H_2 \ . \tag{2}$$
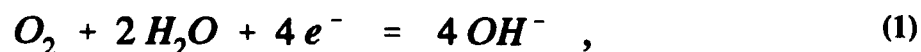
This electrochemical reaction identifies oxygen, water and electrons as the required reactants. Oxygen and water are capable of diffusion through polymer coatings although the rates vary widely with polymer type, coatings formulation and film thickness. Nonetheless, transport of oxygen and water usually occurs at a sufficient rate to support the reaction. Possible exceptions will be discussed later. The electrons are provided by the metal substrate conductivity from anodic sites. Another prerequisite for this cathodic reaction is availability of cations for charge balance (electroneutrality). The degree to which the electrochemical reaction causes damage to the coating/metal interface depends upon the nature of cations present at or transported to the interface[18]. The greatest damage occurs with alkali metal cations such as sodium or potassium. Alkali cations allow the attainment of the highest alkalinity (pH) at the coating metal interface. Values greater than pH = 14 have been measured[19]. High alkalinity is greatly damaging to many polymers useful for coatings purposes; dissolves oxides, phosphates and many types of surface treatment layers; and promotes the corrosion of metals such as iron and zinc by shifting the electrode potential to more active values. A schematic of the general cathodic delamination process is shown in Figure 2. The rate and specific mechanism for the cathodic delamination process depend on the nature of the substrate metal, interphase layers, polymer and fillers, and coating thickness, morphology and uniformity.

Cathodic delamination is a generally applicable mechanism for many types of polymer/metal systems such as ships, pipelines, bridges, appliances, food container liners, circuit boards and electronic components. Specific details for automotive coatings disbondment depend upon materials, thickness and coatings system design. There are two circumstances which should be considered for cathodic delamination contributions to the disbondment process with automotive systems: Defect-free coatings and physically damaged coatings. In the former case, reactants for degradation process diffuse through the coating very slowly establishing what is often the rate-controlling mechanism. Thus, premature coatings system failure is not likely for systems having adequate barrier properties or low interfacial reaction rates for oxygen reduction. This statement presumes other coatings properties are adequate such as hardness, flexibility and toughness and processes such as osmotic blistering due to contaminants and controlled by proper attention to material and application quality. In the latter case, reactants are transported to the reaction sites through the physical defects. Accordingly, degradation can occur rapidly, dependent upon the aggressiveness of the environmental factors and the ability of the coating system to resist corrosive attack associated with the physical defect. A subset of this latter case occurs when the physical damage does not perforate completely the polymer coating system. In the case of partial perforation, the result can be cathodic blister formation with little or no rust formation until the blister cracks or breaks.

Anodic undermining is the dissolution of the metal beneath the phosphate layer and is associated with the presence of cathodic regions formed at defects where the oxygen concentration level is higher or the metal coating becomes galvanically coupled to the more

noble steel substrate in automotive systems. This process is associated with acidification resulting from hydrolysis of metal ions formed in the anodic reaction, for example,

$$Fe^{++} + 2H_2O = Fe(OH)_2 + 2H^+ \quad . \tag{3}$$
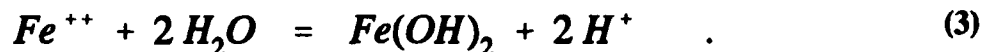
Thermal cycling, alone or in conjunction with other disbondment processes, causes stresses on the coating which can break adhesive bonds to the substrate.

Experimental Methods

Electrochemical impedance spectroscopy (EIS) and positron annihilation lifetime spectroscopy (PALS) are the major focus of recent and on-going work on protective polymer coatings characterization in our laboratory. The former[4,7,9,20] and latter[10,11] methods have been described in detail and are presented briefly here.

EIS Method

Data were obtained from a system consisting of an EG&G Princeton Applied Research Corp. Model 173/179 potentiostat with a computer-controlled Solartron 1250 frequency response analyzer. The impedance spectra were determined from 65.5 kHz to 3.1 mHz. The input amplitude was 15 mV above 100 mHz and 50 mV below 100 mHz. A diagram of the impedance measurement system is shown in Figure 3.

The electrochemical cell was a glass cylinder clamped and o-ring sealed to the specimen surface. The seal exposed 8.8 cm^2 of specimen surface to the distilled water test medium. The reference electrode was Ag/AgCl, and a high density graphite rod served as the counter electrode. Spectra obtained for polymer coated specimens were evaluated using equivalent circuit models shown in Figure 4. Model 1 was satisfactory in cases of a single inflection in log |Z| versus log f plots obtained on defect-free coatings, whereas Model 2 was useful in more complex cases involving coating degradation. Typical coating degradation versus exposure time as monitored with EIS is shown in Figure 5.

Studies were conducted on separate sets of specimens, each at room temperature (RT), and at one of three elevated temperature excursions (40, 60 or 80°C). The typical sequence consisted of: (1) the impedance spectrum taken at RT (this procedural step was designated, RT1); (2) the specimen incubated at the test temperature for 1.5 h and the impedance spectrum taken at the elevated temperature (this step was designated by the temperature used, e.g. 60°C); (3) the specimen equilibrated at RT for 1.5 h and a spectrum recorded (designated RT2); and (4) specimens equilibrated at ambient laboratory conditions (22°C and 50% RH) for 1 week and a final spectrum was begun immediately after filling with electrolyte (final step designated RT3). Defect-free coatings yielded impedance spectra similar to those shown in Figure 6 when subjected to hydrothermal measurement sequences.

Additional impedance measurements were made using powdered graphite as the conductive phase between the specimen and counter electrodes to determine the response to temperature without an electrolyte or water.

PALS Method

The lifetime measurements were made with a standard fast-fast coincidence system based on fast plastic scintillators, RCA photomultipliers, and EG&G Ortec electronics. A diagram of the experimental setup is shown in Figure 7. The sources of positrons used were 10 μCi (water uptake measurements) and 15 μCi (nitrobenzene uptake measurements) ^{22}Na, each sealed in 1.1 mg/cm^2 Kapton foils. In a typical experiment, the positron source was placed between two coated specimens of approximately equal thickness, where the coated side was in direct contact with the source. The spectrum was measured until 60K counts were accumulated in the peak channel. The positron lifetimes and intensities, and their uncertainties were obtained from the raw data using the POSITRONFIT[21] program. Data obtained with four materials are presented in Figure 8. Note the curve shapes to the left of the main peak which clearly demonstrate differences between copper or nitrobenzene (small intensity, short lifetime) versus water or polytetrafluoroethylene (PTFE).

Specimen preparation

Specimens were prepared from 10 x 20 x 0.05 cm SAE-1010 steel panels. The panels were wet ground with 240 grit SiC paper, rinsed with ethanol and dried in warm air with a blow-drier. Table 1 describes the components for the coatings. The coatings formulations and cure conditions are given for the PALS and EIS studies in Tables 2 and 3, respectively. Formulations were applied by draw bar at a thickness of 0.015 cm wet. After curing, the panels were cut into 5 cm squares. Final cured thicknesses ranged from 0.0025 to 0.0040 cm.

Polybutadiene. Substrates for polybutadiene specimens were also prepared in the same manner, but were cut into 5 cm squares before applying the coating. Polybutadiene was applied by spin-coating and cured by baking at 195°C for 30 min. Cured-film thickness was 0.003 cm.

Polyester Baking Enamel. The polyester coating formulation consisted of the following components: Components (weight %) - Polyester resin-N.V. (33.39); TiO$_2$ (35.58); Melamine Resin (11.12); Flow aid (0.076); Catalyst (0.894); Solvents (18.94). The blended formulation was applied by spin-coating. The wet specimen was protected from dust, baked at 190°C for 20 min and equilibrated at 22°C and 50% RH for 1 d before testing.

Urethane. A general-purpose, two-part urethane was applied by spin-coating and cured under ambient conditions of 22°C and 50% RH for 7 d before testing. Cured-film thickness was 0.004 cm.

Results and Discussion

EIS

Hydrothermal responses typically observed with polymer matrices are presented in Figure 9. The sensitivity limit for the measurement system with 8.8 cm^2 specimen area is approximately 10^{11} ohm·cm^2. The 60°C log |Z| values show 1-5 log units changes. The urethane coating showed the largest change and failed to return to its initial value upon equilibration at RT. Permanent degradation of the urethane coating occurred at 60°C during the short exposure period. The epoxy, polybutadiene and polyester exhibited smaller changes than the

urethane and no permanent changes to these coatings were observed due to the single, short duration thermal exposure. These observations demonstrate the general impedance responses obtained for polymeric coatings subjected to transitory exposures to heat and aqueous media.

Figure 10 plots the responses of 15 epoxy coatings to thermal transitions during water exposure. Examination of Figure 10 suggests the cured polymer structure can be more important than the presence of hydrophilic or hydrophobic tail solvents. Hydrophobic solvents may be somewhat beneficial versus hydrophilic solvents. The absence of solvents in the epoxy formulation does not appear to adversely affect the water resistance of the coating. Additional details are provided in another paper[22].

PALS

Figure 11 shows the relationship between the equilibrium volume of water absorbed (v_1) and the change in coating free volume fraction upon water saturation (Δf_p) for two types of polymer structures. The behaviors of the polymers are strikingly different with respect to infusion of water. Free volume of the bisphenol epoxy decreases with water uptake. Conversely, the aliphatic epoxy free volume increases with water uptake. These changes have been related to solvent/polymer interactions[23]. Additionally, the coatings making up the negatively sloped line offered excellent corrosion protection while the coatings making up the positively sloped line offer extremely poor corrosion protection. The addition of the aliphatic epoxide resin to the bisphenol epoxide resin caused the resulting coating (BG1) to fall on the positively sloped line, and consequently this coating was found to offer poor corrosion protection. Thus, the addition of the aliphatic epoxide, which is used as a reactive diluent and plasticizer, to the bisphenol epoxy system causes a loss of corrosion protection which can be predicted by PALS data. Table 4 lists calculated values for molecular cavity size, solvent/polymer interaction parameter, χ , and volume fraction of the solvent in the coating. For comparison, values for PTFE are listed to emphasize the importance of χ -- No water or nitrobenzene occupies the large free volume sites in PTFE due to large (unfavorable) interaction parameters. The combined effects of polymer crosslink structure and solvent interaction strongly affect the degradation resistance of the coating material. These combined effects can be directly measured by PALS and isolated into respective contributions by subtracting the solvent effect obtained by theoretical calculation.

Relationship to Internal Coatings

The major degradation processes for internal coatings used for hot petroleum production involve infusion of materials into the polymer coating. After infusion, coatings can be damaged by a rapid pressure loss or by cyclic pressure transients, chemical interactions resulting in adhesion losses, or electrochemical reactions which damage the polymer/metal interface. The damage can be avoided by enhancing the barrier properties of the coatings systems. EIS and PALS methods presented here provide measurements of the barrier properties which are useful in accessing the coatings performance in hot production service. Both techniques can be performed in situ using thermal and pressure conditions appropriate for petroleum production.

Summary
Polymer coatings degradation processes have been described which are related to internal vessel and tubular cnvironments for hot petroleum productions. Ingress of materials into polymer matrices is an essential step in most coatings degradation mechanisms including those for blistering, wet adhesion, cathodic delamination and general (chemistry-related) adhesion losses. Barrier properties are important criteria for coatings used in pressurized, hot petroleum environments. Coating properties can be evaluated using EIS and PALS techniques under conditions similar to those encountered in hot production. Hydrothermal behavior of polymer coating materials can be rapidly evaluated. Free volume measurements provide details on materials interactions critical to barrier property appraisal. Information obtained by the property evaluations should be useful in the accessment current coating materials for specific conditions and in the development of new polymeric formulations.

References
1. A.K. Dunlop, D.H. Patrick and D.E. Drake in Metals Handbook, Vol. 13: Corrosion, 9th edition, (ASM International, Metals Park, OH, 1987), p. 1235.
2. G.E. Peck, Material Performance 21, 10 (1982): p. 44.
3. M. Roche and J.P. Samaran, Material Performance 26 11 (1987): p. 28.
4. H. Leidheiser, Jr. and R.D. Granata, IBM Journal of Research and Development, 32 5 (1988): p. 582.
5. R.D. Granata, M.A. De Crosta, J.F. McIntyre, and H. Leidheiser, Jr., Industrial Engineering and Chemical Product Research and Development, 26 (1987): p. 427.
6. J.M. Atkinson, R.D. Granata, H. Leidheiser, Jr., and D.G. McBride, IBM Journal of Research and Development 29 1 (1985): p. 27.
7. R.D. Granata, P. Deck and H. Leidheiser, Jr., Journal of Coatings Technology, 60 763 (1988): p. 41.
8. H.E. Townsend, R.D. Granata, D.C. McCune, W.A. Schumacher, R.J. Neville, Proceedings of the Fifth Automotive Corrosion and Prevention Conference and Exposition, Dearborn, MI, October 21-23, 1991, SAE Technical Paper Series, paper no. 912275 (Warrendale, PA: SAE International, 1991).
9. R.D. Granata, K.W. Tiedge and H.L. Vedage, Second International Symposium on Corrosion and Reliability of Electronic Materials and Devices, The Electrochemical Society Meeting, Toronto, CANADA, October 11-16, 1992, accepted.
10. R.D. Granata, M. Moussavi-Madani and R.C. MacQueen, CHEMTECH, December (1992): p. 724.
11. R.C. MacQueen and R.D. Granata, Journal of Polymer Science, accepted for publication.
12. H. Leidheiser, Jr., Journal of Adhesion Science and Technology, 1 1 (1987): p. 79.
13. H. Leidheiser, Jr. and W. Wang, Journal of Coatings Technology, 53 672 (1981): p. 77.
14. H. Leidheiser, Jr., Industrial Engineering and Chemical Product Research and Development, 20 3 (1981): p. 547.
15. H. Leidheiser, Jr., W. Wang, R. D. Granata, H. Vedage and M. L. White, Journal of Coatings Technology, 56 717 (1984): p. 55.

16. M. Kendig, S. Tsai and F. Mansfeld, Materials Performance, 23 6 (1984): p. 37.
17. J.J. Ritter and J. Kruger, in "Corrosion Control by Organic Coatings," H. Leidheiser, Jr., Ed., (Houston, TX: National Association of Corrosion Engineers, 1981), p. 28.
18. H. Leidheiser, Jr. and R.D. Granata, IBM Journal of Research and Development, 32 5 (1988), p. 582.
19. J.J. Ritter, Journal of Coating Technology, 54 695 (1982), p. 51.
20. R.D. Granata and K.J. Kovaleski, in "Electrochemical Impedance: Analysis and Interpretation, ASTM STP 1188," J.R. Scully, D.C. Silverman and M.W. Kendig, eds., (Philadelphia, PA: American Society for Testing and Materials, 1993), p. 450.
21. P. Kirkegaard, M. Eldrup, O.E. Mogensen, N.J. Pedersen, Comp. Phys. Commun., 23 (1981): p. 307. The program was modified by D.M. Granata, (Naval Air Development Center) and recompiled by K. Süvegh, (Laboratory of Nuclear Chemistry, Eötvös University, Budapest,Hungary).
22. R.D. Granata and K.J. Kovaleski, This proceedings.
23. R.C. MacQueen, PhD Dissertation, Lehigh University, October, 1992.

TABLE 1.   EPOXY COATING COMPONENTS

Material	Equiv. Wt.	Description	Solvent	Solubility in H_2O
Resin-1	172-176	diglycidyl ether of bisphenol A (DGEBA)	none	none
Resin-2	175-205	polyglycol diepoxide	none	slight
TETA	24.4	triethylenetetramine	none	complete
AEP	43	aminoethylpiperazine	none	complete
Hardener-1	116	polyamide resin	none	0.5%
Hardener-2	325	polyamide resin	30% xylene	0.4%
Surfactant - polyether modified dimethyl- polysiloxane copolymer	---	solution of a monophenyl glycol 11.5-1-3.5%	xylene	----

TABLE 2.   EPOXY COATINGS SYSTEMS[1] FOR PALS MEASUREMENTS

Coating	Epoxide	Curing Agent	phr[2]	Curing Conditions
B1	Resin-1	TETA	14.0	2 h, 100°C
B2	Resin-2	Hardener-1	66.7	2 h, 100°C
B3	Resin-1	Hardener-2	187.0	2 h, 100°C
B4	Resin-1	AEP	24.7	2 h, 100°C
G1	Resin-2	TETA	12.8	2 h, 100°C
G2	Resin-1	Hardener-1	61.0	2 h, 100°C
G3	Resin-2	Hardener-2	171.0	2 h, 100°C
BG1[3]	Resin-1 & Resin-2	TETA	13.4	2 h, 100°C

1. All coatings have 0.1 parts per 100 by mass of surfactant.

2. phr = (amine H EW x 100)/(Epoxide EW).

3. 1:1 ratio of Resin-1 : Resin-2 by mass.

TABLE 3. EPOXY COATINGS SYSTEMS FOR IMPEDANCE MEASUREMENTS

POLYMER SYSTEM	CODE		
	NO SOLVENT	HYDROPHOBIC SOLVENT	HYDROPHILIC SOLVENT
Resin-1 TETA	E1	E1-O	E1-I
Resin-1 Hardener-1	E2	E2-O	E2-I
Resin-2 Hardener-1	E4	E4-O	E4-I
Resin-1:Resin-2 (1:1) TETA	E5	E5-O	E5-I
Resin-1:Resin-2 (1:1) Hardener-1	E6	E6-O	E6-I

15 Systems: Solventless, Hydrophobic* and Hydrophilic*
5% solvent before oven cure

TABLE 4. FREE VOLUME AND SOLVENT INTERACTION COMPARISON
BETWEEN WATER AND NITROBENZENE

Material	Water			Nitrobenzene		
	molecules per cavity	χ	v_1	molecules per cavity	χ	v_1
B1	2.3	4.88	0.0256	0.41	0.58	0.005
B2	3.2	"	0.0482	0.57	"	0.259
B3	3.7	"	0.0560	0.65	"	0.349
B4	2.2	"	0.0383	0.39	"	0.028
G1	3.1	4.52	0.246	0.55	0.82	0.398
G2	3.6	"	0.176	0.64	"	0.416
G3	4.1	"	0.133	0.72	"	0.498
PTFE	12	17	~0	2.1	18	~0

χ - solvent interaction parameter; $\chi = 0.34 + (V_m/RT)(\delta_1 - \delta_2)$, where V_m is the molar volume of the solvent, and δ_1 and δ_2 are the solubility parameters of the solvent and polymer, respectively.

v_1 - volume fraction of the solvent in the coating.
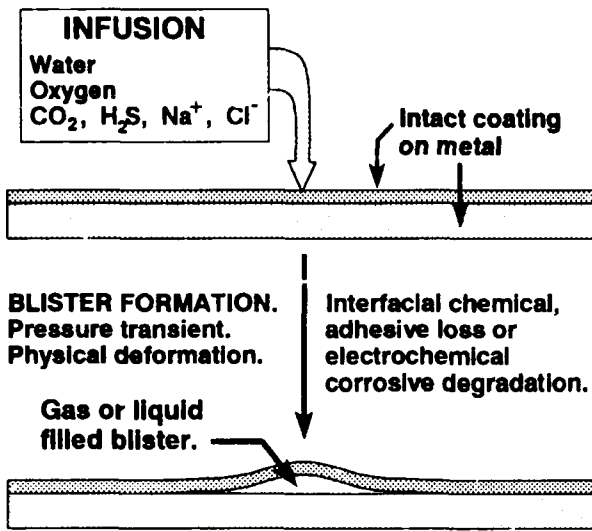
Figure 1. Generic blister processes.

CATHODIC DELAMINATION MECHANISM
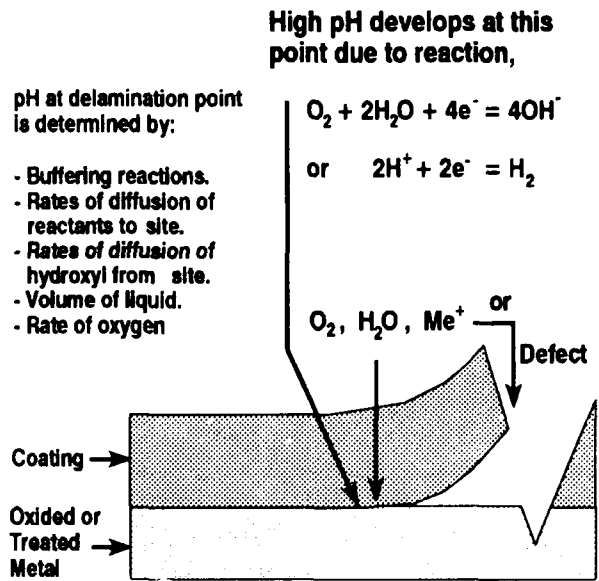
Figure 2. Diagram showing mechanism of cathodic delamination.
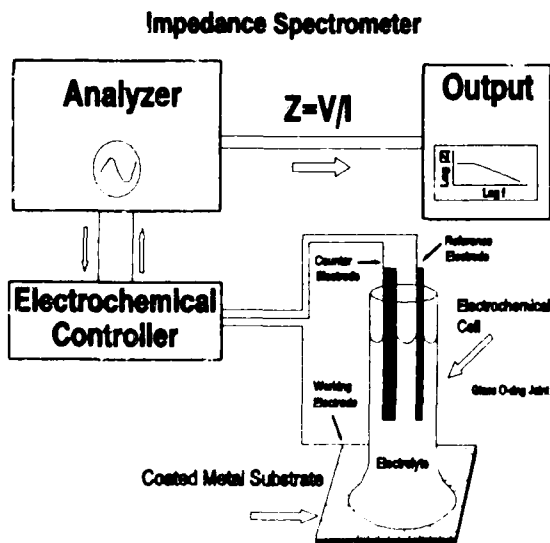
Figure 3. EIS instrumentation.
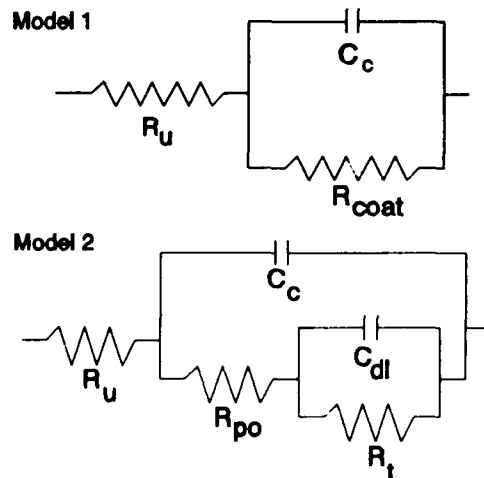
R_u - Uncompensated solution resistance
C_c - Intact coating capacitance
R_{po}- Pore resistance of the coating
C_{dl} - Double-layer capacitance of the metal/solution interface
R_t - Charge transfer resistance of the metal/solution interface

Figure 4. Equivalent circuit models.

Impedance versus Time
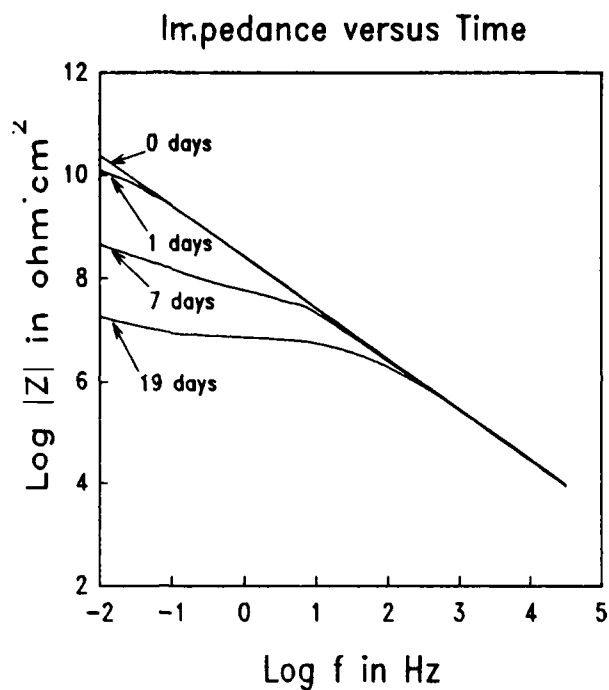
Figure 5. Impedance versus time for polybuta-diene.

Epoxy Coating
Impedance versus Temperature
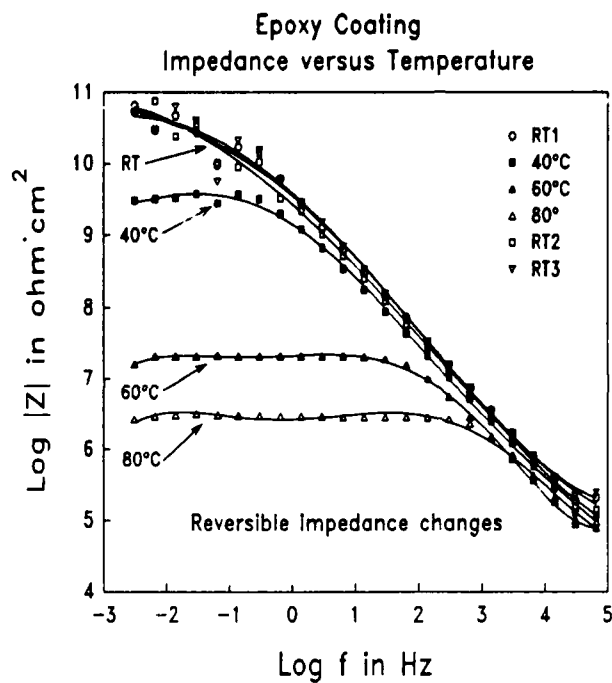
Figure 6. Epoxy coating exhibiting large hydro-thermal impedance change at low frequency.
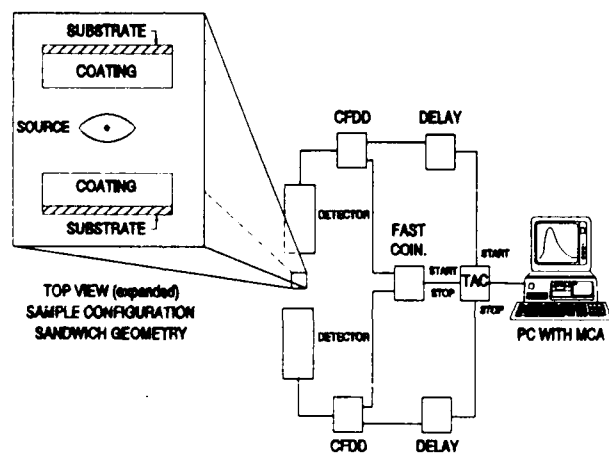
Figure 7. PALS instrumentation.

FOUR PALS SPECTRA
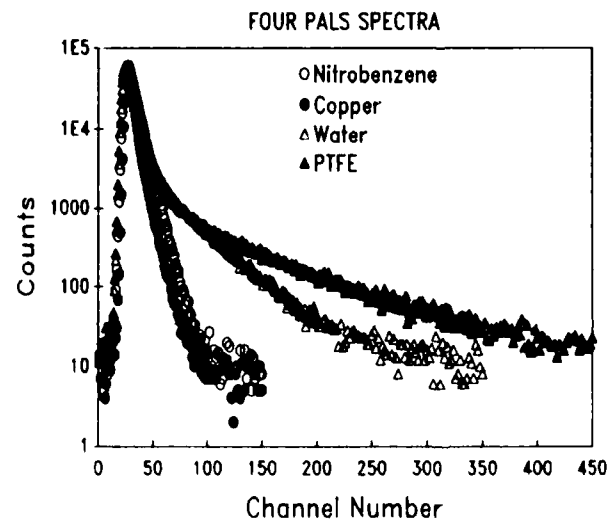
Figure 8. PALS data for four materials with differing long lifetime characteristics.
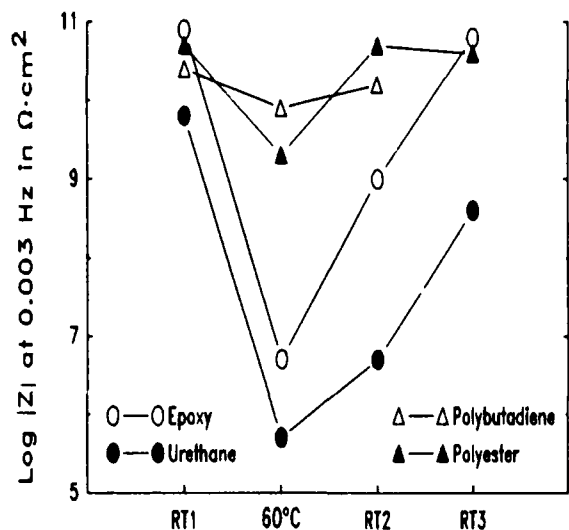
Figure 9. Coatings exhibiting large and small hydrothermal impedance changes at low frequency.
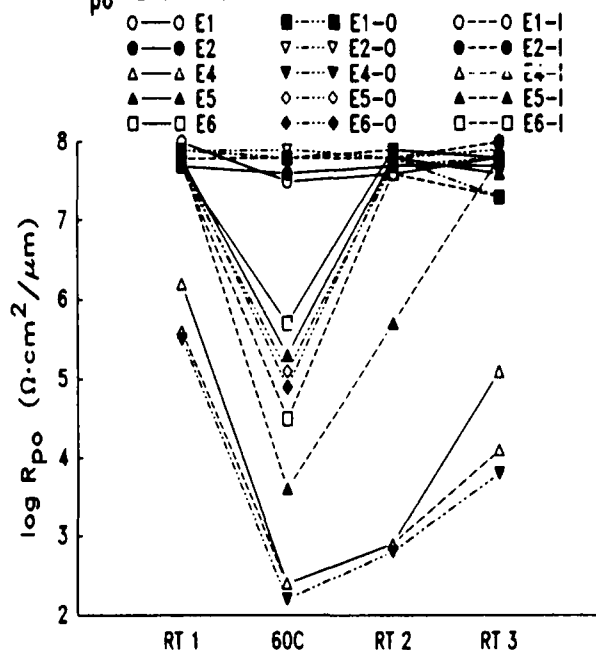
Figure 10. Hydrothermal impedance behavior of 15 epoxy coating systems: Room temperature-60°C transitions.

Figure 11. Equilibrium volume fraction of water absorbed versus free volume fraction after water absorption.

Oxidation of Carburised and Coked Heat-Resistant Steels

D. R. G. Mitchell and D. J. Young
School of Materials Science and Engineering
University of New South Wales
P.O.Box 1, Kensington 2033, Kensington
Sydney, New South Wales, Australia.

W. Kleeman
Schmidt & Clemens GmbH
Edelstahlwerk Kaiserau
D 5253 Lindlar, Germany.

Abstract

The coking and carburisation, decoking and subsequent oxidation of several cast heat-resistant steels have been observed. A commercial HP grade, a high silicon version of this steel and an experimental aluminium-containing steel were found all to coke similarly at $1000^{\circ}C$ in hydrogen-propylene. The aluminium steel did not carburise extensively, being protected by an Al_2O_3 surface layer, but the other two steels underwent rapid internal carburisation.

Subsequent exposure of these reacted steels to air-steam mixtures led to rapid coke burn-off according to linear kinetics. This left the steels with a surface scale of M_7C_3 which covered the surface of the HP grade and the high silicon modification, but formed as islands on the aluminium steel. Further exposure to air-steam at 800 and $900^{\circ}C$ led to slow oxidation of this carbide. This reaction proceeded initially according to slow, parabolic kinetics but was later rather irregular due to occasional scale spallation. The practical consequence of this behaviour was that it proved impossible to passivate the steel surfaces in a reasonable time under the conditions employed.

Key terms: high temperature corrosion, pyrolysis, scale formation, decoking.

Introduction

Pyrolysis tubes in steam-cracking furnaces must withstand the effects of a strongly reducing, highly carburising process stream on their interior and an oxidising environment on their exterior, which is fired to temperatures of up to $1150^{\circ}C$. The materials used in these applications are cast, austenitic steels most commonly of HP grade. A typical composition is shown as alloy A in Table 1.

In service, these materials fail ultimately as a result of carburisation, caused by carbon dissolution into the steel at the tube wall inner surface. Because of this, there is considerable interest in the possibility of protecting the steel from the carbon with an appropriate coating or scale. The possibility of finding an effective scale is particularly attractive because, in the normal course of operations, the

interior of the tubes is periodically subjected to strongly oxidising conditions. This is necessary in order to burn out accumulated carbon deposits, which would otherwise constrict the tube diameter. This procedure, known as "decoking", might afford the possibility of developing a protective oxide scale on the metal surface, if suitable reaction conditions can be defined.

As part of a larger program [1,2] on alloy modifications for improved performance in steam-cracking furnaces, a study of the oxidation of heat-resistant steels which have already undergone carburisation and coke deposition, has commenced. The present paper reports the results of a preliminary investigation of the oxidation behaviour of a current technology commercial steel, together with two developmental steels.

Experimental

The compositions of the three alloys used in this work are given in Table 1. Alloy A is a commercial HP grade material produced by Schmidt & Clemens GmbH and known as G4852 Mod A. Alloys B and C are experimental materials, produced by the same company. Alloy B is very similar to the commercial material but possesses an unusually high silicon content. Alloy H is a complex material containing significant levels of a number of reactive elements as well 14.3 w/o (weight percent) cobalt, 3.1 w/o molybdenum and 1.65 w/o aluminium. The latter two alloys were chosen for use in this study because of the potential benefits which might be expected from the strong oxide formers, silicon and aluminium.

Sample coupons were approximately 2 mm thick and had a total surface area of approximately 2 cm^2. Specimen surfaces were ground to a 600 grit finish and ultrasonically degreased in acetone immediately prior to use.

The kinetics of coking, decoking and oxidation were monitored continuously using a Combustion Instruments Electronics MK2B Microforce microbalance with a sensitivity of 0.02 mg. An alloy specimen was suspended from the balance on a silica cradle and thread inside a Vycor tubular reactor. The reactor was heated externally with an electric furnace, and the temperature of the specimen was controlled within ± 2°C. The required reaction gas mixtures were flowed through this reactor at rates fast enough to ensure that mass transfer was not rate controlling. The coking/carburising gas was 89% hydrogen, 11% propylene at a total pressure of 1 atm and the flow rates yielded a residence time in the hot zone of the furnace of approximately 5 seconds. Coking was always carried out at 1000°C. The decoking and oxidising gas was 55% air, 45% steam which was flowed through the reactor with an inlet gas residence time of about 4 seconds.

In a typical experiment, the system was purged first with argon and then with hydrogen. The pre-heated furnace was then raised over the reactor tube and, once thermal equilibrium was established, propylene was added to the gas flow and the weight gain accompanying carbon uptake was observed to commence. When the desired degree of carbon uptake was achieved, argon was again purged through the system whilst the temperature of the furnace was slowly lowered to the level chosen for decoking and oxidation. Values of 720, 800 and 900°C were used. Once the desired value was reached, the air steam mixture was introduced and coke burn-off commenced. Unfortunately the first 30 seconds or so of reaction could not be

observed due to mechanical instabilities of the balance following the change in viscous drag of the test gas flow. After this period, a weight loss was observed until most of the coke had been removed. From this point on, the weight gain due to oxidation was followed. At the conclusion of each experiment the specimen was allowed to cool in flowing argon.

After reaction, specimen surfaces were examined using scanning electron microscopy and energy dispersive X-ray spectroscopy as well as X-ray diffraction. In addition, metallographic cross-sections were prepared and examined.

Results

The sequential stages of coking, coke burn-off and oxidation are dealt with separately.

Coking/Carburisation

Alloy B gained weight at a slightly slower rate than Alloy A, while the rate for alloy H was significantly slower. Weight uptake kinetics for alloys A and B were parabolic, as shown in Fig. 1, and reasonably reproducible. Regression on the parabolic rate equation

$$\Delta W/A + W' = (2 k_p t)^{\frac{1}{2}} \tag{1}$$

where $\Delta W/A$ is the weight change per unit area formed in time, t, and W', k_p are constants, yielded estimates for the rate constant which are shown in Table 2. The behaviour of alloy H was quite irreproducible with kinetics ranging from linear in some cases to parabolic in others. In a number of cases initial, slow, linear kinetics were succeeded by rather slow, parabolic kinetics as shown in Figure 1.

Analysis by in-situ XRD of the deposits formed on the alloys identified the metal carbide, M_7C_3, and graphitic coke. The appearance of these deposits on alloys A and B was very similar and an example is shown in Figure 2(a). In both cases the deposit had the appearance of pyrolytic graphite. The deposit on alloy H was also mainly pyrolytic coke, but in addition, filamentary coke was present, as shown in Fig. 2(b).

Cross-sections of the alloys after exposure to the coking and carburising gas revealed that alloys A and B behaved rather similarly, but alloy H was different. Alloys A and B both formed poorly adherent, brittle external carbide scales, but also underwent extensive internal carburisation. An example is shown in Fig 3(a). Alloy H formed very little external scale, and the degree of internal carbide formation was very much less than for the other alloys, as seen in Fig 3(b). Internal carburisation was uniform for alloys A and B, but for alloy H occurred only in localised areas.

Decoking

After coking for two hours at 1000^oC, weight gains of approximately 3 mg/cm^2 for Alloys A and B and 0.5 mg/cm^2 for Alloy H were recorded. Subsequent decoking in steam-air mixtures led to linear weight loss kinetics at 720, 800 and 900^oC. These linear kinetics were observed after an initial period of about 30 sec, during which

data was unobtainable because of balance instabilities. Typical data are shown in Figure 1 and linear rate constants are listed in Table 2.

Once a significant proportion of the coke on the specimen surface had gasified, the rate of weight loss was found to slow until all the coke had been removed. At this point weight gain due to oxidation was observed to commence.

Oxidation

The oxidation in air-steam mixtures at 800 and 900°C of decoked surfaces was found to follow parabolic kinetics initially, but subsequently displayed much more complex behaviour, including periods of weight loss. Typical data is shown in Figure 1. Kinetic data for the initial post-coking oxidation was subjected to regression on equation 1, yielding the estimates for the rate constants which are shown in Table 2. Oxidation at 720°C was too slow to measure.

For comparison purposes, fresh alloy samples which had not been exposed to the carburising/coking gas, were oxidised in the same air-steam mixture and the kinetics observed. Results are shown in Figure 4 where it is seen that at 900°C all three alloys oxidised according to parabolic kinetics with alloy H reacting very much more slowly than the other two. However, at 800°C alloys A and B oxidised initially according to parabolic kinetics and subsequently showed a very irregular pattern of behaviour, including occasional weight losses. At this lower temperature, the oxidation of alloy H was too slow to be measured.

Parabolic rate constants for steam-air oxidation of fresh alloys are compared with the corresponding values for early stage steam-air oxidation of coked and carburised alloys in Table 2. The rates at which coked and carburised samples oxidise in the steam-air atmosphere are generally slower than the corresponding values for previous unreacted alloy surface. An exception appears to be alloy A at 900°C, for which a slightly higher rate is recorded for post-coking steam oxidation. These comparisons are valid only for the initial stage of reaction. In the longer term, steam oxidation at 900°C of pre-coked alloys A and B departs dramatically from parabolic kinetics, whereas for non-coked alloys parabolic oxidation kinetics continue.

Analysis by X-ray diffraction was carried out on the sample surfaces after steam oxidation. The results are summarised in Table 3 where it is seen that the effect of coking prior to steam oxidation is reflected in the persistence of M_7C_3 in the surface layer even after subsequent oxidation treatment. It was also found that whereas Cr_2O_3 was the majority species in the scale formed by steam oxidation of fresh metal surfaces, the proportion of spinel was increased in the products of post- coking steam oxidation so that Cr_2O_3 and spinel were present in approximately equal proportions.

Alloys oxidised in air-steam mixtures without prior coking and carburisation were examined metallographically. It was found that alloys A and B were very similar in appearance and a cross-sectional view is shown in Figure 5(a). A thin continuous external scale is seen to have formed. Alloy H behaved quite differently as is seen in Figure 5(b) where significant internal oxidation is apparent.

Cross-sectional views of alloys subjected first to coking and then to steam-oxidation were rather similar in appearance to those of the same materials after simple steam oxidation. One critical difference however is that the external scale formed in this procedure is not continuous. An example is shown in Figure 6 where a thin patchy external scale is visible on the surface. Immediately beneath the surface a narrow zone in which carbides have been dissolved is seen. This zone forms as a result of outward chromium diffusion to form external chromium-rich scale during both the carburisation/coking stage and the oxidation stage.

The difference in reaction products produced by simple steam-air oxidation and steam-air oxidation after precoking is most clearly shown by SEM examination of the external topography. It is seen in Figure 7(a) that the scale formed by air-steam oxidation of alloy B has reproduced the grinding marks on the original alloy surface. Steam oxidation of precoked specimens of the same alloy produced a very different appearance as shown in Figure 7(b). Here a rather fine grained surface has formed, which bears no relationship to the original alloy surface grinding marks. The origin of this oxide morphology was investigated by examining the surface of an alloy which had been precoked and then undergone carbon burn-off but for which the reaction had been stopped before the commencement of weight uptake, that is prior to the beginning of oxidation. Such a sample is shown in Figure 8 where a fine, nodular appearance is apparent. Analysis by X-ray diffraction revealed that the surface region was composed entirely of carbide, M_7C_3. It is apparent, therefore, that the appearance of the subsequently oxidised surface is dictated by the fact that it is the surface carbide which is oxidising under these circumstances.

Alloy H developed surface deposits of quite different appearance. The surface of a sample which had been air-steam oxidised after precoking is shown in Figure 9. The smooth, featureless region which makes up most of the surface was found to be aluminium-rich and is presumed to be Al_2O_3. The dark regions were chromium-rich oxide, and the lighter coloured nodules were found to contain reactive elements. The surface of a similar sample prior to the onset of oxidation, that is after the burning off of coke, is shown in Figure 10. Again the smooth region is aluminium-rich and the dark, localised regions are chromium-rich, but in this case the chromium-rich phase is carbide.

Discussion

The carbon uptake shown by these alloys when exposed to hydrogen-propylene mixtures was due to two different processes, coking and carburisation. Coke deposition on the surface from the gas phase is known [3,4,5] to proceed with linear kinetics. At 1000°C, coke deposits are formed mainly by gas phase pyrolysis, and similar coking rates are observed for all materials. The coke deposits formed in the present work had the appearance and the graphite structure expected of a pyrolytic process. Only in the case of alloy H was some additional coke of filamentary morphology present. Coke of this type is generally thought [6,7] to result from catalysis at metal surfaces of hydrocarbon degradation reactions. Its presence therefore indicates the presence of a somewhat different surface on this alloy during exposure to these gases.

Carburisation takes the form of internal precipitation of chromium-rich carbides resulting from the dissolution of carbon into the alloy and its inward diffusion. As is well known, [8-11] the diffusion-controlled nature of these processes causes the kinetics to be parabolic.

The observed parabolic weight uptake kinetics for alloys A and B show that the majority of the carbon is incorporated into the alloy itself in a carburisation process. The amount of coke deposit is relatively small. Alloy B carburises more slowly than alloy A as a result of its higher silicon content, which depresses carbon solubility and diffusivity in the austenitic matrix [12].

The irreproducible carbon uptake behaviour of alloy H clearly results from the very variable carburisation behaviour of this alloy. The small extent of carburisation of this material is known[2] to be due to formation of an almost continuous aluminium-rich surface oxide layer. Localised failure of this layer is a consequence of the rather low alloy aluminium content and leads to local regions of carbon entry into the alloy. It has been shown[13] that a level of at least 2.7 wt % aluminium is necessary to enable a stable, protective oxide layer to form under the strongly reducing, carburising conditions employed here. The localised failure of the Al_2O_3 surface film not only permits internal chromium carbide formation, but exposes the remnant alloy matrix, principally iron and nickel, to the hydrocarbon gas. These metals are strongly catalytic to coking reactions, and the observed filamentary coke results.

The linear kinetics observed for coke burn-off are to be expected for a surface controlled reaction [4,6,14]. As the coke is mostly pyrolytic, similar combustion rates would be expected for the deposits on all alloy surfaces. Differences arise in measured burn-off rates through the somewhat different morphologies of the deposits and their consequently different surface areas. In addition, the deposit on alloy H was observed to contain some filamentary or catalytic coke. This material is known to burn extremely fast[4] and it was probably removed during the very initial stages of decoking.

The oxidation of non-coked alloys in air-steam mixtures led to parabolic kinetics at 900°C, but irregular reactions at 800°C. At the lower temperature the irregularities were caused by occasional, local spallation of the oxide scale. Alloys A and B formed scales made up largely of Cr_2O_3 and containing also some spinel. The same pattern of reaction products has already been found for cast heat-resistant materials exposed to high temperature air[15]. Alloy B was considerably more resistant to oxidation than alloy A, presumably because of its high silicon content. No discrete silicon-rich layer was found in the oxide scale on alloy B. However, EDAX analysis did indicate some silicon enrichment at the scale metal interface. The much slower oxidation rates observed for alloy H are a consequence of the formation of a protective Al_2O_3 scale over much of the alloy surface. As noted above, this alloy contained insufficient aluminium to form a continuous and truly protective scale. In consequence, localised ares of chromium-rich oxide were also produced. An additional consequence of this alloy's rather low aluminium content was the formation of internal oxide.

The occurrence of spallation during air-steam oxidation of alloys A and B at 800°C was surprising. Oxidation of this sort of material in air does not lead to spallation[15], and the mechanism whereby the steam has this effect is not apparent.

The initial oxidation in air-steam mixtures of pre-coked and carburised alloys was in general substantially slower than air-steam oxidation of fresh alloy surfaces. Although the kinetics are complicated by the subsequent spallation of reaction product from the alloy surfaces, it is nonetheless clear that carburised alloys oxidise more slowly than new material.

This difference in oxidation rate can be ascribed to the fact that alloys subjected to coking/carburisation treatments, followed by coke burn-off, are left in a state where their surfaces are covered by a chromium-carbide scale. The subsequent oxidation of this material

$$4\,Cr_7C_3 \;+\; 27O_2 \;=\; 14\,Cr_2O_3 + 12\,CO \tag{2}$$
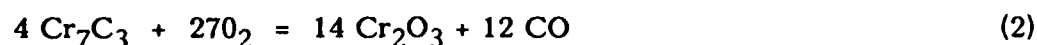
is evidently a rather slow process. This has been noted before in a qualitative fashion[16], but actual kinetic data has not previously been available.

The much greater tendency to spallation during oxidation of a carburised surface can be understood from reference to equation 2. A substantial volume expansion accompanies the conversion of carbide to oxide. It can be calculated from the densities of these compounds that the volume expansion amounts to 77%. Substantial stress accumulation is expected to accompany this change. The effect would be exacerbated by the release of gas implied by reaction 2. In view of these factors, it is not at all surprising that localised failure of the reacting carbide scale is a common event.

The carbide, M_7C_3, can contain quite high levels of iron[17]. The solubility limit at 1000°C corresponds to about 38 atom percent of the carbide metal component being iron. Oxidation of this mixed carbide obviously leads to the formation of a substantial amount of iron-rich spinel in addition to the Cr_2O_3. This explains the much higher proportion of spinel found in products of steam-air oxidation of pre-carburised material than in the oxide scale formed on a fresh alloy surface.

Conclusions

The phenomena observed during sequential coking, coke burn-off and subsequent oxidation are all easily understood in terms of the materials chemistry involved.

The most important finding is that steam-air oxidation of pre-coked and carburised alloy surfaces is surprisingly slow. This was exemplified by the fact that oxidation for 24 hours at 900°C failed to establish a continuous, protective, oxide scale. Even in the case of alloy H, which was in large part protected by an aluminium-rich oxide layer, the surface regions where this layer had failed did not form a useful oxide scale in a reasonable time at 900°C.

The reason for the failure of these alloys to passivate by oxidation was slow oxidation of the prior carbide scale.

References

1. D.R.G. Mitchell, D.J. Young and W. Kleeman, CORROSION/92, p. 302, (Houston, TX: National Association of Engineers, 1992).
2. D.R.G. Mitchell, D.J. Young and W. Kleeman, Proc. Corrosion Asia Conference, paper 189 (Houston, TX: National Association of Corrosion Engineers, 1992).
3. P.R.S. Jackson, D. L. Trimm and D.J. Young, J.Mat.Sci., 21 (1986): p. 3125.
4. P.R.S. Jackson, D.J. Young and D.L. Trimm, J. Mat.Sci. 21 (1986): p. 4376.
5. D.R.G. Mitchell and D.J. Young, J. Mat. Sci., accepted for publication.
6. D.L. Trimm, Catal. Rev. Sci. Eng., 16 (1977): p. 155.
7. P. Tomaszewicz, P.R.S. Jackson, D.L. Trimm and D.J. Young, J. Mat. Sci., 20 (1985): p. 4035.
8. A. Schnaas and H. J. Grabke, Oxid. Met., 12 (1978): p. 387.
9. G.M. Smith, D.J. Young and D. L. Trimm, Oxid. Met., 18 (1982): p. 229.
10. R. H. Kane, Corrosion, 37, (1981): p. 187.
11. K. Ledjeff, A. Rahmel and M. Schorr, Werkst. Korros. 31 (1980): p. 83.
12. R. P. Smith, J. Amer. Chem. Soc., 70 (1948): p. 2724.
13. S. Ando, Y. Nakayama and H. Kimura, ISIJ International, 29 (1989): p.511.
14. T. Y. Yan and M. P. Rosynek, Coke Formation on Metal Surfaces, eds L. F. Allbright and R.T.K. Baker, ACS Symposium Series 202, ACS, Washington (1982).
15. D.J. Young, High Temperature Technology, 1 (1982): p. 101.
16. S.P. Kinniard, D.J. Young and D.L. Trimm, Oxid. Met., 26 (1986): p. 417.
17. R. Benz, J.F. Elliott and J. Chipman, Met. Trans. 5 (1974): p. 2235.

Table 1 Chemical Composition of alloys (wt%) (Fe balance).

Alloy	C	Si	Mn	Cr	Mo	Ni	Zr	Nb	Ti
A	0.45	1.8	1.1	24.0	0.0	32.3	0.1	0.8	0.2
B	0.4	2.6	1.0	24.0	0.0	32.4	0.0	0.8	0.1
H*	0.4	0.7	0.4	17.7	3.1	31.3	0.5	0.4	0.3

* contains 0.1 w/o Y, 1.65w/o Al, 1.2w/o Ta, 1.3w/o Hf and 14.3w/o Co.

Table 2 Rate Constants

Alloy	Coking $k_p \times 10^2$ $(mg^2 cm^{-4} min^{-1})$	Decoking in air-steam $k_{lin} \times -1 \times 10^2$ $(mgcm^{-2} min^{-1})$		
	1000°C	720°C	800°C	900°C
A	3.3 ± 0.75	1.9	3.8	15
B	3.3 ± 0.3	3.5	5.5	30
H	0.27 ± 0.1	2.8	4.5	25

Alloy	Steam oxidation $k_p \times 10^5$ $(mg^2 cm^{-4} min^{-4})$		Post-coking steam-oxidation $k_p \times 10^5$ $(mg^2 cm^{-4} min^{-1})$		
	800°C	900°C	720°C	800°C	900°C
A	1.5	7.0	0	0.1	8.6
B	1.3	2.0	0	0.1	0.6
H	-	0.4	0	0	0.1
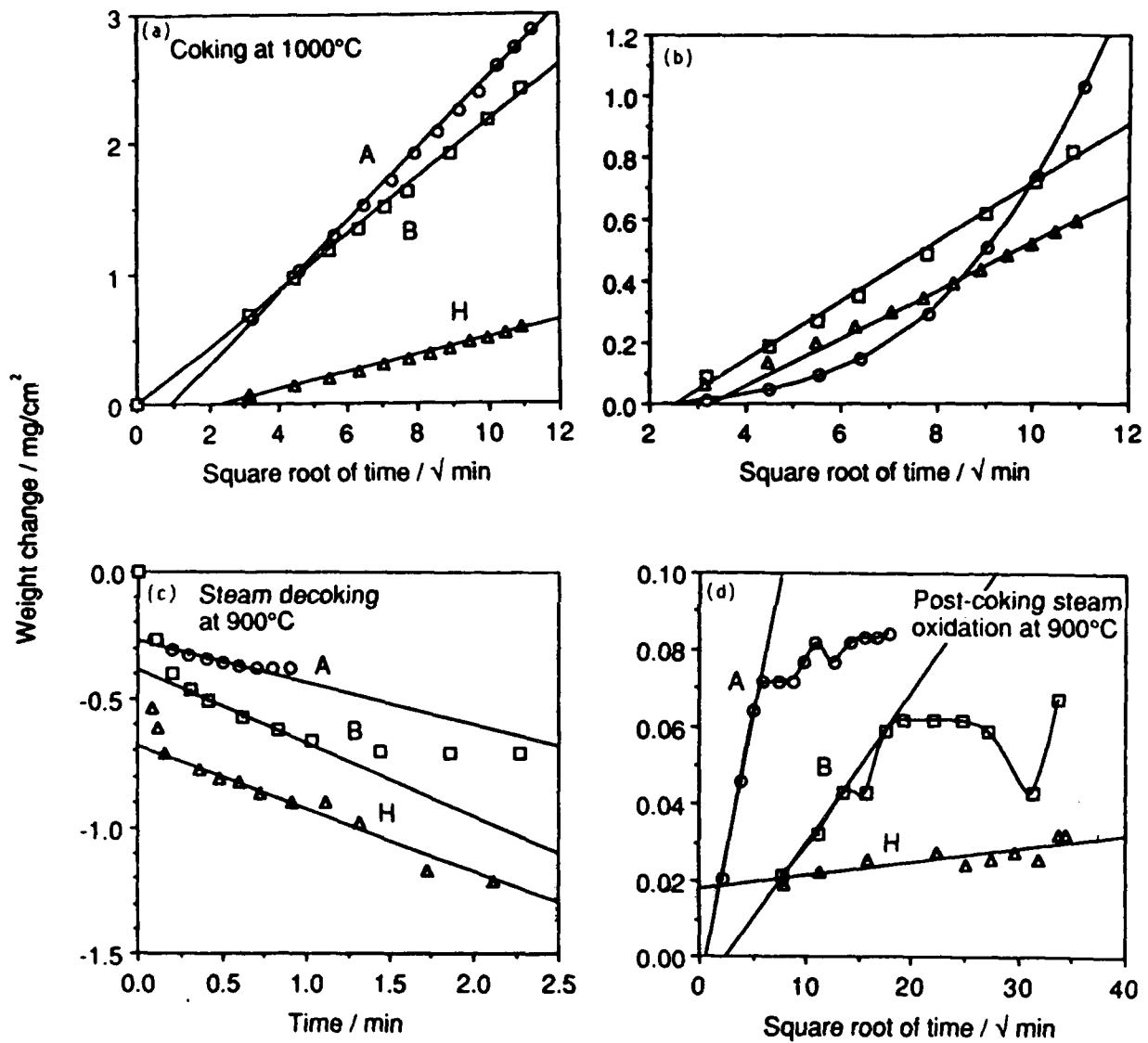
Fig.1. Weight change kinetics for:

(a) coking/carburisation at 1000°C

(b) replicate coking experiments for alloy H at 1000°C

(c) decoking at 900°C

(d) post-coking oxidation at 900°C
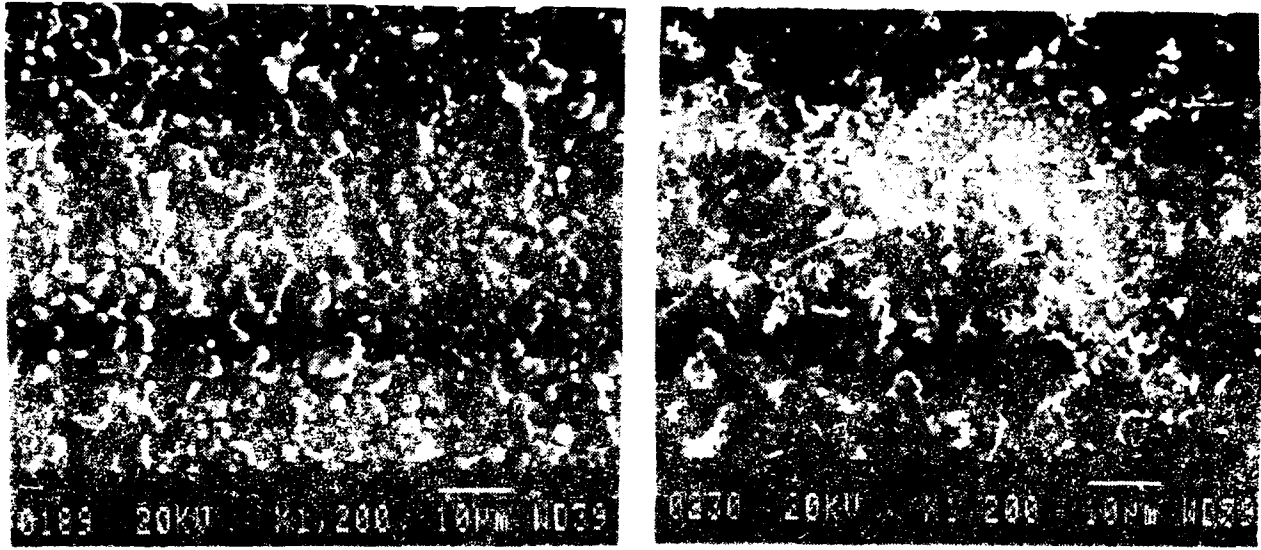
Fig.2.   Topographic views after coking at 1000°C of Alloy A (left)
              and Alloy H (right)
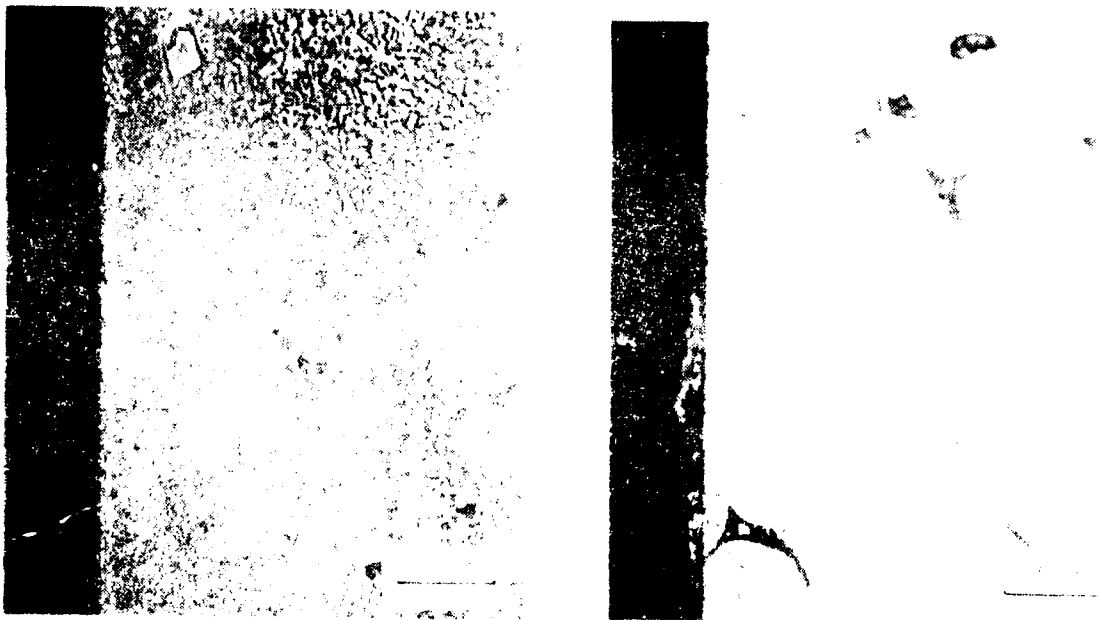
Fig.3.   Cross-sections of Alloy B (left) and Alloy H (right) after coking
              at 1000°C for 2h. Carbides are stained dark.
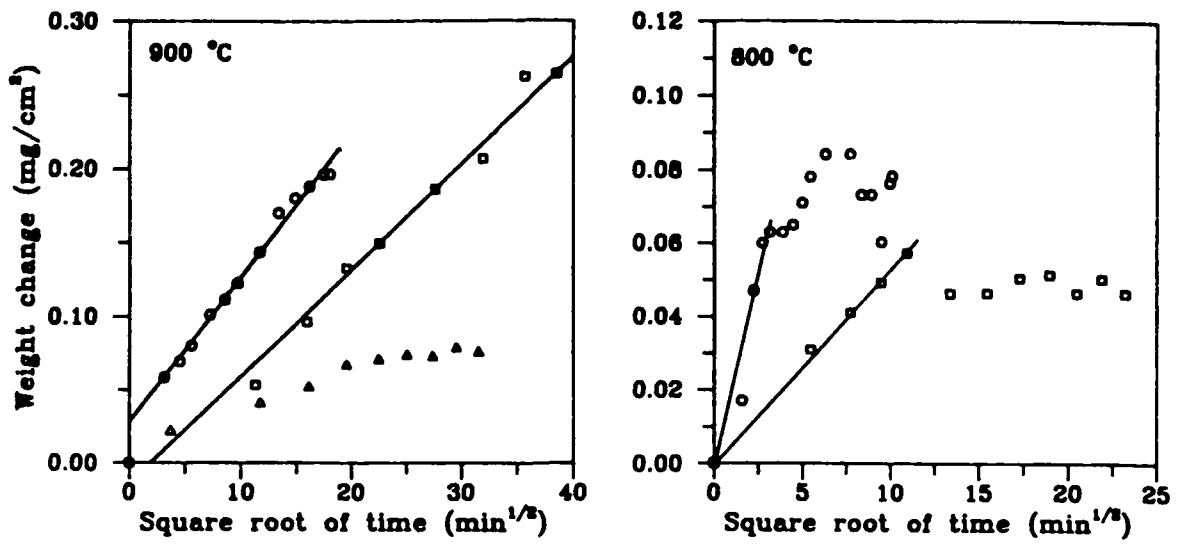
Fig.4. Air-steam oxidation of fresh alloy surfaces.
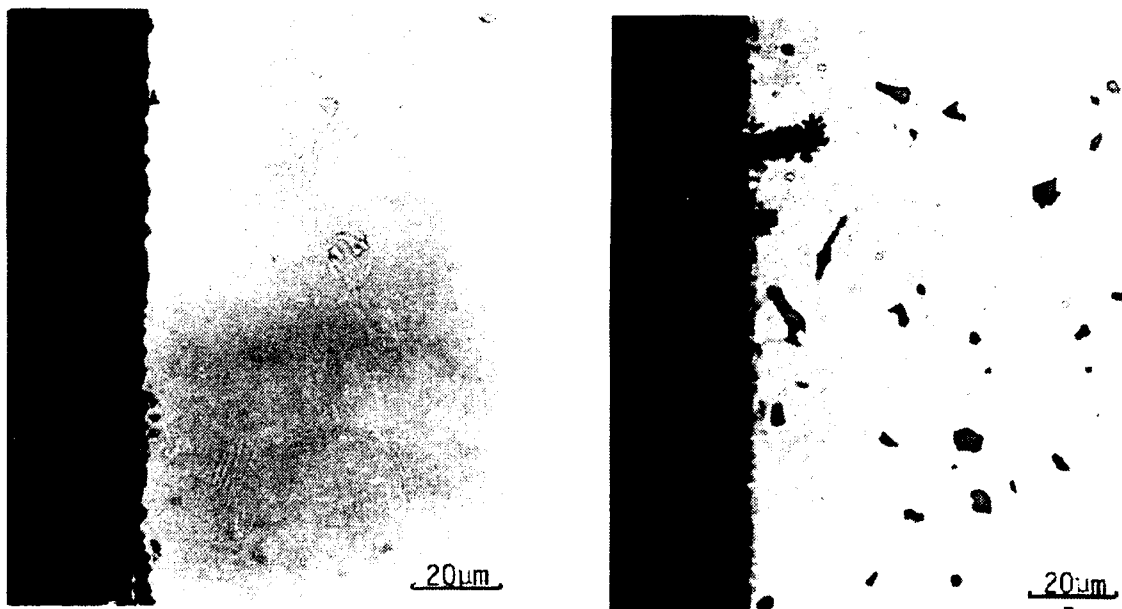
Fig.5. Cross-section of Alloy A (left) and H (right) after steam-air oxidation at 900°C for 24h.
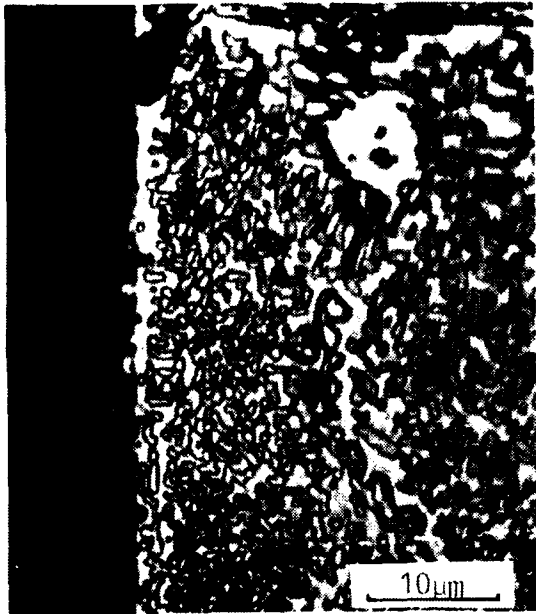
Fig.6. Cross-section of Alloy A, steam-air oxidation at 900°C for 24h, after pre-coking.
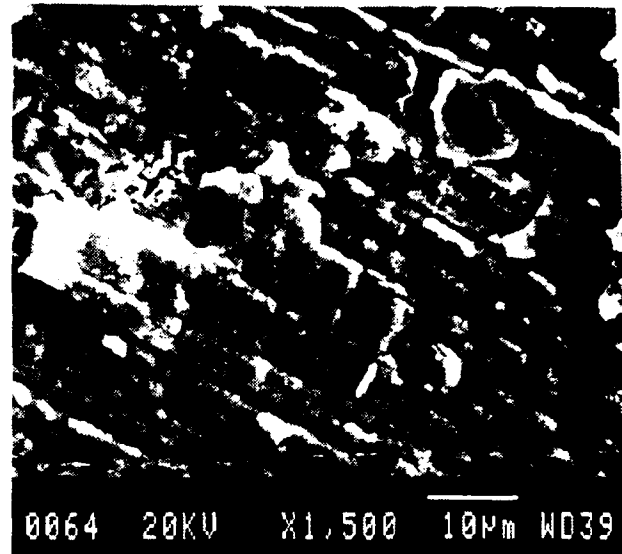
Fig.7(a). Surface of Alloy A after steam-air oxidation for 24h.
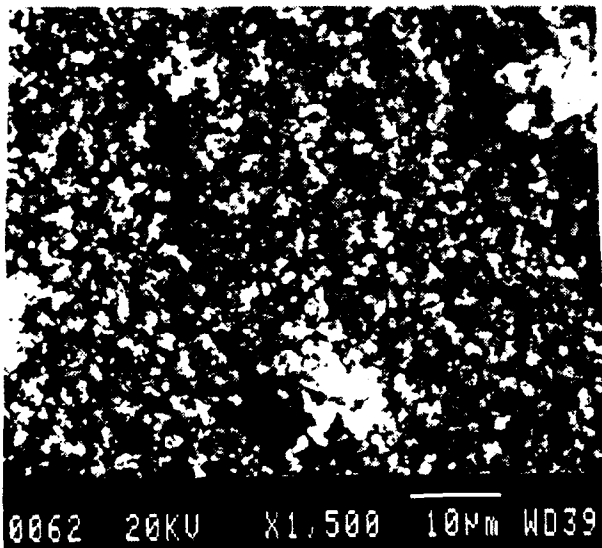
Fig.7(b). Surface of Alloy A after steam-air oxidation at 900°C of pre-coked surface.
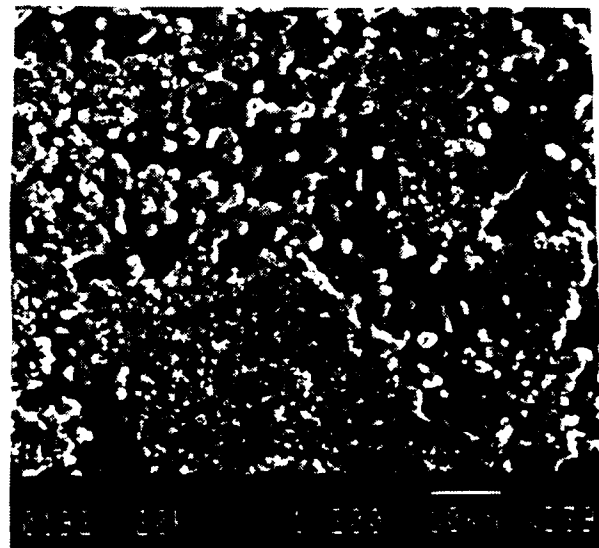
Fig.8. Surface of Alloy A after carbon burn-off of pre-coked surface.
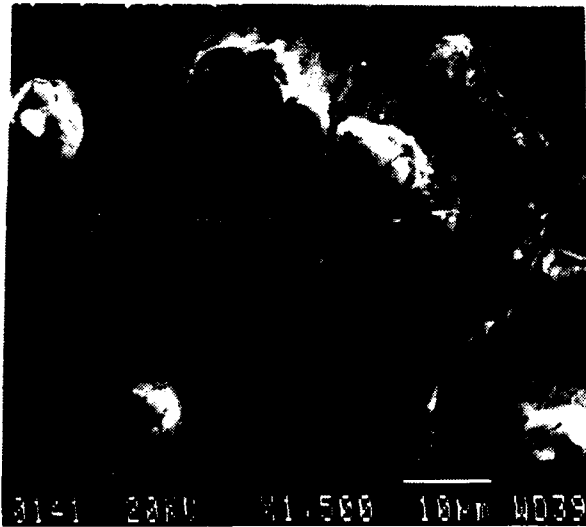
Fig.9.   Surface of Alloy H after
         steam-air oxidation at 900°C
         of pre-coked sample.
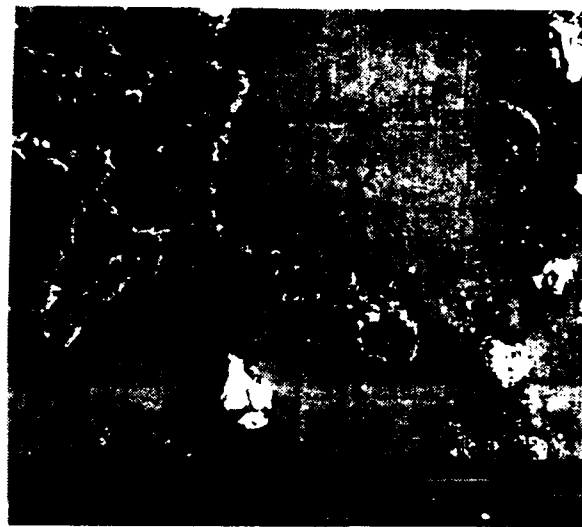
Fig.10. Surface of Alloy H after
         carbon burn-off of pre-
         coked sample.

The Effect of Environmental Variables on Crack Propagation of Carbon Steels in Sour Media

M B Kermani, R G MacCuish, J T A Smith
BP Group Research and Engineering
Sunbury on Thames, UK

R Case and J R Vera
INTEVEP
Los Teques, Venezuela

Abstract

The ability to predict the performance of materials in H_2S-containing environments is becoming increasingly important in the search for oil and gas. In this context, resistance to sulphide stress cracking (SSC) is essential, since the occurrence of SSC can result in a catastrophic and potentially hazardous failure. Therefore, SSC performance of several grades of downhole tubular were evaluated using a combination of test methods over a wide range of testing conditions.

The results have identified that the susceptibility to SSC, the crack growth rate and the resultant fracture morphology are dependent on the solution chemistry. The dominant effect of H_2S presence is found in acidic solutions where hydrogen adsorption increases and causes enhanced hydrogen entry into the steel. Results derived from different test methods showed a good correlation and were complementary. The use of double cantilever beam (DCB) specimens backed by crack growth monitoring using alternating current potential drop (ACPD) technique enabled the identification of a threshold stress intensity factor and crack propagation rate. The results have led to both mechanistic and engineering data providing qualitative and quantitative information on the performance of materials in sour service media.

Key terms: carbon and low alloy steels, crack propagation rate, sour service, sulphide stress cracking, test methods

Introduction

Corrosion is a natural potential hazard associated with downhole tubulars. This results from the fact that an aqueous phase is inevitably co-produced with the oil and/or gas. The inherent corrosivity of this aqueous phase is heavily dependent on the levels of CO_2 and H_2S acidic gases which are also co-produced. The appropriate choice of materials for downhole applications is an important factor in the economic success of oil and gas activities. This is becoming increasingly important as wells are drilled deeper and downhole conditions tend to become more corrosive and contain higher levels of acidic gases. Materials choice is governed by mechanical properties, resistance to both corrosion damage and sulphide stress cracking (SSC), availability and cost. The presence of H_2S, CO_2 and brine in wells not only gives rise to increased corrosion rates, but also can lead to environmental fracture associated with enhanced uptake of hydrogen atoms into the steel. Resistance to SSC is often the principal factor

affecting the choice of materials for H_2S-containing environments, since the occurrence of SSC can result in a catastrophic and potentially hazardous failure. The risk of SSC and lack of a realistic knowledge on the corrosivity of produced fluids often leads to the selection of highly alloyed, highly priced materials with an abundant cost penalty. Therefore, it is important to have a method of assessing the performance of candidate materials that leads to the most appropriate and cost-effective choice.

The SSC performance of materials has long been recognised and has prompted extensive studies of the subject [1-5]. Effort has been expended in studying factors controlling the performance of materials in production environments in an attempt to define the safe operating limits of candidate materials in terms of the environmental and mechanical conditions. This knowledge is gained, in part, from service experience. Nonetheless, it is imperative that candidate materials are assessed in the laboratory prior to their application in the field, so that costly and potentially hazardous failures are avoided. Many test methods have been developed to assess the degree of susceptibility of candidate materials to SSC [6]. However, such approaches are often fraught with danger. This is because the tests have to be "accelerated" to produce results within an acceptable time frame, so that the environments and/or loads used are often unduly severe when compared to the expected service conditions. Furthermore, the relevance of some of these short term tests to long term performance had been exceedingly difficult to establish other than by long term experience or evaluation. Recent application of a finite number of test methods and appropriate solution chemistry has proved extremely effective in drawing a realistic picture of the SSC performance of tubular goods [3,4,8].

In this study, a selected range of techniques were utilised to evaluate the SSC behaviour of downhole materials. Based on this an alternative test procedure has been developed showing discriminatory data and providing qualitative and quantitative information on the performance of a wide range of oil country tubular good (OCTG) steels exposed to sour service environments.

Experiments

Materials

Four grades of oil country tubular good (OCTG) carbon steels were used for the test programme. These included grades K55, L80, C90 and P110 steels. The chemical composition and mechanical properties of these are tabulated in Tables 1 and 2, respectively.

Environments

The test solution was based on that specified in NACE TM0177-90 [6] and contained 5% NaCl and 0.5% acetic acid. The solution was prepared with analytical grade reagents and distilled water. Prior to the commencement of each test, the solution was purged with nitrogen for an hour and then saturated with H_2S (or a mixture of H_2S and nitrogen) for an additional hour. Details of experimental procedures are presented elsewhere [3,4,8].

The initial pH of NACE solution was found to be 2.8 and little or no variation in pH was recorded during each test. All tests were carried out at room temperature (23 °C) as this represents the worst case conditions for the occurrence of SSC [4].

SSC Test Methods

Three standard categories of test were utilised in the present study. These included smooth specimen tensile (ST) test, constant extension rate tensile (CERT) testing and pre-cracked double cantilever beam (DCB) testing. In using ST testing, both constant load and sustained load arrangements were employed

in order to find out the extent to which the results derived from each test method differ. ST and DCB testing were in accordance with NACE TM0177-90 standard test method whereas details of CERT testing are described elsewhere [3,8].

Cylindrical tensile test specimens taken in parallel to the pipe axis, were used for both ST and CERT testing having a 2.5mm diameter over a 25mm gauge length. Specimens were prepared in accordance with the requirement specified in NACE TM0177-90. Prior to exposure, the specimens were degreased with acetone and dried in a stream of warm air. ST tests were run for a period of 720 hours. CERT data were analysed on the basis of normalised strain to failure, i.e. the ratio of strain to failure in solution over the corresponding value produced in air [3,8].

K_{Issc} was identified through both the method defined in TM0177-90 [6] and using Equation (2). In both cases a factor for the effect of the side grooves was included. The specimens were machined from each tubing in the longitudinal direction measuring 100 mm long, 25 mm high and 9.5 mm thick. Side grooves 1.9 mm deep were used to control the crack direction. This geometry was in accordance with the procedures specified in NACE TM0177-90. All specimens were fatigue pre-cracked to at least 1.5 mm beyond the root of chevron notch following the procedures described in NACE TM0177-90 and taking ISO 7539-6: 1989 (E) recommendations into account. DCB specimen loading was made by means of a screw placed through one arm. Arm deflections recommended in NACE TM0177-90 were applied. In DCB testing, test duration was kept to 360 hours.

In defining the KIssc, calculations were made on the crack tip stress intensity so that, where the crack came to a halt, plane strain criteria were satisfied, i.e.

$$B > (K_{Issc}/\sigma_y)^2 \qquad\qquad (1)$$

where: σ_y is the yield strength.

Crack Growth Rate Studies

In studying the crack propagation rate of the OCTG materials, DCB specimens were used. In these cases, the crack tip stress intensity factor (K) was calculated using the load-line displacement equation for DCB specimens (ISO 7539-6: 1989(E)) which includes a factor for the effect of the side grooves as described by Heady [9]. This equation is as follows:

$$K = \frac{[\delta E h[3h(a+0.6h)^2+h^3]]}{[4[(a+0.6h)^3+ah^2]]}\left(\frac{B}{B_n}\right)^{\sqrt{\left(\frac{B}{B_n}\right)}} \qquad\qquad (2)$$

where δ is the displacement at the load line, E is the Young's modulus of the material, a is the crack length measured from the load line, h is the specimen half height and B and B_n are the width of the grooved and ungrooved specimen, respectively.

Continuous crack length measurements were made during the tests using an alternating current potential drop (AC/PD) system. Figure 1 shows the positioning of the four point probe system used in monitoring crack length with elapsed time. This arrangement provided satisfactory sensitivity to crack increment across the specimen width. The load setting bolts of the DCB specimens were fitted with insulated inserts to avoid a low resistance path across the crack. Measurements of crack length (a) and elapsed time were converted to crack growth rate (da/dt) using a computer program based on a seven data point polynomial curve fitting method as described in ASTM E-647. Equation (2) was used to calculate the corresponding stress intensity factor.

Results

SSC Test Results

SSC test results of grade L80 steel using different test techniques are presented in Figures 2, 3 and 4.

The time to failure data using constant load and constant displacement arrangements are presented in Figure 2 showing minor disparity. However, the constant load arrangement or using a sustained load arrangement with a compensation for the load relaxation during the testing [2,5] are preferred methods. This is due to the possibility of load relaxation resulting in lowering of effective applied load on the specimen and subsequent crack halt.

The analyses of CERT data based on normalised strain are shown in Figure 3 illustrating an excellent ranking of materials with respect to their SSC performance. Normalised strain to failure was used based on its proven sensitivity to detect the susceptibility to SSC [3,8].

Crack Growth Rate Studies

A typical crack length/time curve is shown in Figure 4 for grade P110 material in the NACE solution saturated with gas containing 10% H_2S. A region of constant crack velocity is apparent.

Crack growth rate data were displayed correlating crack growth increment (da/dt) with crack tip stress intensity factor (K) on a semi-logarithmic basis. An example of the effect of the crack tip stress intensity factor (K) upon the crack propagation rate (da/dt) is shown in Figure 5. The curve clearly exhibits three distinct stages. At low values of K, threshold stress intensity value (K_{Issc}) is set, below which cracking does not occur. K_{Issc} was defined as the value at which the crack velocity became less than 10^{-9} m/s. At intermediate values of K, da/dt is strongly dependent on K (region I) and at higher values of K, da/dt becomes relatively independent of K (region II).

The Effect of H_2S Concentration

The effect of H_2S concentration on the K_{Issc} values are recorded in Table 3 and Figure 6 showing that the threshold stress intensity decreases with H_2S concentration. K_{Issc} values for grade P110 material were found to be lower than that of grade C90, as expected, since grade P110 material is a more susceptible steel to SSC. Little or no experimental scatters were experienced in the generation of K_{Issc}. Furthermore, K_{Issc} calculated using both NACE TM0177-90 and Equation (2) showed good consistency.

Discussion

Based on the data presented using a number of materials and employing a combination of test methods, an overall approach to materials selection with respect to the SSC behaviour is summarised in Figure 7. This is based on using data generated through CERT, ST and DCB testing. A combination of these techniques provides both qualitative and quantitative information on the SSC behaviour of materials. The test methods are as follows:

    i.   Qualitative information was achieved through constant extension rate tensile (CERT) testing. This method was used as a rapid and efficient method of ranking materials with respect to resistance to the environment under consideration.

    ii.   Quantitative information was provided by means of a fracture mechanics approach through which the threshold stress intensity (K_{Issc}) value for a material/environment system was identified. The K_{Issc} value represents the threshold stress intensity factor below which the material can be used without risk of failure due to SSC.

iii.   Complementary information was provided by testing smooth specimens under constant load. This was the conventional method of testing for resistance to SSC and gave meaningful and plain engineering data. These data provide additional confidence in the interpretation of results.

For SSC to occur, a combination of mechanical, environmental and metallurgical parameters is required. Mechanical parameters are portrayed by the manner by which tensile stress is applied. Environmental variables are illustrated by solution chemistry and metallurgical parameters by the type of material. The above approach caters fully for mechanical parameters combining the conventional methods with the ease of CERT testing and the accuracy of fracture mechanics. The data presented in Figure 6 and Table 3 have shown the importance of solution chemistry in defining the SSC behaviour of steels, reiterating the findings of previously published works [2-4]. The importance of solution chemistry was conveyed through a domain diagram relating solution pH with H_2S partial pressure - the two principal parameters in the occurrence of SSC [4].

The results produced by the three methods were found to be complementary in providing sufficient information in materials ranking.   The use of these methods enabled a realistic picture of the SSC performance of a range of OCTG steels paving the way towards establishing long term performance of tubular goods.   This is in support of results produced by other workers using a combination of test techniques [16].

It is apparent from Figure 5 that there are three regions of velocity versus stress intensity factor. In region I velocity varies exponentially with the stress intensity factor. In region II the velocity is virtually independent of stress intensity. Region III where the velocity is again exponentially related to stress intensity factor was not identified in this study, simply because the stresses in this region are well beyond those anticipated in service and were considered irrelevant to the performance of tubulars in sour service conditions. However, region III data emerge with the fracture toughness properties of materials and should be dealt with separately.

It can be seen from Figure 5 that the conventional method of time to failure tests to define materials performance is not very relevant for mechanistic studies, because time to failure may span over these regions as well as the initiation period and super critical crack growth. The general shape of velocity vs. stress intensity plot was found to be similar in all environments studies. However, the position of region I and region II changed with the concentration of H_2S in the solution. The behaviour in the regions I and II are characteristic of hydrogen-assisted cracking [10].

Observations made on the dependency of crack propagation rate with stress intensity factor show that region I velocity is governed by electrochemical kinetics at the crack tip wherein the equilibrium is reached between the hydrogen available in the metal lattice just below the crack tip surface and hydrogen available in the solution. Through the elastic interaction between this interstitial solute and the effective strain rate at the crack tip hydrogen is transported ahead of crack tip thus resulting in a progressive increase in da/dt with increasing K. A somewhat similar conclusions has been put forward for other systems using a da/dt vs. K relationship [10]. The relationship shown in Figure 5 illustrate the intermittent nature of crack increment. This is considered to be the result of either an optimum requirement for hydrogen build up at the crack tip to cause the sudden crack increment or the build up of a brittle layer at the crack tip causing discontinuous cracking. Other workers using different systems have reported a somewhat similar phenomena [13-15].

The crack growth behaviour observed in region II, is the result of some rate limiting mass transport reaction. Additional tests are reported elsewhere [12] confirming this overview by determination of the apparent activation energies for both these crack velocity regions.

At K_{Issc}, hydrogen fugacity is thought to be below a certain value (with all other experimental conditions remaining constant) and the crack comes to rest. This is supported by other workers using a combination of DCB testing and hydrogen permeation measurement [13,14]. Threshold stress intensity is an extremely important parameters in design of tubulars. By using K_{Issc}, material's behaviour can be predicted with a greater degree of confidence since it takes into account the manufacturing defects and anomalies which are present on the tubular sections. Design of tubular components based on stresses below the K_{Issc} would result in their safe use.

Precracked DCB specimen testing provided qualitative as well as quantitative information on the SSC performance of materials. The latter was gained through a fracture mechanics approach [7]. The data led to the identification of a threshold stress intensity (K_{Issc}) value for a material/environment system. The K_{Issc} value represents the threshold stress intensity factor below which the material can be used without risk of failure due to SSC. K_{Issc} derived using either the procedure recommended in NACE TM0177-90 or Equation (2) at regions where crack growth rate approaches 10^{-6} mm/s were found to be somewhat similar and within the experimental scatter of each other. It is therefore, recommended that for ease of testing, NACE TM0177-90 procedure should be used for ranking purposes. However, da/dt data provides complementary information both in terms of confidence in K_{Issc} and in terms of mechanistic information. This is particularly relevant to the SSC performance of corrosion resistant alloys where test duration may be prolonged [13,14].

It is apparent that factors which promote hydrogen embrittlement would in turn affect the SSC behaviour of materials. These include factors which influence hydrogen availability, entry and its transport within the metal lattice [3,8]. Thus solution chemistry, as defined by its acidity, can govern the performance of materials in sour environments. Solution acidity in the presence of sulphide ions (sour environments) both facilitates the hydrogen evolution reaction, making it the dominant cathodic reaction and enhances the amount of hydrogen absorbed within the lattice, thus increasing the degree of susceptibility to SSC. Therefore, a knowledge of solution chemistry, and in particular the in-situ pH, can lead to the establishment of the SSC performance of materials. This is in support of earlier published data on the SSC behaviour of steels [3,4] which in turn leads to a better definition of materials suitability for sour service exposure. Laboratory test results and the understanding of the mechanism of SSC suggest that the severity of the corrosive medium should be expressed in the form of a pH - H_2S partial pressure diagram.

CONCLUSIONS

1. The slow strain rate tensile method has been successfully used to assess the relative aggressivity of environments and define susceptibility to SSC.

2. The use of DCB method backed by the AC/PD system has shown mechanistic as well as engineering information. This information is highlighted by crack growth rate behaviour and threshold stress intensity factor below which the material can be used safely with no risk of SSC.

3. The overall procedure using a combination of three test methods has offered qualitative and quantitative information on the SSC performance of tubular steels. All the three test methods provides effective means of materials ranking with respect to SSC.

4. Crack growth rate data has shown that SSC time to failure based on engineering stress can be inappropriate.

5. Crack growth monitoring using an alternating current potential drop (ACPD) technique enabled accurate identification of a threshold stress intensity factor and crack propagation rate. These led to both mechanistic and engineering information on the performance of materials in sour service media.

ACKNOWLEDGMENT

NOMENCLATURE

a	Crack length	B	Specimen width
B_n	Specimen width at grooved area	E	Young's modulus
J	Hydrogen flux	h	DCB specimen height
K	Stress intensity factor	K_{Issc}	Threshold stress intensity factor
t	Elapsed time	σ_y	Yield strength
da/dt	Crack growth rate		

REFERENCES

1. H$_2$S Corrosion in Oil & Gas Production - A Compilation of Classic Papers, R N Tuttle and R D (Russ) Kane, eds., NACE (1981).

2. Bonis, M R and Crolet, J L, Corrosion Science, Vol. 27, pp. 1059-1070 (1987).

3. Kermani, M B, Harrop, D, MacCuish, R G and Vera, J R, NACE Annual Conference, Corrosion '91, Paper No. 271, Cincinnati, Ohio (1991).

4. Kermani, M B, Harrop, D, Truchon M L R and Crolet, J L, NACE Annual Conference, Corrosion '91, Paper No. 21, Cincinnati, Ohio (1991).

5. Crolet, J L and Bonis, M R, NACE Annular Conference '89, Paper No 17, New Orleans, Louisiana (1989).

6. NACE Standard TM0177, National Association of Corrosion Engineers (1990).

7. Kermani, M B and MacCuish, R G, Society of Petroleum Engineers, SPE 20457, Vol. D, pp. 525-535, New Orleans (1990).

8. Kermani, M B, Creamer, D A, Smith, J T A and Vera, J R, NACE Annual Conference, Corrosion '93, Paper No. 122, New Orleans (1993).

9. Heady, R.B., Evaluation of Sulphide Corrosion Cracking Resistance in Low Alloy Steels, Corrosion, Vol 33, pp 98-107 (1977)

10. Nelson, H.G. And Williams, D.P., Proc. NACE Conf. Stress Corrosion Cracking and Hydrogen Embrittlement of Iron Base alloys (R.W. Staehle, J Hochmann, R.D. McCright and J.E. Slater, Eds.), pp. 390-404, NACE, Houston (1977).

11. Sponseller, D L, Corrosion, Vol 48, No 2, 159 (1992).

12. Vera, J and Kermani, M B, to be published.

13. Barker, J C, Yu, J, Brook, R and Kermani, M B, ISOPE-93, Singapore (1993).

14. Barker, J C, Yu, J and Brook, R, 12th International Corrosion Congress, Houston (1993).

15. Kermani, M B and Scully, J C, Corrosion Science, Vol 19, p 111 (1979).

16. Miyasaka, A and Ogawa, H, Corrosion 91, Paper No 27, Cincinnati, Ohio (1991).

TABLE 1
CHEMICAL ANALYSIS

MATERIAL	ELEMENTAL COMPOSITION (wt%)						
	C	S	Si	Cr	Mn	Fe	Mo
Grade K55	0.28	<0.01	0.15	0.52	1.3	Bal.	<0.05
Grade L80	0.14	0.001	0.243	0.013	1.24	Bal.	0.006
Grade C90	0.26	<0.01	0.16	1.0	0.47	Bal.	0.53
Grade P110	0.25	<0.01	0.18	0.17	1.4	Bal.	<0.05

TABLE 2
MECHANICAL PROPERTIES

MATERIAL	0.2% Prrof Stress (MPa)	Ultimate Tensile Strength (MPa)	Elongation to Fracture (%)
Grade K55	469	713	16**
Grade L80	660	772	21.1**
Grade C90	653	778	8.8*
Grade P110	840	857	5.5*

TABLE 3
THRESHOLD STRESS INTENSITY FACTOR RESULTS

H_2S Conc.	OCTG Grade		
(%)	C90	P110	L80
100	39.6	22.1	38.6
10	69.6	18	
1.0	74.6	32.2	
0.1	>73	43.3	
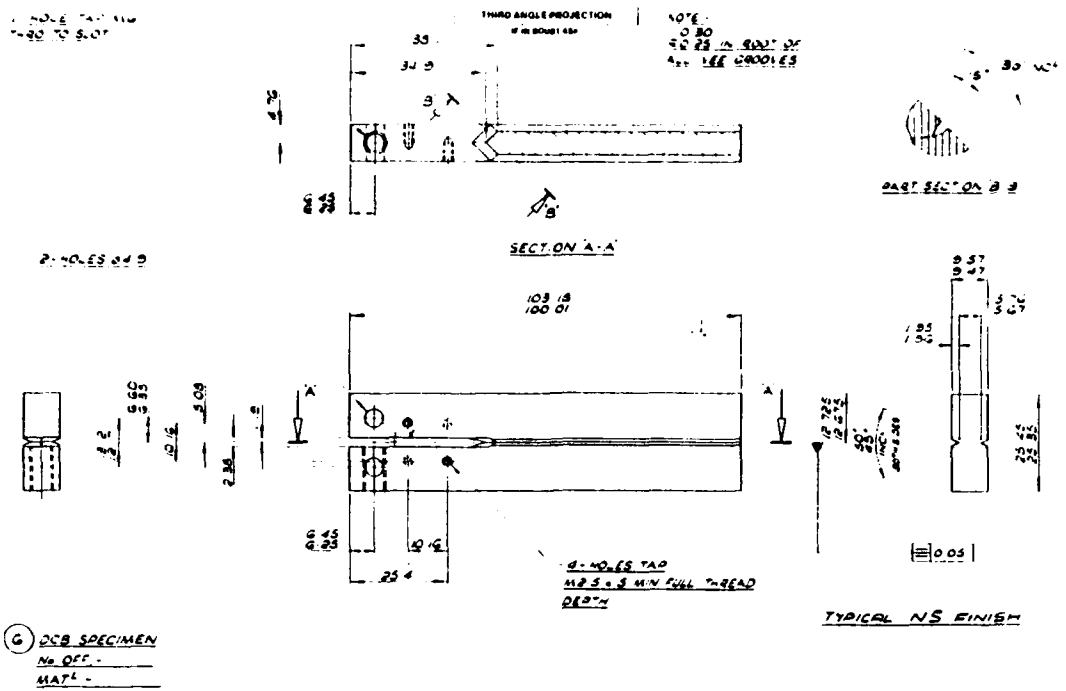
Figure 1.   DCB specimen geometry
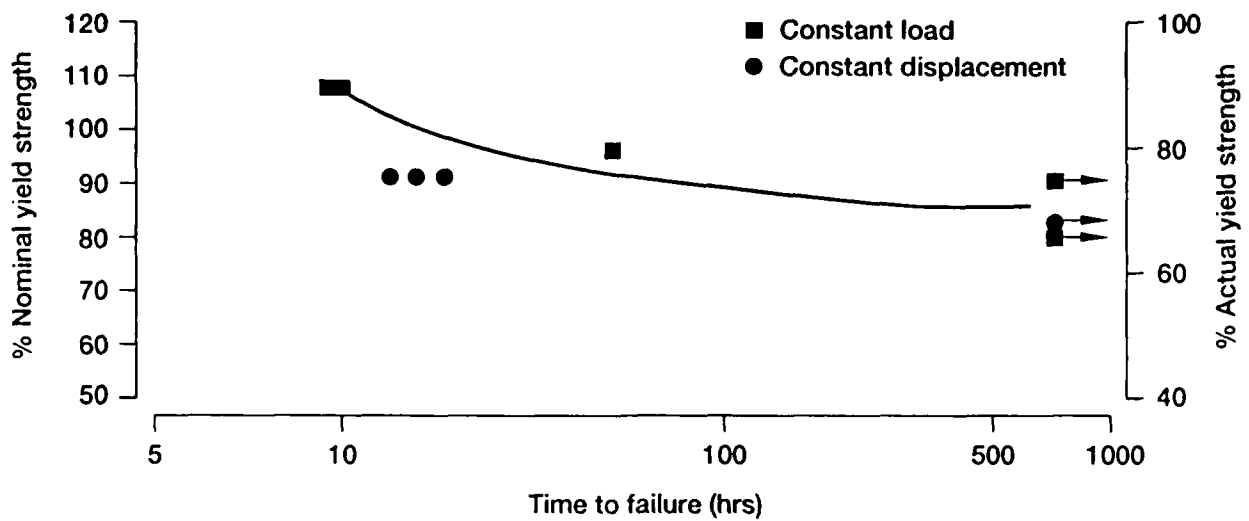
Figure 2.   Time to failure of grade L80 steel in NACE standard solution
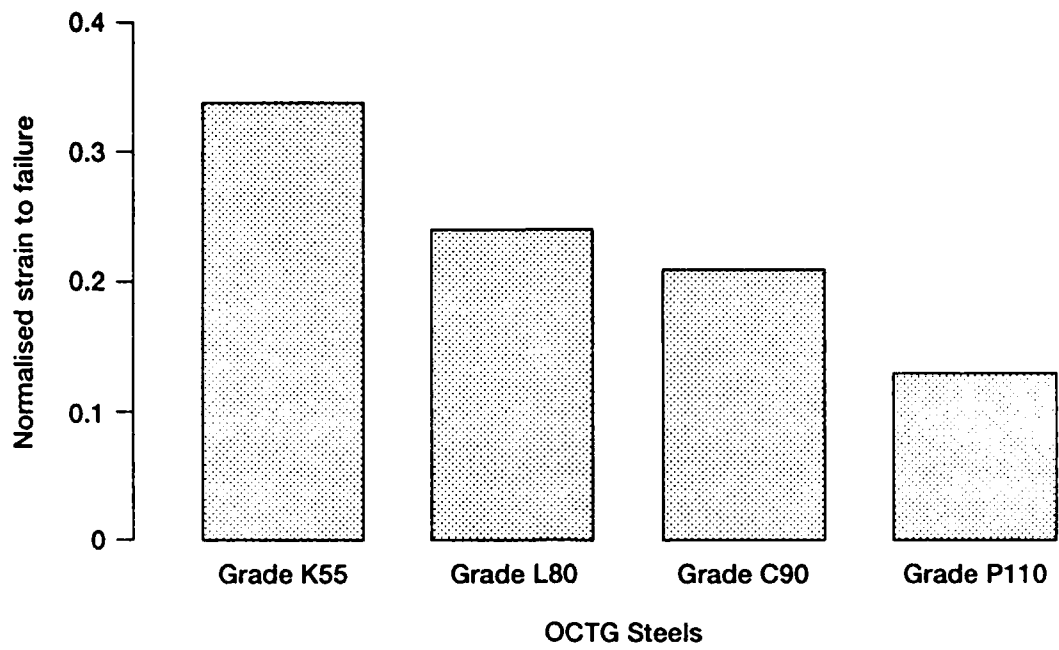
Figure 3.   A comparison of SSC performance of OCTG steels in standard NACE solution
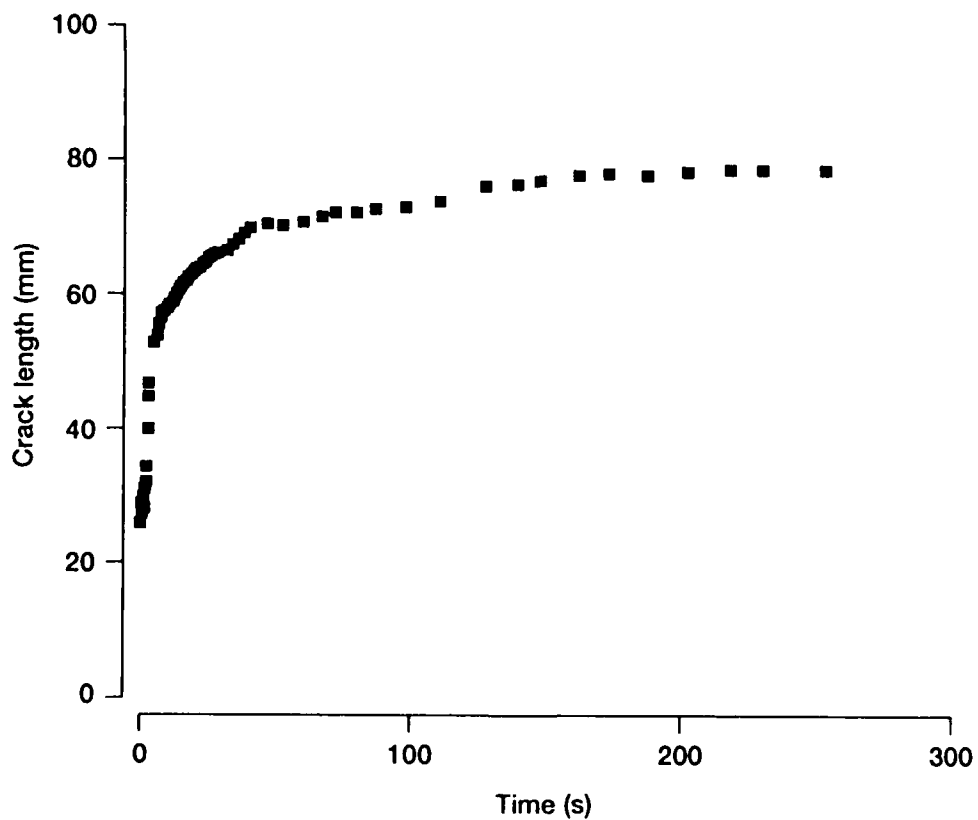
Figure 4.   Crack length vs. time representation of grade P110 specimen in the NACE solution saturated with a gas containing 10% H_2S.
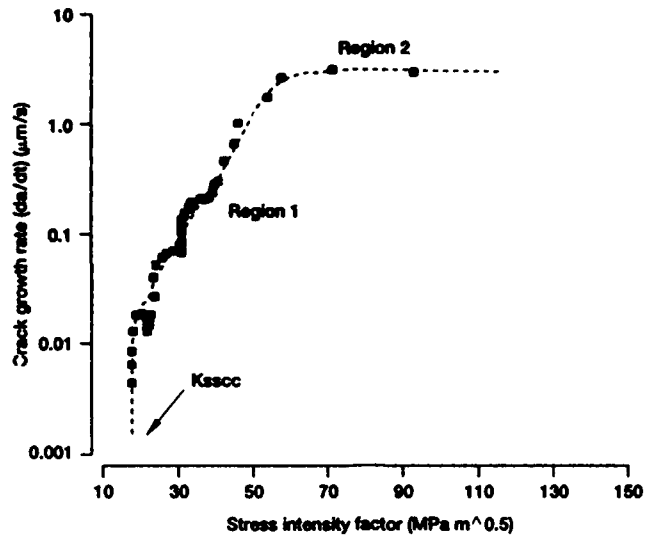
Figure 5. Crack growth rate as a function of stress intensity factor of grade P110 specimen in the NACE solution saturated with a gas containing 10% H_2S.
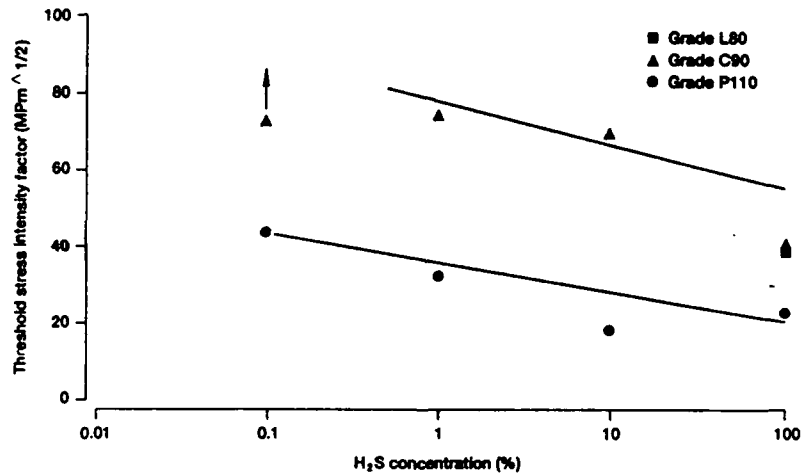
Figure 6. The effect of H_2S concentration on the threshold stress intensity factor.
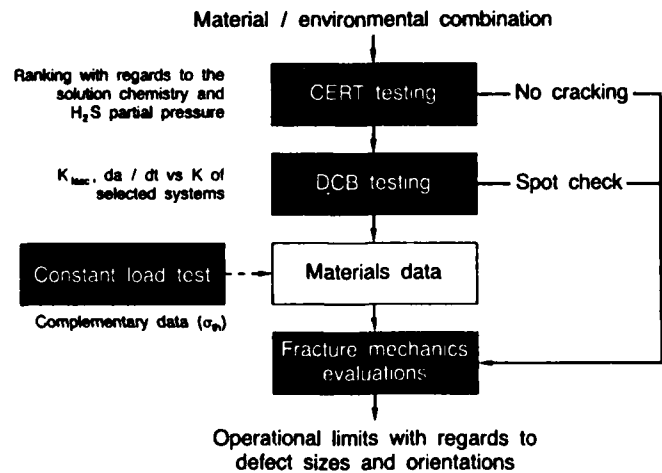
Figure 7. Materials performance assessment chart.

Sulfide Scales for the Protection of Steels in H$_2$S-Containing Atmospheres

M. Schulte
Karl-Winnacker-Institut der DECHEMA e.V.
Theodor-Hcuss-Allee 25
6000 Frankfurt/Main 15, Germany

M. Schütze
Karl-Winnacker-Institut der DECHEMA e.V.
Theodor-Heuss-Allee 25
6000 Frankfurt/Main 15, Germany

Abstract

In several high temperature processes in chemical and petrochemical industry conditions are encountered in which lifetime of the components is determined by H$_2$S-corrosion in atmospheres of sulfidizing nature.
The damage cases observed are not only a consequence of the relatively rapid growth of the sulfide scales but are also due to cracking and spallation resulting from scale growth stresses and temperature changes.
An exclusive materials solution to prevent metal wastage often was unsatisfactory considering costs and results. Another approach can be based on avoiding conditions for scale failure due to stresses which originate during scale growth. In this case even sulfide scales can play a quasi-protective role. Therefore the work to be reported in the paper aims at a quantitative approach to assess the conditions leading to sulfide scale failure taking component geometry into account.

A carbon steel, a low chromium steel (1Cr-0.5Mo-steel, T12), a ferritic chromium steel (12Cr-1Mo-steel) and an austenitic steel (18Cr-9Ni-steel, AISI 321) were investigated concerning scale growth and failure in Ar/H$_2$/H$_2$S in a temperature range of 400-600°C with subsequent cooling down to room temperature. Acoustic emission measurements accompanied the experiments in order to detect cracking and spallation of the sulfide scales. First results of this study are presented.

Key terms: Sulfidation, steels, scale stresses, acoustic emission

Introduction

The rate of metal loss caused by a high temperature corrosion process is decreased if the chemical reaction between the metal and the gaseous species is retarded by its own corrosion products. On the premises of non-volatile reaction products they can form a compact layer on the metal surface preventing it from a direct access of the gaseous phase. Thus, material transport for continuing the reaction is realized by diffusion through a solid phase which - in a common temperature range - is much slower than a gasphase transport. This protective mechanism is maintained as long as the scales are intact. Cracking or even spallation of the scales result in the loss of any protective effect and a regain of protection during operating conditions is only possible by subsequent scale formation.
In technical processes exposing plant equipment to high temperature gaseous environments with high sulfur activity and low oxygen partial pressure, e.g. in coal gasification, in the distillation of tar and in waste pyrolysis H$_2$S-corrosion becomes the major life-limiting factor.

Sulfide scales are formed on the surface of e.g. heat exchangers operating in a temperature range of 300 - 600°C. Although the transport properties of metal sulfides are not as beneficial as they are known from metal oxides the sulfide scales can be considered to be quasi-protective in the way described above if they are mechanically intact.

Damage on the steel components is predominantly observed at "hot spots", zones of high temperature gradients and on bends of tubes, sites where high stresses are expected in the scales.
Cracking and spallation of sulfide scales is caused by growth stresses (isothermal conditions) and stresses resulting from differences in the thermal expansion coefficients of the metal substrate and the scale (temperature change conditions). Aim of the study to be reported was to elucidate the scale growth and failure mechanisms. The first step is the characterization of the sulfides formed on the metal surface. The conditions leading to damage can be characterized by critical stresses or strains, in the case of thermocyclic service by critical temperature changes.

Experimental

The commercial steels investigated were a carbon steel, a low chromium steel (1Cr-0.5Mo, German mat. no. 1.7335, American designation T12), a ferritic chromium steel (12Cr-1Mo, German mat. no. 1.4922) and an austenitic steel (18Cr-9Ni, German mat. no. 1.4541, American designation AISI 321). Their actual composition is given in table 1.

Table 1:

Steel	C	Si	Mn	Cr [Wt.-%]	Mo	Ni	Ti	V
Carbon	≤ 0.17	Traces	0.2-0.5	-	-	-	-	-
1Cr-0.5Mo	0.17	0.22	0.6	0.88	0.46	-	-	-
12Cr-1Mo	0.20	0.20	0.46	11.6	0.89	0.45	-	0.25
18Cr-9Ni	0.058	0.38	1.75	17.17	-	10.75	0.35	-

Samples were machined from seamless heat exchanger tubes ($\varnothing$ 38x4mm or $\varnothing$ 38x5mm) in the form of tube segments (L:20mm, W:14mm). To investigate a possible influence of different surface treatments before sulfidation specimens of the carbon steel were tested as received (oxidized in production process), with a ground surface, and additionally pickled. Samples of the low chromium steel were either formed on a lathe or ground. The 12Cr-1Mo-steel was sandblasted and pickled, AISI 321 was investigated without additional surface treatment. All specimens were cleaned and dried with alcohol.

The experiments were carried out at temperatures of 400, 500 and 600°C by means of electric furnaces heating the specimens either in a horizontal silica tube or in a vertical silica tube adapting the specimen to an acoustic emission transducer by a platinum wire.
The required gas composition (1 Vol.% H_2S in Ar/H_2) was obtained by mixing an Ar/5%H_2 gas mixture with H_2S. The equilibrium sulfur pressures were: 5×10^{-11} bar at 400°C, 3×10^{-9} bar at 500°C and 8×10^{-8} bar at 600°C.

Experiments under isothermal conditions for 50-700 hours were carried out to investigate scale growth, scale morphology and -composition and appearance of surface damage on the various steels by means of weight-gain measurements, optical and scanning electron microscopy and electron probe microanalysis (EPMA). Additionally Pt-Marker experiments were performed to elucidate scale growth mechanisms concerning the direction of material transport. Furthermore samples were monitored during isothermal annealing and subsequent cooling by means of the acoustic emission technique in order to detect cracking and spallation of the sulfide scales.

Results

Scales formed on the surface of the commercial steels were always duplex and consisted of an outer layer of large columnar crystals grown perpendicularly to the metal surface and an inner fine-grained equiaxed layer. The latter were rather porous and inhomogenious on the carbon and the low chromium steel. On contrast the 12Cr-1Mo and the Cr-Ni-steel formed relatively compact inner scales. Pt-Marker experiments showed that the outer layer grows in outward direction whereas the inner layer grows in inward direction starting from the former metal surface.

The outer scales consist of pure $Fe_{1-x}S$ in all cases (with a partial enrichment of Ni in the case of AISI 321). With the exception of the carbon steel the inner regions contained chromium in various concentrations depending upon the metal composition. EPMA-investigations identified the spinell $FeCr_2S_4$ within the inner scale of the Cr-Ni-steel whereas the 12Cr-1Mo steel contained a mixture of sulfides ((Fe,Cr)S).

The kinetic of scale growth derived from discontinuous weight change measurements shows an approximately constant rate at 400°C and 500°C for the carbon and the low chromium steel (linear kinetics). This type of behaviour confirms previous results [1,2]. Concerning the kinetics no significant influence of surface treatment before sulfidation could be observed. The 12Cr-1Mo steel also sulfidizes at constant rate but at a lower level whereas AISI 321 shows a parabolic behaviour at 400°C and 500°C. Investigations of ferritic chromium steels with similar chromium contents and austenitic steels with similar chromium and nickel contents are in agreement with these observations [3].

The FeS scales formed on all steels tended to detach and frequently spalled after removal of the specimens from the furnace at the end of the experiments. An influence of surface treatment before sulfidation was observed in so far that pickled specimens showed an improved scale adherence due to their enhanced surface roughness. The inner scales adhered to the metal substrate in all cases. On the carbon and the low chromium steel through scale cracking was observed (See fig. 1).

On monitoring specimens by the acoustic emission equipment it was intended to find out whether scale failure occurs during isothermal annealing or during temperature change conditions. The rate of acoustic emission signals was highest in the case of temperature change conditions and showed a remarkable increase when the temperature fell below approximately 330°C.
However acoustic emission could also be detected during scale growth. As an example fig. 2 shows the development of counts (cumulative counts of impulses exceeding a threshold of 1V) during isothermal annealing of a 12Cr-1Mo steel specimen at 500°C in the H_2S-containing atmosphere for 300 hours and subsequent cooling. The average cooling rate was 1°C/minute. The results indicate that a significant damage occurs already during scale growth.

Optical and scanning electron microscopic investigations confirm this observation. Fig. 3 manifests a completely new FeS scale growing beneath the detached outer scale. The different FeS layers with deviant grain sizes are additionally depicted in fig. 4 A, B. The detached outer scale also shows cracks predominantly at the grain boundaries.

Discussion

The formation of duplex scales on carbon steels and Cr-containing steels is in agreement with previous observations [2,3]. The outer scale is formed through the outward diffusion of metal ions while the inner layer grows by means of inward penetration of sulfur [4].

The mechanism of scale growth and the specimen geometry can have a large effect on stress generation [5,6]. Especially for the formation of relatively thick scales (as observed in the case of sulfidation) geometrical aspects of scale growth become evident [7]. For the convex and concave surfaces of the heat exchanger tube segments investigated different stresses result from scale growth (due to volume changes caused by the transformation of the substrate material into metal sulfide). The outer FeS scale growing in outward direction is submitted to compressive stresses at the outside of a tube segment but suffers tensile stresses at the tube inside.

This can lead to the following failure situations:

1. Through scale cracking at the inside of the tube segment.
2. Detachment of the FeS scales in both cases because stresses parallel to the interface lead to tensile stresses perpendicular to the interface.

A quantification of the strains resulting from scale growth on curved surfaces can be carried out by means of a scale displacement vector M [5]:

$$M = \Theta \cdot (1 - a) - (1 - V) \tag{1}$$

where
Θ = Pilling-Bedworth-ratio
a = amount of sulfide formed at the scale surface
V = gain of volume due to vacancy injection into the metal

In general for a surface scale two types of stresses can arise: Tangential stresses parallel to the material surface and radial stresses at the scale/metal interface perpendicular to it.
The tangential strain is calculated from [7]

$$\varepsilon_t = \frac{M}{R \cdot \Theta} \cdot d \tag{2}$$

where
R = radius of the surface curvature
d = mean scale thickness

The radial strain can be estimated from [7]:

$$\varepsilon_r \cong \frac{d}{R} \cdot \varepsilon_t \tag{3}$$

The resulting tangential and radial stresses or strains, respectively can be compared to critical values for tensile or compressive scale failure as performed in the following.

A simplified criterion for scale failure in the form of detachment is the surface energy which is necessary to produce the two new surfaces.

The critical strain is calculated from equation (4), which was developed based on considerations in [8].

$$-\varepsilon_c \quad \sqrt{\frac{2 \cdot \gamma_0}{E_s \cdot d}} \tag{4}$$

where $2 \cdot \gamma_0$ = energy to create two new surfaces (i.e. detachment)

           E_s = elastic modulus of the sulfide

Equation (4) neglects the size of possible defects in the plane of detachment and the geometry of the interfaces. Furthermore it is assumed that all energy stored in the scale is released by detachment. However this is not very realistical because a part of the energy remains as elastically stored energy in deformed parts of the scale.

A different approach regards that in brittle scales - as it should be justified in the case of sulfide scales at relatively low temperatures - failure always starts at stress concentrations, i.e. at physical defects. Fig. 5 schematically illustrates the different types of scale failure conceivable in this approach.

Assuming linear elastic behaviour the critical strain for failure under tensile stresses either tangential or radial (comp. fig.5 A=tangential, i.e. through scale cracking, D=radial, i.e. detachment at the interface) is defined by equation (5) [9]:

$$\varepsilon_c \quad \frac{K_{IC}}{f \cdot E_s \cdot \sqrt{\pi \cdot c}} \tag{5}$$

where K_{IC} = fracture toughness of the sulfide

           c = size of the physical defect (here: halflength of an embedded defect)

           f = factor to regard local geometrical aspects (usually $\geq$ 1)

If a scale with a wavy interface is submitted to a global tangential stress also stresses normal to the interface are produced [10] as shown in fig.5 B_1, B_2 Derived from model calculations in [10] the resulting maximum values of strain normal to the interface are [7]

$$\varepsilon_r^{max} \quad \Delta\varepsilon \cdot \frac{2}{\left(1 + \frac{r}{d}\right) \cdot (1 + \nu_s)} \tag{6}$$

where $\Delta\varepsilon$ = tangential strain

r/2 = Amplitude of the wavy interface (comp. fig 5)

v_s = Poisson ratio of the scale

As a conservative approach it is assumed that physical defects of the size 2c lie at the sites of maximum interfacial strains.

Combining eq. (5) and (6) leads to a quantification of the critical tangential strain for detachment of the scale (see eq. (7)).

$$|\varepsilon_c| = \frac{K_{lc}}{f \cdot \sqrt{\pi \cdot c}} \cdot \frac{\left(1 + \frac{r}{d}\right) \cdot (1 + v_s)}{2 \cdot E_s} \tag{7}$$

The condition for shear failure under compressive stresses (comp. fig.5 C) is a modification of eq. (5) under the assumption $K_{IC} \le K_{IIC}, K_{IIIC}$ [11]:

$$-\varepsilon_c = \frac{2 \cdot K_{lc}}{f \cdot E_s \cdot \sqrt{\pi \cdot c}} \tag{8}$$

For the present case, strains were calculated for all situations given in fig. 5. The maximum strains due to FeS scale growth are tangential and tensile and occur at the inside of a tube wall (lowest radius Ri=14mm, comp. eq. (2)). Fig. 6 depicts these growth strains (straight line) and the different critical values from the calculations as a function of scale thickness.

Radial growth strains are orders of magnitude lower and therefore uncritical. They are left out of the further considerations. The fracture toughness of the sulfide was calculated from equation (9) [12]

$$K_{lc} = \sqrt{2 \cdot E_s \cdot \gamma_s} \tag{9}$$

Data for γ_0, E_s and v_s were taken from [13]

From fig. 6 it becomes evident that

- thicker scales are more susceptible to failure than thin scales
- critical strains for scale failure increase with increasing interface amplitudes
- the size of physical defects within a scale significantly determines the value of the critical strains

Thus, from a plot as shown in fig. 6 a critical scale thickness d_c for failure due to growth stresses (without regard to intrinsic growth stresses being independent of the surface geometry) can be estimated by setting $\varepsilon_t = \varepsilon_c$.

The surface energy criterion leads to a conservative value for d_c for detachment on the premises of small physical defects (comp. fig 6 A)

However regarding physical defects of e.g. 5μm or more the critical strains according to eq. (7) are exceeded at comparable or even smaller FeS scale thickness values.
Failure in the form of through scale cracking by tangential tensile stresses due to scale growth (= interception with horizontal lines in fig. 6) should not occcur below d = 50μm except for c ≥ 10μm.

Experimental results obtained from optical micrographs so far confirm the tendency of FeS scales to detach already during isothermal conditions due to growth stresses. To remind of the example given in fig. 3 the detached layer is about 32±3μm thick which is in the range of values calculated. Experimental data for the size of physical defects range from 1 to 20μm and thus correspond to the values for c in the model calculations. The quantitative analysis of experimental results has to be considered with caution at the present time because materials data (such as K_{IC} values) are calculated on the basis of pure substances (e.g. FeS). Values for ((Fe,Cr)S, $FeCr_2S_4$) are unknown.
A distinction has to be made between scale damage due to growth stresses and scale failure as a consequence of thermal induced stresses during cooling at the end of the experiments.

At the present time no reliable data concerning the thermal expansion coefficient of FeS (or other metal sulfides) α_s as a function of temperature is available. As a consequence of phase transformations of FeS at 135°C and 325°C [14] the dependence of α_{FeS} on temperature is expected to be non-linear. It is, however, intended also to quantify the strains arising from cooling within this work.
The event causing strong acoustic emission observed at approximately 330°C can be correlated to the transformation of FeS at 325°C [15].

Conclusions

The formation of iron-sulfide scales on bent surfaces of steels (e.g. carbon steel, low Cr, 12-Cr and 18Cr-9Ni steel) such as on heat exchanger tubes generates growth stresses that can lead to scale failure. This is shown by acoustic emission results and by the formation of new thin FeS scales beneath outer detached thick FeS scales.
The extent of scale deformation on cylindrical components increases with decreasing radius.
The susceptibility to damage rises with scale thickness and is decisively determined by the size of physical defects. Critical tangential strains for detachment processes increase with increasing interface amplitudes.

In model calculations it is possible to assess a critical time t_c, at which during isothermal exposure geometrically induced strains by scale growth lead to mechanical scale failure. This time t_c is synonymous with a critical scale thickness d_c (provided the physical defect size 2c remains constant) and depends largely on the surface curvature. The results of the present experiments show that the calculations yield the correct order of magnitude.

Thus a first step for a quantitative assessment of the stress situation in the sulfide scales relevant for failure could be achieved. Using the model equations for component design allows the assessment of the role of surface curvature for maintaining intact sulfide scales over larger periods, thus providing a quasi-protective behaviour of the scales which should decrease metal wastage by sulfidation.

References

1. W.Grosser, D. Meder, W.Auer, H. Kaesche: <u>Werkstoffe u. Korrosion</u>, 43, 145-153 (1992)

2. F. Gesmundo, W. Znamirowski, F. Viani, F. Bregani: <u>Inter. Symph. High Temp. Corr. Prot.</u>, 1990, Shenyang, China (1990)

3. W. Grosser: <u>PhD-Thesis</u>, Erlangen, Germany (1980)

4. S. Mwrovec, K. Przybylski: <u>High Temp. Mat. and Proc.</u>, 6, No. 1 u. 2 (1984)

5. M.I. Manning: <u>Corr. Sci.</u>, 21, 301-316 (1981)

6. P. Hancock, R. C. Hurst: <u>Adv. in Corosion Science and Technology</u>, Plenum Press, New York (1974)

7. M. Schütze: <u>Proc. of the Workshop on High Temp. Corr. of Advanced Materials and Protective Coatings</u>, Tokyo, Japan (1990), p. 43

8. H.E. Evans, R.C. Lobb: <u>Proc. EUROCORR '87</u>, DECHEMA, Frankfurt (1987), p. 135

9. M. Schütze: Die Korrosionsschutzwirkung oxidischer Deckschichten unter thermisch-chemisch-mechanischer Werkstoffbeanspruchung, Materialkundl.-Technische Reihe, Vol. 10 (eds. G. Petzow and F. Jeglitsch), Gebr. Borntraeger Verlag, Berlin-Stuttgart (1991)

10. A.G. Evans, G.B. Crumley, R.E. Demaray: <u>Ox. of metals</u>, 20, 193-216 (1983)

11. M. Schütze: <u>Corrosion Science</u>, (in press)

12. M. Schütze: <u>Int. J. Pres. Ves. & Piping</u>, 45, 1-23 (1991)

13. J. Robertson, M.I. Manning: <u>Mat. Science and Technology</u>, 6, 81-86 (1990)

14. E. Becker: <u>Stahl u. Eisen</u>, 32, 1018 (1912)

15. H. J. Grabke, Lin Gang, S. Wegge: <u>Proc. 11 th International Corrosion Congress</u>, Florence (1990), AIM, Florence (1990)
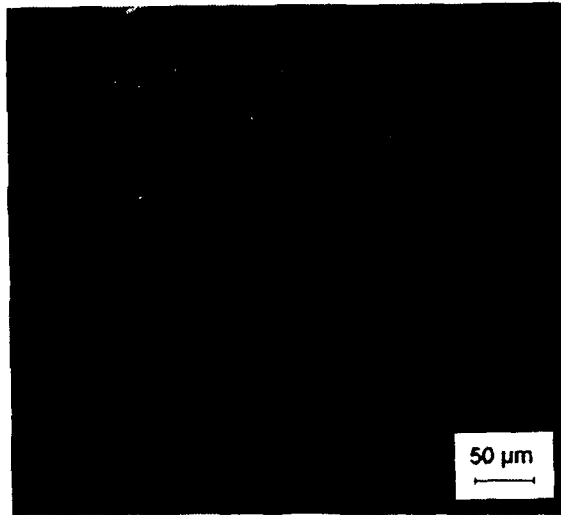
Fig. 1: SEM micrograph of the inner scale formed on the low chromium steel (400°C, 100hrs)
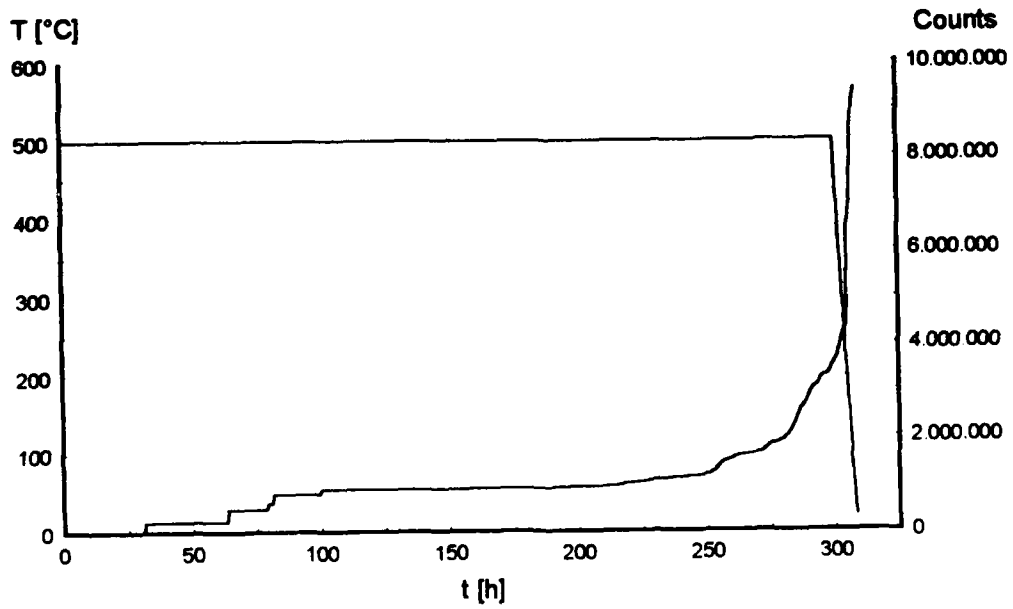
Fig 2: Acoustic emission of the 12Cr-1Mo steel during sulfidation at 500°C and subsequent cooling

Fig 3   Optical micrograph of the 12Cr-1Mo steel after 300 hrs sulfidation at 500 °C

A   B
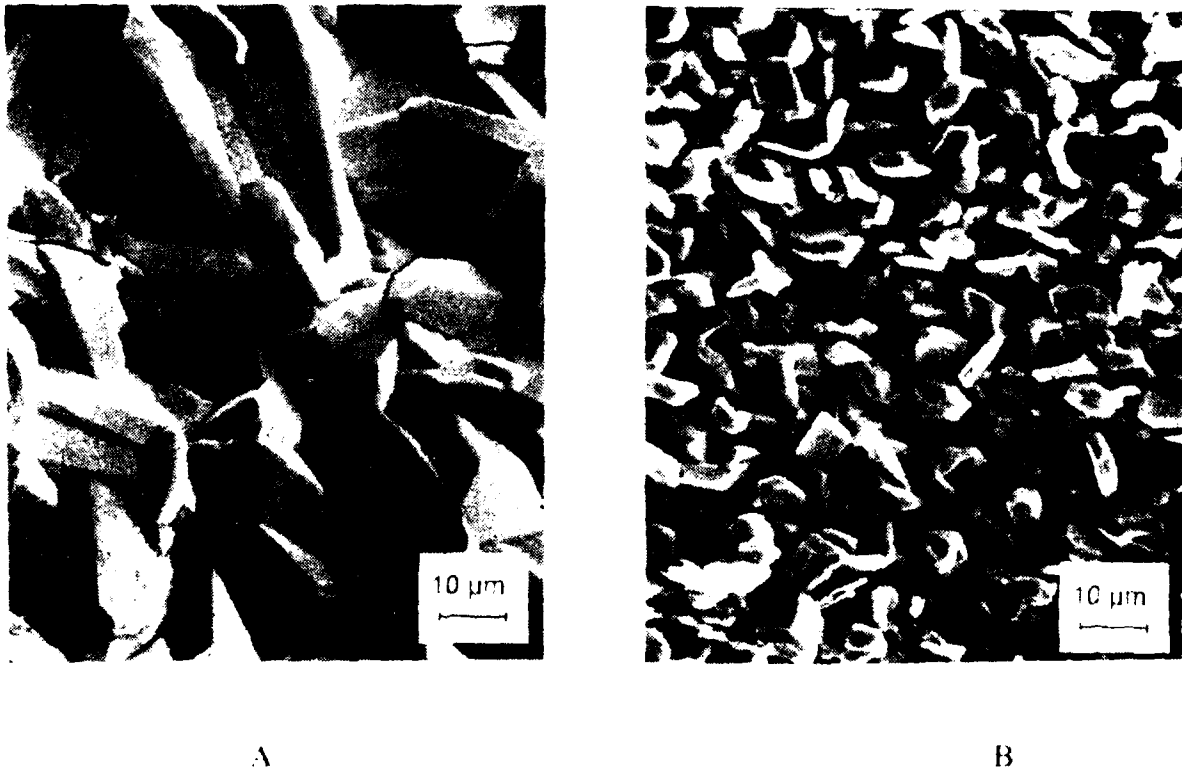
Fig 4   SEM micrograph of the 12Cr-1Mo steel (300 hrs 500 °C)
         A Outer FeS scale
         B FeS scale formed beneath the outer scale
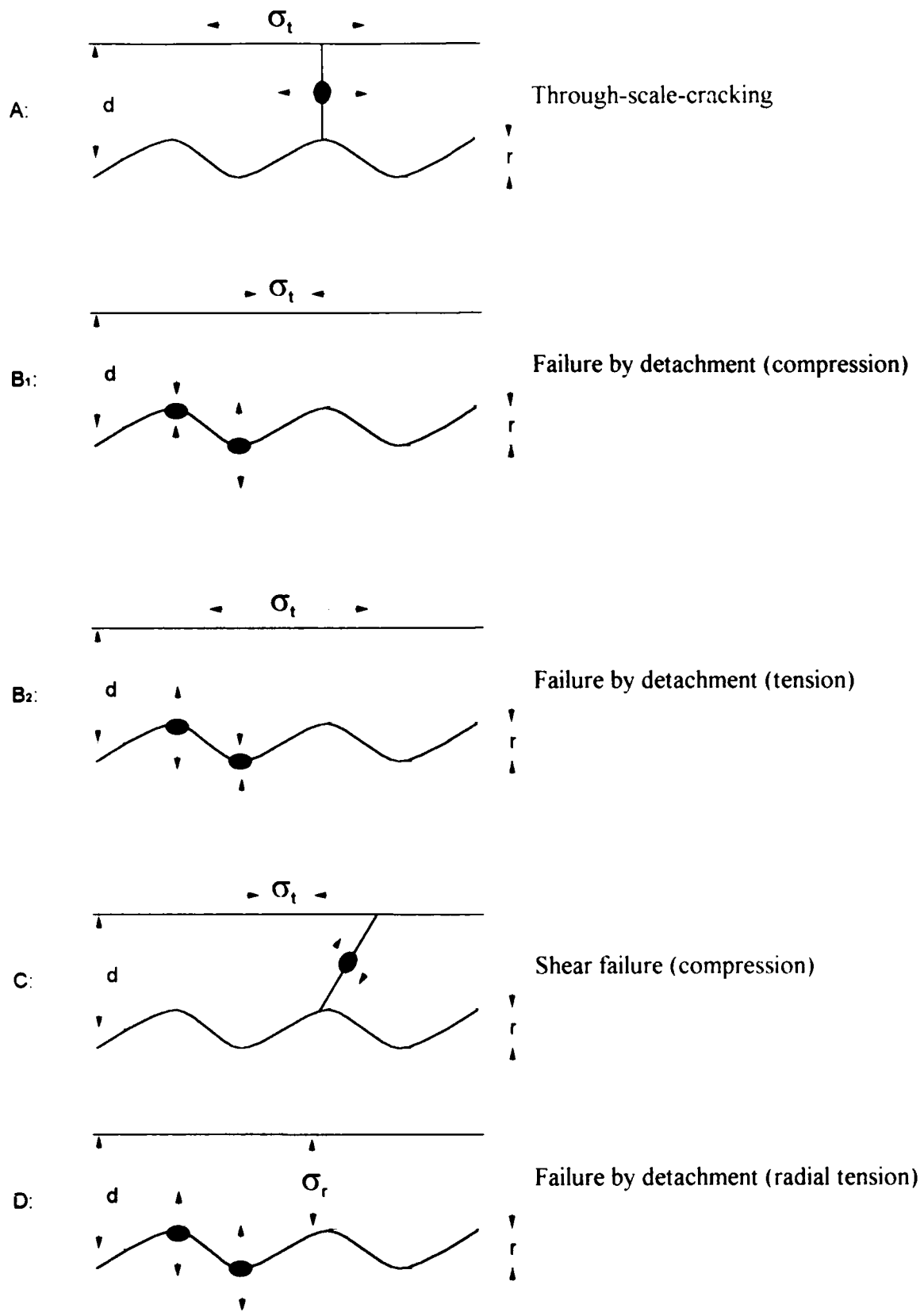
Fig 5   Local stresses at physical defects under global tensile and compressive scale
deformation and parameters describing scale geometry
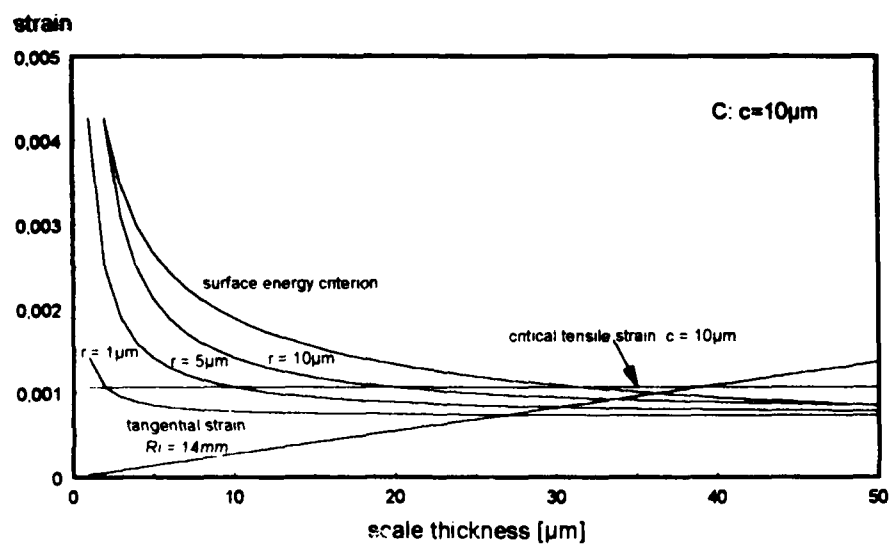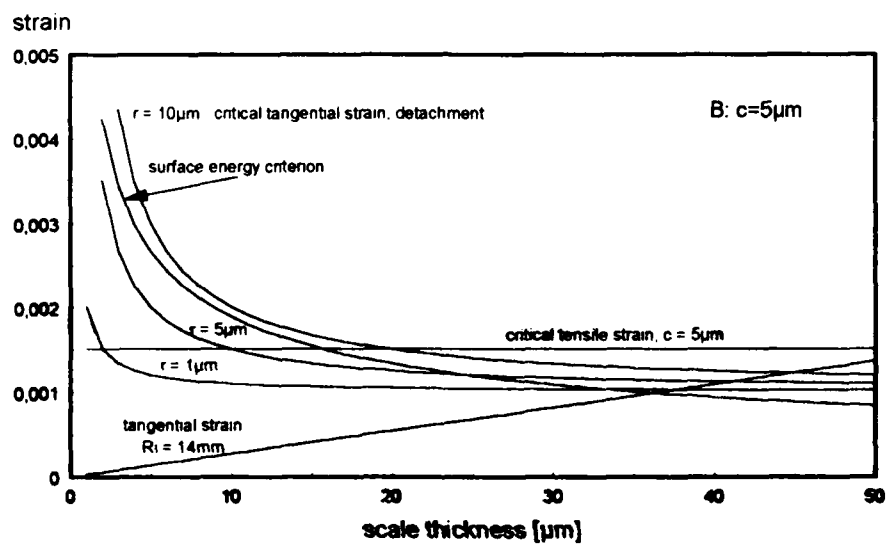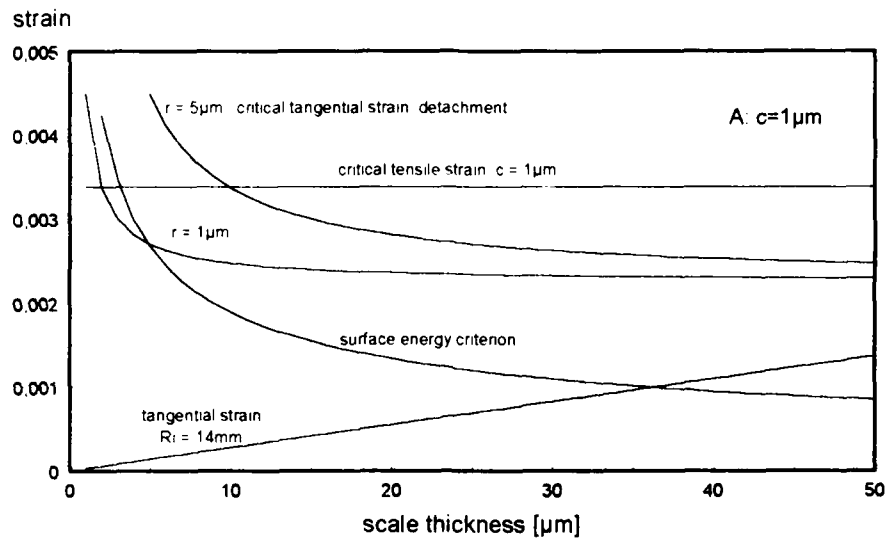
Fig. 6 Tangential strains developed by scale growth (straight line) at the inner site of a tube wall (R_i=14mm) and critical strains as a function of scale thickness

Wall Shear Stress and Flow Accelerated Corrosion of Carbon Steel in Sweet Production

K. D. Efird, E. J. Wright, J. A. Boros and T. G. Hailey
Exxon Production Research Company
Houston, Texas , U.S.A.

Abstract

An investigation of flow accelerated corrosion of carbon steel was conducted employing carefully designed jet impingement and pipe flow hydrodynamic test apparatus. The corrosion rates measured for jet impingement and pipe flow directly correlate on an equivalent wall shear stress basis, and scale up to 4 inch pipe flow corrosion was experimentally verified. This successful scale up allows application of flow accelerated corrosion results from the jet impingement test to field systems based on the concept of equivalent wall shear stress, and will allow more rapid development of flow accelerated corrosion data than is possible using the flow loop.

The general equation for flow accelerated corrosion of carbon steel based on the interrelationship of hydrodynamic parameters, solution chemistry and environmental variables for single phase, sweet, aqueous systems for wall shear stress in the range $0.2 < \tau_w < 100$ N/m^2 is expressed as:

$$R_{cor} = a \, \tau_w^b$$

where "R_{cor}" is the carbon steel corrosion rate in mm/y, and "τ_w" is the wall shear stress in N/m^2. Based on the results to date, the coefficient "a" and exponent "b" in the basic equation are functions of solution chemistry (pH, Fe^{++}, O$_2$, P$_{CO2}$, etc.) and other environmental parameters (total pressure and temperature). All the necessary hydrodynamic variables (ρ, μ, e, etc.) are accounted for in the wall shear stress term. The equation effectively combines the hydrodynamic, solution chemistry and environmental variables for flow accelerated corrosion of steel without the need for correction factors. Further experimental determination of the effect of important solution parameters and environmental factors on the equation coefficient and exponent will provide a complete definition of flow accelerated carbon steel corrosion in sweet systems. A minimum wall shear stress of 0.2 N/m^2 is applied, based on the wall shear stress for the test solution at a pipe flow Reynold's number of 2000, the approximate lower limit for turbulent flow in pipes. The use of wall shear stress as the correlating factor does not imply a shear mechanism for corrosion acceleration. The wall shear stress is simply a hydrodynamic factor that can be effectively used to relate fluid flow in different geometries, allowing accurate comparison of laboratory tests and field operations.

The basic test fluid employed was 3.0% NaCl + 1000 ppm HCO$_3^-$ aqueous solution at 50°C. Carbon dioxide partial pressures of 0.14, 1.4, and 4.1 bar (2, 20 and 60 psig) were utilized, with a measured solution pH of 6.8, 6.0 and 5.8 respectively. Pipe diameters of 12.7, 25.4 and 90 mm were included. The flow accelerated corrosion of steel was strongly affected by the Fe^{++} concentration in solution. Below an Fe^{++} concentration of approximately 8 ppm no measurable effect on steel flow accelerated corrosion was observed. Therefore, a limit of 5 ppm dissolved Fe^{++} in the test solution is recommended for credible flow accelerated corrosion experiments in this environment.

Introduction

Fluid velocity was long used as the primary parameter for scale up of laboratory test results to field applications, but this concept began changing in the 1970's. Data relating the calculated hydrodynamic parameter of wall shear stress to corrosion were first published by Efird in 1977 [1] for copper alloys in flowing seawater. Corrosion science now understands that fluid flow must be expressed in terms broadly related to fluid flow parameters common to all hydrodynamic systems to allow application of laboratory test data to field operations [1-4]. These parameters are calculated from empirical equations developed to characterize fluid flow. The parameters most often employed are wall shear stress (τ_w) and mass transfer coefficient (k).

The basic procedure used to relate laboratory fluid flow corrosion data to field applications is diagrammed in Figure 1. Laboratory corrosion tests are conducted in a manner that allows calculation of the basic hydrodynamic parameters that are geometry independent, e.g., wall shear stress. The laboratory corrosion rates are then applied to the field application for identical calculated wall shear stress. The basic assumptions are that the calculation of the parameters is valid, the calculated parameters are those controlling corrosion or are intimately related to them, and the scale up of these parameters to field operations with respect to corrosion is valid. Note that both wall shear stress and mass transfer coefficient meet these basic criteris. Wall shear stress is utilized here because it is more amenable for application to oil field production operations.

Experimental test design and techniques carefully designed to allow accurate calculation of the hydrodynamic parameters are used in this study of flow accelerated corrosion of carbon steel in single phase (aqueous), sweet environments. The test methods employed are parallel pipe flow (12.7, 25.4 and 90 mm inside diameter) and jet impingement. The details of the techniques and design are given in a previous publication [5].

A clear distinction must be made between flow accelerated corrosion and erosion-corrosion. They are not the same, but are often confused in the literature. Flow accelerated corrosion is defined here as increased corrosion from increasing turbulence intensity and mass transfer as a result of the flow of a fluid over a surface. Erosion-corrosion is defined as increased corrosion due to the impingement of second phase particles contained in the fluid, e.g., solid particles in a liquid, liquid droplets in a gas or solid particles in a gas, on a solid surface as a result of the flow of fluid over the surface. This paper addresses flow accelerated corrosion only, and erosion-corrosion is not considered.

The Turbulent Boundary Layer

When a fluid flows over a solid surface, the flow is characterized as either laminar or turbulent. In virtually all oil and gas situations where fluid flow is of interest the flow is turbulent, so the physical structure of turbulent flow is a primary consideration. Fully developed turbulent flow consists of a turbulent core where the mean velocity is essentially constant, and a boundary layer near the solid/fluid interface. The majority of the changes in fluid stress characteristics, turbulence, mass transfer and fluid interaction with the wall occur within this boundary layer. Because of the specialized nature of this subject, a number of possibly unfamiliar terms will be introduced. These terms are defined in the attached Glossary and Table of Nomenclature.

The turbulent boundary layer consists of three regions: an outer "logarithmic" region (30<y+<100), an intermediate "buffer" region (5<y+<30), and, very close to the solid wall, a "viscous" region (y+<5), where y+ is the dimensionless viscous length perpendicular to the wall, defined [6] as $y+ = yu_\tau/v$. A diagram of these layers along with an idealized plot of the normalized turbulent velocity variation is shown in Figure 2 [6]. Experimental details of the variation in turbulence with distance from the wall are given by Kline et. al.[7] in their extensive study into the structure of the turbulent boundary layer.

The nature of the turbulent boundary layer dictates that this is where the processes that control corrosion and film formation will occur. All movement of corroding species to and of corrosion products from the wall, and all chemical reactions with the wall, must occur in this region. As a result, any disturbance in the turbulent boundary layer, particularly within the viscous region, must be a primary factor affecting the corrosion process.

Disruption of the boundary layer in turbulent flow occurs primarily by the formation of turbulent bursts and sweeps. The turbulent burst is an ejection of fluid from the wall, which also causes fluid to impinge on the wall by the simultaneous formation of sweeps, or movement of fluid toward the wall. Turbulent bursts and sweeps occur through the formation of vortices and the lift-up of wall streaks [8].

One process of vortex formation and evolution into a turbulent burst proposed by Praturi and Brodkey [9] is illustrated in Figure 3. The vortex moves with the flow and is increasingly tilted by the mean shear in the viscous region (Stages 1 to 4). At some point the vortex becomes unstable and a strong ejection occurs along with a rapid sweep of fluid into the viscous region (Stage 5). It is evident that severe pressure fluctuations must occur with the formation of a turbulent burst and during the rapid ejection of fluid.

A slightly different model of the bursting process is given by Offen and Kline [10], where a description of the complete burst cycle is given. In this model, bursting is associated with wall streaks and stretched and lifted vortices. All of the current theories of wall turbulence agree in the basic structure of the turbulence, i.e., the existence and interaction of turbulent bursts, ejections, sweeps and wall streaks. The differences lie in the mechanisms of formation of these structures and the details of their interaction.

An excellent review of the present understanding of the turbulent boundary layer structure is given by Robinson [11]. As a result of this exhaustive review, Robinson concluded that coherent motions exist in the viscous region, that they consist of elongated, unsteady regions of high and low speed streaks, and that sweep motions dominate the viscous region. The majority of the coherent flow structures occur in the buffer region of the turbulent boundary layer, with only sweeps and ejections penetrating into the viscous layer [11]. Laser Doppler measurements have clearly shown the presence of turbulence in the viscous region as shown in Figure 4 [6].

The relationship of turbulent structures in the boundary layer, specifically near wall bursting activity, and fluctuations in the wall shear stress and wall pressure have been measured by Thomas and Bull [12]. A side view diagram of their results is given in Figure 5. This work provides evidence of significant variations in wall shear stress related to the boundary layer turbulence generation process that could have a major effect on corrosion processes.

Wall Shear Stress Defined

There is a great deal of misunderstanding about precisely what is signified by the term "wall shear stress." Wall shear stress is often perceived as a force acting to remove corrosion product films from the surface of a metal. This perception is incorrect. Wall shear stress is a direct measure of the viscous energy loss within the turbulent boundary layer, and is related to the intensity of turbulence in the fluid acting on the wall. It is not a force on the wall from the fluid, but is a force in the fluid at the wall.

Wall shear stress is defined as the isothermal pressure loss in a moving fluid within an incremental length due to fluid friction as a result of contact with a stationary wall. The mathematical definition of wall shear stress is as follows [13]. The total shear stress in a fluid moving past a fixed wall is the sum of the viscous and Reynolds stresses, expressed as:

$$\tau = v\left(\frac{\partial U}{\partial y}\right) - u_x u_y \tag{1}$$

The Reynolds stresses ($u_x u_y$) go to zero at the wall, leaving only the viscous stress in the fluid. The wall shear stress is defined as this viscous shear stress at $y = 0$, expressed as:

$$\tau_w = v\left(\frac{\partial U}{\partial y}\right)_{y=0} \tag{2}$$

Mass transfer is intimately linked to wall shear stress, and at present the two cannot be practically separated either experimentally or mathematically for flow accelerated corrosion. Thus, changes in flow parameters that affect one result in changes in the other. This linking is not totally independent of geometry, however, and the relationship between mass transfer and wall shear stress may change from one flow geometry to another. The violent, rapidly fluctuating nature of the turbulent boundary layer and its interaction with the solid surface is the primary reason that wall shear stress must be a fundamental criterion to include hydrodynamic factors in the definition of flow accelerated corrosion. Additionally, wall shear stress is a parameter that can be readily calculated for most field situations. For these reasons, wall shear stress is used in this research rather than mass transfer coefficient to evaluate flow accelerated corrosion, but this does not imply the assumption of a shear mechanism for flow accelerated corrosion.

Wall Shear Stress Equations

Momentum transfer from a moving fluid to the solid surface over which it is flowing and the degree of fluid turbulence at the solid surface is expressed as the wall shear stress (τ_w), generally manifested as a pressure gradient in the flowing fluid. The wall shear stress is the primary fluid dynamics parameter used to measure the interaction of a flowing fluid with a solid surface, and can be related back to any flow geometry, since it is a basic fluid/wall interaction phenomena and not a function of the specific flow geometry [1,4]. This implies that a test method that determines the wall shear stress acting on the test specimen can be effectively used for research into flow accelerated corrosion, and for correlation among flow geometries. The applicable wall shear stress equations used for parallel pipe flow and jet impingement flow are given below. Details of the derivations for the equations are given by the authors in a previous publication [5].

Pipe Flow. The effect of wall shear stress on pressure loss in a pipe segment of length (dL) and diameter (d) for isothermal flow with no change in elevation is derived by establishing a force balance between pressure forces and the wall shear stress (τ_w). The pressure drop (dP) in segment dL is expressed by the equation:

$$dP = \frac{4\tau_w}{d}(dL) \tag{3}$$

This equation precisely defines the wall shear stress, in terms that can be experimentally measured, i.e., the pressure drop (dP) in a specific length of pipe (dL) with a specific diameter (d). The necessary requirement is the elimination of all other sources of pressure loss. This analogy can be mathematically defined for any surface with a fluid flowing over it.

The ratio of the wall shear stress to the kinetic energy pressure loss per unit volume exactly defines a dimensionless friction factor (f) that is a measure of the pressure loss due to wall turbulence, accounting for both fluid viscous shear and the wall roughness and is expressed as:

$$f \equiv \frac{\tau_w}{\frac{\rho U^2}{2}} \equiv \frac{2\tau_w}{\rho U^2} \tag{4}$$

Solving Equation 4 for the wall shear stress gives the relationship:

$$\tau_w = \frac{f U^2 \rho}{2} \tag{5}$$

The wall shear stress for isothermal parallel pipe flow can be calculated either from fluid properties using Equation 5, or from pressure drop measurements in a pipe section of known dimensions and known fluid properties using Equation 3.

Jet Impingement. Jet impingement is a widely used test technique to study flow accelerated corrosion [14-16]. The flow field established when a circular jet impinges on a flat plate with its central axis normal to the plate is illustrated in Figure 7 [15]. Under these conditions, a stagnation point will exist at the intersection of this axis with the plate and the flow will be symmetric about the axis. Because the flow is axisymmetric, only the flow and fluid properties in the radial plane normal to the disk need to be considered. A detailed description of the flow regions from Figure 6 are given in reference 5, and will not be repeated here, except for Region B for correlation with pipe flow.

Region B is a region of rapidly increasing turbulence intensity, with the flow developing into a wall jet, i.e., the primary flow vector is parallel to the solid surface. This region extends radially to approximately $r = 4r_0$. The flow pattern is characterized by high turbulence intensity, a large velocity gradient at the wall and high wall shear stress. Because of its characteristics, Region B is of primary interest for studying fluid flow effects on corrosion in high turbulence areas and areas of flow disruption. The region has not been rigorously mathematically characterized, but published work to date indicates that the surface shear stress is proportional to the square of the velocity. Giralt and Trass [17,18] have experimentally derived an equation for the wall shear stress in this region. This equation, with the numerical constant recalculated for the use of the jet radius instead of the jet diameter as the normalizing factor, is written as:

$$\tau_w = 0.0112 \rho U^2 Re^{-0.182} \left(\frac{r}{r_0}\right)^{-2.0} \tag{6}$$

where the jet Reynolds number is defined as:

$$Re = \frac{2r_0 U}{\nu} \tag{7}$$

Experimental Procedures and Equipment

The basic apparatus used in this research allows simultaneous experiments using both test methods (pipe flow and jet impingement) under identical environmental conditions. This minimizes the possibility that environmental variables could influence the results of the experiments, allowing direct comparison of the experimental methods. A diagram of the test apparatus is given in Figure 7.

The test material used for all the corrosion rate studies was annealed AISI 1018 carbon steel. The measuring surface exposed to the test environment for all test samples was polished on 600 grit SiC metallurgical paper, degreased, methanol rinsed and air dried before exposure. All experiments were conducted at a controlled temperature of 50°C ± 2°C.

The basic test solution used for all of the experiments was a single phase aqueous solution of 3.0% NaCl with 1000 ppm HCO_3^- as $NaHCO_3$ to buffer the solution and to minimize pH fluctuation during a test. The solution was deaerated by purging with CO_2, or mixed CO_2/N_2 gas, depending on the CO_2 partial pressure being studied, for 12 hours minimum before testing, followed by the injection of 1.0% hydrazine chloride solution immediately before the test initiation to remove any residual dissolved oxygen. Dissolved oxygen and iron concentrations were checked using Chemetrics Corp. Chemets, with a 0 to 40 ppb analytical range for oxygen and 20 ppb to 10 ppm analytical range for iron. The oxygen concentration in the solution was maintained at less than 40 ppb, normally

ranging from 20 to 30 ppb. The ferrous ion concentration was monitored during the test and a test was terminated when the Fe^{++} concentration exceeded 400 ppb, except for the investigation of Fe^{++} effects.

Steel corrosion rates were determined from linear polarization measurements. A Cortest IN4300B Potentiodyne Analyzer instrument employing Potentiodyne software, Ver. 3.01a on a Toshiba T3100 computer in conjunction with a W4300C Potentiostat was used. Linear polarization tests were conducted with a ±15 mv potential scan range from the free corroding potential, at a scan rate of 10 mv/min. Electrochemical impedance measurements were made using an EG&G Model 273 potentiostat interfaced with a Schlumberger Solartron 1250 Frequency Response Analyzer, all under computer control. Impedance measurements were carried out in the frequency range of 10^4 Hz to 5×10^{-2} Hz, with a sinusodial signal amplitude of 5 mv.

Pipe Flow Apparatus

The pipe flow apparatus utilizes a 12.7 mm (0.50 inch) or 25.4 mm (1.00 inch) diameter circular flow test section, with flow stabilizing sections installed before and after the test section. It is extremely important to prevent flow disturbances that can affect the test results and introduce errors into the correlations. All three sections are machined to the same internal diameter and connected using flanges with o-rings to minimize flow disturbance. Differential pressure measurement across the flow section allows accurate determination of the mass flow rate as well as calculation of the wall shear stress in the test area.

The 90 mm (3.5 inch) diameter test section experiments were conducted in the flow loop at the Ohio University Corrosion in Multiphase Systems Center in Athens, Ohio. A test section identical in design to the smaller test section (except for the pipe diameter) was constructed and inserted into the Ohio University test loop, and identical test solutions and corrosion rate measuring equipment were employed.

Disk electrodes in the test section, mounted to form an integral part of the pipe wall, are used for the electrochemical measurements. Details of the corrosion measurement section, showing the electrode placement and locations of the reference salt bridge are given in Figure 8. The electrodes are arranged with the working (test) electrode located between the reference salt bridge opening and the counter electrode. Locating the counter electrode downstream of the working electrode ensures that any reaction products generated at the surface of the counter electrode do not pass across the working electrode and affect its corrosion. The electrode arrangement also ensures that current from the counter electrode does not pass across the reference cell.

The working electrode is a 1.0 mm thick disk machined from AISI 1018 carbon steel, with an accurately machined center hole of the appropriate diameter. The exposed surface area of the working electrode is 39.9 mm^2, 79.9 mm^2 and 282.7 mm^2 for the 12.7 mm, 25.4 mm and 90 mm diameter test assembly respectively. The counter electrode is a 6 mm thick platinum cylinder pressed into a titanium cylinder, providing a counter electrode area of 6 times the working electrode area. Nonmetallic spacers 1.0 mm thick are placed between the working and counter electrodes. The reference cell salt bridge is connected to the reference cell by 6.4 mm diameter Teflon tubing. Both the tubing and the test cell cavity are filled with natural cotton saturated with the test solution. The 2.5 mm diameter hole through the pipe wall is carefully filled with the cotton so it is flush with the internal surface before assembly of the test cell section.

Jet Impingement Apparatus

The general arrangement of the jet impingement test cell is shown schematically in Figure 9. This test cell utilizes impingement of a jet of fluid onto a flat surface, electrochemical corrosion probe.

The fluid jet is formed by a 12.5 mm diameter nonmetallic cylinder with a 2.0 mm diameter machined center hole with a tapered inlet to smooth the flow. The length of the cylinder is set to ensure flow stabilization before the fluid exits, providing a stable, reproducible jet impinging on the sample surface. The platinum counter electrode is fixed to the end of the jet cylinder before drilling the center hole.

The jet impinges on the center line perpendicular to the flat surface of the working electrode probe. The working end of this electrochemical corrosion probe consists of a 1.0 mm thick concentric ring working electrode with a 6.0 mm inside diameter. The back section of the probe is threaded to allow precise adjustment of the distance from the end of the probe test surface to the end of the jet, which is 4.0 mm for a 2.0 mm diameter jet. The concentric ring working electrode lies in the high turbulence Region B of the jet, with the center thickness of the ring at $r/r_0 = 3$. The ring position is shown with respect to the jet flow regions in Figure 10.

Results and Discussion

The results of the fluid flow experiments are given in the following figures. All data are plotted with respect to the wall shear stress. The pipe flow wall shear stress was calculated using Equation 5. The jet impingement wall shear stress was calculated using Equation 6. All experiments were conducted in the same basic environment: 3.0% NaCl + 1000 ppm HCO_3^- aqueous solution at 50°C ± 2°C temperature and 20-30 ppb dissolved oxygen.

Solution Contamination by Ferrous Ion

Ferrous ion contamination of the recirculating fluid from the corrosion of the steel test samples is a significant experimental problem, since the presence of dissolved iron in CO_2 containing brines can greatly reduce the measured corrosion rate of steel. The concentration of dissolved iron allowable in the test solution without significantly affecting the steel corrosion rate must, therefore, be determined. A series of tests were conducted in the 12.7 mm pipe flow apparatus at a range of dissolved iron concentrations. The results of these experiments are shown in Figure 11. There is no apparent effect on the steel corrosion rate at dissolved iron concentrations up to 8 ppm. A dissolved iron concentration of 44 ppm significantly lowered the steel corrosion rates at all wall shear stress levels, however.

These results demonstrate that uncontrolled Fe^{++} in the test solution gives erroneous results for flow accelerated corrosion of steel in sweet environments. For these environments, a limit of 5 ppm Fe^{++} was established for future fluid flow experiments, which is a significant increase over the 400 ppb that was adhered to for the experiments reported here.

Flow Accelerated Corrosion and Wall Shear Stress

The effect of wall shear stress on flow accelerated corrosion of carbon steel for 12.7, 25.4 and 90 mm diameter pipe flow is given in Figure 12. The tests were conducted to ensure there were no extraneous factors in the 12.7 mm diameter pipe to invalidate the equations for wall shear stress and to verify scale up of the flow accelerated corrosion data.

A comparison of regression results for the carbon steel flow accelerated corrosion data for varying pipe diameters is given in Table 1. The slope,"b", of all three curves is similar. The steel corrosion rate difference compared to flow in the 12.7 mm diameter pipe is +7% for flow in the 25.4 mm diameter pipe and -16% for flow in the 90 mm diameter pipe. These data lie within the range of experimental error for the fluid flow corrosion tests, and validate the use of flow accelerated corrosion data from the 12.7 mm diameter pipe for simulation of pipe flow in larger diameter pipes based on wall shear stress.

Flow accelerated corrosion rates of carbon steel for a range of CO_2 partial pressures were determined to evaluate the interactive effect of CO_2 partial pressure and wall shear stress. The results for the pipe flow apparatus are given in Figure 13. There is a significant increase in the steel flow accelerated corrosion rate on increasing CO_2 partial pressure, from 0.14 bar (2.0 psia) to 1.4 bar (20 psia), but only a slight increase at high wall shear stress on further increase to 4.1 bar (60 psia). The corresponding measured solution pH was 6.8, 6.0 and 5.8 respectively, which correlates with the observed change in steel corrosion rate.

Flow accelerated corrosion rates of carbon steel for a range of CO_2 partial pressures using the jet impingement apparatus are given in Figure 14. The results are essentially the same as for the pipe flow apparatus.

Correlation of Pipe Flow and Jet Impingement

Jet impingement tests are significantly easier to conduct than pipe flow experiments, but the flow accelerated corrosion correlation with pipe flow based on equivalent wall shear stress criteria must be established experimentally if there is to be any real confidence in application of the jet impingement test results to field operations. The results for jet impingement and pipe flow are directly compared for different CO_2 partial pressures in Figure 15 for 0.14 bar (2 psia) CO_2, Figure 16 for 1.4 bar (20 psia) CO_2 and Figure 17 for 4.1 bar (60 psia) CO_2. Comparisons of regression results for steel flow accelerated corrosion data at varying CO_2 partial pressures in jet impingement and pipe flow are given in Table 2.

Electrochemical impedance measurements were conducted for corrosion of carbon steel at 10 N/m^2 wall shear stress for both pipe flow and jet impingement in the base solution with 1.4 bar (20 psia) CO_2 partial pressure and a temperature of 50°C. The objective was to produce a more complete comparison of the two flow methods through a more detailed look at the corrosion characteristics as revealed by electrochemical impedance. The results as Nyquist plots are shown in Figure 18. Although there are some differences in detail between the Nyquist plots for the two flow methods, the basic form is the same, and this basic form was reproducible. There was no attempt to investigate the detailed differences in the curves, since this research was not intended to include detailed studies into corrosion mechanisms.

This research demonstrates that flow accelerated corrosion results for the jet impingement test with the test ring set at $r/r_o = 3$ effectively correlate with pipe flow results based on the wall shear stress for carbon steel in sweet environments. Therefore, the jet impingement test can be used to generate flow accelerated corrosion data for application to field systems using equivalent wall shear stress criteria.

The Equation Relating Flow Accelerated Corrosion and Wall Shear Stress

In a previous publication, the authors proposed an equation that relates flow accelerated corrosion of steel to the wall shear stress [5]. This proposal was based on the striking similarity in the logarithmic plots of steel corrosion rate as a function of wall shear stress, implying a general equation describing the effect of wall shear stress on steel corrosion rate. The general equation for flow accelerated carbon steel corrosion in single phase, sweet, aqueous systems is expressed as:

$$R_{cor} = a \, \tau_w^{\ b}$$

where "R_{cor}" is the carbon steel corrosion rate in mm/y and "τ_w" is the wall shear stress in N/m^2. The coefficient "a" and exponent "b" are as yet undefined. This equation is valid for wall shear stress in the range $0.2 < \tau_w < 100$ N/m^2. A minimum wall shear stress of 0.2 N/m^2 is applied based on the wall shear stress for the test solution at a pipe flow Reynold's number of 2000, the approximate lower limit for turbulent flow in pipes.

The results confirm the previous proposal, and demonstrate that the values of the coefficient, a, and exponent, b, are functions of environmental parameters, e.g., P_{CO2}, and solution chemistry, e.g., pH. These factors require further definition, however, before this equation can be universally applied.

The solution chemistry and environmental parameters are accounted for in the coefficient and exponent of the equation, and the necessary hydrodynamic variables are accounted for in the wall shear stress term. Therefore, this equation effectively combines the hydrodynamic and chemistry variables for flow accelerated corrosion without the need for mathematical correction factors. As a result, detailed determination of the effect of important

solution parameters and environmental variables on the exponent and coefficient can provide a complete definition of flow accelerated general corrosion of steel in sweet systems.

The nature of the wall shear stress calculation dictates that it cannot be effectively used for mechanistic interpretation. Specifically, the correlation with wall shear stress does not imply a shear mechanism for flow accelerated corrosion of steel. Neither does it imply that there is no shear component to flow accelerated corrosion. The correlation exists, and the determination of whether the corrosion is charge transfer or mass transfer controlled must be determined separately.

Conclusions

1. Flow accelerated corrosion results from experiments using a 12.7 mm diameter pipe flow simulation can be applied to larger diameter pipes based on equivalent wall shear stress criteria.

2. Flow accelerated corrosion results for the jet impingement test with the test ring set at $r/r_0 = 3$ effectively correlate with pipe flow results based on wall shear stress for carbon steel in sweet environments. Therefore, the jet impingement test can be used to generate flow accelerated corrosion data for application to field systems using equivalent wall shear stress criteria.

3. Flow accelerated corrosion of steel in sweet environments is strongly affected by the Fe^{++} concentration in solution, therefore uncontrolled Fe^{++} in the test solution gives erroneous results for flow accelerated corrosion of steel. A limit of 5 ppm dissolved Fe^{++} in the test solution is recommended for credible fluid flow experiments in this environment.

4. The general equation for flow accelerated carbon steel corrosion based on the interrelationship of hydrodynamic parameters, solution chemistry and environmental variables for single phase, sweet, aqueous systems for wall shear stress in the range $0.2 < \tau_w < 100$ N/m² is expressed as:

$$ R_{cor} = a \, \tau_w{}^{b} $$

where "R_{cor}" is the carbon steel corrosion rate in mm/y and "τ_w" is the wall shear stress in N/m². The coefficient "a" and exponent "b", not fully defined, are functions of the solution chemistry (pH, Fe⁺⁺, O_2, P_{CO2}, etc.) and other environmental parameters (total pressure and temperature). The necessary hydrodynamic variables are accounted for in the wall shear stress term.

References

1. K. D. Efird, "The Effect of Fluid Dynamics on the Corrosion of Copper Base Alloys in Seawater", Corrosion, Vol 33, No. 1, January, 1977, pp. 3-8.

2. T. Y. Chen, A. A. Moccari, D. D. Macdonald, "The Development of Controlled Hydrodynamic Techniques for Corrosion Testing", CORROSION/91, National Association of Corrosion Engineers, Cincinnati, OH, March 11-15, 1991, Paper No. 292.

3. E. Heitz, "Chemo-mechanical Effects of Flow on Corrosion", MTI Publication No. 23, MTI Project No. 15, Materials Technology Institute, Columbus, Ohio, 1986.

4. B. T. Ellison and C. J. Wen, "Hydrodynamic Effects on Corrosion", Tutorial Lectures in Electrochemical Engineering and Technology, Richard Alkire and Theodore Beck Editors, AIChE Symposium Series, Vol. 77, AIChE, New York, 1981, pp. 161-169.

5. K. D. Efird, E. J. Wright, J. A. Boros and T. G. Hailey, "Experimental Correlation of Steel Corrosion in Pipe Flow with Jet Impingement and Rotating Cylinder Laboratory Tests", NACE CORROSION/93, Technical Paper No. 93081, New Orleans, March, 1993.

6. J. T. Davies, "Eddy Transfer Near Solid Surfaces", Turbulence Phenomena, Academic Press, New York, pp. 121-143 (1972).

7. S. J. Kline, W. C. Reynolds, F. A. Schraub and P. W. Runstadler, "The Structure of Turbulent Boundary Layers", Journal of Fluid Mechanics, Vol. 30, 1967, pp. 741-773.

8. M. T. Landahl and E. Mollo-Cristensen, Turbulence and Random Processes in Fluid Mechanics, Cambridge University Press, Cambridge, 1987, pp. 111-120.

9. A. K. Praturi and R. S. Brodkey, "A Stereoscopic Visual Study of Coherent Structures in Turbulent Shear Flow", Journal of Fluid Mechanics, Vol. 89, Part 2, 1978, pp. 251-272.

10. G. R. Often and S. J. Kline, "A Proposed Model of the Bursting Process in Turbulent Boundary Layers", Journal of Fluid Mechanics, Vol. 70, 1975, pp. 209-228.

11. S. K. Robinson, "Coherent Motions in the Turbulent Boundary Layer", Annual Review of Fluid Mechanics, Vol. 23, 1991, pp. 601-639.

12 A. S. Thomas and M. K. Bull, "On the Role of Wall Pressure Fluctuations in Deterministic Motions in the Turbulent Boundary Layer", Journal of Fluid Mechanics, Vol. 128, 1983, pp. 283-322.

13. A. A. Townsend, The Structure of Turbulent Flow, Cambridge University Press, Cambridge, 1956, pp. 194-196.

14. P. A. Lush, S. P. Hutton, J. C. Rowlands, and B. Angell, "The Relation Between Impingement Corrosion and Fluid Turbulence Intensity", 6th European Congress on Metallic Corrosion, Society of the Chemical Industry, London, 1977, pp. 137-146.

15. J. L. Dawson and C. C. Shih, "Electrochemical Testing of Flow Accelerated Corrosion Using Jet Impingement Rigs", CORROSION/87, National Association of Corrosion Engineers, San Francisco, March 1987, Paper No. 453.

16. M. B. Glauert, "The Wall Jet", Journal of Fluid Mechanics, Vol. 1, 1956, pp. 625-643.

17. F. Giralt and D. Trass, "Mass Transfer from Crystalline Surfaces in a Turbulent Impinging Jet, Part 1: Transfer By Erosion", Can. J. Chem. Eng., Vol. 53, 1975, pp. 505-511.

18. F. Giralt and D. Trass, "Mass Transfer from Crystalline Surfaces in a Turbulent Impinging Jet, Part 2: Erosion and Diffusional Transfer", Can. J. Chem. Eng., Vol. 54, 1976, pp. 148-155.

Selected Glossary of Fluid Flow Terms

Boundary Layer The wall region in turbulent flow where the flow changes from fully turbulent to viscous, composed of the logarithmic region, the buffer region and the viscous region.

Buffer Region That portion of the wall region, defined as $5 \leq y_+ \leq 30$.

Burst A violent eruption or localized ejection of fluid away from the wall, caused by the passage of one or more vortices.

Coherent Structure A morphologically invariant, three dimensional region of the flow possessing an identifiable flow pattern. See also, "turbulent structure."

Ejection The movement of fluid away from the wall at an angle to the nominal flow direction.

Lift-up Movement of a wall streak away from the wall due to a local pressure gradient.

Logarithmic Region That portion of the wall region, defined as $30 \leq y_+ \leq 100$.

Sweep The movement of fluid toward the wall at an angle to the nominal flow direction.

Turbulent Structure A morphologically invariant, three dimensional region of turbulent flow possessing an identifiable flow pattern. See also, "coherent structure."

Viscous Region That portion of the wall region, defined as $0 \leq y_+ \leq 5$.

Vortex An area of spiral or circular flow normal to a defined axis.

Wall Region That portion of the boundary layer comprising the viscous sublayer, the buffer region and the logarithmic region, defined as $y_+ \leq 100$.

Wall Streak A coherent segment of fluid moving parallel to the nominal flow direction, but at a significantly different velocity.

Nomenclature

d	diameter (m)	**y**	direction $\perp$ to the surface (m)	**Subscripts**
e	roughness factor (m)	**y+**	viscous length $= yu_\tau/v$ (dimensionless)	**b** boundary layer
I	current density (A/m²)	**z**	direction parallel to the surface	**cor** corrosion
L	characteristic length (m)		but $\perp$ to the flow direction (m)	**d** diffusion
P	pressure (Pa, kg/m s²)			**f** final or ending
R	resistance (Ω m²)	**Greek Symbols**		**i** initial or beginning
R$_{cor}$	corrosion rate (mm/y, mpy)	**Δ**	gradient of a property	**j** species "j"
r	radius or radial distance (m)	**δ**	boundary layer thickness (m)	**lim** limiting
T	temperature (°C)	**ρ**	density (kg/m³)	**o** standard or primary
t	time (s)	**μ**	dynamic viscosity (kg/m s)	**t** value at time t
U	mean velocity (m/s)	**v**	kinematic viscosity (m²/s)	**w** wall or electrode surface
u	local velocity (m/s)	**τ**	shear stress (N/m²)	**x** direction parallel to surface
x	direction parallel to surface (m)			**y** direction $\perp$ to surface
				+ normalized dimensionless form

2672

TABLE 1

PIPE FLOW DIAMETER EFFECT ON REGRESSION RESULTS FOR
CARBON STEEL CORROSION RATE VARIATION WITH WALL SHEAR STRESS

PIPE FLOW DIAMETER	b	a, mm/y (mpy)	R^2	a % DIFF. from 12.7 mm
12.7 mm DIAMETER PIPE	0.12	7.06 (278)	0.80	0%
25.4 mm DIAMETER PIPE	0.10	7.56 (298)	0.80	+7%
90 mm DIAMETER PIPE	0.12	5.9 (233)	0.87	-16%

TABLE 2

COMPARISON OF PIPE FLOW AND JET IMPINGEMENT POWER FUNCTION
REGRESSION RESULTS FOR CARBON STEEL CORROSION RATE VARIATION
WITH WALL SHEAR STRESS

ENVIRONMENT/FLOW TYPE	b	a, mm/y(mpy)	R^2
2.0 psi CO_2 + 1000 ppm HCO_3, pH 6.8			
PIPE FLOW (12.7 mm)	0.28	1.27 (50)	0.80
JET IMPINGEMENT	0.25	1.37 (54)	0.92
20 psi CO_2 + 1000 ppm HCO_3, pH 6.0			
PIPE FLOW (12.7 mm)	0.12	7.06 (278)	0.80
JET IMPINGEMENT	0.10	8.10 (319)	0.90
60 psi CO_2 + 1000 ppm HCO_3, pH 5.8			
PIPE FLOW (12.7 mm)	0.16	7.42 (292)	0.91
JET IMPINGEMENT	0.17	8.36 (329)	0.94
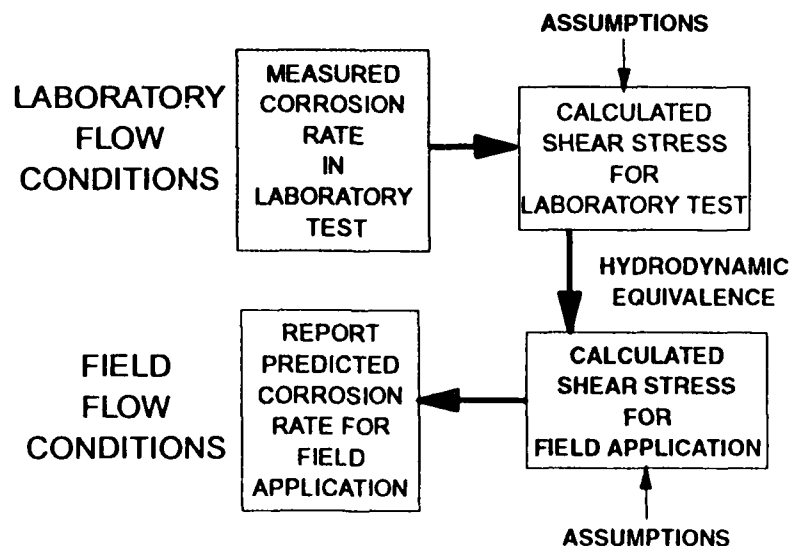
FIGURE 1. The process for determination of field corrosion rates from laboratory data using fluid
mechanics considerations.
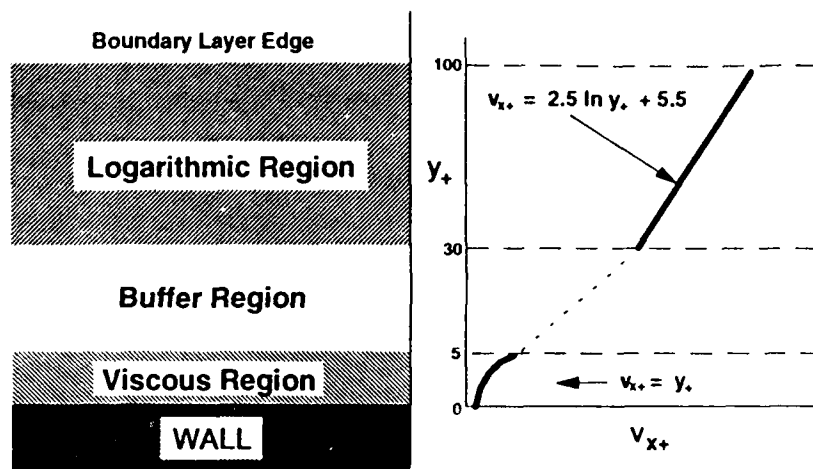
FIGURE 2. Structure of the turbulent boundary layer with an idealized plot of the normalized turbulent velocity variation with distance from the wall, expressed as dimensionless viscous length (from Davies, 1972).
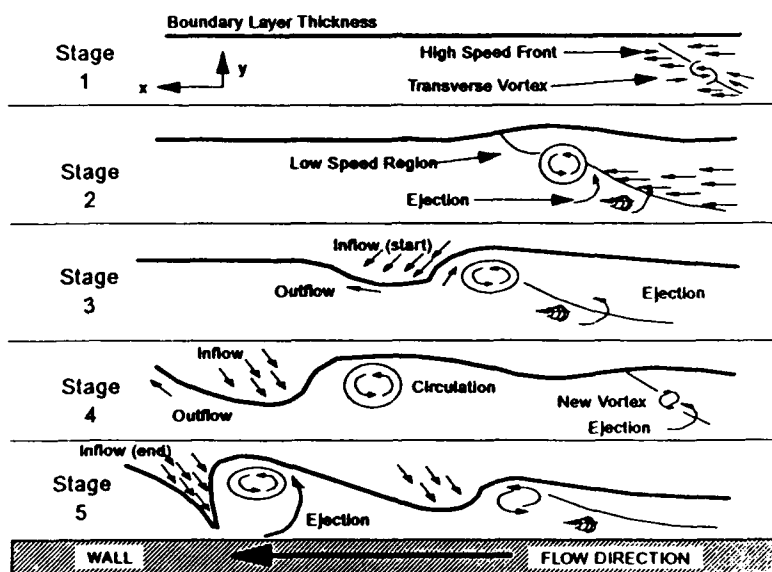
FIGURE 3. Progression of flow illustrating the formation of shear layer vortices and evolution into turbulent bursts (from Praturi and Brodkey, 1978).
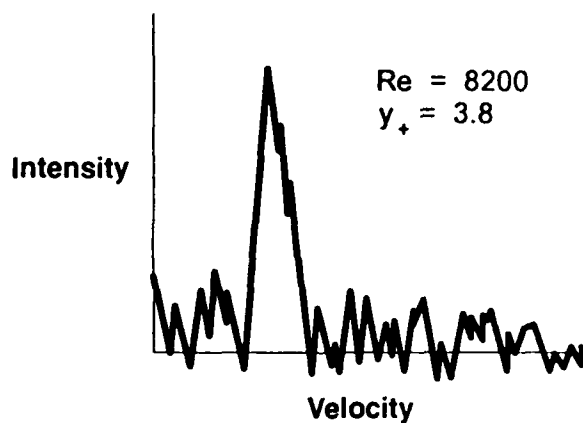
FIGURE 4. Laser Doppler measurements at y+ = 3.8, showing eddies inside the viscous region of water flowing at Re = 8200 in a rectangular pipe. The large peak is the main velocity component, and the small peaks represent instantaneous velocity fluctuations. (from Davies, 1972).
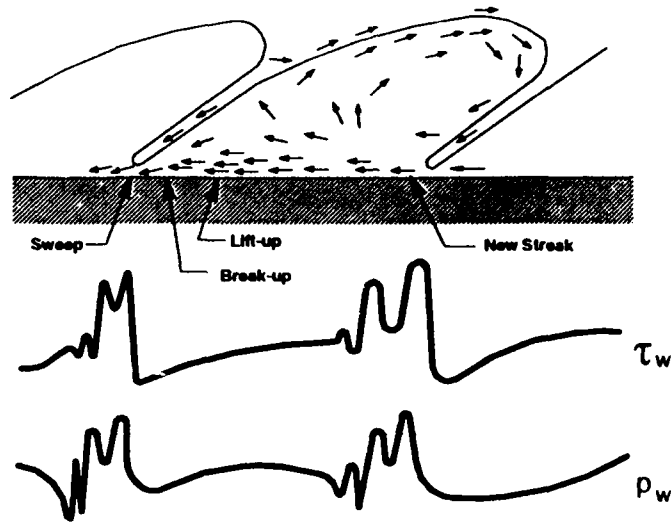
FIGURE 5. Wall shear stress and wall pressure fluctuations in relation to the location of near wall bursting activity in the turbulent boundary layer (from Thomas and Bull, 1983).
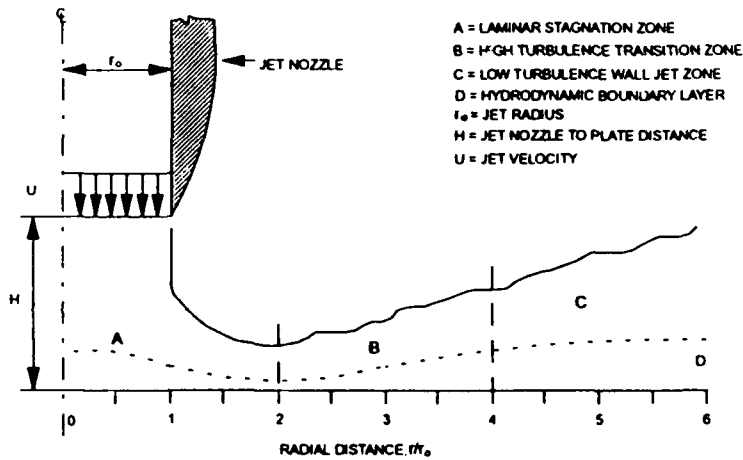
FIGURE 6. Hydrodynamic Characteristics of Jet Impingement on a Flat Plate showing the four characteristic flow regions (from J. L. Dawson and C. C. Shih, 1987).
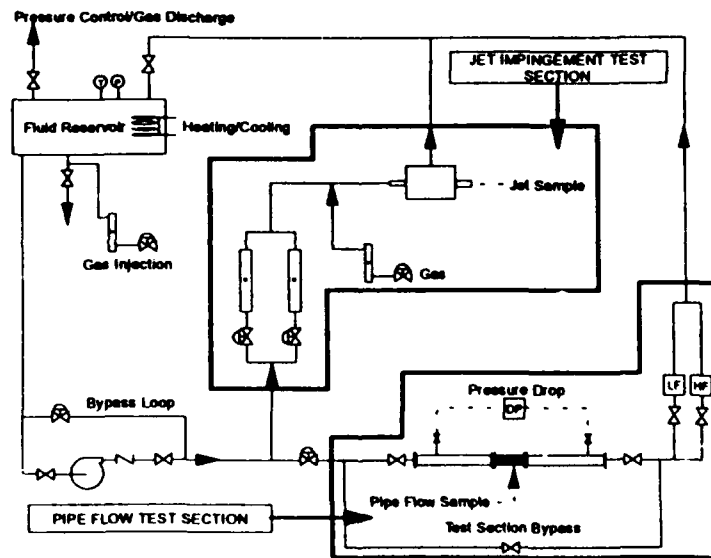
FIGURE 7. Schematic diagram of the test apparatus, including the parallel (pipe) flow and jet impingement test sections.
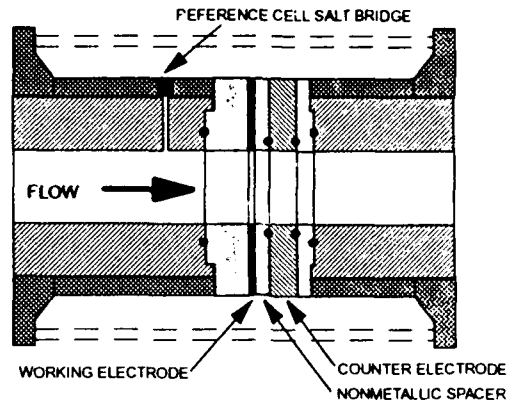
FIGURE 8. Schematic diagram of the parallel flow (pipe) test cell, showing the electrode placement and locations of the reference salt bridge.
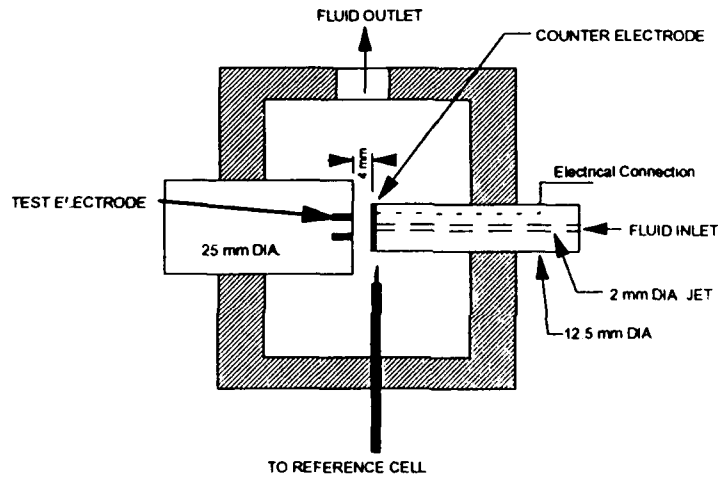
FIGURE 9. Schematic diagram of the jet impingement test cell, showing the relative placement of the jet, test electrode ring, reference cell luggin probe and the counter electrode.
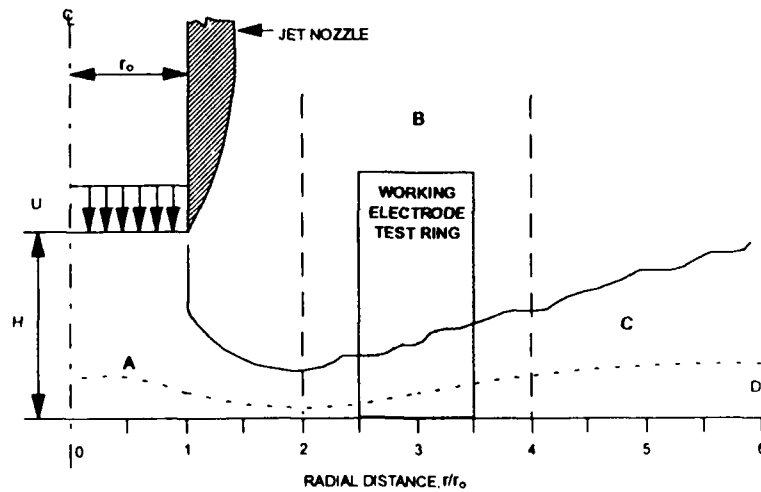
FIGURE 10. Placement of the working electrode test ring with respect to the jet flow regions.
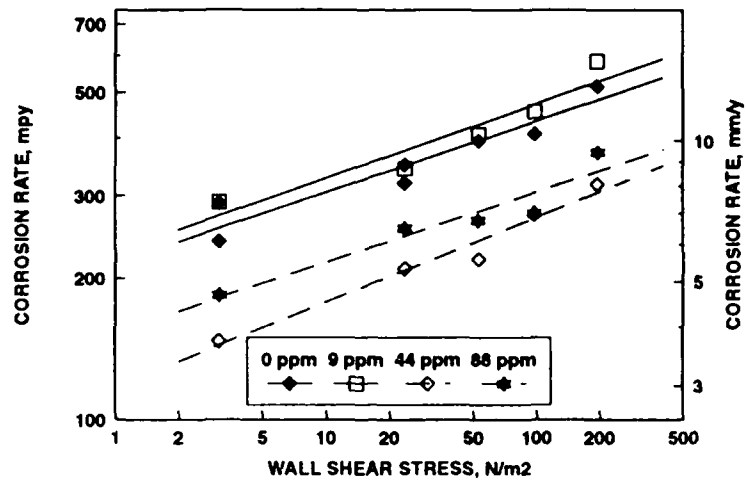
FIGURE 11. The effect of dissolved iron (Fe++) on flow accelerated corrosion of carbon steel in pipe flow as a function of wall shear stress under 1.3 bar (20 psia) CO_2 partial pressure.
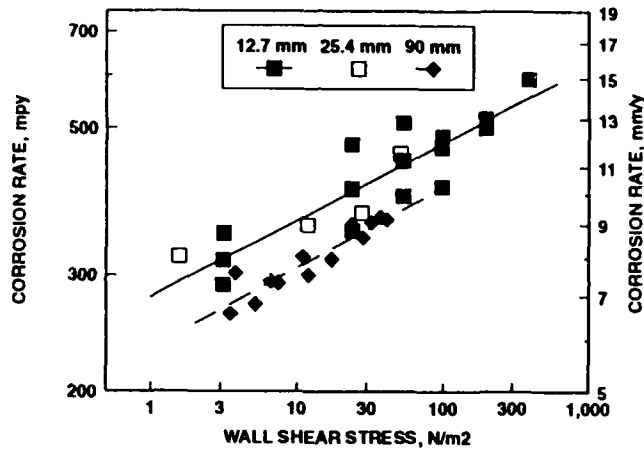
FIGURE 12. The effect of pipe diameter (12.7, 25.4, and 90 mm) on flow accelerated corrosion of carbon steel as a function of wall shear stress under 1.3 bar (20 psia) CO_2 partial pressure.
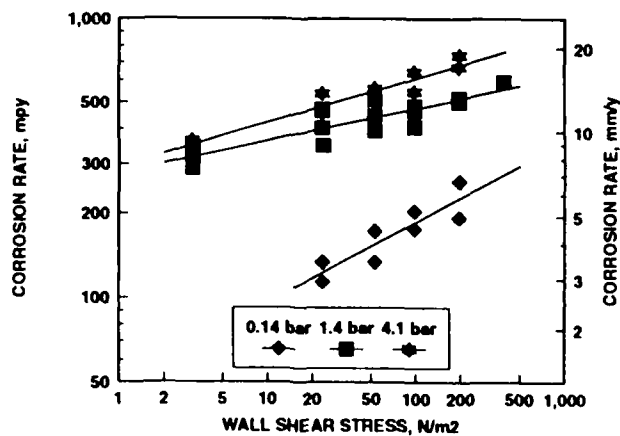
FIGURE 13. The effect of CO_2 partial pressure on flow accelerated corrosion of carbon steel as a function of wall shear stress for pipe flow.
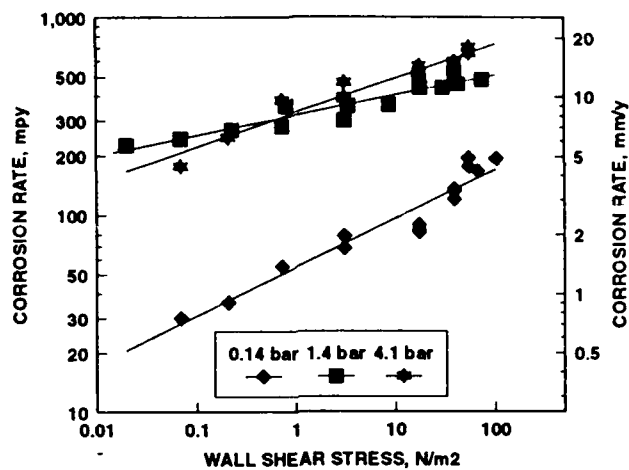
FIGURE 14. The effect of CO_2 partial pressure on flow accelerated corrosion of carbon steel as a function of wall shear stress for jet impingement.
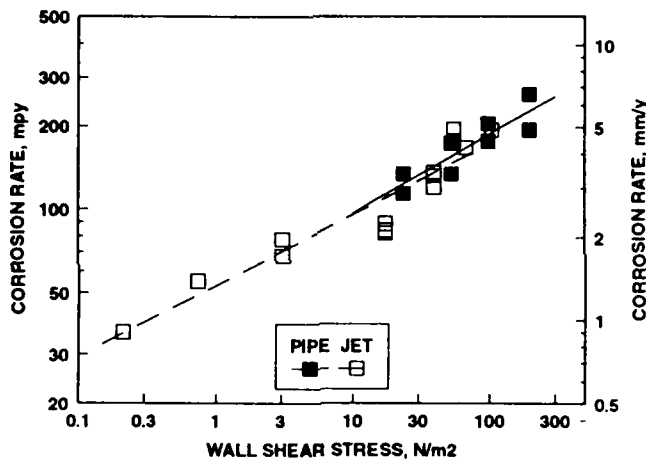
FIGURE 15. Comparison of flow accelerated corrosion of carbon steel as a function of wall shear stress for pipe flow and jet impingement at 2.0 psia CO_2 partial pressure and pH 6.8
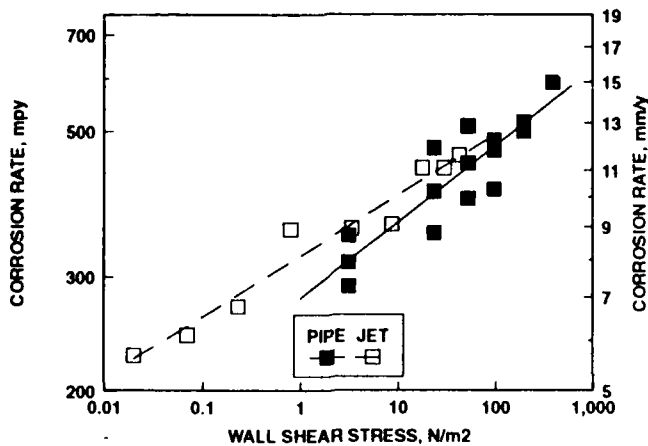
FIGURE 16. Comparison of flow accelerated corrosion of carbon steel as a function of wall shear stress for pipe flow and jet impingement at 20 psia CO_2 partial pressure and pH 6.0.
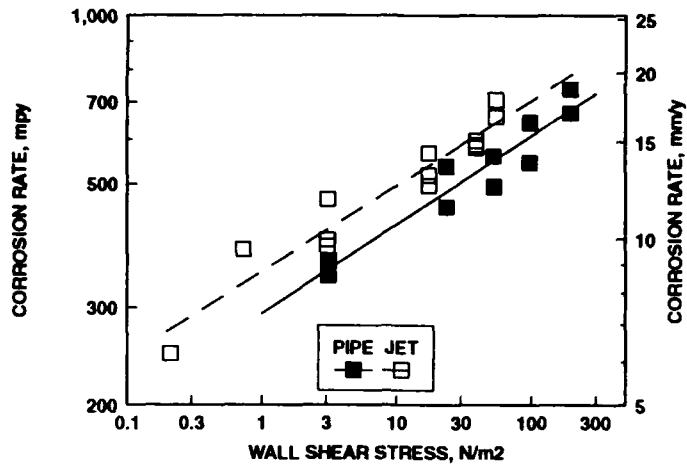
FIGURE 17. Comparison of flow accelerated corrosion of carbon steel as a function of wall shear stress for pipe flow and jet impingement at 60 psia CO_2 partial pressure and pH 5.8.
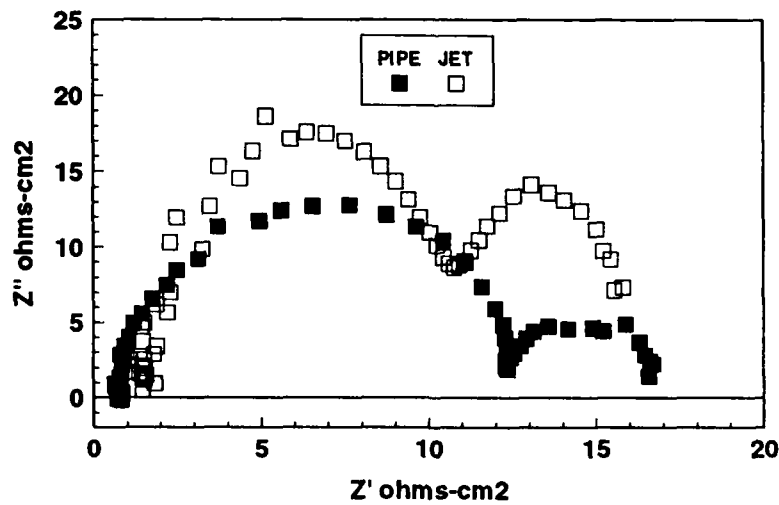
FIGURE 18. Electrochemical impedance Nyquist plot for the corrosion of 1018 carbon steel at a wall shear stress of 10 N/m^2 for pipe flow and jet impingement at 20 psia CO_2 partial pressure and 50 °C.

Effect of Flow Velocity on Carbon Steel CO_2 Corrosion and Surface Films using a Dynamic Field Tester

José R. Vera, José L. Morales, Alfredo Viloria
INTEVEP S.A.
Apartado 76343, Caracas Venezuela

Akio Ikeda, Masakatu Ueda
SUMITOMO METAL INDUSTRIES Ltd.
5-33, Kitahama 4-chome, Chuo-kuOsaka, Japan 451

ABSTRACT

The corrosion behavior of different grades of low alloy carbon steels (e.g., L80, C90, 5LX52 and 2%Cr) has been studied at 10.6-13.8 MPa total pressure, 6.7 % CO_2, 85 ºC and superficial gas velocities from 3 to 62 m/s, using a Dynamic Field Tester (DFT) installed at a Gas/Condensate well head located near ANACO, Venezuela.

The effect of flow velocity on the corrosion/erosion behavior of carbon steels was found to depend significantly on the chromium content of the steel. C90 and 2 % Cr steels showed a critical flow velocity of about 13 m/s, corresponding to a wall shear stress close to 80 N/m^2, above which penetration rates increased substantially with velocity. Line pipe and L80 steels showed a completely different fluid velocity effect, with localized corrosion rates decreasing with increasing fluid velocities up to 32 m/s. This decrease in corrosion rate was related to an increase in the relative presence of Fe_3C and Fe_3O_4 in the corrosion products. At higher velocities, or wall shear stresses over 300 N/m^2, penetration rates tend to increase due to erosion of protective films.

The properties of corrosion products, under the same temperature and CO_2 partial pressure, was associated not only to the chemical composition of materials, but also to the fluid velocity or wall shear stress. High fluid velocities affect kinetics of iron dissolution and $FeCO_3$ nucleation, producing a thin but more protective and erosion resistant film, taking advantage of an anchorage effect of the uncorroded Fe_3C particles left behind.

Key words: Carbon dioxide, corrosion-erosion, localized corrosion, iron carbonate, carbon steel, flow velocity, flow patterns.

Introduction

Current practice in the oil and gas production industry to prevent flow induced CO_2 corrosion generally limits fluid velocities in carbon steel pipelines and equipment based on field experience or empirical equations, such as the one included in the API RP 14E [1] guideline. Therefore, there is a need for developing a reliable method for predicting corrosion rates under hydrodynamic and environmental conditions relevant to oil and gas operations.

A great deal of effort has been directed towards understanding the complex mechanisms involved in the CO_2 erosion/corrosion process[2,3] and the relationship between hydrodynamics and corrosion[4,5]. Most of the research work has been carried out in laboratory recirculating test loops, which can simulate CO_2 partial pressures, water composition, temperatures and gas/liquid flow velocities. However, few research works have been reported using production fluids coming from a gas/condensate well[6], where the flow effect on corrosion can be investigated under controlled operational conditions. These experiments are considered important since the effect of a hydrocarbon phase without oxygen contamination can be assessed.

Experimental results, obtained from a Dynamic Field Tester (DFT) installed at a Gas/Condensate well head, have indicated that the effect of flow rate on the CO_2 corrosion/erosion behavior of different grades of steel depends on the chemical composition of the material[7,8]. This article includes data on the effect of flow velocity on the localized corrosion attack, using different arrangement of the test sections and higher flow velocities (up to 62 m/s). The effect of calculated wall shear stress (from 20 to 660 N/m^2) on the corrosion rates and surface films are also shown and discussed.

Experimental

Dynamic Field Tester (DFT)

The Dynamic Field Tester consists of a set of flow lines and equipment specially designed for corrosion testing of materials in contact with fluids coming from oil/gas wells, under real but well-controlled conditions. The circuit is schematically shown in Figure 1 and has been more extensively explained in previous communications [7,8].

In order to study four flow velocities during each test period, the DFT was designed with straight test sections housing tubular specimens of different internal diameters (52, 27, 20 and 15 mm). The specimens are mounted along the center line of the test section by means of Teflon holders, in such a way that only the internal surface of the specimens is exposed to corrosive fluids (see Figure 2). Test specimens are isolated from each other by Teflon or ceramic washers. A pre-flow section of more than 50 diameters long is installed at the beginning of each straight section to allow the flow regime to be fully developed before entering to the test section. The 15 mm ID specimens, however, are positioned in the last testing section directly after the reduction from 20 mm ID, to reduce pressure drop that occurs at these high velocities. Actual gas and liquid flow rates, temperatures and pressures are continuously monitored throughout the test by detectors installed at different locations.

Materials tested

The chemical composition and the mechanical properties of the materials tested are shown in Tables 1 and 2. Metallographic analysis [8] showed typical quenched and tempered martensitic structure in all materials, with the exemption of the carbon steel with 2 % Cr used in the 52 mm section (2CrNb) and the line-pipe steel. These two materials presented a normalized ferritic-perlitic structure.

Testing Conditions

The DFT was installed using a duplex by-pass line at the CORPOVEN gas/condensate well JM-101, located near Anaco, Venezuela, which had been completed with 13 % Cr tubing. Typical gas composition is shown in Table 3. During the tests, the average well production was 270 Nm^3/min (13.8 MMscf/D) of gas, 0.021 L/m^3 (3.8 MMscf/bbl) of a 42° API condensate and 0.022 L/m^3 (4.0 MMscf/bbl) of condensed water (less than 20 ppm of chlorides).

In tests primarily designed for studying CRA alloys, all fluids coming from the well went through the DFT, obtaining superficial gas velocities ranging between about 20 to 250 m/s. Results reported in the present paper were obtained from Tests N°2, N°3 and N°5, in which fluids were partially by-passed to reduce volumetric flow rates down to 34, 46 and 112 Nm^3/min, respectively. For comparison purpose, carbon steel corrosion data from Test N°1 [7] (at 52 mm ID, 20 m/s) were included in some of the figures.

Unless otherwise noted, test sections were located in a vertical position, in such a way that fluids coming from the well passed through the different internal diameters in the following sequence: 52 mm, 27 mm, 20 mm and 15 mm. Test N°5, however, was designed with the vertical test sections in the opposite sequence (i.e., 20-27-52 mm ID) to rule out possible systematic errors.

The variation of flow rates and pressures in different sections of the DFT are shown in Figure 3, and the average conditions recorded for these tests are summarized in Table 4. The average CO_2 partial pressure was 0.71 ± 0.03 MPa (103 ± 4 psi), the temperature was 80 ± 3 °C (176 ± 5 °F) and the superficial fluid velocity varied between 3 to 62 m/s (9 to 205 ft/s). Note that most of the pressure drop occurs through the small diameter sections, which caused a slight decrease in CO_2 partial pressure. The estimated carbon steel corrosion rates, calculated by the modified De Ward and Milliams equation[9], were also included in Table 4 to indicate the highly aggressive conditions of these tests (12.8 ± 0.4 mm/y).

A testing time of about 2 months was selected for these experiments, since preliminary tests and experience had shown that this exposure time was adequate for studying both general and localized CO_2 corrosion of carbon steel.

Fluid properties, superficial gas velocity, V_{sg}, liquid velocity, V_{sl}, and mixture velocity, V_s, for each testing condition were calculated using the CORRODIS[10] computer model. Flow pattern at each conditions, according to Taitel and Dukler[11] and calculated using vertical upward correlation based on Duns & Ros[12] dimensionless parameters, are shown in Table 5 and displayed in Figure 4. It is important to note that the flow pattern in the 15 mm ID test specimens may have not been fully developed, since it had no stabilization section.

Wall Shear Stress (WSS) at each test section condition, shown in Table 5, was calculated using the frictional pressure gradient ($\Delta P/L$) computed by the NAPS program[13], with the Gray and Ros correlation for Gas/Condensate wells, and the following equation[14] :

$$WSS = \frac{ID}{4} (\Delta P/L) \qquad (1)$$

It is important to note that calculated WSS are sensitive not only to the correlation selected but also to the pipe roughness used in the computation (in this case, 0.046 mm) and the physical-chemical properties of the fluids involved[5,13,14]. A modification in the DFT is been included to measure experimentally the frictional pressure gradient continuously at the different test sections.

Determination of corrosion rate.

At least three specimens were installed in the testing sections for each experimental condition (i.e., material, specimen type, internal diameter). The specific location of each specimen inside the test section was randomly chosen and recorded for future analysis. One specimen was used for destructive analysis in studying the corrosion product morphology and composition, by means of SEM, EDAX and x-ray diffraction. The other specimens were descaled and utilized for corrosion rate measurements. Internal surface of each specimen was also analyzed and low magnification photographs were taken before and after descaling.

Weight loss corrosion rates were calculated using an analytical balance (± 0.1 mg) and the geometric internal surface area of the specimens. Localized corrosion, on the other hand, was quantified by scanning the internal surface of the tubular specimens using a profilometer. For data reduction, only the deepest measurement recorded away from the edges was used in calculating the maximum localized corrosion. Higher localized corrosion was observed close to the interface between some specimens and their Teflon spacer, but these data were not reported in this article since they were regarded as being caused by turbulence produced by slight misalignment of the specimens.

In calculating corrosion rates, weight loss or maximum penetration data were divided by the actual testing time of 1464, 1542 and 1496 hours for test $N^{\circ}2$, $N^{\circ}3$ and $N^{\circ}5$, respectively. Unless otherwise noted, average corrosion rates will be shown with confidence intervals calculated at 95 % confidence.

Results

Effect of Fluid Velocity on Corrosion Behavior of different Steel Grades

L80 Steel

Corrosion behavior of L80 specimens is shown in Figure 5, as a function of superficial fluid velocity. Analysis of Variance (ANOVA) of these results revealed that velocity effects on both general and localized corrosion rates were statistically significant at 99 % confidence.

Weight loss corrosion rates increased with velocity from 2.5 mm/y at 3 m/s up to a maximum of about 7 mm/y at 4 m/s. After this maximum, they decreased with increasing superficial velocities (up to 33 m/s) and approached values not statistically different from those obtained at 3 m/s. At higher velocities, corrosion rates tend to increase significantly with velocity.

Similar conclusions were obtained from the ANOVA of localized corrosion results. That is, a maximum penetration rate of 7.3 ± 0.5 mm/y was obtained in the range from 4 to 20 m/s. Increasing velocities tend to decrease penetration rates, reaching a minimum close to 33 m/s and augmenting at higher velocities.

Analysis of corrosion morphology showed that L80 steel specimens suffered ring worm and some mesa corrosion at flow velocities lower than 13 m/s. It is important to note that the tendency for localized corrosion decreased with velocity. In fact, specimens exposed at fluid velocities higher than 20 m/s, did not show any pitting or mesa corrosion. At these velocities, corrosion rates calculated by weight loss agreed very well with maximum penetration measured, which confirms the lack of localized corrosion. At velocities higher than 33 m/s, flow induced marks were found in the internal surface, and external corrosion was evident. This may account for the fact that weight loss corrosion rates obtained in those specimens were higher than localized corrosion measured in the middle of the coupon.

It is important to note that corrosion rates obtained at about 10 m/s from test Nº2 (27 mm ID) and Nº5 (52 mm ID) were very close, even though experiments were run with different internal diameters and with the test sections placed in opposite sequence related to the gas flow entrance. This indicates that the reduction in corrosion with increasing velocities was not due to a systematic error caused by the position of the test sections (e.g., iron dissolution or pH change).

Line Pipe Carbon Steel

Line pipe material showed higher corrosion rates at low velocities than all the other grades of materials tested. As shown in Figure 6, increasing flow velocity seems to slightly reduce weight loss corrosion rates. Analysis of variance of these results indicated that flow velocity, however, did not have a statistically significant effect on the weight loss corrosion rate up to 42 m/s (5.5± 0.7 mm/y). At 62 m/s, weight loss corrosion rate increased significantly (11.4± 0.3 m/s), obtaining higher value than the internal penetration measured at the middle of the coupons, due primarily to some external corrosion.

As mentioned in a previous communication [8], flow velocity did affect both corrosion morphology and penetration rates. Maximum localized corrosion rates of 8.1± 0.6 mm/y were obtained at low velocities (≤ 20 m/s), on specimens where mesa or ring-worm corrosion was observed. At higher velocities, penetration rates decreased down to about 4 mm/y at 33 and 42 m/s, on specimens where only uniform corrosion was found. Experiments performed at 38 and 62 m/s showed a significant increase in penetration rates, which were statistically similar to the values obtained at lower velocities (i.e., 8.1 ± 0.6 mm/y) but with a different morphology: Corrosion appeared to be uniform, but with evidence of shallow flow induced erosion marks.

C90 Steel

C90 specimens (Figure 7) showed the lowest weight loss corrosion rates of all materials at low flow velocities (1.1 ± 0.5 mm/y at flow velocities ≤ 13 m/s). At flow velocities comprised between 19 and 33 m/s, the weight loss corrosion rate and the standard error increased significantly to 3.8 ± 2.1 mm/y. At even higher velocities, corrosion rates increased substantially up to about 13 mm/y, which were higher than values obtained on any other grade of steel.

Analysis of variance of penetration rates also showed a significant effect of flow velocity. Localized corrosion rates and standard error increased sharply at velocities higher than 13 m/s, from 2.9 ± 0.8 to 7.5 ± 1.2 mm/y. Note that corrosion rates calculated by maximum penetration at low velocities were much higher (about 3 times) than those calculated by weight loss and that the ratios tend to decrease to about 2 at more elevated velocities. These results confirm the need of measuring the penetration rate and not relying solely on weight loss for calculating CO_2 corrosion rates.

These results can also be correlated with a change in the surface morphology. At low flow velocities, the specimens exhibited pitting and ring-worm corrosion, which implies high penetration but not covering a large area. At higher velocities, the tendency to suffer mesa-type corrosion (larger area) was found to increase, which may explain the reduction in the ratio penetration rate/weight loss corrosion. At 38 m/s, it was found that most of the internal surface had suffered mesa corrosion and that both localized and weight loss corrosion rates were close to 10 mm/y. At 62 m/s, corrosion morphology appeared to be uniform, with flow induced erosion marks. As mentioned before, weight loss corrosion rates at this high velocity were calculated to be higher than internal penetration rates, primarily due to external corrosion.

2Cr Steel

Corrosion rates of steels with 2 % Cr are shown in Figure 8. Analysis of variance of these results showed that weight loss corrosion rates seem to increase from 1.4 ± 0.8 mm/y at velocities lower than 13 m/s to a "plateau" at 3.5 ± 1.0, augmenting significantly at higher velocities.

One factor ANOVA for penetration rates obtained from 2Cr specimens, on the other hand, did show a significant flow velocity effect. Penetration rates increase sharply from 2.7 ± 0.8 mm/y, for superficial velocities lower than 13 m/s, up to 7.4 ± 0.6 mm/y at velocities higher than 20 m/s.

The corrosion morphology of 2 Cr specimens had similar tendency to the one found on C90. That is, pitting and ring-worm corrosion was predominant at low velocities and mesa corrosion between 20 to 38 m/s. At 62 m/s, 2 Cr steel specimens showed apparent uniform corrosion, with some flow induced erosion marks. Also, some external corrosion was evident, which accounted for the weight loss corrosion rates to be higher than the penetration rate.

Effect of Flow Velocity on Corrosion products.

Table 6 shows the primary corrosion products, as analyzed by x-ray diffraction, which were obtained for each material at different flow velocity ranges.

X-ray diffraction of corrosion products on C90 and 2Cr specimens showed iron carbonate ($FeCO_3$) as the main corrosion product at all velocities. Under these test conditions, iron carbonate layers were found not to be very adherent. This fact may increase the localized or mesa-type corrosion at the regions where the corrosion product is lost due to the flow effect.

L80 and line pipe materials also presented iron carbonate as the main corrosion product at low velocities (3-4 m/s). When the velocity increased, however, it was found a decrease in the relative intensity of iron carbonate peaks and an increase in the iron carbide x-ray diffraction signals.

Specimens exposed to superficial fluid velocities greater than 33 m/s did not show enough corrosion products to perform x-ray analysis.

Therefore, it is proposed that mass transfer or wall shear stress significantly affects corrosion product properties, by increasing precipitation kinetics, in similar way as reported by Ikeda et al[2,3] for the temperature effect. A similar effect has also been found in DFT galvanic coupling tests[17].

There also appears to be a relationship between the corrosion product and the morphology of attack. C90 specimens showed mesa corrosion at all superficial flow velocities, where the main corrosion product was iron carbonate. L80 specimens, on the other hand, presented mesa corrosion only at low velocities, where the main corrosion product was also iron carbonate, and changed to general corrosion at high velocities, where the primary corrosion product was iron carbide. This situation was similar for line pipe steel. This fact highlights the importance of concentrating research on the type of corrosion product and its relationship with material properties and environmental conditions to further assess the corrosion behavior in CO_2 environments.

Discussion

Experimental results have shown that superficial flow velocity significantly affects both the corrosion rate and the morphology of corrosion, and that velocity effect was dependent on the grade of the steel tested.

On Figures 9 and 10, the ratio between experimentally obtained penetration rates and those calculated from the de Waard and Milliams correlation[9], using average conditions of each test section (see Table 4), are shown as a function of calculated wall shear stress. The relative presence of each of the main corrosion products ($FeCO_3$, Fe_3C and Fe_3O_4) is also exhibited in these figures.

It can be seen that the calculated values were up to 10 times higher than the measured penetration rates, depending on the grade of steel and flow velocity or wall shear stress. This difference has been discussed in a previous communication[8] on basis of the inhibiting effect of the oil phase and on the grade of steel. Besides, the kinetics of CO_2 corrosion of steels in thin film electrolytes, typical of annular mist flow, may be significantly different to those in bulk electrolytes commonly used in laboratory experiments.

CO_2 Corrosion/Erosion of C90 and 2 % Chromium Steels

As shown in Figures 7 and 8, and summarized in Figure 9, carbon steel specimens tested with chromium content between 1 to 2 % showed penetration rate vs. superficial fluid velocity and wall shear stress curves typical of an erosion/corrosion process. From these figures, it can be identified a critical flow velocity Ve of about 13 m/s. This experimental erosion/corrosion critical velocity agreed very well with the values obtained from the API RP 14 E equation [1]

$$Ve = 0.3 \frac{C}{\rho^{1/2}} \qquad (2)$$

which were calculated to be comprised between 13.2 to 13.6 m/s, using the fluid density estimated by the CORRODIS computer model (ρ = 5.3 to 4.9 lb/ft^3 at average DFT testing conditions) and the recommended C value of 100. It is important to emphasize that the critical velocity should be, in general, function of the materials properties, as shown in previous communications[7,8].

Also, the critical erosion velocity coincided with the region of changing flow patterns from churn or transition flow to annular mist flow, as indicated by the 27 mm ID./test N°3 data point displayed on Figure 4. Therefore, results for carbon steels with 1-2 % Cr are consistent with the hypothesis that

the API formula is a reasonable indicator of the onset of the annular mist flow condition, as suggested by Smart [18].

Annular mist flow is the regime that occurs at high superficial gas velocities, and is characterized by the continuity of the gas phase along the pipe core and by the presence of a liquid phase moving partly as an annular film, on permanent contact with the pipe walls, and partially as drops or mist entrained in the gas core. Therefore, it has been proposed that the erosion/corrosion mechanism could be related to that of corrosion product removals by liquid impingement. Craig [19] developed the following equation for the erosive removal of corrosion product films by liquid impingement:

$$Ve = 0.3 \frac{C'}{\rho^{3/7}} \tag{3}$$

where C' is a constant that depends on the properties of the corrosion product, i.e., 150 for Fe_3O_4 and 90 for $FeCO_3$. Experimental results are again consistent with the erosion velocity calculated assuming $FeCO_3$ corrosion product (13.4 to 13.7 m/s). This equation would also predict the beneficial effect of the presence of a protective iron oxide film (Ve between 22 and 23 m/s).

The influence of multiphase flow velocity on corrosion has also been expressed in terms of the effect of the wall shear stress either on removing the corrosion products or on preventing their formation or adherence onto the pipe wall [4,20,21]. Therefore, a critical wall shear stress (or frictional pressure drop) would appear to be preferred engineering parameters, rather than a critical velocity to assess the onset of erosion/corrosion. From Figure 9, it is apparent that the critical wall shear stress is close to 80 N/m^2 for these two grades of steel. In general, the authors believe that critical wall shear stress should be function of the steel metallurgy, temperature, CO_2 partial pressure and mass transfer conditions, which in term would affect corrosion product properties.

Effect of velocity on CO_2 corrosion of L80 and Line/Pipe material

Fluid velocity affects steel specimens with chromium concentration lower than 0.5 % in a completely different way than steels with higher chromium content. As shown in Figures 5 and 6, and consolidated in Figure 10, L80 and line pipe steels presented a significant decrease in penetration rates at fluid velocities comprised between 13 m/s and 33 m/s. Also, the susceptibility to mesa or pitting corrosion was found to be negligible at these velocities.

This unexpected reduction on corrosion rates with increasing fluid velocities was correlated with a change in the morphology and composition of corrosion products [8]. As mentioned earlier, the corrosion products at low velocities were primary $FeCO_3$, whilst at high velocities, a tight thin film with a relatively high concentration of Fe_3C and Fe_3O_4 was found. This fact strongly suggests that flow velocity affects kinetics of iron dissolution and $FeCO_3$ nucleation, producing a more protective and erosion resistant film, taking advantage of an anchorage effect of the uncorroded Fe_3C (cementite) particles left behind. The significant increase in penetration rates at superficial velocities over 33 m/s (Wall Shear Stress of about 300 N/m^2) suggest the presence of an erosion/corrosion velocity, which is consistent with the onset of removal of this tight film.

Conclusions

A critical flow velocity of about 13 m/s, corresponding to a wall shear stress of about 80 N/m^2, was found for C90 and 2Cr steels, above which penetration rates increased substantially with velocity. This experimentally found critical velocity was close to the value calculated by the API RP 14E equation. This correlation, however, should not be generalized because the critical velocity depends on the steel and corrosion product properties.

Line pipe and L80 steels, with chromium content lower than 0.5 %, showed a completely different fluid velocity effect, with localized corrosion rates decreasing with increasing fluid velocities up to 33 m/s. This decrease in corrosion rate was related to an increase in the relative presence of Fe_3C and Fe_3O_4 in the corrosion products. At higher velocities, corresponding to wall shear stresses in the order of 300 N/m^2, penetration rates tend to increase due to erosion of the protective film.

The properties of corrosion products, under the same temperature and CO_2 partial pressure, was found to be associated not only to the chemical composition of materials, but also to the fluid velocity or wall shear stress. High fluid velocities affect kinetics of iron dissolution and $FeCO_3$ nucleation, producing a thin but more protective and erosion resistant film, taking advantage of an anchorage effect of the uncorroded Fe_3C particles left behind.

Acknowledgements

REFERENCES

1. Americam Petroleum Institute. Recommended Practice 14E (API RP 14E). Recommended Practice for Design and Installation of Offshore Production Platform Piping Systems. Washington DC, December 1981.

2. A. Ikeda, M. Ueda, S. Mukai. CO_2 Corrosion Behaviour and Mechanism of Carbon Steel and Alloy Steel. Paper 45. *CORROSION/83*. NACE. Anaheim. 1983

3. A. Ikeda, S. Mukai, M. Ueda.. Prevention of CO_2 Corrosion of Line Pipe and Oil Country Tubular Goods. Paper 289. *CORROSION/84*. NACE. New Orleans. 1984

4. *Meeting of the Advisory Board for The Erosion/Corrosion Research Center at the University of Tulsa.* Universtity of Tulsa. Nov. 1990.

5. G. Schmitt and W. Bücken. Effect of Inhibitors and Surfactants on the Fluid Dynamic Properties of Multiphase Annular Mist Flow in Carbon Dioxide Corrosion Systems. Paper 6. CORROSION 92. NACE 1992.

6. S.E. Lorimer, W.J. Daniels. Shell's CO_2 Corrosion Research Program at the Dynamic Test Facility. *CORROSION/87*. Paper 441. 1987.

7. A. Ikeda, M. Ueda, J.Vera, M. Castillo, A.Viloria. Introduction of New Dynamic Field Tester and Preliminary Results on Flow Effects on CO_2 Corrosion. Paper 48. *CORROSION/92*. NACE. Nashville. 1992.

8. J. Vera, A. Viloria, M. Castillo, A. Ikeda, M. Ueda. Flow Velocity Effect on Carbon Steel CO_2 Corrosion Using a Dynamic Field Tester. Proceeding of 1st Pan-American Corrosion and Protection Congress. Vol. I. p.115-139. Mar del Plata. Argentina. 1992.

9. C. de Waard, U. Lotz, and D.E. Milliams. Predictive Model for CO_2 Corrosion Engineering in wet natural gas pipelines. Paper 577. *CORROSION/91*. NACE. 1991.

10. CORRODIS. *A Computer Model for Optimizing Corrosion Design of Oil Production Facilities. Materials Technology Department.* INTEVEP S.A.

11. Y.Taytel, D. Bornea, A.E.Dukler. Modelling Flow Pattern Transitions for Steady Upward Gas-Liquid Flow in Vertical Tubes, *AIChE Journal*. May,1980.

12. H. Duns, Jr., N.C.J.,Ros. Vertical Flow of Gas and Liquid Mixtures from Boreholes, *Proc. 6th World Petroleum Congress*. Frankfurt. June 1963.

13. NAPS. J. Brill. The University of Tulsa.

14.. R. W. Fox and A.T. McDonald. Introduction to Fluid Mechanics. New York: John Wiley, 4th Edition. 1992.

15. A.E. Dukler, M. Wicks, ,III, R.G. Cleveland. Frictional Pressure Drop in Two Phase Flow: B. An Approach Through Similarity Analysis. AIChE Journal. pp 44-51. 1964.

16. J. Brill, D. Beggs. *Two Phase Flow in Pipes*. The University of Tulsa. Dec. 1988.

17. J. Morales, J. Vera, A. Viloria, A. Ikeda, M. Ueda. Galvanic Effects on CO_2 Corrosion of Carbon Steels. *Submitted to CORROSION 94*.

18. J.S. Smart, III. The Meaning of the API-RP-14-E Formula for Erosion Corrosion in Oil and Gas Production". *CORROSION/91*. paper 468. 1991.

19. B. Craig. Critical Velocity Examined for Effects of Erosion-Corrosion. *Oil and Gas Journal*. pp 99-100. May 27, 1985.

20. M.M. Salama, E.S.Venkatesh. Evaluation of API RP 14E Erosional Velocity Limitations for Offshore Gas Wells". *Proceeding of OTC Conference*. paper 4485. 1983.

21. J.L Dawson, C.C. Shih. Corrosion Under Flowing Conditions - An Overview and Model". CORROSION/90.Paper 21. 1990.

TABLE 1.
CHEMICAL COMPOSITION OF MATERIALS TESTED.

MATERIAL	TYPE	C	Si	Mn	P	S	Cu	Cr	Mo	Ti	Nb
L80	BAR	0.24	0.27	1.04	0.017	0.014	0.01	0.2	<0.1	0.03	<0.01
	PIPE	0.24	0.28	1.19	0.018	0.009	0.01	0.5	<0.1	0.03	<0.01
C90	BAR	0.27	0.31	0.48	0.004	0.003	0.01	1.0	0.5	0.02	0.03
	PIPE	0.27	0.32	0.49	0.004	0.004	0.01	1.0	0.5	0.02	0.03
21/4Cr-1Mo	BAR	0.11	0.30	0.43	0.016	0.005	0.02	2.1	1.0	<0.01	<0.01
2Cr-Nb	PIPE	0.04	0.28	0.98	0.002	0.003	<0.01	1.9	<0.1	<0.01	0.03
C-Steel (L/P)	BAR	0.08	0.22	1.13	0.007	0.001	0.30	<0.1	<0.1	0.02	0.04

TABLE 2.
MECHANICAL PROPERTIES OF MATERIALES TESTED.

MATERIAL	TYPE	Y.S (Kg/mm2)	Y.S (MPa)	T.S (Kg/mm2)	T.S (MPa)	E l (%)	R.A (%)
L80	BAR	49.5	4.85	62.1	6.08	30.8	76.4
	PIPE	61.6	6.03	73.6	7.21	26.4	75.0
C90	BAR	58.8	5.76	70.6	6.92	28.4	74.1
	PIPE	66.8	6.54	76.4	7.49	27.2	74.2
21/4Cr-1Mo	BAR	56.0	5.49	65.8	6.45	30.8	82.6
2Cr-Nb	PIPE	35.4	3.47	56.6	5.54	28.0	71.6
C-Steel(L/P)	BAR	37.1		46.2		42.4	85.3

TABLE 3.
TYPICAL GAS COMPOSITION DURING TESTS AT THE JM-101 WELL.

Component	% Molar
CO_2	6.65
C1	90.36
C2	1.49
C3	0.56
IC4	0.14

TABLE 4.
AVERAGE OPERATING CONDITIONS OBTAINED FOR EACH TEST AND ID SECTION AND ESTIMATED CORROSION RATES.

TEST	ID	Pp CO_2		TEMP		Vs		D&M Vcorr
	mm	MPa	psi	°C	°F	m/s	ft/s	mm/y
2nd	52	0.71	104	82	180	2.8	9	12.5
	27	0.71	103	81	178	10.2	33	12.7
	20	0.70	102	76	169	18.5	61	13.5
	15	0.69	101	76	169	33.1	109	13.5
3rd	52	0.75	109	79	175	3.5	11	13.0
	27	0.74	108	79	175	13.0	43	13.0
	20	0.73	107	78	173	23.9	78	13.2
	15	0.73	107	77	170	42.3	139	13.3
5th	52	0.65	94	82	180	10.3	34	12.4
	27	0.65	94	85	185	38.1	125	12.0
	20	0.71	104	85	185	62.4	205	12.0

TABLE 5
ESTIMATED FLOW PATTERNS AND WALL SHEAR STRESS AT TEST SECTIONS.

TEST	SECTION I.D.(mm)	Vsg (m/s)	Vsl (m/s)	WSS (N/m^2)	N_{gv}	N_{Lv}	flow pattern*
2nd	52	2.8	0.01	21	23.9	0.10	slug flow
	27	10.2	0.04	57	88.2	0.36	transition
	20	18.4	0.08	126	159.6	0.66	anular mist
	15	32.9	0.14	281	285.5	1.17	anular mist
3rd	52	3.5	0.01	24	31.1	0.12	slug flow
	27	13.0	0.05	80	116.1	0.46	transition
	20	23.8	0.09	180	213.2	0.84	anular mist
	15	42.2	0.17	398	377.7	1.49	anular mist
5th	52	10.3	0.04	47	89.2	0.31	transition
	27	38.0	0.13	245	329.9	1.14	anular mist
	20	62.2	0.24	658	539.9	2.07	anular mist

N_{Lv} = 1.938 Vsl $(\rho_{liq}\,\gamma)^{-1/4}$
N_{gv} = 1.938 Vsg $(\rho_{liq}\,\gamma)^{-1/4}$
Vsl = Superfitial liquid velocity
Vsg = Superfitial gas velocity
ρ_{liq} = Liquid (water + condensate) density (lb/ft^3)
γ = Surface tension (dyne/cm)

TABLE 6.
X-RAY DIFFRACTION ANALYSIS OF CORROSION PRODUCTS

MATERIAL	V (m/s)	FeCO$_3$	Fe$_3$C	Fe$_3$O$_4$
L/P	3-4	s	w	m
	10-15	-	s	-
	18-23	w	s	s
	33-62	*	*	*
L80	3-4	s	w	-
	10-15	s	m	m
	18-23	w	s	w
	33-62	*	*	*
C90	3-4	s	ww	-
	10-15	s	w	-
	18-23	s	w	-
	33-62	*	*	*
2CrNb	3-4	s	w	w
	10-15	s	ww	-
	18-23	s	w	-
	33-62	*	*	*

s: strong (80-100%)   m: medium (50-79%)

w: weak (20-49%)   ww very weak (<15%)

* : Not detectable.
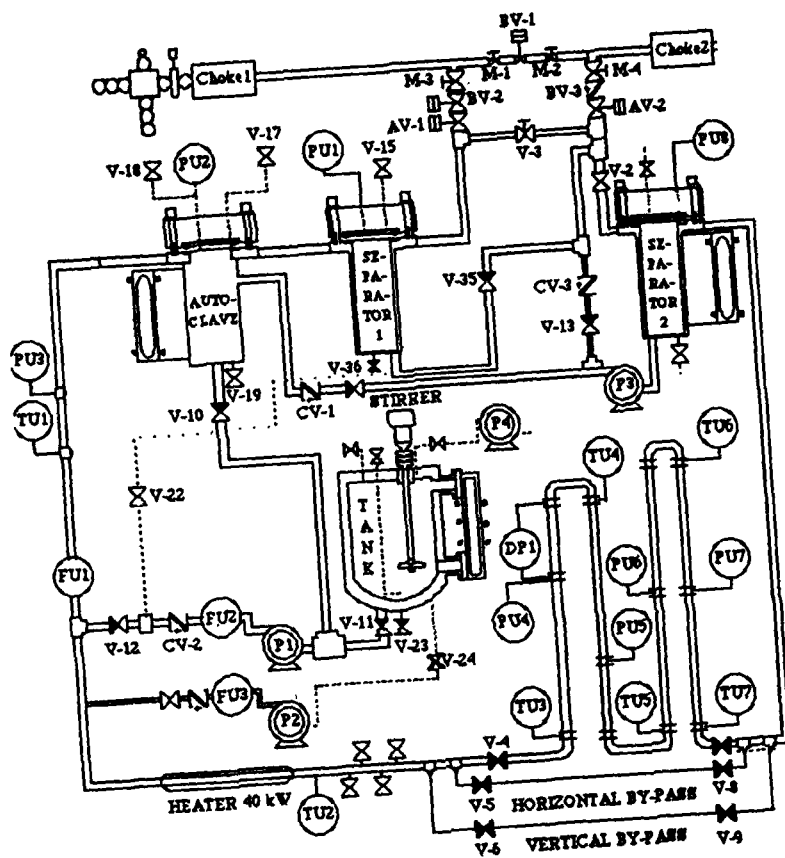
Figure 1   Flow model schematics of the DFT.
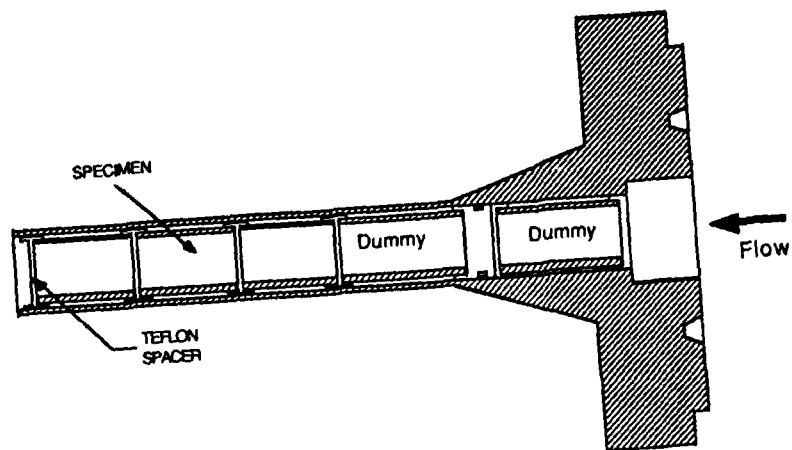
Figure 2   Schematics of tubular specimen arrangement used in studying flow effect on CO_2 corrosion of carbon steels.
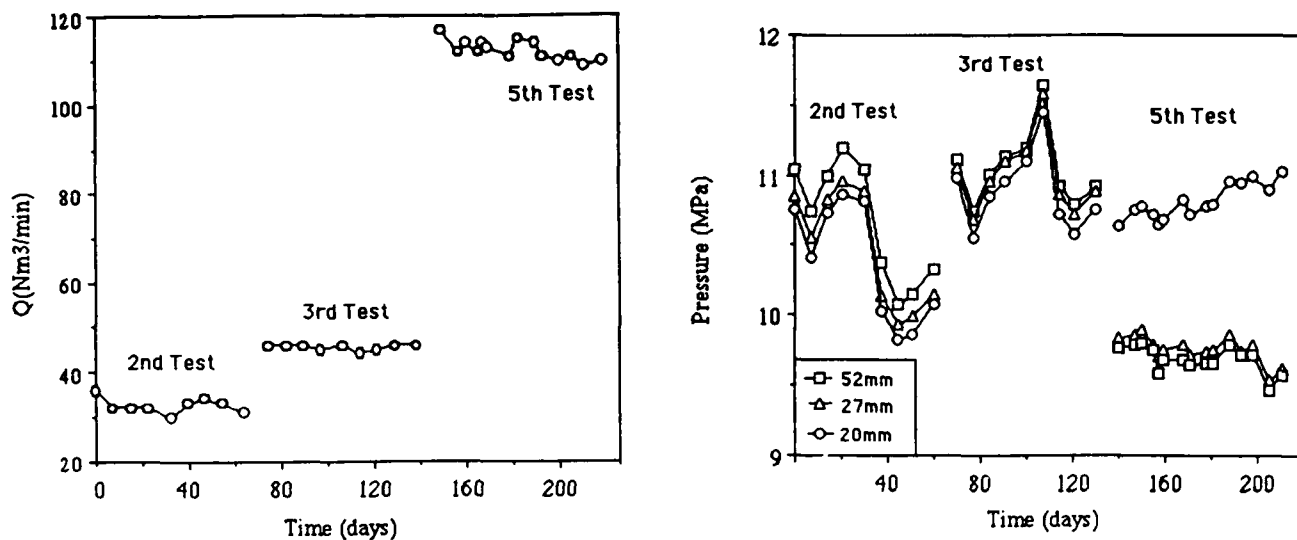
Figure 3   Variations in Pressure and Gas Flow Velocity Q during 2nd, 3rd and
5th DFT Test.
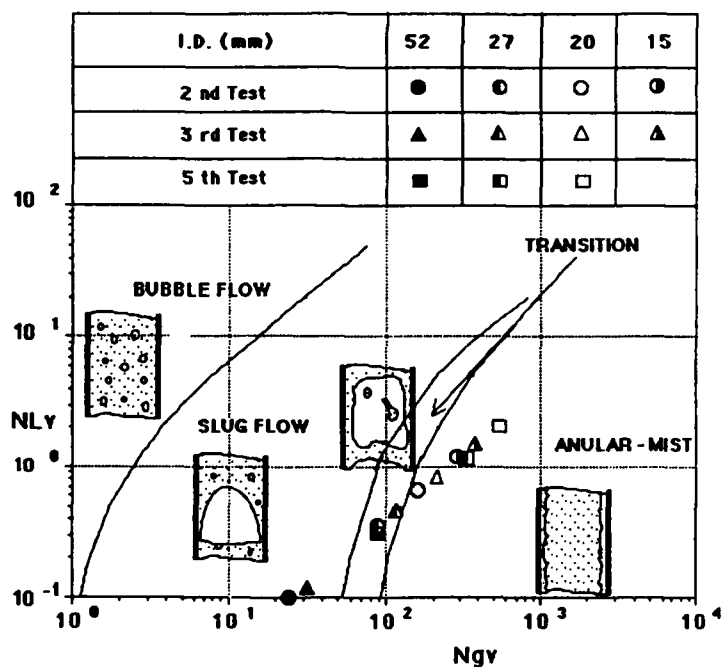
Figure 4   Typical Vertical Two-phase Flow regime map, showing the conditions
of Test N° 2, 3, and 5.
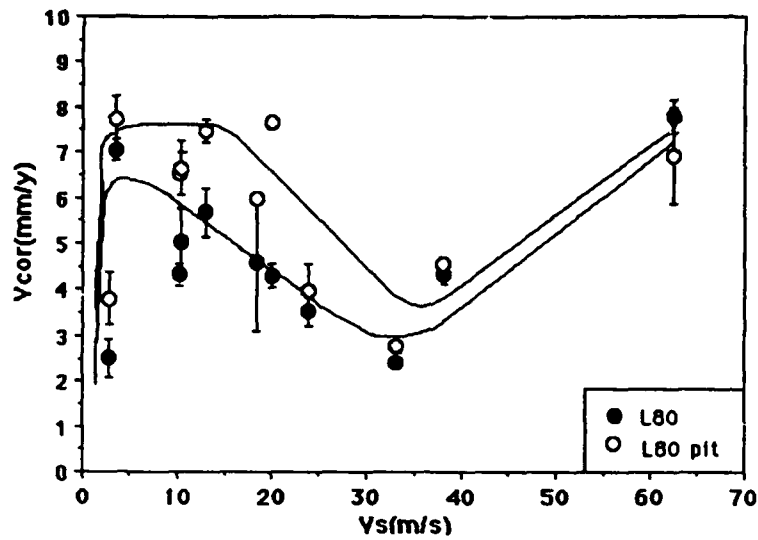
Figure 5   Effect of flow velocity on L80 uniform and localized corrosion rate.
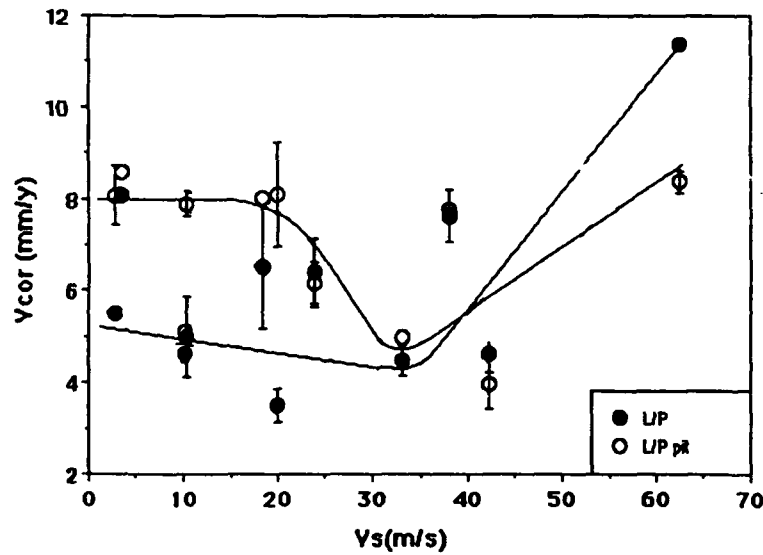
Figure 6   Effect of flow velocity on line pipe steel uniform and localized corrosion rate.
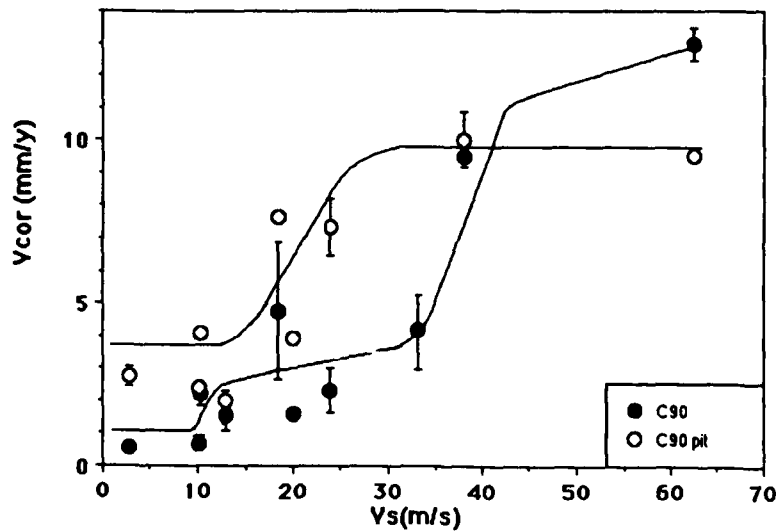
Figure 7   Effect of flow velocity on C90 uniform and localized corrosion rate.
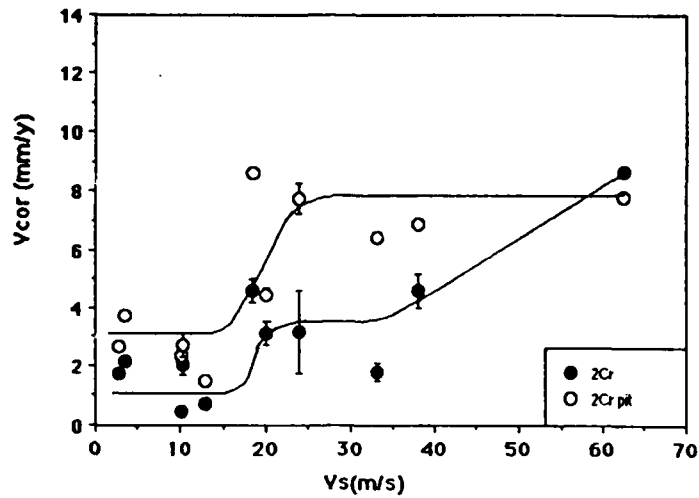
Figure 8   Effect of flow velocity on 2Cr steel uniform and localized corrosion rate.
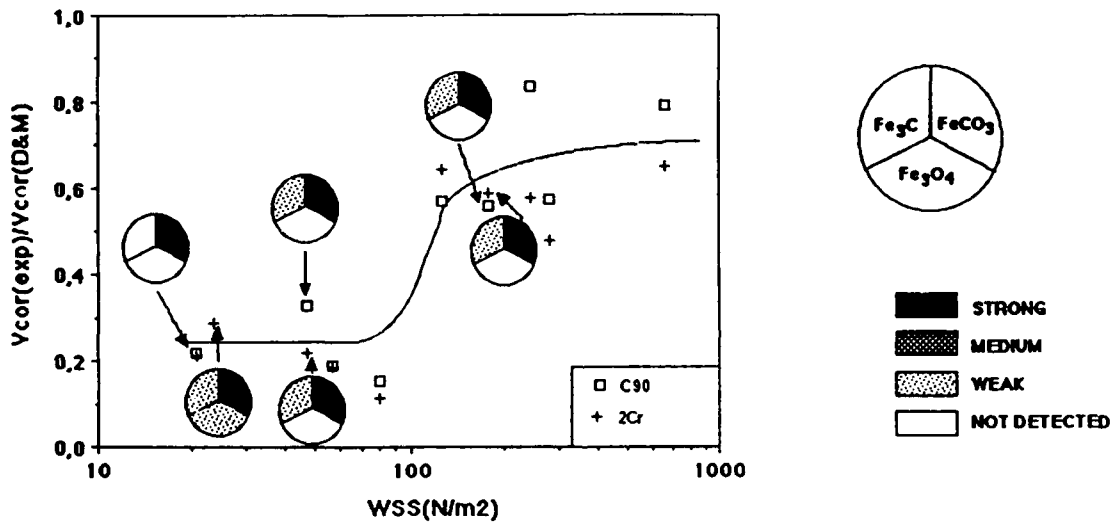
Figure 9   Effect of wall shear stress on the ratio between experimental corrosion rates obtained for C90 and 2 Cr steels and those calculated using new de Waard & Milliams correlation.
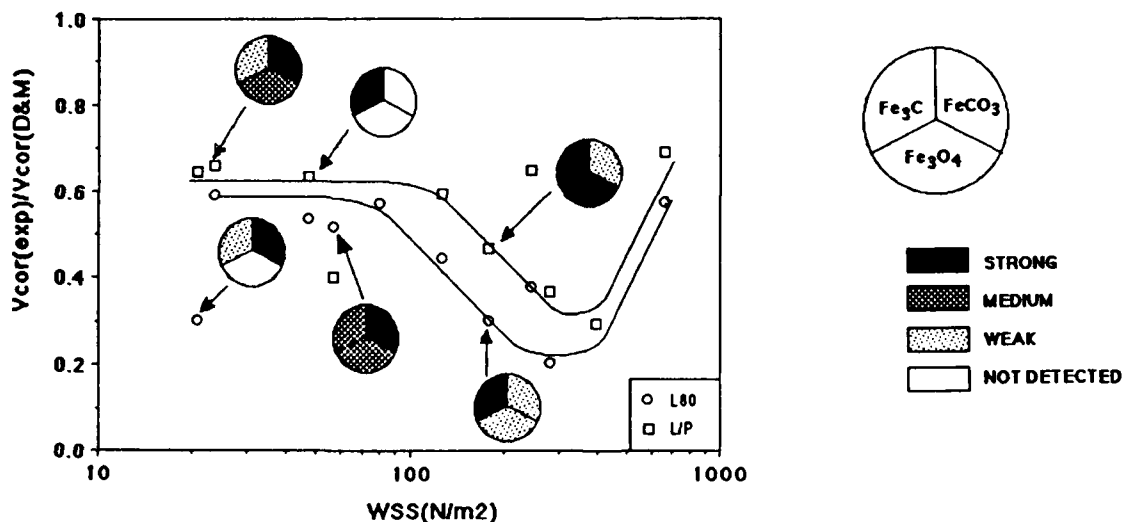
Figure 10 Effect of wall shear stress on the ratio between experimental corrosion rates obtained for L80 and line pipe steels and those calculated using new de Waard & Milliams correlation.

A Proposed Mechanism for Corrosion in Slightly Sour Oil and Gas Production

Stephen N. Smith
Exxon Production Research Co.
P.O. Box 2189
Houston, Texas 77001

Abstract

A corrosion model is proposed to explain corrosion in oil and gas production environments that contain CO_2 and small quantities of H_2S. Although a number of studies have been conducted into the mechanism of corrosion by CO_2 and there has been some study of the corrosion mechanism by H_2S, information about the transition between these corrosion mechanisms has not received much attention. The proposed model is based upon the formation of a meta-stable form of iron sulfide, mackinawite, which has been observed as a corrosion product both in the laboratory and in the field. Mackinawite has been observed as the corrosion product that forms when small concentrations of H_2S are present in the corrosive fluids. A simple partial pressure or solution concentration guideline for the amount of H_2S required to form mackinawite on the iron surface cannot be developed since factors such as temperature, H_2S activity, pH and the ionic strength of the solution are all involved in the determination of the conditions required for formation. Mackinawite is believed to form as a surface reaction between the H_2S in solution and the iron rather than as a precipitation reaction of ferrous sulfide from solution. Therefore, even when the conditions for mackinawite formation are favorable on the iron surface, mackinawite can remain soluble in the bulk solution. This means that as mackinawite forms on the surface, the mackinawite immediately begins to dissolve. However, since the formation reaction has been shown to be much more rapid than the dissolution reaction, a mackinawite film will form and influence the rate of further corrosion.

The interface between the mackinawite region and the CO_2 corrosion region is believed to be independent of the CO_2 corrosion reaction and is defined solely by the chemistry of mackinawite formation. As the concentration of H_2S is increased, an upper H_2S boundary to the mackinawite region is reached. This boundary is defined by the conditions where the solubility product for iron sulfide is exceeded. Under these conditions the thermodynamically stable iron sulfide, pyrrhotite, precipitates on the metal surface. Once pyrrhotite forms, any remaining mackinawite rapidly dissolves or transforms to the slower growing pyrrhotite.

Key terms: Mackinawite, Sour Corrosion, H_2S Corrosion

Introduction

The formation of an iron sulfide corrosion product at low H_2S concentrations can have many practical implications to oilfield corrosion control. Several situations have been encountered in which the change from a CO_2 controlled reaction to H_2S controlled corrosion altered the corrosion rate and the physical location of the most corrosive point within the production system. In some cases, the changeover increased corrosion and in others the change significantly reduced the amount of corrosion to levels below what was expected. The morphology of corrosion is also generally different between CO_2 and H_2S control. Where CO_2 corrosion often produces either general or mesa corrosion, H_2S control is typified by discrete local pitting attack. Thus, the change can have an important effect upon design factors such as corrosion allowance considerations or in the selection and location of the most appropriate corrosion monitoring system.

Although a number of studies of the CO_2 corrosion mechanism have been conducted and there has been some study of the corrosion mechanism by H_2S, the transition region between these two corrosion mechanisms in environments with low to moderate levels of CO_2 and H_2S has not received much attention. This is especially true in the oil and gas industry where the majority of the effort has concentrated on defining the mechanism of CO_2 corrosion and the remaining research has looked at the mechanism of corrosion in high concentrations of H_2S and/or elemental sulfur.

For corrosive conditions where CO_2 is present with virtually no H_2S, the current theories state that the corrosion mechanism will be determined by the fate of the Fe^2 ion corrosion product. If the Fe^2 remains in solution, the corrosion mechanism will follow the chemistry originally described in deWaard and Milliams[1,2]. If conditions conducive to $FeCO_3$ formation are favorable, further corrosion is determined by the quantity and quality of the $FeCO_3$ corrosion product[3,4]. When significant concentrations of H_2S are present in the system, the corrosion mechanism is controlled by the formation of the pyrrhotite form of FeS[5-7]. None of these mechanisms explains the formation of the mackinawite form of iron sulfide that was originally named kansite by Prange[8]. The practical existence of mackinawite as a corrosion product has subsequently received extensive discussion[8-14].

In work performed at the Canadian AEC[10,15-20], a mechanism for the formation of a mackinawite scale was reported for the Girdler-Sulfide method for concentrating heavy water, which utilizes H_2S. The Girdler-Sulfide H_2S concentrations studied were significantly lower than those studied by Ramanarayanan[5,6] and Vedage[7]. The mackinawite corrosion product may therefore exist somewhere between the two CO_2 corrosion regions (Fe^2 and $FeCO_3$) and the pyrrhotite corrosion product region, as illustrated in Figure 1.

This paper will utilize the work of the Canadian AEC and others[10-24], to propose a mechanism for mackinawite formation under oilfield production conditions. The paper will also describe the proposed chemistry required for mackinawite formation. Methods for predicting the boundary conditions that separate the mackinawite region from the other three corrosion product regimes are also discussed along with suggestions for further laboratory work to verify the model.

Mackinawite

Mackinawite was first identified as a corrosion product by Prange[8], who named it kansite. Prange identified mackinawite as the corrosion product that had been observed in a number of sour oil production systems in Kansas and West Texas. The official mineralogical name, Mackinawite, was adopted many years later in 1964[21]. Early corrosion literature citations of kansite are therefore usually describing mackinawite.

Mackinawite is a thermodynamically meta-stable form of iron sulfide. Mackinawite will decompose to the pyrrhotite form of iron sulfide. However, provided favorable conditions are maintained, this decomposition may

not occur for weeks or months. Like pyrrhotite, mackinawite is ferromagnetic and can be highly reactive when fine powders are exposed to oxygen.

Mackinawite exists as the non-stoichiometric form of iron sulfide with the imbalance toward the ferrous ion side. Although the non-stoichiometry has not been proven to be an excess of ferrous ions, as opposed to sulfide ion vacancies, some literature seems to favor the excess ferrous ion option[12, 13] where the composition would be expressed as $Fe_{(1+x)}S$. Other literature[22] presents evidence that mackinawite may exist as the sole example of a sulfur deficient metal sulfide. In this case the composition would be expressed as $FeS_{(1-x)}$.

Mackinawite Corrosion Mechanism

Thermodynamics favors either pyrrhotite or pyrite as the iron sulfide corrosion product over mackinawite. However, the rapid formation kinetics of mackinawite appear to give it the edge as the initial iron sulfide corrosion product. Mackinawite can be observed to form rapidly (virtually instantaneously) on the surface of carbon steel coupons dipped into H_2S saturated deionized water at room temperature. Shoesmith[15] proposed that "the first stage in the corrosion of carbon steel in aqueous H_2S is the formation of a mackinawite layer, via a solid-state mechanism."

An explanation for the preference for solid-state mackinawite formation over pyrrhotite is that the equilibrium Fe^2 and H_2S concentrations in the bulk solution are not conducive to pyrrhotite precipitation as determined by the pyrrhotite solubility product. However, the activity of Fe^2 on a carbon steel surface approaches 1.0 since the Fe activity on the solid steel surface is defined as 1.0. If the combination of the increased Fe^2 ion activity and the local H_2S activity exceeds the equilibrium constant for mackinawite formation on the metal surface, a mackinawite tarnish will form as a surface reaction on the steel. Rickard[23] studied kinetics of this reaction and found them to be extremely fast. Mackinawite was observed after exposures of less than 0.1 seconds in solutions of 10^{-3} M Na_2S at pH 7.0. By comparison, pyrrhotite formation kinetics appear to be quite slow. Shoesmith[16] and Wikjord[20] both reported observing troilite (stoichiometric FeS) and pyrrhotite only after exposures greater than 5 hours. Mackinawite formation would therefore be favored kinetically over pyrrhotite.

However, if the Fe^2 activity of the bulk solution is below the solubility product for mackinawite, the mackinawite is still soluble and will immediately begin to dissolve as the Fe^2 ions diffuse away from the steel surface. If the Fe^2 activity of the bulk solution is above the solubility product for the more stable FeS, pyrrhotite, FeS will start to precipitate from solution. The driving force for mackinawite dissolution will also be reduced as the Fe^2 ion concentration increases. This combination provides the conditions that are conducive to pyrrhotite formation.

Since mackinawite formation kinetics are so fast, Tewari[10] found that the rate of corrosion on a mackinawite covered surface is determined by the combined FeS dissolution and corrosion product diffusion reactions. In fact, Tewari hypothesized the existence of an $Fe(HS)^+$ complex based upon his corrosion product diffusivity values. Shoesmith[16], Taylor[17] and Ogundele[24] also have discussed the existence of an $Fe(HS)^+$ complex based upon FeS dissolution.

Therefore, mackinawite would be expected to form under conditions where the combined Fe^2 and H_2S bulk solution activities are inadequate to precipitate FeS, but where the H_2S activity is sufficient to form mackinawite if the Fe^2 activity on the steel surface is assumed to be 1.0. As illustrated in Figure 2, the H_2S diffuses to the metal surface and reacts with the steel surface to first form adsorbed molecular FeS which then combines to form mackinawite. However, since the FeS is still soluble in the bulk solution, the mackinawite immediately begins to dissolve to form $Fe(HS)^+$, probably through a reaction sequence such as:

$$FeS + H_2S \rightarrow Fe(HS)_2 \rightarrow Fe(HS)^+ + HS^- \qquad (1)$$

As soon as the Fe(HS)$^+$ has had an opportunity to diffuse away, a fresh steel surface is exposed which can immediately react with the H$_2$S to form more mackinawite. The mechanism therefore assumes the following:

- FeS(pyrrhotite) is saturated in solution,
- H$_2$S will diffuse toward the Fe surface,
- A reaction between Fe and H$_2$S occurs on the surface to form FeS,

- FeS begins to dissolve to form Fe(HS)$^+$ and HS$^-$,
- The Fe(HS)$^+$ diffuses away from the metal surface, and
- More H$_2$S immediately moves in to react with the exposed Fe.

This produces a very thin tarnish of mackinawite that is continually forming and dissolving. This is consistent with observations where mackinawite is never observed as the thick scale that often forms when pyrrhotite is the corrosion product. This also explains the poor x-ray diffraction patterns frequently encountered with mackinawite. Tne thin FeS film, combined with the extremely fine crystal size found in a tarnish layer, produces a very broad set of diffraction peaks, as illustrated in Figure 3. This occurs even for the (001) crystal lattice reflection that produces the 100% I peak for mackinawite[21]. This often results in mackinawite not being detected by routine, computerized x-ray diffraction analyses as the peak is too broad for the computer to identify. The problem is further complicated by the low angle diffraction produced by the 5.03 Å spacing of the (001) plane, which can disappear into the background noise produced by the commonly used Cu-K$_\alpha$ excitation signal.

Definition of Corrosion Product Boundaries

Assuming that this explanation for mackinawite formation is correct, the boundary conditions between the mackinawite corrosion product region and the other corrosion products can be defined.

Boundary with Fe^2 Region

Since most oilfield waters have pH values in range of 3 to 6, the majority of the aqueous sulfide found in oilfield waters exists as H$_2$S rather than as HS$^-$ or S^{-2} ions. The equilibrium reaction between the corrosion product regions for Fe^2 and mackinawite can be expressed by the reaction:

$$Fe^2 + H_2S \rightarrow FeS_{mackinawite} + 2H^+ \tag{2}$$

Although equilibrium constant information for mackinawite formation as a function of temperature is not known to be available, Berner[25] reported the standard free energy of formation for mackinawite and MacDonald[14] described a procedure to estimate mackinawite free energy as a function of temperature. The calculated free energy can then be used to develop a value for K$_{eq}$ as a function of T.

For temperature T and assuming a 1.0 molal activity of all reactants and products,

$$\Delta G^T_{reaction} = (G^T_{mackinawite} + 2 * G^T_{H^+}) - (G^T_{Fe^2} + G^T_{H_2S}) \tag{3}$$

Correcting for the fact that the reactants and products are normally not present at unit activity:

$$\Delta G^T_{reaction} = \Delta G^T_{reaction} - RT \ln K_{FeS} \tag{4}$$

where the equilibrium constant for reaction described by equation 2 is:

$$K_{FeS/Fe^2} = \frac{(a_{mackinawite} * (a_{H^+})^2)}{(a_{Fe^2} * a_{H_2Saq})} \tag{5}$$

where $a_{mackinawite}$ is the mackinawite activity on the tarnish surface,

     a_{H^+} is the H^+ activity in the solution,

     a_{H_2Saq} is the activity of the H_2S dissolved in the solution, and

     a_{Fe^2} is the Fe^2 activity in the solution.

The H_2S value that defines the mackinawite/Fe^2 boundary can then be calculated by equation 5. However, the activity of the H_2S dissolved in solution is generally not a readily available value. This can be corrected by determining the aqueous H_2S activity from the H_2S fugacity in the gas phase.

$$H_2S_{vap} \rightarrow H_2S_{aq} \tag{6}$$

$$K_{H_2Saq/H_2Svap} = \frac{a_{H_2Saq}}{a_{H_2Svap}} \tag{7}$$

Since $a_{mackinawite} \equiv 1.0$ and a_{Fe^2} is assumed equal to 1.0 on the surface, equations 5 and 7 can be combined and reduced to:

$$K_{FeS/Fe^2} = \frac{a_{H^+}^2}{K_{H_2Saq/H_2Svap} * a_{H_2Svap}} \tag{8}$$

It is interesting to note that critical H_2S activity for mackinawite formation is highly dependent upon pH. In fact, H^+ activity is a second order function and is therefore far more important than H_2S activity in defining the boundary. Attempts to use a single H_2S value, such as a gas phase concentration of 50 ppm, would therefore appear to be misguided without first specifying a pH.

Although this equation appears to be fairly simple, the fact that the H_2S values appear as activities, as opposed to an aqueous H_2S concentration or a gas phase partial pressure, makes application of this relationship difficult. If the aqueous phase H_2S solution concentration is known, the activity coefficient for dissolved H_2S, which often deviates substantially from 1.0, must be known before the boundary can be defined to any useful degree of accuracy. If a gas phase partial pressure of H_2S is known, then the fugacity coefficient must be defined and the gas and aqueous phases must be assumed to be in equilibrium before an aqueous phase H_2S activity can be determined.

Boundary with $FeCO_3$ Region

$FeCO_3$ is known to be the corrosion product that is favored at elevated temperatures when a mildly acidic aqueous solution containing dissolved CO_2 is the corrosive. Similar to the mackinawite/Fe^2 boundary, the boundary between the $FeCO_3$ and mackinawite regions can be defined by the reaction:

$$FeCO_3 + H_2S \rightarrow FeS_{mackinawite} + H_2CO_3 \tag{9}$$

Tabulated K_{eq} values as a function of temperature are available for $FeCO_3$ and using the thermodynamic data for mackinawite that was described above, an equilibrium constant for this reaction can be determined by:

$$K_{FeS/FeCO_3} = \frac{(a_{mackinawite} * a_{H_2CO_3})}{(a_{FeCO_3} * a_{H_2Saq})}$$

(10)

where $a_{mackinawite}$ is the mackinawite activity on the surface,

     $a_{H_2CO_3}$ is the solution activity of H_2CO_3,

     a_{H_2Saq} is the solution activity of H_2S, and

     a_{FeCO_3} is the $FeCO_3$ activity on the corrosion product surface.

However since $a_{solids} \equiv 1.0$, equation 10 becomes:

$$K_{FeS/FeCO_3} = \frac{a_{H_2CO_3}}{a_{H_2Saq}}$$

(11)

Since the vapor phase CO_2 activity is related to the H_2CO_3 solution activity through the following reactions, the usefulness of this expression can be enhanced by making the following substitutions for $a_{H_2CO_3}$ and a_{H_2Saq}.

$$H_2CO_3 \rightarrow H_2O + CO_{2aq}$$

(12)

$$K_{H_2CO_3/CO_2aq} = \frac{(a_{H_2O} * a_{CO_2aq})}{(a_{H_2CO_3aq})}$$

(13)

$$CO_{2vap} \rightarrow CO_{2aq}$$

(14)

$$K_{CO_2aq/CO_2vap} = \frac{a_{CO_2aq}}{a_{CO_2vap}}$$

(15)

Rearranging terms and substituting expressions 7, 13 and 15 for $a_{H_2CO_3}$ and a_{H_2Saq} into equilibrium expression 11, the equation becomes:

$$K_{FeS/FeCO_3} = \frac{a_{H_2O} * K_{CO_2aq/CO_2vap} * a_{CO_2vap}}{K_{H_2CO_3/CO_2aq} * K_{H_2Saq/H_2Svap} * a_{H_2Svap}}$$

(16)

This can be further simplified by combining the equilibrium constants into a single term and making the simplifying assumption that the activity of water is ≈ 1.0 to produce:

$$K_{FeS/FeCO_3} = C * \frac{a_{CO_2vap}}{a_{H_2Svap}}$$

(17)

If the oversimplifying assumption is made that activity equals partial pressure for CO_2 and H_2S in the gas phase, the form of this equation is consistent with the concept of critical CO_2/H_2S ratios that have been reported for various fields[26, 27].

Mackinawite Upper Temperature Boundary

Since mackinawite is a meta-stable phase of FeS, it is intuitively satisfying that there should be an upper temperature limit to the phase's meta-stability. Takeno[28, 29] synthesized mackinawite by reacting iron with a 1 atm solution of H_2S in distilled water at 50°C. He then heated the mackinawite under vacuum to temperatures ranging from room temperature to 300°C for periods up to 34 days. X-ray diffraction analyses were then conducted on the thermally treated FeS samples to determine the stability region for mackinawite.

Takeno found that mackinawite went through a solid state transformation to pyrrhotite at temperatures between 170° and 200°C. This was illustrated by the sample baked at 170°C for 30 days, which showed signs of both pyrrhotite and mackinawite whereas the 200°C sample was completely transformed to pyrrhotite. Taylor[17] stated that the upper limit of thermal stability is 130°C. Either way, it is not known whether this limit represents a theromodynamic limit or is somehow tied to the sluggish kinetics of the mackinawite/pyrrhotite transformation at this low temperature.

It is therefore possible to conclude that an upper boundary exists and that it appears to be somewhere in the range of 130° to 170°C. The transition temperature may be toward the lower end of the range if exposure times longer than Takeno used are considered.

Pyrrhotite Boundary

Studies of the mechanism that defines the low temperature boundary between the two iron sulfides, mackinawite and pyrrhotite, have not been reported. Extension of the mechanism proposed in this work to the pyrrhotite/mackinawite boundary presumes that the boundary is defined by the saturation of pyrrhotite in the bulk solution. If the solution is undersaturated with respect to pyrrhotite, then mackinawite tarnish will be the kinetically preferred iron sulfide corrosion product. As the solution activity of H_2S and Fe^2 ion (including $Fe(HS)^+$ and any other Fe/S complex ions that may exist) approaches the saturation value for pyrrhotite, the mackinawite dissolution reaction may slow or stop as the effects of the increased bulk Fe^2 activity reduce the Fe^2 ion flux from the surface. This provides the time required for pyrrhotite nucleation kinetics to form pyrrhotite crystals on the surface. The pyrrhotite crystals then grow, cover the surface and thereby gain control of the corrosion mechanism, as described by Ramanarayanan.

Therefore, the boundary between the mackinawite and pyrrhotite regions is defined by pyrrhotite saturation in the bulk solution. The boundary chemistry is determined in the same overall manner as the Fe/mackinawite boundary, except that a_{Fe^2} is no longer defined as 1.0 but is defined by the Fe^2 ion activity in solution and the K_{eq} is based upon the free energy of formation of pyrrhotite rather than mackinawite.

$$K_{pyrr/Fe^2} = \frac{(a_{pyrrhotite} * (a_{H^+})^2)}{(a_{Fe^2} * a_{H_2Saq})} \tag{18}$$

since $a_{pyrrhotite} \equiv 1.0$,

$$K_{FeS/Fe^2} = \frac{a_{H^+}^2}{(a_{Fe^2} * a_{H_2Saq})} \tag{19}$$

As with other activity values, extreme care must be taken when converting from solution concentrations to activity values. This is especially true for divalent ions like Fe^2. A modified Bromley formalism[30] for calculating activity coefficients was used to estimate the activity coefficient for Fe^2 in a 3 wt% NaCl solution at 50°C. The activity coefficient was determined to be less than 0.2. Using the simplifying assumption that the activity coefficient is equal to 1.0 would therefore result in the under-estimation of the critical Fe^2 content for pyrrhotite formation by a factor of _five_ times.

The complexing nature of Fe^2 ions in aqueous chloride media also complicates the matter of determining the critical Fe^2 level to form pyrrhotite. Oilfield produced water analysis procedures intentionally acidiz·· the water to yield a total iron ion value and this acidification breaks down most of the iron complexes that would be found in service. Only ferrous ions that exist as free Fe^2 or as $Fe(HS)_x^y$ complexes are probably available for the pyrrhotite formation reaction. If significant quantities of iron/chloride, iron/oxy-hydroxide and/or iron bicarbonate type complexes exist, they may reduce a_{Fe^2} sufficiently to influence the location of the pyrrhotite/mackinawite boundary.

Suggestions for Further Work to Verify Model

There is surprising little corrosion laboratory data reported about the formation of mackinawite. The vast majority of the work that is reported was conducted in water saturated with H_2S at atmospheric pressure and at temperatures significantly less than 100°C. The numerous difficulties in conducting carefully controlled experiments in this area certainly explains the limited volume of data. Besides the safety problems related to working with H_2S, the problems include:

- the meta-stability of mackinawite,
- the complication of the corrosion reaction consuming H_2S, which must be available in ppm level concentrations to limit pyrrhotite formation,
- changing Fe^2 ion buildup in solution through the experiment,
- the complication that the corrosion reaction increases the pH of the bulk solution by consuming H^+ and releasing HS^-, which decreases the calculated amount of H_2S required for mackinawite formation, and
- the physical difficulty of conducting experiments at the elevated temperatures and pressures representative of oilfield production conditions.

The answer to conducting this type of experiment is the use of a continuously replenished flow system that is capable of handling H_2S containing salt solutions at temperatures up to 150°C and 150 atmospheres. Such systems are complex, expensive to build and can be difficult to operate safely.

An additional area that needs to be addressed is the question of activity coefficients, especially for Fe^2, H^+, H_2S, and CO_2. Existing activity coefficient estimation procedures can be used, but their accuracy for highly concentrated oilfield brine solutions is debatable. This has been a long standing physical chemistry problem, so there is little hope for a theoretical breakthrough. However, collection of the multi-component interaction parameters specific to oilfield waters for the Bromley, Meissner or Pitzer activity coefficient formalisms might help to improve the accuracy of these predictions.

A final suggested area of research is the upper temperature meta-stability limit of mackinawite. Takeno conducted studies that lasted up to 34 days. Longer studies at more temperatures than just 170° and 200°C would help to improve the definition of the upper temperature limit of mackinawite.

Summary

The existence of a corrosion product regime between the sweet corrosion products, Fe^2 and $FeCO_3$, and the sour corrosion product pyrrhotite(FeS) has been postulated. The existence of this FeS corrosion product, mackinawite, has been confirmed in both the field and the laboratory. Equilibrium relationships between mackinawite and the other known corrosion products have been developed and are illustrated in the graph shown in Figure 4. The numbers on the graph reference the appropriate equations in the text.

However, application of these equilibrium relationships may be very difficult to achieve in the field. The thermodynamically non-ideal nature of oilfield gas and aqueous phases means that the use of solution concentrations and gas phase partial pressures for the activities of the various chemical species can introduce substantial errors. Unfortunately, calculation of activity coefficients in many oilfield brine systems is also not an accurate science with the current level of technology.

Therefore, extensive laboratory investigations will be required under carefully control conditions to confirm the corrosion model proposed by this paper. Even more investigation will then be required before the thermodynamic equilibrium relationships could be extended to the kinetic calculations that will be required to predict practical corrosion rates.

Bibliography

1. deWaard, C. and Milliams, D.E., "Prediction of Carbonic Acid Corrosion in Natural Gas Pipelines," Proc. First International Conference on the Internal and External Protection of Pipes. Paper F2. September 1975.
2. deWaard, C. and Milliams, D.E., "Carbonic Acid Corrosion of Steel," Corrosion, Vol. 31, No. 5, pp. 177-181, 1975.
3. Schmitt, G., "CO_2 Corrosion of Steels, An Attempt to Range P. .ameters and Their Effects," Advances in CO_2 Corrosion, NACE, Houston, 1984.
4. Burke, P.A., "Synopsis: Recent Progress in the Understanding of CO_2 Corrosion," Advances in CO_2 Corrosion, NACE, Houston, 1984.
5. Ramanarayanan, T.A. and Smith, S.N., "Scaling Phenomena in High Temperature Aqueous and Gaseous Environments Containing Sulfur," Proc. International Symposium of Corrosion Science and Engineering, Brussels, March 1989.
6. Ramanarayanan, T.A. and Smith, S.N., "Corrosion of Iron in Gaseous Environments and in Gas-Saturated Aqueous Environments," Corrosion, Vol. 46, No. 1, pp. 66-74, 1990.
7. Vedage, H., Ramanarayanan, T.A., Mumford, J.D. and Smith, S.N., "Electrochemical Growth of Iron Sulfide Films in H_2S Saturated Chloride Media," Corrosion, Vol. 49, No. 2, pp. 114-121, 1993.
8. Meyer, F.H., Riggs, O.L., McGlasson, R.L. and Sudbury, J.D., "Corrosion Products of Mild Steel in Hydrogen Sulfide Environments," Corrosion, Vol. 14, No. 2, pp. 69t-115t, 1958.
9. Smith, J.S. and Miller, J.D.A., "Nature of Sulfides and their Corrosive Effect on Ferrous Metals: A Review," Br. Corrosion J., Vol. 10, No. 3, pp. 136-143, 1975.
10. Tewari, P.H. and Campbell, A.B., "Dissolution of iron during the initial corrosion of carbon steel in aqueous H_2S solutions," Canadian J. Chemistry, Vol. 57, pp. 188-196, 1979.
11. Pankow, J.F. and Morgan, J.J., "Dissolution of Tetragonal Ferrous Sulfide (Mackinawite) in Anoxic Aqueous Systems, 1. Dissolution Rate as a Function of pH, Temperature and Ionic Strength," Environmental Science and Technology, Vol. 13, No. 10, pp. 1248-1255, 1979.
12. Pound, B.G., Abdurrahman, M.H., Glucina, M.P., Wright, G.A. and Sharp, R.M., "The Corrosion of Carbon Steel and Stainless Steel in Simulated Geothermal Media," Australian J. Chemistry, Vol. 38, pp. 1133-1140, 1985.
13. Pound, B.G., Wright, G.A. and Sharp, R.M., "The Anodic Behavior of Iron in Hydrogen Sulfide Solutions," Corrosion, Vol. 45, No. 5, pp. 386-392, 1989.
14. MacDonald, D.D. and Hyne, J.B., "The Thermodynamics of the Iron/Sulfide/Water System," Atomic Energy of Canada Ltd. Report AECL-5811, 1979.
15. Shoesmith, D.W., "Formation, Transformation and Dissolution of Phases Formed on Surfaces," Lash Miller Award Address, Electrochemical Society Meeting, Ottawa, Nov. 27, 1981.

16. Shoesmith, D.W., Taylor, P., Bailey, M.G. and Owen, D.G., "The Formation of Ferrous Monosulfide Polymorphs during the Corrosion of Iron by Aqueous Hydrogen Sulfide at 21°C," J. Electrochemical Society, Vol. 127, No. 5, pp. 1007-1015, 1980.

17. Taylor, P., "The stereochemistry of iron sulfides -- a structural rationale for the crystallization of some metastable phases from aqueous solution," American Mineralogist, Vol. 65, pp. 1026-1030, 1980.

18. Tewari, P.H., Wallace, G. and Campbell, A.B., "The Solubility of Iron Sulfides and Their Role in Mass Transport in Girdler-Sulfide Heavy Water Plants," Canadian Atomic Energy Commission, Report AECL-5960, 1978.

19. Tewari, P.H., Bailey, M.G. and Campbell, A.B., "The Erosion-Corrosion of Carbon Steel in Aqueous H_2S Solutions Up to 120°C and 1.6 MPa Pressure," Corrosion Science, Vol. 19, pp. 573-585, 1979.

20. Wikjord, A.G., Rummery, T.E., Doern, F.E. and Owen, D.G., "Corrosion and Deposition During the Exposure of Carbon Steel to Hydrogen Sulfide-Water Solutions," Corrosion Science, Vol. 20, pp 651-671, 1980.

21. Milton, C., "Kansite = Mackinawite, FeS", Corrosion, Vol. 22, No. 7, pp. 191-192, 1966.

22. Morse, J.W., Millerao, F.J., Cornwell, J.C. and Rickard, D., "The Chemistry of the Hydrogen Sulfide and Iron Sulfide Systems in Natural Waters," Earth Science Reviews, Vol. 24, pp. 1-42, 1987.

23. Rickard, D., "Experimental concentration-time curves for the iron(II) sulfide precipitation process in aqueous solutions and their interpretation," Chemical Geology, Vol. 78, pp. 315-324, 1989.

24. Ogundele, G.I. and White, W.E., "Some Observations on the Corrosion of Carbon Steel in Sour Gas Environments: Effects of H_2S and $H_2S/CO_2/CH_4/C_3H_8$ Mixtures," Corrosion, Vol. 42, No. 7, pp. 398-408, 1986.

25. Berner, R.A., "Tetragonal Iron Sulfide," Science. Vol. 137, p. 669, 1962.

26. Dunlop, A.K., Hassell, H.L. and Rhodes, P.R., "Fundamental Considerations in Sweet Gas Well Corrosion," Corrosion/83, Anaheim California, Paper 46.

27. Milliams, D.E. and Kroese, C.J., "Aqueous Corrosion of Steel by H_2S and H_2S/CO_2 Mixtures," Third International Conference on the Internal and External Protection of Pipes, London, Paper H1, September 1979.

28. Takeno, S. Zoka, H. and Niihara, T., "Metastable Cubic Iron Sulfide -- With Special Reference to Mackinawite," American Mineralogist, Vol. 55, pp. 1639-1649, 1970.

29. Takeno, S., "Thermal Studies on Mackinawite," J. Science Hiroshima Univ., ser. C, 4, pp. 455-478, 1965.

30. Zamaitis, J.F., Clark, D.M., Rafal, M. and Scrivner, N.C., Handbook of Aqueous Electrolyte Thermodynamics, Am. Inst. of Chemical Engr., New York, 1986.
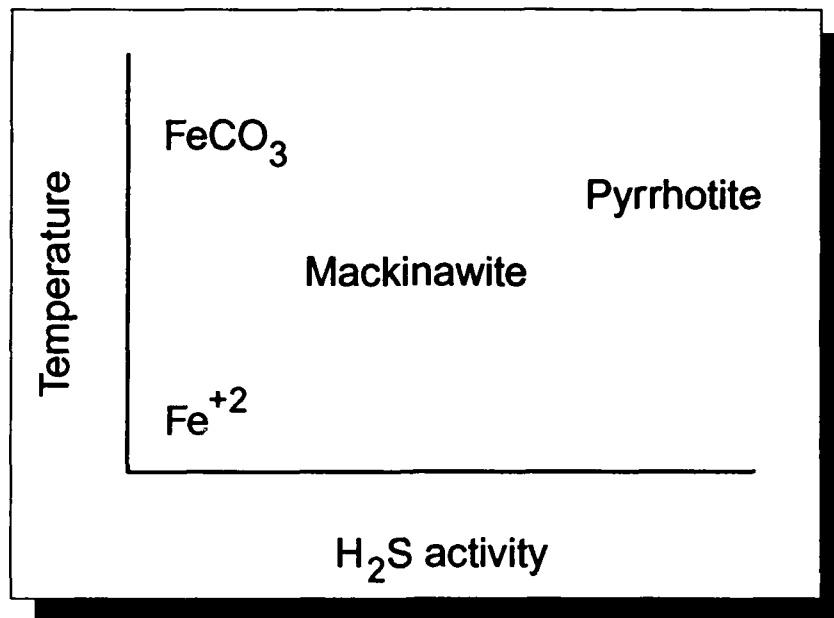
Relationship of Oilfield Corrosion Products
Figure 1
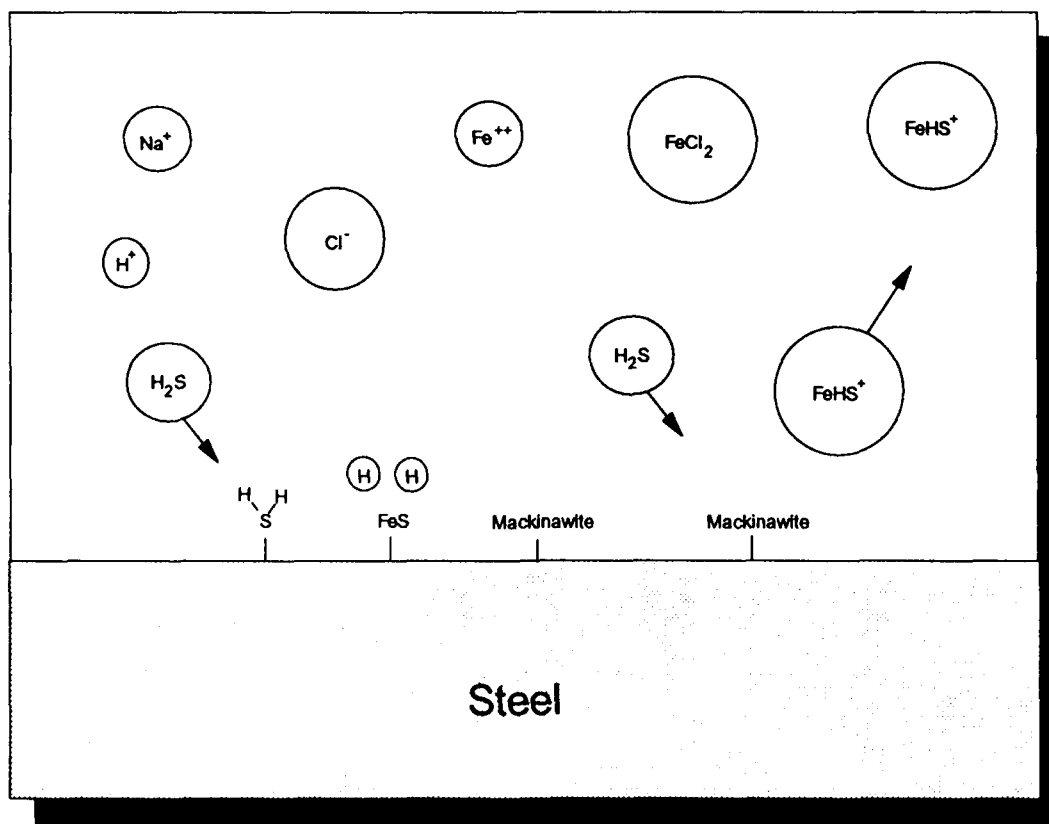
Slightly Sour Corrosion Surface Reactions
Figure 2
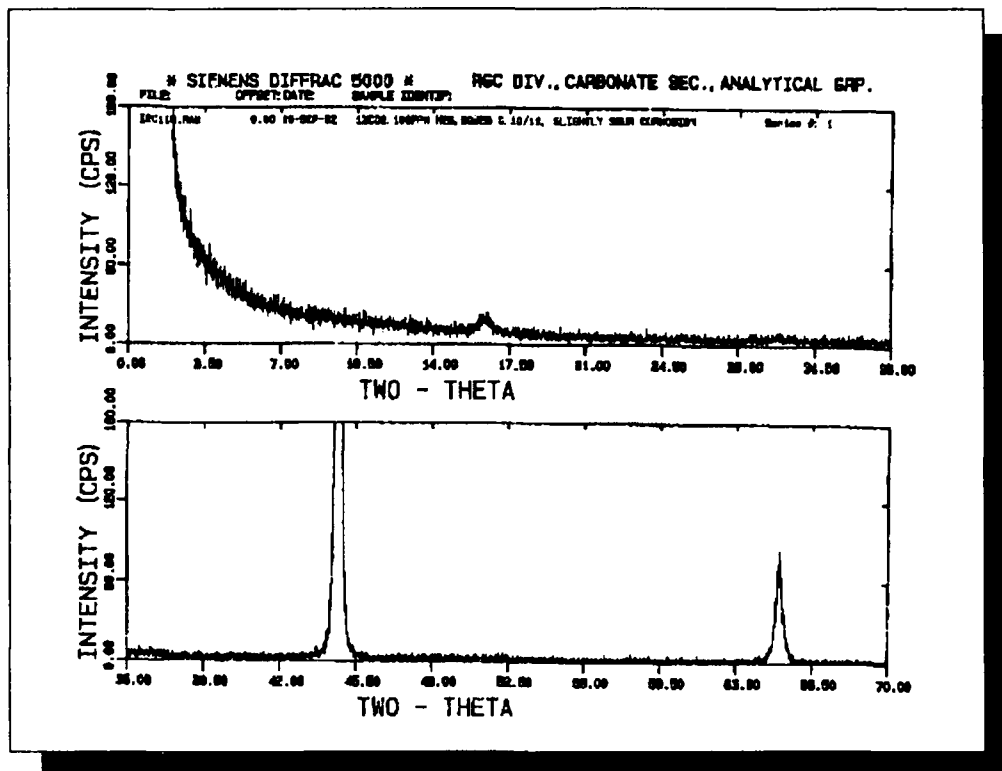
Typical X-ray Diffraction Pattern for Mackinawite Tarnish

Figure 3
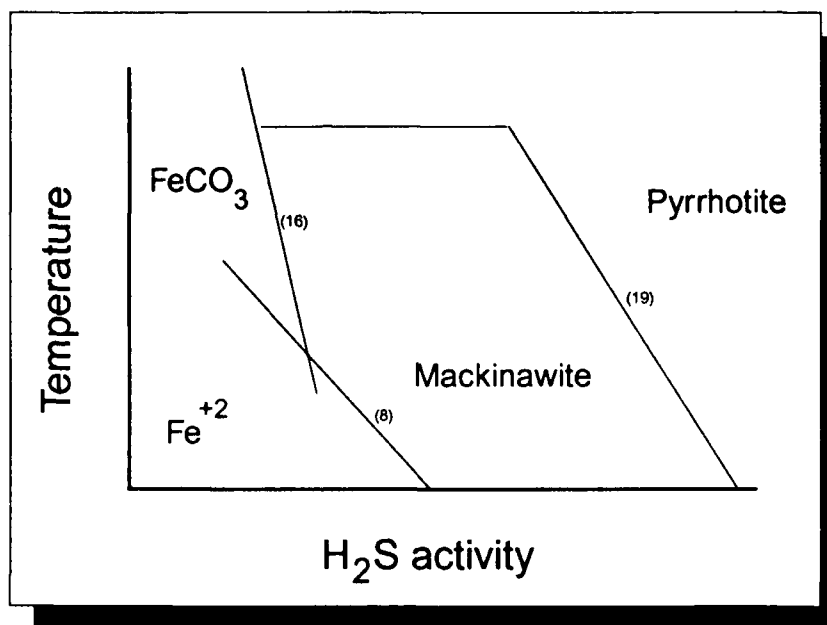
Relationship between Oilfield Corrosion Products
(Numbers Relate to Equation Number of Equilibrium Reaction in Text)

Figure 4

Rotating Cylinder Electrode (RCE) Simulation of Flow Accelerated Corrosion in Sweet Production

E. J. Wright, K. D. Efird, J. A. Boros and T. G. Hailey
Exxon Production Research Company
Houston, Texas, U. S. A.

Abstract

The major application of the rotating cylinder electrode in oil and gas operations is as a fluid flow corrosion test device for inhibitors. However, results reported previously[1] demonstrated that while steel corrosion rates measured in a CO_2-containing brine using a parallel pipe flow apparatus, and a jet impingement apparatus correlate with each other based on calculated wall shear stress, the RCE rotating cylinder corrosion rates do not correlate with either. Clearly, this lack of correlation has implications for the use of the RCE to simulate flow accelerated corrosion in sweet production. This paper presents the results of an investigation to determine first, why the RCE results do not correlate to parallel pipe flow based on the calculated wall shear stress, and second, whether the RCE can be modified to achieve correlation. Electrochemical corrosion testing of AISI 1018 carbon steel in CO_2-containing brines was carried out using direct current (DC) linear polarization and alternating current (AC) impedance techniques. Most of the tests were conducted in a 3.0 % NaCl aqueous solution with the addition of 1000 ppm HCO_3^- at a CO_2 partial pressure of 14.7 psia and a temperature of 50°C. The equation for the effect of calculated RCE wall shear stress on the carbon steel corrosion rate in this environment (for wall shear stresses in the range of $0.2 < \tau_w < 100$ N/m^2) is expressed in the form:

$$R_{COR} = 2.8\,\tau_w^{0.10}$$

where R_{COR} is the corrosion rate in mm/y and τ_w is the calculated wall shear stress. An equation of similar form is shown for pipe flow. However, the coefficient for the pipe is significantly higher, at 7.7, compared to 2.8, because the corrosion rate measured on the pipe is greater than that the RCE corrosion rate at an equivalent wall shear stress. Therefore, the RCE corrosion rate of carbon steel does not directly correlate with pipe flow corrosion rate as a function of calculated wall shear stress. Furthermore, the RCE corrosion rate of carbon steel does not directly correlate with pipe flow corrosion rate as a function of calculated mass transfer coefficients. Tests investigating the influence of CO_2 partial pressure and initial bicarbonate ion concentrations on the corrosion rate of carbon steel showed that the RCE responds very differently from pipe flow to changes in solution chemistry.

AC impedance data indicate that there are significant differences between the RCE and pipe flow electrodes. Specifically, there is increased polarization on the RCE, possibly resulting from film formation and also an inductive loop indicating the presence of an adsorbed film. Scanning electron microscope examinations of the RCE surface after corrosion testing confirmed the presence of a film ~ 2 microns in thickness which is probably iron carbonate. These results suggest that a localized environment exists around the RCE that is conducive to film formation and therefore less corrosive than in pipe flow. This is probably the principal reason the RCE corrosion rate does not correlate with pipe flow and also why the RCE does not respond to the effects of solution chemistry on the corrosion rate similar to pipe flow. Experiments using RCE electrodes of different diameters and using a rotating *strip* electrode did not overcome the basic problem of lack of correlation with pipe flow.

In conclusion, these results indicate that the RCE cannot be used to simulate correctly flow accelerated corrosion of carbon steel to scale up to sweet production.

Key terms: carbon dioxide, flow accelerated corrosion, rotating cylinder electrode, sweet corrosion, wall shear stress.

Introduction

There is a need for a realistic laboratory corrosion fluid flow test facility to investigate the corrosion behavior of carbon steel in CO_2-brine environments. However, it is difficult to simulate effectively both the chemistry and the flow components of the sweet production environment in the laboratory. The traditional approach used for such investigations is a flow loop that is generally large and expensive both in terms of capital and operational costs. There is, therefore, an incentive to investigate the use of other techniques, such as the rotating cylinder electrode (RCE) and jet impingement, that potentially offer fluid flow corrosion testing in a more compact and inexpensive form. However, it is essential to correlate corrosion data obtained from these apparatus with pipe flow, so that the data can be effectively scaled up to service. Therefore, corrosion data obtained using the RCE must be correlated with corresponding tests carried out using pipe flow.

The overall objective of this project is to develop a valid, reliable operational envelope for the application of carbon and low alloy steels in sweet production based on laboratory fluid flow corrosion test data. The work includes the design and construction of a flow loop facility for the simultaneous determination of carbon steel corrosion data in three types of flow apparatus: parallel pipe flow, jet impingement and the RCE. This approach eliminates any experimental artifacts caused by differences in the chemical composition of the fluid in each apparatus and changes in the corrosion behavior of specimen surfaces with exposure time.

Wall shear stress is a fundamental fluid flow parameter in the definition of flow accelerated corrosion, and can be readily calculated for most field situations. For these reasons, wall shear stress is used in this research, instead of mass transfer coefficient to evaluate flow accelerated corrosion. However, the use of this fluid flow parameter does not imply the assumption by the authors of a shear stress mechanism for flow accelerated corrosion in this test environment. Conversely, any demonstration of an experimental correlation between the wall shear stress and the measured corrosion rate cannot be, and has not been, used to derive conclusions regarding the mechanism of corrosion.

Results reported previously[1] demonstrated that steel corrosion rates measured in a parallel pipe flow apparatus, and in a jet impingement apparatus correlate with each other based on calculated wall shear stress, while the RCE corrosion rates do not correlate with either. This paper presents the results of an investigation to determine first, why the RCE results do not correlate to parallel pipe flow based on the calculated wall shear stress, and second, whether the RCE can be modified to achieve a correlation.

Background and Literature Review

Hydrodynamics of the RCE

The RCE consists of a cylindrical metallic electrode mounted on a corrosion resistant alloy shaft that is enclosed in an electrically insulating, non-metallic material which is flush with the electrode surface (see figure 1). Electrical connection for electrochemical corrosion testing is made by silver-graphite brushes that are pressed against the metallic shaft. The electrode is immersed in the corrosion test environment and is then rotated at a defined, stable rate. This arrangement provides controlled hydrodynamic conditions at the electrode surface and can be used to investigate the effects of fluid flow on the corrosion and electrochemical processes occurring on that surface. Corrosion weight-loss measurements can also be made on the rotating cylinder either independently or together with electrochemical tests. The RCE and the accompanying electrochemical cell form a compact, relatively inexpensive system which uses small volumes of test fluids compared to alternative fluid flow corrosion testing apparatus such as flow loops.

The hydrodynamic mass transfer characteristics and the applications of the RCE in the fields of electrochemistry and corrosion have been comprehensively reviewed by Gabe et al.[2, 3]. Two of the major influences on corrosion processes occurring on the surface of an electrode rotating in a corrosive environment are wall shear stress and mass transfer. The magnitude of these effects on the corrosion processes is a function of the rotational rate of the

electrode, generally both effects increasing with rotational rate. It should be noted that these two effects are not independent, i.e., changes in the wall shear stress will also affect the rate of mass transfer to the electrode surface. The wall shear stress (τ_w) is defined by the generally accepted equation: (Please refer to Table 1 for detailed symbol nomenclature.)

$$\tau_w = 0.0791 \, Re^{-0.30} \rho r^2 \omega^2 \qquad [1]$$

where Re is the Reynolds number. This relationship was proposed in the corrosion literature by Silverman[4] and its derivation is based on the empirically determined drag measurements of Theodoresen and Regier[5] on rotating cylinders in various gases and liquids.

The first dimensionless correlation of the mass transfer to hydrodynamic conditions of the RCE was achieved by Eisenberg et al.[6] from an investigation of a nickel electrode-alkaline ferricyanide/ferrocyanide system. An empirical relationship between the mass transfer (Sh), and the Reynolds number (Re) and the Schmidt number (Sc), was derived from the data. This relationship is represented by the equation:

$$Sh = 0.0791 \, Re^{0.7} \, Sc^{0.356} \qquad [2]$$

that has been independently confirmed by Gabe et al.[7] for copper plating solutions, Cornet et al.[8] and also Silverman[4] for oxygen reduction on *Monel Alloy 400*. This relationship can also be expressed more directly in terms of the limiting current density measured for a mass-transfer controlled reaction at a RCE as a function of electrode rotational rate. Essentially the limiting current (i_{lim}) for a mass transfer controlled reaction has been related to the electrode rotational rate (ω) by the following equation:

$$i_{lim} = 0.0791 \, nFC_b \omega^{0.7} d^{-0.3} D^{0.644} \nu^{-0.344} \qquad [3]$$

where d is the characteristic dimension of the RCE equal to the diameter of the electrode.

The wall shear stress and mass transfer equations presented above are based on predictions and measurements, respectively, on hydraulically smooth cylinders. The effects of surface roughness on the mass transfer characteristics have been investigated by Kappesser et al.[9] who developed a modification of the correlation developed by Eisenberg that includes a surface roughness factor. This is important when examining the behavior of corroding surfaces that may show localized corrosion and pitting attack, thereby altering the wall shear stress and mass transfer on the metal surface from those theoretically predicted.

Corrosion applications of the RCE

Silverman[4] has pointed out that most pipe and tubular components operate under turbulent conditions. He notes that the turbulent conditions predicted for the RCE can be used to investigate the effect of fluid flow on the corrosion behavior of engineering components under realistic flow conditions. The Reynolds number is uniform over the entire surface of the RCE. Potentially the RCE has significant advantages for the investigation of the effects of flow on the corrosion of engineering materials. Silverman[10, 11] has presented a theoretical derivation to show hydrodynamic "equivalences" involving mass transfer and wall shear stress between jet impingement, parallel pipe flow and the RCE.

Equivalences based on mass transfer assume that the corrosion rate is under mass transfer control. Furthermore, equations 2 and 3 define overall mass transfer from the RCE to the bulk environment. However, MacDonald and McKubre[12] have described a rotating-cylinder collector electrode which consisted of a nickel strip insulated from and embedded in a copper cylinder. Species produced on the nickel could be reduced on the copper and vice versa. In the first case, a collection efficiency of 67 % was measured and in the second 7.2 %. Reller et al.[13]

have shown that the limiting current density for the oxidation of ferricyanide on strip microelectrodes is significantly larger than that obtainable on a conventional RCE. For the thinnest microelectrode in their work (20 microns) they showed an enhancement of a factor of 30 compared to the RCE. These works suggest that mass transfer *across the RCE surface* influences the mass transfer characteristics of the RCE.

In summary, there are factors which are unique to the RCE flow test apparatus that may complicate correlations of corrosion rate data obtained with corresponding parallel pipe flow and jet impingement tests. Therefore, an empirical correlation of RCE corrosion rates with those measured in parallel pipe flow is required for a given corrosion test system. Two major studies have examined the behavior of alloys using different fluid flow corrosion test apparatus to establish such correlations. MacDonald et al.[14] have examined pipe flow, annular flow and the RCE for 90:10 cupronickel in an aerated sodium chloride solution at room temperature and reported a correlation between the techniques based on mass transfer comparisons. However, these comparisons were complicated by the formation of surface films on the electrodes. Dawson et al.[15] examined the corrosion behavior of carbon steel in sweet environments using jet impingement, RCE and a flow loop and reported a correlation between the techniques based on calculated wall shear stress for each of the test geometries but without the presentation of detailed data to support this conclusion.

The RCE has been used for the investigation of a variety of corrosion systems including UNS S44627 stainless steel in sulfuric acid[16], and carbon steel in sulfuric acid under isothermal[17] and heat transfer conditions.[18] The work on carbon steel, by evaluating corrosion rates as a function of electrode rotational rate, demonstrated that the corrosion rate is controlled by the mass transfer of ferrous ion through a ferrous sulfate film. The RCE has also been used to determine cathodic protection requirements for steel in seawater.[19] In the above studies the corrosion processes under investigation have been under mass transfer (diffusion control) and the experiments have focused on variations of corrosion rate with electrode rotational rate and comparisons with the original work of Eisenberg et al.[6] The main application of the RCE in oil and gas production operations is as a screening test for corrosion inhibitors. Several test approaches[20, 21] have been used, including prefilming of the electrodes and the observation of hysteresis effects between high and low rotational rates to evaluate inhibitor effectiveness. Generally, these tests examine the variation of inhibited corrosion rate versus the calculated wall shear stress created at the electrode surface. Inhibitor efficiency tests are frequently carried out to a defined maximum wall shear stress as calculated from equation 1. There has been some work on the fundamental investigation of CO_2 corrosion of carbon steel using rotating cylinder weight-loss specimens[22, 23] but only limited work with the RCE.[24]

Experimental

Rotating Cylinder Electrodes

The rotating cylinder electrode is mounted on a 304 stainless steel shaft that is enclosed in *Torlon. Torlon* washers provide sealing. Figure 1 shows the electrode configuration. The specimen surface is finished to a 600 grade silicon carbide paper, rinsed in deionized water and finally degreased in reagent grade methanol. Electrical connection is made by silver-graphite brushes pressed against the 304 stainless steel shaft. The corrosion behavior of AISI 1018 carbon steel electrodes of two types was examined. First, conventional cylinder electrodes of three sizes: 1.27, 2.54 and 3.79 cms in diameter respectively. Second, a rotating cylinder strip electrode consisting of a modified 1.27 cm diameter cylinder electrode that had been machined down to 0.8 cm diameter, except for a strip 0.1 mm in width. The electrode outer diameter was then mounted in an epoxy resin and then finish-machined to obtain an exposed, flush-mounted strip of steel of 0.1 mm thickness in a dimensionally accurate cylinder. This functioned as the rotating *strip* electrode for corrosion tests and permitted a comparison of the corrosion data obtained from a conventional RCE.

RCE - Apparatus and Electrochemical Test Cell

The RCE used is an *EG&G Princeton Applied Research* Model 636 Electrode rotator. The electrochemical cell is based on a standard two liter reaction kettle. The assembled cell with the electrode in place is shown schematically in Figure 2. The cover is fabricated from polypropylene and has threaded holes in it for: the Luggin capillary to the external reference electrode, solution inlet and outlet, a combined gas inlet and outlet, two platinum auxiliary electrodes and a thermocouple pocket. The lower surface of the cover also has six polypropylene baffles mounted at sixty degree angles to each other. These baffles minimize vortex formation and axial flow in the solution produced by the rotation of the electrode. The lateral position of the baffles is adjustable for optimum placement around the electrode. The electrode rotator fits with a small clearance (~ 0.5 mm) through a neoprene stopper connected to a nitrogen purge (to prevent oxygen contamination) and is mounted centrally in the cell cover. The auxiliary electrodes are two platinum foils, each 100 mm X 50 mm, curved symmetrically around the specimen electrode. Potential measurements are made using a Luggin capillary probe connected to an external reference electrode. Once-through cell test fluid is supplied from an external flow loop. The cell temperature is monitored by an immersed thermocouple and is controlled to within 1°C of the test temperature by an external heating jacket.

Electrical and Mechanical Characterization of the RCE System

Electrical characterization of the silver-graphite brushes used to connect the cylinder electrode for electrochemical polarization measurements was carried out to ensure that these did not introduce any artifacts into these measurements. The total contact resistance across the brushes was measured as a function of rotational rate. Oscilloscope measurements were also made across the brushes to determine the degree of electrical noise generated. The accuracy of the electrode rotational rate was determined using a *Shimpo* DT-25 tachometer to ensure that both accurate and stable electrode rotation could be achieved with the system.

Mass Transfer Characterization of the RCE

It is important to characterize the mass transfer behavior of the RCE within this test cell to ensure that the RCE system performs as predicted from the technical literature. For this purpose, the oxygen reduction reaction was used as a model system that, on a film-free electrode, is defined as being under mass transfer control in aqueous solutions at room temperature. Therefore, the limiting current densities for the oxygen reduction on a platinized *Monel Alloy 400* surface were measured at a range of electrode rotational rates and the results compared to those predicted from the empirical equations presented by Eisenberg et al.[6]. The test electrolyte for these tests was an air-saturated (~ 6.8 ppm oxygen), 0.5 M anhydrous, reagent grade sodium sulfate solution made up with distilled water. The pH was 7.0 ± 0.2. The platinized *Monel Alloy 400* specimen was cathodically polarized from the stable, free corrosion potential to - 0.75 vs. S.C.E. and the electrode was held at this potential. The limiting current density was measured across the entire range of electrode rotation rates. Triplicate experiments were conducted at 25°C.

Procedure for the RCE Corrosion Tests

The test solution used for the carbon dioxide experiments was a 3.0 % NaCl solution containing a controlled concentration of initial bicarbonate ion (as sodium bicarbonate) to provide system pH buffering. The solution was prepared in the reservoir tank of the flow loop. This solution was circulated through the loop and deaerated with oxygen-free nitrogen for 2 hours followed by sparging with the appropriate carbon dioxide/nitrogen gas mixture for 10 hours to achieve saturation under the particular experimental conditions. The residual oxygen level was monitored with *Chemets* sampling tubes. The acceptable level for this work was determined as 20 - 30 ppb. The assembled RCE test cell was flushed with nitrogen gas for one hour. Solution at the required test temperature was then pumped from the loop to the RCE cell. The cell overflow was flushed to drain. The cell replenishment rate was ~ 3 cm³/sec to minimize any effects on the measured corrosion rates due either to pH changes or dissolved ferrous ion accumulation. Preliminary experiments demonstrated that the concentration of dissolved ferrous ion

must be controlled to < 5 ppm to obtain valid corrosion data. The control value established for testing was 400 ppb ferrous ion.

Corrosion rates of AISI 1018 carbon steel were determined as a function of electrode rotational rate which can be theoretically related to wall shear stress by equation 1. The steel electrodes were allowed to stabilize in the test solution until a constant (i.e., within 2 mV) corrosion potential was measured (typically ~15 minutes). The corrosion rates were then measured by the linear polarization technique (LPR) that involved polarization from -15 mV below the open circuit potential to + 15 mV above at a sweep rate of 0.17 mV/s. AC Impedance spectra were determined for the carbon steel specimens using an *EG&G Princeton Applied Research* Model 273 Potentiostat with a *Solartron* Model 1250 Frequency Response Analyzer operated by a PC running an *EG&G* software package for the data acquisition and analysis. The AC sinusoidal signal voltage applied to the electrode was 5 mV. The frequency range investigated was 0.005 Hz - 10 kHz. Weight-loss determinations were made to validate LPR corrosion rate estimates. Selected electrodes were examined by scanning electron microscopy. The influence of two solution chemistry parameters on the corrosion rate of carbon steel in this test environment was determined: (a) the effect of CO_2 partial pressures of 2.5 and 14.7 psia and (b) the effect of an initial bicarbonate ion concentration of 1000 ppm HCO_3^-.

Results and Discussion

Electrical and Mechanical Characterization of the RCE

The total contact resistance across the silver-graphite brushes used to connect the cylinder electrode for electrochemical polarization was measured as a function of rotational rate. These measurements showed that the low contact resistance (~ 0.15 ohms total) was unaffected by the rotational rate of the electrode. Oscilloscope measurements across the brushes confirmed that the system also exhibited very low electrical noise levels. Therefore no experimental artifacts, due either to varying resistance or electrical noise of the contacts, should occur for this system.

Tachometer measurements confirmed that the unit can maintain accurate and stable rotational rates over extended time intervals. Both the accuracy and the stability of the setting are within 2 - 3 RPM. Whipping of the free end of the electrode was insignificant even at the maximum rotational rate of 9,999 RPM. These observations confirm that the drive system can maintain the cylinder at the specified rotational rate required for corrosion investigations.

Mass Transfer Characterization of the RCE

The equation for mass transfer at cylindrical electrodes rotating inside concentric cells is well established as discussed above. Essentially the limiting current density (i_{lim}) for a mass transfer controlled reaction is related to the electrode rotational rate (ω) by equation 3. For an experiment under a given set of conditions, i.e., one electrode and constant oxygen concentration, temperature and solution, all of the variables are constant except the electrode rotational rate. Therefore the equation can be simplified to:

$$i_{lim} = K\omega^{0.7} \qquad [4]$$

where K is a constant for a given set of experimental conditions and a plot of i_{lim} versus $\omega^{0.7}$ should be linear if the hydrodynamics are as predicted. This is the basis for the mass transfer characterization of the RCE. The results of mass transfer characterization of the system using the reduction of oxygen are presented in Figure 3 which shows a plot of the measured limiting current densities versus the corresponding electrode rotational rates raised to the power 0.7. Triplicate results are presented and show good reproducibility. These results demonstrate that a satisfactory agreement was obtained with equation 4. Therefore, within the limits of experimental error, the

mass transfer/hydrodynamic relationship measured in the RCE cell is consistent with that predicted from the literature.

Corrosion/Calculated Wall Shear Stress Data for AISI 1018 Carbon Steel RCE in CO_2-Brines

Figure 4 shows a plot of the corrosion rate of AISI 1018 carbon steel in the basic test solution (3 % NaCl + 1000 ppm HCO_3^- at 50°C) determined using the LPR technique versus the calculated wall shear stress for the 1.27 cm diameter RCE electrode. This figure shows that the corrosion rate increases as the wall shear stress is increased. A limited number of weight-loss determinations at a constant wall shear stress were made to confirm the validity of the LPR estimates of corrosion rate. These are shown in Table 2 and show acceptable agreement between the two techniques.

Comparison curves reported previously[1] for the wall shear stress effect on carbon steel corrosion rate for the 1.27 cm diameter rotating cylinder electrode and pipe flow are shown in Figure 5 which shows that the corrosion rates for the RCE are significantly lower than for pipe flow. The power function regression analyses for the respective data are presented in Table 3. These analyses imply that the basic equation for the effect of wall shear stress on the carbon steel corrosion rate determined for the rotating cylinder electrode in this environment is expressed in the form:

$$R_{COR} = 2.8 \, \tau_w^{0.10} \hspace{4cm} [5]$$

where R_{COR} is the corrosion rate in mm/y and τ_w is the calculated wall shear stress.

The corresponding equation for pipe flow is:

$$R_{COR} = 7.7 \, \tau_w^{0.10} \hspace{4cm} [6]$$

Comparison of these equations shows, therefore, that the corrosion rate measured on the RCE is significantly less than that measured in pipe flow at an equivalent wall shear stress and does not directly correlate with pipe flow corrosion rate as a function of wall shear stress, using the generally accepted RCE equation for this parameter.

An alternate approach is to attempt to correlate the corrosion rates measured on the RCE and pipe flow using calculated mass transfer coefficients, instead of the calculated wall shear stress. Figure 6 shows a plot of corrosion rate versus calculated mass transfer coefficient[11] for the RCE and pipe flow. This figure demonstrates that the RCE corrosion rate does not correlate with pipe flow based on calculated mass transfer coefficient either.

Figure 7 shows a plot of the corrosion rates of AISI 1018 carbon steel in the same 3.0 % NaCl + 1,000 ppm HCO_3^- solution for the RCE determined for two CO_2 partial pressures, i.e., 2.5 and 14.7 psia at 50°C. The corrosion rate again increases as the calculated wall shear stress increases. As expected, the lower CO_2 partial pressure results in lower corrosion rates. However, as the wall shear stress increases the CO_2 partial pressure exerts less influence on the measured corrosion rate. Figure 8 shows the corresponding plot determined for pipe flow. This figure shows a significantly different corrosion rate at each of the CO_2 partial pressures across the range of wall shear stress.

Figure 9 shows a plot of the corrosion rates of AISI 1018 carbon steel versus calculated wall shear stress in the 3.0% NaCl solution for the RCE at a CO_2 partial pressure of 14.7 psia at 50°C with and without the addition of 1,000 ppm HCO_3^-. The absence of initial bicarbonate was expected to result in a significant increase in corrosion rate. However, the corrosion rates measured are similar in each case at equivalent wall shear stresses. Figure 10 shows the corresponding data obtained for pipe flow which are completely different from the RCE and exhibit the

anticipated influence of bicarbonate ion on the corrosion rate. Specifically, this figure shows that the absence of bicarbonate results in a significant increase in the steel corrosion rate. These results demonstrate that the RCE responds very differently from pipe flow to changes in solution chemistry.

Electrochemical Impedance and Scanning Electron Microscopy (SEM)

Electrochemical impedance measurements were conducted for the RCE and the pipe flow. The objective was to determine if there are any significant differences between these two electrode surfaces which may explain the observed discrepancy in corrosion rates at equivalent calculated shear stress. The description of detailed equivalent circuit models is outside the scope of this paper. Figure 11 shows the Nyquist plot for AISI 1018 carbon steel in the RCE at a calculated shear stress of 10 N/m^2. The RCE spectrum shows a large, depressed semicircle related to charge transfer and also an inductive loop at low frequencies. Figure 12 shows the corresponding plot for the pipe flow which has been rescaled for clarity. The figure shows a similar semicircle attributed to charge transfer resistance. However, there is no evidence of the inductive loop seen in the case of the RCE. In the case of pipe flow, a second semicircle at low frequencies may be related to a slow step in the steel corrosion process.[25]

Representative electrochemical data for the RCE and the pipe are presented in Table 2. Clearly, caution must be used in comparing electrochemical data between these two cell geometries which are inevitably very different. Nevertheless, there are significant, reproducible and stable differences between the two sets of data that are difficult to rationalize in terms of cell artifacts. The major difference is the higher value of the estimated charge transfer resistance measured on the RCE, 121 ohms/cm^2, compared to the pipe at 12.8 ohms/cm^2. This indicates a greater degree of polarization on the RCE, possibly resulting from film formation. The higher apparent solution resistance measured on the RCE, compared to the pipe, also indicates the presence of a film on the RCE as does the inductive loop.[26, 27] Finally, the greater degree of depression observed in the RCE semicircle suggests a heterogeneous electrode surface, e.g., partially filmed.[28] The DC corrosion potential on the RCE is also consistently lower by ~ 30 mV, compared to the pipe flow.

Visual observations of the exposed RCE and pipe electrodes showed that after testing the RCE was covered with a very thin dark gray film, unlike the corresponding pipe electrode. Therefore, a RCE exposed surface and a metallographic cross section prepared from the same electrode were examined using a scanning electron microscope. Figure 13 is a scanning electron micrograph of the RCE surface after four hours' exposure to the test solution at 10 N/m^2 and shows that corrosion attack on the surface is non-uniform, certain areas still show the original grinding marks, while others are attacked. Figure 14 is a corresponding micrograph of the metallographic cross-section and shows an unattacked area protected by a thin (~ 2 microns thick) film, probably of iron carbonate. These observations are consistent with the interpretation of the AC impedance data, i.e., that the RCE has a heterogeneous, partially-filmed surface.

Corrosion/Calculated Wall Shear Stress Data for AISI 1018 Carbon Steel RCEs of Various Diameters and for the Rotating _strip_ Electrode in CO_2-Brines

Figure 15 shows the corrosion rate versus calculated wall shear stress results for the three diameters of RCE examined, i.e., 1.27, 2.54 and 3.79 cms in the basic test environment. These experiments were designed to examine the effect of RCE diameter on the observed corrosion rates. Reference to equation 3 shows that each of the electrodes has different mass transfer characteristics. Nevertheless, this figure shows essentially the same corrosion rate versus calculated wall shear stress for the three electrodes. Therefore the effect of electrode diameter on the RCE calculated shear stress is consistent with equation 1.

Figure 16 shows a plot of the corrosion rate of AISI 1018 carbon steel determined using the LPR technique versus the calculated wall shear stress on the surface of the 1.2/ cm diameter rotating _strip_ cylinder electrode in the basic environment. The corresponding plot for the conventional RCE is shown for comparison. This shows that the corrosion rates measured on the strip are similar to those for the conventional cylinder electrode under equivalent

environmental and wall shear stress conditions. Therefore the use of a rotating *strip* electrode does not overcome the basic problem of lack of correlation with pipe flow.

Why does the RCE Corrosion Rate not Correlate with Pipe Flow?

The AC impedance data and SEM examinations demonstrate that there are significant differences between the RCE and pipe flow electrodes. Specifically, there is increased polarization on the RCE, resulting from the presence of a film. These results suggest that a localized environment exists around the RCE that is more conducive to film formation and therefore less corrosive than in pipe flow. This is proposed to be the principal reason the RCE corrosion rate does not correlate with pipe flow and also why the RCE does not respond to the effects of solution chemistry in the same manner as pipe flow. Two interrelated factors may be responsible for the creation of this localized environment. First, the generally accepted equation for calculating the wall shear stress on a rotating cylinder electrode may overestimate the actual wall shear stress because the original equation was derived from drag measurements of rotating cylinders in various liquids. These drag measurements inevitably include, in addition to the wall shear stress, stress contributions from *within the liquid layers* around the rotating cylinder. Therefore, only a small portion of the total measured wall shear stress may act on the electrode surface, producing a lower corrosion rate than would be expected.

A second potential factor is that there are unique features of the fluid flow around rotating cylinders, e.g., at low rotational rates, the formation of *Taylor Vortices* that contain significant radial components of fluid velocity. At higher rotational rates, these are considered to break up to produce fully turbulent flow.[29] Therefore, the effect of fluid turbulence on the RCE corrosion rate of steel may be intrinsically different to that in pipe flow. Specifically, the fluid flow may be less effective in removing corrosion products from the surface which would produce a localized environment, different from and less corrosive than that produced in pipe flow. The corrosion results from the rotating *strip* electrode were similar to those obtained from the conventional RCE and this agreement shows that even a narrow strip appears to create a localized environment similar to that of a conventional RCE. This observation is consistent with the major flow component from the cylinder being in a radial (perpendicular to the surface), rather than in a parallel direction to the surface as in pipe flow. The detailed nature of turbulent flow and its effect on corrosion are discussed in a separate paper at this symposium by these authors.[30]

Conclusions

1. The RCE corrosion rate of carbon steel does not directly correlate with pipe flow corrosion rate as a function of calculated wall shear stress, using the generally accepted equation for RCE wall shear stress.

2. The RCE corrosion rate of carbon steel does not directly correlate with pipe flow corrosion rate as a function of calculated mass transfer coefficients.

3. The RCE corrosion rate responds very differently from pipe flow to changes in solution chemistry. Based on these results, corrosion rates generated by the RCE cannot be used to scale-up flow-accelerated corrosion of carbon steel in sweet production.

4. The AC impedance data and scanning electron microscope (SEM) examinations show that there are significant differences between the RCE and pipe flow electrodes. Specifically, there is increased polarization on the RCE, resulting from the presence of a film, confirmed by SEM examinations and probably consisting of iron carbonate. These results suggest that a localized environment exists around the RCE that is more conducive to film formation, and therefore, less corrosive than in pipe flow.

References

1. K. D. Efird, E. J. Wright, J. A. Boros and T. G. Hailey, "Experimental Correlation of Steel Corrosion in Pipe Flow with Jet Impingement and Rotating Cylinder Laboratory Tests", NACE CORROSION/93, Technical Paper No. 93081, New Orleans, March 1993.

2. D. R. Gabe, "The Rotating Cylinder Electrode", Journal of Applied Electrochemistry, Vol. 4, pp. 91 - 108, 1974.

3. D. R. Gabe and F. C. Walsh, "The Rotating Cylinder Electrode: A Review of Development", Journal of Applied Electrochemistry, Vol. 13, pp. 3 - 21, 1983.

4 D. C. Silverman, "Rotating Cylinder Electrode for Velocity Sensitive Testing", Corrosion, Vol. 40, No. 5, pp. 22^ - 226, 1984.

5. T. Theodorsen and A. Regier, "Experiments on Drag of Revolving Disks, Cylinders, and Streamline Rods at High Speeds", National Advisory Committee for Aeronautics, Report No. 793, 1945.

6. M. Eisenber ;, C. W. Tobias and C. R. Wilke, "Ionic Mass transfer and Concentration Polarization at Rotating Electrodes", Journal of the Electrochemical Society, Vol. 101, No. 6, pp. 306 - 320, 1954.

7. D. R. Gabe and D. J. Robinson, "Dendritic Formation and the Effects of Addition Agents in The Electrodeposition of Copper from Acid Sulfate Solutions", Transactions of the Institute of Metal Finishing, Vol. 49, pp. 17 - 21, 1971.

8. I. Cornet and R. Kappesser, "Cathodic Protection of a Rotating Cylinder", Transactions of the Institute of Chemical Engineers, Vol. 47, pp. 194 - 197, 1969.

9. R. Kappesser, I. Cornet and R. Grief, "Mass Transfer to a Rough Rotating Cylinder", Journal of the Electrochemical Society, Vol. 118, No. 12, pp. 1957 - 1959, 1971.

10. D. C. Silverman, "Rotating Cylinder Electrode-Geometry Relationships for Prediction of Velocity-Sensitive Corrosion", Corrosion, Vol. 44, No. 1, pp. 29 - 49, 1988.

11. D. C. Silverman, "Rotating Cylinder Electrode - An Approach for Prediction of Velocity Sensitive Corrosion", CORROSION/90, Technical Paper No. 90013, Las Vegas, March 1990.

12. M. C. H. McKubre and D. D. Macdonald, "The Rotating Cylinder-Collector Electrode (RCCE)", Journal of the Electrochemical Society, Vol. 27, No. 3, pp. 632 - 640, 1980.

13. H. Reller, I. Feldstein-Hallakoun and E. Gileadi, "Rotating Cylindrical Strip Microelectrodes", Electrochimica Acta., Vol. 33, No. 1, pp. 95 - 101, 1988.

14. T. Y. Chen, A. A. Moccari and D. D. Macdonald, "The Development of Controlled Hydrodynamic Techniques for Corrosion Testing", CORROSION/91, Technical Paper No. 91292, Cincinnati, March 1991.

15. J. J. Dawson, C. C. Shih, R. G. Miller and J. W. Palmer, "Inhibitor Evaluations Under Controlled Hydrodynamic Shear", CORROSION/90, Technical Paper No. 90014, Las Vegas, March 1990.

16. D. C. Silverman and M. E. Zerr, "Application of the Rotating Cylinder Electrode: E-Brite 26-1/Concentrated Sulfuric Acid", Corrosion, Vol. 42, No. 11, 633 - 640, 1986.

17. B. T. Ellison and W. R. Schmeal, "Corrosion of Steel in Concentrated Sulfuric Acid", Journal of the Electrochemical Society, 125, No. 4, pp. 524 - 531, 1978.

18. M. Shirkhanzadeh, "A Rotating Cylinder Electrode For Corrosion Studies Under Controlled Heat Transfer Conditions", Corrosion, Vol. 43, No. 10, pp. 621 - 623, 1987.

19. R. A. Holser, G. Prentice, R. B. Pond and R. Guanti, "Use of Rotating Cylinder Electrode to Simulate Turbulent Flow Conditions in Corroding Systems", Corrosion, Vol. 46, No. 9, pp. 764 - 769, 1990.

20. S. D. Bhakta and S. Hettiarachchi, "In situ Electrical Injection of Corrosion Inhibitors for Protecting the Trans-Alaska Pipeline", SRI Bimonthly Report, Project No. 1909, September 1991.

21. J. L. Dawson, R. G. Miller, D. G. John, D. Gearey and R. A. King, "Inhibitor Evaluation Methodology for Oil Field Applications", CORROSION/88, Technical Paper No. 88361, National Association of Corrosion Engineers, St. Louis, March 1988.

22. A. K. Dunlop, H. L. Hassel and P. R. Rhodes, "Fundamental Considerations in Sweet Gas Well Corrosion", CORROSION/83, Technical Paper No. 83046, Anaheim, 1983.

23. S. D. Kapusta, P. R. Rhodes and S. A. Silverman, "CO_2 Testing - Inhibitor Testing Procedures for CO_2 Environments", CORROSION/91, Technical Paper No. 91471, Cincinnati, March 1991.

24. E. Dayalan, "Velocity Correlations in a Small Scale Apparatus for Inhibitor Evaluations", Presentation to Industrial Advisory Board, University of Tulsa, May 1992.

25. D. D. Macdonald, "The Advantages and Pitfalls of Electrochemical Impedance Spectroscopy", CORROSION/89, Technical Paper No. 89030, New Orleans, April 1989.

26. D. C. Silverman, "Corrosion Rate Estimation from Pseudo-Inductive Electrochemical Impedance Response", CORROSION/89, Technical Paper No. 89023, New Orleans, April 1989.

27. I. Epelboin, C. Gabrielli, M. Keddam and H. Takenouti, Proc. of the ASTM Symp., "Progress in Electrochemical Corrosion Testing", May 1979, Ed. F. Mansfeld and U. Bertocci, pp. 150 - 166, ASTM, 1981.

28. W. J. Lorenz and F. Mansfeld, "Determination of Corrosion Rates by Electrochemical DC and AC Methods", Corrosion Science, Vol. 21, No. 9, pp. 647 - 672, (1981).

29. "Electrochemical Systems", J. Newman, Prentice-Hall, New York, 1973.

30. K. D. Efird, E. J. Wright, J. A. Boros and T. G. Hailey, "Wall Shear Stress and Flow Accelerated Corrosion of Carbon Steel in Sweet Production.", Technical Paper TS 14 194, 12th International Corrosion Congress, Houston, Texas, U. S. A. , September 1993.

TABLE 1
NOMENCLATURE

Symbols		R	resistance ($\Omega\,m^2$)	v	kinematic viscosity (m^2/s)
c	concentration (mol/l)	R_{cor}	corrosion rate (mm/y, μm/y)	τ	shear stress (N/m^2)
d	diameter (m	r	radius or radial distance (m)	ω	rotation rate (rad/s)
F	Faraday's constant (96487	T	temperature (°C)	Subscripts	
	C/mol)	U	mean velocity (m/s	b	mass average or bulk
i	current density (A/m^2)	z	charge number of a species	cor	corrosion
k	mass transfer coefficient (m/s)	Greek Symbols		d	diffusion
L	characteristic length (m)	ρ	density (kg/m^3)	lim	limiting
P	pressure (Pa, kg/m s^2)	μ	dynamic viscosity (kg/m s)	w	wall or electrode surface

TABLE 2
ELECTROCHEMICAL DATA FOR AISI 1018 CARBON STEEL IN THE RCE AND PIPE FLOW AT A CALCULATED WALL SHEAR STRESSES OF 10 N/m^2.

Test Apparatus	Corrosion Potential vs. S.C.E (mV)	"Solution" Resistance (ohms/cm²)	Charge Transfer Resistance [1] (ohms/cm²)	Corrosion Rate from LPR [2] (mpy)	Corrosion Rate from weight-loss (mpy)
RCE (1.27 cm dia.)	-742	6.6	121	93	69
Pipe Flow (1.27 cm dia.)	-717	0.7	12.8	641	460

1. Charge transfer resistance estimated after the method of Epelboin et al. in reference 27.
2. Corrosion rate estimates derived from DC polarization resistance.

TABLE 3
POWER FUNCTION REGRESSION RESULTS FOR CARBON STEEL CORROSION RATE VARIATION WITH SHEAR STRESS

FLOW APPARATUS	R^2	b	a, mm/y(mpy)
1.27 cm Rotating Cylinder Electrode	0.77	0.101	2.8 (111)
1.27 cm Diameter Pipe	0.85	0.103	7.7 (304)
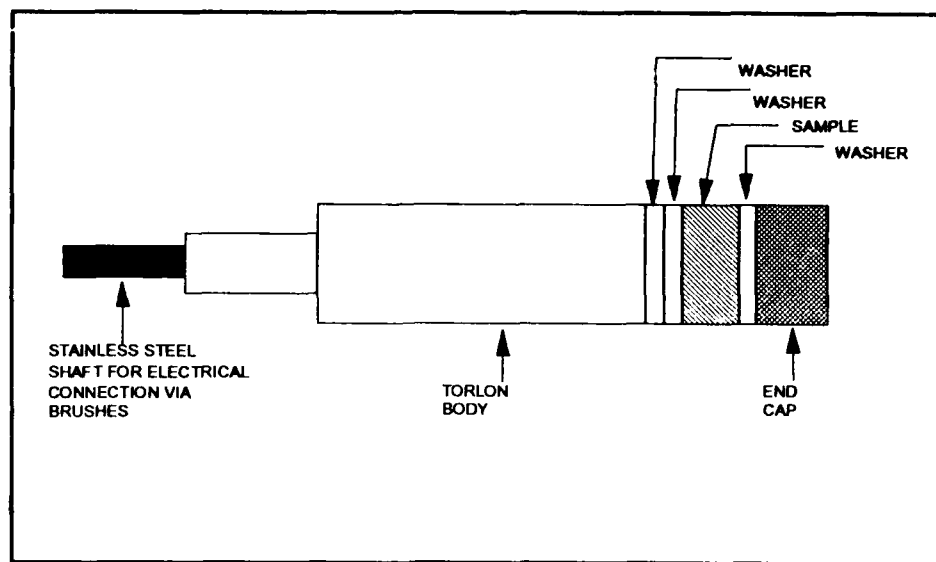
Figure 1.   *Rotating Cylinder Electrode.*
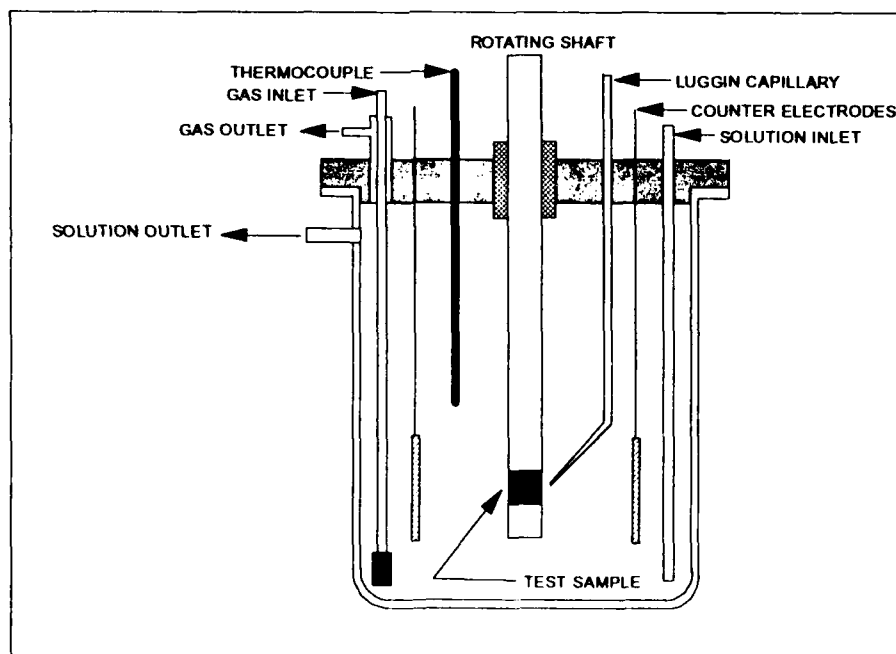
Figure 2.   *Schematic of Rotating Cylinder Electrochemical Cell.*
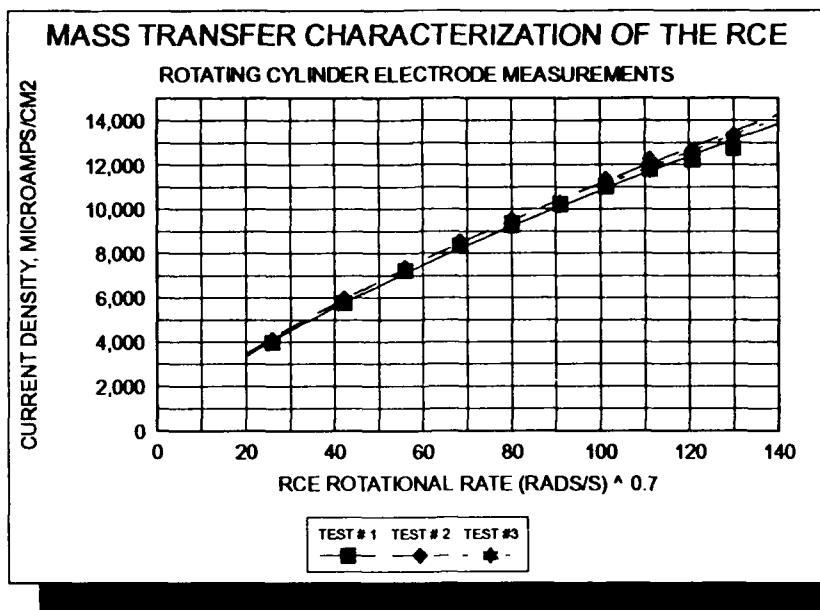
Figure 3. Limiting current density measured for the oxygen reduction reaction versus RCE rotational rate (rads/s)$^{0.7}$ showing a linear relationship in accordance with Eisenberg et. al.[6]
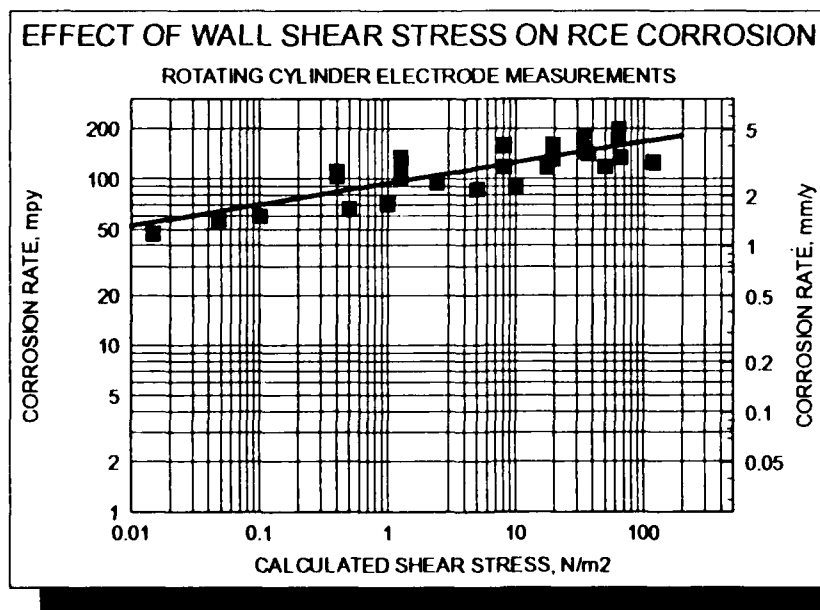
Figure 4. The effect of wall shear stress on the flow accelerated corrosion of carbon steel for the RCE of 1.27 cm diameter.
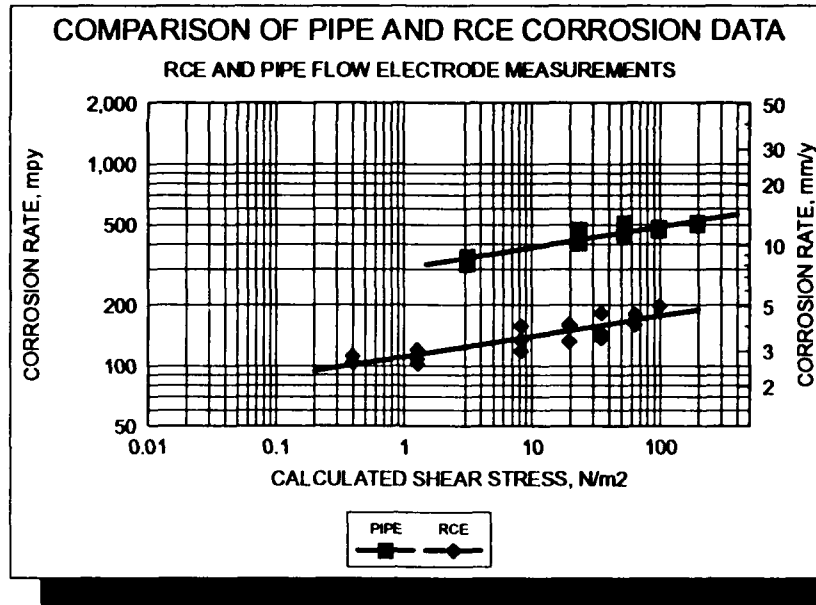
Figure 5. Comparison of the effect of wall shear stress on the flow accelerated corrosion of carbon steel for the RCE (1.27 cm) and pipe flow.
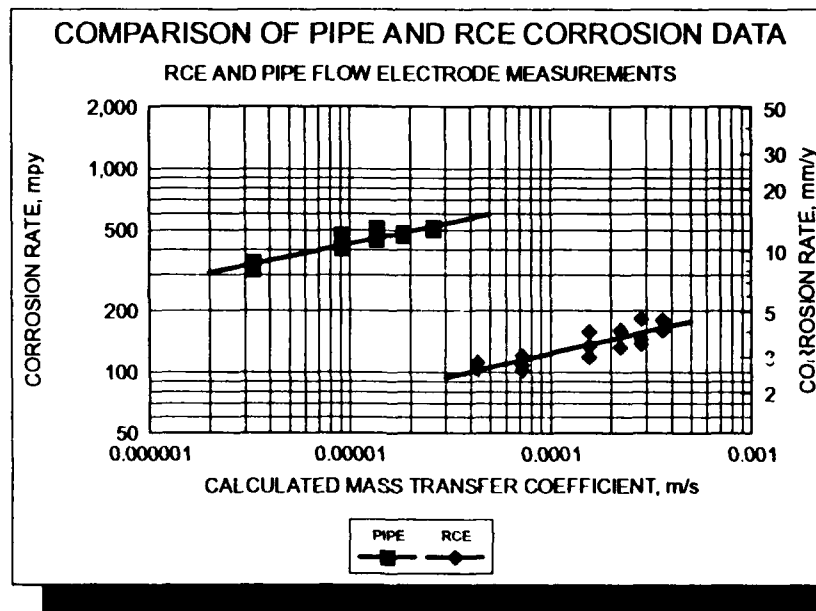
Figure 6. Comparison of the flow accelerated corrosion of carbon steel as a function of calculated mass transfer coefficient for the RCE and pipe flow.
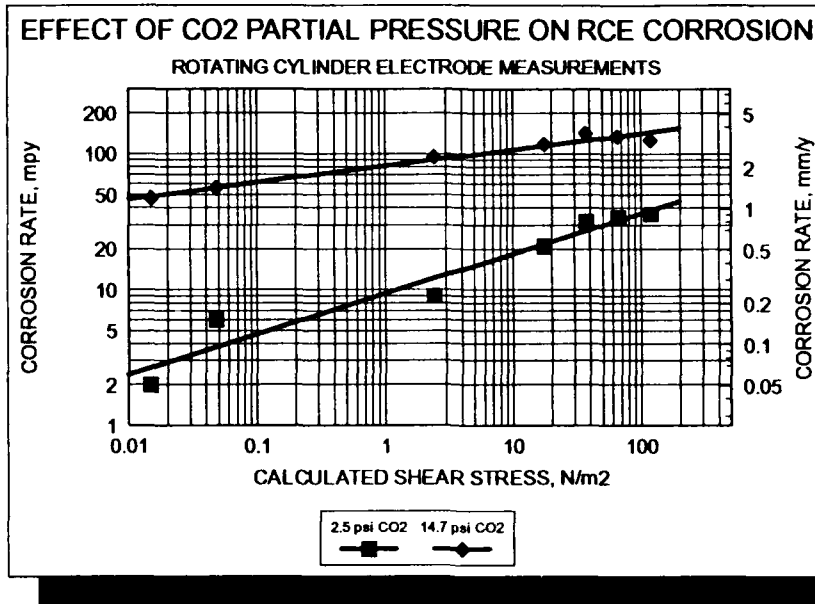
Figure 7. The effect of CO_2 partial pressure on the flow accelerated corrosion of carbon steel as a function of wall shear stress for the RCE.
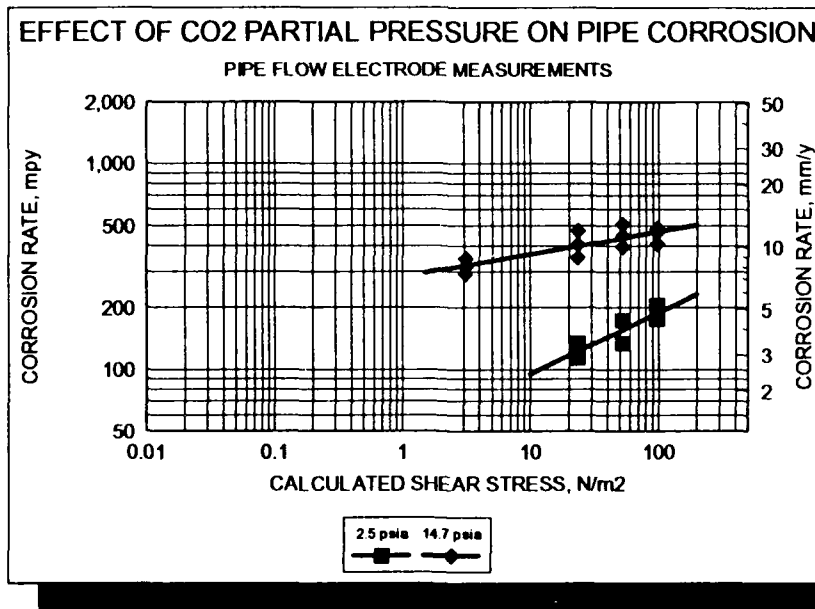
Figure 8. The effect of CO_2 partial pressure on the flow accelerated corrosion of carbon steel as a function of wall shear stress for pipe flow.
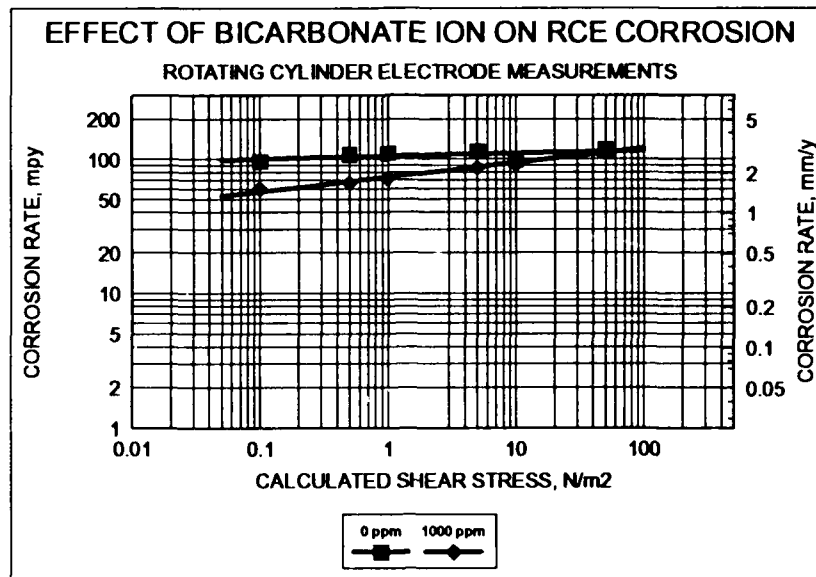
Figure 9. The effect of initial bicarbonate ion concentration on the flow accelerated corrosion of carbon steel as a function of wall shear stress for the RCE.
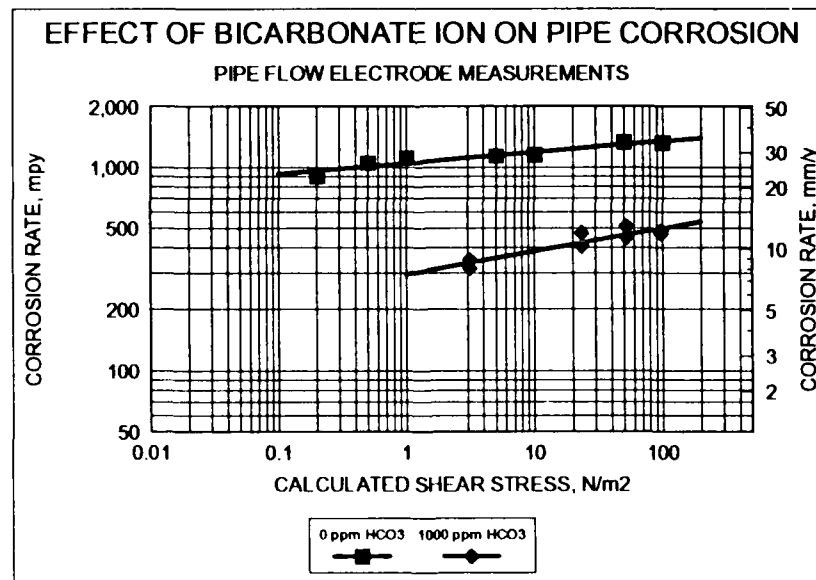
Figure 10. The effect of initial bicarbonate ion concentration on the flow accelerated corrosion of carbon steel as a function of wall shear stress for pipe flow.
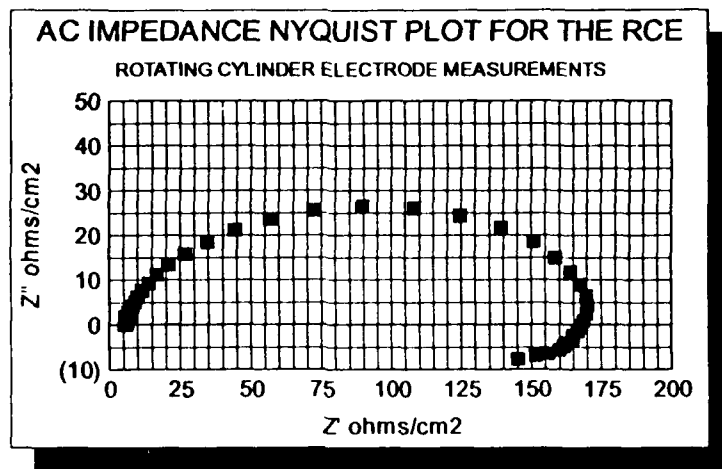
Figure 11. AC Impedance Nyquist plot for the flow accelerated corrosion of carbon steel in the RCE at a constant wall shear stress of 10 N/m².
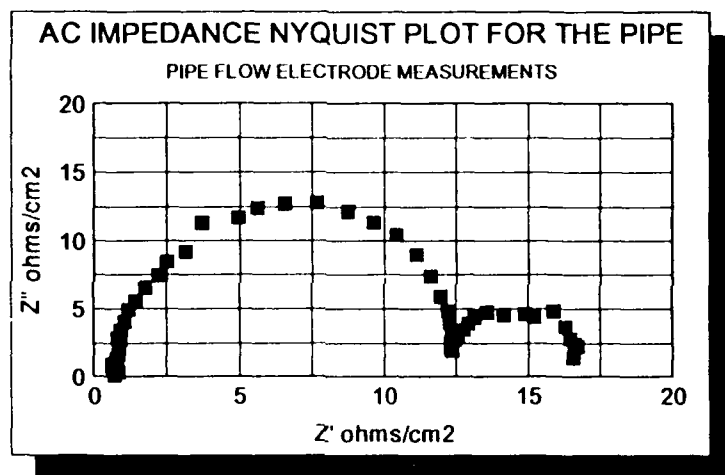
Figure 12. AC Impedance Nyquist plot for the corrosion of carbon steel in the pipe flow at a constant wall shear stress of 10 N/m².
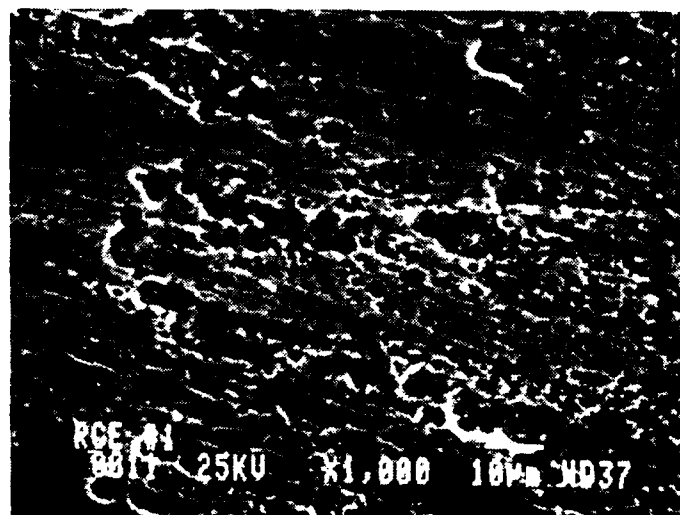
Figure 13. Scanning electron micrograph of RCE surface (Magnification = 1,000 X).
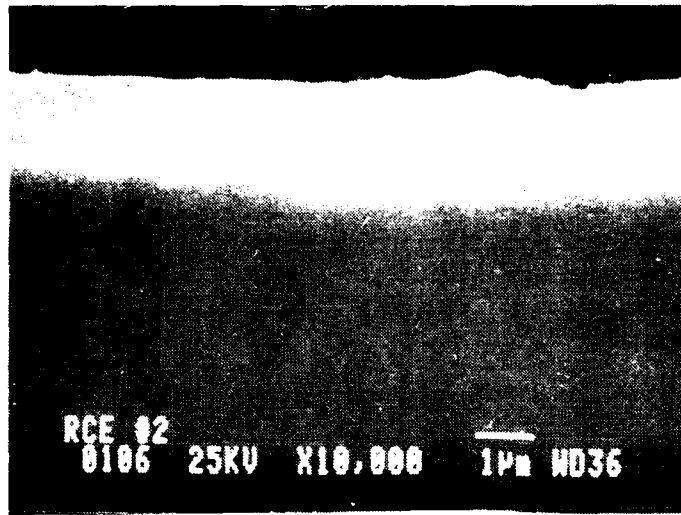
Figure 14. Scanning electron micrograph of section of RCE surface (Magnification = 10,000 X).
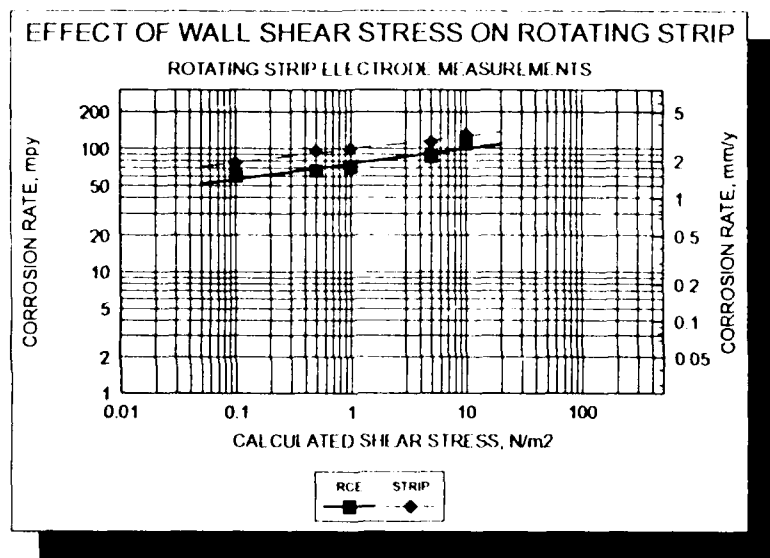
Figure 16. Comparison of the effect of wall shear stress on the flow accelerated corrosion of carbon steel for the conventional RCE and the rotating strip electrode.
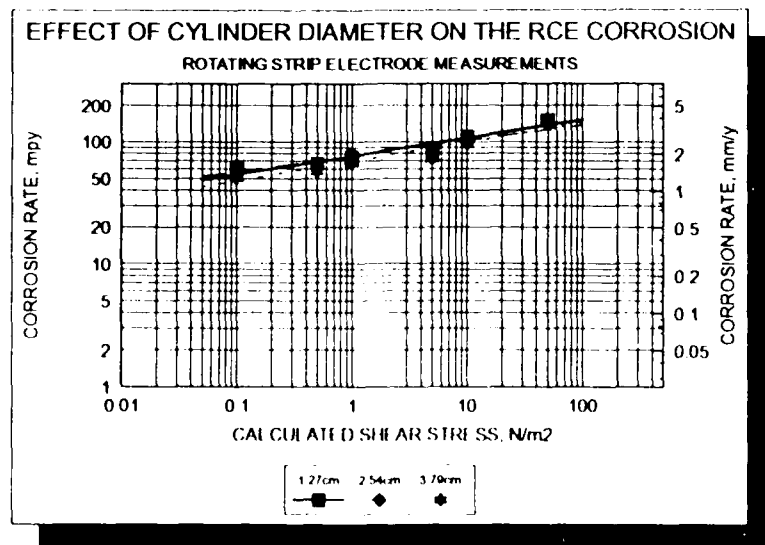
Figure 15. The effect of electrode diameter on the flow accelerated corrosion of carbon steel for the RCE as a function of wall shear stress.

Inhibitor Performance In Annular Mist Flow

J.H. Gerretsen and A. Visser
Shell Research
Billiton Research Arnhem
P.O. Box 40, 6800 AA Arnhem
The Netherlands

Abstract

Removal of inhibitor films by erosion may provoke unacceptable corrosion. In gas production, operating in the annular mist flow regime, such erosion is probably due to impact of liquid droplets. Shear stresses induced by the impinging droplets, flowing out over the surface can be high, leading to failure of the inhibitor film. The effects of droplet impingement on the performance of inhibitors as a function of operating parameters, such as temperature, CO_2 partial pressure, pH and impact velocity (i.e. gas production velocity), are being studied using a specially designed test facility. Recently, some results have been presented at the NACE Corrosion Conference[1]. Additional results are presented here. It is shown that a critical velocity can be obtained at which the inhibitor fails. This critical erosion velocity appears to be a function of inhibitor concentration. Increasing inhibitor concentration resulted in a higher critical velocity. It becomes apparent from such results that inhibitor handling in the operations should be quality controlled, e.g. avoiding situations of under-dosage or, temporary, enhanced production.
Some of the impingement results have been compared with results from liquid-full flow loop tests, using the same inhibitor. In these tests the inhibitor failed at a lower liquid velocity. Localised attack at a flow constriction could not be suppressed by applying a higher inhibitor dosage. The results indicate the advantages of testing an inhibitor with equipment dedicated to operation conditions, including its specific flow regimes.

Key terms: inhibition, carbon dioxide corrosion, shear stress, erosion, droplet impact, annular mist flow

Introduction

Whenever well fluids are, or become, corrosive the question arises what measures should there be taken to combat corrosion. In principle, the first consideration is, of course, of an economical nature: what is the most cost effective way to operate? Can alloyed steels be applied or is the use of carbon steel combined with an inhibitor programme more appropriate? As to the latter, a suitable inhibitor has to be selected. To minimise the risk of unpleasant surprises in the form of expensive work-overs, or repairs, in future operation, the selection procedure should give as much confidence as possible in the performance of the chosen inhibitor.
For gas production facilities, the inhibitors applied are commonly of the film forming type. A thin inhibitor film then stifles corrosion. When corrosion attack occurs it is, in many cases, found to be of localised nature[2,3]. In the particular case of operating in the annular mist flow regime, where the water is entrained in the gas phase as liquid droplets, the inhibitor films may fail due to the repetitive impact of liquid droplets. Flow becomes disturbed e.g. near chokes, valves, welds etc., but a disturbance of the flow can also be triggered by already corroded areas. A

critical velocity above which erosion, and subsequent corrosion, may occur is currently derived from the API RP 14E formula[4]. The formula, however, does not take any credit for inhibitors. The predicted velocity may well be too conservative for one inhibitor, or worse, too optimistic for another. At present, there are no test methods commercially available, or universally agreed upon, for performance ranking of inhibitors for application in the mist flow regime. Furthermore, the general understanding of inhibitor performance under the conditions of mist flow, is very limited.

To test an inhibitor, field testing in a side stream is probably the best option. However, this is not always possible and also extremely expensive. Besides, erroneous results may be obtained when different inhibitors are tested consecutively due to their chemical interaction. Alternatively, laboratory tests should be performed, matching operation conditions as closely as possible. Obviously, the tests should include establishing the physical/chemical behaviour of the inhibitor, like its foaming tendency, partitioning and temperature stability. Inhibitors should furthermore be tested under relevant flow conditions. Currently, there are only few laboratory facilities which allow for testing of inhibitors for the specific case of mist flow regime. Some laboratories are equipped with dedicated flow loops, but these are usually difficult to operate with inhibitors and very elaborate.

In our laboratories we have developed a test rig especially for the conditions of mist flow. It focusses on the study of the effects of droplet impingement. Maximum production velocities can be assessed for (wet gas) production systems operating in the annular mist flow regime, with and without inhibitors. The existence of a critical velocity, for a specific inhibitor, is revealed and it is shown to be concentration dependent. Sensitive on-line hydrogen measurements provide for continuous corrosion monitoring in-situ. Among other things, the use of such dedicated equipment is discussed by comparison with liquid-full flow loop tests.

Experimental

The operational practice of high velocity gas production conditions have been simulated with a so-called Jet And Wheel apparatus (JAW). A detail of the JAW is shown in Figure 1. The principles of the equipment have been described in detail elsewhere[1,5]. In this test rig horizontally rotating steel coupons collide repetitively against a continuous, vertical, water jet, mimicking repetitive impact of liquid droplets. In addition to hitting the jet once every rotation, the coupons are continuously wetted during rotation via a horizontal liquid supply. In this manner drying due to the centrifugal forces is avoided. The experiments are carried out in a conditioned environment. The aim of the erosion-corrosion tests is to establish a critical operation velocity above which the inhibitor fails, under a given set of conditions. The variable condition parameters are temperature, water cut, type and concentration of inhibitor and water chemistry (ferrous concentration, pH). Corrosion can be monitored in several ways. The most important one is by a sensitive hydrogen probe, which measures the hydrogen evolving during the corrosion reaction very sensitively. Concentration dependency tests were carried out at 70 °C. During the tests the jet is switched on after injection of inhibitor and stabilisation of the corrosion rate. The impingement velocity is increased until the inhibitor fails, after which an additional dosage of 100 ppm is injected. In another experimental sequence the inhibitor is injected at 30 °C, after which the temperature is increased gradually to 90 °C, to assess the residual corrosion rates.

The liquid full experiments were carried out in a flow loop which is almost completely constructed from PVDF, which enables relatively easy cleaning procedures. In the loop, schematically given in Figure 2, a cylindrical test section can be mounted in a 44 10^{-3} m ID piping. The test section consists of three stacked samples, separated by PVDF washers. To

provide high shear conditions, a constricted sample, with an ID of 40 10^{-3} m, is placed within the test section.

The loop contains about 5 10^{-2} m^3 and can be operated at a maximum velocity of 5 m/s. Inhibitor can be injected in a by pass in which also oxygen and pH is measured. To avoid gas entrainment under the high turbulent operating conditions, a pipe is attached to the entrance of the loop where the liquid is admitted to the main vessel. This pipe ends under the liquid level. Consequently some phase separation occurred in the top part of the main vessel. Hence, the exact concentration of the inhibitor is not known.

Corrosion could be monitored with AC impedance, but its results will not be discussed here. The liquid velocity was 5 m/s. After the tests, the samples were cleaned and weighed to determine weight loss. Subsequently, the samples were examined microscopically.

In general, the test conditions for the JAW experiments were: 0.4 MPa CO_2, 1% NaCl in de-ionised water. Shellsol K was used as a gas condensate substitute at a water cut of 90%. In the flow loop a CO_2 partial pressure of 0.13 MPa was used and a water cut of 99%. Samples were machined from steel 52-3. Prior to the actual corrosion testing, the equipment was purged with pure nitrogen to remove oxygen. Experiments were run with less than 10 ppm oxygen in the gas phase, typically 1 ppm. The samples were pre-corroded prior to injection of inhibitor. The inhibitor applied in the tests was of the oil soluble, water dispersible, film forming, type. The concentration as advised by the supplier is for gas production facilities: 100 ppm on total liquid and for oil transport: 10 ppm in the water phase.

Results

It can be seen from Figure 3 that the critical velocity is dependent on the concentration of the inhibitor. At a concentration of about 100 ppm on total liquid, the inhibitor failed at an impact velocity of about 15 m/s. When an additional 100 ppm was added, the inhibitor became effective once again, despite of the continuous impact. The critical velocity shifted to 25 m/s. After a subsequent increase of the inhibitor concentration with another 100 ppm, the samples were again protected. This time the inhibitor remained protective up to the highest velocity tested; 30 m/s.

Once being damaged the corrosion rate, normalised with respect to the attacked area, reached a value of the same order as the corrosion rate predicted by the nomogram of de Waard/Milliams[6]. At 45 °C and a concentration of 100 ppm, a similar critical velocity was obtained. For the particular conditions of the test, a tentative engineering curve can be produced indicating conditions for save operation (Figure 4). In several inhibitor tests, the base case corrosion rates with inhibitor were measured. The inhibited corrosion rate for this inhibitor, appeared dependent on temperature. At 70 °C the lowest residual corrosion rates was obtained (Table I). It appeared that under impinging conditions at a temperature of 30 °C, the inhibitor became hardly effective within the duration of the test (20 h). Increasing the temperature resulted in an improved performance.

In the liquid full experiments with flow restriction, corrosion could not be fully suppressed, even not under extremely high dosages of the inhibitor for liquid full systems. It became apparent that at low concentrations of 10 ppm, the inhibitor performance was poor. Neither the flush mounted rings upstream and downstream were fully protected. The upstream side of the constriction was not protected at all. Increasing inhibitor concentration (Table II) improved protection. However, even at 300 ppm, pitting was observed at the upstream side of the constriction. At 45 °C, applying a similar concentration as in the JAW experiments, 100 ppm, the inhibitor did not perform satisfactory in the flow loop at a liquid velocity of 5 m/s. Localised attack was observed. No local damage was found in the JAW experiments at an impingement velocity of 10 m/s. The general corrosion rate of the constriction was of the same order as

during the liquid droplet tests at 45 °C, at an impact velocity of 10 m/s. The corrosion rates of two other samples in the test section, one upstream and one downstream of the constriction, were significantly lower.

Discussion

In many cases the inhibitor performance as obtained in lab tests is expressed in terms of efficiency:

$$Efficiency \equiv \frac{(CR - CR_{inhibited})}{CR} \times 100\%, \qquad (1)$$

Where CR is the corrosion rate without inhibitor. Such an efficiency is then used as the characteristic value for the specific inhibitor.

The actual use of such an efficiency, however, is doubtful. First, there are no generally accepted guidelines on how to assess the corrosion rate even in the absence of an inhibitor. It is well known that, after an inititial increase, the corrosion rate decreases as function of time during a constant inventory test due to the increase of pH[6] To overcome this, the maximum in corrosion rate during a test can be taken. Dugstad[7], among others has shown that the increase in pH is dependent on the tests conditions, however. Secondly, the reduction of the corrosion rate by the inhibitor is not necessarily constant. For example, the tested inhibitor gave a minimum residual corrosion rate at 70 °C (Table I). Actually, it is the residual corrosion rate which is of interest, rather than the effectiveness. Yet, even more important is that the efficiency of the inhibitor reflects only its protection against general corrosion where, maybe, the main criterion should be its susceptibility towards localised failure. The latter can occur at places with increased turbulence, or at places with different micro-structures, like at welds. Hence, information should be obtained about the inhibitor performance under the worst conditions expected. As far as flow is concerned, in multi-phase, L-L-G, the worst condition exists when droplets impinge perpendicularly against the wall.

In the mechanism causing damage by liquid droplet impact two separate events can be distinguished. Damage can result from high stresses on the surfaces, induced by the pressure accumulation in the droplet and from the local wall shear stresses arising after the pressure in the droplet is released and the liquid flows out over the surface. The pressure at the wall is given by the water hammer pressure, $\rho c v$, where ρ is the density of the droplet, c the velocity of sound in the liquid and v the impact velocity. According to Lesser and Field[8], the pressure at the contact ring of the droplet can sweep up to a higher value than given by the water hammer pressure. The pressure may damage either the metal or any surface film present by a fatigue mechanism. The harm done depends on the hardness of the surface. The pressure may lead to the initiation of erosion.

The results show a similar characteristic erosion behaviour as with a metal, i.e. there exists a critical velocity above which erosion occurs. This velocity depends on inhibitor concentration. The residual general corrosion rates, before damage, were independent of concentration. On the other hand the resistance towards erosion alters when increasing the inhibitor concentration, indicating the formation of a mechanical stronger, or a thicker, film. The presence of a critical velocity also shows that the repair of the film is relatively slow compared to the peripheral velocity of the wheel; once damage occurs, high corrosion rates, of the order of the corrosion rate as predicted for pure CO_2 corrosion with the nomogram, are encountered. Clearly, the system behaves in an on/off manner.

In actual practice the liquid loading of the gas phase will cause higher impingement frequencies than in our equipment. The frequency dependency has not been addressed, yet. Thus, at the moment, it cannot be excluded that the inhibitor fails at a somewhat lower impact velocity if the impingement frequencies were higher, due to fatigue. Future work can give more insight about this.

It becomes clear from the results that the API formula cannot be used straight forwardly in the case inhibitors are applied; the formula predicting one single critical velocity, irrespective of concentration or flow regime. It has been argued by Smart that the formula predicts the onset of annular mist flow[9]. This seems indeed probable, giving rough information for multi-phase operations where no inhibitors are applied. The results indicate that a higher velocity can be accepted, applying a suitable inhibitor at a sensible concentration, however. Of course, it is of utmost importance that the concentration required is maintained at all times. It has been shown before that a temporary under-dosage situation may trigger continuous corrosion[5]. A feature which appeared also strongly dependent on temperature.

Because of the complexity of tests in annular mist flow, other inhibitor screening methods are to be preferred. Initially, the objective of the flow loop experiments was to screen inhibitors for the droplet impingement tests. Fully developed pipe flow was regarded not to be of direct relevance, because the corrosion attack found in practice is usually of a localised nature, triggered by a flow disturbance. Therefore a constricted sample was used. When the results of these liquid-full experiments are compared with the results obtained in the JAW it appears that in the former case the inhibitor was not fully effective, irrespective of concentration at the velocity tested: 5 m/s. It was not possible to fully protect the upstream side of the protrusion and there was almost no difference in the tests carried out at 50, 100 or 300 ppm, although pitting appeared to be more severe at the lowest concentration. At an even lower concentration the inhibitor performed poorly. It appeared that by using a flow constriction it is difficult to obtain a concentration at which the whole system is protected. The broad range of concentration for which almost no difference in performance was observed, suggest that it is difficult to use such a test for assessing a concentration dependence. Probably, a concentration can be found at which flow induced corrosion is completely suppressed, but in the case of the inhibitor examined, such a concentration is expected to be excessively high. The test may, however, be used for pre-selection purposes.

An interesting side-observation was that the preferential attack at the upstream side of the constriction was not always located at the leading edge of the constriction only, but the attacked region extended to about half way of the protrusion (Figure 5) This phenomenon is not understood, as yet.

To assure a proper choice of inhibitor and to establish a suitable concentration, tests should be carried out using dedicated equipment, mimicking the flow conditions in actual practice.

Conclusion

The use of equipment like the JAW can fill the existing gap in test methodology for establishing maximum production velocities for annular mist flow conditions, typically encountered in gas production systems. An inhibitor should be tested for the whole range of expected operating conditions, including tests in the expected flow regime. The inhibitor efficiency on its own is not sufficient to characterise inhibitor performance. Among other things, an integral inhibitor testing programme should contain tests focusing at localised failure such as persistency tests and tests to assess the capacity of the inhibitor to restore a protective film once the film has been damaged by a process upset.

The API formula, of which the validity has never been fully proven in laboratory tests, can now

be scrutinised for different operating conditions. At a given temperature, a critical production velocity can be assessed for different concentrations of inhibitors.

Liquid-full experiments may well be used as a tool for pre-selection of inhibitors for the liquid droplet impact tests. These experiments cannot easily be translated to their performance in mist flow and certainly no-critical concentration or velocity can be assessed from such tests for a L-G multiphase system.

The characteristic on/off performance of the inhibitor as function of velocity illustrates the possible risk of under-dosage situation related to production velocity.

References

1. J.H. Gerretsen et all, NACE corrosion conference,New Orleans paper 84, 1993
2. J.C. Smart, NACE corrosion conference,Las Vegas, paper 10, 1990
3. P.H.M. Geelen, K. Groenewoud, 6th Chem. Ind. Soc. et al Europe Metallic Corrosion Congress, London,1977
4. API Recommended Practise for Design and Installation of Offshore Production Platform Piping Systems, API Washington D.C.
5. Corrosion Science, accepted for publication.
6. C.de Waard, D. Milliams, U. Lotz, Nace Corrosion conference, Cincinnati, paper 577, 1991
7. A. Dugstad, NACE corrosion conference, Nachville , paper 14 1992
8. J.E Field and M.B. Lesser, J.P. Dear, Proc. R. Soc. Lond. A 401, 225-249, 1985
9. J.S. Smart, NACE corrosion confer ce, Cincinnati, paper 468, 1991

TABLE I	**TABLE II**

Residual corrosion rate , after 10 hours of exposure to droplet impacts with a velocity of 10 m/s.

Inhibitor performance in test loop with a flow constriction.

Temperature (°C)	Corrosion rate (mm/y)
27	3.7 (nomogram = 7)
45	0.4
70	0.02
90	1

Inh. conc. (ppm)	Observation	
	constriction	up/downstream
10	poor protection	pitting
50	severe pitting	some shallow pits
100	pitting	good protection
300	pitting	good protection
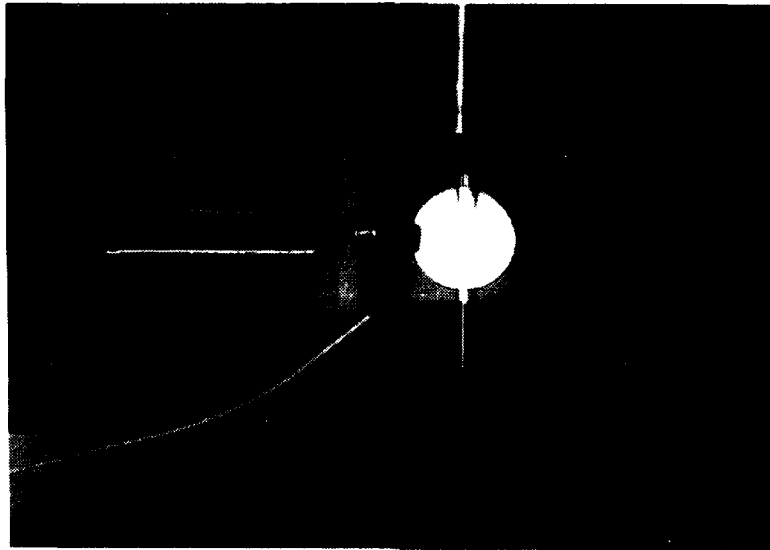
Figure 1. Jet and Wheel arrangement
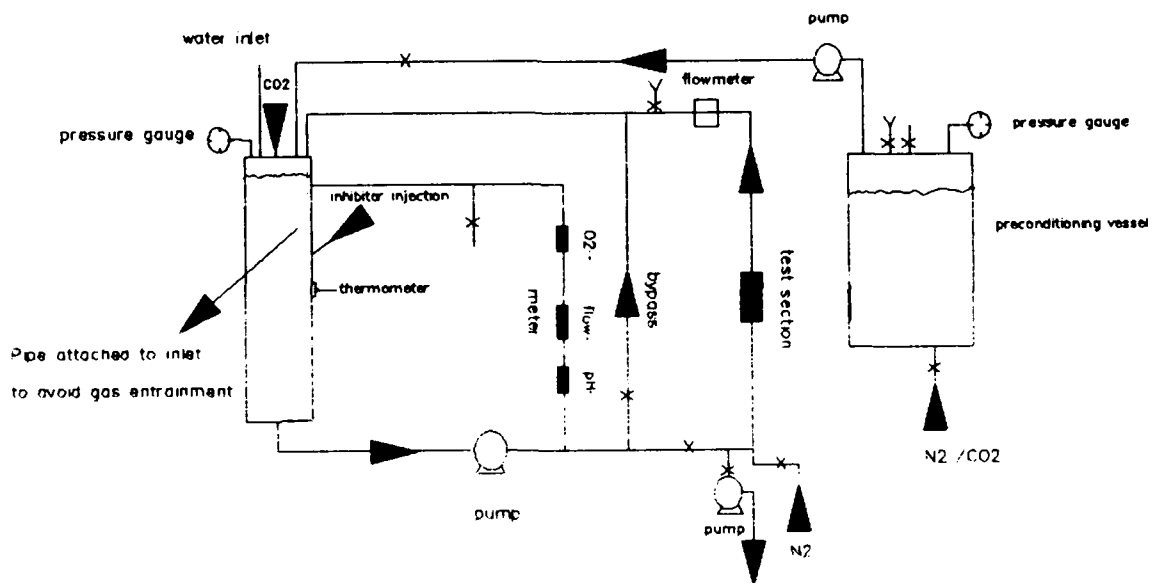
Figure 2. Schematic presentation of flow loop
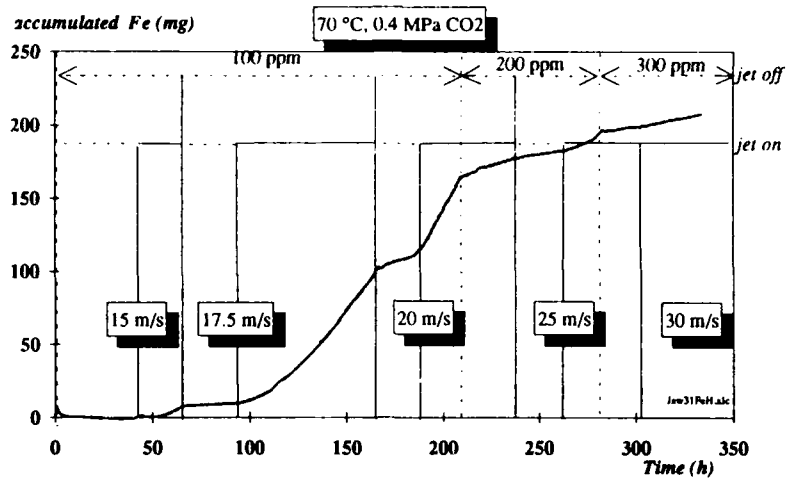
Figure 3. Inhibitor performance as function of inhibitor concentration
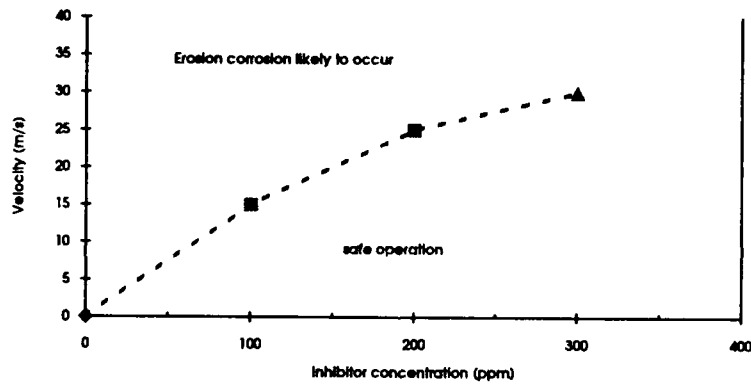
Figure 4. Tentative engineering curve for establishing a critical velocity for operating with the tested inhibitor at 70 °C, 0.4 MPa.

Figure 5. Photo micrograph of the upstream side of the protrusion, after a test with 100 ppm inhibitor. (magnification 20 x).

Evaluation of Magnetic Flux Leakage (MFL) Intelligent Pigging Results from Recurring Arctic Pipeline Inspections

G. C. Williamson, III
ARCO Alaska, Inc.,
P. O. Box 100360
Anchorage, Alaska 99510

A. L. Dahlquist
ARCO Alaska, Inc.
P. O. Box 1966449
Anchorage, Alaska 99519

P. D. Hain
ARCO Alaska, Inc.
P. O. Box 100360
Anchorage, Alaska 99510

B. A. Servin
ARCO Alaska, Inc.
P. O. Box 1966449
Anchorage, Alaska 99519

Abstract

This paper compares the severity of pipeline corrosion as indicated by magnetic flux leakage (MFL) intelligent pigs to the actual severity of pipeline damage. Inspection results from a very comprehensive five-year field verification program are summarized. The inspections were conducted on aboveground insulated pipelines at Prudhoe Bay, Alaska. The pipelines transport corrosive multiphase fluids that contain oil, water, natural gas, carbon dioxide, and hydrogen sulfide. Numerous pig-detected internal and external corrosion features have been inspected by radiographic testing (RT) and ultrasonic testing (UT) over a five-year recurring pigging program. The accuracy and repeatability of the MFL pigs are evaluated. In addition, the limits of detection for corrosion features in the pipe and welds are presented. Operational parameters and other variables affecting MFL pig inspection results are reviewed.

The results show that MFL pigs perform well under extremely adverse conditions. The analysis shows that the MFL pigs are conservative in that they tend to overpredict wall loss. The degree of conservatism increases with severity of the wall loss. The increased difficulty of detecting corrosion in pipeline girth welds and bends is quantified.

Key terms: pipeline corrosion, high-resolution, magnetic flux leakage (MFL), intelligent pig, smart pig, accuracy, statistical analysis, detection limits

I. Introduction

Magnetic flux leakage (MFL) intelligent pigs are used for recurring inspection of pipelines at Prudhoe Bay, Alaska. MFL pig inspection represents one part of a comprehensive on-going inspection program. The program includes frequent recurring radiographic testing (RT) and ultrasonic testing (UT) inspection of known corrosion features. In addition, real-time radiographic testing (RTR) is employed to inspect long segments of piping. Even though high-resolution MFL pigs are used for inspection, historically the results have been used for flagging corrosion features and prioritizing verification inspections. Verification inspections have been conducted on nearly all of the MFL intelligent pig-detected corrosion damage for the majority of the five-year program. Nondestructive examination (NDE) methods such as manual RT and UT are utilized for verification of internal corrosion damage; after removal of the insulation, pit gages and UT are utilized for verification of external corrosion.

As a result of the inspection program at Prudhoe Bay, extensive data has been accumulated on the severity of corrosion features as measured by MFL pigs versus the actual severity of damage. This data results from field verification of previously unknown damage detected by the pigs as well as from the routine monitoring of known damage that is also detected by the pigs.

Most of the data presented in this paper were collected in 16" and 24" diameter pipelines. The 16" diameter line pipe was made by a seamless process while the 24" diameter line pipe was formed by the "U & O" process and seam welded (double submerged arc welded). Table 1 includes a summary of the pipeline parameters. The pipelines are aboveground, insulated, and transport corrosive multiphase fluids. Expansion loops and anchors are located approximately every 1,500 feet along the pipelines (Figure 1). Each expansion loop contains four 90° elbows. A typical five-mile pipeline will contain approximately 70-75 bends. The aboveground pipelines are supported by saddles and stanchions about every 50 feet. This is very significant to verification of damage detected by MFL pigs: the support saddles are detected by the pigs, thereby yielding an excellent reference point every 50 feet along the pipeline. In addition, at least one pipeline girth weld is located between two adjacent support saddles; these girth welds are also detected by the MFL pigs. Thus, any detected damage will have at least three reference points within fifty feet (Figure 2).

II. Preparation and Inspection Procedure

Since permanent pigging facilities were not originally installed for the multiphase piping systems, temporary pig launchers and receivers are installed prior to pipeline cleaning and inspection. Saline water is a major component of the fluids carried within the pipelines. Because the MFL pigs applied cannot operate in saline environments, the liquids must be removed from the pipelines prior to running the MFL pigs. The liquids are removed by sweeping the pipelines with dry natural gas at rates of 40-60 MMSCFD for 4-6 hours. The production fluids in these pipelines tend to carry solids such as formation sand and hydraulic fracture proppant. The solids tend to settle-out and collect along the bottom of the pipelines, especially upstream of elevation changes. Complex flow regimes in multiphase piping systems are conducive to the accumulation of liquids and solid debris.[1] Because solids can interfere with the MFL pig inspections, as much of the solids as possible are removed prior to inspection. The solids are removed using various combinations of conventional brush, disk, and cupped cleaning pigs. The cleaning pigs are often run with water or a high viscosity polymer gel ahead of the pigs to aid in solids pick-up and removal. Dry natural gas is used as the cleaning pig propulsion medium; line pressure is 250-300 psig and pig velocities are maintained at 3-5 ft/sec.

Gage and profile pigs are run prior to the MFL intelligent pig after the liquids and solids have been removed from the pipeline. The gage and profile pigs ensure that the pipeline geometry is suitable for the MFL intelligent pig. Dry natural gas is used as the propulsion medium for the gage, profile, and inspection pig runs. The line pressure during the pig runs is 500 psig and 400 psig for the 16" and 24" diameter pipelines, respectively. In all cases, pig velocity between 8-13 ft/sec is acceptable; 10 ft/sec is considered optimal. In the case of the MFL pigs, velocity is continuously measured and recorded on-board throughout the inspection run for subsequent analysis.

III. General Discussion of Verification Inspection

Intelligent pig accuracy is evaluated by comparing pig-detected damage to the actual wall loss (accepted "true" values) measured by some other NDE method. The purpose of verification inspection is to: 1) evaluate areas suspected of having the worst damage or defects, 2) evaluate the overall performance of the intelligent pig, and 3) establish confidence levels for the data. First and most significantly, pig-detected damage must be properly located and compared to the corresponding damage on the pipeline. Several factors affect the feasibility for making determinate comparisons. Some of these factors are: distance measurement errors by the intelligent pig or surveying method, the extent and characteristics of corrosion in the piping, and the number and distance reference points to pig-detected damage. In addition to technical and physical considerations, other factors can affect the reliability of data comparisons. A natural tendency often exists to force fit intelligent pig data to field inspection results. Insufficient knowledge of pig measurement capabilities and the lack of experienced personnel can exaggerate this tendency and affect the reliability of post inspection analysis. Many of these obstacles can be overcome by employing regimented verification methods and utilizing multiple reviewers.

Verification inspections should always be conclusive regarding pipeline integrity at the verification location. However, if there is reasonable uncertainty about the match-up of the pipeline location to the pig-detected damage, findings can be inconclusive for evaluating intelligent pig performance and data reliability. As discussed earlier, the Prudhoe Bay piping typically has at least three reference points, a girth weld and two support saddles, within fifty feet of pig-detected damage. Even with nearly ideal conditions regarding reference points, it is still not always possible to make an exact one-to-one determinate comparison. Assuming that the correct pipeline location is being verified, there are three possible outcomes when comparing pig-detected damage: underestimation of wall loss, overestimation of wall loss, correct estimation within some decided tolerance limit. At the extremes are failure to detect existing damage and falsely reporting damage in undamaged pipe.

Four different parameters are used to locate pig-detected damage and evaluate the reliability of the inspection results. The parameters are distance comparison, wall loss comparison, repeatability comparison, and azimuth comparison. Distance comparison is the comparison of pig-measured distances to known or actual distances between reference points (welds, fittings, anchors, etc.) or from a reference point to a pig-detected feature. Wall loss comparison is the comparison of pig-measured wall loss values to actual or more accurate wall loss values (measured by a more accurate NDE technique). Repeatability comparisons evaluate an intelligent pig's ability to detect and locate known corrosion features over recurring inspection runs in a given pipeline. Azimuth comparison is the comparison of the pig-measured azimuth for a detected feature to the "true" azimuth value.

The most critical parameter for evaluating intelligent pig results is distance measurement. Distance measurements affect the comparison of all other parameters. Given the level of criticality, distance measurement errors are discussed in further detail. Numerous comparisons between pig-measured distances and known distances in the Prudhoe Bay pipelines show that the pigs are typically within ±2% of actual values (true for short and long segments). The comparisons also show that measurement errors vary throughout a pig run from segment-to-segment in a pipeline. Even though the pigs generally measure distance quite well, it is still important to make several distance comparisons for each inspection run. Occasionally, measurement errors as high as several hundred percent have been seen in short pipeline segments. Measurement errors appear in or tend to be exaggerated by pipeline bends. This may be attributed to inspection vehicle velocity fluctuations and loss of odometer wheel contact at pipeline bends.

Distance comparisons or simple ratio analysis techniques are used to enhance the value of pig inspection results. These techniques can often resolve distance measurement discrepancies or identify pipeline segments with questionable inspection results. In addition to improving the reliability of verification inspections, these techniques have helped reduce the overall cost of verification inspections. Initially, a nominal plus-or-minus tolerance limit was used to account for

pig measurement errors. For example, if a pig's general measurement error was believed to be ±2%, an increment of 4% of the pig-measured distance was inspected along the pipeline at the centerline around the suspected location of a pig-detected corrosion feature. Subsequent analysis of distance measurements indicated that if the measurement error was better known for a given segment of pipeline, damage location could be improved while conducting verification inspections on shorter pipeline increments. Instead of a nominal plus-or-minus tolerance to account for measurement errors, a calculated tolerance is utilized. Both the magnitude and direction of the tolerances is adjusted. The principal assumptions for ratio analysis techniques are that the pig's distance measurement error occurred uniformly across the segment in question and that the surveying method determines the "true" distance. The ratio technique is most successful when applied to short segments of straight piping that do not include bends.

IV. Analysis and Discussion of Inspection Results

The results from five years of recurring MFL pig inspections are included in this analysis. A total of 43 different pipeline inspections were completed from 1988-1992. The 1988 inspection results have been included only in a few parts of the analysis; most of the data are from the 1989-1992 inspections. The intelligent pig inspection history for each individual pipeline is shown in Table 1. The majority (41 out of 43) of the inspections were performed by one contractor. The different inspection tools have simply been identified as A and B in Table 1.

Pig-detected features which could not be matched to actual pipeline features have been omitted from the analysis; only those pig-detected features which could be matched with certainty to actual pipeline features were included in this analysis. As discussed earlier, pig-detected damage is first located and then verified by various NDE methods. Manual RT and/or UT were used to quantify internal corrosion; pit gage and UT measurements were used to quantify external corrosion. As employed, the accuracy for each of the NDE methods is approximately ±2% for internal and ±4% for external corrosion. The remaining wall or wall loss values measured by these NDE methods were considered the actual or "true" values.

The MFL pig inspection results were reported in four different wall loss categories or damage classes. Qualitatively these classes can be thought of as light, moderate, severe, and very severe damage. The range for wall loss percentages in the four different damage classes varied from time-to-time between the following two combinations: 1) <20%, 20%-40%, 40%-60%, and >60% or 2) <30%, 30%-50%, 50%-70%, and >70%. Rather than repeating the cumbersome percentages for each different combination, where possible, we will use the qualita... class descriptions of light, moderate, severe, and very severe damage. Some of the subseq... analysis will involve data interpretations applicable to a specific damage class. Due to very limited and statistically insignificant observations for the severe and very severe damage classes, at times it was necessary to group them into one damage class.

Pig-detected damage from the 1989-1992 inspection results was compared to actual wall loss values. The results were analyzed and categorized as follows: the MFL pig inspection result equals the actual wall loss value, the MFL pig inspection result overestimates (conservative) the actual wall loss value, the MFL pig inspection result underestimates the actual wall loss value. The results from each year are summarized line-by-line in Tables 2 through 5. Although some of the observations were statistically insignificant on a line-by-line basis, the results have been included for completeness. An annual and overall summary for the results is provided in Table 6. Overall, the MFL pigs correctly evaluated 50.5% of the 2,121 corrosion features in the study. Moreover, the MFL pigs overestimated 39.5% and underestimated 10.0% of the total corrosion features. A total of 90.0% of all the corrosion features were either evaluated correctly or overestimated. There was, however, considerable variability in the results from year-to-year. On a year-to-year basis, 47.0%-57.7% of the damage was correctly identified, 31.0-56.9% of the damage was overestimated, and 1.1%-18.9% of the damage was underestimated.

The overall MFL pig results from the Prudhoe Bay pipelines were compared to the results published in another comprehensive field study.[2] The referenced study compared MFL and UT pig performance in the Trans-Alaskan Pipeline. The damage class ranges reported by the UT pigs (10%-20%, 20%-40%, >40%) are comparable to the classes reported by the MFL pigs at

Prudhoe Bay. The results were reviewed and an overall percentage for correct calls by UT pigs was calculated (as done by the author for each damage class). The overall result was that 41% of the total features were correctly (pig-graded wall loss equals field verification inspection) evaluated by the UT pigs. This value is actually less than the 50.5% for correct calls by MFL pigs in the Prudhoe Bay study. Based on the comparison of two comprehensive field studies, the simple accuracy of high-resolution MFL pigs is at least comparable to that of UT pigs. This conclusion contradicts the conventional wisdom that UT pigs are more accurate than MFL pigs. However, the foundation for this conventional wisdom is primarily based upon hypotheses regarding the physics involved with each inspection technique and the results of laboratory bench-top or controlled pull-through tests, all of which ignore or do not duplicate most pipeline inspection conditions. Intelligent pig accuracy is dependent upon the total system (pipeline conditions, etc.), not just the measurement instruments. When the limitations of each technology (such as false-calls and the affects of even small quantities of debris on UT pigs and difficulties with weld inspection for MFL pigs) and inspection conditions in most pipelines are considered, high-resolution MFL pigs may consistently detect and size anomalies better than UT pigs.

In regard to pipeline integrity and leak prevention, overestimation of damage is clearly preferred to underestimation. However, overestimation of damage can be a nuisance and reduce the overall value of pig inspection results. Most important is the degree (how much) to which MFL pigs either underestimate or overestimate damage and how these trends vary in the specific damage classes (light, moderate, severe, very severe). An analysis to quantify underestimation and overestimation errors was completed. First, we simply counted the number of corrosion features that were underestimated (as compared to the actual wall loss values) by more than one damage class. Only 6 or 0.4% of all the 1376 detected and verified corrosion features from the 1991 and 1992 data were underestimated by more than one wall loss category.

In order to quantify variations between pig-predicted damage and corresponding actual wall loss values, data from individual pig-graded damage classes were segregated and further examined. Statistical parameters for five different pig-graded damage classes (2 light, 2 moderate, 1 severe) are shown in Table 7. The mean actual wall loss values were: 18.2% and 21.8% for the light pig-graded damage, 25.4% and 23.5% for the moderate pig-graded damage, and 30.0% for the severe pig-graded damage. Frequency distributions for the actual wall loss values were generated for the five pig-graded damage classes. With exception of the light pig-graded damage classes, the frequency distributions for actual wall loss were all shifted leftward (to lower or more conservative values) relative to the pig-predicted values. The frequency distributions were all positively skewed. As the severity of pig-graded damage classes increased (low to moderate, moderate to severe), the frequency distributions were shifted more leftward and the degree of positive skew decreased. The MFL intelligent pigs graded the more severe pig-predicted damage classes with increasing conservatism. A probability table, Table 8, was constructed for the five different pig-graded damage classes. The table provides probability calculations for actual wall loss ranges for each pig-graded damage class. It should be noted that normality was assumed and that the results are specific to our data set (collected under adverse conditions). However, the results may offer a predictive guideline for other MFL pigging projects.

The pigging results were analyzed for trends simply due to variation in pipe size or wall thickness. The trends were highly variable and no significant conclusions were reached. Relative to other variables, pipe size and wall thickness are believed to be insignificant for our range of parameters. Pipe wall thickness varies from 0.281" to 0.406" for the different pipelines. All of these thicknesses should have easily reached full magnetic saturation, and therefore not appreciably affected the inspection results.

The data were segregated by pipe manufacture method for further analysis. The 16" diameter line pipe was made by a seamless process while the 24" diameter line pipe was formed by the "U & O" process and seam welded (double submerged arc welded). The manufacture method for the 12" diameter line pipe varied; therefore, it was excluded from this analysis. The results in Table 9 show a significant difference in MFL pig performance in the two types of line pipe. The MFL pigs performed much better in seam-welded versus seamless line pipe. The MFL pigs evaluated only 29.9% of all damage correctly in seamless line pipe as compared to 65.5% of all

damage in seam-welded line pipe. Significantly 62.0% of all damage was overestimated in seamless line pipe as compared to only 22.8% in seam-welded line pipe. The percentages for underestimated damage were similar with values of 8.1% and 11.7% for seamless and seam-welded line pipe, respectively. The probable cause for reduced MFL pig accuracy in seamless line pipe is discussed in the next section of this paper.

A total of 154 corrosion features that the MFL pigs did not detect or underestimated were further analyzed. The damage was segregated into the following four different categories based on actual feature length: 1) less than 2 inches, 2) 2 to 6 inches, 3) 6 to 12 inches, and 4) greater than 12 inches. The results are shown in Figure 3. The MFL pigs clearly had more problems detecting or quantifying damage with actual lengths of less than 2 inches (31.2% of the total) or greater than 12 inches (50.6% of the total). Only 18.2% of the anomalies involved features with actual lengths ranging from 2 to 12 inches. One possible explanation for the apparent trend is that: MFL pigs actually derive average wall loss or thickness values from measurements that are a function of feature geometry or three dimensional metal loss. The larger corrosion features require a greater number of successful measurements and averaging over a larger surface area. More opportunity for measurement errors and the inherent errors associated with the volumetric to wall thickness conversion are present. Moreover, if a corrosion feature is too large, it may behave similar to an area of general wall thinning, hence not generating measurable magnetic flux lines perpendicular to the pipe wall or in a geometric pattern that complicates detection throughout the corrosion feature length. Conversely, damage with actual lengths of less than 2" may simply be near or below detection limits.

A breakdown for the percentages of known damage detected and not detected (missed) by the MFL pigs in welds, bends, and welds in bends is illustrated in Figure 4. The majority of the damage included in this analysis was at least 20% wall loss and 1.5 inches in diameter. The pig missed or did not detect known corrosion as follows: 77% of the known damage in welds, 46% of the known damage in bends, and 82% of the known damage at welds in bends. Based on our experience, the MFL inspection tools clearly have increased difficulties with detecting corrosion in bends, welds, and in pipe adjacent to welds. Welds appear to affect detection of damage as far as 1 to 1.5 inches away. Figure 5 shows a radiograph and the corresponding graphical presentation of undetected corrosion adjacent to a pipeline girth weld. Under the adverse pigging conditions in the ARCO multiphase lines, damage of this areal extent (up to 30% wall loss) is often not detected. Error sources associated with MFL inspection at welds are discussed in the next section.

Figure 6 shows a repeatability plot for three short sections of a pipeline. The location of pig-detected damage from three different year's pig inspections is illustrated. Segment No. 1 shows excellent repeatability. The other two sections, No. 2 and No. 3, show reduced degrees of repeatability. Several factors are discussed in the next section that can influence the repeatability of MFL pig results. The repeatability plot illustrates how well the tools can perform and introduces a simple graphical method for evaluating intelligent pig location repeatability.

V. Discussion of MFL Inspection Variables and Data Error Sources

A number of technical factors that affect quantitative accuracy and damage detection limits for MFL pigs are reviewed. Many of these factors relate to physical and metallurgical characteristics of the pipeline. Others relate to conditions inside the pipeline and variation in inspection run parameters. Pipeline design configurations that contain numerous bends and elevation changes can greatly affect the quality of the MFL inspection results in gas pipelines. Given the fact that low pressure gas is a highly compressible fluid, pigs can experience chronic velocity fluctuations during inspection runs.[1] These velocity fluctuations are accentuated as the inspection pigs tend to get temporarily lodged at pipeline bends or elevation changes. It is well known that inspection pig velocity significantly affects magnetic flux leakage signal intensity.[3] Velocity fluctuations can significantly reduce the accuracy of MFL pig results. In fact if the fluctuations are too extreme, data can be worthless at these locations. Certain pipeline segments can essentially go without inspection. An inspection pig that monitors velocity throughout inspection runs is essential.

When using gas as the pig propulsion medium, it is preferable to inspect at the highest acceptable line pressure. Given safety and other design considerations this is not always a viable option. We have found significant dampening of velocity fluctuations when pressures are greater than 400 psig. Figure 7 shows the improvements in a 24" diameter pipeline with the back pressure control valve set at 425 psig and 320 psig, respectively. Decreased velocity fluctuations improved the acceptable inspection results from 83% to 100% of the total line length. Although velocities were within overall limits, the 425 psig velocity plot shows that fluctuations can still be significant in pipelines with several bends and/or elevation changes. We anticipate more dramatic improvements in a straight pipeline under the same conditions. Raising total line pressure increases stress levels in the pipe. If stress levels in the pipe wall eclipse certain thresholds, MFL signal-to-noise ratios are significantly improved.[4,5,6]

Another cause for error in the MFL data is sensor lift-off. The MFL sensors are actually lifted away from the pipe wall as they pass over debris (corrosion products, scale, or produced solids) in the pipeline. The sensors are also lifted away from the pipe wall at pipeline girth welds. As the sensors are lifted away from the pipe wall, their trajectory path and relative velocity are altered throughout the magnetic field. Consequently, the measured voltage signal is corrupted. Although pipeline cleanliness is not as critical as for UT pig applications, its importance is often under-emphasized for MFL pig applications.

The "magnetic signature" or a specific flux pattern associated with seamless line pipe is another cause for error in MFL data. Each joint of seamless line pipe tends to have a spiral patterned "magnetic signature" as a result of the manufacturing process. This particular type of "magnetic signature" is not present in seam-welded line pipe. Essentially the "magnetic signature" is "noise" that must be filtered from information carrying signals. The root cause of the "noise" is likely a combination of variations in the seamless pipe's wall thickness, concentricity, and total applied stresses. The effects of stress on magnetization are well documented.[5,6] The same type of "noise" is often present in fittings and influences MFL inspection results in pipeline bends.

Welds also tend to have a particular "magnetic signature" or a specific flux pattern. The flux pattern developed at welds is partially a function of variation in metallurgy, but also relates to weld geometry. If welds are post weld heat treated and the weld crowns are ground flush, MFL anomalies are eliminated or reduced to insignificant levels. However, full heat treating and grinding are not practical for pipeline girth welds. Pipeline girth welds generally have significant "magnetic signatures." These "magnetic signatures" must be normalized or filtered out of signal measurements to detect corrosion in welds. If welds are similar in geometry and metallurgical variations are limited by tight welding procedures, the likelihood of corrosion detection can be increased. However, detection is still difficult. Even more difficult is quantitative evaluation of corrosion detected in welds.

VI. Conclusions
1) Accuracy for pig-measured distances is critical for the verification of pig-detected damage. Our experience indicates that pig-measured distances are generally within ±2% of actual distances. Distance measurement errors vary in magnitude and direction throughout a pig run in different pipeline segments. Distance measurement errors up to several hundred percent can occur in short pipeline sections. Distance measurement errors tend to be exaggerated near or in pipeline bends. It is not always possible to make one-to-one or exact comparisons between pig-detected damage and subsequent verification inspections. Even when multiple reference points are located within fifty feet of pig-detected damage, the match-up of pig-detected damage and actual pipeline corrosion can be difficult. Intelligent pig inspections should utilize as many reference points as possible.

2) Distance measurement errors can be calculated for different pipeline segments using known reference distances. These values can be used to calculate adjusted measurement tolerances for subsequent verification inspections. Both the direction and magnitude of the tolerances can be adjusted. When applied to short pipeline segments, these adjustments can increase verification efficiency and reduce subsequent inspection costs

3) MFL pig results and repeatability varies from run-to-run or year-to-year in any given pipeline. However, the variation tends to be within reasonable limits. The results from recurring intelligent pig inspections and subsequent verification inspections can help determine the general trend for a given inspection run. Knowledge of these trends can help reduce subsequent verifications and add confidence to pipeline mechanical integrity assessments.

4) Given the pipeline design characteristics, multiphase production fluids, and a gas propulsion medium for pigging, the Prudhoe Bay pipeline conditions represent extremely adverse conditions for MFL pigging. In spite of adverse conditions, generally the MFL pigs perform well and tend to be conservative in their evaluation of detected corrosion. In ARCO's experience at Prudhoe Bay with high-resolution MFL pigs, overall 50.5% of all identified corrosion features are categorized in the correct wall loss category. The MFL pigs overestimated (conservative) 39.5% and underestimated 10.0% of the total corrosion features. In general, a total of 90.0% of all the corrosion features were either evaluated correctly or overestimated. Based on the comparison of two comprehensive field studies, the simple accuracy of high-resolution MFL pigs is at least comparable to that of UT pigs. When the limitations of each technology and inspection conditions for most pipelines are considered, high-resolution MFL pigs may consistently detect and size anomalies better than UT pigs.

5) Pig-detected damage is rarely underestimated by more than one wall loss category. Only 6 or 0.4% of all the 1,376 detected and verified corrosion features from the 1991 and 1992 data were underestimated by more than one pig-graded damage class. The MFL intelligent pigs grade the more severe pig-predicted damage with increasing conservatism. Probability calculations for actual wall loss values were produced for light, moderate, and severe pig-graded damage classes. The results are specific to our data set, but may offer a predictive guideline for other MFL pigging projects.

6) MFL pig's quantitative accuracy is affected by the pipe manufacture method. The pigs perform much better in seam-welded versus seamless line pipe. The percentage of damage correctly sized is 65.5% and 29.9% for seam-welded versus seamless line pipe. Coincidentally, the overall results are similar with approximately 90% of all the values either correctly sized or overestimated and only 8%-12% underestimated. MFL pig results were less accurate and more conservative in seamless line pipe. The probable explanation is MFL "noise" that arises during magnetic saturation of seamless line pipe. The root cause of the "noise" is likely a combination of variations in the seamless pipe's wall thickness, concentricity, and variation of total applied stresses.

7) MFL pigs have increased difficulty with detection of damage in or near pipeline girth welds (up to distances of 1 to 1.5 inches from welds) and in pipeline bends. MFL pigs missed or did not detect known corrosion as follows: 77% of the known damage in welds, 46% of the known damage in bends, and 82% of the known damage at welds in bends. The majority of the damage included in this analysis was at least 20% wall loss and 1.5 inches in diameter.

8) MFL pigs have increased difficulty with detection and sizing corrosion features with actual lengths of less than 2 inches or greater than 12 inches.

9) Increasing total gas pressure from 320 psig to 425 psig significantly mitigated intelligent pig velocity fluctuations. Consequently, inspection coverage was improved from 83% to 100% of total line length in a Prudhoe Bay pipeline.

10) All of the ARCO pigging inspections were conducted under extremely adverse conditions. We anticipate that MFL pig inspection results could be significantly better under more optimal conditions. Given the detection difficulties in welds and bends, the criticality of our pipelines, and extremely adverse inspection conditions, we conclude that high-resolution MFL pigs are not a stand alone inspection technique in our multiphase fluid pipelines. Therefore, supplemental inspections are required to assure pipeline integrity and prevent leaks.

References

1. Rodningen, M., "Pigging of Multiphase Flow Pipelines," Pipes and Pipelines Int. Subsea Pigging Conf., Haugesund, Norway, September 23-25, 1986.

2. Harle, J. C., "Corrosion Inspection of the Trans-Alaska Pipeline," Pipes and Pipelines International, Vol. 36, No. 3, pp. 14-18, May-June1991.

3. Atherton, D.L., Jagadish, C. , Laursen, P. , Strom, V. , Ham, F., Scharfenberger, B., "Pipeline Inspection Tool Speed Alters MFL Signals," Oil and Gas Journal, Vol. 88, No. 5, pp. 84-86, January 1990.

4. Atherton, D.L., "Effect of Line Pressure on the Performance of Magnetic Inspection Tools for Pipelines," Oil and Gas Journal, Vol. 84, No. 43, pp. 86-89, October 1986.

5. Atherton, D.L., Jiles, D.C., "Effects of Stress on Magnetization," NDT International, Vol. 19, No. 1, pp. 15-19, February 1986.

6. Atherton, D.L., Dhar, A., Hauge, C., Strom, V., Ham, F., Scharfenberger, B., "Line Stresses Affect MFL Defect Indications," Oil and Gas Journal, Vol. 90, No. 27, pp. 81-83, July 1992.

TABLE 1
PIPELINE PARAMETERS

LINE NO.	PIPE SIZE (in)	LINE LENGTH (ft)	WALL THK. (in)	PIPE GRADE	PIPE MANUFACTURE METHOD	DESIGN PRESS. (psig)	OPER. PRESS. (psig)	DESIGN CODE	SMART PIG INSPECTED (YEAR)				
									1988	1989	1990	1991	1992
A	24	14,534	0.375	X-65	Seam-welded	708	200	B31 4	A	A	A	A	A
B	16	15,354	0.344	X-56	Seamless	1440	220	B31.4	none	A	none	A	A
C	24	7,299	0.281	X-65	Seam-welded	708	200	B31.4	A	A	none	A	A
D	12	10,528	0.406	X-56	(varied)	1440	791	B31.4	none	none	none	A	none
E	24	15,982	0.375	X-65	Seam-welded	708	220	B31.4	A	A	A	none	none
F	16	16,239	0.406	X-65	Seamless	1320	230	B31.4	none	A	none	A	none
G	24	16,340	0.375	X-65	Seam-welded	720	228	B31.4	none	none	none	none	A
H	16	2,264	0.312	X-65	Seamless	1440	200	B31.4	none	A	none	none	none
I	12	7,200	0.406	X-56	(varied)	1440	742	B31.4	none	none	none	A	none
J	24	6,650	0.281	X-65	Seam-welded	750	234	B31.4	none	A	A	A	none
K	24	26,531	0.281	X-65	Seam-welded	708	200	B31.4	A	A	A	none	A
L	24	9,372	0.281	X-65	Seam-welded	708	200	B31.4	none	none	none	none	A
M	16	17,582	0.344	X-56	Seamless	1440	220	B31 4	none	none	none	A	none
N	24	18,769	0.281	X-65	Seam-welded	708	190	B31.4	none	A	none	none	A
O	24	21,530	0 281	X-65	Seam-welded	750	248	B31.4	none	A	A	A	A
P	24	13,982	0.281	X-65	Seam-welded	720	234	B31 4	none	none	none	none	A
Q	16	25,877	0.312	X-65	Seamless	1440	296	B31.4	none	A	A	B	A
R	16	25,651	0.312	X-65	Seamless	1440	200	B31.4	none	A	none	B	A

Different company's inspection tools; A and B.

TABLE 2
1989 VERIFICATION SUMMARY

LINE	COMPARED	NUMBER OF LOCATIONS MFL = RT/UT	MFL > RT/UT	MFL < RT/UT	% EQUAL	% OVER ESTIMATED	% UNDER ESTIMATED
A	113	76	24	13	67.3	21.2	11.5
B	39	5	34	0	12.8	87.2	0.0
C	3	0	2	1	0.0	66.7	33.3
O	35	14	11	10	40.0	31.4	28.6
E	3	1	2	0	33.3	66.7	0.0
F	40	13	17	10	32.5	42.5	25.0
H	10	10	0	0	100.0	0.0	0.0
N	4	0	4	0	0.0	100.0	0.0
J	30	15	11	4	50.0	36.7	13.3
K	13	9	2	2	69.2	15.4	15.4
Q	67	28	11	28	41.8	16.4	41.8
R	24	8	12	4	33.3	50.0	16.7
TOTAL	381	179	130	72	47.0	34.1	18.9

TABLE 3
1990 VERIFICATION SUMMARY

LINE	COMPARED	NUMBER OF LOCATIONS MFL = RT/UT	MFL > RT/UT	MFL < RT/UT	% EQUAL	% OVER ESTIMATED	% UNDER ESTIMATED
A	138	96	25	17	69.6	18.1	12.3
O	2	1	0	1	50.0	0.0	50.0
E	1	1	0	0	100.0	0.0	0.0
J	2	2	0	0	100.0	0.0	0.0
K	71	47	3	21	66.2	4.2	29.6
Q	150	37	111	2	24.7	74.0	1.3
TOTAL	364	184	139	41	50.5	38.2	11.3

TABLE 4
1991 VERIFICATION SUMMARY

LINE	COMPARED	NUMBER OF LOCATIONS MFL = RT/UT	MFL > RT/UT	MFL < RT/UT	% EQUAL	% OVER ESTIMATED	% UNDER ESTIMATED
A	86	48	21	17	55.8	24.4	19.8
B	48	26	18	4	54.2	37.5	8.3
C	42	22	11	9	52.4	26.2	21.4
O	182	131	34	17	72.0	18.7	9.3
D	149	88	51	10	59.1	34.2	6.7
F	56	29	21	6	51.8	37.5	10.7
M	39	14	25	0	35.9	64.1	0.0
J	30	14	14	2	46.7	46.7	6.7
I	93	55	25	13	59.1	26.9	14.0
Q	73	34	33	6	46.6	45.2	8.2
R	30	17	4	9	56.7	13.3	30.0
TOTAL	828	478	257	93	57.7	31.0	11.2

TABLE 5
1992 VERIFICATION SUMMARY

| | | NUMBER OF LOCATIONS | | | | | |
LINE	COMPARED	MFL = RT/UT	MFL > RT/UT	MFL < RT/UT	% EQUAL	% OVER ESTIMATED	% UNDER ESTIMATED
A	206	169	33	4	82.0	16.0	1.9
B	19	1	18	0	5.3	94.7	0.0
C	8	4	3	1	50.0	37.5	12.5
O	7	0	7	0	0.0	100.0	0.0
G	1	1	0	0	100.0	0.0	0.0
N	4	3	0	1	75.0	0.0	25.0
P	1	1	0	0	100.0	0.0	0.0
K	11	10	1	0	90.9	9.1	0.0
Q	239	32	207	0	13.4	86.6	0.0
L	36	9	27	0	25.0	75.0	0.0
R	16	0	16	0	0.0	100.0	0.0
TOTAL	548	230	312	6	42.0	56.9	1.1

TABLE 6
1989-1992 VERIFICATION SUMMARY

| | | NUMBER OF LOCATIONS | | | | | |
YEAR	COMPARED	MFL = RT/UT	MFL > RT/UT	MFL < RT/UT	% EQUAL	% OVER ESTIMATED	% UNDER ESTIMATED
1989	381	179	130	72	47.0	34.1	18.9
1990	364	184	139	41	50.5	38.2	11.3
1991	828	478	257	93	57.7	31.0	11.2
1992	548	230	312	6	42.0	56.9	1.1
TOTAL	2121	1071	838	212	50.5	39.5	10.0

TABLE 7
STATISTICAL PARAMETERS FOR ACTUAL WALL LOSS VALUES
IN DIFFERENT PIG-GRADED DAMAGE CLASSES*

Qualitative Description for Damage Class	Pig-Graded Damage Class	Actual Wall Loss			Total Count
		Mean	Std. Dev.	Skew	
Light	<20%	18.2	8.1	1.31	161
Light	<30%	21.8	11.1	0.69	199
Moderate	20%-40%	25.4	8.7	0.29	371
Moderate	30%-50%	23.5	10.8	0.54	412
Severe	>50%	30.3	10.8	0.00	53

* 1991 and 1992 data only.

TABLE 8
PROBABILITY TABLE FOR PREDICTED ACTUAL WALL LOSS VALUES

Pig-Graded Damage Class	Probability that Actual Wall Loss is in the Specified Range						
	<20%	20-30%	30-40%	40-50%	50-60%	60-70%	>70%
Light(<20%)	0.587	0.341	0.069	P(x)>40% 0.003	•	•	•
Light(<30%)	0.436	0.334	0.179	0.045	0.005	P(x)>60% 0.001	•
Moderate (20%-40%)	0.268	0.434	0.252	0.044	P(x)>50% 0.002	•	•
Moderate (30%-50%)	0.375	0.351	0.211	0.056	0.007	P(x)>60% <0.0001	•
Severe (>50%)	0.171	0.317	0.328	0.150	0.031	0.003	<0.0001

TABLE 9
VERIFICATION SUMMARY FOR DIFFERENT PIPE MANUFACTURE METHODS

MANUFACTURE METHOD	NUMBER OF LOCATIONS						
	COMPARED	MFL = RT/UT	MFL > RT/UT	MFL < RT/UT	% EQUAL	% OVER ESTIMATED	% UNDER ESTIMATED
Seamless	850	254	527	69	29.9	62.0	8.1
Seam-welded	1029	674	235	120	65.5	22.8	11.7
TOTAL	1879	928	762	189	49.4	40.6	10.1
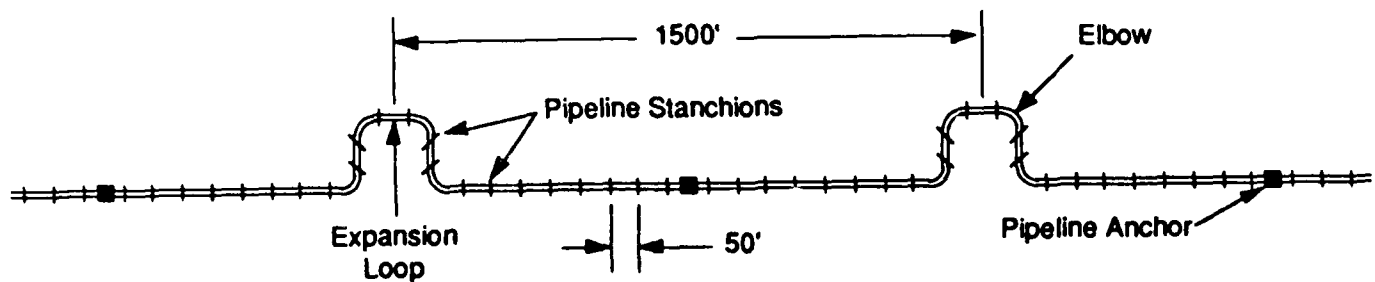
Figure 1. General Overview of Pipeline Design
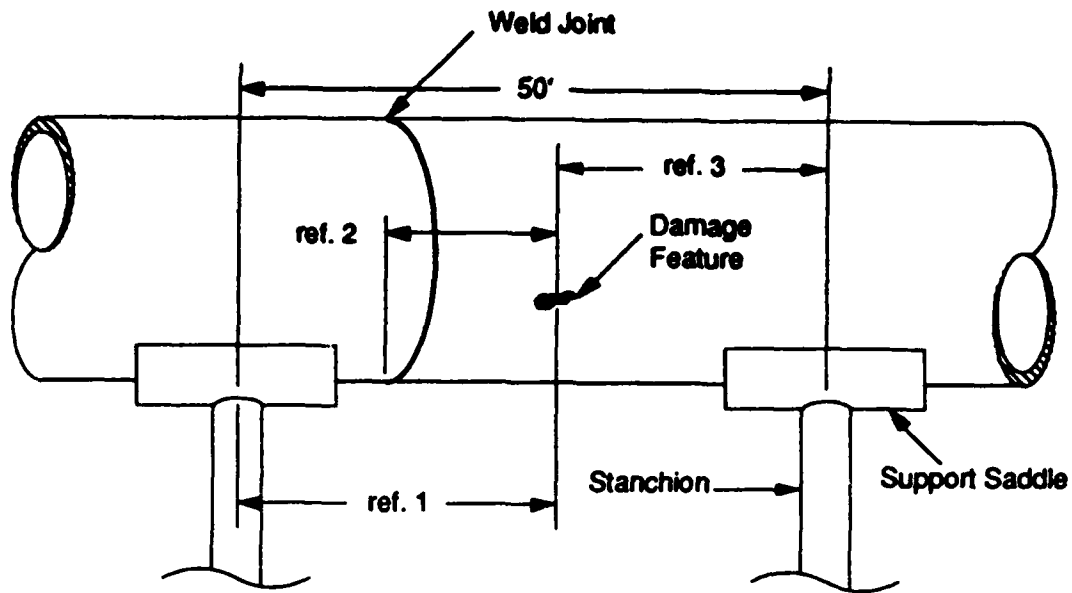
Figure 2. Basic Diagram of Pipeline Installation

81.8% of the total discrepancies involved features with actual lengths of less than 2 or greater than 12 inches.
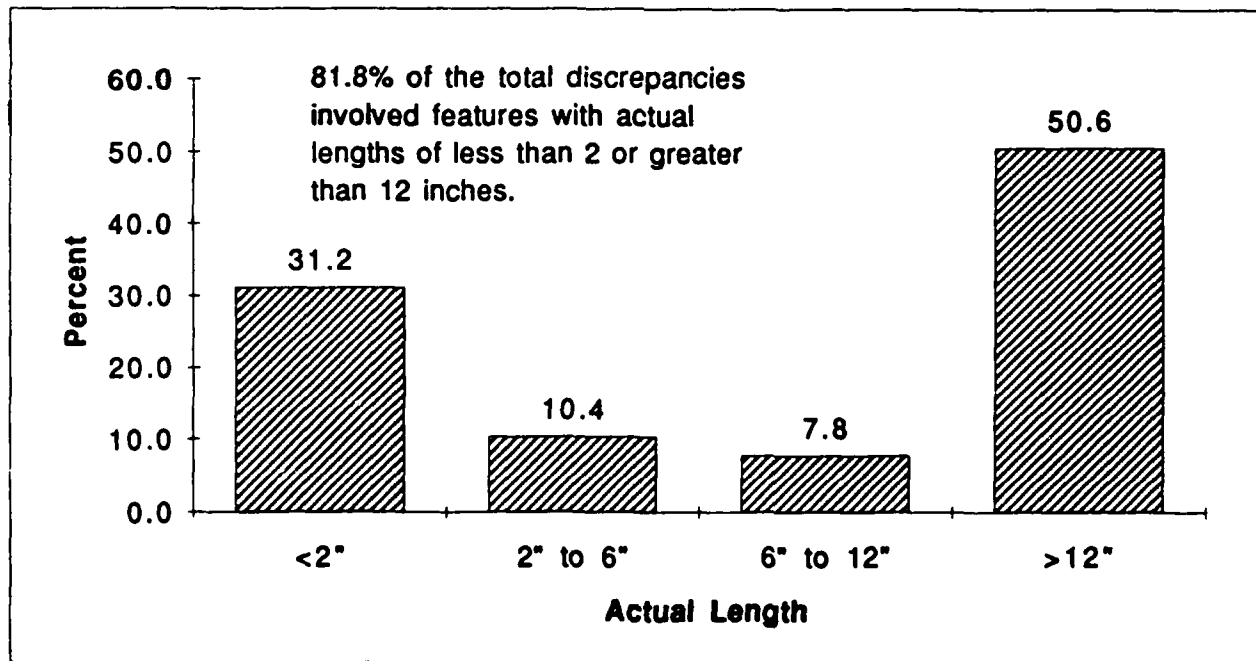
Figure 3. Corrosion Features Not Detected or Underestimated as Compared Actual Length
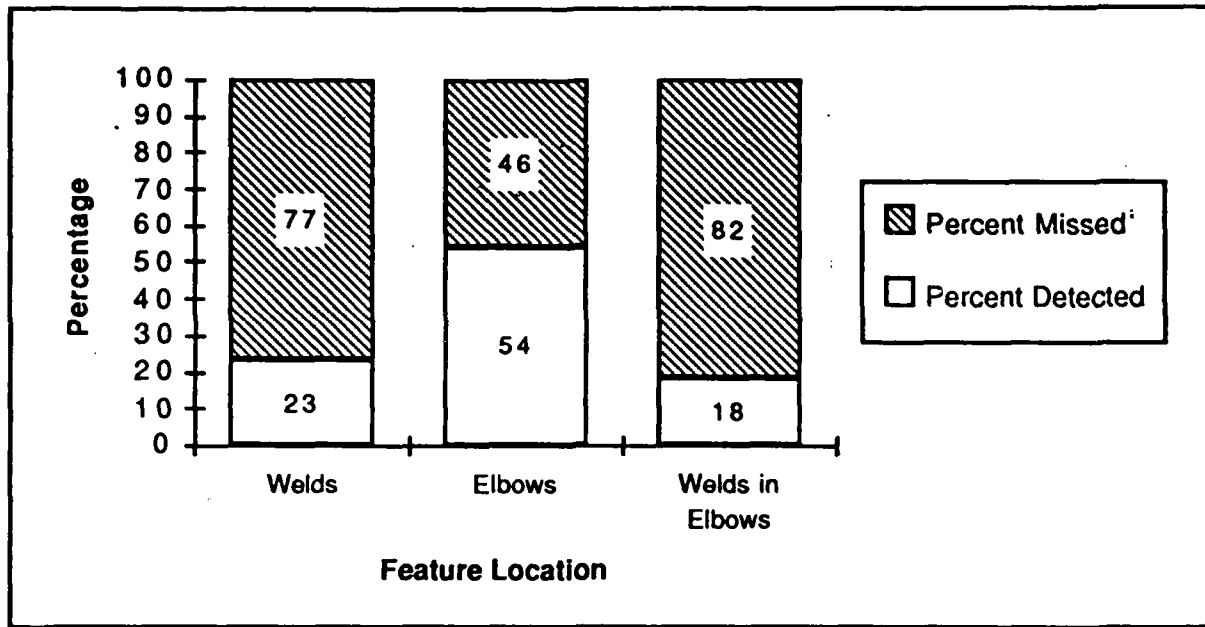
Figure 4. Detected and Missed Corrosion Features in Welds, Elbows, and Welds in Elbows
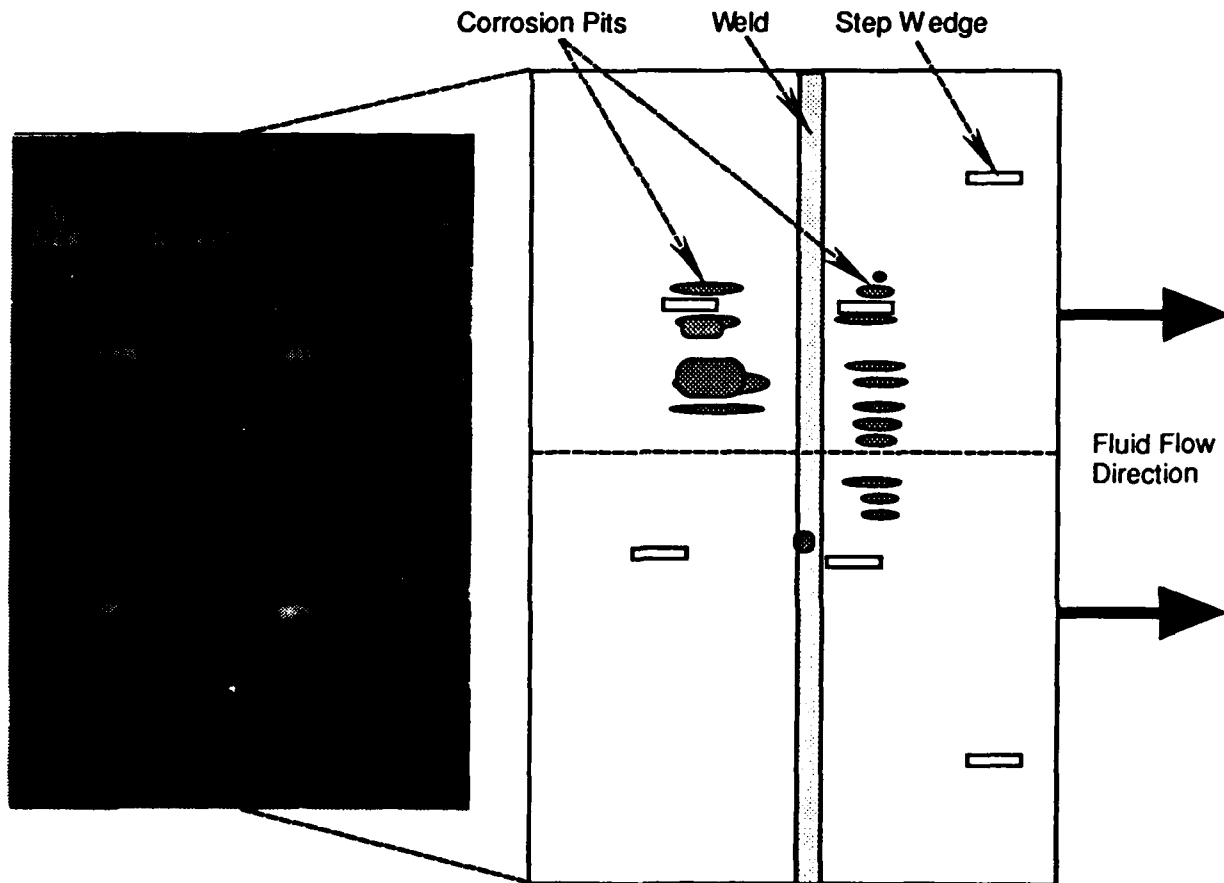
Figure 5. Radiograph and Corresponding Diagram of Undetected Corrosion Damage Near Pipeline Weld
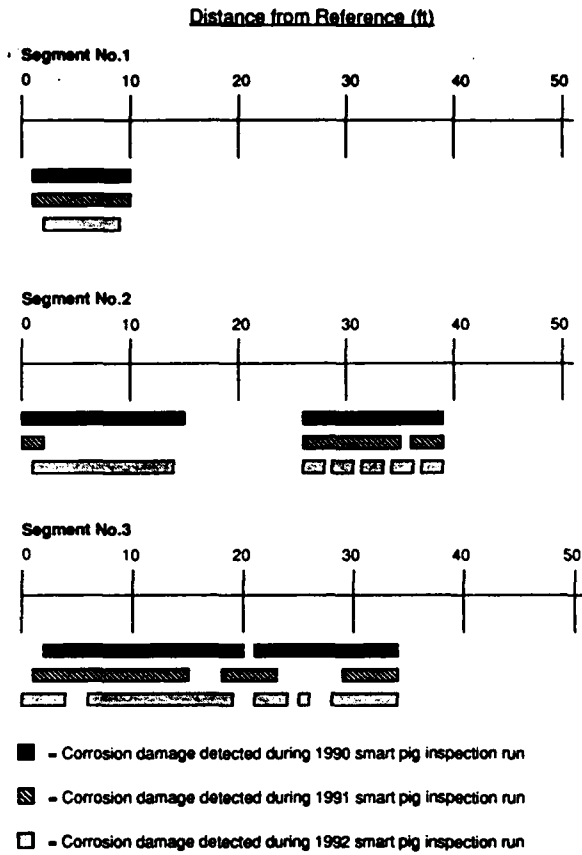
FIGURE 6. Repeatability Diagram for Short Segments in Pipeline A
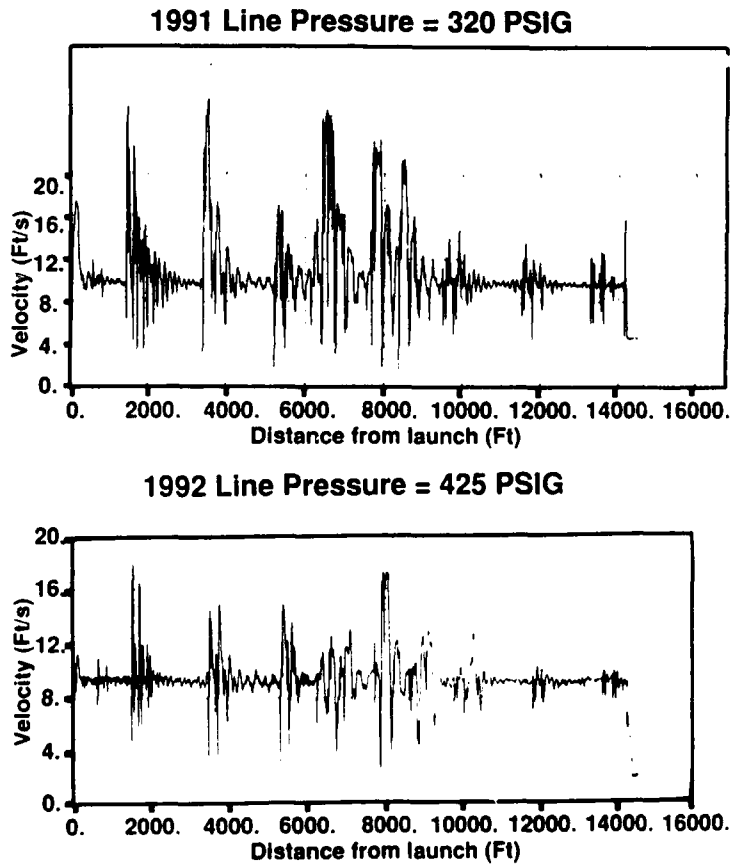
Figure 7. Plots of MFL Pig Velocity vs. Distance Along the Pipeline for Two
Different Total Line Pressures

Practical Approach To Evaluating A Corrosion and Scale Inhibition Program in a Gathering System

Dr. Robert C. Bess
Caltex Pacific Indonesia
Rumbai, Pekanbaru 28271
Sumatra, Indonesia.

Doc Monical
Champion Technologies
AKA Build. 6th Floor Jl. Bangka 2
Jakarta 12720, Indonesia.

Eddy Yanto/ Bill Black - Contributors
Champion Technologies
AKA Build. 6th Floor Jl. Bangka 2
Jakarta 12720, Indonesia.

ABSTRACT

An integrated corrosion and scale treatment program was evaluated using a special gas/liquid separation sidestream apparatus in conjunction with an electrochemical potentiostat. The Electrochemical Sidestream Apparatus (ESA) was custom designed by Champion Technologies for use by P.T. Caltex Pacific Indonesia in Sumatran oil gathering systems. It was found to be a very effective system for evaluating corrosion tendencies in gas/liquid matrices, by electrochemical methods.

The field investigations had historically been followed using in-line pre-weighed, commercial weight loss corrosion coupons for monitoring the inhibition program. A comparative corrosion monitoring program was conducted using both commercial corrosion weight loss coupons and electrochemical techniques based on polarization resistance, cyclic voltammetry, and Tafel extrapolation. Three main phenomena were investigated: (1) localized corrosion, primarily due to solvated carbon dioxide; (2) erosion corrosion due to the production of sand, and (3) the effect of an oil in water reverse emulsion on the corrosion processes.

Scaling tendencies were evaluated from real time scaling coupon data, historical scale formation data, simulation runs using Oddo-Tomson Calculations.

The efficacy and cost effectiveness of using a dual function corrosion/scale inhibitor versus a unifunctional corrosion inhibitor was examined in light of the current research data.

The project was a joint research effort of Champion Technologies, Inc., P.T. Champion Kurnia Djaja Technologies, and P.T. Caltex Pacific Indonesia.

Key Terms: CO2, Electrochemical, Corrosion Rate (mpy), Corrosion Inhibitor, ESA, Calcium Carbonate Scale, Dual Function Inhibitor.

INTRODUCTION

A integrated corrosion/scale mitigation program was evaluated in an oil gathering system located in Central Sumatra, Riau Province, Republic of Indonesia. The gathering system produces light gravity crude oil with an average water cut of 92% and an average well head temperature of 180 degrees Fahrenheit. The gathering lines consist of 2 inch to 20 inch ID mild carbon steel pipelines. The production contains an average of about 29% free CO_2 in the separated gas phase, and an average of about 150 ppm of solvated carbon dioxide in the field area examined in this study. The untreated produced water contains an oil in water (reverse) emulsion of 2800 - 4000 ppm oil in the water phase coming into the gathering stations. The operating pressure of the various pipelines in the system varies from about 50 psi to 120 psi depending on particular section of the gathering system. The only present method of corrosion monitoring used in the area routinely is a weight loss coupon. Coupons are installed on the pipelines at the six o'clock (bottom) position.

Due to the large amount of CO_2 solvated in the water, a variety of unique conditions can exist within the producing area that exhibit scaling, corrosion or both depending on the well water chemistry and the operating conditions at the specific location. In some of the lines localized corrosion has occurred due to carbon dioxide attack (Figure 1) while calcium carbonate scale has occurred mainly in the separation facilities with only limited instances of scale in upstream producing lines and equipment.

Because of the problems of some scale and corrosion simultaneous occurring in locations within the field, the current practice has been to apply a combination scale and corrosion inhibition product commonly referred to as a "dual function" inhibitor.

The present chemical is a completely water soluable combination chemical that is formulated to inhibit both corrosion and scale at a produced fluid temperature of 180 degrees F. The average treatment rate has been 3.0 to 4.0 ppm continuous injection.

I. Evaluation of Corrosion Inhibition Program

The present research involved designing a gas/liquid separation vessel and sidestream with an electrochemical potentiostat interfaced to it in order to make instantaneous electrochemical measurements in the operating system. The sidestream apparatus successfully separated the gas, oil, and water to an acceptable level for electrochemical data acquisition. Previous attempts by other investigators in this producing area had always resulted in unreliable data due to electrode fouling.

The actual dimensions of the separation vessel were three feet in height and 12 inches in diameter interfaced into the producing line to simulate a gas boot. The electrochemical electrodes were inserted into the bottom of the apparatus. The vertical separator allowed for sufficient oil separation from the water not only for electrochemical investigations, but also provided good quality produced water samples for chemical analysis by bottom sampling the

apparatus. The sidestream system design allowed for obtaining good quality samples under dynamic operating conditions.

All electrochemical data were obtained with a portable potentiostat with the working electrode area for cyclic scans designed to obtain a current density of 5 milliamperes per square centimeter for estimated pitting rate determinations 1-3. All data was calculated to express corrosion rates in mils per year (MPY).

A. Background Uninhibited Corrosion Rates

The ESA unit was installed at seven coupon and wellhead locations within the gathering system network to determine uninhibited corrosion rates. The effect of the stabilized oil in water emulsion and sand production on the corrosion rate could also be monitored under the uninhibited conditions.

The ESA sidestream also provided a method of comparing instantaneous electrochemical corrosion rates with the present and past weight loss coupon data.

The uninhibited corrosion measurements by electrochemistry were somewhat higher than the coupon rates. This was felt not to be an experimental artifact; but an indication that the ESA design was able to produce a much cleaner water to examine versus the line water which contained a 2000 - 4000 ppm oil in water (reverse) emulsion as well as possibly some coupon exposure to produced oil in pipelines with sufficient flow turbulence. This was supported by previous studies which indicated that under nonfouling and nonconcentration polarization conditions, the electrochemical data can agree very closely with carefully monitored coupon data 4- 6. The higher electrochemical corrosion rates were also consistent with the examination by scanning electron microscopy of several coupons that indicated little contribution from erosion to the corrosion rates in most producing lines. These coupons showed no etching or abrasion along their edge surfaces perpendicular to the direction of flow.

Figure 2 depicts the corrosion rates in MPY of corrosion coupons compared with the electrochemically determined general and pitting corrosion rates.

As mentioned previously, the difference in the electrochemical and coupons rates is somewhat due to the inhibiting effect of the produced oil and oil in water emulsion found in the produced water.

B. Inhibited Corrosion Rates

1. Dual Function Inhibitor

The chemical injection of the dual function scale corrosion inhibitor was initiated after the acquisition of all background data. The ESA sidestream was installed and the electrodes were allowed to reach steady state. Steady state corrosion rate measurements were then taken for five hour periods and an average value calculated for each five hour exposure period. The reported electrochemical values are the five hour averaged values (Figure 3).

Corrosion coupons were installed and the general corrosion rates determined by 45-60 day exposures. The corrosion rates of the two methods are compared in Figure 3. The two methods agree well and both were determined to be satisfactory methods for measuring corrosion rates in the gathering system. The electrochemical methods have the advantage of providing more detailed and instantaneous data.

2. Single Inhibitor Amine Bases

The corrosion performance of the dual function chemical was investigated by examing its mitigation efficiency versus two single function corrosion inhibitor only formulations.

The dual function chemical injection was discontinued and a microliter chemical injection pump was installed into the feed line of the cleaned separator of the ESA unit. Corrosion inhibitor bases were blended to 1% solutions for microliter chemical injection.

The inhibitor bases evaluated were:

(a) Blend A -- a water soluable quaternary amine.
(b) Blend B -- water soluable oxyalkylated amines
(c) Blend C -- the water soluable dual function scale/corrosion product.

Figure 4 compares the inhibited corrosion rates of the three product blends. Blend B gave the best corrosion mitigation with an average estimated pitting rate of 3.0 +/- 1.0 MPY.

II. Evaluation of Scale Inhibitor Program

An investigation of various ratio blends of the water soluable dual functions inhibitor were examined to find the most effective ratio of scale inhibitor to corrosion inhibitor for areas of the field with different water chemistries. Blends in decade per cent increments of 70% scale inhibitor to 30% corrosion inhibitor to 30% scale inhibitor to 70% corrosion inhibitor were examined for total effectiveness and cost effective application.

A calcium carbonate scale simulation was conducted on the produced water at the gathering station. The produced water was sampled through the separation gas boot. The pH, CO2 in water, and bicarbonates were determined immediately (Table 1). The Oddo-Tomson 7 calcium

carbonate scaling tendencies was calculated at variable operating conditions experienced in the production and gathering system. The Valone-Skillern method was used to calculate calcium carbonate scale deposition in the facilities at atmospheric pressure. The results indicate a positive scale index of 0.69, but the amount of calcium carbonate scale is limited to 42 pounds per thousands barrels.

As the operating pressure and CO2 content drops in the system, the calcium carbonate scale potential increases (Figure 5 & 6). This would indicate a potential for scale after degassing in the separation facility on the water injection system.

Previous field records and performance reports of oil wells and surface equipment have shown virtually no calcium carbonate scale has formed in the gathering system during the last two years in the producing area studied. Secondly, no serious scaling has taken place upstream of the dual function chemical injection points. This would indicate calcium carbonate scale is not dropping out upstream carbonate from Valone scale simulation program. The dual function inhibitor provides phosphonate residuals in the produced water to an average of 0.45 ppm. Field results indicate this residual seems to be sufficient to inhibit scale downstream in the separation facility.

Based on this study, a dual function inhibitor is not required in this area of the production and a more cost effective single function water soluable corrosion inhibitor based on oxyalkylated amine chemistry will be used in a new chemical treatment program specifically designed for this production area of the field.

III. CONCLUSION

The ESA electrochemical sidestream system is an accurate and reliable method for examing corrosion phenomena on-line in operating systems where the oil/water separation can be accomplished with reasonable efficiency.

The standard in-line commercial weight loss corrosion coupons are a valid corrosion monitoring method for the gathering system.

The level of CO2 in the gas and water provide a mechanistic pathway for high levels of corrosion if untreated.

Erosion corrosion due to unconsolidated sand flow is not a significant corrosion influence in the studied area.

The reverse emulsion in the produced water enhances the corrosion inhibitor process and reduces the severity of the corrosion by oil wetting pipe surfaces.

Single function corrosion inhibitors are more cost effective for this system, as the incidence of scaling is insignificant. The dual function treatment will be discontinued and a new treatment program based on oxyalkylated amine chemistry will be implemented.

Calcium carbonate scale upstream of the separation factory is not a major concern.

Any scaling problems would occur after degassing as the calcium carbonate scaling index increase with reduced CO_2 and pressures. A chemically compatible scale inhibitor if necessary could be injected at low concentrations upstream of the gas boot. This would control the calcium carbonate scale at lower operating pressures in the separation facilities. The use of two separate single function compatible corrosion and scale treatment chemicals will be more cost effective in this system than a dual function product.

REFERENCES:

1. R.L. Martin, Application of Electrochemical Polarization to Corrosion Problems, (St. Louis, MO: Petrolite Corporation, 1981), p. 7-66.

2. Robert Baboian, G.S. Haynes, "Cyclic Polarization Measurements-Experimental Procedure and Evaluation of Test Data," (Philadelphia, PA: ASTM STP 727, Electrochemical Corrosion Testing, 1984), p. 274-281.

3. M.G. Fontana, Corrosion Engineering, 3rd edition, (New York, NY: McGraw-Hill Company, 1986), p. 41-503.

4. R.C. Bess, K.M. Koshy, "Comparative Study of Wheel Oven vs. Electrochemical Methods for Evaluation of Corrosion Inhibitors in a CO2 Saturated Saudi Arabian Brine", Proceedings of the Second Saudi Engineering Conference, (Dhahran, KSA: University of Petroleum & Minerals, 1985).

5. R.C. Bess, "Application of DC Electrochemical Techniques to the Study of Corrosion Processes," Proceedings of the Second Saudi Chemists Conference, (Riyadh, KSA: King Saud University, 1986).

6. R.C. Bess, P.E. Frazer, and C.F. Hurley, "On-Line Electrochemical Cell For the Laboratory Performance Evaluation of Corrosion Inhibitors Used in Well Squeeze Applications," 5th NACE/BSE Corrosion, (Manama, Bahrain: NACE/BSE, 1991).

7. J.E. Oddo, M.B. Tomson, Journal of Petroleum Technology, 34 (1982): p. 1583-1590.

TABLE I

WATER ANALYSIS & SCALING TENDENCY

COMPANY:
FIELD: Sumatran Field
SAMPLE LOCATION: Wash Tank
SAMPLE DATE: Jan. 11, 1993
SERVICE ENGINEER:

WATER ANALYSIS

CHEMICAL COMPONENT		Pipeline	After Degassing	Water Inj.
CHLORIDE (Cl)	MGS/L	1203	1203	1203
SULFATE (SO4)	MGS/L	40	40	40
CARBONATE (CO3)	MGS/L	48	48	48
BICARBONATE (HCO3)	MGS/L	1144	1144	1144
CALCIUM (Ca)	MGS/L	80	80	80
MAGNESIUM (Mg)	MGS/L	63	63	63
IRON (Fe)	MGS/L	1.5	1.5	1.5
BARIUM (Ba)	MGS/L	0	0	0
STRONTIUM (Sr)	MGS/L	0	0	0
SODIUM (Na)	MGS/L	1051	1056	1056
IONIC STRENGTH		0.06	0.06	0.06
DISSOLVED SOLIDS	(TDS)	3645	3645	3645
SPECIFIC GRAVITY @60F		1.00	1.00	1.00
TEMPERATURE	(F)	165	155	200
Is (TOMSON-ODDO)		0.50	2.42	1.71
PRESSURE	(PSIA)	50	25	500
pH CALCULATED	(TOMSON)	6.38	8.41	7.28
SURFACE pH	(METER)	7.25	7.80	7.80
% CO2	(MOLE %)	29.00	0.50	0.50

ANALYST:

SCALING TENDENCIES

PTB CACO3		45.3	69.6	68.3
PTB BASO4	(TOMSON)	-0.4	-0.3	-0.5
PTB CASO4	(TOMSON)	-1012.0	-1039.5	-953.7
PTB SRSO4	(TOMSON)	-48.3	-50.6	-42.6

Figure 1
Pitting Corrosion Rates vs Solvated CO2 Concentration

Background Corrosion Rates conducted with ESA
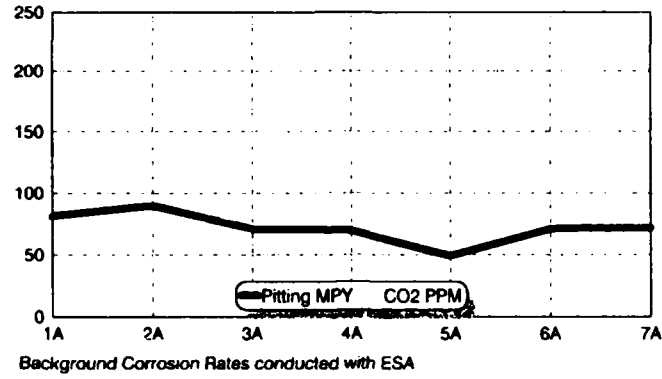
Figure 2
Background Corrosion Rates
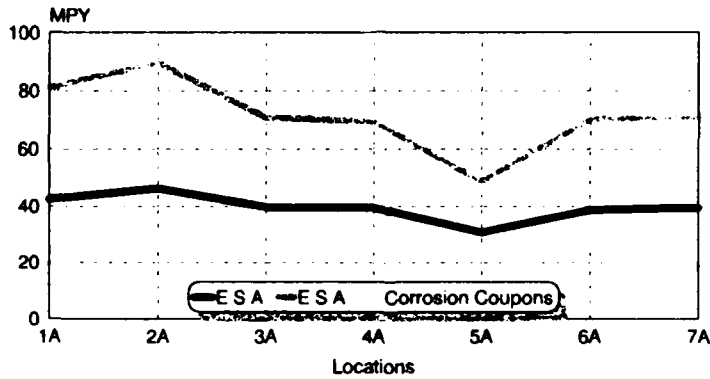
Figure 3
Dual Function General Corrosion Rates

System Treated at 4 ppm
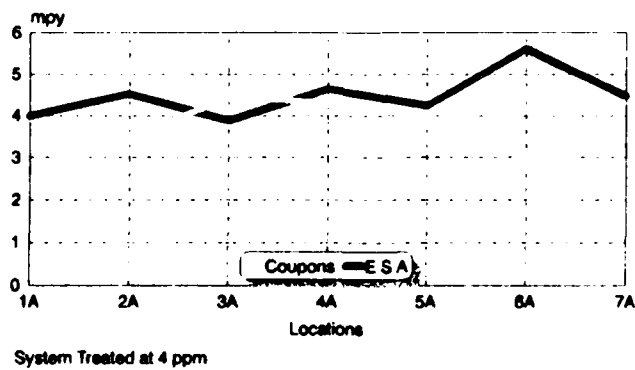
FIGURE 4

Pitting Rates of Three Types of Inhibitor Bases

Treated with 4 ppm of chemical

Figure 5

Calcium Carbonate Stability Index Scaling Curve
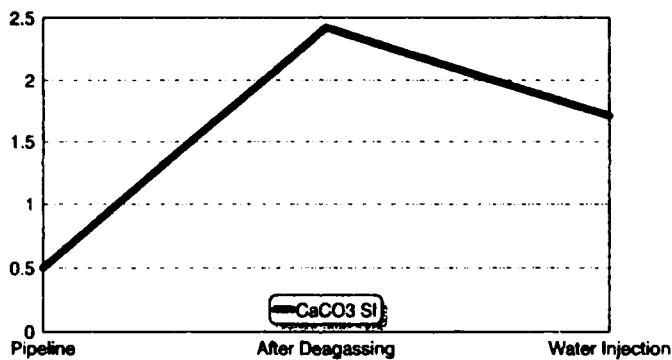
Oddo-Tomson Method

Figure 6

Calcium Carbonate Scale Deposition Curve
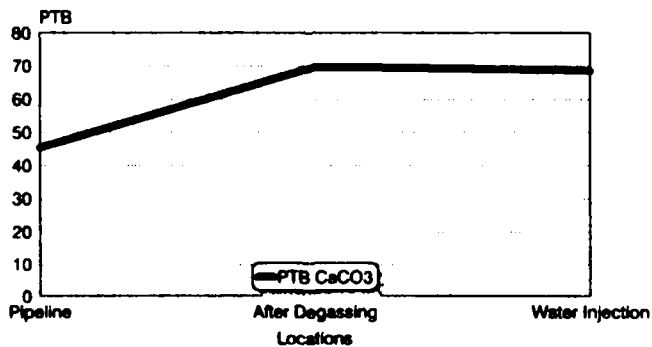
Oddo-Tomson Method

THE IMPORTANCE OF WETTABILITY IN OIL AND GAS SYSTEM CORROSION

John S. Smart, III
John Smart Consulting Engineers
14210 Carolcrest Drive
Houston, TX   77079
tel/fax 713 493 5946

ABSTRACT

Wettability is one of the most important factors in determining if corrosion will occur in oil and gas systems, but is little understood. Factors involved in determining the oil vs. water wettability of metal and corrosion product surfaces are presented. The data are applied to corrosion under producing well and production equipment conditions to estimate when corrosion can be expected to occur and 'he effect of wettability on corrosion rates.

KEYWORDS: Corrosion, wettability, oil-wet, water wet, surfactants, water cut, problem wells, sulfonates, amines, contact angle, inhibitors, carboxylic acids, interfacial energy, adhesion tension

INTRODUCTION

With today's technology, corrosion engineers are very good at explaining corrosion once they find it, but they are not always so successful at predicting when and where it will occur in the first place. One of the major factors in determining when and where corrosion actually occurs, but which has received little attention in the corrosion literature, is the subject of wettability.

Wettability helps determine when and where metal surfaces can become water wet, and thus are subject to corrosion. Surfaces which remain oil wet do not corrode.

Further, even surfaces which do become water wet can have substantially modified corrosion characteristics due to oil wetting parameters. These wettability effects are the reason that several authors have found such a strong effect when oil is present when testing system corrosion parameters. If wettability can be predicted, or measured for a system, then a major factor in corrosion can be better understood and costly errors avoided.

Wettability has been recognized as an important factor in corrosion for over 40 years, with significant research efforts by at least three major oil companies (1,2). Wettability was thought to affect corrosion in two ways, by reducing the interfacial tension between water and oil, and by increasing the tendency of oil to wet steel. Early workers concentrated in the development of oil wetting agents as corrosion inhibitors. Researchers performed sessile drop size ratio tests to determine the wettability of various oils in the presence of their produced brines. From the results, however, they concluded that they were doing something wrong. There is no mention of the requirement that air contamination of the samples be avoided, which is one likely source of their problems. As a result, early efforts in this field were not successful, and were terminated.

Wettability

Wettability is defined as "the tendency for one fluid to spread on or adhere to a solid surface in the presence of another immiscible fluid."(3) Applied to corrosion, wettability is a measure of the preference of the corrosion product layer or metal surface for either water or oil. When the corrosion product layer is water wet, there is a tendency for water to contact the majority of the corrosion product film and to fill cracks and interstices in the corrosion product film. It is important to note, however, that the term wettability is used to denote the wetting preference of the surface, and does not necessarily refer to the fluid with which it is wet at any given time.

Measurement of wettability

To understand some wettability characteristics, consider the idealized oil-water-mineral system shown in Figure 1. The surface energies in this system are related by the Young-Dupre equation as follows:

$$\sigma_{os} - \sigma_{ws} = \sigma_{ow} \cos \theta_c \qquad \text{[Eqn. 1]}$$

where

σ_{os} = interfacial energy between the oil and solid, dynes/cm

σ_{ws} = interfacial energy between the water and the solid, dynes/cm

σ_{ow} = interfacial energy (interfacial tension) between the oil and water, dynes/cm

θ_c = angle at the oil-water-solid interface measured through the water, degrees.

The oil-solid and the water-solid interfacial energies cannot be measured directly, however, the oil-water interfacial tension and the contact angle can be determined in the laboratory. Therefore, the contact angle, θ_c, has achieved significance as a measure of wettability. It can range from zero to 180°, signifying completely water wet surfaces and completely oil wet surfaces.

Wettability can range from strongly oil wet to strongly water wet, depending upon the type of surface and the properties of oil and water in contact with it. In rock core wettability studies, water advancing contact angles less than 75°,

measured through the water, are considered as water wet, while a contact angle greater than 105° is considered oil wet(4,7). Contact angles between 75° and 105° are considered as neutrally or intermediate wet. Besides oil and water wet, systems can have mixed wettability, with some areas water wet and some oil wet. Another type of wetting in crude oil brine systems is called "hybrid" wetting, in which the water advancing contact angle is greater than 90° and the water receding contact angle is less than 90°. In a hybrid system, whichever liquid is in contact with the surface tends to remain in contact with the surface until it is displaced because of overriding forces.

Andersen, et al (7) have recently developed an improved device for measuring the wettability preference of crude oil/brine/water systems based upon the Wilhelmy plate technique. Wilhelmy described the basic technique for measuring surface tension and interfacial tensions in 1863 (8), and it is still a standard technique in surface chemistry.

In the modified Wilhelmy technique, a thin plate of the mineral to be tested is suspended from a computer controlled microbalance over a vessel containing oil and brine. A computer controlled stepper motor moves the vessel upwards, causing the plate to pass through the air-oil and oil-brine interface. The change in force on the plate as it passes a fluid-liquid interface is related to the adhesion tension of the mineral surface. Adhesion tension is the product of the Interfacial Tension and the cosine of the contact angle as given in Equation 1. If the lower liquid preferentially wets the plate, an upward meniscus forms on the plate and the adhesion tension is positive. Alternately, if the solid prefers wetting by the upward liquid, a downwards meniscus forms as the interface passes the bottom of the plate, and the adhesion tension is negative. Figures 2 and 3 illustrate the types of meniscus that form under water wet and oil wet conditions. This one test gives both a visual and a quantitative measure of wettability. Because the test can be run both upwards and downwards, hybrid wettability can be determined, as well as determining aging effects such as caused by exposure of crude oils to air.

WETTABILITY FACTORS

Reservoir rock wettability has been extensively studied by petrophysicists, and an exhaustive literature survey has been recently performed(4-6). Corresponding data on corrosion related wettability is very limited. However, since corrosion products such as iron oxide, iron carbonate, and iron sulfide are similar in many respects to reservoir minerals such as silica, magnesium carbonate, and calcium carbonate, much information on the wettability characteristics of corrosion products can be obtained from reservoir rock studies.

Reservoir rock is originally water wet due to its sedimentary formation, and is made up of many minerals, each with different surface chemistry and adsorption characteristics. It was soon discovered, however, that reservoir rock can also be oil wet, and that oil wettability of reservoir rock was controlled by the adsorption and/or precipitation of surface active or polar compounds from crude oil (4).

Smart (9) recently reviewed the factors important in the wettability of reservoir rock, which are summarized as follows:

Surface Active Compounds in Crude Oil

There are more than 1500 separately identified surface active compounds in crude oils. It is the presence or absence of these surface active compounds which is the major factor in the oil wetting tendency of an oil (4). The total quantity of these compounds is usually only a few ppm, and, unfortunately, no analytical technique is yet able to identity these compounds and relate their chemistry to the wetting characteristic of the oil.

While the surface active components of crude oils are found in a wide range of petroleum fractions, they are more prevalent in the heavier fractions of crude, such as resins and asphaltenes (4). The surface active agents in oil are generally believed to be polar compounds that contain oxygen, nitrogen and/or sulfur. The oxygen compounds, which are usually acidic, include the phenols and a large number of different carboxylic acids, which are interfacially active at alkaline pH. Sulfur compounds include sulfides, thiophenes, mercaptans and polysulfides. Nitrogen compounds are usually basic or neutral, and include carbazoles, amides, pyridenes, quinolines, and porphyrins. Porphyrins can form interfacially active metal/porphyrin complexes with a number of different metals, including nickel, vanadium, iron, copper, zinc, titanium, calcium, and magnesium.

Wettability Effect of Polar Compound Chemistry

The surface active compounds in crude oils have different effects on wettability.(4) Positively charged, cationic surfactants such as amines tend to stick to negatively charged surfaces such as silica. Negatively charged anionic surfactants such as organic acids tend to stick to positively charged surfaces such as carbonates, and Sulfonates seem to have no systematic differences between mineral surfaces. Adsorption of precipitated asphaltenes promotes crude oil wettability on mineral surfaces.

The implications for corrosion of these polar compounds is that "black" oils should tend to give corrosion problems at higher water fractions than would light oils such as gas condensate. This is only a tendency, however, as each oil in unique and must be measured. Deasphalted and refined oils did not show oil adhesion at any tested pH level (4), meaning that petroleum product pipelines, for instance, could be especially susceptible to corrosion, even at very low water levels.

Effect of pH

The surface charge of silica and calcite in water is positive at low pH, but negative at high pH. For silica, the surface becomes negatively charged when the pH is increased above about 2 to 3.7, while calcite does not become negatively charged until the pH is greater than 8 to 9.5. Thus calcite will tend to adsorb anionic surfactants such as organic acids in the pH range of interest in corrosion, 4-7, while silica tends to adsorb amines.

```
Silica surface charge              pos  <  pH 2-3.7  <  neg
Carbonate surface charge           pos  <  pH 8-9.5  <  neg
```

pH also affects the ionization of surface active organic acids and bases in the crude oil.

For a given oil, only slight changes in pH at close to neutral conditions can cause a drastic change in oil adhesion behavior. Morrow (10) has studied the transition of oil to water wettability of minerals in different crude oils. His results for two crude oils: Moutray Crude and NS-3 Crude at 50°C are shown in Figure 4 as a function of water pH and molar concentration of sodium ions. The reservoir rock showed oil wetting behavior for brine pH values below about 6 for these two crudes. At a pH above 6, water wetting behavior was observed. For nearly all crude oils tested, the transition from oil wet to water wet fell within the band of pH 6.5 +/- 2. Higher salinity decreased the pH at which an oil wet system became water wet.

Effect of Multivalent Metal Cations

Multivalent metal cations in brine can reduce the solubility of the crude surfactants and/or promote adsorption at the mineral surfaces, causing the system to become more oil wet. Multivalent metal cations also act as "activators" by

binding to the surface and providing negatively charged sites for the surfaces to bond.

Exposure to Air

A number of researchers (4,7,13) have shown that exposure to air and drying can alter the wettability of mineral surfaces. Crudes not exposed to air showed very little interfacial activity. Upon exposure to air, the crudes developed moderate to strong film-forming tendency and the Interfacial Tension (IFT) was lowered by as much as 50%, indicating that surfactants were formed by oxidation of the crude. Anderson et al (7) found that exposure of crude oils to air changed their wetting characteristics in non-systematic ways, but that normal paraffins such as hexadecane remained stable.

Natural State Mineral Wettability

Work on mineral flotation indicates that coal, graphite, sulfur, talc, and many sulfides are probably neutrally wet to oil wet. Metal oxides and many other naturally occurring inorganic minerals are usually wetted by water, but also can be wetted by oil, making them intermediately wetted compounds. Most other minerals, such as quartz, carbonates and sulfates are strongly water wet in their natural states (4). Hematite shows intermediate and hybrid wettability, but tends to be more oil wet than water wet in various oils used to formulate oil based muds. (11) This indicates that iron oxide corrosion products can be strongly affected by the properties of the oil, and is controlled by the relative effects of the amount of polar compounds in the oil, the brine chemistry, and the relative amounts of oil and water. This makes the use of wettability extremely complex as a predictive indicator in corrosion.

WETTABILITY: CORROSION STUDIES

Several authors have studied the effect of wettability on corrosion, but in some cases have not explicitly recognized wettability as a determining factor. Efird and Jacinski (12) studied the effect of crude oil on corrosion of steel in crude oil/brine mixtures. They concluded that:

1. Crude oil has a significant effect on the corrosion of steel in crude oil brine mixtures, and that these effects are significantly different for different crude oils.

2. The differences in the observed steel corrosion behavior for different crude oils are in the degree of corrosion product protectiveness and not in the formation rate of the corrosion product.

3. Tests conducted on steel in brine environments without the crude oil present do not give accurate representation of the behavior of steel in the crude oil/brine production environment, and that this can lead to gross errors when using the test results to estimate the potential corrosion problems and effects of corrosion inhibitor treatments in a crude oil production system.

These conclusions can be readily understood in the context of wettability and the adsorption of surface active components on the surface of steel.

Efird (13) also studied the water-oil ratio required for the onset of accelerated corrosion in various crude oils, recognizing that the onset of accelerated corrosion in crude oil production cannot be reliably predicted by "rule of thumb" produced water levels, by "the occurrence of free water" in the produced fluids, or by "water external mixtures and emulsions." He determined the produced water level in five crude oils at which accelerated corrosion occurred, which he termed the "Corrosion Rate Break Produced Water Level," or more simply "The Efird Number." The corrosion rate break tests were followed by test for corrosion

inhibitor effectiveness at produced water levels above the Corrosion Rate Break Level. These tests determined at what produced water level corrosion inhibitor would be required, which inhibitor to use, and what materials should be used for tubing and well head equipment.

Efird also stated that several principles MUST be followed to accurately determine the produced water level for accelerated corrosion of steel. These include:

1.   The Production environment must be duplicated for all corrosion testing, and its composition other than the relative amounts of crude oil and produced water should not be altered in any way.

2.   The actual production crude oil must be used for all corrosion testing, however, artificial produced water may be used.

3.   Oxygen must not be allowed to contact the crude oil at any time before or during the corrosion testing.

4.   Each individual corrosion test must be completed before the chemistry of the test environment is changed by the corrosion process.

The first three of these "MUSTS" are directly related to the surface active properties of the oil as was discussed previously, especially for the presence of polar compounds in the oil.

Efird's results are equally as interesting as his methods. The produced water level for the accelerated corrosion of steel, the Efird Number, range from 2% water up to above 60% water for the crudes he tested. Three of the five crudes reported had Efird Numbers less than 10%. This should not be taken as typical of the range of Efird Numbers in crude oil, however, as Efird was investigating "problem" crudes (14).

Efird concluded that:

1.   the produced water level where accelerated corrosion of steel in crude oil production will occur can be identified with a high degree of accuracy, and

2.   that the expense of failure and replacement of downhole equipment and tubulars can be minimized by identifying the produced water level where accelerated corrosion will begin before it actually occurs.

Other examples of wettability influenced corrosion also exist in the literature, such as the corrosion failures reported in the Ekofisk and Prudhoe Bay fields at very low water levels. The author has also experienced corrosion failures in North Sea oil wells at water levels reported as "Trace or 0.1%" water in oil (15). In this case, corrosion occurred as drop sized pits strung along the bottom of highly deviated wells. The production rate of oil in these wells was apparently just right to allow drops of water to stratify along the bottom of the tubing in this highly deviated section. It is not possible to differentiate whether water wetting was established by long term contact beneath stationary water drops or by wetting at low produced water levels. Exactly the same situation has been reported by Gunalton (16) for producing oil wells in the Zakum Field in The United Arab Emirates.

SWEET GAS CONDENSATE WELLS AND PIPELINES

Several recent authors have made measurements of the water oil ratio at which corrosion begins to occur. Adams and Garber (17), in their study of gas condensate well corrosion, report that the onset of corrosion occurs when the water is at least 30% of the liquids, with the rate affected up to about 50% water. Above 50% water, the corrosion rate was apparently not affected by the

water fraction. The 30% number remained valid in all 48 wells that they had investigated. The amount of water and oil in a gas condensate well is determined by the in-situ phase equilibrium in the well tubulars, which is not the same as separator conditions. They report that water and hydrocarbon dew points occur at different depths in the well, but only when the in-situ liquids are 30% water or more does corrosion occur.

deWaard and Lotz (18) report the same number in their model of carbon dioxide corrosion of steel, in which they indicate that corrosion occurs when the water fraction is 30% or more.

Gerritson et al (19) measured the water fraction at which corrosion began to occur under disturbed flow conditions in kerosine and water at 70°C. In their laboratory tests, no corrosion occurred below a water fraction of 40%, and corrosion was roughly proportional to water fraction above 40% water.

Choi (20) studied the sweet corrosion mechanism of dynamic oil-brine two phase flows, and proposed a mechanism for the pitting corrosion and mesa type corrosion he observed in flowing crude oil brine mixtures. He concluded that the surface condition of the steels in conjunction with local turbulence determined the initiation of pitting rather than metallurgical heterogeneities such as second phase inclusions or anisotropy. Local turbulence and wettability of a steel by a water phase surface at an active corrosion site controlled pit propagation. Flow dependency of sweet corrosion was greater as CO_2 partial pressure was lower, and because of the importance of local turbulence and surface heterogeneities in sweet corrosion, a proper simulation of field conditions is required in performing oilfield chemical or material evaluation in a laboratory. The effect of wettability on Choi's findings of the effect of turbulence and flow lies in the water advancing contact angle.

CONCLUSIONS

1. Wettability is a major factor in oil and gas system corrosion, controlling the occurrence of corrosion and having a major effect on corrosion rates.

2. The effect of wettability on corrosion can be measured in the laboratory to determine which oils are potentially corrosive and what methods of control need to be employed.

3. Data on the wettability of metals and corrosion product minerals is needed to better understand the effect of wettability on corrosion.

REFERENCES

1. Private Communication, Harry Byers, Dallas, Texas

2. Corrosion Magazine, March 1947

3. F. F. Craig, Jr. The Reservoir Aspects of Waterflooding SPE of AIME, Dallas, 1971

4. W. G. Anderson, "Wettability Literature Survey - Part 1: Rock/Oil/Brine Interactions and the Effects of Core Handling on Wettability" Journal of Petroleum Technology 38 (10) 1986 Pgs. 1125-1144

5. W. G. Anderson, "Wettability Literature Survey - Part 2: Wettability Measurement" Journal of Petroleum Technology 38 (11) 1986 Pgs. 1246-1262

6. W. G. Anderson, "Wettability Literature Survey - Part 3: The Effects of Wettability on the Electrical Properties of Porous Media" Journal of Petroleum Technology 38 (12) 1986 Pgs. 1371-1378

7. M. A. Andersen, D. C. Thomas, "A New Formation Wettability Test: The Dynamic Wilhelmy Plate Wettability Technique" SPE/DOE Paper #17368 presented at the SPE/DOE Enhanced Oil Recovery Symposium, Tulsa, OK April 17-20, 1988

8. L. Wilhelmy, "Ueber die Abhangigkeit der Capillaritats-Constanten des Alkohols von Substanz und Gestait des benetzten festen Korpers," Ann. Physik., 119 (6) (1863) 117-217

9. Smart, J. S. "Wettability, A Major Factor in Oil and Gas System Corrosion" CORROSION'93 Paper 93070

10. N. R. Morrow, "Wettability and Its Effect on Oil Recovery" JPT Dec. 1990 pages 1476-1484 (Trans SPE 21621)

11. J. T. Cline, D. C. Teeters, and M. A. Andersen, "Wettability Preferences of Minerals used in Oil Based Drilling Fluids" SPE 18476, presented at the 1989 SPE International Symposium on Oilfield Chemistry, Houstoon, TX Feb 8-10, 1989

12. K. D. Efird and R. J. Jacinski, "Effect of Crude Oil on Corrosion of Steel in Crude Oil/Brine Production" CORROSION Vol 45 #2 (1989) pages 165-171

13. K. D. Efird, "Preventative Corrosion Engineering in Crude Oil Production" OTC Paper #6599, 1991 Offshore Technology Conference, Houston, TX

14. Private Conversation, K. D. Efird

15. Unpublished field results, J. S. Smart

16. Gunalton, Y. "Corrosion in Zakum Field" SPE No.

17. Adams, C. D., and J. D. Garber, "Verification of Computer-Modelled Tubing Life Prediction by Field Data" CORR'93 Paper 93082

18. deWaard, C. W. and U. Lotz, "Prediction of CO2 Corrosion" CORR'93 Paper 93069

19. Gerritsen, J. H., A. Visser, S. Damen, U. Lotz, "CO_2 Corrosion and Its Inhibition Under Liquid, Full, Disturbed Flow and Under Liquid Droplet Impact Corrosion" CORROSION'93 Paper 93084

20. Ho Jin Choi, "Sweet Corrosion Mechanism of Dynamic Oil-Brine Two Phase Flows" CORROSION'90 Paper 31, NACE, Las Vegas, 1990
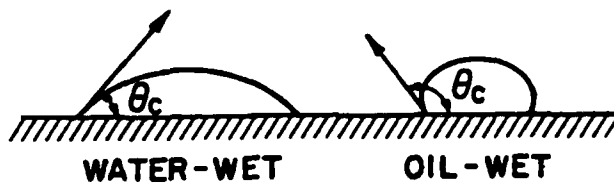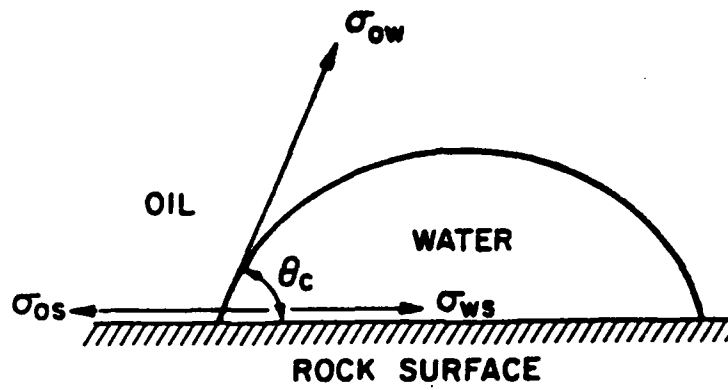
Figure 1. Idealized Water Oil Mineral System, indicating contact angles for water wet and oil wet surfaces.
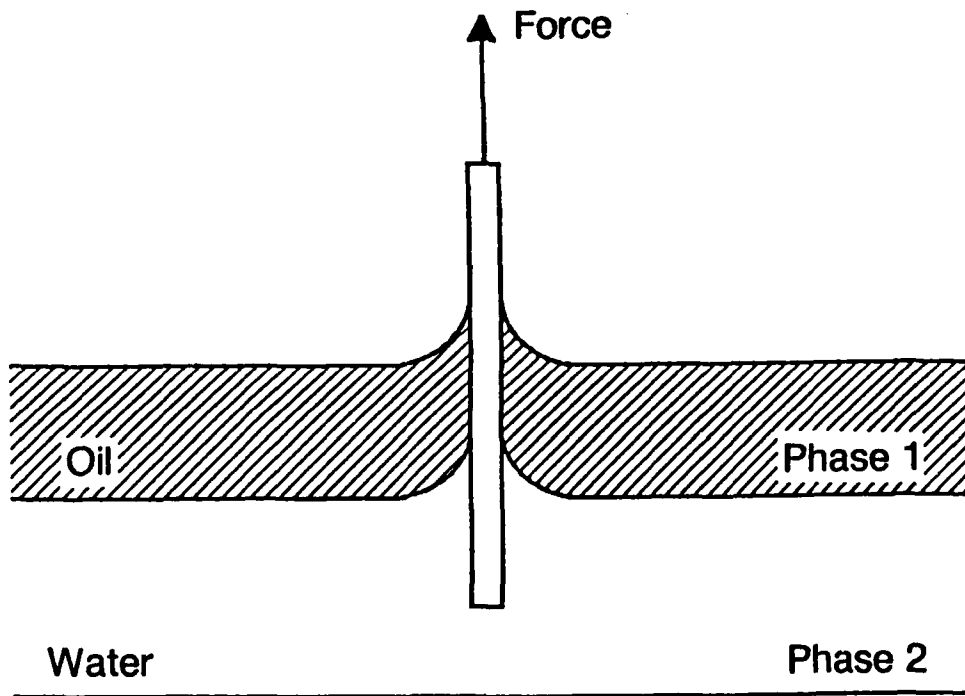
Figure 2. The types of meniscus formed on water wet surfaces using the Wilhelmy Technique to measure surface adhesion tension.

Meniscuses For Oil–Wetting System
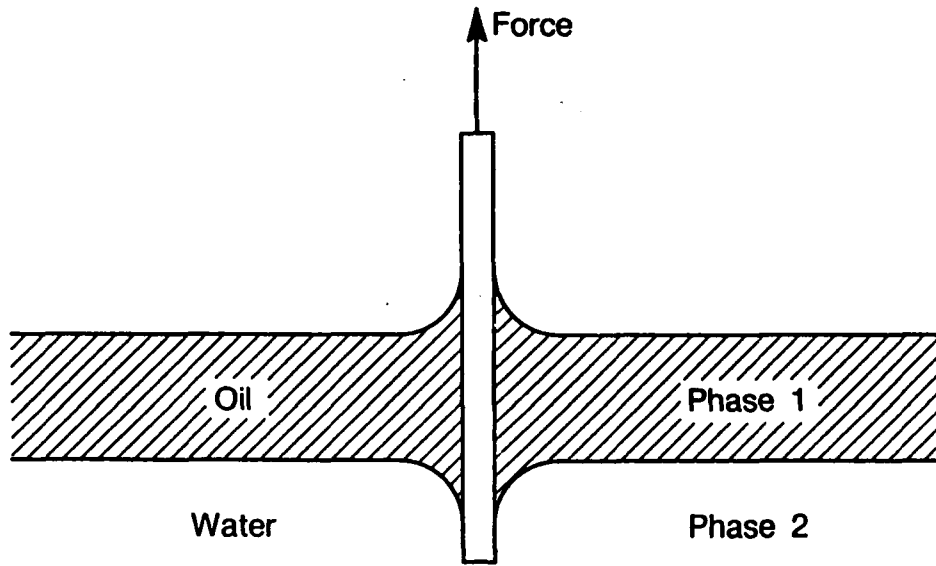
Figure 3. The types of meniscus formed on oil wet minerals using the Wilhelmy Technique.

Wettability of Crude Oil-Brine-Solids Systems
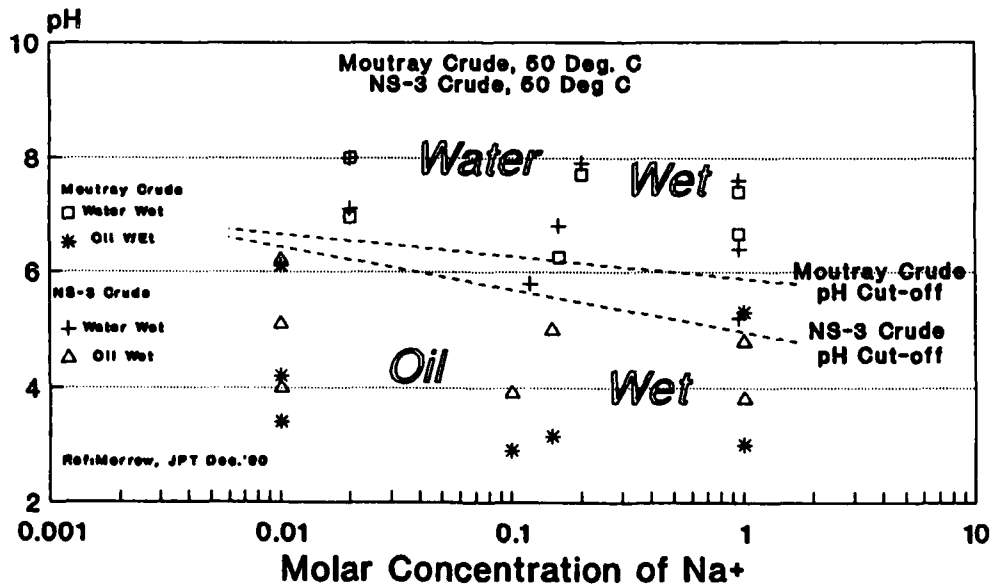
Figure 4. Wettability of Crude Oil-Brine-Solids Systems as a function of pH and Water Salinity.

Corrosion Inhibition in Wet Gas Pipelines

J.W. Palmer,
CAPCIS Ltd.,
Bainbridge House,
Granby Row,
Manchester, M1 2PW

J.I. Dawson,
CAPCIS Ltd.,
Bainbridge House,
Granby Row,
Manchester, M1 2PW.

K. Lawson,
CAPCIS-MARCH Ltd.,
Bainbridge House,
Granby Row,
Manchester, M1 2PW.

J. Palmer,
Total Oil Marine Plc.,
Crawpeel Road,
Altens,
Aberdeen, AB9 2AG.

I. Fonczek,
Southern California Gas Company,
555 West Fifth Street,
Los Angeles,
California CA 90013-1011,
USA.

Abstract

Transportation of wet natural gas is of increasing importance in the development of gas producing fields. The corrosivity of a particular system, and the extent to which corrosion can be controlled, are significant factors in determining whether wet gas transportation is economically viable.

The paper describes how flow conditions can influence inhibitor performance in wet gas pipelines. Experience in the field is used to illustrate some of the problems that can occur. The use of appropriate laboratory test systems for the evaluation of inhibitors for application in wet gas systems is considered.

Key terms: Wet gas, Inhibition, Hydrodynamics, Carbon Dioxide
            Electrochemical Monitoring

Introduction

Inhibition is the standard method used to mitigate the effects of corrosion in pipelines. However, economic pressures to both improve on the optimisation of inhibitor treatments and devise new treatments for mixed fluid lines means that inhibitor selection and on-site evaluations have a continuning and important role for future developments.

Of the many factors which must be taken into account when selecting an appropriate inhibition programme for a gas pipeline, consideration of the flow conditions is perhaps the most important. Fluids in transportation lines are often operated in a relatively dry state but the increasing interest in being able to transport wet and mixed fluids means that more appropriate inhibition packages are required.

A wide range of flow conditions can exist in such systems and each regime poses its own particular problems. These may relate either to enhanced corrosion caused by increased flow and/or removal of protective corrosion products under highly turbulent flow. These effects result from enhanced mass transport of corrodents and high local momentum transfer (the fluid to wall shear stress) respectively. The hydrodynamic conditions can also significantly influence inhibitor transport to the pipe wall or inhibitor film removal due to high wall shear stresses. Such processes and their influence on corrosion are well documented, particularly for single phase and two phase liquid systems (1,2,3). In the case of two phase gas/liquid or three phase gas/liquid/liquid flow the interactions between fluid hydrodynamics and corrosion more complex and required detailed evaluation. A number of studies (4,5) including a Gas Phase project at CAPCIS (6) have been undertaken over the past few years to investigate the factors which influence corrosion and corrosion inhibition in wet gas pipelines. The major parameters of interest will first be summarised below.

The transition from one flow regime to another can be illustrated by a flow diagram such as the Mandhane plot (7). Figure 1 shows that for a horizontal pipe, the dominant flow regimes at low liquid velocities are stratified smooth flow, stratified wavy flow and annular or mist flow. Transitions occur with increasing superficial gas velocity.

Inhibitor transport in pipelines operating under high gas velocities producing annular or mist flow is not normally a problem because mixing of the turbulent gas and liquid phases provides good contact of inhibitor with the pipe wall. However, in high production gas systems where water droplet impingement onto the pipe walls occurs, inhibitor films can be removed (5). Similarly, at local disturbances such as weld beads, effective inhibition is more difficult because of the high local shear stress conditions.

If a pipeline is operating under stratified flow the wall shear stress tends to be low and is therefore less significant. In this case, inhibitor transport to the pipe wall could be a greater problem. Corrosion problems can occur at the top of the line where condensed water absorbs carbon dioxide and becomes corrosive. Such conditions can be simulated in an designed flow loop test rig (6) with the corrosion monitored using suitably designed insert probes and advanced electrochemical techniques. Inhibition in this case requires vapour transport of inhibitor to the top of the line or frequent batch treatment must be considered.

One area of concern is at low spots in the line where stagnant liquid may collect. This can be a particular problem in gas systems containing low levels of liquids. In these regions, local turbulence at the hydrocarbon/aqueous phase interface may not be sufficient to allow adequate mixing or partitioning of inhibitor leading to reduced protection.

Another problem caused by low spots is the development of slug flow. As fluid accumulates, the apparent pipe diameter available to the moving gas decreases until the gas gathers the standing liquid into a slug which is pushed up the inclined pipe. Beyond the next crest the fluid spreads out on the pipe bottom and allows the gas to move free from the liquids. Under these conditions, periods of high shear stress are produced in an otherwise low shear stress system. Inhibitor film removed under slug flow conditions has recently been detected using Electrochemical Noise Monitoring (8).

Two examples of the type of problem described above are given in the following sections. How different operating conditions might best be simulated in the laboratory in order to select the most appropriate inhibitor programme are discussed. These evaluations may involve rotating cylinder, jet impingment and/or flow loop apparatus.

Case History 1

Approximately 18 months after commissioning, a wet gas flowline was found to be suffering severe preferential weld corrosion with up to 6mm weld metal loss just downstream of the choke.

Operating conditions were as follows:

Gas production : 2000 m$_s$m^3/day (maximum)
Condensate : 500 m^3/day (maximum)
Carbon dioxide : 1.7 mol %
Pressure : 70 bar
Temperature : 76"C

The weld root contained 0.7-0.9% Ni and 0.25-0.45% Cu with the filler metal containing 0.4% Si, 0.6% Ni, 0.4% Cu.

Attempts to control the problem had included injection of a water soluble corrosion inhibition and later an oil soluble corrosion inhibitor but neither product proved effective.

The mechanism of weldment corrosion is believed to have resulted from differences in the tenacity of carbonate films formed on the parent pipe and the nickel containing weld metal under the conditions of operation of the flowline. The high shear stress conditions led to removal of the surface film on the weld metal while that on parent pipe remained intact. This caused a switch from cathodic to anodic weld metal behaviour. Further research is about to be carried out to determine the exact cause of this type of failure and the range of conditions under which it occurs.

Laboratory Data

With regard to the immediate mitigation of the problem a laboratory test programme was carried out in order to simulate the corrosion behaviour and then select an inhibitor which was capable of protecting the flowline weldments.

Tests were carried out in a Rotating Segmented Electrode (RSE) cell (Figure 2) and a Jet Impingement loop (Figure 3). The techniques for sectioning weldments and monitoring weld corrosion have been described in previous publications (9,10).

Initial tests in the RSE under simulated operating conditions at up to 66N/m^2 shear stress showed that the weldment corrosion behaviour could be simulated in the laboratory with weld metal corrosion rates up to an order of magnitude higher than that of parent metal. Figure 4 shows the effect of increasing shear stress on corrosion rate.

Inhibitor tests showed that with some products protection was lost above a certain critical shear stress (Figure 5) while others proved effective at 66N/m^2 (Figure 6).

The worst case shear stress levels in the flowline exceeded 200N/m^2 with a maximum of 258N/m^2 calculated at the highest production rates. Further tests were therefore carried out in a Jet Impingement rig in which shear stresses of up to 240N/m^2 could be generated. It was found that effective inhibition could be achieved at these shear stress levels.
The corrosion inhibitor selected from these tests continues to provide good protection of the flowline weldment in service.

Case History 2

The second case history relates to the problems of inhibition in a gas storage facility operated by Southern California Gas. This facility consists of a number of gas wells which are connected to a common withdrawal header system. Although the gas is supplied dry, upon withdrawal, the gas is produced "wet" with approximately 9000-13000ppm chloride and 0.8-1.2% CO$_2$. The produced fluids comprise 50:50 oil:brine ratio with operating temperatures of 60-100°C at line pressures of up to 700 psig.

The produced fluids were expected to be highly corrosive. Previous experience had shown that attack occurred predominantly at the bottom dead centre at low spots in the withdrawal line. A rigorous procedure of draining produced fluids from low spots was carried out twice a day and corrosion inhibitor was injected into the system. However, regular inspection indicated that corrosion was not being alleviated.

It was suspected that corrosion was not continuous and that variations in the operation of the gas storage field could generate service environments which exacerbated corrosion and others which limited it. High pressure sensor probes were installed in the withdrawal line at the most vulnerable locations in order to study variations in corrosion during normal field operations.

The probes were configured for use with the CAPCIS-MARCH portable Multi System corrosion (MUSYC) monitor which incorporates the simultaneous logging of coupling current using a Zero Resistance Ammeter (ZRA), Electrochemical Potential and Current Noise (EPN and ECN) and Linear Polarisation Resistance (LPR). The multi-technique approach was adopted since one technique alone would not satisfactorily detect all corrosion conditions. The use of a number of powerful and complimentary techniques provides a useful investigative tool for determining the factors that lead to corrosion and the resulting morphology of attack (11).

Field Data

Typical responses from the CML MUSYC system are presented in Figures 7 to 9. The data exhibits some interesting and characteristic features:

(i)   Pronounced step changes in signal responses were observed at specific times during plant operation.

(ii)   A large range of corrosion rates was measured (0.2 to 250 mpy) but of greater significance was that the corrosion rate changed almost instantaneously.

(iii)   At certain periods the signal responses became highly variable, however, by comparison with the pronounced 'steps' the changes occurred more frequently, varying in an almost oscillatory fashion.

(iv)   In all cases, transient changes in the corrosion rate were observed despite dosing the system with inhibitor.

It was possible to interpret the data by correlating the signals with changes in the relevant process parameters. It was found that the corrosion rate was a function of the withdrawal status of gas wells upstream, although no individual well was responsible for causing enhanced corrosion attack.

It is postulated that the observed corrosion behaviour is a function of the local gas velocity since velocities would increase dramatically once wells upstream were switched over to withdrawal and vice-versa when shut-in. The step changes in signal responses would appear to reflect the tendency for fluid drop-out which occurred at low local velocities.

The oscillating corrosion data at certain periods probably corresponds to slugs of fluid being forced through the line at intermediate gas velocities.

Corrosion inhibition of this form of attack proved to be ineffective even at substantially increased dosage levels.

Under these circumstances where the corrosivity of the system is very specific to its operation, on-line corrosion monitoring (rather than laboratory simulation of process changes) is the most effective approach to determining how best to control the problem.

Discussion and Conclusions

The two examples described above illustrate some of the types of corrosion/inhibition problems which can occur in gas transportation. The data also demonstrate how the range of electrochemical monitoring techniques now available can be used to assess the various forms of corrosion encountered in practice, such as pitting, corrosion caused by condensation at the top of a pipe and slug flow. On-line monitoring can obviously be used to advantage in a trouble shooting excercise, as described above, however these real time measurements can also be employed in the final stage of an inhibitor selection programme.

The success of any monitoring excercise will depend on the design of the probe, its position in the system and the measurement techniques. Linear polarisation and zero resistance ammeter readings may be appropriate in high conductivity environments but under low conductivity or condensing conditions either impedance or electrochemical noise would be required. All these techniques are employed in laboratory studies, the selection being based on the type of corrosion problem and the flow conditions under evaluation.

The type of laboratory equipment which is appropriate for simulating system operating conditions in order to select appropriate inhibitor programmes needs careful consideration. It is most important that the system chosen must incorporate controlled hydrodynamics. Other factors such the pipeline steel and weldment compositions, aqueous chemistry and concentration of corrodent must also be considered in addition to partitioning characteristics and compatibility of the inhibitor with other treatment chemicals (12).

Rotating cylinder type systems such as that used in preliminary studies for Case History I described above, allow close control of the wall shear stress over a limited range of conditions and are useful for conducting batch treatment or inhibitor persistency studies. However, under circumstances where shear stress levels are high ($-70N/m^2$) or where inhibitor transport is perceived to be a problem, then use of rotating cylinder cells of is limited relevance.

Jet Impingement systems can reproduce high shear stress conditions and can simulate the effects of droplet impingement or local disturbances in wet gas systems. As yet there have been no reported attempts to correlate either Rotating Cylinder or Jet Impingement data with the effects of slug flow. Again, if inhibitor transport across liquid/liquid phase boundaries is likely to be a problem then Jet Impingement rigs are not appropriate.

The main use of flow loops must relate to simulation of inhibitor transport. Examples given in the introduction of this paper such as inhibitor transport to low spots or to the condensing phase can be simulated in flow loop systems. A Group Sponsored Project to assess Gas Phase Inhibition has recently been completed using a flow loop in which condensing phase corrosion and inhibition was successfully simulated by means of a cooled probe at the top of 4" diameter flow loop tubing (6). Inhibitor transport to low spots was also studied.

Laboratory studies on the effects of slug flow require simulation in flow loop studies with probes mounted flush with the pipe wall. Rapid response electrochemical monitoring techniques such as Electrochemical Noise seem to be the most effective method of evaluating the effects of a moving slug of liquid.

In circumstances where the corrosivity of a system is very specific to its operation, such as in Case History 2, then online corrosion monitoring is perhaps the most appropriate method of determining the best method of corrosion control.

Acknowledgements

References

1.   J.L. Dawson, C.C. Shih, R.G. Miller, J.W. Palmer, Mats. Perf. 30, 43 (1991).

2.   J.L. Dawson, C.C. Shih, P.K.N. Bartlett, U.K. Corrosion/90 3, pp 259-268, Pub. I.Corr, U.K. 1990.

3.   C.A. Palocios, J.R. Shadley, Corrosion/91, Paper 476, Pub. NACE, Houston, 1991.

4.   R. Nyborg, A. Dugstad, L. Lunde, Corrosion 93, New Orleans, Paper 77, Pub. NACE, Houston, 1993.

5.   J.H. Gerretsen, S. Damen, A. Visser, U. Lotz. NACE Corrosion, New Orleans, Paper 84, 1993.

6.   Gas Phase Corrosion Inhibition. CAPCIS report, (1992).

7.   J.M. Mandhane, G.A. Gregory, K. Aziz, Int. J. Multiphase Flow, Vol 1, p537, (1974).

8.   S. Webster, L. Nathanson, A.G. Green, B.V. Johnson, U.K. Corrosion, Manchester, Vol 2, 1992.

9.   J.W. Palmer, J.L. Dawson, T. Ulrich, A.N. Rothwell, NACE Corrosion, New Orleans, Paper 119, 1993.

10.   J.L. Dawson, A.N. Rothwell, D.A. Eden, J.W. Palmer. NACE Corrosion, New Orleans, Paper 108, 1993.

11.   D.A. Eden, A.N. Rothwell. NACE Corrosion, Nashville, Paper 292, 1992.

12.   S. Webster, D. Harrop, A.J. McMahon, G.J. Partridge. NACE Corrosion, New Orleans, Paper 109, 1993.
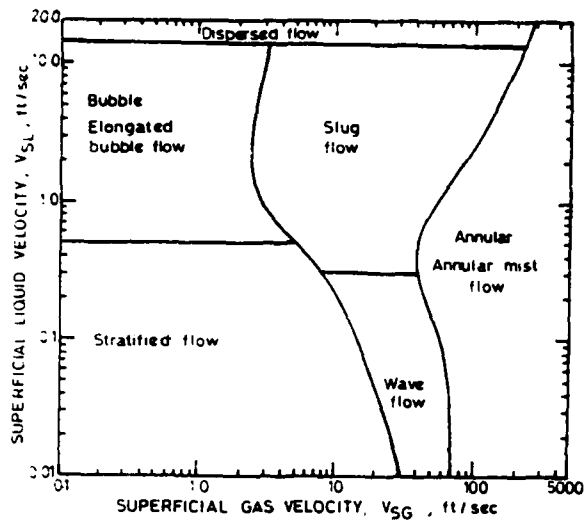
FIGURE 1. Flow pattern map after Mandhane.
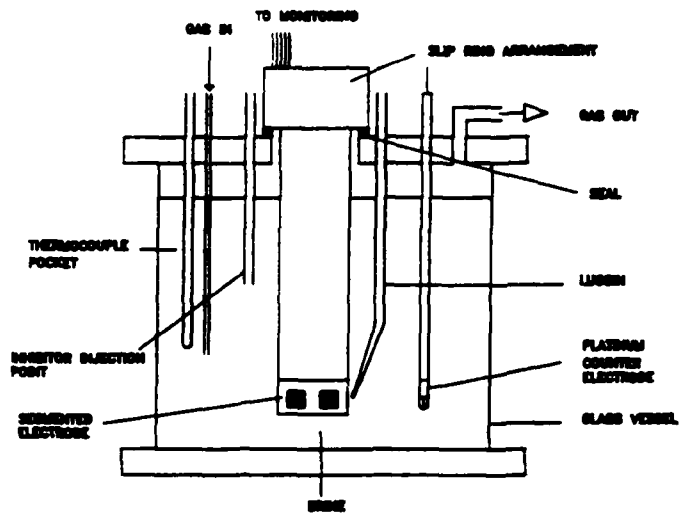
FIGURE 2. Rotating cylinder cell.
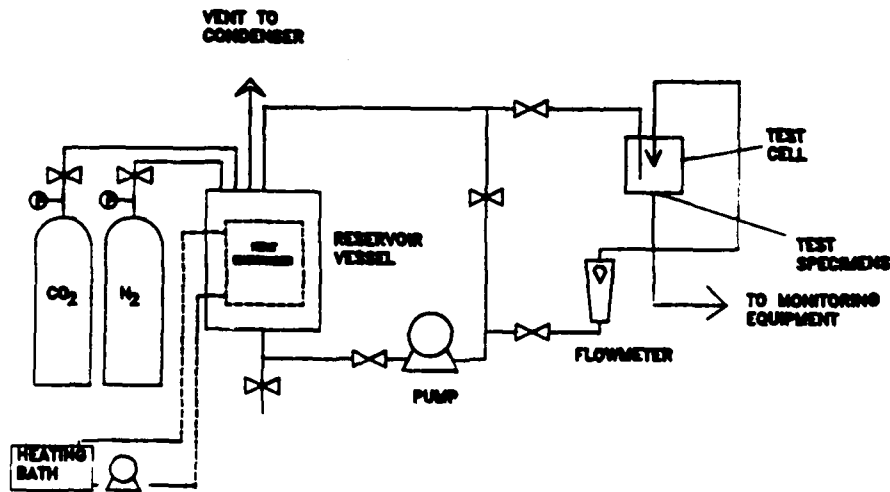
FIGURE 3. Jet Impingement rig.

FIGURE 4.
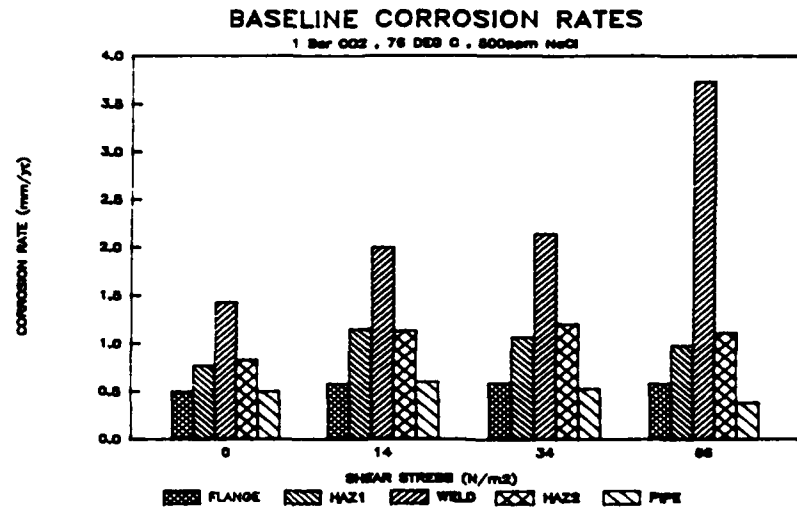
FIGURE 5.
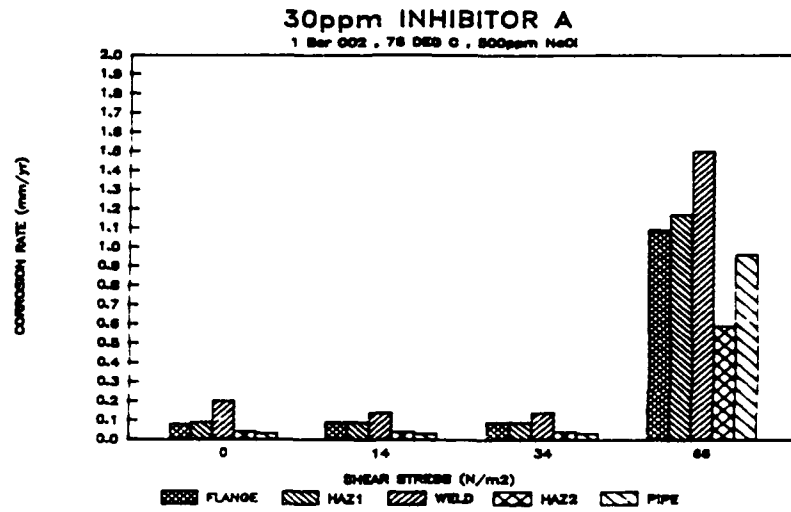
FIGURE 6.
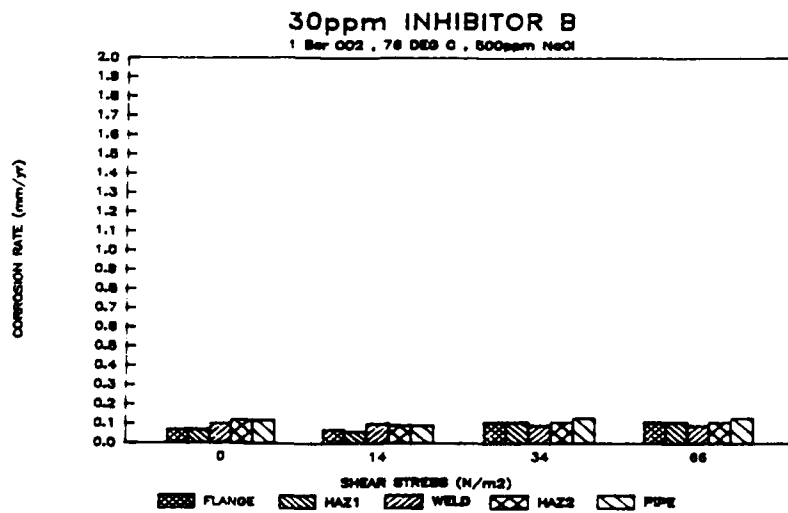
FIGURE 4-6. Baseline weldment corrosion behaviour and the effects of 30ppm
inhibitor A and B on weldment corrosion over a range of wall
shear stresses.

FIGURE 7. ZRA, Electrochemical Noise (ECN, EPN) and LPRM data showing a step change in corrosion behaviour in a gas gathering system.

FIGURE 8.   ZRA, Electrochemical Noise and LPRM data showing a step change in corrosion behaviour in a gas gathering system.

	ZRA	Channel : 2
1 mA		Min : 335 nA
		Max : 251 uA
		Mean: 89 uA
		SDev: 66 uA
100 nA		CVar: 737 E-3

	ECN	Channel : 3
1 uA		Min : 4.7 nA
		Max : 1 uA
		Mean: 759 nA
		SDev: 356 nA
100 pA		CVar: 469 E-3

	EPN	Channel : 4
10 mV		Min : 351 uV
		Max : 9.6 mV
		Mean: 2.9 mV
		SDev: 1.0 mV
1 uV		CVar: 353 E-3

	LPRM	Channel : 5
10 Ohm		Min : 33 Ohm
		Max : 100 KOhm
		Mean: 4.7 KOhm
		SDev: 7.5 KOhm
100 KOhm		CVar: 1.5
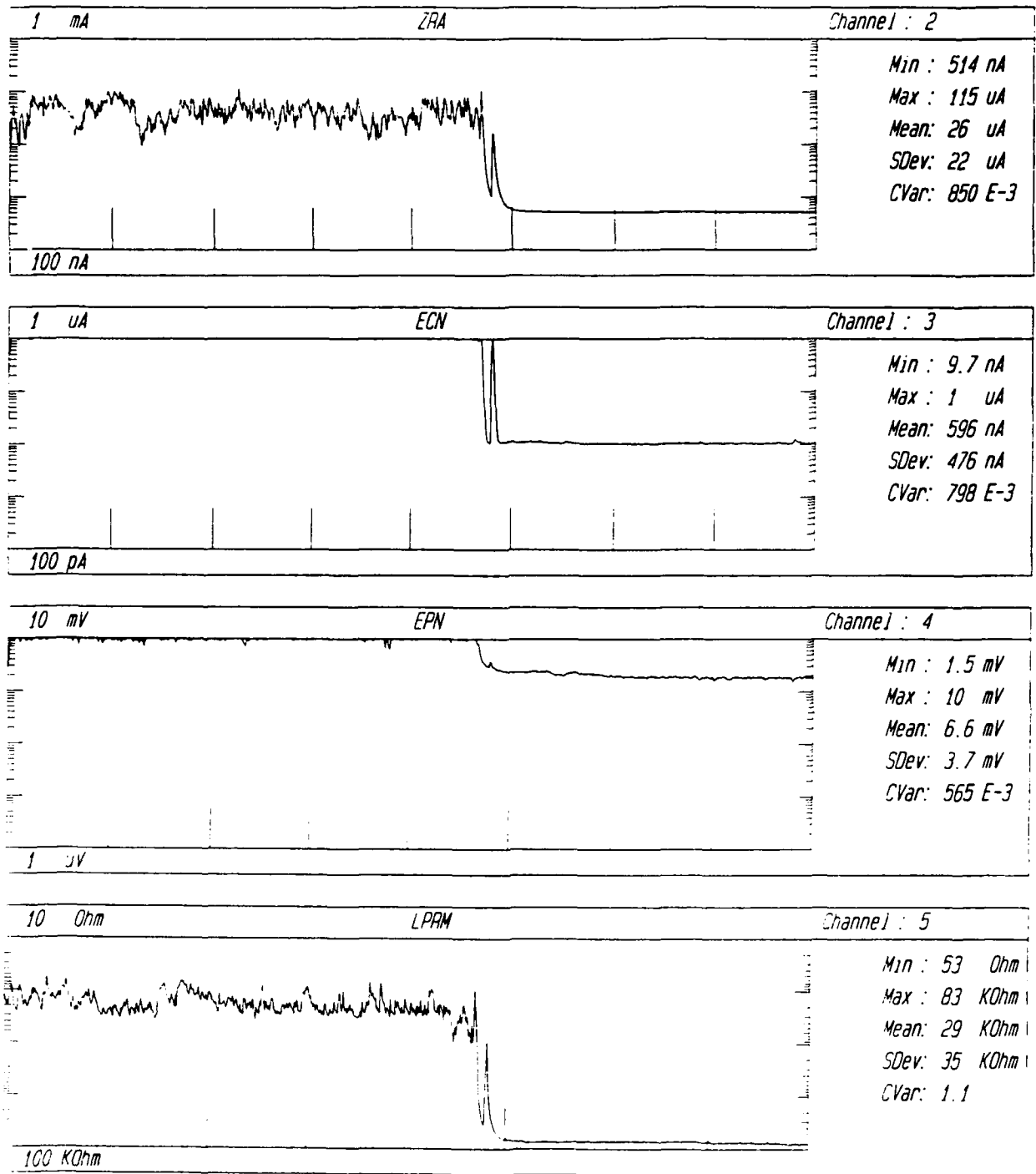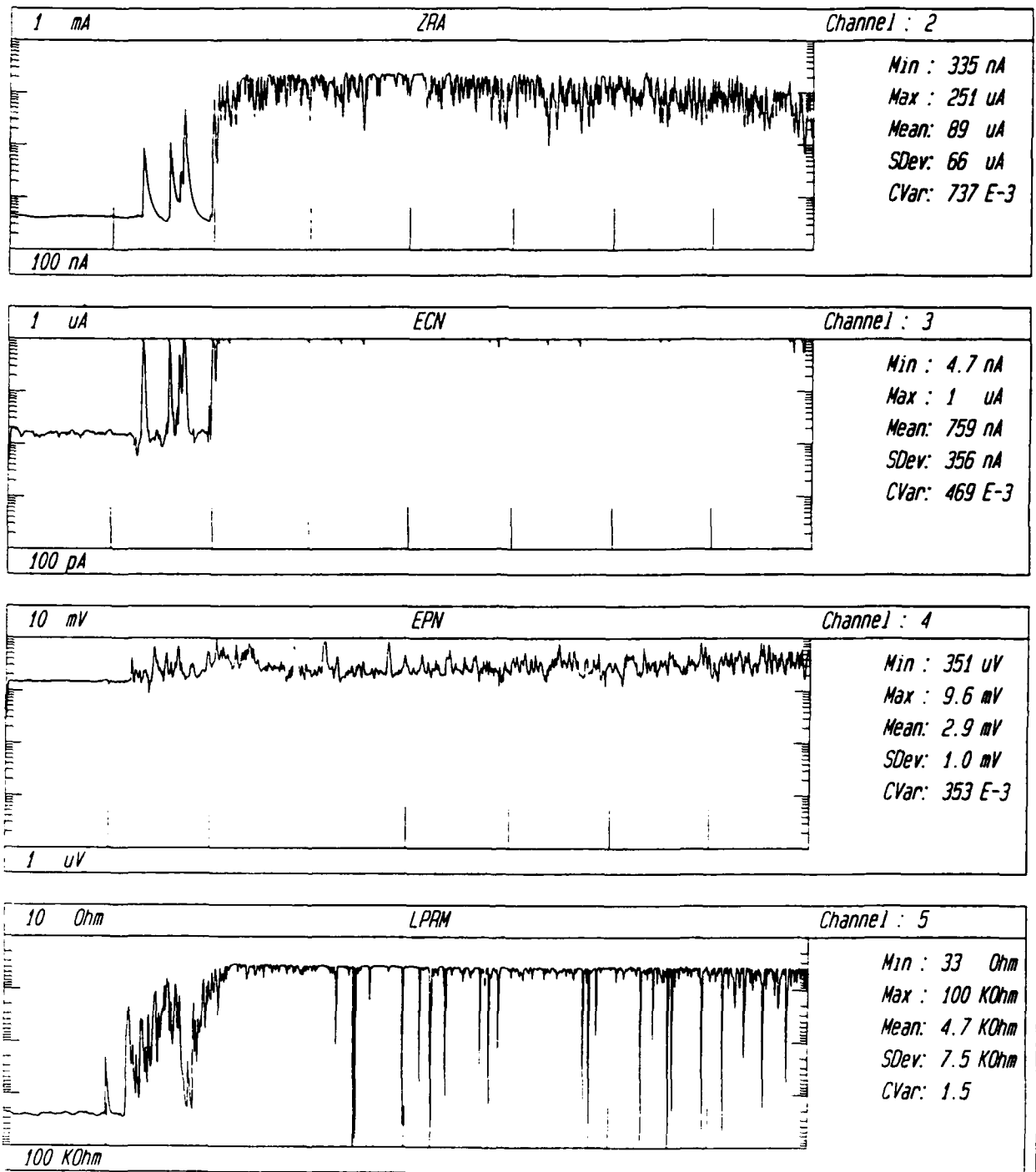
File   : 92B02N37.D2A
Time Span : 7 hrs 58 mins 59 secs

FIGURE 9.   ZRA, Electrochemical Noise and LPRM data showing a step change
            in corrosion behaviour and rapid fluctuations in corrosion
            rate possibly due to slug flow.

Behavior of Corrosion Resistant Alloys in Stimulation Acids, Completion Fluids, and Injected Waters

Dr. Russell D. Kane
Cortest Laboratories, Inc.
P.O. Box 691505
Houston, Texas 77269-1505

Abstract

The use of corrosion resistant alloys (CRAs) for oilfield applications has expanded greatly in recent years. For the most part, selection of CRAs is based on resistance to corrosive species in the production environment (i.e. H_2S, CO_2, sulfur, brine). In may cases, however, there are non-production environments to which these materials must also be resistant for either short term or prolonged duration. These environments include: (1) Stimulation acids and brine, and (2) Completion and Workover Fluids. This paper discussed the requirements and methodology of selection of CRAs for resistance to corrosion and stress corrosion cracking in these non-production oilfield environments. It provides service experience and information obtained through laboratory investigations which identify the critical aspects of each type of environment and the requirements of a sound materials evaluation and selection program.

Key terms: corrosion resistant alloys, stress corrosion cracking, materials selection, testing, oil and gas operations.

Introduction

Over the past decade, the use of corrosion resistant alloys (CRAs) for downhole tubulars and equipment and topside piping, wellheads and flowlines has become increasingly more prevalent. In these applications, use of CRAs is based on their high resistance to corrosion in environments containing high levels of CO_2, H_2S, chloride and in some cases elemental sulfur. A listing of many commonly used CRA materials is given in Table 1. If properly selected, their use allows elimination of chemical inhibition conventionally used with steel, costly workovers and the need for equipment repair or replacement during the project lifetime. It is typically the benefit derived from the elimination of these costly operations which directly or indirectly results in a significant reduction in the costs associated with corrosion control. In these circumstances, even though the initial capital costs may be higher than for conventional "steel and inhibitor" completions, it has been shown that total project costs associated with corrosion mitigation can be significantly reduced through the use of CRAs.

As indicated above, the principal technical concern in the application of CRA technology was initially resistance to corrosive production environments. The effects of H_2S, CO_2 and chloride and sulfur predominate the early literature (i.e. 1975 through 1988).[1-3] However, in recent years, there has been increasing awareness of the additional need for compatibility of CRA materials with various non-production environments which can be equally or even more aggressive to CRAs.

The purpose of this paper is to define the nature of these non-production environments, highlight the current areas of concern for the serviceability of CRAs and define parameters which can be utilized for the selection of CRAs for compatibility with both production and non-production

environments. Particular emphasis will be placed on both laboratory data and service experience and methodologies to determine which environments define the safe use limits for CRAs in oilfield operations.

Background

Over the past several years, Cortest Laboratories, Inc. (CLI-Houston), has been extensively involved in evaluation, selection and specification of materials for use in corrosive oilfield environments. These studies have included work on a number of large scale international projects involving production environments ranging from corrosive sweet (CO_2) gas conditions to sour conditions containing low levels of H_2S to liquid H_2S with elemental sulfur. CLI has also worked to incorporate its technical experience with that of a broadly based group of oil companies, equipment manufacturers and materials suppliers in the development of the SOCRATES™* expert system (see Appendix I for a list of companies). The aim of this effort was to assist engineers in selection of the appropriate materials of construction through the development of rules which define the applicable limits of materials used in oil and gas operations. [4]

During this expert system development effort, it was determined that under certain circumstances, the limiting parameters for materials selection was not always defined by the corrosivity of the production environment (i.e. H_2S, CO_2, chloride, composition of the produced water etc.). In situations particularly where stainless steels and nickel alloys were utilized, major operational problems from corrosive degradation could be expected which did not arise from prolonged exposure to the production environment, but rather to relatively short term exposure to stimulation acids, workover and completion fluids and/or injected or surface waters.

Based on the above mentioned considerations, it was decided to extend the program to include rules which define (1) the limits of CRAs in non-production environments and (2) the use of inhibitors on carbon and low alloy steels and CRAs. This paper summarizes some of the background work and data assessment that was conducted prior to undertaking this activity. It identifies specific areas of concern for commonly used alloys and situations where the selection of materials based solely on the corrosivity of the production environment would likely result in non-conservative designs.

Definition of Non-Production Environments

Stimulation Acids

A common oilfield practice is to inject concentrated, inhibited acid formulations down the production tubing and into the formation to increase (stimulate) the formation permeability and thereby increase the production of hydrocarbons. The acid formulations utilized in the acidizing process typically have a combination of additives which include corrosion inhibitors as well as other chemicals to control reaction rates with formation rock and to modify flow characteristics. The more commonly used stimulation acids are based on HCl (15 and 28 %), HCl+HF mixtures (mud acids) or organic acids such as formic acid. Presently, even more complex acid formulations are available which contain combinations of both inorganic and organic acids which allow careful control of the reaction rate of the formulation with temperature.

The corrosion rate of acidizing on conventional steel equipment has typically been controlled to an acceptable level with corrosion inhibitors.[5] These are commonly organic filming inhibitors that minimize localized corrosion and reduce the corrosion rate of steel to ≤ 2000 mpy (0.005 inch per day; 0.12 mm per day). It has been found in some cases, that these inhibitors can be

---

* TM - SOCRATES: Selection of Corrosion Resistant Alloys Through Environmental Specifications (Cortest Laboratories, Inc., PO Box 691505, Houston, Texas 77269-1505)

substantially less effective in protecting CRA materials which have high levels of Cr, Ni, and Mo leading to localized corrosion and stress corrosion cracking (SCC). Therefore, stimulation acids represent a class of non-production environments which constitute a major concern in terms of compatibility with CRA equipment.

Workover and Completion Fluids

In modern workover and completion operations, a variety of clear (non-particulate containing) fluids are utilized depending on the specific characteristics of the wells in question.[6] These are well control fluids typically consisting of chloride, bromide and chloride/bromide salt solutions of high density used to produce a high hydrostatic pressure in the wellbore needed to counterbalance the formation pressure. In some cases, these fluids are utilized for only short duration while running and setting downhole equipment, but in other cases exposure can be for prolonged periods as in the case of packer fluids which are held in the casing/tubing annulus for years. Additionally, sometimes workover fluids are lost into the formation especially during period of prolonged overbalanced pressure conditions (i.e. wellbore pressure > formation pressure). In this case, these fluids can become commingled with the formation fluids often adding to the severity of the production environment for an extended period at the start of well production.

Injected Waters

Another widely varying type of non-production environment to which CRAs can be exposed are chloride containing waters which are either injected downhole or utilized at the surface. Typically, water is injected into underground rock formations for either secondary recovery (formation pressure maintenance in hydrocarbon bearing rock to maximize well productivity) or for disposal of produced water. The composition of this injected water may vary greatly in condition from raw acid gas containing brine (which may also be contaminated with air due to leaks in the pumping system or due to ineffective deaeration), aerated brine to treated (chlorinated and deaerated) brine or fresh water.

These systems have considerably different concerns regarding corrosion than those of the production environment.[7] These concerns may also vary greatly depending on the nature of the injected water. Additionally, when CRAs are utilized in topside systems offshore, they can be exposed to both corrosive waters internally and to aerated seawater on the outside from the marine environment which in turn can be concentrated by evaporation. Therefore, in some cases, these environments are less severe than production environments, such as with treated, deaerated seawater. In other cases, they may be much more aggressive as observed in aerated seawater or sour brine which has been contaminated with air.

Serviceability of CRAs in Non-Production Environments

Due to the highly specific nature of corrosion in non-production environments, separate guidelines must be utilized for ranking the severity of each type of environment and the resistance of CRAs to that environment. The limiting environment can then be determined by the situation which requires the highest alloy requirements to resist corrosion or SCC. Alternatively, changes in operating procedures can be assessed which can limit or eliminate exposure to the non-production environment to maximum performance and minimize alloy cost. In this section, each of the three classes of non-production environments will be discussed separately in terms of the critical parameters which govern CRA performance.

Stimulation Acids

In terms of assessing the severity of stimulation acids from the standpoint of corrosion and SCC the following conditions must be considered:

1.	Acid type and concentration.	4.	Inhibitors performance.
2.	Maximum temperature.	5.	Duration of exposure and well
3.	Acid gas concentration		clean-up procedure.

Typically, higher rates of corrosive attack are associated with stronger acid formulations, HF containing acids, and higher formation temperatures.

Secondly, the required alloy performance needs to be determined. Typically, the initial period of exposure to the inhibited concentrated acid is most severe from the standpoint of weight loss and localized corrosion.[8] Corrosion rates of CRA materials can range from 100 - 50,000 mpy (2.5 - 12,500 mm per year; 0.005 - 34 mm per day!). Corrosion rates are highest for HF containing mud acids followed by HCl. The organic acids such as formic are typically the most benign in terms of weight loss corrosion on CRAs. Greatest rates of attack are commonly found in the lower alloy stainless materials such as 13Cr, 22-25Cr and 28 Cr. In most cases, materials with more than 42Ni exhibit acceptable rates of attack except in concentrated HCl or HCl+HF at high temperature (approaching 200 C or at high H_2S levels) where 50Ni alloys or Alloy C-276 should be considered. Organic acids such as formic typically do not pose major problems in terms of corrosion or SCC of CRAs.

Particular concern is for the performance of the individual inhibitor formulations which are to be utilized in the actual service application for fluids containing inorganic acids. There has been an evolution of acid inhibitors for CRAs over time especially for duplex stainless steels, but substantial variation in inhibitor performance still exists.[8]

No one inhibitor type has been found which works well in all combinations of alloy and acid. Typically, CRAs require higher inhibitor concentrations ($\geq$2 percent) than do carbon and low alloy steels particularly in the stronger, more aggressive inorganic acids.[9] One of the most difficult situations is the tendency of 22-25Cr duplex stainless steel to exhibit selective phase corrosion in a wide variety of acids whereby the ferritic phase is selectively attacked. Some inhibitors have been found which can successfully impart resistance to this form of corrosive attack. Successful inhibition of 15 percent HCl on duplex stainless steels has been reported up to 185 C and at higher temperatures if HCl+formic acid mixtures are utilized at an equivalent strength to 15 percent HCl. [10]

In general, due to the high variability in inhibitor performance (See Figures 1 and 2), screening tests for evaluation of the corrosivity of the actual concentrated inhibited acid formulations under consideration on CRA materials are recommended. Additionally, the evaluation of CRAs for acidizing conditions should also include exposure of stressed coupons to the spent (i.e. reacted and uninhibited) acid to simulate acid returns which can occur for an extended period after returning the well to production. Under these circumstances, it appears that SCC may be of greater concern than weight loss corrosion in the acidizing process. SCC has been observed in materials which have had acceptable weight-loss corrosion resistance in various acidizing formulations. SCC severity is typically greatest in the spent acid environment. Therefore, careful attention to post acidizing, well clean-up procedures should be taken to minimize exposure of CRAs to these spent acid returns.[8]

Workover and Completion Fluids

In terms of assessing the severity of workover and completion fluids from the standpoint of corrosion and SCC the following conditions must be considered:

1.	Acid gas partial pressure.	3.	Inhibitor type and concentration.
2.	Temperature.	4.	Conditions of aeration.

5. Fluid composition (i.e. chloride
   and bromide content; cation species
   present, and ionic strength)

6. Duration of exposure.

Only limited documented service experience has been obtained, but there is evidence from laboratory studies which lead to concern for CRAs in workover and completion fluids. Examples of common fluid types are shown below:

Single brine systems		Mixed brine systems	
1.	NaCl (specific gravity, SG, up to 1.20)	1.	NaCl/NaBr (SG up to 1.50)
2.	KCl (SG up to 1.20)	2.	$CaCl_2/CaBr_2$ (SG up to 1.80)
3.	$CaCl_2$ (SG up to 1.40)	3.	$NaBr/ZnBr_2$ (SG up to 2.00)
		3.	$CaCl_2/CaBr_2/ZnBr_2$ (SG up to 2.20)
		4.	$CaBr_2/ZnBr_2$ (SG up to 2.40)

These fluids can be classified as either light or heavy (high) brine systems. Typically, light brines have a specific gravity (SG) of 1.05 to 1.40 while the SG of the heavy brines can range from 1.30 to 2.40. They derive their SG from the amount and type of salt species dissolved in solution. Adding to the complexity of the situation, there can also be a variety of inhibitors in these brine systems. These include formulations based on both organic filming amines and inorganic thiocyanate salts.

Test results have indicated that maximum corrosivity of these brine systems occurs with temperature from <100 to 250 C and SG over the range 1.30 to 2.30. Corrosion rates for steel range from <0.1 mm per year for NaCl/NaBr brine (SG = 1.32 to 1.42) to approximately 1.5 mm per year for the $CaBr_2/ZnBr_2$ brine (SG = 2.30) at 200 C (See Figure 3). Additionally, corrosion rates can be a factor of ten higher in light brine fluids under aerated conditions (;1mm per year) versus deaerated conditions (0.1mm per year).[11] In some cases, galvanic interactions between the steel casing and CRA tubing in the casing/tubing annulus can increase the corrosion rate of steel by galvanic interactions through packer fluids (See Figure 4).[12]

Both organic and inorganic inhibitors can be effective for reducing corrosion rate at temperatures up to between 80 and 150 C. At higher temperatures these compounds have been shown to have limited long term benefit partially due to their limited solubility and stability in these concentrated brine systems. Specific combinations of inhibitors have been examined which may inhibit corrosion under specific conditions in heavy brine systems. Unfortunately, some inhibitors have been found to actually promote corrosion in some stainless steels and nickel base alloys exposed to heavy brine fluids.[13] 9Cr-1Mo and 13Cr alloys appear to be particularly susceptible to general and localized attack in these environments. In some cases, even higher alloy materials such as duplex stainless through Alloy 718 can also be attacked. However, more work is needed before special formulations of inhibitors can be reliably utilized for the effective long term inhibition in heavy brine packer fluids.

Another aspect of CRA behavior in workover and completion fluids is environmentally induced cracking. It has been observed that 9Cr-1Mo, 13Cr and 22-25Cr duplex stainless steels can exhibit cracking failures in inhibited brine $CaCl_2/CaBr_2$ completions fluids. These are typically failures which have occurred after prolonged exposures at high temperature (at or above 200 C). Some of these failures have been associated with decomposition of inorganic inhibitors to form H_2S which promotes sulfide stress cracking (SSC) in 9Cr-1Mo and 13Cr alloys and SCC in 22-

25Cr duplex stainless steels (See Figure.[11, 14]

There have been reports which indicate that prolonged exposure to high brine $CaCl_2$ workover fluids and acid gas can induce localized corrosion and SCC in 22Cr duplex stainless steels and possibly nickel base alloys under conditions which normally would not affect these alloys.[15] The main effect in this case, is the increased chloride content of the environment resulting from excessive fluid losses in the formation during workover and drilling operations. Once the well is put on production, the chloride content can be up to three orders of magnitude higher than the normal production environment. This situation can have a significant affect on the initiation of localized corrosion and SCC particularly under conditions in which (1) H_2S is present or (2) prolonged exposure has occurred.

Injected Waters

In terms of assessing the severity of injected waters from the standpoint of corrosion and SCC the following conditions must be considered:

1. Level of aeration/deaeration.
2. Residual Chlorine from water treatment gasses
3. Chloride concentration and possibility for chloride concentration through evaporation.
4. pH as may be affected by dissolved acid
5. Presence of absence of H_2S.

In most cases where water is being injected into hydrocarbon bearing formations, care will be taken to control the quality of the injected water. That is, procedures will be set-up and maintained to deaerate (≤ 20 ppb) and chlorinate this water and possibly treat the water with additional biocide formulations to minimize corrosion causing and H_2S producing bacterial growth. In these cases, the actual corrosivity of the water will be very low (≤ 0.1 mm per year on steel; see Figure 6) at normal injection temperatures (<60 C).[16] Therefore, carbon steel and conventional austenitic stainless steels will perform well in terms of resistance to both weight-loss corrosion and SCC. Residual chlorine in the system can increase the severity to localized corrosion and SCC in stainless steels and should be maintained at levels ≤ 0.5 ppm. In addition, corrosion will be higher at lower pH. Therefore, efforts in water treatment particularly in closed systems are often directed toward pH control to maintain higher pH (i.e. pH >6.0).

In other situations, however, the corrosivity of chloride containing water can vary greatly due to the numerous environmental variables and materials of construction in these systems. These may include steel, stainless steels, nickel base alloys and copper alloys. Additionally, effects of galvanic interactions and differential aeration cells at crevice sites can be strong in these environments leading to cathodic protection of certain alloys and localized corrosion in others depending on their electrochemical behavior (See Table 2).[17] However, under conditions where the fluids are contaminated with sulfide species, substantial change in electrochemical behavior can occur causing dramatic changes in galvanic interactions (see Sour Water below). In order to understand these relationships, it is necessary to subdivide these applications depending on their service environment. NACE Standard RP0475 provides some guidelines for the consideration of environmental factors for selection of materials for water injection service.

CO2 Containing Water. The most direct affect of CO_2 in water is the lowering of the solution pH. This can greatly increase the corrosion rate of steels as shown in Figure 7.[19] Typically, deaerated systems with less than 0.2 bar partial pressure CO_2 are not considered excessively corrosive to steel[20], but can exhibit corrosion rates of up to 0.2 mm/yr (10 mpy). Under these circumstances, minor amounts of buffering ions such as bicarbonate produce pH

values 5 or higher which reduce the corrosion severity. As the partial pressure increases, corrosion rate increases. At 0.5 bar partial pressure CO_2, the corrosion rate of steel [1 mm/yr (40 mpy)] is high enough to consider inhibition particularly if the bicarbonate level is low as in condensed water systems. At 2.0 bar partial pressure CO_2, the system would be at a pH in the range of 3.5 to 4.5 and be considered severe from the standpoint of weight loss corrosion [corrosion rate of >2.5 mm/yr (>100 mpy). In all cases, increased velocity would be expected to increase the corrosion rate of steel.

In terms of severity of corrosion on stainless alloys, CO_2 corrosion is effectively mitigated by the addition of Cr. As shown in Figure 8, the addition of at least 12 percent Cr, reduced the corrosion rate to less than 0.1 mm per year (0.4 mpy). Additionally, up to 9 percent Ni also appears to have significant beneficial effects on the mitigation of corrosion in CO_2/brine environments.[21] This is the basis for the use of 9Cr-1Mo, AISI 410 and 13Cr stainless steels for many wet CO_2 handling systems along with the recent development of alloys with enhanced CO_2 corrosion resistance which have 13Cr-5Ni-2Mo. However, the nature of the corrosive attack in 12Cr and 13Cr materials is commonly observed to be more localized in nature than found in carbon or low alloy steels. The most severe corrosion is often found under static conditions (<1 meter/second) and high levels of chloride ion. Velocity tends to reduce the conditions for local attack and decrease formation of deposits on the material surface which can cause crevice or under-deposit corrosion. In these mildly acidic environments, SCC of Ni-containing stainless steels is not a major factor if deaerated conditions are maintained and high chloride concentrations are not observed.

Sour Water. Sour water systems are usually significantly more difficult to handle since problems can result from either weight loss corrosion or sulfide stress cracking in susceptible steels. In addition, the combination of high levels of chloride and H_2S can also produce SCC in some grades of stainless alloys. The corrosion scaling tendencies of sour water systems is much more variable than in CO_2 systems. Generally, corrosion rates of steel are not as high in sour water systems than CO_2 systems due to the somewhat protective nature of the sulfide scale relative to the iron carbonate unless oxygen contamination has occurred.[21]. Since protective hydrocarbon films may not be present in these systems, corrosion rates would be at the upper boundaries of those observed in oilfield production systems (i.e. those usually observed in high GOR wells with high water cut).

If deaerated sour water conditions are present, the guidelines for oil and gas production environments usually provide acceptable results. Resistance of materials to SSC can be handled through the application of NACE Standard MR0175[23]. The primary concern in this case would be to select SSC resistant materials and fabrication practices when the H_2S partial pressure was ≥0.05 psia (≥0.003 bar).

The rules for general corrosion, pitting, SCC and SSC developed in the expert system program for sour production environments also apply to sour water systems. The only major difference would be if aerated sour water conditions exist. Under these conditions, very severe weight loss corrosion of steel and severe pitting and SCC of stainless and nickel base alloys occurs. Even very highly alloyed materials such as Alloys G and C-276 exhibit marginal resistance to localized corrosion as shown in electrochemical tests[24] In these cases, most titanium alloys can provide added resistance to localized corrosion at less than 150 C. At higher temperatures, however, only a few special titanium alloys such as Alloy Beta C can provide the necessary corrosion resistance.

Aerated Seawater. Probably the largest group of applications relates to the exposure of

materials to aerated seawater. These include a variety of platform topside piping and vessels, firewater systems and desalination equipment. In these types of systems the major environmental variables are oxygen content, temperature and chloride concentration. In aerated seawater, the materials are typically stainless steel or nickel base alloys depending on the degree of severity of the service environment. Alloys are selected for resistance to localized (crevice) corrosion or SCC. Figure 9, shows the limits for crevice corrosion in stainless steels in terms of alloy content and chloride concentration. It indicates the generally higher resistance of super duplex and super austenitic stainless steels over conventional austenitic stainless steels.[25] In some very severe cases, base alloys or Ti-alloys are required due to the requirements for resistance to localized corrosion or SCC at temperatures ≥ 60 C.

Figure 10 indicates the relative crevice corrosion resistance of several stainless steels based on the depth of crevice attack for temperatures between 5 and 70C [26]. The data is plotted in terms of Cr + 3.3Mo + XN for the various alloys. Pitting resistance can generally be attained in seawater up to high temperatures with 22-25 Cr duplex stainless steels. Crevice corrosion requires very highly alloyed 6Mo stainless steels or nickel base alloys. New super duplex stainless steels with 4 Mo and 0.2 - 0.3 N have also been found to provide excellent resistance to localized corrosion in seawater.[27] Additionally, Figure 10 indicates that in materials which are susceptible to crevice corrosion, the depth of attack can be minimal at low temperatures (;5C) but increases rapidly with temperature. The selection of stainless alloys is a function of both the type of application and the effect of this attack on serviceability (i.e. piping or sealing application).

One additional aspect of the use of CRAs in seawater service is the affect of chlorination. As shown in Figure 11, the corrosion potential of the materials depends on both the amount of chlorine concentration and method of chlorination. Amounts of residual chlorine in seawater as low as 0.1 - 0.2 ppm can elevate the corrosion potential enough to increase susceptibility to pitting and crevice attack. By comparison intermittent chlorination has been found to produce corrosion potentials in stainless alloys which are more cathodic and therefore less damaging than potentials produced in seawater at 0.1 and 100 ppm chlorine.

Conclusions

Based on the results of this study, the following conclusions were made:1. Oilfield production environments do not always determine the serviceability limits for CRA materials.

2.   In many cases, non-production environments have a higher degree of corrosivity and can result in attack of materials acceptable from the standpoint of the production environment.

3.   In the selection of CRAs, the evaluation process must isolate the various production and non-production environments. Relevant non-production environments include the following:

        a.   Stimulation Acids
        b.   Workover and Completion Fluids
        c.   Injected Water.

4.   Each of the environments given in Item 3 must be considered separately in terms of (a) their aggressiveness to steel, and (b) to CRAs and the minimum alloy requirements for each environment.

5.   The alloys selected must meet the requirements of the most severe environment (production or non-production). Alternately, modifications in operating procedures to

minimize exposure to severe non-production environments.

6. Careful evaluation and selection of inhibition chemicals must be used to minimize corrosive attack of both steel and CRAs in these non-production environments. This procedure will allow for the use of generally lower alloy materials and the most cost effective corrosion engineering approach.

References

1. R.D. Kane, et. al., "Factors Influencing the Embrittlement of Cold Worked High Alloy Materials in H_2S Environments", Corrosion Journal, Vol. No. 9, September, 1977 pp 309-320.

2. R.D. Kane, et. al., "Stress Corrosion Cracking of Nickel and Cobalt Based Alloys in Chloride Containing Environments", CORROSION/79, Paper No. 174, Atlanta, GA, NACE March, 1979.

3. S.M. Wilhelm, "Effect of Elemental Sulfur on Stress Corrosion Cracking of Nickel Base Alloys in Deep Sour Gas Well Production", CORROSION/88, Paper No. 77, St. Louis, MO, NACE, March 1988.

4. R.D. Kane and S. Srinivasan, "Selection of Martensitic and Duplex Stainless Steels for Oil and Gas Service", CORROSION/92, Paper No. 56, Nashville, TN, NACE, April, 1992.

5. M.L. Walker and T.H. McCoy, "Effect and Inhibition of Stimulation Acids on Corrosion Resistant Alloys", CORROSION/86, Paper No. 154, Houston, Texas, NACE, March 1986.

6. D.D. Schmidt, "......", Petroleum Engineer International, August, 1983.

7. Standard RP0475, Selection of Metallic Materials to be Used in All Phases of Water Handling for Injection into Oil-Bearing Formations, NACE, Houston, TX, Oct. 1991.

8. R.D. Kane and S.M. Wilhelm, "Compatibility of Stainless and Nickel Base Alloys in Acidizing Environments", CORROSION/89, Paper No. 481, New Orleans, LA, NACE, April 1989.

9. A.I. Williamson and M.G. Hay, "Selection of CRA Tubing and HCl Corrosion Inhibitors for Burnt Timber/Limestone Wells", CORROSION/91, Paper No. 11, Cincinnati, OH, NACE, March, 1991.

10. M.J. Walker, Halliburton Services, Private Communications, October, 1992.

11. A. Ikeda, et. al., "Corrosion Behavior of Low and High Alloy Tubular Products in Completion Fluids for High Temperature Deep Wells", CORROSION/92, Paper No. 46, Nashville, TN, NACE, April, 1992.

12. S.M. Wilhelm, "Galvanic Corrosion in Oil and Gas Production", Corrosion Journal, Vol. 48, No. 8, August, 1992, p 699.

13. R.G. Asperger, Cortest Laboratories, Inc., Private Communication, September, 1992.

14. P.A. Berke, et. al., "CO_2 Corrosion Behavior of Carbon and Alloy Steels in High Concentration Brine Solutions", CORROSION/88, Paper No. 212, St. Louis, MO, NACE, March 1988.

15. R.D. Kane and S.M. Wilhelm, Cortest Laboratories, Inc., Proprietary Report, May, 1992.

16. J.W. Oldfield et. al., "Corrosion of Metals in Deaerated Seawater", Proceedings of the 2nd BSE-NACE Corrosion Conference, Bahrain, January, 1981, pp 48-60.

17. Standard Guide G-82, "Development and Use of a Galvanic Series for Predicting Galvanic Corrosion Performance", NACE, Houston, TX.

18. Material Requirement MR0175, "Sulfide Stress Cracking Resistant Metallic Materials for Oilfield Equipment", NACE, Houston, TX.

19. DeWaard, C. and Milliams, D.E., "Carbonic Acid Corrosion of Steels", Corrosion Journal, Vol. 31, No. 5, May, 1975, pp 121-135.

20. Corrosion of Oil and Gas Well Equipment, Book 2 of the Vocational Training Series, American Petroleum Institute, Dallas, Texas, p 8.

21. Publication No. 50-3, The Field Testing of 32 Alloys in the Flow Streams of Seven Condensate Wells, NACE, Houston, Texas, July, 1950, p 103.

22. A.C. Coates, R.D. Kane and M.J. Schofield, "Corrosion Mitigation Technology for Oil and Gas Production", Proceedings of the Zee Pipe Conference, Oseberg, Belgium, October, 1989.

23. Recommended Practice RP0475, "Selection of Metallic Materials to be Used in All Phases of Water Handling for Injection into Oil Bearing Formations", NACE, Houston, TX.

24. R.D. Kane, S.M. Wilhelm and W.G. Ashbaugh, "Applications of Laboratory Simulation of Process Corrosion", CORROSION/92, Paper No. 285, Nashville, TN, NACE, April, 1992.

25. R.M. Kain and J.W. Oldfield, "Crevice Corrosion Behavior of Stainless Steels in Chloride and Sulfate Containing Waters", CORROSION/90, Paper No. 384, Las Vegas, NV, April 1990.

26. J.W. Oldfield, "Crevice Corrosion of Stainless Steels in Seawater", Proceedings of the International Congress on Metallic Corrosion, Madras, India, 7-11, Nov. 1987.

27. B. Walden et al, "Experience of High Performance Duplex Stainless Steel in Marine Environments" Proceedings of CORRASIA/92, Paper No. 188, NACE, Singapore, Sept 1992.

Appendix I List of Companies
Using SOCRATES™

1.	Abu Dhabi National Oil Company	14.	Kawasaki Steel
2.	AGIP S.p.A., Italy	15.	Mobil R & D
3.	Amerada Hess	16.	Nippon Steel
4.	Amoco Corporation	17.	NKK America
5.	Baker Oil Tools, Inc.	18.	Oryx Energy
6.	British Gas	19.	Otis Engineering
7.	Cabval	20.	Petro-Canada Resources
8.	Camco, Inc.	21.	Sumitomo Metal America
9.	Chevron Research and Technology	22.	Texaco, Inc.
10	Exxon Production Research	23.	Teledyne Wah Chang
11	FMC Corporation	24.	VDM Technologies
12	Inco Alloys International	25.	UNOCAL
13	O.N.G.C., India	26.	Vetco Gray

TABLE 1

Ferritic Stainless Steels		Martensitic Stainless Steels		Duplex Stainless Steels	
UNS No.	Common Name	UNS No.	Common Name	UNS No.	Common Name
S40900	409	S50400	9CR-1MO-1	S31500	3RE60
S40500	405	K90941	9CR-1MO-2	S32900	329
S42900	429	J91150	CA-15	S32404	URANUS-50
S43000	430	S41000	410	S31200	44LN
S44200	442	J91151	CA-15M	S31803	2205-22-Cr
S43400	434	S42000	420	S32550	FERRALIUM-255
S43600	436	J91540	CA-6NM	S31260	DP-3-25-Cr
S44600	446	S42400	F6NM-1		
S44400	18-2	S41500	F6NM-2		
S44626	26-1-Ti				
S44627	26-1-Cb				
S44660	SC-1				
S44635	26-4-4				
S44700	29-4				
S44800	29-4-2				
S44735	29-4C				

Precipitation-Hardened Stainless Steels		Conventional Austenitic Stainless Steels		High Alloy Austenitic Stainless Steels	
UNS No.	Common Name	UNS No.	Common Name	UNS No.	Common Name
S45500	CUSTOM-455	S30200	302	N08020	20-CB-3
S36200	ALMAR-362	J92500	CF-3	N08904	904L
S15500	15-5PH	S32100	321	N08024	20MO-4
S17600	STAINLESS-W	S31600	316	N08028	ALLOY-28
S17400	17-4-PH	S34700	347	N31254	254-SMO
S45000	CUSTOM-450	S38100	18-18-2	N08367	ALLOY-6XN
S17700	17-7-PH	S30500	305		
S66286	ALLOY-A286	S30400	304		
S13800	PH-13-8-Mo	S30403	304L		
S15700	PH-15-7-Mo	J92600	CF-8		
S35500	AM-355	S30800	308		
		S30900	309		
		J92800	CF-3M		
		S31000	310		
		J92900	CF-8M		
		S31603	316L		
		S20910	22-13-5		
		S31700	317		

TABLE 1 (cont.)

Solid Solution Nickel base alloys		Precipitation-Hardened Nickel base alloys		Cobalt base alloys	
UNS No.	Common Name	UNS No.	Common Name	UNS No.	Common Name
N08825	ALLOY-825	N07750	ALLOY-X-750	R30260	ALLOY-2602
N06975	ALLOY-2550	N07031	ALLOY-31	R30155	N-155
N06985	ALLOY-G-3	N09925	ALLOY-925	R30031	STELLITE-31
N06007	ALLOY-G	N07718	ALLOY-718	R30006	STELLITE-6
N06625	ALLOY-625	N07716	625-PLUS	R30003	ELGILOY
N06110	ALLCORR	N07725	ALLOY-725	R30188	ALLOY-188
N06455	ALLOY-C-4	N06625	ALLOY-625	R30605	ALLOY-L-605
N06022	ALLOY-C-22			R30159	MP159
N10276	ALLOY-C-276			R30035	MP35N
N10002	ALLOY-C				
N06975	ALLOY-G-2				
N06030	ALLOY-G-30				

Zirconium Alloys		Titanium Alloys		Nickel Copper Alloys	
UNS No.	Common Name	UNS No.	Common Name	UNS No.	Common Name
R60702	Zr-702	R50400	TI-GRADE2	N04400	MONEL-400
R60704	Zr-704	R53400	TI-GRADE12	N04405	MONEL-R405
R60705	Zr-705	R58640	TI-6246	N05500	MONEL-K500
		R56401	TI-6Al-4V		

Note: Dark boxes indicate active behavior of active-passive alloys

Graphite
Platinum
Ni-C-Mo alloy C
Titanium
Ni-Cr-Mo-Cu-Si alloy B
Nickel-Iron-Chromium alloy 825
Alloy "20" Stainless Steels, cast and wrought
Stainless Steel - Types 316, 317
Nickel-Copper Alloys 400, K-500
Stainless Steel - Types 302, 304, 321, 347
Silver
Nickel 200
Silver Braze Alloys
Nickel-Chromium Alloy 600
Nickel-Aluminum Bronze
70-30 Copper Nickel
Lead
Stainless Steel - Type 430
80-20 Copper Nickel
90-10 Copper Nickel
Nickel Silver
Stainless Steel - Types 410, 416
Tin Bronzes (G&M)
Silicon Bronze
Manganese Bronze
Admiralty Brass, Aluminum Brass
Pb-Sn Solder (50/50)
Copper
Tin
Naval Brass, Yellow Brass, Red Brass
Aluminum Bronze
Austenitic Nickel Cast Iron
Low Alloy Steel
Mild Steel, Cast Iron
Cadmium
Aluminum Alloys
Beryllium
Zinc
Magnesium

-1.6 -1.4 -1.2 -1.0 -0.8 -0.6 -0.4 -0.2 0 +0.2
(Active) Volts vs Saturated Calomel Reference Electrode (Noble)

Table 2 — Galvanic series in seawater. Flowing seawater at 2.4 to 4.0 m/s for 5 to 15 days at 5 to 30°C

Test	1A-1		1A-2		1A-3		1A-4	
Conditions	200°F/CO2		400°F/CO2		200°F/H2S		400°F/H2S	
Stage	1	1,2,3	1	1,2,3	1	1,2,3	1	1,2,3
4130								
13 Cr	O		O		O			
22 Cr	O	-	O		O			
25 Cr	O	-	O		O			
28 Cr	O	O	O	X 2	O	O	O	X 2
42 Ni	O	O	O	X 3	O	O	O	X 3
925	O	O	O	X 3	O	O	O	X 3
718	O	O	O	X 3	O	O	O	X 3
52 Ni	O	O	O	X 3	O	O	O	X 3
ALLCORR	O	O	O	X 3	O	O	O	X 2
C-276	O	O	O	X 3	O	O	O	

Weight Loss Corrosion
▓ Either > 2000 MPY or Specimens Destroyed by Corrosion During Test Period
☐ < 2000 MPY (5.5 MPD)
⊠ Not Tested

Stress Corrosion Cracking
O – No Failure
X – Failure (2, 3 refers to stage of test)
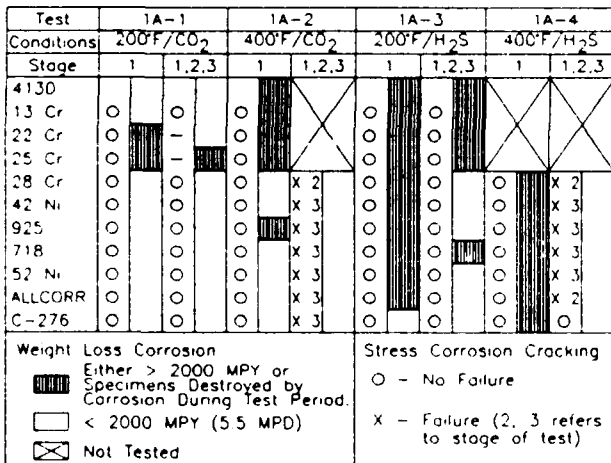
Figure 1a — Results of Corrosion Tests with 15% HCl + Inhibitor 1

Test	1B-1		1B-2		1B-3		1B-4	
Conditions	200°F/CO2		400°F/CO2		200°F/H2S		400°F/H2S	
Stage	1	1,2,3	1	1,2,3	1	1,2,3	1	1,2,3
4130								
13 Cr	O	X 3			O			
22 Cr	O	X 3			O			
25 Cr	O	O			O	X		
28 Cr	O	O	O	X 2	O	O	O	X 2
42 Ni	O	O	O	X 2	O	O	O	X 2
925	O	O	O	X 2	O	O	O	X 2
718	O	O	O	X 2	O	X 2	O	X 2
52 Ni	O	O	O	X 2	O	O	O	X 2
ALLCORR	O	O	O	X 2	O	O	O	X 2
C-276	O	O	O	X 2	O	O	O	X 2

Weight Loss Corrosion
▓ Either > 2000 MPY or Specimens Destroyed by Corrosion During Test Period
☐ < 2000 MPY (5.5 MPD)
⊠ Not Tested

Stress Corrosion Cracking
O – No Failure
X – Failure (2, 3 refers to stage of test)
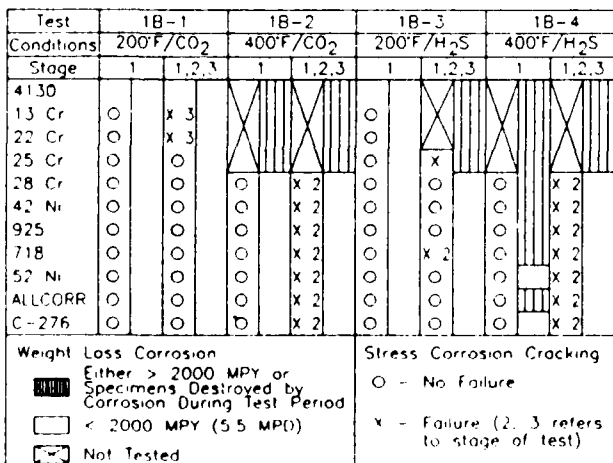
Figure 1b — Results of Corrosion Tests with 15% HCl + Inhibitor 2

Test	2A-1		2A-2		2A-3		2A-4	
Conditions	200°F/CO2		400°F/CO2		200°F/H2S		400°F/H2S	
Stage	1	1,2,3	1	1,2,3	1	1,2,3	1	1,2,3
4130								
13 Cr	O	-	-		O	-		
22 Cr	O	-	-		O	-		
25 Cr	O	X 3	-		O	X 2		
28 Cr	O	O	X		O	O		
42 Ni	O	O	O	X 2	O	O	O	
925	O	O	O	X 2	O	O	O	X 2
718	O	O	O	X 2	O	O	O	X 2
52 Ni	O	O	O	X 2	O	O	O	X 2
ALLCORR	O	O	O	X 2	O	O	O	X 2
C-276	O	O	O	X 2	O	O	O	X 2

Weight Loss Corrosion
▓ Either > 2000 MPY or Specimens Destroyed by Corrosion During Test Period
☐ < 2000 MPY (5.5 MPD)
⊠ Not Tested

Stress Corrosion Cracking
O – No Failure
X – Failure (2, 3 refers to stage of test)

Figure 2 — Results of Corrosion Tests with 28% HCl + Inhibitor 1

Mark	Chemicals	Specific gravity
O—O ●—●	NaCl-NaBr	1.32 1.42
×—×	CaCl2	1.32
△—△ ▲—▲	CaCl2-CaBr2	1.45 1.75
□---□ ■---■	CaCl2-CaBr2 -ZnBr2	1.90 2.20
O—O ●—●	CaBr2-ZnBr2	2.00 2.30
◇—◇ ◆—◆	NaBr-ZnBr2	1.55 1.75

Figure 3 — Effect of temperature on corrosivity of brine (Carbon steel A, 30 days, 2mℓ/cm²)

2792

Figure 4a – Galvanic corrosion of 9 Cr in 12ppg $CaCl_2$, 400psia CO_2, 200°C. Baseline corrosion rate of 9 Cr = 5.1mpy.
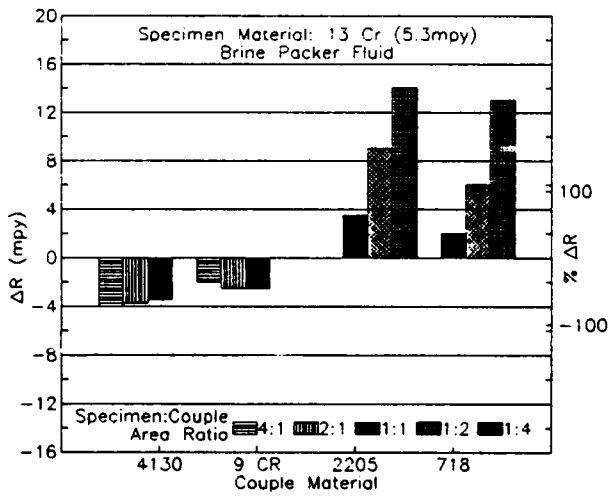
Figure 4b – Galvanic corrosion of 13 Cr in 12ppg $CaCl_2$, 400psia CO_2, 200°C. Baseline corrosion rate of 13 Cr = 5.3mpy.
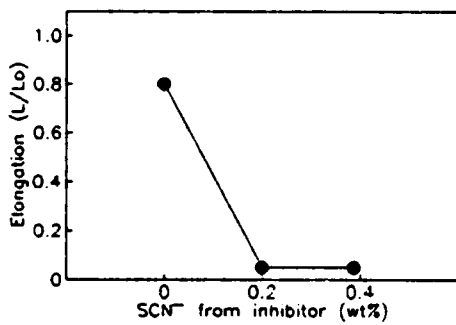
Figure 5 – Effect of SCN⁻ concentration on environmental cracking susceptibility index (L/Lo) of 13Cr in SSRT test. (380°F(193°C), 42wt%NaBr, 0.1MPaN$_2$, $\epsilon=4 \times 10^{-6}s^{-1}$)
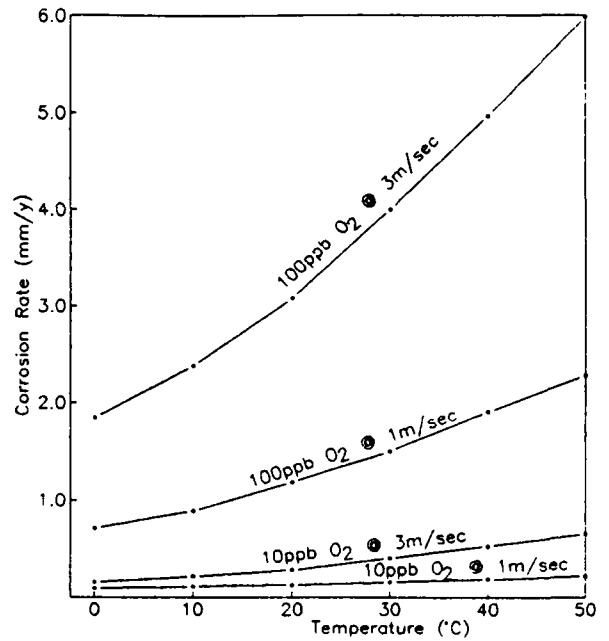
Figure 6 – Corrosion Rate of Steel in Deaerated Saltwater (10 to 100ppb O_2)
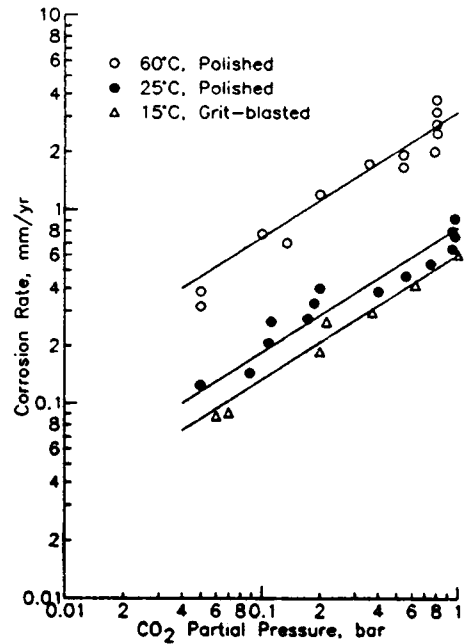
Figure 7 – Influence of CO_2 pressure and temperature on corrosion rate of carbon steel.
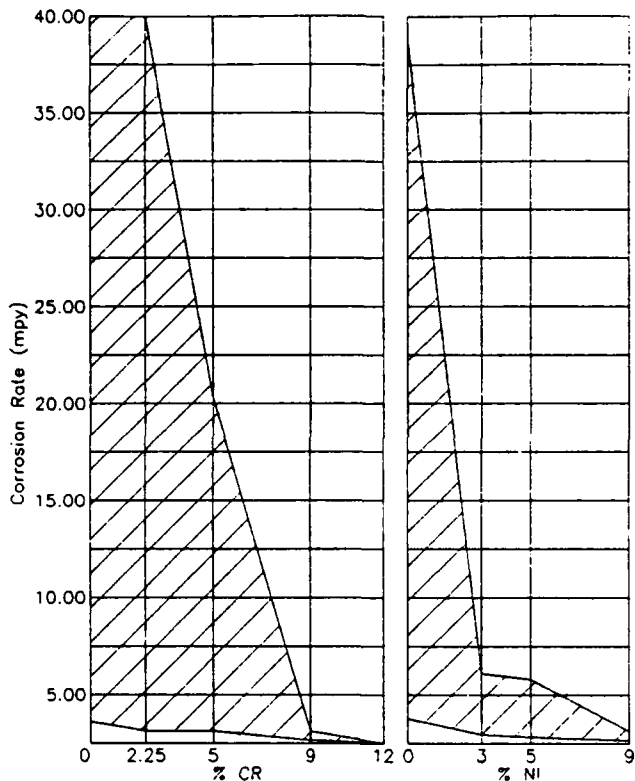
Figure 8 — Effect of Cr and Ni on CO_2 Corrosion: field test data in seven condensate wells.
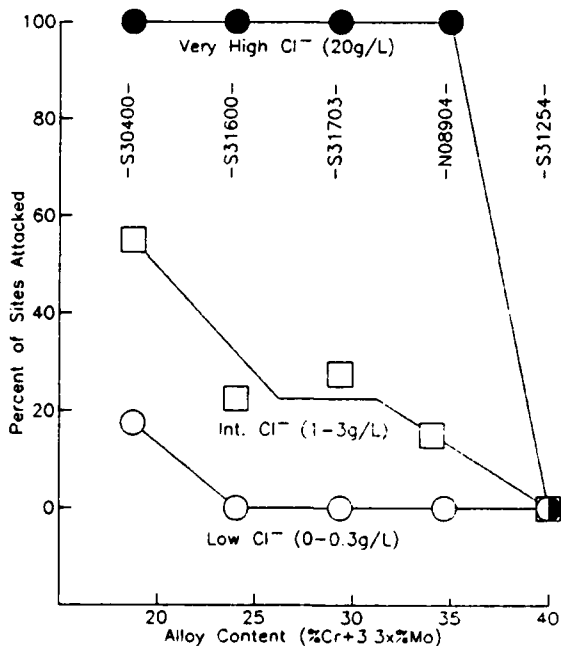
Figure 9 — Effect of alloy content on overall resistance to crevice corrosion initiation in waters containing up to 20 g/L Cl⁻
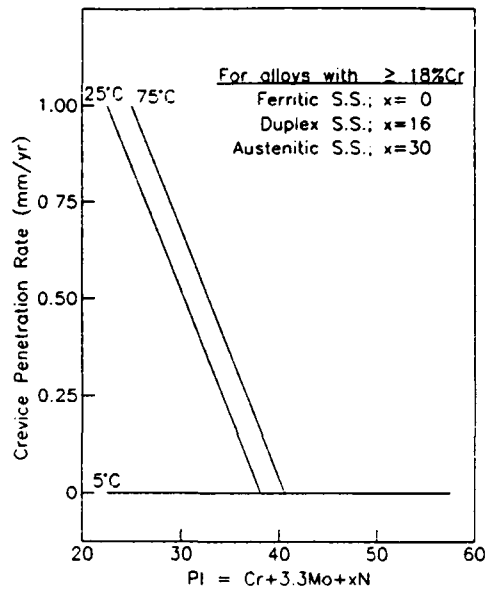
Figure 10 — Rate of crevice attack in seawater versus service temperature and Pitting Index (PI).
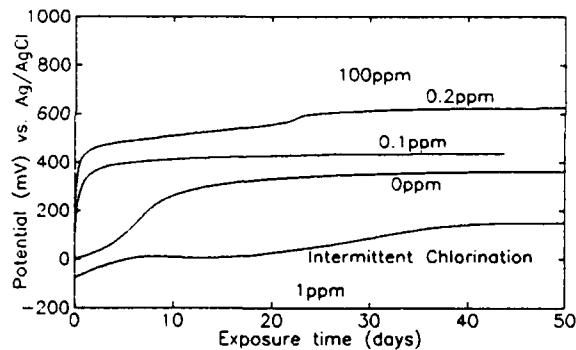
Figure 11 — Corrosion potential versus time for UNS S31254 in natural sea water with different chlorine concentrations at 9°C. For intermittent chlorination (1ppm 30min/d) the potential immediately before chlorination each day is shown.

Effects of Acidizing on High Alloy Springs After H$_2$S Exposure

Bill Bailey
Baker Oil Tools
P.O. Box 3048
Houston, Tx.

Abstract

Both compression and torsion springs made from MP35N, Elgiloy, X-750, and Beta-C titanium were stressed and exposed to severe H$_2$S, CO$_2$, and chloride environments at 350°F (177°C) for 30 days. This was followed by exposure to 38°C (100°F) simulated HCl acidizing solutions. Variables evaluated include materials, heat treatments, inhibitors, acid concentration, contaminant chloride concentration, and low alloy couple.

Key terms: acidizing, springs, H$_2$S, hydrogen embrittlement, nickel base alloys, cobalt base alloys, galvanic couple, corrosion inhibitors.

Introduction

Springs used in downhole oil and gas completion equipment are frequently exposed to corrosive produced fluids followed by acidizing treatments to enhance the flow of hydrocarbons. Failures of springs have been reported[1] by several manufacturers. Laboratory tests attempting to reproduce this cracking have been relatively unsuccessful. A testing program was developed in hopes of producing laboratory cracking. It was further hoped that a determination could be made of the effects of selected environmental, material, and processing variables. These included spring type, material, low alloy couple, inhibitor, MP35N aging temperature, and potential fluid composition and concentration during acidizing.

Experimental

Compression springs were designed and manufactured from 4.11 mm (0.162") MP35N, Elgiloy, X-750, and Beta-C titanium. Torsion springs were manufactured from 1.14 mm (0.045") MP35N and Elgiloy. The springs were assembled in fixtures designed to produce the high stresses typically required in downhole completion equipment applications. Torsion springs were stressed to 1792 MPa (260 ksi) corrected stress. Compression springs were stressed to 758 MPa (110 ksi) for MP35N, Elgiloy, and Beta-C and 689 MPa (100 ksi) for X-750. Each spring was serialized and load tested to establish the required compression height or, for torsion springs, the required angular deflection. Half of the compression springs were assembled with steel end flanges to provide low alloy galvanic couple. The other compression springs used alloy C-276 end flanges. All of the torsion springs were assembled on fixtures made from C-276 with MP35N pins (see fig. 1).

The springs were installed in two large capacity autoclaves and exposed to the same brine solution containing 100,000 ppm chlorides. The gas phase was 100 psia H_2S, 100 psia CO_2, and sufficient Argon to bring the total system pressure to 5000 psi at 350 °F (177 °C). The test duration was 30 days. Two autoclaves were used in order to separate the springs with low alloy couple and provide a larger fluid volume. The 18 steel coupled compression springs were tested in a 5.2 gal. (20 liter) autoclave. The 18 remaining compression and 18 torsion springs were tested in a 3.3 gal. (12.4 liter) autoclave. After removal from the autoclaves, the springs were individually stored in glass bottles filled with analytical toluene and sealed until the subsequent HCl testing was performed.

HCl acid exposure tests were performed at ambient pressure. Plastic bottles containing 300 ml of a specified concentration of HCl (with and without chloride salts and inhibitors) were placed in a constant temperature bath until the fluid reached the bath temperature, 38 °C (100 °F). The springs, still stressed, were then placed in individual bottles and periodically checked for cracks.

Results

A.   30 Day Autoclave H_2S, CO_2, Cl^-, 350°F Exposure of Stressed Springs

No cracking was found on any of the springs regardless of type (compression/torsion) or galvanic couple (low alloy/C-276).

B.   Acid Exposure

1.   Spring type. Some of the compression springs were shown to be susceptible to cracking in the low temperature acid exposure tests. None of the torsion springs experienced cracking in the low temperature acid exposure tests.

2.   Materials. The following spring materials were found to be resistant to cracking in the laboratory simulated acidizing cracking tests: MP35N aged 4 hours at 704°C/1300°F [MP1300], Elgiloy, Beta-C titanium. Cracking was observed under certain conditions for alloys MP35N aged 4 hours at 649°C/1200°F [MP1200] and X-750.

3.   Chlorides. Chlorides appear to be an essential variable to produce cracking. A lower limit was not established, but 10,000 ppm sea salts (4,750 ppm chloride) was sufficient for MP1200 and cracking was also observed when straight NaCl was used (20,000 ppm NaCl, 15 % HCl).

4.   Low Alloy Couple. Low alloy couple was found to be an essential variable to produce cracking, however this should be qualified since it may not be entirely related to galvanic coupling. See discussion below.

5.   Inhibitors. Inhibitors, at concentrations recommended by the manufacturer, prevented cracking in susceptible materials.

6.   Acid concentration. Both the X-750 and MP1200 compression springs were shown to be susceptible to cracking in HCl acid concentrations as low as 10% (lower concentrations were not tested).

Discussion

The environment in contact with downhole internal spring components can vary significantly during acidizing. Some of the variables include: type of fluids used to cool down the well prior to acidizing (e.g. sea water, fresh water, ammonium chloride, etc.), initial acid composition and concentration, inhibitor concentration and type, temperature of the acid treatment fluids at the downhole location of interest (both injected and produced), pH of the "spent" acid being produced, the concentration of the remaining inhibitor, dissolved formation minerals, duration of contact with the spring components, contamination of H_2S (indirectly from acid reaction with iron sulfide on the tubing I.D as the acid is pumped in, or directly from the formation when the "spent" acid returns), etc. Combinations of these fluids can vary significantly in their effect on cracking of ultra high strength, corrosion resistant alloy spring materials.

Type of stress appeared to be very important in influencing cracking. Compression springs seemed to be much more susceptible to low temperature cracking. This is contrary to what one would normally expect for the springs used downhole. Torsion springs are smaller in wire size, higher in strength, and frequently stressed closer to yield strength. The *highest fiber stresses for compression springs are located along the coil ID and are torsional*. The highest fiber stresses for torsion springs are located along the coil OD and at 'legs'. The wire in this case is loaded by tension or bending stress.

Alloy type was also very influential in determining cracking susceptibility in the low temperature tests.

Heat treat condition was shown to influence the cracking performance of MP35N compression springs. Higher aging temperatures provide better cracking resistance but this must be weighed against the loss in tensile strength. This loss was 379 MPa (55 ksi) in yield strength for the single heat and wire size used in this test.

Low alloy couple was shown to be an essential variable. The cracking observed is due to hydrogen embrittlement and without galvanic charging, no cracking was observed. Neither the C-276 coupled compression springs nor any of the torsion springs were galvanically coupled to an active material and none of these springs cracked. The presence of iron sulfide on the low alloy couple is believed to be a factor that helps to promote this low temperature type of cracking. This is due to the evolution of H_2S

upon contact with HCl. The availability of H_2S increases the amount of atomic hydrogen entering the spring[2]. When MP1200 compression springs were exposed to acidizing fluids while in contact with low alloy end washers, cracking was only produced if the end washers had not been previously exposed to acid. To explain, two MP1200 springs that had received their $H_2S/CO_2/Cl^-$ exposure with C-276 washers were disassembled and reassembled with different 4140 end washers. One spring was restressed with 4140 washers still containing iron sulfide corrosion product from the autoclave testing. The other spring was assembled with 4140 washers "cleaned" by HCl acid exposure . Cracking was observed only on the iron sulfide covered, 4140 coupled, MP1200 spring.

However, cracking was observed on two occasions where the acid solution was replaced after the initial exposure with a fresh acid solution that now contained chlorides. In these cases, the iron sulfide would have been removed and H_2S would not have been generated in the second exposure. In these cases an accelerated hydrogen charging rate was the cause of the cracking. This was due to the increased corrosion rate of the steel end washers resulting from a second exposure containing chlorides and fresh acid.

Steel end washers may not be the most severe cracking condition. The corrosion rate of ferrous materials in HCl is closely tied to chromium content. During acidizing, higher alloys such as 9 Cr, 13 Cr, 2205 duplex, and many other stainless steels have higher corrosion rates (and galvanic charging rates) compared to low alloy steel.

Inhibitors effectively prevented cracking in materials/environments combinations that previously demonstrated cracking susceptibility. However, inhibitors are always reported to have been used when investigations of field failures are made. There are a number of possible explanations for this conflict, including differences in inhibitor type, concentration, quality, time of exposure, depletion of the inhibitor in the formation resulting in the most severe attack occurring when the "spent" acid is produced, etc. Sulfur and non-sulfur containing inhibitors were tested in acid environments with spring materials that previously produced cracking and both effectively eliminated cracking.

Conclusion

- Galvanic coupling is a contributor to acidizing spring failures.
- The presence of H_2S increases cracking susceptibility.
- Higher aging temperatures for MP35N, above the 649°C (1200°F) specified by NACE MR0175, reduce the risk of cracking.
- X-750 and MP1200 are more susceptible to this low temperature cracking than MP1300, Elgiloy, and Beta-C titanium.
- Methods for limiting the risk of cracking include: limiting exposure time, sufficient use of inhibitors, selection of the more resistant spring materials, and minimizing chlorides and galvanic coupling.

Acknowledgments

The author would like to thank the management of Baker Oil Tools for supporting this investigation and encouraging the publication of this paper. Art Cizek (Baker Performance Chemicals) and Brian Wilfahrt (Baker Oil Tools) were invaluable in their help and advise in this work.

References

1   G. Chitwood, "Environmental Cracking History of High Alloy Downhole Springs", Corrosion/87, paper 298, (Houston, Tx: National Association of Corrosion Engineers, 1987)

2   R.S. Treseder, "Stress Corrosion Cracking and Hydrogen Embrittlement of Iron Based Alloys", NACE, p. 147-161, 1977.

3   R.D. Kane, B.J. Berlowitz, "Effect of Heat Treatment and impurities on the Hydrogen Embrittlement of a Nickel-Cobalt Base Alloy", Corrosion 36,(1) Jan. 1980, p. 29-37

Compression Springs

	C	Mn	P	S	Si	Cr	Ni	Mo	Fe	Co	Ti	
MP35N	.006	<.01	.002	.001	<.01	20.6	34.9	9.5	.53	33.6	.69	.01B
Elgiloy	.058	2.0	.007	.001	.50	19.7	15.3	7.1	Bal	39.6	-	.06Be
X-750	.05	.06	.006	.001	.14	15.6	Bal	-	6.7	-	2.59	2.6Cb
Beta-C	.03	-	-	-	-	5.8	-	4.0	.10	8.0V	3.3Al	3.8Zr

Torsion Springs

	C	Mn	P	S	Si	Cr	Ni	Mo	Fe	Co	Ti	
MP35N	.012	.04	.005	.0006	.05	19.9	34.7	9.5	.86	34.2	.60	.003B
Elgiloy	.060	2.0	.008	.002	.5	20.0	15.5	7.2	14.3	40.4	-	.001Be

Tensile Properties

	Yield mPa (ksi)	Tensile mPa (ksi)	elongation %
MP35N c 649°C Age	2140 (310)	2207 (320)	4.0
MP35N c 704°C Age	1758 (255)	1805 (262)	5.7
Elgiloy c 527°C Age	2158 (313)	2170 (315)	5.1
X-750 c 649°C Age	1582 (230)	1754 (254)	4.2
Beta-C c 510°C Age	1275 (185)	1289 (187)	9.0
MP35N t 649°C Age	2249 (326)	2364 (343)	2.0
MP35N t 704°C Age	1903 (276)	2020 (293)	2.1
Elgiloy t 527°C Age	2604 (378)	2642 (383)	3.0

c=compression spring; t=torsion spring

Compression Springs with 4140 Steel Galvanic Couple

Sample	Material	HCl Conc.	NaCl or Sea Salts ppm	Hours	Results
1T	Elgiloy	10%	10,000 Sea Salt	100	No Cracks
1M	Elgiloy	15% 15%	20,000 Sea Salt 20,000 Sea Salt	48 100+	No Cracks No Cracks
1B	Elgiloy				Not Tested
2T	MP1300	10%	10,000 Sea Salt	100	No Cracks
2M	MP1300	15%	20,000 Sea Salt	48	No Cracks
2B	MP1300				Not Tested
3T	X-750	15% 15%	0 20,000 NaCl	~36 ~60	No Cracks Cracked
3M	X-750	10%	10,000 Sea Salt	72	No Cracks
3B	X-750	10% 10%	10,000 Sea Salt 20,000 Sea Salt	48 30-40	No Cracks Cracked
4T	MP1200	15% 15%	0 20,000 NaCl	~36 ~60	No Cracks Cracked
4M	MP1200	15%	20,000 NaCl	9-24	Cracked
4B	MP1200	10%	10,000 Sea Salt	~8	Multi-Cracks
5T	MP1200	10%	10,000 Sea Salt	100	No Cracks
5M	MP1200	10%	10,000 Sea Salt	72	No Cracks
5B	MP1200	10%	10,000 Sea Salt	14	Cracked
6T	Beta-C	10%	10,000 Sea Salt	48	No Cracks
6C	Beta-C				Not Tested
6B	Beta-C	15%	20,000 Sea Salt	100	No Cracks
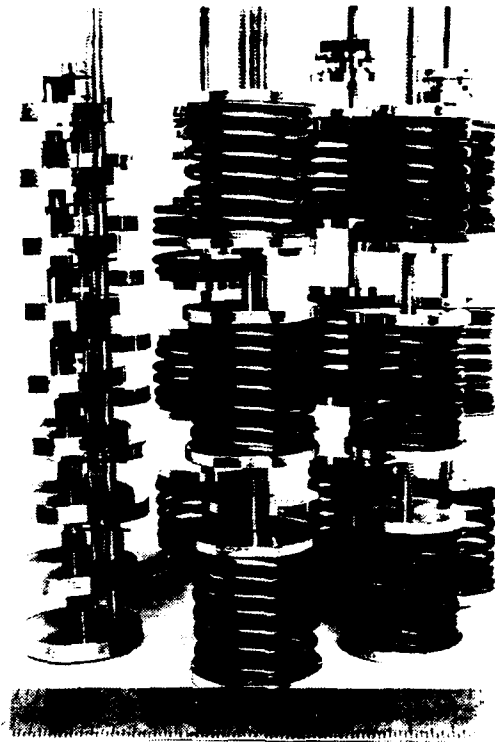
Figure 1: 0.8X Photograph of the compression and torsion springs prior to assembly in the autoclave. Each spring is loaded to a specific compression height or angle of rotation to obtain the desired stress level.
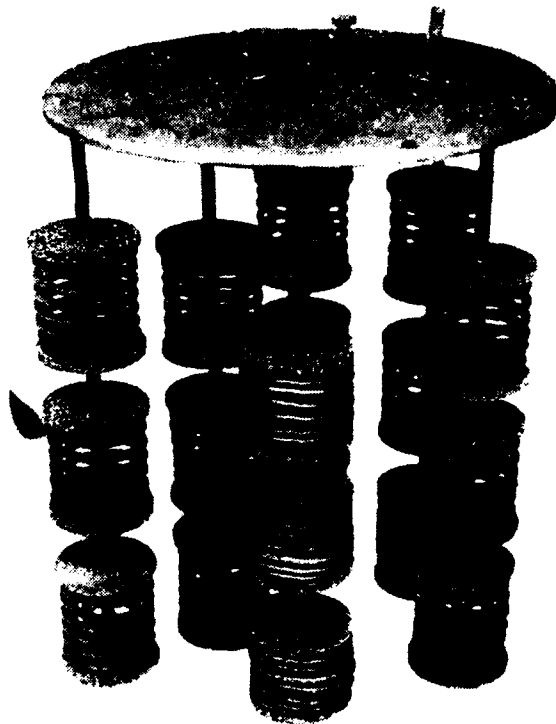
Figure 2: 0.6X Photograph of the compression springs with low alloy steel end flanges after 30 days in the autoclave environment. Crystals of corrosion product are visible on end flanges and springs.

Figure 3: 0.5X Photograph of the X-750 compression spring which cracked after 60 hours of exposure in a 15% HCl and 20,000 ppm NaCl solution at 38°C (100°F). The torsional fracture is typical for compression springs.

Figure 4: 14X Photomicrograph of the cracked X-750 spring of figure 3. The fracture originated at the ID. No other cracks were found.

Study of Corrosion Inhibitors in Waste Water Reuse System in the Oilfield*

L. Zhu

The Preparation of Corrosion Inhibitor for Water Flooding in the Oilfield and Mechanism Evaluation

Lu Zhu, Huang Guangtuan and Yan Wenjun

East China University of Chem. Tech., Shanghai 200237, China

Abstract

A various of imidazoline corrosion inhibitors were prepared by reacting aliphatic acids with diethylenetriamine and further quaterized to form derivatives of imidazolines. Several test methods, e.g., weightloss and electrochemical methods such as linear polarization, polarization curve and Ac-impedance, were used to evaluate the performance of corrosion inhibitor. The optimum corrosion inhibitor HO-8 was screened from the measurement. The effect of H2S in water flooding on the properties of corrosion inhibitors was studied. The effects of temperature, minerization and other water treatment chemicals on the speed of film forming were discussed. The Ac-impedance and modern instrument analysis methods, e.g., FT-IR, NMR and AES, were applied to study the inhibition mechanism of corrosion inhibitors. It was indicated that imidazoline molecules were adsorbed on the metal surface to inhibit metal corrosion. Under the action of hydrogen sulfide, corrosion inhibitors react with FeS to form surface complexes and enhance the protection performance of film. Corrosion inhibitor HO-8 can be used as multi-functional water treatment chemicals in oilfield flooding water.

Introduction

With the development of oil recovery, the amount of sewage containing oil was increasing rapidly. A serious problem appeared about the treatment and discharge of sewage in oilfield. On one hand, the flooding water source was required for the secondary oil recovery; On the other hand, it was required to solve the discharge of sewage. It was natural for people to use oilfield sewage as the flooding water of oil recovery. then, the two problems mentioned above can be solved simultaneously. However, the sewage components in oilfield are very complex.The high minerization and several types of gases, e.g., H2S, CO2 and dissolved oxygen can cause the corrosion of the equipment and pipeline easily. The scaling salts contained in sewage, such as calcium, magnesium, strontium and barium carbonates or sulfates can form the scales in equipment. Moreover, the organic substances and microorganism, e.g., sulfate reduced bacteria and ferrobacillus can also lead to the bacterium corrosion and plug by the slime. Beside treating with sewage to meet the requirement of flooding water quality to prevent corrosion, scale and microorganism slime, some corrosion inhibitors, scale inhibitors

and bactericides, including organic amines (monoamines. diamines, amides), imidazolines and quaternary ammonium salts etc., need to be added into sewage.

The study of corrosion inhibitors of oilfield flooding water began from 1950's. In 1950's, Farriss[1] used 13 ppm zinc chromate to inhibit the corrosion of iron in 5.2% NaCl solution. Bergman[2] proposed to use quaternary ammonium salts and rosin amine as inhibitors. In 1960's, A. Ostroff[3] used 75 ppm derivatives of cacao amine to inhibit the corrosion of mild steel in NaCl solution (containing 100 ppm H_2S and CO_2) at 50 °C and the inhibition efficiency was above 90%. In 1970's, P. W. Walk and F. T. Bobalek [4] used 20 ppm amines with elements S and O to inhibit the corrosion of steel in 5% NaCl acid solution. Now, the new types of corrosion inhibitors have been developing and more works were based on the conbination of conventional chemcals as to raise the inhibition efficiency. In recent years, several types of corrosion inhibitors, e.g., SO-1 and SL-2B etc., had been used successfully in Sheng Li Oilfield. However, generally, the patterns and efficiency of corrosion inhibitors need to be improved.

Based on investigation for extensive information and the consideration of characteristics of corrosion inhibition and bactericidal function, the quaternary ammonium group was introduced into imidazoline molecules to increase its solubility in water and the efficiencies of corrosion inhibition and anti-bacteria. Therefore, a series of imidazoline inhibitors with high efficiencies for corrosion inhibition and anti-bacteria were syntherized successfully and the influence factors and mechanism were discussed.

The Evaluation of Corrosion inhibitor in Oilfield

1.weightloss test

A sheet of mild steel readily polished was wholly immersed in high minerization (30000ppm.), 10±2 ppm H_2S and 75±5 ppm CO_2 simulative oilfield sewage. Seven days later, the corrosion products were cleared away and the specimens were weighed with a analysis balance. Then the corrosion rate and the inhibition efficiency can be calculated as shown in Table I.

Table 1 The results of HO series of inhibitors with weightloss

No.	blank	1	2	3	4	5	6	7	8	SL-2B
CR (mm/y)	10.8	6.41	1.70	3.27	7.53	3.96	0.76	0.79	0.75	1.19
IE (%)	--	40.6	84.3	69.7	30.4	63.3	93.0	92.7	93.1	89.0

CR--corrosion rate. IE--inhibition efficiency
All figures about CR n table 1 was divided by 10 Exp 3
T: 60+1 C; pH:7.4: Dosage: 20 ppm

It was indicated in Table 1 that the inhibition efficiencies of HO-6, HO-7 and HO-8 were higher than those of the other six inhibitors tested simultaneously and it may get to above 90%. They were better than SL-2B inhibitor (a commerial inhibitor). Especially HO-8 is the best one. Moreover, the surfaces of specimens were shine and there was not the occurence of pitting corrosion. It was shown from these results that HO-8 was effective in the treatment of oilfield sewage containing H2S,CO2 and high minerization.

2.liner polarization measurement

The corrosion rate of inhibitors mentioned above can be measured by Model M-1120 corrosion rate measurement instrument. The result was shown in Fig.1. It was shown from Fig.1 that all the inhibitors are effective compared with the blank. Especially, HO-8 corrosion rate decreased fastest and the final corrosion rate was lowest, which meaned that HO-8 rate of film formation was fastest and the efficiency was highest of all. The reason was that negative HS ions Adsorbed primarily on the surface under the action of H2S and the quaternary ammonium group in the HO-8 molecules would strengthen the ability of adsorption by interactions of charges. The effect of concentration, temperature, minerization and the H2S content on HO-8 were shown in Fig.2 to Fig.5.

It was known from Fig.2 that HO-8 was very effective when its concentration got to 20 ppm. In Fig.3 and Fig.4, there was almost no effect when the temperature changed from 40° to 80 °C and the minerization changed from 10000 ppm to 30000 ppm. In Fig.5, the corrosion rate was high when the concentration of H2S changed from 30 to 50 ppm, but the decreasing tendency with time was high too.

In practical application, corrosion , scale inhibitors and bactericides were used simultaneously, so their compatibility was important. The experiment followed was to study the efficiency of the conbination of HO-8, HEDP and 1227 (a kind of bactericide) and the results were shown in Fig.6. It was indicated from Fig.6 that the rate of film forming was more rapidly than that of HO-8 used only when these three chemicals were used at same time. The one of reason was that HEDP and 1227 were effective in corrosion inhibition for themselves and the synergestic effect existed when they were used with HO-8.

3. polarization curve measurement

The results of polarization curve measurement of seven inhibitors were shown in Fig.7. It was known from Fig.7 that all corrosion inhibitors were effective at a certain degrees of inhibition action comparing with the blank. In particular, the polarization curve of HO-8 had a large slope than the others, which meaned that HO-8 had the highest polarizability, the fastest rate of film forming and the most protective film. This result was consistent with that of weightloss test and liner polarization

measurement.

4.Ac-impedance measurement

The total impedance IzI and phase angle of corrosion system can be measured by Model 4194A Ac-impedance measurer. Then the solution resistance Rl, the polarization resistance Rr, differential capacity Cd and the figure of impedance complex plane can be obtained by computer simulation. Fig.8 and Fig.9 showed respectively the change of C_d and R_s with time under the condition of 20 ppm HO-8. It was indicated form Fig.8 that with the increasing immersion time, R_s became larger and C_d became smaller obviously. the reason was that the film became thicker and denser.

The Study of Machanism

1.FT-IR spectrum analysis

The FT-IR spectrum of corrosion inhibition system could be obtained by Model FT-IR 20XS measurer and the result was shown in Fig.10. It was indicated from Fig.10 that there was a great adsoption peak at 1600 cm or so which is the characteristic peak of imidazoline. Apart form it, there were two adsoption peaks at 1560 cm and 1660 cm, which meaned that there was quaternary ammonium group in HO-8 molecule.

2.NMR spectrum analysis

The NMR spectrum of HO-8 could be obtained by Model WP-100SY nuclear magnetic resonator and the result was shown in Fig 11. It was indicated from Fig.11 that there were imidazoline rings in HO-8 obviously. Moreover, tertiary amine group in the side chain of HO-8 has been substjtuted by benzyl group, which meaned that HO-8 has been quaterized.

3.SEM analysis

The SEM of HO-8 could be obtained by Model Steroscan 250MK3 measurer and it was indicated from SEM photographs that there was serious corrosion on blank specimens, but the corrosion only took place at a small degrees under the condition of HO-8 used, which meaned that HO-8 was very effective.

4.AES analysis

The AES of HO-8 could be obtained by Model PHI 550 ESCA/SAM combined spectrum measurer made by Perkin-Elmer Company and the result was shown in Fig.12. The relationship of the percent of atoms and sputtering time could be calculated by experimental AES and standard ES. Then the Fig.13 could be drawn. It was indicated from Fig.12 and Fig.13 that the content of element S and O was higher at the outside of film and there was a maximum value when the sputtering time was 30s, which meaned that FeS and oxide of

iron were rich in the outside of film and their combination strengthened the protection under the condition of HO-8 used. In general, some conclusions about the machanism could be made based on the experiment mentioned above: HO-8 could form positive ion when it combined with hydrogen ion and it would be adsorbed on the cathodic area of metal surface because of electrostatic gravitational force, which stopped the hydrogen ion from further closing to metal and lowed the energy of activation of discharge of hydrogen ion. Then the corrosion was inhibited effectively. This kind of adsorption because of electrostatic gravitational force or Vander wal force was physical adsorption.

Apart from these, there is no-share electron pair around the central atom N in HO-8. The lone-pair electrons of central atom of polar group will form coordinate bond with d orbit of metal surface when the orbit is empty. Thus, the molecule of HO-8 can adsorb on the metal surface. This kind of adsorption because of the forming of coordinate bond was named as chemical adsorption. As to HO-8, chemical adsorption and physical adsoption existed at the same time. On the one hand, the polar group in molecule can adsorb on the surface of metal, which changed the structure of electric double layer and raised the energy of activation of the ionization process of metal ; On the other hand, the nonpolar group had directional arrangment far away the surface and formed a layer of hydrophobic film which was the obstacle of diffusion for corrosion reactants. Thus the corrosion was inhibited.

Conclusion

1. corrosion inhibitor HO-8 had good efficiency under the condition of H2S and CO2.
2. the inhibition efficiency almost was not influenced by using HEDP and 1227 at the same time.
3. by modern analysis technique, it was known that the machanism of HO-8 was that: the molecule of HO-8 could form a layer of adsorbed film, which hindered the diffusion of corrosive substances. Moreover, HO-8 could take part in the corrosion reaction and formed a kind of complex combining with FeS which could also take part in the film forming under the condition of H2 S.
4. the synthesis process of HO-8 was simple and its efficiency was high. Apart from these, HO-8 was also a kind of bactericides. So it could be widely used in oilfield flooding water .

Reference

1. R. E. Farriss. USP 2,695,876 Nov. 30 (1954)
2 J. I. Bregman. Corrosion inhibitors (1963)
3. A. G. Ostroff. USP 3,412,025 Nov. 19 (1968)
4. C. C. Nathan. Corrosion Inhibitors. (1973)
5. F. Mansfeld. Corrosion Mechanisms. (1987)

Curve o — blank
Curve 7 — HO-8 (20ppm)
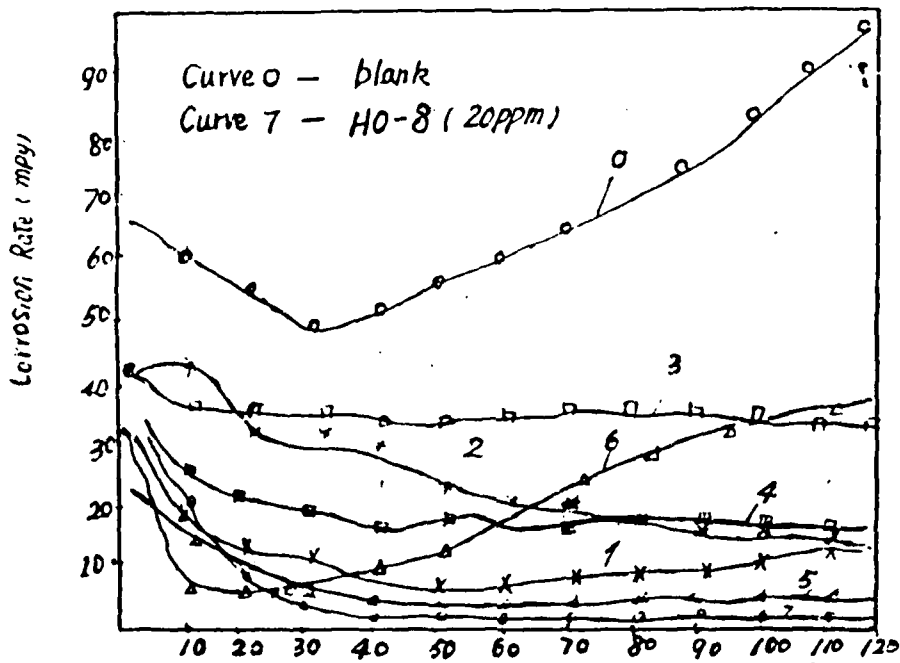
Fig.1 The Corrosion rate of Several Corrosion Inhibitor (min)

1 — 10 ppm
2 — 20ppm
3 — 30ppm
4 — 40ppm
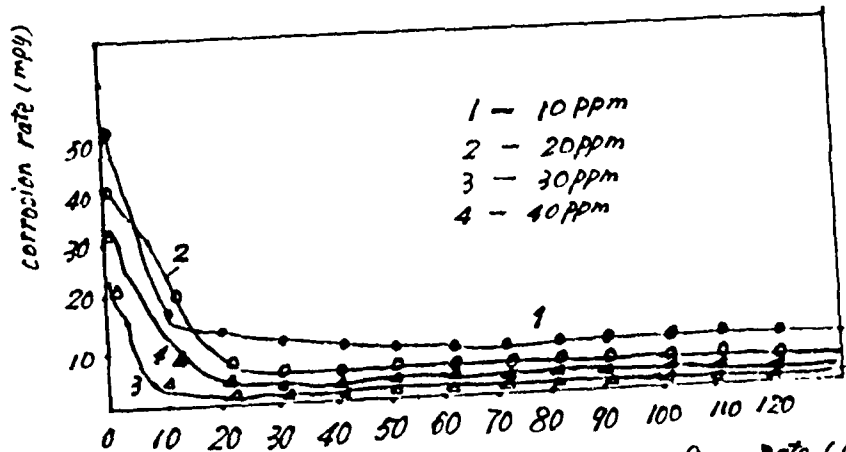
Fig.2 the Effect of Ho-8 Dosage on Corr. Rate (min)

1 —— 40°C
2 —— 60°C
3 —— 80°C
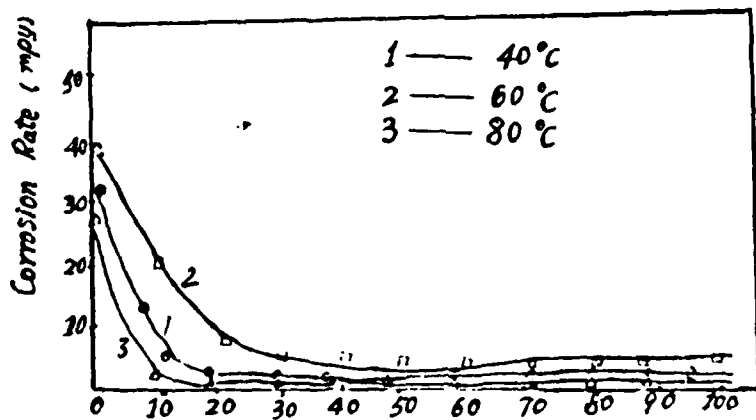
Fig.3 The Effect of Temperature on Corrosion Rate (min)
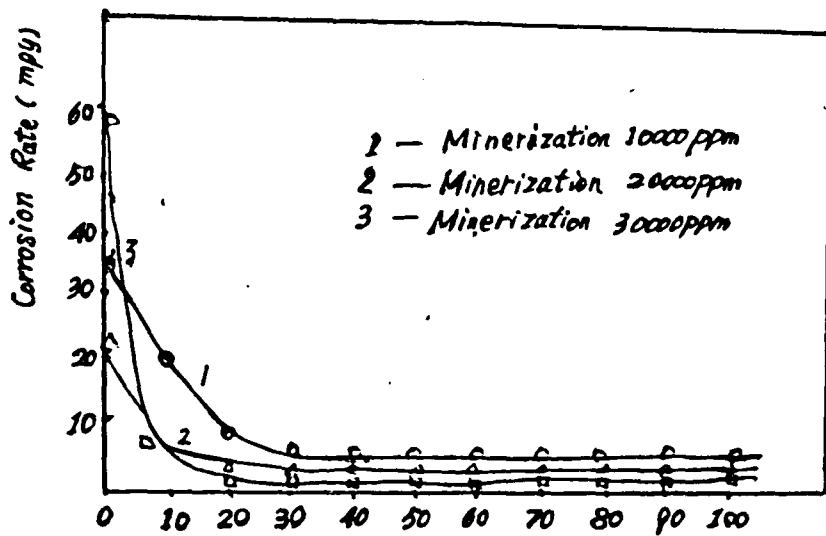
Fig 4 The Effect of Minerization on Corrosion Rate (min)
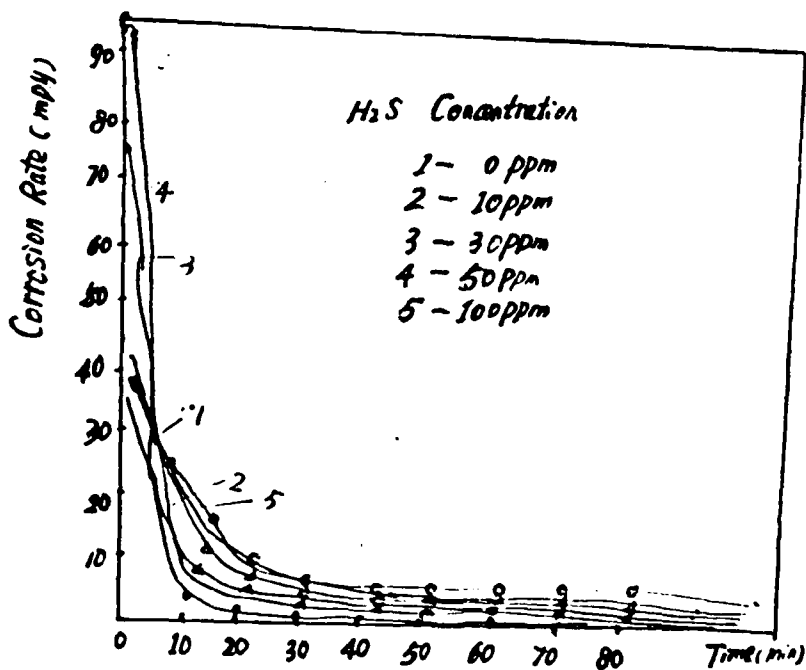
Fig 5 The Effect of H₂S Concentration Corrosion Rate
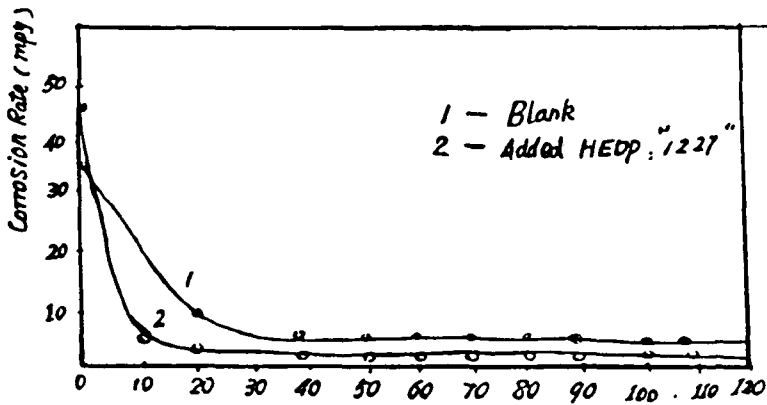
Fig.6 the Effect of HEDP and "1227" on HO-8 Corr. Rate (min)

1 — Blank
2 — Added HEDP. "1227"
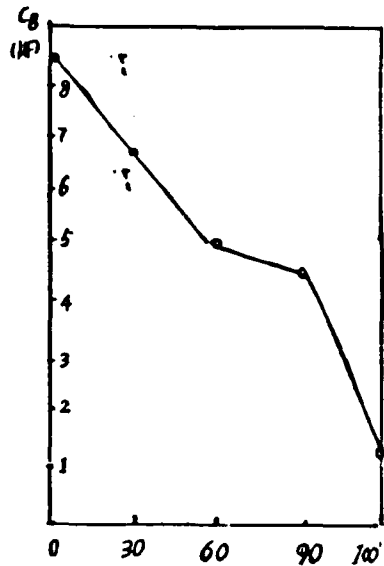
Fig.8 the Relationship of C_B and Time Being Added Ho-8
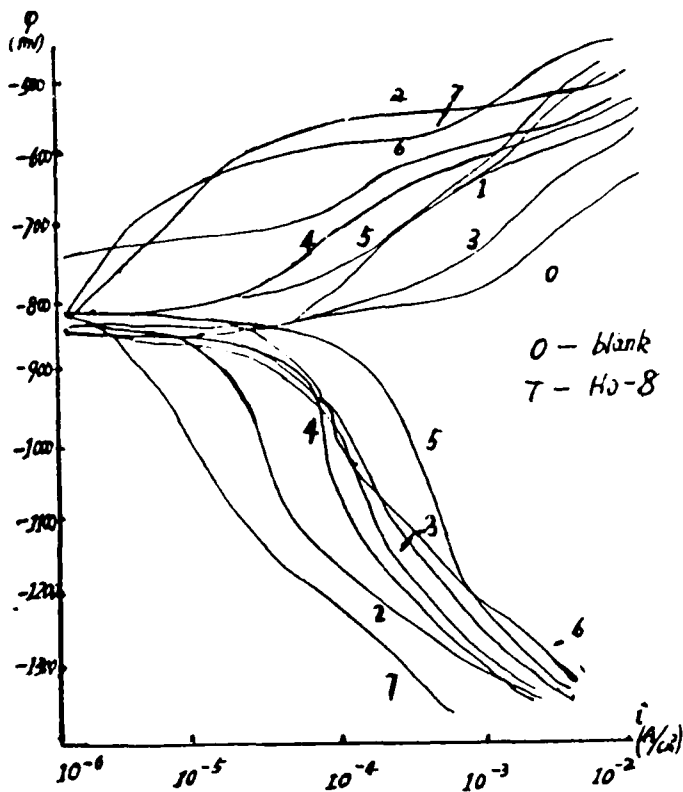
Fig.7 the Polarilation Curves of Several Corr. Inhibitors

O — blank
7 — Ho-8
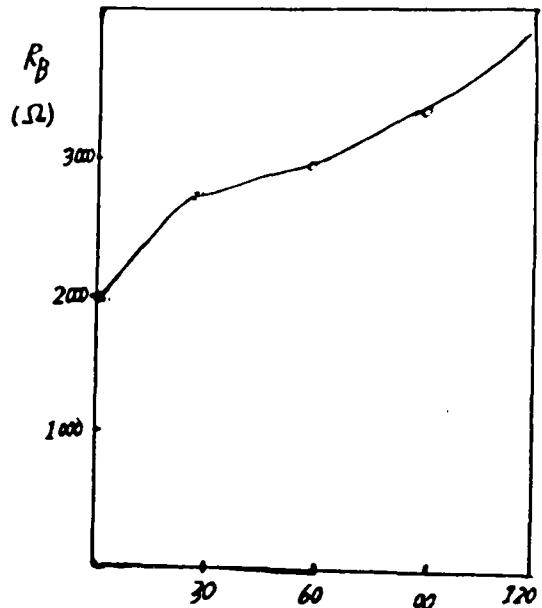
Fig.9 the Relationship of R_B and Time Being Added Ho-8 (min)

2811
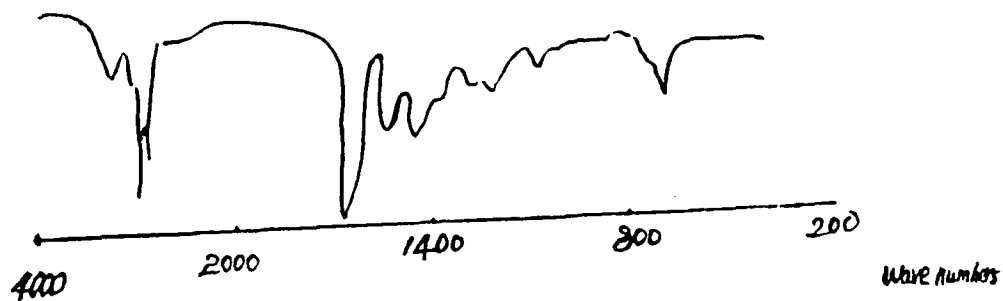
Fig.17   FI-IR Spectrum of Ho-8
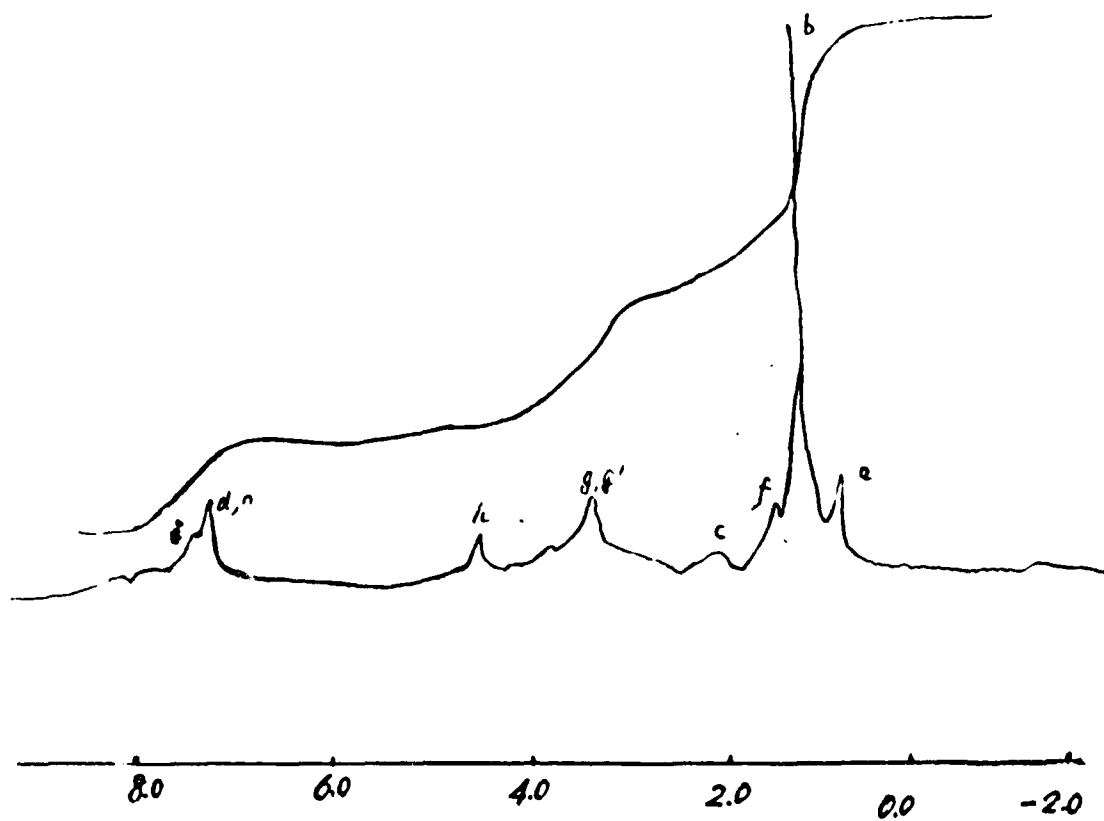
Fig.18 NMR Spectrum of Ho-8
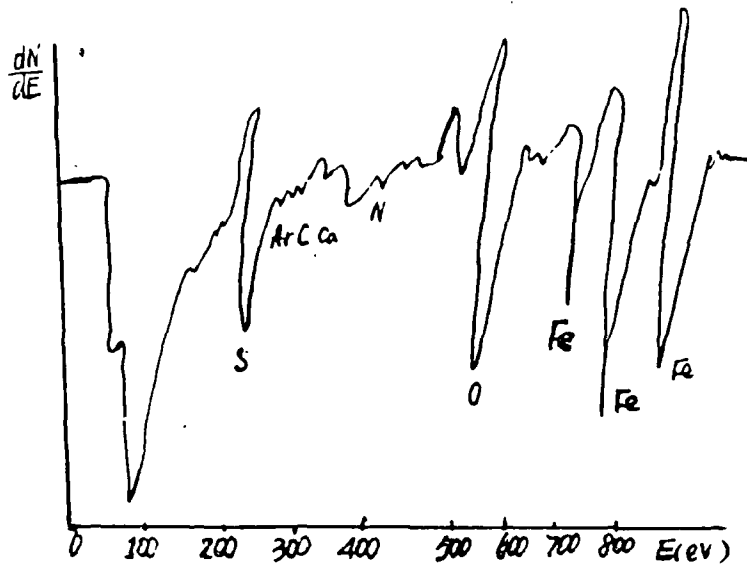
Fig.12 AES Spectrum of Corrosion inhibitor Ho-8
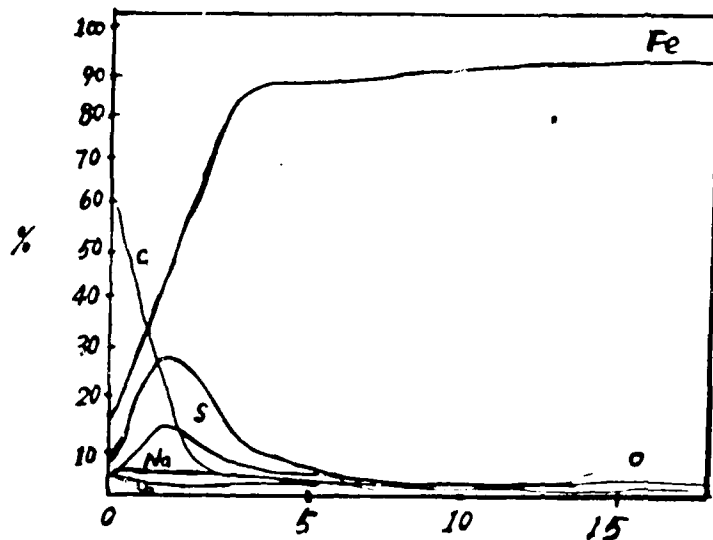
Fig.13 the Relationship of the percent of Atoms with Sputtering Time (min)

Low Cost Material Selection
for
Produced Water Tank

Torfinn Havn
Aker Engineering a.s
P.O. Box 589, N-4001 Stavanger, Norway

Abstract

Based on an investigation of 5 various materials it turned out that the most cost effective solution for a Produced Water Tank on a North Sea platform was to use stainless steel UNS S31603 in combination with simple carbon steel anodes.

This untraditional solution is verified by electrochemical potential measurements.

Current measurements show that the anodes work. The current demand was measured to a higher value than design value. However, usually the current demand decreases after some weeks and most probably the design life of 20 years are met.

Key terms: Produced water, cathodic protection, carbon steel anodes.

Introduction

Tanks for handling produced water is reported to suffer from heavy corrosion. This due to the fact that produced water at atmospheric pressure is about as corrosive as seawater.

Corrosion attack often requires repair welding and of course blasting and re-lining. This causes high direct and indirect costs.

Knowing the external impact and the strong and weak properties of the materials, it is in some cases possible to re-think material selection and go for untraditional solutions.

The weak property of the stainless steels is the low resistance against pitting corrosion in chloride containing solutions. However, by moving the electrochemical potential slightly (100-150 mV) in negative direction, the resistance against pitting corrosion is increased to an acceptable level. This can be obtained by cheap carbon steel anodes. Even at temperatures as high as 80 °C the pitting resistance will be acceptable.

Process Data and Tank Design

The temperatures, medium and tank operation are as follows:

Operating temperatures: Minimum/normal/maximum 5 °C / 10 °C / 85 °C

Design temperatures: Minimum - 7 °C, Maximum 115 °C

Medium: Produced water and oil at atmospheric pressure, water/oil ratio = 0.25. No sand.

Operation: At liquid level of 3.5 m and 0.5 m the pump starts and stops respectively.

Produced water level: At highest 3.5 m x 0.25 m = 0.875 m

Tank size: L x w x h = 5 m x 1.62 m x 5 m
Tank is divided in two equal parts, making each part 2.5 m x 1.62 m x 5 m

Material Evaluation and Cost Impact

Five material alternatives were investigated. The various alternatives are summarised as follows:

1. Lined carbon steel with Zn or Al anodes is the alternative with lowest initial cost. However, the lining can not be expected to last for more than 2-4 years. During periods with high operating temperature, the anodes will not work as intended. Depending on time span between damage of lining and relining, weld repair might be carried out. The cost of one relining offshore is higher than the initial cost of the tank which is about NOK 300.000,-.

2. Stainless steel UNS S31603 does not need lining and as shown in this paper, can be protected against pitting corrosion even at a temperature of 80 °C by simply using carbon steel anodes. The initial cost is higher compared to alternative 1, a total of about NOK 800.000,-. However, this alternative is maintenance free.

3. Higher alloyed stainless steel grades as UNS N08904 and 6Mo stainless steel will suffer from pitting corrosion at temperatures above 30 - 40 °C. And when a pit is formed it will continue to grow at lower temperatures. The increased cost, about NOK 1.4 mill. is therefore not justified.

4. Glass fibre reinforced plastic (GRP) is also a maintenance free alternative. However, due to limited experience with tanks having such a high amount of nozzles both in top and bottom, this alternative was not found favourable. In addition the risk of falling objects and decreasing stiffnes at 80 °C, made the GRP solution less attractive.

5. The Titanium grade 2 alternative was found maintenance free for the whole design life of 30 years. However, the initial cost was estimated to NOK 2.5 mill. Compared to the stainless steel alternative of NOK 0.8 mill. This alternative was rejected.

Cathodic Protection Requirements and Anode Design

Design Life of Anodes

The design is based on 20 years life time. The reasons for not designing for overall process equipment life time of 30 years are that retrofitting of anodes is very easy, quick and cheap. No welding is needed on the platform. And for periods the water level will be below the design level. This means that actual life of anodes will be longer than their design life.

Calculation of Current Demand

Area to be protected The area to be protected is calculated to 11 m². This is for one part of the tank and at a water level of 0.875 m.

Current demand The current density requirement is obtained through following
equations: $i_t = i_o + k \times dT$ (1)
        i_o = current density for oxygenated seawater = 120 mA/m²
        k = constant for temperatures above 25 °C = 1 mA/m² °C

An average temperature of 40 °C is used and gives.

i_t = 120 mA/m² + 1 x (40-25) mA/m² = 135 mA/m²   (2)
The total current demand is then
i_t = 135 mA/m² x 11 m² = <u>1.5 A</u>

Protection Potential

The protection potential in a produced water environment under atmospheric pressure is assumed to be as for seawater.

The breakdown potential of UNS S31603 versus pitting corrosion is in the literature found to vary between 0 mV, (SCE) (1), -50 mV (SCE) (4) and -200 mV (SCE) (2) at 80 - 90 °C.

To be on the conservative side, a protection potential Epr of -300 mV (SCE) is to be designed for.

Calculation of Anode Potential E_A

To enabling anode potential calculation, one first have to make an assumption about anode area, calculate numbers of anodes, and then control the assumptions.

It is assumed that the surface area ratio carbon steel to stainless steel is 1:12 or 8.3 %. Further, the calculation is based on same current density of stainless steel surface as of carbon steel surface: 135 mA/m² which is an estimated limit for oxygen containing seawater in a tank at a temperature of 40 °C.

The anodes then have to supply:

1.5A + 8.3 % x 1.5A = 1.62A   (3)

or $I_t + I_a = I_{cc}$ (4)

where
I_t = total current demand on stainless steel surface
I_a = current consume on anodes (self corrosion)
I_{cc} = total cathodic current

The carbon steel anodes are assumed to have a free corrosion potential at 40 °C of about: E_F = -620 mV (SCE)

The Tafel slope varies in the literature. However, a value of 60 mV per decade is anticipated. Coupled to the stainless steel tank with an area ratio of 1:12, the electro-chemical potential on the anodes will increase to:

$E_A = E_F + (\log (I_t+I_a) - \log I_a) \times 60$ mV   (5)
$E_A = -553$ mV (SCE)

Anode Design

The driving potential is the difference between the potential of the polarized anode surface and the protection potential of the stainless steel surface.

The driving potential:

$dV = E_{pr} - E_A = -300 - -553$mV = 253 mV   (6)

The anodes are designed for easy handling.

Anode size: 350 x 350 x 35 mm³.

The ohmic resistance of such an anode is according to Lloyd (3):

$R = S/L2$ (7)
S = specific resistivity (ohmcm)
L = arithmetic mean of anode length and width

For seawater:

S = 30 ohmcm
$R = \dfrac{30 \text{ ohmcm}}{2 \times 35 \text{ cm}} = 0.43$ ohm

Each anode is then able to supply :

$$I = \frac{U}{R} = \frac{0.253}{0.43} \text{ A} = 0.59\text{A} \tag{8}$$

Number of anodes needed based on current density capacity:

$$N_1 = \frac{1.62\text{A}}{0.59\text{A}} = \underline{3 \text{ anodes}}$$

Anode mass needed for the life time is calculated by Faradays law.

$$\frac{dn}{dt} = \frac{IM}{zF} \text{ (g/sec)} \tag{9}$$

M: molar mass
F: Faradays constant
z: number of electrons

Total anode mass:

$$W = \frac{1.62\text{A} \times 56 \times 10^3 \times 3600 \times 8700 \times 20}{2 \times 96500} = 294 \text{ kg}$$

Number of anodes:

$$N_2 = W/\text{anode mass} \times f$$
f = anode efficiency = 0.90

Anode mass is calculated to 32.8 kg.

$$N_2 = \frac{294 \text{ kg}}{32.8 \text{ kg} \times 0.90} = 10 \text{ anodes}$$
$$N_2 > N_1$$

A total of 10 anodes are to be used.

As shown in fig. 1 the anodes are painted on one side. Therefore, the 10 anodes will have a surface area of: (350 x 350 - 100 x 100) x 10 mm² = 1.125 m²
(Area used for anode fitting represents 100 x 100 mm²).

This area is: $\frac{1.125}{11.2}$ = 10 % of stainless steel surface

The assumption of 8.3 % is fulfilled. The 10 % instead of 8.3 % means a slight increase of I_{cc} and a slight decrease of anode potential (5 mV).

The anode details, fitting device, anode locations and tank are shown in figures 1, 2, 3 and 4.

Temperature Effects

The design is based on an average temperature of 40 °C. However, pitting corrosion at max. operating temperature of 80 °C is also to be prevented. And as shown later potential measurements for design verification is carried out at ambient temperature.

A temperature increase from 40 °C to 80 °C causes a potential increase of about 7 mV. This is based on equations 2 and 5. Therefore, if a protection potential of -300 mV (SCE) is needed at 80 °C, a potential of -307 mV is needed at 40 °C, and at ambient temperature the potential should read about -310 mV (SCE).

Electrochemical Potential and Current Measurements

Results

After construction of the tank and installation of the carbon steel anodes, one part of the tank was filled with seawater from the harbour of Stavanger. The level of the seawater should have been 0.875 m. However, due to practical difficulties by entering the 5 m high tank from the top, the manhole located on front side was used. Therefore the seawater level was to be reduced to 0.525 m. The seawater temperature and pH were 7 °C and 8.1 respectively.

The voltmeter and reference cell (saturated calomel electrode) was calibrated versus calibrated laboratory equipment.

The electrochemical potentials on the 10 anodes, on stainless steel wall behind the anodes, on stainless steel wall at mid-distance between anodes and in bottom of tank at longest distance from anodes were measured to:

Anode no.	Anode surface	Stainless steel behind anodes	Stainless steel at mid-distance between anodes	Bottom of tank
1	- 535	- 487	- 479	- 377
2	- 552	- 532	- 521	- 387
3	- 538	- 501	-468	- 385
4	- 533	- 494	- 485	- 380
5	- 529	- 427	- 469	
6	- 537	- 488	- 458	
7	- 5.8	- 481	- 478	
8	- 532	- 485	- 482	
9	- 527	- 425	- 492	
10	- 524	- 490	- 480	
Average:	- 533	- 481	- 481	- 382

<u>Table 1</u>   Potential measurements mV (SCE)

The measurements were carried out about 4-6 hours after the seawater was pumped into the tank. As reference, uncoupled stainless steel (UNS S31603) was placed in the tank and a potential of -260 to -270 mV was measured.

One anode was electrically isolated from the internal of the tank and earthed through an ampere-meter. Results ranging from 250 mA to 327 mA with an average value of 282 mA were measured.

Discussion and Conclusions

As can be seen from test results, the cathodic protection system is working. The carbon steel anodes do supply the necessary current for protection of the stainless steel surface.

The measurements gave results of limited scatter.

The electrochemical potential found on anode surfaces is slightly more positive (about 25 mv) than calculated.

The "mismatch" of only 25 mV may indicate that these calculations are close to correct values. The "mismatch" would have been zero if the free corrosion potential was reduced from E_F = -620 mV to -645 mV. By more negative E_F the "mismatch" would start to increase. A steeper Tafel slope (more than 60 mV per decade) would also have reduced the "mismatch".

However, all experience tells that the electrochemical potentials in a system decrease with time (days and weeks) due to build-up of deposits on the surfaces.

Therefore, the main conclusion is that the designed anodes most probably will maintain the stainless steel surface at an electrochemical potential below the critical pitting potential.

This is also the case at 80 °C since the most positive value was found to be -377 mV which is well below -310 mV (SCE).

Close to the carbon steel anodes (100 - 300 mm) the potential on the stainless steel surface was about 50 mV more positive compared to the anodes. At longer distances (600 - 700 mm) this difference increased to 150 mV.

Regarding current output measurements the anode supplied more current than calculated. The max. current output from one anode is calculated to 590 mA. By 10 anodes the supply is calculated to be 150 mA from each anode. Measured value was 282 mA. Taking into consideration the temperature of 7 °C (reduction of 12.5 % from 40 °C) and water level of 0.525 m instead of 0.875 m (reduction of 26 %) the calculated value is: $\dfrac{150 \text{ mA}}{1.125 \times 1.26}$ = 106 mA

The measured initial value (282 mA) is 2.6 times higher than calculated value. This result is not unexpected. The initial current demand is always high. After som time (days) the current demand is expected to decrease due to build-up of deposits.

Following is concluded:

1. Stainless steel of UNS S31603 can be protected against pitting corrosion by carbon steel anodes. The anodes are working.

2. Design based on overvoltage curves, known Tafel slope, current requirements and Faradays law give a design which is found verified by practical potential measurements.

3. Current demand is higher than design value. Most probably the current demand decreases after some weeks and restore anode life time calculation, thereby enabling anodes to protect the tank for 20 - 30 years. If no deposits form and current demand doesn't decrease, some anodes may need to be replaced after 8 years.

4. Protecting stainless steel by carbon steel anodes in this environment is a very cost effective utilization of the inherent material properties of said material combination. Compared to the other maintenance free solution, the Titanium tank, initial cost saving is about NOK 1.7 mill.

5. Retrofitting of anodes is very cheap, quick and no welding offshore is involved.

References

1. Szklarska-Smialowska, Review of Literature on Pitting Corrosion Published since 1960. Corrosion Nace Vol. 27 No. 6 June 1971.

2. Drugli, Bardal. A short duration Test Method for Prediction of Crevice Corrosion Rates on SS. Corrosion Vol. 34 December 1978.

3. Nisanciogles K., An analysis of resistance formular for sacrificial anodes. Material Performance, December 1984.

4. Drugli, Rogne, Valen, Johnsen, Olsen. Corrosion Test Methods for evaluating stainless steel for Well flow applications. Corrosion 90, paper no. 270.

Acknowledgement
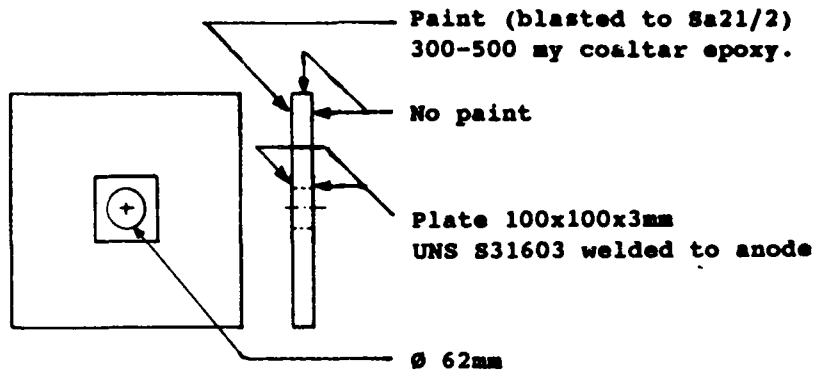
Fig. 1. Carbon steel anode. Size: 350x350x35mm.
Chemical composition: 0.13%C, 0.20%Si, 1.05%Mn, 0.009%P & 0.012%S.
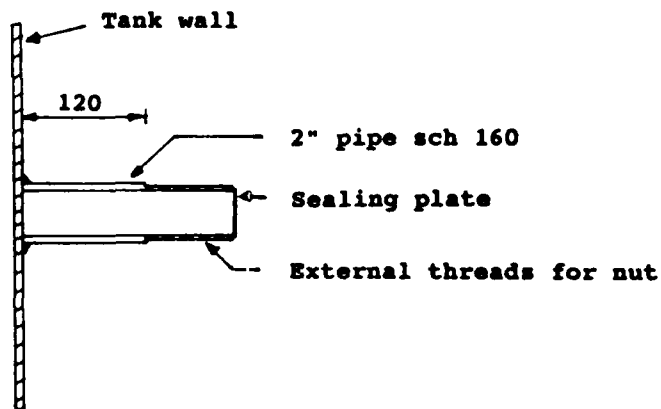
Fig. 2.
Pin for fixing of anode.
All fillet welds: 100% DP
inspected. All UNS S31603.
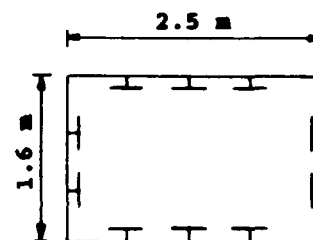
Fig. 3.
Tank bottom seen from above. Anodes
schematically shown. All anodes
placed within 0.5 m from tank-bottom.
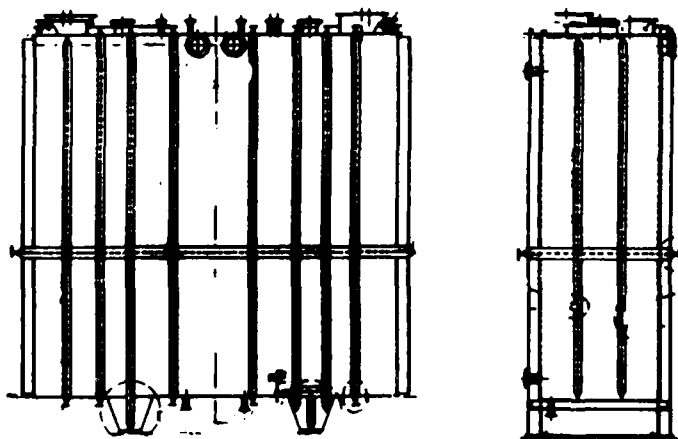
Fig. 4. Tank schematically shown. Size: LxWxH = 5mx1.6mx5m.

Corrosion Prevention on the Iroquois Gas Transmission System by a Reliability Based Design
Philosophy

Tom Hamilton
Iroquois Gas Transmission System L.P.
One Corporate Drive, Suite 606
Shelton CT 06484

Abstract

A reliability based design philosophy used on a newly constructed large diameter high pressure
natural gas pipeline is described.

The design process of the corrosion prevention measures is described, both protective coatings
and cathodic protection systems.

The operation of the cathodic protection system, and its interaction with previously existing
utilities is described, along with strategies implimented to overcome interference situations.

Key words : Corrosion prevention; Cathodic protection; Reliability ; Gas pipeline

Introduction

Reliability of the pipeline system is of paramount importance to the Iroquois Gas Transmission System.(IGTS) The pipe is a new source of energy, serving the Northeast, which is a market where the primary energy source previously was oil. The line is not currently looped, which means that any disruption in the flow of gas can affect customer takes in a relatively short period of time. Since the market conditions are competitive, such disruptions would be capitalized upon in short order by the oil factions. The prospect of insecure supply, in addition to the scare tactics currently being used by the oil dealers, would slow the displacement of the sulfur laden offshore product by the clean domestic alternative!

Having dispensed with the market picture, we turn to the engineering aspects of the reliability based design philosophy. Although not as ripe with opportunities for humor, the basic concepts of continuous access to the product by the customer, and the provision of safety for people living adjacent to the pipeline, remain.

Although all facilities are built using a projected or "design" life, a properly designed, constructed, and maintained pipeline system can operate indefinitely. The depreciation schedules on line pipe do not relate to the expected service life of the pipe in the same way that they do with compression units or valve seats. If the IGTS pipeline is ever temporarily out of service, the last thing that I would expect to be the cause is a failure of the line pipe.

Our committment to top flight reliability began with the design, followed through with the construction, and continues with the operation. The focus of the present paper is on the coatings and cathodic protection of the line. The design philosophy of reliability engineering[1] was utilized in all stages of the implimentation of a corrosion prevention program for the system. Others may present the facilities design considerations or welding and metallurgical concerns at a later date.

The Iroquois Gas Transmission System currently consists of a single pipeline connecting a source of western Canadian gas to U S markets between the St. Lawrence river and Long Island New York. The pipe is 30" (762 mm) diameter for its northern 190 miles,(304 km.) and 24" (609 mm) for its remainder of its 370 miles.(592 km.) No compressor units are installed on the line, the gas free flows from Canada to Long Island. Sales points on the system feed customers along the way. This configuration will evolve with the market, in fact the first compressor station is being built in Wright New York this year.

The line is protected from corrosion by coating with a thin film coating of epoxy. Field joints and valves and fittings are coated with a liquid epoxy urethane. A system of rectifiers and deepwell groundbeds provides cathodic protection. Since the pipeline route includes many miles of collocation with high voltage electric power lines, the corrosion prevention systems are augmented by over one hundred miles of zinc ribbon which was installed in the pipeline trench during construction.

Code Compliance

High pressure gas pipelines are governed by the Code of Federal Regulations Title 49, Part 192.

These requirements represent the minimum mandatory standards for the design, construction and operation of high pressure gas pipelines. We do not believe that following these standards to

the letter would lead to the lowest lifetime cost or highest level of reliability for a pipeline system. In most cases, IGTS standards are significantly in excess of the federal minimums. In others, such as records management, the federal guidelines are followed closely, providing a good chronological record of the pipeline and its cathodic protection system.

Design Considerations

Gas is compressed in Canada from less than 1000 psi (6895 kPa) in the multiple looped mainline system of TransCanada PipeLines, to 1440 psi (9928 kPa), for delivery to the Iroquois pipeline. Coolers downstream of the compression units are used to reduce the temperature of the gas for efficiency and practicality. Serving high compression ratio units, the coolers are beneficial to the longevity of the pipeline coating. Since the coolers may be out of service for a period of time, and gas deliveries would not be curtailed, the worst case operating condition is defined. The pipeline coating must be able to withstand operating temperatures in excess of 160 degrees fahrenheit (70 degrees C) for some indeterminent length of time, as well as the general expectation that the coating should continue to perform its task for the economic life of the asset.

This temperature consideration was the most challenging aspect of the technical design. All compressor stations to be built in the future are to be of the high compression ratio type, which demands that the coatings on the entire line be capable of withstanding the excursion conditions.

The cathodic protection system was designed to hold the polarized potential of the pipeline between -0.850 and -1.100 V vs. copper/copper sulphate ($Cu/CuSO_4$). The line was not looped, and each customer's sales point was isolated from the mainline, so a series of point source current drains spaced equally along the route was determined to be the most economic and effective design to accomplish the objective described above.

Modifying this design somewhat was the non-uniform positioning of zinc ribbon runs, to be installed parallel to the pipe in the same ditch during construction, for High Voltage Alternating Current (HVAC) effects mitigation. One mainline isolation joint was installed, at the landfall in Connecticut, at the start of the 26.3 mile (42 km.) crossing of Long Island Sound. The offshore line is provided with zinc bracelet anodes, spaced at 500 foot (152 m) intervals following conservative offshore guidelines. The 8.9 miles (14.2 km.) on Long Island itself is protected by zinc ribbon.

The sites of two groundbeds were also moved when, during construction, two creeks were crossed by directional drilling, and it seemed opportune to site groundbeds in the immediate vicinity "just in case".

The use of fusion bond epoxy, based on experience with previous pipelines, allows the wide spacing between rectifier/groundbed units to be utilized. Attenuation studies indicated that the thirty mile distance is totally attainable given consistent coating quality. This quality must be obtained both in the coating mills and in the field on joints, valves and fittings.

Coatings

The overall design philosophy centers around the concept that buried facilities are protected from corrosion by groundwater by protective coatings. All of our experience with underground plant indicates that the only significant challenge to corrosion prevention is on facilities where the

coatings are inadequate. This most often occurrs with coatings which have aged, and which have failed to some extent due to soil stress or other failure mechanisms.

Failure of a pipeline coating occurs when, by whatever mechanism, moisture is allowed to contact the steel. The coating can fail during application, if voids are created, during shipping to site or handling at site, if the integrity of the coating is compromised by mechanical damage, and most importantly, during its service life after backfill.

We could be very conscientious of pipe handling during construction, but the longevity of the coating system is directly dependent on the coating choice, fitness for service, and the reaction of the coating to its service environment.

Based on our previous experience with many types of pipeline coatings, and after analysis of the expected operating conditions, thin film epoxy coating was chosen for the line pipe. It was our conclusion that FBE exhibits the best combination of adhesion, film integrity, and resistance to cathodic disbondment, with acceptable toughness and flexibility for practical pipeline use. Appropriate high temperature performance had been demonstrated by FBE, in the lab, and in many field environments, for many operators, giving us confidence that during thermal excursions the coatings would not undergo a significantly accelerated rate of deterioration. Combined with a strict monitoring of the applicators' quality assurance programs in the mills, we felt confidant that we had the best line pipe coating for the intended service. In service, the epoxy products are not known to fail in a manner where they would shield cathodic protection current.

It was a significantly more challenging task to specify a coating for the field joints, valves and fittings. The high operating temperatures are generally not compatible with liquid coatings. We had the option of field applied FBE for the field welds, but needed coatings for valves and fittings as well. We had been looking for years for liquid coatings to be used on weld joints, as repair coatings, and for valves and fittings which could withstand the rigors of field application and cathodic protection at normal operating temperatures. We had subjected all products submitted to an extensive battery of laboratory tests. The cathodic disbond test and the low temperature flexibility testing seemed to be the most challenging. Very few coatings have been found which can pass these tests. Following successful lab testing, the coatings must pass a field trial for ease of application and handling.

Only one coating has been found, to date, which can handle the rigors of pipeline field application and survive in the high temperature environment. This epoxy urethane coating was used extensively on the IGTS line, with great success.

The coating was initially challenging for the contractors to apply in the field and in the fab shops, since most had had minimal previous exposure to such liquid coatings. After a short learning curve however, all six spreads easily attained acceptable production rates, and all left the job feeling that the product was no problem for normal pipelining. This factor cannot be overlooked, since the world's greatest products or application specifications mean nothing if the contractor who actually applies the product has to fight with an impractical situation. The field people are an integral part of the overall system which is to produce a defect free pipeline.

Coating Reliability

Some pipeline companies use coatings incorporating an outer plastic film which provides mechanical protection for the "corrosion coating" underneath. Some of these products are capable of withstanding very high operating temperatures, with the polypropylene serving the extreme high end, and polyethylene serving the range that we were considering. Here, the reliability concept comes into play with respect to coating choice.

No pipeline coating is 100 % void free. Additionally, at some point in each product's service life the coating will begin to fail. As defined above, coatings fail to perform their intended service

when moisture is allowed to come in contact with the substrate. This is the point when the utilization of a thin film coating is superior to a multi-layer coating system in underground service.

When the coating on a pipeline fails, between the day of its backfill and the day of its retirement, the operating company supplies cathodic protection so that the pipe retains its integrity. The thin film coatings generally fail via underfilm migration of moisture from coating holidays, or by through film transport of water. The layered coatings have similar risk of undercut at holidays, but virtually nil chance of through film transport. Unfortunately, when failure occurs with a multilayered plastic system, the task of the operator to supply cathodic protection to the steel surface, or to successfully monitor the effect of the cathodic protection system is at best extremely challenging.

The new pipeline coatings are extremely effective. The current demand of the installed pipe is very low, microamps per running foot on large diameter lines. The challenge with a new pipeline is not provision of sufficient current, but provision of very small amounts of current to the necessary locations.

If a pipe coating begins to fail, the volume of current needed goes up. If a coating fails by water absorption as the old asphalt coatings did,or as our thin film coatings may, the rectifier outputs can be simply increased. The current density has increased, but the current distribution remains essentially the same. A half amp output groundbed can be increased to five amps output quickly and easily should the need arise. If however, the current demands go from fifty micro amps per foot to seventy microamps per foot due to coating undercut, and your pipe to soil survey is not sophisticated enough to indicate the increased need due to shielding, the pipe could be subject a considerable increase in corrosion rate without the operator being aware. Then a corrosion pig is run or random bellhole examination uncovers the unpleasant truth.

If a thin film coating fails, by undercut or by through film water transport, at least I know that the pipe to soil survey will indicate the situation, and that I have the technology to fix the problem. Time will tell if our coating choices are appropriate for the actual operating conditions.

Cathodic Protection

The cathodic protection system consists of a series of eleven rectifier/groundbed units spaced approximately equally along the line. Around thirty miles (48 km.) of pipe is protected by each rectifier. The coating system is so effective that only milliamps of current are required to protect a mile 1.6 km.) of pipe.

In addition, at locations where zinc ribbon has been installed in the pipe trench during construction to mitigate the effects of high voltage AC lines in parallel rights-of-way, and this system aids the provision of cathodic protection to over one hundred miles (160 km.) of line pipe. There were also a few hundred zinc anodes installed in the pipe trench during construction to provide adequate current in areas of rock trench where there was not sufficient soil cover to allow passage of cathodic protection current in surface waters. All sacrificial elements are attached to the pipeline through above ground test lead posts to allow them to be disengaged for polarized potential testing purposes.

The original cathodic protection design, which was based on a soil resistivity survey at approximately one mile (1.6 km.) intervals prior to construction, and theoretical pipe coating performance in forced drainage attenuation calculations, has been validated by field surveys following rectifier commissioning.

The principal field survey was an on/off pipe to soil survey using a spacing of three feet.(one metre) Prior to beginning the survey, the optimum interrupter timing was determined by theoretical calculation (computer modeling), and the predictions confirmed by field measurments after the installation of the groundbeds. [2] This pre survey work assured us of capturing valid data so as to draw the most reliable conclusions from the survey results. With the interrupters set at a one second cycle, one third second off, two thirds on, and using a field data logger capable of storing readings available after any spiking had settled down, we were able to survey between four and eight miles of line pipe per four man crew in a ten to twelve hour day. Up to seven interrupters were used at a time, with four typically being necessary to interrupt the Iroquois supplied current.

A major challenge to data interpretation turned up during the surveys. Telluric currents were especially active during the summer of 1992, and our principally north-south pipeline was heavily influenced. Many of the lows found during the surveys will be investigated further by detail survey before they may be classified as coating defects etc. Even our annual test lead pipe to soil surveys may require potential logging in the future if this situation continues. To determine the effect of earth voltages and separate the effects of DC traction systems in certain areas also becomes challenging.

The pipe to soil results confirmed the original cathodic protection design, identified areas of interference with adjacent utilities, located minor construction related coating damage and some cases of broken zinc ribbon, and identified one area of underprotection where the current from a rectifier did not cross a major river.

Cathodic Protection Criteria

Two criteria are used to assess the propensity for active corrosion. We are totally committed to the scientific basis of each criterion used, and have been encouraged by recent findings on this topic.[3]

The commonly used -0.850 V $Cu/CuSO_4$ is most widely applied. Familiarity with this criterion, and the comfort we all feel when we read something less negative than this on our meters, plus the fact that it is readily achieved on a new pipeline, makes it the most common criterion on our system.

We have many miles of concrete coated (rock jacket, approximately one inch, (25mm) thick) pipe in the southern end of our system. This pipe may be overprotected if polarized to 850 mV. In addition, other pipe, due to its immediate environment, may not readily polarize to that level. In these cases, we institute the use of the 100mV cathodic polarization criterion. We measure this effect by comparing the depolarized pipe to soil potential with the interrupted p/s at the same location.

Because of our dedication to an extended service life for this pipeline system, we have also instituted the use of a threshold polarized potential criterion. By not exceeding -1.100 V we will prevent the formation of hydrogen at the steel surface, and avoid excessive coating disbondment from cathodic protection. Of course, the preservation of our primary corrosion prevention system allows the use of the minimum possible amount of cathodic protection, which extends the life of the overall system as much as possible. This strategy should maximize the reliability of the system.

Although a cathodic protection system consisting totally of sacrificial elements could be argued to be maximally reliable, it is not as effective in the cost benefit analysis. We are trying not only to engineer a reliable system, but to do so in a manner that exhibits responsible economic performance.

Cathodic Protection System Operation

Each of the rectifiers has been outfitted with a data acquisiton and storage unit which continuously monitors the condition of the rectifier. The units can be polled by telephone at will by the corrosion technicians, for instance after an electrical storm to check the condition of the fuses. This ability to record the status of the rectifier and review as needed will confim the continuous operation of the rectifiers, cut down on the number of actual field visits to the units, and provide an accurate record of the time of service interruptions. Using these systems, the availability of the cathodic protection system to the pipeline should approach 100 %.

Pigging

Pigging is, in general, outside the scope of this paper. Reliability of a pigging program is of interest to us. With the advent of higher resolution inspection tools, we have a leg up on the technology of the past. A cost benefit analysis can now be done comparing the relative cost of determining the line's fitness for service using a conventional tool, a higher resolution tool or a very high resolution tool. To achieve an adequate level of confidence in the inspection data, we felt we should do some preliminary work.

Since we have a considerable offshore pipe segment that we know is presently well protected from corrosion, and since the concept of calibration digs is not feasible for this line, we elected to perform a baseline survey of this line segment. All of the magnetic anomalies found during this baseline survey must be due to metallurgical reasons, and not corrosion. Future pig runs should reproduce indications in these original locations. New indications should represent corrosion activity which has taken place since the baseline run. This strategy should provide maximum data reliability and minimize inspection costs.

This is another example of where we have elected to spend money on work in excess of regulated minimums following the belief that it will lead to the lowest long-term cost of operation, and provide maximum system reliability.

Interference

When the pipeline passes through the sphere of influence of an adjacent underground utility's cathodic protection system, or when another's underground plant encroaches on ours, the probability of interference between the two CP systems is very high. When a conductor picks up, due to alternative electrical paths for the direct current, and transmits the CP current from a foreign rectifier, the current must at some point leave that conductor to return to the originating rectifier. This discharge point is the dangerous part of underground interference. The current, leaving the pipeline through a small holiday in the coating can in relatively short order, pit the discharging line. We had already controlled the pickup end of the equation to the best of our ability using coatings with a high insulating value, and now needed to identify and control the discharge points.

To maximize reliability of the Iroquois system, a close pipe to soil survey was carried out immediately after energizing the cathodic protection system. This survey identified areas of interference concern, all as it turned out being caused by adjacent high pressure pipelines.

The coping strategy for these interference problems is to provide a low resistance path for the current to return to the originating pipeline. Usually this is in the form of a string of zinc anodes attached to our pipeline. In this fashion, there is no maintenance associated with a unidirectional bond, nor is there any adverse consequence to the line if either or both CP systems are out of commission for a period of time.

The foreign source of current must simultaneously be interrupted with the Iroquois current so that an accurate representation of the discharge area is obtained, since during operation the area of discharge is affected by a voltage gradient caused by the flow of current back to the "offending" pipeline.

It is planned that time dependent interference from electric railways will also be easily dealt with through the use of low resistance return paths, or some sort of greater shielding at the pick-up areas, so that a fail-safe philosophy can be maintained throughout the system.

Summary

Throughout the design, construction and maintenance of the Iroquois Gas Transmission System, the concept of overall system reliability has been at the forefront. The idea that the system should be, if not foolproof, at least as fool resistant as possible has been on the minds of the entire management team. Regarding corrosion prevention, that meant specifying the best possible coating materials, seeing that they were installed using the best possible techniques, so that the load on the cathodic protection system could be minimized, and the installed CP system could be as simple as possible.

With most of the corrosion prevention done before the pipe is backfilled, the task of maintaining the line, for whatever period of time, becomes a matter of course. Overall, with emphasis on reliability engineering, isolation and failsafe interaction strategies, we have provided a very reliable system.

References

1.) J Justice, "The Role of Reliability Considerations in Design and Operating Strategies" International Conference on Pipieline Reliability, Calgary, June 1992

2.) J Dabkowski, T Hamilton, "A Review of Instant-Off Polarized Potential Measurement Errors", CORROSION /93 Paper No. 561(New Orleans LA : National Association Of Corrosion Engineers, 1993

3.) T Kazmierczak, R Gummow, "Cathodic Protection Criteria - A Literature Survey" Papers selected and reviewed by NACE Task Group T - 10 - 1, 1989

Pitting Corrosion Behaviour of Pipeline Steel in Solutions with Coating Disbonded Area Chemisrty and in Bicarbonate Solutions

X. Liu
Department of Mechanical Engineering
The University of Calgary
2500 University Drive, N.W.
Calgary, Alberta
Canada T2N 1N4

X. Mao
Department of Mechanical Engineering
The University of Calgary
2500 University Drive, N.W.
Calgary, Alberta
Canada T2N 1N4

R. W. Revie
Metals Technology Laboratories, CANMET
Energy, Mines and Resources Canada
568 Booth Street
Ottawa, Ontario
Canada K1A 0G1

Abstract

The corrosion behaviour of Grade 550 (X-80) pipeline steel with coating disbondments was studied in a range of bicarbonate solutions using a potentiodynamic polarization technique. The corrosion morphology of the steel was examined using optical and scanning electron microscopy.

The shape of the polarization curves and the sensitivity of the steel to pitting corrosion were found to vary with bicarbonate concentration. Increase in bicarbonate concentration results in a wider passive region and a more noble breakdown potential, resulting in greater resistance to pitting corrosion. The surface morphology showed no pit formation in solutions with HCO_3^- concentration greater than 0.05 M, but pits did develop at a concentration of 0.05M. With further decrease in HCO_3^- concentration, the size and density of corrosion pits increased. The graph of corrosion potential versus HCO_3^- concentration showed a peak at 0.05M, whereas the corrosion current density increased monotonically with increased bicarbonate concentration.   Low concentrations of chloride ion greatly affect the polarization characteristics and can cause the elimination of passivity in specific solutions.

Key terms: Pipeline steel, pitting corrosion, coating disbondments, bicarbonate concentration

I. Introduction

Recent research [1] has shown that coating disbondments on pipelines in Canada contain solutions with much lower bicarbonate and carbonate concentrations, and hence lower pH, compared with those that have been analyzed on US pipelines. [2] Coating disbondments on pipelines in Canada were found to contain solutions with relatively low concentrations of bicarbonate and chloride ions. The composition of the NS-4 Solution, shown in Table 1, is typical of solution compositions in disbondments on Canadian pipelines. [1] Although much research [2-6] has already been carried out to understand the corrosion and stress-corrosion cracking behaviour of pipeline steel in more concentrated carbonate/bicarbonate solutions, less research has been focused on the corrosion problems of carbon steel in dilute carbonate/bicarbonate solutions in the presence of chloride ion. Since the results of field investigations have indicated that pitting corrosion may, in some cases, be the first step for pipeline fracture in CO_3^{--}/HCO_3^- environment, the research described in this paper was carried out with the following objectives: (1) to establish the effects of bicarbonate concentration on the polarization characteristics and corrosion behaviour of pipeline steel, and (2) to examine the effects of chloride ion on passivation and pitting of pipeline steel in bicarbonate solution.

II. Experimental

The steel samples used in this study were cut from Grade 550 (X-80) linepipe, 914 mm diameter and 10 mm wall thickness. The chemical composition and tensile properties of the steel are presented in Table 2.

The corrosion behaviour of the steel was investigated by potentiodynamic polarization using a PAR/EGG Model 273 potentiostat. The samples were mounted in epoxy and wet-ground with emery paper to a 600 grit finish. The test solutions were NS-4 Solution [1] and sodium bicarbonate solutions varying in concentration from 0.005M to 1M, with corresponding pH values from 8.2 to 9.5. To investigate the effects of chloride ion on pitting corrosion in HCO_3^- solution, sodium chloride was added to the 0.005M sodium bicarbonate solution, to yield sodium chloride concentrations of 0.001M and 0.01M. The test solution was deaerated by bubbling nitrogen gas for 1 hour at a rate of 15 cm³/min before the sample was immersed in the solution. Polarization tests were carried out at room temperature, based on ASTM standard G5-87, with a scan rate of 0.33 mV/s. After each polarization test, the surface condition of the sample was examined using an optical microscope and a scanning electron microscope (SEM).

III. Results and Discussion

A. Effects of Bicarbonate Concentration on Polarization Characteristics

Figures 1A), 1B), and 1C) illustrate polarization curves of the steel in bicarbonate solutions of different concentration. The shape of the polarization curves changes with bicarbonate concentration in terms of the number of anodic peaks. As shown in Figure 1A), in 1M and 0.5M sodium bicarbonate solution, there is one anodic peak, at a potential of about -600 mV (the

primary passive potential, E_p), noble to which the passive region exists. It was observed that a white-grey film formed on the specimen surface when the potential was increased to that corresponding to the anodic current peak.

At lower bicarbonate concentrations, 0.1M and 0.05M, a well-defined second anodic peak appeared, at potentials of about -300 mV, and there was little change in the first anodic peak, as shown in Figure 1B). In bicarbonate solution of further lower concentration, 0.005M and 0.01M, the two anodic peaks overlapped to form a wide and blunt peak, as shown in Figure 1C). Yellow-brown surface films formed in the 0.01M and 0.005M bicarbonate solutions in the potential region immediately above E_p, corresponding to the decrease in anodic current density with increasing potential. The more noble E_p in the solutions of lower concentration, resulted in a narrower passive region.

Since corrosion behavior depends on the tenacity and stability of the protective films on the sample surface, the different passivation behavior of the steel in solutions of different concentrations mentioned above is believed to be the results of change in the protective films.

The relationship of corrosion potential (E_{corr}) with bicarbonate concentration, Figure 2, shows a maximum at 0.05M concentration. On the other hand, the corrosion current density (I_{corr}), measured by the Tafel back extrapolation method, increases monotonically with bicarbonate concentration, as shown in Figure 3. This is most likely attributable to the higher conductivity at the higher concentration. Figure 4 shows the relationship of breakdown potential (E_b) with bicarbonate concentration. At bicarbonate concentrations of 0.05M and lower, E_b is about 820 mV. At bicarbonate concentrations above 0.05M, the breakdown potential increases gradually until it stabilizes at a higher value, about 920 mV. Since lower breakdown potential means lower pitting corrosion resistance, increased sensitivity to pitting corrosion is expected in more dilute bicarbonate solutions.

Figure 5 shows the surface morphology of specimens tested in 1M, 0.5M, 0.1M, 0.05M, 0.01M and 0.005M HCO_3^- solutions. The density and size of corrosion pits increased with decreased bicarbonate concentration. The specimen tested in 0.005M solution showed larger shallow pits about 80 um in diameter and a rather high density. The size and density of pits decreased gradually with increasing bicarbonate concentration, and pits did not form in solutions above a concentration of 0.1M bicarbonate. Low HCO_3^- concentration results in a relatively active pitting potential and larger pits; whereas high HCO_3^- concentration results in a more noble pitting potential, small pits, and a smaller number of pits or no pits.

From both polarization characteristics and surface morphology of the polarized samples, it is clear that the pitting corrosion resistance of the steel decreases with decreased bicarbonate concentration. Pitting corrosion will become an important process in dilute bicarbonate solutions of 0.05M or lower concentration.

B. Effects of chloride ion on pitting corrosion behaviour

Figure 6 shows the polarization curves of carbon steel in NS-4 Solution, 0.005M NaHCO$_3$ and 0.005M NaHCO$_3$ + 0.001M NaCl solutions. As shown, a passive region exists in 0.005M NaHCO$_3$ solution; however, a small amount of chloride ion significantly changed the passivation behaviour. The addition of 0.001M NaCl to the 0.005M NaHCO$_3$ solution completely eliminated the passive region, as shown in Figures 6 and 7. In addition, no passivation was found to exist in NS-4 Solution, containing 0.006M HCO$_3^-$ and 0.004M Cl$^-$. It is clear that chloride ion is harmful to passivation in HCO$_3^-$ solution. Increasing Cl$^-$ concentration from 0.001M to 0.01M in the 0.005M NaHCO$_3$ solution, however, has little influence on the polarization characteristics, as shown in Figure 7.

Figure 8 shows the corrosion morphologies in 0.005M NaHCO$_3$, 0.005M NaHCO$_3$ + 0.001M NaCl, and NS-4 solutions. The corrosion pits are larger in the NaHCO$_3$ solutions with Cl$^-$ than in the chloride-free solution.

The detrimental influence of chloride ion on passivation is believed to result from its catalytic effect on liberating Fe^{3+} from the ferric oxide film, [7] which causes the breakdown potential of the ferric oxide film to be reduced to its Flade potential. [8]

IV. Conclusions

The polarization characteristics and the pitting corrosion behaviour of Grade 550 (X-80) pipeline steel in NS-4 Solution and in bicarbonate solutions with and without Cl$^-$ have been investigated using a potentiodynamic polarization technique. The following conclusions have been reached:

1. The presence of small amounts of chloride ion greatly reduced the passivating tendency of the steel. A passive region did not exist in NS-4 Solution and in the 0.005M NaHCO$_3$ solutions with 0.001M and 0.01M chloride ion, and pitting corrosion is more severe in these solutions than in the chloride-free solutions. Since carbon steel does not show passive behaviour in HCO$_3^-$ solutions in the presence of Cl$^-$, it may be reasoned that the mechanism of stress-corrosion cracking of pipeline steel in NS-4 Solution is not explained by the film rupture, at least not by rupture of a passive film.

2. The shapes of the polarization curves vary with bicarbonate concentration of the solution. At high concentrations, one anodic peak exists, followed by a wide passive regime. In the solutions of intermediate concentration, a well-defined second anodic peak appears at a potential of about -300 mV. In solutions of low concentration, the first and the second anodic peaks overlap to form one wide blunt peak. The different shapes of the polarization curves are attributed mainly to the difference in stability of the FeCO$_3$ film in the different solutions.

3. Lower bicarbonate concentration resulted in higher sensitivity of the steel to pitting corrosion. The steel was immune to pitting corrosion at 0.1M and higher concentration. Pitting occurred in 0.05M bicarbonate solution, and the size and density of corrosion pits

increased with decrease in bicarbonate concentration. These results are consistent with the change of breakdown potential and indicate that pitting corrosion may be an important process in these types of environment.

Acknowledgement

References

1. B. Delanty, J. O'Beirne: Oil & Gas Journal, June 15 (1992), p. 39.
2. R. L. Wenk: Proc. of 5th Symposium on Line Pipe Research, Houston, Texas, (1974) T1.
3. J. M. Sutcliffe, R. R. Fessler, W. K. Boyd, and R. N. Parkins: Corrosion, 28, (1972), p. 313
4. R. W. Revie, and R. R. Ramsingh: Canadian Metallurgical Quarterly, Vol. 22, p. 235.
5. J. Stiksma, and S. A. Bradford: Corrosion, 41 (1985), p. 446.
6. R. N. Parkins, and P. M. Singh: Corrosion, 46 (1990), p. 485.
7. J. G. N. Thomas, T. J. Nurse, and R. Walker: British Corrosion Journal, 5 (1970), p. 87.
8. D. H. Davies and G. T. Burstein: Corrosion, 36 (1980), p. 416.

Table 1. Composition of NS-4 Solution

Compound	NaHCO$_3$	KCl	CaCl$_2$	MgSO$_4$.7H$_2$O
Concentration (g/l)	0.483	0.122	0.137	0.131
(Mole/l)	0.00575	0.00164	0.00123	0.00053

Table 2. Chemical composition (wt.%) and mechanical properties of the steel, Grade 550 (X-80)

C	Si	Mn	P	S	Cu	Ni	Cr	Nb	V	Ti	Al	Y.S.(MPa)	T.S.(MPa)	El(%)
0.06	0.30	1.81	0.006	0.001	0.22	0.20	0.02	0.064	0.039	0.006	0.036	629	740	28.3
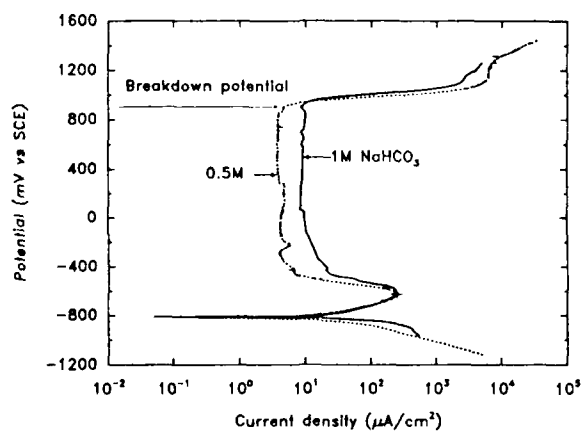
Figure 1A). Polarization curves in 1M and 0.5M bicarbonate solutions.
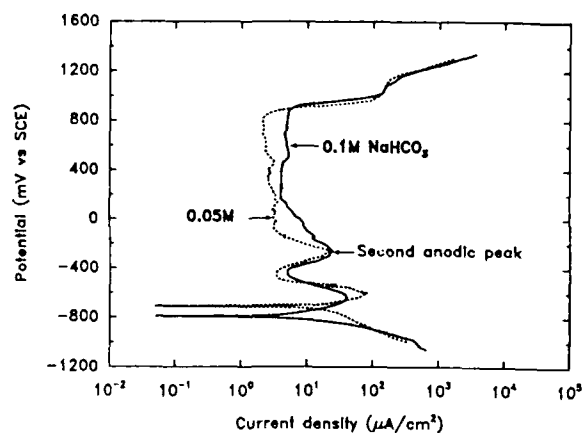
Figure 1B). Polarization curves in 0.1M and 0.05M bicarbonate solutions.
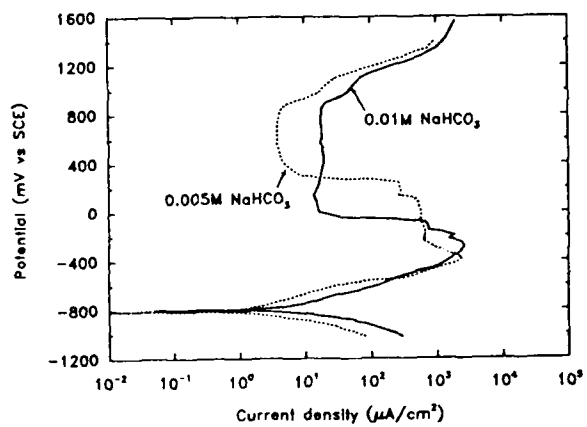
Figure 1C). Polarization curves in 0.01M and 0.005M bicarbonate solutions.
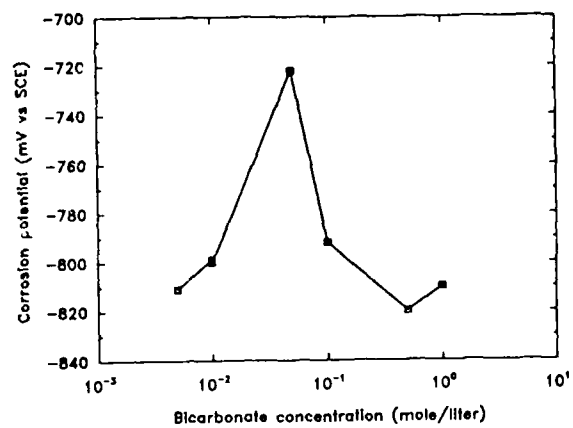
Figure 2. Effects of bicarbonate concentration on corrosion potential.
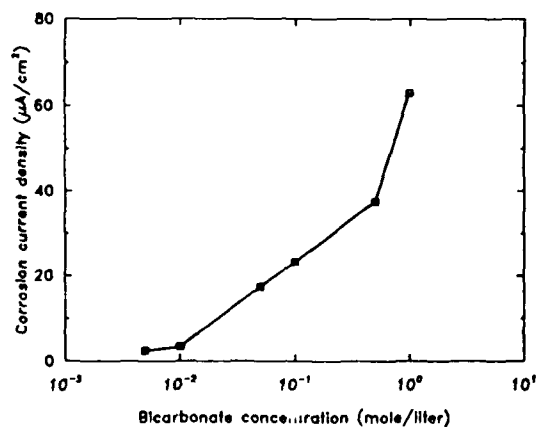
Figure 3. Effects of bicarbonate concentration on corrosion current density.
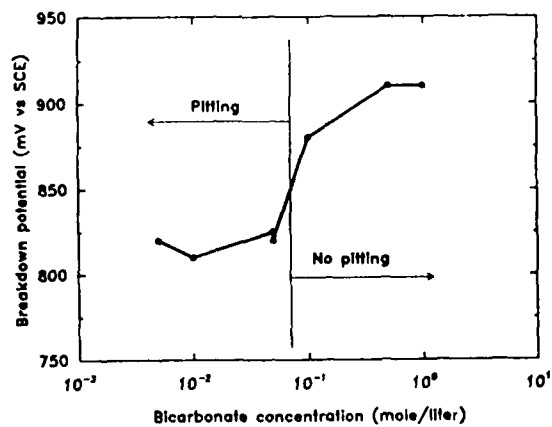
Figure 4. Effects of bicarbonate concentration on breakdown potential.
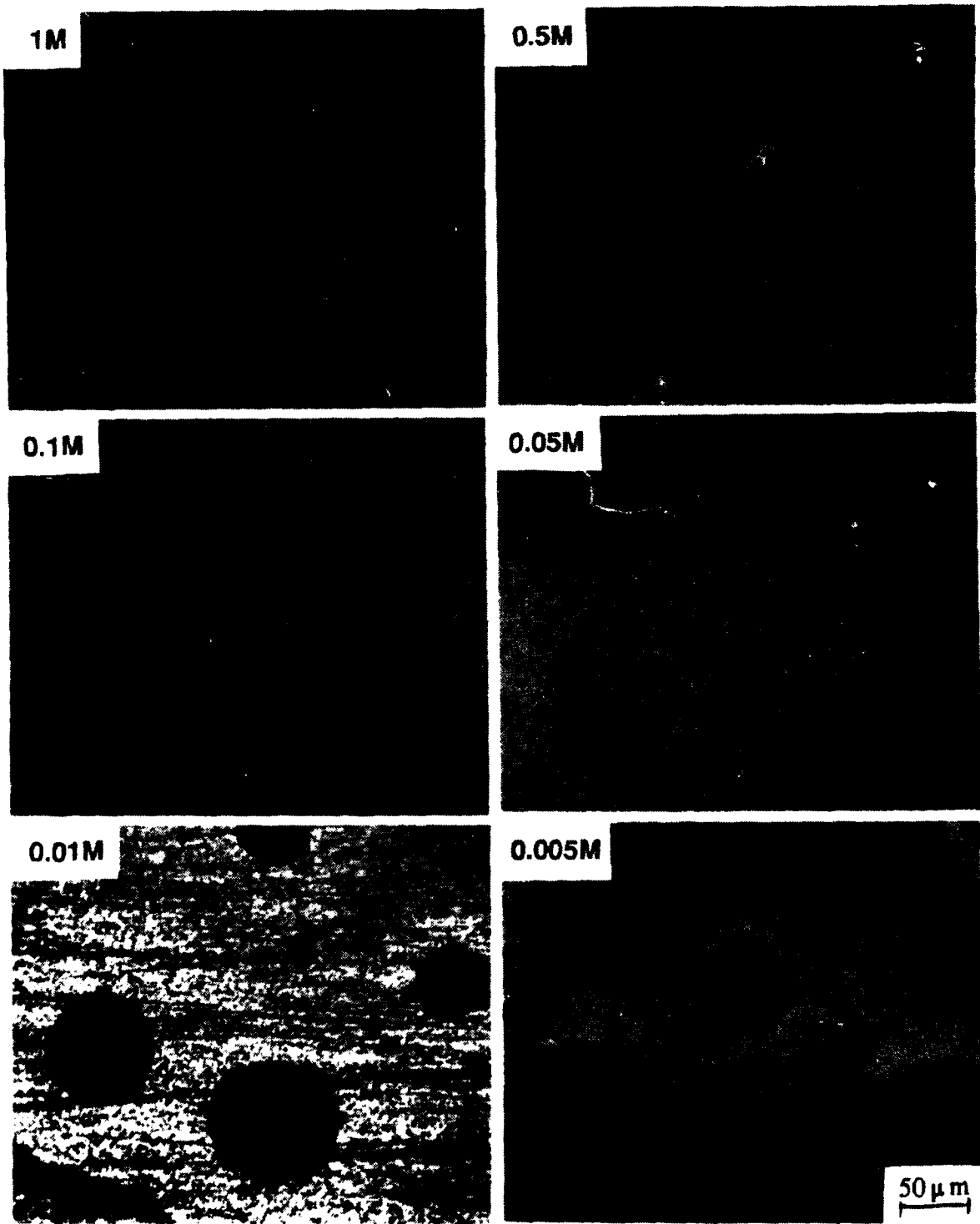
Figure 5. Surface morphology of the specimens tested in bicarbonate solutions.
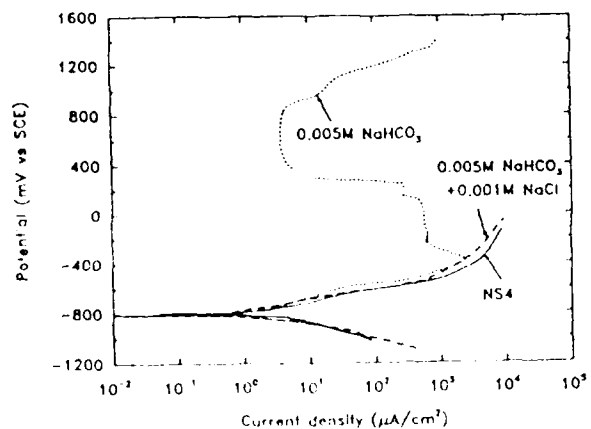
Figure 6. Polarization curves in NS-4 Solution and in 0.005M NaHCO$_3$ solutions with and without Cl$^-$ ions.
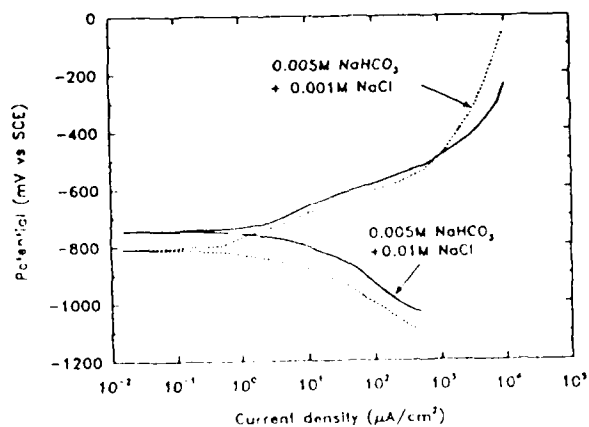
Figure 7. Effects of Cl$^-$ concentration on polarization characteristics.
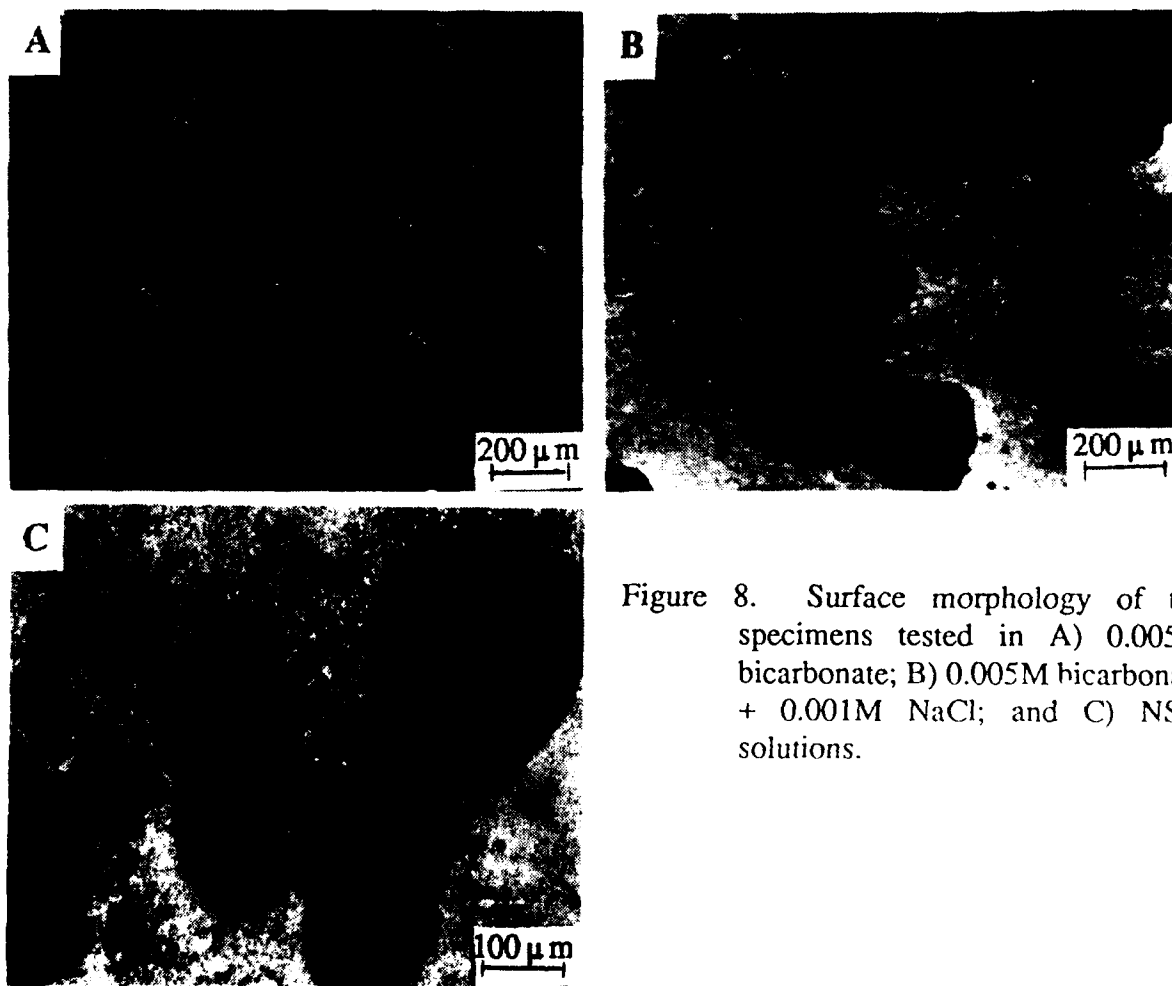
Figure 8. Surface morphology of the specimens tested in A) 0.005M bicarbonate; B) 0.005M bicarbonate + 0.001M NaCl; and C) NS-4 solutions.

The Effect of Microstructure on Corrosion of Linepipe Steels in CO_2-Brine Solution

Brajendra Mishra
Center for Welding and Joining Research
Colorado School of Mines, Golden, CO 80401

David L. Olson
Center for Welding and Joining Research
Colorado School of Mines, Golden, CO 80401

Mamdouh M. Salama
Production Technology
Conoco Inc., Ponca City, OK 74603

Abstract

Dissolved carbon dioxide in water or aqueous solutions is known to cause severe corrosion of linepipe steels used in the oil and natural gas production. CO_2 corrosion in a wet gas pipeline is influenced by pH, temperature, partial pressure of CO_2, oxygen content, H_2S level, flow rate of the solution, solid particles content, surface condition, water chemistry and oil condensate drop out. The microstructure of steel has also been found to affect the corrosion rate because of its impact on the corrosion scale characteristics.

The volume fraction and distribution of various phases have been measured for different heat treatments. A predominantly interface controlled mechanism of corrosion is found to be operative below 60 °C, whereas a diffusion controlled mechanism is dominant above 60°C when a stable carbonate scale is formed. Conditions that promote tight and adherent scale result in lower corrosion rate than conditions that promote the formation of porous and less tenacious scale. The volume and thicknesses of the primary and secondary layers of the carbonate scale are found to be a strong function of the microstructural feature of the steel, particularly those involving ferrite-pearlite type of microstructure. The effect of microstructure diminishes under a transport controlled mechanism.

A predictive model relating the microstructure and composition of the steel with the corrosion rate is being developed on the basis of experimental measurements. The model will be used to suggest proper heat treatment condition for the linepipe steel on the basis of its corrosion behavior.

Key terms: Linepipe steel, heat-treatment, microstructure, carbon dioxide, iron carbonate, aqueous corrosion, pH, CO_2 partial pressure, stability diagram.

I. Introduction

The feasibility of transporting wet, untreated natural gas is becoming an important factor in the development of many gas fields, since the traditional practice of avoiding condensation of an aqueous phase in pipelines by using offshore dehydration of gas prior to its pipeline transport is very costly. The wet corrosive conditions in various linepipe and downhole tube steels in the presence of carbon dioxide present severe problems and operational risk due to the potential of significant internal corrosion since

the associated water and carbon dioxide form weak but corrosive carbonic acid. A knowledge of carbon dioxide corrosion, therefore, is important in determining the reliability of equipment for production, processing, and transportation of hydrocarbon oil and gas. Consequently, a corrosion control program is considered critical to proper operation of wet gas pipelines. For lines operating in annular mist flow regimes, continuous injection of a corrosion inhibitor represents a viable corrosion control system. However, for lines operating in stratified flow, continuous inhibition is not effective because the inhibitor mist is not expected to be stable beyond a point 10-20 pipe diameters from the injection point[1]. Therefore, corrosion may occur at the top of the line due to condensation of an aqueous phase. In such a case, corrosion control can be achieved by batch application of corrosion inhibitors, ensuring full-bore wetting of the internal surface of the pipe. This technique, however, poses several operational problems, such as reliability of inhibitor performance, frequent interruptions of the operation and handling of large slugs of inhibitor[2].

It is critical to the operation of wet gas pipelines to evaluate factors that influence corrosion rate of carbon steel in the presence of CO_2 with particular emphasis on understanding conditions that allow the formation of protective scales. Various attempts to explain the mechanisms involved in CO_2-induced corrosion of steels have been made[3-6]. Regardless of the exact mechanisms involved in corrosion of bare steel, the formation and tenacity of protective scales or passive films are major controlling factors that influence the final corrosion rate. With respect to low alloy-carbon steels, corrosion rates are dominated by chemical or physical stability of precipitation type scales which consist primarily of iron carbonate. Parameters affecting iron carbonate scale formation (dissolution) were found to be temperature, pH, CO_2 partial pressure, brine content, material composition, flow velocity and time. Furthermore, laboratory simulation of the production of iron carbonate type scales is strongly dependent upon experimental conditions such as the surface to volume ratios, surface preparation, testing apparatus, etc. The relationship of CO_2 corrosion to testing parameters and the correlation of these results to in service damage is important to determine, since meaningful laboratory corrosion testing procedures which can evaluate the susceptibility of a given material to corrode under given service conditions are desirable.

Four types of corrosion have been identified in wet CO_2 atmosphere in steels, viz. uniform corrosion, pitting corrosion, stress corrosion cracking and mesa attack. The uniform corrosion of steel in CO_2 containing environments is controlled by the protectiveness of the corrosion product layer and is unaffected by the fluid flow velocity if the scale is not removed.

Significant amount of work has been done to relate the corrosion rate of different grades of steel from the environment side of the application, such as the temperature, solution pH, partial pressure of the gas phases, inhibitor effects, flow condition, solution composition, etc. In this research, an attempt has been made to carry out a fundamental analysis of the corrosion behavior from the material side. A structure-property relationship is being developed which can be used to predict the corrosion rate under a set of conditions by carefully measuring the microstructural features of steel.

A. Factors affecting CO_2-Corrosion

A comprehensive survey of all the important parameters and their effects on the corrosion behavior has been done by Mishra et.al[7]. Various constitutive equations and nomograms relating the corrosion rate and these parameters have been developed and modified over the years[8-14]. These equations, with applied scaling factors, are very useful in predicting the rates and can be used for material selection. Some of the relationships have been industrially used for monitoring the process. The parameters affecting CO_2 corrosion of steel can be divided into two groups: (1) environmental parameters which include temperature, CO_2 partial pressure, pH, flow velocity, contents of oxygen, iron, crude oil, solid particles and hydrogen sulfide in the solution, etc, and (2) metallurgical parameters which include alloy

composition, microstructure, surface roughness, etc.

The equations generally accepted and concerned with the effects of pH, temperature (T) and p_{CO2} and the effect of steel heat-treatment have been discussed by Mishra et. al[15]. The actual measurements made for the corrosion rate shows an agreement within thirty percent of the predicted value.[8]. Simon Thomas et al.[14] have also developed various scaling factors for other parameters, such as the flow rate, hydrocarbon content, glycol and methanol effect, etc., that should be used to calculate a more precise corrosion rate. A spread-sheet computer program has also been developed to predict the corrosion rate with inputs defining the flow parameters, pH, temperature, inhibitor efficiency and gas content, pressure and dew point[14].

B. Corrosion Mechanisms

Studies have been conducted by Schmitt[16], Burke[3], Ogundele and White[4] and DeWaard and Milliams[5] who have explained the salient differences in mechanisms based on the fact that cathodic hydrogen evolution proceeds catalytically by the direct reduction of carbonic acid[5] or through the reduction of HCO_3^- ions[4] with the final corrosion product being iron carbonate after anodic dissolution of iron. The rate of uniform corrosion of bare iron has been reported to be controlled by kinetics of H_2 evolution, which involves the heterogeneous hydration of chemisorbed CO_2 as the rate-determining step[1]. However, if the metal surface is coated with corrosion product layers, mass transfer through this layer can become the limiting factor, which indeed is the reported phenomenon above 60°C temperature.

However, a possibility of the cathodic reaction through reduction of both H_2CO_3 and HCO_3^-, has also been suggested[6]. An extensive research has been carried out to explain the bicarbonate contribution to steel corrosion in carbon dioxide containing environment[17]. The results suggest that the corrosion product is $Fe(HCO_3)_2$ initially, which then forms iron carbonate scale after prolonged exposure. The final scale observed, therefore, consists of iron carbonate only. However, some evidence of bicarbonate in the final scale product has also been found in API X-42 grade of linepipe steel[17].

Iron carbonate is not a very protective film and, thus, corrosion is not stifled. It has been reported that the final iron carbonate scale consists of a primary scale which is thicker than the secondary scale[18] and further explained how cementite platelets (during ferrite phase dissolution) assist in anchoring the iron carbonate scale and improved adhesion. This observation explains why cementite was found in scales on steels after exposure to CO_2 - containing environment, not as a product formed by corrosion process[19]. Also, the role of microstructure in controlling the corrosion behavior becomes evident from this scale behavior. Protectiveness of iron carbonate growing on steel is said to be increasing at 60 °C and above[16]. Above 100 °C, iron oxides (mainly Fe_3O_4) are known to form. Iron carbonate layers grown in conditions below 40 °C and below five bars of carbon dioxide pressure are amorphous and exhibit poor adherence.

C. Heat Treatment

It has been reported that low-alloy carbon steels and hardenable steels are most resistant when quenched and either tempered or double tempered to form martensitic microstructures in the hardness range of HR_C 22 maximum[20]. The microstructure of carbon and low alloy steels are known to influence their corrosion resistance in acid environment, and in CO_2 environment in particular[21]. Furthermore, experiments carried out on API N-80 specimens in conditions, where CO_2 partial pressure of 1.03 MPa and a temperature of 71°C were maintained, revealed two types of scales[18]. The primary iron carbonate scale formed on normalized specimens were thicker, less porous and more tenacious than those formed on quenched and tempered ones. The secondary scale has the same characteristics for both types of heat-treatment. It has

also been mentioned that the thickness of the primary $FeCO_3$ scale is more uniform and the crystals are larger in the normalized steel than for the Q&T steel. This behavior is observed because the pearlite phase in normalized steels is well distributed within the metal matrix. Furthermore, this condition helped to anchor the iron carbonate crystals to the surface when ferrite corrodes leaving the pearlite to form platelets[18]. The results of Palacias[18] and Fincher[20], therefore, are contradictory.

A study[22] found that the corrosion rate of steel in carbonic acid increases significantly with carbon content. The rate was found to be 11.5, 75 and 340 mdd for 0.05, 0.38 and 0.46 wt. pct. carbon steels, respectively, for seven days exposure. Corrosion rate decreased to 12.2 and 32 mdd for 0.38 and 0.46 wt. pct. carbon steels while it increased to 49 mdd for the 0.05 wt. pct. carbon steel after 70 days of exposure. It indicated that corrosion rate of medium and high carbon steels increases with carbon content, which related to higher percentage of carbides formed. It is well known that iron carbide is more cathodic than the ferrite phase. Earlier study[23] found that medium carbon steels were more resistant than the low carbon steels. It was also concluded that steels with pearlite structure corrode slower than similar steels with spheroidized structure. Furthermore, an attempt was made to correlate the ring-worm corrosion at welds and upset tube ends with the structure of carbide caused by heat input[24]. The effect of flow velocity on the corrosion rate of different grades of special steels has been studied by Ikeda et al.[25]. Myasaka[26] has compared the different microstructural effect under CO_2 and H_2S corrosion. Pearlite has been found to enhance the corrosion rate, which is inconsistent with Holmberg's[23] results. The exact role of microstructure in the formation of scales and in the rate of corrosion, therefore, needs to be studied.

As far as the electrochemical principles are concerned, it was established that cementite has a lower overpotential for hydrogen evolution reaction[27], which suggests microgalvanic cells are formed between cementite particles and ferrite matrix which lead to selective attacks at surfaces that are confined to pearlite bands[21].

II. Experimental

Different grades of steel with specific heat-treatments were corrosion tested under fixed conditions of pH, p_{CO2} and temperature. The set of parameters and experiments being conducted include steel grades, such as (a) linepipe steel grades, API X-52 and X-60, (b) downhole tube grade, N-80 and (c) chromium bearing steel [2.25 Cr + 1.0 Mo] under different heat treated condition, such as, thermo-mechanical controlled processed [TMCP], annealed, normalized and quenched and tempered at three temperatures of 350°, 400° and 475°C to vary the amount and morphology of ferrite, pearlite, cementite, martensite, bainite and various carbide phases. This paper includes the results of experiments conducted with API X-52 steel grade only, the chemical composition for which is shown in Table 1.

Experiments have been conducted in three percent sodium chloride synthetic brine solution under pure carbon dioxide atmosphere at 12.5, 50 and 120 psi pressures and at 25°, 38°, 52°, 58°, 65° and 80°C temperatures. The experiments at 50 and 120 psi pressures of CO_2 are being conducted at 52° and 80°C only, whereas, the tests at 12.5 psi pressure have been conducted only up to 65°C temperature. Thus far, a static solution flow condition has been used through out the tests which have been saturated with carbon dioxide at a pressure of 12.5 psi. Four specimens were prepared from each steel condition for weight-loss and microstructural study after 100, 200, 400 and 800 hours of exposure time. Specimens were cleaned and the scale was removed (if precipitated on the surface) with a steel brush, and rinsed with distilled water and acetone before weighing for the loss of weight. The desired temperature was set with only a ± 0.7°C fluctuation throughout the tests. Solution pH varied in the range of 5.2-5.7 during the tests. The calculated pH, using the equation developed by DeWaard & Milliams[8], for the temperature range of 25°-65°C falls between 5.0 and 5.2 which is on the lower end of the measured pH.

38 mm x 38 mm x 4 mm samples were exposed up to 800 hours with a solution to surface ratio of 4.8 ml/mm^2. Specimens were polished to grit # 400 paper and ultrasonically cleaned. The dissolved iron ion concentration of the solution at the end of the experiment was found to be 7 x 10^{-4} g/l.

Corrosion rates were determined by the weight-loss method and the scale morphology has been recorded using the optical metallography. Microstructural analysis has been done with an image-analyzer to measure the phase-volumes.

III. Results and Discussion

Corrosion rates, as weight loss in mg/mm^2, for API X-52 grade of steel under different heat treated conditions and at 25°, 38° and 52° have been shown as best-fit straight lines in Figures 1-3, respectively. The data in Figures 1-3 show that the corrosion rate starts to lose its linear behavior with time after a certain length of exposure for a given heat-treated condition, as indicated by the arrows. The linear behavior is characteristic of an interface controlled corrosion mechanism. As the iron carbonate scale begins to adhere to the steel surface after prolonged exposure, the corrosion mechanism shifts to transport controlled and a parabolic relationship is observed between the corrosion rate and time, indicated by the arrows. The time for the onset of a parabolic behavior is different for different heat-treatments, since the microstructural effect on sacle adherence changes with the heat-treatment. The time required to obtain an adhering scale is also a function of temperature, as is evident from Figures 1-3. The linearity is lost after a longer exposure at 25°C for, e.g. TMCP condition, as indicated by the preliminary results obtained. More data at intermediate times and temperature can provide further insight.

It is evident that the corrosion mechanism is different at 65°C [Figure 4] from the other three temperatures. However, there is a delayed start of approx. 100 hours, since the formation of a stable scale is associated with a time lag. This lag is significantly lower than the linear corrosion range between 25° and 52°C. A distinct parabolic rate is observed at the higher temperature of 65°C, signifying a change to diffusion controlled reaction under all heat-treated conditions. All the heat-treated conditions show an increase in corrosion rate at 52°C. However, the effect of microstructure tends to diminish with an increase in temperature. The lines in Figures 3 and 4 tend to merge as the temperature is increased. This effect is observed due the increasing stability of carbonate scale at higher temperature. Annealed grade of steel shows the lowest rate of corrosion at 38° and 52°C. Microstructures consisting of ferrite and pearlite show a larger variation in corrosion rate at any given environmental condition compared with a martensitic structure. Figure 5 compares the effect of tempering temperature on the corrosion rate of a quenched steel indicating a decrease in the rate with an increase in tempering temperature.

Figure 6 shows an almost linear relationship for the weight loss at 65°C when plotted as a function of the square-root of time. However, the delay-time, t$_1$, is also shown in this plot which is consistent with Figure 4. Since the lines for different heat-treatments do not deviate significantly due to proximity of data-points, it further supports the observation that microstructure is no longer a dominant factor in the corrosion behavior beyond 60°C. Figure 7 shows the region for linear, parabolic and paralinear rates of corrosion as a temperature vs. log[time] plot. As discussed earlier, the time required for a change in the corrosion mechanism from interface control to transport control, i.e. linear to parabolic rates, increases with a decrease in temperature.

Figure 8 shows the plot for log [Corr. rate] as a function of the reciprocal of temperature for different heat treatments as parallel straight lines with an average activation energy of approx. -10.3 kCal, determined by the slopes. Corrosion rates at 65°C have been shown by dotted lines with an approximate slope to indicate the non-linearity of the corrosion rate with time, since the rate controlling mechanism is no longer interfacial. Corrosion rate in mm/year, based on the linear slopes in Figures 1-3, is shown

in Table 2, which indicates that the corrosion rates at 52°C are significantly higher than 25°, or 38°C, essentially due to the predominance of microstructural effect over the temperature effect. However, the quench and tempered microstructures do not show a similar increase due to its martensitic nature. The corrosion rate at 65°C is calculated after 800 hours of exposure and is also listed in Table 2. A stable adherent non-porous carbonate scale is formed beyond 60°C which slows the corrosion down after prolonged exposures. The tenacity of the carbonate film is known to increase with temperature.

Figures 9 and 10 show the optical micrographs of the steel samples. Mixed size, large grains are observed in the as received X-52 steel [Figure 9(a)]. X-52 grade also shows large pearlite colonies with a banded structure. The quenched and tempered X-52 steel [Figure 10] shows small grain size with high volume fraction of tempered martensite. Little change in microstructure is observed by increasing the tempering temperature from 350 to 475°C [Figures 10(a-c)]. Normalizing the X-52 grade [Figure 9(b)] gives a uniform fine grain size with evenly distributed pearlite. Figure 9(c) shows a banded large grained structure upon annealing. Table 3 shows the measured volume fractions of various phases. The variations in size and volume fractions of various phases are responsible for the variation in the corrosion rates observed at any temperature.

The data in Table 3 do not indicate a direct correlation between the phase fractions of ferrite and pearlite and corrosion rate of the as-received, annealed and normalized samples. However, the distribution of pearlite has an effect on the corrosion rate. The pearlite is redistributed in the ferrite matrix as a result of heat treatment while the pearlite has a banded structure in the as-received condition. This ferrite-carbide morphology results in bands of cathodes which increases the dissolution rate of the small anodes (ferrite) that are close to and around the band, rather than a general slower dissolution of ferrite. This dissolution of ferrite grains around the pearlite band (small anodes and large cathodes) could also result in formation of pits which could cause the specimen to lose the pearlite colony itself after complete dissolution of all the ferrite component around it.

It has been demonstrated that structures like bainite are more anodic than a structure consisting of ferrite and pearlite[28]. A bainitic structure is often preferred from the toughness point of view and results from a thermo-mechanical treatment [TMCP]. Therefore, the as-received TMCP steel is likely to corrode faster than in other heat-treated conditions. Another study shows that in a corrosion couple between quenched and tempered N-80 grade and normalized J-55 grade, N-80 preferentially corrodes[29]. Corrosion of ferrite and anchoring of carbonate by cementite is the operative mechanism as a uniform dissolution of normalized structure has been observed in comparison with the uneven scale-matrix interface of as-received steel[15].

A constitutive equation can be developed which will thus relate the corrosion rate and the microstructural features, such as the grain size and volume fraction of ferrite, pearlite, martensite, carbide, etc., once significant data is generated. A direct correlation between the material parameters and the corrosion rate can provide the guidance for selection and design of steel to combat the problem. If constituents of the microstructure play the role of anodic and cathodic sites and control the rate of corrosion, it is logical to conclude that their shape, size and distribution will be directly related to the measured rate at any given set of solution conditions.

IV. Conclusions

Microstructure of steel plays a prominent role in the corrosion of linepipe steels in CO_2-brine environment at temperatures below 60°C. The difference in the rates of corrosion between different heat-treatments become less as the temperature is increased, i.e. role of microstructure diminishes at higher temperatures. Formation of a stable adherent carbonate scale is responsible for increased protectiveness.

Ferrite-pearlite based microstructures show larger effects on the rate of corrosion compared with a quenched and tempered microstructure. The finer the ferrite grain size slower is the rate of corrosion. A non-uniform distribution of phases make the steel susceptible to enhanced corrosion. Rate of corrosion decreases with an increase in tempering temperature for a quenched steel.

V. References

1.   L. van Bodegom, K. van Gelder, J.A.M. Spaninks and M.J.J. Simon Thomas, "Control of CO_2 Corrosion in Wet Gas Lines by Injection of Glycol", Corrosion 88, Paper No. 187, NACE, Houston, TX, (1988).

2.   K. van Gelder, L. van Bodegom and A. Visser, "Inhibition of CO_2 Corrosion of Carbon Steel Pipelines Transporting Wet Gas", Corrosion 87, Paper No. 56, NACE, Houston, TX (1987).

3.   P.A. Burke, "Recent Progress in Understanding of CO_2 Corrosion", Advances in CO_2 Corrosion, Vol. 1, p.3, NACE, Houston, TX, (1985).

4.   G.I. Ogundele and W.E. White, "Some Observations on Corrosion of Carbon Steel in Aqueous Environment Containing CO_2", Corrosion, Vol. 42 (2), p. 71, (1986).

5.   C. deWaard and D.E. Milliams, "Carbonic Acid Corrosion of Steel", Corrosion, Vol. 31 (5), p. 177,(1975).

6.   K. Masamura and I. Matsushima, "Corrosion and Electrochemical Behaviour of Steel in CO_2 Bearing Water", Transaction of the Iron and Steel Institute of Japan, Vol. 23(8), p. 676, (1983).

7.   B. Mishra, D.L. Olson, S. Al-Hassan and M.M. Salama, "Physical Characteristics of Iron Carbonate Scale Formation in Linepipe Steels," CORROSION/92, Paper No. 13, (Houston, TX: NACE, 1992)

8.   C. deWaard, U. Lotz and D.E. Milliams, "Predictive Model for CO_2 Corrosion Engineering in Wet Natural Gas Pipelines," CORROSION/91, Paper No. 577, (Houston, TX: NACE, 1991)

9.   K. Videm and A. Dugstad, "Corrosion of Carbon Steel in an Aqueous Carbon Dioxide Environment: Part 1," Material Performance, Vol. 28(3), p. 63, (1989).

10.   T. Murata, E. Sato and R. Matsuhashi, "Factors Controlling Corrosion of Steels in CO_2 Saturated Environment," Advanced in CO_2 Corrosion, p. 64, NACE, Houston, TX, (1985).

11.   A.K. Dunlop, H.L. Hassell and P.A. Rodes, "Fundamental Considerations in Sweet Gas Well Corrosion," Advances in CO_2 Corrosion, p. 52, NACE, Houston, TX, (1985).

12.   E.C. Greco and W. B. Wright, "Corrosion of Iron in an H_2S-CO_2-H_2O System," Corrosion, Vol. 18, p. 119t, (1962).

13.   C. deWaard and D.E. Milliams, "Prediction of Carbonic Acid Corrosion in Natural Gas Pipelines," BHRA Conference at University of Durham, The Netherlands, Industrial Finishing and Surface Coatings, Vol. 28, p. 24, (1976).

14. M.J.J Simon Thomas, C. deWaard and L.M. Smith, "Controlling Factors in the Rate of CO_2 Corrosion", Shell Internationale Petroleum Maatschappij B.V., UK Corrosion '87, Brighton, England, P. 147, (1987).

15. B. Mishra, D.L. Olson, S. Al-Hassan and M.M. Salama, "Prediction of Microstructural Effect on Corrosion of Linepipe Steels in CO_2-Brine Solution," CORROSION/93, Paper No.90, (Houston, TX: NACE, 1993)

16. G. Schmitt, "Fundamental Aspects of CO_2 Corrosion", Advances in CO_2 Corrosion, P. 10, NACE, Houston, TX, (1985).

17. Z. Xia, K.C. Chou and Z. Szklarska-Smialowska, "Pitting Corrosion of Carbon Steel in CO_2-Containing NaCl Brine", Corrosion, Vol. 45(8), p. 636, (1989).

18. C.P. Palacias and J.R. Shadley, "Characteristics of Corrosion Scale on Steels in a CO_2-Saturated NaCl Brine," Corrosion, Vol. 47(2), P. 122, (1991).

19. B.D. Craig, "The Occurrence of Cementite as a Corrosion Product of Low Temperature [50°C(120°F)] in a Gas Environment," Material Performance, Vol. 16 (2), P. 34, (1977).

20. D.R. Fincher, J.W. Ward and M.R. Chance, "How To Control Corrosion in Sour Gas Pipelines", Pipeline Industry, Vol. 48 No. 6, P. 67, (1978).

21. U. Lotz and T. Sydberger, "CO_2 Corrosion of C. Steel and 13Cr Steel in Particle-Laden Fluid", Corrosion, Vol. 44(11), p. 800, (1988).

22. C.K. Eilerts, F. Greene, F.G. Archer, B. Hanna and L.M. Burman, "Alloying Steels for Corrosion Resistance to Gas-Condensate Fluids: Part 2", Corr., Vol. 4(7), (1948), p. 321.

23. M.E. Holmberg, "Some Metallurgical Observations with Respect to Corrosion in Distillate Wells", Corr., Vol. 2 No. 11, p. 278, (1946).

24. R.W. Manuel,"Effect of Carbide Structure on the Corrosion Resistance of Steel", Corr., Vol. 3 No. 9, 1947, p. 415.

25. J.R. Vera, A. Viloria, M. Castillo, A. Ikeda and M. Ueda, "Flow velocity effect on carbon steel CO_2 corrosion using a dynamic field tester", 1st Pan-American Cong. Corrosion and Protection, 1992.

26. A. Myasaka, Nippon Steel Corp., Private Communication, 1992.

27. H.J. Cleary and N.D. Greene, " Electrochemical Properties of Fe and Steel", Corr. Sci., Vol. 9 No. 1, 1969, p. 3.

28. S. Endo, M. Nagae, S. Fujita and O. Hirano, "Preferential corrosion of weldment of carbon steel in CO_2 containing environment", Matls. Engg.,Volume III-A ASME 1992, 1992 OMAE, p 95, 1992.

29. B.D. Craig,"Practical Oil-Field Metallurgy", PennWell Publishing Co., Oklahoma, p. 110, 1984.

Table 1: Chemical Composition and Properties of API X-52 Grade of Steel

Elements Wt. Pct.	C	Mn	Si	S	P	Nb	YS kg/mm²	UTS kg/mm²	CVN, kg-m -50 °C
	0.14	1.26	0.22	0.002	0.018	0.022	37.5	42.2	54.1

Table 2: Corrosion Rate [mmy] as a Function of Temperature for API X-52 Steel

HEAT TREATMENT	25°C	38°C	52°C	65°C	CONST*, mmy/$P_{CO_2}^{2/3}$ (Eqn.9)
As received [TMCP]	1.58	2.01	2.52	1.81	0.42×10^{15}
Quench & tempered	1.00	1.34	1.76	1.74	0.29×10^{15}
Annealed	---	1.12	1.59	---	0.26×10^{15}
Normalized	1.30	1.91	2.25	1.76	0.37×10^{15}

CORROSION RATE [mm/year]; pCO_2: 12.5 psi;
Test time: 800 hours; pH: 5.2-5.7
Final Fe^{++} Conc.: 7×10^{-4} g/l
* Calculated at T = 52 °C, Q = -10.3 kCal, pH = 5.5 and p_{CO_2} = 0.83 atm.

$$CR = CONST. \cdot [H^+]^{1.3} \cdot P_{CO_2}^{0.7} \cdot e^{-Q/kT} \qquad (7)$$

Table 3: Measurement of Microstructural Parameters

Heat Treatment	Ferrite %	Pearlite %	Retained Austenite	Martensite %	Grain size, μm, α	Grain size, μm, P
As-received	53.02	46.98			7.4	37
Quench & Tempered, 350°C	67.08		4.34	28.58		
Quench & Tempered, 400°C	60.78		2.79	36.43		
Quench & Tempered, 475°C	64.27		2.77	32.96		
Annealed	44.42	55.58			2	20
Normalized	56.65	43.35			6	9
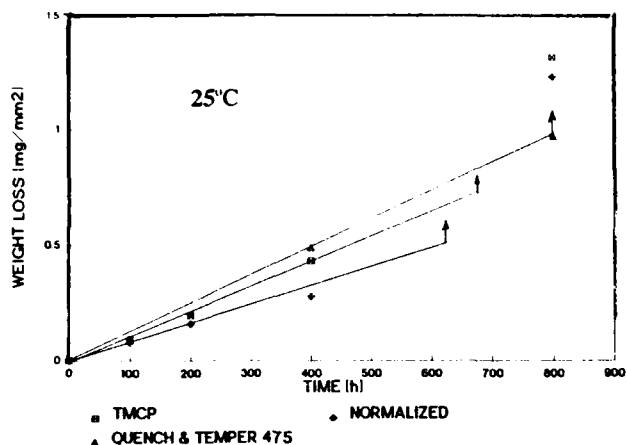
Figure 1: Change in weight as a function of time at 25°C for API X-52 linepipe steel under different heat-treated conditions.
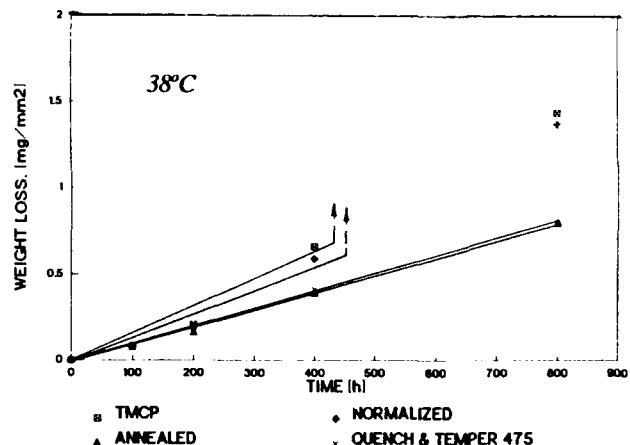
Figure 2: Change in weight as a function of time at 38°C for API X-52 linepipe steel under different heat-treated conditions.
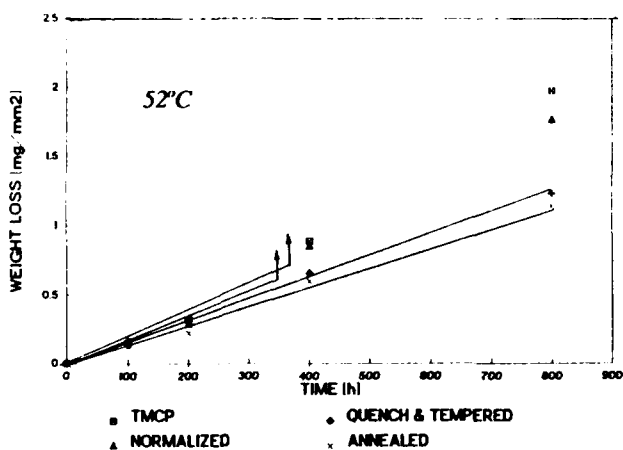
Figure 3: Change in weight as a function of time at 52°C for API X-52 linepipe steel under different heat-treated conditions.
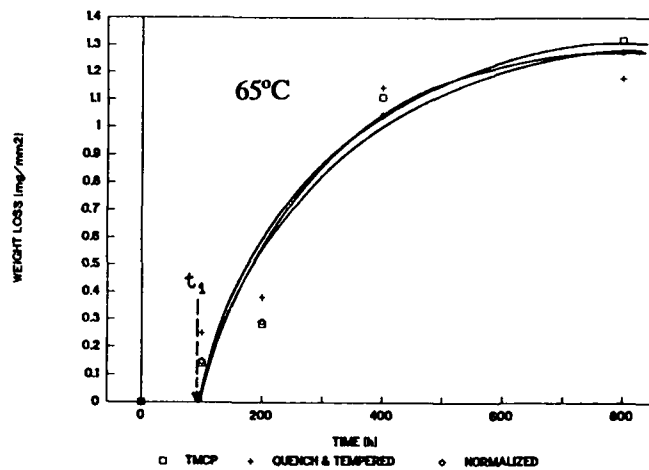
Figure 4: Change in weight as a function of time at 65°C for API X-52 linepipe steel under different heat-treated conditions.
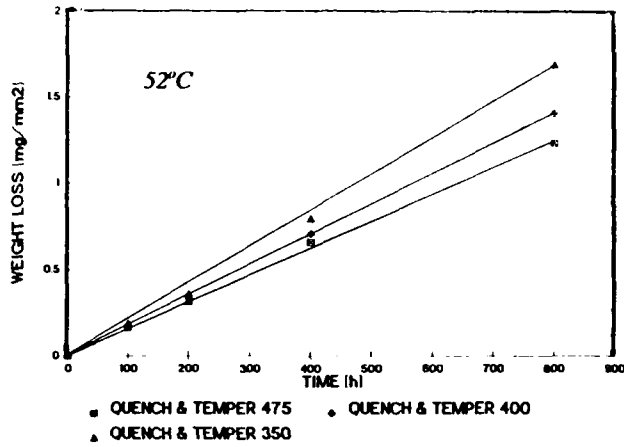
Figure 5: Change in weight as a function of time at 52°C for API X-52 linepipe steel at different tempering temperatures.
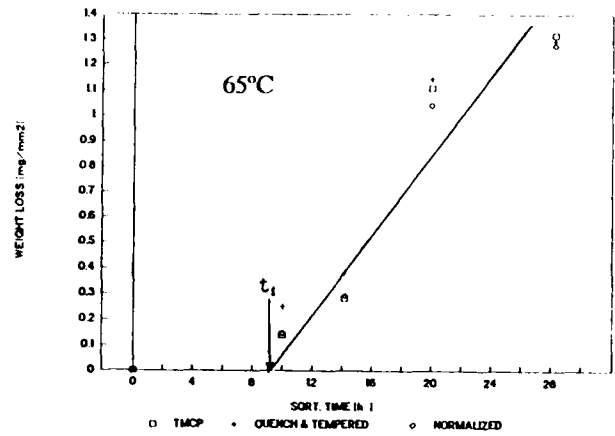
Figure 6: Change in weight as a function of square root of time at 65°C indicating a diffusion controlled corrosion mechanism.
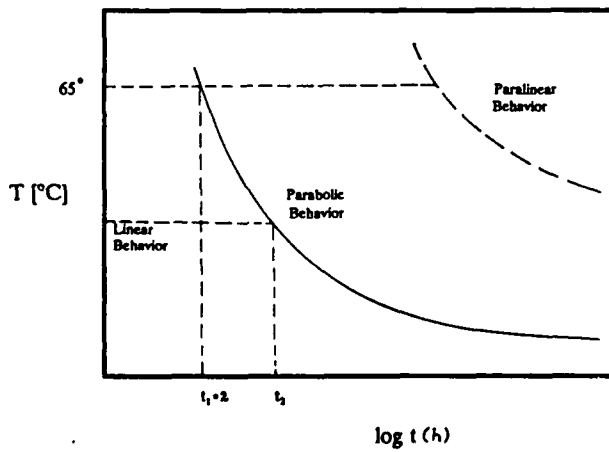
Figure 7: Temperature versus log (time) plot showing the regions of linear and parabolic corrosion rates.
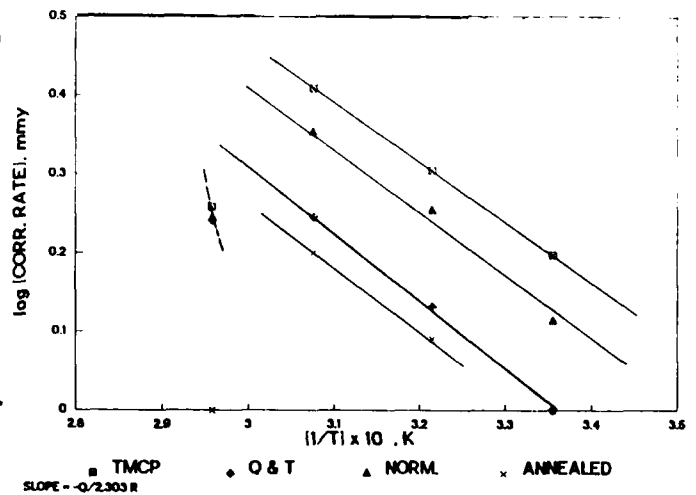
Figure 8: Corrosion rate as a function of the reciprocal of temperature.
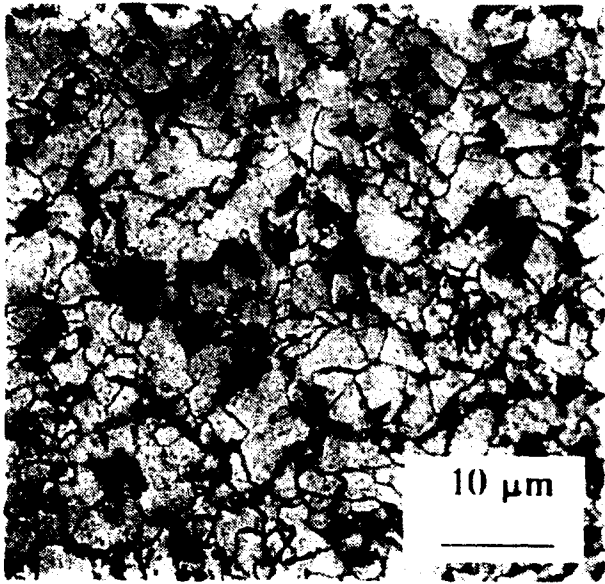
Figure 9(a): Photomicrograph of as-rolled
API X-52 linepipe steel.
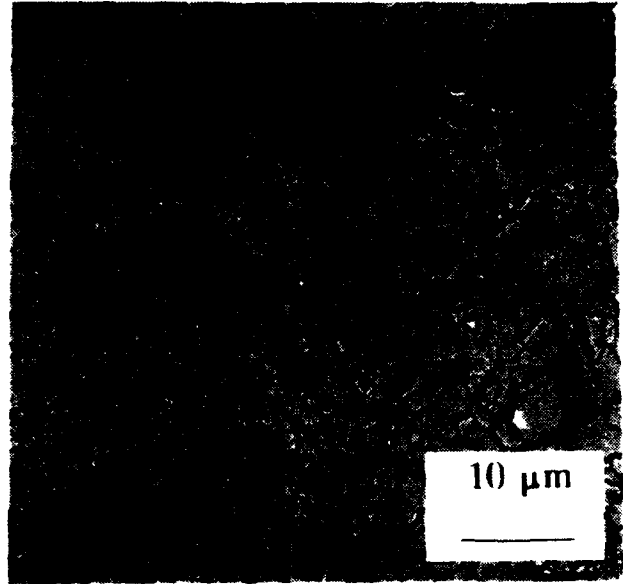
Figure 9(b): Photomicrograph of normalized
API X-52 linepipe steel.
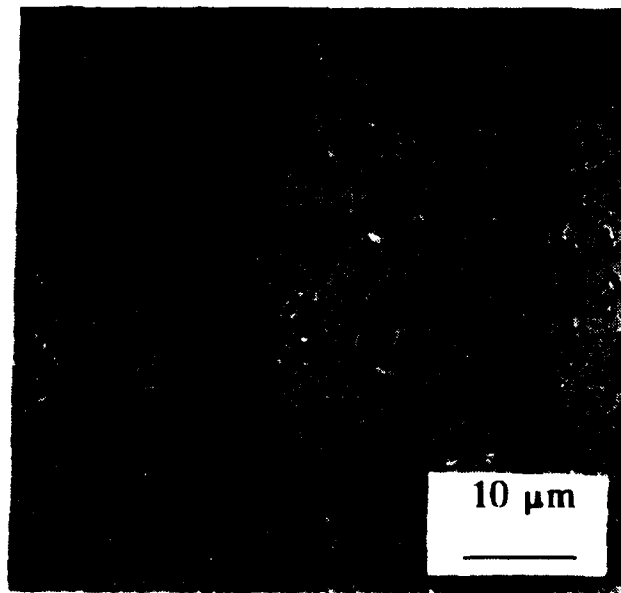
Figure 9(c): Photomicrograph of annealed
API X-52 linepipe steel.
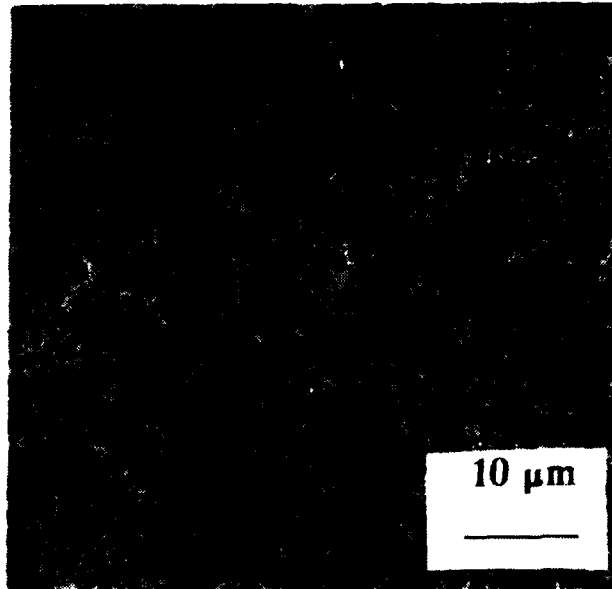
Figure 10(a): Photomicrograph of quenched and tempered [350°C] API X-52 linepipe steel.
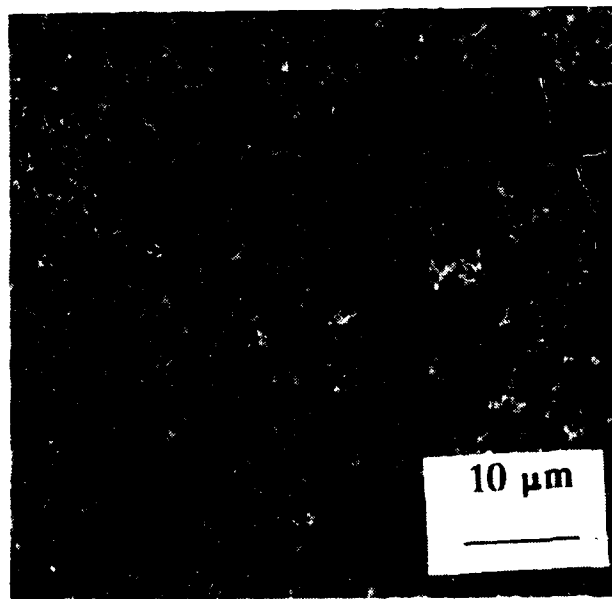
Figure 10(b): Photomicrograph of quenched and tempered [400°C] API X-52 linepipe steel.
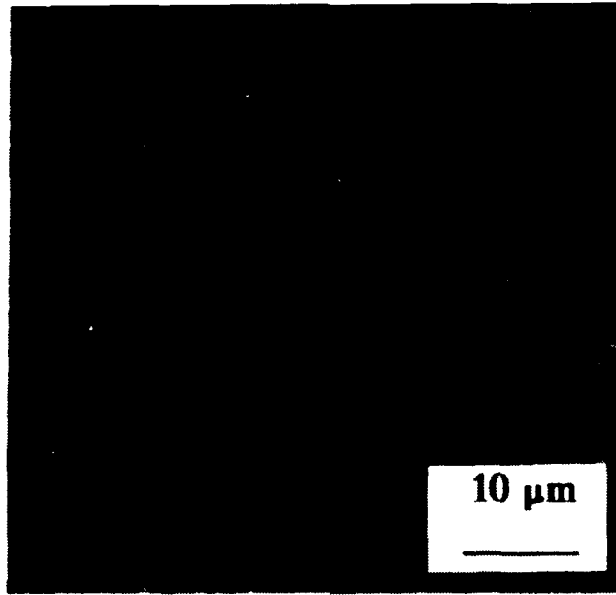
Figure 10(c): Photomicrograph of quenched and tempered [475°C] API X-52 linepipe steel.

The Effects of Latex Additions on Centrifugally Cast Concrete for Internal Pipeline Protection

R.G. Buchheit, T.E. Hinkebein, P.F. Hlava
Sandia National Laboratories
Albuquerque, New Mexico 87185

D.G. Melton
LaQue Center for Corrosion Technology, Inc.
Wrightsville Beach, North Carolina 28480

Abstract

Centrifugally-cast concrete liners applied to the interiors of plain steel pipe sections were tested for corrosion performance in brine solutions. An American Petroleum Institute (API) standard concrete, with and without additions of a styrene-butadiene copolymer latex, was subjected to simulated service and laboratory tests. Simulated service tests used a mechanically pumped test manifold containing sections of concrete-lined pipe. Linear polarization probes embedded at steel-concrete interfaces tracked corrosion rates of these samples as a function of exposure time. Laboratory tests used electrochemical impedance spectroscopy to study corrosion occurring at the steel-concrete interfaces. Electron probe microanalysis (EPMA) determined ingress and distribution of damaging species, such as Cl, in concrete liners periodically returned from the field. Observations of concrete-liner fabrication indicate that latex loading levels were difficult to control in the centrifugal-casting process. Overall, test results indicate that latex additions do not impart significant improvements to the performance of centrifugally cast liners and may even be detrimental. Corrosion at steel-concrete interfaces appears to be localized and the area fraction of corroding interfaces can be greater in latex-modified concretes than in API baseline material. EPMA shows higher interfacial Cl concentration in the latex-modified concretes than in the API standard due to rapid brine transport through cracks to the steel surface.

Key terms: concrete, corrosion, concrete lined steel pipe, electrochemical impedance spectroscopy.

Introduction

The U.S. Strategic Petroleum Reserve (SPR) stores upwards of 500 million barrels of crude oil in caverns formed in naturally occurring underground salt domes situated along the Gulf Coast of Louisiana and Texas. The majority of these storage caverns have been formed by a solution mining process that uses low salinity water, usually from a nearby intracoastal source. This water is injected into the dome in a controlled fashion, dissolving away the salt to form a storage cavern with the desired dimensions. This solution mining process generates large quantities of brine that is transported through 0.91 to 1.07 m (36 to 42 in.) diameter steel pipelines to diffusers located in the Gulf of Mexico, or to disposal wells in sandy, porous formations near the storage site. At sites where solution mining has been completed, the brine disposal pipelines must be used on a periodic basis to accommodate normal site activities. Currently, the SPR operates approximately 65 miles of these brine disposal pipelines[1].

Over the 15 year history of the SPR, the brine disposal pipelines have, in certain instances, experienced aggressive erosion and corrosion damage. To combat erosion and corrosion damage, internal cement linings on the steel pipe are being considered as a replacement strategy to offer extended service life and lower pipeline maintenance costs. Concrete liners are expected to provide a buffer against erosion damage and provide corrosion protection by passivation of the steel in the high pH cement paste.

Latex additions to concrete are reported to improve concrete properties important in the SPR application including durability, adhesive properties, resistance to chloride ingress, shear bond strength, and tensile strength[2]. Because of the potential for improvements in concrete properties, latex modified concretes are candidate liner materials.

Currently, the performance of a variety of industrial standard and experimental concrete compositions for use in SPR brine disposal pipelines are being explored. In this paper, interim results are reported from on-going studies involving an American Petroleum Institute (API) standard cement consisting of 60% high sulfate resistance Portland Cement with 40% silica fume fly ash and this API standard concrete modified by additions of a styrene-butadiene copolymer latex emulsion. The performance of these concrete liners has been evaluated in a testing manifold using actual brine generated at an SPR site. Additional specimens have been subjected to SPR brine under non-flowing conditions, and have been returned to the laboratory at regular intervals to analyze brine penetration and concrete deterioration as a function of exposure time. Laboratory scale specimens have also been constructed so that the concrete liners can be evaluated using electrochemical impedance spectroscopy.

Experimental Procedures

Materials and Specimen Preparation. Concrete lined steel pipe specimens were prepared using commercially available materials. Plain carbon steel pipe sections 5.8 to 6.8 m (19 to 22 ft) in length with a 76 mm (3 inch) inner diameter were prepared for lining by sandblasting the pipe interior. The baseline concrete mixture consisted of 60% (by weight) API Class C (0% C3A) high sulfate resistance Portland cement, and 40% API Class F (<10% CaO, 5 -10% C) fly ash[2]. Latex additions of 5%, 10%, and 15% by weight were made by adding a styrene-butadiene copolymer emulsified in water to the concrete mix prior to application in pipe sections. The emulsion contained approximately 50% solids by weight. Table 1 lists the amounts of the above ingredients used to make the baseline and latex modified concretes.

The concrete lined pipe was fabricated at Permian Enterprises, Odessa, TX using their standard centrifugal casting production methods. The concretes were prepared in a mixing bin then pumped through a delivery lance into the pipe section to be lined. For the latex modified concretes, the emulsion was added directly to the mixing bin without any other alterations in the standard fabrication process. The pipe section was capped at one end and the concrete was pumped at a predetermined rate through the lance as it was withdrawn. After charging the pipe section, the remaining end of the pipe was capped and the section was loaded onto rollers for the spinning operation. Pipe sections were spun at speeds ranging from 12.7 m/s (2500 ft/min) to 14.2 m/s (2800 ft/min) for 1.5 to 4 minutes generating forces in excess of 20 g. After spinning, the pipe section was removed from the rollers, the ends were uncapped and excess water and latex were drained from the pipe. The fact that latex was observed in the run-off when pipe sections were drained indicated that not all the latex was retained in the liner. Pipe section ends were then recapped and kiln cured at 65° C for approximately 18 hours. Full details of the centrifugal casting process can be found in reference 4.

Liner thicknesses and densities are listed in Table 1. Densities were determined using a high precision balance to determine mass, and gas pyncnometry to determine volume. The densities for the latex modified concretes are lower than the baseline concrete indicating that latex was incorporated into the liner. However, the densities for all three latex loading levels were nearly identical suggesting that the amount of latex retained after centrifugal casting was similar. In spite of this apparent similarity, the latex modified concretes performed quite differently in corrosion experiments and are referred to according to their intended loading levels (5%, 10%, and 15%) throughout the remainder of the text.

On-site Simulated Service Testing. A scaled test system was constructed at the Big Hill SPR Site in Winnie, TX. This test was performed to measure the concrete liner durability and pipe corrosion rate using actual brine generated from normal site operations. The advantages of this test was that real service environments were encountered, and test results were quickly interpreted. The primary disadvantages were that brine concentrations varied during the test period compromising experimental control, and the emergence of performance trends was slow since this was not an accelerated test.

Concrete lined test pipes were placed into a manifold through which site brine was mechanically pumped. Brine was withdrawn from a settling ponds, pumped through the system and deposited back into the settling pond at a distance removed from the system intake (approximately 20 m). The flow rate through the 5.0 cm (2 in.) inner diameter piping used in the manifold was selected to generate a pipe wall shear stress equal to that of a 0.91 m (36 in.) pipe carrying brine flowing at 2.36 m/s (7.75 ft/s). Corrosion rates were measured using a linear polarization probes fitted into diametrically opposing ports in the pipe section prior to the concrete lining operation. Instantaneous corrosion rate measurements were made by determining the polarization resistance using a 10 mV voltage perturbation about the free corrosion potential. Corrosion rates were determined from the polarization resistance using the Stearn-Geary equation[5] assuming a value of 25 mV for B where $B = \beta_a \beta_c / 2.3(\beta_a + \beta_c)$, with β_a and β_c representing the anodic and cathodic Tafel slopes. The appropriateness of the linear polarization method for these tests is discussed in the 'Results' section.

Electrochemical Impedance Spectroscopy (EIS). To supplement on-site testing, laboratory-based EIS was performed on cells constructed from concrete lined pipe sections. Test specimens, 100 mm in length, were cut from pipe sections and sealed with rigid plastic at one end. Specimens were placed on end and filled with air sparged saturated solution consisting of 300 g/l NaCl, 4.0 g/l CaSO$_4$, and 1.0 g/l MgCl$_2$, which approximated saturated SPR brine[6]. Air sparging kept the dissolved oxygen concentration constant near its saturation value of 2 ppm[6], while the use of a saturated solution insured that composition variations were minimized during the lengthy tests.

EIS experiments were made using a two electrode measurement, where the working electrode was the steel pipe and the counter electrode was a cylindrical nichrome mesh inserted into the cell symmetrically about the pipe centerline. The EIS measurement systems consisted of either a PAR 273 potentiostat/Solartron 1250 frequency response analyzer (FRA) combination, or a Solartron 1286 electrochemical interface/1255 FRA combination. Each system was controlled by Scribner Associates' Z plot impedance software package installed on an IBM personal computer. Typically, measurements were made at frequencies ranging from 65 kHz to 1 mHz by sampling at 10 points per decade frequency using a 20 mV sinusoidal voltage perturbation. At any frequency, the measured current was integrated to minimize the effects of spurious components to the signal. EIS

measurements were made at weekly intervals for the first 4 weeks, biweekly from 4 to 24 weeks, and monthly thereafter.

Electron Probe Microanalysis (EPMA). EPMA of the concrete liners was used to track ingress of brine and degradation of the cement liners as a function of exposure time. Specimens were exposed at the Big Hill SPR site and returned to the laboratory for analysis at regular intervals. Sections of liners were removed, potted in epoxy and polished with successively finer papers and diamond pastes until the surface was sufficiently smooth for X-ray microanalysis. X-ray linescans were performed using a JEOL 8600 electron microprobe. Analyses were conducted by stepping the beam in 50 μm increments from the steel-concrete interface to the concrete-brine interface. Quantitative wavelength dispersive X-ray data were generated using a 25 nA beam at an accelerating voltage of 15 keV. The data were corrected for fluorescence, atomic absorption, and atomic number using the Bence-Albee technique. All of the major elements in the system were measured, although the focus in this paper is on the distribution of Cl.

Results and Discussion

On-site Simulated Service Testing. Table 2 lists maximum corrosion rates detected at the steel-concrete interface over 314 days of test manifold operation. The steady state corrosion rate for bare steel in the test manifold is listed for comparison. No corrosion was detected at the linear polarization probes in the baseline concrete. Some indication for corrosion was found for the latex modified concretes, however. Overall, these values were small compared to the steady state corrosion rate determined for the bare steel control. The data in Table 2 were calculated using a B value of 25 mV, and were not corrected for iR drop occurring in the concrete. Accepted values for B are 26 mV for corroding steel, and 52 mV for passive steel[7], hence the value used here is comparatively low. Additionally, visual inspection of samples returned from the site showed that corrosion at the steel-concrete interface was localized. For these reasons, these data are taken only to indicate that concrete liners impart significant corrosion protection compared to unprotected steel, and to indicate the relative presence or absence of corrosion among the concrete lined specimens.

EIS. A complex plane plot representative of the response for both the baseline and latex modified concrete liners is shown in Figure 1. The inset shows the small arc or 'spur' observed at high frequencies. The low frequency arc was semicircular and depressed with respect to the real axis. The high frequency arc was not always fully resolved, but also appeared to be a depressed semicircle. Both arcs were consistently observed throughout the duration of the exposure period for both the baseline and latex modified concretes. The time constant for the high frequency arc was typically in the range of 10^{-3} to 10^{-4} s, while that for the low frequency arc was usually between 300 and 1000 s. The impedance response of these systems was interpreted using the equivalent circuit model (Figure 2a) developed by Macdonald[8] for corrosion of rebar in chloride-contaminated concrete. In this model, two parallel subcircuits are used to represent corroding and passivated regions of the steel cement interface. These parallel subcircuits are arranged in series with a concrete resistance, R_c. The subcircuit for the passivated area of the interface is comprised of a capacitance, C_{pa}, in parallel with a charge transfer resistance R_{pa}. The subcircuit for the corroding area of the interface is comprised of a capacitance, C_{ca}, in parallel with a charge transfer resistance, R_{ca}, and a diffusional impedance, Z_w. A_{pa} and A_{ca} in Figure 2a denote the passivated area fraction and the corroding area fraction respectively. Inspection of specimens returned from the field showed that corrosion at

the steel-concrete interface was localized, indicating that this model was physically realistic for the present situation.

For complex nonlinear least squares (CNLS) fitting of the low frequency arc, a more generalized form of the model in Figure 2a was adopted. In the modified equivalent circuit shown in Figure 2b, the low frequency arc was modeled using a resistor in parallel with a constant phase element (CPE); a combination otherwise known as the ZARC impedance function[8]. As shown in Figures 3a and b, this equivalent circuit was capable of accurately fitting spectra from baseline and latex modified concrete lined pipe specimens. Good fits were regularly obtained even for long exposure times. The ZARC function is often used to model depressed arcs in the complex plane, so the level of agreement between the model and the data in Figures 3a and b is not surprising. The high frequency arc was not always fully resolved, and fitting was not performed. The Z' intercept of the low-frequency side of the arc was used for estimating R_{pa}.

The generalized model was used to reflect the fact that charge transfer and diffusional impedances were not clearly distinguished in the impedance response of these systems. Use of the ZARC function is appropriate for modeling systems where the relaxation time is not single valued but distributed about some mean value[9]. In concretes, the conductive pathways are the paste (Portland plus water), and shrinkage cracks filled with intruding brine. A multitude of these pathways exist in the liner with similar, though not identical relaxation times. Additionally, this and previous studies[10] suggest that the mean time constant for diffusional processes in the concrete, and the time constant due to charge transfer at a corroding steel-concrete interface are similar. Separating out the diffusional impedance is further complicated by the fact that good mass transport data are not readily available for concretes of the type under study here. The ZARC function used in the CNLS fitting allowed a lumped quantity, R_{ca}, to be determined without having to distinguish between diffusion and charge transfer components.

Figure 4 shows the measured charge transfer resistance associated with the passivated interface, $R_{pa}{}^m$, as a function of exposure time for the baseline and latex modified concretes. The measured resistance is given by:

$$R_{pa}{}^m = \rho_{pa}{}^o / A_{pa} \qquad \text{(eq. 1)}$$

where $\rho_{pa}{}^o$ is the area specific resistivity of the passive interface and, A_{pa} is the interfacial area. This equation illustrates the inverse relationship between the measured resistance and the passive interface area. Assuming $\rho_{pa}{}^o$ is similar for each type of concrete, Figure 5 indicates that the baseline material exhibits the largest passive interfacial area for exposure times up to 100 days. After this time, $R_{pa}{}^m$ for the 5% latex concrete appears to fall, suggesting that corroding interface is passivated. The 10% and 15% latex modified concretes exhibit high $R_{pa}{}^m$ presumably indicating smaller passive interface areas.

Figure 5 shows the charge transfer resistance of corroding areas as a function of exposure time. These data are highly scattered, but the general trend appears to be that largest R_{ca} values are exhibited for the latex modified concretes. The R_{ca} value plotted in Figure 5 includes a contribution due to diffusional impedance, Z_w, and evaluation of these data by the method used above is not believed to be valid due to intrinsic variations in Z_w caused by the latex additions.

EPMA. Figure 6a is a plot of chloride concentration as a function of position in the 5% latex modified concrete liner after 60 days exposure to brine at the SPR. This plot illustrates how brine is transported and partitioned in the concrete. The predominant feature of this plot is the high Cl concentration near the concrete-brine interface due to penetration of the brine through the paste. Away from this large Cl spike, smaller spikes are observed. These are due to shrinkage cracks in the concrete liner that filled with brine during exposure. These cracks appear to deliver brine to the steel-concrete interface because the Cl levels there are clearly elevated. Elevated Cl levels at the steel cement interface were observed after 30 days exposure to SPR site brine indicating that transport of brine through cracks is relatively rapid.

Figure 6b shows the chloride profile measured in the baseline concrete after 60 days exposure. Compared to Figure 6a, Cl accumulation at the interface is considerably less. Table 3 shows peak Cl concentrations measured within 0.5 mm of the steel-concrete interface for the baseline and latex modified concretes. Chloride concentrations in excess of 0.1 w/o were regularly detected for the latex modified concretes, but were not detected for the baseline concrete. The variation in the measured peak Cl level in the latex modified concretes suggests that chloride did not accumulate in a uniform way at the interface. It is likely that cracks allowed rapid transport of brine to the steel surface where it then diffused along the interfacial region. Local regions high in chloride were then created at the base of cracks.

The absence of high interfacial chloride concentrations for the baseline concrete is noteworthy. It is possible that a chloride rich region has not yet been encountered in a baseline concrete sample prepared for EPMA. However, the low interfacial chloride concentrations of the baseline concrete are consistent with EIS data that indicated that large passive interfacial areas were sustained during exposure.

It is possible that latex additions interfere with the concrete's ability to provide corrosion protection for the steel. Latex in the paste may inhibit mobility of cement forming calcium species thereby suppressing self healing of cracks. These open cracks may, in turn, be responsible for the elevated Cl concentrations detected at the steel-concrete interface for the latex modified cements. Reduced mobility of Ca-species at the interface may also inhibit the chemical passivation of the steel since the high pH in the paste may not be maintained over time.

The position of the Cl "front" as a function of exposure time is plotted in Figure 7 as a measure of brine ingress through the paste. Contrary to expectations, brine penetrated further into the latex modified concrete than in the baseline concrete. These data also suggest that the penetration rate for both types of concrete in the first 30 days is much greater subsequent rates.

Summary

Latex modified concrete liners can be prepared using standard centrifugal lining procedures, however it is not clear that latex loading levels can be accurately controlled. Although latex modified concretes have been used successfully in other applications, corrosion test results obtained for these centrifugally cast latex modified concretes do not show a performance improvement over the API standard material. EIS results indicate that the amount of passivated area at the steel concrete interface can be lower when latex is added to the cement mix. EPMA results show that higher Cl concentrations exist at the steel-concrete interface for latex modified concretes. This observation may be traceable to inhibition of crack self healing in the latex bearing concretes. These cracks provide a path for rapid transport of brine to the steel-concrete interface, and may cause locally high

concentrations of Cl in the vicinity of the crack base. Locally high Cl concentrations may result in localization of corrosion damage.

Acknowledgments

References

1. W.J. Smollen, personal communication, February, 1992.

2. S.H. Kosmatka, W.C. Panarese, Design and Control of Concrete Mixtures, (Skokie, IL: Portland Cement Association, 1988), p. 194.

3. S.H. Kosmatka, W.C. Panarese, Design and Control of Concrete Mixtures, (Skokie, IL: Portland Cement Association, 1988), p. 68.

4. B. Jackson, J.F. Armstrong, Materials Performance, 29 2 (1990), p. 36.

5. M. Stearn, A.L. Geary, Journal of the Electrochemical Society, 104 (1957), p. 56.

6. Daily Meter Reading Data Sheets, Big Hill SPR site, Winnie, TX, 1990-1991.

7. C. Andrade, V. Castelo, C. Alonso, J.A. Gonzales, "Determination of the Corrosion Rate of Steel Embedded in Concrete", ASTM STP 906, (Philadelphia, PA: ASTM, 1986), p. 43.

8. D.D. Macdonald, M.C.H. McKubre, M. Uruquidi-Macdonald, Corrosion, 44 1 (1988), p. 2.

9. J.R. Macdonald, D.R. Franschetti, "Physical and Electrochemical Models", Impedance Spectroscopy, (New York: John Wiley & Sons, Inc., 1987), p. 90.

10. D.G. John, P.C. Searson, J.L. Dawson, British Corrosion Journal, 16 2 (1981), p. 102.

Table 1. Concrete mixes, final liner thicknesses, and densities for the concretes used in this study.

Material	Cement (kg)	Fly Ash (kg)	Latex Emulsion (kg)	Water (kg)	W/S* Ratio	Final Liner Thickness (mm)	Density (g/cm^3)
Baseline	90.4	60.2	0	54.4	0.36	11.85	2.45±0.07
5% Latex	90.4	60.2	8.8	54.4	0.38	14.50	2.22±0.06
10% Latex	107.8	71.8	22.6	54.4	0.34	12.85	2.24±0.02
15% Latex	98.0	65.3	29.5	41.3	0.31	12.85	2.24±0.02

* Water to Solids Ratio

Table 2. Maximum Corrossion Rates Detected fom Simualted Service Testing.

Liner Material	Corrosion Rate (mpy)
Bare Steel	20*
Baseline	0.0‡
5% Latex	0.6
10% Latex	1.6
15% Latex	0.6

* approximate steady state value

‡ no corrosion detected

Table 3. Peak Cl Concentrations Measured Within 0.5 mm of the Steel-Concrete Interface.

Exposure Time (days)	Baseline	5% Latex	10% Latex	15% Latex
30	0.09		0.01	0.67
60		0.15	0.04	0.03
120	0.08	0.15	0.05	0.20
180	0.08	0.83	0.15	0.04
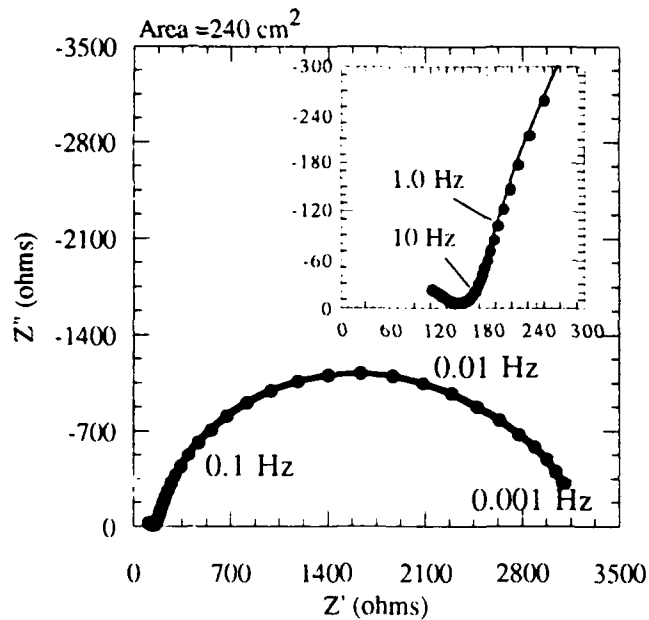
Figure 1. Typical Complex plane plot for the concrete lined steel pipe used in EIS experiments.
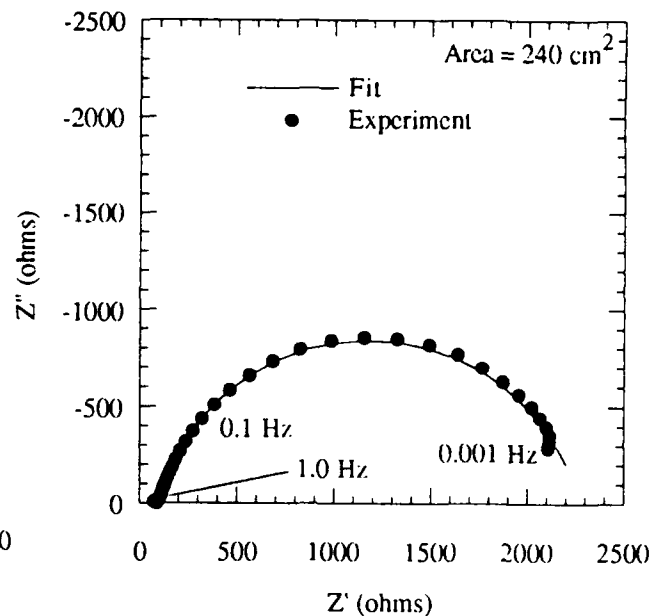
Figure 3a. Experimental EIS data and CNLS fit using the model shown in Figure 2b for the baseline concrete liner.
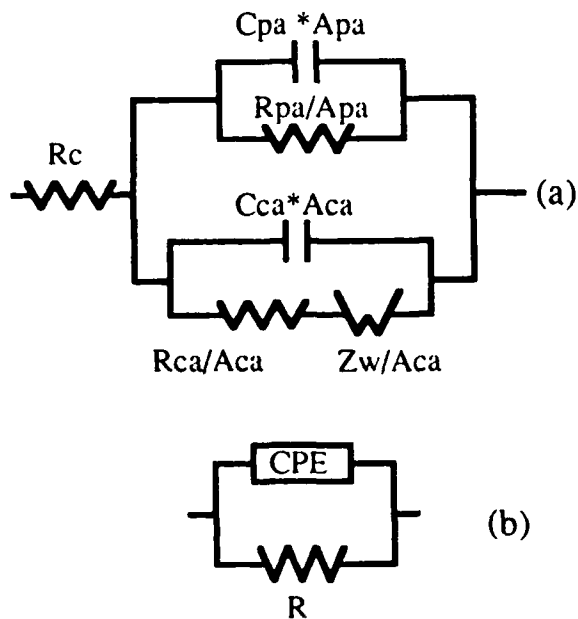
Figure 2. (a.) Equivalent circuit used for interpreting EIS data, (b.) generalized form used for CNLS modeling of the low frequency arc.
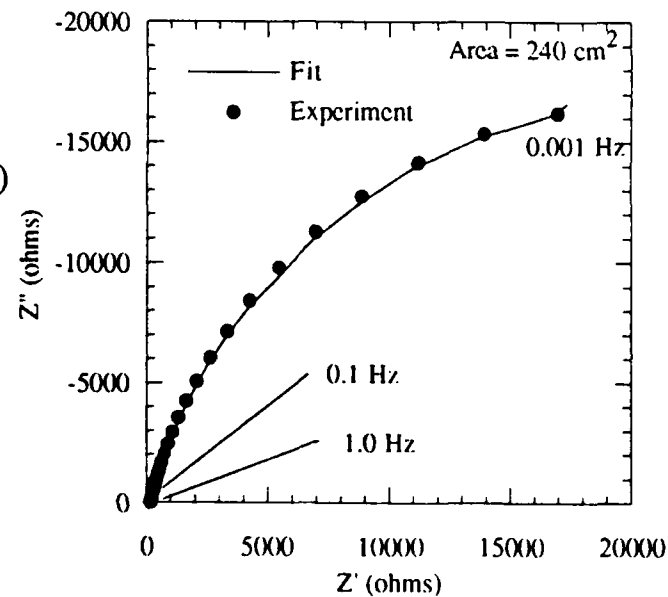
Figure 3b. Experimental EIS data and CNLS fit for 5% latex modifed concrete liner after 14 days exposure.
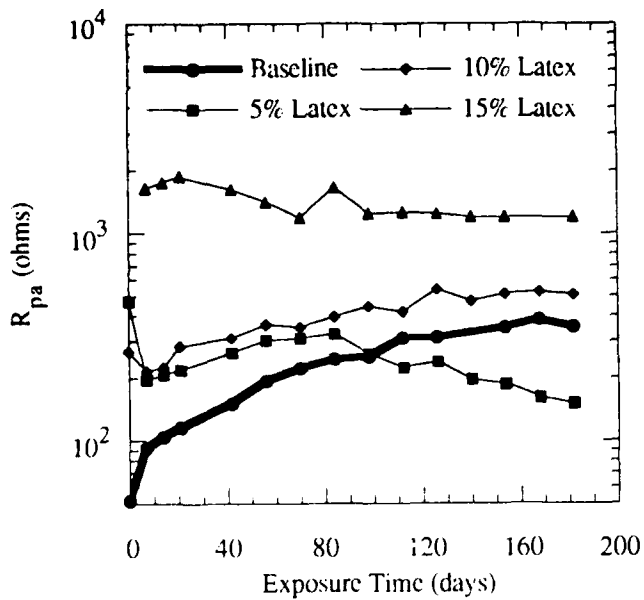
Figure 4. $R_{pa}{}^m$ versus exposure time for the baseline concrete and the latex modified concretes.
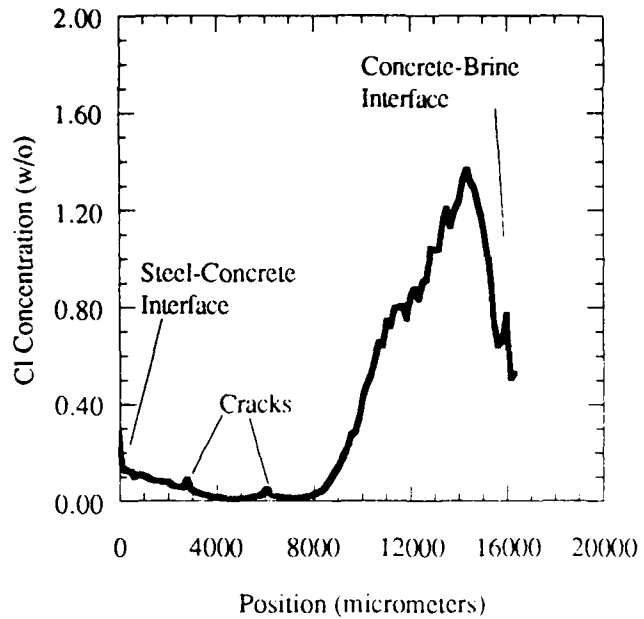
Figure 6a. Cl concentration versus position for the 5% latex modified concrete liner exposed to brine for 60 days.
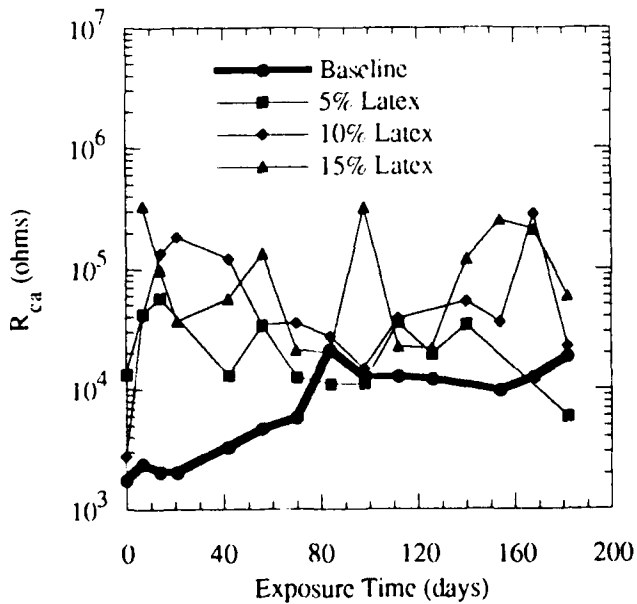
Figure 5. $R_{ca}{}^m$ versus exposure time for the baseline and latex modified concretes.
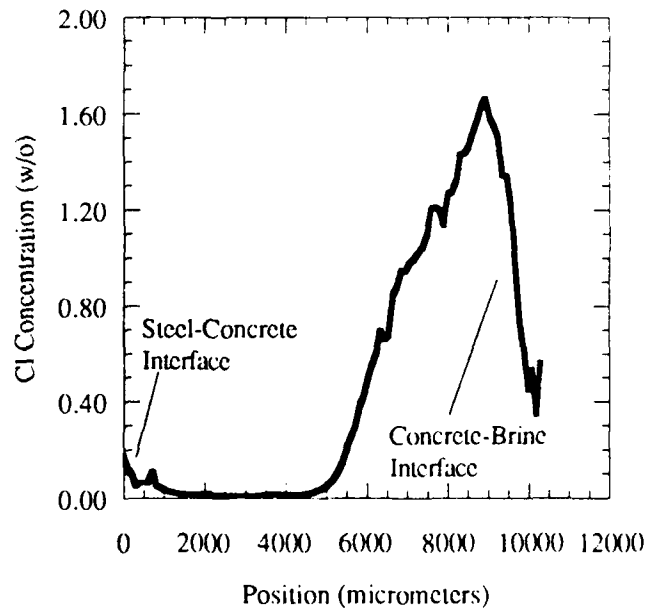
Figure 6b. Cl concentration versus position for the baseline concrete liner exposed to brine for 60 days.
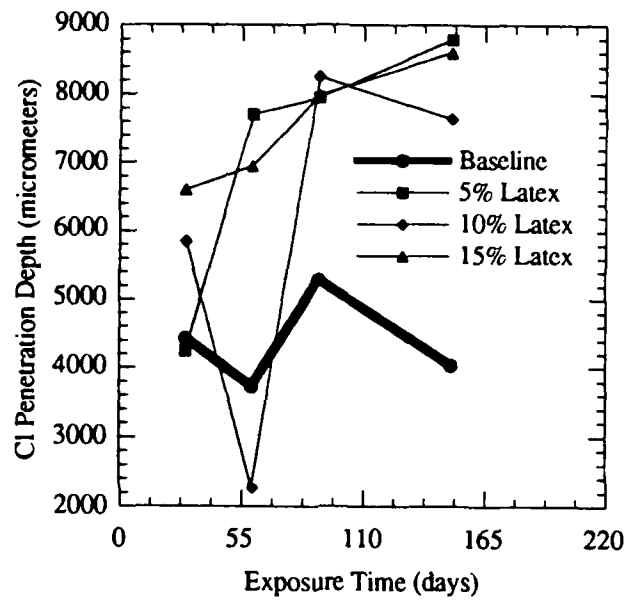
Figure 7. Cl penetration versus exposure
time for the baseline and latex modified
concretes.

A New Process for Internal Welding Joint Corrosion Protection of a Pipeline with Cement Liners

Lin Fa
Daqing Oilfield Construction Design & Research Institute
Daqing, Heilongjiang
P. R. China, 163712

Chen Jimin
Daqing Oilfield Construction Design & Research Institute
Daqing, Heilongjiang
P. R. China, 163712

Abstract

A new process for internal welding joint corrosion protection of a pipeline with cement mortar liners is discussed in the paper. A closed circular cavity is created with a piece of spring steel plate at the inside of the welded area, into which a corrosion protection material is injected through a tiny hole after welding, so that the liners of the sections of two pipes to be connected will be bound into a continuous liner at the welding joint. The paper reviews the various aspects of the technology, constructing process, technical parameters as well as the test results such as hydraulic test of the structure, air—tightness and corrosion resistance.

Introduction

Serious industrious damage will result from corrosion of the internal surface of a pipeline, e. f. loss of pipeline—transported products or their purity deterioration, production cost rise, environmental contamination etc. Applying a coating or liner to the internal wall of a pipe has proved to be one of the most reliable, cost—effective and the simplest technologies of pipeline internal corrosion protection.

In the recent years thousands of kilometres of water pipelines with internal coatings and liners have been in operation across China's oilfields. As for the materials for pipeline internal walls corrosion protection, cement mortar and modified cement mortar liners, due to their long service life and low—cost, has been used widely in water supply pipelines and oilfield water injection pipelines. The pipeline internal walls have thus been effectively protected from corrosion. As a result, the quality of the water will meet the requirement.

Most of the linered pipelines are connected with each other by welding since it is simple and reliable. High pressure water injection pipeline in particular has been welded together without exception. However, since the applicable technology of internal welding joint corrosion protection are not available, most of

the pipelines have not been finished with corrosion protection coatings or liners at a welding joint. So the corrosion protection for them is incomplete. Therefore we will review the experiment and development of the process in the paper.

Desription of the Process

A corrosion protection material is injected to the internal welding joint of the pipeline with cement mortar liner to protect the area from corrosion. The details of the structure is shown in Figure 1.
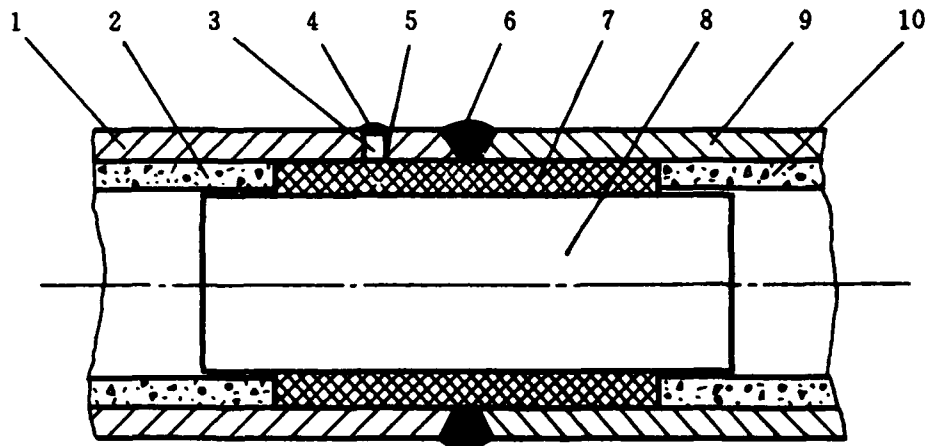
Fig. 1   Schematic of the section
1,9—pipe,   2,10—liner,   3—rivet,   4—weld,   5—hole
6—welding joint,   7—injecting material,   8—spring plate

The fabricating process is to be briefed as follows:
Keep sections without liners toward both ends of a pipe,and drill a hole there in the field. Then insert a circular spring plate into the pipes on the welding joint. After the two pipes are aligned,take away the bandage from the spring steel plate,so that it will spring against the internal wall. Just by this way a closed cavity is created. The material is injected to the cavity through the hole,connecting the liners with each other at the weld joint. Finally place a revit into the hole and weld it on the outside of the pipe to keep the hole plugging complete sealed and desired strength.

Test and Results

We finished the test of the process described above. The test consisted of selecting material,injecting technology,mode of hole plugging, and test of completeness of the section of the pipe.

1. Selecting material for corrosion protection
Cement mortar,polymer cement mortar,epoxy and polyurethane were tested for flowing characteristic when injected,and corrosion protection,strength and deformation characteristics,as well as binding strength with liners.
The comparison of various materials with each other is shown as follows:

(1) Cement mortar is characterized by its higher heat resistance, but has lower binding strength with the existing liners, and it is brittle as well.

(2) Polymer cement mortar has desired bond with the existing liners. In addition, its efficiency of corrosion protection is as high as that of the existing liners. Also it exceeds the common cement mortar in flowing characteristic, so it is easy to handle. But its heat resistance is not good.

(3) Epoxy, polyurethane are satisfactory as to its binding capacity with the existing liners, water—tight capacity and corrosion resistance. But it is unable to withstand higher temperature.

2. Injecting process

The tested steel pipe, $\varnothing$76 mm ~ $\varnothing$245 mm, was linered of 6 mm cement mortar. We have developed a injecting device which can control the volume of material to be injected, and the injecting process applicable to the liners of pipes of various sizes. We have also collected a set of injecting parameters. The test shows that to insert a circular spring steel plate into a pipe is very applicable. It is easy to put in place. And it will ensure smooth injection of material, so sections without liners will be filled out adequately, and the injected material will form a perfect corrosion protection liners.

3. Hole plugging

Revit made of the same material as that of the pipe is used to avoid corrosion of electric couple and to ensure the strength and seal of the hole. And weld it on the external wall of the pipe. We investigated the effects of spot welding on the injected material by testing the maximum temperature rise at the internal wall of the pipe. Based upon the data collected in the process we selected the right material.

Under the conditions of temp. 20℃, normally welding current and speed, maximum temperature rises at the internal walls of pipes of different thickness is shown in Figure 2.
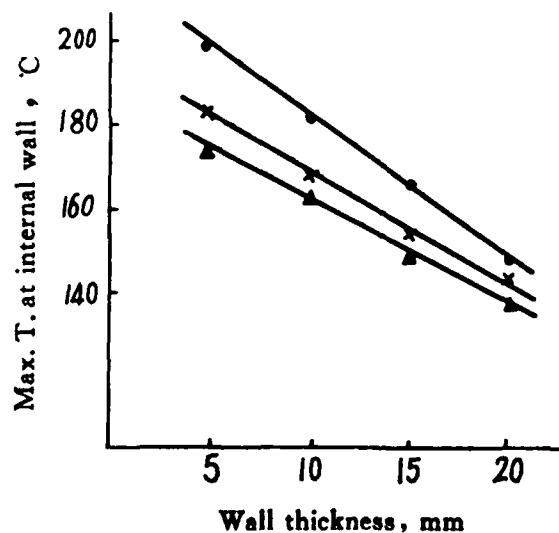
Fig. 2 Max. T. at internal wall Vs. wall thickness

1—epoxy, 2—polymer cement mortar, 3—cement mortar

From the figure, it is clear that the material to be injected is required to withstand temperature of 200℃ with wall thickness greater than 5 mm, and with wall thickness greater than 10 mm, heat resistance of the material is required to be 150℃ . And the test of property of the material is in agreement with the conclusion.

4. Test of completeness of the corrosion protection section

(1) Hydraulic test

The tested pipe is 76 mm in diameter, 6 mm in wall thickness and 5 mm in liner thickness, to which hydraulic pressure 25 MPa / 15 min. was applied. The tested piece was then opened up to be inspected. And it was found that the material remained undamaged. Accordingly it can be seen that the injected material and the hole plugging survived the hydraulic pressure. And this section was able to stand the pressure as high as that of the pipe liners. In other words, this method is not restricted in fluids pressure.

(2) Test of air—tightness

The size of the tested piece was the same as that of the hydraulic tested one. Leak did not occure to the section when 0. 6 MPa pressure / 30 min. was applied to it.

(3) Test of corrosion protection

Immersion corrosion test was conducted with the corrosion media such as water, sewage water, salted solution, dilute acid solution and dilute alkali solution. The test shows that corrosion protection of the section is as effective as that of the existing pipe liners, which can meet the requirement for long service.

Conclusion

1. The process is simple, reliable and cost—effective. In addition, it is not restricted in fluids pressure, and can be applied to the pipeline of small size with a cement mortar liner or modified cement mortar liner.

2. Volume of material for corrosion protection to be injected is easily controlled.

3. Wall thickness of the pipe is to be considered to select material to be injected to ensure that welding heat will not have impact on the material property.

Progress Toward a Modified B31G Criterion

Patrick H. Vieth
Kiefner & Associates, Inc.
P.O. Box 268
Worthington OH 43085

John F. Kiefner
Kiefner & Associates, Inc.
P.O. Box 268
Worthington OH 43085

Abstract

A criterion known as the ANSI/ASME B31G criterion is currently used to assess the remaining strength of corroded pipelines. From its inception, the B31G criterion has embodied a large factor of safety to protect pipelines from failure. Experience has proven that the excessive conservatism present in the B31G criterion has resulted in the repair or replacement of more pipe than is necessary to maintain adequate integrity.

A modified criterion has been developed to eliminate the excessive conservatism and still preserve adequate pipeline integrity. Details of the modified criterion along with a description of the on-going work to further validate and implement the modified criterion are presented in this paper. These projects are based primarily upon research funded and directed under contract with the American Gas Association (A.G.A.) on behalf of the Pipeline Research Committee.

Key terms: corroded pipe, pipeline, pressurized piping, pipeline rehabilitation, B31G

Introduction

In the late 1960s and early 1970s, a criterion was developed through research sponsored by Texas Eastern Transmission Corporation and the Pipeline Research Committee of the American Gas Association (A.G.A.) to evaluate the serviceability of corroded pipe. This criterion has been embodied in both the B31.4 and B31.8 pipeline design codes and is described in detail in a separate document: "ANSI/ASME B31G - 1991 Manual for Determining the Remaining Strength of Corroded Pipelines". The criterion, commonly referred to as the "B31G criterion", can be used by a pipeline operator to assess corroded pipe for rehabilitation purposes. The remaining pressure-carrying capacity of a pipe segment is calculated on the basis of the amount and distribution of metal lost to corrosion and the yield strength of the material. If the calculated remaining pressure-carrying capacity exceeds the maximum allowable operating pressure of the pipeline by a sufficient margin of safety, the corroded segment can remain in service. If not, it must be repaired or replaced. Applying this criterion, pipeline operators have saved millions of dollars by not removing corroded pipe which is still fit for service in spite of having sustained some loss of metal.

From its inception, the B31G criterion was intended to embody a large factor of safety to protect pipelines from failure. Experience has shown that the amount of conservatism embodied in the criterion is excessive, resulting in the removal or repair of more pipe than is necessary to maintain adequate integrity. Therefore, it is desirable to have a modified criterion which will still preserve adequate pipeline integrity but will result in less removal of pipe. A modified criterion which meets this requirement is described in this paper and presented in detail in Reference 1. Papers similar to this paper have been previously presented at other conferences.

Background

The B31G criterion is based upon a semiempirical fracture-mechanics relationship conceived by Maxey (2) and is described in detail in Reference 3. It was based upon a "Dugdale" plastic-zone-size model, a "Folias" analysis (4) of an axial crack in a pressurized cylinder, and an empirically established flaw-depth-to-pipe-thickness relationship. The extensive data base of flawed-pipe burst tests presented in Reference 3 demonstrated its usefulness and validity for axial flaws in line pipe. Subsequently, Kiefner (5) conducted a series of burst tests of corroded pipes which demonstrated the applicability of the NG-18 surface flaw equation to predicting the remaining strengths of such pipes. Reference 6 presents details of these burst tests along with a compilation of additional burst tests conducted on corroded pipe. The applicability of this approach to the analysis of corroded pipe was further substantiated in a program of research conducted by British Gas (Shannon, Reference 7). From the work of Reference 5, the B31G criterion was derived.

Basis of the B31G Criterion

Basic Equation. The B31G criterion is based upon Equation 1

$$S = \overline{S} \left[\frac{1 - A/A_o}{1 - (A/A_o)(M^{-1})} \right] \qquad (1)$$

where

M is the "Folias" factor, a function of L, D, and t

S is the hoop stress level at failure, psi (Pa)

$\overline{S}$ is the flow stress of the material, a material property related to its yield strength, psi, Pa

A is the area of crack or defect in the longitudinal plane through the wall thickness, in^2 (mm^2)

A_o is Lt, in^2 (mm^2)

L is the axial extent of the defect, inches (mm)

t is the wall thickness of the pipe, inch (mm)

D is the diameter of the pipe, inches (mm).

Equation 1 is used to calculate the failure stress level of a pressurized pipe containing a longitudinally oriented crack or defect. It is also used to predict the remaining strength of corroded pipe where the parameters of the metal loss are handled as shown in Figure 1. The overall axial length of the corrosion is taken as L even if the corrosion is an array of pitting not necessarily lined up along an axial line. The projection of the pitted profile onto the axially oriented plane through the wall thickness as shown in Figure 1 yields the area, A, to be used in Equation 1. The maximum depth of a corroded area, d, as shown in Figure 1 does not appear in Equation 1 but is used in the analysis of corroded pipe as will be shown.

Assumptions Embodied in the B31G Criterion

In adapting Equation 1 to predicting the remaining strength of corroded pipe, the following assumptions were made. First, the Folias factor M was represented as follows

$$M = \left[1 + \frac{0.8L^2}{Dt}\right]^{1/2} \tag{2}$$

Secondly, the flow stress of the material, $\bar{S}$, was taken as 1.1 SMYS where SMYS is the specified minimum yield strength of the material.

To simplify the evaluation of corroded pipe, the area of metal loss, A, was represented by a parabola as shown in Figure 2. This permits one to calculate A on the basis of two simple parameters of the metal loss, its overall length, L, and its maximum depth, d. The resulting area, A, is equal to (2/3)Ld. A_o, of course, is Lt.

The format of Equation 1 as used in the B31G criterion is

$$S_f = 1.1 \; SMYS \left[\frac{1 - 2/3(Ld/Lt)}{1 - 2/3(Ld/Lt)M^{-1}}\right] \tag{3}$$

$$= 1.1 \; SMYS \left[\frac{1 - 2/3(d/t)}{1 - 2/3(d/t)(M^{-1})}\right]$$

$$M = \left[1 + \frac{0.8L^2}{Dt}\right]^{1/2} \tag{2}$$

Factor of Safety

Equation 3 predicts the hoop stress level which will cause the failure of a corroded pipe with diameter, D, wall thickness, t, and minimum yield strength, SMYS, where the metal loss has an axial length L and a maximum depth, d. Sound engineering judgement requires that corrosion should not be allowed to reach a size (L and d) so large that the predicted failure stress level is at or below the maximum operating stress level. Therefore, a factor of safety must be applied to Equation 3. The basis for the factor of safety consists of the reasonable

requirement that the failure stress level, S_f, not be less than 100 percent of SMYS. In that manner, the acceptance or rejection of corroded areas by the criterion would embody the same factor of safety as a hydrostatic test of the pipeline to 100 percent of SMYS. For those pipelines in which the maximum operating stress level does not exceed 72 percent of SMYS, the factor of safety embodied in the B31G criterion (not considering any other built-in conservatism of which there is some) is 100/72 = 1.39.

Format of the B31G Criterion

**Evaluating a Corroded Region**. A given corroded region in a pipeline is evaluated on the basis of its maximum length, L, and maximum depth, d, via a transformation and combination of Equations 2 and 3.

$$L = 1.12 \sqrt{\left(\frac{d/t}{1.1 d/t - 0.15}\right)^2 - 1} \ \sqrt{Dt} \tag{4}$$

The corroded area L is acceptable if L is less than or equal to the value given by Equation 4.

The B31G document provides the relationship shown in Figure 3 and the equation

$$L \leq 1.12 \ B\sqrt{Dt} \tag{5}$$

as a means of evaluating a given anomaly.

Pits with depths greater than 0.8 of the wall thickness are not permitted because of the chances that very deep pits would develop leaks even though the criterion predicts that they will not cause ruptures. Because the parabolic representation becomes less and less an accurate representation of the actual area of metal loss as the length increases, the use of B values greater than 4.0 is not permitted. A value of B equal to 4.0 corresponds to a d/t of 0.175. Anomalies with depths in terms of d/t greater than 0.125 but less than 0.175 are not allowed to have lengths exceeding $4.48\sqrt{Dt}$. Anomalies of depths in terms of d/t less than or equal to 0.125 may be of unlimited length since such cases would be expected to have the same remaining strength as a pipe which just meets the minimum wall thickness requirement.

**Calculating a Reduced Operating Pressure Level**. The B31G criterion provides that if L exceeds the allowable length, an acceptable reduced operating pressure may be calculated by keeping the factor of safety equal to 1.39. The reduced operating pressure is defined as follows:

$$P' = 1.1 \ P \left[\frac{1 - (2/3)(d/t)}{1 - (2/3)(d/t)(M^{-1})}\right] \tag{6}$$

where p is the safe maximum pressure for the corroded area and p' is the greater of the MAOP or the pressure determined by the equation in Title 49, Part 192 of the Code of Federal Regulations. Equation 6 is embodied in a set of curves in the B31G document which permits the calculation of reduced pressure levels in the event that the length of the corroded area is found to be unacceptable via Equation 5. Because of the previously mentioned inadequacy of the parabolic approximation of a long corroded area, Equation 6 is used only for Q*

---

*In the B31G document, the M value is shown as $(1 + Q^2)^{1/2}$ because one must calculate $Q = \frac{0.893L}{\sqrt{Dt}}$ to use the curves.

values less than or equal to 4.0. When Q is greater than 4.0, the 2/3 factor on Ld is converted to 1.0 (a rectangular rather than a parabolic representation) and M is assumed to approach infinity. The result is that P' is calculated as follows:

$$P' = 1.1 \, P \, [1 - d/t] \tag{7}$$

except that p' must be less than or equal to p.

Enhancements and Extension of the B31G

As a result of excess conservatism embodied in the original B31G criterion, too much serviceable pipe is being removed during rehabilitation efforts. For the sake of optimizing safety, it is better to concentrate rehabilitation efforts on the portions of the systems which truly need repair as soon as possible rather than stretch out rehabilitation efforts to meet a criterion known to contain an unnecessarily large margin of safety. To obtain the desired improvement in the criterion, the sources of excess conservatism and the serious limitations of the original approach were reconsidered as described below.

Sources of Excess Conservatism

The sources of excess conservatism in the original B31G criterion are:

- The expression for flow stress
- The approximation used for the Folias factor
- The parabolic representation of the metal loss (as used within the B31G limitations), primarily the limitation when applied to long areas of corrosion
- The inability to consider the strengthening effect of islands of full thickness or near full thickness pipe at the ends of or between arrays of corrosion pits.

Modified Flow Stress

It was known even when the original B31G criterion was developed that 1.1 SMYS substantially underestimates the flow stress of a line-pipe material. In Reference 3, it was clearly demonstrated that yield strength + 10,000 psi (68.9 MPa) closely approximates the flow stress for line-pipe materials. Even if one takes yield strength to be SMYS, this latter value would exceed the 1.1 SMYS value for all available grades of line pipe. For the modified criterion, then, the value of flow stress will be taken as SMYS + 10,000 psi (68.9 MPa).

Modified Folias Factor

The two-term approximation for M, the Folias factor, used in the original B31G criterion has been presented herein in Equation 2. A more exact and less conservative approximation of M_T is as follows. For values of $(L^2/Dt) \leq 50$:

$$M_T = \left[1 + 0.6275 \, \frac{L^2}{Dt} - 0.003375 \, \frac{L^4}{D^2 t^2} \right]^{1/2} \tag{8}$$

For values of $(L^2/Dt) > 50$

$$M_T = 0.032 \ (L^2/Dt) + 3.3 \qquad \textbf{(8a)}$$

The alternate form of M_T is illustrated in Figure 4. It is needed for very long anomalies because the negative term of the three-term series starts to dominate and the three-term approximation is no longer valid beyond the stated limit. It is derived by extrapolating the M_T versus L^2/Dt relationship by means of a straight line tangent to the curve of Equation 8 at $L^2/Dt = 50$.

Modified Representation of Metal-Loss Area

Parabolic Area (Original B31G Criterion). The exact area of metal loss as portrayed in Figure 1 is difficult to represent in terms of simple geometric shapes definable by maximum length and depth. Two shapes which were considered in the development of the original B31G criterion were the rectangle (A = Ld) and the parabola (A = 2/3Ld). On the basis of the 47 burst tests of corroded pipe presented in Reference 5, it was easily shown that the parabolic method was preferable. Predictions of remaining strength using the rectangular method were too conservative, but those made using the parabolic method as described in the form of Equation 3 consistently underestimated the actual failure stress levels as shown in Reference 5 (Table 4). The ratios of actual-to-predicted failure stress levels range from 1.07 to 3.07. It is apparent that even with the parabolic method, many of the predictions greatly underestimated the strengths of the pipes.

In reality, the parabolic method has significant limitations. Obviously, if the corroded area were very long, the effect of the metal loss would be underestimated and the remaining strength would be over estimated. The fact that the method of Equation 3 underestimated the strengths in all 47 cases is probably the result of circumstances such as the pits not being lined up axially and the deepest areas being separated by islands of greater remaining wall thickness. To prevent misuse of the criterion in cases where long, deep corroded areas might actually have lower strengths than the criterion would predict, the method was limited as described earlier to defects where the B values obtained from Figure 3 are less than or equal to 4.0. This forces all long areas to be considered essentially on the basis of 1 - d/t.

Effective Area. A more accurate method to predict the remaining strength involves calculations based upon various subsections of the total area of metal loss. For example, one could calculate 16 different predicted failure pressures based upon the profile shown in Figure 6. Each calculation involves the length, L_i where i varies from 1 to 16. The area of each individual flaw is calculated as the sum of the areas of the trapezoids made up by the discrete depth points within L_i. The area of each is slightly more than $L_i d_{avg}$ because the endpoint d values are nonzero. The procedure usually, though not always, results in a minimum predicted failure stress that is less than the value corresponding to the exact-area total-length method. This method is referred to as the "effective area" method. It is based upon the effective area and effective length of the defect.

One of the most important results of the PR 3-805 project sponsored by the A.G.A. Corrosion Supervisory Committee(1) was the development of a PC program called RSTRENG. RSTRENG facilitates the analysis of corroded areas via the effective-area method. RSTRENG and its use are explained in more detail later.

New Area Representation. It was recognized that the parabolic area representation left a few things to be desired and that some pipeline operators might not choose to use the effective-area method because of the detailed measurements required. Therefore, in addition to the RSTRENG option, a new area representation relying solely on maximum length, L, and maximum depth of pitting, d, was conceived. The new representation is

$$A = 0.85 \, dL \qquad \text{(8a)}$$

The new A can be used in Equation 1 with the modified Folias factor (Equations 8 or 8a) to calculate predicted failure pressures when only d and L are known.

The calculation of remaining strength via one or more of these more exact methods tends to give predictions that are in better agreement with actual burst-test results than those made using the parabolic representation of metal loss. However, there is no fixed relationship between the results predicted by the various methods.

A final point that must be made with regard to any type of profile representation of metal loss is that some excess conservatism will always be present when the deepest parts of the corrosion are not lined up along the axis of the pipe and when deeper portions of the pitting are separated by islands of greater remaining wall thickness. Within the present state of technology, it is not practical to deal analytically with these variables.

RSTRENG

A personal-computer program, titled RSTRENG, was developed as part of Project PR-3-805 (Reference 1). This software was developed as a tool for pipeline operators to easily evaluate sections of corroded pipelines. Since the development of RSTRENG, an additional A.G.A. project has been carried out to enhance the usability of RSTRENG. As a result of this project, RSTRENG2 was developed and is provided along with a users manual in Reference 8. RSTRENG2 is based on the same equations as those in RSTRENG but is formatted in a more usable and versatile format.

RSTRENG2 resides on a single 5-1/4-inch floppy disk that can be used on any IBM-compatible PC. RSTRENG permits the analysis of corroded pipe by use of the effective-area method. It finds the minimum failure pressure and effective flaw length automatically and quickly, saving much time over the long-hand calculations.

To illustrate its use, let us consider a sample problem involving a 30-inch O.D. by 0.375-inch wall (762-mm O.D. by 9.53-mm wall) X52 pipe with a 20-inch-long (508-mm) corroded area. The maximum depth of corrosion is 0.140 inch (3.56 mm) and the pipeline operator has made detailed depth measurements at 1-inch (25-mm) intervals along the axis of the pipe deviating occasionally to pick up the locally deepest portions of the affected region. The pipeline operates at maximum allowable operating pressure, P, of 936 psig (645 MPa).

First, let us see what the existing B31G criterion tells us. Since d is 0.140 inch (3.56 mm), d/t = 0.373. According to Equation 5 or Figure 3, our B value then is 1.025. The acceptable length of corrosion then is

$$L \leq 1.12B\sqrt{Dt} = 1.12(1.025)\sqrt{30 \times 0.375} = 3.85 \; inches \qquad \text{(10)}$$

The length is too long and we must calculate a safe operating pressure. When we calculate $Q = \dfrac{0.893 \, L}{\sqrt{Dt}}$, we find that Q is 5.32. This forces us to use Equation 7 as follows:

$$P' = 1.1 \, P \left[1 - \frac{d}{t}\right] = 1.1(936)[1 - 0.373] \qquad \text{(11)}$$

Thus, under the existing B31G criterion, the operator must reduce the operating pressure to 645 psig or remove or repair the pipe.

The results using the more sophisticated RSTRENG2 analysis are presented in Figure 7. The input data are presented across the top portion of this figure (diameter, wall thickness, SMYS, and Pressure). Below this data is a corrosion profile. This profile represents each of the corrosion pit depths (y-axis) along the length of the corrosion (x-axis). Each asterisk, "*", represents a corrosion pit depth measurement.

Below the corrosion profile is a summary of the results for CASE 1, CASE 2, and CASE 3. CASE 1 results are based on the modified criterion where the area of missing metal due to corrosion is modelled using the effective area method. CASE 2 is also based on the modified criterion except that the area of missing metal is modelled as $0.85 \, dL$. CASE 3 results are based on the current B31G analysis methods.

For each case, a safe maximum pressure, a predicted burst pressure, and a factor of safety is presented. The safe maximum pressure is a function of the established maximum operating pressure rating for a given pipeline. The predicted burst pressure is based on the SMYS and does <u>not</u> account for any factor safety. The calculated factor of safety is the predicted burst pressure divided by the operating pressure (936 psig) in this example. Additional results of the effective area method analysis (CASE 1) are presented below the results along with the length and pit depth input data.

Based on the RSTRENG2 analysis, the safe maximum pressure is calculated to be 892 psig (6,146 kPa). This pressure is much higher than the pressure level of 645 psig (4,444 kPa) obtained via the existing B31G analysis (CASE 3).

This example illustrates the most valuable feature of the effective-area method and the greatest weakness for the existing B31G criterion. The new method permits the calculation of the realistic failure pressure of long corroded areas whereas the existing criterion restricts the analysis to relative short corroded areas falling back on the overconservative net-thickness concept when the corrosion is extensive in length.

Summary

This paper has described an improved method for evaluating the remaining strength of corroded pipe. The pipeline industry currently uses the "B31G" criterion to evaluate corroded pipe for removal or repair or for leaving it in service if the metal loss is within safe size limits as defined in the B31G criterion. An improved criterion was desired because of the known excess conservatism in the original B31G method. Even though the use of the B31G criterion has undoubtedly helped pipeline operators to avoid many unnecessary cut outs, the excess conservatism continues to cause some unnecessary cut outs that could be avoided without compromising safety.

The proposed modified criterion presented herein is less conservative than the existing B31G criterion. It will permit metal-loss anomalies of greater size to remain in service at the current maximum operating pressure. And, for anomalies which exceed the newly recommended allowable size, the modified criterion will require less pressure reduction to maintain an adequate margin of safety.

The new criterion was made less conservative by means of a change in the manner in which the flow stress of the material is considered and by means of a change in the format of the stress-intensifying effect of the metal loss. The proposed modified criterion can be used with detailed measurements of the metal loss and successive trial calculations to predict a minimum failure pressure for an area of metal loss based upon its "effective" area.

As part of Project PR 3-805, software was developed to assist pipeline operators in conducting the calculations necessary to predict the remaining strength of a section of corroded pipe. This software, titled RSTRENG, has been used widely by pipeline operators as a tool to make timely decisions during renovation or inspection. Since the software has been used in industry, some modifications to the software have been incorporated into a revised software program titled RSTRENG2.

Acknowledgements

References

(1)   Kiefner, J. F., and Vieth, P. H., "A Modified Criterion for Evaluating the Remaining Strength of Corroded Pipe", Project PR-3-805, Pipeline Research Committee, American Gas Association, Catalog No. L51609.

(2)   Maxey, W. A., Kiefner, J. F., Eiber, R. J., and Duffy, A. R., "Ductile Fracture Initiation, Propagation, and Arrest in Cylindrical Vessels", Fracture Toughness, Proceedings of the 1971 National Symposium on Fracture Mechanics, Part II, ASTM STP 514, American Society for Testing and Materials, pp 70-81 (1972).

(3)   Kiefner, J. F., Maxey, W. A., Eiber, R. J., and Duffy, A. R., "Failure Stress Levels of Flaws in Pressurized Cylinders", Progress in Flaw Growth and Fracture Toughness Testing, ASTM STP 536, American Society for Testing and Materials, pp 461-481 (1973).

(4)   Folias, E. S., "The Stresses in a Cylindrical Shell Containing an Axial Crack", ARL 64-174, Aerospace Research Laboratories (October 1964).

(5)   Kiefner, J. F., and Duffy, A. R., Summary of Research to Determine the Strength of Corroded Areas in Line Pipe, presented at a Public Hearing at the U.S. Department of Transportation (July 20, 1971).

(6)   Vieth, P. H., and Kiefner, J. F., Database of Corroded Pipe Tests, Pipeline Research Committee, American Gas Association, (To be published).

(7)   Shannon, R. W. E., "The Failure Behavior of Line Pipe Defects", International Journal of Pressure Vessels and Piping, (2) (1974) - Applied Science Publishers, Ltd., England, Printed in Great Britain (1974).

(8)   Vieth, P. H., and Kiefner, J. F., RSTRENG2 User's Manual, Pipeline Research Committee, American Gas Association, (To be published).
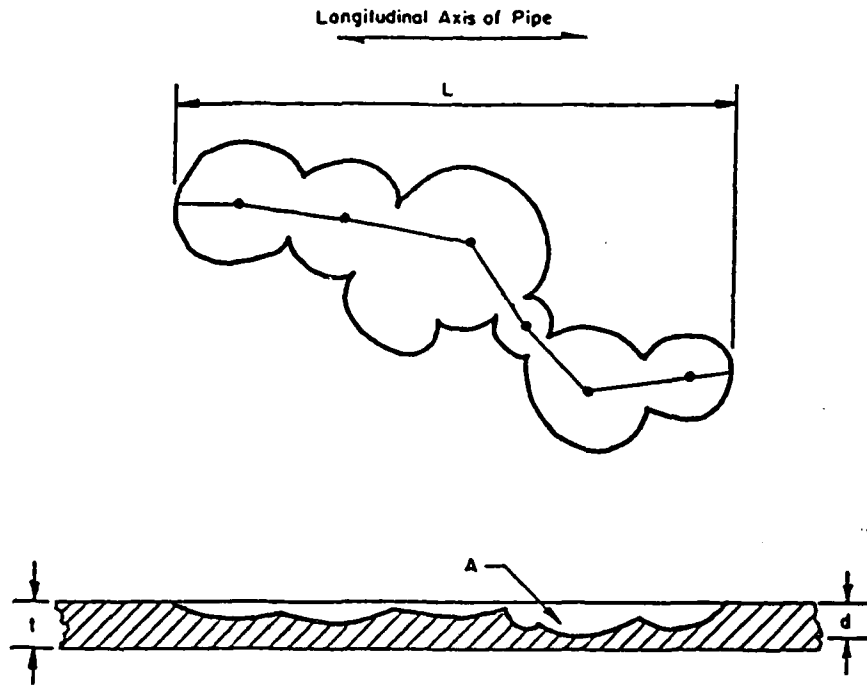
Figure 1. Parameters of Metal Loss Used in B31G Analysis
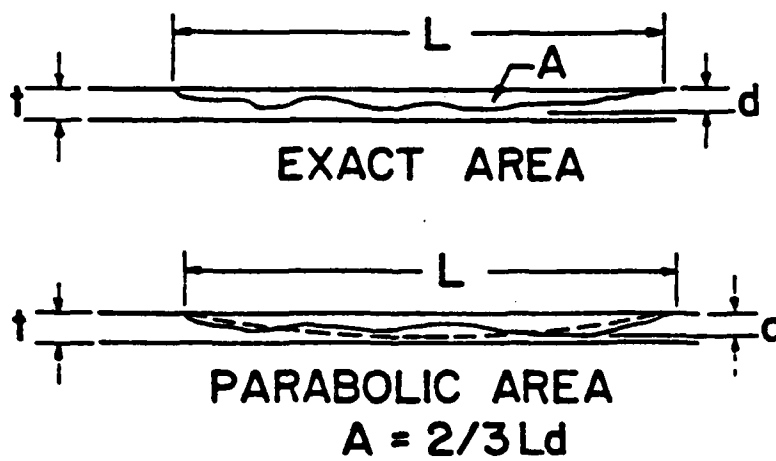
Figure 2. Parabolic Representation of Metal Loss as Used in the B31G Criterion

$$B = \sqrt{\left(\frac{d/t}{1.1\, d/t - 0.15}\right)^2 - 1}$$
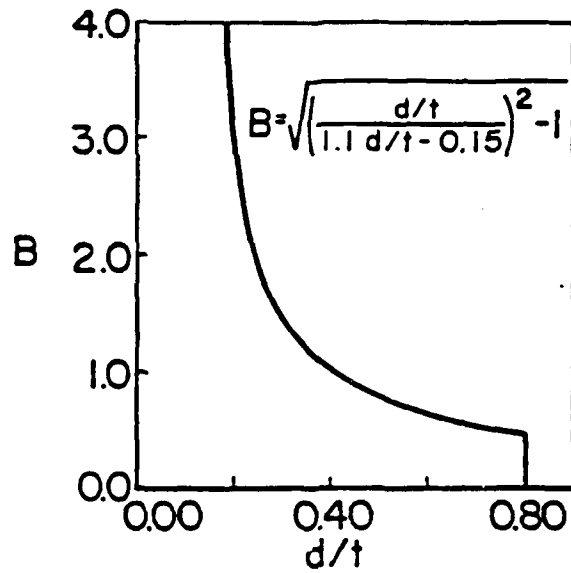
$$L \leq 1.12\ B\sqrt{Dt}$$

Figure 3. The B31G Criterion for Acceptable Length of a Corroded Region

$$M_T = 0.032\, \frac{L^2}{Dt} + 3.3$$

$$M_T = \left[1 + 0.6275\, \frac{L^2}{Dt} - 0.003375\left(\frac{L^2}{Dt}\right)^2\right]^{1/2}$$

$$\frac{L^2}{Dt} = 50$$
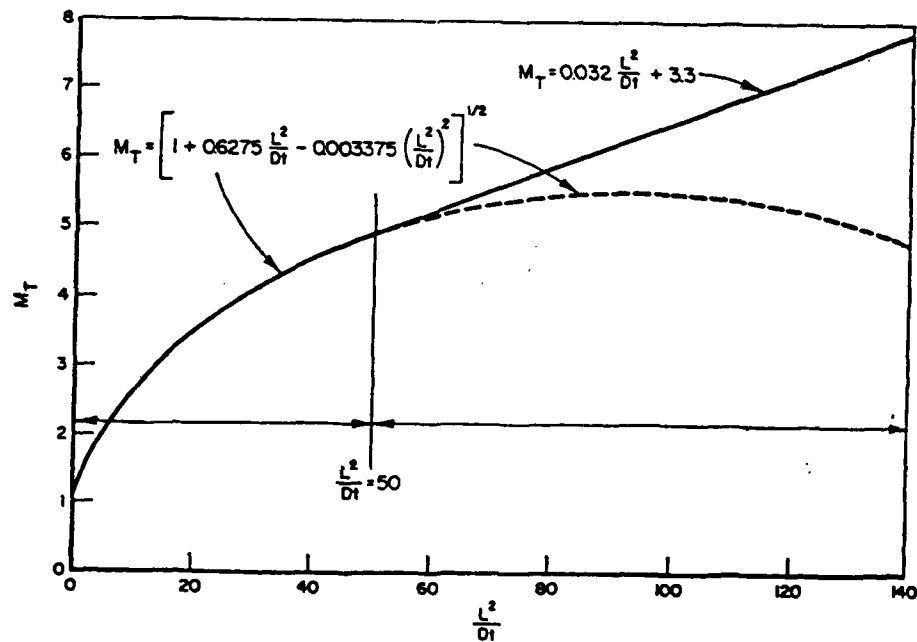
Figure 4. Graphical Representation of Folias Factors Used in the Modified Criterion
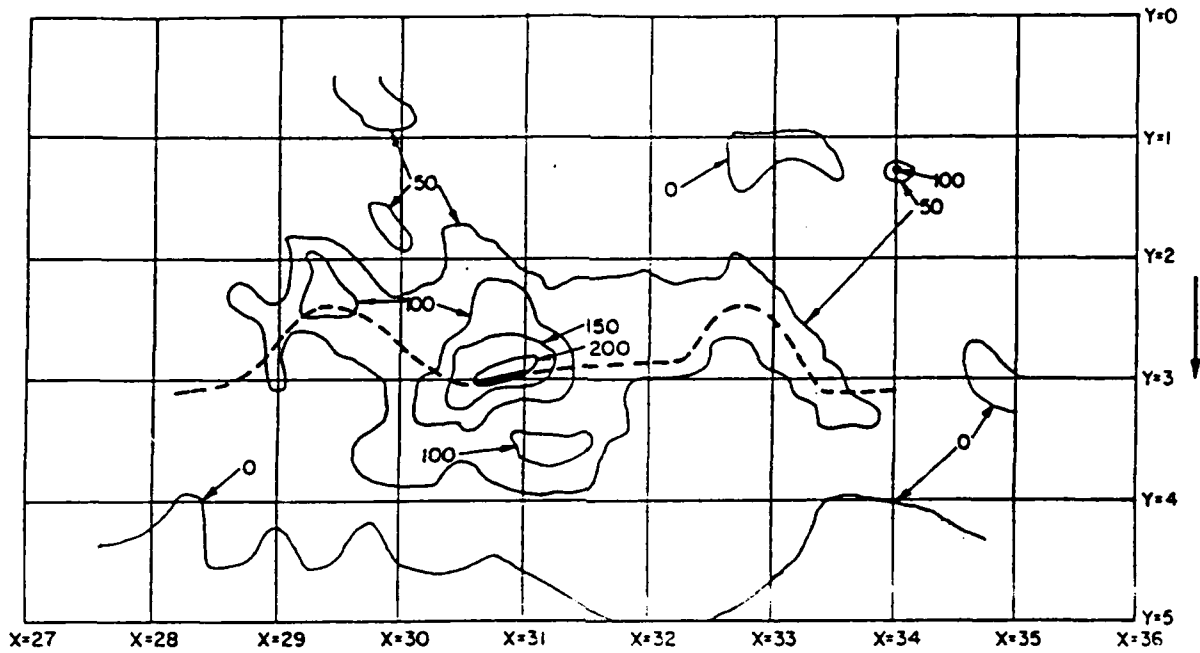
Figure 5. Contour Map of Pit Depths
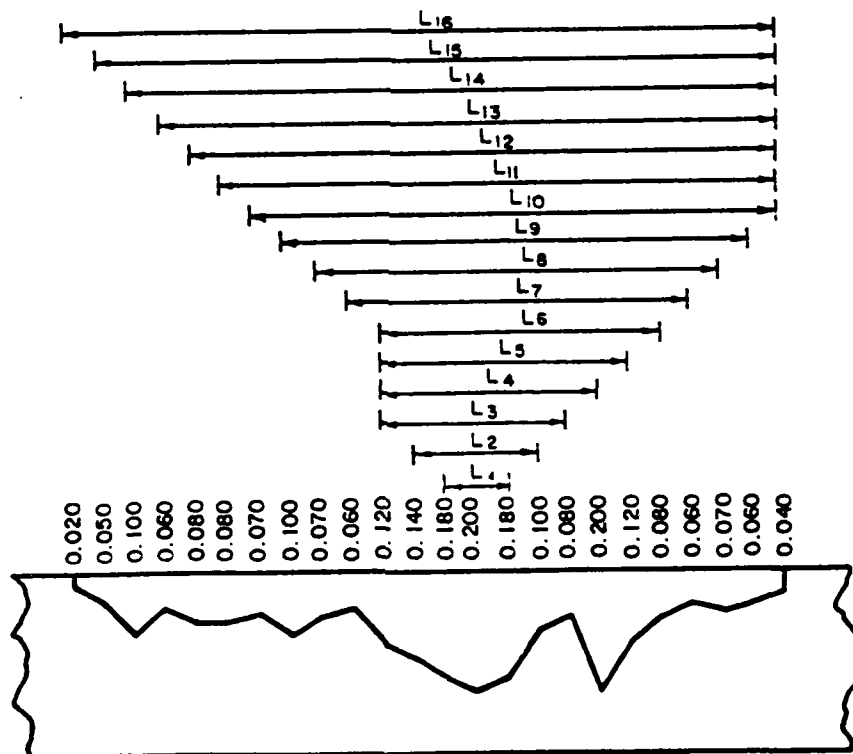
Figure 6. Profile of Pit Depths Along "River-Bottom" Path in Figure 5 (in inches)

```
FILENAME: C:\RSTRENG2\DATA\X.DAT          Date: 05-18-1993
   Diameter, inches     30.00     Wall Thickness, inches     0.375
   SMYS, psi            52,000     Pressure, psi                936
              !-----------------Leff-----------------!
        0             5            10            15            20
0.000   *-*-----------+-------------+-------------+-----------*--*
0.038   +    *                                 *            *
0.075   +       *             *      *  *      *  *        *
0.113   +           *  *  *  *  *      *                 *
0.150   +
0.188   +
0.225   +
0.263   +
0.300   +
0.338   +
0.375   +


        -------------------------------------------------------------

              Pressure, psi =    936
                              Safe        Predicted
                             Maximum        Burst        Factor
                             Pressure      Pressure        of
                             psi (*)         psi         Safety
                             --------      --------      --------
CASE 1 - Effective Area        892          1,239         1.32
CASE 2 - 0.85 dL Area          822          1,141         1.22
CASE 3 - B31G                  645            896          0.96


                                  Max. Pit Depth, inch =    0.140
Total Length, inch =    20.00     Max. Depth/Thickness =    0.37
 Eff. Length, inch =    14.00        Eff. Area, inch^2 =    1.390
        Start, inch =     3.00             Stop, inch  =   17.00

(*) If the calculated safe maximum pressure for the criteria that
    the user follows (CASE 1, CASE 2, or CASE 3) is less than
    the established pressure, remedial action must be taken.




-------------------- Lengths and Pit Depths --------------------
    Length    Depth        Length    Depth        Length    Depth
    inch      MIL          inch      MIL          inch      MIL
    --------  -----        --------  -----        --------  -----
     0.00      0           10.00     110          20.00      0
     1.00      20          11.00      90
     2.00      40          12.00      70
     3.00      90          13.00      40
     4.00     110          14.00      90
     5.00     110          15.00     100
     6.00     120          16.00     110
     7.00     140          17.00      90
     8.00     110          18.00      40
     9.00     100          19.00      20
```
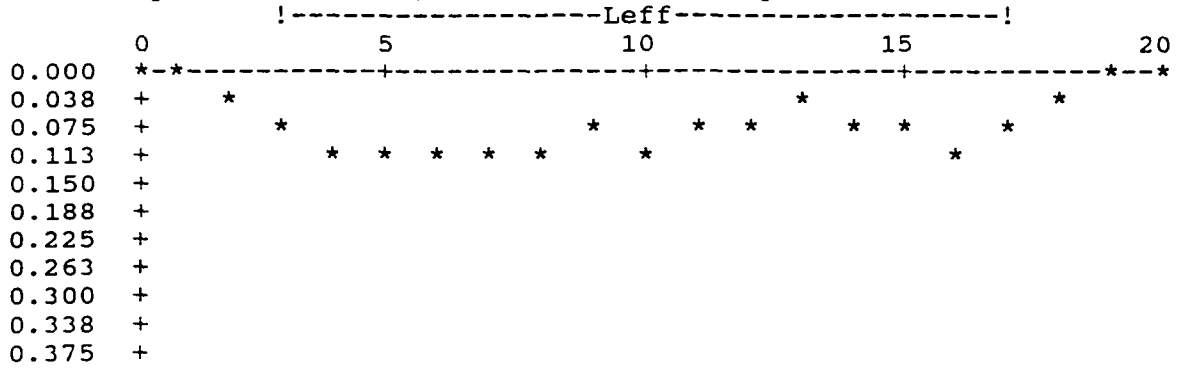
Figure 7. Results from RSTRENG2 Analysis

Welding of UNS S32654 - Corrosion Properties and Metallurgical Aspects

Mats Liljas
Avesta Sheffield AB
S-774 80 Avesta, Sweden

Peter Stenvall
Avesta Sheffield AB
S-774 80 Avesta, Sweden

Abstract

Welding trials have been carried out on a very highly alloyed, nitrogen-enhanced superaustenitic stainless steel, Avesta Sheffield 654 SMO™ (UNS S32654). Welding was performed automatically in a laboratory welding fixture with gas tungsten arc, plasma arc, gas metal arc and submerged arc welding. The welding was executed both with a nickel-base filler, Avesta P16™, and autogenously. Different nitrogen-containing torch and plasma gases were tested in order to study the influence on nitrogen content in the weld metal and the pitting resistance.

Welding trials were also carried out with manual gas tungsten arc in order to study the influence of dilution from parent material and the effect of two different shielding gases on pitting resistance, mechanical properties, microstructure, and microsegregation of molybdenum.

The effect of different post weld cleaning methods on the pitting resistance was studied on gas tungsten arc welds and shielded metals arc welds.

The tests showed that welding with addition of the overalloyed nickel-base filler gave high pitting corrosion resistance. However, the resistance was surprisingly high also in autogenous plasma arc welds and in gas tungsten arc welds when nitrogen addition in the torch gas was used.

The investigations also showed that the nitrogen loss of the weld deposit was strongly reduced when nitrogen-bearing gases were used as torch gas in gas tungsten arc welding. The pitting resistance is substantially improved when welding was performed with nitrogen-containing torch gas instead of pure argon. This effect was accentuated for autogenously welded joints. The tungsten electrode wear was, however, increased when nitrogen was added to the torch gas.

In plasma arc welding, there appeared to be only a minor nitrogen loss, or no loss at all in welds produced autogenously. The pitting resistance was very high in all plasma arc welds. The tungsten electrode wear was very low if nitrogen and hydrogen were added to the plasma gas. The very high pitting resistance and good plasma arc weldability indicate that the plasma arc welding process is very useful when automatic welding is applicable.

Post weld cleaning strongly influenced the pitting resistance. The best pitting resistance was achieved when acid pickling was performed in a heated pickling bath. Good results were also obtained when the weldment was cleaned with abrasive means (grinding or 3M-polymer-abrasive-grinding) followed by pickling with paste.

I. Introduction

The interest in nitrogen alloying of stainless steels is growing rapidly and many stainless grades, both austenitic and duplex, containing considerable amounts of nitrogen have been presented during the last 10 years. It is well established that nitrogen, especially in combination with molybdenum, greatly improves the pitting resistance. Nitrogen also increases the yield strength by solution hardening of the austenite. Austenitic steels are eminently suited for high nitrogen levels because the nitrogen solubility is very high in the austenite, and in fact higher than in the liquid phase. Hence, superaustenitic stainless steels have a great potential for being strongly improved by high nitrogen contents.

Since their introduction at the end of the 1970's, superaustenitic stainless steels have been used successfully in a wide range of severe environments due to their excellent corrosion resistance. There is, however, a demand for alloys with even better resistance to localized corrosion. The principal alloying elements to improve the corrosion resistance are chromium and molybdenum. Fortunately, both chromium and molybdenum increase the solubility of nitrogen in the steel and, therefore, nitrogen contents of about 0.5% can be added to a superaustenitic steel with high chromium and molybdenum levels without requiring too high manganese content. Several of new superaustenitic stainless steels, using the beneficial effects of very high nitrogen contents, have been developed to meet the requirements in the most aggressive environments.

One example is UNS S32654. This new grade is alloyed with unusually high amounts of molybdenum and nitrogen. The composition is presented in Table 1. High contents of chromium, molybdenum and nitrogen give S32654 excellent resistance to pitting and crevice corrosion. In Table 2 the mechanical properties are compared to those of Avesta Sheffield 254 SMO[*] (UNS S31254), the first generation superaustenitic steels. The high nitrogen level in S32654 contributes to a very high strength. Due to the balance among chromium, molybdenum, nitrogen and nickel, the stability against precipitation of intermetallics and carbides is similar to that of the lower alloyed S31254. The corrosion properties of S32654 are reported elsewhere[1, 2].

Welding of high alloy superaustenitic stainless steels has been discussed extensively in the literature[3-6] and it is for example generally agreed that overalloyed nickel-base filler metals should be used for optimum pitting corrosion resistance. However, the acceptable level of dilution from the parent material for best properties is seldom presented. Specific concerns when welding high nitrogen alloys could be porosity and nitrogen loss[7, 8]. Also post weld cleaning procedures, particularly of welds intended for use in very aggressive environments, need attention[9-11]. Welding of the new 7Mo superaustenitic stainless steel has been discussed in general elsewhere[12]. The object of this paper is to illustrate the influence of different welding methods, dilution levels and post weld cleaning methods on microstructure and properties, especially pitting resistance.

II. Experimental

A. Automatic Welding

Four automatic welding processes were studied: gas tungsten arc welding (GTAW), plasma arc welding (PAW), submerged arc welding (SAW) and gas metal arc welding (GMAW).

Gas tungsten arc welding was carried out on 3 mm sheet by automatic welding in a welding fixture. The welding trial was made both autogenously and with addition of P16 filler metal. Different torch gases were tested. Tubes 25 mm in diameter with a 1 mm wall thickness

were produced from strip in fully automatic machines where forming, welding, bead working, sizing, eddy current testing and cutting took place in a continuous process. The welding was performed autogenously using two torches, see Table 3. About 12 m of the total weld length of 150 m was subjected to dye penetrant testing and about 6 m was radiographed .

Plasma arc welding was also performed on 3 mm sheet in a welding fixture. Different torch gases were tested. The shielding gas consisted of argon + 10% nitrogen. The welding was executed autogenously and with filler addition. Plasma arc welding of tubes 60.3 mm in diameter with a 2.77 mm wall thickness was carried out on strips in a fully automatic welding machine as described above. The welding was performed with filler addition. The shielding gas consisted of argon + 10% nitrogen. See Table 4. About 12 m of the total weld length of 150 m was subjected to dye penetrant testing and about 6 m was radiographed.

Submerged arc welding was executed on 10 and 15 mm plate in a welding fixture. A basic flux, Avesta 803, was used. Joint preparation and welding parameters were as shown in Table 5. The welds were subjected to X-ray testing.

Gas metal arc welding was carried out on 3 mm sheet and 10 mm plate. Torch gas and joint preparation were as shown in Table 5.

All weldments in sheet or plate were tensile and bend tested transverse to the weld. Impact toughness of the weld metal was evaluated on the gas metal arc and submerged arc weldments at ambient temperature and -90°C. Five Charpy V-notch specimens per temperature and weldment were tested. Hardness measurements (Vickers) were carried out on weld deposits and parent material.

The pitting resistance was evaluated in ferric chloride according to ASTM G48, Practice A, using 24 h exposure. New duplicate specimens were used at each test temperature. The testing was performed with 2.5°C intervals. The critical pitting temperature (CPT) was defined as the lowest temperature at which attack occured. All specimens were pickled thoroughly before testing.

Microstructure was studied in weld metal and HAZ. The amount of second phases in weld metal was measured by linear analysis in light optical microscope. In the weld deposit, the nitrogen content was measured using the LECO method. In order to calculate the dilution from the parent metal in automatically performed welds with filler, the average composition of the weld metal was measured in electron probe microanalyzer (EPMA).

B. Dilution from Parent Material

The welding trials were performed from one side on 3 mm sheet using manual gas tungsten arc welding (GTAW). In order to achieve the different dilution levels, 30%, 50%, 80% and 100% (i.e. autogenous), the joint was varied from square butt joint (autogenous) to V-joints with different gaps.

Two different torch gases were used, pure argon and argon + 5% nitrogen. For backing, a gas mix consisting of nitrogen + 10% hydrogen was used.

The dilution from parent material was calculated from electron probe microanalyses (EPMA) in the weld deposits. Electron probe microanalyses was also used in order to measure the microsegregation. The nitrogen content of the weld metals was measured according to LECO. The amount of second phases was measured in light optical microscope using linear analysis.

Prior to the pitting corrosion tests the specimens where thoroughly pickled in order to eliminate any disturbance from oxidation, chromium depletion and surface contamination. Pitting corrosion tests were performed as above.

Tensile strength was tested transverse the welds. Bend tests were carried out over a mandrel having a diameter of 9 mm (3 x t). The bend tests were performed on the welds with both root side and face side in tension.

C. Post Weld Cleaning

The effect of post weld cleaning methods on the pitting resistance was studied on welds produced with manual gas tungsten arc welding (GTAW) and shielded metal arc welding (SMAW) on 3 mm sheet and 8 mm plate.

The gas tungsten arc welding was performed from both sides using argon + 5% nitrogen as torch gas and nitrogen + 10% hydrogen as root gas. The welding was carried out with addition of filler rod. The shielded metal welding was carried out from both sides using a coated electrode. On the 3 mm sheet material, a square butt joint was used with a 1.5 mm gap for gas tungsten arc welding and a 2 mm gap for shielded metal arc welding. On the 8 mm plate material 70° V-joint, having 2 mm land, without gap was used for the gas tungsten arc welding. For the shielded metal arc welding a 60° V-joint, having 2 mm land, with 2 mm gap, was used. In Table 7 the different cleaning methods tested are listed. Prior to the second pass, the root was ground.

Subsequent to the post weld cleaning the surfaces were protected with tape and specimens were cut out for pitting tests in ferric chloride solution according to ASTM G48. Prior to testing the samples were degreased in acetone. The determination of critical pitting temperature (CPT) was performed as described elsewhere in this paper.

III. Results and Discussion

A. Properties of Welds Produced with Automatic Welding

1. Gas Tungsten Arc and Plasma Arc Welds. The dye penetrant test of the tube welds showed no cracks on either the gas tungsten arc or the plasma arc welds. No pores could be detected in the X-ray tests.

The microstructures of the weld metals consisted of an austenitic matrix with small amounts of interdendritic second phases. In the heat affected zone (HAZ), the austenite grain boundaries were decorated with fine precipitates of intermetallic phase.

Weld transverse tensile strengths ranged between 750 and 850 MPa with all fractures in the parent material. Bend tests transverse to the welds over a mandrel having a diameter of 3 or 4 x t were carried out without any cracking. All mechanical tests demonstrated that gas tungsten arc and plasma arc welding produced sound welds with high strength and ductility.

Measured nitrogen contents, dilution from parent material, second phase content and critical pitting temperatures of gas tungsten and plasma arc welds are shown in Tables 9 and 10.

Table 9 shows that the nitrogen content in the weld metal is reduced by the gas tungsten arc process irrespective of shielding gas composition, even if the loss is somewhat less when nitrogen is added to the torch gas. For plasma arc welding, there is no nitrogen loss but rather a nitrogen take-up in the weld metal when argon and, particularly, argon and 5% nitrogen is used in the plasma gas. The nitrogen take-up occuring when pure argon was used as plasma gas could be due to the nitrogen-bearing shielding gas. See Table 10. When 5% hydrogen was added, a slight loss was observed. As expected, both welding processes gave a reduction of the nitrogen content in the weld metal when a nickel-base filler addition with virtually no nitrogen

is used.

The dilution from the parent material was around 85% for the gas tungsten arc welds due to the V-joint, whereas, the plasma arc welds with a butt joint had a dilution of ~92%. For the autogenous welds, the dilution is, of course, set to 100%. The amount of second phase in the autogenous weld metals appeared to decrease with increasing nitrogen content. Addition of a nickel-base filler metal seemed to have a similar effect.

The pitting corrosion tests in ferric chloride showed a great influence of shielding gas for gas tungsten arc welding. Pure argon in autogenous welding resulted in a CPT of <70°C while addition of 5 and 10% nitrogen increased the CPT to 80 and 87.5°C, respectively. Nitrogen addition was also beneficial when filler was used even if the CPT level had been raised by the addition of over-alloyed consumable. The plasma arc welds showed consistently high CPT levels, with all welds above 90°C. For the autogenous welds, 5% nitrogen in the plasma gas improved the pitting resistance but 10% nitrogen plus 5% hydrogen reduced the CPT. Both results could be coupled to the nitrogen contents in the weld metals. Plasma arc welds with filler gave a high pitting resistance.

The influence of second phase content on pitting corrosion resistance was difficult to assess possibly because it is overshadowed by the nitrogen content. All pitting attack occurred in the weld metal but no detailed study was made to determine the exact initiation sites of the pitting. However, the HAZ was not attacked despite the presence of intergranular precipitates, which is consistent with earlier experience with welds in superaustenitic steels[5].

Welding with commercially pure argon resulted in different problems depending on welding method. In gas tungsten arc welding, argon gave a calm welding process and a smooth weld surface. However, the pitting resistance for autogenously performed welds is much lower. When pure argon was used as plasma gas, the weld had undercut and a rough surface. The pitting resistance, however, was excellent.

The nitrogen addition gave a considerable tungsten electrode wear in both gas tungsten arc and plasma arc welding. An addition of hydrogen to the argon-nitrogen mixture, however, resulted in a strong reduction of the electrode wear when welding with plasma arc. The pitting resistance was somewhat lower in autogenously produced welds when using argon+10% nitrogen+5% hydrogen instead of argon+10% nitrogen.

2. Gas Metal Arc and Submerged Arc Welding. The X-ray tests of the submerged arc welds showed sound welds without porosity.

The tensile strength was on the same level as the parent material (800-880MPa) for both welding processes and with the rupture in the parent material. The Charpy V-notch impact toughness was fairly high both at room temperature and at -90°C, see Table 11.

Low nitrogen contents were measured in both gas metal arc and submerged arc welds. This is explained by low dilution. The levels of dilution shown in Table 11, reflect the different welding procedures. Low dilutions were measured in cap runs of multipass welds. The amount of second phase in the weld metal was about 1-2%.

The critical pitting temperatures in ferric chloride are on a high level for both gas metal arc weldments, 97.5°C, as seen in Table 11. This is explained by a considerable addition of over-alloyed filler material. The submerged arc welds showed somewhat lower CPT, the weld produced with the highest arc energy having the lowest value. One reason for the lower CPT in the submerged arc welds could be the higher level of non-metallic inclusions as a result of a higher oxygen content. Another reason could be the considerably higher arc energy for the submerged arc welds.

B. Influence of Dilution from Parent Material

The results from the study of the effect of dilution from parent material on pitting resistance are shown in Figure 1. When pure argon was used as torch gas there was no significant difference between the various dilution levels, 30%, 50% and 80%. However, the autogenous weld showed a markedly lower CPT. When argon + 5% nitrogen was used as torch gas no significant difference could be seen among any one of the four different dilution levels.

The results in Table 12 show that there was no clear correlation between tensile strength and dilution. However, for the autogenous welds, welding with argon + 5% nitrogen resulted in significantly higher tensile strength compared to welding with pure argon. The results from the bend tests show that all welds, except for the autogenous welds, passed bending to 180° without cracking. Only one of the specimens of the weld performed with the nitrogen-bearing torch gas failed, indicating that the ductility was on the border line. In the previous investigation on gas tungsten arc welds presented in this paper (paragraph A.), autogenous welds performed with argon + 5% nitrogen passed the bend test. These results indicate that the ductility is on the border line for autogenous welds performed with argon + 5% nitrogen.

Nitrogen contents of the weld deposits are shown in Table 12. Welding with nitrogen-bearing torch gas resulted in a higher nitrogen content in the weld metal. This resulted in a lower amount of second phases in the weld deposits, see Figure 2. The influence of dilution on the content of second phases seems to be limited in the interval 30-80% dilution. However, from 80 to 100% there is a significant increase in the content of second phases. These high contents of second phases at 100% dilution are most likely the main reason for the drop in ductility causing failures in the bend testing.

The microsegregation of molybdenum was measured using electron probe microanalyser (EMPA). The lowest molybdenum contents measured — in the dendrite cores — were used for calculating segregation indices for molybdenum, by deviding the minimum values by the average molybdenum content of the weld deposit ($\%Mo_{min}/\%Mo_{aver}$). In Figure 3 the segregation indices for the different dilution levels are plotted. For welds performed with argon + 5% nitrogen there seemed to be a correlation to the dilution (i.e., the nickel content). This phenomenon has been shown before[13]. However, no correlation could be found when pure argon was used. The lack of trend in the latter case could be due to the difficulties in finding the lowest molybdenum content of the dendrite. The difference between the two curves in Figure 3 indicates that nitrogen has a retarding effect on the microsegregation of molybdenum, although the difference between the curves is small.

These trials indicate that the importance of the dilution from parent material is limited to the dilution interval 80-100% when welding is performed with pure argon as torch gas. If argon + 5% nitrogen is used as torch gas there seems to be no clear influence of dilution on the properties.

C. Influence of Post Weld Cleaning

In Figures 4 and 5 the critical pitting temperatures determined in ferric chloride (ASTM G48, Pracatice A), are presented. The results from these post weld cleaning trials indicate that abrasive cleaning methods alone are not sufficient in order to achieve optimum pitting resistance of the welds. For shielded metal arc welding in 3 mm sheet, the critical pitting temperatures for the ground welds were even lower than for that of the joint in the as welded state. The

pitting resistance was in most cases clearly improved if the abrasive cleaning was followed by pickling. The results show that optimum pitting resistance was obtained if blasting was combined with thorough pickling in a bath. However, different abrasive methods followed by pickling with paste did also give good results.

The results also indicate that the pitting resistance in many cases is better for gas tungsten arc welds compared to shielded metal arc welds. The difference is most pronounced for welds in 3 mm sheet. This phenomenon indicates that the best corrosion resistance for welds in light gauges is obtained if manual gas tungsten arc welding is used instaed of shielded metal arc welding. For medium and heavy gauges the difference seems to be smaller and shielded metal arc welding is probably more advantageous for practical reasons.

Pitting resistance of weldments in stainless steels is almost always reduced compared to the unaffected parent material. For UNS S32654, the CPT in ferric chloride of the parent material is above the boiling point, while the CPT of manually produced welds in most cases falls below 80-85°C. These trials have shown that different post weld cleaning methods can offset the reduction of pitting resistance for welds in S32654. Although the post weld cleaning is important for pitting resistance, the level of CPT is generally very high for S32654. In most cases it is possible to achieve a pitting resistance of weldments in S32654 comparable to that of the parent material of the lower alloyed so called 6Mo grades, e.g. UNS S31254, or super duplex grades.

IV.   Practical Implications

Most of the welding methods described in this paper - GTAW, SMAW, PAW, GMAW and SAW - work excellently in UNS S32654. In spite of the high nitrogen content there is no practical problem with porosity. The welding characteristics of this material are similar to those of other superaustenitic stainless steels. However, there are restrictions to be observed. Post weld cleaning is very important in order to obtain optimum corrosion resistance. For welding in the field abrasive post weld cleaning combined with subsequent pickling is recommended. Abrasive cleaning only seems to give a lower pitting resistance compared to the as welded condition.

Autogenous gas tungsten arc welding should not be performed using pure argon as torch gas, although this gas gives good properties when welding with filler addition. If there is a risk of dilution levels above 80%, argon + 5% nitrogen is preferable.

The only welding process, dealt with in this paper, which needs further development is gas metal arc welding (GMAW). The torch gas used in these trials (argon + 30% helium + 1% oxygen) gave rise to sputter. A new gas mixture is under development in order to give a calmer welding process. However, the properties of gas metal arc welded joints presented here are comparable to those of welds produced with the other welding methods.

V.   Conclusions

A large number of welding trials on UNS S32654 have been performed and the following conclusions can be made:

-      Welding of S32654 can be performed using GTAW, PAW, SAW, and SMAW giving
       good welding performance, sound welds and excellent material properties. GMAW gives
       sound welds and acceptable properties but requires some further development of welding

practice.

- Autogenous gas tungsten arc welding led to a nitrogen loss in the weld metal and a reduction of pitting resistance. Nitrogen addition to the torch gas is therefore necessary for best pitting resistance of autogenous welds.

- Welding with addition of the overalloyed nickel-base filler gave high pitting corrosion resistance. However, the resistance was surprisingly high also in autogenous plasma arc welds and in gas tungsten arc welds when nitrogen addition in the torch gas was used.

- Nitrogen addition to torch or plasma gas resulted in tungsten electrode wear. Hydrogen addition to the nitrogen-mixed gas reduces the electrode wear.

- Dilution from parent material seems to affect the material properties between 80% and 100% dilution. In the interval 30-80% dilution, there seems to be little influence.

- Nitrogen in the weld deposit seems to have a moderating effect on the microsegregation of molybdenum.

- Post weld cleaning has a significant effect on the pitting resistance. Optimum pitting resistance is obtained if abrasive cleaning is combined with subsequent pickling.

VI. References

1. B. Wallén, M. Liljas, P. Stenvall, CORROSION/92, Paper no 322 (National Association of Corrosion Engineers, 1992)
2. B. Wallén, M. Liljas, P. Stenvall, Applications of Stainless Steels '92, Stockholm, Sweden (The Institute of Metals, London 1992), vol.1, p.23.
3. A. Bäumel, Werkstoffe und Korrosion, 27(1976), Heft 10, 687.
4. A. Garner, CORROSION/78, Paper no 20 (National Association of Corrosion Engineers, 1978)
5. M. Liljas, B. Holmberg, A. Ulander, Stainless Steels '84, Göteborg, Sweden (The Institute of Metals, 1985), p.323.
6. R. M. Davison et. al., CORROSION/86, Paper no 185, (National Association of Corrosion Engineers, 1986)
7. J. R. Kearns, H E Deverell, Corrosion/86, NACE (1986), Paper no 188.
8. O. Jonsson, M. Liljas, P. Stenvall, Duplex Stainless Steels '91, Beaune, France (Société Française de Métallurgie et de Matériaux, 1991), vol 1, p.461.
9. R. Ericsson, L. Schön, B. Wallén, 8th Scandinavian Corrosion Congress, Helsinki (1978) p. 321.
10. G. E. Coates, CORROSION/90, Paper no 539, (National Association of Corrosion Engineers, 1990)
11. M. B. Rockel, W. R. Herda, Werkstoffe und Korrosion, 43(1992) p.354.
12. M. Liljas, P. Stenvall, B. Holmberg, O . Jonsson, Applications of Stainless Steels '92, Stockholm, Sweden (The Institute of Metals, London, 1992), vol.2, p.971.
13. T. Koseki, T. Ogawa, Quarterly Journal of the Japan Welding Society, vol. 9, no 1 (1991) p. 143.

Table 1. Typical composition of parent material, UNS S32654, and nickel-base filler.

Material	C	Mn	Cr	Ni	Mo	Cu	N
UNS S32654	0.01	3.5	24	22	7.3	0.5	0.5
Filler wire	0.01	0.5	23	bal.	16	-	-
Coated electrode	0.02	4.0	25	bal.	14	-	-

Table 2. Mechanical properties of UNS S32654 and S31254. Typical values, 10 mm plate.

UNS	Rp0.2 (MPa)	Rp1.0 (MPa)	Rm (MPa)	A5 (%)
S32654	460	500	830	55
S31254	350	390	700	50

Table 3. Welding data of welds performed with automatic gas tungsten arc welding.

Weld number	Filler	Material thickn. (mm)	Joint prep	Torch/plasma gas	Arc energy (kJ/mm)
TA	-	3	Sq butt	Ar	0.4
T5N	-	3	Sq butt	Ar+5%N$_2$	1.0
T10N	-	3	Sq butt	Ar+10%N$_2$	0.8
TFA	P16	3	V-joint	Ar	1.1
TF5N	P16	3	V-joint	Ar+5%N$_2$	1.3

Table 4. Welding data of welds performed with plasma arc welding.

Weld number	Filler	Material thickn. (mm)	Joint prep	Torch/plasma gas	Arc energy (kJ/mm)
PA	-	3	Sq butt	Ar	0.5
P5N	-	3	Sq butt	Ar+5%N$_2$	0.5
P10NH	-	3	Sq butt	Ar+10%N$_2$+5%H$_2$	0.7
PFA	P16	3	Sq butt	Ar	0.8
PF10NH	P16	3	Sq butt	Ar+10%N$_2$+5%H$_2$	0.9
PF-tube	P16	2.77	Sq butt	Ar + 10%N$_2$ + 5%H$_2$	0.5

Table 5. Welding data of welds performed with gas metal arc and submerged arc welding.

Weld number	Method	Filler	Material thickn. (mm)	Joint prep	Torch gas / flux	Arc energy (kJ/mm)
M3	GMAW	P16	3	Sq butt	Ar+30%He+1%O_2	0.6
M10	GMAW	P16	10	V-joint	Ar+30%He+1%O_2	0.6
SX15	SAW	P16	15	X-joint	basic	1.0
SV15	SAW	P16	15	V-joint	basic	1.4-2.5
SV10	SAW	P16	10	V-joint	basic	1.1

Table 6. Welding data of welds performed with manual gas tungsten arc welding.

Dilution	Torch gas	Material thickn. (mm)	Joint prep.	Filler	Arc energy (kJ/mm)
30 %	Ar	3	V-joint	P16	0.8-0.9
50 %	Ar	3	V-joint	P16	0.6-0.9
80 %	Ar	3	V-joint	P16	0.6-0.7
100 %	Ar	3	Sq butt	-	0.6-1.2
30 %	Ar + 5%N_2	3	V-joint	P16	0.6-0.8
50 %	Ar + 5%N_2	3	V-joint	P16	0.4-0.7
80 %	Ar + 5%N_2	3	V-joint	P16	0.6-0.9
100 %	Ar + 5%N_2	3	Sq butt	-	0.4-0.9

Table 7. Post weld cleaning of gas tungsten arc and shielded metal arc welds in 3 mm sheet and 8 mm plate.

Post Weld Cleaning	Weldments tested, SMAW and GTAW
1) Grinding	3 mm
2) Grinding + pickling paste, 4h	3 mm and 8 mm
3) Grinding (polymer-abrasive)	3 mm and 8 mm
4) Grinding (polymer-abrasive) + pickling paste, 4h	3 mm and 8 mm
5) Sand blasting	3 mm
6) Sand blasting + pickling paste, 4h	3 mm
7) Sand blasting + pickling bath, 24h	3 mm and 8 mm
8) As welded	3 mm

Table 8. Welding data of welds for post weld cleaning.

Weld	Joint prep	Gap (mm)	Arc energy (kJ/mm)
GTAW, 3 mm sheet	Square butt	1.5	0.3-0.4
SMAW, 3 mm sheet	Square butt	2.0	0.4-0.5
GTAW, 8 mm plate	V-joint, 70°	1.5	0.6-1.0
SMAW, 8 mm plate	V-joint, 60°	2	0.6-1.0

Table 9 . Tests of welds performed with gas tungsten arc welding.

Weld number	% N	Dilution (%)	Second phase (%)	CPT (°C)
TA	0.36	100	1.4	<70
T5N	0.38	100	1.2	80
T10N	0.41	100	0.6	87.5
TFA	0.31	84	1.2	85
TF5N	0.32	85	1.6	90
TA-tube, AW	0.46	100	n.a	<70
TA-tube, PWHT	0.46	100	0.3	95

Note: AW = as welded. PWHT = post weld heat treated.

Table 10. Tests of welds performed with plasma arc welding.

Weld number	% N	Dilution (%)	Second phase (%)	CPT (°C)
PA	0.50	100	0.8	97.5
P5N	0.61	100	0.3	BP
P10NH	0.44	100	0.7	95
PFA	0.43	91	0.7	BP
PF10NH	0.38	93	0.5	BP
PF-tube, AW	0.42	84	0.8	90
PF-tube, PWHT	0.42	84	0.0	BP

Note: AW = as welded. PWHT = post weld heat treated. BP = Boiling point.

Table 11. Tests of welds performed with gas metal arc and submerged arc welding.

Weld number	%N	Dilution (%)	Second phase (%)	CPT (°C)	Charpy V (J), RT	Charpy V (J), -90°C
M3	0.28	70	1.0	97.5	26[1]	23[1]
M10	0.22	22-51	0.6-1.7	97.5	80	67
SX	0.13	22-53	0.9-1.5	82.5	81	78
SV15	0.18[3]	43[3]	0.9[3]	90	106	88
SV10	0.26[3]	57[3]	1.0[3]	87.5	105[2]	67[2]

1) Subsize 1/4 specimen.
2) Subsize 3/4 specimen.
3) Cover pass.

Table 12. Tests of gas tungsten arc welds with different dilution from the parent material.

Dilution (%)	Torch gas	Rm (MPa)	Bend test[1] (d=3xt) Face bend	Root bend	N-content (%)	Second phases (%)
30	Ar	753	180° n.c.	180° n.c.	0.15	1.2
30	Ar + 5%N$_2$	742	180° n.c.	180° n.c.	0.21	1.0
50	Ar	753	180° n.c.	180° n.c.	0.18	1.3
50	Ar + 5%N$_2$	842	180° n.c.	180° n.c.	0.31	1.0
80	Ar	856	180° n.c.	180° n.c.	0.24	1.3
80	Ar + 5%N$_2$	791	180° n.c.	180° n.c.	0.30	1.0
100	Ar	738	70° cracks 75° cracks	70° cracks 75° cracks	0.29	3.8
100	Ar + 5%N$_2$	805	180° n.c. 115° cracks	180° n.c.	0.40	3.2

1) Duplicate specimens
Note: n.c. = no cracks
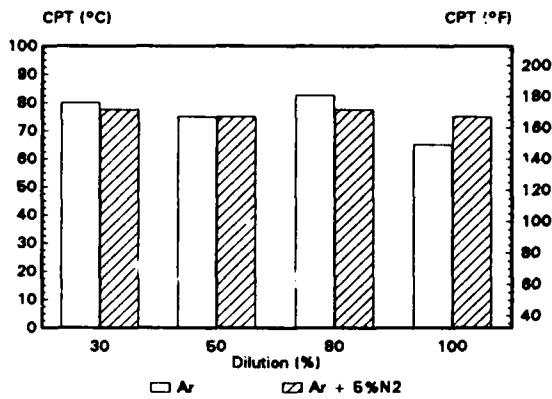
Figure 1. Influence of dilution from parent material on CPT in ferric chloride (ASTM G48).
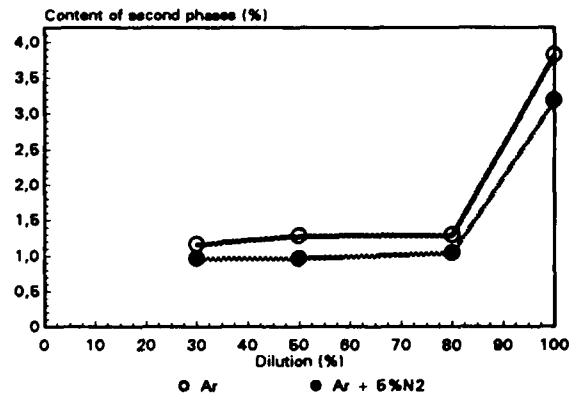
Figure 2. Influence of dilution from parent material on the content of second phases.
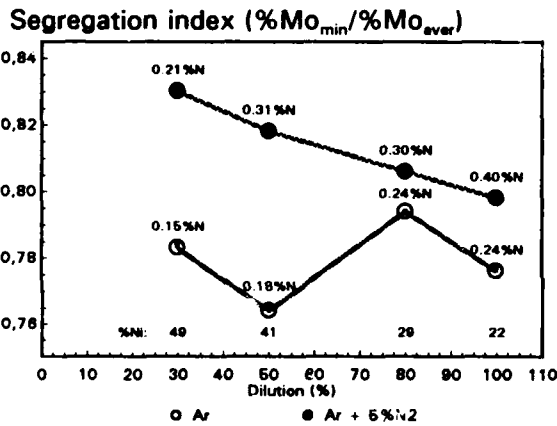
Figure 3. Segregation index for molybdenum as a function of dilution from parent material.
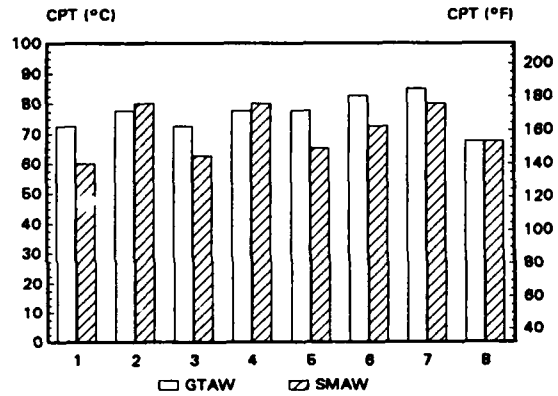
Figure 4. Influence of post weld cleaning on CPT in ferric chloride (ASTM G48). GTAW and SMAW in 3 mm sheet.
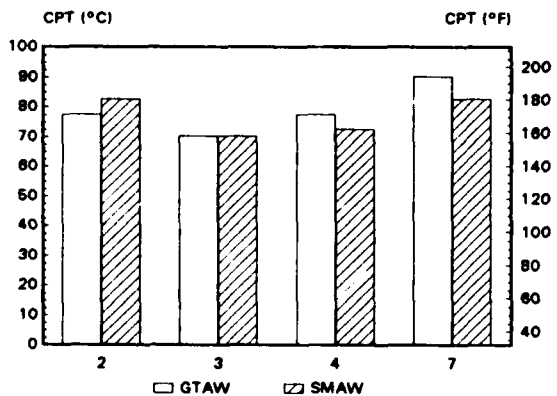
Figure 5. Influence of post weld cleaning on CPT in ferric chloride (ASTM G48). GTAW and SMAW in 8 mm plate.

Cleaning methods, Figures 3 and 4:

1. Grinding wheel.
2. Grinding wheel + pickling paste.
3. Polymer-abrasive grinding wheel.
4. Polymer-abrasive grinding wheel + pickling paste.
5. Sand blasting
6. Sand blasting + pickling paste
7. Sand blasting + pickling bath
8. As welded.

Pitting Resistance of Autogenous Welds in UNS S31254 High Alloy Austenitic Stainless Steel

B J Ginn and T G Gooch
TWI
Abington Hall
Abington
Cambridge CB1 6AL, UK

Abstract

Normal welding practice for UNS S31254 steel is to use overalloyed, Ni-base consumables to avoid weld metal corrosion, but the necessity for adequate filler addition complicates welding, for example of pipe root runs. The present work sought to optimise pitting resistance of autogenous welds in chloride media. Melt runs and butt welds were produced in plate and tube using the gas tungsten arc process, the butt welds employing autogenous root runs with subsequent passes incorporating ERNiCrMo-3 filler. Welding was carried out with arc energy from 0.25 to 2.5kJ/mm, and with pure argon or argon/3% nitrogen shielding gas.

Tests were undertaken in $10\%FeCl_3.6H_2O$ to define a critical pitting temperature, and potentio-dynamic scans were carried out in 3%NaCl at 70°C to derive pitting potential data. The test welds were examine metallographically, with analysis of weld metal nitrogen contents. X-ray diffraction (XRD) examination was used to identify subsidiary phases, with energy dispersive X-ray (EDX) analysis of the solidification structure.

All autogenous welds produced were susceptible to preferential pitting corrosion, associated with segregation of alloying elements. Interdendritic sigma phase was also observed. Relative to base metal, pitting potentials were reduced by up to 500mV, and critical pitting temperatures by up to 30°C. However, weld metal pitting resistance was influenced by arc energy, high arc energy being detrimental. Using Ar shielding, the nitrogen content of the fused zone was below that of the parent steel; loss was prevented with $Ar/3\%N_2$ shielding and, although nitrogen recovery was not entirely consistent, nitrogen levels above the base metal were obtained, giving improved pitting characteristics by both test methods.

It was concluded that, in many applications, high alloy austenitic steels can be welded autogenously without unacceptable loss of corrosion resistance. Further, by using low arc energy and $Ar/3\%N_2$ shielding gas, the pitting resistance of autogenous joints was equivalent to that of weldments produced with ERNiCrMo-3 filler.

Key terms: pitting corrosion, stainless steel, weld metal.

Introduction

High alloy austenitic stainless steels, typified by the UNS S31254 specification, resist pitting, crevice attack and stress corrosion cracking in chloride media and are used extensively for sea water applications, eg piping and process systems in offshore oil and gas rigs, and desalination units (1). In addition, such materials have found use in bleach plants, where demands for energy conservation and pollution control have resulted in increased plant operating temperatures and higher chloride concentrations.

The corrosion resistance of weld metals in highly alloyed austenitic stainless steel produced autogenously or with matching composition fillers is invariably inferior to that of the base metal (2-6). As a consequence of the primary austenite solidification, Mo and Cr segregate to the interdendritic regions in the weld metal. This leaves the dendrite cores lean in these elements, and they become sites for preferential attack.

To overcome preferential weld metal corrosion, current industrial practice is to adopt Ni-based fillers with circa 20%Cr and 9%Mo (6). Although segregation still occurs, the Mo and Cr levels in the dendrite cores remain above that of the parent material, and satisfactory service over many years has been achieved by the use of such fillers. However, the necessity to add sufficient filler complicates the welding operation, and for applications, such as root runs in pipe welds, autogenous welding is of considerable practical advantage.

This paper summarises work undertaken at TWI to examine the effects of welding arc energy, travel speed and shielding gas practice on the pitting resistance of autogenous gas tungsten arc (GTA) welds. Pitting corrosion resistance studies were undertaken using potentiodynamic scanning and the ferric chloride immersion test.

Experimental Programme
Materials and Welding

Two parent steel plates (1C380 and 1C757) and one tube sample (1C638), conforming to UNS S31254, were investigated. The two plates were 5mm thick whilst the tube had a wall thickness of 6mm and an outside diameter of 50mm (Table 1).

Mechanised autogenous GTA bead on plate (BOP) melt runs were produced on the plate steels in the flat position at a range of arc energies. The runs were made at the same travel speed, with one exception at a higher traverse rate. A "V" joint preparation, with an included angle of 100°, was used for multi-pass circumferential butt welds in the pipe, the root face being varied according to arc energy. Again, arc energy and travel speed were varied, although because of process instability at high currents, it proved impractical to make a satisfactory root pass at arc energy conditions greater than 1.75kJ/mm. Pure Ar backing gas was employed and 1.6mm ERNiCrMo-3 filler wire was used for the fill passes. Two series of BOP melt runs and butt welds were produced, one with pure Ar shielding, the other with Ar/3%N_2 shielding.

Examination

Transverse sections were taken for metallographic examination from each weld. Two etchants were used, namely 20%H_2SO_4 + 0.1g/L NH_4SCN at approximately 2V, and an aqua regia based solution (50ml HCl, 5ml HNO_3, 50ml H_2O + 0.5g $SnCl_2$ and 0.5g As_2O_3 at 55°C). A Magne-Gage was employed to check for the presence of any magnetic phases. In addition, X-ray diffraction analysis was carried out on a longitudinal section of the root of a butt weld and a parent material sample, with energy dispersive analysis (EDX) analysis of the solidification structures developed over the arc energy range used. Triplicate nitrogen

determinations were made on the melt runs and root deposits, although samples from the low arc energy weldments may have contained some parent material.

Corrosion Testing

Potentiodynamic studies. Potentiodynamic scans were undertaken on coupons extracted longitudinally from the melt zones made with pure Ar shielding gas in material 1C380. The coupons, of approximately 40x100mm, were ground back to remove any overfill (or undercut) and prepared by grinding all faces to a 600 grit finish. Each coupon contained weld metal, HAZ and parent steel, all of which were exposed to the test solution. The test solution of 3%NaCl at +70°C was purged with nitrogen for approximately 1 hour after the sample was loaded. The scan rate was 0.1mV/sec, and cell voltage was increased in the anodic direction until the specimen current density reached approximately $1.0mA/cm^2$, at which point the direction of scanning was reversed. To avoid crevice effects, the samples were not masked off in any way, but a convenient length was dipped into the test solution. The surface area of each coupon exposed to the solution was obtained after it had been loaded in the cell.

Ferric chloride tests Direct exposure tests in $10\%FeCl_3.6H_2O$ were conducted following ASTM G-48 on all autogenous GTA runs from both parent steels and on the butt weld root pass regions ie the inner tube surface. Longitudinal test coupons approximately 20mmx40mm were extracted from each melt run in the parent plates. The overfill and undercut were again dressed off to produce a uniformly flat sample and all faces were finished to 220 grit. Test coupons from the welded tube material were slightly smaller, 20x30mm, and were prepared by descaling using wire brushes and pickling in a $20\%HNO_3+10\%HF$ solution at 40-50°C. In this case the weld overfill was not removed. As for the potentiodynamic tests, the ferric chloride coupons contained fusion zone, HAZ and parent steel, and all three regions were exposed to the test solution. Exposure to the ferric chloride solution was for periods of 23 hours at set temperatures, the temperature increasing by 2.5°C for each exposure period. Coupons were weighed at the start and finish of each exposure and examined visually for the onset of pitting. Testing was continued until gross pitting occurred or a substantial weight loss was recorded.

Results

Metallurgical examination

Chemical analyses of the base steels are given in Table 1, with a representative microstructure in Fig 1. The microstructure in all three steels was fine grained and fully austenitic.

Sections through weld metals are illustrated in Fig.2. All fused regions showed dendritic solidification to austenite, with the arm spacing increasing from about 2 to 10μm as the heat input was raised from 0.25 to 2.5kJ/mm (Fig.3). Little difference was observed between the microstructures of the 1.25kJ/mm welds made at different travel speeds. The expected segregation was evident from EDX analysis, but was not clearly related to welding conditions (Table 4). Small amounts of a second phase were observed in sections from all arc energies. The proportion of this interdendritic phase apparently increased with arc energy, particularly when pure Ar shielding was used (Table 3). There was no magnetic attraction from the samples using a Magne-Gage indicating that the phase was not ferrite. However, the XRD scans indicated the presence of sigma phase in the weld metals, but not in base metal.

Nitrogen analysis

In both the melt runs and butt welds, the introduction of nitrogen into the shielding gas generally increased the weld metal nitrogen level relative both to the parent steels and to runs made with pure argon shielding, as illustrated in Fig.4. There was no obvious systematic effect of arc energy on deposit nitrogen level, although nitrogen seemed to be increased by higher travel speed. Nitrogen recovery varied by up to 0.03% along a weld (Table 5), and to some degree between the steels.

Corrosion Tests

Potentiodynamic Studies. Typical scans on melt runs made in material 1C380 with pure Ar shielding are given in Fig 5. Noting that the current increase at above 1V stems largely from oxygen evolution, Fig 5 shows a constant increase in current with increasing potential. For base metal, once the scan was reversed, the passive film reformed and current flow was reduced: with weld samples, significant film breakdown and pitting occurred, and the current continued to increase after scan reversal, giving a hysteresis loop.

The samples tested incorporated melt zone, HAZ and base steel, while the area of melt zone in the test sample varied depending upon the welding conditions. However, pitting appeared to develop initially in weld metal, and from Fig 6, an increase in arc energy led to a reduction in potential for both pit initiation (0.05mA/cm^2) and pit propagation (1mA/cm^2).

Ferric chloride tests. In all cases, as the test temperature was raised there was good agreement between visual identification of pitting and commencement of weight loss. Critical pitting temperatures (CPTs) defined by first observation of a pit or, say, 10mg weight loss were within 5°C, and generally 2.5°C. Results for a 10mg weight loss criterion are shown in Fig 7 for the melt runs and in Fig 8 for the butt welds. Regardless of whether Ar/3%N$_2$ shielding gas was used, increasing the arc energy reduced the corrosion resistance of the melt zone. Further, addition of 3% nitrogen to the shielding gas generally resulted in an increase in the CPT, the effect being more consistent with the butt welds, although even with the addition of nitrogen to the shielding gas, and given a low arc energy, the CPT of the melt zones were 10-15°C lower than that for the parent material. Increasing the travel speed did not have a consistent effect on the CPT in either melt runs or butt welds for the shielding gases investigated.

Pitting in some of the test coupons occurred in the root weld deposit. Higher magnification examination suggested that the pitting attack occurred along the second phase boundaries (Fig.9). Pitting in other coupons, especially those made with Ar/3%N$_2$ shielding, initiated along the weld fusion boundary, with some growth into the heat affected zone (Fig.10).

Discussion
Control of Weld Metal Nitrogen Content

The beneficial effects of nitrogen on pitting corrosion resistance in highly alloyed stainless steels, as illustrated by the high factor attributed to nitrogen in various pitting indices, have been well documented (4-6). It is also well recognised that autogenous welding with inert gas shielding (or in vacuum) leads to nitrogen loss. It is therefore important to control the weld

metal nitrogen level. As found by other workers (7), the addition of nitrogen to the shield gas does effectively increase deposit nitrogen content (Fig 4).

Nitrogen recovery was not entirely consistent, and could vary by up to some 0.03% along a weld, although the variation was normally less than this value. Further, nitrogen pickup differed somewhat between the steels, some melt runs in 1C380 made with $Ar/3\%N_2$ shielding gas having nitrogen contents below the base metal level. The reasons for this behaviour are not clear, although the process instability noted at above about 1.75kJ/mm may have been contributory. More consistent nitrogen recovery was obtained in the butt welds, and it may be possible to obtain even higher weld metal nitrogen contents by the addition of more than $3\%N_2$ to the shielding gas. Caution is, however, necessary, since this approach is likely to cause unacceptable degradation of the tungsten electrode.

Other work has shown (8) that nitrogen segregation may be less significant in weld metal than suggested by its high factor in pitting indices derived for wrought base metal. Nonetheless, Figs 7 and 8 indicate an overall beneficial effect of nitrogen on weld metal pitting resistance. Considering the melt runs, welds made in 1C757 with $Ar/3\%N_2$ shielding performed better than either series of welds in 1C380. This difference is attributed to different nitrogen levels since other elements which determine corrosion resistance (namely Cr and Mo) are similar for both steels, (Table 1).

Effect of Welding Conditions

The reduction in corrosion resistance with increase in arc energy was consistent for melt runs in both parent steels welded using two shielding gases, and for the tube butt welds. For the melt runs, this trend was found by both corrosion methods used. The polarisation data in Fig 6 indicate a drop in pitting potential of up to some 500mV from the parent steel value. Similarly, for the $FeCl_3$ corrosion tests, an increase in arc energy from 0.25kJ/mm to 2.5kJ/mm is accompanied by a reduction in CPT of approximately 10–30°C, depending upon alloy composition, weld configuration, shielding gas and pitting resistance criterion. These shifts are significant, and there is clearly an advantage in welding high alloy steels at minimal arc energy. It does not appear that travel speed has a major influence on pitting behaviour, although the range employed was fairly small.

A similar effect of arc energy on weld metal behaviour has been reported previously (3) but the mechanism has not been identified. While Garner considered it due to a change in the orientation of the columnar dendrites at the surface of the weld metal, this is unlikely to be the cause in the general case. Certainly, the microstructures in Fig 2 do not indicate any clear change in solidification pattern with varying arc energy. Three reasons can be postulated for degradation in corrosion resistance with increasing arc energy, namely loss of nitrogen, an increase in second phase particles and more extensive residual segregation at higher arc energy levels.

On the basis of the current results, nitrogen level was shown to be effectively independent of arc energy. Hence, an effect due to varying nitrogen can essentially be discounted.

The volume fraction of the second phase determined in the root pass of the butt welds increased with arc energy (Table 3). The phase was non–magnetic, and, from the XRD studies, is most probably sigma, or other intermetallic, phase. Its formation would be

enhanced by the segregation of Cr and Mo to interdendritic regions, and it would increase in volume fraction with cooling time, as experienced in higher arc energy runs. The effect of such intermetallic particles on corrosion behaviour is likely to be adverse by denuding the surrounding matrix of Cr and/or Mo. At the same time, the amount of sigma phase did not clearly increase in the $Ar/3\%N_2$ weld beads, even though these also displayed reduction in pitting resistance at high arc energy, and further work is necessary to clarify the situation.

Autogenous GTA melt runs in this alloy class solidify as primary austenite, with rejection of ferrite–stabilising elements at the advancing liquid/solid interface. The EDX data in Table 4 do not show an obvious effect of arc energy on segregation, but the spot analysis size of some $2\mu m$ is of the same order as the solidification structure. Hence, the extremes of segregation are unlikely to be identified by EDX analysis. While diffusion will occur in both liquid and solid states, the effects of varying arc energy and cooling cycle on resultant weld metal segregation have not been defined. Segregation during solidification would be less marked with more rapid solidification (9), but it is likely that solidification rate was in fact fairly constant over the range of welding conditions used. The fine dendrite spacing at low arc energy indicates a reduction in cooling time between liquidus and solidus (10), but given the accompanying steeper temperature gradient, this does not necessarily mean a marked change in solidification rate. Homogenisation by solid state diffusion would be limited by the low diffusion coefficients particularly of substitutional elements in austenite, although it can be remarked that homogenisation would be enhanced by the fine structure at low arc energy.

Practical Implications

It can be concluded that, to optimise autogenous GTA weld metal corrosion resistance, low arc energies and nitrogen bearing shielding gases should be employed. Such practice could be adopted in, for example, the root pass of a pipe weld, and a major point is that the CPTs obtained in $FeCl_3$ of about 50–55°C are directly comparable with reported data on welds made using Ni–base fillers (4–8). The arc energies employed in this study were selected to investigate the effect of corrosion behaviour and values as low as 0.25kJ/mm may not be achieved in practice. Nevertheless, arc energy levels of say 0.50 to 0.75kJ/mm for autogenous TIG root passes are practicable, and, given such small beads, some degree of elemental diffusion and homogenisation by fill passes may also be of benefit. In this regard, it should be feasible to use higher arc energy for second and subsequent fill passes, provided that the root is not remelted.

Conclusions

1. The arc energy used affected melt zone corrosion resistance, with a high arc energy being detrimental. Over the arc energy range studied of 0.25 to 2.5kJ/mm, critical pitting temperatures in ferric chloride were reduced by up to 30°C, and pitting potentials by 500mV. Varying travel speed from 100–150mm/min did not have a major effect on pitting behaviour.

2. Weld metal nitrogen content was increased by employing Ar shielding gas containing $3\%N_2$. Autogenous GTA runs with higher nitrogen contents possessed superior corrosion resistance compared with lower nitrogen weld beads.

3. In many applications, high alloy austenitic stainless steels can be welded autogenously without unacceptable loss of pitting resistance. Optimum results are expected by keeping arc energy low and by the use of nitrogen-bearing shielding gases.

Acknowledgements

References

1. Olsson J: Stainless Steel Industries, Jan, 1990.
2. Garner A: Welding Journal January 1983 **62** 1 27–34.
3. Garner A: Corrosion 1979 **35** 3 March 108–14.
4. Suutala N and Kurkela M: Proc conf Stainless Steels 84. The Metals Society 1984 240–247.
5. Ogawa T, Aoki S, Salcameter T and Zauzen T: Welding Journal May 1982 **61** 5 139s–148s.
6. Rabensteiner G: Welding in the World **27** 1/2 1989 2–13.
7. Suutala N, Grekula A and Kemppainen J: Paper presented at "Sixth international symposium on corrosion in the pulp and paper industry", Helsinki.
8. Marshall P I and Gooch T G: Proc conf "Corrosion '92", NACE, Nashville, paper 296.
9. Nakao Y and Nishimoto K: IIW Doc IX-1666-92.
10. Bower T F, Brody H D and Flemings M C: Trans ASME, **236** May 1966 624–634.

Table 1   Chemical compositions of parent steels

Steel identity	Element, wt %										PI*
	C	S	P	Si	Mn	Ni	Cr	Mo	Cu	N_2	
1C380	0.016	0.011	0.029	0.62	0.50	18.0	19.8	6.2	0.71	0.184	43.3
1C757	0.016	<0.001	0.018	0.39	0.37	18.1	19.8	6.0	0.64	0.207	42.9
1C638	0.018	0.007	0.03	0.72	0.80	17.7	19.5	6.19	0.80	0.207	43.8
UNS31254	0.020 max	0.010 max	0.030 max	0.80 max	1.00 max	17.50–18.50	19.50–20.50	6.00–6.50	0.50–1.00	0.180–0.220	

*Pitting Index = PI = Cr + 3.3Mo + 16N

Table 2   Welding conditions, bead on plate (BOP) runs, root and fill passes

Weld	Current, A	Voltage, V	Travel speed, mm/min	Arc energy, kJ/mm
BOP/Root runs	56	8.0	100	0.25
	83	10.0	100	0.5
	120	10.4	100	0.75
	180	11.5	100	1.25
	260	12.0	150	1.25
	220	13.0	100	1.75
	240	14.0	100	2.00
	260	16.0	100	2.50
Fill passes	110	10.0	340	0.20

Polarity = DC, electrode negative

Table 3 Percentage of second phase in root weld metal

Arc energy, kJ/mm	Ar shielding	Ar/3%N$_2$ shielding
0.25	0.5	3.5
0.50	2.5	2.0
0.75	2.5	3.0
1.25	5.0	3.5
1.25*	6.5	2.0
1.75	4.5	3.0

*150mm/min

Table 4 Results of EDX analysis: GTA runs in 1C380 with Ar shielding

Region analysed	Arc energy, kJ/mm	Element*, wt % (Mean of 6 readings)		
		Mo	Cr	Ni
Dendrite cores	0.5	5.0	18.4	17.5
	0.75	5.2	18.4	17.2
	2.50	4.7	18.3	17.6
Interdendritic regions	0.5	7.0	20.0	17.4
	0.75	6.9	19.5	17.7
	2.5	7.1	19.7	17.8

Table 5 Nitrogen contents of butt weld root passes

Arc energy, kJ/mm	Nitrogen content, wt %	
	Ar shielding	Ar/3% N$_2$
0.25	$\dfrac{0.171-0.190}{0.180}$	$\dfrac{0.199-0.218}{0.212}$
0.5	$\dfrac{0.211-0.242}{0.228}$	$\dfrac{0.263-0.291}{0.274}$
0.75	$\dfrac{0.174-0.184}{0.179}$	$\dfrac{0.248-0.249}{0.248}$
1.25	$\dfrac{0.204-0.207}{0.206}$	$\dfrac{0.256-0.262}{0.259}$
1.25 (150mm/min)	$\dfrac{0.205-0.207}{0.206}$	$\dfrac{0.265-0.279}{0.272}$
1.75	$\dfrac{0.204-0.207}{0.205}$	$\dfrac{0.249-0.256}{0.254}$

Parent material $\dfrac{0.205-0.209}{0.207}$, Three readings and expressed as $\dfrac{minimum-maximum}{average}$
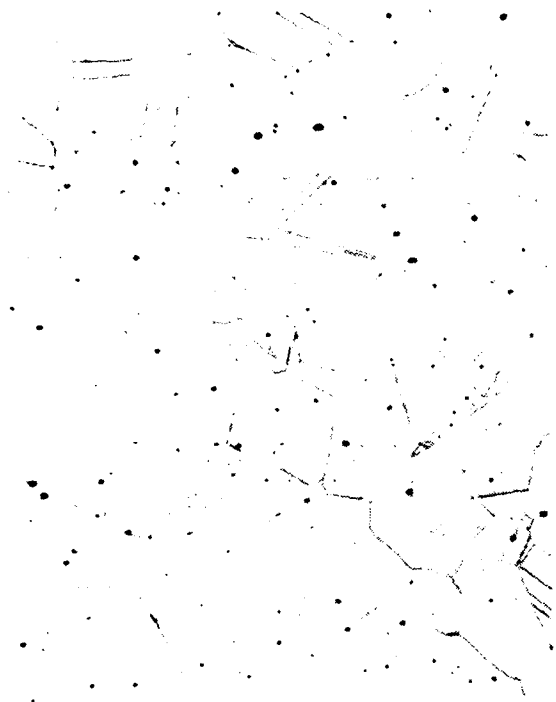
Fig.1 Microstructure of steel 1C 757, ×200.
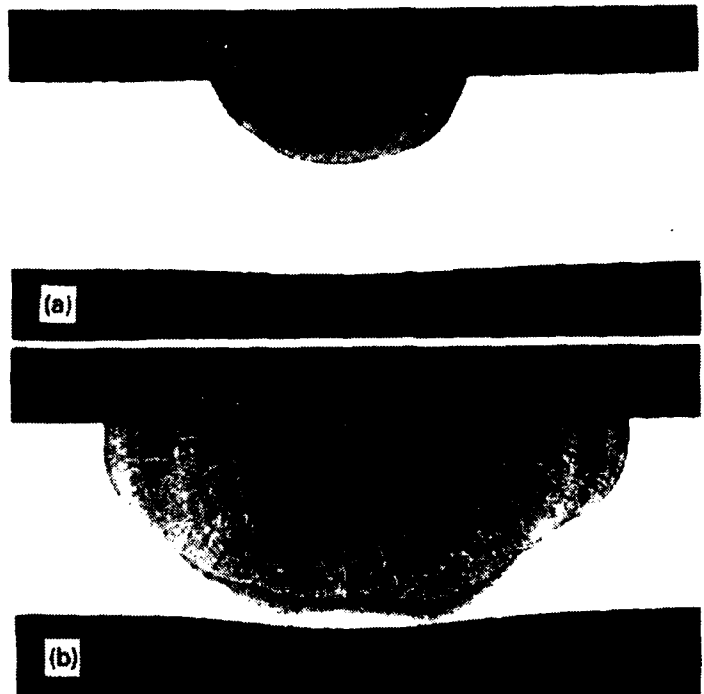
Fig.2 Representative melt run cross-sections: 1C 380: Ar, ×5:

a) 0.75 kJ/mm; b) 2.0 kJ/mm.
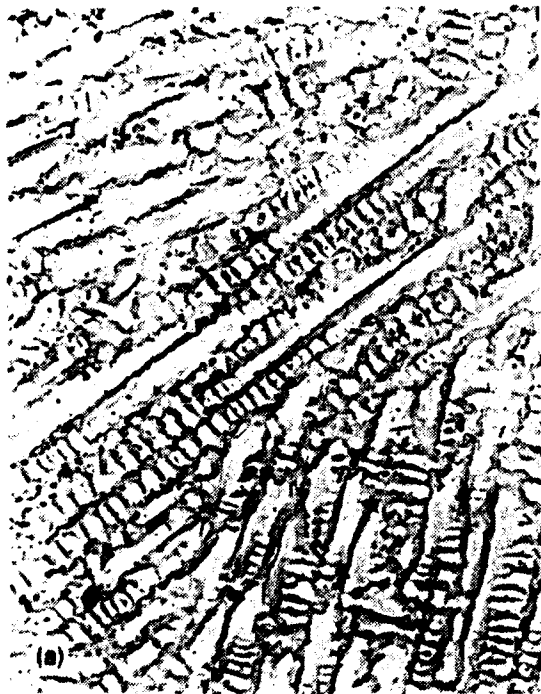
Fig.3 Melt run microstructures: 1C 380: Ar, ×500:

a) 0.75 kJ/mm; b) 2.5 kJ/mm.
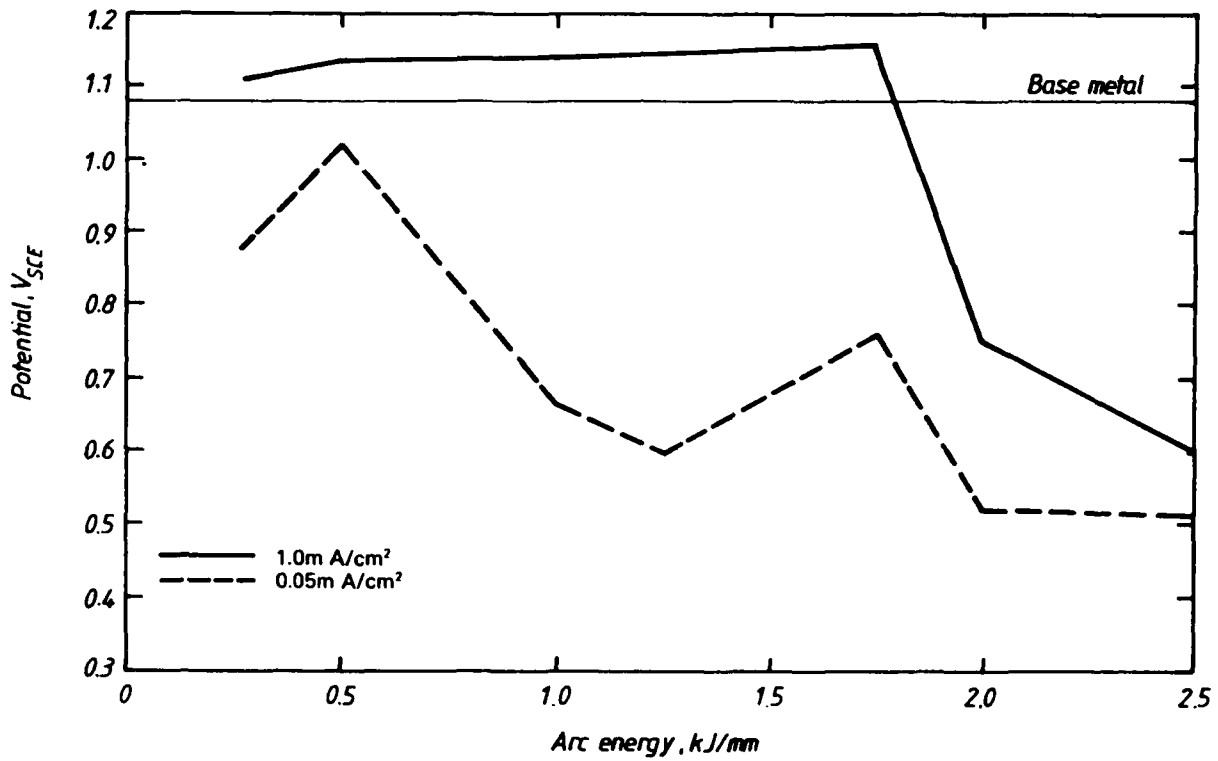
Fig.6 Effect of arc energy on pit initiation (0.05 mA/cm²) and propagation (1.0 mA/cm²) potentials: 1C 380 melt runs: Ar shielding.
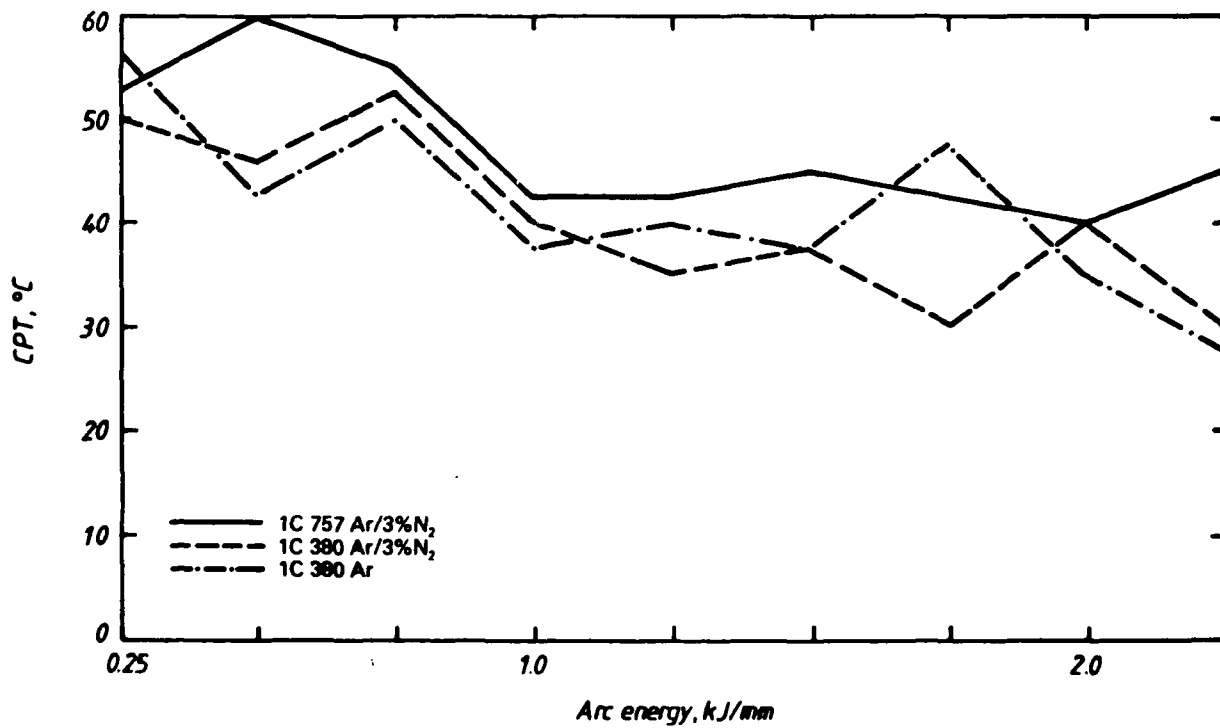
Fig.7 Effect of arc energy on FeCl₃ CPTs: GTA melt runs.
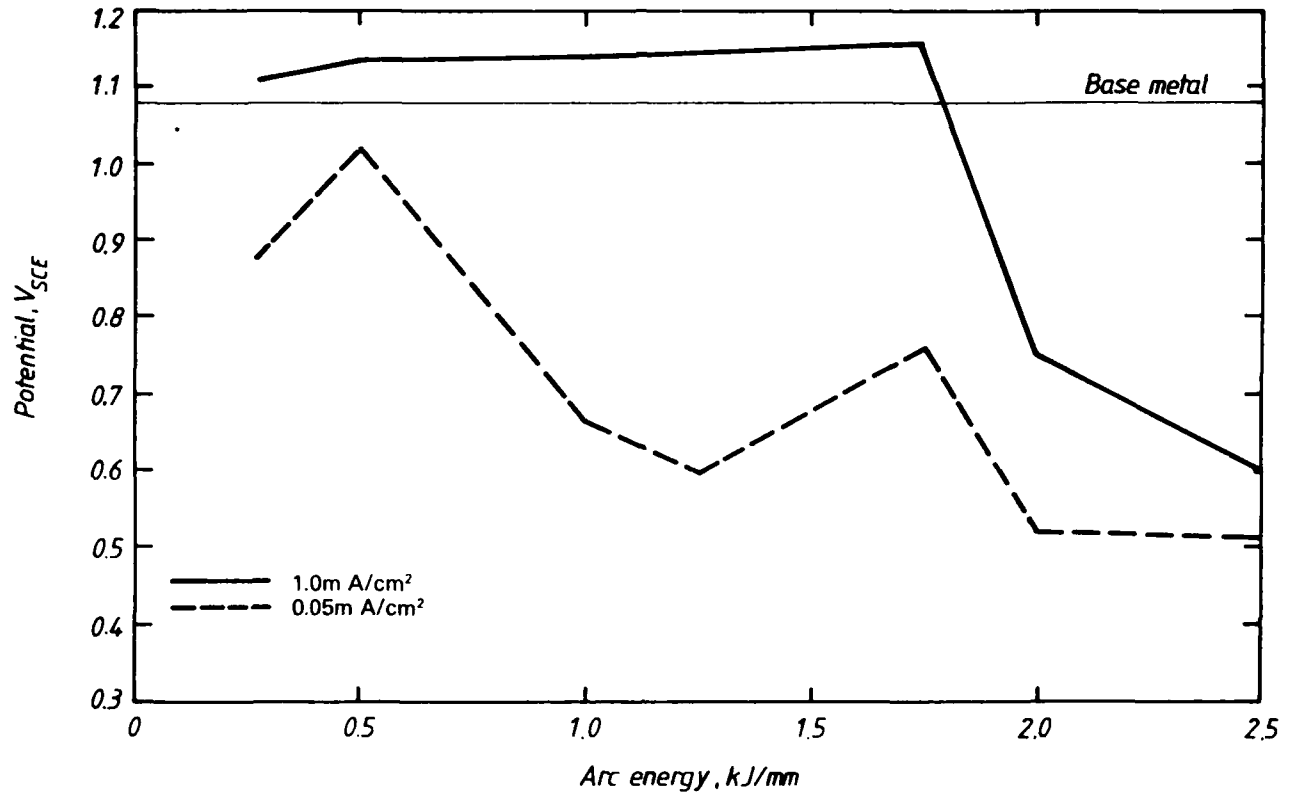
Fig.6 Effect of arc energy on pit initiation (0.05 mA/cm²) and propagation (1.0 mA/cm²) potentials: 1C 380 melt runs: Ar shielding.
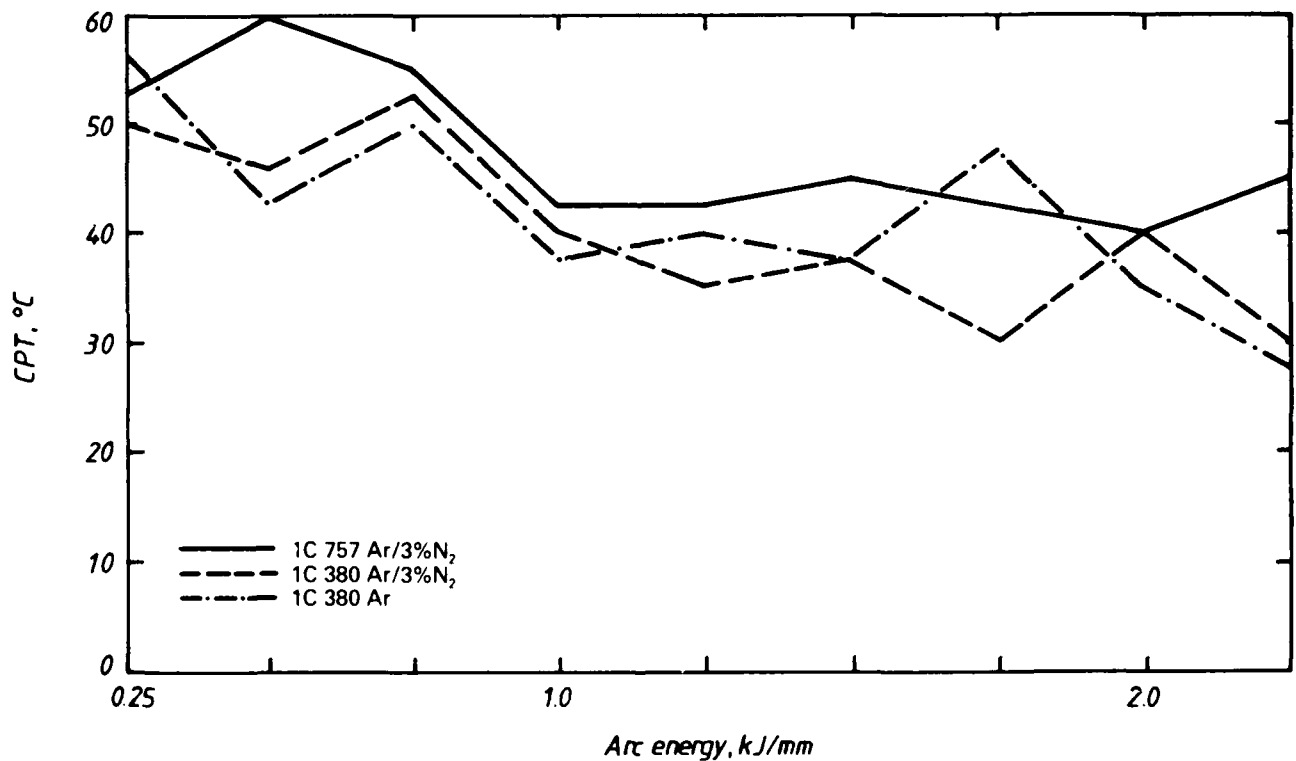
Fig.7 Effect of arc energy on FeCl₃ CPTs: GTA melt runs.
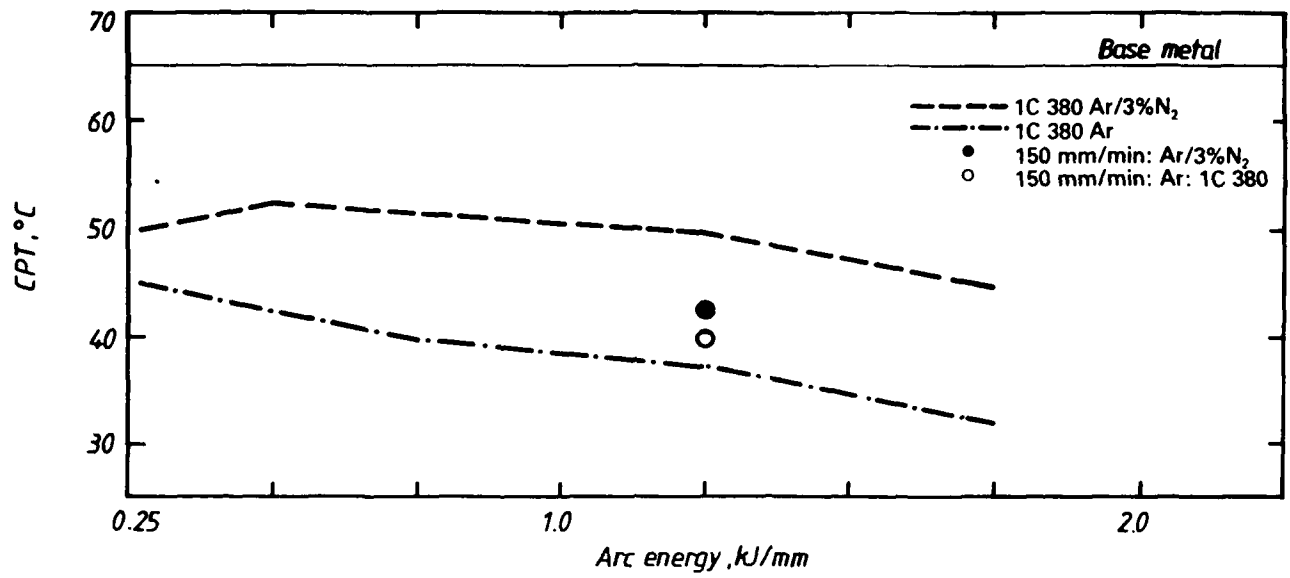
Fig.8 Effect of arc energy on FeCl₃ CPTs: butt weld roots.
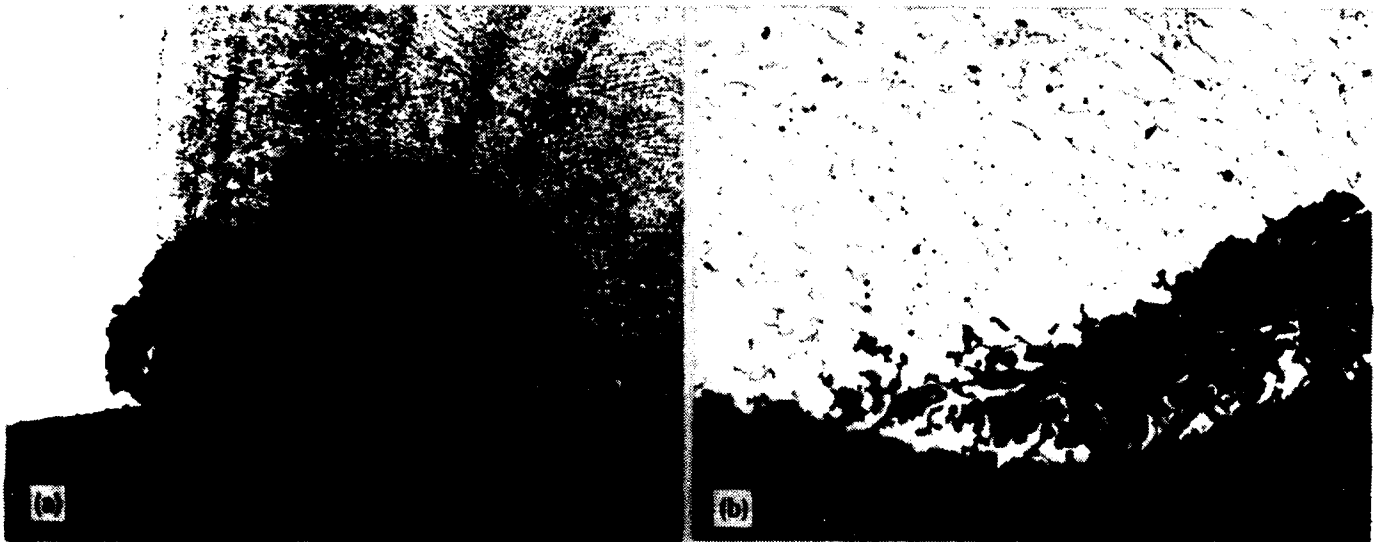
Fig.9
a) Corrosion pit in butt weld root bead: 0.75 kJ/mm: Ar shielding, ×25;
b) Preferential corrosion at second phase in butt weld root run: 0.75 kJ/mm: Ar shielding, ×200.
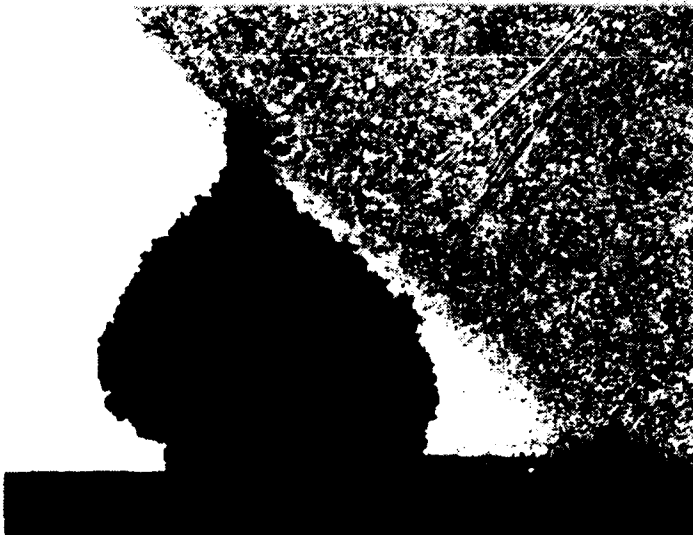
Fig.10 Fusion boundary pitting in butt weld root: 1.25 kJ/mm: Ar/3%N₂ shielding, ×25.

Localized Corrosion of the Unmixed Zone in Nickel-Base Alloy Weldments

L. H. Flasche
Haynes International, Inc.
1020 West Park Avenue
Kokomo, Indiana

H. S. Ahluwalia, PhD
Haynes International, Inc.
1020 West Park Avenue
Kokomo, Indiana

Abstract

The existence of an unmixed zone at the fusion line of a weldment has been recognized for more than 20 years. The effect of that distinct region on the corrosion resistance of high alloy weldments has not, however, been addressed in any detail. This paper examines the extent and the corrosion resistance of the unmixed zone in a nickel-base solid solution strengthened material (UNS number N06985) welded using both matching filler material (UNS N06985) and overalloyed welding filler material (UNS N06022).

Laboratory immersion corrosion testing was conducted in an oxidizing acid environment and an oxidizing acid-chloride environment. These environments were used to characterize the uniform and pitting corrosion resistance of the base material, as well as various weldment conditions. Weldment corrosion results were then compared with the results of unwelded base material to assess total weldment corrosion resistance. From this, it was concluded that unmixed zones have increased susceptibility in oxidizing acid-chloride (pitting corrosion) environments. On the other hand, no preferential attack was noted at the unmixed zone in the oxidizing acid (uniform corrosion) environment.

In addition to immersion corrosion testing, Auger electron spectroscopy (AES) was conducted on several weldments to characterize the solidification structure of both the unmixed zone and the fusion zone. AES area scan microchemical analysis confirmed that a narrow cast microstructural region exists, between the wrought base material and an overalloyed weld fusion zone, which has the composition of the wrought base material. In addition, by using point count AES analysis techniques, it was confirmed that the unmixed zones, as well as the fusion zones, have regions depleted in molybdenum. The molybdenum ratio of the bulk material to these depleted regions was between 0.7 and 0.8.

Key terms: GMAW, GTAW, nickel-base alloys, overalloyed weldments, pitting corrosion, SMAW, uniform corrosion, unmixed zone, welding

Introduction

The use of nickel-base welding filler materials to join lower alloy base materials has been suggested and recommended for many years. It is generally believed that when overalloyed filler materials are used, the fusion zone (the weld metal) will be immune to corrosion attack relative to the base material and thus the base material will become the governing factor in the corrosion resistance of the weldment. From an aqueous corrosion standpoint, alloy 625 (UNS N06625) is often considered for such overalloyed filler metal applications.

As C-22™ alloy (UNS N06022) has improved corrosion resistance when compared to N06625, N06022 is a natural upgrade over N06625 and is being increasingly considered for such overalloyed welding situations. As noted in the Background Section, local corrosion attack has been noted at the fusion boundary when various nickel-base filler metals have been used to join lower alloyed base material. One example of such attack is shown in Figure 1. In this case, N06022 welding coated electrodes were used to join HASTELLOY® alloy G-3 (UNS N06985) base material.

Because welding was performed using the shielded metal arc welding (SMAW) process, the level of nonmetallic inclusions in the fusion zone is expected to be high and uniformly distributed. On close examination of the interface (see lower photomicrograph in Figure 1), however, there is a region of cast microstructure that contains no inclusions. Such a cast region that appeared not to have mixed with the welding filler material was identified as an example of an "unmixed zone" and as such could explain the local fusion boundary attack. Other accounts of fusion boundary corrosion attack are discussed in the literature review presented in the Background section of this paper.

The purpose of this work was to investigate the effect of unmixed zones on the corrosion resistance of overalloyed weldments. In this work, a 7% molybdenum containing nickel-base material (UNS N06985) was welded using a matching filler material (N06985) and an overalloyed filler material (N06022). Two immersion corrosion tests were used to simulate oxidizing acid environments (designed to promote uniform-type corrosion attack) and oxidizing acid-chloride environments (designed to promote localized pitting-type attack). In each case, the region at the fusion line was carefully examined for selective corrosion attack that might have been caused by the presence of an unmixed zone. In addition to corrosion testing, optical metallography and Auger electron spectroscopy (AES) were performed to characterize the structure and composition of the various weldment regions.

Background

The existence of an "unmixed" region at the fusion line in weldments was identified nearly 30 years ago. Savage referred to this region as the "superheat-melt-back-region" in a paper in 1966.[1] In later work, this region was redefined as the "unmixed zone."[2,3] Matthews reports that such unmixed zones form "when the melting range of the consumable electrode is equal to or greater than the melting range of the base material."[2] A proposed definition for the unmixed zone was presented in the Szekeres paper in 1976.[3] The current American Welding Society definition of the unmixed zone is: A thin boundary layer of weld metal, adjacent to the weld interface, that solidifies without mixing with the remaining weld metal.[4]

Measurements of unmixed zone widths for several welding processes were investigated using 304 base metal and 316 filler material. It was concluded that "the width of the unmixed zone increases with increasing arc energy and dilution."[5]

Limited information is available on the effect of the unmixed zone on corrosion resistance of weldments. One major welding study examined the effect of unmixed zones on the stress corrosion cracking of 304L stainless steel welded with 310 and 312 stainless steel filler materials.[6] The unmixed zones that were investigated in that work solidified with a two-phase (austenite + ferrite) microstructure. The corrosion attack noted in that work either showed environmentally assisted cracking resulting from dissolution of the ferrite phase in the unmixed zone or base metal SCC unrelated to the unmixed zone.

Concerns over corrosion of unmixed zones in single-phase solid-solution strengthened corrosion-resistant alloys are raised in two papers. First, Garner in a paper on pulp bleach plant corrosion made several references to possible selective attack at the unmixed zone when nickel-base overalloyed filler metals (N06625) were used on lower alloy base materials.[7] More recently, Norby reported preferential interface corrosion attack of nickel-base alloys in a nitric + hydrofluoric acid environment.[8]

Procedure

Immersion Corrosion Testing

Corrosion test samples were fabricated using the gas tungsten arc (GTAW) and the gas metal arc (GMAW variable pulse mode) welding processes. Samples were prepared using both matching welding filler material and overalloyed welding filler material. The welding parameters used in this work are detailed in Table 1. Nominal chemical compositions of the various alloys are indicated in Table 2.

Corrosion testing was conducted on duplicate samples per standard laboratory procedures. Before testing, coupons were grit blasted in a mild alumina abrasive slurry. Testing was conducted using the ASTM G-28A (boiling ferric sulfate - 50% sulfuric acid) test, an oxidizing acid environment, and the NaCl-HCl test, an

oxidizing acid-chloride environment. The chemical compositions of the environments are detailed in Tables 3 and 4.

The ASTM G28A testing was conducted for 120 hours at boiling and was used to determine the resistance to uniform (i.e., nonpitting) corrosion attack. Results from this test are reported as millimeters per year (mmpy) of corrosion attack.

The NaCl-HCl test was conducted to determine resistance to localized corrosion (pitting) attack. NaCl-HCl corrosion testing was conducted for 24 hours at various test temperatures to determine the transition temperature, measured at 2.5°C increments, between a pitting and a nonpitting condition. This transition temperature is called the critical pitting temperature (CPT). Pitting was determined by visual inspection using a stereomicroscope at a magnification of 10X. To provide complete corrosion attack documentation, weight loss data was determined and is reported as millimeters per year (mmpy) of corrosion attack at the critical pitting temperature.

Comparative Chemical Analysis
Chemical analyses of the various weld fusion zones were determined using a scanning electron microscope (SEM) equipped with an energy dispersive X-ray spectrometer (EDS). Analysis of each weld pass for the four weldment conditions was determined and then divided by the actual composition of the wrought base material. Standard SEM laboratory procedures were used. The accelerating voltage was 30 KV.

Metallography
Metallographic samples were mounted, polished and etched using standard laboratory techniques. After final alumina polishing, samples were electropolished in a solution of sulfuric acid + methanol and then electrolytically etched in a solution of hydrochloric + oxalic acids.

Auger Electron Spectroscopy
Small cross-section gas tungsten arc welded (GTAW) samples were removed from matching and overalloyed corrosion testing coupons. The samples were mounted and polished through the diamond polishing stage. Samples were then removed from the mount and lightly electrolytically etched in a solution of 10% hydrochloric acid + methanol. The polished and etched samples were thoroughly cleaned and examined in the as-etched condition. Analysis was conducted using a Perkin Elmer Phi 660 Scanning Auger Microprobe. The surface was sputter cleaned for at least 5 minutes before analysis and was sometimes sputter cleaned between analyses. Raw chemical analysis data was reported in atomic percent. Raw (atomic percent) data was converted into weight percent for comparison to nominal chemical analysis information.

Results
Immersion Corrosion Testing
Corrosion results for the oxidizing acid environment are documented in Table 3. Corrosion results for the oxidizing acid-chloride environment are documented in Table 4. Graphical presentations of those results are shown in Figure 2. Photomicrographs showing the key metallurgical features of the various weldment conditions (both uniform and pitting environments) are shown in Figures 3 through 6.

The results of ASTM G28A corrosion testing (see Table 3 and Figure 2) are as expected for such a highly oxidizing environment. Preferential fusion zone etching was noted for each welding condition. Such selective attack of the fusion zone accounts for the generally higher corrosion rates in the as-welded condition as compared to the wrought unwelded base material. The higher corrosion rates noted for the overalloyed filler metal coupons result from the inherently higher corrosion rates noted for N06022 alloy as compared to N06985 alloy in highly oxidizing environments. For example, wrought unwelded N06022 base material corrosion rates in ASTM G28A are 1 mmpy as compared to 0.3 mmpy for N06985 alloy. Of greatest importance to this work, however, is the fact that metallographic examination (see Figure 3) did not reveal preferential fusion line attack under any weldment condition.

Results of the oxidizing acid-chloride corrosion testing are summarized in Table 4. The CPT for each welding condition is plotted in Figure 2. The critical pitting temperature for unwelded wrought base material was 67.5 C (based upon the minor edge pits noted on both samples). The critical pitting temperature, if edge pits were ignored, was 70°C. These results compare well with previously published CPT data for N06985.[9] In contrast, the matching filler metal weldments (N06985 filler metal) showed critical pitting temperatures in the 40-42.5 C range. This represents a drop of about 25 C in critical pitting temperature as compared to the wrought unwelded base material. This lowering in CPT, while larger than seen in other environments (20°C is more typical) and alloy systems, is expected in oxidizing acid-chloride environments. It is attributed to molybdenum segregation that occurs upon solidification.

Results of NaCl-HCl testing of the overalloyed weldment samples again show a lowering of critical pitting temperatures when compared to the unwelded base material. However, the difference here is 10°C rather than 25°C as noted above. This increase in CPT represents an improvement in weldment pitting resistance, but clearly the overalloyed filler material weldments did not achieve corrosion resistance equivalent to the wrought base material.

Results from NaCl-HCl weldment testing show nearly all reported pits were confined to the weld fusion zone. For weldments made using matching filler materials, the pits were usually randomly distributed over the fusion zone surface. On the other hand, results of overalloyed filler metal testing show pitting attack to be more often confined to the boundary between the base material and the weld metal. This was particularly true for the GMAW overalloyed weldment where all observed weld pits were identified as fusion line pits. For the GTAW overalloyed weldments, some fusion zone pitting was observed in addition to fusion line pitting. Examples of fusion line attack are shown in Figures 4 and 5. Notice that pitting initiates at the fusion line, propagates along the fusion line, and then into the wrought base material (probably by crevice corrosion).

These differences in pitting response are due to differences in the chemical compositions among the various welding conditions. The SEM-EDS chemical analysis data shown in Table 5 provides relative composition data as compared to the unwelded base material. The overalloyed weld passes show higher molybdenum and lower iron than the N06985 alloy composition. Further, the GTAW (overalloyed) weldment shows higher iron content and lower molybdenum when compared to the GMAW (overalloyed) weldment. This suggests that the GTAW process produced higher base metal dilution when compared to the GMAW process. The higher molybdenum and lower iron content of the GMAW (overalloyed) weldment, as compared to the GTAW (overalloyed) weldment, would be expected to improve the fusion zone pitting resistance and thus tend to force corrosion attack elsewhere.

Metallographic Examination
Differences in fusion line etching response are clearly visible among the various weldment conditions. Samples that contain matching welding filler materials show an abrupt transition between the wrought base metal and the cast weld metal (see upper photomicrograph in Figure 6). On the other hand, the overalloyed samples show a narrow region at the fusion line that etches very differently (see Figures 1, 3, 4 and 6). Examination of the overalloyed weldment fusion lines at high magnification (see Figure 6) shows a narrow region to have a cast microstructure that is quite different from the bulk as-cast weld fusion zone microstructure. This region is identified as an unmixed zone. It represents base material that melted and then solidified but did not mix with the overalloyed filler material.

It should be noted that unmixed zones are expected no matter what the base/filler metal combination. That is, the matching filler metal weldments also contain unmixed zones. However, because the nominal compositions of the base material and the filler material have the same as-cast composition, the unmixed zone is nominally the same as the fusion zone. Such a condition would therefore not be expected to show differences in etching effects or corrosion resistance. The difference in chemical composition between the thin as-cast N06985 base metal composition and the as-cast composition of the overalloyed filler material accounts for the difference in etching response.

Auger Electron Spectroscopy

AES was used to characterize the chemical composition of the unmixed zone because composition analysis can be obtained in a region 0-3 nanometers from the surface for all elements except hydrogen and helium.[10] The Auger electrons are emitted from a region very near the surface as opposed to the primary x-ray excitation region that can be as large as 1 cubicmicrometer. This near surface capability allows analysis of cast (dendritic) microstructure with a minimum of subsurface composition interaction.

Results of Auger electron spectroscopy chemical analysis (converted to weight percent) are presented in Tables 6, 7, and 8. Table 6 contains data on area scans for both the matching and overalloyed weldment configurations. Table 7 contains data on point analysis of the matching weldment configuration for both the fusion zone and the unmixed zone regions. Table 8 contains data on point analysis for the overalloyed GTAW weldment. Table 9 provides partitioning data for the various fusion and unmixed zones. Finally, Figure 8 provides reproductions of original polaroid scanning photomicrographs of the GTAW weldments used in this investigation. Differences in fusion line structure are evident in these scanning photomicrographs.

It should be understood that the reported microchemical analysis data are not intended to represent absolute composition levels. As the data was collected without benefit of calibrated standards, the data is being used to compare one area or point against another within the microstructure.

The results of area scan analysis show that the chemical analysis of the unmixed zone (overalloyed filler metal weldment) has the same chemical composition as the transition region (unmixed zone) of the matching weldment (see Table 6 and Figure 7). As shown, the molybdenum content for the three regions of the matching filler metal weldment, and two regions of the overalloyed weldment, is near 11%. On the other hand, the molybdenum content of the fusion zone for the overalloyed weldment is reported to be greater than 15%. Iron content as well is shown to decrease significantly in the fusion zone of the overalloyed weldment when compared to either the base material or the unmixed zone. These differences in molybdenum, as well as the differences in other alloying elements, are plotted in Figure 7.

It should be noted that during this area analysis work, care was taken to have the scanned regions significantly larger than any individual microstructural feature such as wrought grains or dendritic structure of the cast material. This should insure that these results represent a true average composition for each region.

Besides the area scan information, individual point analysis information also confirms that the unmixed zone has the composition of the wrought base material. For example, the molybdenum contents of the dendrites of the matching weldment fusion zone and unmixed zone are 9.2% and the dendrite molybdenum content of the overalloyed weldment unmixed zone is 7.4%. This compares with molybdenum content of 12.8% for the fusion zone dendrites of the overalloyed weldment. The very low level of molybdenum in the dendrites of the unmixed zone is a clear indication that no mixing occurred between the overalloyed filler metal and the unmixed zone.

As data is available for both bulk composition (area scan) and composition of the dendrite and interdendritic regions, it is possible to determine partitioning coefficients for the various cast weldment conditions. Such information concerning the segregation of alloying elements is presented in Table 9. Clearly, the most obvious element to show significant segregation is molybdenum. In both the matching and the overalloyed filler metal situations, the ratio of molybdenum in the dendrites compared with the bulk analysis is between 0.7 and 0.8.

Discussion

As molybdenum is the most important alloying element in determining localized (pitting) corrosion resistance in oxidizing acid-chloride environments[11], the differences in molybdenum content among the various regions can help explain the reduced pitting corrosion resistance found during immersion corrosion testing. From the matching filler metal standpoint, the random occurrences of pits over the various fusion zone surfaces

can be explained by the fact that the matching filler metal samples have the same molybdenum content in both the unmixed zone and the fusion zone.

On the other hand, the unmixed zone of the overalloyed weldment has molybdenum content at the dendrite cores of 7.4% compared to 12.8% molybdenum content for the overalloyed fusion zone dendrite cores. Such differences in as-cast minimum molybdenum content will have an effect on pitting corrosion resistance of the various regions in the overalloyed weldments. Further, as the molybdenum content of the dendrites of the overalloyed fusion zones is higher than that of the wrought base material, it is argued that the overalloyed fusion zones possess superior pitting corrosion resistance when compared to the wrought base material. This leaves the unmixed zones with lower molybdenum content than any other region of the overalloyed weldment. Given this, there are three regions, from a corrosion susceptibility standpoint, in an overalloyed weldment. Those regions are the wrought base material, the cast base material (unmixed zone) and the cast welding filler material. Of those regions, the unmixed zone region is the most susceptible to pitting corrosion attack.

Because the unmixed zone region of the overalloyed weldment has a cast microstructure of N06985 alloy composition, that region would be expected to have the same critical pitting temperature as the fusion zone of the matching filler material weldment. Therefore, this should lead to selective pitting attack in the unmixed zone at or near the established critical pitting temperature (40-42.5°C) of the matching composition weldment.

Clearly, the critical pitting temperature of the overalloyed filler metal weldments is about 15°C higher than that of the matching composition filler material. This difference in CPT between the observed matching filler material and the overalloyed filler materials cannot be explained based upon the work conducted. However, it has been established that a susceptible region at the fusion boundary does exist. Because this region has a composition that of the base material, the corrosion resistance of an overalloyed weldment is still controlled by the base material. Further improvements in weldment corrosion resistance can therefore only be obtained by increasing the alloy content of the base material.

Conclusions

1. Based upon immersion corrosion testing in an oxidizing acid-chloride environment, differences in critical pitting temperatures were measured between the wrought unwelded base material and samples welded with matching and overalloyed welding filler materials. The critical pitting temperature was lowest when matching filler materials were used. When overalloyed welding filler materials were used, the critical temperatures increased but did not equal the critical pitting temperature of the unwelded wrought base material.

2. Auger electron spectroscopy (AES) area scan microchemical analysis and optical metallography confirm that a narrow cast region exists between the wrought base material and an overalloyed filler metal fusion zone, which has the composition of the wrought base material. By using point count AES analysis techniques, it was shown that the unmixed zones, and the fusion zones, have regions depleted in molybdenum content. The ratio of the bulk material to these depleted regions was between 0.7 and 0.8.

3. The existence of molybdenum depleted regions in the unmixed zone of an overalloyed weldment explains the preferential pitting corrosion attack that was noted at the weld fusion line.

4. Unmixed zones were observed using three different welding processes (GTAW, GMAW and SMAW). The widest unmixed zone was noted with the gas metal arc welding process and the narrowest zone was noted with the gas tungsten arc welding process.

5. As the unmixed zone has a composition that of the base material, the corrosion resistance of an overalloyed weldment is ultimately controlled by the base material. Therefore, improvements in weldment corrosion resistance may have to be obtained by increasing the alloy content of the base material.

References

1. Savage, W. F.; "What is a Weld?" Aerospace Symposium at Lockheed Aerospace Division, Palo Alto, CA, September 1966, pp 36-37. Addison-Wesley Publishing Co., Inc., 1968.

2. Matthews, S. J. and Savage, W. F.; "Heat-Affected Zone Infiltration by Dissimilar Liquid Metal." Welding Journal, Research Supplement, April 1971.

3. Savage, W. F., Nippes, E. F., Szekeres, E. S.; "A study of Weld Interface Phenomena in Low Alloy Steel." Welding Journal, Research Supplement, September 1976.

4. Standard Welding Terms and Definitions, ANSI/AWS A3.0-89, American Welding Society, Miami, FL.

5. Lukkari, J., Moisio, T.; "The Effect of the Welding Method on the Unmixed Zone of the Weld." Microstructural Science Volume 7 (Proceedings of the Eleventh Annual Technical Meeting of the International Metallographic Society), Elsevier North Holland, Inc. 1979.

6. Baeslack, W. A., Lippold, J. C., Savage, W. F.; "Unmixed Zone Formation in Austenitic Stainless Steel Weldments." Welding Journal, Research Supplement, June 1979.

7. Garner, A.; "Corrosion of Weldments in Pulp Bleach Plants." Welding Journal, September 1986.

8. Norby, B. C.; "Improved Corrosion Resistance of UNS N06030 in Nitric/Hydrofluoric Acid Solutions by Welding with a Dissimilar Weld Wire." Paper number 107, Presented at Corrosion/92, Nashville, TN, April 1992.

9. **HASTELLOY C-22** ALLOY, Brochure H-2019C; Published by Haynes International, Inc., Kokomo, IN, USA.

10. Joshi, A.; "Auger Electron Spectroscopy." Metals Handbook, Ninth Edition, Volume 10, Materials Characterization, American Society for Metals, Metals Park Ohio, 1986.

11. Sridhar, N.; "Effect of Alloying Elements on Localized Corrosion Resistance of Nickel-Base Alloys." International Conference on Localized Corrosion, National Association of Corrosion (NACE), June 1-5, 1987.

Table 1

Welding Parameter Information

Welding Parameters	GTAW	GMAW	SMAW
Base Metal Thickness	UNS N06985 3.2 mm	UNS N06985 3.2 mm	UNS N06985 3.2 mm
Matching Filler Metal Diameter	UNS N06985 3.2 mm	UNS N06985 3.2 mm	n/a
Overalloy Filler Metal Diameter	UNS N06022 3.2 mm	UNS N06022 3.2 mm	UNS N06022 3.2 mm
Preheat temperature	RT	RT	RT
Interpass Temperature	100°C max.	100°C max.	100°C max.
Shielding gas Flow rate	100% Argon 14 L/min	Ar+He+CO_2 mix 16.5 L/min	n/a

Electrical parameters
   Amperage
   Volts
   Travel speed
	DCEN
	250 amps
	9 - 12 volts
	23 cm/min
		DCEP
		90 -110 amps
		18 - 20 volts
		25 - 38 cm/min
			DCEP
			90 amps
			22 - 24 volts
			19 cm/min

Welding Techniques	Airline system; Copper backup	Variable pulse synergic system	manual welding

Table 2

Nominal Chemical Composition of Base and Filler Materials
(weight percent)

Elements	UNS N06985	UNS N06022
Carbon	0.015 max	0.015 max
Chromium	22.0	22.0
Cobalt	5.0 max	2.5 max
Copper	2.0	-
Iron	19.5	3.0
Manganese	1.0 max	0.5 max
Molybdenum	7.0	13.0
Nickel	44.0	56.0
Niobium	0.5 max	-
Phosphorous	0.04 max	0.02 max
Silicon	1.0 max	0.08 max 0.2 max *
Sulfur	0.03 max	0.02 max
Tungsten	1.5 max	3.0

* = Limit for Coated Electrodes (SMAW)

Table 3

Corrosion Results in Oxidizing Acid Test Environment
(reported in mm/y)

	Unwelded Base Metal	GTAW (matching)	GMAW (matching)	GTAW (overalloy)	GMAW (overalloy)
Test 1	0.29	0.41	0.44	0.45	0.49
Test 2	0.32	0.43	0.41	0.44	0.54
Average	0.31	0.42	0.43	0.45	0.52

ASTM G-28A = 25 grams $Fe_2(SO_4)_3$ + 236 mL H_2SO_4 + 400 mL H_2O

Table 4

Corrosion Results in Oxidizing Acid-Chloride Test Environment
(reported in mm/y)

	Corrosion rates	CPT (°C)	Comments
Unwelded Base metal	0.01 0.01	67.5	Minor edge pitting Minor edge pitting
GTAW (matching)	0.08 0.03	40.0	Pit on weld face No pitting noted
GMAW (matching)	0.01 0.01	42.5	No pitting Fusion zone edge pitting
GTAW (overalloy)	0.03 0.03	57.5	No pitting Fusion zone pitting
GMAW (overalloy)	0.03 0.36	57.5	Fusion line pitting Fusion line edge pitting

NaCl-HCl solution = 40 grams NaCl + 1 gram $Fe_2(SO_4)_3$ + 1 mL HCl + 957 mL H_2O

Table 5

Ratio of Weld Fusion Zone Chemical Analyses Compared to Wrought Base Material

Elements	GTAW (matching)		GMAW (matching)		GTAW (overalloy)		GMAW (overalloy)	
	Pass 1	Pass 2	Pass 1	Pass 2	Pass 1	Pass 2	Pass 1	Pass 2
Chromium	1.01	1.00	1.02	1.00	0.98	0.93	0.94	0.96
Iron	1.00	1.01	0.97	1.01	0.70	0.58	0.47	0.40
Molybdenum	0.75	0.62	0.95	0.69	1.08	1.28	1.56	1.18
Nickel	0.95	0.95	0.91	0.93	1.02	1.07	1.01	0.95
Tungsten	1.04	0.96	0.96	0.88	1.12	1.04	1.44	1.28

Table 6

Auger Electron Spectroscopy Area Scan Chemical Analysis
(weight percent)

Elements	Base Metal	Unmixed Zone	Fusion Zone
Matching Filler Metal Analysis			
Chromium	25.6	26.0	25.4
Molybdenum	11.1	11.1	11.0
Iron	20.6	23.4	26.1
Nickel	41.7	38.6	37.2
Overalloyed Filler Metal Analysis			
Chromium	25.0	26.01	23.4
Molybdenum	10.5	11.2	15.3
Iron	21.7	22.2	16.4
Nickel	40.9	39.1	43.2

Table 7

GTAW Auger Spectroscopy Point Analysis of Matching Weldment Configuration
(weight percent)

Elements	Weld Fusion Zone		Unmixed Zone	
	Interdendritic	Dendrite	Interdendritic	Dendrite
Chromium	25.7	24.5	27.5	26.2
Molybdenum	10.9	9.2	13.9	9.2
Iron	23.5	24.4	21.9	23.7
Nickel	38.8	40.7	35.8	39.7

(Average of 2 analysis points per region)

Table 8

GTAW Auger Spectroscopy Point Analysis of Overalloyed Weldment Configuration
(weight percent)

Element	Weld Fusion Zone		Unmixed Zone	
	Interdendritic	Dendrite	Interdendritic	Dendrite
Chromium	26.7	26.4	26.3	24.4
Molybdenum	16.4	12.8	13.1	7.4
Iron	15.6	16.2	20.0	23.4
Nickel	39.0	41.7	38.2	42.0

(Average of 2 analysis points per region)

Table 9

Partitioning of Elements for the Various Fusion and Unmixed Zones
(weight percent)

Elements	Bulk Area	Dendrite	Dendrite Ratio	Interdendritic	Interdendritic Ratio
N06022 Fusion Zone Partitioning Ratios					
Molybdenum	15.3	12.8	0.8	16.4	1.1
Chromium	23.4	26.4	1.1	26.7	1.1
Iron	16.4	16.2	1.0	15.6	1.0
Nickel	43.2	41.7	1.0	39.0	0.9
N06985 Fusion Zone Partitioning Ratios					
Molybdenum	11.0	9.2	0.8	10.9	1.0
Chromium	25.4	24.5	1.0	25.7	1.0
Iron	26.1	24.4	0.9	23.5	0.9
Nickel	37.2	40.7	1.1	38.8	1.0
Matching Filler Metal Unmixed Zone Partitioning Ratios					
Molybdenum	11.1	9.2	0.8	13.9	1.3
Chromium	26.0	26.2	1.0	27.5	1.1
Iron	23.4	23.7	1.0	21.9	0.9
Nickel	38.6	39.7	1.0	35.8	0.9
Overalloyed Filler Metal Unmixed Zone Partitioning Ratios					
Molybdenum	11.2	7.4	0.7	13.1	1.2
Chromium	26.0	24.4	0.9	26.3	1.0
Iron	22.2	23.4	1.1	20.0	0.9
Nickel	39.1	42.0	1.1	38.2	1.0
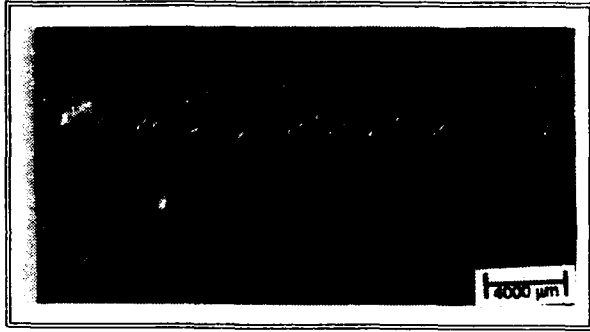
SMAW weld coupon showing fusion line
corrosion attack

SMAW weld cross-section showing fusion line pitting attack
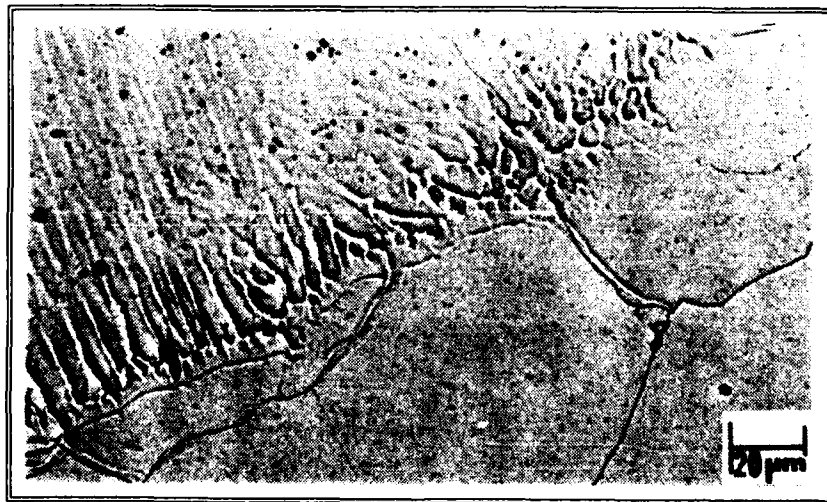
High magnification photomicrograph showing narrow zone at
fusion line that does not contain nonmetallic particles

Figure 1: Example of Local Corrosion Attack Noted Adjacent to Fusion Zone
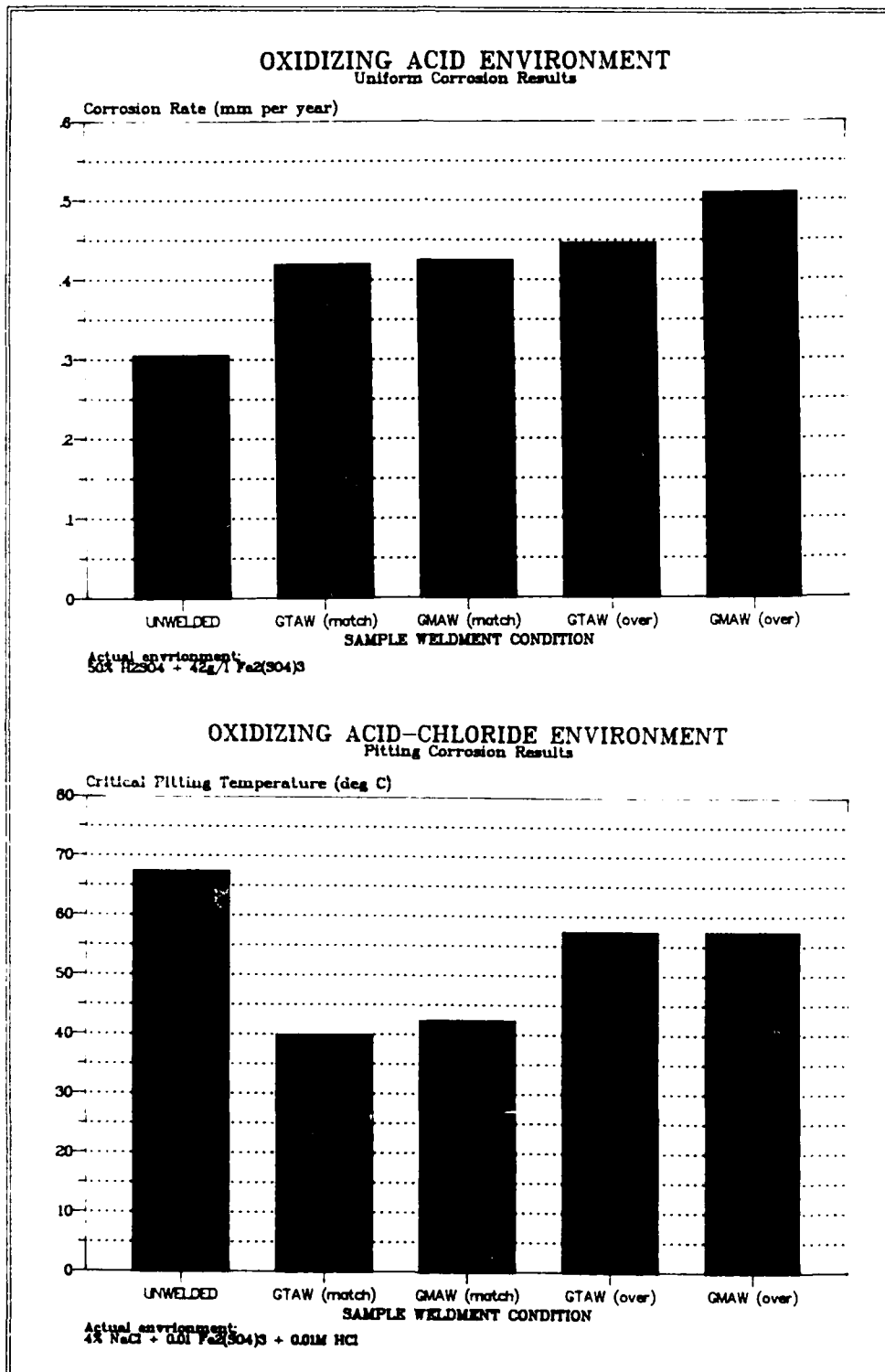
Figure 2: Corrosion Results for Uniform and Pitting Environments

Figure 3: Oxidizing Acid Environment Results for GTAW (overalloy) Specimen

Figure 4: Example of Fusion Line Pitting in GMAW Overalloy Weldment
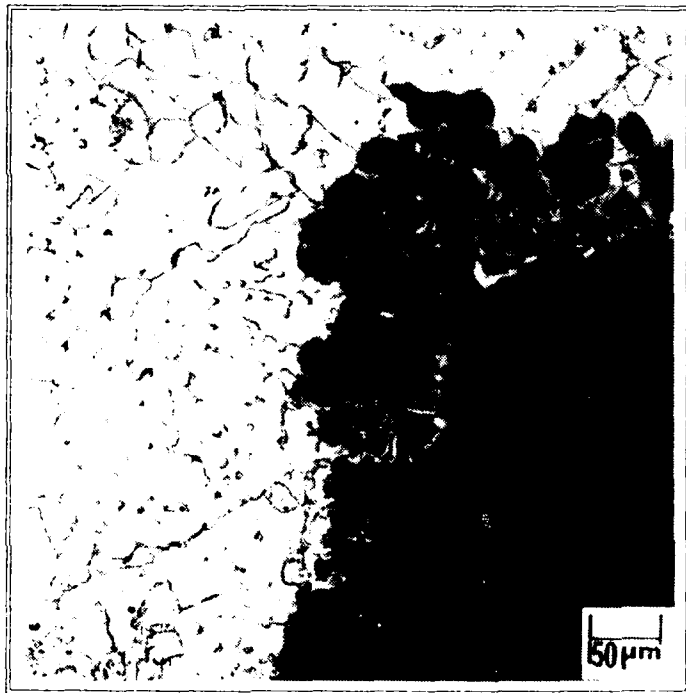
Insert showing root pass pitting attack at
high magnification

Figure 5: Example of Fusion Line Pitting Attack in GTAW Overalloy Weldment
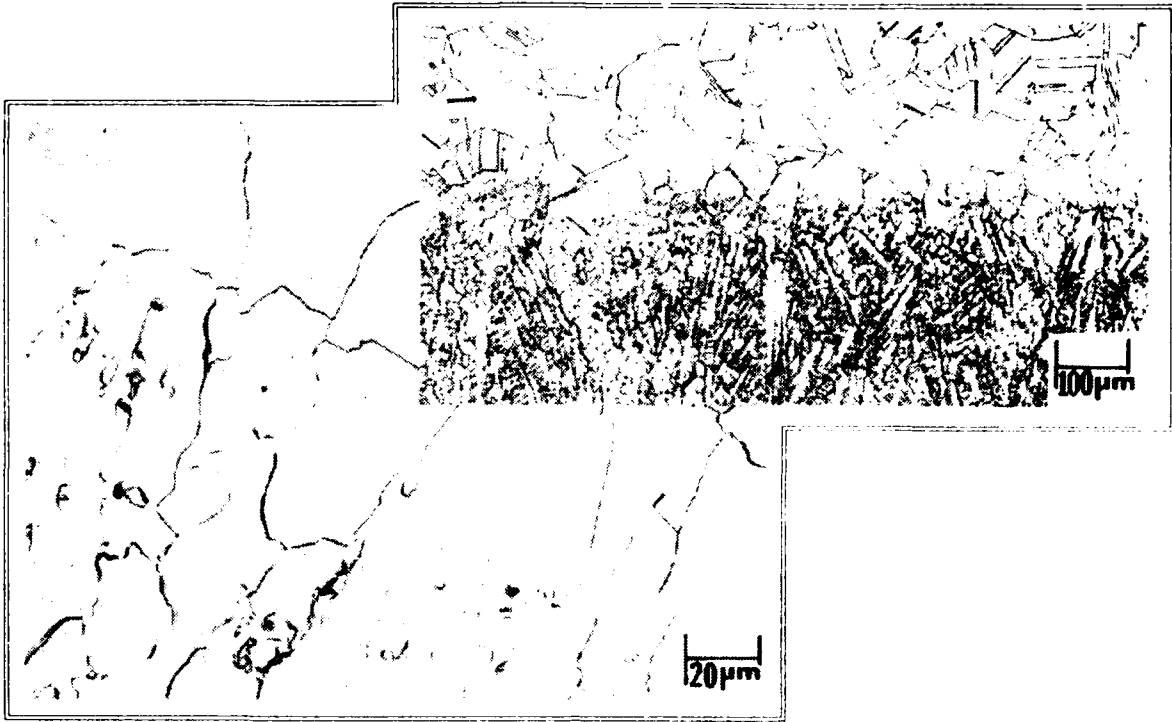
Matching filler metal
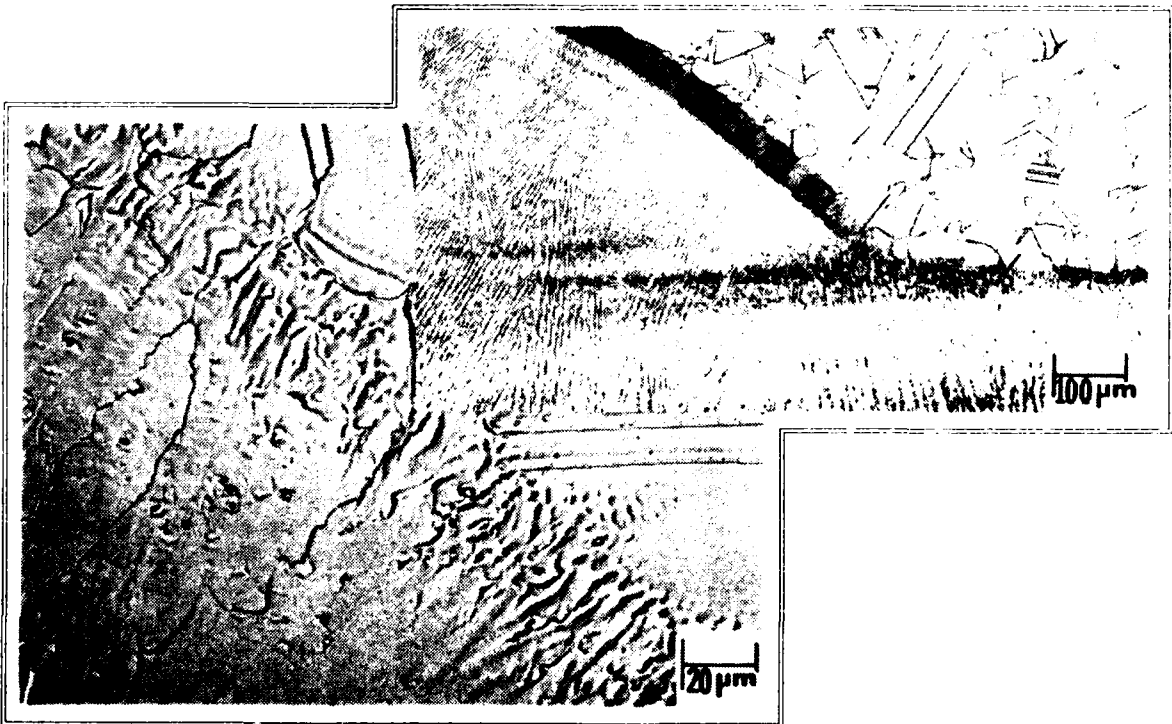
Overalloy Filler Metal

Figure 6: GMAW Weld Fusion Line Structure
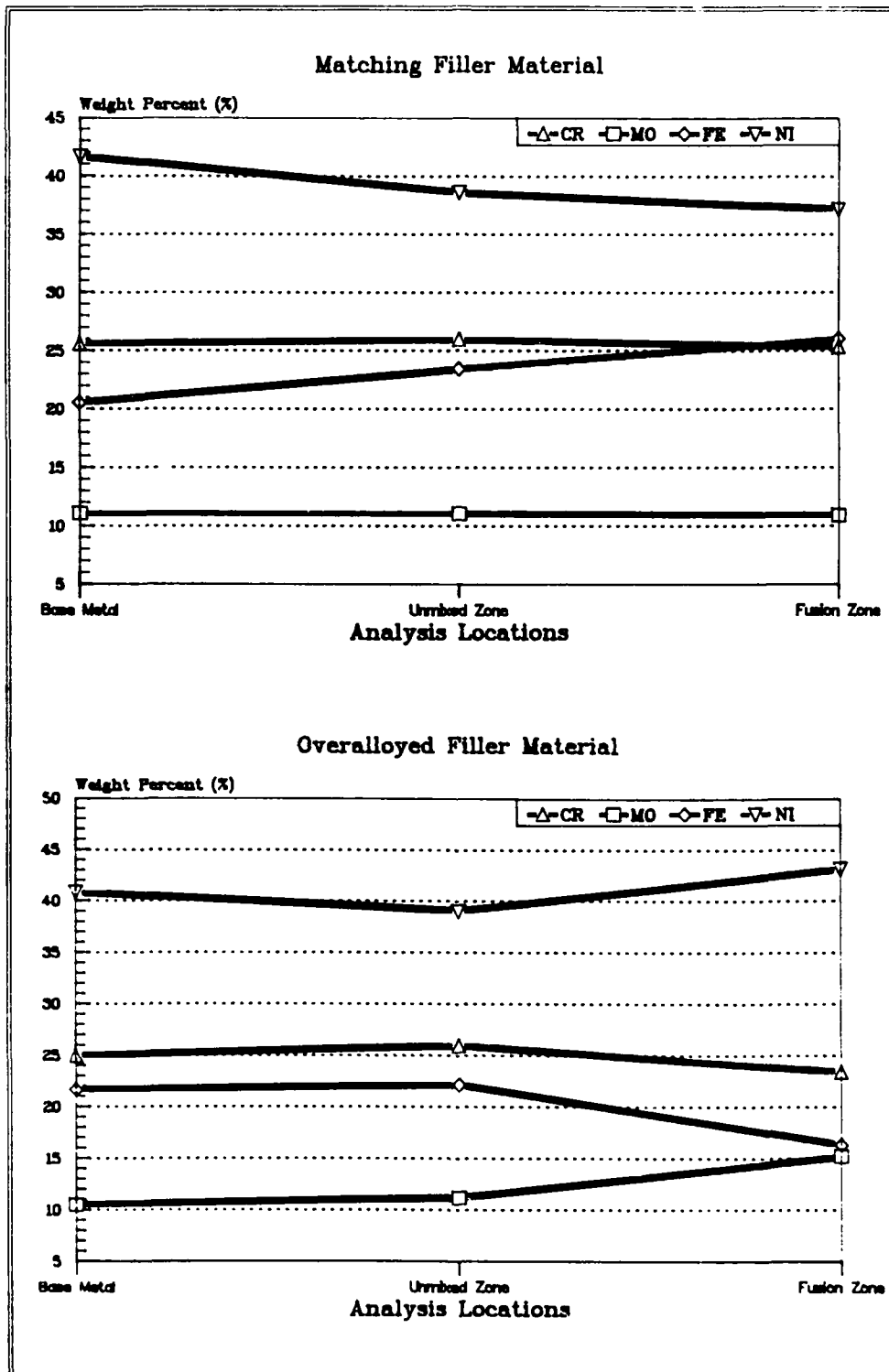
Figure 7: AES Area Scan Chemical Analysis Results

Matching Filler Metal
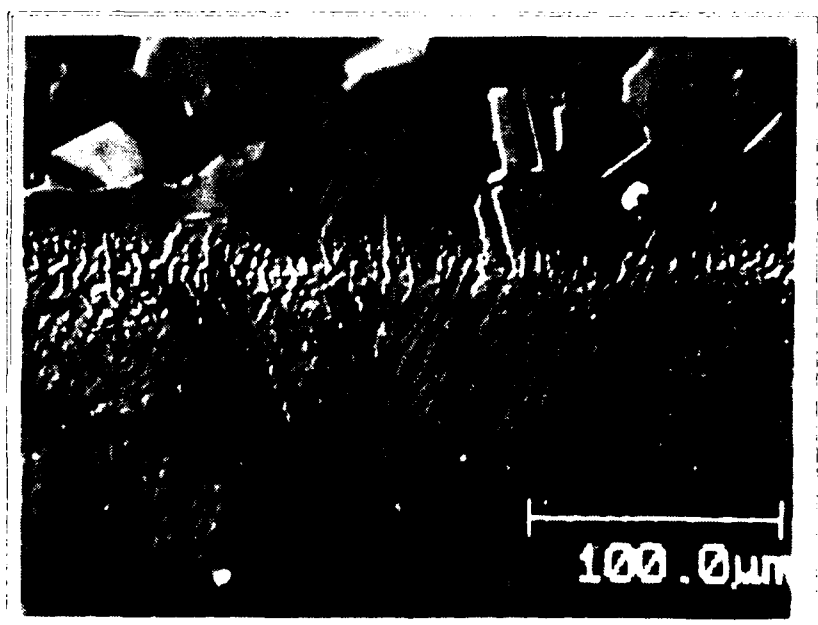
Overalloyed Filler Metal

Figure 8 Scanning Electron Micrographs of GTAW Fusion Line and Unmixed Zones

Corrosion and Behavior of SAW Stainless Steel Filler Metals with N_2 and Mn*

Al. Gil-Negrete

* Paper not available at time of publication.

BENEFICIAL EFFECTS OF NITROGEN ADDITIONS
ON THE MICROSTRUCTURE STABILITY AND CORROSION PROPERTIES
OF WELDED UR 52 N+ SUPER DUPLEX STAINLESS STEELS

Jacques CHARLES, Michel VERNEAU, Bernard BONNEFOIS
CREUSOT-LOIRE INDUSTRIE
PO Box 56
F - 71202 LE CREUSOT

Abstract

The paper outlines the effects of nitrogen additions on the microstructure stability of the duplex stainless steels alloys.
The case of welded joints is particularly investigated. It is shown that both base metal and HAZ are less sensitive to α/γ ratio evolutions.
Nitrogen additions contribute also to the improvement of the corrosion resistance properties of both base metal and welded joint.
The paper presents practical data about the ways to increase the nitrogen content in the weld metal. Welding parameters including heat input, shelding gas and backing gas compositions are discussed. Corrosion and microstructure investigation are presented.

General Considerations : more nitrogen in duplex alloys ?

The duplex stainless steels are characterized by a two phase structure comprised of a mixture of f.c.c. austenite and b.c.c. ferrite grains. A rolling texture is usually exhibited for wrought products *(figure 1)*.

Although the list of duplex alloys presented *TABLE I* is long, It is far from exhaustive ! This table also gives the corresponding values of the pitting resistance equivalent PREN = Cr + 3.3 Mo + 16 N. It should be recalled that the superduplex grades are characterized by a value of PREN > 40. The large number of grades illustrated wrought products is due in part to the gradual optimization of the chemical composition to meet new property requirements and to take advantage of new technological developments.

However, in the case of wrought products, there are, to-day, essentially only three principal grades :

a) The composition 22% Cr - 5% Ni - 3% Mo - 0.17% N (UR 45N, SAF 2205, etc...) which can be considered as the standard duplex stainless steel, and whose nitrogen content has recently been increased to further improve its corrosion resistance in oxydizing chloride-rich acid media (essentially an increase in pitting resistance). Its corrosion resistance lies between those of the austenitic grade AISI 316 and the 5-6 % Mo super austenitic alloys.

b) The super duplex grade with a pitting index PREN > 40, containing 25% Cr, 6.8% Ni, 3.7% Mo and 0.27% N, with or without copper and/or tungsten additions (UR 52N+, SAF 2507). They are especially designed for marine, chemical, and oil engineering applications, requiring both high mechanical strength and resistance to corrosion in extremely aggressive environments (chloride-containing acids, etc.).

The corrosion resistance is equivalent to that of the super austenitic steels containing 5-6 % Mo.

c) The 23% Cr - 4% Ni - 0.10% N, molybdenum-free grade (UR 35 N), an economical material, which, for the majority of applications, can be used to replace the austenitic grades AISI 304 and/or 316

It is noteworthy in *TABLE I* that several commercial grades with different analytical balances can be covered by the same specification (e.g. by UNS S32550 for the grades UR 52 N, FERRALIUM 255 and UR 52 N+). *Figure 2* illustrates the large compositional ranges permetted for a given specification. The corresponding maximum and minimum values of the pitting index PREN = Cr + 3.3. Mo + 16 N are also indicades. This example clearly shows that standards such as the UNS specifications are insufficient to define a material with a precise range of properties. It is recommended to apply additional restrictions on chemical composition, and/or complementary acceptance tests, particularly as regards corrosion resistance. This point is of great importance for industrial applications.

Effects of nitrogen on the microstructure of duplex alloys

The alloys used up to now have roughly equivalent volume fractions of ferrite and austenite. This is obtained by work-hardening, followed by solution annealing and quenching, and involves the simultaneous control of the chemical composition and annealing temperature. *Figure 3* shows a schematic isoplethal section of the Fe-Cr-Ni diagram, for an iron content of 68%. The proportions of each of the phases and their respective compositions are indicated for a given alloy analysis and annealing temperature (at temperature To, Ao is the composition of the ferrite and Bo that of the austenite) [1-2].

The difficulty in predicting the microstructure is due essentially to the effects of the other alloying elements, which modify the phase diagram. Alloy producers use empirical formulae, in which proportionality coefficients are attributed to each elemer˙ and the latter are grouped together, depending on their tendency to stabilize either the ferrite α , ˙ Mo, Si, etc.) or the austenite γ (Ni, N, C, Cu, etc...)

TABLE II gives the partition coefficient between the ferrite and austenite phases determined by micro-analysis. Some data issued from the litterature are also reported. Examination of this table reveals severals points :

a) The ferrite is enriched in α - stabilizing elements, in the following order : P > W > Cr ≅ Si

b) The austenite is enriched in γ stabilizing elements in the following order : N > >Ni >Cu > Mn

c) The partition coefficients for a given element vary very little from an alloy to another except for nitrogen. This latest point is explaii.ed by the fact that the solubility limit of nitrogen in the ferrite is very low and that almost all of the nitrogen goes into solution in the austenite.

It can thus be concluded that the PREN (Cr + 3.3 Mo + 16 N) values of ferritie and austenite grains are different and that the nitrogen containing duplex alloys have PREN values for both phases more close from each other, due to the fact that the PREN value of the austenite is increased by the over alloying in nitrogen while the PREN value of the ferrite grains remains almost unaffected by an increase of the nitrogen level.

Figure 4 shows the variation with temperature of the ferrite content (determined by optical microscopy, using the grid method), for the different α/γ steels studied, including in particular a range of nitrogen contents.

As regards the high temperature stability of the duplex structure, it is important to note the marked effect of nitrogen compared to those of chromium and molybdenum. The gamma stabilising action of nitrogen is clearly revealed, since, in spite of larger additions of ferrite-stabilising molybdenum, for about 0.25% N, the volume fraction of ferrite at 1050°C is close to 50% , compared to nearly 60% in the 25 % Cr heat containing only 0.18 %N.
Furthemore, the reversion to ferrite increases more slowly with rise in temperature. This stabilisation of the duplex structure at high temperatures by the addition of nitrogen is of particular interest in the heat affected zone (HAZ) of welds.

Figure 5 shows TTT diagrams for the grades UR 35N, UR 45N, and UR 52N+. In the temperature range 600-1050°C, the diagrams are based on optical microscope observations of the time necessary for the appeerence of intergranular precipitation, while in the range 300-600°C, they are determined from hardness measurements. The diagrams are conservative in nature and do not imply that the mechanical properties or corrosion resistance are modified as soon as the boundaries indicated are reached. This is particularly true for the low temperature ferrite hardening field. The TTT curves are mainly affected by molybdenum and chromium additions. Nitrogen addition on the opposite have only slight influence on those diagram since the phases transformations occur mainly in the ferrite which is few concerned by nitrogen content fluctuations as described previously (main effect on austenite grains) - figure 6. On the opposite, in cost structure, nitrogen additions are very beneficial since they lower the microsegregation, and so reduce the Cr and Mo contents of the ferrite.

Effects of nitrogen additions on the mechanical properties of duplex alloy

Mechanical properties

Figure 7 shows typical tensile properties obtained on hot-rolled duplex steel plate. They should not be extrapolated to thin section products, such as cold-rolled sheet, or to forgings or castings. Like all other metals and alloys, their mechanical properties depend on factors such as the grain size, texture and degree of segregation.

The major characteristic of the duplex stainlesss steels for equivalent corrosion resistance properties is their extremely high yield strength, twice that of austenitic grades of equivalent PREN (figure 7). The ultimate tensile strength is also high, while the elongation is greater than 25%. These property levels allow the use of thinner sections, leading to considerable savings in weight and capital investment.

The high mechanical strength is the result of several simultaneous mechanisms :

  - interstitial solid solution hardening (C, N) ;
  - substitutional solid solution hardening (Cr, Mo, Ni, etc...)
  - strengthening by grain refinement, the presence of two phases preventing their mutual growth during heat treatment ;
  - Possible hardening due to the formation of γ_2 phase,
  - strengthening due to the presence of ferrite, since, for a similar composition, this phase is harder than the austenitic structure.

The interstitial solid solution hardening of nitrogen additions in duplex alloys occurs mainly between 0 and 0,14% Nitrogen additions. For higher nitrogen additions (> 0.14%) no

complementary hardening effects are observed since in that case the weaker phase is the ferrite and undergo the first plastic deformation as observed *figure 8*.

Figure 9 shows the variation of impact strength with temperature for the different families or stainless steels. The behaviour of the duplex alloys is seen to fall between those of the austenitic and ferritic grades. It is important to note that the toughness of the duplex materials remains satisfactory down to temperatures as low as -50°C. However, the superduplex steels appear to have a slightly lower toughness than the other two-phase grades. Also, a certain scatter in the toughness values is observed at room temperature. This can probably be explained by texture variations, but could also be due to differences in residual elements. Indeed, the impact strength can be improved by reducing the oxygen content.

Too high nitrogen levels, may also affect the toughness at low temperature of the duplex alloys by an over-saturation of the phases in nitrogen, which is known to affect the low temperature toughness of properties of both phases.

Relation between the chemical composition of the plate, welding conditions of the microstructure of the HAZ

Experimental procedure

Single pass manual welds were made with different heat inputs on each test plate, without preheating. The cooling rates, at 700°C, were either monitored using thermocouples stuck into the weld pool, or calculated according to Adam's formulas [3]. The width of the HAZ and the max. ferrite contents were checked micrographically, with a high magnification (x 800 minimum) by the grid method.

Parameters influencing the width of the HAZ

In the case of duplex stainless steels, we have defined a "micrographic HAZ" as the base metal area where, because of the welding thermal cycle, a more or less complet $\alpha \Rightarrow \gamma$ transformation of the high temperature ferrite has occurred. Its witdth is easily measured but varies with the welding conditions and the chemical composition of the plate.

Figure 10 shows the effect of the welding heat input on the maximum width of the HAZ for two different plate thicknesses (UNS 31803). It is obvious from the curves that the welding heat input cannot be considered alone.

Figure 11 shows that the cooling rate at 700°C can provide an accurate prediction of the maximum width of the HAZ.

The composition of the plate, and particularly the nitrogen content, which increases the stability of austenite at very high temperatures has an important effect on the HAZ width. This effect appears in *figure 12*. The higher nitrogen grade has a thinner HAZ, for similar welding conditions.

Accurate measurement of the max. ferrite content of the HAZ

The high nitrogen duplex steels can exhibit very thin HAZs (about 0.1 mm). For this reason, the magnification used for the metallographic check must be high enough to ensure that the grid used to measure the ferrite contents always falls in the $\delta \Rightarrow \gamma$ transformed area of the HAZ.

The micrographs of *figure 13* show that, at 400 x magnification, a part of the unaffected base metal is taken into account for the ferrite determination, which is not the case at 1000 x magnification.

To determine accurately the maximum ferrite content of the HAZ of a duplex stainless steel containing more than 0.20% nitrogen, it is necessary to use magnifications over 800 x. This was not necessarily the case for lower nitrogen contents, because their HAZ is normally wider (see *TABLE III*).

In the case of multipass welds, the maximum ferrite content is normally found in the unreheated HAZ, near the last pass, which does not normally show secondary austenite precipitates. In all cases, the number of fields should be high enough (> = 30) to obtain a sufficiently accurate ferrite content (± 4 % normally).

Welding parameters and maximum ferrite content in HAZ

The max ferrite content in the HAZ is plotted in *figure 14* against the cooling rate at 700°C (for 25% Cr duplex steels). These curves become linear when the logarithm of the cooling rate is used as the variable. The formulas determined in our laboratory are the core of the "Premic" software which gives the max. ferrite content in HAZ using the welding parameters (thickness of plates, welding heat input, or welding conditions and efficiency of each process). We have tested other criteria to introduce the cooling rate effect, Vr 1100°C (°C/s) or ΔT 500-800°C (s) but the accuracy of the predictions is not improved.

"Premic" can also be used to calculate the minimum heat input (or the maximum cooling rate) which guarantees a given maximum ferrite content in the HAZ of a duplex weld, in the as welded condition. This version of "Premic" applies only to CLI grades, with the same "air analysis".

Different methods to introduce nitrogen in the duplex weld metal

Nitrogen can be overalloyed in the filler material itself (in addition or in susbstitution to the nickel increase) to obtain an acceptable ferrite content in the as welded condition. This addition of nitrogen is not difficult through the metallic powder in the case of cored wire or for electrode coatings. In the case of solid welding wire, it can be limited by the hot workability of the wire at the hot rolling stage. For this reason and for welding processes without filler materials (electron beam for instance) and also in the case of very thin plates, it was essential to develop other methods of nitrogen addition in the weld pool.

The differents methods that have been studied in greater depth are summarized in *TABLE IV*.

Some of these methods are still experimental (use of very high nitrogen duplex steel plates, use of nitride wire). But the others are now used as industrial applications such as the nitrogen addition in the welding gas in GTAW or PAW.

The studied weld metal compositions are based on the standard 22% Cr duplex (used to weld UNS 31803 plates) or the 25% Cr superduplex family (such as UNS 32550). In each case, several nitrogen levels have been tested in order to quantify its effect on the parameters under study.

Effect of nitrogen addition on thet technological welding properties

Depending on the welding process, nitrogen alloying can have some measurable effects on differents aspects of the technological weldability. For instance, for GMAW, the curve of *figure 15* shows that the nitrogen addition in the welding gas increases the arc instability, particularly at high nitrogen levels, corresponding to the cases where nitrogen pick up is very effective. This undesirable effect of nitrogen in gas exists for GTAW and does not affect the GTAW or PAW of duplex steels.

On the other hand, an effect of nitrogen additions on the bead geometry has been observed more frequently in welding without filler and with filler. For instance, in GTAW with nitrided wire, the ratio D/W, which determines the bead shape, increases when the nitrogen content of the wire increases as shown in *figure 16.*

The two curves of this *figure 16* show that the relations between the nitrogen content of the wire and the bead geometry are also depending on the other welding parameters (the welding speed in this case). These results mean that in the case of welding automation when a constant bead geometry is required, the selection of the welding parameters should include the effect of the desired nitrogen content in the wire or in the welding gas.

An other property of the weld, which can be affected by nitrogen additions, is the compactness. In *figure 17*, the compactness has been measured by counting the number of porosities detected by X Ray examination of a 100 mm length weld. The results obtained here (GTAW weld) indicate that the number of porosities increases with the nitrogen content of the wire. However, here again, the welding parameters have also an important effect and for instance, the number of porosities detected by X Ray examination decreases when the weld speed increases.

With a welding speed of 15 cm/mm, the nitrided wire 0.4% nitrogen can be used to obtain an ASME IX acceptable weld, in terms of X Ray compactness.

Study of nitrogen transfer for different methods of introduction

For welds without filler under inert gas or vacuum, a more or less important part or the plate nitrogen is transferred into the molten metal.

In EBW, the results given in *TABLE V* show that for duplex plates with similar thicknesses, the ratio of transferred nitrogen remains constant (about 80%) even for the very high nitrogen experimental plate.

In laser welding, a study carried out by the INSTITUT DE SOUDURE (PARIS) [4] shows that the nitrogen losses cannot be compensated by nitrogen additions in the shielding gas.

For GTAW or PAW, nitrogen additions in the gas are industrially uesd. The amount of nitrogen added to argon can vary from 3 % (welding with filler) to 20 % (welding without filler with high cooling rates, in the case of thin plates).

The curves of *figures 18* and *19* show that, for GMAW, the transfer of nitrogen strongly depends upon the welding conditions. For instance, nitrogen is easily introduced when the carrying gas is a Ar + 1.5% O_2 mixture *(figure 18)* and when the metal transfert is the short circuiting type *(figure 19)*

Nitrogen introduction and weld metal microstructure

Whatever the selected method, the main effect of the nitrogen introduction in the weld metal is to decrease the ferrite content of its microstructure in the as welded condition.

In fact, the two parameters which determine the weld metal ferrite content are the actual content of nitrogen in the weld metal and the cooling rate of the weld.

As shown, in *figure 20*, for GTAW, the required nitrogen content in the shielding gas will be higher for a welding at low heat input (high cooling rate) than for a high heat input (low cooling rate). A similar effect exists also in PAW where a higher cooling rate implies a higher nitrogen addition in the plasma gas. For GMAW (*figure 21*), the lowest weld metal ferite content is obtained for the most efficient nitrogen transfer (*figures 18 and 19*) which corresponds to an Ar + 1.5% O_2

Another effect of the nitrogen introduction in the weld metal is the higher stability of the microstructure (in terms of transformation of the ferrite into intermetallic phases). The results given in *TABLE VI* show that in the case of high alloy duplex multipass welds (25% Cr, Mo) involving several thermal cycles, high nitrogen additions are necessary to avoid a transformation of the ferrite non magnetic intermetallic phases.

Nitrogen introduction and corrosion resistance of the duplex base and weld metal

In addition to its stabilizing effect on the weld metal microstructure, nitrogen increases the pitting corrosion resistance. Consequently, nitrogen losses during welding can decrease the corrosion resistance. This could occur during GTA welding, particularly, if the nitrogen content of the wire is too low.

The pitting potential values of *Table VII*, for UNS 31803 weld metals with two different nitrogen contents confirm this decrease in corrosion resistance if nitrogen losses during welding are not taken into account.

The addition of nitrogen in the gas for welds improves very significantly the critical pitting temperature (ASTM G48), of UR 52N+ welds (using the same wire composition as that for the base material) both in the as welded and heat treated conditions (*figure 22*)

Regarding the rather standard off-sore industry requirement of 35°C minimum CPT-ASTM G48-A) the 3% nitrogen addition in the welding gas gives a sufficient safety margin in both conditions (as welded and solution annealed + water cooled).

Conclusion

A new family of duplex stainless steels containing increased nitrogen additions has been developped. Those alloys present a significant step in safer use of duplex alloys since the structural differences between the as welded and annealed conditions have been reduced. Furthermore, the high nitrogen additions increase the corrosion resistance of the alloys and contribute to the microstructure stability i.e intermetallic phase precipitations are delayed. All those advantages explain why duplex alloys are undergoing now for developments for most of the applications requiring corrosion resistant alloys. Nevertheless, the cost saving aspects of those materials will be successfully achieved when properly used. Technical background is thus recommended.

References

[1] J. CHARLES - The duplex stainless steels : materials to meet your needs (Ed. de Physique)
Proc. DSS'91 International Conference Beaune - France, 1991 - pp 1-48

[2] J. CHARLES - Super Duplex Stainless steels : structure and properties
DSS'91- 1991 - pp 151-168

[3] B. BONNEFOIS - J. CHARLES - F. DUPOIRON - P. SOULIGNAC
How to predict welding properties for duplex stainless steels ?
DSS'91 - pp 347-360

[3] B. BONNEFOIS - P. SOULIGNAC - J. CHARLES
Some aspects of nitrogen introduction in the duplex weld pool
DSS'91 - pp 469-478

TABLE I - Typical chemical composition of some wrought duplex stainless steels

Standard	Trade mark	Typical chemical composition					PREN
		Cr	Ni	Mo	N	Others	
UNS S 32304￼WNr 1.4362￼Z3CN 2304 AZ	SAF 2304￼UR 35 N	23	4	.2	.1	-	25
UNS S 32404￼Z3CNDU 2107	UR50	21	7	2.5	.07	1.5 Cu	31
UNS S 31500￼W Nr 1 4417	3 RE 60￼VEW A903	18.5	5	2.7	.07	1.5 Si	23
UNS S 31803￼WNr 1 4462￼NFA 36209￼Z3CND 2205 AZ	UR45N￼SAF 2205￼223 FAL￼AF22￼VS22￼...	22	5.3	3	.16	-	35
UNS S 32900	10 RE 51	25	4.5	1.5	-	-	30
UNS S 31200￼WNr 1. 4460	44LN	25	6.2	1.7	.17	-	33
UNS S 31260	N.A.R. DP-3	25	6.5	3	.16	.5CU.3W	38
UNS S 32550￼Z3CNDU2507 AZ	UR52N￼FERRALIUM 255	25	6.5	3	.18	1.6 Cu	38
UNS (S 32200)￼Z3CND 2507 AZ	UR47N	25	6.5	3	.18	-	38
	VEW A 905	26	3.7	2.3	.34	6 Mn	39
UNS S32760	ZERON 100	25	7	3.6	.25	.7Cu.7W	41
UNS S32550￼Z3CNDU 2506	UR52N$^+$	25	6	3.8	.26	1.5Cu	42
UNS S32750	SAF 2507	25	7	3.8	.27	-	42

TABLE II - Partition coefficient α/γ between ferrite and austenite phases
for several elements in duplex stainless steels

Grade	T°	Cr	Ni	Mo	N	Si	Cu	Mn	W	P
AF 22	1000	1.20	.54	1.65	-	-	-	-	-	-
* UR 35 N	960	1.19	.61	1.65	-	1.16	.68	.89	-	2.38
* UR 35 N3Cu	975	1.2	.60	1.7	-	1.19	.66	.87	-	-
* UR45 N	980	1.1	.61	1.66	-	1.16	.67	.86	-	2.31
SAF 2205	980	1.2	.58	1.72	.2°	-	-	-	-	-
DP3 (SEM)	1020	1.1	.74	1.49	-	1.19	-	1.01	2	-
* UR52N	1040	1.15	.65	1.6	-	1.19	0.69	.87	-	2.9
* UR52N+	1060	1.11	.66	1.49	-	1.15	.71	-	-	-
SAF 2507	1060	1.13	.70	1.3	.125°°	-	-	-	-	-
* SAF 2507	1060	1.12	.60	1.58	-	1.19	-	.95	-	-
* ZERON 100	1080	1.16	.65	1.57	-	1.10	.73	.94	-	-

° [N] = .05 in α and [N] = 0.25 in γ
°° [N] = .06 in α and [N] = 0.48 in γ
* CLI-CRMC Results

TABLE III - Effect of the magnification on the HAZ ferrite content
measured by a metallographic method

Grade	Cooling rate Vr 700 (°C/s)	Magnification	HAZ Ferrite %
UNS 32 550 (N = 0.16%)	13	400	80
		1000	79
UR 52 N+ (N = 0.25 %)	12	400	56
		1000	67

TABLE IV - Different methods to introduce nitrogen in duplex welds

NITROGEN INTRODUCTION METHODS	WELD METAL TYPE	WELDING PROCESSES	DIFFERENT CONTENTS OF NITROGEN			
% NITROGEN IN PLATE	UNS 31803	EBW GTAW (Without Filler)	0,13	0,18	0,40	
% NITROGEN IN NITRIDED WELDING WIRE	UNS 32550	GTAW	0,225	0,405	1,04	
% NITROGEN IN ARGON SHIELDING GAS	UNS 32550	GTAW (WITHOUT OR WITH FILLER)	3	9	14	20
% NITROGEN IN ARGON + 1.5% O2 SHIELDING GAS	UNS 32550	GMAW	0	2,8	5,5	8,3

TABLE V - Effect of nitrogen losses in EBW of duplex plates

Plate Grade	Thickness (mm)	Nitrogen % in base metal	Nitrogen % in fused metal	F.M. N% / B.M. N%	Ferrite % in fused metal
UNS 31803	7	0.137	0.111	0.810	91
UNS 32550	7	0.166	0.135	0.813	95
Experimental 675	8	0.400	0.328	0.820	42

Table VI - Effect of nitrogen on ferrite transformation in carbides and sigma phases in duplex weld metals

Weld Ref.	eq.Cr %	Ni %	N %	Predicted Espy ferrite %	Magntic ferrite of reheated pass	Transformed ferrite %
P1	29.4	13.0	0.069	23	0.4	98
P2	29.9	7.3	0.279	33	34	0

Table VII - Effect of nitrogen content on the pitting corrosion resistance of the weld metal

Weld type	Cr %	Mo %	N %	PRE	Pitting Potential E (mV/sce)
UNS 31803	22.35	2.99	0.159	33.9	900 to 1000
UNS 31803	22.31	2.93	0.086	32.4	300 to 400

PRE : % Cr + 3.3 % Mo + 16 % N   NaCl 30 g/l desaerated 40°C
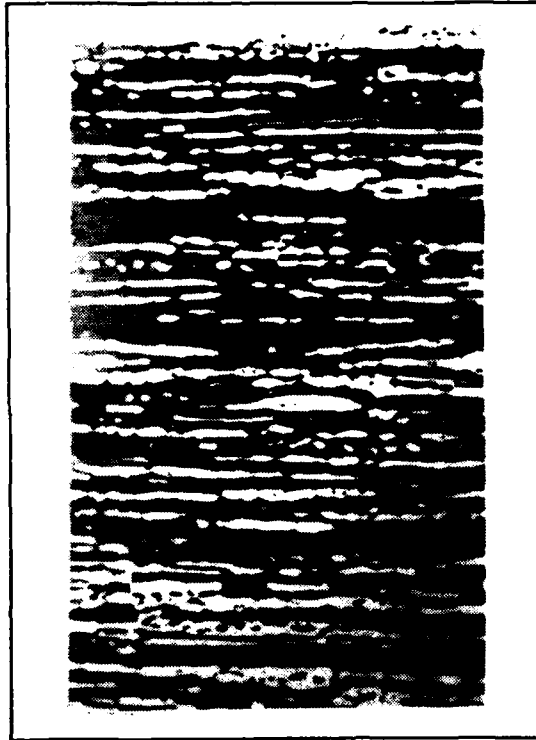
Figure 1 - Typical microstructure of hot-rolled duplex
stainless steels plates

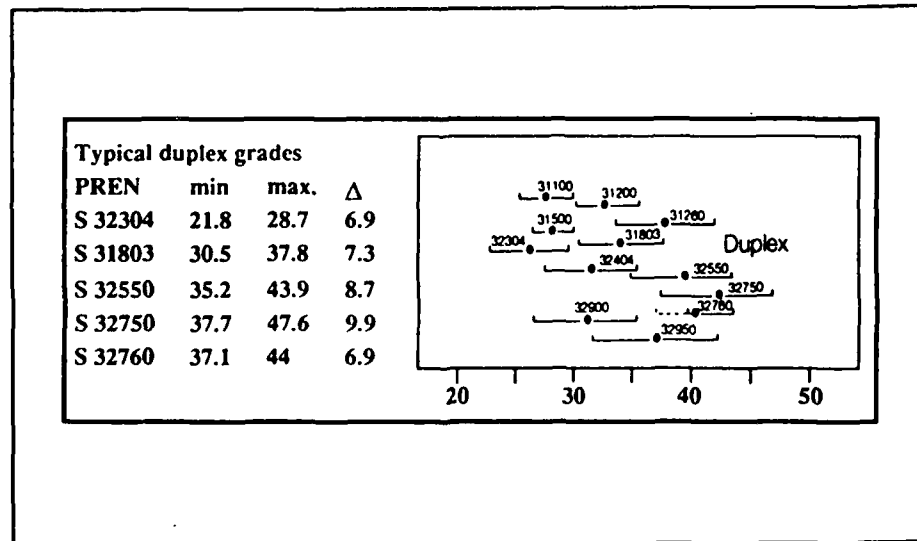| Typical duplex grades			
PREN	min	max.	Δ
S 32304	21.8	28.7	6.9
S 31803	30.5	37.8	7.3
S 32550	35.2	43.9	8.7
S 32750	37.7	47.6	9.9
S 32760	37.1	44	6.9

Figure 2 - UNS numbers and PREN equivalent values
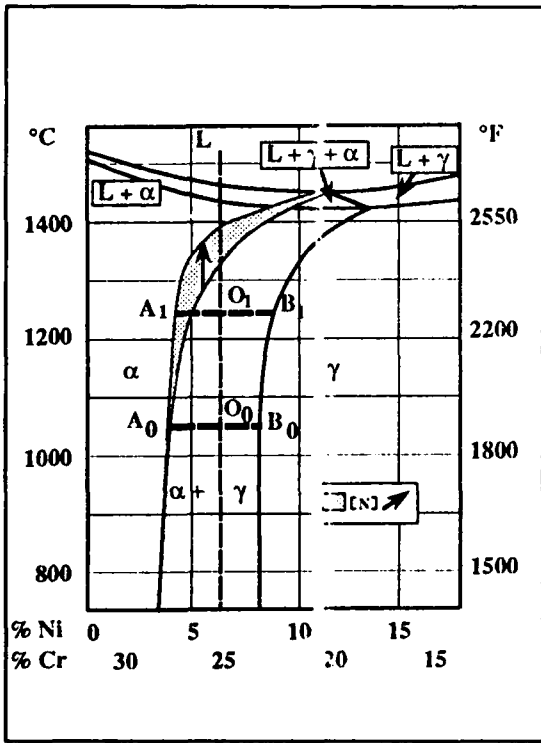of duplex alloys

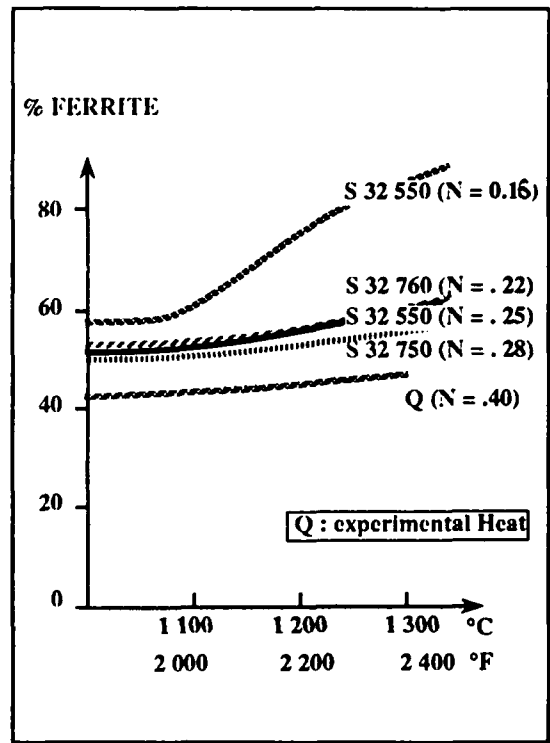**Figure 3** - Schematic effect of nitrogen additions on the pseudo binary Cr - Ni - 68 Fe phase diagram

Figure 4 - Variation of ferrite content with increase of temperature for 25 Cr Duplex stainless steels
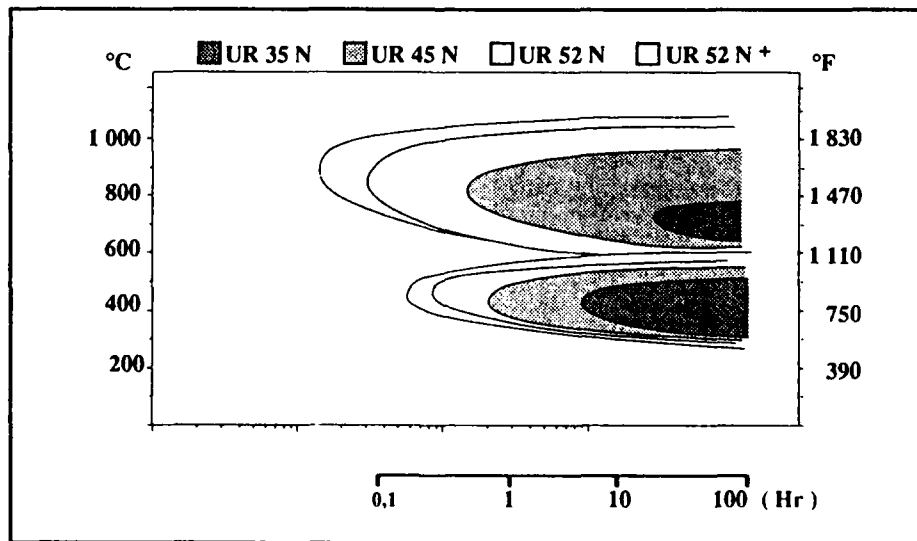

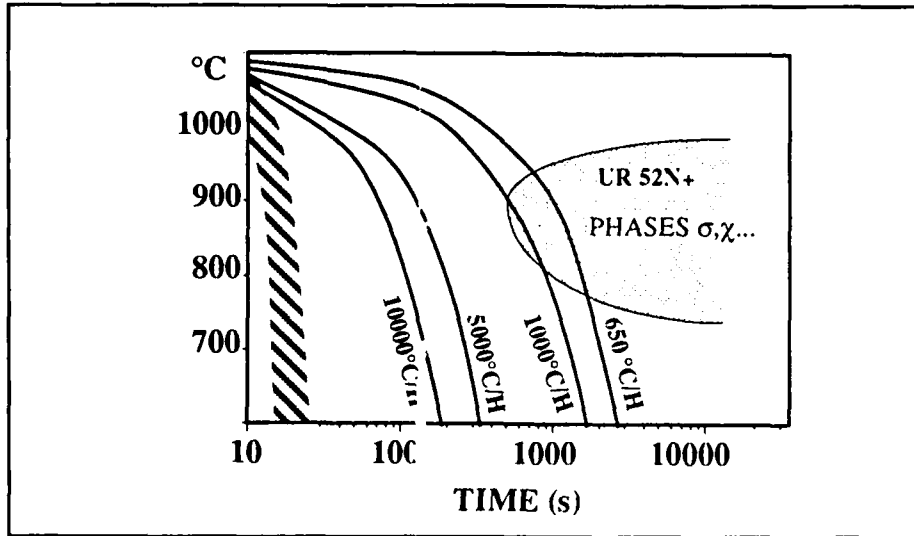**Figure 5** - T.T.T. diagrams of Duplex Stainless Steels

Figure 6 - Continous cooling diagram (heating at 1080°C)

 Typical HAZ cooling rates
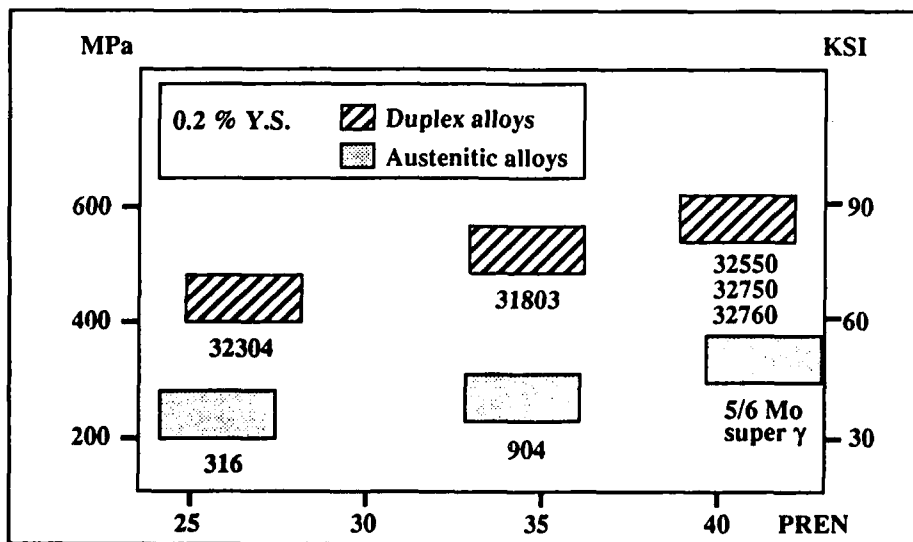
Figure 7 - Typical 2% yield and ult. tensile strengths of hot
rolled stainless steels
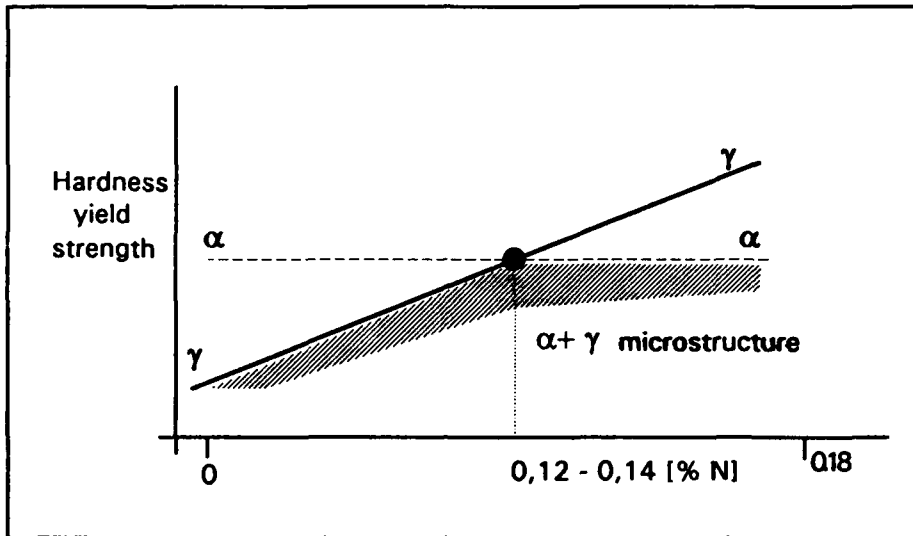
Figure 8 - Effects of nitrogen additions on the
mechanical properties of duplex alloys
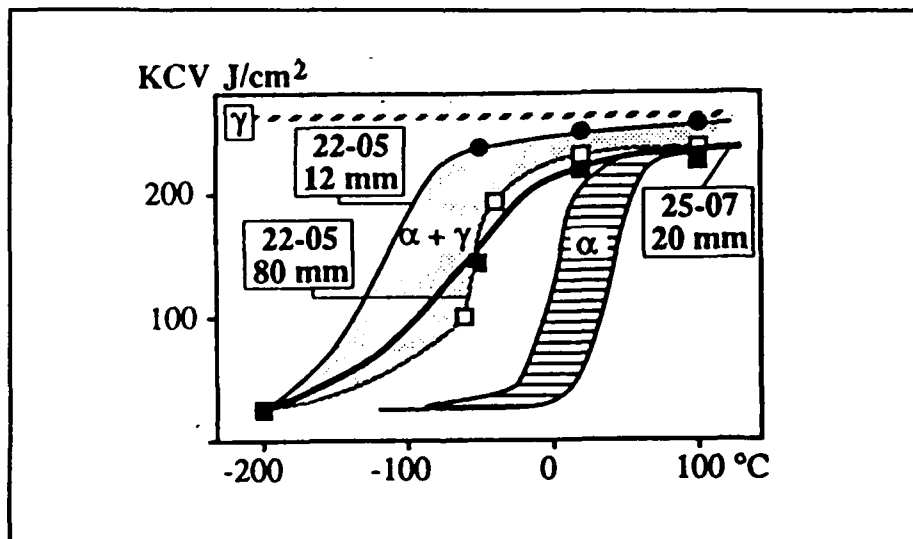
Figure 9 - Impact Charpy energy versus testing temperature
measured for several stainless steels
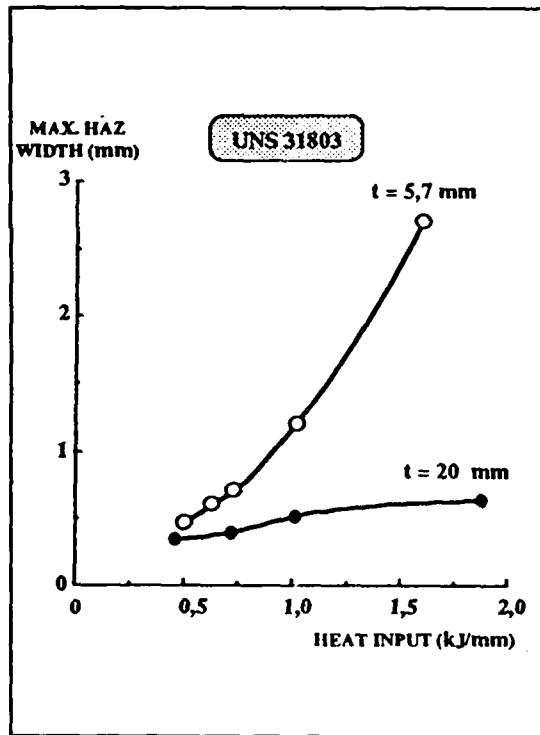
Figure 10 - Effect of the heat input on the
Max.HAZ width
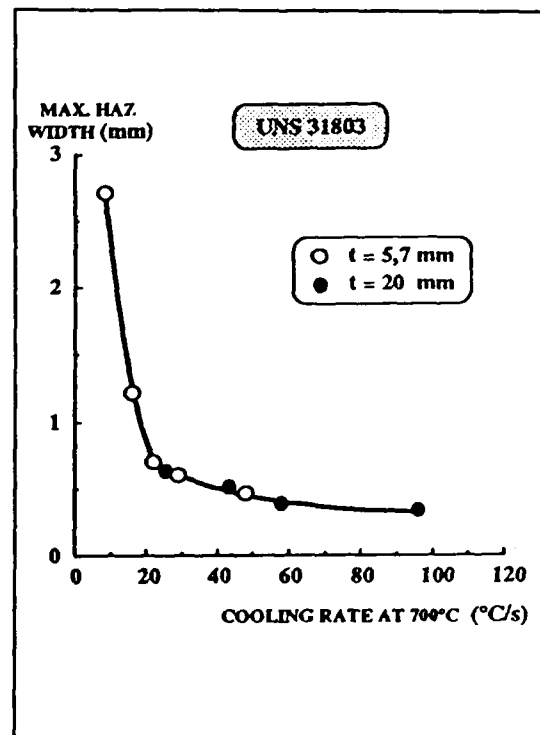
Figure 11 - Relation between max. HAZ
width and cooling rate
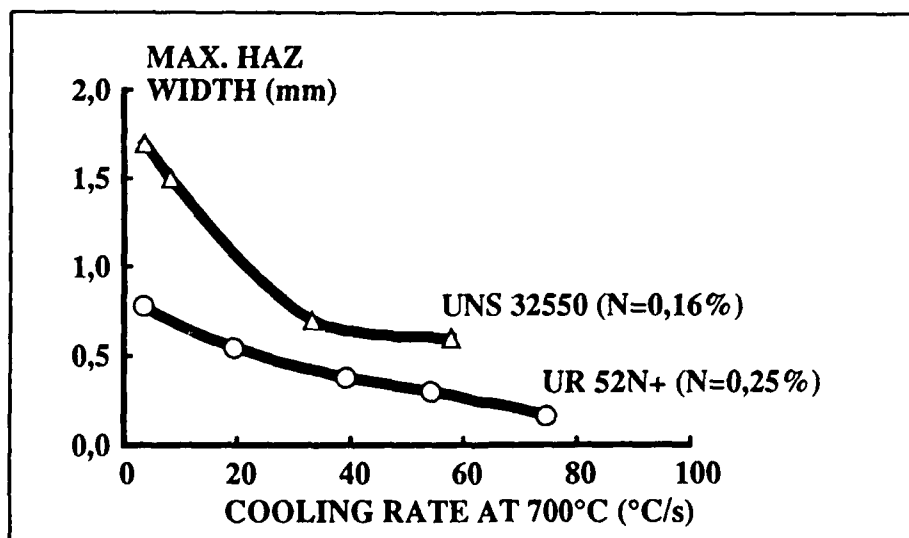
Figure 12 - Effect of the N2 Content of the
plate on the max. HAZ width
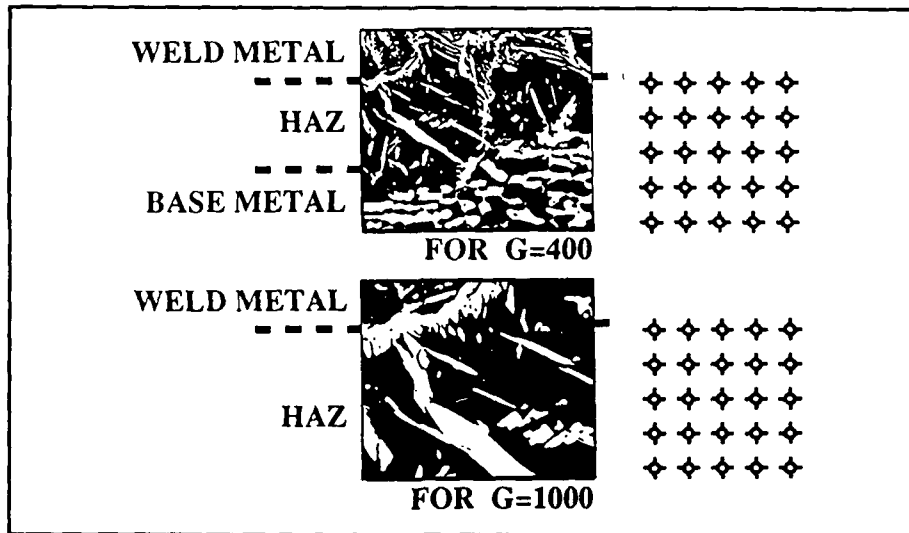
Figure 13 - Choice of the magnification for the metallo-graphic measurement of max. ferrite content in the HAZ
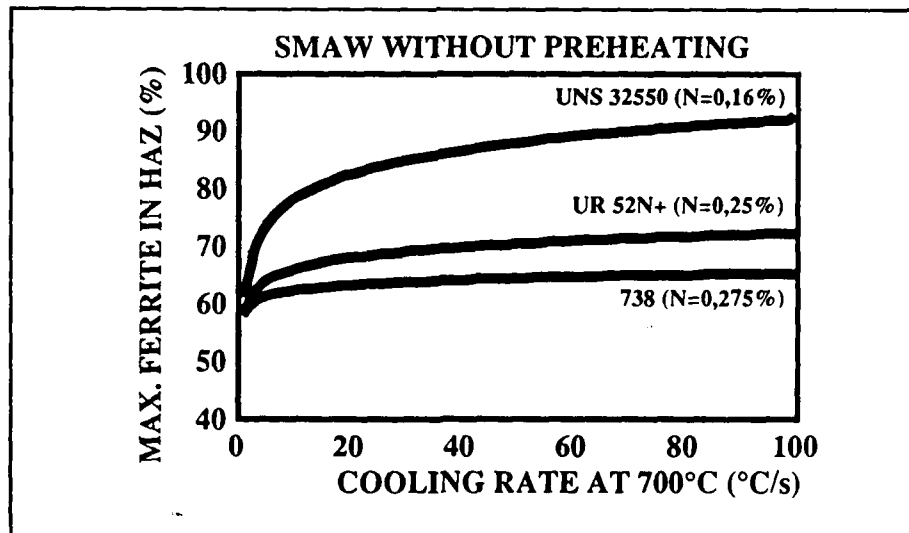
Figure 14 - Effect of the cooling rate on the max. ferrite content in the HAZ for superduplex plates
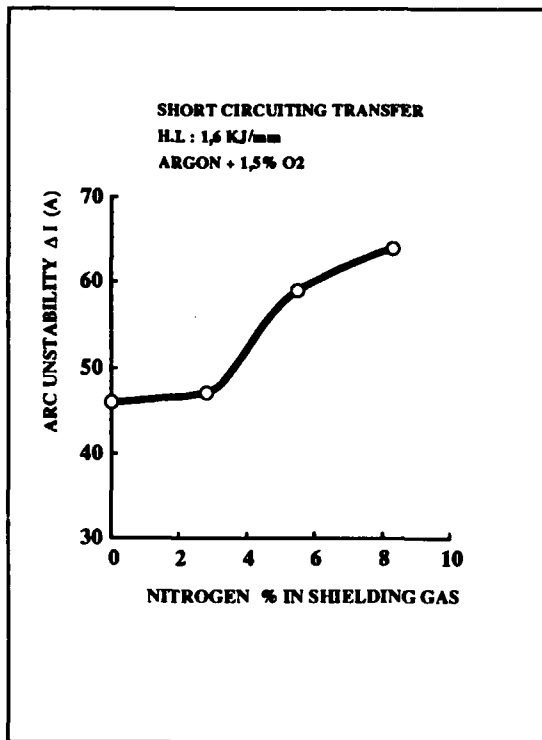
Figure 15 - Effect of nitrogen addition in shielding gas on arc unstability (GMAW)
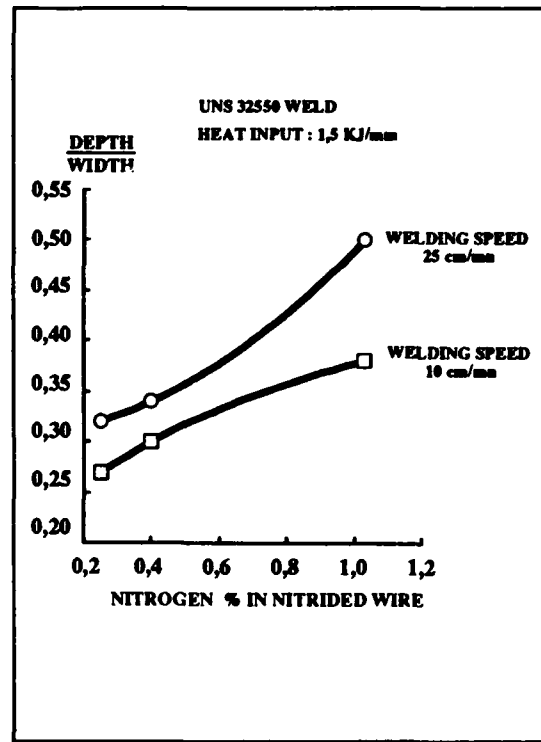
Figure 16 - Effect of nitrogen addition in the wire on the geometry of the bead (GTAW)
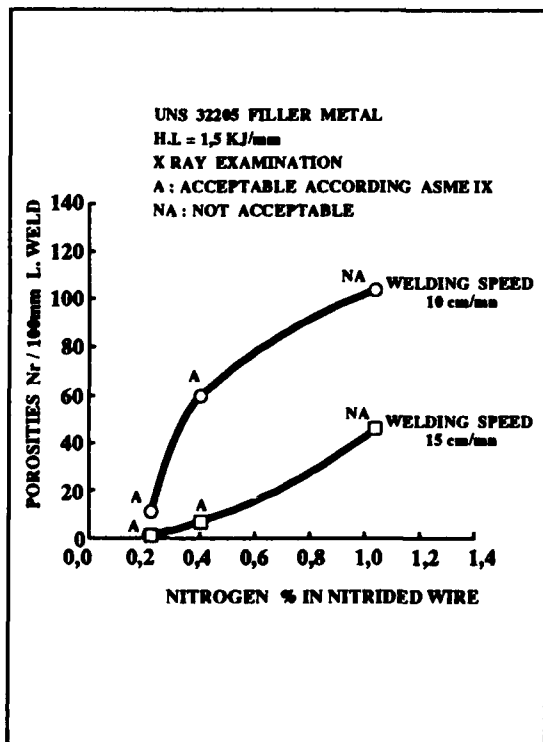
Figure 17 - Effect nitrogen addition in the wire on the porosities number (GTA weld)
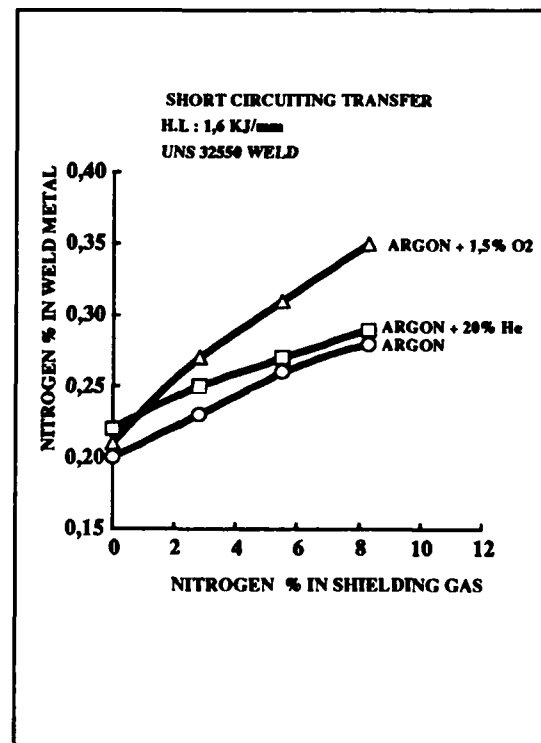
Figure 18 - Efficiency of nitrogen addition for different carrying gas (GMAW)
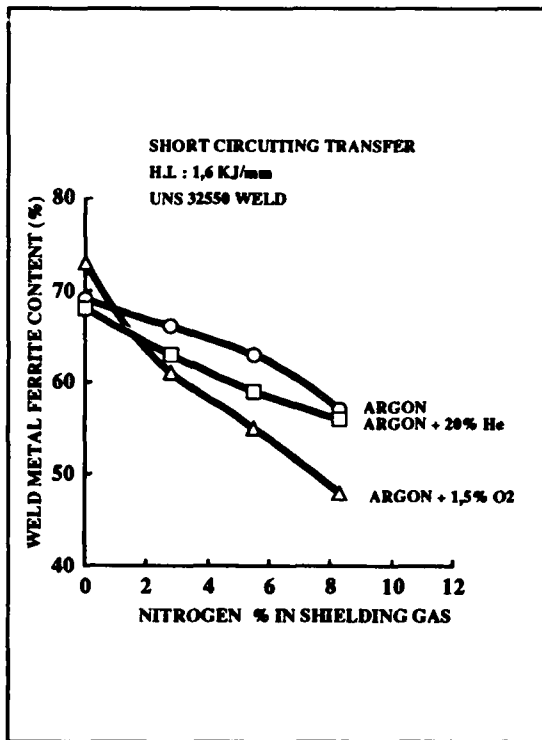
Figure 19 - Efficiency of nitrogen addition for two metal transfers (GMAW)
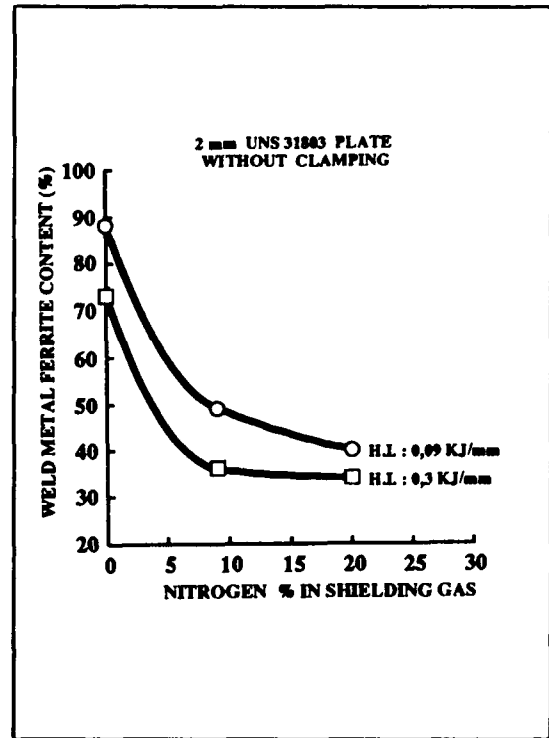
Figure 20 - Effect of nitrogen % in gas on the weld metal ferrite content (GTAW without filler metal).
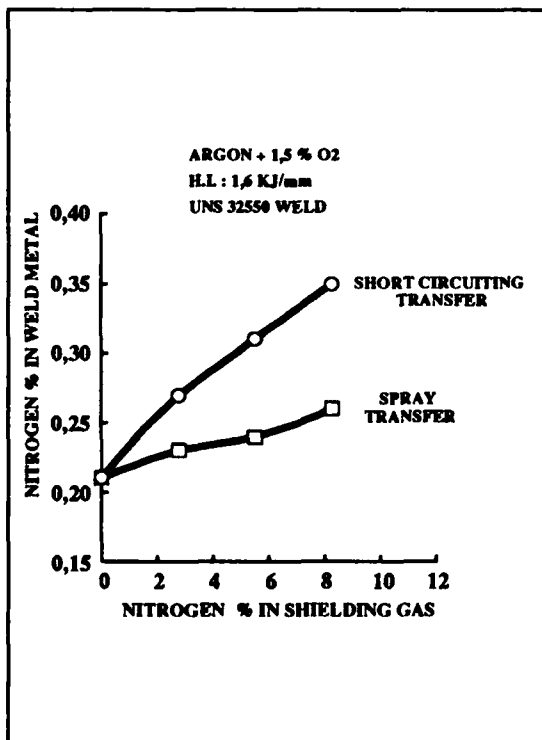
Figure 21 - Effect of nitrogen in gas on weld metal ferrite content for different carrying gas (GMAW)
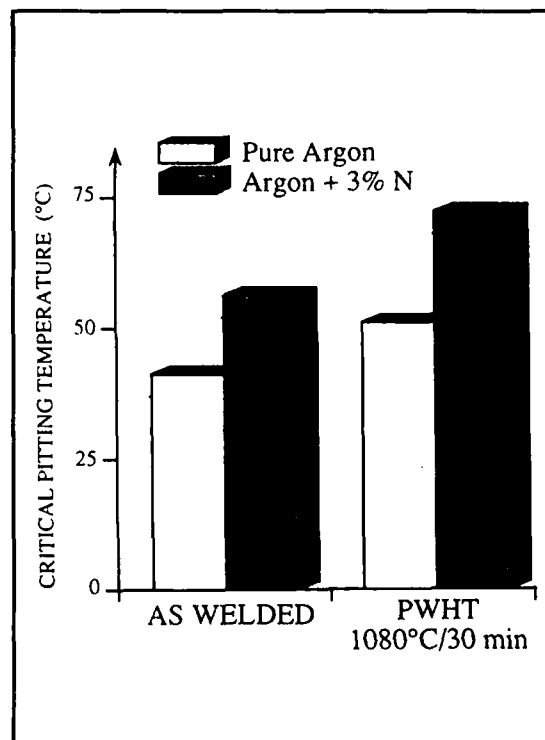
Figure 22 - Pitting corrosion test : ASTM G48 ON PAW + GTAW welds of UR 52 N +

Corrosion Properties of Duplex and Super Duplex Stainless Weld Metals After Isothermal Aging

Leif Karlsson
The Esab Group
Esab AB
Box 8004
S-402 77 Göteborg, Sweden

Susan Pak
The Esab Group
Esab AB
Box 8004
S-402 77 Göteborg, Sweden

Abstract

Corrosion resistance and mechanical properties was studied for duplex (22%Cr 9%Ni 3%Mo 0.15%N) and super duplex (25 %Cr 10 %Ni 4 %Mo 0.25 %N) SMAW weld metals in as welded condition and after isothermal aging between 700 and 1000°C. R-phase precipitated rapidly below 800°C in the duplex weld metal. σ-phase successively replaced R-phase at 800°C and was the only phase forming at higher temperatures. The impact strength decreased most rapidly around 900°C and deteroriation of corrosion resistance took place most quickly at 700 and 900°C. Corrosion resistance and toughness was affected simultaneously above 800°C whereas loss of corrosion resistance preceded embrittlement at lower temperatures. Ferrite content or hardness can be used as an indication of loss of corrosion resistance and embrittlement but not to guarantee unaffected properties. The solidification mode is important for super duplex weld metals. A fully ferritic solidification gives a "normal duplex" microstructure whereas ferritic-austenitic solidification gives a microstructure that is very susceptible to formation of σ-phase. Loss of corrosion resistance or embrittlement of duplex and super duplex weld metals will not occur if suitable consumables are used and recommended welding procedures are followed.

Key terms: weld metals, shielded metal arc welding, duplex, super duplex ,heat treatment, precipitation, intermetallic phases, corrosion, hardness, impact toughness, solidification mode, ferrite morphology,

Introduction

Duplex (ferritic-austenitic) and super duplex[1] stainless steels are today used in a wide variety of applications. In particular their combination of good corrosion resistance and high mechanical strength is attracting interest. The strength and corrosion resistance of duplex stainless steels generally increase with increasing alloying content. However, also the susceptibility to formation of intermetallic phases, which will impair properties, is higher for higher alloying contents. Formation of intermetallic phases is a cause of concern during production and use of duplex and super duplex stainless steels and can be caused by either heat treatments or improper welding.

Precipitation in duplex and super duplex stainless steels has been investigated rather thoroughly[1-3]. In the temperature range 600-1000°C embrittlement is mainly due to formation of σ-phase but also other intermetallic phases, as well as carbides and nitrides, have been observed[1-3]. However, duplex and super duplex stainless weld metals, intended for use without post weld heat treatments, are overalloyed in Ni to ensure formation of a sufficient amount of austenite during cooling. The weld metals also have a different ferrite morphology and are less homogeneous than the steels. Therefore, the precipitation kinetics of duplex and super duplex stainless steels cannot directly be used to predict the behaviour of the corresponding weld metals.

---

(1)   Super duplex steels are defined as duplex steels with PRE > 40 (PRE = %Cr + 3.3·%Mo + 16·%N).

Only limited information about the aging response of duplex and super duplex weld metals is available[4-6]. In particular detailed information about precipitation in the temperature range 600-1000°C, where most rapid precipitation can be expected during welding, is lacking. Most studies have been concerned mainly with the effects on mechanical properties[1, 5-7]. However, it is well known that the effect on corrosion resistance of small amounts of precipitates is more pronounced than the effect on mechanical properties[8].

In the present investigation the formation of intermetallic phases in the temperature interval 700-1000°C was studied for 22%Cr 9%Ni 3%Mo 0.15%N type duplex and 25%Cr 10%Ni 4%Mo 0.25%N type super duplex weld metals. These weld metals are used mainly for welding of the 22%Cr duplex UNS S31803 and the super duplex 25%Cr UNS S32750 steel grades, respectively. The aim of the first part of the investigation was to study the kinetics of intermetallic phase formation and its dependence on weld metal composition, ferrite morphology and elemental distribution[8-10]. In the second part the main object was to clarify the effects of precipitation on mechanical properties and corrosion resistance[9-11]. The possibilities to monitor deteroriation of impact strength and corrosion resistance by measuring ferrite content and hardness is also considered. The results are compared to the behaviour of duplex and super duplex steels and are discussed in terms of practical implications on welding.

Experimental

Weld Metals

Duplex and super duplex weld metals deposited by covered electrodes for shielded metal arc welding (SMAW) have been examined. The two groups of weld metals had nominal compositions of 22.5% Cr 9.5%Ni 3%Mo 0.16%N and 25.5%Cr 9.5%Ni 4%Mo 0.26%N (Table 1). Standard and experimental types of duplex and super duplex weld metals were produced using ø 3.25 mm electrodes[(2)].

Most of the studies were performed on all weld metal specimens from weld pads (Table 2). Impact test specimens from the standard type duplex weld metal, used for isothermal aging studies, were produced by welding according to AWS standard procedure. Thin weld beads were deposited using a low heat input and a low interpass temperature (Table 2). The intention was to make the weld susceptible to further heat treatments by producing a "worst case" starting condition with a large fraction of microstructure already subjected to one or more reheating thermal cycles.

A range of heat inputs in combination with different interpass temperatures were used for welding of the standard type super duplex weld metal. Specimens for isothermal aging were prepared from a weld pad welded with medium heat input (0.9 kJ/mm) and low interpass temperature (<100°C).

Further details about the consumables and the welding procedures are given in Table 2. Heat treatments were performed according to Table 3. The 1 and 5 minutes heat treatments were made in a weld simulator using rapid resistance heating (≈ 5 s heating up time) whereas longer heat treatments were performed in a laboratory furnace. All heat treatments were followed by rapid quenching in water.

Metallography and Mechanical Testing

The ferrite content of the weld metals was determined in Ferrite Numbers (FN) using a Magne-Gage instrument. Overviews of the microstructures were obtained by light optical microscopy. Etching in Murakamis etchant and colour etching were used to produce contrast between the ferrite and the austenite and to reveal the presence of precipitates[12]. More detailed studies of the microstructure were performed by scanning electron microscopy (SEM) combined with microanalysis (EDX) and by transmission electron microscopy (TEM). Precipitates were identified by electron diffraction and analytical transmission electron microscopy (ATEM).

---

(2)   The electrodes are all from experimental batches. The corresponding rutile duplex and basic-rutile super duplex production electrodes are Esab OK 67.50 and Esab OK 68.53, respectively.

The impact toughness was determined for standard Charpy-V impact specimens (10x10x55 mm) with the notch located at the center of the weld metal. Three specimens were tested at room temperature for each heat treatment. Hardness testing was performed using the Vickers method with a 10 kg load.

Corrosion Testing

All weld metal specimens in the as welded condition, prepared from large weld pads, were used for testing the resistance to pitting corrosion and to intergranular corrosion. The Critical Pitting Temperature (CPT) in 10% $FeCl_3 \cdot 6H_2O$ (ASTM G48) was determined for the super duplex weld metals. Specimens were tested for 24 hours at each temperature, starting at 40°C and increasing the test temperature stepwise by 5°C. Visible pitting attack or > 5 mg weight loss was used as evaluation criteria. Two or three specimens were tested for each weld metal and for each combination of heat input and interpass temperature.

The resistance to intergranular corrosion of the experimental duplex and the standard super duplex weld metals was evaluated using the Streicher test (ASTM A262 practice B) and the Huey test (ASTM A262 practice C). Two specimens were tested for each weld metal and for each welding condition. All surfaces were wet ground using 120 grit SiC-paper before testing.

Fractured impact test specimens from the heat treated standard duplex weld metal were corrosion tested by electrochemical etching in oxalic acid. The specimens were embedded in epoxy exposing only the fracture surface. The fracture surface were ground flat removing enough material to avoid any effect of deformation during impact testing. Etching was performed in 10% oxalic acid at room temperature, with a current of 1 A/cm^2 and an etching time of 30 seconds. The resulting etch structures were then evaluated by light optical microscopy.

Results

Microstructure

Ferrite Morphology. The weld metals could be divided into two groups according to their microstructure; a) those having a "typical duplex" microstructure throughout (Fig. 1) and b) those in which also "austenitic" regions where the ferrite had a lacy or vermicular appearance (Fig. 2) occurred. The "normal duplex" microstructure consisted of primary ferrite grains with austenite mainly precipitated in a Widmannstätten manner. Some finely dispersed intragranular austenite was also found. The second type of microstructure was termed "austenitic" since this ferrite morphology is identical to that seen in weld metals used for welding of austenitic stainless steels.

All three duplex weld metals and the standard super duplex weld metal had a "typical duplex" microstructure throughout. However, the experimental super duplex weld metal had a predominantly "austenitic" structure. The orientation relationship between ferrite and austenite was studied by electron diffraction for both types of microstructure. The Kurdjumov-Sachs orientation relationship was always obeyed by the ferrite and austenite in the "duplex" regions (Fig. 3). However, this orientation relationship was usually not found in the "austenitic" regions where the ferrite had a vermicular appearance.

Precipitation in Duplex Weld Metals. No precipitates were found in any of the duplex weld metals in the as welded condition except for the inevitable microslag inclusions introduced by welding. However, precipitates were found in the ferrite and at ferrite/austenite boundaries after aging. Basically two morphologies of precipitates appeared (Fig. 4). Small precipitates dominated after aging at 700°C and were common up to 30 minutes aging at 800°C. Larger precipitates, that had almost completely replaced the ferrite after long aging times, were in majority after 3 hours at 800°C and the only type seen after aging above 800°C. Some large precipitates were also found after 3 hours heat treatment at 700°C.

Three different intermetallic phases were identified in the heat treated standard duplex weld metal; tetragonal σ-phase, rhombohedral R-phase and cubic χ-phase[1, 3]. The larger particles seen in light optical micrographs were mainly σ-phase that formed rather large, elongated particles in the ferrite and gave an even contrast in TEM (Fig. 5).

R-phase was found after heat treatments at 700 or 800°C. These particles had a characteristic irregular shape and uneven contrast in TEM (Fig. 6). Most of the R-phase appeared as small particles ($\approx$0.01-0.1 μm), mainly at ferrite/austenite phase boundaries, but also to some extent inside the ferrite grains. Small amounts of precipitates with a rounded, rectangular shape and a typical size of around 0.5 μm were found in the specimen heat treated at 800°C for 5 minutes. These precipitates were identified as χ-phase. However, R- and σ-phase were the only two phases present in sufficient quantities to be of significance for mechanical properties and corrosion resistance[10, 11].

Precipitation in Super Duplex Weld Metals. σ-phase was found in the experimental super duplex weld metal in the as welded condition and in the heat treated standard super duplex weld metal. σ-phase had precipitated almost only in "austenitic" regions in the experimental weld metal (Figs. 5 and 7). Optical microscopy indicated that also other intermetallic phases might be present after aging below 800°C. However, this was not verified by TEM.

Volume Fractions of Precipitates. The volume fractions of precipitates in the standard duplex weld metal were estimated from a combination of image analysis of SEM images, the decrease in ferrite content and information from optical and TEM micrographs. The phase present in largest volume fractions is clearly σ-phase. The only exception to this is below 800°C when R-phase is present in relatively large amounts. The results are summarized in a TTT-diagram for R- and σ-phase together with results from oxalic acid testing in Figure 8.

No estimation of the volume fractions of precipitates was made for the super duplex weld metals. However, it has been shown that a clear increase in hardness can be measured when approximately 2 vol.% of σ-phase has formed. Therefore, the more rapid hardness increase in the super duplex weld metal during aging suggests that σ-phase forms more rapidly than in the duplex types at 600, 700 and 800°C and most probably also at 900 and 1000°C.

Chemical Composition of Precipitates. A summary of the results of EDX analysis of precipitates in the heat treated standard duplex weld metal and the as welded experimental super duplex weld metal is given in Table 4 (see also ref. 10). σ-phase was rich in Cr but only slightly enriched in Mo, whereas R-phase had a high Mo content and a Cr content similar to that of the ferrite. χ-phase had an intermediate composition compared to R- and σ-phase. The composition of σ-phase was similar in both weld metals.

Corrosion

Oxalic Acid Etching Test. The dissolution rate of precipitates during oxalic acid etching was very high compared to that of austenite and ferrite (Fig. 9). Ferrite was etched somewhat more strongly than austenite. The rapid etching of precipitates produced a very distinct contrast in light optical micrographs. Two types of etch structures could be seen. Small, spotlike localized attacks taken as indications of the presence of individual small precipitates and larger continuous regions (Fig. 9) suggesting the presence of larger precipitates.

According to the ASTM A262-practice A standard for oxalic acid etching test the etch structure should be classified as step, dual or ditch structure. A ditch structure shows that the material has become sensitized to intergranular corrosion. This method of classifying the etch structures could not be used for the weld metals since the etch structure was of the step type also when precipitates were present. Grain boundary etching giving the ditch type etch structure was not observed in any of the specimens.

Oxalic acid etch structures of the standard duplex weld metal is shown in Fig. 9. Small precipitates in the ferrite and at ferrite/austenite phase boundaries appear in some regions already after 1 minute aging at 700 or 800°C. The number of precipitates is very small after 1 minute aging at 800°C but is significant after the 1 minute heat treatment at 700°C. Larger precipitates are the only type after heat treatment at 900°C and are frequent after longer aging times at lower temperatures. The ferrite is almost completely replaced by rapidly etching precipitates after 3 hours aging at 800 or 900°C.

Streicher and Huey Tests. The corrosion rate in the Streicher and Huey tests was higher for the rutile than for the basic experimental duplex weld metal (Table 5). The difference in corrosion rate was 13 % for the Streicher test and 50 % for the Huey test.

A lower corrosion rate was measured in Streicher testing for the standard super duplex weld metal than for the duplex weld metals (Table 5). However, there was clearly a relation between heat input and corrosion rate. An increase in heat input from 0.62 to 1.44 kJ/mm caused the corrosion rate to increase from 0.09 to 0.22 mm/year. No corresponding dependence of corrosion rate on interpass temperature was found.

Pitting Corrosion. The CPT-value (the lowest temperature were pitting and/or significant weight loss occurred) was 55±5°C for the standard super duplex weld metal. No difference in CPT could be seen between the different combinations of heat inputs and interpass temperatures used. However, a significantly lower CPT-value of 40°C was found for the experimental super duplex weld metal.

Ferrite Content, Hardness and Impact Toughness

Duplex Weld Metals. The ferrite content decreased and the hardness increased with increasing aging times for the standard duplex weld metal (Table 6). At 900°C there was a significant change in ferrite content already after 1 minute whereas a clear decrease could not be seen until after 3 hours at 700°C. The hardness increased with longer aging times and the highest hardness values were measured after 3 hours at 800°C and 900°C. Also at 700°C a clear increase in hardness was found but the hardness did not increase with aging time.

The changes in impact strength were most pronounced for long aging times when all specimens were clearly brittle (Table 6). However, the decrease was much more rapid at higher temperatures. At 700 embrittlement could not be seen until after 3 hours whereas a clear decrease was seen already after 5 minutes at 80(' and 900°C.

Super Duplex Weld Metals. A higher ferrite content and hardness, in as welded condition, was measured for the standard super duplex weld metal compared to the duplex types (Table 6). The hardness increased further during aging and the highest hardness levels were found after aging at 900°C. The hardness increase was more rapid than for the duplex weld metal. The experimental super duplex weld metal, with a predominantly "austenitic" microstructure, had a significantly lower ferrite content as welded compared to the standard type (33 and 44 FN, respectively).

Discussion

Microstructure

Solidification Modes. The microstructure of the experimental super duplex weld metal was mainly "austenitic" with lacy or vermicular ferrite (Fig. 6) whereas the duplex and the standard duplex weld metals all had a typical duplex microstructure. According to eg Suutala[13] and Elmer et al[14] the solidification mode has been ferritic-austenitic in "austenitic" regions and fully ferritic in the "normal duplex" regions. When plotting the ferrite content (FN) against the Cr_{eq}/Ni_{eq} ratio (Cr_{eq}= %Cr + 1.37·%Mo + 1.5·%Si, Ni_{eq}= %Ni + 0.31·%Mn + 22·%C + 14.2·%N)[15] for different super duplex weld metals (Fig. 10) it is found that the change from fully ferritic solidification to a combination of ferritic-austenitic and fully ferritic solidification occurs at approximately Cr_{eq}/Ni_{eq} = 2.25. The Cr_{eq}/Ni_{eq} ratios were 2.12 and 2.29 for the experimental and the standard super duplex weld metals, respectively, which is in agreement with the observed ferrite morphologies.

Precipitation in Super Duplex Weld Metals. Hardness measurements indicate that formation of significant amounts of precipitates during heat treatment occurred more rapidly in the standard super duplex weld metal than in the standard duplex weld metal. This is in agreement with the more rapid precipitation in super duplex stainless steels than in duplex stainless steels[3, 6, 7]. Although, it was not possible to study the start of precipitation by following the hardness it was clear from corrosion testing and microscopy, that no precipitation occurred during welding of the standard super duplex weld metal.

The σ-phase in the experimental super duplex weld metal almost only appeared in the "austenitic" regions where the weld metal had solidified as a mixture of ferrite and austenite. This can be understood in terms of differences in austenite/ferrite phase boundary energy and differences in ferrite composition for the two ferrite morphologies. The Widmannstätten type austenite forming after a fully ferritic solidification grows across the solidification

structure. Therefore, there is no clear correlation between the location of the ferrite dendrites formed during solidification and the location of the room temperature ferrite (Fig. 11). However, the ferrite in regions solidified as a mixture of ferrite and austenite is located at the centres of the as solidified ferrite dendrites. These regions are richer in Cr and Mo due to segregation during solidification[16].

The ferrite and austenite in "normal duplex" regions obeyed the Kurdjumov-Sachs orientation relationship whereas this was usually not the case where the ferrite had a vermicular appearance. This orientation relationship leads to low energy ferrite/austenite boundaries, in particular for planar interfaces, whereas phase boundaries with orientation relationships that deviates from this relative orientation have a higher interfacial energy. Studies on 304L austenitic stainless steel weld metals have shown that σ-phase forms most rapidly in regions with high energy interfaces not obeying the Kurdjumov-Sachs orientation relationship[17]. Therefore, the more rapid σ-phase formation in regions with vermicular ferrite is due to the combined effect of a more highly alloyed ferrite and higher energy interfaces.

Precipitation in Duplex Weld Metals. R-phase nucleated and grew quickly but was replaced by σ-phase after longer aging times. Obviously σ-phase is the more stable phase after long aging times[3]. The measured compositions of precipitates (Table 4) are in good agreement with those reported in literature[6, 7]. Other intermetallic phases, carbides and nitrides have earlier been identified in duplex stainless steels and weld metals[1, 3] but none of these were detected. R- and σ-phase were clearly the only two phases present in sufficient quantities to be of practical importance for mechanical properties and those most influencing the corrosion resistance.

Corrosion Resistance

Oxalic acid test. Two temperature regimes can be distinguished when plotting the approximate time for significant etching attack in the oxalic acid test on a TTT-diagram for R- and σ-phase precipitation (Fig. 8). Above 800°C the oxalic acid attack curve closely follows the curve for σ-phase precipitation. However, at 700°C significant etching attack was found already after 1 minute whereas 1% R-phase was estimated to have formed after approximately 1 hour.

In 22%Cr duplex stainless steels etching attack in the lower temperature regime is considered to be an effect of nitride and carbide precipitation[18]. However, no carbide or nitride precipitation could be detected in the weld metal suggesting that it is either insignificant or occur simultaneously as precipitation of intermetallic phases. Anyhow, the effect on corrosion resistance must be small compared to the effect of intermetallic precipitates. Consequently, the TTT-diagram for R-phase precipitation (Fig. 8) describes the time to formation of larger volume fractions of R-phase (>1%) whereas the curve showing the time to significant attack in oxalic acid more accurately describes the time to start of of R-phase formation.

Streicher and Huey test. The presence of σ-phase or other Mo-rich intermetallic phases, like Laves and χ-phase, is known to cause high corrosion rates in Huey and Streicher tests[11,19]. However, precipitation cannot explain the observed differences in corrosion rate (Table 5) since no precipatates were found in any of the weld metals subjected to Huey and Streicher testing.

A higher corrosion rate was found for the rutile than for the basic duplex experimental weld metal (Table 5). Previous studies have shown that the ferrite was more highly alloyed in this weld metal than in the basic weld metal due to greater partitioning of alloying elements during solidification and cooling[9]. There was a correlation between the alloying content and the corrosion rate also for the standard super duplex weld metal. Higher heat inputs gave higher corrosion rates. A higher heat input is well known to give a lower cooling rate and a more pronounced partitioning of elements between the ferrite and the austenite[20]. Therefore, differences in corrosion rates were due to differences in ferrite and austenite composition rather than precipitation in the as welded condition.

Pitting corrosion. The content of Cr, Mo and N largely determines the pitting corrosion resistance of stainless steels. However, also other factors than those included in the index are important. No effect of heat input and interpass temperature on CPT could be seen for the standard super duplex weld metal whereas a significantly lower CPT-value was found for the experimental weld metal. It is known for duplex weld metals that the ferrite

morphology does not directly influence the pitting resistance[21]. However, precipitation of intermetallic phases lowers the pitting resistance markedly. Therefore, the large difference in pitting corrosion resistance of the two super duplex weld metals was clearly caused by extensive precipitation of σ-phase in the experimental weld metal. In this case the ferrite morphology was of great importance via its effect on the nucleation and growth of σ-phase.

Ferrite Content, Hardness and Corrosion Resistance. Corrosion resistance and toughness deteroriated almost simultaneously during aging above 800°C whereas corrosion resistance was affected more quickly than toughness at lower temperatures in the standard duplex weld metal. The reason was the relatively strong effect on corrosion resistance of small amounts of precipitates. Therefore, a significant decrease in ferrite content or an increase in hardness, compared to the as welded condition, should be taken as an indication of a seriously lowered corrosion resistance (Table 6). However, the same approach cannot be used to guarantee an unaffected corrosion resistance.

Mechanical Properties

Embrittlement. The impact toughness of the standard duplex weld metal dropped drastically when 3-5 vol.% of intermetallic phases had formed (Table 6 and Fig. 8). A similar effect on impact strength has been reported for the duplex and super duplex steels where the presence of approximately 4 vol.% σ-phase decreased the toughness to unacceptable levels[7, 10]. The impact toughness had decreased to below 27 J after approximately 3-4 minutes at 850-950°C (Table 6) whereas the corresponding duplex steel (UNS S31803) will be embrittled after 10-40 minutes[7]. However, the time to embrittlement leaves a broad margin for the cooling rates normally obtained with recommended welding procedures. It should also be pointed out that the critical times determined here are conservative since "a worst case" weld metal with a large fraction of multiply reheated regions was studied.

Embrittlement will occur more quickly in super duplex steel grades than in duplex grades due to the more rapid precipitation in the more highly alloyed material[3]. The deteroriation of toughness can be expected to proceed more rapidly in the weld metal than in the steel. However, embrittlement of super duplex weld metals should normally not occur during welding.

Ferrite Content, Hardness and Impact Toughness. A significant decrease in ferrite content or an increase in hardness in the standard duplex weld metal clearly indicated serious embrittlement by precipitation of intermetallic phases (Table 6). However, ferrite content and hardness cannot be used as tools to guarantee the absence of embrittlement since impact toughness is affected before any increase in hardness can be seen. This is in line with the finding that precipitation of approximately 2 vol. % σ-phase is needed to give a clearly noticeable effect on hardness whereas effects on toughness can be seen for smaller amounts of precipitates[3].

Practical Welding

Practical experience shows that lowered corrosion resistance or embrittlement, of 22%Cr duplex steels and weld metals, due to slow cooling after welding is very uncommon. Quite contrary, any corrosion problems in connection with welding are most often due to nitride precipitation caused by overly rapid cooling or caused by poor gas protection of the root in one sided welding[5]. Therefore, embrittlement or loss of corrosion resistance will not occur in duplex weld metals when recommended welding procedures are followed.

The higher alloying content of super duplex weld metals, compared to duplex types, gives a higher strength and a better corrosion resistance. However, super duplex stainless steels are inherently more sensitive to precipitation and it is, therefore, even more important than for duplex grades that proper welding procedures are used. An important point is that the tendency to precipitation in super duplex weld metals is very dependent on the weld metal composition via its effect on the solidification mode. This effect is much stronger than the effect of heat input. A weld metal with a composition that with certainty gives a fully ferritic solidification should always be used for welding of super duplex steels to minimize the risk of precipitation and to optimize the weld metal properties.

Conclusions

Precipitation of intermetallic phases in the temperature interval 700-1000°C and its effects on corrosion resistance and impact toughness was studied for 22%Cr 9%Ni 3%Mo 0.15%N duplex and 25%Cr 10%Ni 4%Mo 0.25%N super duplex SMAW weld metals.

- R-phase formed rapidly at 700°C in the duplex weld metal whereas σ-phase replaced R-phase after longer aging times at 800°C and was the only phase found after aging at higher temperatures. Some χ-phase formed at 800°C. No carbides or nitrides were detected.

- R-phase was Cr- and Mo-rich, σ-phase was Cr-rich and χ-phase had an intermediate composition.

- Significant etching attack in the oxalic acid test occurred after shortest aging times (1 min.) at 700 and 900°C.

- Corrosion resistance and toughness deteroriates almost simultaneously during aging of duplex weld metals above 800°C whereas corrosion resistance is affected before toughness at lower temperatures.

- Ferrite content or hardness can be used as an indication of loss of corrosion resistance and embrittlement but not to guarantee unaffected properties.

- Corrosion rates in Streicher and Huey testing increased with increasing partitioning of elements between ferrite and austenite.

- The effect of solidification mode on corrosion resistance is much stronger than the effect of variations in heat input and interpass temperature for super duplex weld metals. A fully ferritic solidification gives a "normal duplex" microstructure with good resistance to σ-phase formation whereas ferritic-austenitic solidification results in a microstructure that is more susceptible to formation of detrimental phases.

Precipitation occurs somewhat more rapidly in duplex and super duplex weld metals than in the corresponding steels. However, embrittlement or loss of corrosion resistance will not occur in the weld metal if properly designed consumables are used and if recommended welding procedures are followed.

Acknowledgements

References

1. B. Josefsson, J.-O. Nilsson, A. Wilson, Duplex Stainless Steels'91, (Beaune, France: Les Éditions de Physique, 1991), p. 67.
2. J.-O. Nilsson and A. Wilson, B. Josefsson, T. Thorvaldsson, Applications of Stainless Steels'92, (Stockholm, Sweden: Jernkontoret, 1992), p. 280
3. J.-O. Nilsson, Mater. Sci. Techn., 8 8 (1992): p. 685.
4. D. J. Kotecki, Welding Journal, 68 11 (1989): p. 431s.
5. L. van Nassau, H. Meelker, J. Hilkes, Duplex Stainless Steels'91, (Beaune, France: Les Éditions de Physique, 1991), p. 303.
6. J.-O. Nilsson, P. Liu. Mater. Sci. Techn., 7 9 (1991): p. 853.
7. E. M. L. E. M. Jackson, L. M. Matthews: Stainless Steels'91, (Chiba, Japan: ISIJ, 1991), p. 730.
8. L. Karlsson, S. Pak, S.L. Andersson, ibid., p. 1093.
9. L. Karlsson, S. Pak, ibid., p. 1101.
10. L. Karlsson, L. Bengtsson, U Rolander, S. Pak, Applications of Stainless Steels'92, (Stockholm, Sweden: Jernkontoret, 1992), p. 335.
11. L. Karlsson, S. Pak, Corr. of Welded Constr. and Pressure Vessels, (Madrid, Spain: CENIM, 1992), p. 13.
12. G.F. Vander Voort, J O M, 41 3 (1989): p. 6.
13. N. Suutala: Acta Univ. Oulu, C26 (1983): p. 53.
14. J. W. Elmer, S. M. Allen, T. W. Eagar, Met. Trans. A, 20A (1989): p. 2117.
15. Hammar, U. Svensson, Solidific. and Casting of Metals, (London, UK: The Metals Society, 1979), p. 401.
16. E. Folkhardt, Welding Metallurgy of Stainless Steels, (Wien, Austria: Springer-Verlag, 1988), p. 72.
17. H. Kokawa, T Kuwana, A. Yamamoto, Welding Journal, 68 3 (1989): p. 92s.
18. C. Honglu, S.Hertzman, Intern. Rep. No 2689, (Stockholm, Sweden: Swedish Inst. for Metals Res., 1991).
19. G. Herbsleb, P. Schwaab, 1986.Werkstoffe und Korrosion. 37 1 (1986): p. 24.
20. T. G. Gooch, Duplex Stainless Steels'91, (Beaune, France: Les Éditions de Physique, 1991), p. 325.
21. S. Pak, L. Karlsson, Scand. J. Metallurgy, 19 (1990): p. 9.

Table 1   Chemical composition (wt.%) of weld metals[a].

Element:	C	Si	Mn	P	S	Cr	Ni	Mo	N	O
Duplex Weld Metals:										
D-standard:	0.022	0.86	0.86	0.017	0.006	22.32	9.68	2.91	0.17	0.07
D-exp. R.:	0.018	1.00	0.80	0.021	0.012	23.24	10.30	3.10	0.15	0.09
D-exp. B.:	0.043	0.72	1.61	0.013	0.011	22.49	9.41	2.84	0.14	0.05
Super Duplex Weld Metals:										
SD-standard[b]:	0.03	0.6	0.7	0.02	0.007	25.6	9.5	4.1	0.26	0.07
SD-exp. B.-R.:	0.023	0.53	0.62	0.015	0.008	25.09	10.23	3.90	0.27	0.08

[a] The chemical analysis of the weld metals were determined using an Optical Emission Spectrometer, except for C, O and N, where combustion furnaces were used.

[b] Typical composition.

Table 2.   Welding conditions

Weld metal	Coating type	Heat input (kJ/mm)	Max. interpass temp. (°C)	"Joint" type
Duplex weld metals:				
D-standard	Rutile	0.6	100	Weld pad/ AWS-joint
D-exp. R.	Rutile	0.8	150	Weld pad
D-exp. B.	Basic	"	"	"
Super duplex weld metals:				
SD-standard	Basic-rutile	0.62, 1.16 or 1.44	100	Weld pad
"		0.9	100	"
"		1.08	150	"
SD-exp. B.-R.	"	0.8	125	"

Table 3   Heat treatments.

Temperature:			600°C	700°C	800°C	900°C	950°C	1000°C
Duplex:		**Time**						
D-standard	1	minute		X	X	X		
"	5	minutes			X	X		
"	30	minutes		X	X	X	X	X
"	3	hours		X	X	X		
Super duplex:		**Time**						
SD-standard	30	minutes	X	X	X	X		X
"	1	hour	X	X	X	X		X
"	2	hours	X	X	X	X		X
"	4	hours	X	X	X	X		X

Table 4   Typical chemical composition (wt.%) of precipitates.

	Fe	Cr	Ni	Mo	Si
D-standard:					
σ-phase:	55	34	4	6	1
Small R-phase:	36	19	3	38	4
Large R-phase:	43	25	4	25	2
χ-phase:	49	28	3	18	1
SD-exp. B.-R.:					
σ-phase:	54	32	6	7	1

Table 5.   Corrosion rates in Huey and Streicher tests.

Weld metal	Heat input (kJ/mm)	Max. interpass temp. (°C)	Corrosion rate (mm/year) Huey test	Streicher test
Duplex weld metals:				
D-exp. R.	0.8	150	0.45	0.30
D-exp. B.	"	"	0.27	0.24
Super duplex weld metal:				
SD-standard	0.62	100		0.09
"	1.16	"		0.15
"	1.44	"		0.21
"	1.08	150		0.10

Table 6   Ferrite content, room temperature impact strength and hardness.

Heat treatment		Duplex: D-standard			Super duplex: SD-standard	
		Ferrite content (FN)[a]	Impact strength (J)[a]	Hardness (HV$_{10}$)[a]	Ferrite content (FN)[a]	Hardness (HV$_{10}$)[a]
As welded		30	50	256	44	293
600°C/	30 min					295
"	1 h					294
"	2 h					293
"	4 h					309
700°C/	1 min	28	63	272		
"	30 min	29	59	278		294
"	1 h					296
"	2 h					342
"	3 h	16	8	272		
"	4 h					356
800°C/	1 min	26	66	272		
"	5 min	24	25	274		
"	30 min	17	11	292		332
"	1 h					400
"	2 h					397
"	3 h	1	2	322		
"	4 h					385
900°C/	1 min	24	51	258		
"	30 min	11	4	295		345
"	1 h					398
"	2 h					411
"	3 h	1	3	311		
"	4 h					433
950°C/	30 min	7	3	294		
1000°C/	30 min	20	12	261		320
"	1 h					360
"	2 h					360
"	4 h					366

[a]   The spread for a given heat treatment is typically ±2 J, ±2 FN and ± 10 HV$_{10}$.

Figure 1 Typical microstructure of duplex weld metal with Widmanstätten type austenite in ferrite (dark phase).

Figure 2 Super duplex weld metal with a micro-structure consisting of regions with a "normal duplex" microstructure (left) and "austenitic" regions in which the ferrite (dark phase) had a lacy or vermicular appearance.

Kurdjumov-Sachs orientation relationship

$(111)_\gamma \mathbin{/\!/} (011)_\alpha$

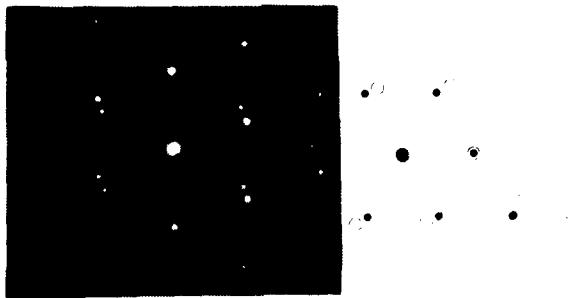$[\bar{1}01]_\gamma \cdot [\bar{1}\bar{1}1]_\alpha$

Figure 3 Electron diffraction pattern showing Kurdjumov-Sachs orientation relationship in the "normal" duplex microstructure.
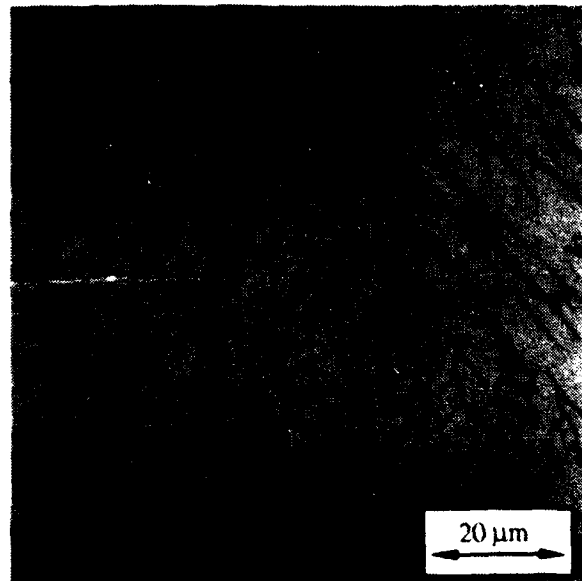

Figure 4 Light optical micrograph showing extensive precipitation of small (dark spots) and larger (dark grey) precipitates in ferrite (light grey) of duplex weld metal aged for 30 minutes at 800°C.

Figure 5 TEM-micrograph of σ-phase precipite in an "austenitic" region of a super duplex weld metal.

Figure 6 TEM images of R-phase particles at ferrite/austenite boundaries formed in a duplex weld metal during isothermal heat treatment.

Figure 7 Optical micrograph showing the preferential precipitation of σ-phase (dark) in "austenitic" regions in a super duplex weld metal.
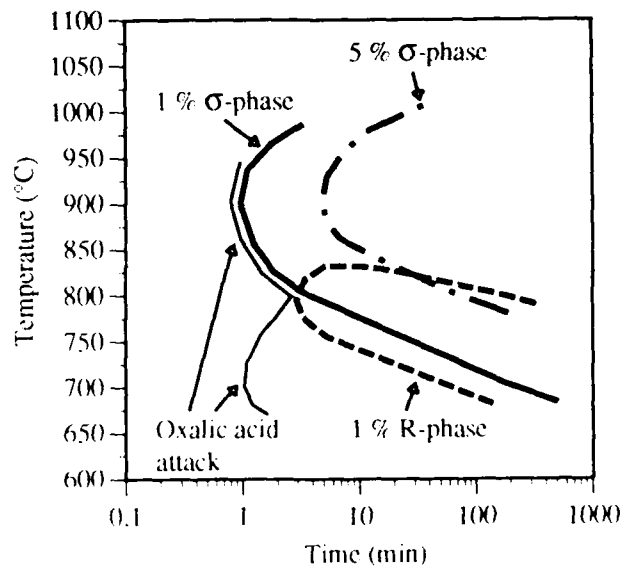
Figure 8 Time for significant attack in oxalic acid superimposed on TTT-diagram for R- and σ-phase precipitation in a duplex weld metal.
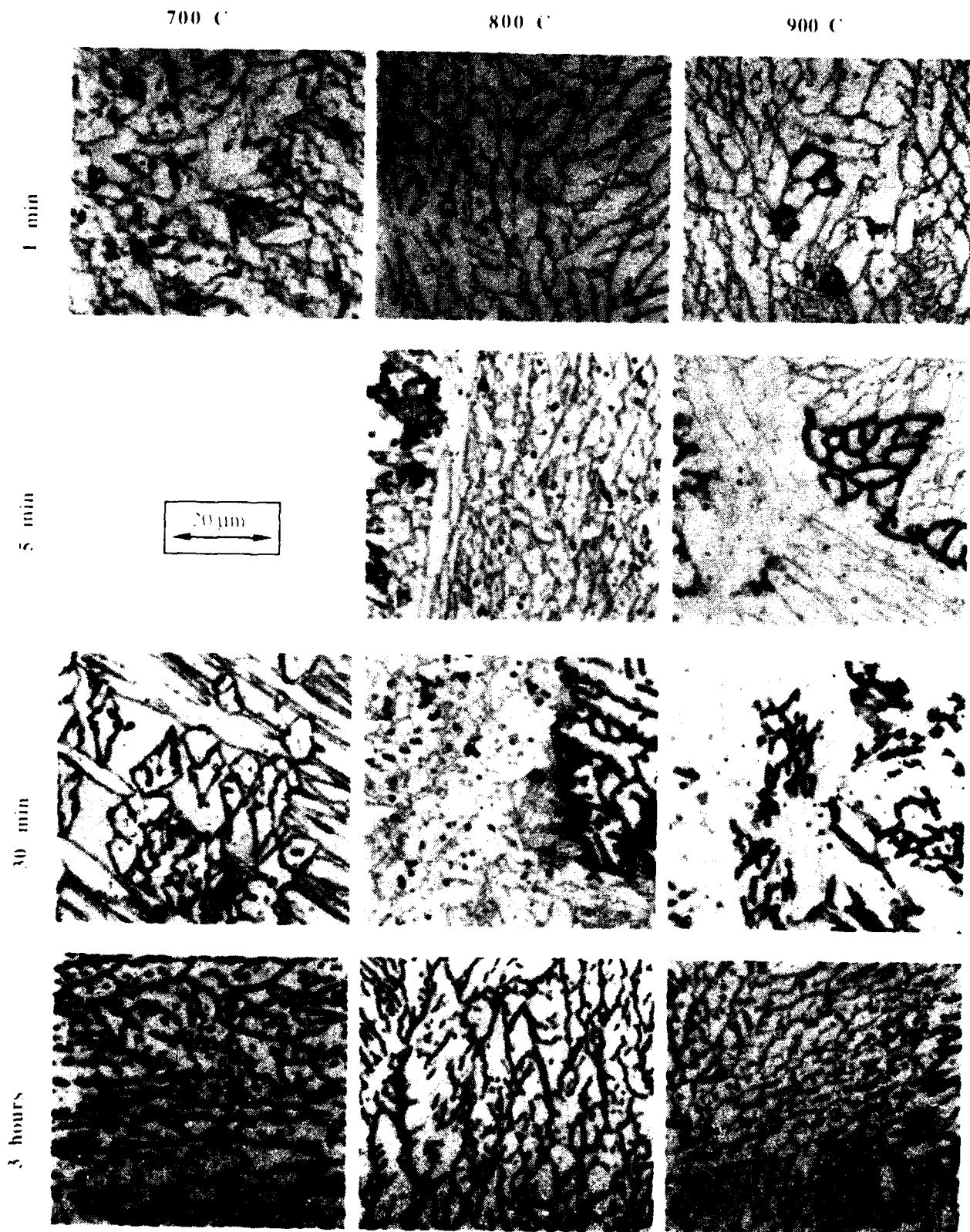
Figure 9 Light optical micrographs showing the microstructure of the standard duplex weld metal after oxalic acid etching. Precipitates are etched preferentially and give a dark contrast. Small precipitates formed at 700 and 800°C. Only larger precipitates were found after heat treatment at 900°C and were also seen after longer aging times at 700 and 800°C.
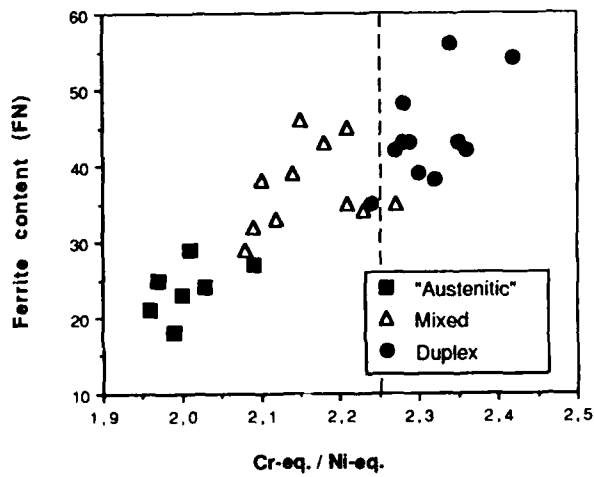
Figure 10   Ferrite Numbers (FN) plotted as a function of Cr_{eq}/Ni_{eq} for super duplex SMAW weld metals. The weld metals are grouped according to their microstructure.
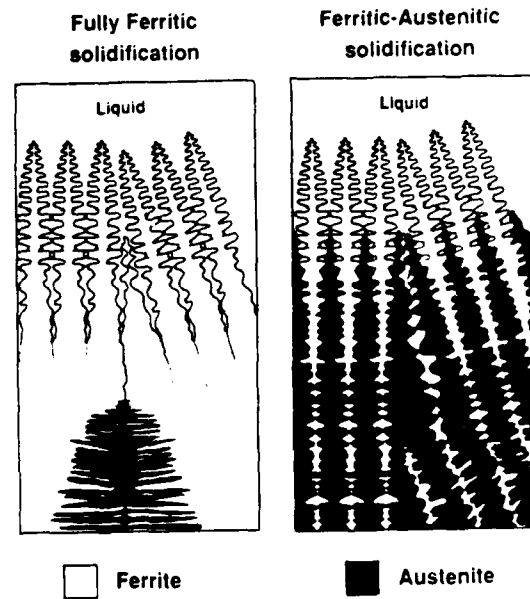
Figure 11   Schematic illustration of fully ferritic and ferritic-austenitic solidification.

Corrosion Characteristics of Plasma Weld Surfacing with the Duplex Materials, X 2 CrNiMo 22 5 3 and X 2 CrNiMoN 25 7 4

Ulrich Draugelates
Technische Universität Clausthal, ISAF
Agricolastraße 2
3392 Clausthal-Zellerfeld, Germany

Belkacem Bouaifi
Technische Universität Clausthal, ISAF
Agricolastraße 2
3392 Clausthal-Zellerfeld, Germany

Andreas Stark
Technische Universität Clausthal, ISAF
Agricolastraße 2
3392 Clausthal-Zellerfeld, Germany

Irmgard Garz
Technische Universität Magdeburg, IWW
PO Box 41 20
3010 Magdeburg, Germany

Sabine Schulze
Technische Universität Magdeburg, IWW
PO Box 41 20
3010 Magdeburg, Germany

Abstract

During recent years, claddings for protecting against corrosion have gained increased importance as far as the development of new materials is concerned. For producing composite materials of this kind, weld surfacing has steadily gained importance as an economical cladding technique. In comparison with conventional methods, plasma hot wire weld surfacing (PHS) is characterized by the application of thin claddings with very low dilution and high deposition efficiency, [1-5]. Within the scope of the present investigations, corrosion-resistant claddings of duplex steels have been applied by the PHS welding method with a thickness of 1 to 2 mm and a dilution of less than 10 percent.

Key terms: surface protection, plasma hot wire weld, corrosion resistance, electrochemical noise

I. Introduction

Duplex materials possess a structure with austenitic and ferritic components and exhibit considerably higher strength as well as improved corrosion resistance in comparison with austenitic steels. Because of their corrosion resistance, the duplex materials of types X 2 CrNiMo 22 5 3 and X 2 CrNiMoN 25 7 4 are employed to an increasing extent in chemical apparatus and plant construction as well as for flue gas desulfurization chambers and in offshore engineering. This stability is due to a pore-free passive layer, which results from the high chromium content; this passivating layer impedes the passage of metal ions from the metal into the electrolyte and thus strongly decreases the corrosion rate. With the addition of molybdenum as alloying partner, the resistance of the passive layer to attack by chloride ions is enhanced, and the breakdown potential is thus shifted to higher values. Because of the low carbon content of 0.03 percent at the most, this material group likewise exhibits high resistance to intercrystalline corrosion (IC). Further alloying elements enhance the effect of chromium.

The protective duplex claddings applied by the PHS technique have been examined with respect to structure, variation of the austenite-ferrite ratio, and corrosion resistance. The corrosion tests comprise the determination of resistance to intercrystalline corrosion and pitting.

The results thus achieved are presented and discussed in this article.

II. Experimental procedure

A. Materials
Table 1 shows the chemical composition of the steels in the hot rolled (wrought) and the PHS (clad) state. The two claddings of type X 2 CrNiMoN 22 5 3 (called duplex in the following) differ only slightly in carbon content. The nickel content is somewhat higher than usual for this type. The thermal history of the wrought duplex and type X 2 CrNiMoN 25 7 4 (called super duplex) is not known.
The welding ferrite content determined by magnetoinductive measurement of the permeability with the Ferritoscope MP3 (Fischer Company, Germany) is likewise low; this may be caused to some extent by the procedure applied. Some specimens have been aged and subsequently water-quenched (WQ). Some claddings were mildly annealed (MA) at 1050°C / 30 min / WQ. Thermal treatments and ferrite contents are summarized in table 3.
The microstructure was investigated with the use of the optical and scanning microscope (REM-EDX/WDX type DSM 960/Zeiss, Germany). Some results are given in table 4.

1. Corrosion testing procedures: Specimens were taken as sheets. From claddings the upper (second) layer (2.L) was used (2 to 3 mm) after mechanical separation. For electrochemical measuements specimens were electrically contacted with a wire of the same material by spot welding and embedded in resin; hence, the working area of about 1 cm² consisted of the welded surface only.

2. Iron III chloride test: The critical pitting temperature (CPT) and the critical crevice temperature (CCT) were evaluated from the iron III chloride test in accordance with ASTM G48 method A or B, but applied in a slightly modified manner [6]. Wrought sheets are wet ground (600 grit abrasive paper). Claddings (2L) were exposed in the as-welded, ground or pickled (acid) state. The mechanically separated (bottom) surface was always ground. In both tests the temperature of the 10 percent FeCl₃·6 H₂O solution was varied by 2.5 K after each immersion period of 24 hours.
For the investigation of crevice corrosion (modified method B), specimens of about 38 x 58 x 2 mm with a central borehole (average: 9 mm) were used. Two Teflon® blocks with six perpendicular grooves [6] were fastened on each side by a Teflon® screw M8.
The specimens were examined under 20 x magnification. At the first appearance of pits or fine crevices, the pit depth and density were examined.

3. Electrochemical (EC) pitting tests: Single-cycle potentiodynamic pitting scan (PPS) tests as described in [7] were conducted in the usual trielectrode cell with a platinum counterelectrode and a saturated calomel reference electrode (SCE). A microprocessor-controlled potentiostat IMP 83 PC (Jaissle, Germany) was operated at a scan rate of 0.5 mV/s in argon-purged solutions of NaCl (0.01 to 1 M) at 25, 40, and 70°C. After measuring the stable free corrosion potential (about -650 mV), the potential was scanned from -700 m ′ in the noble direction and reversed once a preset threshold current density of 50 A/m² had been reached. The potential associated with 1 A/m² in the noble scan is taken as pitting potential. The repassivation potential is characterized by the closure of the anodic hysteresis loop which occurs during the reverse scan.
In a second step, potentiostatic potential versus time curves were taken at potentials in the neighborhood of the pitting potential U_p derived from PPS. The potential at which the passive current begins to increase slowly within 2 hours and results in visible pits is regarded as the pitting potential.

4. Modified Strauss test and Huey test As specified in SEP 1877/DIN 50914, a copper - copper sulfate - 35 percent sulfuric acid solution was used during a boiling period of 15 h. The conditions correspond to ASTM 262A-E or -F with a medium aggressivity of the test solution. After boiling, the

specimens were bent through 90° over a diameter equal to one-fourth of the specimen thickness. Longitudinal and transverse sections were examined (100 to 250 x magnification) in order to determine the existence and depth of intergranular attack (IGA).
The Huey test was used in accordance with ASTM A 262-86 C.

5. Electrochemical potentiodynamic repassivation (EPR) test: With the use of the equipment described above, an attempt was made to demonstrate the tendency toward IGA by a double-loop EPR-test [8,9] under the following conditions:
0.5 M H_2SO_4 + 0.01 M KSCN, Ar-deaerated, 70 °C, scan rate: 2 mV/s.
The specimens were wet-ground (600 grit). After reaching a stable corrosion potential, the scan proceeds from -500 mV to +300 mV (anodic loop) and reverses immediately. The IGA is indicated by the charge relation (double loop EPR quotient),

$$C = Qr/Qa,$$

from the repassivation current peak of the reverse scan and the higher current peak of anodic passivation in connection with metallographic examination of the tested surfaces.

III. Results and discussion

A. Microstructure
The duplex SS with a ferrite content of about 38 percent exhibits elongated ferritic grains arranged in layers between the austenite in longitudinal wrought specimens (figure 2). The (Cr/Ni)eq values of 2,30 (wrought) and 1,93 (cladding), respectively, as given by De Long [10] implies primary ferritic solidification. The claddings show Widmanstetten structure with lath of austenite (figure 3). In contrast to the superduplex with its high N content and $(Cr/Ni)_{eq}$ of 1,36 (wrought) and 1,18 (cladding), respectively, primary austenitic solidification is to be expected.

B. Resistance to pitting and crevice corrosion
1. Results of the iron III chloride immersion test: The results are summarized in table 2; the better resistance of the X2CrNiMoN 25 8 5 as compared with the X2CrNiMoN 25 5 3 SS (PRE: 45 and. 45) is evident. This finding agrees with its higher pitting resistance equivalent [11].

    PRE = %Cr + 3,3x %Mo + 16x %N   (1)

The PHS claddings do not reach the same high values of CPT and CCT. It is interesting to note that CPT is strongly influenced by surface treatment. Ground and pickled surfaces are more resistant than those in the welded state (see the next section). On the other hand, the upper thin coat or "skin" resulting from the welding process leads to a higher pit density but markedly lowered average pit depth; this seems to be a decisive advantage over the ground wrought reference material.

C. Electrochemical behavior in sodium chloride solutions
1. Influence of the surface state of claddings: In agreement with the immersion tests, PPS-curves also show the better resistance of ground and pickled surfaces as compared with the as-welded state (figure 4). The latter shows a pitting potential more negative by some hundred mV than for the wrought material, whereas in the ground state no marked difference is observed between PHS and wrought duplex SS. Because the potentiodynamic measured U_p are higher than the breakdown potential in sulfuric acid (~900 mV with respect to SCE), the precise value may be masked by anodic currents corresponding to oxygen evolution [7]. The superior pitting resistance of wrought duplex SS as compared with cast SS, which may be partially compared with claddings, has also been demonstrated in [7]. The pronounced hysteresis found in the as-welded state, which results in a very negative repassivation potential, is caused by pits which behave as crevices. Authors suppose that pitting begins at small failure

sites or thermal cracks or fissures in the upper "skin", which consists of high temperature oxides. Therefore, the pits grow preferentially in the underlying metal and are stimulated by lowering of the pH value as a result of hydrolysis of corrosion products inside the pit and the hindrance of anion exchange with the bulk solution. In practice, the necessity of removing oxide films after welding is the subject of controversy. In most cases, as in [12], pickling followed by repassivation is recommended.

The lower resistance of the as-welded state may be caused by thermal chromium depletion in the oxide and in the underlying alloy substrate, as is known for SS [12]. Moreover, the pitting resistance of duplex SS is influenced by the ferrite-austenite ratio [13]. The ferrite content is decreased from 39 to 33 percent by grinding; in accordance with [13], this results in the better pitting resistance measured. The higher ferrite content of the upper film may be caused by the higher cooling rate after welding.

2. Influence of the test temperature: It is generally known that the pitting resistance of SS decreases with increasing temperature, but that the kind of characteristic depends of the chemical composition and type of SS [6,14,15]. Molybdenum- bearing SS with high pitting potentials at room temperature usually exhibits pronounced decay at about 40 to 60 °C. For duplex SS, this is expected at lower temperatures [15]. As indicated in figure 5, U_P decreases mainly between 25 and 40 °C in a manner not yet characterized precisely from the transpassivation range to about 400 mV (wrought materials) and about 100 mV (claddings). From our measurements we can give the following ranking order for the pitting resistance at 40 °C:

superduplex (wr.) > duplex (wr.) > claddings (both types)

At 70 °C there are no decisive differences at all.

Wallis [16] has pointed out that Mo as an alloying constituent exerts no influence in the range of transpassive breakdown potential, but that it promotes the formation of Cr-rich resistant passive layers because of the oxidizing properties of the MoO_4^{2-} anions known as anodic inhibitors. This takes place only in the transpassive range for Mo at potentials above 600 mV/SHE (about 350 mV/SCE). Below this range, molybdenium exerts little influence on the pitting potential. The results in figure 5 coincide well with these characteristic features. For the claddings, one must take into account the segregation properties of molybdenum and the possibility of precipitation of Mo-rich phases which may lower the pitting resistance [16]. In order to find the exact reason for the lower resistance of the claddings at 40 °C, further investigations are required. The general differences in pitting behavior of the two steels show the PPS in figure 6a for the wrought and figure 6b for the cladding specimen.

3. Influence of chloride concentration: As indicated in figure 7, the potentiodynamically measured pitting potentials of the duplex SS decrease with rising concentration of chlorides (0.01 M to 1 M NaCl, 70 °C) and obeys essentially the well known expression,

$$U_P = a - b \cdot \lg c_{Cl^-} \qquad (2)$$

Deviations of the cladding pitting potential in dilute solution may be caused by the potentiodynamic measurement and perhaps by the kind of definition of U_P which is more suitable for more concentrated solutions. Long-term potentiostatic measurements are in preparation.

The better resistance of the wrought material is particularly evident in dilute solution; in 1 M NaCl, the difference from the as welded state is decreased to about 75 mV.

4. Location of pits: Pitting behavior and topography of duplex SS may differ from that of single phase alloys because of solute partitioning effects between austenite (γ) and ferrite (α) phases and the presence of α / γ-interfaces. As can be seen from table 4, the ferrite is enriched mainly in chromium and molybdenum and therefore ought to be more resistant to pitting than the austenite. Phase transformations and segregations such as chi- and σ-phase precipitations may result in regions depleted with respect to chromium and molybdenum. As expressed in the PRE number, nitrogen strongly increases the pitting resistance. In detail, the higher solubility of N in the γ-phase increases mainly the resistance of austenite. Furthermore, the situation is influenced by thermal treatment and environment.

As shown by PPS experiments, large pits extend over α and γ regions. Stopping the anodic loop immediatly after increasing of current density or after suitable potentiostatic experiments indicates that

pitting can also be associated with the ferritic regions (figures 8a, 8b). Therefore, the stabilizing effect of nitrogen on austenite seems to overcome the effect of the higher Cr and Mo content of ferrite. Equal resistance in NaCl/H$_2$S solution requires about 0.18 percent N [17].

5. Influence of aging : Increasing the aging temperature shifts the pitting potential in the cathodic direction (figure 9). At 850 °C this is caused by σ-phase precipitation (see table 4). Potgieter [18] has found that in NaCl a small σ-phase content is sufficient to severely impair the pitting corrosion resistance of duplex SS, to displace the pitting potential to less noble values, and to cause pitting in both phases. The poor resistance at 750 °C may be due to the Mo- and Cr-rich chi-phase which is surrounded by a matrix depleted with respect to molybdenum and chromium [19]. It is supposed that the σ-phase acts in the same way in inducing pit nucleation at the phase boundary of the depleted matrix / intermetallic phase because of lattice irregularities in the passive layer [16].

D. Intergranular corrosion

1. Modified Strauss test: This test may be applied to evaluate the susceptibility of as-received material to IGA as a result of chromium carbide precipitation, M$_{23}$C$_6$, and the resistance of extra-low-carbon grades to sensitization caused by welding and heat treatments. As indicated in the TTP diagram [20] for duplex SS (figure 10) in the range from 550 to 1000 °C, chromium nitrides, chi-phase, M$_{23}$C$_6$ carbides, and, after a longer time, σ-phase are to be expected. However, as indicated by the Strauss test (figure 11), there are no fissures after bending, and this implies the absence of IGA caused by chromium depletion following M$_{23}$C$_6$ precipitation. The brittle fracture of the bent specimen after aging at 800 °C and higher is caused by σ-phase precipitation, followed by an increase in hardness (see table 3). Though not usual, the measured rate of general attack increases considerably at 750 and 850 °C. The former may be caused by chi-phase, the latter by σ-phase precipitation. Probably the highest attack is also caused by unstable austenite as a result of transformation of ferrite to sigma and austenite.

2. Results of the Huey Test: The test shows the good resistance of duplex SS in the as-received state with a corrosion rate less than 0,5 mm/a. It is interesting to note that the cladding exhibits a somewhat lower rate (0.28 mm/a, in comparison with 0.41, figure 12). The maximal depth of attack on the upper side in the as-welded state is 8 μm; on the mechanically treated lower side the value is 28 μm (as compared with 12 μm for wrought duplex). From this observation, it can be concluded that under practical conditions the claddings are more resistant than in this test. Figure 13a shows that the lines of attack are controlled preferentially by the welding direction, whereas on the underside of second layers, the attack occurs preferentially at primary ferritic grain boundaries. Short-term aging at 750 °C is caused by the preferential attack on ferrite with finely dispersed chi-phase precipitations. The corrosion rate decreases with the beginning of σ-phase precipitation, although chi-phase exists, too. Therefore, the better resistance may be caused by a transformation from ferrite to austenite (residual ferrite content: 3 percent) and thus by the high resistance of austenite in the potential range of the Huey test.

3.Results of the double loop EPR test: Proper test procedures for determinig the IGA susceptibility of duplex SS have been studied to a far lesser extent than those for austenitic SS. In spite of its higher resistance, the test has to be intensified, for instance, by increasing the concentration of acid or activator [21].
The EPR curves (figures 14a to c) [22] show a first anodic peak at about -320 mV, which is attributed to preferential ferrite dissolution, and a second, higher peak at about -230 mV, which is attributed to the austenitic matrix. Both peaks exhibit a tendential increase with aging temperature and aging time, but the ferrite peak degenerates to a shoulder or vanishes, if the ferrite content decreases to less than 10 percent as a result of the transformation. During the reverse scan, the shift to more cathodic potentials for the ferritic repassivation peak is clearly expressed in the aging state (figures 14a and b). Mill annealing (MA) of the claddings before aging suppresses the anodic ferritic peak as well as the repassivation peak and results in full IGA-resistance (see table 3). In accordance with the EPR-quotient (table 3) and metallographic investigations, sensibilization of wrought duplex occurs after aging (750 °C / 5 h and 850 °C / 3 h) and causes IGA in austenite, besides preferential attack in the former ferritic regions (figure 15) This agrees with the σ- and chi-precipitation at the γ / γ-grain boundaries and the dispersed morphology of the σ-phase which results from the ferrite transformation (figure 16). The dispersed σ-phase causes the most

severe decrease in corrosion resistance [23]. The claddings are susceptible only at 750 °C. In the microstructure, parts of coherent grooves exist in the neighborhood of austenitic lathes; this marks the primary ferrite grain boundaries (figure 17). As as result of aging at higher temperatures and longer times, the known healing effect is realized sooner with claddings than with wrought material.

It can be concluded that in the as-received state neither the wrought duplex nor the PHS claddings are susceptible to IGA, and that the results of the EPR test under the conditions considered are in accordance with the chemical tests.

References

1. U. Draugelates, B. Bouaifi, Mat.-Wiss u. Werkstofftech., 19 (1988) p. 201-205
2. U. Draugelates, B. Bouaifi, Int. Kongreß und Fachausstellung für Beschichtungstechnologie, Wiesbaden/Germany, Coat Tech (1989) p. 231-249
3. Th. Hoffmann, U. Draugelates, B. Bouaifi, R. Reiter, VDM-Report 13 (1989) p. 1-9
4. U. Draugelates, B. Bouaifi, Industrieanzeiger 79 (1990)
5. B. Bouaifi, Dissertation, TU Clausthal, 1988
6. M. Reuner, U. Heubner, M.B. Rockel, E. Willis, Werkstoffe und Korrosion 37 (1986) p. 183
7. R. Siram, D. Tromans, Corrosion 45 (1989) p. 804
8. V. Chihal, A. Desestret, M,Froment, G. H. Wagner,
   5th Conf. European Federation of Corr., Paris/France 1973
9. J. R. Kearns, Draft Internat. Standard ISO/TC 156 WG N 39 Austenitic Stainless Steels, EPR-Test (1989)
10. W. T. De Long, Welding Research Supplement (1973) p. 281
11. M. Pokl, A. Ibach, K.H. Lange, Pract. Met 28 (1991) p. 70
12. S. Turner, F. P. A. Robinson, Corrosion 45 (1989) p. 710
13. Y Ishizawa, T. Inazumi, Duplex Stainlees Steels 86, The Haag / Netherlands (1986) p. 392
14. I. Garz, E. Dörfler, Korrosion (Dresden / GDR) 5 (1978) p. 242
15. N. N., Current Events,Werkstoffe und Korrosion 37 (1986) p. 183
16. E. Wallis, Werkstoffe und Korrosion 41 (1990) p. 155
17. H.Tsuge, Y. Tarutani, T. Kudo, Corrosion 44 (1988) p. 305
18. J.H. Potgieter, British Coros. Journ. 27 (1992) p. 537
19. A. Sedriks, Corrosion 42 (1986) p. 376
20. R. Grundmann, P. Gümpel, R. Ortmann, P. Roth, Thyssen Edelst. Techn. Ber. 14 (1988) p. 57
21. J. R. Scully, R.G. Kelly, Corrosion 42(1986) p. 537
22. I. Garz, S. Schultze, B. Bouaifi, to be published
23. A. Zingales, G. Quartarone, G. Moretti, Corrosion 41 (1985) p. 141

Table 1 Chemical composition (by mass, in %) and PRE number

Material	C	Si	Mn	P	S	Cr	Mo	Ni	N	Cu	Fe	PRE %
X 2CrNiMoN 22 5 3												
wrought	0,023	0,32	1,70	0,01	0,005	22,35	3,06	5,35	0,15	0,30	66,35	34,8
cladding 1	0,017	0,52	1,55	0,01	0,005	22,34	3,20	7,81	0,15	0,69	64,49	35,3
cladding 2	0,029	0,51	1,65	0,02	0,005	22,51	2,85	7,61	0,13	0,34	64,35	34,3
X 2CrNiMoN 25 7 4												
wrought	0.026	0,39	0,65	0,03	0,002	25,44	3,95	6,95	0,50	0,51	61,56	46,5
cladding	0,028	0,27	0,51	0,02	0,003	24,78	3,91	8,58	0,50	0,07	61,33	45,7

Table 2 Modified Ferric Cloride Test (ASTM G48 , A and B)

Material	state	CCT °C	CPT °C	pit density $z \cdot 10^{-3}$ m^{-2}	$\varnothing$ pit depth mm
X 2CrNiMoN 22 5 3 cladding	as welded	-	20,0	11,0	0,34
	pickled	-	27,5	1,4	1,40
	ground	15,0	27,5	1,6	1,30
X 2CrNiMoN 22 5 3 wrought	ground	27,5	42,5	0,5	0,51
X 2CrNiMoN 25 7 4 cladding	as welded				
X 2CrNiMoN 25 7 4 wrought	ground	32,5			

Table 3 Thermal treatment, ferrite content, hardness and data of EPR test

Material	ageing T / °C	t / h	α / %	HV 10	C (Qr / Qa)	Ir / Ia	Remarks
X 2 CrNiMoN 22 5 3 wrought	-	-	36	249	0,02	0,06	
	750	0,5	29	231	0,06	0,19	
	750	5	18		0,22	0,37	
	850	3	9	312	0,14	0,29	IGA in γ select A in α
X 2 CrNiMoN 22 5 3 cladding	-	-	34	250	0,06	0,17	
	750	0,5	31	240	0,19	0,38	
	750	5	25		0,28	0,55	IGA at GB
	850	3	3	308	0,04	0,07	of prim.struct.
	800	100	0		0,002	0	
X 2 CrNiMoN 22 5 3 cladding + MA (1050°C / 0,5h)	-	-	35		0	0	
	750	0,5	30		0,002	0,01	
	850	3	7		0,04	0,05	
X 2 CrNiMoN 25 7 4 wrought			49				
X 2 CrNiMoN 25 7 4 cladding			33				

Table 4 REM / EDX characterization of different phases in X 2CrNiMoN 22 5 3

state	ageing		phase	chemical composition - loy mass, in %						
	T / °C .	t / h		Cr	Fe	Ni	Mo	Mn	Si	% α
wrought			α	24.65	64.40	4.28	4.29	1.95	0.42	35
			γ	21.40	66.60	7.26	2.41	1.99	0.35	
cladding			α	24.54	64.76	4.17	3.24	1.62	0.83	34
			γ	21.33	66.28	7.75	2.06	1.86	0.55	
wrought	850	3	α	25.89	66.81	2.88	2.53	1.66	0.24	9
			γ	21.06	66.76	7.42	2.63	2.05	0.36	
			σ	19.87	58.08	3.19	6.60	1.90	0.51	
			χ	24.05	57.68	3.86	11.51	1.68	1.04	
cladding	850	3	α							3
			γ	20.61	65.43	9.21	2.43	1.73	0.54	
			σ	30.48	57.28	3.28	6.81	1.39	0.77	
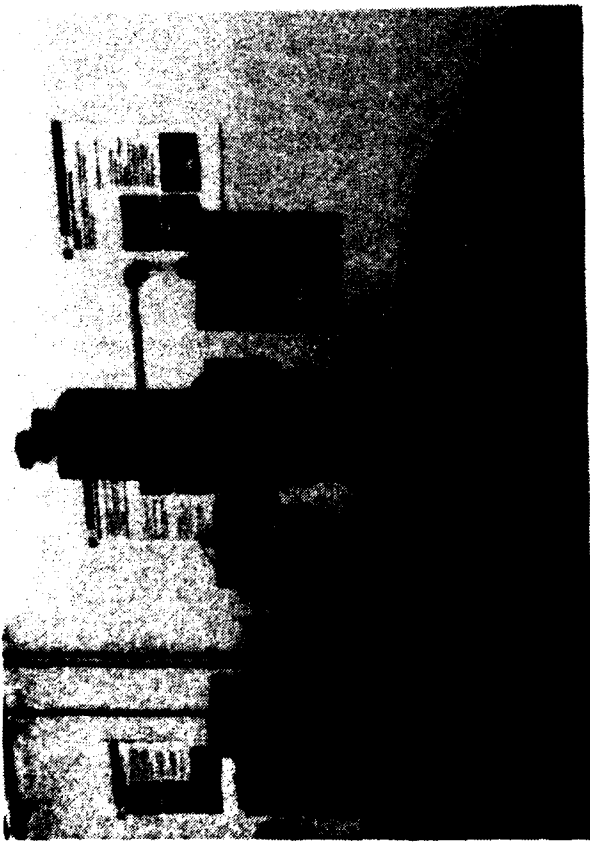
Fig. 2 X 2 CrNiMoN 22 5 3 Wrought Structur
Etched (10%HNO$_3$, 3%HF)

Fig. 3 X 2 CrNiMoN 22 5 3, Cladding, as Welded
Etched (Kalling's Reagent [7])

Fig. 1 PHS - Apparature

X 2CrNiMoN 22 5 3
1 M NaCl
25°C
0,5mV/s

as welded + grinded

as welded + pickled

as welded

wrought

Potential U in V(SCE)

current density i in A/m^2
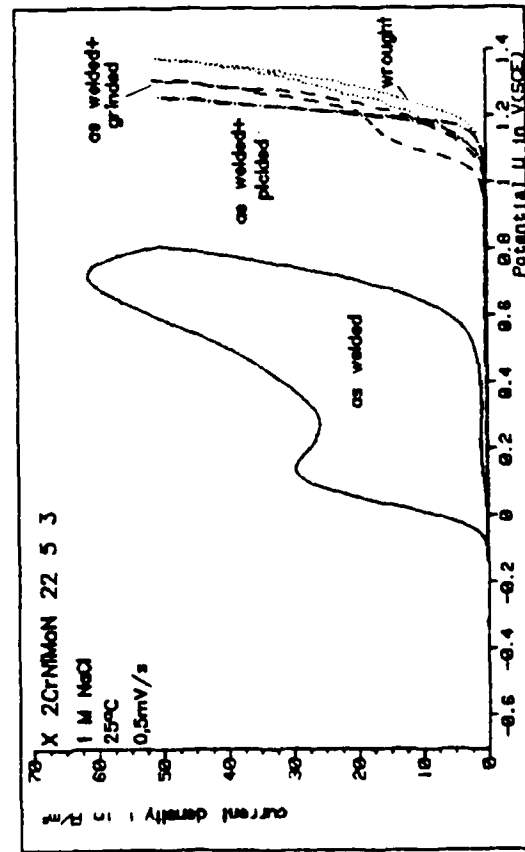
Fig. 4 Influence of Surface State on Pitting Behaviour of Duplex SS

Fig. 6 Influence of Temperature on Pitting Behaviour
a) Wrought Duplex SS , b) Claddings

Fig. 5 Pitting Potential of Duplex and Super-Duplex SS
Influence of Temperature

Fig. 7 Influence of NaCl - Concentration at 70°

Fig. 9 Influence of Ageing on Pitting Corrosion of Duplex Claddings
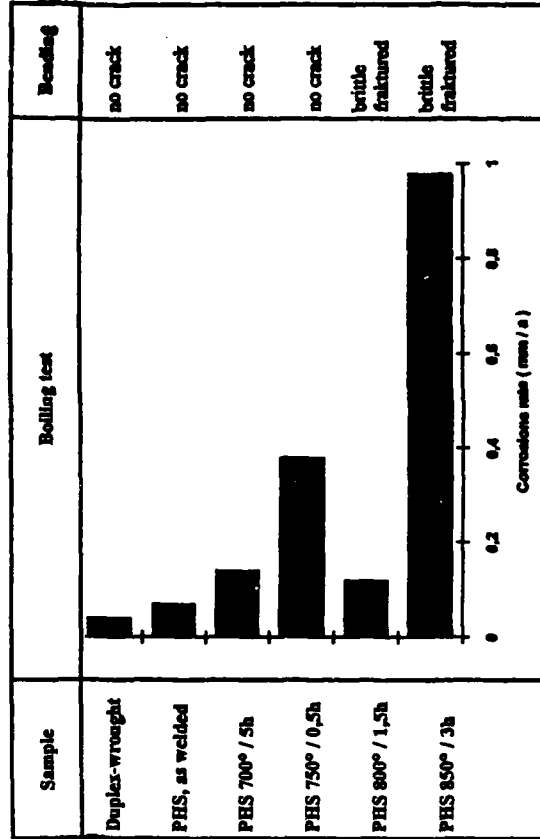
Fig. 11 Results of Modified Strauss-Test

Fig. 8 Pits in the Ferritic Regions (1M NaCl , 40°)
a) Wrought , b) Cladding Duplex SS

Fig. 10 Time Temperature Precipitation Diagram [20]
for X 2 CrNiMoN 22 5 3

Corrosion rate (mm / a)   X 2CrNiMoN 22 5 3

Legend:
- □ wrought
- ▣ L, as welded
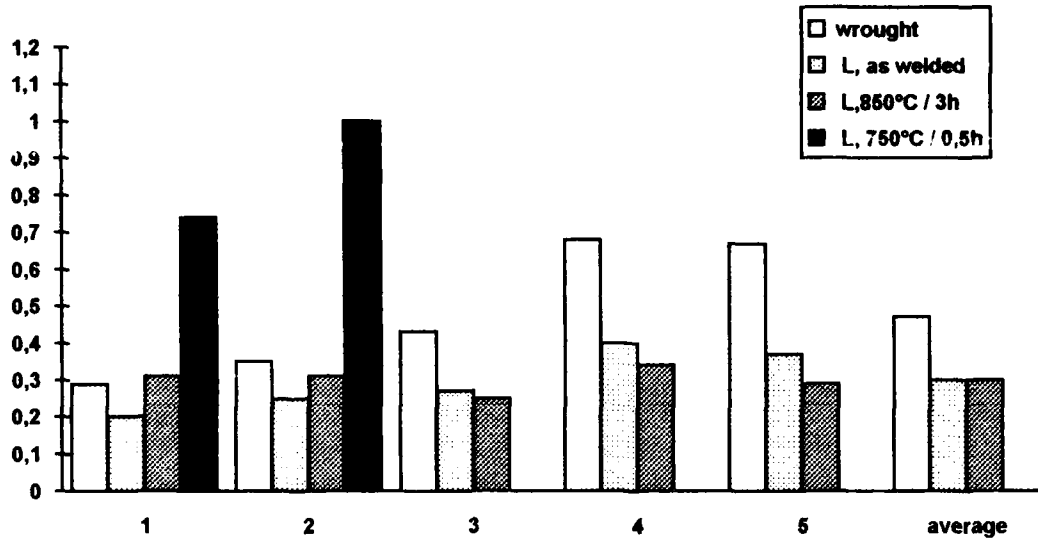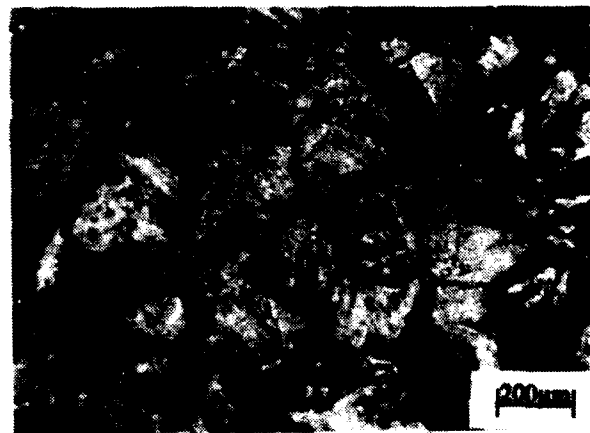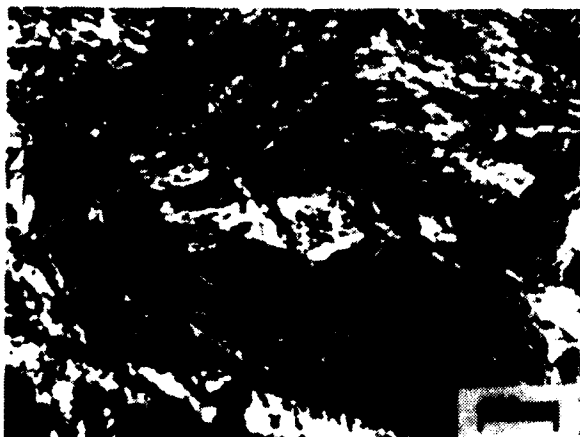- ▨ L, 850°C / 3h
- ■ L, 750°C / 0,5h

Fig. 12 Corrosion Rate in Huey- Test ASTM A262- C
for five individual 48 hour periods (L = second layer)

a)

b)

c)

Fig. 13 Attack after Huey-Test (5 periods)
a) Cladding, as Welded state,
b) Under Side of second Layer,
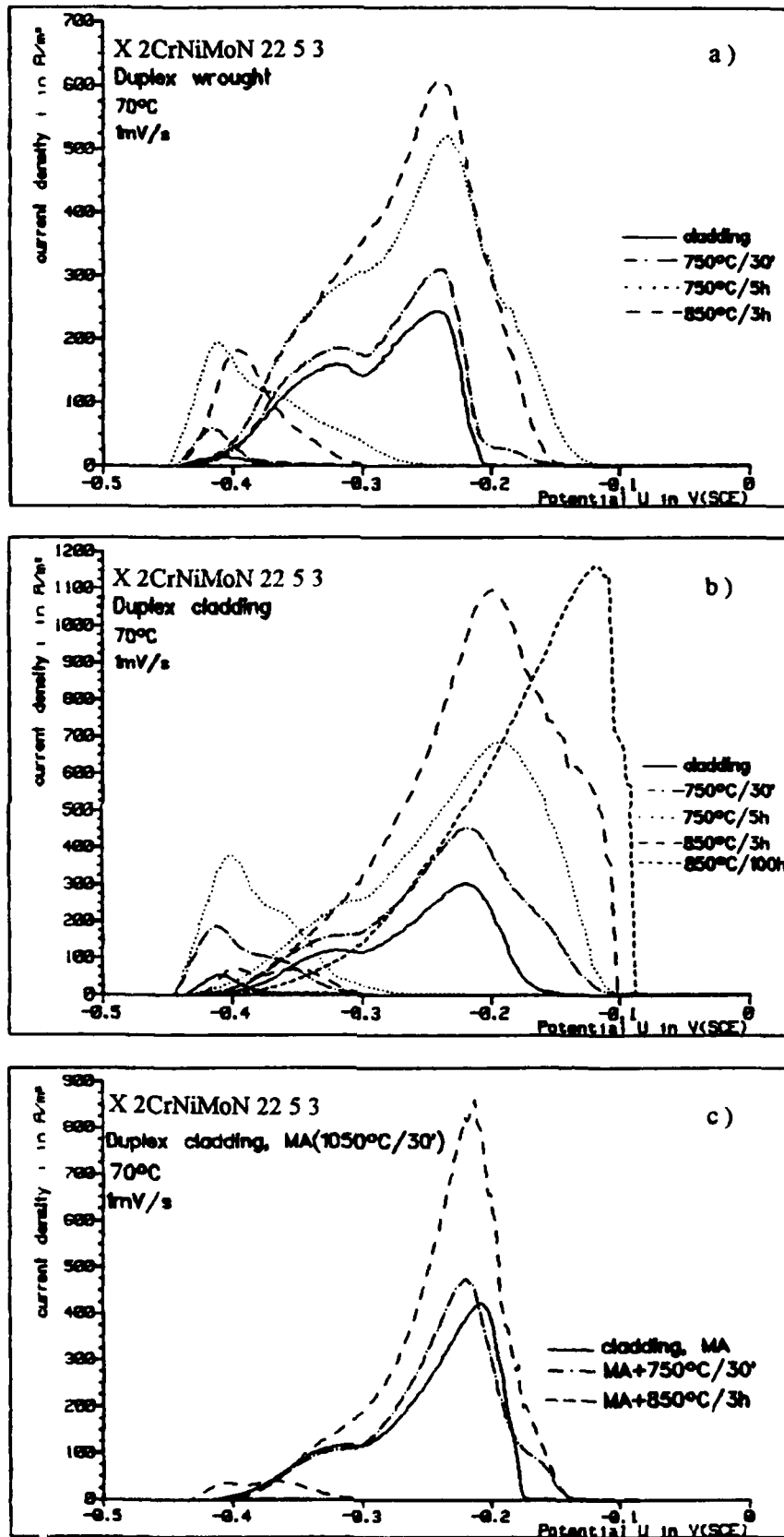c) Aged at 750 °C / 0.5 h

2970

Fig. 14   EPR- Curves of Duplex SS
        a) Wrought specimen , b) Claddings , c) Claddings , MA
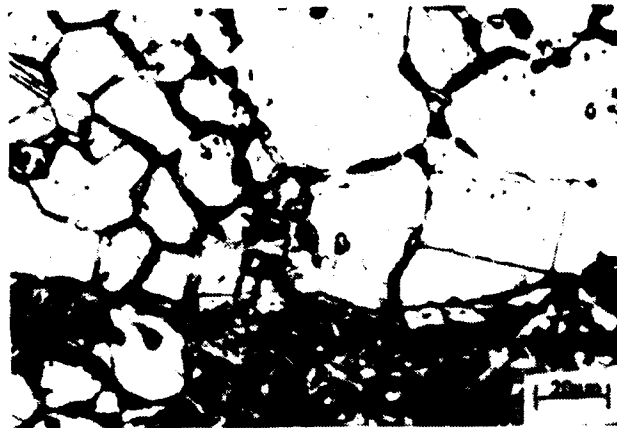
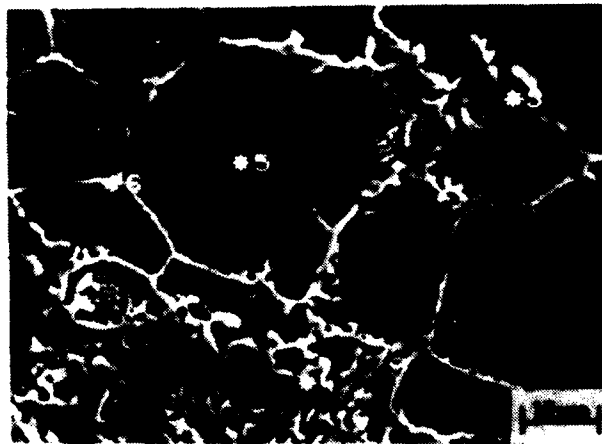Fig. 15   IGA of Wrought Duplex (850 °C / 3h) after EPR- Test

Fig. 16   Precipitations of χ-phase (* 6) and σ-phase in
wrought Duplex SS after Ageing (850 °C / 3h)

Fig. 17   Aged (750 °C / 3h) Cladding after EPR-Test

Alloy 625 Weld Overlays for Offshore and Onshore Projects

Dan Capitanescu, Welding Specialist
Capitan Welding Technologies Inc.
9304 Horton Road S.W.
Calgary, Alberta, T2V 2X4 , Canada

Abstract

This technical report presents an in-depth design, research and fabrication information for Alloy 625 weld overlayed carbon steel pipe and fittings such as: 90 degree and 45 degree LR Elbows, Tees, Dished Heads, Reducers, Weld Neck Flanges, Valves, Spools, Manifolds, Nozzles, and Blinds. Major developments for Offshore Projects took place in Calgary, Canada during 1989, 1990 and continued through 1991 such as:

- Development of an entire range of Alloy 625 weld overlay and butt welding procedures to cover a majority of the welding processes: SAW, Pulsed GMAW, SMAW, GTAW, FCAW and base materials such as: P1 and 4130 with thicknesses from .250 in. (6.3mm) to no limit to be weld overlayed or butt welded.

- Development of a wide range of welding procedures to join dissimilar and similar materials such as: P1 to P1, P43 to P43, P1 to P45, P43 to P45, 4130 to 4130, 4130 to P43 etc. All using the same filler metal: Alloy 625.

- Development of special welding consumables with special formulation to be used on Offshore Projects.

- Development of a unique welding technology and welding technique to provide a low iron content Alloy 625 weld deposit on carbon steel base material.

- Development of a specialized welding equipment to perform weld overlay on 45 degree and 90 degree LR Elbows with any exotic welding filler metal including Alloy 625, employing a high productivity SAW System with near zero defect rate.

- Corrosion tests performed on Alloy 625 weld overlay deposits and corrosion tests performed on self contained Alloy 625 weld overlayed Autoclaves.

- Complete study of Alloy 625 flux cored wire: weldability, corrosion testing and weld defect occurrence while weld deposits performed using FCAW fillers available today.

I. Introduction

As the Earth's Oil and Gas Reserves diminish and the search for additional and deeper resources increases, there is a growing tendency towards Offshore Developments as the answer to self-sufficiency or to at least reducing Oil and Gas dependability on other oil producing countries. The search for and findings of Oil and Gas at such great depths are marked with high pressures, high H2S and CO2 contents and very often elevated temperatures. Complicating the situation and making the project engineer's life even more challenging is the issue of materials. Those proven acceptable for such projects just a few years ago are now not good enough because of the increased pressures, H2S and CO2 concentrations and temperatures.

Just a few years ago an "Exotic Material" was a material used for a multitude of corrosion resistant applications. Today for the majority of the Onshore and Offshore Oil and Gas Developments "Exotic Material" has to be "Super Alloy".

Such major developments combining the drastic changes in the environment awareness and the ever increasing cost of maintenance and equipment repair has put the Super Alloys in the spotlight and the Alloy 625 on the top of the list as one of the most flexible alloys to be used as a "Corrosion Barrier" for most applications. From an economical point of view Alloy 625 looks very unattractive to many potential users because of its very high price tag. As a direct result of the high price of Alloy 625 solid fittings, Alloy 625 weld overlayed pipe and fittings is an obvious alternative with excellent technical results and remarkable cost reductions.

II. Alloy 625 Weld Overlays: Welding Processes And Welding Technologies

Choosing the right combination of welding process and welding technique for the proper application is the secret of Alloy 625 weld overlays.

As shown in Table I, Alloy 625 displays properties that will make welding anything but an easy task.

The bottom line is that Alloy 625 weld deposits will allow a good appearance and sound weld deposit only if the welding process used falls into the category of "Hot" processes such as: SAW, GTAW, PLASMA TRANSFER ARC, etc. On the other hand, with any "Hot" process high dilution comes as a normal attachment.

A smart compromise has to be found and an ideal balance of sound weld deposit - low dilution occurrence has to be found. One of the most successful candidates in achieving most of the advantages in weld overlaying with Alloy 625 is Submerged, Arc Welding System. With a proper welding technique that is tailored differently to various base metal thicknesses and shapes the SAW process will definitely show the following positive aspects:

- High deposition rates.
- Near zero weld deposit defects.
- Almost perfect "Smooth" weld deposit appearance.

- Controllable dilution rates.
- Minimum filler metal waste.
- Very good consistency in weld overlay deposit chemistry.
- Equipment flexibility to produce weld overlays in a very small bore(1 in. dia.) pipe and fittings.
- Low cost of labour (machine operator versus skilled welder).

Very successful attempts were made to qualify Alloy 625 weld overlays on F1 and 4130 base materials. Table II is a summary of various overlay and butt welding procedures all having one thing in common: Alloy 625 filler metal.

Very valuable data have been compiled, some reinforcing former developments on Alloy 625 welding but most of the findings are new. An integral part of the welding technology developed are four factors that were found to be most influential in achieving the best end results: filler metal diameter, welding position, welding speed and flux type (for SAW).

III. Filler Metal Diameter

It has been many years since researchers have established the direct relationship between Alloy 625 cracking during welding and the weld puddle size and shape. Mathematical formulas will eventually help to establish the stress forces that occur at the surface line of an Alloy 625 weld puddle. What these formulas will not provide is the practical means to avoid such occurrences. What is an ideal puddle shape that will allow a crack free weld? The size and shape of a weld puddle will be decided mainly by the wire diameter, welding speed and weld position.

With the SAW process used to perform about 90% of the Alloy 625 weld overlays on this development and an approximate 20,000 lbs of Alloy 625 (ERNiCrMo-3) filler metal being melted, the one diameter that emerged as being the most suitable for SAW process was 1/16" (1.6mm). A smaller diameter filler metal was used (approximately 400 lbs of Alloy 625, .045" (1.2mm)) and displayed poorer results then 1/16" diameter as far as weld deposit appearance and deposit defects are concerned. With the Pulsed GMAW the only diameter with excellent results was .045" (12mm).

With the SMAW process after an approximate quantity of 2000 lbs of Alloy 625 welding rods were used, the most successfully used diameters in achieving weld deposits free of defects were 1/8" 3.2mm) and 5/32" (4.0mm). On GTAW even though the quantities used were significantly lower than the ones used with SAW and SMAW we can conclude that one diameter provided defect free weld deposits : 1/8" (3.2mm).

In conclusion we can say the following:

- Smaller diameter Alloy 625 filler metals allow zero crack weld deposits.
- Small weld puddles are preferred to large ones in order to reduce stress cracking and bring the two expansion coefficients of the carbon steel base metal and Alloy 625 weld deposit to a common ground.

- In the case of SAW process feeding small filler metal diameters definitely help to maintain a continuous flow that directly helps in maintaining welding parameters (current and voltage) to a constant level which translate into a sound weld deposit.
- Pulsed GMAW has emerged as the process that will replace completely the slower, low productivity SMAW process.

IV.   Welding Position, Welding Speeds And Flux Type

Welding positions and welding speeds are very important factors in producing a sound Alloy 625 weld deposit. For SAW process Alloy 625 combined with a proper welding flux has the characteristic of "Fast Freeze" weld puddle which makes it a very good candidate for "Out of Position" welds with very good results for SAW welding near the " 3 o'clock" position.

The negative side is that in order to perform a SAW weld in a near "3 o'clock" position the welding speed has to be somewhere near 18-25 IPM and this situation will lead to "Higher" than normal dilution rates. Very good quality SAW Alloy 625 weld overlays were achieved in near "3 o'clock" position especially in performing the weld overlays on 90 degree elbows. Figure 1 shows a schematic of such near "3 o'clock" SAW weld overlay on 90 degree elbows with several production chemistries performed on 10% of the elbows showing excellent results.

From a practical point of view SAW Alloy 625 weld overlays can be successfully achieved in "Out of Position" situations only on the condition that while the welding puddle solidifies it has the kind of support that will not let it "RUN AWAY" and be disturbed to any extent.   A "RUN AWAY" puddle will create weld cracks throughout the entire weld.

V.   Flux Type Used For SAW Overlays With Alloy 625

The most valuable finding during this development was the influence of the flux used for SAW overlay in regards to the occurrence of cracking in the weld deposit. As a normal practice the liquid penetrant test is the test that will decide if a corrosion resistant weld overlay will perform, depending on the overlay's surface condition. "Defect free" weld overlay deposits will "read" in a similar manner as a 100% radiography test of a butt weld with no defects.

During the development, after a sizable number of fittings were finalized and ready to be butt welded to the corresponding clad pipe, multiple cracks were detected in the weld overlay deposit during a radiographic
test. The findings were surprising due to the surface quality following liquid penetrant test. There were approximately 150 fittings (elbows, tees, flanges, blinds, reducers, caps, etc.) varying in sizes from 6" to 18" that after radiographic testing showed cracks varying in number from 4 to 20 on the same fitting and from 1/4" to 2" in length.

A large amount of filler metal and flux were wasted. After a thorough technical investigation one element stood out in our findings: high amounts of silicon were found in the weld deposits. The cracks were consistent from one point of view - all "embedded" in the weld deposit. There was no finding to show a crack propagated either into the base material or to the weld overlay surface. A typical crack found in Alloy 625 weld deposit is shown in Figure 2.

As has been previously established in the welding community, solidification cracking occurs when the solidifying weld pool is subjected to transverse shrinkage. Very often, in the center of the weld which solidifies last, there is an important amount of low melting point impurities. Due to this occurrence, the weld loses a good portion of its ductility. High strain in conjunction with low ductility leads to cracking in the weld. The occurrence of such cracks very often takes place in alloys rich in low melting points or low ductile elements such as silicon combinations. As mentioned above during a very thorough lab test investigation significant amounts of silicon were found around the crack, as can be seen in Figure 3.

It is known that SAW weld overlay deposits with Alloy 625 are anything but an easy job due to the very high nickel content of the filler. An easy way of producing SAW weld overlay deposits with smooth appearances is to use a silicon rich flux which will automatically ensure a very "fluid" slag in combination with "silent" arc and no occurrence of heavy slag or slag "bubbling" effect. This was the case of Flux #805, which produced very good appearance weld deposits but with "under surface" cracks. Immediate steps were taken and new welding procedures were developed using a silicon free flux. The new flux, Flux #7, is very difficult to weld with due to very poor flow characteristics in molten state; but there followed an approximate 10,000 lbs of Alloy 625 weld deposits with ERNiCrMo-3 filler and Flux #7 with not one single occurrence of cracks.

VI. Low Iron Alloy 625

The idea of producing a low iron Alloy 625 weld deposit occurred at the very first stage of development. Extensive corrosion tests were conducted by various parties interested in Mobile Bay Development and for that environment solid Alloy 825 was found appropriate to successfully withstand the corrosion produced by known H2S - CO2 concentrations. Table III shows the typical chemistries of Alloy 825 and Alloy 625.

During the course of this development, great difficulty was experienced in procuring Alloy 825 fittings in time and at an acceptable price tag. As a result a decision was made that all fittings larger than 4" dia. would be weld overlayed with Alloy 625 in order to ensure a weld deposit with an acceptable iron level. Due to the quantity of fittings to be weld overlayed a total review of the project specifications took place in order to accommodate an "achievable" production weld overlay chemistry throughout the entire range of fittings of various diameters and shapes.

To ensure that the weld deposit chemistry limits were going to be achieved for production weld overlays a further step was taken in producing "Special

chemistry Low Iron" Alloy 625 filler metals. Table IV shows the special chemistries of the three types of filler metals used on the project.

During the course of the development, many welding procedures were developed and an important number of chemical tests on Alloy 625 weld overlays were performed. The conclusion was that regardless of the welding process used a great chemistry consistency was achieved throughout the entire project and all the results were well within the project specifications - Table V.

In conclusion, achieving the levels set through the projects specifications, and producing and using a low iron filler metal was most helpful and also proved economically feasible. This was due to weld overlaying that was performed in normal "Shop Production Conditions" on various items with a multitude of diameters, shapes and configurations as shown in Figure 4 a,b,c,d,e & f. This was done without making use of any sophisticated welding technology or technique more appropriate for Research and Development or laboratory conditions.

VII. Corrosion Tests Of Alloy 625 Weld Overlayed Deposits

Even though corrosion tests on Alloy 825 proved it suitable for use on the environment occurring from Mobile Bay conditions, extensive corrosion tests were conducted on Alloy 625 weld overlay deposits performed on various items such as: P1 base material plates, 4130 base material plates, P1 base material fittings (tees, etc.) or whole self contained autoclaves with a multitude of weld overlayed items as can be seen in Table VI.

The tests were very elaborate and under more severe conditions then the production ones. Excellent results were somewhat expected. It was very reassuring to demonstrate that Alloy 625 weld overlay deposits on carbon steel base materials are at least as corrosion resistant as solid Alloy 825.

VIII. Specialized Equipment To Perform Alloy 625 Weld Overlays Of Small Bore Pipe And Fittings

The application of Alloy 625 weld overlaying to fittings with a large variety of shapes and diameters can be achieved only with highly specialized welding equipment. "Shape Welding" and "Shape Weld Overlaying" are ideas many people were dealing with for quite some time, but bringing it from theory to practice has been demonstrated during this project.

Besides the normal range of welding equipment to weld overlay pipes, flanges, tees, and reducers, a major development took place during the course of this project: a unique SAW Welding System to weld overlay 90 degree Long Radius Elbows with diameters starting as low as 6". As can bee seen in Table VII an entire range of fittings were weld overlayed as part of the Mobile Bay Development.

IX. Economical Aspects Of Alloy 625 Weld Overlay

The significant savings of using Alloy 625 weld overlayed pipe fittings versus solid Alloy 625 or 825 fittings made this project possible from the very beginning. Choosing Alloy 625 weld overlayed fittings over solid centrifugally clad, hip clad etc. proved to be a very big economic success, besides having a technical advantages from the safety and corrosion resistant point of view. Figure 5 shows a clear picture of the above statement.

X. Conclusions

With the completion of the Mobil Bay Development, a solid precedant is created: Alloy 625 weld overlayed fittings for an entire project with no exception. There are very certain conclusions that can be drawn at the time of closing this project.

1. "Shape Weld Overlay" is a reality and can be achieved with specialized equipment, personnel and research and development.

2. A 100% sound weld overlay deposit can be obtained with a controllable chemistry.

3. Silicon content in the flux must be kept under strict control when Submerged Arc weld overlays with Alloy 625 filler is being considered. A maximum of .5% Silicon in the weld deposit will ensure a "crack free" overlay.

4. Economical Alloy 625 weld overlayed fittings, small pipes and spools fabrication is the obvious choice for substantial savings regardless of the size of the project.

5. For both, Onshore and Offshore Projects with highly corrosive environment Alloy 625 weld overlay is a proven choice that is feasible from technical and economical point of view.

6. Specialized weld overlaying equipment and weldingtechnology already tested makes it easier to continue the search for answers on similar future projects.

References

1. D. Capitanescu, "Weld Surfacing of Small Pipe Interiors", Welding Journal, August 1989, 29-34.

2. R. A. Kane, S. M. Wilhelm (Cortest Laboratories Inc.), T. Yoshida, S. Matsui, T. Iwase (Kawasaki Heavy Industries), "Analysis of Bimetalic Pipe For Mobile Bay Service", (Paper presented at the OTC , Houston, Texas, 7-10 May 1990), 115-128.

3. T. F. Lemke, "Heavy Section Welding of Inconel Alloy 625", (Paper presented at AWS Welding Conference, Anaheim, California, 24-26 April 1990), 1-36.

4. N. Stephenson, "Versatility of Highly Alloyed Ni-Cr-Mo Welding Consumables", Welding & Metal Fabrication, August/September 1990, 376-387.

"Table I" - Physical Constants and Thermal Properties

Physical Constants and Thermal Properties						
Density, lb/cu in. ... 0.305			Melting Range, °F ... 2350-2460			
Modulus of Elasticity, psi			Specific Heat, Btu/lb/°F			
Tension ...30,000,000			70°F ... 0.098			
Torsion ...11,000,000			Curie Temperature, °F ... <-320			
Poisson's Ratio ... 0.31			Permeability (70°F, H = 200 oersted) ... 1.0006			
	70°F	200°F	500°F	1000°F	1500°F	2000°F
Thermal Expansion, in./in./°F x 10⁻⁶ ...	5.5	7.1	7.4	7.8	8.7	—
Thermal Conductivity, Btu/sq ft/hr/in./°F ...	68	—	93	121	151	—
Electrical Resistivity, ohm/circ mil/ft ...	776	—	809	830	821	806

"Table II" - Summary of All Mobile Bay Qualifications

WELDING Process	BASE METAL P1	BASE METAL 4130	THICKNESS Qualified	CONSUMABLES Filler	CONSUMABLES Flux	CONSUMABLES Gas	One layer E/ER NiCrMo-3	Two layer E/ER NiCrMo-3
SAW	■		.250" to No max.	625	#7			
SAW		■	.250" to No max.	625	#7			
GTAW	■		.250" to No max.	625		Ar		
GTAW		■	.250" to No max.	625		Ar		
SMAW	■		.250" to No max.	112				
SMAW			.250" to No max.	112				
Pulsed GMAW	■		.250" to No max.	625		Ar	■	
Pulsed GMAW			.250" to No max.	625		Ar		
F CAW		■	.250" to No max.	625		Ar·CO_2		

WELDING Process	BASE METAL P1	BASE METAL P43	BASE METAL P45	BASE METAL 4130	THICKNESS Qualified	CONSUMABLES Filler	CONSUMABLES Electr.	CONSUMABLES Gas	Remarks
GTAW root SMAW fill & cap		■			.1875" - 1.000"	625	112	Ar	Overlay ERNiCrMo-3
			■		.1875" - 1.436"	625	112	Ar	Overlay(P1) ERNiCrMo3
		■			.1875" - 1.436"	625	112	Ar	Overlay (P1) ERNiCrMo3
	■				.0625" - .674"	625	112	Ar	
		■			.0625" - .674"	625	112	Ar	
	■				.0625" - .674"	625	112	Ar	
				■	.1875" - 1.500"	625	112	Ar	PWHT 1100°F, HRC≤22
GMAW					.1875" - 2.500"	625	112	Ar	Fill&Cap Pulsed GMAW *

"Table II" - Typical Chemistries of Alloy 825 and Alloy 625

	alloy 825	alloy 625
Nickel	38.0-46.0	Balance
Carbon	0.05 max.	0.10
Manganese	1.0 max.	0.50
Iron	Balance	5.0
Sulfur	0.03 max.	0.015
Silicon	0.5 max.	0.50
Copper	1.5-3.0	
Chromium	19.5-23.5	20.0-23.0
Aluminum	0.2 max.	0.40
Titanium	0.6-1.2	0.40
Molybdenum	2.5-3.5	8.0-10.0
Cb+Ta		3.15-4.15
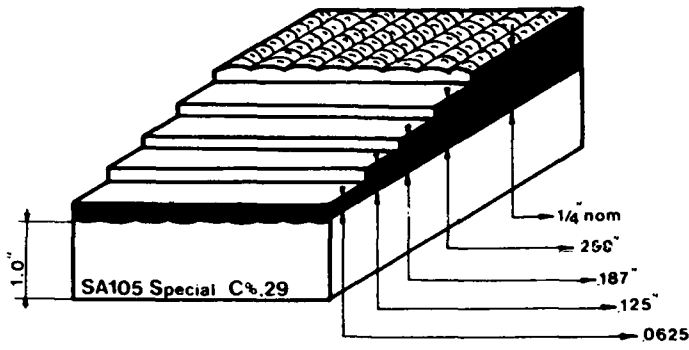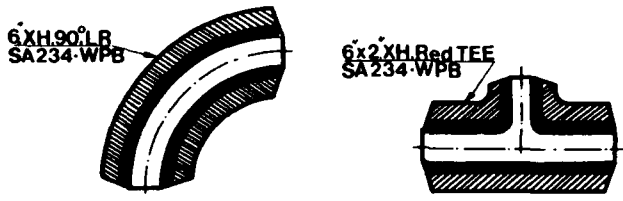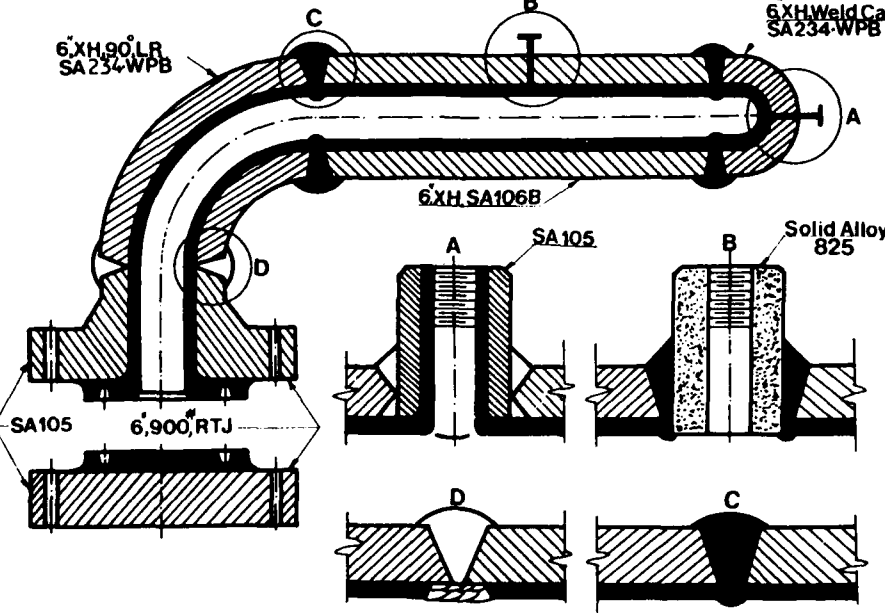
"Table IV" - "Special Chemistry Low Iron" Alloy 625 Filler Metals

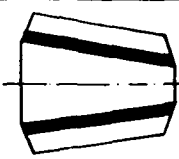| WELDING PROCESS	FILLER CLASS	FILLER TRADE NAME	ø in	C	Cr	Ni	Mn	Si	Mo	Fe	Ti	Cu	NbTa	S	Al
SAW	ERNiCrMo.3	NICROFER 6020	1/16	.013	22.2	64.0	.02	.05	9.1	.6	.18	.01	3.5	.002	0.12
SMAW	ENiCrMo-3	INCONEL 112	5/32	.004	21.0	63.1	.01	.38	8.9	1.0	.20	.04	3.4	.003	0.13
GTAW pulsed	ERNiCrMo3	NICROFER 6020	1/8	.012	22.2	63.0	.05	.06	9.2	.7	.20	.03	3.5	.003	0.12
GMAW	ERNiCrMo3	NICROFER 6020	.045	.015	22.0	64.0	.02	.04	9.2	.69	.20	.01	3.4	.003	0.14
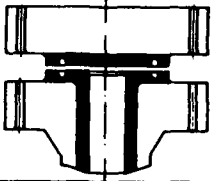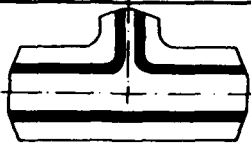
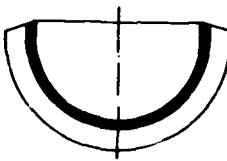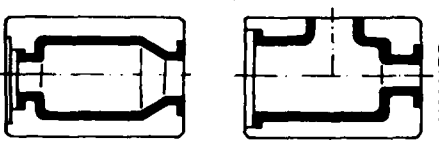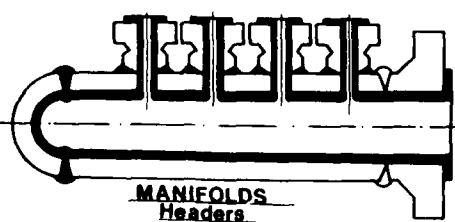## "Table V" - Chemical Analysis Results for Project

Welding process	Number of layers	Depth of chemistry sample	Number of chemistries	%C P	%C S	%Cr P	%Cr S	%Ni P	%Ni S	%Mo P	%Mo S	%Fe P	%Fe S	Nb+Ta P	Nb+Ta S	%Si P	%Si S
SAW	ONE	.125"	34	02	.1	18	14	53	40	8	6	20	30	3.7	2	.3	75
SAW	TWO	.156"	70	02	.1	20	15	55	45	8.5	6	12	15	38	2	.2	55
SMAW	TWO	.125"	20	05	.1	20	15	57	45	8	6	11	12	25	2	.3	55
GTAW	TWO	.125"	15	05	.1	21	15	60	45	8.6	6	6	12	27	2	.1	55
Pulsed GMAW	ONE	.125"	20	01	.1	22	15	61	50	8.5	7	25	10	41	25	.2	5
Pulsed GMAW	TWO	.156"	17	01	.1	22	17	61	55	8.5	7.5	2	8	40	3	.2	5

Weldment corrosion test
"2 Layer" E/ERNiCrMo·3 OVERLAY on P1 BASE MAT.

TYPE OF TEST	TYPE OF PROBE		TESTED BY:	RESULTS
FUSION LINE	PLATE	SA105 Special C%.29 — 1/4" nom — 250" — .187" — .125" — .0625" 1.0"	CORTEST LAB. INC & MOBIL USA	★ ★ ★ ★ ★
ASTM A272 Practice C	FITTINGS	6"XH.90°LR SA234·WPB 6"x2"XH.Red TEE SA234·WPB		★ ★ ★ ★ ★
ASTM G28 ASTM G48	AUTOCLAVE	6"XH.90°LR SA234·WPB 6"XH.Weld Cap SA234·WPB 6"XH.SA106B SA105 Solid Alloy 825 SA105 6,900# RTJ	SHELL OFFSHORE INC. Westhollow, Texas, USA.	★ ★ ★ ★ ★

"Table VII" - Fittings Weld Overlayed with E/ERNiCrMo-3 (Alloy 625)

E/ERNiCrMo-3 (Alloy 625) Weld Overlays

WELD OVERLAYED COMPONENENT	Base Material	Weld Process	NDE	Remarks
BLINDS & FLANGES	P1 P4 4130	SAW Pulsed GMAW SMAW GTAW	100%PT 100%RT	RF & RTJ
TEES	P1 P4 4130	SAW Pulsed GMAW GTAW	100%PT 100%RT	STRAIGHT & REDUCING
ELBOWS	P1 P4 4130	SAW	100%PT 100%RT	90°&45° ø4"min.
REDUCERS	P1 P4 4130	SAW Pulsed GMAW SMAW	100%PT 100%RT	CONC.&ECC.
CAPS	P1 P4 4130	SAW Pulsed GMAW	100%PT 100%RT	ø4"min.
VALVES	P1 4130	SAW Pulsed GMAW SMAW GTAW	100%PT	CHECK&BALL
MANIFOLDS Headers	P1	SAW Pulsed GMAW GTAW	100%PT 100%RT Part UT	RF&RTJ
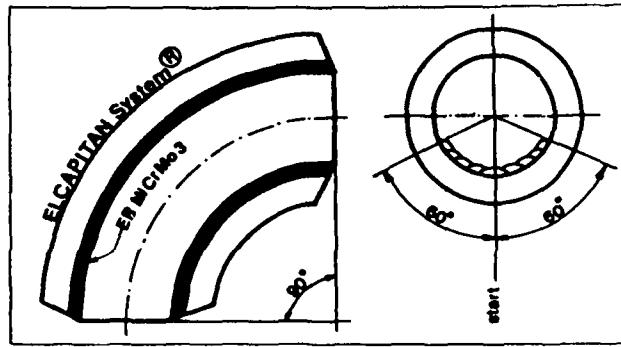
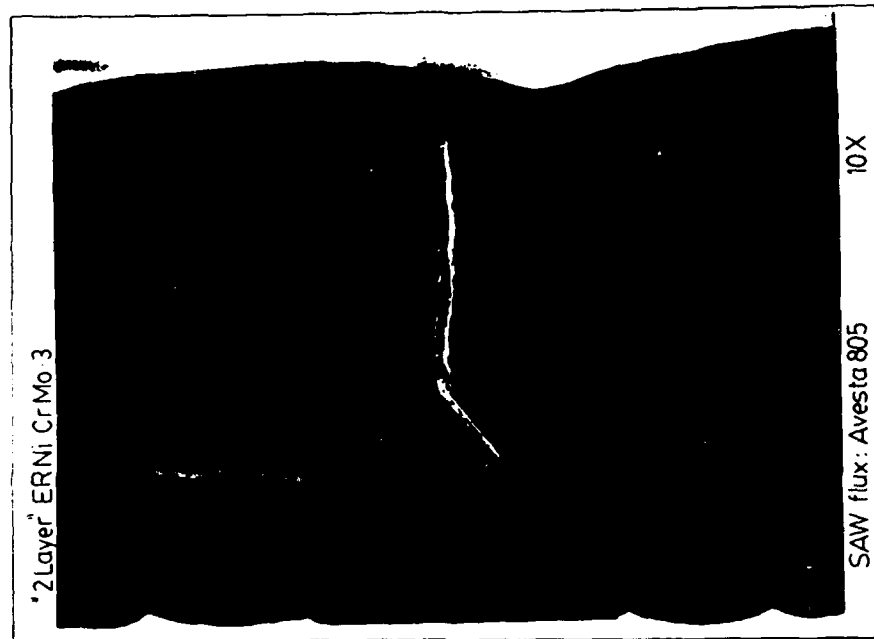"Figure 1" - "Out of Position" Elbow Overlay

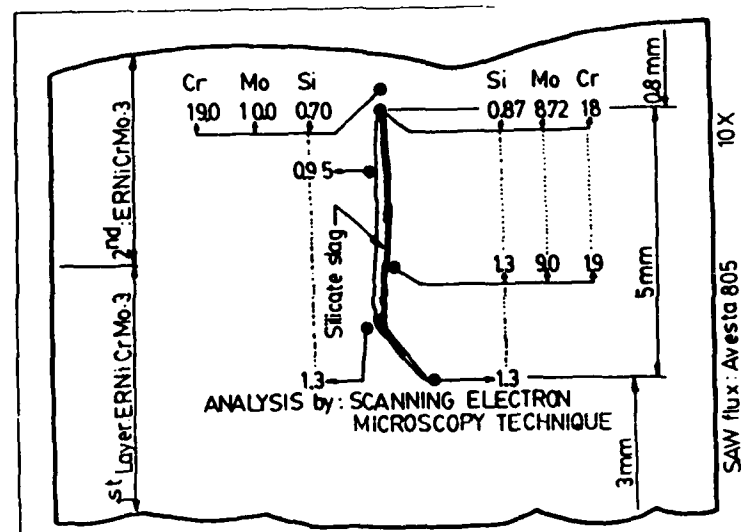"Figure 2" - Alloy 625 Cracking Due to High Silicon Content of Saw Flux
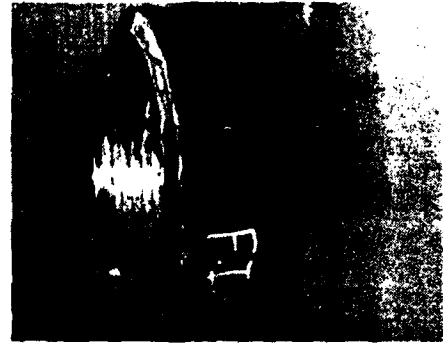

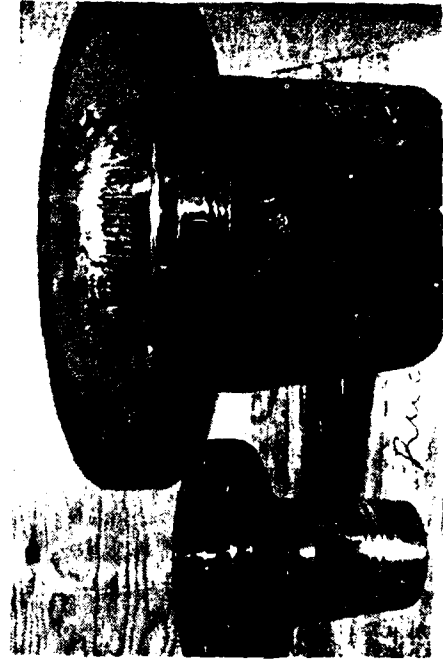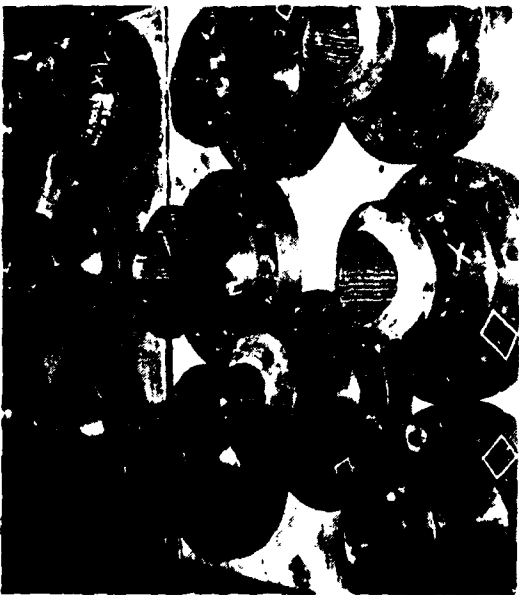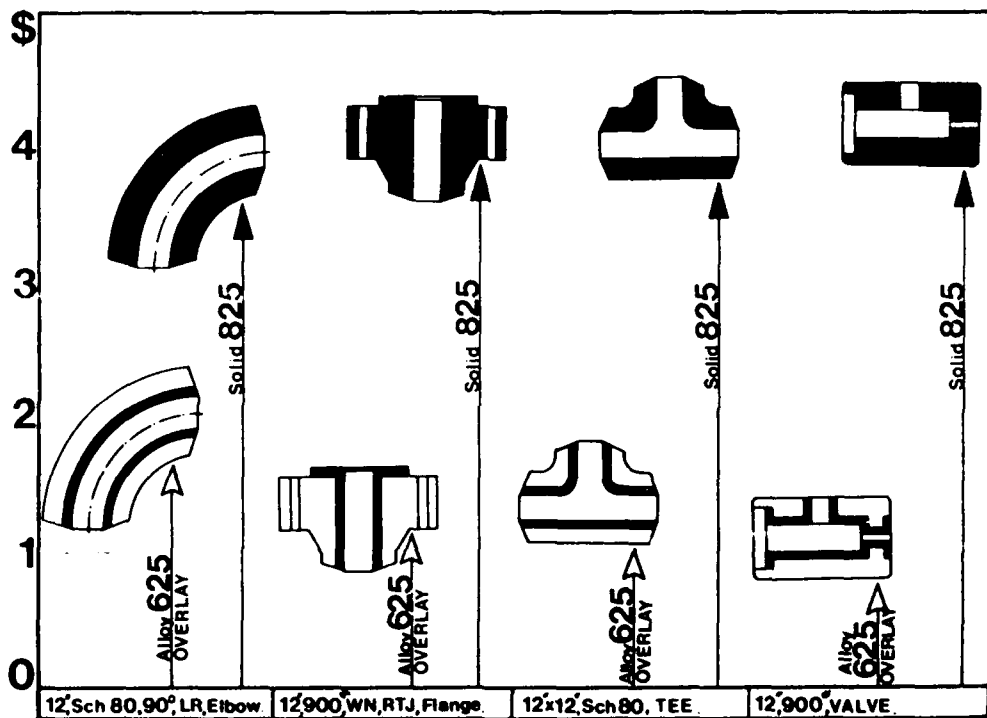"Figure 3" - The "ANATOMY" of Alloy 625 Crack

Figure 4" - Various Shapes and Configurations - Weld Overlayed Fittings

"Figure 5" - Economical Considerations of Weld Overlayed Fittings Versus Solid Fittings

Characterization of the Corrosion Behavior of Surface Welded Protective Claddings of Nickel and Titanium Alloys

Belkacem Bouaifi
Technische Universität Clausthal, ISAF
Agricolastraße 2
3392 Clausthal-Zellerfeld,   Germany

Ulrich Draugelates
Technische Universität Clausthal, ISAF
Agricolastraße 2
3392 Clausthal-Zellerfeld,   Germany

Helmut Steinberg
Technische Universität Clausthal, ISAF
Agricolastraße 2
3392 Clausthal-Zellerfeld,   Germany

Joachim Göllner
Technische Universität Magdeburg, IWW
PO Box 41 20
3010 Magdeburg,   Germany

Andreas Burkert
Technische Universität Magdeburg, IWW
PO Box 41 20
3010 Magdeburg,   Germany

I. Introduction

The continuing development of technical processes in the chemical industry and in the field of apparatus and machine construction often imposes demands which exceed the load limits of conventional materials. For this purpose, the application of corrosion- and oxidation-resistant protective claddings by weld surfacing is steadily gaining importance. Components clad by surface welding are thereby characterized by a subdivision of functions: the surface requirements are satisfied by an appropriate protective cladding, whereas the substrate supports the mechanical stresses encountered during operation. Consequently, the corrosion properties of claddings applied by plasma weld surfacing with titanium- and nickel-based alloys had to be investigated.

Titanium and titanium alloys exhibit high corrosion resistance with respect to many aggressive media, even at high pressure and temperature; this feature is not achieved by any conventional protective materials under similar conditions. In the case of titanium, this property is due to its stability under oxidizing conditions. Cladding with special-purpose metals occupies a particular position in cladding technology. The engineering problems involved in weld surfacing are associated with the relatively high melting point of titanium in comparison with that of the substrate, such as structural steel, and the very high reactivity with noninert gases and other metals. Weld surfacing with special metals on a heterogeneous substrate has hitherto not been regarded as feasible because of brittle reaction products which form in the bonding zone.

High-content nickel-based alloys have increasingly proved their worth in chemical apparatus and plant construction as well as environmental and power engineering. These alloys are employed wherever comparatively aggressive conditions, such as highly concentrated alkaline or acidic

media in combination with additional contaminants, such as chlorides or fluorides, as well as high temperature and pressure, are encountered. These materials are successfully employed in the construction of chemical apparatus because of their high corrosion resistance in strongly oxidizing acids. By virtue of their composite structure with the application of thin claddings, they present an economical solution by saving raw materials.

The results achieved in the course of these investigations on the corrosion behavior of claddings applied by plasma weld surfacing with gas-sensitive titanium- and nickel-based alloys susceptible to dilution are presented and discussed [1 to 7].

II. Investigation of corrosion on titanium and nickel claddings

A. Titanium claddings

The single-layer titanium claddings have been investigated in detail by metallographic and zone analysis as well as by corrosion chemical methods [4; 6]. The results indicate the possibility of applying corrosion-resistant claddings of titanium by the plasma method, provided that the welding process is shielded against contamination by atmospheric gases, and that the formation of undesirable reaction products in the bonding zone between the substrate and filler material is minimized with the application of an intermediate layer, *figure 1*.

The corrosion behavior of the applied claddings has been investigated by means of chemical and electrochemical analyses; the corrosion properties of standard commercial rolled materials were thereby taken as reference. Unless otherwise mentioned, the original surface was examined. The surfaces were prepared only by degreasing (acetone, ultrasonic bath). For the chemical analyses, the rear surface of the samples were worked until dilution effects were essentially eliminated.

1. Chemical investigations - autoclave tests: The titanium samples (surface area: 22 cm²) were exposed to a weakly acidized sodium chloride solution (150 g/l NaCl, pH value: 4) in an autoclave for 7, 14, and 21 days. The results are presented in *figure 2*. No appreciable mass loss was thereby detected on the surface welded titanium claddings with an intermediate nickel layer, as well as on the reference material (not indicated in the figure). A measurable mass loss of about 1 g/m² (1.5; 1.2, 0.7 g/m²) was observed only on 10 percent of the surface welded samples. The microscopic examination of the surface did not indicate any signs of corrosion. Small scratches and grooves already present before the test were not enlarged by the corrosive exposure. In the case of the titanium claddings applied over an intermediate copper layer, in contrast, large mass losses occurred, especially during the first week. These losses are due especially to inhomogeneities in the copper distribution. Moreover, x-ray examinations revealed high residual stresses in the applied claddings; in part, these stresses resulted in disintegration of the samples during the test. However, an optimistic feature is the fact that several samples suffered only a very slight mass loss. By means of further improvements in welding technology, with low and uniform copper dilution as primary objective, useful results can certainly be achieved in the case of cladding over intermediate copper layers, too.

2. Electrochemical analyses: For better appraising the corrosion resistance of the surface welded claddings, curves have also been recorded for the quasisteady-state current density versus the potential. A 15 percent sodium chloride solution with a pH value of 3 (adjusted with HCl) was employed as corrosive medium. The tests were performed in the aerated electrolyte at a temperature of 70 °C. From the respective rest potential, the measuring electrode (surface area: 1 cm²) was polarized by 25 mV in the anodic direction every 10 min, and the corrosion current established after 10 min was recorded. On the basis of these investigations, the surface welded claddings with an intermediate nickel layer can be regarded as equivalent to ʾference material with respect to their corrosion behavior in the selected medium. The pitting corrosion potentiaᴵ

determined for the reference material is about 1750 mV, that measured for the claddings on an intermediate nickel layer is about 1650 mV. (All indicated potentials are referred to the standard hydrogen electrode.) In contrast, the surface welded claddings on an intermediate copper layer already exhibit a decided increase in the corrosion current above 500 mV (*figure 3*). The brief increase in current at about 250 mV is due to selective copper dissolution. After the tests, the surfaces of these samples were coated with a gray deposit, which was interrupted by small metallically lustrous areas at a few sites. The considerably inferior corrosion behavior of the surface welded cladding over intermediate copper layers is due to pronounced dilution of the copper and its nonuniform distribution in the surface welded cladding, as already mentioned in conjunction with the chemical tests.

On the basis of these current density versus potential curves, electrochemical noise measurements were performed at selected potential values [7]. Battery-operated potentiostats and amplifiers with extremely low noise from the *Forschungsinstitut* "Kurt Schwabe", Meinsberg, and the Jaissle Company, Waiblingen, were employed for the purpose. The measured data were recorded with the use of an analog-digital converter circuit board (resolution: 14 bit) integrated in a battery-operated laptop. A thermostatted, doubly jacketed vessel was employed as measuring cell.

Even at room temperature, a holding experiment at 350 mV revealed decided differences in noise characteristics between the claddings on an intermediate copper layer and the other two materials tested (*figure 4*). At frequencies around 1 Hz, the titanium cladding on an intermediate copper layer exhibits a noise power level which is higher by almost three powers of ten than that for the reference material or the titanium claddings on nickel. The cumulative current indicated at the same time by the ammeter of the potentiostat was around 400 nA/cm² for all three materials and thus provides no evidence of differences in corrosion behavior.

The electrochemical noise measurements thus confirm the conclusion that the surface welded claddings on an intermediate copper layer do not satisfy the requirements imposed under this condition, whereas the titanium claddings on an intermediate nickel layer are qualitatively equivalent to the reference material.

B. Nickel-based alloys

1. Chemical investigations - immersion tests on nickel-based alloys: The examination for intergranular corrosion was performed by means of the modified Streicher test in analogy with SEP 1877/II. For this purpose, the mass loss rate and the formation of furrows (cracks) was determined after exposure of the samples to boiling sulfuric acid with added iron sulfate for 24 h. A crack depth of 50 μm was taken as criterion for susceptibility to intergranular corrosion.

Upon visual inspection, all investigated samples exhibited a general mass loss, which was highest in the case of C 276, as shown in *figure 5*. This trend is due especially to the effect of the alloying elements and can be predicted in correspondence with the percentage ratio of Cr to (Mo + W), as indicated by U. Heubner and M. Köhler [8], as well as F. G. Hodge and R. W. Kirchner [9]. At a low ratio, the mass loss due to corrosion is very high and corresponds to the following sequence:

C 276 > C 4 > C 22

The surface welded claddings exhibit a mass loss rate which is lower by one-half than that for the reference material; this observation is associated primarily with the fine-grained structure of the weld.

As far as the crack depth is concerned, a comparison between the reference and weld materials reveals inverse behavior (*table 1*). No crack depth greater than 50 μm was measured in any case; hence, all materials can be classified as resistant toward intergranular corrosion. After annealing in the sensitizing range, however, susceptibility to intergranular corrosion was observed with all alloys, that is, with the reference material as well as the surface welded claddings.

The pitting corrosion test was conducted in conformance with ASTM G 48-76 [10]. The critical pitting temperature is thereby determined in FeCl₃ solution. (The procedure begins at 50 °C with an increase by 5 °C every 24 h.)

No pitting was observed on any of the surface welded claddings in this solution up to 90 °C. As in the case of the rolled goods, the critical temperature is above the temperature range attainable in this medium, in correspondence with the effective sum $(1 \times \% \, Cr + 3.3 \times \% \, Mo$, after [11]). Nevertheless, the investigations revealed a dependence of the general corrosion mass loss on the surface condition. Unetched surface welded claddings exhibit higher corrosion rates than etched or polished samples. The rolled material behaves somewhat better in comparison with the weld.

2. Electrochemical investigations: The electrochemical experiments were performed on alloys C 4, C 22, and C 276 in the welded condition and on rolled material under the same conditions as on titanium. The current density versus potential curves thereby indicate approximately identical behavior for all materials investigated. The pitting potential was about 1000 mV (with respect to NHE) for all samples. For investigating the surface welded claddings more closely, the electrochemical noise was measured at selected potential values in this case, too. The conclusion concerning the approximately identical corrosion behavior of alloys C 4 and C 22 in the selected medium was confirmed. The surface welded cladding of C 276 exhibits increased noise during holding experiments (900 mV). This finding is in agreement with the immersion tests, which also yielded decidedly inferior results with C 276 in the welded state than with the other two alloys. As expected, noise tests on rolled goods at 900 mV yielded decidedly higher noise levels; this observation indicates higher surface activity. In *figure 6*, examples of power density spectra are presented for the surface welded claddings of C 4 and C 276, as well as the C 276 rolled material. The power spectra for surface welded claddings of C 22 concur with those for C 4 and have therefore not been included in the figure. In contrast, the noise level for the rolled goods is decidedly higher, as confirmed by the power spectrum of the C 276 reference. In the case of the nickel-based alloys, too, the results of the electrochemical noise measurements correlate with the data obtained by chemical test methods. These results indicate superior corrosion behavior for the surface welded claddings in comparison with the rolled material, as was also the case with the chemical corrosion tests.

III. Conclusions

In t' present article, the corrosion behavior of claddings applied by plasma weld surfacing with ti ...um- and nickel-based alloys is discussed. From the standpoint of corrosion resistance, the surface welded claddings are equivalent to the rolled materials, with the exception of the titanium claddings on an intermediate copper layer. If dilution of the substrate or intermediate layer material in the welded top cladding layer is kept low, the problems with the titanium claddings on intermediate copper layers can certainly be be solved, too. As demonstrated by the claddings with nickel-based alloys, surface welded claddings can even exhibit corrosion properties superior to those of the rolled material because of their fine-grained structure.

The results of electrochemical noise measurements on claddings of titanium and nickel-based alloys demonstrate that noise diagnostics provides valuable assistance in optimizing the welding parameters. By means of noise diagnostics, the corrosion susceptibility of surface welded claddings can be determined with very high sensitivity in a considerably shorter time than with conventional methods of investigation. The effect of appropriate variations of the welding parameters on the corrosion behavior of the cladding, as well as possible differences in quality due to random fluctuations of parameters, can thus be ascertained.

In summary, the results confirm the possibility of applying homogeneous, highly corrosion resistant claddings by plasma weld surfacing if the process is optimized in combination with electric arc control by accurately adjustable and reproducible heat transfer.

References

1. U. Draurelates, B. Bouaifi, Schweißen und Schneiden, 41 (1989): p. 551.

2. U. Draugelates, B. Bouaifi, Coat Tech, (1989): p. 231.

3. U. Draugelates, B. Bouaifi, Industrieanzeiger, 79 (1990): p. 30.

4. U. Draugelates, B. Bouaifi, V. Wesling, DVS-Bericht, 131 (1990): p. 196.

5. B. Bouaifi, Stahl Eisen, 12 (1990): p.128.

6. U. Draugelates, B. Bouaifi, Jahrbuch Oberflächentechnik, 47 (1991): p. 358.

7. J. Göllner, I. Garz, Wiss. Zeitschrift der TU Magdeburg, 39 (1990): p. 21.

8. U. Heubner, M. Köhler, Werkstoffe und Korrosion, 43 (1992): p. 181.

9. F. G. Hodge, R.W. Kirchner, Corrosion, 32 (1976): p. 332.

10. M. Renner, U. Heubner, M.B. Rockel, E. Wallis, Werkstoffe und Korrosion, 37 (1986): p. 183.

11. U. Heubner, W. Heimann, R. Kirchheimer, Werkstoffe und Korrosion, 38 (1987): p. 746.

Nickel-alloys	As welded	Reference material
C 276	40 μm	25 μm
C 4	25 μm	10 μm
C 22	no cracks detected	no cracks detected

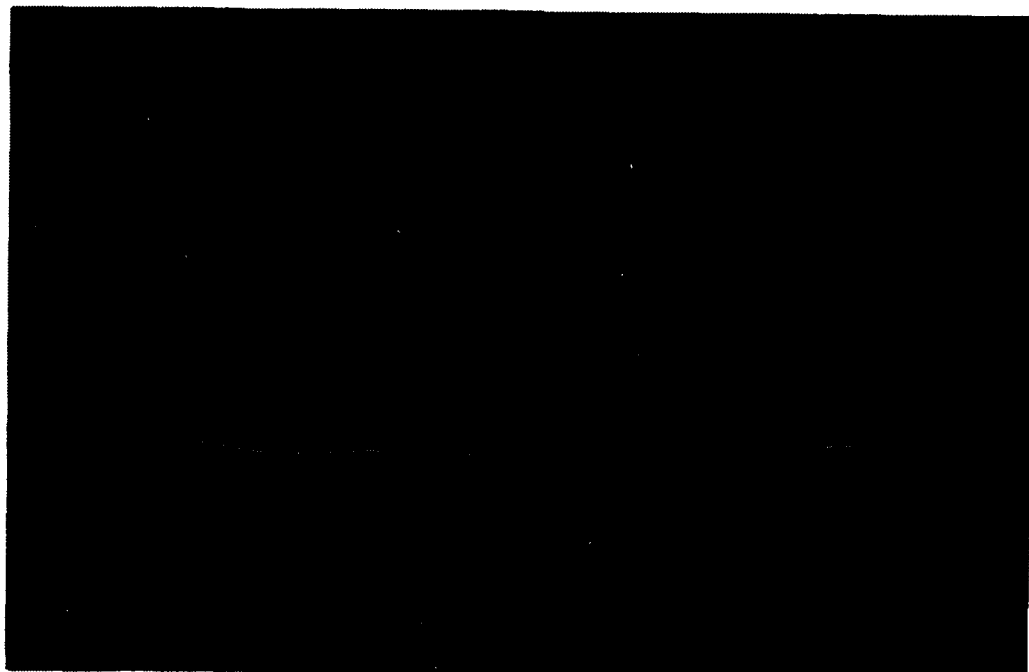**Table 1:** Crack depths measured on nickel-based alloys

Figure 1: Ni-Ti transition zone of a cladding applied by plasma weld surfacing with Ti code 12
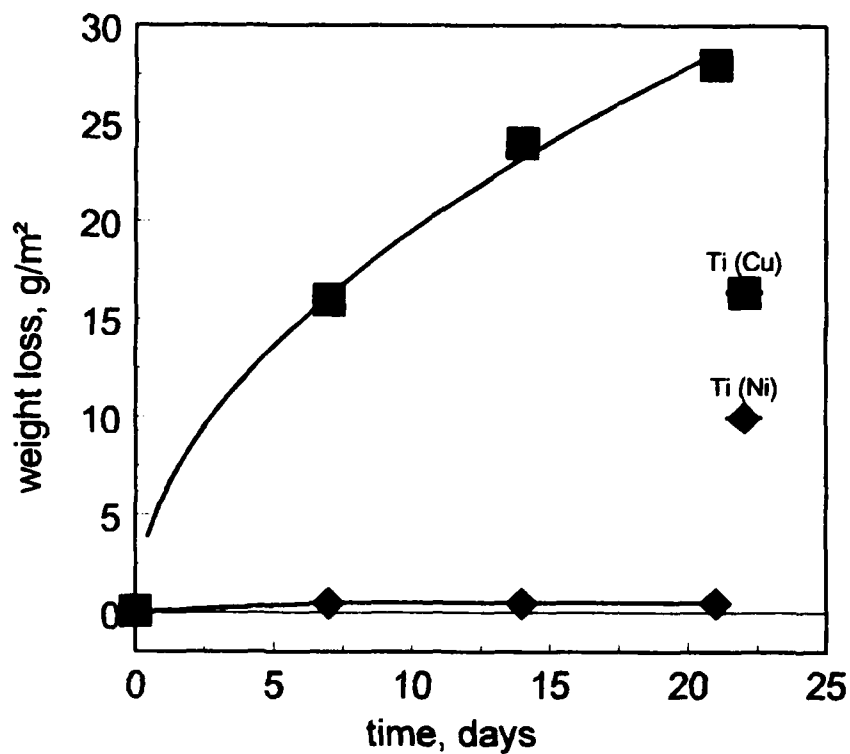
Figure 2: Autoclave tests on surface welded titanium claddings on intermediate copper or nickel layers in 150 g/l NaCl, pH value: 4, T: 180 °C
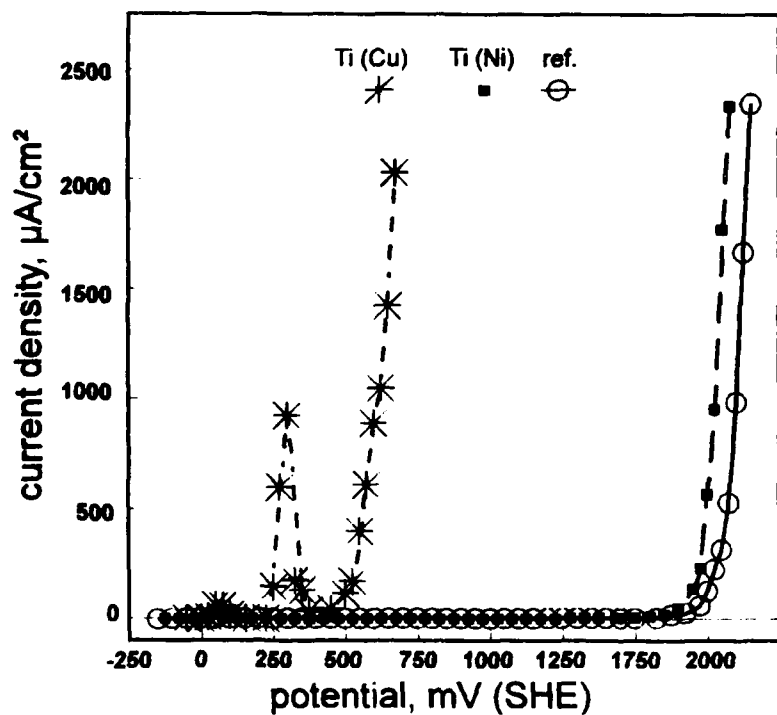

Figure 3: Quasisteady-state current density versus potential curves on surface welded titanium claddings and reference material in 150 g/l NaCl, pH value: 3, T: 70 °C, ΔU: +25 mV, holding time: 10 min
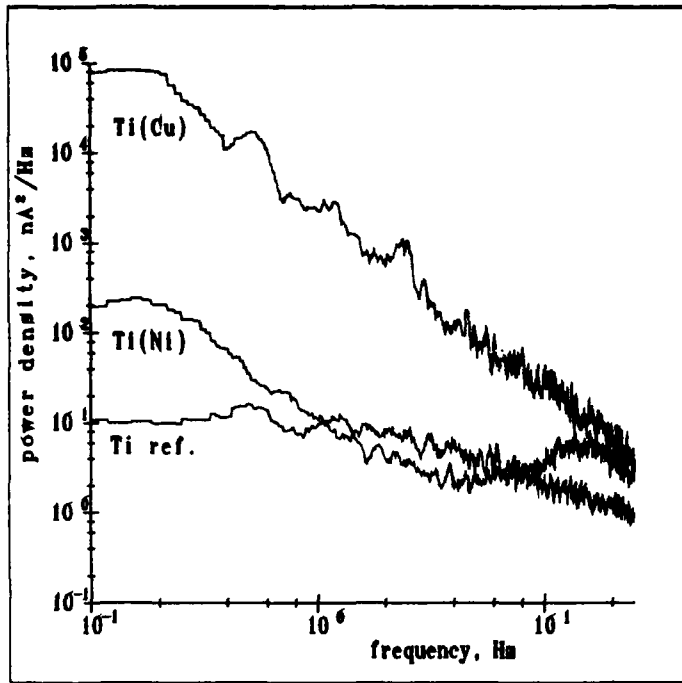
Figure 4: Power density spectrum for current noise on titanium alloys in 150 g/l NaCl, pH value: 3, T: 70 °C, measuring area: 1 cm² (polished to 20 μm grain size), U_{SHE}: +350 mV
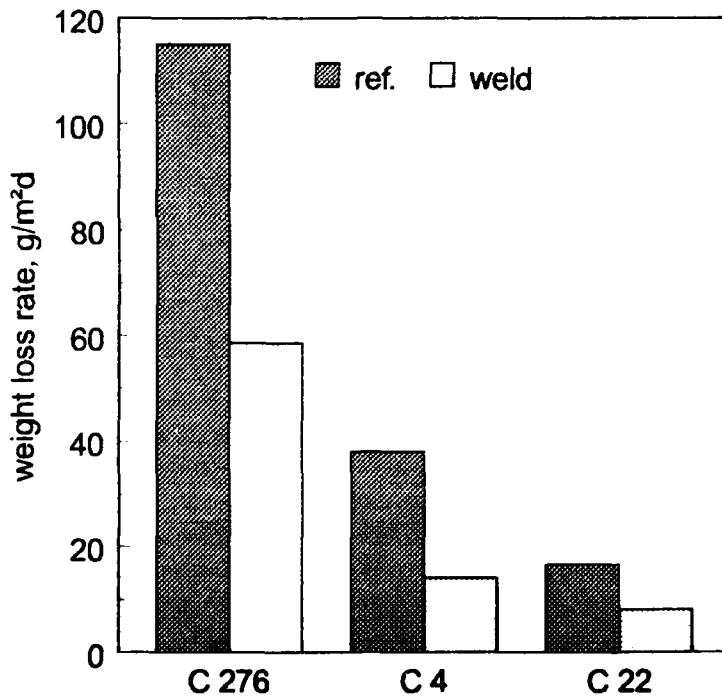

Figure 5: Corrosion rate for various nickel-based alloys (rolled material: reference; surface welded cladding: weld) from the Streicher test (SEP 1877/II, modified after [X1])
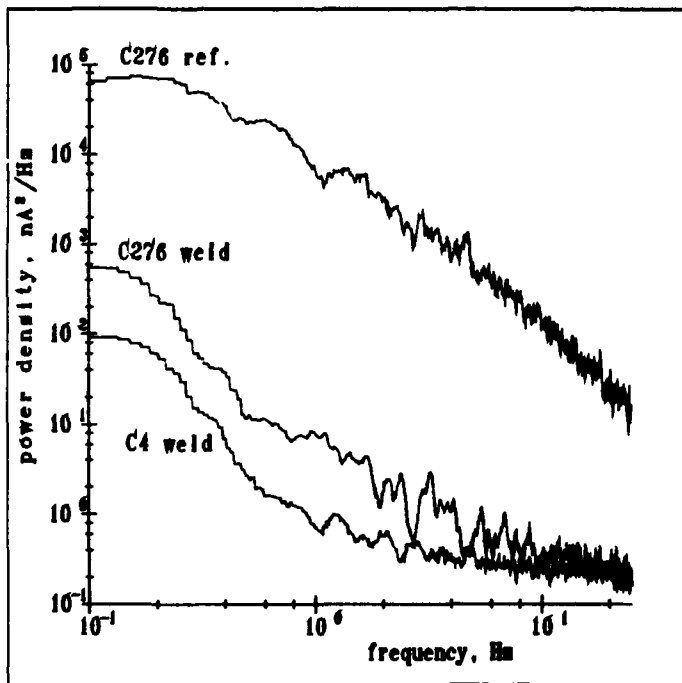
Figure 6: Power density spectrum for current noise on nickel alloys in 150 g/l NaCl, pH value: 3, T: 70 °C, measuring area: 0.25 cm² (polished to 20 μm grain size), U_{SHE}: +900 mV

Some More About Electrochemical Tests to be Performed on the Field as Non-Destructive Quality Control Inspection

Michel Verneau
Creusot-Loire Industrie
Centre de Recherche des Matériaux
56 rue Clémenceau
71200 Le Creusot France

François Dupoiron
Creusot-Loire Industrie
Centre de Recherche des Matériaux
56 rue Clémenceau
71200 Le Creusot France

Jacques Charles
Creusot-Loire Industrie
56 rue Clémenceau
71200 Le Creusot France

Abstract

The fabrication of stainless steels plates must be controlled, in order that the products have the required corrosion resistance properties. Moreover, in service, periodical quality control inspection is mandatory for many chemical process apparatus. The quality of the surface of stainless steels is primordial for their corrosion resistance and therefore, it must be maintained during all their service life.

The aim of these inspections is to control that no damage has occured, which could weaken the corrosion and mechanical properties of the materials. This paper presents recent advances in the use of an electrochemical technique to determine the degree of sensitization of stainless steels and alloys. The results are very promising, since the method looks rapid, sensitive and reliable. The development of on-site measurements will be discussed.

Key terms : intergranular corrosion, stainless steels, sensitization, on-site technique, electrochemical test, non-destructive test.

Introduction

The corrosion resistance of stainless steels depends on their ability to build a uniform protective passive film against the corrosive medium. However, many phenomena may weaken this passivity : The presence of impurities or precipitations in the materials, which may occur during all the process of fabrication of the products, or while assembling apparatus, can favour

selective attack, since the surface and the passive film will be modified. Stainless steels need to be solution annealed and quenched in order to put in solution all the different precipitates and to homogenize their structure. If stainless steels are associated with carbon steel, the post-welding heat treatment of carbon steel must be carefully determined. If badly chosen, this latter treatment can favour precipitations in the material. This partial or full sensitization will increase the risk of intergranular corrosion (figure 1). The same phenomenon can be encountered in service, when an exceptional increase of the temperature occurs, due to a drift in the chemical process. When it happens, an inspection of the apparatus is necessary to determine the influence of this technical hitch on the security of the installation.

Welding operations induce a thermal effect near the weld metal. Therefore, the heat affected zone can present a lower corrosion resistance than the base metal, due to carbide or phase precipitations and chromium depleted areas around the precipitates (figure 2). Today, it is very difficult to control the welding effect on the sensitization of the materials, since the method must be non-destructive, and most of the equipments are often built according to the "know-how" of the constructor. The problem is the same when repairs are made on an in-service apparatus : The possibility of control of the sensitization that is induced would be appreciated.

Pickling is necessary after heat treatments or welding operations on stainless steels, in order to remove the oxides and underlying chromium depleted layer, and to clean their surface. Indeed, chromium bearing oxides that have been formed on the surface of the steel during the thermal cycle need to be removed, in order to decrease the risks of corrosion that they could induce. The chromium depleted areas, generated by superficial oxides, may be the source of localized or intergranular corrosion (figure 3). For this reason, they also need to be removed.

I.   Intergranular Corrosion Tests

The most usual intergranular corrosion tests are the ASTM Standard Practices for Detecting Susceptibility to Intergranular Attack in Austenitic Stainless Steels (A262, practices A to F). However, these techniques present many deficiencies, particularly when one wants to use them on assembled apparatus :

- All of them are destructive methods : they require to cut a sample off the material, before carrying the test out.
- Except practice A, the duration of the tests is between 4 hours and 240 hours of immersion. Moreover, the time of preparation of the samples (i.e. machining and polishing) must be added to this time of immersion.
- Lastly, these methods do not precisely quantify the degree of sensitization of the steels. Some of them are even purely qualitative.

These different lacks explain why another method has been required to qualify the susceptibility of stainless steels to intergranular corrosion, and the surface condition of these materials. Today, users cannot easily measure the real state of their apparatus, either when they receive it, or when they have repaired it. Most of the time, the only information that they have is the performance of the materials before assembling, which cannot be checked later. The

welding operations particularly require to be very cautious, and a non-destructive method would be appreciable to verify the result of that work. Systematic controls after assembling on representative areas of the welded joints would probably avoid many corrosion problems in service.

In conclusion, the main qualities that would be required for a better method of testing the susceptibility of stainless steels to intergranular corrosion would be :

1. non-destructive
2. test rapidity
3. reproducibility
4. accuracy
5. quantitative measurement.

II.   Electrochemical Potentio-kinetic Reactivation Test

Electrochemical methods have known a wide expansion during the recent past, and some techniques have been promoted to study the surface condition of stainless steels. This is particularly the case of the Electrochemical Potentiokinetic Reactivation (EPR) technique [1][2].

A.   The EPR test

Originally, the EPR method has been developed for the quantification of the susceptibility to intergranular corrosion of common austenitic stainless steels (AISI 304 or 304 L grades) [3][4]. The principle of the test is based on the reactivation curve of the material in an appropriate chemical solution.

For AISI 304 and 304L grades, the chemical solution that is generally used[2] is a mixture of sulfuric acid (H_2SO_4) and potassium thiocyanate (KSCN) : 0.5 M H_2SO_4 + 0.01 M KSCN.

KSCN acts as a depassivating chemical species which enhances the reactivation of the material. The temperature of the solution is maintained at 30° C. At the beginning of the test, the sample is maintained about 2 min at the free-corroding potential. Then, the potential is set in the passive area (+ 200 mV/SCE) for 2 min. The time of passivation must be controlled, in order that the method keeps reproducible. After that, the potential back scan begins, using a sweep rate of 6V/h. In the single-loop test, the potentiodynamic reactivation curve is drawn, from the passive potential, towards the rest potential of the steel (figure 4).

Precipitations in the material or localized chromium depletions generally induce a weakening of the passive film. This will appear on the reactivation curve as a high peak that means that the material has been sensitized. Conversely, no peak will appear for materials which are not sensitized, since the passive film is not attacked.

The total weight loss of the material is directly proportional to the intensity of the dissolution reaction, itself proportional to the quantity of Coulombs exchanged during the reaction (Faraday's law):

$$m/M = Q/nF \qquad (1)$$

where m = weight loss (g)
     M = atomic weight (g)
     Q = reactivation charge (C)
     n = valency of the metal
     F = Faraday's number (C)

Since this weight loss directly depends on the total surface of the chromium depleted areas, the area under the reactivation peak, which is proportional to the reactivation charge, is also proportional to the chromium depleted area. This means that the measurement of the total surface under the reactivation peak can quantify the sensitization of the stainless steel.

Softwares have been developed to calculate the integral of the peak, and the result is expressed in mC/cm^2. Waterquenched stainless steels, which do not have any phase or carbide precipitation, usually present a reactivation curve without any peak or with only a small loop. Conversely, sensitized materials will show high and wide reactivation peaks, that will depend on their degree of sensitization.

B.   Discussion on the EPR method

The EPR method can be applied to a wide range of stainless steels or alloys [5][6]. However, the parameters of the test must be calibrated for each material. Indeed, they directly depend on the corrosion resistance of the steels. This induces difficulties for the standardization of the parameters of the test.

For each grade of stainless steel, the following parameters have to be calibrated :

1.   The composition of the solution in H_2SO_4 and KSCN : H_2SO_4 concentration increases both the aggressivity and the sensitivity of the test. KSCN has basically a similar effect. Nevertheless, pits may be initiated on the steel when a high KSCN concentration is used. Therefore, the KSCN concentration will be limited to low values. Figure 5 presents the influence of H_2SO_4 concentration on the reactivation peak of a 23% Cr - 4% Ni sensitized stainless steel.

2.   The temperature of the solution : it activates the electrochemical reactions and weakens the corrosion resistance (figure 6). The use of high temperatures may induce pits on the materials, though the sensivity would be better. So, it is often necessary to limit the temperature of the test. Similar results have been previously obtained on 304 stainless steels [4].

3.   The surface condition of the steel : the effect of surface finish has been clearly observed on 304 stainless steels [4]. The reproductibility of the chemical and electrochemical reactions requires to know perfectly the conditions of surface at the beginning of the test. It is

recommended to use freshly polished specimens.

4. The passivation potential and the duration of the passivation : an optimum value for the passivation potential is near the pitting potential. In these conditions, the sensitivity of the test is almost the best, although it is sometimes difficult to avoid pits formation. Usually, the passive potential is maintained about 10 to 15 minutes. This time is sufficient for the construction of the passive film.

5. The potential scan rate : the sensitivity of the test decreases when the potential scan rate increases (figure 7). This explains why low scan rates are often used for the realization of the EPR test[4].

Two specimens are always necessary for the calibration of the test : one is sensitized, the other is free of any precipitation. The optimum parameters of the test are determined in order that the sensitized specimen presents the highest peak, while no peak is observed on the other one. Then, each lightly or highly sensitized sample will present a reactivation peak.

Finally, as soon as the test has been calibrated for a special steel, it becomes very easy to use and presents many advantages :

- Non destructive test : this is one of the major advantages of this electrochemical test that does not require to cut a sample off the material. Neither weight loss measurement, nor bending test is done. All the reactions are only surperficial. The test can be easily carried out on the material, in laboratory or directly on-site, with the use of a specific cell.

- Rapidity : for most of the steels, the duration of the test does not exceed two hours. This is a real advantage in comparison with the usual chemical tests which last from 4 to 240 hours.

- Reproductibility : the EPR test shows a very good reproductibility on stainless steels, provided that their structure is homogeneous, and that all the parameters of the test are carefully controlled[4]. This property has been verified on different steels, with different conditions of testing.

- Sensitivity : the sensitivity of the EPR test is very good, and after a fine calibration, one can observe the very beginning of sensitization on most of the steels. A quantitative measurement of the degree of sensitization of the materials can be obtained with a good precision. However, some authors have observed a saturation of the EPR test, that becomes insensitive when the measurements are greater than 10 C/cm^2 [4].

III.   Some Applications of the EPR Test

A.   Characterization of Pickling Operations :

The EPR method has been applied to 317 LN stainless steel plates, to determine the influence of the duration of pickling on their corrosion behaviour. The chemical analysis of such plates is given in Table 1. The test has been performed on hot rolled plates after a solution annealing heat treatment.

Table 2 presents the results obtained for different conditions of pickling in a solution containing hydrofluoric acid (HF) and nitric acid (HNO_3). The parameters of the EPR test have

been calibrated as follows :

H_2SO_4 concentration : 0.5 M
KSCN concentration : 0.01 M
Temperature : 30 °C
Scan rate : 6 V/h
Passivation potential : + 200 mV/SCE
Passivation time : 2 min.

For each temperature of pickling, the results indicate that the reactivation charge decreases when the duration of pickling is increased. An increase of the temperature of the pickling solution also results in decreasing the reactivation peak obtained with the EPR test (figure 8). These observations mean that the quality of pickling is improved both with a raise of temperature or a longer time of immersion. The surface condition of the specimens appears to be directly linked with the result of the EPR test which is in total agreement with micrographic examinations. High reactivation peaks indicate that pickling of the samples has not been sufficient to remove surface encrusted oxides. In such conditions, these chromium bearing oxides create chromium depleted zones around them, which are local preferential sites of attack in service. During the EPR test, they are severely corroded and the reactivation peak grows. In contrast, well pickled surfaces do not reactivate during the test.

Finally, the EPR test appears to be an easy and reliable method to characterize the quality of pickling operations.

B.   Measurement of the Degree of Sensitization on Inconel 600 Plates.

Recent work has been done on two Inconel 600 plates with different carbon levels, to determine the degree of sensitization after heat treatment. Two tests have been conducted : ASTM G28 A intergranular corrosion test, and EPR test. The results are presented on table 3. They clearly indicate a detrimental effect of high carbon content on the intergranular corrosion resistance of Inconel 600 : A sharp increase of the corrosion rate, the maximum penetration depth, and the reactivation peak is observed for the 0.066 %C containing alloy, compared with the 0.019 %C containing one.

The evolution of the EPR result looks directly correlated with that of the ASTM G28 test. In fact, an important advantage of the EPR test in this case is that the results only concern the real surface of the plate. Therefore, the reliability must be better. Conversely, ASTM G28 test takes into account the reverse face and the ends of the samples, which will never be immersed in-service.

The conclusion of this study is that EPR tests can easily supply the classical intergranular corrosion tests for some nickel-base alloys. The main advantages of this method could be the determination of the sensitization of the real surface of the material, since immersion tests are not always representative of the conditions of use.

IV.   On-Site Measurements Technique

The electrochemical potentiokinetic reactivation method does not require to remove a sample from the material. A specific electrochemical cell can be directly put on the surface of the steel to be tested, regardless of size. This constitutes an important advantage of the EPR test, compared with other intergranular corrosion practices.

Once calibrated, users can easily apply the test to evaluate the susceptibility of stainless steels plates or pipes to intergranular corrosion, or to detect eventual phase precipitation in their apparatus. The EPR method could advantageously supplant the classical corrosion tests (Strauss, Streicher,etc) in many cases, all the more so as they are almost ineffective for non-destructive quality control inspection. The rapidity of the test and its high sensitivity enhance the advantages of applying the method for such applications.

For example, the method could be used for periodical control of the quality of assembled vessels or apparatus, like :

1. Control of the sensitization after heat treatment or welding
2. Surface investigations with qualification of the pickling operations
3. Checking of the structural state after repairs.

Different equipments exist in this field of investigations. In practice, we have just conceived a portable equipment. Easy to use on site, this prototype consists of an electrochemical cell, with its three electrodes (working, reference and auxiliary), coupled with a portable computerized potentiostat. The cell is fixed on the steel that constitutes the working electrode. Many different positions are possible, due to some articulations. This will make easier the development of the cell to work either on plates or pipes, elbows, welds, etc. All shapes of metallic surfaces can be tested, provided that they are easily accessible with the cell. The computerized potentiostat drives the experiment, and records the data instantaneously. At the end of the experiment, all the data are stored, and the computer calculates the integral of the reactivation peak. The degree of sensitization of the steel investigated is thus known in a few minutes only, without any damage on the material.

V.   Conclusion

The paper has presented the development and some potential applications of an electrochemical method used to evaluate the degree of sensitization by phase or carbide precipitation of stainless steels and alloys. The main characteristics of the EPR test are its rapidity, its high sensitivity, its reliability and the possibility of use as a non-destructive test.

These different qualities are very important, as far as on-site quality control inspection is expected. Recently, a specific portable prototype has been conceived, to realize on-site measurements. A good correlation has been observed between the results of the test and the real

surface state of the materials. The development of the method should interest both fabricators and final users, since it will solve many problems and questions concerning the reliability of their materials, which could not be easily verified until now.

References :

1.   V.Cihal, "Advances in Potentiodynamic Reactivation Method," Use of special steels, alloys and new materials in chemical process industries, paper 17 (Lyon, France : Cercle d'Etudes des Métaux, 1991).
2.   W.L. Clarke, R.L. Cowan and W.L. Walker, Intergranular Corrosion of Stainless Alloys, ASTM STP 656, (Philadelphia, PA : American Society for Testing Materials, 1978), p. 99.
3.   A.P. Majidi and M.A. Streicher, Electrochemical Techniques for Corrosion Engineering, (Philadelphia, PA : National Association of Corrosion Engineers, 1985).
4.   A.P. Majidi and M.A. Streicher, Corrosion, 40 8 (1984) : p. 393.
5.   M. Verneau, J. Charles and C. Lojewski, "Technique de Contrôle In Situ de la Sensibilité à la Corrosion Intergranulaire d'Aciers Inoxydables et Alliages de Nickel", European Conference on Corrosion in Chemical and Parachemical Industries, (Lyon, France : Société de Chimie Industrielle, 1991).
6.   M. Verneau, J. Charles and C. Lojewski, Duplex Stainless Steels'91, (Beaune, France : Editions de Physique, 1991).

C	S	P	Si	Mn	Ni	Cr	Mo	N
0.016	0.001	0.024	0.362	1.756	13.75	18.24	3.41	0.13

Table 1 : Chemical composition of a 317 LN plate (w/o)

	Reactivation charge (mC/cm^2)		
Duration of pickling (min)	20 °C	40 °C	60 °C
0	1840	---	---
5	1763	800	26
10	---	52	0
15	575	10	0
20	93	3	0
25	---	0	0

Table 2 : Influence of the conditions of pickling
on the reactivation peak

Carbon content	Corrosion rate ASTM G28 A (mm/yr)	Integral of the reactivation peak (mC/cm^2)
0.066 %	5.58	16.1
0.019 %	3.69	9.9

Table 3 : Results of G28 A and EPR tests
on Inconel 600 plates
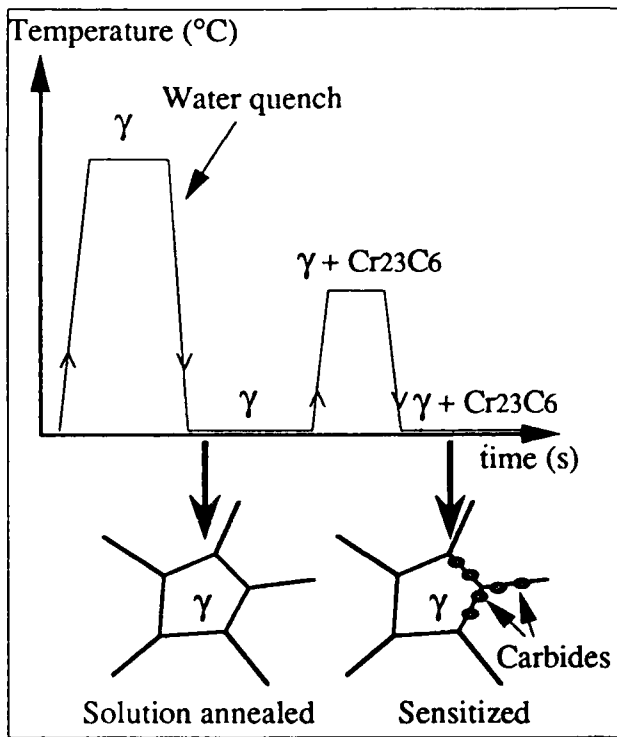
Figure 1 : Effect of heat treatment on the
sensitization of stainless steels
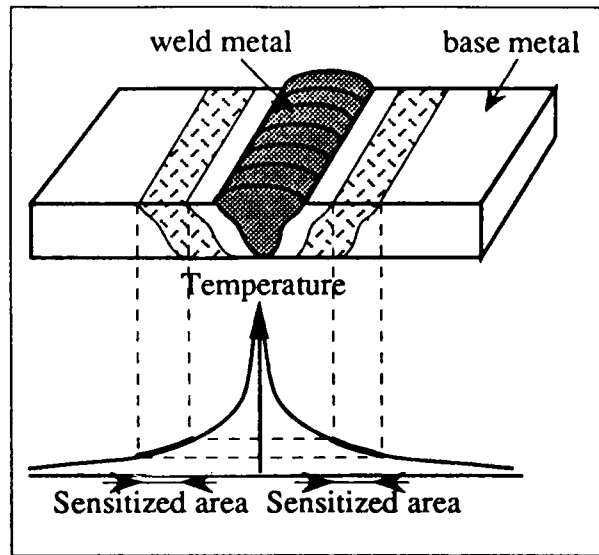
Figure 2 : Effect of welding on the
sensitization of stainless steels
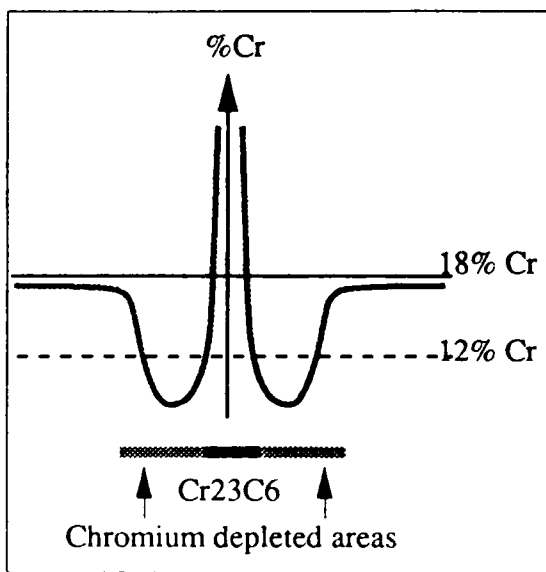
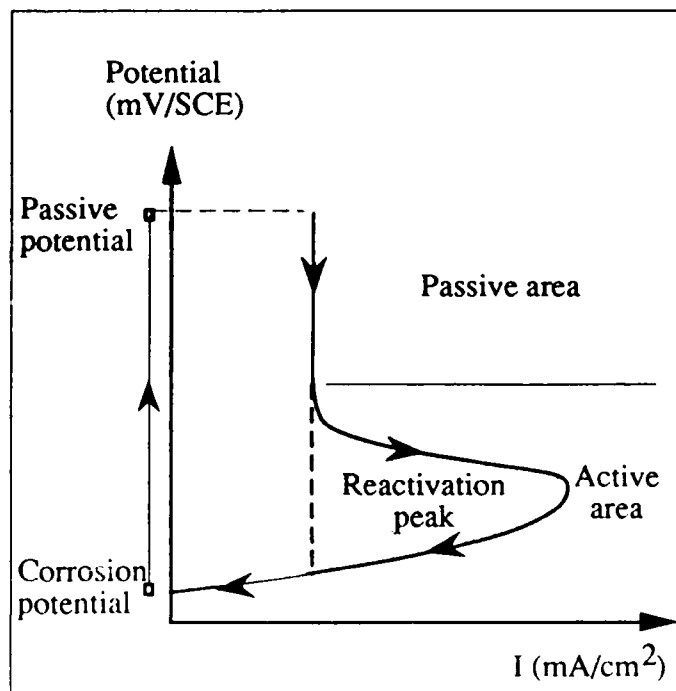Figure 3 : Intergranular corrosion
on Cr-depleted areas

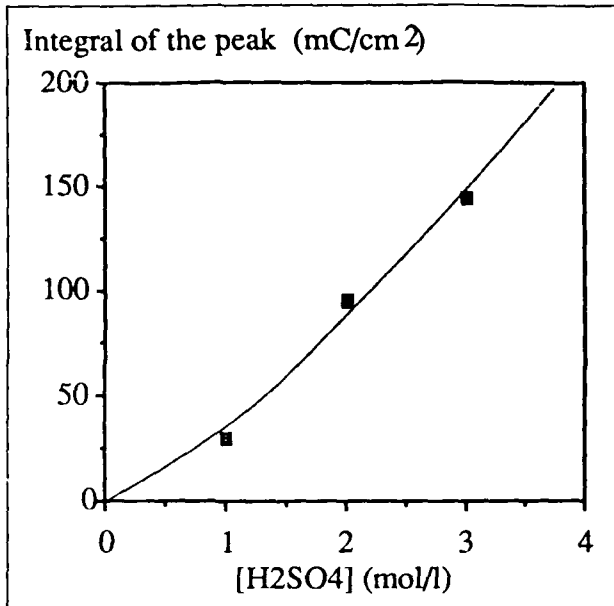Figure 4 : Reactivation curve on stainless steels

Figure 5 : Influence of the sulfuric acid concentration on the integral of the reactivation peak of a 23 %Cr-4 %Ni sensitized stainless steel
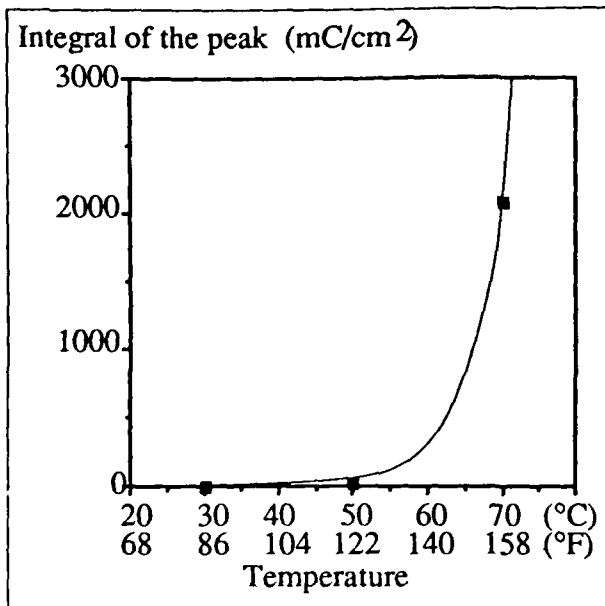

Figure 6 : Influence of the temperature on the integral of the reactivation peak of a 23 %Cr-4 %Ni sensitized stainless steel
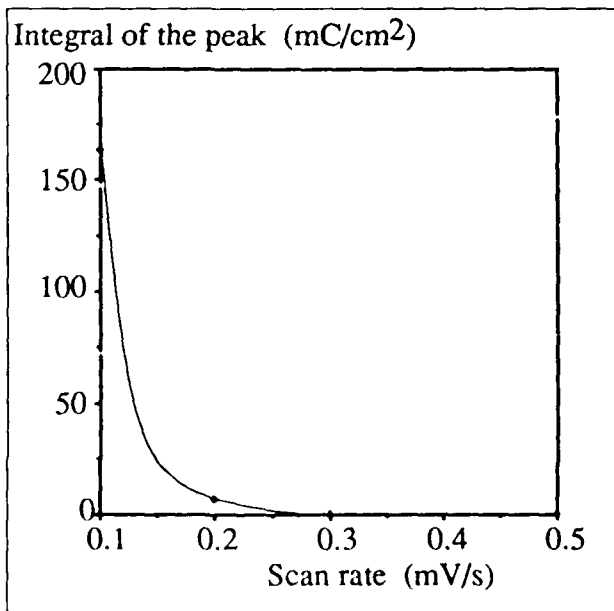

Figure 7 : Influence of the scan rate on the integral of the reactivation peak of a 23 %Cr-4 %Ni sensitized stainless steel
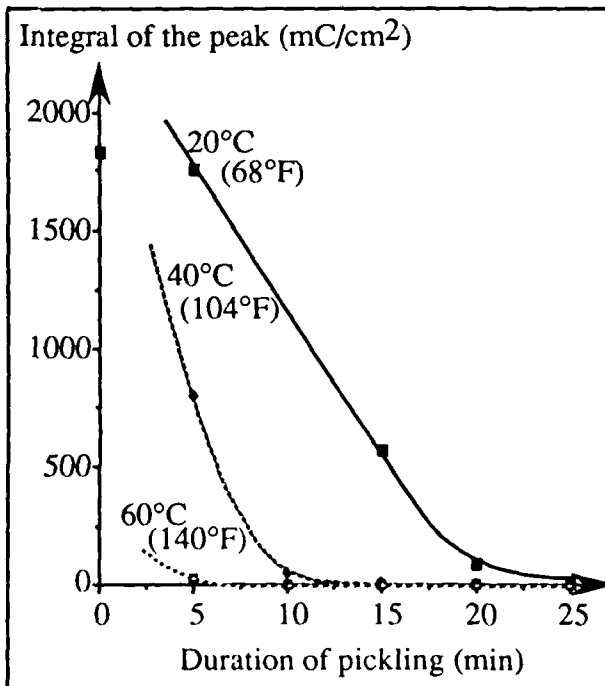

Figure 8 : Influence of the temperature and the duration of pickling on the integral of the reactivation peak of a 317LN stainless steel